Pierre Sagaut · Claude Cambon

Homogeneous Turbulence Dynamics

Second Edition

Springer

Homogeneous Turbulence Dynamics

Pierre Sagaut · Claude Cambon

Homogeneous Turbulence Dynamics

Second Edition

Springer

Pierre Sagaut
Laboratoire de Mécanique, Modélisation et Procédés Propres, UMR CNRS 7340, Ecole Centrale de Marseille
Aix-Marseille Université
Marseille
France

Claude Cambon
Laboratoire de Mécanique des Fluides et d'Acoustique, UMR CNRS 5509
Ecole Centrale de Lyon
Écully
France

ISBN 978-3-319-73161-2 ISBN 978-3-319-73162-9 (eBook)
https://doi.org/10.1007/978-3-319-73162-9

Library of Congress Control Number: 2017962025

Enlarged Second Edition

Printed on acid-free paper

This Springer imprint is published by Springer Nature
The registered company is Springer International Publishing AG
The registered company address is: Gewerbestrasse 11, 6330 Cham, Switzerland

To Pierre Nicolas and Solène
To Lydia

Foreword to Second Edition

This monograph by Pierre Sagaut and Claude Cambon, a revision of an earlier edition, is extraordinary in scope and audacious in outlook: It is not often that one encounters a coherent account of more than 900 pages on turbulence. I will not list the contents of the book or provide a detailed critique, but mention a few aspects that appeal to me.

The cliché that turbulence is the last unsolved problem of classical physics, repeated *ad nauseam* by everyone who wants to give a talk on the subject to non-specialist audience, or wishes to write for a general audience outside the subject, while being literally true, does considerable injustice to both the practitioners of the subject and the external audience. The statement at once diminishes the important work that has occurred and robs an outsider of the curiosity that she may otherwise have had for the subject. The authors make no claim that the problem has been solved (whatever that might mean, exactly) but present accurately the progress that has occurred in quantitative predictions of turbulence. This progress is based on combinations of theories and models, combining exact dynamical equations with sophisticated closure assumptions, supported by increasingly powerful experiments and numerical simulations. This book attempts to provide a synthesis of much of that work, which has taken place roughly since the 70s, providing a complement to A. S. Monin and A. M. Yaglom's well-known second volume. It does not touch, except very briefly, either the considerable work on modern scaling approaches, exemplified well, at the time it was written, by U. Frisch in his popular book of 1995, or present plots of engineering calculations justifying the pragmatic success of the authors' approaches; rather, it presents a philosophy of turbulence research covering a vast range of material that treads carefully from what G. K. Batchelor called analytical theories of turbulence to how such theories can be put to use in practical circumstances. The authors retain rigor where possible but do not shy away from ad hoc modeling where necessary—and they do this, in 18 chapters that are readable and comprehensive, for various classes of flows from homogeneous and isotropic turbulence to geophysical flows to quantum turbulence.

It is not that I agree with everything that the authors say, or that the selection of their material is perfect from my point of view, but what is admirable is the authors' ambition as well as the balance between skepticism and optimism that they display. Their philosophy is that, while a full understanding of turbulence is still lacking, the quantitative description has advanced to a phenomenal degree. Just consider numerical simulations. Many of us remember well the excitement created by S. A. Orszag's simulations of homogeneous and isotropic turbulence on a 32^3 box: now P. K. Yeung and collaborators have advanced it to cubes of $16{,}384^3$ grid points. Similar advances have occurred in Nagoya, Madrid and elsewhere, from passive scalars to wall-bounded flows. Experiments in a variety of flows have in recent years pushed the parameter space (such as the Reynolds number, Rayleigh number, rotation rates, etc) to incredible levels. All of this has enhanced our ability to query the flow characteristics immensely, but we need to create tools with which to query the data. That ability to query will clearly depend on the theoretical tools we develop, and on our willingness to reject the splintering of the field by creating silos that become so specialized as to be almost meaningless.

The authors themselves regard their book as an important medium for provoking "an honest and up-to-date survey of turbulence theory, with the special purpose of reconciling different angles of attack". I agree with this hope wholeheartedly and congratulate the authors on this book: I am sure it will undergo further modifications with time and will provoke more interesting work.

K. R. Sreenivasan
New York University
New York, USA

Preface to Second Edition

This book aims to build on an earlier edition, published under the same title by CUP, NY in 2008. As in that book, Chap. 2 presents the basic equations of fluid motion, in both Eulerian and Lagrangian forms, while Chap. 3 is an addition concerning compressible flows. These chapters provide a basis, subsequently used to rigorously derive the statistical-moment equations, in particular those of multi-point moments.

Roughly half the book treats statistically homogeneous turbulence rendered anisotropic by, e.g. uniform velocity gradients, density stratification or rotation. This framework encompasses a very wide class of models and theoretical analyses, from linear theory (which includes rapid distortion theory) to triadic closures, which allow for nonlinear interactions between Fourier components. As far as possible, we aim to provide a unified presentation in which weak turbulence, dominated by resonant interactions between dispersive waves (e.g. inertial, internal and gravity waves), gives way to strongly nonlinear interactions as the turbulent intensity increases. Strong turbulence involves modelling and we discuss many applications of the anisotropic EDQNM approach, while keeping in mind the less sophisticated RANS single-point models which remain the mainstay of industrial calculations.

Classical isotropic turbulence has not been neglected. Indeed, Chap. 4 reviews the state of the art in that area, while also making some connections with other subject areas, such as visco-elastic structural vibration (Chap. 5) and quantum turbulence (Chap. 6). These openings into other fields illustrate the power of the theoretical tools and concepts employed in this book, in particular the Lagrangian formalism. There are also paybacks from these other fields, e.g. the analogy between the equations of visco-elastic fluids and those of magneto-hydrodynamics.

Chapter 10, originally devoted to turbulence in stably stratified flow, now includes a review of more recent work on unstable stratification and mixing layers due to Rayleigh/Taylor instability. Among other things, these studies, which have parallels in geo- and astrophysics, extend the classical homogeneous approach by allowing for forcing of the mean flow by non-uniformities of the Reynolds stresses. Chapter 11, which concerns the effects of rotation, stratification and shear, has been augmented by applications to accretion disks, and, more notably, models of transient

growth and transition. The new Chap. 12 concerns magneto-hydrodynamic turbulence, of particular interest in astrophysics and possible fusion reactors, and focuses on Alfvén waves and anisotropic Ohmic dissipation.

Chapters 13–16 concern compressible flows, their modelling and DNS, in particular Chap. 13, whose subject is isotropic compressible turbulence, while Chap. 14 discusses combined effects of shear and compressibility and Chaps. 15 and 16 shock-turbulence interactions.

The final two chapters allow for the increased scope of the new book and aim to provide an improved overview of the theoretical principles and models which form its centre of gravity. Chapter 17 focuses more on technical aspects (e.g. detailed equations and numerical techniques), whereas Chap. 18 provides an overall conclusion.

We would like to warmly acknowledge all very nice colleagues who helped us in writing this book by providing us figures and also for rich and fruitful discussions about the content of the book: Antoine Briard, Alexandre Delache, Diego Donzis, Gabriel Farag, Benjamin Favier, Boris Galperin, Fabien Godeferd, Benoit-Joseph Gréa, Jérôme Griffond, César Huete, Danaila Luminita, Raffaele Marino, Marcello Meldi, Vincent Mons, Jim Riley, Abdelaziz Salhi, Julian Scott, Gustavo Wouchuk, with special and warm thanks for Katepalli Sreenivasan for writing a wonderful foreword for this book.

Marseille, France
Lyon, France
September 2017

Pierre Sagaut
Claude Cambon

Contents

Abstract

This book provides state-of-the-art results and theories in homogeneous turbulence, including anisotropy and compressibility effects with extension to quantum turbulence, magneto-hydrodynamic turbulence and turbulence in non-Newtonian fluids. Each chapter is devoted to a given type of interaction (strain, rotation, shear, etc.), and presents and compares experimental data, numerical results, analysis of the Reynolds stress budget equations and advanced multipoint spectral theories. The role of both linear and non-linear mechanisms is emphasized. The link between the statistical properties and the dynamics of coherent structures is also addressed. Despite its restriction to homogeneous turbulence, the book is of interest to all people working in turbulence, since the basic physical mechanisms which are present in all turbulent flows are explained. The reader will find a unified presentation of the results and a clear presentation of existing controversies. Special attention is given to bridge the results obtained in different research communities. Mathematical tools and advanced physical models are detailed in dedicated chapters.

Chapter 1
Introduction

1.1 Scope of the Book

Turbulence is well known to be one of the most complex and exciting field of research, which raises many theoretical issues and which is a key feature in a large number of application fields, ranging from engineering to geophysics and astrophysics. It is still a dominant research topic in fluid mechanics, and several conceptual tools developed within the framework of turbulence analysis have been applied in other fields dealing with non-linear, chaotic phenomena (e.g.: non-linear optics, non-linear acoustics, econophysics ...).

Despite more than a century of work and a number of important insights, a complete understanding of turbulence remains elusive, as witnessed by the lack of fully satisfactory theories of such basic aspects as transition and the Kolmogorov $k^{-5/3}$ spectrum. Nevertheless, quantitative predictions of turbulence have developed. They are often based on theories and models which combine *exact* dynamical equations and closure assumptions, and are supported by physical and —more and more— numerical experiments.

Homogeneous turbulence remains a timely subject, even half a century after the publication of Batchelor's book (Batchelor 1953) in 1953, and this framework is pivotal in the present book. Isotropic homogeneous turbulence (HIT) is the best known canonical case; it is very well documented — even if not completely understood— from experiments/simple models to recent $12,288^3$ full Direct Numerical Simulation (DNS) (Ishihara et al. 2016). Of course, this case is addressed (in Chap. 4) but more generally emphasis is put on Homogeneous Anisotropic Turbulence (HAT) in the presence of mean (velocity, temperature ...) gradients and/or body forces. This context is illustrated by several physical and numerical experiments (the latter being easy to perform by slightly modifying pseudo-spectral numerical methods designed for DNS of isotropic turbulence following the method introduced by Rogallo in the late 1970s), but its interest to develop fundamental understanding and to improve theories/models is largely underestimated, regarding the existing literature. Depending on the strength of the distortion (by mean gradients and/or body forces) and its time

P. Sagaut and C. Cambon, *Homogeneous Turbulence Dynamics*,
https://doi.org/10.1007/978-3-319-73162-9_1

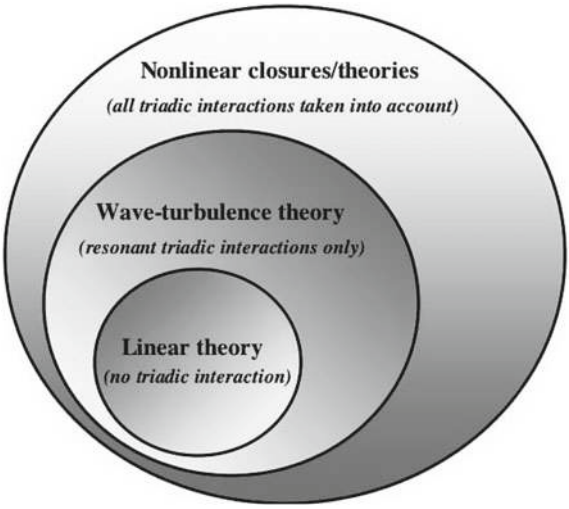

Fig. 1.1 Sketch of the hierarchy of embedded turbulence theories and closures

of application, it is possible to move from pure linear approaches, such as the *Rapid Distortion Theory* (RDT), to fully nonlinear statistical theories, with the important intermediate step of 'weak' turbulence theories, such as the *wave-turbulence theory*. As far as possible, it is proposed to pass from 'weak' to 'strong' turbulence by following a strict hierarchy of embedded models/theories, which is illustrated in Fig. 1.1.

This strategy was introduced by the second author in its contribution to the book *Theories of turbulence* (Oberlack and Busse 2002). Even if the most original part of the present book deals with two-point statistics, the Reynolds stress budget is very informative and therefore Reynolds stress equations are discussed before addressing more complex approaches. Limits or failure of single-point closures are enlighted in each case.

A discussion of the physical relevance of the HAT cannot be eluded, and we show that homogeneous turbulence in the presence of space-uniform mean gradients is not so ideal and restrictive. In addition to physical and numerical experiments which are capable of reproducing HAT, some typical equations (e.g. Townsend or Craya equations) are shown to remain relevant for analysing flows with non-uniform mean gradients (e.g. short-wave stability analyses, WKB Rapid Distortion theory). In some cases, pedagogical explanations for "purely" homogeneous turbulence can be extended towards inhomogeneous turbulence (e.g. near wall turbulent shear flow). Another important point is that homogeneous sheared turbulence exhibits self-sustained cycles, which are very a key features of turbulence dynamics in near-wall regions.

A large number of books devoted to turbulence are available, which put the emphasis on three aspects: statistical properties of isotropic, incompressible turbulence (e.g. Batchelor 1953; Frisch 1995; Tsinober 2009; McComb 1992, 2014), description of global dynamics and statistical properties of some academic flows (boundary layer,

mixing layer, jet, wake, ... e.g. Townsend 1976; Smits and Dussauge 2006) and modeling of turbulent motion for engineering purpose (among other Durbin and Petersson Reif 2001; Wilcox 2004; Sagaut 2005; Sagaut et al. 2013). Only little information on the *dynamics* of turbulent scales is usually provided, and most authors put the emphasis on a particular feature. One should of course mention general purpose textbooks (see Pope 2000; Tennekes and Lumley 1994; Bailly and Comte-Bellot 2003), which provide the reader with a general survey of different issues related to turbulence research. Therefore, recent results dealing with dynamics of turbulent motion obtained from direct numerical simulations, advanced statistical models (linear theories and models, nonlinear triadic closures, ...) and experiments are not available to the reader in a single book. Results are disseminated among a huge number of journal articles, technical reports and conference papers that do not always use the same terminology.

The present book aims at providing a state-of-the-art sum of results and theories dealing with homogeneous turbulence, including anisotropic effects and compressibility effects. The underlying idea is to gather most recent results dealing with dynamics of homogeneous turbulence when it interacts with external forcing (strain, rotation, ...) and when compressibility effects are at play. Each chapter will be devoted to a given type of interactions, and will present and compare experimental data, DNS/LES results, analysis of the Reynolds stress budget equations and advanced linear and nonlinear theoretical models. The role of both linear and non-linear mechanisms are emphasized. The link between the statistical properties and the dynamics of coherent structures is also addressed. Despite it is restricted to homogeneous turbulence, the book will be of interest to all people involved in turbulence studies, since it will enlight basic physical mechanisms which are present in all turbulent flows.

Another interest of the book is the possibility for the reader to find a unified presentation of the results, and also a clear presentation of existing controversies and lacks in the theoretical background. A special attention is paid to bridging between the results obtained in different research communities. This last point is developed concerning both results dealing with turbulence dynamics and the tools used to investigate it.

1.2 Structure and Contents of the Second Edition of the Book

As in the first edition of the book, the presentation of the results is carried out in such a way that it allows for two levels of reading: a first level for readers interested in the results but who do not want to enter the details of the tools (i.e. linear and nonlinear theoretical models) employed to get them, and a second level for readers interested in these details. The Chap. 2 has been enlarged and now incorporates more elements that result from rigorous, not to say "exact", equations of conservation in both Eulerian and Lagrangian formalisms, along with their optimal treatment. This

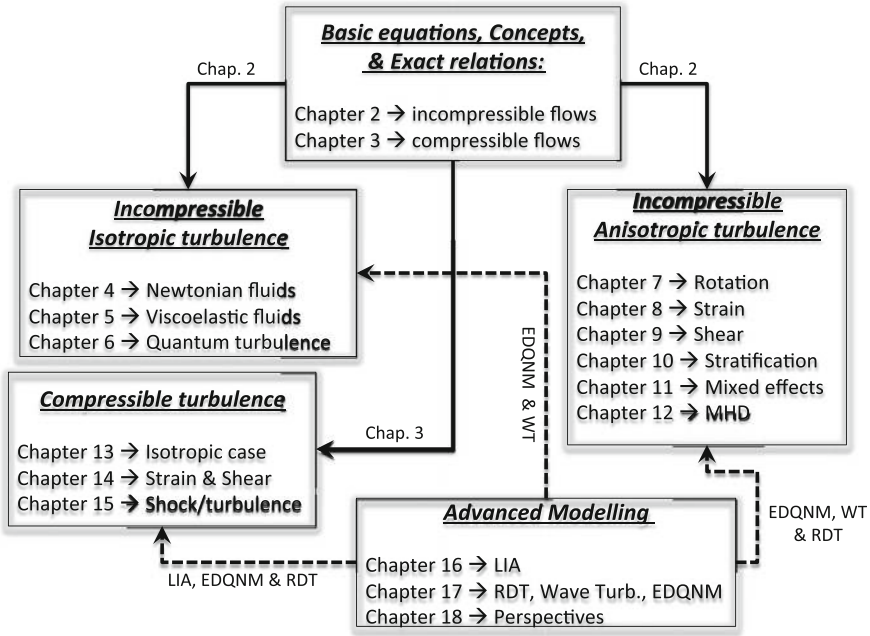

Fig. 1.2 Organization of the book

involves an enhanced use of the Lagrangian formalism and direct use of Green's tensors for solutions of equations, from basic Navier–Stokes-type equations for the fluctuating field to three-point third-order statistical equations. Accordingly, some modeling approaches, ranging from the modeling of the pressure Hessian in the equation for the perceived velocity gradient, to the application of main nonlinear closures, appear as byproducts of rigorous Green-function-based equations. More background for compressibility effects have been also added in this chapter. The most specific aspects of compressibility, from this viewpoint, are put in the new complementary Chap. 3.

The book is now organized in 18 chapters (see Fig. 1.2), with turbulent flow cases ranging from homogeneous isotropic turbulence (without distortion in Chap. 4, along with new chapters dealing with non-Newtonian effects, see Chap. 5, and Quantum Turbulence in superfluids and Bose-Einstein condensates, see Chap. 6) to HAT subjected to various distorting processes (rotation, strain, shear, stratification, and now Magnetohydrodynamics (MHD) in Chaps. 7–12. Flows subjected to coupled forcing effects are gathered in Chap. 11 and in the new Chap. 12 on Magnetohydrodynamic turbulence, whereas compressible turbulence is addressed in Chaps. 13–16.

The mathematical details of Linear Interaction Theory for shock/turbulence interaction are presented in Chap. 16, with extension to mixture of perfect gas, detonation waves and rarefaction waves.

Constraints for ensuring consistency of statistical homogeneity — for turbulence — with the distorting processes are given in the most general way, for both incompressible (particularly in Chaps. 2 and 8) and compressible flows (Chap. 14). The physical relevance of this framework is also discussed, especially for the analysis of both explicit and implicit effects of compressibility on turbulent shear flows.

The essentials of linear and nonlinear theories and models for incompressible anisotropic turbulence are now gathered in Chap. 17, that replaces Chaps. 13 and 14 in the former edition. Finally, our concluding comments are presented in Chap. 18.

Every typical flow case is revisited under different angles of attack, from observations/simulations, models, to theories, combining dynamical, statistical and structural aspects, as follows:

(i) Observations, physical and numerical experiments
(ii) Analysis through *Reynolds Stress Tensor* (RST) equations, balance and coupling terms
(iii) Refined analysis using linear theory
(iv) Refined analyses through full nonlinear theories and models for two-point statistics (if available)
(v) Phenomenological (and possibly dynamical) approach to structures, evolution, coupling

It is worth noting that two classes of flows are discussed in the book. The first one is the class of flows without turbulence production mechanism (e.g. decaying isotropic turbulence, rotating homogeneous turbulence, stably stratified homogeneous turbulence, ...) and flows with turbulent kinetic energy production mechanism (e.g. homogeneous sheared turbulence, new case of unstably stratified turbulence). In the former case, nonlinear dynamics and its modification by the mean flow effects are the sole features of the flow, while in the later case linear mechanisms are the main dynamical characteristic features. Therefore, nonlinear models will be privileged tools in the first case (but eigenfunctions of the linear theories can provide optimal basis to write them), while they will be more briefly discussed in flows with production for which linear theories are very powerful.

The most complete illustration of the hierarchy of embedded models in each other is the case of pure rotation (Chap. 7). Common models, such as RST closure models, are shown to present definite flaws in this case, and some limited attempts to improve single-point closure techniques are only briefly reviewed. As an important related point, linear theories such as the Rapid Distortion Theory have almost been reviewed for irrotational mean flows only in other recent monographs about turbulence (e.g. Pope 2000; Durbin and Petersson Reif 2001), with the only exception of pure shear in the book of Townsend (1976), written long time ago. In contrast, linear theory for HAT subjected to more general rotational mean flows is a very important part of the present book. In addition, our extended linear theory is a building block which may be useful for a wider community (*e.g.* the elliptical flow instability from the viewpoint of stability analysis, the rotating and/or stratified shear flow, in Chap. 11). The domain of application of RDT has evolved during the last one or two decades,

and this change is discussed in depth in the present edition of the book, especially in Chap. 11. The linear spectral theory, that underlies RDT, is now almost forgotten in the Engineering community that used it for calibrating some constants in statistical models for Reynolds-Averaged Navier–Stokes equations, e.g. in modeling "rapid" pressure-strain rate tensors. In turn, it is increasingly used in geophysics and astrophysics, taking advantage of the possibility to recovering non-modal stability analysis and thereby to predict explosive transient growth and bypass transition to turbulence. Applications to the stability and transition to accretion discs are provided.

The domain of application of two-point nonlinear closures is even more restricted in existing monographs (e.g. Monin and Yaglom 1975; Leslie 1973; Lesieur 1997; Frisch 1995; McComb 1992, 2014). Only isotropic turbulence is treated in a straightforward way, and only few attempts to deal with small anisotropy are offered, whereas the linkage to linear models and wave-turbulence is ignored. The effort to integrate and reconcile a holistic spectral approach from "RDT" to fully nonlinear triadic closures has been further developed in the present second edition. About wave turbulence theory, there is a wealth of recent studies, but much more devoted to vibrating plates and surface waves than for 3D turbulence modified by internal waves (e.g. inertial waves, gravity waves, Alfvén waves, and combination of them). In addition, the very old terminology, that is used in most of these studies, often masks the asymptotic quasi-normal markovian character of the basic theory. This point is addressed in Chaps. 7 and 12.

The last item about "structures" deserves some clarification. On the one hand, it is recognized that typical structures can be evidenced in snapshots, or random realizations, of statistically homogeneous flows. The first example is the occurence of vortex tubes in isotropic turbulence. Other well-known structures are streak-like structures (in shear flows), cigar-like (in flows with dominant rotation) or pancake-like (in flows with dominant stable stratification) structures. On the other hand, the relevance of low-order statistics to identify and quantify these structures is controversial. Second order statistics, if they include fully anisotropic two-point correlations, can give a real insight into these structures, with quantitative informations such as elongation parameters and aspect ratios. It is sometimes objected that phase coherence is lost in homogeneous statistics. This is true only for single-time second-order correlations. Linear operators identified in spectral linear theory affect any realization of the fluctuating field. If this anisotropic effect is not directly reflected in second-order statistics — as in the cases without production — it appears on three-point third-order correlations, where phase information is recovered. The sketch displayed in Fig. 1.3 illustrates how the distribution in Fourier space, via angle-dependent spectra, underlies the presence of anisotropic structures, in several flow cases of shear-driven or buoyancy-driven turbulence.

It is worthwhile to stress that our detailed anisotropic description includes *dimensionality*, with a possibility to quantify the transition between 3D state to either a 2D or a 1D state. For instance, the structure-based modelling by Kassinos and Reynolds, which allows to distinguish between dimensionality and componentality, becomes a by-product of our general description, at least for homogeneous turbulence.

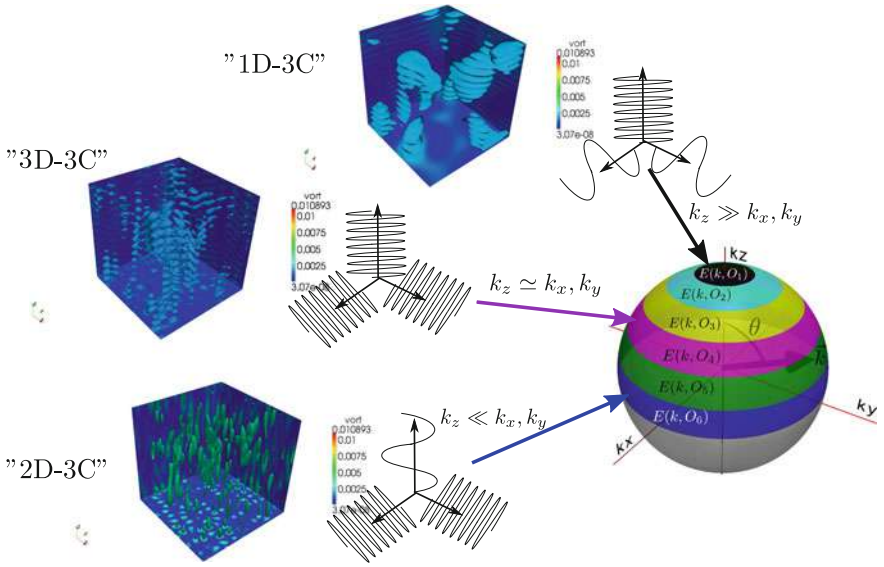

Fig. 1.3 Sketch of the linkage of angle-dependent spectral distribution to anisotropic structures. Anisotropy affects both dimensionality and componentiality, or, as illustrated in the whole book, directional anisotropy and polarization anisotropy. Courtesy from Alexandre Delache

The advanced models and theories selected here systematically incorporate dynamical operators which are really based on Navier–Stokes equations, even if they deal with "weak" turbulence only (e.g. linearized models, wave-turbulence), not to mention exact triadic equations and conventional two-point closures based on them. 3D Fourier space is an unavoidable tool in HAT analysis; it is first considered here as a mathematical convenience to account for solenoidal properties (in isovolume turbulence) and to simplify related *modal decompositions*. A special use is made of a decomposition of the fluctuating velocity in Fourier space, often referred to as the Craya–Herring decomposition, which amounts to a general Helmholtz decomposition, in terms of two solenoidal (toroidal–poloidal type), or vortical, modes and one dilatational (or divergent) mode. In incompressible turbulence, the Poisson equation for the pressure fluctuation is immediately recovered by projecting momentum equations onto the dilatational mode, the dilatational velocity mode being zero, so that dynamical equations only deal with the two solenoidal modes. This decomposition readily generates the helical mode decomposition, and various "vortex-wave" decompositions when a buoyancy fluctuation is accounted for (see Chaps. 10–12). The dilatational mode recovers its dynamic role, together with the pressure mode, when compressibility is introduced. The increase of the complexity of the system can be presented as follows:

(i) Two mode-turbulence, in which the two independent unknowns are $u^{(1)}, u^{(2)}$ using the toroidal-poloidal decomposition, or $u^{(2)} \pm \imath u^{(1)}$ considering the helical

mode variant. The dilatational mode $u^{(3)}$ is strictly zero so that the pressure mode $u^{(4)}$ is completely enslaved to the two solenoidal ones, and therefore removed from consideration (Chaps. 4–12).

(ii) Three mode-turbulence. Same situation as before, but an additional buoyancy term is incorporated as a pseudo-dilatational mode. The physical problem with 5 components (3 for velocity fluctuations, one for pressure fluctuations, one for buoyancy fluctuations) is turned into a three-mode one thanks to the Boussinesq approximation (divergence-free velocity field and related Poisson equation for pressure holds again, even if the buoyancy term can fluctuate). This case is met in Chaps. 10 and 11.

(iii) Four-mode-turbulence $u^{(1)}, ..., u^{(4)}$, as in the quasi-isentropic flow cases addressed in Chaps. 13 and 14. If the acoustic equilibrium hypothesis holds, $u^{(3)}$ and $u^{(4)}$ can be combined like $(u^{(4)} \pm \imath u^{(3)})$, $u^{(3)}$ corresponding to the kinetic energy of acoustic waves, and $u^{(4)}$ giving their potential counterpart, respectively.

In this rapid survey, the exact definition of the modes denoted as "toroidal", "poloidal", "divergent" and "pressure" is not mandatory. They will be identified later on, with $u^{(1)}, u^{(2)}, u^{(3)}$ being the three components of the Fourier mode of the fluctuating velocity in the Craya–Herring frame, and $u^{(4)}$ being the Fourier mode of the pressure fluctuation, scaled as a velocity. In buoyant flows affected by mean stratification, within the Boussinesq approximation, the component $u^{(3)}$ characterizes the fluctuating buoyancy term, again scaled as a velocity. In the case of incompressible Magnetohydrodynamic turbulence, both solenoidal velocity field $\boldsymbol{u}$ and magnetic field $\boldsymbol{b}$ amount to 4 modes, say $u^{(1)}, u^{(2)}, b^{(1)}, b^{(2)}$, with possible linear recombination under helical modes and/or Elsaesser ones. What happens if full compressibility is considered? Instead of considering a possible fifth mode, identified as the entropy mode, we prefer to keep the principle of a four-modes decomposition, but consider their further decomposition according to small parameter(s), related to the Mach number or/and a typical ratio such as the dilatational to the solenoidal dissipation rate. For instance, the Chu–Kovaznay decomposition, introduced in Chap. 3, amounts to a first-order decomposition, in which the "vortical mode" is only a part of the solenoidal mode generated by the full set $(u^{(1)}, u^{(2)})$, whereas the "entropic mode" only concerns the bulk dissipation related to them. The decomposition used for shock-turbulence interaction in Chaps. 15 and 16, and anticipated in the Chap. 3, is now better connected to the general four-mode decomposition (excluding MHD) used in the rest of the book. As a final remark, the difficulty of designing an optimal modal decomposition in fully compressible turbulence is also connected to the use of mass-weighted variables (velocity, momentum $\rho\boldsymbol{u}$, or intermediate mixed quantity $\rho^x\boldsymbol{u}$?). The problem is not solved in this book, anyway, but relevant discussions are displayed in the dedicated chapters.

We can say now what aspects are not addressed, or only incidentally, in this book, and what are emphasized, as follows:

(i) Theoretical stochastic models (as used by physicists to work on internal intermittency) are not generally considered in the present book except if explicitly

stated in dedicated sections, as in the end of Chap. 2, with Langevin models. Indeed, we favour models that retain dynamical aspects of basic Navier–Stokes-type equations. From this viewpoint, shell-models are briefly addressed in Chap. 12 when they incorporate helical modes. Other exceptions concern the "Kinematic Simulation", when exact linear operators (RDT-type) are incorporated in it (see Chap. 11). Shell-models mimic a simplified triadic interaction, between only three adjacent shells in Fourier space, but statistical moments of any order can be predicted from them in principle. On the other hand, second-order empirical (spherically averaged) shell-models exist. Because recent progresses were made, with the possibility to disentangle in them directional anisotropy and polarization anisotropy, their general linkage to rigorous expansions in terms of angular harmonics is discussed in Chap. 2 and results are presented in Chap. 8.

(ii) Phenomenological theories about scaling and (internal) intermittency, from the legacy of Kolmogorov, are touched upon but in a minimal way, since they retain very little from Navier–Stokes equations. Only the Kolmogorov equation for the third order structure function is partly based on Navier–Stokes-type equation, but its "exactness" depends on the Reynolds number, as revisited in Chap. 4. In addition, we consider as highly controversial the interpretation (Bohr et al. 1998; Frisch 1995) of "anomalous exponents"[1] departure from the original Kolmogorov (1941) theory (which leads to $\zeta_n = n/3$) as internal intermittency. Generally, the pure statistical description based on anomalous exponents, or ESS laws, mixes anisotropy, inhomogeneity and possible internal intermittency in an intricated way. More discussion is given, case by case, with a sum of arguments given in Chap. 18.

(iii) Statistical two-point "triadic" closures, the simplest one being EDQNM, are reconciled with linear models and wave-turbulence theory, and finally are shown to be still useful and relevant (especially with respect to the phenomenological theories quoted just before). Their limitation to low order moments precludes in principle the description of internal intermittency, but the three-point description of third-order moments gives much more information on cascades than a third-order structure function based on only two points. Low-order two-point (or more) moments are shown to be very informative: second-order moments for energy distribution, third-order moments for energy transfers (cascade), fourth-order ones for typical closure, especially in connection with associated dynamical equations. Higher-order moments, via n-structure functions and full probability density functions are very briefly discussed.

At last, results dealing with Lagrangian statistics and passive scalar transport are sparsely provided, but all the background exists in Chap. 2, and some applications are addressed, case by case. It is worthy to note that the case of "active" scalars, as the buoyancy in Chap. 10 cannot be disconnected from the simpler case of passive scalar.

[1] Often denoted ζ_n in the literature, n being the order of the structure function which is supposed to decay as $r^{-\zeta_n}$.

Let us go back to Chaps. 13–16, dealing with dynamics of compressible turbulence. This issue is almost absent in most previous books dealing with turbulence fundamentals. Chapter 13 is devoted to presentation of state-of-the-art knowledge about the dynamics of compressible isotropic turbulence. The Chu–Kovazsnay modal decomposition of the turbulent fluctuations introduced in Chap. 3, is extended to provide the reader with a physical insight into coupling between acoustics, entropy and vorticity. Then, the different regimes observed in numerical simulations and theoretical analyses are described: the pseudo-acoustic regime, the subsonic regime (both pseudo-acoustic and thermal régimes are considered) and the supersonic régime. In each case, details of the interactions and transfers among scales and modes are discussed and the link with the dynamics of coherent events (vortical structures, acoustic waves, shocklets, ...) is made. Some low-Mach triadic interaction theory results are included, together with simplified models. Chapter 14 presents the coupling of compressible turbulence with mean gradient effects. In this chapter, the emphasis is put on linear theory and DNS results since they are well suited to describe dominant dynamical mechanisms in such strongly anisotropic flows. The theory of compressible Rapid Distortion Theory is enlightened. Chapters 15 and 16 are dedicated to the shock/turbulence interaction, which has been proved to be very accurately predicted by the *Linear Interaction Approximation* (LIA) for a large class of flows. The LIA is presented in Chap. 16 in its most achieved version, and it is used to illustrate the physics of the interaction of a shock with different kinds of fluctuations corresponding to the Chu–Kovazsnay modes. The comparison with DNS and experimental results is also made. Despite it is restricted to simple flow configurations, the basic physical mechanisms emphasized in this part are the building blocks for the interpretation and understanding of the properties of compressible turbulent flows in complex configurations.

References

Bailly, C., Comte-Bellot, G., Turbulence, CNRS Editions (2003) (in french)
Batchelor, G.K.: The Theory Of Homogeneous Turbulence. Cambridge University Press, Cambridge (1953)
Bohr, T., Jensen, M.H., Paladin, G., Vulpiani, A.: Dynamical Systems Approach To Turbulence. Cambridge University Press, Cambridge (1998)
Davidson, P.A.: Turbulence. Oxford University Press, USA (2004)
Durbin, P.: Petersson Reif. Statistical Theory And Modeling For Turbulence Flow. Wiley & Sons, B.A. (2001)
Frisch, U.: Turbulence. Cambridge University Press, Cambridge (1995)
Ishihara, T., Morishita, K., Yokokawa, M., Uno, A., Kaneda, Y.: Energy spectrum in high-resolution direct numerical simulations of turbulence. Phys. Rev. Fluid. **1**, 082403 (R) (2016)
Kolmogorov, A.N.: The local structure of turbulence in incompressible viscous fluid for very large Reynolds number. C.R. Acad. Sci. USSR (Dokl. Akad. Nauk SSSR), **30**(4) (1941). English translation in Proc. Roy. Soc. Lond. A **434**, 9–13 (1991)
Lesieur, M.: Turbulence in Fluids, 3rd edn. Kluwer Academic Press, Dordrecht (1997)
Leslie, D.C.: Developments in the Theory Of Turbulence. Clarendon Press, Oxford (1973)

Mathieu, J., Scott, J.F.: Turbulent Flows: An Introduction. Cambridge University Press, Cambridge (2000)
McComb, W.D.: Homogeneous, Isotropic Turbulence: Phenomenology. Oxford Science Publication, Renormalization and Statistical closures (2014)
McComb, W.D.: The Physics of Fluid Turbulence. Oxford Science Publication (1992)
Monin, A.S., Yaglom, A.M.: Statistical fluid Mechanics, MIT Press, Cambridge (MA), 1971 (Vol. I), 1975 (Vol. II)
Oberlack, M., Busse F.H (eds.): Theories of Turbulence, CISM 442. Springer, Berlin (2002). (Chapter IV, p. 197–251, from Claude Cambon.)
Piquet, J.: Turbulent Flows - Models And Physics, 2nd revised printing. Springer, Berlin (2001)
Pope, S.B.: Turbulent flows. Cambridge University Press, Cambridge (2000)
Sagaut, P., Deck, S., Terracol, M.: Multiscale and Multiresolution Approaches In Turbulence, 2nd edn. Imperial College Press (2013)
Sagaut, P.: Large-Eddy Simulation For Incompressible Flows, 3rd edn. Springer, Berlin (2005)
Smits, A.J., Dussauge, J.P.: Turbulent Shear Layers In Supersonic Flows, 2nd edn. Springer, Berlin (2006)
Tennekes, H., Lumley, J.L.: A First Course In Turbulence. MIT Press, USA (1994)
Townsend, A.A.: The Structure Of Turbulent Shear Flow, 2nd edn. Cambridge University Press, Cambridge (1976)
Tsinober, A.: An Informal Conceptual Introduction To Turbulence: Second Edition Of An Informal Introduction To Turbulence. Springer, Berlin (2009)
Wilcox, D.C.: Turbulence Modeling For CFD, 2nd edn., DCW Industries (2004)

Chapter 2
Governing Equations, from Dynamics to Statistics

2.1 Background Deterministic Equations

2.1.1 Mass Conservation

The equation of mass conservation is well known and do not need long explanations to be derived. Both Eulerian and Lagrangian forms will be given below. The latter is less common in fluids dynamics but it deserves some attention, since it brings in some fundamental *Lagrangian* concepts and relationships.

Let us begin addressing the Eulerian description. To this end, we consider a fixed arbitrary control volume $\mathcal{V}$, delineated by a surface S. The total mass of the fluid is governed by the following integral balance equation

$$\underbrace{\frac{d}{dt}\iiint_{\mathcal{V}} \rho(\boldsymbol{x},t)d^3\boldsymbol{x}}_{variation} = \underbrace{-\iint_S \rho(\boldsymbol{x},t)\boldsymbol{u}(\boldsymbol{x},t)\cdot\boldsymbol{n}d\sigma}_{flux} + \underbrace{\iiint_{\mathcal{V}} m(\boldsymbol{x},t)d^3\boldsymbol{x}}_{production}. \tag{2.1}$$

in which ρ, $\boldsymbol{u}$ and m are the density, the velocity and the rate of mass production, respectively. All these fields are assumed to be continuous fields in terms of time t and Eulerian and Cartesian coordinates $\boldsymbol{x}$. In this equation, $d^3\boldsymbol{x}$ is the elementary volume of a fluid particle, $d\sigma$ is the elementary surface with outward normal and $\boldsymbol{n}$ the unit vector. The classical Ostrogradsky formula yields $\iint_S \rho\boldsymbol{u}\cdot\boldsymbol{n}d\sigma = \iiint_{\mathcal{V}} \nabla\cdot(\rho\boldsymbol{u})d^3\boldsymbol{x}$, so that the previous equation is rewritten as

$$\iiint_{\mathcal{V}} \left[\frac{\partial\rho}{\partial t} + \nabla\cdot(\rho\boldsymbol{u}) - m\right] d^3\boldsymbol{x}.$$

For the sake of clarity, the divergence of a vector $\boldsymbol{V}$ will be denoted $\nabla\cdot(\boldsymbol{V})$ or $\frac{\partial V_i}{\partial x_i}$ alternatively in the following. The classical local and instantaneous counterpart of the above equation is the continuity equation

P. Sagaut and C. Cambon, *Homogeneous Turbulence Dynamics*,
https://doi.org/10.1007/978-3-319-73162-9_2

$$\frac{\partial \rho}{\partial t} + \nabla \cdot (\rho \boldsymbol{u}) = m. \tag{2.2}$$

In the Lagrangian description, fluid particles follow trajectories, which are given by the relationship

$$x_i = x_i^L(\boldsymbol{X}, t, t_0) \tag{2.3}$$

which links the position of the fluid particle at time t to its initial position $\boldsymbol{X}$ at time t_0. The Lagrangian coordinates $\boldsymbol{X}$ characterize the initial position, and therefore label the trajectory. In order to avoid any confusion, the trajectory equation is denoted x_i^L, different from the Eulerian coordinates x_i. In the following, the superscript ^{L} will be often omitted, but different notations will be used for time-derivatives.

On the one hand, $\frac{\partial}{\partial t}$ denotes the Eulerian time derivative, at constant $\boldsymbol{x}$, as in Eq. (2.2). On the other hand, the overdot is related to the Lagrangian time derivative, at constant $\boldsymbol{X}$. As a first example, the differential term associated to Eq. (2.3) can be expanded as

$$dx_i = u_i dt + F_{ij} dX_j \tag{2.4}$$

(in which dx_i holds for dx_i^L), straightforwardly leading to

$$\dot{x}_i = \frac{\partial x_i^L}{\partial t} = u_i$$

and

$$F_{ij}(\boldsymbol{X}, t, t_0) = \frac{\partial x_i^L}{\partial X_j}. \tag{2.5}$$

The latter matrix, referred to as the Cauchy matrix,[1] will be denoted only $\partial x_i / \partial X_j$ from now on, for the sake of brevity. It is related to the classical semi-Lagrangian displacement gradient in continuum mechanics (see Eringen 1971, to whom notations are borrowed).

The brief reminder above is needed for deriving the continuity equation in the Lagrangian description. Now, one considers that the mass of an ensemble of fluid particles is conserved during its motion

$$\frac{d}{dt} \iiint_{\mathcal{V}} \rho(\boldsymbol{X}, t, t_0) d^3\boldsymbol{x} = \underbrace{\iiint_{\mathcal{V}} m(\boldsymbol{X}, t, t_0) d^3\boldsymbol{x}}_{M}$$

but the moving domain $\mathcal{V}$ has to be considered as the mapping of an initial domain $\mathcal{V}_0$ following all individual trajectories with positions in this domain (m ought to be considered in Lagrangian coordinates, too, but a new specific notation is not needed

[1] According to a recent historical investigation by U. Frisch, a more complete nomenclature would be "The Jacobian matrix of Cauchy–Lagrange".

for the sake of simplicity). From the very definition of F_{ij}, its determinant (always nonzero positive) is the Jacobian of the $\boldsymbol{x}$-to-$\boldsymbol{X}$ transformation, so that

$$d^3\boldsymbol{x} = J d^3\boldsymbol{X},$$

with

$$J(\boldsymbol{X}, t, t_0) = \det \boldsymbol{F} \tag{2.6}$$

being the local and instantaneous volumetric ratio following a trajectory. The conservation equation can be written as

$$\frac{d}{dt} \iiint_{\mathcal{V}_0} \rho J d^3\boldsymbol{X} = M,$$

and the (Lagrangian) time derivative holds inside the integral, so that

$$\iiint_{\mathcal{V}_0} \left(\dot{\rho} J + \rho \dot{J}\right) d^3\boldsymbol{X} = M.$$

From

$$\dot{F}_{ij} = \frac{\partial \dot{x}_i}{\partial X_j} = \frac{\partial u_i}{\partial x_n} F_{nj} \tag{2.7}$$

one derives

$$\dot{J} = \nabla \cdot (\boldsymbol{u}) J. \tag{2.8}$$

Finally, the continuity equation can be expressed as $(\dot{\rho J}) = Jm$, or

$$J(\boldsymbol{X}, t, t_0) = \frac{\rho(\boldsymbol{X}, t_0)}{\rho(\boldsymbol{X}, t)} + \oint_{t_0}^{t} (Jm) dt, \tag{2.9}$$

using $J(\boldsymbol{X}, t_0, t_0) = 1$ (where the time integral of m is computed along a trajectory), or alternatively

$$\dot{\rho} = -\rho \nabla \cdot (\boldsymbol{u}) + m. \tag{2.10}$$

Of course, the identity of the latter equation with Eq. (2.2) can be checked, using

$$\dot{\rho} = \frac{\partial \rho}{\partial t} + \dot{x_j} \frac{\partial \rho}{\partial x_j} = \frac{\partial \rho}{\partial t} + u_j \frac{\partial \rho}{\partial x_j}. \tag{2.11}$$

2.1.2 The Momentum, Navier–Stokes, Equations

In the same way as for the mass, the conservation of momentum yields

$$\underbrace{\frac{d}{dt}\iiint_{\mathcal{V}} \rho u_i d^3\boldsymbol{x}}_{variation} = \underbrace{-\iint_S \rho u_i \boldsymbol{u}\cdot\boldsymbol{n} d\sigma}_{flux} + \underbrace{\iiint_{\mathcal{V}} \rho f_i(\boldsymbol{x},t) d^3\boldsymbol{x}}_{production}, \tag{2.12}$$

in which the 'production' involves a body force per mass unit, denoted $\boldsymbol{f}$, but the domain of fluid is not isolated: a *surfacic* strain tensor σ_{ij} is acting on it. Accordingly, a pure kinematic balance, as in the previous subsection for the mass, is no longer valid, and *dynamics* must be accounted for. Replacing $u_i \boldsymbol{u}\cdot\boldsymbol{n} = u_i u_j n_j$ by $(u_i u_j - \sigma_{ij})n_j$, one obtains

$$\frac{\partial(\rho u_i)}{\partial t} + \frac{\partial(\rho u_i u_j - \sigma_{ij})}{\partial x_j} = b_i, \tag{2.13}$$

or

$$\rho \dot{u}_i = \frac{\partial \sigma_{ij}}{\partial x_j} + \rho f_i, \tag{2.14}$$

using the continuity equation with $m = 0$.

Finally, the classical Navier–Stokes equations[2] correspond to the following expression of the strain tensor in Eq. (2.14):

$$\sigma_{ij} = -p\delta_{ij} + \underbrace{\mu\left(\underbrace{\frac{\partial u_i}{\partial x_j} + \frac{\partial u_j}{\partial x_i}}_{S_{ij}} - \frac{2\delta_{ij}}{3}\frac{\partial u_n}{\partial x_n}\right) + \frac{3\lambda + 2\mu}{3}\frac{\partial u_n}{\partial x_n}\delta_{ij}}_{\sigma_{ij}^{visc}}, \tag{2.15}$$

in which the threefold decomposition includes a spherical term linked to pressure p, a shearing viscous term which involves the symmetric, tracefree velocity-gradient tensor, and a viscous 'bulk' term. The fluid-dependent parameters μ and λ are the counterpart of the Lamé coefficients (for a solid), and are often linked together by the Stokes relationship $3\lambda + 2\mu = 0$, which removes from consideration the pure volumic 'bulk' dissipation process.

2.1.3 Incompressible Turbulence

Strict incompressibility is recovered assuming $\rho(\boldsymbol{x},t) = \rho_0$ in the continuity equation, so that the velocity field is divergence-free or solenoidal. Ignoring the mass

[2] These equations were established by Claude Navier in 1823 and rediscovered or rederived at least four times: by Cauchy in 1823, by Poisson in 1829, by Saint-Venant in 1837 and by Stokes in 1847 (Darrigol 2005). Navier already distinguished two types of motion, 'régulier' (mean) and 'tumultueux' (turbulent), foreshadowing the Osborne's Reynolds decomposition. The idea that two length scales are present was also considered by Saint-Venant.

production term m for the sake of simplicity, mass conservation reduces to the divergence-free (solenoidal) condition, or to $J = 1$ from the Lagrangian viewpoint, and the momentum equation reduces to

$$\dot{u}_i = -\frac{1}{\rho_0}\frac{\partial p}{\partial x_i} - \nu\nabla^2 u_i + f_i, \tag{2.16}$$

in which the left-hand-side term is the acceleration, or

$$\dot{u}_i = \frac{\partial u_i}{\partial t} + \dot{x_j}\frac{\partial u_i}{\partial x_j} = \frac{\partial u_i}{\partial t} + u_j\frac{\partial u_i}{\partial x_j} \tag{2.17}$$

as for Eq. (2.11). $\nu = \mu/\rho_0$ is the kinematic viscosity, which will be considered as a constant parameter. The problem is self-consistent and well-posed, with four dependent variables (u_1, u_2, u_3, p) and four equations (one for the divergence-free constraint, three for the system of Navier–Stokes equations above).

The pressure is no longer a thermodynamic, autonomous, variable, but a simple Lagrange multiplier connected to the solenoidal constraint for velocity. Taking the divergence of Eq. (2.16), and accounting for the incompressibility constraint $\partial u_i/\partial x_i = 0$, one obtains

$$\frac{1}{\rho_0}\nabla^2 p = -\frac{\partial^2}{\partial x_i \partial x_j}\left(u_i u_j\right) - \frac{\partial f_i}{\partial x_i}. \tag{2.18}$$

This Poisson-type equation shows how the pressure is connected to the terms which are not divergence-free in the Navier–Stokes equations[3]: the acceleration term itself (contributing to the first term in the r.h.s.) and possibly the body force term (second term in the r.h.s.). In contrast, divergence-free terms, such as $\partial u_i/\partial t$ and $\nu\nabla^2 u_i$ are removed. This relationship between velocity and pressure is essential in many turbulent flows as the ones discussed in Chaps. 4–11. Two remarks can be made from the very beginning:

- this nonlocal and *instantaneous* relationship is not physical, since it implies that the speed of sound is infinite, so that a pressure disturbance in a remote position instantaneously responds to a velocity disturbance.
- however, this unphysical problem is very relevant to study and to understand low-Mach number turbulence. It is now clear that the 'problem of turbulence' is not only due to the nonlinearity of the acceleration term (2.17), as often advocated, and not only due to the lack of integrability of trajectories (2.3) (e.g. Lagrangian chaos). The 'pressure-released' turbulence, illustrated by the Burger's equation in the one-dimensional case, and by the cosmological gas in three dimensions (e.g. Polyakov 1995) is essentially solved! Hence, the role of pressure, or identically, the restriction to solenoidal modes (projection onto a solenoidal subspace) is an essential point to understand why turbulence is so complex. In addition, 'solenoidal

[3]It is important to note that such terms exist even if the velocity field is solenoidal.

turbulence', as calculated using pseudo-spectral DNS at the highest order available (e.g. 4096^3, Kaneda et al. 2003), mimics all characteristics of — low-speed — 'real' physical turbulence.

2.1.4 First Insight into Compressibility Effects

As soon as the solenoidal constraint is relaxed, the coupling between pressure and velocity becomes very different. First of all, the problem with five components (ρ, u_1, u_2, u_3, p) is only governed by four equations, i.e. mass and momentum conservation, the latter with given σ_{ij}. The state law of the fluid provides a new equation, but also introduces a new variable, usually temperature or entropy. Consequently, a new conservation equation (for energy, enthalpy, entropy) is needed. As illustrated in Chap. 3, the entropy term s can be chosen, so that the six-component $(\rho, u_1, u_2, u_3, p, s)$ compressible problem will be addressed using a six-component system of equations: 1 (mass conservation) + 3 (momentum conservation) + 1 (state law) + 1 (entropy conservation).

As a first illustration, it is possible to derive a wave propagation-like equation for ρ, combining mass and momentum equations. Taking the time-derivative of the mass conservation equation and the divergence of the momentum equation, one obtains after some algebra:

$$\frac{\partial^2 \rho}{\partial t^2} - a_0^2 \nabla^2 \rho = \frac{\partial^2}{\partial x_i \partial x_j} \left(\underbrace{\rho u_i u_j - \sigma_{ij}^{visc} + \delta_{ij}(p - a_0^2 \rho)}_{T_{ij}} \right). \tag{2.19}$$

The characteristic speed of sound, a_0, is assumed to be space-uniform in this equation, which is 'exact' in this limit (only 'production' terms m and $\boldsymbol{f}$ are ignored, for the sake of simplicity). For instance, with isentropic and low Mach number additional assumptions, T_{ij} reduces to its first term, and (2.19) can be used as a cornerstone to derive acoustic analogies (e.g. Lighthill and many followers). An equation similar to (2.19) can be found for the pressure, so that Eqs. (2.18) and (2.19) illustrate the different dynamics when compressibility is called to play.

2.1.5 Splitting the Velocity Field: Helmholtz Decomposition, Poloidal-Toroidal Decomposition and Clebsh Potentials

2.1.5.1 The Helmholtz Decomposition

The Helmholtz decomposition is an exact, purely kinematic decomposition for the velocity field. It reads

$$\boldsymbol{u}(\boldsymbol{x},t)=\boldsymbol{u}^{(sol)}(\boldsymbol{x},t)+\boldsymbol{u}^{(dil)}(\boldsymbol{x},t)+\boldsymbol{u}^{(sd)}(\boldsymbol{x},t), \tag{2.20}$$

which appears as the sum of a solenoidal contribution $\boldsymbol{u}^{(sol)}(\boldsymbol{x},t)$, a dilatational one $\boldsymbol{u}^{(dil)}(\boldsymbol{x},t)$, and a mixed one, $\boldsymbol{u}^{(sd)}(\boldsymbol{x},t)$. The third part is a purely harmonic contribution such that $\nabla\times\boldsymbol{u}^{(sd)}(\boldsymbol{x},t)=0$ and $\nabla\cdot\boldsymbol{u}^{(sd)}(\boldsymbol{x},t)=0$. In the absence of relevant boundary effects, or in the case of periodic boundaries (as used in DNS for approaching realizations of an homogeneous flow), the harmonic component is space-uniform and can therefore be taken equal to zero. More generally, even in the presence of solid boundaries, the harmonic term can be absorbed, e.g. in the dilatational term. This is illustrated by the RDT solution for an irrotational straining process in the presence of a wall based upon the Helmholtz decomposition of the linearized Weber equation (8.20) originating from Eq. (2.31).

The solenoidal mode corresponds to a purely vortical mode, with null divergence, i.e. $\nabla\cdot\boldsymbol{u}^{(sol)}=0$ and $\boldsymbol{\omega}=\nabla\times\boldsymbol{u}=\nabla\times\boldsymbol{u}^{(sol)}$. The dilatational mode has a non-zero divergence and has zero Curl, yielding $\nabla\times\boldsymbol{u}^{(dil)}=0$ and $d=\nabla\cdot\boldsymbol{u}=\nabla\cdot\boldsymbol{u}^{(dil)}$. Their properties are satisfied by introducing a *stream function vector* $\boldsymbol{\psi}$ for the first one and a scalar potential φ for the second one, such that

$$\boldsymbol{u}^{(sol)}(\boldsymbol{x},t)=\boldsymbol{\nabla}\times\boldsymbol{\psi}(\boldsymbol{x},t),\quad \boldsymbol{u}^{(dil)}(\boldsymbol{x},t)=\boldsymbol{\nabla}\varphi(\boldsymbol{x},t). \tag{2.21}$$

It may be noted that instead of the symbolic notation $\nabla\times\boldsymbol{\psi}$, a tensorial expression using the third-order alternating pseudo-tensor ε_{ijn} (often referred to as the *Levi-Civita tensor*), can be used for safer calculations since the symbolic operator $\boldsymbol{\nabla}$ is not a vector, and some permutation rules do not hold for it.

The fact that the dilatational mode is one-dimensional is obvious; on the other hand, the two-dimensional (or two-component) structure of the solenoidal term is not easily transfered to the stream function vector. Exhaustive discussions about Gauge conditions are outside our scope, but we use the toroidal-poloidal decomposition as a practical way to express $\boldsymbol{u}^{(sol)}$ in Eq. (2.25).

Note that the Helmholtz decomposition is useful even in strictly incompressible flow cases: considering any type of incompressible Navier–Stokes equations as

$$\frac{\partial\boldsymbol{u}}{\partial t}+\boldsymbol{S}+\boldsymbol{\nabla}p=0, \tag{2.22}$$

in which $\boldsymbol{S}$ represents any linear or nonlinear term, the solenoidal condition for $\boldsymbol{u}=\boldsymbol{u}^{(sol)}$ yields

$$\frac{\partial\boldsymbol{u}^{(sol)}}{\partial t}+\boldsymbol{S}^{(sol)}=0,\quad \boldsymbol{\nabla}(p+S^{(dil)})=0.$$

Accordingly, one recovers the fact that the pressure term balances the dilatational part of the arbitrary contribution $\boldsymbol{S}$, whereas the first equation, as a reduced purely solenoidal equation in which the pressure is removed from consideration, only involves the contribution $\boldsymbol{S}^{(sol)}$. Of course, for practical applications, the Curl of the first equation gives the Helmholtz equation for vorticity, whereas the divergence of

the second equation gives the Poisson equation for pressure in the incompressible case. In short, if the full Helmholtz decomposition is not useful for $\boldsymbol{u}$ in the pure incompressible case, it can be transferred to any $\boldsymbol{S}$, which governs the velocity-time-derivative, in addition to the pressure gradient term.

Going back to the general case of compressible turbulence, is there a systematic way to separate "compressible" from "incompressible" components of flow variables other than the velocity? Generally speaking, the Helmholtz decomposition is static, in the sense that it does not rely on the evolution equations which govern the dynamics, up to some exceptions mentioned throughout this book. Accordingly, this decomposition does not provide any help in the task of splitting the pressure, the density and the entropy between compressible and incompressible components. Therefore, the splitting given by Eq. (2.20) must be supplemented by some arbitrary definition of "incompressible" and "compressible" parts of other physical variables.

The pressure is usually split as

$$p = p_s + p_d \tag{2.23}$$

where p_s is *defined* as the part of the pressure field which satisfies the Poisson equation found for the pressure in the incompressible case, leading to

$$\nabla^2 p_s = -\nabla \cdot \nabla \cdot (\boldsymbol{u}^{(sol)} \otimes \boldsymbol{u}^{(sol)}). \tag{2.24}$$

The component p_d is then defined as the remainder, i.e. $p_d = p - p_s$.

An important remark is that the solenoidal field $(\boldsymbol{u}^{(sol)}, p_s)$ does not include acoustic waves, but that the residual field $(\boldsymbol{u}^{(dil)}, p_d)$ is not restricted to acoustic phenomena. The characteristic velocity scale associated to $(\boldsymbol{u}^{(sol)}, p_s)$ is the fluid velocity, while $(\boldsymbol{u}^{(dil)}, p_d)$ can have two characteristic scales in the most general case: the fluid velocity and the speed of sound. The former will hold if $(\boldsymbol{u}^{(dil)}, p_d)$ is dominated by heat transfer (convective phenomenon), while the latter will be relevant in acoustics-governed cases.

Another point is the possible interest to use density-weighted variables. Instead of applying the Helmholtz decomposition to the velocity field, or to the $\boldsymbol{S}$ term in Eq. (2.22), it can be applied to the momentum $\rho\boldsymbol{u}$. One can introduce this way a hierarchy of embedded levels of approximation, among which the anelastic approximation. As a second example, following Kida and Orszag (1990a, b, 1992), Miura and Kida (1995) extend the usual Helmholtz decomposition by applying it to the vector field $\boldsymbol{w} = \sqrt{\rho}\boldsymbol{u}$. Using this definition, the authors enforce the positive-definiteness of the spectra of the compressive and rotational kinetic energies.

It must be mentioned that looking at mathematical details, rather complex non-local relationships are found when inverting some above mentioned equations, e.g. when extracting velocity from vorticity, stream vector function and scalar potential function from velocity, toroidal and poloidal potential scalars from solenoidal velocity. The use of Fourier space, consistent with our homogeneous framework, yields algebraic simplified relations for all these mathematical projections, as it will be shown everywhere in this book.

2.1.5.2 The Poloidal-Toroidal Decomposition and Clebsh Potential

The toroidal-poloidal decomposition can provide a useful alternative for expressing the solenoidal field, in terms of two components:

$$\boldsymbol{u}^{(sol)}(\boldsymbol{x},t) = \underbrace{\boldsymbol{\nabla}\times(s_{tor}(\boldsymbol{x},t)\boldsymbol{n})}_{toroidal\ part} + \underbrace{\boldsymbol{\nabla}\times[\boldsymbol{\nabla}\times(s_{pol}(\boldsymbol{x},t)\boldsymbol{n})]}_{poloidal\ part} \tag{2.25}$$

in which s_{pol} and s_{tor} are scalar potentials. Of course, this definition involves an arbitrary direction $\boldsymbol{n}$, but it is important noting that there is no important lack of generality, and that the toroidal-poloidal decomposition is not restricted to axisymmetric flows, even though it yields dramatic simplifications in that case. One recovers an explicit three-terms description with three scalar potentials (toroidal-poloidal-dilatational) for any velocity field, combining Eqs. (2.21) and (2.25).

Another decomposition, with a most general definition of the toroidal mode, deserves some attention, especially for deriving the expansion in terms of spherical harmonics for a vector field (Chandrasekhar 1981; Rieutord 1987), as discussed in Sect. 2.5.2.1.

Another alternative consists of using Clebsch potentials $\lambda(\boldsymbol{x},t)$ and $\mu(\boldsymbol{x},t)$, with

$$\boldsymbol{u} = \lambda\boldsymbol{\nabla}\mu + \boldsymbol{\nabla}\varphi''. \tag{2.26}$$

It is less practical because the part generated by Clebsch decomposition has both solenoidal and dilatational contributions, to be disentangled, according to

$$\boldsymbol{u}^{(sol)} = (\lambda\boldsymbol{\nabla}\mu)^{(sol)}, \quad \boldsymbol{u}^{(dil)} = (\lambda\boldsymbol{\nabla}\mu)^{(dil)} + \boldsymbol{\nabla}\varphi''.$$

In contrast, both toroidal and poloidal contributions are explicitly and separately divergence-free.

2.1.6 Reminder About Circulation and Vorticity

The reader is referred to basic textbooks for the fundamentals about circulation, related Kelvin theorem and vorticity, e.g. Saffman (1995). The vorticity is defined as the $Curl$ of velocity, i.e. $\boldsymbol{\omega} = \mathrm{Curl}(\boldsymbol{u})$, leading to

$$\boldsymbol{\omega} = \boldsymbol{\nabla}\times\boldsymbol{u} \quad \text{or} \quad \omega_i = \varepsilon_{ijn}\frac{\partial u_n}{\partial x_j}. \tag{2.27}$$

It is found that $\boldsymbol{\omega} = \boldsymbol{\nabla}\times\boldsymbol{u}^{(sol)}$, and

$$\boldsymbol{\omega} = -\nabla^2\psi, \tag{2.28}$$

in which only solenoidal terms are involved.

From the momentum conservation law (2.14) it follows that

$$\dot{\omega}_i + \frac{\partial u_j}{\partial x_j}\omega_i - \frac{\partial u_i}{\partial x_j}\omega_j = \varepsilon_{ijn}\frac{\partial}{\partial x_j}\left[\frac{1}{\rho}\frac{\partial \sigma_{nm}}{\partial x_m} + f_n\right].$$

The right-hand-side is exactly the $Curl$ of the acceleration $\dot{\boldsymbol{u}}$. Ignoring the viscous and body force terms, this equation can be rewritten as

$$\left(\frac{\dot{\omega}_i}{\rho}\right) = \frac{\partial u_i}{\partial x_j}\frac{\omega_j}{\rho} + \frac{1}{\rho^3}\varepsilon_{ijn}\frac{\partial \rho}{\partial x_j}\frac{\partial p}{\partial x_n}, \tag{2.29}$$

in which the *baroclinic torque* appears as the second term in the right-hand-side.

This term vanishes in the barotropic case $p = p(\rho)$, and not only in the pure incompressible case. In such a situation, the Eq. (2.7) for F_{ij} is the same as the above equation for ω_i/ρ at fixed j. As a consequence, the evolution of the vorticity vector along trajectories is governed by the Cauchy matrix according to the following law

$$\omega_i(\boldsymbol{x}, t) = \frac{1}{\det \mathbf{F}} F_{ij}(\boldsymbol{X}, t, t_0)\omega_j(\boldsymbol{X}, t_0). \tag{2.30}$$

A similar but less common equation for the velocity is the *Weber equation*

$$u_i(\boldsymbol{x}, t) = F^{-1}_{ji}(\boldsymbol{X}, t, t_0)u_j(\boldsymbol{X}, t_0) + \frac{\partial \varphi'}{\partial x_i}. \tag{2.31}$$

where φ' is a scalar potential, similar those found in Eq. (2.21) and in the Clebsch decomposition. It is easy to derive Eq. (2.30) from Eq. (2.31) via the $Curl$ operator, but the reciprocal is much more difficult to establish. An alternative way (Julian Hunt, private communication) for proving (2.31) is to start from the Kelvin circulation theorem

$$\oint_C \boldsymbol{u}(\boldsymbol{x}, t) \cdot \delta\boldsymbol{x} = \oint_{C_0} \boldsymbol{u}(\boldsymbol{X}, t_0) \cdot \delta\boldsymbol{X}$$

in which the closed chains of fluid particles, respectively C_0 at initial time and C at final time, are connected via trajectories. Since the result has to be independent of the form of the (e.g. initial) loop C_0, a differential formula can be derived from the integral one, as in thermodynamics for first and second principles, yielding

$$\boldsymbol{u}(\boldsymbol{x}, t) \cdot \delta\boldsymbol{x} - \boldsymbol{u}(\boldsymbol{X}, t_0) \cdot \delta\boldsymbol{X} = d\phi$$

in which $d\phi$ is a total differential. The Weber equation is recovered from the former differential equation using $\delta X_i = F^{-1}_{ij}\delta x_j$ and $d\phi = \frac{\partial \phi}{\partial x_i}\delta x_i$.

2.1.7 Evolution Equation for Velocity Gradient and Vorticity

Even in the purely incompressible case, to which the rest of the present chapter is devoted, the vorticity dynamics is essential but is not the whole story: The vortex stretching effect illustrates the important interaction of the symmetric part of the velocity-gradient with the vorticity, related to its antisymmetric part. Consequently, fundamental evolution equations for velocity-gradient related quantities are very important to get a full understanding of flow dynamics. Introducing the velocity gradient tensor $\mathbf{A} = \nabla \boldsymbol{u}$, its symmetric part (the strain) $\mathbf{S} = \frac{1}{2}(\mathbf{A} + \mathbf{A}^T)$, its antisymmetric part $\mathbf{W} = \frac{1}{2}(\mathbf{A} - \mathbf{A}^T)$, the Navier–Stokes equations straightforwardly lead to

$$\dot{\mathbf{A}} = \frac{\partial}{\partial t}\mathbf{A} + \boldsymbol{u} \cdot \nabla \mathbf{A} = -\mathbf{A}^2 + \nu \nabla^2 \mathbf{A} + \mathbf{H} \tag{2.32}$$

where $H_{ij} = (\partial^2 p / \partial x_i \partial x_j)$ is the Hessian of pressure fluctuations, along with

$$\dot{\mathbf{W}} = \frac{\partial}{\partial t}\mathbf{W} + \boldsymbol{u} \cdot \nabla \mathbf{W} = -(\mathbf{S}\mathbf{W} + \mathbf{W}\mathbf{S}) + \nu \nabla^2 \mathbf{W} \tag{2.33}$$

$$\dot{\mathbf{S}} = \frac{\partial}{\partial t}\mathbf{S} + \boldsymbol{u} \cdot \nabla \mathbf{S} = -\left(\mathbf{S}^2 - \frac{1}{3} Tr(\mathbf{S}^2)\mathbf{I}\right) - \left(\mathbf{W}^2 - \frac{1}{3} Tr(\mathbf{W}^2)\mathbf{I}\right) + \nu \nabla^2 \mathbf{S} + \mathbf{H}^p \tag{2.34}$$

where $\mathbf{H}^p$ denotes the deviatoric part of the pressure Hessian:

$$H^p_{ij} = -\left(\frac{\partial^2 p}{\partial x_i \partial x_j} - \frac{1}{3}\nabla^2 p \delta_{ij}\right) \tag{2.35}$$

Now considering the vorticity vector $\boldsymbol{\omega}$ and reminding that $\omega_i = \varepsilon_{ijk} W_{jk}$ where ε_{ijk} denotes the Levi-Civita tensor, one obtains

$$\dot{\boldsymbol{\omega}} = \frac{\partial \boldsymbol{\omega}}{\partial t} + \boldsymbol{u} \cdot \nabla \boldsymbol{\omega} = \mathbf{S}\omega + \nu \nabla^2 \boldsymbol{\omega} \tag{2.36}$$

and

$$\frac{\partial}{\partial t}\mathbf{S} + \boldsymbol{u} \cdot \nabla \mathbf{S} = -\left(\mathbf{S}^2 - \frac{1}{3} Tr(\mathbf{S}^2)\mathbf{I}\right) - \left(\boldsymbol{\omega}\boldsymbol{\omega}^T - \frac{\omega^2}{3}\mathbf{I}\right) + \nu \nabla^2 \mathbf{S} + \mathbf{H}^p. \tag{2.37}$$

One recover the incompressible version of Eq. (2.29), and its couplings with the $\mathbf{S}$-equation are displayed.

Being a traceless second-rank tensor in three dimensions, $\mathbf{A}$ can be reduced to the following five scalar invariants, which are often used to describe turbulence properties:

$$Q = -\frac{1}{2}A_{lk}A_{kl},\ R = -\frac{1}{3}A_{ij}A_{jk}A_{ki},\ Q_S = -\frac{1}{2}S_{lk}S_{kl},$$
$$R_S = -\frac{1}{3}S_{ij}S_{jk}S_{ki},\ V^2 = S_{in}S_{im}\omega_n\omega_m. \tag{2.38}$$

The set of independent scalars can be given as well by two eigenvalues of $\mathbf{S}$ (three eigenvalues for a symmetric tensor, but with zero sum, because it is trace-free) and the three components of vorticity, seen in the eigenframe (principal axes) of $\mathbf{S}$.

A first look at Eq. (2.32) shows that $\mathbf{A}$ is subjected to advection by the velocity field, quadratic self-amplification or self-attenuation, viscous damping and pressure effects. It is worth reminding that $\mathbf{H}$ is both non-local and linear, while the $\mathbf{A}^2$ is a local non-linear term. Equation (2.36) shows that the vorticity is amplified or damped by the vortex stretching term $\mathbf{S}\boldsymbol{\omega}$ depending on the sign of the eigenvalues of $\mathbf{S}$ and the relative orientation of $\boldsymbol{\omega}$ with respect to its eigenvectors. The first term in the right-hand side of Eq. (2.37) is responsible for a local, quadratic self-amplification of self-attenuation of the velocity gradient, since it is diagonal in the eigenframe of $\mathbf{S}$. The second term, which is related to vorticity effect on the local rate of strain, is also a gradient amplification mechanism coupled to a local rotation of the eigenframe of $\mathbf{S}$.

From the above equations one can recover evolution equations for the enstrophy $\omega^2/2$ and the total strain $S^2 = S_{ij}S_{ij}$. In the absence of external forcing, one has (making indices to appear for the sake of clarity)

$$\frac{1}{2}\frac{\partial\omega^2}{\partial t} + u_j\frac{\partial\omega^2}{\partial x_j} = \omega_i\omega_j S_{ij} + \nu\omega_i\nabla^2\omega_i \tag{2.39}$$

$$\frac{1}{2}\frac{\partial S^2}{\partial t} + u_j\frac{\partial S^2}{\partial x_j} = -S_{ik}S_{kj}S_{ij} - \frac{1}{4}\omega_i\omega_j S_{ij} - S_{ij}\frac{\partial^2 p}{\partial x_i x_j} + \nu S_{ij}\nabla^2 S_{ij}. \tag{2.40}$$

2.1.8 *Biot–Savart Relationship and Non-local Closure of Vorticity Equation*

The vorticity vector includes all the information on the velocity field in the incompressible case, up to possible complex boundary conditions ignored here for the sake of simplicity. But the Helmholtz equation is not closed in terms of vorticity, because the strain tensor responsible for the vortex stretching effect is also affected by the pressure Hessian. As for the nonlocal relationship of pressure to velocity (see Eq. (2.53) and associated discussions), it is necessary to look at the relationship of velocity to vorticity, which is found by *inverting* the Curl operator.

Taking the Curl of vorticity, one obtains,

$$\varepsilon_{imn}\frac{\partial}{\partial x_m}\omega_n = -\frac{\partial^2 u_i}{\partial x_m\partial x_m} + \frac{\partial}{\partial x_i}\frac{\partial u_m}{\partial x_m},$$

which simplifies as

$$\boldsymbol{\nabla} \times \boldsymbol{\omega} = -\nabla^2 \boldsymbol{u} \tag{2.41}$$

in the incompressible case, so that $\boldsymbol{u}$ can be expressed in terms of $\boldsymbol{\nabla} \times \boldsymbol{\omega}$ using the Green's function of the Laplacian operator, as for solving the Poisson equation for the pressure (see Eq. (2.53)). A slightly more direct relationship is given by Biot–Savart as

$$\boldsymbol{u}(\boldsymbol{x}, t) = \frac{1}{4\pi} \iiint \boldsymbol{\omega}(\boldsymbol{x}', t) \times \frac{\boldsymbol{x} - \boldsymbol{x}'}{| \boldsymbol{x} - \boldsymbol{x}' |^3} d^3\boldsymbol{x}'. \tag{2.42}$$

An explicit non-local relationship follows for the strain tensor in terms of the velocity (Constantin 1994; Majda and Bertozzi 2002) as

$$\mathbf{S}(\boldsymbol{x}) = \frac{3}{8\pi} \mathcal{P}V \iiint \left[\frac{(\boldsymbol{x} - \boldsymbol{x}') \otimes [(\boldsymbol{x} - \boldsymbol{x}') \times \boldsymbol{\omega}(\boldsymbol{x}')]}{| \boldsymbol{x} - \boldsymbol{x}' |^5} + \frac{[(\boldsymbol{x} - \boldsymbol{x}') \times \boldsymbol{\omega}(\boldsymbol{x}')] \otimes (\boldsymbol{x} - \boldsymbol{x}')}{| \boldsymbol{x} - \boldsymbol{x}' |^5} \right] d^3\boldsymbol{x}', \tag{2.43}$$

where the integral is understood as a Cauchy Principal Value (denoted $\mathcal{P}V$) and $\otimes$ is the tensor product, i.e. $(\boldsymbol{x} \otimes \boldsymbol{y})_{ij} = x_i y_j$.

The Helmholtz equation is eventually closed using the latter equation. A technical problem is that the kernel operator appearing in Biot–Savart law is not differentiable in the sense of classical functions, but in the sense of distributions only. In addition to the detailed analysis by Majda and Bertozzi (2002), the reader is referred to Pereira et al. (2016) for a recent application to a dissipative random velocity field.

Beyond homogeneous turbulence, the Biot–Savart relationship is shown by Garry L. Brown and Anatol Roshko to be essential for the clumping of the vorticity with instability in turbulent shear layers and wakes (Brown and Roshko 2012).

2.1.9 Adding Body Forces or Mean Gradients

In the absence of external forcing or turbulence production via interaction with a non-uniform mean velocity field, the 'incompressible' turbulence (only this case will be discussed here) decays, and, but this is more controversial, returns, at least partially at small scales, towards isotropy. Therefore, decaying isotropic turbulence, which is addressed in Chap. 4, is the best illustration of turbulence dynamics. Statistical homogeneity is a mandatory requirement to study such a turbulence, so that the concepts of homogeneity and isotropy are intimately connected in various fundamental approaches to *Homogeneous Isotropic Turbulence* (HIT). A main theme of this book is to illustrate how the framework of *Homogeneous Anisotropic Turbulence* (HAT) is informative and useful … up to careful definitions and some caveats. In this context, the emphasis is put on anisotropic forcings, which can render the turbulence anisotropic and inject energy, so that the ultimate decay is altered or even prevented.

How such a forcing can preserve homogeneity, as far as possible, while representing a *physical* process, is the first question. Our experience is that forcing processes often used in fundamental studies have nothing to do with actual flows. On the other hand, mean rotation, strain, shear, density-stratification are physically relevant effects, consistent or not with statistical homogeneity.

The case of turbulence in a rotating frame is helpful to introduce our concept of HAT. On the one hand, a solid body motion

$$x_i^{(0)} = F_{ij}(t - t_0)X_j \tag{2.44}$$

can be superimposed to a disturbance motion which will be considered as 'turbulent'. In the above equation, the solid body motion can be considered as a base flow. $\boldsymbol{X}$ denotes the Lagrangian coordinates *associated to the base flow motion*, and $F_{ij}(t)$ is also the base flow counterpart of the general matrix introduced at the beginning of this chapter. In agreement with the usual solid body motion description, the velocity field is characterized by the angular velocity vector $\Omega\boldsymbol{n}$ with magnitude Ω and orientation $\boldsymbol{n}$, so that

$$\boldsymbol{u}^{(0)} = \Omega\boldsymbol{n} \times \boldsymbol{x} \quad \text{with} \quad \nabla \times \boldsymbol{u}^{(0)} = 2\Omega\boldsymbol{n}$$

up to a constant term, which can set equal to zero by changing the frame of reference thanks to the Galilean invariance property. In other words, the base flow is characterized by a constant velocity gradient matrix $\mathbf{A}$

$$\mathbf{A} = \left(\frac{\partial u_i^{(0)}}{\partial x_j}\right) = \begin{pmatrix} 0 & -\Omega & 0 \\ \Omega & 0 & 0 \\ 0 & 0 & 0 \end{pmatrix} \tag{2.45}$$

choosing $n_i = \delta_{i3}$ without loss of generality. Accordingly, it is possible to replace u_i by $u_i^{(0)} + u_i'$ in the background equations, and to study the turbulent flow (i.e. $\boldsymbol{u}'$) in the presence of a particular base flow $\boldsymbol{u}^{(0)}$ with constant, antisymmetric gradient matrix. In our simple example dealing with solid body rotation, the base displacement gradient matrix is

$$\left(F_{ij}^{(0)}\right) = \begin{pmatrix} \cos\Omega(t - t_0) & -\sin\Omega(t - t_0) & 0 \\ \sin\Omega(t - t_0) & \cos\Omega(t - t_0) & 0 \\ 0 & 0 & 1 \end{pmatrix}. \tag{2.46}$$

On the other hand, it is well known that it is easier to study turbulence in the rotating frame, projecting both position and velocity in this non-Galilean frame of reference. Replacing x_i by X_i and u_i by v_i, defined in the same way as in Eq. (2.44) by

$$u_i = F_{ij}^{(0)}(t - t_0)v_j,$$

it is seen that v_i and X_i satisfy the same equations as u_i and x_i in the Galilean reference frame, up to additional centrifugal and Coriolis forces. This non-Galilean

acceleration term is defined as

$$\boldsymbol{f} = \underbrace{-2\Omega \boldsymbol{n} \times \boldsymbol{v}}_{Coriolis} - \Omega^2(\boldsymbol{n} \times (\boldsymbol{n} \times \boldsymbol{X})).$$

This simple example, addressed with more details in Chap. 7, is used here to illustrate the relevance of adding a constant base velocity gradient, or adding a body force. For solid body rotation, energy is not directly injected into turbulence, since the Coriolis force produces no work (and the centrifugal force can be removed from consideration if it is incorporated in the pressure term), but the energy cascade is strongly altered and rendered highly anisotropic. Without anticipating the results dealing with statistical properties of this flow, which will be presented in Chap. 7, the presence of solid body rotation can be shown to be consistent with statistical homogeneity of the turbulent flow: removing the base flow motion for defining homogeneity (and hence restricting the analysis to disturbances) in the first case, $\boldsymbol{u}' = \boldsymbol{u} - \boldsymbol{u}^{(0)}$,[4] and considering homogeneity for $\boldsymbol{u}' \to \boldsymbol{v}$ in the rotating frame in the second case.

To what extent the pure antisymmetric base velocity gradient matrix can be replaced by a more general one, including both symmetric and antisymmetric part? Craya introduced in 1958 a relevant formalism for this purpose, which has been completely revisited in Cambon's thesis (1982), and rediscovered later in the context of stability analysis, e.g. Craik and Criminale (1986). In a large part of this book, a constant mean velocity gradient matrix $\mathbf{A}$ will be used to study the turbulent velocity field

$$u_i' = u_i - A_{ij}x_j,$$

The following comments can be made prior to the analysis:

(i) A special form of $\mathbf{A}$ is required to preserve statistical homogeneity of the turbulent field. In the incompressible case, however, these conditions are not very stringent, allowing hyperbolic, linear and elliptical streamlines for the mean motion. As soon as $\mathbf{A}$ has a nonzero symmetric part, kinetic energy can be directly injected into the turbulent flow, i.e. some turbulence production mechanisms can take place.

(ii) The strict analogy with the effect of body forces holds for solid body motion only. The advection of the turbulent motion by the mean flow can be removed by a convenient change of frame, even if $\mathbf{A}$ is not purely antisymmetric, but all other terms in the equations for $\boldsymbol{u}'$ are then rendered more complicated, since they will involve $\mathbf{F}^{(0)}(t - t_0)$-dependent factors (Rogallo 1981; Cambon 1982).

(iii) Both linear (as in the *Rapid Distortion Theory* (RDT) or in similar stability analyses) and *full* nonlinear approaches can be carried out with the additional constant-mean-velocity-gradient-matrix effect, keeping the context of homogeneous, but often highly anisotropic, turbulence.

(iv) What is the physical relevance of a mean flow without boundaries having the same $\mathbf{A}$ matrix over the whole space (often called *extensional base flow* in the

[4] It is worth noting that the base flow is not invariant by translation.

community of hydrodynamic stability)? This question is essential. It received a clear answer, at least for the linear theory, ranging from WKB RDT to short-wave disturbance analyses: one has to consider that the spatial homogeneity, and therefore the region in which the mean gradient is almost constant, is restricted to a domain which is large with respect to the size of relevant 'turbulent' structures (turbulence in general), or large with respect to the wavelength of disturbances, from the linear stability viewpoint.

The last point (iv) suggests that the HAT in the presence of constant $\mathbf{A}$ is not only a marginal domain in the field of turbulence research. We therefore propose to use it as one of the main thread in this book. Of course, this point has to be discussed with care, in order to delineate its relevance to understand the dynamics of realistic shear flows of practical interest. In addition, it is shown in Chap. 16 that turbulence in the presence of a shock wave can be handled using the HAT formalism. Even if the effect of the shock is very far from a mean gradient effect, it is consistent with the absence of typical lengthscale L for the distorting mechanism: L is considered as infinite (or very large with respect to the size of turbulent structures) in the first case; it is zero (the thickness of the shock-wave), in contrast, in the second case (or very small with respect to the size of turbulent or organized structures passing through the shock-wave).

2.2 Briefs About Statistical and Probabilistic Approaches

A presentation of statistical tools is a 'compulsory figure' in any book on turbulence. The reader is referred to, e.g., the Tennekes and Lumley's monograph (Tennekes and Lumley 1972) and to Chap. 3 of the more recent book (Mathieu and Scott 2000) for a deep and comprehensive review. Since this aspect is well documented, only key definitions and procedures are recalled in this subsection.

2.2.1 Ensemble Averaging

The most fundamental statistical averaging deals with an ensemble of independent realizations of a random variable V and will be denoted either by an overbar $\overline{V}$ or by brackets $\langle V \rangle$ in the following. Possible approximations using temporal or spatial averaging are not discussed here. We assume that the ensemble averaging has all the properties of commutation (with time and spatial derivatives) which are often referred to as the Reynolds axioms, and can therefore be referred to as a Reynolds averaging. Discussing ergodicity is also beyond the scope of this book. The *probability density function* (pdf) which underlies the calculation of any statistical moment, as $\overline{V^n}$ for a scalar, or $\overline{\boldsymbol{V}^n}$ for a vector, will be introduced only when it will be used in a specific context.

2.2.2 Single-Point and Multi-point Moments

It is important to point out that the Reynolds decomposition in terms of a mean (velocity $\overline{\boldsymbol{u}}$) and a fluctuating (velocity $\boldsymbol{u}'$) motion remains useful in many applications. It is used as a mandatory requirement before applying the statistical tools to u_i', e.g. evaluating statistical moments of the turbulent field. In this sense, statistical modelling is restricted to a *centered* random variable $\boldsymbol{u}' = \boldsymbol{u} - \overline{\boldsymbol{u}}$. In addition, N$th$-order moments of $\boldsymbol{u}'$ can be taken at the same point in the spatial domain, or at different points, from 2 to N. Evolution equations can be derived for all these quantities, with a problem of closure revisited in the last section of this chapter. A given level of description can be labelled as $[N,\ P]$, with N the order of correlations, and P ($P \leq N$) the number of undependent points. Emphasis will be put in this book on low-order moments, with N ranging from 2 to 4, but possibly in a multi-point description.

2.2.3 Statistics for Velocity Increments

An alternative to the two-point description, for instance based on the velocity correlation tensor

$$R_{ij}(\boldsymbol{x}, \boldsymbol{r}, t) = \overline{\boldsymbol{u}_i(\boldsymbol{x}, t)\boldsymbol{u}_j(\boldsymbol{x} + \boldsymbol{r}, t)} \tag{2.47}$$

is to work with velocity increments

$$\delta u_i = u_i(\boldsymbol{x} + \boldsymbol{r}, t) - u_i(\boldsymbol{x}, t)$$

and to consider their moments only. This analysis will be discussed in Chap. 4. A local scaling (in terms of $\boldsymbol{r}$) of related moments, or structure functions, is easier to justify, following Kolmogorov, since the velocity increments are naturally smaller and smaller as the distance $r = |\boldsymbol{r}|$ decreases. This analysis is restricted to an inertial range of scales, with r being significantly larger than the Kolmogorov scale and significantly smaller than a typical integral lengthscale. High order moments, i.e. high order structure functions, are investigated in order to characterize the internal intermittency, but the multi-point approach is always a two-point one.

2.2.4 Application of the Reynolds Decomposition to Dynamical Equations

The velocity and pressure fields are first split into mean and fluctuating components and equations for their time evolution are derived from the basic equations of motion of the fluid. Assuming incompressibility, as done in this chapter unless explicitly stated, one obtains the following mean flow equations

$$\frac{\partial \overline{u}_i}{\partial t} + \overline{u}_j \frac{\partial \overline{u}_i}{\partial x_j} = -\frac{\partial \overline{p}}{\partial x_i} + \nu \frac{\partial^2 \overline{u}_i}{\partial x_j \partial x_j} - \underbrace{\frac{\partial \overline{u'_i u'_j}}{\partial x_j}}_{\text{Reynolds stress term}} \tag{2.48}$$

$$\frac{\partial \overline{u}_i}{\partial x_i} = 0 \tag{2.49}$$

and the equations for the fluctuating component

$$\frac{\partial u'_i}{\partial t} + \overline{u}_j \frac{\partial u'_i}{\partial x_j} + u'_j \frac{\partial \overline{u}_i}{\partial x_j} + \underbrace{\frac{\partial}{\partial x_j}(u'_i u'_j - \overline{u'_i u'_j})}_{\text{Nonlinear term}} = \underbrace{-\frac{\partial p'}{\partial x_i}}_{\text{Pressure term}} + \underbrace{\nu \frac{\partial^2 u'_i}{\partial x_j \partial x_j}}_{\text{Viscous term}} \tag{2.50}$$

and

$$\frac{\partial u'_i}{\partial x_i} = 0. \tag{2.51}$$

Here, $\overline{u}_i$ and $\overline{p}$ are the mean velocity and static pressure (divided by density), while u'_i and p' are the corresponding fluctuating quantities, usually interpreted as representing turbulence.

At various points, we will mention related works in the area of hydrodynamic stability. It is worth noting that in the inhomogeneous case Eqs. (2.50) and (2.51) for the fluctuating flow are essentially the same as those for a perturbation u'_i, about a basic flow $\overline{u}_i$, with an additional forcing term $\partial \overline{u'_i u'_j}/\partial x_j$. Although the aims of stability theory (to characterize growth of the perturbations) and of the theory of turbulence (to determine the statistics of u'_i) are different, it is nonetheless valuable to draw parallels between these two fields. It is our hope that doing so we will encourage specialists in both areas to become more conversant with each others work.

Equation (2.50) is now used to derive equations for the time evolution of velocity moments, i.e. averages of products of u'_i with itself at one or more points in space. Setting up the equations for the nth-order velocity moments at n points, one discovers that there are two main difficulties. Firstly, the term in (2.50) which is nonlinear with respect to the fluctuations leads to the appearance of (n + 1)th-order moments in the evolution equations for nth-order moments. Secondly, the pressure term brings in pressure-velocity correlations.

The pressure field is intimately connected with the incompressibility constraint. Indeed, taking the divergence of (2.50) one obtains a Poisson equation for the pressure fluctuations

$$\nabla^2 p' = -\frac{\partial^2}{\partial x_i \partial x_j}(u'_i \overline{u}_j + \overline{u}_i u'_j + u'_i u'_j - \overline{u'_i u'_j}). \tag{2.52}$$

The solution of this equation based on Green's functions expresses p' at any point in space in terms of an integral of the velocity field over the entire fluid domain,

together with integrals over the boundaries, the details of whose expression in terms of velocity do not concern us here.

The solution of the Poisson equation $\nabla^2 p' = f'$ can be written as

$$p'(\boldsymbol{x}, t) = \int_{\mathbb{R}^3} \mathcal{G}(\boldsymbol{x}, \boldsymbol{x}') f'(\boldsymbol{x}', t) d^3\boldsymbol{x}', \tag{2.53}$$

with the related Green's function given by

$$\mathcal{G}(\boldsymbol{x}, \boldsymbol{x}') = \frac{1}{4\pi} \frac{1}{|\boldsymbol{x}' - \boldsymbol{x}|}, \tag{2.54}$$

in a three-dimensional unbounded domain, getting rid of specific boundary conditions.

Replacing f' in Eq. (2.53) by the whole right-hand-side of Eq. (2.52) yields both linear and nonlinear, nonlocal contributions from fluctuating velocity. Thus, the pressure at a given point is nonlocally determined by the velocity field at all points of the flow, leading to integro-differential equations for the velocity moments when the pressure-velocity moments are expressed in terms of the sole velocity. It must be observed that nonlocality is not specific to the use of statistical methods, but is an intrinsic feature of incompressible fluids, in which the pressure field responds instantaneously and nonlocally to changes in the flow to enforce incompressibility. The source term in the Poisson equation (2.52) consists of parts which are linear and nonlinear with respect to the velocity fluctuation. Therefore, the pressure can be decomposed as the sum of two components: a pressure term $p'^{(r)}$ associated to linear terms (and referred to as the *rapid pressure term*, since it responds immediately to a change in the mean flow) and a second one, $p'^{(s)}$, which is associated to the nonlinear ones (referred to as the *slow pressure term*, since it is not directly sensitive to a change in the mean flow):

$$\nabla^2 p'^{(r)} = -\frac{\partial^2}{\partial x_i \partial x_j} (u_i' \overline{u}_j + \overline{u}_i u_j'), \tag{2.55}$$

$$\nabla^2 p'^{(s)} = -\frac{\partial^2}{\partial x_i \partial x_j} (u_i' u_j' - \overline{u_i' u_j'}). \tag{2.56}$$

2.3 Reynolds Stress Tensor and Related Equations

2.3.1 RST Equations

In addition to simple closure models for the Reynolds-averaged Navier–Stokes equations, such as models of turbulent viscosity using a mixing length assumption, second-

order single-point [2, 1] models offer both a dynamical and a statistical description of the turbulent field. The governing equations for the Reynolds stress tensor, turbulent kinetic energy, and for its dissipation rate can reflect the effects of convection, diffusion, distortion, pressure and viscous stresses, which are present in the equations that govern the fluctuating field u_i'.

The exact evolution equation for the Reynolds Stress tensor $R_{ij} = \overline{u_i' u_j'}$ (with $\boldsymbol{r} = 0$ in Eq. (2.47)), derived from Eq. (2.50), has the form

$$\frac{\partial R_{ij}}{\partial t} + \overline{u}_k \frac{\partial R_{ij}}{\partial x_k} = \mathcal{P}_{ij} + \Pi_{ij} - \varepsilon_{ij} - \frac{\partial \mathcal{D}_{ijk}}{\partial x_k}, \tag{2.57}$$

where

$$\mathcal{P}_{ij} = -\frac{\partial \overline{u}_i}{\partial x_k} R_{kj} - \frac{\partial \overline{u}_j}{\partial x_k} R_{ki} \tag{2.58}$$

is usually referred to as the production tensor and is the only term on the right-hand-side of Eq. (2.57) which does not require modelling, since it is given in terms of the basic one-point variables $\overline{u}_i$ and R_{ij}. The remaining terms are not exactly expressible in terms of the basic one-point variables and heuristic approximations, forming the core of the model, are introduced to close the equations.

The second term in the right hand side of Eq. (2.57) is associated with the fluctuating pressure and is given by

$$\Pi_{ij} = \overline{p' \left(\frac{\partial u_i'}{\partial x_j} + \frac{\partial u_j'}{\partial x_i} \right)}, \tag{2.59}$$

consisting of one-point correlations between the fluctuating pressure and rate of strain tensor. As discussed in the introduction, p' is nonlocally determined from the velocity field by the Poisson equation (2.52) which, in principle, requires multi-point methods for its treatment. It is usual to decompose Π_{ij} into three parts

$$\Pi_{ij} = \Pi_{ij}^{(r)} + \Pi_{ij}^{(s)} + \Pi_{ij}^{(w)} \tag{2.60}$$

corresponding to the three components of the Green's function solution of (2.52). The first is known as the "rapid" pressure component and arises from the pressure component defined by Eq. (2.55). Being linear, this component is present in RDT, hence the term "rapid" component. The second term in (2.60) is the "slow" component and comes from (2.56). Finally, $\Pi_{ij}^{(w)}$ is the wall component and corresponds to a surface integral over the boundaries of the flow in the Green's function solution for p' which is additional to the volume integrals expressing the rapid and slow components. The three components of Π_{ij} have zero trace, and are assumed to represent physically distinct mechanisms. Hence, they are modelled separately. The pressure-strain tensor is traceless (because of the incompressibility constraint) and therefore corresponds to a mechanism of redistribution of energy between the different components of the Reynolds stress tensor. Linear and nonlinear mechanisms reflected in its 'rapid' and

'slow' parts, respectively, will be discussed at the end of this subsection. In simple models, a mechanism of *isotropization of the production* is attributed to $\Pi_{ij}^{(r)}$, and a mechanism of *return to isotropy*, or *isotropization of the Reynolds stress tensor*, is attributed to $\Pi_{ij}^{(s)}$.

The dissipation tensor

$$\varepsilon_{ij} = 2\nu \overline{\frac{\partial u_i'}{\partial x_k} \frac{\partial u_j'}{\partial x_k}} \tag{2.61}$$

accounts for the destruction of kinetic energy by viscous effects. The usual scalar dissipation rate, denoted ε, is defined as

$$\varepsilon \equiv \frac{1}{2}\varepsilon_{ii}. \tag{2.62}$$

The last term in Eq. (2.57) vanishes in homogeneous turbulence. This term is expressed as a flux of a third order correlation tensor $\mathcal{D}_{ijk}$, which gathers triple velocity correlations, pressure-velocity terms and viscous diffusion terms:

$$\mathcal{D}_{ijk} = \overline{u_i' u_j' u_k'} + \frac{1}{\rho}\left(\delta_{jk}\overline{p' u_i'} + \delta_{ik}\overline{p' u_j'}\right) + \nu\left(\overline{u_i' \frac{\partial u_j'}{\partial x_k}} + \overline{u_j' \frac{\partial u_i'}{\partial x_k}}\right). \tag{2.63}$$

Its role is essential to spatial transfer of the turbulent kinetic energy (and anisotropy), which is created near a wall, away from it. It will be ignored, however, as far as strict statistical homogeneity will be assumed in this book.

Given the importance of $\mathcal{K} - \varepsilon$ model in engineering, together with the specific role of trace-free terms in the Reynolds stress equations, it is useful to introduce a trace-deviator decomposition for the Reynolds stress tensor

$$R_{ij} = 2\mathcal{K}\left(\frac{\delta_{ij}}{3} + b_{ij}\right), \quad \mathcal{K} = \frac{1}{2}R_{ii}, \quad b_{ij} = \frac{R_{ij}}{2\mathcal{K}} - \frac{\delta_{ij}}{3} \tag{2.64}$$

and to write the governing equations for both the kinetic energy $\mathcal{K}$ and the deviatoric, tracefree and dimensionless, anisotropy tensor b_{ij}.

The evolution equation for the kinetic energy derived from Eq. (2.57) is

$$\frac{\partial \mathcal{K}}{\partial t} + \overline{u}_k \frac{\partial \mathcal{K}}{\partial x_k} = \mathcal{P} - \varepsilon - \frac{\partial \mathcal{D}_k}{\partial x_k}, \tag{2.65}$$

and a similar equation is derived for b_{ij}. All the terms present in the Reynolds stress equation contribute to the equation for the kinetic energy, except the — traceless — pressure-strain tensor. The scalar production term $\mathcal{P} = \mathcal{P}_{ii}/2$ can be rewritten as

$$\mathcal{P} = -\mathcal{K}\left[\frac{1}{3}\left(\frac{\partial \overline{u}_i}{\partial x_j} + \frac{\partial \overline{u}_j}{\partial x_i}\right) + \left(\frac{\partial \overline{u}_i}{\partial x_k} b_{kj} + \frac{\partial \overline{u}_j}{\partial x_k} b_{ki}\right)\right]. \tag{2.66}$$

The deviatoric part of the dissipation tensor is either neglected or simply modelled similarly as the 'slow' part of the pressure-strain tensor. Only the scalar dissipation rate ε is considered as an independent variable, which is governed by its own equation. Since the exact evolution equation for ε is very complex, the model equation used in practice is obtained deriving the equation for $\dot{\varepsilon}/\varepsilon$ from the one for $\dot{\mathcal{K}}/\mathcal{K}$, which is much easier to derive.

The terms which appear in the evolution equations for Reynolds stress models in homogeneous turbulence can be exactly expressed as integrals in Fourier space of contributions derived from the second order spectral tensor $\hat{R}_{ij}$, which is the Fourier transform of double correlations at two point, and from the third-order 'transfer' spectral tensor T_{ij}, which involves the Fourier transform of two-point triple velocity correlations (see Sect. 2.5).

2.3.2 *The Mean Flow Consistent with Homogeneity Restricted to Fluctuations*

If we consider a mean flow, filling all the space, with space-uniform velocity gradients, which generalizes the solid body motion $\boldsymbol{u}^{(0)}$ introduced in Sect. 2.1.9:

$$\bar{u}_i(\boldsymbol{x}, t) = A_{ij}(t)x_j + u_i^0, \tag{2.67}$$

its presence can be consistent with statistical homogeneity for the fluctuating flow. This is a common background for homogeneous turbulence and recent linear stability analyses (see Craik and Criminale 1986, among others).[5] Equations (2.48) and (2.50) can be simplified by dropping the Reynolds stress term in both, so that (2.48) reduces to a particular Euler equation with solution of type (2.67). As a consequence, the trace-free matrix $\mathbf{A}$ is subjected to the condition that $d\mathbf{A}/dt + \mathbf{A}^2$ must be symmetric, or equivalently

$$\varepsilon_{ijk}\left(\frac{dA_{jk}}{dt} + A_{jn}A_{nk}\right) = 0 \quad A_{ii} = 0. \tag{2.68}$$

Irrotational mean flows, which are the flow with a symmetric gradient matrix $\mathbf{A}$, i.e. with $A_{ij} = A_{ji}$, are obvious solutions. Rotational mean flows yield more complicated linear solutions, and only the steady case has received much attention (Craik and coworkers, Bayly and coworkers performed recent developments in unsteady cases,

[5] It is important to stress that the feedback of the Reynolds stress tensor in (2.48) vanishes due to statistical homogeneity (zero gradient of any averaged quantity), so that the mean flow (2.67) has to be a particular solution of the Euler equations and can be considered as a base flow for stability analysis. In turn, the form (2.67) is consistent with the preservation of homogeneity of the fluctuating flow governed by (2.50) and (2.51), provided that homogeneity holds for the initial data. This explains why homogeneous RDT can have the same starting point as a rigorous and complete linear stability analysis in this case, before the random initialisation of the fluctuating velocity field is considered.

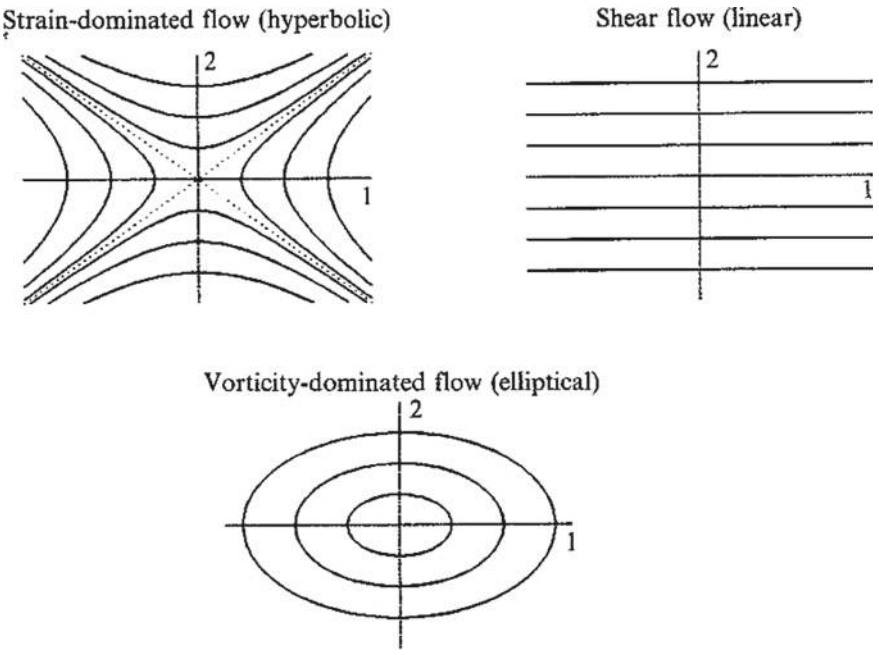

Fig. 2.1 Sketch of isovalues of the streamfunction for the steady mean flow in homogeneous RDT: the three canonical cases, **a** elliptical $\Omega^2 > S^2$, **b** hyperbolical $\Omega^2 < S^2$, **c** linear $\Omega^2 = S^2$

see e.g. Bayly et al. 1996). Conditions (2.68) imply that $\mathbf{A}$ writes as

$$\mathbf{A} = \begin{pmatrix} 0 & S-\Omega & 0 \\ S+\Omega & 0 & 0 \\ 0 & 0 & 0 \end{pmatrix} \tag{2.69}$$

in the steady, rotational case, when axes are chosen appropriately, where $S, \Omega \geq 0$. This corresponds to steady plane flows, combining vorticity 2Ω and irrotational straining S. The related (scalar here and related to the two-dimensional mean flow) streamfunction (sketched on Fig. 2.1) is

$$\Psi = \frac{S}{2}(x_1^2 - x_2^2) + \frac{\Omega}{2}(x_1^2 + x_2^2) \tag{2.70}$$

with $\overline{u}_i = \varepsilon_{i3j}\frac{\partial \Psi}{\partial x_j}$. The problem with arbitrary S and Ω was analysed in order to generalise classical RDT results, which were restricted to pure strain and pure shear. For $S > \Omega$, the mean flow streamlines are open and hyperbolic. For $S < \Omega$, the mean flow streamlines are closed and elliptic about the stagnation point at the origin. The limiting case, $S = \Omega$, correspond to pure shearing of straight mean streamlines (see Chap. 9 for fundamentals of RDT analysis).

2.3.3 *Homogeneous RST Equations. Briefs About Closure Methods*

Classical closure methods are now briefly addressed. The reader is referred to reference books for an exhaustive discussion about turbulence modelling, e.g. Piquet (2001). If we restrict our attention to homogeneous turbulence in the presence of mean velocity gradients previously defined, the Reynolds Stress tensor is *unsteady*: the steadiness of RST equations, often assumed in RANS methods, comes from the use of time averaging, and does not concern us here. Historically, basic concepts for deriving statistical closures were introduced in this unsteady homogeneous framework (Launder et al. 1975; Lumley 1975). The most difficult term to close in homogeneous turbulence is the linear (rapid) contribution to the pressure-strain tensor in Eqs. (2.57) and (2.60), which can be written as

$$\Pi_{ij}^{(r)} = 2A_{mn}\left(M_{inmj} + M_{jnmi}\right), \tag{2.71}$$

with

$$M_{ijpq} = \frac{1}{4\pi}\frac{\partial^2}{\partial r_p \partial r_q}\iiint \frac{1}{\mid \boldsymbol{r} - \boldsymbol{r}' \mid} R_{ij}(\boldsymbol{r}', t)d^3\boldsymbol{r}', \tag{2.72}$$

using Eqs. (2.53) and (2.54). A slightly different form of M_{ijpq} can be found in Launder et al. (1975), Lumley (1978). The alternative relationship for M_{ijpq} in Fourier space, more tractable from our viewpoint, will be given in Sect. 2.6.2, in exact agreement with, e.g., Kassinos et al. (2001). In general, there is no direct link between M_{ijpq} and the Reynolds Stress tensor, even if the identity $M_{ijpp} = R_{ij}$ holds, and the problem of closure arises from the two-point structure in Eq. (2.72). In classical closures, the non-dimensional tensor $M_{ijpq}/(2\mathcal{K})$ is sought as a tensorial function of the nondimensional deviatoric tensor b_{ij} defined in Eq. (2.64). Models range from linear (Launder et al. 1975) to cubic tensorial expansions.

Similarly, the slow pressure-strain tensor is assumed to be an isotropic tensorial function of b_{ij}. In the simplest version, $\Pi_{ij}^{(s)}$ is proportional to $-b_{ij}$, in agreement with an heuristic principle of return-to-isotropy.

Finally, the ε-equation is usually closed by pure analogy with the $\mathcal{K}$-equation. This can be understood considering the following evolution equations for their logarithmic derivatives:

$$\frac{1}{\mathcal{K}}\frac{d\mathcal{K}}{dt} = \frac{\mathcal{P}}{\mathcal{K}} - \frac{\varepsilon}{\mathcal{K}} \tag{2.73}$$

and

$$\frac{1}{\varepsilon}\frac{d\varepsilon}{dt} = C_{\varepsilon 1}\frac{\mathcal{P}}{\mathcal{K}} - C_{\varepsilon 2}\frac{\varepsilon}{\mathcal{K}}. \tag{2.74}$$

where $C_{\varepsilon 1}$ and $C_{\varepsilon 2}$ are two real arbitrary parameters, which are tuned to optimize the results on some very simple flows (e.g. decaying isotropic turbulence, homogeneous shear flow, turbulent flat-plate boundary layer, …) The first equation can be consid-

ered as exact in the homogeneous unsteady limit, if the production term, given by Eq. (2.66) is known (it derives from the Reynolds Stress tensor, but it is evaluated from simplified b_{ij}-models in linear and nonlinear $\mathcal{K}-\varepsilon$ models). On the other hand, the second equation is only a carbon copy of the first one, using two empirical constants, without linkage to the true enstrophy equation.

2.3.3.1 KRR's New Tensors

Even if the Reynolds Stress tensor is recovered in contracting the last two indices of M_{ijpq}, the closure of this whole tensor in terms of the Reynolds Stress tensor only is an heuristic method, which was questioned, especially in the presence of a rotational mean flow. In order to capture more of the components of M_{ijpq}, Kassinos, Reynolds and Rogers (see Kassinos et al. 2001) proposed to introduce a *Dimensionality tensor*

$$D_{pq} = M_{iipq}, \tag{2.75}$$

along with a *Circulicity tensor*, denoted F_{ij} in Kassinos et al. (2001) but f_{ij} here to avoid any confusion with the Cauchy matrix, and a *Stropholysis tensor* Q_{ijn}

$$f_{ij} = \varepsilon_{ipm}\varepsilon_{jqn}M_{mnpq}, \quad Q_{ijn} = \varepsilon_{ipq}M_{jqpn}, \tag{2.76}$$

with an alternative fully symmetrized version Q^*_{ijn}. In homogeneous turbulence, the circulicity tensor is not an independent one, in agreement with

$$f_{ij} = \mathcal{K}\delta_{ij} - D_{ij} - \overline{u'_i u'_j}. \tag{2.77}$$

Alternative definitions (also valid in inhomogeneous turbulence) were given by using a vector potential, or *turbulence stream function vector* ψ'_i, first introduced in Eq. (2.21), or

$$u'_i = \varepsilon_{imn}\psi'_{n,m},$$

so that

$$\overline{u'_i u'_j} = \varepsilon_{imn}\varepsilon_{ipq}\overline{\psi'_{n,m}\psi'_{q,p}}, \qquad D_{ij} = \overline{\psi'_{n,i}\psi'_{n,j}}, \qquad f_{ij} = \overline{\psi'_{i,n}\psi'_{j,n}}. \tag{2.78}$$

The reader is referred to Kassinos et al. (2001) for the definition of a last tensor, denoted C_{ij} and specifically inhomogeneous. As for M_{ijpq}, a new insight to this structure-based modelling will appear using spectral formalism.

2.4 Anisotropy in Physical Space. Single-Point Correlations

In single-point modelling used in RANS methods, the deviatoric part of the Reynolds stress tensor is used as the unique anisotropy indicator. An equation for b_{ij} is readily derived from (2.57), as the $\mathcal{K}$-equation (2.65).

The anisotropy tensor b_{ij} defined in Eq. (2.64) can be used to characterize the structure of the anisotropic flows. Following the Cayley–Hamilton theorem, one has

$$b_{ij}^3 + I_2 b_{ij} - I_3 \delta_{ij} = 0 \tag{2.79}$$

where the second and third invariants of the anisotropy tensor are defined as $I_2 = -b_{ij}b_{ji}/2$ and $I_3 = \det(b)$, respectively. It was shown by Lumley and Newman (1977) that all physically admissible turbulent flows are contained within a finite region (often referred to as the *Lumley triangle*) in the space spanned by I_2 and I_3 (or equivalently in the space spanned by the two non-vanishing eigenvalues of the anisotropy tensor). Each admissible point in the anisotropy map corresponds to a specific shape of the ellipsoid generated by the three diagonal components of the Reynolds stress tensor. The classification of the main anisotropy states was recently clarified by Simonsen and Krogstadt (2005). The main elements of the classification are summarized in Table 2.1 and illustrated in Fig. 2.2.

This analysis can be applied to any 'deviatoric' tensor, dimensionless and tracefree, derived from a definite-positive symmetrical tensor. The complete with possible prefactors in terms of $n!$, that are absorbed or not in the definition of extendees Lagrange polynomials. Definite-positive tensor, be the Reynolds stress tensor, the dimensionality tensor, yields three positive eigenvalues related to the orthogonal frame of eigenvectors (principal axes), which can be used instead of the λ_i

Table 2.1 Characteristics of Reynolds stress tensor and the anisotropy tensor. Adapted from Simonsen and Krogstad (2005)

State of turbulence	Invariants	Eigenvalues of b_{ij}	Shape of Reynolds stress ellipsoid
Isotropic	$I_2 = I_3 = 0$	$\lambda_1 = \lambda_2 = \lambda_3 = 0$	Sphere
Axisymmetric (one large λ_i)	$\frac{-I_2}{3} = \left(\frac{I_3}{2}\right)^{2/3}$	$0 < \lambda_1 < \frac{1}{3}$ $-\frac{1}{6} < \lambda_2 = \lambda_3 < 0$	Prolate spheroid
Axisymmetric (one small λ_i)	$\frac{-I_2}{3} = \left(-\frac{I_3}{2}\right)^{2/3}$	$0 < \lambda_1 < \frac{1}{3}$ $0 < \lambda_2 = \lambda_3 < \frac{1}{6}$	Oblate spheroid
One-component	$I_3 = \frac{2}{27}$ $I_2 = -\frac{1}{3}$	$\lambda_1 = \frac{2}{3}$ $\lambda_2 = \lambda_3 = -\frac{1}{3}$	Line
Two component (axisymmetric)	$I_3 = -\frac{1}{108}$ $I_2 = -\frac{1}{12}$	$\lambda_1 = -\frac{1}{3}$ $\lambda_2 = \lambda_3 = \frac{1}{6}$	Disk
Two component	$-\frac{I_2}{3} = \left(\frac{1}{27} + I_3\right)$	$\lambda_1 + \lambda_2 = \frac{1}{3}$ $\lambda_3 = -\frac{1}{3}$	Ellipsoid

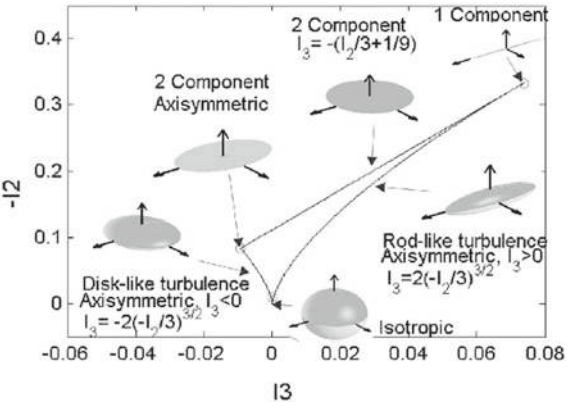

Fig. 2.2 Lumley's anisotropy invariant map and related Reynolds stress ellipsoids. Admissible turbulent states are located inside the triangle-like subdomain. From Simonsen and Krogstad (2005), with permission of the AIP

eigenvalues. Many instances will be given throughout this book, including structure-based modelling and spectral tensors as well.

Note that the initial reference to dimensionality (1D, 2D) for discussing the Lumley invariant map was confusing, because the Reynolds stress tensor gives only access to componentiality. This was partly clarified by Kassinos et al. (2001), and the concepts of dimensionality and componentiality for single-point structure tensors can be exactly derived from the irreducible decomposition of the spectral (or two-point) tensor of second-order velocity correlations in terms of directional anisotropy and polarization anisotropy.

2.5 Spectral Analysis, from Random Fields to Two-Point Correlations. Local Frame, Helical Modes

2.5.1 Second Order Statistics

Regarding homogeneous turbulence, we aim at taking into account the possible distorting effects of a mean flow defined by Eqs. (2.67) and (2.68), or effects of body forces, so that anisotropy is essential. Therefore, the emphasis is put on *Homogeneous Anisotropic Turbulence* (HAT). The Fourier transform is a valuable tool to handle equations for velocity and pressure fluctuations, considered as random variables, as well as their statistical multipoint correlations matrices. The relations between second-order tensors defined in both physical and Fourier spaces are displayed in Fig. 2.3.

The inverse Fourier transform which connects $\boldsymbol{u}'$ to $\hat{\boldsymbol{u}}$ is expressed as

$$u_i'(\boldsymbol{x}, t) = \int \hat{u}_i(\boldsymbol{k}, t) \exp(\imath \boldsymbol{k} \cdot \boldsymbol{x}) \, d^3\boldsymbol{k}. \tag{2.80}$$

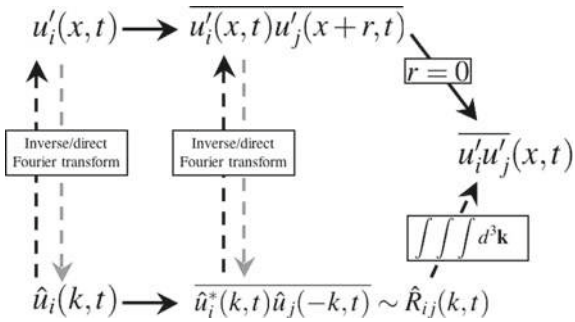

Fig. 2.3 Schematic view of the relations which exist between second-order tensors defined in both physical and Fourier spaces

Applying it to the two-point correlation tensor, one obtains

$$\overline{u_i'(\boldsymbol{x},t)u_j'(\boldsymbol{x}+\boldsymbol{r},t)} = \int \hat{R}_{ij}(\boldsymbol{k},t)\exp(\imath\boldsymbol{k}\cdot\boldsymbol{r})d^3\boldsymbol{k}. \tag{2.81}$$

One may recall here that the direct Fourier transform writes

$$\hat{R}_{ij}(\boldsymbol{k},t) = \frac{1}{(2\pi)^3}\int R_{ij}(\boldsymbol{r},t)\exp(-\imath\boldsymbol{k}\cdot\boldsymbol{r})d^3\boldsymbol{r}. \tag{2.82}$$

It is worth noting that the prefactor $1/(2\pi)^3$ appears in Eq. (2.82), and not in Eq. (2.81). According to (2.81), the Reynolds Stress tensor, which is obtained by setting $\boldsymbol{r}=\boldsymbol{0}$ in R_{ij}, derives from its spectral counterpart $\hat{\mathbf{R}}$ through a 3D integral

$$\overline{u_i'(\boldsymbol{x},t)u_j'(\boldsymbol{x},t)} = \int \hat{R}_{ij}(\boldsymbol{k},t)d^3\boldsymbol{k}. \tag{2.83}$$

The last interesting equation is

$$\overline{\hat{u}_i^*(\boldsymbol{p},t)\hat{u}_j(\boldsymbol{k},t)} = \hat{R}_{ij}(\boldsymbol{k},t)\delta^3(\boldsymbol{k}-\boldsymbol{p}). \tag{2.84}$$

Two alternative ways can be used to derive evolution equations for statistical quantities in spectral space. On the one hand, an equation for $\overline{u_i'(\boldsymbol{x},t)u_j'(\boldsymbol{x}+\boldsymbol{r},t)}$ can be derived by first using Eq. (2.50) and then obtaining the equation for $\hat{R}_{ij}$, by applying (2.82), following Craya and Oberlack (2001). On the other hand, an equation for $\hat{u}_i(\boldsymbol{k},t)$ can be directly obtained in Fourier space, from which the equation for $\hat{R}_{ij}$ is derived using Eq. (2.84). At least in homogeneous turbulence, the second way is simpler since the pressure term can be solved in the simplest way in the equation for $\hat{u}_i$. As a consequence, it will be used in the following. The first way (Craya 1958), even if more cumbersome, has the advantage of applying Fourier-transform only on statistical (smooth) quantities, without need for distribution theory. The reader

is referred to Batchelor (1953) and to Chap. 6 of Mathieu and Scott (2000) for a detailed analysis of Fourier expansions of both random variables and their statistical moments and their limit in an infinite box.

2.5.2 Poloidal-Toroidal Decomposition, and Craya–Herring Frame of Reference

The simplified *poloidal-toroidal decomposition* was given by Eq. (2.25). It is used to represent a three-component divergence-free velocity field in terms of two independent scalar terms, taking advantage of the presence of a privileged direction $\boldsymbol{n}$:

$$\boldsymbol{u}' = \underbrace{\boldsymbol{\nabla} \times (s'_{tor}\boldsymbol{n})}_{toroidal\ part} + \underbrace{\boldsymbol{\nabla} \times [\boldsymbol{\nabla} \times (s'_{pol}\boldsymbol{n})]}_{poloidal\ part}.$$

The axial vector $\boldsymbol{n}$ is chosen (Chandrasekhar 1981) along the vertical direction, without loss of generality. As a caveat, some care is needed to represent *vertically sheared horizontal flows* (VSHF) (as coined in Smith and Waleffe 2002) which are defined as $\boldsymbol{u}' = \boldsymbol{u}'(\boldsymbol{x} \cdot \boldsymbol{n}, t)$ with $\boldsymbol{u}' \cdot \boldsymbol{n} = 0$.

In Fourier space, the above decomposition yields a pure geometrical representation

$$\hat{\boldsymbol{u}} = \underbrace{\boldsymbol{k} \times \boldsymbol{n}(\imath \hat{s}_{tor})}_{toroidal\ mode} - \underbrace{\boldsymbol{k} \times (\boldsymbol{k} \times \boldsymbol{n})(\hat{s}_{pol})}_{poloidal\ mode} \tag{2.85}$$

and it appears immediately that the Fourier mode related to the vertical wavevector direction, $\boldsymbol{k} \parallel \boldsymbol{n}$, has zero contribution. This gap in the spectral description precludes the capture of the VSHF mode in physical space. In order to cure this problem, one can define an orthonormal frame of reference, which is nothing but the local reference frame of a polar-spherical system of coordinates for $\boldsymbol{k}$ (see Fig. 2.4)

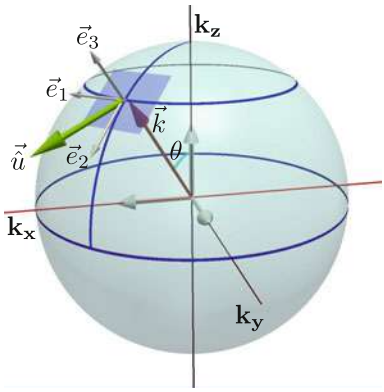

Fig. 2.4 Polar-spherical system of coordinates for $\boldsymbol{k}$ and related 'Craya–Herring' frame of reference

$$\boldsymbol{e}^{(1)} = \frac{\boldsymbol{k} \times \boldsymbol{n}}{|\boldsymbol{k} \times \boldsymbol{n}|}, \quad \boldsymbol{e}^{(2)} = \boldsymbol{e}^{(3)} \times \boldsymbol{e}^{(1)}, \quad \boldsymbol{e}^{(3)} = \frac{\boldsymbol{k}}{k} \tag{2.86}$$

with $\boldsymbol{k} \times \boldsymbol{n} \neq 0$. Local frame vectors $\boldsymbol{e}^{(1)}, \boldsymbol{e}^{(2)}, \boldsymbol{e}^{(3)}$ may coincide with the fixed frame of reference, with $\boldsymbol{e}^{(3)} = \boldsymbol{n}$ for $\boldsymbol{k} \parallel \boldsymbol{n}$. In the turbulence community, the local frame $(\boldsymbol{e}^{(1)}, \boldsymbol{e}^{(2)})$ of the plane normal to the wave vector is often referred to as *Craya–Herring frame*. Accordingly, the divergence-free velocity field in Fourier space has only two components in the Craya–Herring frame

$$\hat{\boldsymbol{u}}(\boldsymbol{k}, t) = u^{(1)} \boldsymbol{e}^{(1)} + u^{(2)} \boldsymbol{e}^{(2)}. \tag{2.87}$$

For $\boldsymbol{k} \times \boldsymbol{n} \neq 0$, $u^{(1)}$ and $u^{(2)}$ are directly linked to the *toroidal mode* and the *poloidal mode*, respectively. For $\boldsymbol{k} \times \boldsymbol{n} = 0$, they correspond to the VSHF mode. For the vorticity fluctuation, a similar decomposition is found:

$$\hat{\omega}_i(\boldsymbol{k}, t) = \imath k \left(u^{(1)} e_i^{(2)} - u^{(2)} e_i^{(1)} \right), \tag{2.88}$$

so that $u^{(1)}$ and $u^{(2)}$ are directly related to the spectral counterparts of Orr–Sommerfeld/Squires variables: $\hat{\omega}_3 = -k_\perp u^{(1)}$ for ω_3' and $-k^2 \hat{u}_3 = -k k_\perp u^{(2)}$ for $\nabla^2 u_3'$, with $k_\perp = |\boldsymbol{k} \times \boldsymbol{n}|$. A similar decomposition is used in Bayly et al. (1996). Finally, the *wave-vortex decomposition* introduced in Riley et al. (1981) in the particular context of stably stratified turbulence (see Chap. 10), is also a particular case of Eq. (2.25).

Rapid Distortion Theory equations (and fully nonlinear ones, too) can be written in the Craya–Herring frame, resulting in a reduced Green's function with only four independent components (Cambon 1982). Details will be given in next Sect. 2.5.7, then in next chapters, in which RDT solutions are discussed.

The poloidal-toroidal decomposition gives access, for instance, to the potential vector in Eq. (2.21) as

$$\psi_i' = s_{tor}' n_i + \varepsilon_{ipq} \frac{\partial s_{pol}'}{\partial x_p} n_q. \tag{2.89}$$

The usual way to recover the two scalar functions s_{pol}' and s_{tor}' from the solenoidal velocity field is not recalled here for the sake of brevity.

2.5.2.1 Towards Vectorial Spherical Harmonics

The Craya–Herring decomposition, as a spectral counterpart of the simplified toroidal-poloidal decomposition is used throughout this book, with several variants. The problem of expanding a vector field in terms of spherical harmonics, however, cannot be solved using Eq. (2.25). For this purpose, the alternative way of using vectorial spherical harmonics given by Chandrasekhar (1981), Rieutord (1987) is now introduced and discussed. Expansion of the scalar field in terms of spherical

harmonics is well known. Using a system of polar-spherical coordinates (r, θ, ϕ) for any scalar s, e.g. in physical space, the SSH (Scalar Spherical Harmonics) $Y_n^m(\theta, \phi)$ use extended Legendre polynomials $P_n^{|m|}$ as follows

$$s(r, \theta, \phi) = \sum_{n=0}^{N} \sum_{m=-n}^{m=n} s_n^m(r) P_n^{|m|}(\theta) \exp(\imath m \phi), \tag{2.90}$$

with possible prefactors in terms of $n!$, that are absorbed or not in the definition of extended Legendre polynomials. What about a vector (or tensorial) field? One may immediately extend expansions in terms of SSH to toroidal and poloidal potentials in Eq. (2.25) . . . but the problem of null contribution to the "pole" ($\boldsymbol{r} \parallel \boldsymbol{n}$) rears its ugly head! Following the study by Rieutord (1987), a different toroidal mode is defined as

$$\boldsymbol{u}^{(tor)} = \boldsymbol{\nabla} \times (s''(\boldsymbol{r})\boldsymbol{r}/r), \tag{2.91}$$

with a related expansion in terms of vectorial spherical harmonics

$$\boldsymbol{u}^{(tor)}(r, \theta, \phi) = \sum_{n=0}^{N} \sum_{m=-n}^{n} w_n^m(r) \boldsymbol{\nabla} \times \left(Y_n^m(\theta, \phi) \frac{\boldsymbol{r}}{r} \right).$$

Details on the rest of the decomposition, with a spheroidal field for $\boldsymbol{u}$, or $\boldsymbol{u} - \boldsymbol{u}^{(tor)}$, also related to an extended poloidal field (Chandrasekhar 1981; Rieutord 1987), is not given here for the sake of brevity. Let us retain only that the radial vector of the polar-spherical system of coordinates is used for defining the toroidal field instead of the polar axis. The problem of the "hole in the pole" is solved, but translation in Fourier space raises new difficulties. An expansion of a scalar field, from $s(r, \theta, \phi)$ in physical space to $\hat{s}(k, \theta_k, \phi_k)$ in 3D Fourier space is very simple, using the same SSH. On the other hand, the counterpart of basis of the vectorial spherical harmonics should use a modified toroidal field as

$$\hat{\boldsymbol{u}}^{(tor)} = \boldsymbol{k} \times \left(\frac{\partial s'''(\boldsymbol{k})}{\partial \boldsymbol{k}} \right),$$

with a *differential operator*, now contaminating the 3D Fourier space representation, that is purely algebraic with the Craya–Herring decompositions and its variants. Accordingly the vectorial spherical harmonics (VSH) decomposition deserves further investigation, but it brings out new difficulties. Keeping in mind the invaluable role of Fourier decomposition in HAT, we will continue to privilegiate the Craya–Herring decomposition and its variants in the following.

2.5.3 The Helical Mode Decomposition

This decomposition is an alternative to the Craya–Herring decomposition, and presents some advantages regarding frame-invariance properties, treatment of background nonlinearity, and rotating turbulence. The *helical modes* are defined from

$$N_i(\boldsymbol{k}) = e_i^{(2)}(\boldsymbol{k}) - \imath e_i^{(1)}(\boldsymbol{k}) \tag{2.92}$$

so that the solenoidal velocity field in Fourier space is decomposed as

$$\hat{\boldsymbol{u}}(\boldsymbol{k}, t) = \xi_+(\boldsymbol{k}, t)\boldsymbol{N}(\boldsymbol{k}) + \xi_-(\boldsymbol{k}, t)\boldsymbol{N}(-\boldsymbol{k}). \tag{2.93}$$

The definition above is the same as in the Cambon's thesis (1982). It was used in all the subsequent papers (e.g. Cambon and Jacquin 1989) from the same team. Particularly, this definition ensures Hermitian symmetry

$$\boldsymbol{N}(-\boldsymbol{k}) = \boldsymbol{N}^*(\boldsymbol{k})$$

since $\boldsymbol{e}^{(1)}(-\boldsymbol{k}) = -\boldsymbol{e}^{(1)}(\boldsymbol{k})$ and $\boldsymbol{e}^{(2)}(-\boldsymbol{k}) = \boldsymbol{e}^{(2)}(\boldsymbol{k})$. The most useful property is

$$\imath\boldsymbol{k} \times \boldsymbol{N} = k\boldsymbol{N}, \tag{2.94}$$

which means that $\boldsymbol{N}e^{\imath\boldsymbol{k}\cdot\boldsymbol{x}}$ and its complex conjugate are eigenmodes of the *Curl* operator. Accordingly, the vorticity fluctuation in Fourier space is written as

$$\hat{\omega}_i(\boldsymbol{k}, t) = k\left(\xi_+(\boldsymbol{k}, t)N_i(\boldsymbol{k}) - \xi_-(\boldsymbol{k}, t)N_i(-\boldsymbol{k})\right). \tag{2.95}$$

Helical modes (2.92) were also used by Waleffe (1992). Only looking at the literature from the turbulence community, similar modes were introduced in the 1970s as *helicity waves* (Uriel Frish and Marcel Lesieur, private communication), but they were not used to get simplified dynamical equations.

Key elements of three spectral decompositions presented above are summarized in Table 2.2.

2.5.4 On the Use of Projection Operators

Even when pure incompressible flows are considered, the solenoidal property for the velocity field is not satisfied by some terms in the governing equations, so that projection onto a solenoidal subspace is needed. The Helmholtz decomposition, which was addressed in Sect. 2.1.5, with Eq. (2.21) can be used in a simple way to define longitudinal and transverse projection operators.

Table 2.2 Local frame of reference in the Fourier space. The general form is $\hat{\mathbf{u}}(\boldsymbol{k},t) = \chi_1(t)\boldsymbol{V}_1(\boldsymbol{k}) + \chi_2(t)\boldsymbol{V}_2(\boldsymbol{k})$, where $(\boldsymbol{V}_1(\boldsymbol{k}), \boldsymbol{V}_2(\boldsymbol{k}))$ is a local frame in the plane orthogonal to $\boldsymbol{k}$ This local basis is supplement by a third vector $\boldsymbol{V}_3$. The vector $\boldsymbol{n}$ is an arbitrary parameter in the three decompositions

Decomposition name	$\boldsymbol{V}_3(\boldsymbol{k})$	$\boldsymbol{V}_1(\boldsymbol{k})$	$\boldsymbol{V}_2(\boldsymbol{k})$
Poloidal-toroidal	$\boldsymbol{n}$	$\imath\boldsymbol{k}\times\boldsymbol{n}$	$-\boldsymbol{k}\times(\boldsymbol{k}\times\boldsymbol{n})$
Craya–Herring	$\dfrac{\boldsymbol{k}}{k}$	$\dfrac{\boldsymbol{k}\times\boldsymbol{n}}{\lvert\boldsymbol{k}\times\boldsymbol{n}\rvert}$	$\dfrac{\boldsymbol{k}}{k}\times\dfrac{\boldsymbol{k}\times\boldsymbol{n}}{\lvert\boldsymbol{k}\times\boldsymbol{n}\rvert}$
Helical	$\dfrac{\boldsymbol{k}}{k}$	$\dfrac{\boldsymbol{k}}{k}\times\dfrac{\boldsymbol{k}\times\boldsymbol{n}}{\lvert\boldsymbol{k}\times\boldsymbol{n}\rvert} - \imath\dfrac{\boldsymbol{k}\times\boldsymbol{n}}{\lvert\boldsymbol{k}\times\boldsymbol{n}\rvert}$	$\dfrac{\boldsymbol{k}}{k}\times\dfrac{\boldsymbol{k}\times\boldsymbol{n}}{\lvert\boldsymbol{k}\times\boldsymbol{n}\rvert} + \imath\dfrac{\boldsymbol{k}\times\boldsymbol{n}}{\lvert\boldsymbol{k}\times\boldsymbol{n}\rvert}$

A simple geometric decomposition is obvious for any vector $\boldsymbol{V}$ into a component along a given direction spanned by a unit vector $\boldsymbol{a}$ and a component contained in the plane normal to $\boldsymbol{a}$

$$\boldsymbol{V} = \boldsymbol{V}^{\parallel} + \boldsymbol{V}^{\perp},$$

with $\boldsymbol{V}^{\parallel} = (\boldsymbol{V}\cdot\boldsymbol{a})\boldsymbol{a}$ and, by difference $\boldsymbol{V}^{\perp} = \boldsymbol{V} - (\boldsymbol{V}\cdot\boldsymbol{a})\boldsymbol{a}$. This decomposition brings in two projection matrices, $P^{\parallel}_{ij} = a_i a_j$, with $V_i^{\parallel} = P^{\parallel}_{ij}V_j$, and $P^{\perp}_{ij} = \delta_{ij} - a_i a_j$ with $V_i^{\perp} = P^{\perp}_{ij}V_j$.

If we now consider $\boldsymbol{V}(\boldsymbol{k})$ as the Fourier transform of any term in the background equation which governs $\hat{\boldsymbol{u}}$, and set $\boldsymbol{a}$ equal to the unit vector along $\boldsymbol{k}$, i.e. $a_i = k_i/k$, the above geometric decomposition gives a simplified instance of the Helmholtz decomposition. Accordingly,

$$V_i^{\parallel}(\boldsymbol{k}) = \frac{k_i k_j}{k^2} V_i(\boldsymbol{k})$$

corresponds to the projection onto the *dilatational mode*, and

$$V_i^{\perp}(\boldsymbol{k}) = \left(\delta_{ij} - \frac{k_i k_j}{k^2}\right) V_j(\boldsymbol{k})$$

corresponds to the projection onto the *solenoidal mode*. This immediately suggests to define a longitudinal projection operator

$$P^{\parallel}_{ij} = \frac{k_i k_j}{k^2} \tag{2.96}$$

and a transverse projection operator as

$$P^{\perp}_{ij} = \delta_{ij} - \frac{k_i k_j}{k^2}. \tag{2.97}$$

Let us consider the generic model equation, Eq. (2.22)

$$\frac{\partial u_i'}{\partial t} + S_i + \frac{\partial p'}{\partial x_i} = 0$$

with a solenoidal $\boldsymbol{u}'$ and an arbitrary term S_i. Its counterpart in Fourier space is

$$\frac{\partial \hat{u}_i}{\partial t} + \hat{S}_i + \imath k_i \hat{p} = 0,$$

and the solenoidal property is replaced by the condition that $\hat{\boldsymbol{u}}$ and $\boldsymbol{k}$ are orthogonal. Application of the longitudinal projection operator yields

$$P_{ij}^{\parallel} \hat{u}_j = 0,$$

and

$$P_{ij}^{\parallel} \hat{S}_j + \imath k_i \hat{p} = 0,$$

which corresponds to the Poisson equation for the pressure term, whereas the transverse projection operator gives

$$P_{ij}^{\perp} \hat{u}_j = \hat{u}_i$$

and

$$\frac{\partial \hat{u}_i}{\partial t} + P_{ij}^{\perp} \hat{S}_i = 0.$$

The latter equation is a pure solenoidal equation, which no longer includes the pressure term. Putting the emphasis on solenoidal turbulence, only the latter form of the dynamical equation is useful (as far as the specific information on the pressure term is not needed), and only the tranverse projection operator $P^{\perp}(\boldsymbol{k})$ is needed. For the sake of simplicity the adjective 'transverse' and the superscript $^{\perp}$ will be omitted from now on. Of course, the projection operator has a simple expression in terms of Craya–Herring and helical modes

$$P_{ij} = e_i^{(1)} e_j^{(1)} + e_i^{(2)} e_j^{(2)} = \Re \left(N_i N_j^* \right). \tag{2.98}$$

The decomposition of an arbitrary vector field $\boldsymbol{V}(\boldsymbol{k})$, which is not a priori divergence-free, requires the use of the three vectors $(\boldsymbol{e}^{(1)}, \boldsymbol{e}^{(2)}, \boldsymbol{e}^{(3)})$ of the Craya–Herring base, with $e_i^{(3)} = k_i / k$. One recovers here the fact that the third component is related to the dilatational mode (which is a one-dimensional mode in the local reference frame) and that the first two components represent the solenoidal mode (which is a priori two-dimensional in the local reference frame), in agreement with both the Helmholtz and toroidal-poloidal decompositions in physical space.

2.5.5 Nonlinear Dynamics

Considering a mean flow which preserves the statistical homogeneity of the fluctuating motion, the nonlinear equation (2.50) can be recast as follows

$$\hat{\widehat{u}}_i + M_{ij}\widehat{u}_j = s_i - \nu k^2 \widehat{u}_i, \tag{2.99}$$

where

$$\hat{\widehat{u}}_i = \frac{\partial \hat{u}_i}{\partial t} + \frac{\partial \hat{u}_i}{\partial k_m}\frac{dk_m}{dt} = \frac{\partial \hat{u}_i}{\partial t} - A_{lm}k_l \frac{\partial \hat{u}_i}{\partial k_m} \tag{2.100}$$

is related to linear advection by the mean flow (see Eq. (2.67)), and $M_{ij} = A_{mj}(\delta_{im} - 2k_i k_m/k^2)$ gathers linear distortion and pressure terms (see Chap. 8). Once nonlinear and viscous terms have been summed, Eq. (2.99) generalises the linear inviscid equation.

The nonlinear term s_i is given by

$$s_i(\boldsymbol{k}, t) = -\imath P_{ijk}(\boldsymbol{k}) \int_{\mathbf{p}+\mathbf{q}=\mathbf{k}} \widehat{u}_j(\mathbf{p}, t)\widehat{u}_k(\mathbf{q}, t) d^3\mathbf{p}, \tag{2.101}$$

in which the third-order tensor $P_{ijk} = \frac{1}{2}(P_{ij}k_k + P_{ik}k_j)$ arises from the elimination of pressure using the incompressibility condition $k_i \widehat{u}_i(\boldsymbol{k}, t) = 0$, in agreement with the use of the projection operator (2.97) as discussed in the previous subsection.

The equations (2.99)–(2.101) are completely generic, and hold for other cases, including body forces and additional random variables. This is achieved in a straightforward manner only changing the matrix $\mathbf{M}$ of the linear operator, and/or the influence matrix P_{ijk} in the convolution product which reflects quadratic nonlinearity. The evolution equation for $\hat{R}_{ij}$ (Craya 1958) derived from Eqs. (2.84) and (2.99) is

$$\dot{\hat{R}}_{ij} + M_{ik}\hat{R}_{kj} + M_{jk}\hat{R}_{ik} = T_{ij} - 2\nu k^2 \hat{R}_{ij}, \tag{2.102}$$

where the left-hand side arises from the linear inviscid part of Eq. (2.99). The term $\dot{\hat{R}}_{ij}$ is a convective time derivative in $\boldsymbol{k}$-space with distortion components. The second term in the right-hand-side is the spectral counterpart of the dissipation tensor. The generalized transfer tensor T_{ij} is mediated by nonlinearity as

$$< \hat{u}_i^*(\boldsymbol{p}, t)s_j(\boldsymbol{k}, t) + s_i^*(\boldsymbol{p}, t)\hat{u}_j(\boldsymbol{k}, t) >= T_{ij}(\boldsymbol{k}, t)\delta(\boldsymbol{p} - \boldsymbol{k}). \tag{2.103}$$

This tensor involves triple velocity correlations as shown by Eq. (2.101) for s_i. More details on it will be given in Chap. 4.

Although the purely linear theory closes the equations and simplifies mathematical analysis, its domain of applicability is rather limited since it neglects all interactions of turbulence with itself, including the physically important cascade process. Multipoint turbulence models which account for nonlinearity via closure lead to moment

equations with a well-defined linear operator and nonlinear source terms. The view taken in this chapter is that, even when nonlinearity is significant, the behaviour of the linear part of the model often has a significant influence. Thus, it is important to first understand the properties of the linearised model. An additional interesting output of the linearised analysis is that it often allows for the definition of a simplified formulation of the nonlinear model using more appropriate variables.

2.5.6 *Background Nonlinearity in the Different Reference Frames*

Equations given in Sect. 2.5.5 express background linear and nonlinear terms in three-dimensional Fourier space. They can be rewritten in the different local reference frames introduced above (results are summarized in Table 2.3).

In the Craya–Herring frame of reference, the $\hat{\boldsymbol{u}}$ vector with three components is replaced by the $u^{(\alpha)}$ vector which has two components, and Eq. (2.99) becomes

$$\dot{u}^{(\alpha)} + m_{\alpha\beta} u^{(\beta)} = -\imath \int_{\boldsymbol{p}+\boldsymbol{q}=\boldsymbol{k}} P_{\alpha\beta\gamma} u^{(\beta)}(\boldsymbol{p},t) u^{(\gamma)}(\boldsymbol{q},t) d^3\boldsymbol{p}, \tag{2.104}$$

with

$$m_{\alpha\beta}(\boldsymbol{k}) = e_i^{(\alpha)} M_{ij} e_j^{(\beta)} - \dot{e}_i^{(\alpha)} e_j^{(\beta)} \tag{2.105}$$

and Chandrasekhar (1981)

$$\begin{aligned} P_{\alpha\beta\gamma}(\boldsymbol{k},\boldsymbol{p}) = \frac{k}{2} \big[& (\boldsymbol{e}^{(\alpha)}(\boldsymbol{k}) \cdot \boldsymbol{e}^{(\beta)}(\boldsymbol{p}))(\boldsymbol{e}^{(3)}(\boldsymbol{k}) \cdot \boldsymbol{e}^{(\gamma)}(\boldsymbol{q})) \\ & + (\boldsymbol{e}^{(\alpha)}(\boldsymbol{k}) \cdot \boldsymbol{e}^{(\gamma)}(\boldsymbol{q}))(\boldsymbol{e}^{(3)}(\boldsymbol{k}) \cdot \boldsymbol{e}^{(\beta)}(\boldsymbol{p})) \big]. \end{aligned} \tag{2.106}$$

More details will be given in Chaps. 4 and 10. Using the helical modes decomposition, with $\xi_s = (1/2)\hat{\boldsymbol{u}}_i(\boldsymbol{k}) N_i(-s\boldsymbol{k})$, the background equation (2.104) becomes

$$\dot{\xi}_s + m_{ss'} \xi_{s'} = -\imath \int_{\boldsymbol{p}+\boldsymbol{q}=\boldsymbol{k}} P_{ss's''} \xi_{s'}(\boldsymbol{p},t) \xi_{s''}(\boldsymbol{q},t) d^3\boldsymbol{p}, \tag{2.107}$$

with

$$m_{ss'}(\boldsymbol{k}) = (1/2) N_i(-s\boldsymbol{k}) M_{ij} N_j(s'\boldsymbol{k}) - (1/2) \dot{N}_i(-s\boldsymbol{k}) N_j(s'\boldsymbol{k}) \tag{2.108}$$

and

$$\begin{aligned} M_{ss's''} = \frac{k}{4} \big[& (\boldsymbol{N}(-s\boldsymbol{k}) \cdot \boldsymbol{N}(s'\boldsymbol{p}))(\boldsymbol{e}^{(3)}(\boldsymbol{k}) \cdot \boldsymbol{N}(s''\boldsymbol{q})) \\ & + (\boldsymbol{N}(-s\boldsymbol{k}) \cdot \boldsymbol{N}(s''\boldsymbol{q}))(\boldsymbol{e}^{(3)}(\boldsymbol{k}) \cdot \boldsymbol{N}(s'\boldsymbol{p})) \big]. \end{aligned} \tag{2.109}$$

Table 2.3 Expressions of the nonlinear momentum equation in both fixed Cartesian and local (Craya–Herring, helical) reference frames in Fourier space. The tensor M_{ij} accounts for linear convective and pressure terms: $M_{ij} = A_{mj}(\delta_{im} - 2k_i k_m/k^2)$, where $A_{ij} = \partial \bar{u}_i/\partial x_j$

Reference frame	Convective term	Equation
Fixed Cartesian		$\dot{\widehat{u}}_i + M_{ij}\widehat{u}_j = s_i$
		$M_{ij}(\boldsymbol{k}) = A_{mj}(\delta_{im} - 2k_i k_m/k^2)$
	Conservative	$s_i(\boldsymbol{k}) = -\imath P_{ijk}(\boldsymbol{k}) \int_{\mathbf{p}+\mathbf{q}=\mathbf{k}} \widehat{u}_j(\mathbf{p},t)\widehat{u}_k(\mathbf{q},t)d^3\mathbf{p}$
Craya–Herring		$\dot{u}^{(\alpha)} + m_{\alpha\beta}u^{(\beta)} = -\imath \int_{\boldsymbol{p}+\boldsymbol{q}=\boldsymbol{k}} P_{\alpha\beta\gamma}u^{(\beta)}(\boldsymbol{p},t)u^{(\gamma)}(\boldsymbol{q},t)d^3\boldsymbol{p}$
		$m_{\alpha\beta}(\boldsymbol{k}) = e_i^{(\alpha)}M_{ij}e_j^{(\beta)} - \dot{e}_i^{(\alpha)}e_j^{(\beta)}$
	Conservative	$P_{\alpha\beta\gamma}(\boldsymbol{k},\boldsymbol{p}) = \frac{k}{2}\left[(\boldsymbol{e}^{(\alpha)}(\boldsymbol{k})\cdot\boldsymbol{e}^{(\beta)}(\boldsymbol{p}))(\boldsymbol{e}^{(3)}(\boldsymbol{k})\cdot\boldsymbol{e}^{(\gamma)}(\boldsymbol{q})) + (\boldsymbol{e}^{(\alpha)}(\boldsymbol{k})\cdot\boldsymbol{e}^{(\gamma)}(\boldsymbol{q}))(\boldsymbol{e}^{(3)}(\boldsymbol{k})\cdot\boldsymbol{e}^{(\beta)}(\boldsymbol{p}))\right]$
	Rotational	$P_{\alpha\beta\gamma} = \frac{1}{2}\varepsilon_{\beta\delta 3}e^{(\alpha)}(\boldsymbol{k})\cdot\left(qe^{(\delta)}(\boldsymbol{p})\times e^{(\gamma)}(\boldsymbol{q}) + pe^{(\delta)}(\boldsymbol{q})\times e^{(\gamma)}(\boldsymbol{p})\right)$
Helical modes		$\dot{\xi}_s + m_{ss'}\xi_{s'} = -\imath \int_{\boldsymbol{p}+\boldsymbol{q}=\boldsymbol{k}} M_{ss's''}\xi_{s'}(\boldsymbol{p},t)\xi_{s''}(\boldsymbol{q},t)d^3\boldsymbol{p}$
		$m_{ss'}(\boldsymbol{k}) = (1/2)N_i(-s\boldsymbol{k})M_{ij}N_j(s'\boldsymbol{k}) - (1/2)\dot{N}_i(-s\boldsymbol{k})N_j(s'\boldsymbol{k})$
	Conservative	$M_{ss's''} = \frac{k}{4}\left[(\boldsymbol{N}(-s\boldsymbol{k})\cdot\boldsymbol{N}(s'\boldsymbol{p}))(\boldsymbol{e}^{(3)}(\boldsymbol{k})\cdot\boldsymbol{N}(s''\boldsymbol{q})) + (\boldsymbol{N}(-s\boldsymbol{k})\cdot\boldsymbol{N}(s''\boldsymbol{q}))(\boldsymbol{e}^{(3)}(\boldsymbol{k})\cdot\boldsymbol{N}(s'\boldsymbol{p}))\right]$
	Rotational	$M_{ss's''} = \frac{1}{2}(s'p - s''q)\boldsymbol{N}(-s\boldsymbol{k})\cdot\left(\boldsymbol{N}(s'\boldsymbol{p})\times\boldsymbol{N}(s''\boldsymbol{q})\right)$

The signs s, s', s'' take only the values ± 1, and the Einstein convention on repeated indices is used. The last equation will be revisited in Chaps. 4 and 10.

It is worth noting that Eqs. (2.106) and (2.109) directly use the expression of the basic nonlinearity as the solenoidal part of $\boldsymbol{\nabla}(\boldsymbol{u} \otimes \boldsymbol{u})$. A very interesting variant is obtained starting from the solenoidal part of $\boldsymbol{\omega} \times \boldsymbol{u}$ (e.g. Waleffe 1992). The counterpart of (2.106) is

$$P_{\alpha\beta\gamma} = \frac{1}{2}\varepsilon_{\beta\delta 3} e^{(\alpha)}(\boldsymbol{k}) \cdot \left(q e^{(\delta)}(\boldsymbol{p}) \times e^{(\gamma)}(\boldsymbol{q}) + p e^{(\delta)}(\boldsymbol{q}) \times e^{(\gamma)}(\boldsymbol{p}) \right), \tag{2.110}$$

whereas the counterpart of (2.109) is

$$M_{ss's''} = \frac{1}{2}(s'p - s''q)\boldsymbol{N}(-s\boldsymbol{k}) \cdot \left(\boldsymbol{N}(s'\boldsymbol{p}) \times \boldsymbol{N}(s''\boldsymbol{q}) \right). \tag{2.111}$$

Applications of the first equation is given in Chap. 10, whereas applications of the second equations appear in Chaps. 4 and 7.

2.5.7 *Inverting Linear Operators: Introduction to Green Functions*

Our basic equations, mainly seen in Fourier space, involve both linear operators induced by mean gradients and/or body forces, and quadratic nonlinearities. Solving (or inverting) these linear operators, for models ranging from RDT approximation to fully nonlinear equations recast in an adequate way, is useful even in the absence of any closure application. Such mathematical operation will help to clarify the structure of many two-point or triadic closures, anyway.

For this purpose, we anticipate some developments presented in Chaps. 7–11.

A basic tensorial Green's function is identified in the viscous RDT approximation. Considering the nonlinear problem Eq. (2.99), it leads to the following formal solution:

$$\hat{u}_i(\boldsymbol{k}(t), t) = G^{(0)}_{ij}(\boldsymbol{k}, t, t_0)\hat{u}_j(\boldsymbol{k}(t_0), t_0) + \int_{t_0}^{t} G^{(0)}_{ij}(\boldsymbol{k}, t, t'')s_j(\boldsymbol{k}(t''), t'')dt'', \tag{2.112}$$

in which the first term gives the purely linear solution, or viscous RDT solution, and the second one accounts for the nonlinear term and any given forcing added to it. It is worth noting that it is based on a Lagrangian approach (for the mean flow only, see Sect. 2.8) and that the time dependence of the wave vector resulting from the advection by the mean flow is involved. The use of a time-dependent wave vector is equivalent of solving the advection term in Eq. (2.100) following characteristic lines; details are given in Sect. 8.4, with Eq. (17.28).

The associated form of this solution in the Craya–Herring frame of reference (which leads to the definition of the problem with the minimal number of components) is

$$u^{(\alpha)}(\boldsymbol{k}(t),t) = g^{(0)}_{\alpha\beta}(\boldsymbol{k},t,t_0)u^{(\beta)}(\boldsymbol{k}(t_0),t_0) + \int_{t_0}^{t} g^{(0)}_{\alpha\beta}(\boldsymbol{k},t,t'')s_\beta(\boldsymbol{k}(t''),t'')dt'', \tag{2.113}$$

with

$$g_{\alpha\beta}(\boldsymbol{k},t,t'') = e_i^{(\alpha)}(\boldsymbol{k}(t))G_{ij}(\boldsymbol{k},t,t'')e_j^{(\beta)}(\boldsymbol{k}(t'')), \quad \alpha,\beta = 1,2. \tag{2.114}$$

In order to gather both contributions from initial data and from the forcing nonlinear term, the previous equations can be compacted as

$$\hat{u}_i(\boldsymbol{k}(t),t) = \int_{-\infty}^{t} G^{(0)}_{ij}(\boldsymbol{k},t,t'')f_j(\boldsymbol{k}(t''),t'')dt'', \tag{2.115}$$

with $\boldsymbol{f}(\boldsymbol{k}(t''),t'') = \hat{\boldsymbol{u}}(\boldsymbol{k}(t''),t'')\delta(t''-t_0) + \boldsymbol{s}(\boldsymbol{k}(t''),t'')H(t''-t_0)$, where δ and H denote the Dirac and Heaviside temporal distributions, respectively.

2.5.7.1 Single-Time Statistics

The formal solution of the Craya equation (2.102) for the single-time second-order spectral tensor is

$$\hat{R}_{ij}(\boldsymbol{k}(t),t) = G^{(0)}_{im}(\boldsymbol{k},t,t_0)G^{(0)}_{jn}(\boldsymbol{k},t,t_0)\hat{R}_{mn}(\boldsymbol{k}(t_0),t_0)$$

$$+ \int_{t_0}^{t} G^{(0)}_{im}(\boldsymbol{k},t,t'')G^{(0)}_{jn}(\boldsymbol{k},t,t'')T_{mn}(\boldsymbol{k}(t''),t'')dt''. \tag{2.116}$$

Going to third-order statistical moment, one obtains

$$S_{ijm}(\boldsymbol{k}(t),\boldsymbol{p}(t),t) = G^{(0)}_{iu}(\boldsymbol{q},t,t_0)G^{(0)}_{jv}(\boldsymbol{k},t,t_0)G^{(0)}_{mw}S_{uvw}(\boldsymbol{k}(t_0),t_0)$$

$$+ \int_{t_0}^{t} G^{(0)}_{iu}(\boldsymbol{q},t,t'')G^{(0)}_{jv}(\boldsymbol{k},t,t'')G^{(0)}_{mw}(\boldsymbol{p},t,t'')\tau_{uvw}(\boldsymbol{k}(t''),\boldsymbol{p}(t''),t'')dt'', \tag{2.117}$$

in which S_{ijm} is related to three-point third-order correlations, via

$$\overline{\imath\hat{u}_i(\boldsymbol{q},t)\hat{u}_j(\boldsymbol{k},t)\hat{u}_m(\boldsymbol{p},t)} = S_{ijm}(\boldsymbol{k},\boldsymbol{p},t)\delta^3(\boldsymbol{k}+\boldsymbol{p}+\boldsymbol{q}), \tag{2.118}$$

with

$$T_{ij}(\boldsymbol{k},t) = k_m \iiint \left(S_{ijm}(\boldsymbol{k},\boldsymbol{p},t) + S^*_{jim}(\boldsymbol{k},\boldsymbol{p},t)\right)d^3\boldsymbol{p}, \tag{2.119}$$

and where τ_{ijm} accounts for all contributions originating in fourth-order correlations.

Of course, this procedure can be extended to any statistical moments with arbitrary order N (see also Sect. 2.6.3), without any additional assumption other than incompressibility and statistical homogeneity restricted to fluctuations.

A direct closure in terms of single-time statistics can be found for three-point third-order correlations, replacing the "bare" Green's function in the nonlinear part of Eq. (2.116) by a nonlinear Green's tensor $G_{ij}^{(NL)}$ similar to the Kraichnan's response tensor discussed below, and simultaneously replacing the contribution from fourth-order correlations τ_{uvw} by its quasi-normal approximation $\tau_{uvw}^{(QN)}$, leading to

$$S_{ijm}(\boldsymbol{k}(t),\boldsymbol{p}(t),t) = G_{iu}^{(0)}(\boldsymbol{q},t,t_0)G_{jv}^{(0)}(\boldsymbol{k},t,t_0)G_{mw}^{(0)}S_{uvw}(\boldsymbol{k}(t_0),t_0)$$

$$+\int_{t_0}^{t} G_{iu}^{(NL)}(\boldsymbol{q},t,t')G_{jv}^{(NL)}(\boldsymbol{k},t,t')G_{mw}^{(NL)}(\boldsymbol{p},t,t')\tau_{uvw}^{(QN)}(\boldsymbol{k}(t'),\boldsymbol{p}(t'),t')dt'. \tag{2.120}$$

The quasi-normal expression $\tau_{uvw}^{(QN)}$, which appears as a factorization of fourth-order correlations in terms of second-order ones, is not detailed here. Because τ_{uvw} differs from its quasi-normal expression $\tau_{uvw}^{(QN)}$ via fourth-order *cumulants*, these cumulants generate the departure of $G_{ij}^{(NL)}$ from its purely linear counterpart $G_{ij}^{(0)}$. Equation (2.120) can therefore give the structure of generalized EDQNM, or TFM (Test Field Model) once reduced to single-time statistics, if the derivation of the nonlinear tensorial Green's function is not specified.

2.5.7.2 Towards Two-Time Statistics, and Discussion

The concept of response tensor, as a nonlinear Green's tensor, was introduced by Kraichnan, so that we should introduce, at least for the sake of formal comparisons, some background from DIA (Direct Interaction Approximation) (Kraichnan 1958). To this end, it is useful to look at two-time correlations as well, because they are essential for the derivation of all theories inspired from DIA. In the absence of mean advection effect, the two-time counterpart of $\hat{R}_{ij}$ is immediately found as

$$\overline{\hat{u}_i^*(\boldsymbol{p},t')\hat{u}_j(\boldsymbol{k},t)} = \hat{R}_{ij}(\boldsymbol{k},t,t')\delta^3(\boldsymbol{k}-\boldsymbol{p}). \tag{2.121}$$

The response tensor is introduced for expressing the infinitesimal velocity perturbation in terms of the nonlinear forcing perturbation as

$$\delta\hat{u}_i(\boldsymbol{k},t) = \int_{t_0}^{t} G_{ij}(\boldsymbol{k},t,t'')\delta f_j(\boldsymbol{k},t'')dt''. \tag{2.122}$$

Putting aside the advection term, this equation is similar to the linear equation (2.115), but linearization is performed around a fully nonlinear state, so that an additional convolution term $\delta\hat{\boldsymbol{u}}\otimes\hat{\boldsymbol{u}}$ is generated in linearized Navier–Stokes-type

equations from the quadratic nonlinearity. Incidentally, Eq. (2.122) is an oversimplification, because the nonlinear response tensor should be nonlocal in space, as $G_{ij}(\boldsymbol{k}, \boldsymbol{k}'', t, t'')$ is, at least before specifying statistical properties such as homogeneity or isotropy that should hold for its statistical moments only. This point will be rediscussed in Chap. 17.

Now, analogies with single-time Eqs. (2.117) and (2.120) are sought, but it must be kept in mind that DIA relies on perturbative expansions. In the equation governing the two-time second-order spectral tensor $\hat{\mathbf{R}}(\boldsymbol{k}, t, t')$, nonlinearity calls into play the following *two-time and perturbative* counterpart of $-\imath S_{ijm}$:

$$S_1 = \overline{\delta\hat{u}_i(\boldsymbol{q}, t')\hat{u}_j(\boldsymbol{k}, t)\hat{u}_m(\boldsymbol{p}, t')} + \overline{\hat{u}_i(\boldsymbol{q}, t')\delta\hat{u}_j(\boldsymbol{k}, t)\hat{u}_m(\boldsymbol{p}, t')} + \overline{\hat{u}_i(\boldsymbol{q}, t')\hat{u}_j(\boldsymbol{k}, t)\delta\hat{u}_m(\boldsymbol{p}, t')}.$$

The second term on the right hand side may be written as

$$\overline{\hat{u}_i(\boldsymbol{q}, t')\delta\hat{u}_j(\boldsymbol{k}, t)\hat{u}_m(\boldsymbol{p}, t')} =$$

$$-\imath P_{uvw}(\boldsymbol{k}) \int_{t_0}^{t} \overline{G_{ju}(\boldsymbol{k}, t, t'')\hat{u}_m(\boldsymbol{p}, t')\hat{u}_v(-\boldsymbol{p}, t'')\hat{u}_i(\boldsymbol{q}, t')\hat{u}_w(-\boldsymbol{q}, t'')}dt'', \tag{2.123}$$

and similarly for the other two terms, where G_{ij} denote the Kraichnan's response tensor for infinitesimal perturbations. Only its ensemble-average, finally involved in closure equations, will be referred to as *response tensor* in the following.

Considering now the procedure inherited from Kraichnan's initial DIA, the closure relationship from Eq. (2.123) yields

$$\overline{\hat{u}_i(\boldsymbol{q}, t')\delta\hat{u}_j(\boldsymbol{k}, t)\hat{u}_m(\boldsymbol{p}, t')} =$$

$$-\imath P_{uvw}(\boldsymbol{k}) \int_{t_0}^{t} \overline{G}_{ju}(\boldsymbol{k}, t, t'')\overline{\hat{u}_m(\boldsymbol{p}, t')\hat{u}_v(-\boldsymbol{p}, t'')} \cdot \overline{\hat{u}_i(\boldsymbol{q}, t')\hat{u}_w(-\boldsymbol{q}, t'')}dt'', \tag{2.124}$$

in which the *weak dependence principle* implies quasi-normal factorization of fourth-order velocity correlations, as done in Eq. (2.120). Finally, how to reconcile Eq. (2.120) and Eq. (2.124)? If we accept to identify $G_{ij}^{(NL)}$ and $\overline{G}_{ij}$, the apparent difference is a three-fold product of response tensors in the first equation, and a single response tensor in the second one. In fact, the three-fold product is recovered when "converting" two-time second-order statistics into single-time ones: The response tensor is used for this purpose, in agreement with a so-called *fluctuation-dissipation theorem*, which amounts to write

$$\hat{R}_{vm}(\boldsymbol{p}, t', t'') = \overline{G}_{mr}(\boldsymbol{p}, t'', t')\hat{R}_{vr}(\boldsymbol{p}, t'', t''), \tag{2.125}$$

with $t'' \leq t' \leq t$ for instance, and similarly for $\hat{R}_{wi}(\boldsymbol{q}, t'', t')$ from Eq. (2.124).

This preliminary discussion of DIA gives a link between single-time and two-time approaches to triadic closures, but we have eluded important technical problems. This point is further discussed with care in Chap. 17. Three points can be specified from now on as follows.

- To our best knowledge, the correct zeroth-order response tensor, denoted $G_{ij}^{(0)}$ here, is never used to get practical results in two-time theories, even when homogeneous anisotropic shear-driven flows are addressed. In contrast, perturbation expansions are started with a purely isotropic zeroth-order expansion, so that only very weak anisotropy is considered in the homogeneous context. The mean-shear-advection, which amounts to link different wave vectors and different times is not taken into account, and this reflects an oversimplification of the (random) response tensor for perturbations, before and even after averaging it. Accordingly, two-time theories ought to be completely re-formulated in order to address arbitrary anisotropy.
- DIA is applied to inhomogeneous flows, both shear driven and thermally driven in Kraichnan (1964). Is it possible to by-pass the intermediate step of homogeneous arbitrary anisotropic flows? This is a difficult question, almost outside the scope of this book, but a discussion cannot be eluded (see Chaps. 10 and 17.)
- The possible advantage of two-time theories is to use a coupled equation for the nonlinear response tensor, which is not specified a priori, as it might be in single-time EDQNM-type approach. In counterpart, the relevance of this equation, always obtained by a perturbation expansion, depends on its zeroth order.

Finally, it is important to emphasize that nothing is said about small perturbations in exact (before closure) Eq. (2.117) leading to Eq. (2.120). In some cases, the purely linear term in these equations, that reflects *rapid distortion* of three-point third-order correlations, provides very valuable informations about the transient effect of transfer terms. This is exemplified in the present book by many examples, e.g. purely rotating turbulence, in which RDT gives no useful evolution for double correlations started from isotropy. Classical wave turbulence theory, illustrated by rotating turbulence as well, provides an asymptotic case, in which the nonlinear part of Eq. (2.120) can be considered as exact, even without changing ("dressing") the bare Green's tensor $\mathbf{G}^{(0)}$ into $\mathbf{G}^{(NL)}$. In the latter case, the three-fold product of bare Green's tensors generate the three-wave resonant operator.

2.6 Anisotropy for Multipoint Correlations

To describe anisotropic correlations tensors is an important task. Firstly, one has to determine an optimal set of scalar or pseudo-scalar descriptors, in order to describe what was called *componentiality* by W. C. Reynolds. Secondly, we can look at the possible expansion of the preceding set in terms of angular harmonics, with respect to separation vectors, as $\boldsymbol{r}$ in physical space, or with respect to related wave vectors, in Fourier space. For single-point correlations, only the first step is explicit, even if we will see that implicit effects of *dimensionality* can be related to expansions

in terms of first non-trivial angular harmonics for the new structure-based tensors introduced by Kassinos et al. (2001).

Because of the isometric properties of the Fourier transform, expansion of statistical descriptors in terms of angular harmonics is similar in physical space and in Fourier space. We will privilegiate the spectral tensors rather than the multipoint correlations tensors here because the solenoidal property for the velocity field yields a much simpler procedure in Fourier space.

For instance, looking at second-order two-point correlations in physical space, application of group invariance properties (e.g. axisymmetry with or without mirror symmetry) to $\mathbf{R}(\boldsymbol{r}, t)$ must be made prior to application of the incompressibility constraint, and results in the determination of some pseudo-scalar terms. Incompressibility yields implicit differential relationships between these different terms resulting from the symmetry group analysis (Chandrasekhar 1981; Sreenivasan and Narasimha 1978). In contrast, as we shall see below, the incompressibility constraint a priori yields dramatic simplifications (reduction of the number of scalar or pseudo-scalar descriptors) once and for all for the spectral tensor, which is the 3D-Fourier counterpart of $\mathbf{R}(\boldsymbol{r}, t)$, so that application of symmetry group properties, as a second step, is much simpler. The reader is referred to Cambon et al. (2013) for a review of anisotropic description in both physical space and Fourier space.

Another important question is the possibility to use the SO(3) symmetry group, which is the best procedure for the sake of generality, or a SO(2) group, for technical convenience when a dominant direction is used. Anisotropic structure functions, related to two-point correlations, are addressed in the scaling/intermittency community, using SO(3) symmetry group for angular harmonic expansions (Arad et al. 1999). As far as possible, we will try to reconcile the different procedures in the following.

2.6.1 Second Order Velocity Statistics

Independently of closure, the spectral tensor $\hat{R}_{ij}$ is not a general complex matrix, but has a number of special properties, including the fact that it is Hermitian, positive-definite, as follows from Eq. (2.84). The incompressibility condition $k_j \widehat{u}_j = 0$ and Eq. (2.84) also yield $\hat{R}_{ij} k_j = 0$. Taken together, these properties show that, instead of the 18 real degrees of freedom needed to describe a general complex tensor, $\hat{R}_{ij}$ can be represented using only four independent scalars. Indeed, using the spherical polar coordinate system in $\boldsymbol{k}$-space defined by Eqs. (2.86) and (2.87), the tensor simplifies as

$$\hat{R} = \begin{pmatrix} \Phi^{11} & \Phi^{12} & 0 \\ \Phi^{12*} & \phi^{22} & 0 \\ 0 & 0 & 0 \end{pmatrix}. \tag{2.126}$$

Displaying the first two unit vectors of the Craya–Herring frame, one obtains

$$\hat{R}_{ij} = \Phi^{11} e_i^{(1)} e_j^{(1)} + \Phi^{12} e_i^{(1)} e_j^{(2)} + \Phi^{12*} e_i^{(2)} e_j^{(1)} + \Phi^{22} e_i^{(2)} e_j^{(2)}, \tag{2.127}$$

or, in a more compact form:

$$\hat{R}_{ij} = \Phi^{\alpha\beta} e_i^{(\alpha)} e_j^{(\beta)},$$

in which the summation convention over repeated Greek indices, taking only the values 1 and 2, is used.

Similarly, the decomposition in terms of helical modes yields

$$\hat{R}_{ij} = \sum_{s=\pm 1} \sum_{s'=\pm 1} A^{ss'} N_i(-s\boldsymbol{k}) N_j(s'\boldsymbol{k}).$$

Even if these decompositions are essentially the same, and rely on four independent real scalars, an optimal splitting can be found to identify the most 'physical' and the most intrinsic (with respect to any change of the orthonormal frame of reference) quantities. Using

$$N_i N_j^* = P_{ij} - \imath \varepsilon_{ijn} \frac{k_n}{k},$$

in which P_{ij} denotes the projection operator and ε_{ijn} the alternating third-order tensor, the later equation can be rewritten as

$$\hat{R}_{ij} = \mathcal{E}(\boldsymbol{k}, t) P_{ij}(\boldsymbol{k}) + Re[Z(\boldsymbol{k}, t) N_i(\boldsymbol{k}) N_j(\boldsymbol{k})] + \imath \mathcal{H}(\boldsymbol{k}, t) \varepsilon_{ijn} \frac{k_n}{k}, \tag{2.128}$$

where $\mathcal{E}(\boldsymbol{k}, t)$ and $\mathcal{H}(\boldsymbol{k}, t)$ are real scalars, and $Z(\boldsymbol{k}, t) = Z_r + \imath Z_i$ is a complex-valued scalar. The quantity

$$\mathcal{E}(\boldsymbol{k}, t) = \frac{1}{2} \hat{R}_{ii} = \frac{1}{2} \left(\Phi^{11} + \Phi^{22} \right) \tag{2.129}$$

is the *energy density* in three-dimensional $\boldsymbol{k}$-space, whereas

$$k\mathcal{H}(\boldsymbol{k}, t) = -\frac{\imath}{2} k_l \varepsilon_{lij} \hat{R}_{ij} = k \Im \Phi^{12} \tag{2.130}$$

is the *helicity spectrum*. Global kinetic energy $\mathcal{K}$ and global helicity h are given by

$$\mathcal{K}(t) = \frac{1}{2} \overline{u_i' u_i'} = \int \mathcal{E}(\boldsymbol{k}, t) d^3\boldsymbol{k} \quad h(t) = \frac{1}{2} \overline{\omega_i' u_i'} = \int k\mathcal{H}(\boldsymbol{k}, t) d^3\boldsymbol{k}. \tag{2.131}$$

The third term

$$Z = \frac{1}{2} \hat{R}_{ij} N_i^* N_j^* = \frac{1}{2} \left(\Phi^{22} - \Phi^{11} \right) + \imath \Re \Phi^{12}, \tag{2.132}$$

characterizes a *polarization* anisotropy, as discussed below. Equivalent decompositions for vorticity correlations and helicity are gathered in Table 2.4 as well as the linkage of two-point correlations to their spectral counterpart.

Anisotropy is expressed through the variations of these scalars with respect to the direction of $\boldsymbol{k}$, as well as departures of $\mathcal{H}$ and Z from zero at a given wavenumber. Whatever spectral closure is used, the number of real unknowns may be reduced to the above four scalar parameters when carrying out numerical simulations, and analysis of the results can be simplified using these variables, particularly when the turbulence is statistically axisymmetric.

In various homogeneous isotropic or anisotropic configurations, the *radial energy spectrum* $E(k,t)$ is a key quantity,[6] which is obtained from $\mathcal{E}(\boldsymbol{k},t)$ by averaging over spherical shells of radius $k=|\boldsymbol{k}|$

$$E(k,t)=\iint_{k=|\boldsymbol{k}|}\mathcal{E}(\boldsymbol{k},t)d^2\boldsymbol{k}=\int_0^{\pi}\int_0^{2\pi}\mathcal{E}(k,\theta,\phi,t)k^2\sin\theta d\theta d\phi, \tag{2.133}$$

the last integral specifying the use of conventional variables in a polar-spherical system of coordinates. Other one-dimensional energy spectra can be obtained by averaging over planes or cylinders. They will be defined only when specific applications will be addressed. For three-dimensional isotropic turbulence (including mirror symmetry), the general set $(\mathcal{E},Z,\mathcal{H})$ reduces to

$$\mathcal{E}=\frac{E(k,t)}{4\pi k^2},\quad Z=\mathcal{H}=0$$

so that

$$\hat{R}_{ij}(\boldsymbol{k},t)=\underbrace{\frac{E(k,t)}{4\pi k^2}}_{\mathcal{E}}\underbrace{\left(\delta_{ij}-\frac{k_ik_j}{k^2}\right)}_{P_{ij}}. \tag{2.134}$$

2.6.1.1 Directional and Polarization Anisotropy – Intrinsic Form

Equation (2.128) (Chandrasekhar 1981) can be written in any direct orthonormal system of Cartesian coordinates. It can be shown that $\mathcal{E}$, $|Z|$ and $\mathcal{H}$, are invariants. If the fixed frame of reference is changed, or if the specific Craya–Herring frame is rotated around the wavevector $\boldsymbol{k}$, only the phase of Z will be modified. It is therefore possible to have access to the intrinsic (eigen) representation of the spectral tensor by specifying a unique angle, directly related to the phase of Z. For physical convenience, let us discuss only the symmetric, real part of the spectral tensor, ignoring the contribution from helicity. The real part of the spectral tensor can be represented in the orthonormal frame defined by its principal axes. The two nonzero eigenvalues $\mathcal{E}+|Z|$ and $\mathcal{E}-|Z|$ are associated with the two principal axes, which are orthogonal

[6] This quantity is also often referred to as the *three-dimensional energy spectrum*.

Table 2.4 Two-point correlations with their spectral counterparts. With velocity (first line), vorticity (second line) and (mixed) helicity (third line). The generic relationship is, first line, $\hat{R}_{ij}(\boldsymbol{k},t) = \mathcal{E}(\boldsymbol{k})P_{ij}(\boldsymbol{\alpha}) + \Re(Z(\boldsymbol{k})N_i(\boldsymbol{\alpha})N_j(\boldsymbol{\alpha})) + \imath\varepsilon_{ijm}\alpha_m\mathcal{H}(\boldsymbol{k})$

.		Using the irreducible decomposition (iso, dir, pol, hel)		
Two-point correlations	Spectral tensor	Trace ($\mathcal{E}$)	Polarization (Z)	Helicity ($\mathcal{H}$)
	$(\bullet) =$	$(\bullet)\,P_{ij}(\boldsymbol{\alpha})$	$+\Re[(\bullet)N_i(\boldsymbol{\alpha})N_j(\boldsymbol{\alpha})]$	$+\imath\varepsilon_{ijm}\alpha_m(\bullet)$
$\overline{u_i(\boldsymbol{x})u_j(\boldsymbol{x}+\boldsymbol{r})} = R_{ij}(\boldsymbol{r})$	$\hat{R}_{ij}(\boldsymbol{k})$	$\mathcal{E}(\boldsymbol{k})$	$Z(\boldsymbol{k})$	$\mathcal{H}(\boldsymbol{k})$
$\overline{\omega_i(\boldsymbol{x})\omega_j(\boldsymbol{x}+\boldsymbol{r})}$	$-\varepsilon_{imn}\varepsilon_{jpq}k_m k_q\hat{R}_{pq}(\boldsymbol{k})$	$k^2\mathcal{E}(\boldsymbol{k})$	$-k^2 Z(\boldsymbol{k})$	$k^2\mathcal{H}(\boldsymbol{k})$
$\overline{u_i(\boldsymbol{x})\omega_i(\boldsymbol{x}+\boldsymbol{r})}$	$\imath\varepsilon_{imn}k_n\hat{R}_{im}(\boldsymbol{k})$	0	0	$k\mathcal{H}(\boldsymbol{k})$

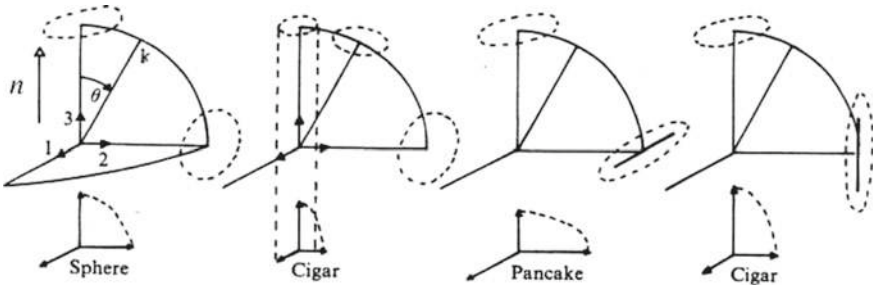

Fig. 2.5 Schematic representation of the anisotropy, from spectral space to its impact on the Reynolds stress tensor. The top line displays the ellipse spanned by the four non-vanishing components of $\hat{R}$ is the local Craya–Herring reference frame (see Eq. (2.126)), giving for every $\boldsymbol{k}$, $\mathcal{E}+ \mid Z \mid$ (length of the largest axis), $\mathcal{E}- \mid Z \mid$ (length of the smallest axis), and their angle in the plane normal to $\boldsymbol{k}$ by means of the phase of Z. The bottom line shows the associated ellipsoid generated by the corresponding Reynolds tensor in the physical space. Adapted from Cambon and Jacquin (1989)

to $\boldsymbol{k}$ and to each other. The third eigenvalue, which is equal to 0, is related to the unit vector spanned by $\boldsymbol{k}$. Finally Z describes the anisotropic structure of the real part of the spectral tensor at a given $\boldsymbol{k}$: its modulus is half the difference of the nonzero eigenvalues, whereas its phase is related to the angle for passing from the Craya–Herring frame to the eigenframe by rotation around $\boldsymbol{k}$ (see Fig. 2.5). Note that the different cartoons in this figure are further illustrated by realistic flow cases in the rest of the book. From left to right, four cases are displayed. The first one is related to purely 3D isotropic turbulence, without directional anisotropy and polarization. The second one illustrates directional anisotropy towards bi-dimensionalization: it is further examplified by the purely linear phase of quasi-static MHD (Magnetohydrodynamics) in Fig. 12.4.2-top-left. When the second one is combined with polarization anisotropy on the third one, they yield together the cases of purely rotating turbulence, that is shown in Fig. 7.17, and the case of fully nonlinear quasi-static MHD in Fig. 12.4.2. Note that the trends to create a cigar shape or a pancake shape in the Reynolds stress tensor are opposite in the second and the third sketches. Finally, the case of Unstable Stratified Homogeneous Turbulence (USHT) combines the second and the fourth cases: A 2D trend for directional anisotropy and a vertical trend for polarization (see Fig. 10.18.) In the latter case, the trends to create a cigar shape for the Reynolds stress tensor are additive, for both directional and polarization anisotropies. Only the case of Stably Stratified Homogeneous Turbulence was not anticipated in Fig. 2.5: it corresponds to concentration of energy towards the polar zone of the sphere in Fourier space, with dimensional anisotropy towards a 1D structure without significant polarization anisotropy, and a pancake trend for the Reynolds stress tensor.

The anisotropic structure is then analyzed by isolating the pure isotropic contribution (2.134) in Eq. (2.128), so that

$$\Re\left(\hat{R}_{ij}\right) = \underbrace{\frac{E(k)}{4\pi k^2} P_{ij}}_{Isotropic\ part} + \underbrace{\left(\mathcal{E}(\mathbf{k}) - \frac{E(k)}{4\pi k^2}\right) P_{ij}}_{Directional\ anisotropy} + \underbrace{\Re\left(Z(\mathbf{k},t) N_i N_j\right)}_{Polarization\ anisotropy} . \quad (2.135)$$

It is now possible to discriminate the *directional anisotropy*, which means that all directions of $\boldsymbol{k}$ on a spherical shell do not have the same amount of energy, from the *polarization anisotropy*, which means that the orientations of the vector $\hat{\boldsymbol{u}}$, located in the plane normal to a given wavevector $\boldsymbol{k}$, are not statistically equivalent. The first kind of anisotropy is quantified by the angular distribution of $\mathcal{E} - E/(4\pi k^2)$, whereas the second kind is measured by Z, whose modulus and phase are related to the intensity and the phase of polarization, respectively.

2.6.1.2 Expansion in Terms of Angular Harmonics

An important step, considering symmetries associated to SO(3) or SO(2) invariance groups,[7] is to expand the typical scalar or pseudo-scalar descriptors, which depend on the separation vector $\boldsymbol{r}$ in physical space or on the related wave vector $\boldsymbol{k}$ in Fourier space, in terms of angular harmonics. The procedure is well known for the 'true' scalar $\mathcal{E}(\boldsymbol{k})$, and a general SO(3)-related expansion yields

$$\mathcal{E}(\boldsymbol{k}) = \frac{E(k)}{4\pi k^2}\left(1 + U_{ij}^{2(dir)}(k)\alpha_i\alpha_j + U_{ijmn}^{4(dir)}(k)\alpha_i\alpha_j\alpha_m\alpha_n + \cdots\right). \quad (2.136)$$

Only angular harmonics of even degree are relevant in the preceding expansion, in which two kinds of quantities appear, namely tensors depending only on the wavenumber $k = |\boldsymbol{k}|$ and tensorial products of the orientation $\boldsymbol{\alpha} = \boldsymbol{k}/k$ of the wave vector. An equivalent, more common, expansion in terms of scalar spherical harmonics is

$$\mathcal{E}(k,\theta_k,\phi_k) = \frac{E(k)}{4\pi k^2}\left(1 + \sum_{n=1}^{N}\sum_{m=-2n}^{2n} U_{2n}^{m(dir)}(k)\underbrace{P_{2n}^m(\theta_k)\exp(\imath m\phi_k)}_{Y_{2n}^m(\theta_k,\phi_k)}\right), \quad (2.137)$$

in which a polar-spherical system of coordinates is used for $\boldsymbol{k}$, with θ_k its polar angle and ϕ_k its azimuthal angle, respectively. The $P_{2n}^m(\theta_k)$ are extended Legendre polynomials, already used in Eq. (2.90). The advantage of Eq. (2.137) is that it relies on orthogonal polynomials, allowing for an easy extraction of individual coefficients from any angular distribution of $\mathcal{E}$ in terms of $\boldsymbol{k}$. On the other hand, it is apparently a SO(2) expansion because it depends on the choice of the polar axis; nevertheless the degree n (m is called the order) of the expansion is self-consistent considering any change of the polar axis. The latter expansion is not restricted to axisymmetric

[7] It is recalled that these multiplicative groups are related to rotations.

turbulence, but it is particularly simple in that case, with $m = 0$, so that the spherical harmonic functions Y_m^{2n} reduce to ordinary Legendre polynomials $P^{(2n)}(\cos\theta_k)$.

Of course, similar expansions are found for the scalar $(1/2)\mathbf{R}(\boldsymbol{r})$ in physical space (see, e.g. Cambon and Teissèdre 1985; Cambon et al. 2013).

Looking now at the anisotropic structure of the polarization, things are more complicated, because a tensor cannot be expanded in terms of angular harmonics as a scalar, and as a matter of fact Z represents a tensor. Following Rubinstein et al. (2015), a SO(3) expansion of the polarization tensor is eventually translated in terms of Z as

$$Z(\boldsymbol{k}) = \frac{E(k)}{4\pi k^2}\left(U_{ij}^{2(pol)}(k) + \imath U_{ijm}^{3(pol)}(k)\alpha_m + U_{ijmn}^{4(pol)}\alpha_m\alpha_n + \cdots\right) N_i^*(\boldsymbol{\alpha})N_j^*(\boldsymbol{\alpha}). \tag{2.138}$$

The role and form of k-modulus-spherical tensors with odd degree (or spin) is now completely clarified: in accordance with Hermitian symmetry, they are purely imaginary, whereas the ones with even degree are real.

A related question is how to relate the angular harmonics in the Z-expansion to the *vectorial spherical harmonics* in Sect. 2.5.2.1. Work is still in progress.

2.6.2 *Induced Anisotropic Structure of Arbitrary Second-Order Statistical Quantities*

The anisotropic decomposition introduced above can be used to obtain a meaningful decomposition of any arbitrary second-order statistical tensor.

The most detailed information on two-point second-order velocity statistics is given by $\hat{\mathbf{R}}(\boldsymbol{k})$, or similarly by $\mathcal{E}$ and Z descriptors in terms of $\boldsymbol{k}$-vector.

One can retain this information only in terms of spherically-averaged descriptors, by spherically integrating the second-order spectral tensor, retaining the basic three-fold splitting

$$\varphi_{ij}(k) = 2E(k)\left(\frac{1}{3}\delta_{ij} + H_{ij}^{(dir)}(k) + H_{ij}^{(pol)}(k)\right). \tag{2.139}$$

This is summarized in Table 2.5. The deviatoric tensors, which are both tracefree and symmetric, are directly related to the generating tensors of angular harmonic expansions in Eqs. (2.136) and (2.138) at the first nontrivial degree, yielding

$$U_{ij}^{2(dir)}(k) = -15H_{ij}^{(dir)}(k), \quad U_{ij}^{2(pol)}(k) = 5H_{ij}^{(pol)}(k), \tag{2.140}$$

in which the exact coefficients of proportionality derive from the following analytical identity

Table 2.5 Description of anisotropy for two-point velocity correlations, using $\boldsymbol{k}$-vector descriptors and their corresponding spherically-averaged contributions. The generic relationship, first line, is $\mathcal{E}(\boldsymbol{k}) = \frac{E(k)}{4\pi k^2}(1 - 15H_{mn}^{(dir)}(k)\alpha_m\alpha_n + \cdots)$. Integral relationship is $\iint \hat{R}_{ij}(\boldsymbol{k})d^2\boldsymbol{k} = 2E(k)(\delta_{ij}/3 + H_{ij}^{(dir)}(k) + H_{ij}^{(pol)}(k))$

.	Spherically averaged descriptors		
$\boldsymbol{k}$-vector descriptors	Isotropy	Directional anisotropy	Polarization anisotropy
$\mathcal{E}(\boldsymbol{k}, t)$	$E(k, t)$	$H_{ij}^{(dir)}(k, t)$	0
$Z(\boldsymbol{k}, t)$	0	0	$H_{ij}^{(pol)}(k, t)$

$$\iint_{k=|\boldsymbol{k}|} \alpha_{i_1}\alpha_{i_2}\ldots\alpha_{i_{2N}}d^2\boldsymbol{k} = \frac{4\pi k^2}{3.5\ldots(2N+1)}\delta^N_{i_1 i_2 \ldots i_{2N}}, \tag{2.141}$$

with $\delta^1_{ij} = \delta_{ij}$, $\delta^2_{ijmn} = \delta_{ij}\delta_{mn} + \delta_{im}\delta_{jn} + \delta_{jm}\delta_{in}\ldots$ etc.

It is now possible to recover single-point correlations by integrating on the wavenumber k the spherically-averaged descriptors.

By integrating Eq. (2.139), the following threefold splitting is obtained for the Reynolds Stress tensor

$$\overline{u_i'u_j'} = \iiint \hat{R}_{ij}(\boldsymbol{k}, t)d^3\boldsymbol{k} = 2\mathcal{K}\left(\frac{\delta_{ij}}{3} + \underbrace{b_{ij}^{(dir)} + b_{ij}^{(pol)}}_{b_{ij}}\right), \tag{2.142}$$

where

$$2\mathcal{K}b_{ij}^{(dir)} = \iiint\left(\mathcal{E} - \frac{E}{4\pi k^2}\right)P_{ij}d^3\boldsymbol{k}, \quad 2\mathcal{K}b_{ij}^{(pol)} = \iiint \Re\left(ZN_iN_j\right)d^3\boldsymbol{k}. \tag{2.143}$$

The fourth-order tensor M_{ijpq} can be expressed as

$$M_{ijpq} = \iiint\left(\frac{k_ik_p}{k^2}\hat{R}_{qj}(\boldsymbol{k}, t) + \frac{k_jk_p}{k^2}\hat{R}_{qi}(\boldsymbol{k}, t)\right)d^3\boldsymbol{k}. \tag{2.144}$$

2.6.2.1 Bridging with Dimensionality and Componentality

Similar decompositions can be found for the *dimensionality structure tensor* (Kassinos et al. 2001)

$$D_{ij} = \iiint \frac{k_ik_j}{k^2}2\mathcal{E}(\boldsymbol{k}, t)d^3\boldsymbol{k} = 2\mathcal{K}\left(\frac{\delta_{ij}}{3} - 2b_{ij}^{(dir)} + 0\right),$$

Table 2.6 Structure-based single-point tensors. The generic relationship, first line, is $\overline{u_i(\boldsymbol{x})u_j(\boldsymbol{x})} = 2\mathcal{K}(\delta_{ij}/3 + b_{ij}^{(dir)} + b_{ij}^{(pol)})$. Integral relationships are: $\mathcal{K} = \int_0^\infty E(k)dk = \iiint \mathcal{E}(\boldsymbol{k})d^3\boldsymbol{k}$, $2\mathcal{K}b_{ij}^{(dir)} = \int_0^\infty 2E(k)H_{ij}^{(dir)}(k) = \iiint(\mathcal{E}(\boldsymbol{k}) - \frac{E(k)}{4\pi k^2})P_{ij}(\boldsymbol{\alpha})d^3\boldsymbol{k}$

.		Using homogeneity (iso, dir, pol)		
Single-point tensors	In terms of stream-function	Isotropy	Directional anisotropy	Polarization anisotropy
	$(\bullet) =$	$\frac{2}{3}(\bullet)\delta_{ij}$	$+2\mathcal{K}(\bullet)$	$+2\mathcal{K}(\bullet)$
Reynolds stress	$\varepsilon_{imn}\varepsilon_{jpq}\overline{\psi_{m,n}\psi_{p,q}}$	$\mathcal{K}$	$b_{ij}^{(dir)}$	$b_{ij}^{(pol)}$
Dimensionality	$\overline{\psi_{m,i}\psi_{m,j}}$	$\mathcal{K}$	$-2b_{ij}^{(dir)}$	0
Circulicity	$\overline{\psi_{i,m}\psi_{j,m}}$	$\mathcal{K}$	$b_{ij}^{(dir)}$	$-b_{ij}^{(pol)}$

and for the *vorticity correlations tensor*.[8] Details are summarized in Table 2.6, along with a reminder of the expressions in terms of the vector streamfunction. The resulting expressions are

$$\overline{\omega_i'\omega_j'} = \omega^2\left(\frac{\delta_{ij}}{3} + b_{ij}^{(k^2e)} - b_{ij}^{(k^2z)}\right), \tag{2.145}$$

with

$$\omega^2 = \iiint k^2\mathcal{E}d^3\boldsymbol{k}, \tag{2.146}$$

$$\omega^2 b_{ij}^{(k^2e)} = \iiint k^2\left(\mathcal{E} - \frac{E}{4\pi k^2}\right)P_{ij}d^3\boldsymbol{k}, \tag{2.147}$$

$$\omega^2 b_{ij}^{(k^2z)} = \iiint k^2\Re\left(ZN_iN_j\right)d^3\boldsymbol{k}. \tag{2.148}$$

Relations (2.147) and (2.148) show that the anisotropy tensor b_{ij} is the sum of two very different contributions: $b_{ij}^{(dir)}$ which originates the directional (or dimensionality) anisotropy and $b_{ij}^{(pol)}$ which accounts for polarization anisotropy. Surprising RDT results in rotating flows are explained by this decomposition (see Chap. 7), and the formalism introduced in Kassinos et al. (2001) appears as a byproduct of Eq. (2.128) in homogeneous turbulence, the decomposition in terms of directional and polarization anisotropy lending support to componental and dimensional anisotropy.

[8] Rather than the vorticity correlations tensor, Kassinos et al. (2001) introduced the *circulicity tensor* f_{ij}, given by Eq. (2.78), which involves larger scales. This tensor corresponds to

$$f_{ij} = 2\mathcal{K}\left(\frac{\delta_{ij}}{3} + b_{ij}^{(dir)} - b_{ij}^{(pol)}\right)$$

with our notations.

The third tensor introduced by Kassinos and coworkers, referred to as *stropholysis* is also connected to the $\mathcal{E} - Z$ decomposition, and its form can be recast as

$$Q_{ijm} = \underbrace{\mathcal{K}\varepsilon_{ijp}\left(2b_{pm}^{(dir)} - \frac{\delta_{pm}}{3}\right)}_{Q_{ijm}^{(dir)}} + \underbrace{\iiint \frac{k_m}{k}\Im(ZN_iN_j)d^3\boldsymbol{k}}_{Q_{ijm}^{(pol)}}. \tag{2.149}$$

A possible contribution from the helicity spectrum may be added, it is not taken into account here for the sake of coherence with the main part of the book, and also for the sake of brevity. Under a fully symmetrized form, only the contribution from polarization $Q_{ijm}^{*} = Q_{ijm}^{*(pol)}$ remains: The spectrum of this single-point tensor is firstly generated by the spin-3 term $U_{mpq}^{3(pol)}(k)$ in Eq. (2.138), and probably by all other possible odd-order terms. Beyond pure kinematics, a *dynamical stropholysis effect* induced by vortical mean flows, is discussed in Chap. 8.

More details on the exact hierarchy between $\boldsymbol{k}$-vector descriptors $(\mathcal{E}, Z)$, spherically-averaged descriptors, and single-point tensors, via straightforward integration, can be found in the appendix of Mons et al. (2016).

In conclusion, it is worthwhile to point out that a fully anisotropic spectral (or two-point) description carries a very large amount of information, even if restricted to second-order statistics. In the inhomogeneous case, the POD (*proper orthogonal decomposition*, see Lumley 1967) has renewed interest in second-order two-point statistics, but this technique is applied to strongly inhomogeneous quasi-deterministic flows. It is only said that POD spatial modes are Fourier modes in homogeneous turbulence, without considering that a spectral tensor such as $\hat{\mathbf{R}}$ ought to be diagonalized in order to exhibit its eigenmodes as POD modes in the *anisotropic* case.

2.6.3 Some Comments About Higher Order Statistics

N-order correlations at N points can be defined in homogeneous turbulence via spectral tensors, similarly as for the second order case ($N = 2$). For instance

$$\begin{aligned} &< \hat{u}_{i_1}^{*}(\boldsymbol{k}_N)\hat{u}_{i_2}(\boldsymbol{k}_1)\ldots\hat{u}_{i_{N-1}}(\boldsymbol{k}_{N-2})\hat{u}_{i_N}(\boldsymbol{k}_{N-1}) > \\ &= \hat{R}_{i_1 i_2 \ldots i_N}(\boldsymbol{k}_1, \boldsymbol{k}_2, \ldots, \boldsymbol{k}_{N-1})\delta\left(\boldsymbol{k}_N - \sum_{i=1}^{N-1}\boldsymbol{k}_i\right). \end{aligned} \tag{2.150}$$

Since the N wave-vectors form a closed polygon, only $N - 1$ of them, $\boldsymbol{k}_1$, $\boldsymbol{k}_2$, …, $\boldsymbol{k}_{N-1}$, are independent, corresponding to the $N - 1$ independent separations vectors $\boldsymbol{r}_1, \ldots, \boldsymbol{r}_{N-1}$ in physical space. The interest of addressing the most complex configuration, with N independent points for representing Nth-order correlations is discussed in the last section of this chapter.

As a first general result, for incompressible turbulence, it is possible to extend Eq. (2.102), which was derived for $N = 2$, to an arbitrary order, yielding an equation for $\hat{R}_{i_1 \ldots i_N}(\boldsymbol{k}_1, \ldots, \boldsymbol{k}_{N-1}, t)$. In this equation, all pressure effects can be exactly incorporated as functions of $\hat{R}_{i_1 \ldots i_N}$ itself, as all the linear effects, and of the $(\mathrm{N}+1)th$-order spectral tensor.

As a second result, it is possible to replace $\hat{u}(\boldsymbol{k}_n)$ by $u^{(\alpha)}(\boldsymbol{k}_n)$ using either of the local Craya or poloidal-toroidal frame attached to $\boldsymbol{k}_n$. Accordingly, the Nth-order spectral tensor is shown to depend on $N + 1$ scalar components only, considering that $u^{(\alpha)}$ has two components and that the spectral tensor is left unchanged when permuting simultaneously the N wavevectors and the N-indices. The latter result was found independently in the Ph.D. theses of Cambon (1982) and Lindborg (1996).

Of course, the most general case has very little applications, but the cases $N = 3$ and $N = 4$ are relevant in triadic and quasi-normal closure theories and models, which are addressed in the following chapters. Orders larger than $N = 4$ are commonly addressed in the 'scaling-intermittency' community, for structure functions, but always restricted to two-point correlations.

2.7 A Synthetic Scheme of the Closure Problem: Non-linearity and Non-locality

Both the nonlinear pressure component and the nonlinear term appearing directly in Eq. (2.50) contribute to the closure problem: the equation for the nth-order velocity moments involves $(\mathrm{n}+1)th$-order moments. As a consequence, no finite subset of the infinite hierarchy of integro-differential equations describing the velocity moments at all orders is closed, reflecting the fundamental difficulty of the turbulence problem, viewed through the classical statistical description in terms of statistical moments. The origin of the closure problem is *nonlinearity* of the Navier–Stokes equations, which is beared by the convective terms and the nonlinear part of the pressure fluctuations. *Non-locality*, by itself, does not lead to problems, although the technical difficulties associated with integro-differential are nontrivial.[9]

The non-local problem of closure is discarded only in models for *multi-point* statistical correlations, e.g. double correlations at two points or triple correlations at three points, so that in such models the problem of closure is determined by the sole non-linearity.

The knowledge of the probability density function (pdf) of the velocity fluctuations is equivalent to the knowledge of all the statistical moments of arbitrary orders. Therefore, the above mentioned problem of the open hierarchy of the moment-equations, is precluded in a pdf-based approach. Consequently, the problem of closure induced

[9] Non-locality ought to be only understood in *physical space* here. Of course, the operators related to pressure and dissipation will appear as local quantities in Fourier space, but this is only for the sake of mathematical convenience. Discussing the possible degree of locality of nonlinear interactions in Fourier space is beyond our scope, too.

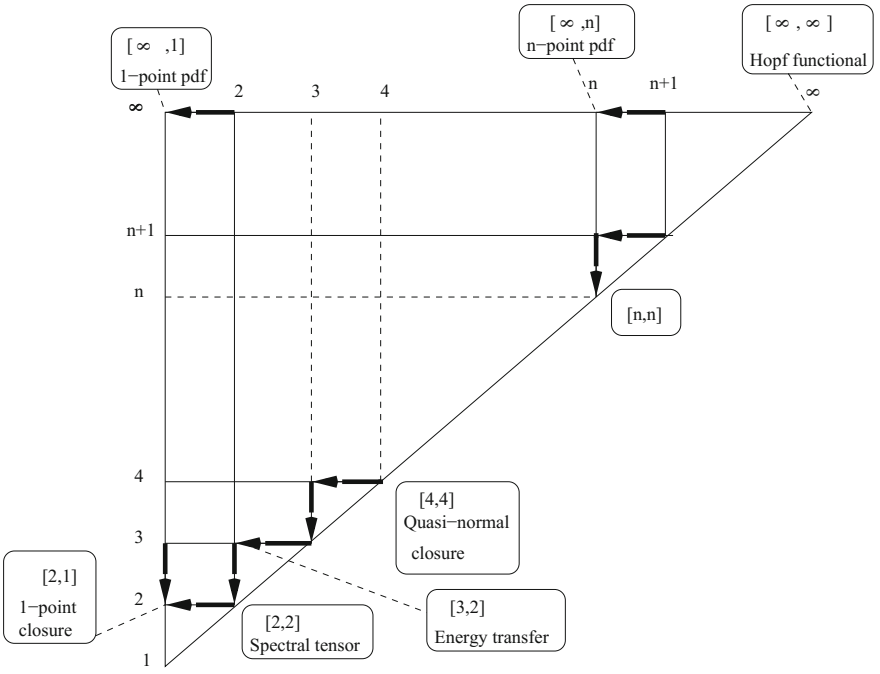

Fig. 2.6 Synthetic scheme for statistical closures

by the non-linearity is precluded using a pdf approach, but the non-local problem of closure remains, so that the equations for a local single-point velocity pdf involve a two-point velocity pdf, and equations for a n-point velocity pdf involve a $(n+1)$-point velocity pdf. This open hierarchy of multipoint pdf is often referred to as the Lundgren–Monin–Novikov hierarchy (Lundgren 1967; Monin 1967; Novikov 1968). Statistical symmetries of this hierarchy were recently addressed by Waclawczyk et al. (2014).

In order to summarize all the consequences of the above discussion, a synthetic scheme using a triangle is shown in Fig. 2.6. The vertical axis bears the order of the statistical moments, from 1 (the mean velocity), 2 (second order moments), up to arbitrary high order moments. For the sake of convenience, the moments of order greater of equal to 2 are centered, so that they only involve the fluctuating velocity field. Along the vertical axis, n corresponds to the number of possible different points for a multi-point description of the nth-order moment under consideration along the horizontal axis. Considering the nth-order moment, the number of points ranges from 1 (single-point correlation), 2 (two-point correlation), up to n. The possible solutions are observed to generate a triangle in this representation.

In other words, the vertical axis displays the open hierarchy due to non-linearity, while the horizontal one deals with non-locality. Each point in the triangle characterizes a level of description. As an example, the point [3, 2] is related to triple

correlations at two points, which are associated with the spectral energy transfer and the kinetic energy cascade. In addition, the problem of closure can be stated by looking at the adjacent points (if any) just above and just to the left. For instance, The main problem which concerns engineering, when solving Reynolds-averaged Navier Stokes equations, is expressing the flux of the Reynolds stress tensor. This can be represented by an arrow from [2, 1] to [1, 1]. Then, the equations that govern the Reynolds-stress tensor [2, 1] need extra information (not given by [2, 1] itself, leading to the appearance of the closure problem) on second-order two-point correlations [2, 2] (involved in the 'rapid' pressure-strain rate term and the dissipation term), on triple-order single-point correlations [3, 1] and triple-order two-point correlations [3, 2] (involved in the 'slow' pressure-strain rate and diffusion terms). Of course, the Reynolds stress tensor [2, 1] is directly derived from second-order correlations at two points [2, 2], illustrating the simple rule of *concentration of the information* when moving from the right to the left. The non-locality issue, due to pressure and dissipation terms, is discarded when looking only at $[n, n]$ correlations (located on the hypotenuse of the triangle in Fig. 2.6), leaving only the hierarchy due to non-linearity. The governing equations for [2, 2] need only extra information on [3, 2]. The equations which govern [3, 3] require only extra-information on [4, 3]. These two examples, which are directly involved in classical two-point closures, will be discussed in Chap. 4.

The arrow from $[n + 1, n]$ to $[n, n]$ gives an obvious generalization of the optimal way to use multipoint closures, and illustrates the open hierarchy of equations *due to the sole non-linearity*. Often the closure relationship holds at the level $[n + 1, n + 1]$, from which is readily derived the level $[n + 1, n]$. For instance, the Quasi-Normal assumption, which is involved in all multi-point closures, as well as in wave-turbulence theories, calls into play the [4, 4] level.

Regarding the pdf approach, we are concerned with the upper horizontal side of the triangle. It seems to be consistent to relate to the point $[\infty, 1]$ a description in terms of a local velocity pdf. Accordingly, the arrow from $[\infty, 2]$ to $[\infty, 1]$ shows the need for extra-information on the two-point pdf in the equations which govern single-point pdfs. In the same way, the arrow from $[\infty, n + 1]$ to $[\infty, n]$ shows the link between n-point and $(n + 1)$-point pdf (Lundgren 1967), and illustrates the open hierarchy of equations due to the sole non-locality.

The last limit concerns the ultimate point $[\infty, \infty]$. It is consistent to consider that the limit of a joint-pdf of velocity values at an infinite number of points is equivalent to the functional pdf description of Hopf (1952). In this case we reach the top left point of the triangle and there is no need for any extra-information. The Hopf equation is closed, and it is possible to derive from it any multi-point pdf or statistical moment. It is interesting to point out that the bottom right point [1, 1] gives the most crude information about the velocity field – its mean value – whereas the opposite point $[\infty, \infty]$ gives the most sophisticated.

As a last general comment, our synoptic scheme clearly shows that the problem of closure, which reflects a loss of information at a given level of statistical description, can be removed from consideration, at least partially, if additional degrees of freedom are introduced in order to enlarge the configuration-space. For instance, to

introduce as a new dependent variable the vector which joins the two points in a two-point second-order description allows for the removal of the problem of closure due to nonlocality, which is present using a single-point second-order description. The introduction, as a new dependent variable, such as the test-value Υ_i of the random velocity field u_i' in a pdf approach

$$P(\Upsilon_i, \mathbf{x}, t) = \overline{\delta(u_i'(\mathbf{x}, t) - \Upsilon_i)}$$

allows for the removal of the problem of closure due to nonlinearity, which is present in any description in terms of statistical moments. Finally, any problem of closure is removed using the Hopf equation but the price to pay is an incredibly complicated configuration-space! The probabilistic description, which is of practical interest regarding a *concentration scalar* field rather than a velocity field, is extensively addressed in the context of combustion modelling, and will no longer be considered in this book.

2.8 On the Use of Lagrangian Formalism

We conclude this chapter on "exact" dynamical aspects by a survey of the use of the Lagrangian formalism with application to both turbulence structure and modeling. A large part of applications are developed within the Eulerian framework, and the synoptic scheme of closures given in the preceding section is essentially drawn in this context.

Equivalence of Eulerian and Lagrangian frameworks is a truism, at least for the fluid considered as a continuum, even if some recent statistical studies from physical and numerical experiments advocate for a richer information of the Lagrangian description. This viewpoint is influenced by the increase of the number of studies related to particle-laden flows, and the fact that statistics are necessary multi-time in the Lagrangian approach. Of course, two-time Lagrangian statistics are richer than single-time Eulerian statistics, but all can be reconciled in principle using the same level — eg. two-time two-point — of statistical description.

It is important noticing that nonlinearity and nonlocality discussed in the last section in the Eulerian context, are radically different in the Lagrangian description. Quadratic nonlinearity due to the convection term is removed from consideration in the Lagrangian framework, but difficulty is transferred to pressure gradient and dissipative term. Let us recall the standard Navier–Stokes equations for Eq. (2.13), with linear Lagrangian acceleration as

$$\rho \ddot{x}_i = -\frac{\partial p}{\partial x_i} + \mu \frac{\partial^2 \dot{x}_i}{\partial x_j \partial x_j},$$

in which the Cauchy matrix, or semi-Lagrangian gradient of displacements, $\mathbf{F}(\boldsymbol{X}, t, t_0)$ in Eq. (2.5), must be used for expressing ρ (as $\rho = \rho_0/\det \mathbf{F}$ from Eq. (2.11)) and for "converting" Eulerian gradient terms into Lagrangian ones, via

$$\frac{\partial}{\partial x_i} = \frac{\partial X_j}{\partial x_i}\frac{\partial}{\partial X_j} = F_{ji}^{-1}(\boldsymbol{X}, t, t_0)\frac{\partial}{\partial X_j}. \tag{2.151}$$

Finally one obtains

$$\ddot{x}_i = \frac{\det \mathbf{F}}{\rho_0}\left(-F_{ji}^{-1}\frac{\partial p}{\partial X_j} + \mu\left(F_{mj}^{-1}F_{nj}^{-1}\frac{\partial \dot{x}_i}{\partial X_m \partial X_n} + F_{nj}^{-1}\frac{\partial F_{mj}^{-1}}{\partial X_n}\frac{\partial \dot{x}_i}{\partial X_m}\right)\right). \tag{2.152}$$

A last modification should consist in replacing $\frac{\partial \dot{x}_i}{\partial X_m}$ by $\dot{F}_{im}$, but there is no need to further emphasize the high complexity of the "Lagrangian" r.h.s. term, which involves plenty of $\mathbf{F}^{-1}$ factors.

Now, the discussion can be organized around the pivotal role of the matrix $\mathbf{F}$ in different approaches, in which a formal or actual analogy with visco-elastic mechanisms can be drawn. The problem of existence and smoothness, at least for large times $t - t_0$, can be discussed for $\mathbf{F}$ in turbulent flow realizations, but we can at least mention some interesting properties in a smooth flow case. Along with the additive decomposition of $\mathbf{A}$ into a divergent part (trace), a symmetric traceless (strain) part and an antisymmetric one linked to vorticity, matrix theory shows that $\mathbf{F}$ has the following multiplicative decomposition

$$\mathbf{F}(\boldsymbol{X}, t, t_0) = (\det \mathbf{F})^{1/3}\mathbf{R} \cdot \mathbf{Q}, \tag{2.153}$$

in which $\mathbf{Q}$ is an orthogonal matrix (cumulated rotation effect along trajectories) and $\mathbf{R}$ (cumulated strain effect along trajectories) a symmetric tensor; $\det \mathbf{F}$ characterizes a bulk cumulated compression if different from one. By forming the Cauchy–Green tensor, $\mathbf{C} = \mathbf{F} \cdot \tilde{\mathbf{F}}$, the symmetric factor is extracted, as $\mathbf{C} = (\det \mathbf{F})^{2/3}\mathbf{R}^2$.

2.8.1 *From RDT to Visco-Elastic Mechanisms*

The role of $\mathbf{F}$ is obvious in nonlinear expressions such as Eqs. (2.30) and (2.31), whose linearized form is useful for deriving analytical RDT solutions for inhomogeneous straining processes. Before linearization, the Helmholtz decomposition can be applied to the Weber equation in the incompressible case, so that

$$\boldsymbol{u}(\boldsymbol{x}, t) = \left(\tilde{\mathbf{F}}^{-1}(\boldsymbol{X}, t, t_0)\boldsymbol{u}(\boldsymbol{X}, t_0)\right)^{(sol)}, \tag{2.154}$$

whereas its projection on the "dilatational subspace" yields

$$\left(\tilde{\mathbf{F}}^{-1}(\boldsymbol{X},t,t_0)\boldsymbol{u}(\boldsymbol{X},t_0)\right)^{(dil)}+\boldsymbol{\nabla}\varphi'=0.$$

The term φ' holds for a temporal integral of the total pressure $p+\frac{1}{2}\rho u^2$ along trajectories. Applications are discussed in Chap. 8.

We can move to "homogeneous" RDT as follows. When a mean flow with space-uniform velocity gradients is introduced, following Craya, it is possible to consider statistical homogeneity restricted to fluctuations and to restrict the Lagrangian approach to the mean flow. In this case, only simplified mean trajectories are accounted for, as linear relationship of $\boldsymbol{x}$ to $\boldsymbol{X}$, and $\mathbf{F}$ is space-uniform as well. Looking at the Green's tensor denoted $\mathbf{G}^{(0)}$ from Eq. (2.112), its purely viscous factor displays $\mathbf{F}$, and its inviscid factor is

$$P_{ij}(\boldsymbol{k}(t))F^{-1}_{ji}(t,t_0),$$

for irrotational mean flows, in accordance with Eq. (2.154). Even if the homogeneous RDT solution can be more complicated for rotational mean flows, the time-dependent wave vector, that reflects mean-flow-advection, is directly linked to $\mathbf{F}$ in all cases by the following relation:

$$k_i(t)=F^{-1}_{ji}(t,t_0)\underbrace{k_j(t_0)}_{\boldsymbol{K}},$$

in accordance to the mean flow trajectories

$$x_i=F_{ij}(t,t_0)X_j.$$

In addition to linear RDT, such a formalism was implicitly used by Rogallo (1981) to extend nonlinear pseudo-spectral DNS in tri-periodic boxes to flows subjected to mean velocity gradients (his formalism corresponds to $x'_i=X_i$ and $B_{ij}=F^{-1}_{ij}$).

The role of $\mathbf{F}$ for building RDT solutions gives a formal support to the analogy of the regime, rapid distortion + nonlinear relaxation, with a visco-elastic mechanism. Such an analogy is still used in some stochastic models, touched upon at the very end of this chapter.

A second application deals with the pressure Hessian in Eq. (2.32), using its Lagrangian counterpart via the exact transform

$$\frac{\partial^2 p}{\partial x_j\partial x_j}=F^{-1}_{jm}F^{-1}_{jn}\frac{\partial^2 p}{\partial X_m\partial X_n}+F^{-1}_{nj}\frac{\partial F^{-1}_{mj}}{\partial X_n}\frac{\partial p}{\partial X_m},\tag{2.155}$$

using Eq. (2.151). At least for its modeling in HIT, revisited in Chap. 4, $\mathbf{F}$ is not dominated by a mean flow effect, as in homogeneous RDT, but it is supposed to be well defined and relatively smooth, related to a "perceived" large-scale mean flow gradient $\mathbf{A}$.

The reader is referred to Chap. 5 for applications to flows with microstructures subjected to viscoelastic mechanisms.

2.8.2 Lagrangian Stochastic Models

Paul Langevin introduced his equation for the Brownian motion in 1908. Many instances of related studies were developed for modeling Lagrangian diffusion. The trajectory of a particle considered as a fluid element is given by

$$\dot{x}_i = u_i(\boldsymbol{x}, t),$$

and the acceleration $\ddot{\boldsymbol{x}} = \dot{\boldsymbol{u}}$ is expressed as

$$\dot{\boldsymbol{u}} = \mathcal{L}(\boldsymbol{u}) + \boldsymbol{\xi}, \tag{2.156}$$

in which the first term in the r.h.s is deterministic and linear, whereas the second one is a stochastic forcing, varying for each realization. The linear operator can simplify as $-\frac{\boldsymbol{u}}{\tau_L}$ using an ad-hoc linear time scale τ_L. One of the most elaborated model was introduced by Thomson (1987), with

$$du_i = a_i(\boldsymbol{x}, \boldsymbol{u}, t)dt + b_{ij}(\boldsymbol{x}, \boldsymbol{u}, t)d\xi_j,$$

in which ξ is a white noise Gaussian process in time with standard deviation dt.

It is chosen to put the emphasis on exact dynamical equations in this chapter, as a starting point for an approach to developed turbulence. We do not question the validity of these equations, even if they imply smooth fields, whereas "turbulent" fields are not. It is worth noting that the classical Kolmogorov (K41) scalings for structure functions in the inertial range are not consistent with such a smooth field, from the fractional exponent induced by $\delta u(r) \sim (\varepsilon r)^{1/3}$ in average. On the other hand, when we address statistical quantities, they are smooth, and their governing equations are really built from "exact" conservation equations given throughout this chapter. This viewpoint allows us to present a well-defined problem of closure, and is consistently addressed from $k - \varepsilon$ modeling to the Hopf equation, with a special emphasis on two-point and three-point statistics, mainly Eulerian, but for a simplified mean, or large-scale, flow.

Accordingly, stochastic modeling is at odds of the main stream of the present book. There are possible linkages, such as a spectral stochastic model that can be consistent with basic DIA, and perhaps with EDQNM (but this is more controversial). In turn, stochastic models are generally not consistent with "exact" dynamical equations. As recalled by Raoul Robert (private communication), a Wiener process can be made fully consistent with Burger equations, but no stochastic model can presently match the Euler equations. On the other hand, internal intermittency is often a byproduct of some stochastic models. This point is touched upon in our introduction and will be rediscussed in the conclusion.

References

Arad, I., Lvov, V.S., Proccaccia, I.: Correlations functions in isotropic and anisotropic turbulence: the role of the symmetry group. Phys. Rev. E **59**, 6753–6765 (1999)

Batchelor, G.K.: The Theory of Homogeneous Turbulence. Cambridge University Press, Cambridge (1953)

Bayly, B.J., Holm, D.D., Lifschitz, A.: Three-dimensional stability of elliptical vortex columns in external strain flows. Philos. Trans. R. Soc. Lond. A **354**, 895–926 (1996)

Brown, G.L., Roshko, A.: Turbulent shear layers and wakes. J. Turbul. **13**(51), 1–32 (2012)

Cambon, C.: Etude spectrale d'un champ turbulent incompressible soumis à des effets couplés de déformation et rotation imposés extérieurement. Université Lyon I, France, Thèse de Doctorat d'Etat (1982)

Cambon, C., Jacquin, L.: Spectral approach to non-isotropic turbulence subjected to rotation. J. Fluid Mech. **202**, 295–317 (1989)

Cambon, C., Rubinstein, R.: Anisotropic developments for homogeneous shear flows. Phys. Fluids **18**, 085106 (2006)

Cambon, C., Scott, J.F.: Linear and nonlinear models of anisotropic turbulence. Ann. Rev. Fluid Mech. **31**, 1–53 (1999)

Cambon, C., Teissèdre, C.: Application dres harmonioques sphériques à la représentation et au calcul des grandeurs cinématiques en turbulence homogène anisotrope. C. R. Acad. Sci. Paris t. **301**, II(2), 65–68 (1985)

Cambon, C., Jacquin, L., Lubrano, J.-L.: Towards a new Reynolds stress model for rotating turbulent flows. Phys. Fluids A **4**, 812–824 (1992)

Cambon, C., Danaila, L., Godeferd, F.S., Scott, J.F.: Third-order statistics and the dynamics of strongly anisotropic turbulent flows. J. Turbul. **14**(3), 121–160 (2013)

Chandrasekhar, S.: Hydrodynamics and Hydrodynamic Stability. Dover, New York (1981)

Constantin, P.: SIAM Rev. **36**, 73 (1994)

Craik, A.D.D., Criminale, W.O.: Evolution of wavelike disturbances in shear flows: a class of exact solutions of the Navier-Stokes equations. Proc. R. Soc. Lond. Ser. A **406**, 13–26 (1986)

Craya, A.: Contribution à l'analyse de la turbulence associée à des vitesses moyennes. P.S.T. n^0, vol. 345. Ministère de l'air. France (1958)

Darrigol, O.: Worlds of Flow. Oxford University Press, Oxford (2005)

Eringen, C.: Continuum Physics. Academic Press, New York, tome 1 (1971)

Hopf, E.: Statistical hydrodynamics and functional calculus. J. Ration. Mech. Anal. **1**, 87 (1952)

Kaneda, Y., Ishihara, T., Yokokawa, M., Itakura, K., Uno, A.: Energy dissipation rate and energy spectrum in high resolution direct numerical simulations of turbulence in a periodic box. Phys. Fluids **15**, L21–L24 (2003)

Kassinos, S.C., Reynolds, W.C., Rogers, M.M.: One-point turbulence structure tensors. J. Fluid Mech. **428**, 213–248 (2001)

Kida, S., Orszag, S.A.: Energy and spectral dynamics in forced compressible turbulence. J. Sci. Comput. **5**(2), 85–125 (1990a)

Kida, S., Orszag, S.A.: Enstrophy budget in decaying compressible turbulence. J. Sci. Comput. **5**(1), 1–34 (1990b)

Kida, S., Orszag, S.A.: Energy and spectral dynamics in decaying compressible turbulence. J. Sci. Comput. **7**(1), 1–34 (1992)

Kraichnan, R.H.: The structure of isotropic turbulence at very high Reynolds number. J. Fluid Mech. **5**, 497–543 (1958)

Kraichnan, R.H.: Direct-interaction approximation for shear and thermally driven turbulence. Phys. Fluids **7**, 1048–1062 (1964)

Launder, B.E., Reece, G.J., Rodi, W.: Progress in the development of a Reynolds stress turbulence closure. J. Fluid Mech. **68**, 537–566 (1975)

Lindborg, E.: A note on Kolmogorov's third-order structure-function law, the local isotropy hypothesis and the pressure-velocity correlation. J. Fluid Mech. **326**, 343–356 (1996)

Lumley, J.L.: The structure of inhomogeneous turbulent flows. In: Yaglom, A.M., Tatarski, V.I. (eds.) Atmospheric Turbulence and Radio Waves Propagation, pp. 166–167. NAUCA, Moscow (1967)
Lumley, J.L.: Pressure strain correlations. Phys. Fluids **18**(6), 750–751 (1975)
Lumley, J.L.: Computation modelling of turbulent flows. Adv. Appl. Mech. **18**, 126–176 (1978)
Lumley, J.L., Newman, G.: The return to isotropy of homogeneous turbulence. J. Fluid Mech. **82**(1), 161–178 (1977)
Lundgren, T.S.: Distribution function in the statistical theory of turbulence. Phys. Fluids **10**(5), 969–975 (1967)
Majda, A., Bertozzi, A.: Vorticity and Incompressible Flows. Cambridge University Press, Cambridge (2002)
Mathieu, J., Scott, J.F.: Turbulent Flows: An Introduction. Cambridge University Press, Cambridge (2000)
Miura, H., Kida, S.: Acoustic energy exchange in compressible turbulence. Phys. Fluids **7**(7), 1732–1742 (1995)
Monin, A.S.: Prikl. Mat. Mekh. **31**, 1057 (1967)
Mons, V., Cambon, C., Sagaut, P.: A spectral model for homogeneous shear-driven anisotropic turbulence in terms of spherically averaged descriptors. J. Fluid Mech. **788**, 147–182 (2016)
Novikov, E.A.: Sov. Phys.-Dokl. **12**, 1006 (1968)
Oberlack, M.: Theories of Turbulence. Springer, Berlin (2001)
Pereira, R.M., Garban, C., Chevillard, C.: A dissipative random velocity field for fully developed fluid turbulence. J. Fluid Mech. **794**, 369–408 (2016)
Piquet, J.: Turbulent Flows. Models and Physics, 2nd edn. Springer, Berlin (2001)
Polyakov, A.: Turbulence without pressure. Phys. Rev. E **52**(6), 6183–6188 (1995)
Rieutord, M.: Linear theory of rotating fluids using spherical harmonics. Geophys. Astrophys. Fluid Dyn. **39**, 163–182 (1987)
Riley, J.J., Metcalfe, R.W., Weissman, M.A.: In: West, B.J. (ed.) Proceedings of the AIP Conference on Nonlinear Properties of Internal Waves, pp. 72–112 (1981)
Rogallo, R.: Numerical experiments in homogeneous turbulence, NASA Technical Memorandum, No 81315 (1981)
Rubinstein, R., Kurien, S., Cambon, C.: Scalar and tensor spherical harmonics expansion of the velocity correlation in homogeneous anisotropic turbulence. J. Turbul. **16**(11), 1058–1075 (2015)
Saffman, P.G.: Vortex Dynamics. Cambridge University Press, Cambridge (1995)
Simonsen, A.J., Krogstad, P.A.: Turbulent stress invariant analysis: clarification of existing terminology. Phys. Fluids **17**, 088103 (2005)
Smith, L.M., Waleffe, F.: Generation of slow, large scales in forced rotating, stratified turbulence. J. Fluid Mech. **451**, 145–168 (2002)
Sreenivasan, K.R., Narashima, R.: Rapid distortion theory of axisymmetric turbulence. J. Fluid Mech. **84**, 497–516 (1978)
Tennekes, H., Lumley, J.L.: A First Course in Turbulence. The MIT Press, Cambridge (1972)
Thomson, D.J.: Criteria for the selection of stochastic-models of particle trajectories in turbulent flows. J. Fluid Mech. **180**, 529–556 (1987)
Waleffe, F.: The nature of triad interactions in homogeneous turbulence. Phys. Fluids **4**, 350–363 (1992)
Waclawczyk, et al.: Statistical symmetries of the Lundgren-Monin-Novikov hierarchy. Phys. Rev. E **90**, 013022 (2014)

Chapter 3
Additional Reminders: Compressible Turbulence Description

3.1 Navier–Stokes Equations for Compressible Flows and Shock Jump Conditions

3.1.1 Governing Conservation Equations

The basic governing equations for such flows are

$$\frac{\partial \rho}{\partial t} + \nabla \cdot (\rho \boldsymbol{u}) = m, \tag{3.1}$$

$$\rho \left(\frac{\partial \boldsymbol{u}}{\partial t} + \boldsymbol{u} \nabla \boldsymbol{u} \right) = -\nabla p - \frac{2}{3} \nabla \left(\mu \nabla \cdot \boldsymbol{u} \right) + \nabla \cdot (\mu \mathbf{S}) + \rho \boldsymbol{f}, \tag{3.2}$$

$$\frac{p}{\mathcal{R}} \left(\frac{\partial s}{\partial t} + \boldsymbol{u} \cdot \nabla s \right) = \nabla \cdot (\kappa \nabla T) + \mu \left(\frac{1}{2} \mathbf{S} : \mathbf{S} - \frac{2}{3} (\nabla \cdot \boldsymbol{u})^2 \right) + Q, \tag{3.3}$$

where $\mathcal{R}$, p, ρ, T, $\boldsymbol{u}$, s, μ and κ denote the perfect gas constant, pressure, density, temperature, velocity, entropy, coefficients of viscosity and heat conduction, respectively. The additional variables m, $\boldsymbol{f}$ and Q are related to the rate of mass injection per unit volume, the body force per unit mass and the rate of heat addition per unit volume, respectively. Both the viscosity and the heat conduction are assumed to be monotonic functions of the temperature, i.e. $\mu = \mu(T)$ and $\kappa = \kappa(T)$. The system is supplemented by the perfect gas law

$$p = \rho \mathcal{R} T, \tag{3.4}$$

and the definition of the entropy

$$s - s_r = c_v \log \left[\left(\frac{p}{p_r} \right) \left(\frac{\rho_r}{\rho} \right)^{\gamma} \right] \tag{3.5}$$

P. Sagaut and C. Cambon, *Homogeneous Turbulence Dynamics*,
https://doi.org/10.1007/978-3-319-73162-9_3

where s_r, p_r and ρ_r are related to a reference state. c_v and c_p denote the specific heat at constant volume and pressure, respectively, and $\gamma = c_p/c_v$. Introducing the viscous stress tensor $\boldsymbol{\tau}$

$$\boldsymbol{\tau} = \mu \left(2\mathbf{S} - \frac{2}{3}(\nabla \cdot \boldsymbol{u})\mathbf{I} \right), \tag{3.6}$$

where the symmetric part of the velocity gradient tensor, $\mathbf{S}$, is defined as in Sect. 2.1.7, the momentum equation can be rewritten as follows

$$\frac{\partial \rho \boldsymbol{u}}{\partial t} + \nabla \cdot (\rho \boldsymbol{u}\boldsymbol{u}) = -\nabla p + \nabla \cdot \boldsymbol{\tau}. \tag{3.7}$$

For the sake of completeness, the evolution equation for the internal energy, $e = c_v T$, the enthalpy, $h = c_p T$, the vorticity $\boldsymbol{\omega} = \nabla \times \boldsymbol{u}$ and the pressure are given below:

$$\frac{\partial \rho e}{\partial t} + \nabla \cdot (\rho \boldsymbol{u} e) = -p(\nabla \cdot \boldsymbol{u}) + \boldsymbol{\tau} : (\nabla \boldsymbol{u}) + \nabla \boldsymbol{q}, \tag{3.8}$$

$$\frac{\partial \rho h}{\partial t} + \nabla \cdot (\rho \boldsymbol{u} h) = \left(\frac{\partial p}{\partial t} + \boldsymbol{u} \cdot \nabla p \right) + \boldsymbol{\tau} : (\nabla \boldsymbol{u}) + \nabla \boldsymbol{q}, \tag{3.9}$$

$$\begin{aligned} \frac{\partial \boldsymbol{\omega}}{\partial t} + (\nabla \boldsymbol{\omega})\boldsymbol{u} = {} & (\nabla \boldsymbol{u})\boldsymbol{\omega} + \nu \nabla^2 \boldsymbol{\omega} - (\nabla \cdot \boldsymbol{u})\boldsymbol{\omega} \\ & + \frac{1}{\rho^2}(\nabla \rho) \times \left(\nabla p - \frac{4}{3}\nabla(\mu(\nabla \cdot \boldsymbol{u})) + \mu \nabla \times \boldsymbol{\omega} \right) \\ & + \nabla \times \left(\frac{2}{\rho}\mathbf{S}(\nabla \mu) - \frac{2}{3}\frac{1}{\rho}(\nabla \cdot \boldsymbol{u})(\nabla \mu) \right) \\ & - \frac{1}{\rho}(\nabla \mu) \times (\nabla \times \boldsymbol{\omega}), \end{aligned} \tag{3.10}$$

$$\frac{\partial p}{\partial t} + \boldsymbol{u} \cdot \nabla p = \frac{\gamma p}{c_p} \left(\frac{\partial s}{\partial t} + \boldsymbol{u} \cdot \nabla s \right) - \gamma p (\nabla \cdot \boldsymbol{u}), \tag{3.11}$$

where the heat conduction flux vector $\boldsymbol{q}$ is defined as

$$\boldsymbol{q} = -\kappa \nabla T. \tag{3.12}$$

Considering constant molecular viscosity and diffusivity, and taking the inner product of (3.10) with $\boldsymbol{\omega}$, one obtains an evolution equation for the enstrophy $\Omega = \boldsymbol{\omega} \cdot \boldsymbol{\omega}/2$:

$$\frac{\partial \Omega}{\partial t} + \nabla \cdot (\boldsymbol{u}\Omega) = -\Omega(\nabla \cdot \boldsymbol{u}) + \boldsymbol{\omega} \cdot \mathbf{S} \cdot \boldsymbol{\omega} - \frac{1}{\rho^2}\boldsymbol{\omega} \cdot (\nabla p \times \nabla \rho) + \frac{\nu}{\rho}\boldsymbol{\omega} \cdot \nabla^2 \boldsymbol{\omega} - \nu \boldsymbol{\omega} \cdot \left(\frac{1}{\rho^2} \nabla \rho \times \left(\nabla^2 \boldsymbol{u} + \frac{1}{3} \nabla (\nabla \cdot \boldsymbol{u}) \right) \right). \tag{3.13}$$

3.1.2 Rankine–Hugoniot Jump Relations

Most cases dealing with shock/turbulence interaction addressed in Chaps. 15 and 16 do not take viscous effects into account. The rationale for that is that viscous effects are negligible compared to other physical mechanisms during the interaction (this will be proved a posteriori comparing theoretical results with DNS and experimental results), and that relaxation times associated to vibrational, rotational and translational energy modes of the molecules are very small with respect to macroscopic turbulent time scales. Therefore, the shock is modeled as a surface discontinuity with zero thickness. An important consequence is that the shock has no intrinsic time or length scale, and its corrugation is entirely governed by incident fluctuations. Its effects are entirely captured writing the Rankine–Hugoniot jump conditions for the mass, momentum and energy.[1]

It is reminded that for a scalar quantity $q(\boldsymbol{x}, t)$ governed by the following global conservation law in a fixed domain $\mathcal{D}$ with boundary $\partial\mathcal{D}$

$$\frac{\partial}{\partial t} \iiint_{\mathcal{D}} q d^3\boldsymbol{x} = \iiint_{\mathcal{D}} P_q d^3\boldsymbol{x} + \iint_{\partial\mathcal{D}} (q\boldsymbol{u} + \boldsymbol{F}_q) \cdot \boldsymbol{n} d^2\boldsymbol{x} \tag{3.14}$$

where P_q, $q\boldsymbol{u}$, $\boldsymbol{F}_q$ and $\boldsymbol{n}$ denote the volume production, the convective flux, the diffusive flux and the outward unit vector, respectively, the jump relation across a discontinuity which moves with velocity $\boldsymbol{u}_s$ is

$$\left[\left[(q(\boldsymbol{u} - \boldsymbol{u}_s) + \boldsymbol{F}_q) \cdot \boldsymbol{n}\right]\right] = 0. \tag{3.15}$$

Applying this result to the compressible Navier–Stokes equations for mass, momentum and total energy, one obtains for a planar shock wave moving at constant speed in the direct $\boldsymbol{e}_x$:

$$[[\rho u_n]] = 0, \tag{3.16}$$

$$\left[\left[\rho u_n^2 + p\right]\right] = 0, \tag{3.17}$$

$$[[\boldsymbol{u}_t]] = 0, \tag{3.18}$$

[1] Extensions to mixtures of perfect gas and reactive shock waves with chemical reactions will be discussed in devoted sections in Chaps. 15 and 16.

$$\left[\left[e+\frac{p}{\rho}+u^2\right]\right]=[[H]]=0, \tag{3.19}$$

where H is the stagnation enthalpy and $\boldsymbol{u}$ is the velocity in the reference frame tied to the shock wave, i.e. $\boldsymbol{u}=\boldsymbol{v}-\boldsymbol{u}_s$ where $\boldsymbol{v}$ and $\boldsymbol{u}_s$ are the fluid velocity and the shock speed in the laboratory frame, respectively. Subscripts n and t are related to the normal and tangential components of vector fields with respect to the shock wave, respectively:

$$u_n\equiv\boldsymbol{u}\cdot\boldsymbol{n},\quad \boldsymbol{u}_t\equiv\boldsymbol{n}\times(\boldsymbol{u}\times\boldsymbol{n}),\quad \boldsymbol{u}=u_n\boldsymbol{n}+\boldsymbol{u}_t, \tag{3.20}$$

where $\boldsymbol{n}$ is the shock normal unit vector. An exact general jump condition for the vorticity can be derived from the relations given above Hayes (1957). First noting that the vorticity vector $\boldsymbol{\omega}=\nabla\times\boldsymbol{u}$ can be decomposed as $\boldsymbol{\omega}=\omega_n\boldsymbol{n}+\boldsymbol{\omega}_t$ with

$$\omega_n=(\nabla\times\boldsymbol{u}_t)_n, \tag{3.21}$$

and

$$\boldsymbol{\omega}_t=\boldsymbol{n}\times\left(\frac{\partial\boldsymbol{u}_t}{\partial n}+\boldsymbol{u}_t\cdot\nabla\boldsymbol{n}-\nabla_{||}u_n\right), \tag{3.22}$$

where $\nabla_{||}$ denotes the tangential (with respect to the shock surface) part of the nabla operator, one obtains the following vorticity jump conditions in unsteady flows in which the shock experiences deformations:

$$[[\omega_n]]=0, \tag{3.23}$$

$$[[\boldsymbol{\omega}_t]]=\boldsymbol{n}\times\left(\nabla_{||}(\rho u_n)\left[\left[\frac{1}{\rho}\right]\right]-\frac{1}{\rho u_n}[[\rho]]\left(D_{||}\boldsymbol{u}_t+u_sD_{||}\boldsymbol{n}\right)\right), \tag{3.24}$$

with

$$D_{||}\boldsymbol{u}_t=\left(\frac{d\boldsymbol{u}_t}{dt}\right)_t+\boldsymbol{u}_t\cdot\nabla_{||}\boldsymbol{u}_t=\left(\frac{\partial\boldsymbol{u}_t}{\partial t}+u_s\frac{\partial\boldsymbol{u}_t}{\partial n}\right)_t+\boldsymbol{u}_t\cdot\nabla_{||}\boldsymbol{u}_t \tag{3.25}$$

and

$$D_{||}\boldsymbol{n}=\frac{d\boldsymbol{n}}{dt}+\boldsymbol{u}_t\cdot\nabla_{||}\boldsymbol{n}=-\nabla_{||}u_s+\boldsymbol{u}_t\cdot\nabla_{||}\boldsymbol{n}. \tag{3.26}$$

It is seen that the normal component of the vorticity is continuous across the shock, while the jump of the tangential component depends on the density jump, the tangential velocity and the shock wave deformation. In steady flows, the jump condition for the tangential vorticity simplifies as

$$[[\boldsymbol{\omega}_t]]=\boldsymbol{n}\times\left(\nabla_{||}(\rho u_n)\left[\left[\frac{1}{\rho}\right]\right]-\frac{1}{\rho u_n}[[\rho]]\,\boldsymbol{u}_t\cdot\nabla_{||}\boldsymbol{u}_t\right). \tag{3.27}$$

3.1.3 Linearization of Rankine-Hugoniot Jump Relations

In the analysis of the interaction between turbulent fluctuations and a shock wave (see Chap. 15) it may be very helpful to use the Linear Interaction Approximation (see Chap. 16) that relies on the linearized Rankine-Hugoniot jump relations for small disturbances. This is done linearizing the usual jump relations (3.16)–(3.19) written in a frame of reference that moves at the local instantaneous speed of the shock wave. Reminding that all quantities, including shock speed $\boldsymbol{u}_s$, shock normal unit vector $\boldsymbol{n}$ and shock tangential unit vector $\boldsymbol{t}$ exhibit a fluctuation and can be expressed as $q = \bar{q} + q'$ (where q is a dummy quantity and q' is assumed to be a first-order perturbation), one obtains

$$\left[\left[(\bar{\rho}+\rho')(\bar{\boldsymbol{u}}+\boldsymbol{u}'-\bar{\boldsymbol{u}}_s-\boldsymbol{u}'_s)\cdot(\bar{\boldsymbol{n}}+\boldsymbol{n}')\right]\right]=0, \tag{3.28}$$

$$\left[\left[\{(\bar{\rho}+\rho')[(\bar{\boldsymbol{u}}+\boldsymbol{u}')\otimes(\bar{\boldsymbol{u}}+\boldsymbol{u}'-\bar{\boldsymbol{u}}_s-\boldsymbol{u}'_s)+(\bar{p}+p')\mathbf{I}\}\cdot(\bar{\boldsymbol{n}}+\boldsymbol{n}')\right]\right]=0, \tag{3.29}$$

$$\left[\left[\{(\bar{\rho}+\rho')(\bar{E}+E')(\bar{\boldsymbol{u}}+\boldsymbol{u}'-\bar{\boldsymbol{u}}_s-\boldsymbol{u}'_s)+(\bar{p}+p')(\bar{\boldsymbol{u}}+\boldsymbol{u}')\}\cdot(\bar{\boldsymbol{n}}+\boldsymbol{n}')\right]\right]=0. \tag{3.30}$$

We now restrict the analysis to the case an unidirectional case with a planar shock wave normal to $\boldsymbol{e}_x$. The mean flow is $\bar{\boldsymbol{u}} = (U_1, 0, 0)$ upstream the shock wave and $\bar{\boldsymbol{u}} = (U_2, 0, 0)$ in the downstream region. The fluctuating velocity is expressed as $\boldsymbol{u}' = (u', v', w')$ in Cartesian coordinates. Introducing $\alpha' = \boldsymbol{n}\cdot\boldsymbol{t}'$ the first order angle between the unperturbed shock front and the local tangent of the corrugated shock, $\bar{j} = \bar{\rho}(U-\bar{u}_s)$ the mean mass flux across the shock front and $j' = \rho'(U-\bar{u}_s)+\bar{\rho}(u'-u'_s)$ the mass flux fluctuation, on obtains the following linearized jump relations

$$\left[\left[j'\right]\right]=0, \tag{3.31}$$

$$\bar{j}\left[\left[u'\right]\right]+j'\left[[U]\right]+\left[\left[p'\right]\right]=0, \tag{3.32}$$

$$\left[\left[U\alpha'+v'\right]\right]=0, \tag{3.33}$$

$$\bar{j}\left[\left[e'+Uu'\right]\right]+j'\left[\left[\bar{e}+U^2/2\right]\right]+\left[\left[\bar{p}u'+p'U\right]\right]=0. \tag{3.34}$$

3.2 Introduction to Modal Decomposition of Turbulent Fluctuations

3.2.1 Statement of the Problem

A natural question which arises when dealing with compressible turbulent flows is: how to characterize the compressibility effects on turbulence? Or, in an equivalent way, what are the differences between the compressible turbulent fluctuations and the

incompressible ones? To answer this question, it is first important to remark that in incompressible flows the full solution is contained in the sole velocity field since the pressure is nothing but an enslaved Lagrange multiplier. In compressible turbulence, this is no longer true since pressure is now an autonomous variable and that at least one additional physical variable is required to describe the solution.[2]

A common way to solve this problem is to try to decompose the observed fluctuations as the sum of a compressible part and an incompressible one, the latter being very often understood as the part of the solution which fulfills the incompressible Navier–Stokes equations, the former being defined as the difference between the full solution and the incompressible part. Unfortunately, no fully general decomposition based on this approach leading to tractable and useful analysis has been proposed up to now. A main reason for that is that such a decomposition does not explicitly distinguish between acoustic waves and other compressible phenomena.

To remedy this problem and to provide a meaningful and powerful decomposition of compressible fluctuations into physical modes, Kovasznay proposed a small-parameter expansion discussed below (Sect. 3.2.2), which is based on the assumption that the turbulent fluctuations will be small in some sense with respect to a uniform mean flow. As it will be seen below, this decomposition provides us with many meaningful informations, but its validity is restricted since it relies on a linearized theory. To handle flows in which nonlinear mechanisms are dominant, another approach consists in using the exact Helmholtz decomposition of the compressible velocity field (see Sect. 2.1.5). Since this decomposition does not rely on any assumption dealing with the amplitude of the turbulent fluctuations, it is valid in all flows. But its weakness its that it does not allow a direct splitting of other flow variables like density, pressure or entropy. Therefore, it must be supplemented with arbitrary splitting procedures for these variables.

3.2.2 *Kovasznay's Linear Decomposition*

The first step in Kovasznay's approach (Kovasznay 1953) consists in expanding the turbulent field as

$$\boldsymbol{u} = \boldsymbol{u}_0 + \epsilon \boldsymbol{u}_1 + \epsilon^2 \boldsymbol{u}_2 + \dots , \tag{3.35}$$

$$\rho = \rho_0 + \epsilon \rho_1 + \epsilon^2 \rho_2 + \dots , \tag{3.36}$$

$$p = p_0 + \epsilon p_1 + \epsilon^2 p_2 + \dots , \tag{3.37}$$

$$s = s_0 + \epsilon s_1 + \epsilon^2 s_2 + \dots \tag{3.38}$$

[2]The discussion in the present chapter is restricted to the case of single-phase, non-reactive, single-species flows of divariant fluids. The case of binary mixtures of perfect gas is addressed in Sect. 16.9.2.

where ϵ is a small parameter related to the amplitude of the perturbation field and $(\boldsymbol{u}_0, \rho_0, p_0, s_0)$ are related to a uniform mean field. It is worth noting that the leading fluctuating terms in the pressure and the density fields are assumed to have the same scaling order with respect to ϵ. Different scaling laws can also be considered (e.g. Zank and Matthaeus 1990, 1991; Bayly et al. 1992). The mean velocity $\boldsymbol{u}_0$ can be set to zero by changing the frame of reference.

Assuming that the source terms in the right-hand sides of Eqs. (3.1)–(3.3) scale like ϵ and inserting the above expansions into these equations, one obtains the following linearized set of equations for the first-order fluctuating field $(\boldsymbol{u}_1, \rho_1, p_1, s_1)$ (the subscript 1 will be omitted hereafter for the sake of clarity):

$$\nabla \cdot \boldsymbol{u} + \frac{\partial p}{\partial t} - \frac{\partial s}{\partial t} = \frac{m}{\rho_0}, \tag{3.39}$$

$$\frac{\partial \boldsymbol{u}}{\partial t} + a_0^2 \nabla p - \nu_0 \nabla^2 \boldsymbol{u} - \frac{1}{3}\nu_0 \nabla(\nabla \cdot \boldsymbol{u}) = \boldsymbol{f}, \tag{3.40}$$

$$\frac{\partial s}{\partial t} - \frac{4}{3}\nu_0 \nabla^2 s - \frac{4}{3}(\gamma - 1)\nu_0 \nabla^2 p = \frac{Q}{\rho_0 c_p T_0}, \tag{3.41}$$

where $\nu_0 = \mu_0/\rho_0$, $\gamma = c_p/c_v$, c_p being the specific heat at constant pressure and c_v that at constant volume. It is to be noted that the pressure and the entropy have been normalized by γp_0 and c_p, respectively (the notations have not been changed for the sake of simplicity). The speed of sound in the undisturbed medium, a_0, is computed as $a_0 = \sqrt{\gamma p_0/\rho_0}$. The Prandtl number $\mu c_p/\kappa$ has been taken equal to 3/4 for the sole purpose of simplifying the algebra. This linear system can be rewritten introducing the fluctuating vorticity $\boldsymbol{\omega} = \nabla \times \boldsymbol{u}$. By a slight manipulation, one obtains

$$\frac{\partial \boldsymbol{\omega}}{\partial t} - \nu_0 \nabla^2 \boldsymbol{\omega} = \nabla \times \boldsymbol{f}, \tag{3.42}$$

$$\frac{\partial s}{\partial t} - \frac{4}{3}\nu_0 \nabla^2 s = \frac{4}{3}(\gamma - 1)\nu_0 \nabla^2 p + \frac{Q}{\rho_0 c_p T_0}, \tag{3.43}$$

$$\frac{\partial^2 p}{\partial t^2} - a_0^2 \nabla^2 p - \frac{4}{3}\gamma\nu_0 \frac{\partial}{\partial t}\left(\nabla^2 p\right) = \left[\left(\frac{\partial}{\partial t} - \frac{4}{3}\nu_0 \nabla^2\right)\frac{m}{\rho_0} - \nabla \cdot \boldsymbol{f} + \frac{\partial}{\partial t}\left(\frac{Q}{\rho_0 c_p T_0}\right)\right]. \tag{3.44}$$

This set of equations is supplemented by additional relations obtained by linearizing the perfect gas law (3.4) and the entropy definition (3.5):

$$\gamma p - \frac{\rho}{\rho_0} - \frac{T}{T_0} = 0, \tag{3.45}$$

$$p + \frac{1}{\gamma - 1}\left(s - \frac{T}{T_0}\right) = 0. \tag{3.46}$$

Using these equations, Kovasznay proposes to define three *physical modes*, each mode corresponding to the solution of a subsystem extracted from (3.42)–(3.44):

- The *vorticity mode*, whose fluctuating field is denoted $(\boldsymbol{\omega}_v, p_v, s_v, \boldsymbol{u}_v)$, is defined as follows

$$\frac{\partial \boldsymbol{\omega}_v}{\partial t} - \nu_0 \nabla^2 \boldsymbol{\omega}_v = \nabla \times \boldsymbol{f}, \tag{3.47}$$

$$p_v = 0, \quad s_v = 0, \quad \nabla \times \boldsymbol{u}_v = \boldsymbol{\omega}_v, \quad \nabla \cdot \boldsymbol{u}_v = 0. \tag{3.48}$$

  The vorticity mode is associated with a solenoidal rotational velocity field, and it can be interpreted as the "incompressible" part of the solution. But it is worth noting that there is no corresponding pressure disturbance because it is expected to be of order ϵ^2. If the source term is set equal to zero, an exact wave-like solution is

$$\boldsymbol{\omega}_v = \boldsymbol{Z}_v \exp\left(\imath \boldsymbol{k}_v \cdot \boldsymbol{x} - \nu_0 k_v^2 t\right), \tag{3.49}$$

$$\boldsymbol{u}_v = \imath \frac{\boldsymbol{k}_v \times \boldsymbol{Z}_v}{k_v^2} \exp\left(\imath \boldsymbol{k}_v \cdot \boldsymbol{x} - \nu_0 k_v^2 t\right), \tag{3.50}$$

  where the wave vector associated with the vorticity mode, $\boldsymbol{k}_v$, and the complex amplitude fluctuation vector $\boldsymbol{Z}_v$ are such that $\boldsymbol{Z}_v \cdot \boldsymbol{k}_v = 0$, i.e. the associated velocity field corresponds to a transverse wave.
- The *entropy mode* whose corresponding perturbation field is $(\boldsymbol{\omega}_s, p_s, s_s, \boldsymbol{u}_s)$, is defined as

$$\frac{\partial s_s}{\partial t} - \frac{4}{3}\nu_0 \nabla^2 s_s = \frac{4}{3}(\gamma - 1)\nu_0 \nabla^2 p_s + \frac{Q}{\rho_0 c_p T_0}, \tag{3.51}$$

$$\boldsymbol{\omega}_s = 0, \quad p_s = 0, \quad \nabla \times \boldsymbol{u}_s = 0, \quad \nabla \cdot \boldsymbol{u}_s = \frac{\partial s_s}{\partial t}. \tag{3.52}$$

  The corresponding wave-like solution for the source-free problem is

$$s_s = S \exp\left(\imath \boldsymbol{k}_s \cdot \boldsymbol{x} - \frac{4}{3}\nu_0 k_s^2 t\right), \tag{3.53}$$

$$\boldsymbol{u}_s = \imath S \frac{4}{3}\nu_0 \boldsymbol{k}_s \exp\left(\imath \boldsymbol{k}_s \cdot \boldsymbol{x} - \frac{4}{3}\nu_0 k_s^2 t\right), \tag{3.54}$$

  where S and $\boldsymbol{k}_s$ are the complex amplitude and the wave vector, respectively. The velocity perturbation is purely dilatational and is induced by the sole viscous effects, and therefore $\boldsymbol{u}_s = 0$ in the inviscid case.

- The *acoustic mode*, which is characterized by $(\boldsymbol{\omega}_a, p_a, s_a, \boldsymbol{u}_a)$. The governing relations for this mode are

$$\frac{\partial^2 p_a}{\partial t^2} - a_0^2 \nabla^2 p_a - \frac{4}{3}\gamma\nu_0 \frac{\partial}{\partial t}\left(\nabla^2 p_a\right) = \left[\left(\frac{\partial}{\partial t} - \frac{4}{3}\nu_0\nabla^2\right)\frac{m}{\rho_0} - \nabla\cdot\boldsymbol{f} + \frac{\partial}{\partial t}\left(\frac{Q}{\rho_0 c_p T_0}\right)\right], \tag{3.55}$$

$$\frac{\partial s_a}{\partial t} - \frac{4}{3}\nu_0\nabla^2 s_a = \frac{4}{3}(\gamma-1)\nu_0\nabla^2 p_a, \tag{3.56}$$

$$\nabla\times\boldsymbol{u}_a = 0, \quad \nabla\cdot\boldsymbol{u}_a = \frac{\partial s_a}{\partial t} - \frac{\partial p_a}{\partial t} + \frac{m}{\rho_0}. \tag{3.57}$$

The wave solution is

$$p_a = P\exp\left(\imath(\boldsymbol{k}_a\cdot\boldsymbol{x} - \sigma t)\right), \tag{3.58}$$

$$s_a = \frac{4}{3}P\frac{(\gamma-1)\nu_0 k_a^2}{c - \frac{4}{3}\nu_0 k_a}\exp\left(\imath(\boldsymbol{k}_a\cdot\boldsymbol{x} - \sigma t)\right), \tag{3.59}$$

$$\boldsymbol{u}_a = \imath P\boldsymbol{k}_a\frac{a_0^2}{c - \frac{4}{3}\nu_0 k_a}\left(\imath(\boldsymbol{k}_a\cdot\boldsymbol{x} - \sigma t)\right), \tag{3.60}$$

where P and $\boldsymbol{k}_a$ are the complex amplitude and the wave vector, respectively. The complex propagation frequency σ is defined as

$$\sigma = -a_0 k_a\left(\sqrt{1 - \frac{4\gamma^2\nu_0^2 k_a^2}{9a_0^2}} - \imath\frac{2}{3}\frac{\gamma\nu_0 k_a}{a_0}\right). \tag{3.61}$$

The imaginary part of σ gives the damping rate of the acoustic waves while the real part is related to the frequency of oscillations. It is observed that the viscous effects lead to the existence of a dispersive solution. The existence of an acoustic entropy fluctuation originates in the viscous dissipation of the pressure waves. In the inviscid case, one recovers $s_a = 0$ and waves travel at the speed a_0 (i.e. $\sigma = -a_0 k_a$).

It is seen that disturbances associated with the entropy mode and the vorticity mode are passively advected by the mean field (velocity $\boldsymbol{u}_0$ in a reference frame at rest), while acoustic disturbances travel at the speed of sound relatively to the mean flow.

Using this three-mode decomposition, all turbulent fluctuations can be decomposed as indicated in Table 3.1.

Table 3.1 Non-vanishing Kovasznay mode contribution to the fluctuating field. Symbols are related to non-vanishing contributions. X: non-zero contribution in the viscous case only; ◯ = non-zero contribution in both viscous and inviscid case

Mode/fluctuation	s	p	$\boldsymbol{u}$	$\boldsymbol{\omega}$
Acoustic	X	◯	◯	
Entropy	◯		X	
Vorticity			◯	◯

The analysis of governing equations for each mode also give some information on the role of the forcing terms m, $\boldsymbol{f}$ and Q.

The mass addition term m leads to a production of the acoustic mode (see Eqs. (3.55) and (3.57)). The effect is twofold: mass addition induces the rise of a non-zero velocity perturbation, and it also generates pressure waves. But it is worth noting that if m obeys the diffusion equation

$$\left(\frac{\partial}{\partial t} - \frac{4}{3}\nu_0\nabla^2\right)\frac{m}{\rho_0} = 0 \tag{3.62}$$

no pressure wave is created. In this case, the generated velocity field is a potential field whose potential ϕ_p satisfies the following Poisson equation

$$\nabla^2\phi_p = \frac{m}{\rho_0}. \tag{3.63}$$

The forcing term $\boldsymbol{f}$ produces both the vorticity mode and the acoustic mode. A closer examination of the governing equations shows that the irrotational (resp. solenoidal) part of $\boldsymbol{f}$ generates the acoustic (resp. vorticity) mode and cannot generate the vorticity (resp. acoustic) mode. If $\boldsymbol{f}$ is an harmonic force field (i.e. it is both solenoidal and irrotational) no fluctuating vorticity and pressure fields are generated. The only effect is the creation of an harmonic velocity field $\boldsymbol{u}_H$ given by

$$\frac{\partial \boldsymbol{u}_H}{\partial t} = \boldsymbol{f}. \tag{3.64}$$

The effect of heat addition (term Q) is to create both entropy mode and acoustic mode. Adding heat obviously yields an increase of the entropy (creation of the entropy mode) and leads to a local dilatation of the medium and a local disturbance in the pressure field (creation of the acoustic mode).

The Kovasznay modes are decoupled in the absence of mean flow gradient, showing that they correspond to eigenmodes of the linearized Euler equations in that case. The associated characteristic propagation velocities correspond to the eigenvalues of the system. This point is further discussed in Sect. 3.2.7.

Table 3.2 Source terms associated with second-order bilateral modal interactions according to Kovasznay decomposition

Modal interaction	Acoustic source	Vorticity source	Entropy source
Acoustic-Acoustic	Steepening and self-scattering $\nabla\cdot\nabla\cdot(\boldsymbol{u}_a\boldsymbol{u}_a)+a_0^2\nabla^2 p_a^2+\frac{\gamma-1}{2}\frac{\partial^2 p_a^2}{\partial t^2}$	$O(\epsilon^2\epsilon')$	$O(\epsilon^2\epsilon')$
Vorticity-Vorticity	Generation $2\nabla\cdot\nabla\cdot(\boldsymbol{u}_v\boldsymbol{u}_v)$	Self-convection and stretching $-\boldsymbol{u}_v\nabla\boldsymbol{\omega}_v+\boldsymbol{\omega}_v\nabla\boldsymbol{u}_v$	$O(\epsilon^2\epsilon')$
Entropy-Entropy	$O(\epsilon^2\epsilon')$	$O(\epsilon^2\epsilon')$	$O(\epsilon^2\epsilon')$
Acoustic-Vorticity	Scattering $2\nabla\cdot\nabla\cdot(\boldsymbol{u}_v\boldsymbol{u}_a)$	Vorticity convection and stretching $-\boldsymbol{u}_a\nabla\boldsymbol{\omega}_v+\boldsymbol{\omega}_v\nabla\boldsymbol{u}_a-\boldsymbol{\omega}_v\nabla\cdot\boldsymbol{u}_a$	$O(\epsilon^2\epsilon')$
Acoustic-Entropy	Scattering $\frac{\partial}{\partial t}\nabla\cdot(s_s\boldsymbol{u}_a)$	Baroclinic source $-a_0^2(\nabla s_s)\times(\nabla p_a)$	Heat convection $-\boldsymbol{u}_a\cdot\nabla s_s$
Vorticity-Entropy	$O(\epsilon^2\epsilon')$	$O(\epsilon^2\epsilon')$	Heat convection $-\boldsymbol{u}_v\cdot\nabla s_s$

3.2.3 *Weakly Nonlinear Corrected Kovasznay Decomposition*

The linear decomposition presented above makes it possible to define the three physical modes, but it does not provide any insight into the interactions between them since the modes evolve independently. Informations dealing with the creation/destruction of fluctuations due to the modal interactions are recovered looking at terms of order ϵ^2 resulting from bilateral interactions (Chu and Kovasznay 1957). The full analysis brings in 18 terms and also involves a second non-dimensional parameter[3] $\epsilon'=\nu_0 k/a_0$ which measures the ratio of the characteristic length scale of the perturbation, $1/k$, and the intrinsic scale of the medium ν_0/a_0. Second-order terms scale as ϵ^2 or $\epsilon^2\epsilon'$. Since for turbulent flows at atmospheric pressure and density one has $\epsilon'\ll\epsilon$,[4] it is chosen to neglect terms of order $\epsilon^2\epsilon'$. Remaining terms and associated production mechanisms are displayed in Table 3.2.

It is important to note that this second-order corrections make all the modes fully coupled, since even self-interactions yield the growth of the other modes. Therefore, the Kovasznay decomposition strictly holds for fully linear approximations only. Statistical theories for the interaction between isotropic turbulence and the acoustic

[3] It is recalled that the first non-dimensional parameter ϵ is related to the amplitude of the perturbations.

[4] Considering $\nu_0=0.15\cdot10^{-4}\,\mathrm{m^2 s^{-1}}$ and $a_0=300\,\mathrm{ms^{-1}}$, one obtains $\nu_0/a_0=5\cdot10^{-8}\,\mathrm{m}$ which is of the order of the mean-free path of the molecules in the gas. For a frequency equal to 1 Hz, one has $1/k=300\,\mathrm{m}$ and $\epsilon'=1.66\cdot10^{-10}$. For 1 kHz one has $\epsilon'=1.66\cdot10^{-7}$ and $\epsilon'=1.66\cdot10^{-4}$ at 1 MHz. Even at 1 GHz, one obtains $\epsilon'=1.66\cdot10^{-1}<1$!

field are addressed in Sects. 13.2.10 and 13.2.11, which are related to noise generation and noise scattering by quasi-isentropic turbulence, respectively. The production of entropy by vorticity self-interactions in low-Mach number isotropic turbulence is discussed in Sect. 13.3.4.

3.2.4 Bridging Between Kovasznay and Helmholtz Decomposition

The Kovasznay decomposition can be related to the Helmholtz decomposition (see Sect. 2.1.5) for the velocity field.

In the case where $\boldsymbol{u}^{(sd)} = 0$ in Eq. (2.20), one obtains in the viscous case:

$$\boldsymbol{u}^{(sol)} = \boldsymbol{u}_v, \quad \boldsymbol{u}^{(dil)} = \boldsymbol{u}_a + \boldsymbol{u}_s. \tag{3.65}$$

It is worth noting that the Helmholtz approach does not rely on a small parameter expansion and is therefore exact, while the Kovasznay decomposition is nothing but a first-order approximation. It is important to remind that $\boldsymbol{u}^{(sol)}$ is associated to a null fluctuating pressure field in this case, since p_s is a second-order quantity.

3.2.5 Helmholtz-Decomposition-Based Kinematic Relations for Isotropic Turbulence

The Helmholtz decomposition $\boldsymbol{u}' = \boldsymbol{u}'_s + \boldsymbol{u}'_d$ can be used to extend the kinematic relations discussed in the incompressible flow framework in Chap. 2. The two-point velocity correlation tensor $R_{ij}(\boldsymbol{x}, \boldsymbol{x}+\boldsymbol{r})$ can be split in isotropic turbulence as follows

$$R_{ij}(\boldsymbol{r}) = \underbrace{\overline{u'_{s_i}(0)u'_{s_j}(\boldsymbol{r})}}_{R^s_{ij}(\boldsymbol{r})} + \underbrace{\overline{u'_{s_i}(0)u'_{d_j}(\boldsymbol{r})} + \overline{u'_{d_i}(0)u'_{s_j}(\boldsymbol{r})}}_{R^{sd}_{ij}(\boldsymbol{r})} + \underbrace{\overline{u'_{d_i}(0)u'_{d_j}(\boldsymbol{r})}}_{R^{d}_{ij}(\boldsymbol{r})}. \tag{3.66}$$

It can be shown that $R^{sd}_{ij}(\boldsymbol{r}) \equiv 0$ in isotropic turbulence. The general formulation for second-order isotropic tensors yields

$$R_{ij}(\boldsymbol{r}) = u'^2 \left[\frac{a(r) - b(r)}{r^2} r_i r_j + b(r)\delta_{ij} \right], \tag{3.67}$$

where $a(r)$ and $b(r)$ are the total longitudinal and lateral two-point velocity correlation functions, respectively. The solenoidal character of $\boldsymbol{u}'_s$ leads to the fact that the expression of $R^s_{ij}(\boldsymbol{r})$ is identical to those found in the incompressible case:

$$R_{ij}^{s}(\boldsymbol{r}) = u'^2\left[-\frac{1}{2r}f_s'(r)r_i r_j + \left(f_s(r) + \frac{1}{2}rf_s'(r)\right)\delta_{ij}\right], \tag{3.68}$$

where $f_s(r)$ denotes the longitudinal correlation function of the solenoidal velocity component $\boldsymbol{u}_s'$. The fact that the curl of $R_{ij}^{d}(\boldsymbol{r})$ vanishes leads to

$$R_{ij}^{d}(\boldsymbol{r}) = u'^2\left[\frac{1}{r}g_d'(r)r_i r_j + g_d(r)\delta_{ij}\right], \tag{3.69}$$

where $g_d(r)$ denotes the transverse correlation function of the dilatational velocity component $\boldsymbol{u}_d'$. Equalizing (3.67) and the sum of (3.68) and (3.69), one obtains

$$rf_s'(r)/2 - rg_d'(r) = b(r) - a(r),\ rf_s'(r) + f_s(r) + g_d(r) = b(r) \tag{3.70}$$

whose solution is:

$$f_s(r) = -\frac{2}{3}\int_0^{+\infty}\frac{h(z)}{z}dz + \frac{2}{3}\int_0^{r}\frac{h(z)}{z}\left(1 - \frac{z^3}{r^3}\right)dz \tag{3.71}$$

$$g_d(r) = \frac{2}{3}\int_0^{+\infty}\frac{h(z)}{z}dz + \frac{1}{3}\int_0^{r}\frac{h(z)}{z}\left(1 - \frac{z^3}{r^3}\right)dz - \int_0^{r}\frac{h(z)}{z}dz + b(r), \tag{3.72}$$

where $h(r) = b(r) - a(r) + rb'(r)$. In the incompressible case, one has $b(r) = a(r) + ra'(r)/2$, leading to $f_s(r) = a(r)$ and $g_d(r) = 0$.

The spectral tensor can also be split into a dilatational and a solenoidal component:

$$\hat{R}_{ij}(\boldsymbol{k}) = \hat{R}_{ij}^{s}(\boldsymbol{k}) + \hat{R}_{ij}^{d}(\boldsymbol{k}), \tag{3.73}$$

where

$$\hat{R}_{ij}^{s}(\boldsymbol{k}) \equiv \iiint R_{ij}^{s}(\boldsymbol{x})e^{-\imath\boldsymbol{k}\cdot\boldsymbol{x}}d^3\boldsymbol{x} = A_s(k)(k^2\delta_{ij} - k_i k_j) \tag{3.74}$$

$$\hat{R}_{ij}^{d}(\boldsymbol{k}) \equiv \iiint R_{ij}^{d}(\boldsymbol{x})e^{-\imath\boldsymbol{k}\cdot\boldsymbol{x}}d^3\boldsymbol{x} = A_d(k)k_i k_j. \tag{3.75}$$

Introducing the associated three-dimensional spectra

$$E(k) = \iint_{k=\|\boldsymbol{k}\|}\hat{R}_{ii}(\boldsymbol{k})d^2\boldsymbol{k}, \tag{3.76}$$

$$E_{ss}(k) = \iint_{k=\|\boldsymbol{k}\|}\hat{R}_{ii}^{s}(\boldsymbol{k})d^2\boldsymbol{k} = -4\pi k^4 A_s(k), \tag{3.77}$$

$$E_{dd}(k) = \iint_{k=\|\boldsymbol{k}\|} \hat{R}^d_{ii}(\boldsymbol{k}) d^2\boldsymbol{k} = 4\pi k^4 A_d(k), \tag{3.78}$$

one obtains $E(k) = E_{ss}(k) + \frac{1}{2}E_{dd}(k)$, along with

$$\hat{R}_{ij}(\boldsymbol{k}) = \frac{1}{4\pi k^4}\left([E_{dd}(k) - E_{ss}(k)]\, k_i k_j + k^2 E_{ss}(k)\delta_{ij}\right). \tag{3.79}$$

The *solenoidal* and *dilatational kinetic energy*, respectively denoted $\mathcal{K}_s$ and $\mathcal{K}_d$, are computed as follows

$$\mathcal{K}_s(t) = \int_0^{+\infty} E_{ss}(k,t)dk, \quad \mathcal{K}_d(t) = \int_0^{+\infty} E_{dd}(k,t)dk \tag{3.80}$$

while the corresponding dissipations are defined as

$$\bar{\varepsilon}_s(t) = 2\nu \int_0^{+\infty} k^2 E_{ss}(k,t)dk, \quad \bar{\varepsilon}_d(t) = 2\frac{4}{3}\nu \int_0^{+\infty} k^2 E_{dd}(k,t)dk. \tag{3.81}$$

Combining the above relations, one can also express the three-dimensional spectra as functions of the correlation functions:

$$E_{ss}(k) = \frac{u'^2}{\pi} \int_0^{+\infty} f_s(r) k^2 r^2 \left(\frac{\sin(kr)}{kr} - \cos(kr)\right) dr, \tag{3.82}$$

$$E_{dd}(k) = \frac{u'^2}{\pi} \int_0^{+\infty} g_d(r) k^2 r^2 \left(\frac{\sin(kr)}{kr} - \cos(kr)\right) dr. \tag{3.83}$$

3.2.6 *On the Faisability of a Fully General Modal Decomposition*

The second-order correction of the linear Kovasznay decomposition provides a meaningful qualitative insight into bilateral interactions. Because of the small amplitude hypothesis, it is not able to lead correct quantitative predictions in fully developed turbulent flows. Therefore, more sophisticated decompositions must be found to deal with genuinely nonlinear dynamics.

The idea of defining nearly independent physical modes which can serve as a basis to decompose turbulent compressible fluctuations is very appealing, but unfortunately it cannot be extended to arbitrary mean fields. The very reason why is that in the general case the mean field gradients bring in new terms in linearized equations which do not allow to decouple the different fluctuating fields. The search for such a system of equations for the acoustic mode developing about an arbitrary mean field is the Holy Graal of aeroacoustics, and a large number of surrogate evolution equations

have been proposed which will not be discussed here. The interested reader is invited to refer to reference books in acoustics.

Other chapters of this book deal with the coupling between the modes induced by the mean field non-uniformity: Chap. 14 is devoted to the interactions induced by a non-uniform smooth mean velocity field while the case of the interaction with a planar normal shock wave is detailed in Chap. 15.

3.2.7 *Remarks on the Energy of Disturbances in Compressible Turbulence*

The definition of the *energy of small disturbances* in compressible turbulence is a non-trivial topic, since several definitions have been proposed for it. For the sake of physical consistency, energy in a disturbance should be defined as a positive definite norm that characterizes the level of fluctuation in the disturbance about a base flow.

The best definition was given by Chu (1965), Joseph et al. (2011). Considering the linearized set of equations for small amplitude viscous disturbances, he proposed to define the energy contained in a control volume V as

$$E(t) = \iiint_V \left\{ \frac{1}{2}\rho_0(u_i' u_i') + \frac{1}{2}\frac{a_0^2}{\gamma\rho_0}\rho'^2 + \frac{1}{2}\frac{\rho_0 c_v}{T_0}T'^2 \right\} d\boldsymbol{x} \tag{3.84}$$

$$= \iiint_V \left\{ \frac{1}{2}\rho_0(u_i' u_i') + \frac{1}{2}\rho_0 a_0^2 \left(\frac{p'}{\gamma p_0}\right)^2 + \frac{1}{2}\frac{\gamma-1}{\gamma}p_0\left(\frac{s'}{R}\right)^2 \right\} d\boldsymbol{x}. \tag{3.85}$$

This definition has the advantage to define an inner product, with respect to which the linearized Euler equations about a uniform base flow are self-adjoint. This is illustrated considering 2D case for the sake of brevity without loss of generality and a uniform base flow $(\rho_0, u_0, 0, T_0)$. Introducing the normalized monochromatic fluctuation vector with wave vector $\boldsymbol{k} = (k_x, k_y)$ as

$$\boldsymbol{V}'(\boldsymbol{x}, t) = \left(\frac{u'(t)}{a_0} e^{\imath \boldsymbol{k}\cdot\boldsymbol{x}}, \frac{v'(t)}{a_0} e^{\imath \boldsymbol{k}\cdot\boldsymbol{x}}, \frac{\rho'(t)}{\sqrt{\gamma}\rho_0} e^{\imath \boldsymbol{k}\cdot\boldsymbol{x}}, \frac{T'(t)}{\sqrt{\gamma(\gamma-1)}T_0} e^{\imath \boldsymbol{k}\cdot\boldsymbol{x}} \right), \tag{3.86}$$

the linearized evolution equations can be recast as

$$\frac{d\boldsymbol{V}'}{dt} = \mathbf{M}\boldsymbol{V}', \quad \mathbf{M} = \begin{pmatrix} -\imath k_x u_0 & -\imath \frac{k_x a_0}{\sqrt{\gamma}} & -\imath \frac{k_y a_0}{\sqrt{\gamma}} & 0 \\ -\imath \frac{k_x a_0}{\sqrt{\gamma}} & -\imath k_x u_0 & 0 & -\imath \frac{k_x a_0 \sqrt{\gamma-1}}{\sqrt{\gamma}} \\ -\imath \frac{k_y a_0}{\sqrt{\gamma}} & 0 & -\imath k_x u_0 & -\imath \frac{k_y a_0 \sqrt{\gamma-1}}{\sqrt{\gamma}} \\ 0 & -\imath \frac{k_x a_0 \sqrt{\gamma-1}}{\sqrt{\gamma}} & -\imath \frac{k_y a_0 \sqrt{\gamma-1}}{\sqrt{\gamma}} & -\imath k_x u_0 \end{pmatrix}. \tag{3.87}$$

The eigenvalues of $\mathbf{M}$ are $(-\imath k_x u_0, -\imath k_x u_0, -\imath k_x u_0 - i\|\boldsymbol{k}\|a_0, -\imath k_x u_0 + i\|\boldsymbol{k}\|a_0)$. $\mathbf{M}$ is purely imaginary and symmetric, hence normal. Reminding that the adjoint of a matrix is its conjugate transpose, the adjoint of $\mathbf{M}$ is simply its negative, leading to the fact that $\mathbf{M}$ is self-adjoint. Therefore, its eigenvectors are orthogonal to each other. They are expressed as

$$\boldsymbol{Y}_1 = \begin{pmatrix} \sqrt{\frac{\gamma-1}{\gamma}} \\ 0 \\ 0 \\ -\frac{1}{\sqrt{\gamma}} \end{pmatrix}, \ \boldsymbol{Y}_2 = \begin{pmatrix} 0 \\ \frac{k_y}{\|\boldsymbol{k}\|} \\ \frac{-k_x}{\|\boldsymbol{k}\|} \\ 0 \end{pmatrix}, \ \boldsymbol{Y}_3 = \begin{pmatrix} \frac{1}{\sqrt{2\gamma}} \\ \frac{k_x}{\sqrt{2}\|\boldsymbol{k}\|} \\ \frac{k_y}{\sqrt{2}\|\boldsymbol{k}\|} \\ \sqrt{\frac{\gamma-1}{2\gamma}} \end{pmatrix}, \ \boldsymbol{Y}_4 = \begin{pmatrix} \frac{1}{\sqrt{2\gamma}} \\ \frac{-k_x}{\sqrt{2}\|\boldsymbol{k}\|} \\ \frac{-k_y}{\sqrt{2}\|\boldsymbol{k}\|} \\ \sqrt{\frac{\gamma-1}{2\gamma}} \end{pmatrix} \tag{3.88}$$

and are related to entropy, vorticity, fast and slow acoustic waves, respectively. These eigenvectors are related to the Kovasznay modes discussed in Sect. 3.2.2, showing that the Kovasznay decomposition is a normal-mode decomposition of small compressible disturbances. Defining the control area as $V = [0, 2\pi/k_x] \times [0, 2\pi/k_y]$, Chu's disturbance energy can be rewritten in terms of the L^2-norm of the state vector as

$$E(t) = \frac{\gamma p_0 \pi^2}{2k_x k_y} \|\boldsymbol{V}'\|_2^2. \tag{3.89}$$

The fact that evolution equations are self-adjoint with respect to the inner product associated to the energy definition is very important, since it allows for an exact energy conservation in the inviscid case with uniform base flow without spurious energy growth due to non-normal modal interactions. Since the eigenvectors form a complete basis, any arbitrary perturbation can be written a linear combination of the eigenvectors:

$$\boldsymbol{V}'(t) = a_1(t)\boldsymbol{Y}_1 + a_2(t)\boldsymbol{Y}_2 + a_3(t)\boldsymbol{Y}_3 + a_4(t)\boldsymbol{Y}_4. \tag{3.90}$$

Thanks to the fact that eigenvectors are orthonormal, the inner product simplifies as

$$\|\boldsymbol{V}'(t)\|_2^2 = |a_1(t)|^2 + |a_2(t)|^2 + |a_3(t)|^2 + |a_4(t)|^2. \tag{3.91}$$

The solution of the linear time evolution problem is

$$\boldsymbol{V}'(t) = a_1(0)e^{\lambda_1 t}\boldsymbol{Y}_1 + a_2(0)e^{\lambda_2 t}\boldsymbol{Y}_2 + a_3(0)e^{\lambda_3 t}\boldsymbol{Y}_3 + a_4(0)e^{\lambda_4 t}\boldsymbol{Y}_4. \tag{3.92}$$

Since all eigenvalues are purely imaginary, one has

$$\|\boldsymbol{V}'(t)\|_2^2 = |a_1(0)|^2 + |a_2(0)|^2 + |a_3(0)|^2 + |a_4(0)|^2 = \|\boldsymbol{V}'(0)\|_2^2, \tag{3.93}$$

leading to exact energy conservation, which is physically relevant. In the case the linearized operator is not self-adjoint with respect to the energy-associated inner

product, energy can exhibit transient fluctuations due to non-normal couplings between physical modes (Chomaz 2005). Such variations are mathematically correct but physically meaningless, and may lead to misleading conclusions about flow dynamics.

3.3 Mean Flow Equations, Reynolds Stress Tensor and Energy Balance in Compressible Flows

3.3.1 Arbitrary Flows

We first address the derivation of the governing equations for the mean field and the associated second-order turbulent stresses. The usual density-weighted average, referred to as the Favre averaging technique,[5] is retained here. For a dummy variable ϕ (either a scalar or a vectorial one), the mean part, $\tilde{\phi}$, and the fluctuating part, ϕ'', are defined as

$$\tilde{\phi} \equiv \frac{\overline{\rho\phi}}{\bar{\rho}}, \quad \phi'' \equiv \phi - \tilde{\phi}, \tag{3.94}$$

where the *bar* symbol is related to the usual statistical average.

Applying the mass-weighted averaging procedure (3.94) to the system (3.1), (3.2) and (3.8) (removing external source terms for the sake of simplicity) and using the binary regrouping[6] approach for the convective terms:

$$\rho\phi u_i = \bar{\rho}\tilde{\phi}\tilde{u}_i + \overline{\rho\phi'' u_i''} = \bar{\rho}\tilde{\phi}\tilde{u}_i + \widetilde{\bar{\rho}\phi'' u_i''}, \tag{3.95}$$

one obtains the following equations for the mean flow variables:

$$\frac{\partial\bar{\rho}}{\partial t} + \frac{\partial(\bar{\rho}\tilde{u}_j)}{\partial x_j} = 0, \tag{3.96}$$

$$\frac{\partial\bar{\rho}\tilde{u}_i}{\partial t} + \frac{\partial(\bar{\rho}\tilde{u}_i\tilde{u}_j)}{\partial x_i} = -\frac{\partial\bar{p}}{\partial x_i} + \frac{\partial\bar{\tau}_{ij}}{\partial x_j} - \frac{\partial\bar{\rho}R_{ij}}{\partial x_j}, \tag{3.97}$$

$$\frac{\partial\bar{\rho}\tilde{e}}{\partial t} + \frac{\partial(\bar{\rho}\tilde{e}\tilde{u}_j)}{\partial x_j} = \underbrace{-\bar{p}\frac{\partial\tilde{u}_i}{\partial x_i}}_{I} \underbrace{-\overline{p\frac{\partial u_i''}{\partial x_i}}}_{II} \underbrace{+\bar{\tau}_{ij}\frac{\partial\tilde{u}_i}{\partial x_j}}_{III} \underbrace{+\overline{\tau_{ij}\frac{\partial u_i''}{\partial x_j}}}_{IV} \underbrace{+\frac{\partial\bar{q}_i}{\partial x_i}}_{V} \underbrace{-\frac{\partial(\widetilde{\bar{\rho}e''u_j''})}{\partial x_j}}_{VI} \tag{3.98}$$

[5] But let us notice that the density-weighted average was introduced by Osborne Reynolds in is seminal paper in 1884!

[6] This term was coined by Chassaing and coworkers (see Chassaing et al. 2002), who developed the alternative ternary regrouping approach.

where the Reynolds stress tensor is now defined as

$$R_{ij} \equiv \widetilde{u_i'' u_j''}. \tag{3.99}$$

An additional equation for the mean kinetic energy $K \equiv \bar{\rho}\tilde{u}_i\tilde{u}_i/2$ is obtained by taking the inner product of the mean momentum equation (3.97) by the mean density-weighted velocity vector $\tilde{\boldsymbol{u}}$:

$$\frac{\partial K}{\partial t} + \frac{\partial (K\tilde{u}_j)}{\partial x_j} = \underbrace{-\frac{\partial (\bar{p}\tilde{u}_i)}{\partial x_i}}_{VII} + \underbrace{\bar{p}\frac{\partial \tilde{u}_i}{\partial x_i}}_{I} \underbrace{-\frac{\partial (\bar{\rho}R_{ij}\tilde{u}_i)}{\partial x_j}}_{VIII} + \underbrace{\bar{\rho}R_{ij}\frac{\partial \tilde{u}_i}{\partial x_j}}_{IX} + \underbrace{\frac{\partial (\bar{\tau}_{ij}\tilde{u}_i)}{\partial x_j}}_{X} \underbrace{-\bar{\tau}_{ij}\frac{\partial \tilde{u}_i}{\partial x_j}}_{III}. \tag{3.100}$$

The physical meaning of source terms in the mean internal energy equation and the mean kinetic energy are

- I: mean pressure-dilatation energy transfer, which is strictly null if the mean velocity field $\tilde{\boldsymbol{u}}$ is solenoidal.
- II: pressure-fluctuation dilatation correlation, which vanishes if the fluctuating velocity field u″ is solenoidal.
- III: viscous heat production associated to mechanical dissipation by the mean flow.
- IV: viscous heat production associated to mechanical dissipation by the fluctuating flow (turbulent dissipation of turbulence kinetic energy).
- V: mean external heat source by conduction.
- VI: turbulent diffusion of internal energy.
- VII: power of the mean external pressure forces in the mean motion.
- VIII: power of the Reynolds stresses
- IX: energy exchange with the turbulence kinetic energy (shear production). This term is null if the mean shear is zero.
- X: power of the mean external viscous stresses in the mean motion.

The evolution equation for the fluctuating velocity is

$$\begin{aligned}\frac{\partial (\overline{\bar{\rho}u_i''})}{\partial t} + \frac{\partial (\overline{\bar{\rho}u_i''}\tilde{u}_j)}{\partial x_j} = &-\frac{\partial (\bar{\rho}R_{ij})}{\partial x_j} - \overline{\bar{\rho}u_j''}\frac{\partial \tilde{u}_i}{\partial x_j} - \overline{\bar{\rho}u_i''\frac{\partial u_i''}{\partial x_j}} \\ &+\overline{\frac{\rho'}{\rho}\frac{\partial p}{\partial x_i}} - \overline{\frac{\rho'}{\rho}\frac{\partial \tau_{ij}}{\partial x_j}}.\end{aligned} \tag{3.101}$$

In the same way as in the incompressible flow case, evolution equations for the Reynolds stresses can be deduced from the Navier–Stokes equations. Still considering the binary regrouping, one obtains:

$$\frac{\partial \bar{\rho} R_{ij}}{\partial t} + \frac{\partial (\bar{\rho} R_{ik} \tilde{u}_k)}{\partial x_k} = -\bar{\rho} \left(R_{ik} \frac{\partial \tilde{u}_j}{\partial x_k} + R_{jk} \frac{\partial \tilde{u}_i}{\partial x_k} \right) + \overline{p' \left(\frac{\partial u_i''}{\partial x_j} + \frac{\partial u_j''}{\partial x_i} \right)}$$
$$- \frac{\partial}{\partial x_k} \left(\overline{\rho u_i'' u_j'' u_k''} + \overline{p' u_i''} \delta_{jk} + \overline{p' u_j''} \delta_{ik} - \overline{\tau_{ik}' u_j''} - \overline{\tau_{jk}' u_i''} \right)$$
$$+ \overline{u_i''} \left(\frac{\partial \bar{\tau}_{jk}}{\partial x_k} - \frac{\partial \bar{p}}{\partial x_j} \right) + \overline{u_j''} \left(\frac{\partial \bar{\tau}_{ik}}{\partial x_k} - \frac{\partial \bar{p}}{\partial x_i} \right)$$
$$- \overline{\tau_{ik}' \frac{\partial u_j''}{\partial x_k}} - \overline{\tau_{jk}' \frac{\partial u_i''}{\partial x_k}}. \tag{3.102}$$

Defining the instantaneous turbulence kinetic energy as $k'' = u_i'' u_i''/2$, one deduces from the Reynolds stress equations the following evolution equation for the mean density weighted turbulence kinetic energy $\mathcal{K} = \bar{\rho} \overline{u_i'' u_i''}/2$:

$$\frac{\partial \mathcal{K}}{\partial t} + \frac{\partial (\mathcal{K} \tilde{u}_j)}{\partial x_j} = \underbrace{- \frac{\partial (\widetilde{\bar{\rho} k'' u_j''})}{\partial x_j}}_{XI} \underbrace{- \bar{\rho} R_{ij} \frac{\partial \tilde{u}_i}{\partial x_j}}_{IX} \underbrace{- \frac{\partial (\bar{p} \overline{u_i''})}{\partial x_i}}_{XII} \underbrace{- \frac{\partial \overline{p' u_i''}}{\partial x_i}}_{XIII} \underbrace{+ \overline{p \frac{\partial u_i''}{\partial x_i}}}_{II}$$
$$\underbrace{+ \frac{\partial (\overline{\tau_{ij} u_i''})}{\partial x_j}}_{XIV} \underbrace{- \overline{\tau_{ij} \frac{\partial u_i''}{\partial x_j}}}_{IV}, \tag{3.103}$$

where the physical mechanisms at play are:

- XI: turbulent diffusion.
- XII: external power of mean pressure forces acting through the fluctuating motion.
- XIII: external power of pressure fluctuations in the fluctuating motion.
- XIV: external power of fluctuating viscous forces in the fluctuating motion.

Direct energy exchanges between the mean flow kinetic energy, the mean internal energy and the mean turbulence kinetic energy are due to common terms appearing in equations (3.98), (3.100) and (3.103), namely terms I, II, III, IV and IX. A schematic view of this dynamical scheme is displayed in Fig. 3.1.

3.3.2 Simplifications in the Isotropic Case

The dynamical scheme presented above simplifies dramatically in isotropic turbulence, due to the absence of mean flow gradient and to the symmetry properties of statistical moments of turbulent fluctuations. In this case, the system (3.98)–(3.100)–(3.103) becomes:

$$\frac{\partial \bar{\rho} \tilde{e}}{\partial t} = \underbrace{- \overline{p \frac{\partial u_i''}{\partial x_i}}}_{II} + \underbrace{\overline{\tau_{ij} \frac{\partial u_i''}{\partial x_j}}}_{IV}, \tag{3.104}$$

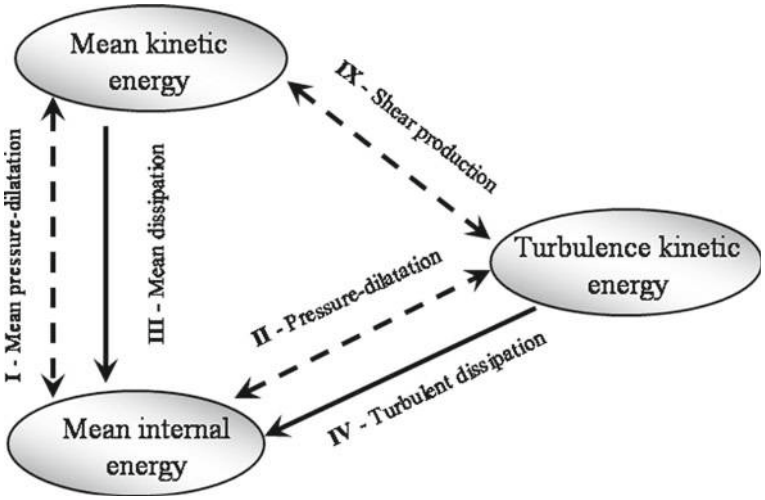

Fig. 3.1 Schematic view of mean energy exchanges in compressible turbulence

$$\frac{\partial K}{\partial t} = 0, \tag{3.105}$$

$$\frac{\partial \mathcal{K}}{\partial t} = \underbrace{\overline{p \frac{\partial u_i''}{\partial x_i}}}_{II} - \underbrace{\overline{\tau_{ij} \frac{\partial u_i''}{\partial x_j}}}_{IV}. \tag{3.106}$$

One observes that, as in the case of incompressible flow, the mean kinetic energy is constant since the turbulent force in the mean momentum equation vanishes. The remaining coupling terms II and IV correspond to energy exchanges between the mean internal energy and the mean turbulence kinetic energy (see Fig. 3.2). It is worth noting that the term II depends on the sole dilatational part of the fluctuating velocity field. Using the Kovasznay decomposition, one can see that this term is associated to the acoustic mode and the entropy mode. In the general case where a temperature-dependent viscosity is considered, term IV also accounts for turbulent fluctuations of the molecular viscosity. This term is also present in the incompressible case, and therefore is associated to the three modes of the Kovsznay decomposition.

The full dynamical scheme in isotropic turbulence consists in energy exchanges at constant total mean energy between the mean turbulence kinetic and the mean internal energy since

$$\frac{\partial}{\partial t}(\tilde{e} + K + \mathcal{K}) = \frac{\partial \tilde{e}}{\partial t} + \frac{\partial \mathcal{K}}{\partial t} = 0. \tag{3.107}$$

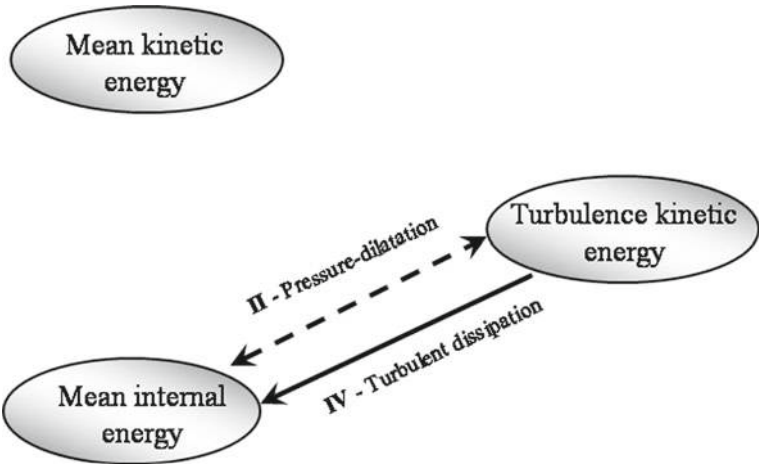

Fig. 3.2 Schematic view of mean energy exchanges in compressible isotropic turbulence

Therefore, the whole dynamics is governed by terms II and IV and most studies dealing with compressible isotropic turbulence have been devoted to the analysis of these two terms and the underlying physical mechanisms.

To get a deeper insight into the contributions of each physical mode, it is useful to decompose the terms II and IV.

The pressure-dilation correlation (term II) can be rewritten like

$$\overline{p\frac{\partial u_i''}{\partial x_i}} = \overline{p'\frac{\partial u_i''}{\partial x_i}} = \overline{p'\frac{\partial u_i'}{\partial x_i}}, \tag{3.108}$$

where it is important to note that $\boldsymbol{u}' \equiv (\boldsymbol{u} - \bar{\boldsymbol{u}})$ is defined using the usual statistical average and not the density-weighted one. This change is possible because, as pointed out by Feiereisen and coworkers (1981), *the density-weighted average and the usual average are equivalent in homogeneous flows*. This is observed writing the following exact decomposition of the density-weighted momentum:

$$\bar{\rho}\tilde{u}_i \equiv \bar{\rho}\bar{u}_i + \overline{\rho u_i'} = \bar{\rho}\bar{u}_i + \overline{\rho' u_i'}, \tag{3.109}$$

from which it follows that

$$\tilde{u}_i = \bar{u}_i + \frac{\overline{\rho' u_i'}}{\bar{\rho}}. \tag{3.110}$$

Since the momentum is conserved in homogeneous turbulence (and more generally in all periodic domains) and that the statistical average can be interpreted as a volume average by invoking the ergodic theorem, the last term in the right-hand side of Eq. (3.110) is constant in space and time. The two velocity fields $\tilde{\boldsymbol{u}}$ and $\bar{\boldsymbol{u}}$ are

related by an additive constant, which can be chosen to be zero selecting the ad hoc frame of reference.

Introducing the Helmholtz decomposition $\boldsymbol{u}' = \boldsymbol{u}'_s + \boldsymbol{u}'_d$ and $p' = p'_s + p'_d$, the pressure-dilatation term is rewritten as

$$\overline{p' \frac{\partial u'_i}{\partial x_i}} = \overline{p'_s \frac{\partial u'_{di}}{\partial x_i}} + \overline{p'_d \frac{\partial u'_{di}}{\partial x_i}}. \tag{3.111}$$

This new expression emphasizes that this term is strictly null in incompressible flows, but also that the solenoidal field has a contribution associated to the correlation between the solenoidal pressure fluctuations and the divergence of the fluctuating velocity field. Since the entropy mode has no pressure fluctuation (at least in the first-order Kovasznay approximation), it is seen that term II is null if there is no acoustic mode. In the true solution of nonlinear problems, it is expected to be very small if no acoustic waves are present or if no very intense entropy source is present.

Neglecting the molecular viscosity fluctuations,[7] the dilatation-dissipation term (term IV) can be decomposed in homogeneous turbulence as[8]

$$\overline{\tau_{ij} \frac{\partial u''_i}{\partial x_j}} = \overline{\tau'_{ij} \frac{\partial u''_i}{\partial x_j}} = \bar{\rho} \bar{\varepsilon}_s + \bar{\rho} \bar{\varepsilon}_d, \tag{3.112}$$

where $\bar{\varepsilon}_s$ and $\bar{\varepsilon}_d$, which are respectively referred to as the solenoidal and the dilatational dissipation rate, are defined as

$$\bar{\varepsilon}_s = 2 \frac{\bar{\mu}}{\bar{\rho}} \overline{W'_{ij} W'_{ij}} = \frac{\bar{\mu}}{\bar{\rho}} \overline{\boldsymbol{\omega}'_i \boldsymbol{\omega}'_i}, \quad W'_{ij} = \frac{1}{2} \left(\frac{\partial u'_i}{\partial x_j} - \frac{\partial u'_j}{\partial x_i} \right), \tag{3.113}$$

$$\bar{\varepsilon}_d = \frac{4}{3} \frac{\bar{\mu}}{\bar{\rho}} \overline{\left(\frac{\partial u''_i}{\partial x_i} \right)^2} = \frac{4}{3} \frac{\bar{\mu}}{\bar{\rho}} \overline{\left(\frac{\partial u''_{di}}{\partial x_i} \right)^2}, \tag{3.114}$$

where $\boldsymbol{\omega}' \equiv \nabla \times \boldsymbol{u}' = \nabla \times \boldsymbol{u}'_s$. It is observed that $\bar{\varepsilon}_s$ (resp. $\bar{\varepsilon}_d$) does not depend on the dilatational (resp. solenoidal) field at all, and will therefore be exactly zero if the solenoidal (resp. dilatational) field is not present in the flow. In high speed flows without strong external entropy source, and restricting the analysis to the linear

[7] This assumption is relevant for most high-speed non-reactive flows.

[8] In non-homogeneous flows a third contribution must be taken into account, which is defined as

$$\bar{\varepsilon}_n = 2 \frac{\bar{\mu}}{\bar{\rho}} \left(\frac{\partial^2}{\partial x_i \partial x_j} \overline{u'_i u'_j} - 2 \frac{\partial}{\partial x_j} \left(\overline{u'_j \frac{\partial u'_i}{\partial x_i}} \right) \right).$$

Kovasznay splitting, it is seen that the solenoidal dissipation $\bar{\varepsilon}_s$ is associated to the sole vorticity mode, while the dilatational dissipation is mainly due to the acoustic mode.

References

Bayly, B.J., Levermore, C.D., Passot, T.: Density variations in weakly compressible flows. Phys. Fluids **4**(5), 945–954 (1992)

Chassaing, P., Antonia, R.A., Anselmet, F., Joly, L., Sarkar, S.: Variable density turbulence. Springer, Berlin (2002)

Chomaz, J.M.: Global instabilities in spatially developing flows: Non-normality and non-linearity. Ann. Rev. Fluid Mech. **37**, 357–392 (2005)

Chu, B.T.: On the energy transfer to small disturbances in fluid flow (part 1). Acta Mechanica **1**, 215–234 (1965)

Chu, B.T., Kovasznay, L.S.G.: Non-linear interactions in a viscous heat-conducting compressible gas. J. Fluid Mech. **3**, 494–514 (1957)

Feiereisen, W.J., Reynolds, W.C., Ferziger, J.H.: Numerical simulation of compressible homogeneous turbulent shear flow, *Report No TF 13*, Stanford University (1981)

Hayes, W.D.: The vorticity jump across a gasdynamic discontinuity. J. Fluid Mech. **2**, 595–600 (1957)

Joseph George, K., Sujith, R.I.: On Chu's disturbance energy. J. Sound Vib. **330**, 5280–5291 (2011)

Kovasznay, L.S.G.: Turbulence in supersonic flow. J. Aero. Sci. **20**, 657–682 (1953)

Zank, G.P., Matthaeus, W.H.: Nearly incompressible hydrodynamics and heat conduction. Phys. Rev. Lett. **64**(11), 1243–1245 (1990)

Zank, G.P., Matthaeus, W.H.: The equations of nearly incompressible fluids. I. Hydrodynamics, turbulence and waves. Phys. Fluids **3**(1), 69–82 (1991)

Chapter 4
Incompressible Homogeneous Isotropic Turbulence

To caricature, it can be jokingly said that, once one has eliminated all features of a flow that one understands, what remains is turbulence. This sentence (Mathieu and Scott 2000) is even more relevant in Homogeneous Isotropic Turbulence (HIT), in which no interaction with a structuring effect (mean flow, body force, shock-wave, wall ...) may occur. HIT, even if it can be described statistically with a few number of quantities, is really the core of the turbulence problem.

4.1 Observations and Measures in Forced and Freely Decaying Turbulence

4.1.1 How to Generate Isotropic Turbulence?

Isotropic turbulence can be investigated using both experimental and numerical approaches, despite it requires the existence of an unbounded domain from the theoretical point of view.

A quasi-isotropic fully developed turbulent state can be reached in wind tunnels using a grid to promote turbulence (see Fig. 4.1). In such a setup, boundary layers develop along solid walls, but a quasi-isotropic flow is recovered in the core of wind tunnel. The grid wake transforms a part of mean flow kinetic energy into turbulent kinetic energy. After a certain distance downstream the grid, the mean flow is uniform and no more turbulence production mechanism takes place. Therefore, the turbulent fluctuations dynamics is entirely governed by the advection due to the uniform mean flow, the non-linear interactions and the linear viscous effects, leading to a monotonic decay of the turbulent kinetic energy $\mathcal{K}$.

Several regions are usually identified downstream the grid, which correspond to different dynamical regimes. These decay regimes are discussed in Sect. 4.1.3.

P. Sagaut and C. Cambon, *Homogeneous Turbulence Dynamics*,
https://doi.org/10.1007/978-3-319-73162-9_4

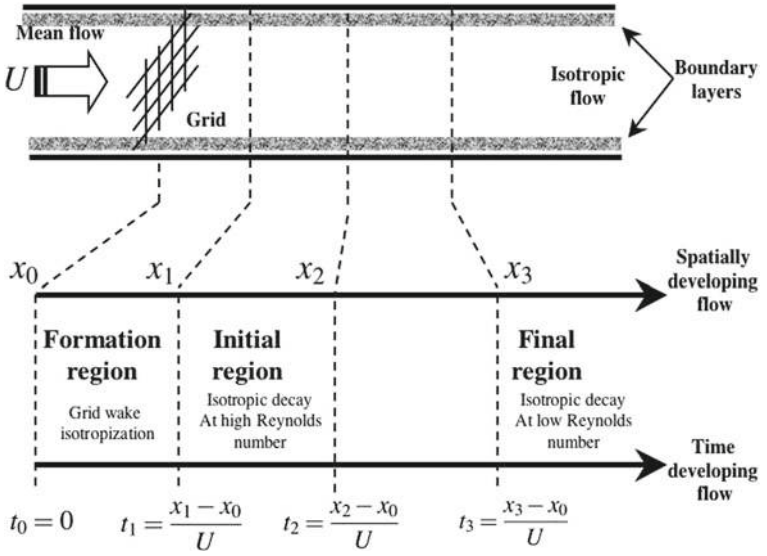

Fig. 4.1 Schematic view of wind tunnel set-up for generating isotropic turbulence

The full-scale spatial development of isotropic turbulence observed in wind tunnels cannot be exactly reproduced in numerical simulations, due to the enormous required computing power. But it is mimicked switching from a spatially evolving flow to a time-developing flow. In this new configuration, periodic boundary conditions are imposed in all space directions, and a pseudo-turbulent initial condition is used. An isotropic time decaying turbulent flow is then obtained. It can be made statistically steady in time inserting an ad hoc forcing term. But it is worth noting that the use of periodic boundary conditions induces spurious couplings at scales of the order of the computational domain size, and that the analysis of large scale dynamics must be carried out with great care.

Spatially-developing and time-evolving flows can be compared thanks to *Taylor's frozen turbulence hypothesis*. In 1938, Taylor hypothesized that the turbulent velocity fluctuation $\boldsymbol{u}(\boldsymbol{x}, t)$ measured by a stationary probe can be interpreted as resulting from the advection of a frozen spatial structure by a uniform steady flow with velocity $\boldsymbol{U}$, yielding

$$\boldsymbol{u}(\boldsymbol{x}, t) = \boldsymbol{u}(\boldsymbol{x} - \boldsymbol{U}t, 0). \tag{4.1}$$

This hypothesis can also be used to find a approximate relation between space and time derivatives. Let us consider consider a new reference frame advected at velocity $\boldsymbol{U}$. Denoting quantities expressed in this new reference frame by a *tilde*, one has:

$$\tilde{\boldsymbol{x}} = \boldsymbol{x} - \boldsymbol{U}t, \quad \tilde{t} = t, \quad \tilde{\boldsymbol{u}}(\tilde{\boldsymbol{x}}, \tilde{t}) = \boldsymbol{u}(\boldsymbol{x}, t) - \boldsymbol{U} \tag{4.2}$$

and

$$\frac{\partial u_i}{\partial t} = \frac{\partial \tilde{u}_i}{\partial x_j}\frac{\partial x_j}{\partial t} + \frac{\partial \tilde{u}_i}{\partial t} = \frac{\partial \tilde{u}_i}{\partial t} - U_j \frac{\partial \tilde{u}_i}{\partial x_j}. \tag{4.3}$$

If one now assumes that the signal is frozen in the advected frame, i.e. if $\partial \tilde{\boldsymbol{u}}/\partial t \approx 0$, then the following relation holds

$$\frac{\partial}{\partial t} \approx U_j \frac{\partial}{\partial x_j}. \tag{4.4}$$

It is important to note that the Taylor hypothesis does not hold in the following cases, at least from the theoretical viewpoint:

- A single advecting velocity cannot be defined. This is the case in compressible flows, in which hydrodynamic and acoustic perturbations do not have the same speed, and in flows in which the advection speed depends on the scale of the perturbation. This last case is met in some shear flows (e.g. mixing layers, boundary layers).
- The rate of change in the moving frame cannot be neglected. Let us consider a structure with characteristic size L and characteristic time T. The Taylor hypothesis is valid if

$$\frac{L}{U} \ll T. \tag{4.5}$$

Now using the relation $\sqrt{\mathcal{K}} \approx L/T$, the validity criterion can be recast as

$$\sqrt{\mathcal{K}} \ll U, \tag{4.6}$$

showing that the mean flow speed must be large compared with the characteristic turbulent velocity scale.

One of the first experiment of decaying grid-generated turbulence, but perhaps one of the most documented, was carried out by Comte-Bellot and Corrsin (1966). In order to achieve a better isotropy, at least measured looking at the Reynolds stress tensor, a convergent duct was placed after the grid, in the "formation region". Without this additional device, the Reynolds stresses exhibit a mild axisymmetry with $\overline{u_1^2} > \overline{u_2^2} \sim \overline{u_2^3}$: the effect of the convergent duct is to diminish the Reynolds stress component in the axial direction (x_1 here) and to increase it in the radial directions, as shown by Rapid Distortion Theory (see Chap. 8). Unfortunately, such experiments cannot reproduce high Reynolds number flows, a typical value of the Reynolds number based on the Taylor microscale $Re_\lambda = \lambda u'/\nu$ being 70–80. Here $u' = \sqrt{\frac{2}{3}\mathcal{K}}$ denotes the characteristic velocity scale of the large, energy-containing

scales, and $\lambda \equiv \sqrt{15\nu u'^2/\varepsilon}$ is the Taylor microscale,[1] where ε is the kinetic-energy dissipation rate (see Sect. 4.2.1 for more details).

DNS began to reach higher Reynolds numbers from the early 1980s. A weakness of these simulations is that the large scale forcing which is present in the simulation prevent recovering reliable information about the smallest wavenumbers. The semi-empirical law

$$N \sim Re_\lambda^{0.74}$$

was recently proposed, where N is the number of grid points along the side of a cubic box in a conventional pseudo-spectral DNS. Using such a high-accuracy method, the recommended mesh size is $\Delta x \sim 4 - 5\eta$, where η refers to the Kolmogorov length scale. This estimate was further refined in the case of freely decaying turbulence by Meldi and Sagaut (2017). To avoid spurious confinement effects, the domain size should be at least ten times larger than the integral scale at the final time of simulation. Therefore, in order to simulate turbulence decay from time t_0 to t_F with an initial turbulent Reynolds number $Re_L(0)$, one should take

$$N = 2\left(1 + \frac{t_F}{t_0}\right)^{2/(\sigma+3)} Re_L^{3/4}(t_0), \tag{4.7}$$

where σ is the slope of the energy spectrum at very large scales, i.e. $E(kL \ll 1) \propto k^\sigma$.

4.1.2 Main Observed Statistical Features of Developed Isotropic Turbulence

The main results retrieved from laboratory experiments and numerical simulations are the following:

- *Typical observed turbulent kinetic energy spectrum shapes* are displayed in Fig. 4.7. An universal inertial range is observed in the turbulent kinetic energy spectrum if the Reynolds number is high enough. At very high wave numbers, viscous dissipation becomes dominant, and the energy spectrum falls very quickly. The physical assumption that the turbulent field is regular in the sense that the L_2 norm of all high order spatial derivatives of the velocity field is finite suggests that the spectrum shape should exhibit an exponential decay at very high wave numbers.
  The spectrum shape at large scales (i.e. small wave numbers) which do not belong to the inertial range is observed to be flow-dependent.

[1] It is recalled that the Taylor microscale is associated with scales at which the spectrum of kinetic-energy dissipation, or equivalently the enstrophy spectrum, exhibits its maximum.

The time evolution of the turbulent kinetic energy spectrum is displayed in Figs. 4.7 and 4.8. Results dealing with both the free decay case and the statistically steady case are presented. In the former case, no source of turbulent kinetic energy is present, and the turbulent kinetic energy is a monotonically decaying function of time, while in the latter a kinetic energy source is used to reach a statistically steady state. In both cases, it is observed that the spectrum shape relaxes towards a universal shape at small scales (provided that the Reynolds number is high enough to allow for the existence of the inertial range). The change in the kinetic energy spectrum shape is due to non-linear interactions between modes. Two mechanisms are obviously at play: a direct kinetic energy cascade from large to small scales (also referred to a the forward cascade) which is responsible for the existence of the inertial range, and an inverse kinetic energy cascade from small to large scales (also named the backward cascade) which yield the growth of the energy spectrum at very small wave numbers.

- *Turbulent velocity fluctuations are not Gaussian random variables.*
  A first manifestation of non-Gaussianity of the turbulent velocity field is that its odd-order statistical moments are not zero, while they are identically zero for a random Gaussian field. A measure of this difference is therefore gained looking at the skewness and the flatness parameters[2] based on velocity increments (or equivalently the velocity gradients). Common reported values of the skewness factor are $S_0 = -0.4 \pm 0.1$ (instead of $S_0 = 0$ for a Gaussian field), while the *flatness factor*, F_0, ranges from 4 to 40, depending on the Reynolds number (instead of $F_0 = 3$ for a Gaussian field).
  It is worth noting that the single point even moments of velocity fluctuations exhibit a quasi-normal distribution (see Fig. 4.2), while velocity increments are not Gaussian random variables. Therefore, the one-point analysis of the turbulent velocity field is not sufficient to analyze the lack of Gaussianity of turbulence: two-point quantities must be considered. Extreme velocity events, which correspond to the very end of the tails of the pdf plots are observed to escape the Normal distribution. As a matter of fact, the tails of the velocity-increment pdf are observed to be exponential or even stretched exponential. The negative value of the skewness factor is associated to a strong asymmetry in the distribution of longitudinal velocity increment with dominating compressive events. A possible explanation is that this extreme events are (at least partially) governed by the physical mechanisms

[2]Let us recall that the flatness factor $F(a)$ and the skewness factor $S(a)$ of the random field $\boldsymbol{a}$ are defined as

$$F(a) \equiv \frac{\langle a^4 \rangle}{\langle a^2 \rangle^2}, \quad S(a) \equiv \frac{\langle a^3 \rangle}{\langle a^2 \rangle^{3/2}}. \tag{4.8}$$

If $\boldsymbol{a}$ is a Gaussian field, then

$$F(a) = 3, \quad S(a) = 0. \tag{4.9}$$

Still assuming that $\boldsymbol{a}$ is a random Gaussian field, and defining $\boldsymbol{\omega}_a = \mathrm{curl}\boldsymbol{a}$ and $\mathbf{S}_a = \frac{1}{2}(\nabla \boldsymbol{a} + \nabla^T \boldsymbol{a})$, one has

$$F(\omega_a) = 5/3, \quad F(S_a^2) = 7/5. \tag{4.10}$$

Another important point is that almost all non-linear functions of $\boldsymbol{a}$ will exhibit a non-Gaussian behavior.

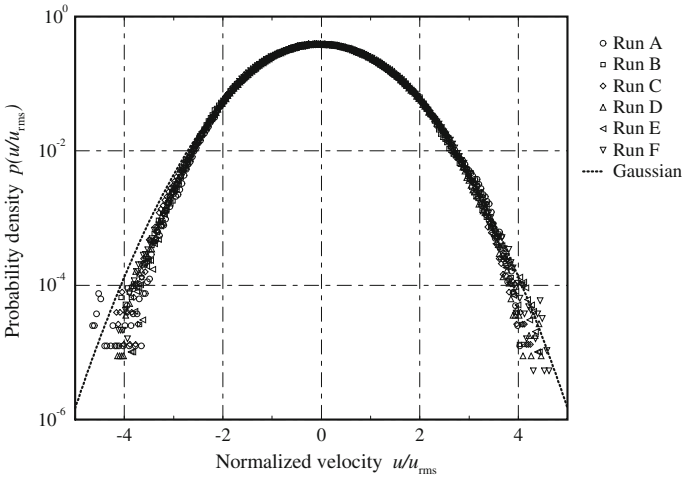

Fig. 4.2 Probability density function of normalized velocity fluctuation in isotropic turbulence. From Noullez et al. (1997) with permission of CUP

responsible for the production of turbulent kinetic energy.[3] Therefore, they are flow-dependent and do not exhibit an universal behavior, since they are sensitive to the characteristic time scale of the turbulence production at large scales.

The analysis of the pdf of the longitudinal velocity increments shows that the lack of Gaussianity is scale-dependent (see Fig. 4.3), in the sense that velocity increments at small scales exhibit larger differences with the Normal distribution than velocity increments at larger scales.

The lack of Gaussianity is an intrinsic feature of turbulence, due to the nonlinearity of the Navier–Stokes equations. This point will be addressed in Sect. 4.11.5.

4.1.3 Energy Decay Regimes

The turbulent kinetic energy $\mathcal{K}$ is observed to follow different regimes, depending on the position in the wake of the turbulence-generating grid. Three regions are usually

[3] It can be shown Falkovich and Lebedev (1997) that a Gaussian random forcing having a correlation scale l_F and a time scale τ_F yields velocity pdf tails of the form

$$\ln P(u) \propto -u^4 \text{ for } u \gg \max(u_{\text{rms}}, l_F/\tau_F),$$

where $P(u)$ is the pdf of the velocity fluctuation u. For a short-correlated forcing such that $\tau_F \ll l_F/u_{\text{rms}}$, one obtains

$$\ln P(u) \propto -u^3 \text{ for } l_F/\tau_F \gg u \gg u_{\text{rms}}.$$

Therefore, it is seen that the interplay between the external forcing and the turbulence non-linearity leads to an automatic breakdown of Gaussianity for very intense events.

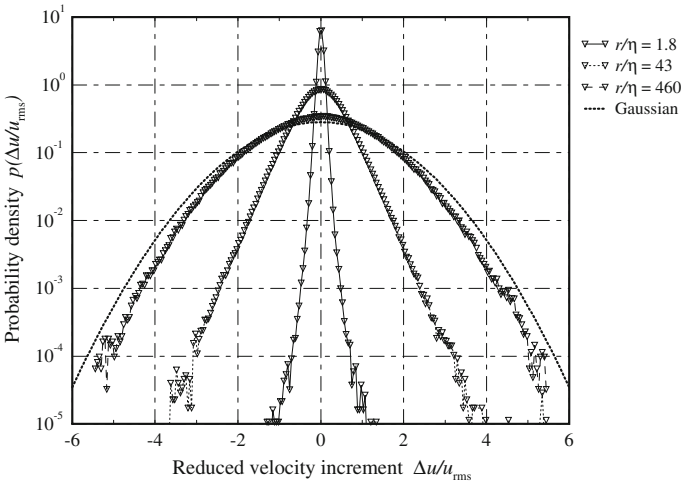

Fig. 4.3 Probability density function of normalized velocity increment in isotropic turbulence. From Noullez et al. (1997) with permission of CUP

identified, which are presented below. They have an universal character, since they are observed in almost all clean experimental data sets.

(i) The **formation region**, in which the wakes of the rods of the grid interact and merge. These interactions lead to a loss of memory of turbulent fluctuations and to the rise of an quasi-isotropic state.[4] It is important noting that this return to isotropy is not observed if the initial Reynolds number is too low.

(ii) The **initial region**, in which the flow can be considered as isotropic and is strongly energetic. In this region, the Taylor-scale-based Reynolds number Re_λ is high, meaning that the non-linear effects are dominant. Both experimental data and theoretical analysis lead to $Re_\lambda \geq 100$ as a minimum to recover the high-Reynolds decay exponent, higher values being required when higher-order statistics are considered. In this region, the turbulent kinetic energy $\mathcal{K}$ is observed to decay approximately like t^{-n} with $n \approx 1.1-1.38$, while the Taylor scale grows like $t^{0.35-0.4}$. Most existing turbulence theories yield $6/5 \leq n \leq 4/3$, but some significant differences with experimental data are reported. It is important to notice that experimental uncertainties dealing with the measure of the decay exponent are high, since this measure relies on several strong assumptions (Mohamed and Larue 1990; Skrbek and Stalp 2000). This is illustrated in Fig. 4.4 in which the histogram of about 600 values of the decay exponent of kinetic energy in grid turbulence published over the last 50 years is displayed. Theoretical analyses based on two-point closures, like EDQNM (see Sect. 4.8.6)

[4]The term quasi-isotropic refers here to a state in which at least second-order statistical moments are isotropic. But some anisotropic effects due to turbulence memory may remain on higher-order moments.

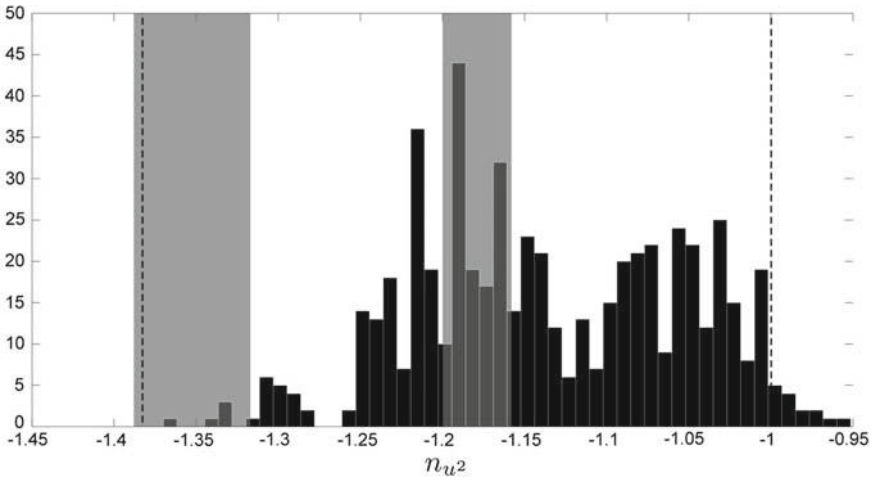

Fig. 4.4 Histogram of about 600 published values of the power law exponent n_{u^2} related to the decay turbulent kinetic energy in DNS and wind tunnel experiments. Grey areas are related to the probabilistic regions predicted by Meldi et al. (2011) for Saffman and Batchelor turbulence using uncertainty quantification techniques to account for possible changes in the initial spectrum. From Meldi and Sagaut (2012) with permission of CUP

reveal that the decay exponent n is sensitive to many parameters related to the initial condition, such as the shape of the turbulent kinetic energy spectrum at very small wave numbers at initial time, but also to possible saturation effects due to the finite size of both experimental facilities and computational domains (Skrbek and Stalp 2000). The analysis of these states is presented in Sect. 4.4.

(iii) The **final region**, which is defined as the region in which the Taylor-based Reynolds number is so low that the viscous linear effects are dominant. The criterion $Re_\lambda \leq 1$ is sometimes used to define the final region, but EDQNM analysis show that $Re_\lambda \leq 0.1$ is a better threshold to observe the asymptotic low-Reynolds behavior. The turbulent kinetic energy now decays more fastly, leading to $\mathcal{K} \sim t^{-n}$ with $n \approx 2-2.5$, while the Taylor microscale grows like $\sqrt{t}$. It is important to note that, at such low Reynolds number, isotropy is very difficult to achieve, either in laboratory experiment and in numerical simulations, due to couplings between large and small scales. As in the previous case, the decay rate is expected to be sensitive to the slope of the spectrum at very low wave numbers and various parameters of the experimental apparatus. Experimental realizations of the final region are very rare, and it seems that the transition between the initial and the final region has never been observed experimentally, since it would require very long wind tunnels (Skrbek and Stalp 2000). Details about this decay regime are displayed in Sect. 4.4.5.

4.1.4 Coherent Structures in Isotropic Turbulence

Statistical isotropy does not imply that isotropic turbulence fluctuations are uncoherent. Since the pioneering simulations of Siggia (1981), it has been observed that vortical coherent events are present in isotropic turbulence. One usually distinguishes elongated vortices, referred to as *worms* or *vortex tubes*, and flat *vortex sheets*. These structures, their dynamics and their role in the turbulence dynamics are discussed in Sect. 4.10.

4.2 Classical Statistical Analysis: Energy Cascade, Local Isotropy, Usual Characteristic Scales

4.2.1 Double Correlations and Typical Scales

Isotropy implies that the two-point second order correlation tensor

$$R_{ij}(\boldsymbol{r}) = < u_i'(\boldsymbol{x}) u_j'(\boldsymbol{x}+\boldsymbol{r}) >$$

(time is omitted for the sake of brevity) can be expressed as $R_{ij} = A(r)\delta_{ij} + B(r) r_i r_j$, or

$$R_{ij}(\boldsymbol{r}) = u'^2 \left(g(r)\delta_{ij} + (f(r) - g(r)) \frac{r_i r_j}{r^2} \right), \tag{4.11}$$

introducing the scaling factor $u'^2 = \frac{2}{3}\mathcal{K}$, and using the longitudinal correlation function

$$u'^2 f(r) = R_{ij}(\boldsymbol{r}) \frac{r_i r_j}{r^2}, \tag{4.12}$$

and its transverse counterpart

$$u'^2 g(r) = R_{ij}(\boldsymbol{r}) n_i n_j, \tag{4.13}$$

in which $\boldsymbol{n}$ is a unit vector normal to $\boldsymbol{r}$ (see Fig. 4.5).

The scalar correlation functions f and g are linked via the incompressibility constraint. Using $\frac{\partial R_{ij}}{\partial r_j} = 0$ one obtains

$$g(r) = f(r) + \frac{r}{2} \frac{\partial f}{\partial r}. \tag{4.14}$$

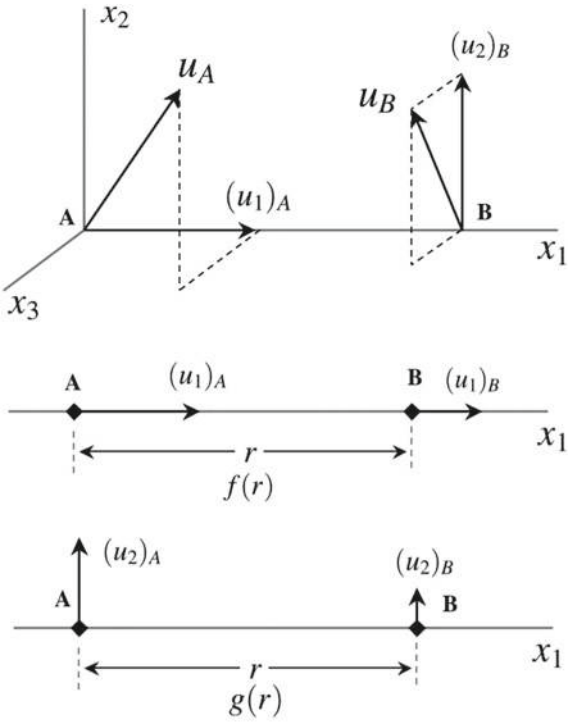

Fig. 4.5 Schematic view of multi-point correlations. Top: general sketch of the correlation between two-velocity components taken at two differents points A and B. Bottom: illustration of the physical meaning of the longitudinal correlation function $f(r)$ and its transverse counterpart $g(r)$

It can be easily seen that

$$\left.\frac{\partial^{2n} g}{\partial r^{2n}}\right|_{r=0} = (n+1)\left.\frac{\partial^{2n} f}{\partial r^{2n}}\right|_{r=0} \tag{4.15}$$

along with

$$f(0) = 1, \quad f'(0) = 0, \quad f''(0) < 0, \tag{4.16}$$

where the notation f' is introduced to denote the derivative of $\partial f/\partial r$ for the sake of simplicity. Finally, reintroducing the time dependency, the evolution equation for the two-point second order tensor amounts to the single scalar equation, e.g. for f, as follows

$$\frac{\partial}{\partial t}(u'^2 f) = \left(\frac{\partial}{\partial r} + \frac{4}{r}\right)\left(R_{LL,L}(r,t) + 2\nu\frac{\partial}{\partial r}(u'^2 f)\right), \tag{4.17}$$

which is referred to as the *Karman–Howarth equation*. The term $R_{LL,L}$ represents the longitudinal two-point third-order correlation function, which is involved via the quadratic non linearity. It is defined as

$$R_{LL,L}(r,t) = \overline{u_i'(\boldsymbol{x},t)u_i'(\boldsymbol{x},t)u_m'(\boldsymbol{x}+\boldsymbol{r},t)}\frac{r_m}{r} = u'^3 h(r,t). \tag{4.18}$$

A slightly different form can be found in Mathieu and Scott (2000).

Typical length scales of turbulence can be defined using functions $f(r)$ and $g(r)$. The *longitudinal and transverse integral lengthscales*, denoted L_f and L_g, respectively, are defined as

$$L_f = \int_0^\infty f(r)dr, \quad L_g = \int_0^\infty g(r)dr. \tag{4.19}$$

Isotropy implies

$$L_g = \frac{1}{2}L_f. \tag{4.20}$$

showing that there is only one independent integral scale. These scales are usually interpreted as the typical scale of the most energetic eddies in the flow. The integral scale L_f is commonly replaced by the characteristic large scale $L_u = \mathcal{K}^{3/2}/\varepsilon$ that can be easily computed using the outputs of most existing statistical turbulence models developed for engineering purposes within the Reynolds Averaged Numerical Simulation (RANS) framework. It is important noting that L_f and L_u are not equal, since

$$L_u = \lim_{Re_L \to +\infty} \frac{3\pi}{4} L_f. \tag{4.21}$$

EDQNM results show that the approximation $L_u \sim L_f$ holds for $Re_\lambda \geq 100$, while at lower Reynolds numbers finite Reynolds effects become significant.

The *longitudinal and transverse Taylor microscales*, λ_f and λ_g, are computed as

$$\lambda_f = \sqrt{-\frac{2}{f''(r=0)}}, \quad \lambda_g = \sqrt{-\frac{2}{g''(r=0)}}, \tag{4.22}$$

respectively, with

$$\lambda_g^2 = \frac{1}{2}\lambda_f^2 \tag{4.23}$$

in isotropic flows. This scale is defined as the point at which the osculatory parabola of $f(r)$ at point $r = 0$ defined by $y(r) = f(0) + f'(0)r + f''(0)\frac{r^2}{2} = 1 + f''(0)\frac{r^2}{2}$ vanishes. Reminding that

$$\frac{\partial}{\partial x_k}\overline{u_i'(x,t)u_j'(x+r,t)} = -u'^2\frac{\partial R_{ij}}{\partial r_k}, \tag{4.24}$$

one has

$$
\begin{aligned}
-u'^2 \left.\frac{\partial^2 f}{\partial r^2}\right|_{r=0} &= -\lim_{r\to 0} \frac{\partial^2}{\partial r^2} \overline{u_1'(x+re_x,t)u_1'(x,t)} \\
&= -\lim_{r\to 0} \left(\overline{\left.\frac{\partial^2 u_1'}{\partial r^2}\right|_{x+re_x} u_1'(x,t)} \right) \\
&= \overline{\left(\frac{\partial u_1'}{\partial x_1}\right)^2} \\
&= \frac{4}{3}\frac{\mathcal{K}}{\lambda_f^2}.
\end{aligned} \tag{4.25}
$$

Combining this results with the isotropic relation

$$
\varepsilon = 15\nu \overline{\left(\frac{\partial u_1'}{\partial x_1}\right)^2}, \tag{4.26}
$$

one recovers the usual expression for the dissipation rate

$$
\varepsilon = 30\nu \frac{u'^2}{\lambda_f^2} = -15\nu u'^2 f''(0). \tag{4.27}
$$

Consequently, the Taylor microscales are commonly interpreted as the typical size of eddies at which the maximum of dissipation occurs.

The fourth-order derivative of f at $r = 0$ can be evaluated by the use of the same procedure:

$$
\begin{aligned}
\overline{u^2} \left.\frac{\partial^4 f}{\partial r^4}\right|_{r=0} &= \lim_{r\to 0} \frac{\partial^4}{\partial r^4} \overline{u_1'(x+re_x,t)u_1'(x,t)} \\
&= \lim_{r\to 0} \overline{\left.\frac{\partial^2 u_1'}{\partial r^2}\right|_{x+re_x} \left.\frac{\partial^2 u_1'}{\partial r^2}\right|_{x+re_x}} \\
&= \overline{\left(\frac{\partial^2 u_1'}{\partial x_1^2}\right)^2} \\
&\propto \overline{\left(\frac{\partial \omega_1'}{\partial x_2}\right)^2}, \\
\Longrightarrow \left.\frac{\partial^4 f}{\partial r^4}\right|_{r=0} &= \frac{G}{\lambda^4},
\end{aligned} \tag{4.28}
$$

where G is the palinstrophy coefficient defined in Eq. (4.47).

Table 4.1 Definitions of characteristic space and time scales associated to the fluctuating velocity field

	Integral scale	Taylor scale	Kolmogorov scale
Space	$L_u = \dfrac{\mathcal{K}^{3/2}}{\varepsilon}$	$\lambda_g = \sqrt{\dfrac{10\mathcal{K}\nu}{\varepsilon}}$	$\eta = \left(\dfrac{\nu^3}{\varepsilon}\right)^{1/4}$
Time	$\tau_u = \dfrac{\mathcal{K}}{\varepsilon}$	$\tau_\lambda = \sqrt{\dfrac{15\nu}{\varepsilon}}$	$\tau_\eta = \sqrt{\dfrac{\nu}{\varepsilon}}$
Reynolds number	$Re_L = \dfrac{\mathcal{K}^2}{\nu\varepsilon}$	$Re_\lambda = \sqrt{\dfrac{20}{3}}\dfrac{\mathcal{K}}{\sqrt{\nu\varepsilon}}$	$Re_\eta = 1$
Remark	Large energy-containing scales	Small scales, maximum of dissipation/enstrophy spectrum	Local Reynolds number equal to 1

A last family of scales was introduced by Kolmogorov in 1941. Assuming local isotropy, he made the hypothesis that two-point two-time statistical moments of the fluctuating field may be evaluated thanks to dimensional analysis using r, the separation distance, τ, the time delay, ν, the fluid viscosity and ε. Here the physical meaning of ε deserves a brief discussion. On can define at least three typical rates looking at time evolution of kinetic energy $\mathcal{K}$ in isotropic turbulence. The first one is the production rate, ε_P, associated to production of kinetic energy by a source term, if any. The second one, ε_T, is associated to the non-linear transfer of kinetic energy toward small scales by the energy cascade mechanisms. It is assumed to be scale-independent within Kolmogorov inertial range in most theories. The last rate is the dissipation rate, ε, which is related to transformation of kinetic energy into heat via viscous mechanisms. In the case of *local equilibrium*, one has $\varepsilon_P = \varepsilon_T = \varepsilon$ and ε can be understood as a non-linear energy transfer rate across scales rather than a viscous phenomenon rate.

Several quantities can be build using ε and ν thanks to dimensional analysis. The Kolmogorov length scale, η, time scale τ_η and velocity scale u_η are given by

$$\eta = \left(\frac{\nu^3}{\varepsilon}\right)^{1/4}, \quad \tau_\eta = \sqrt{\frac{\nu}{\varepsilon}}, \quad u_\eta = (\nu\varepsilon)^{1/4}. \tag{4.29}$$

The physical meaning of Kolmogorov scales is obtained observing that the *local Reynolds number* $Re_\eta = u_\eta\eta/\nu$ =1. Such a low value shows that eddies with size of the order of η are governed by linear diffusive effects. As a consequence, the Kolmogorov scale is commonly accepted as the smallest active scale in a turbulent flow.

Integral, Taylor and Kolmogorov scales whose definitions are summarized in Table 4.1 are tied by scaling laws summarized in Tables 4.2 (for spatial scales) and 4.3 (for time scales).

Table 4.2 Relations between spatial integral scales in isotropic turbulence

	L_u	λ_g	η
L_u	1	$Re_L^{1/2}/\sqrt{10}$	$Re_L^{3/4}$
λ_g	$\sqrt{10}Re_L^{-1/2}$	1	$\sqrt{10}Re_L^{1/2}$
η	$Re_L^{-3/4}$	$Re_L^{-3/4}/\sqrt{10}$	1

Table 4.3 Relations between temporal integral scales in isotropic turbulence

	τ_u	τ_λ	τ_η
τ_u	1	$Re_L^{1/2}/\sqrt{15}$	$Re_L^{1/2}$
τ_λ	$\sqrt{15}Re_L^{-1/2}$	1	$\sqrt{15}$
τ_η	$Re_L^{-1/2}$	$1/\sqrt{15}$	1

4.2.2 (Very Brief) Reminder About Kolmogorov Legacy, Structure Functions, 'Modern' Scaling Approach

Structure functions are interesting alternatives to velocity correlations at two points, using equivalent $\boldsymbol{r}$ (two-point) separation vectors, but velocity increments $\delta\boldsymbol{u}' = \boldsymbol{u}'(\boldsymbol{x}+\boldsymbol{r}) - \boldsymbol{u}'(\boldsymbol{x})$ instead of $\boldsymbol{u}'(\boldsymbol{x})$ or $\boldsymbol{u}'(\boldsymbol{x}+\boldsymbol{r})$. The structure function of order n is defined as

$$S_n(r) = \overline{\left[(\boldsymbol{u}'(\boldsymbol{x}+\boldsymbol{r}) - \boldsymbol{u}'(\boldsymbol{x})) \cdot \frac{\boldsymbol{r}}{r}\right]^n}. \tag{4.30}$$

Now restricting the analysis to the longitudinal structure functions in isotropic turbulence, this expression simplifies as

$$S_n(r) = \overline{[u'(r) - u'(0)]^n}. \tag{4.31}$$

The counterpart of the longitudinal correlation f is the (longitudinal) second-order structure function $S_2(r)$. In homogeneous turbulence, the second-order longitudinal structure function, for instance, is given by

$$S_2(r) = \frac{2}{3}\mathcal{K}\left(1 - f(r)\right). \tag{4.32}$$

More generally, on can keep in mind that structure functions give information on two-point statistics for $\boldsymbol{r} \neq 0$, and tend to zero with vanishing $\boldsymbol{r}$.

The Karman–Howarth equation can be rewritten to obtain an exact evolution equation for $S_2(r)$. In freely decaying isotropic turbulence, one has:

$$\frac{2}{3}\frac{\partial \mathcal{K}}{\partial t} = -\frac{2}{3}\varepsilon = \frac{1}{2}\frac{\partial S_2}{\partial t} + \frac{1}{6r^4}\frac{\partial}{\partial r}(r^4 S_3) - \frac{\nu}{r^4}\frac{\partial}{\partial r}\left(r^4 \frac{\partial S_2}{\partial r}\right). \tag{4.33}$$

Kolmogorov originally proposed to scale the structure functions in terms of r and the dissipation rate ε only, the first and simplest version (denoted K41, since the seminal paper of Kolmogorov was published in 1941) reducing to

$$S_n(r) \sim (\varepsilon r)^{n/3}. \tag{4.34}$$

The scaling only results from dimensional analysis, once the physical parameters have been chosen. Of course, this choice relies on nontrivial phenomenological aspects. The scaling holds for an inertial range, i.e. for $L \gg r \gg \eta$, delineated by a large scale L, comparable to L_f in Eq. (4.19) and the Kolmogorov scale η given by Eq. (4.29). It is important to notice that the classical Taylor series expansion $u_i(\boldsymbol{x} + \boldsymbol{r}) = u_i(\boldsymbol{x}) + \frac{\partial u_i}{\partial r_l} r_l + \cdots$ would yield a different scaling law: $S_n(r) \sim ((\partial u/\partial r)r)^n$. This result, which holds for a smooth, differentiable, velocity field, may be valid for the smallest scales, i.e. $r < \eta$. The simple fact that the K41 exponent $(n/3)$ is fractional means that the velocity field is not differentiable in the inertial range, and that self-similar dynamics is expected at such scales.

Modern phenomenological theories continue in search of a more general scaling, replacing the $n/3$ exponents by new ones, ζ_n, called 'anomalous exponents', since the former are questioned in the case of internal intermittency. The background argument for introducing such new scaling is to consider a local dissipation rate $\varepsilon(r)$ which is no longer independent from the size r. The reader is referred to the following books for more details: Monin and Yaglom (1975), Frisch (1995), and Mathieu and Scott (2000).

Finally, let us just mention the famous *Kolmogorov's four-fifths law*

$$S_3(r) = -\frac{4}{5}\varepsilon r + 6\nu \frac{\partial}{\partial r} S_2(r), \tag{4.35}$$

which appears as a simplified form of the Karman–Howarth equation (4.33) assuming a steady turbulence (and therefore adding a source term to balance viscous dissipation). It can be further simplified neglecting viscous terms, leading to the popular approximate formula:

$$S_3(r) = -\frac{4}{5}\varepsilon r. \tag{4.36}$$

Accordingly, the K41 scaling remains unquestioned (at least in HIT at very high Reynolds number) for $n = 3$.

It is important noting that relation (4.36) is an asymptotic scaling law, which requires very high Reynolds numbers to be accurately recovered. In many practical realizations, *Finite Reynolds Number effects* are present that yield a departure from this relation, as seen from Eq. (4.35). Such departure should not be misinterpreted as intermittency effects.

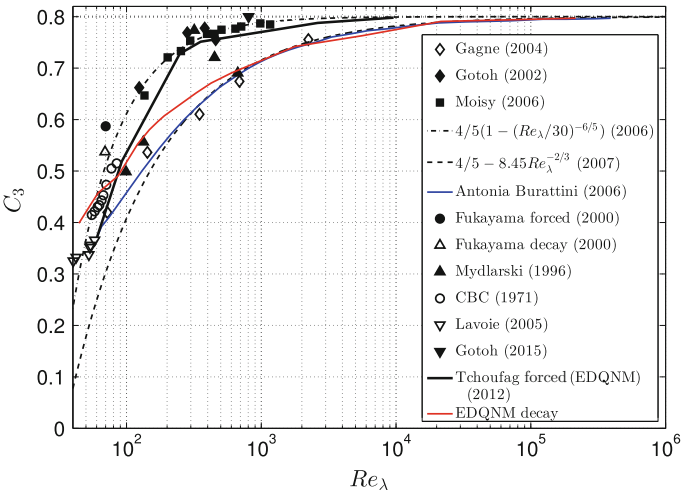

Fig. 4.6 Finite Reynolds Number effects: convergence of C_3 versus the Taylor-based Reynolds number. The Kolmogorov 4/5th-law is recovered when $C_3 = 4/5$. Courtesy of A. Briard, adapted from an original figure in Tchoufag et al. (2012)

Introducing the Reynolds-dependent coefficient

$$C_3 = -\max_r S_3^*(r), \quad S_3^*(r) = \frac{S_3(r)}{-\varepsilon r}, \tag{4.37}$$

one recovers the Kolmogorov law as an asymptotic limit with $\lim_{Re_\lambda \to +\infty} C_3 = 4/5$. The convergence is illustrated in Fig. 4.6, in which it is observed that $Re_\lambda \geq 5.10^4$ is required to recover the 4/5 value in freely decaying turbulence while $Re_\lambda \geq 5.10^3$ is enough in forced turbulence. A few empirical models that account for the Reynolds-dependency of C_3 and $S_3^*(r)$ are displayed in Tables 4.4 and 4.5. Results gathered in this figure follow those of Antonia and Burattini (2006), who proposed one of the best available semi-empirical fit (dotted line) for finite-Reynolds number effects. In addition, EDQNM results are given by solid lines, and the CBC (Comte-Bellot and Corrsin) points were obtained by calculating S_3, using Eq. (4.59), from the spectral transfer terms shown in Fig. 4.21, that are very similar in both experiment and EDQNM calculations.

4.2.3 Turbulent Kinetic Energy Cascade in Fourier Space

It is often easier to investigate two-point statistics using the three-dimensional Fourier space. The counterpart of Eq. (4.11) in the Fourier space is Eq. (2.134), recalled below

Table 4.4 Empirical laws for $S_3^*(r)$

Source	$S_3^*(r)$	Remarks
Qian (1999)	$\frac{4}{5} - C_1 \left(\frac{r}{L}\right)^m - C_2 \left(\frac{r}{\eta}\right)^{-4/3}$	Decaying turbulence, $C1 > 0$, $C_2 = 5.26 K_0$
Moisy (1999)	$\frac{4}{5} - 8\left(\frac{r}{\eta}\right)^{-4/3} - \frac{2}{7} Re_\lambda^{-3} \left(\frac{r}{\eta}\right)^2$	
Lindborg (1999)	$\frac{4}{5} - 2\left(C_\star Re_\lambda^{-1} \left(\frac{r}{\eta}\right)^{2/3} + 4\left(\frac{r}{\eta}\right)^{-4/3}\right)$	$C_\star = \frac{6.4\sqrt{15}}{17}$
Lundgren (2002)	$\frac{4}{5} - \frac{3.34}{\sqrt{15}} \left(\frac{r}{L}\right)^{2/3} - 8\left(\frac{r}{\eta}\right)^{-4/3}$	
Lundgren (2003)	$\frac{4}{5}\left(1 - Re_\lambda^{-2/3}\left(2.678 C_2 \left(\frac{r}{\lambda}\right)^{2/3} + 2.029 C_2 \left(\frac{r}{\lambda}\right)^{-4/3}\right)\right)$	forced turbulence, $C_2 \simeq 2$
Lundgren (2003)	$\frac{4}{5}\left(1 - Re_\lambda^{-2/3}\left(2.678 \left(\frac{2}{3}\frac{1+n}{n}\right) C_2 \left(\frac{r}{\lambda}\right)^{2/3} + 2.029 C_2 \left(\frac{r}{\lambda}\right)^{-4/3}\right)\right)$	decaying turbulence, $\mathcal{K}(t) \propto t^{-n}$

Table 4.5 Empirical laws for C_3

Source	$C_3(r)$	Remarks
Qian (1999)	$\frac{4}{5} - C_\delta Re_\lambda^{-\mu}$, $\mu = \frac{6m}{3m+4}$	Decaying turbulence: $\mu = 2/3$, homogeneous shear: $2/3 \leq \mu \leq 1$, non-homogeneous shear: $\mu \geq 1$
Lindborg (1999)	$\frac{4}{5} - 6C_\star^{2/3} Re_\lambda^{-2/3}$	
Moisy (1999)	$\frac{4}{5}\left(1 - \left(\frac{Re_\lambda}{Re_{\lambda_0}}\right)^{-6/5}\right)$	$Re_{\lambda 0} \sim 30$
Lundgren (2002)	$\frac{4}{5} - 8.45 Re_\lambda^{-2/3}$	Decaying turbulence
Lundgren (2003)	$\frac{4}{5}\left(1 - 2.678 Re_\lambda^{-2/3} C_2 \left(\frac{2.029}{2.678}\right)^{1/3}\right)$	forced turbulence, $C_2 \simeq 2$
Lundgren (2003)	$\frac{4}{5}\left(1 - 2.678 Re_\lambda^{-2/3} C_2 \left(\frac{2.029}{2.678}\right)^{1/3} \left(\frac{2(1+n)}{3n}\right)^{2/3}\right)$	Decaying turbulence $\mathcal{K}(t) \propto t^{-n}$

$$\hat{R}_{ij}(\boldsymbol{k},t) = \underbrace{\frac{E(k,t)}{4\pi k^2}}_{\mathcal{E}(k,t)} \underbrace{\left(\delta_{ij} - \frac{k_i k_j}{k^2}\right)}_{P_{ij}}.$$

It should be borne in mind that isotropy yields a very special form of the spectral tensor. The involved parameters are the following: $E(k,t)$, with $k = |\boldsymbol{k}|$, is the usual energy spectrum, representing the distribution of turbulent kinetic energy over different scales and the quantity in brackets will be recognized as the projection matrix, $P_{ij}(\boldsymbol{k})$. Thus, $\hat{R}_{ij}$ is determined by a single real scalar quantity, E, which is a function of the sole magnitude of $\boldsymbol{k}$. Therefore, both the form of $\hat{R}_{ij}$ at a single point and its distribution over $\boldsymbol{k}$-space are strongly constrained by isotropy.

The evolution of the energy spectrum is governed by the *Lin equation*

$$\frac{\partial E(k,t)}{\partial t} + 2\nu k^2 E(k,t) = T(k,t) \tag{4.38}$$

in which the third-order correlations are involved in the scalar spectral transfer term $T(k,t)$.[5] This equation can be seen as a spectral counterpart of the Karman–Howarth equation (4.17). Exact relationship between $E(k)$, $T(k)$ and all the correlations defined in physical space can be found in Mathieu and Scott (2000). This equation derives from the Craya's equation (2.102) by cancelling mean-gradient terms and by assuming isotropy, so that

$$E(k,t) = 2\pi k^2 \hat{R}_{ii} \quad T(k,t) = 2\pi k^2 T_{ii}. \tag{4.39}$$

Integrating the equation over k yields

$$\mathcal{K}(t) = \int_0^\infty E(k)dk \quad \varepsilon = 2\nu \int_0^\infty k^2 E(k,t)dk \tag{4.40}$$

and

$$\int_0^\infty T(k)dk = 0. \tag{4.41}$$

This allows us to recover the basic equation (4.233), and shows that $T(k,t)$ is a pure redistribution term in the Fourier space. The last relation accounts for the fact that the convection term conserves the total kinetic energy, leading to the well-known result that global kinetic energy is an invariant in inviscid incompressible flows (without boundary conditions).

[5] Let us emphasize here the physical meaning of the sign of $T(k)$. The net effect of nonlinearity on modes k such that $T(k) > 0$ is a kinetic energy gain (which must be balanced by viscous effects in the statistically steady case $\partial E(k,t)/\partial t$), while modes such that $T(k) < 0$ lose more kinetic energy than they gain through nonlinear interactions (these scales must be fed by a forcing term to obtain a statistically steady state). At last, scales such that $T(k) = 0$ are in equilibrium, in the sense that they don't lose or gain kinetic energy on the mean.

Typical shapes of $E(k)$, $2\pi k^2 E(k)$ and $T(k)$ are displayed in Fig. 4.22. It is observed that the peak of the energy spectrum, $E(k)$ is significantly separated from the one of the dissipation spectrum $2\nu k^2 E(k)$ at large Reynolds number. The transfer term is almost zero in a small zone within the inertial range, negative for smallest k and positive for largest k, the areas of both positive and negative values being exactly balanced. The physical meaning is that small wave number modes lose kinetic energy on the mean due to the non-linear interactions, while large wave number modes gain kinetic energy. The scale located within the inertial range have a zero net transfer. The associated dynamic picture is the celebrated *forward energy cascade* process[6]: turbulent kinetic energy is injected in the system (by external forcing, hydrodynamic instabilities, ...) at small wave number modes. The energy is then pumped toward higher wave number modes by the non-linear interactions,'streaming' in some sense toward modes at which it will be transformed into heat by viscous mechanisms. The inertial range is defined as the zone in which the net transfer is zero. In the inertial zone, the classical Kolmogorov scaling[7]

$$E(k) = K_0 \varepsilon^{2/3} k^{-5/3} \tag{4.42}$$

is observed in both experimental an numerical datasets.

The evolution equation for the dissipation ε is recovered from Eq. (4.38) by integrating it over k after multiplication by the factor $2\nu k^2$, yielding

$$\frac{d\varepsilon}{dt} = \int_0^\infty 2\nu k^2 T(k) dk - \int_0^\infty (2\nu k^2)^2 E(k) dk \tag{4.43}$$

$$= -\frac{7}{15}\left(\frac{1}{2} S(t) Re_\lambda(t) + G(t)\right) \frac{\varepsilon^2(t)}{\mathcal{K}(t)} \tag{4.44}$$

$$= \underbrace{-\frac{7}{3\sqrt{15}} S(t) \sqrt{Re_L(t)} \frac{\varepsilon^2(t)}{\mathcal{K}(t)}}_{\text{Generation of dissipation}} \underbrace{-\frac{7}{15} G(t) \frac{\varepsilon^2(t)}{\mathcal{K}(t)}}_{\text{Destruction of dissipation}}, \tag{4.45}$$

where the skewness S and the palinstrophy G parameters are defined as

$$S = -\frac{\overline{(\partial u'/\partial x)^3}}{\overline{(\partial u'/\partial x)^2}^{3/2}} = -\frac{3\sqrt{30}}{14} \frac{\int_0^{+\infty} k^2 T(k,t) dk}{\left[\int_0^{+\infty} k^2 E(k,t) dk\right]^{3/2}} = \frac{h'''(0)}{f''(0)}^{3/2} \tag{4.46}$$

[6]The term cascade was coined by Onsager in the late 1940s.

[7]This scaling is consistent with the content of the papers published by Kolmogorov in 1941. But it is worth noting that Kolmogorov never worked in the Fourier space. The expression of the turbulent kinetic spectrum was given by his PhD student A. Obhukov, and almost independently rendered popular by Heisenberg.

$$G = \frac{30}{7}\frac{\nu\mathcal{K}}{\varepsilon}\frac{\overline{\frac{\partial\omega_i'}{\partial x_j}\frac{\partial\omega_i'}{\partial x_j}}}{\overline{\omega_k'\omega_k'}} = \frac{120}{7}\frac{\nu\mathcal{K}}{\varepsilon}\frac{\int_0^{+\infty}k^4E(k,t)dk}{\int_0^{+\infty}k^2E(k,t)dk} = \lambda^4 f^{(IV)}(0) \tag{4.47}$$

where h is the triple correlation function defined in Eq. (4.18).

This equation is the spectral counterpart of the following evolution equation in the physical space:

$$\frac{\partial\varepsilon}{\partial t} = 2\nu\overline{\omega_i'\omega_j'\frac{\partial u_i'}{\partial x_j}} - 2\nu^2\overline{\frac{\partial\omega_i'}{\partial x_j}\frac{\partial\omega_i'}{\partial x_j}}. \tag{4.48}$$

Looking at Eq. (4.43), it is clear that the second term in the right-hand-side is negative and corresponds to a viscous destruction mechanism. The first term is essentially positive. A part of $T(k)$ (at large k) is privileged by the k^2 weighting factor, and can be interpreted as a *production* of ε by nonlinear interactions. This point will be further discussed in Sect. 4.11.

The fact that the evolution of ε results from the imbalance between two very different terms, whose sum can be efficiently modeled using the purely negative term $-C_{\varepsilon_2}\frac{\varepsilon^2}{\mathcal{K}} = -\frac{n}{n+1}\frac{\varepsilon^2}{\mathcal{K}}$ along with $\mathcal{K}(t) \propto t^{-n}$ is certainly true in HIT at high Reynolds number, but remains not completely understood. As a matter of fact, the exact equation (4.45) leads to

$$C_{\varepsilon_2} = \frac{n}{n+1} = \frac{7}{15}\left(\frac{1}{2}S(t)Re_\lambda(t) + G(t)\right), \tag{4.49}$$

showing that both C_{ε_2} and n should be Reynolds-number and time-dependent in the general case. This point will be further discussed in Sect. 4.6.

We should perhaps say a few words about two-dimensional turbulence. On the one hand, this state corresponds to an extreme anisotropic (axisymmetric) case with respect to three-dimensional HIT, in which two-point correlations are invariant along a direction $x_\parallel$, and with a Dirac distribution of spectral kinetic energy $e(\boldsymbol{k}) = E(k)/(2\pi k)\delta(k_\parallel)$. This viewpoint will be addressed in Chap. 7, showing that the accurate description of a partial transition from three-dimensional to two-dimensional structure needs a very refined anisotropic description. On the other hand, one can just get rid of the third dimension and consider HIT in two dimensions as a self-consistent area of study. In this case the scaling

$$E(k) \sim \overline{\omega'^2}k^{-3}$$

has been proposed by Kraichnan, in connection with the conservation of enstrophy $\overline{\omega'^2}$ and with an inverse cascade.

4.2.4 Bridging Between Physical and Fourier Space: Some Useful Formulas

It is worth reminding that in isotropic turbulence the Karman–Howarth equation and the Lin equation are equivalent, and that quantities defined in physical space can be expressed using spectral quantities, and vice versa.

A few useful relations are recalled below:

(i) Velocity longitudinal integral length scale:

$$L_f \equiv \int_0^{+\infty} f(r)dr = \frac{3\pi}{4}\frac{\int_0^{\infty}\frac{E(k)}{k}dk}{\int_0^{\infty}E(k)dk} = \frac{1}{2}\int_0^{+\infty} g(r)dr = \frac{1}{2}\int_0^{+\infty}\left[f(r)+\frac{2}{r}f'(r)\right]dr \tag{4.50}$$

(ii) Velocity longitudinal Taylor length scale:

$$\lambda_f^2 \equiv -\frac{1}{f''(0)} = \frac{10\mathcal{K}\nu}{\varepsilon} = 5\frac{\int_0^{\infty}E(k,t)dk}{\int_0^{\infty}k^2E(k,t)dk} \tag{4.51}$$

(iii) Turbulent dissipation rate:

$$\varepsilon = \nu\overline{\frac{\partial u_i'}{\partial x_j}\frac{\partial u_i'}{x_j}} = \nu\overline{\omega_i'\omega_i'} = 2\nu\int_0^{+\infty}k^2E(k)dk = 10\frac{\mathcal{K}\nu}{\lambda_f^2} = -10f''(0)\mathcal{K}\nu = 15\nu\overline{\left(\frac{\partial u'}{\partial x}\right)^2} \tag{4.52}$$

(iv) Longitudinal velocity correlation function as a function of the three-dimensional energy spectrum:

$$u'^2 f(r,t) = 2\int_0^{+\infty}E(k,t)\left(\frac{\sin(kr)}{k^3r^3}-\frac{\cos(kr)}{k^2r^2}\right)dk \tag{4.53}$$

(v) Transverse velocity correlation function as a function of the three-dimensional energy spectrum:

$$u'^2 g(r,t) = 2\int_0^{+\infty}E(k,t)\left(\frac{\sin(kr)}{kr}-\frac{\sin(kr)}{k^3r^3}+\frac{\cos(kr)}{k^2r^2}\right)dk \tag{4.54}$$

(vi) Three-dimensional energy spectrum as a function of the longitudinal velocity correlation function:

$$E(k,t) = \frac{u'^2}{\pi}\int_0^{+\infty}kr(\sin kr - kr\cos kr)f(r,t)dr \tag{4.55}$$

(vii) Spectral energy transfer term (in Lin equation) as a function of the triple correlation function $h(r)$ defined in Karman–Howarth equation by Eq. (4.18):

$$T(k,t) = -2\frac{u'^3}{\pi}\int_0^{+\infty}\left[(k^2r^2-3)kr\sin(kr)+3k^2r^2\cos(kr)\right]\frac{h(r)}{r}dr \tag{4.56}$$

(viii) Triple correlation function $h(r)$ as a function of the spectral energy transfer term:

$$u'^3h(r) = \int_0^{+\infty}\left[\frac{(k^2r^2-3)\sin(kr)}{k^4r^4}+\frac{3\cos(kr)}{k^3r^3}\right]\frac{T(k)}{k}dk \tag{4.57}$$

(ix) Second-order velocity structure function

$$S_2(r) = \overline{[u(r)-u(0)]^2} = 2u'^2\left[1-f(r)\right] = 4\int_0^{+\infty}E(k)a(kr)dk, \quad a(x) = \frac{1}{3}-\frac{\sin x - x\sin x}{x^3} \tag{4.58}$$

(x) Third-order velocity structure function

$$S_3(r) = \overline{[u(r)-u(0)]^3} = -12u'^3h(r) = 4\int_0^{+\infty}\frac{T(k)}{k^2}\frac{\partial a(kr)}{\partial r}dk \tag{4.59}$$

4.3 Models for Single-Time and Two-Time Energy Spectra and Velocity Correlation Functions

4.3.1 Models for Three-Dimensional Energy Spectrum $E(k)$

Most existing analytical models for the spectrum $E(k)$ can be recast in the following generic form Pope (2000), Meyers and Meneveau (2008)

$$E(k) = K_0\varepsilon^{2/3}k^{-5/3}f_L(kL)f_\eta(k\eta), \tag{4.60}$$

where f_L and f_η are the dimensionless shape functions at large and small scales, respectively. Some consistency relations exist, that lead to integral constraints on the spectrum shape functions:

$$\int_0^{+\infty}E(k)dk = \mathcal{K} \Longrightarrow \int_0^{+\infty}x^{-5/3}F(xRe^{-3/4})dx = 1, \tag{4.61}$$

$$\int_0^{+\infty}k^2E(k)dk = \varepsilon/2\nu \Longrightarrow \int_0^{+\infty}x^{1/3}F(x)dx = 1/2, \tag{4.62}$$

$$\int_0^{+\infty} k^4 E(k)dk = \overline{\frac{\partial \omega_i'}{\partial x_j}\frac{\partial \omega_i'}{\partial x_j}} \Longrightarrow \int_0^{+\infty} x^{7/3} F(x)dx = \frac{-7S}{12\sqrt{15}}, \tag{4.63}$$

where $x = k\eta$ is a dummy variable and $F(k\eta) = K_0 f_L(k\eta Re_L^{3/4}) f_\eta(k\eta)$. The fluctuating vorticity is defined as $\boldsymbol{\omega}' = \mathrm{curl}(\boldsymbol{u}')$. The skewness parameter S is given by Eq. (4.46).

The celebrated hypotheses proposed by Kolmorogov in 1941 yield the following asymptotic spectrum shapes for small scales for which the local isotropy hypothesis holds:

$$E(k) = K_0 \varepsilon^{2/3} k^{-5/3} f_\eta(k\eta), \tag{4.64}$$

where K_0, ε and η are the Kolmogorov constant, the dissipation rate and the Kolmogorov scale, respectively.

The assumed regularity of the derivatives of the velocity field is ensured by the function f_η, which must be a fastly decaying function, i.e.

$$\int_0^{+\infty} x^n f_\eta(x)dx < \infty \quad \forall n \geq 0. \tag{4.65}$$

Among the numerous proposals made for $f_\eta(x)$ (see Table 4.7), a widely admitted one is

$$f_\eta(x) = Cx^\alpha \exp[-\beta x^n], \tag{4.66}$$

where C, α, β and n are real parameters. Not to mention values of n such as $n = 4/3$ (proposed by Pao, for pure mathematical convenience), $n = 2$ (suggested by Townsend, assuming linear response of small scales), $n = 1$ is consistently predicted by all "triadic" closures (EDQNM, DIA, LHDIA, LRA) (Kaneda 1993) and supported by recent experimental and DNS results. The reader is referred to Ishihara et al. (2005) for a survey including new DNS with the Taylor micro-scale Reynolds number Re_λ and resolution ranging up to about 675 and 4096^3, respectively. In addition to $n = 1$, the values of α and β obtained by the latter DNS decrease monotonically with Re_λ and appear to tend to constants as $Re_\lambda \to \infty$, but the convergence, especially that of β, is slow. A simple power law fitting suggests the following asymptotic (infinite Re_λ) values

$$\alpha = -2.9, \quad \beta = 0.62, \quad C = 0.044.$$

Surprisingly, the above-mentioned closures predict $\alpha = 3$ (Kaneda 1993). This positive value, however, does not yield an overshoot for the spectrum, between the end of the inertial range and the beginning of the dissipative range, because β is sufficiently large.

For small scales much larger than the Kolmogorov scale η, one recovers the inertial-range expression[8]:

$$E(k) = K_0 \varepsilon^{2/3} k^{-5/3}. \tag{4.67}$$

The exact value of the Kolmogorov constant is not known. A large number of estimates are provided in the literature (Sreenivasan 1995), coming from measures in the atmospheric boundary layer, from laboratory experiments and numerical simulations. This uncertainty comes from either the departure from isotropy in many flows or the absence of a large inertial range in the spectrum. An reliable estimate seems to be $K_0 = 1.5 \pm 0.1$.

It is important noting that the Kolmogorov scaling comes from an asymptotic dimensional analysis. Denoting L the integral scale of turbulence, usual estimates for the upper and lower bounds of the inertial range are:

$$L_{\text{upper}} \simeq 5(Re_L)^{-1/2} L, \quad L_{\text{lower}} \simeq 50(Re_L)^{-3/4} L. \tag{4.68}$$

The miminum Reynolds number for an inertial range to exist is an open issue, but there are evidences that the Taylor-scale based Reynolds number Re_λ must be O(100) for any natural inertial range to exist, and that Re_λ = O(1000) for a decade of inertial range.

The shape function at large scale f_L is purely empirical, since no universal theory exist for such scales. Large scale features are very difficult to measure directly in experiments because of confinement problems and statistical convergence issues. Therefore, they are very often inferred using an a priori model for large scales, whose coefficients are tuned to fit available data. Common sense says that there should be a finite cutoff scale, since real fluid flow always occur in a finite domain (even a very large but finite one like Earth's atmosphere). In the same way, one should remember that numerical simulations are performed in finite computational domains. As a consequence, one should assume that $E(k) = 0$ for scales larger than a cutoff scale. Such a limit is never taken into account in existing models (see Table 4.6), in which the constraint $E(k \to 0) = 0$ is enforced.

Several turbulence theories yield to the proposal that $E(k)$ should exhibit an asymptotic algebraic form, i.e.

$$E(k \to 0) \propto k^\sigma \tag{4.69}$$

with σ ranging from 1 to 4. A detailed discussion about the large-scale behavior of the energy spectrum is given in Sect. 4.3.3. Let us just mention here that a detailed analytical analysis show that $E(k)$ might exhibit non-algebraic behaviors in some cases.

[8]It is important to keep in mind that Kolmogorov inertial range theory is a priori derived assuming that turbulence scales are at equilibrium, i.e. that they are statistically steady. Consequences of non-equilibrium, e.g. in freely decaying turbulence, are discussed in Sect. 4.5.6.3.

Table 4.6 Shape function of the kinetic energy spectrum at large scales, f_L. σ denotes the energy spectrum slope at very large scales: $E(k) \propto k^{\sigma}$, $(kL) \ll 1$. The models obtained by an analytical integration of an evolution equation for $E(k)$ are denoted with an asterisk

Author	$f_L(x), x = kL$
Pope (2000)	$\left(\frac{x}{\sqrt{x^2 + c_L}}\right)^{5/3+\sigma}$, $c_L \sim 6.78$
Meyers & Meneveau (2008)	$\left(\frac{x}{(x^p + \alpha_5)^{1/p}}\right)^{5/3+\beta+\sigma} x^{-\beta}$, $\beta = \mu/9$, $\mu = 0.25$, $p = 1.5$
Pao (1965)*	$\left(1 + \frac{3K_0}{2}(k\hat{l})^{-2/3}\right)^{-(3\sigma+5)/2}$, $\hat{l}^{2/3} = \hat{l}_0^{2/3} + \int_0^t \varepsilon(t')dt'$

4.3.2 Models for Longitudinal Velocity Correlation Function $f(r)$

The exact form of the function $f(r)$ is unknown. At small separation distance r, the Taylor series expansion of $f(r)$ yields

$$f(r) = 1 - \frac{r^2}{\lambda_f^2} + \frac{r^4}{\lambda_f^4}\frac{G}{24} + O(r^6/\lambda_f^6). \tag{4.70}$$

The asymptotic behavior of $f(r)$ at very large separation distance is still an open issue, and it is often conjectured that $f(r \to +\infty) \sim r^{-m}$ where m is an integer to be determined.

At asymptotically low Reynolds number, i.e. neglecting $h(r)$ in the Karman-Horwarth equation, some analytical solutions can be derived. The most popular one was provided by Taylor in (1935):

$$f(r) = \exp(-r/\lambda_f). \tag{4.71}$$

Another famous solution is the Gaussian solution provided by Batchelor and Townsend in 1948:

$$f(r) = \exp(-r^2/\lambda_f^2). \tag{4.72}$$

More expression for the asymptotic low-Reynolds case have been proposed (Table 4.7).

At high Reynolds number composite models made of the combination of a Taylor series expansion for $r \to 0$ and an algebraic decay law for $r \to +\infty$ have been proposed, but almost all of them are not fully satisfactory. The reason for that is that

Table 4.7 Shape function of the kinetic energy spectrum at small scales, f_η. The models obtained by an analytical integration of an evolution equation for $E(k)$ are denoted with an asterisk

Author	$f_\eta(x), x = k\eta$
Pope (2000)	$\exp\left(-\beta([x^4 + c_\eta^4]^{1/4} - c_\eta)\right)$, $c_\eta \sim 0.4$, $\beta \sim 5.2$
Meyers & Meneveau (2008)	$\left(1 + \frac{\alpha_2 (x/\alpha_4)^{\alpha_3}}{1 + \alpha_2 (x/\alpha_4)^{\alpha_3}}\right) \exp(-\alpha_1 x)$
Pao (1965)*	$\exp\left(-\frac{3K_0}{2} x^{4/3}\right)$
Kovasznay (1948)*	$\begin{cases} \left(1 - \alpha x^{4/3}\right)^2 & x < 1, \alpha = (2K_0)^{-1/3} \\ 0 & otherwise \end{cases}$
Heisenberg (1948)* Bass (1949)* Chandrasekhar (1949)* Goldstein (1951)*	$\begin{cases} \left(1 + \left(\frac{8}{3\alpha_H^2} - \frac{1}{m^4}\right) \alpha x^4\right)^{-4/3} & x < m \\ 0 & otherwise \end{cases}$
Qian (1984)	$\frac{1.19}{K_0} \left(1 + x^{2/3}\right) \exp\left(-5.4 x^{4/3}\right)$
Saffman (1963)	$\exp\left(-2x^2\right)$
Manley (1992)	$\exp\left(-a_m x^m\right), a_m = \left(\frac{2}{m} K_0 \Gamma(4/3m)\right)^{3m/4}$
Kraichnan (1959)	$A x^\gamma \exp(-\beta x)$ $A = 6.3 \pm 2 \quad or \quad 8.4 \pm 0.6$ $\gamma = -1.6 \pm 0.2, \quad \beta = 4.9 \pm 0.4$
Ishihara et al. (2005)	$A x^\gamma \exp(-\beta x)$ $A = 0.038 + 23.5 Re_\lambda^{-0.42}$ $\gamma = -2.9 + 7.2 Re_\lambda^{-0.47}$ $\beta = 0.62 + 9.3 Re_\lambda^{-0.19}$

the velocity correlation function must verify a number of physical constraints, and it appears that a model that fulfill all these constraints is still lacking. This is illustrated for a couple low-Reynolds models for $f(r)$ in Table 4.8.

A composite model that fulfill almost all constraints was recently proposed par Monte, Meldi and Sagaut:

$$f(r,t) = f_{in}(r/\lambda, Re_\lambda) + f_{out}(r/L, \sigma), \tag{4.73}$$

where $f_{in}(r/\lambda, Re_\lambda)$ and $f_{out}(r/L, \sigma)$ are related to the behavior at small at large separation distances, respectively. The function f_{in} is defined as:

$$f_{in}\left(r/\lambda, Re_\lambda\right) = \frac{1 + c_1 \log\left(1 + c_2 \frac{r}{\lambda}\right) + c_3 \frac{r}{\lambda}}{1 + c_4 \frac{r}{\lambda}} \cdot \frac{\exp(-c_5 \frac{r}{\lambda})}{1 + \exp(-c_5 \frac{r}{\lambda})} \tag{4.74}$$

where the coefficients c_i are positive functions of Re_λ. These coefficients have to be tuned in order to take into account the observed Re_λ dependency at small r. The outer function is defined as:

$$f_{out}\left(r/L, \sigma\right) = \frac{\exp(-c_6 \frac{r}{L})}{1 + \exp(-c_6 \frac{r}{L})} \cdot \frac{1}{1 + c_7 \left(\frac{r}{L}\right)^{m(\sigma)}} \tag{4.75}$$

where m is the parameter governing the decay dynamics of the two-point velocity correlation. The parameter m is related to the energy spectrum parameter σ thanks to

$$m = \begin{cases} \sigma + 1 & \sigma = 1, 2, 3 \\ 6 & \sigma = 4 \end{cases}. \tag{4.76}$$

A least-square optimization procedure based on EDQNM data yields

$$\begin{gathered} c_1 = 0.11 Re_\lambda^{0.45},\ c_2 = 248 Re_\lambda^{-1.14},\ c_3 = 10.6 Re_\lambda^{-0.02} - 9.2, \\ c_4 = \frac{665.5}{Re_\lambda + 282.2},\ c_5 = \frac{15.7}{Re_\lambda - 64},\ c_6 = 0.88,\ c_7 = 5 \times 10^{-5}. \end{gathered} \tag{4.77}$$

4.3.3 *Remarks on Asymptotic Behaviors $E(k \to 0)$ and $f(r \to +\infty)$*

Most existing models and theories for the three-dimensional energy spectrum $E(k)$ and velocity correlation function $f(r)$ assume that $E(k \to 0) \propto k^\sigma$ and $f(r \to \infty) \propto r^{-m}$ where exponents $1 \leq \sigma \leq 4$ and $2 \leq m6$ are tied by a simple univoque relation.

A deeper analysis reveals that this hypothesis stems from an oversimplified mathematical analysis. Starting from the exact relations (4.53) and (4.55) one can show that non-algebraic solutions exists after some rigorous algebra, as shown in Davidson (2011) whose results are summarized in Table 4.9.

The full rigorous solution was given more recently by Llor and Soulard (2013). Considering a correlation function of the form:

Table 4.8 Exact and asymptotic kinematic constraints on the longitudinal correlation function $f(r)$. Analytical: the constraint is exactly satisfied, thanks to the mathematical form of the model; A posteriori: the constraint is not explicitly taken into account in the derivation of the model nor in the coefficient calibration procedure, but can be checked a posteriori; No: the constraint is not satisfied by the model

Physical argument	Constraint on f	$e^{-r/\lambda}$	$e^{-r^2/2\lambda^2}$	$e^{-r/L}$	$e^{-\pi r^2/4L^2}$	Present, Eq. 4.73
Definition of autocorrelation	$f(0)=1$	1	1	1	1	Analytical
f is a decaying function	$\lim_{r\to\infty} f(r,t)=0$	0	0	0	0	Analytical
g is a decaying function	$\lim_{r\to\infty} rf'(r)=0$	0	0	0	0	Analytical
f' vanishes at $r=0$	$f'(r=0)=0$	$-\frac{1}{\lambda_f}$	0	$-\frac{1}{L_f}$	0	Analytical
Integral length scale definition	$\int_0^{+\infty} f(r)dr = L_f$	λ_f	$\lambda_f\sqrt{\frac{\pi}{2}}$	L_f	L_f	Constrainted
Integral length scale definition	$-\int_0^{+\infty} rf'(r)dr = L_f$	λ_f	$\lambda_f\sqrt{\frac{\pi}{2}}$	L_f	L_f	Constrained
Taylor microscale definition	$f''(r=0)=-\frac{1}{\lambda_f^2}$	$\frac{1}{\lambda_f^2}$	$-\frac{1}{\lambda_f^2}$	$\frac{1}{L_f^2}$	$-\frac{\pi}{2L_f^2}$	Constrained
Pressure variance	$\int_0^{+\infty} r\left(f'(r)\right)^2 dr = \frac{\overline{p'^2}}{2\rho^2 u'^4}$	$\frac{1}{4}$	$\frac{1}{2}$	$\frac{1}{4}$	$\frac{1}{2}$	A posteriori
Pressure gradient variance	$\int_0^{+\infty} \frac{1}{r}\left(f'(r)\right)^2 dr = \frac{\overline{(\nabla p')^2}}{12\rho^2 u'^4}$	$+\infty$	$\frac{1}{2\lambda_f^2}$	$+\infty$	$\frac{\pi}{4L_f^2}$	A posteriori
First root of $g(r)$	$g(r_1)=0, r_1=2.25L_f$	$r_1=2\lambda_f$	$r_1=\sqrt{2}\lambda_f$	$r_1=2L_f$	$r_1=2/\sqrt{\pi}L_f$	Constrained
Self-similarity at large scales	$\overline{u^2}f(r\to+\infty)\propto r^{-m}$, with $m=\sigma+1$ if $\sigma\leq 3$ and $m=6$ if $\sigma=4$	No	No	No	No	Analytical

Table 4.9 Asymptotic behaviour of $E(k)$ for fixed algebraic behaviour of $f(r)$. $\mathfrak{I}$ and A are the Loistsyansky integral parameter given in Eq. (4.143) and a constant parameter, respectively. Adapted from Davidson (2011)

$u'^2 f(r \to \infty)$	$E(k \to 0)$
Ar^{-2}	$\frac{A}{2}k$
Ar^{-3}	$\frac{A}{\pi}k^2$
Ar^{-4}	$\frac{A}{4}k^3$
Ar^{-5}	$\frac{A}{3\pi}k^4(D - \ln k),\ D = O(1)$
Ar^{-6}	$\frac{\mathfrak{I}}{24\pi^2}k^4 + O(Ak^5)$

$$f(r) = \sum_{m=m_0}^{+\infty} c_m \left(\frac{r}{L}\right)^{-m}, \tag{4.78}$$

they obtained the following exact asymptotic expression:

$$\frac{\pi}{2u'^2}E(k) = \sum_{n=4}^{+\infty}(\phi_n - c_{n+1}\ln(kL))a_n L^{n+1}k^n + \sum_{m=m_0}^{+\infty} c_m \alpha_m L^m k^{m-1}, \tag{4.79}$$

where $a_n = (-1)^{n/2}(n-2)/(n-1)!$ (n being restricted to even integers) along with

$$\phi_n = \lim_{R\to+\infty}\left(\int_0^R \left[f(r) - \sum_{m=m_0}^{<n+1} c_m \left(\frac{r}{L}\right)^{-m}\right]\frac{r^n}{L^{n+1}}dr - c_{n+1}\ln(R/L)\right) \tag{4.80}$$

and

$$\alpha_m = \lim_{\epsilon\to 0}\left(\int_\epsilon^{+\infty} \xi^{-m}\left[\xi(\sin\xi - \xi\cos\xi) - \sum_{n=4}^{<m-1} a_n\xi^n\right]d\xi\right). \tag{4.81}$$

The first term in this expression for $E(k)$ exhibits a logarithmic correction, showing that non-algebraic behavior for $E(k)$ or $f(r)$ must be considered, which has not been the case in almost all existing theories. It is worth noting that these expressions stem from kinematic analysis, and that there is no evidence that they are solutions of the Lin and Karman–Howarth equations.

4.3.4 Model for Wave-number-frequency Energy Spectrum $E(k, \omega)$

The energy spectrum models can be extended to obtain a wave-number frequency energy spectrum, which will account for advection of the turbulent scales. Introducing

the two-point two-time velocity correlation tensor $R_{ij}(\boldsymbol{r},\tau) = \overline{u_i'(\boldsymbol{x},t)u_j'(\boldsymbol{x}+\boldsymbol{r},t+\tau)}$ and its Fourier transform in the physical space

$$\hat{R}_{ij}(\boldsymbol{k},\tau) = \frac{1}{(2\pi)^3}\iiint R_{ij}(\boldsymbol{r},\tau)e^{-\imath\boldsymbol{k}\cdot\boldsymbol{r}}d\boldsymbol{r}, \tag{4.82}$$

the two-time energy spectrum $E(\boldsymbol{k},\tau)$ is defined as

$$E(\boldsymbol{k},\tau) = \frac{1}{2}\hat{R}_{ii}(\boldsymbol{k},\tau). \tag{4.83}$$

The wave-number-frequency energy spectrum is then obtained applying the Fourier transform in time

$$E(\boldsymbol{k},\omega) = \int E(\boldsymbol{k},\tau)e^{-\imath\omega\tau}d\tau. \tag{4.84}$$

To model $E(\boldsymbol{k},\omega)$ it is necessary to identify advection mechanisms that are at play, the emphasis being put on small scales for which a universal behavior may be expected. At least three advection mechanisms can be taken into account:

(i) *Advection by a mean flow* velocity, which will be uniform in the isotropic turbulence case. Small scales are assumed to evolved slowly compared to the mean velocity and to be advected in a quasi-frozen state, as hypothesized by Taylor in 1938 (see Sect. 4.1.1).
(ii) *Passive advection by large turbulent scales*. This phenomenon was addressed in pioneering works by Kraichnan in 1964 and later by Tennekes in 1975. It is coined as the *random sweeping* of small scales by large ones.
(iii) *Straining by large scale fluctuations*, which results in the nonlinear cascade process.

The effects of the first two advection mechanisms can be understood considering an extended version of Kraichnan's Linear Random Advection model in which both advecting fields are accounted for:

$$\frac{\partial}{\partial t}\boldsymbol{u}(\boldsymbol{k},t) = -\imath\left[\boldsymbol{k}\cdot(\boldsymbol{v}_0+\boldsymbol{v})\right]\boldsymbol{u}(\boldsymbol{k},t), \tag{4.85}$$

where $\boldsymbol{u}$, $\boldsymbol{v}_0$ and $\boldsymbol{v}$ denotes the small scale velocity field, the mean velocity field and the large-scale velocity field with zero mean, respectively. The exact analytical solution is

$$\boldsymbol{u}(\boldsymbol{k},t) = \exp\left[\boldsymbol{k}\cdot(\boldsymbol{v}_0+\boldsymbol{v})t\right]\boldsymbol{u}(\boldsymbol{k},0), \tag{4.86}$$

which corresponds to Eq. (2.112), with $G_{ij}^{(0)}(\boldsymbol{k},t,t_0) = \exp\left[\boldsymbol{k}\cdot(\boldsymbol{v}_0+\boldsymbol{v})t\right]$ and a zero source term $\boldsymbol{s}$. Here, since the mean flow velocity is assumed to be uniform, one has $\boldsymbol{k}(t) = \boldsymbol{k}(t_0)$.

The two-time spectral energy tensor is therefore given by

$$\overline{u_i'(\boldsymbol{k},t)u_j'(\boldsymbol{k}',t')} = \frac{1}{(2\pi)^6}\int \overline{u_i'(\boldsymbol{x},t)u_j'(\boldsymbol{x}',t')}e^{-\imath(\boldsymbol{k}\cdot\boldsymbol{x}+\boldsymbol{k}'\cdot\boldsymbol{x}')}d^3\boldsymbol{x}d^3\boldsymbol{x}'. \tag{4.87}$$

Noting $\boldsymbol{x}' = \boldsymbol{x} + \boldsymbol{r}$ and $t' = t + \tau$ and reminding that

$$\delta(\boldsymbol{k}+\boldsymbol{k}') = \frac{1}{(2\pi)^3}\iiint e^{-\imath(\boldsymbol{k}+\boldsymbol{k}')\cdot\boldsymbol{x}}d^3\boldsymbol{x},$$

one obtains

$$\overline{u_i'(\boldsymbol{k},t)u_j'(\boldsymbol{k}',t+\tau)} = \delta(\boldsymbol{k}+\boldsymbol{k}').\hat{R}_{ij}(\boldsymbol{k}',\tau). \tag{4.88}$$

Now inserting the solution (4.86), one obtains

$$\begin{aligned}\overline{u_i'(\boldsymbol{k},t)u_j'(\boldsymbol{k}',t+\tau)} = \overline{u_i'(\boldsymbol{k},0)u_j'(\boldsymbol{k}',0)} \\ \times\overline{\exp\left[-\imath\boldsymbol{k}\cdot(\boldsymbol{v}_0+\boldsymbol{v})t - \boldsymbol{k}'\cdot(\boldsymbol{v}_0+\boldsymbol{v})(t+\tau)\right]},\end{aligned} \tag{4.89}$$

which can be rewritten as a relation between two-time and single-time spectral tensors:

$$\delta(\boldsymbol{k}+\boldsymbol{k}')\hat{R}_{ij}(\boldsymbol{k}',\tau) = \delta(\boldsymbol{k}+\boldsymbol{k}')\hat{R}_{ij}(\boldsymbol{k}')\overline{\exp\left[-\imath\boldsymbol{k}\cdot(\boldsymbol{v}_0+\boldsymbol{v})t - \boldsymbol{k}'\cdot(\boldsymbol{v}_0+\boldsymbol{v})(t+\tau)\right]}. \tag{4.90}$$

Integration over $\boldsymbol{k}'$ leads to

$$\hat{R}_{ij}(\boldsymbol{k},\tau) = \hat{R}_{ij}(\boldsymbol{k})\overline{\exp\left[-\imath\boldsymbol{k}\cdot(\boldsymbol{v}_0+\boldsymbol{v})\tau\right]}, \tag{4.91}$$

from which one recovers the relation between two-time and single-time energy spectra:

$$E(\boldsymbol{k},\tau) = E(\boldsymbol{k})\overline{\exp\left[-\imath\boldsymbol{k}\cdot(\boldsymbol{v}_0+\boldsymbol{v})\tau\right]}. \tag{4.92}$$

This expression can be further developed assuming that the sweeping velocity field $\boldsymbol{v}$ is a Gaussian random field. In this case, one has

$$\begin{aligned}\overline{\exp\left[-\imath\boldsymbol{k}\cdot(\boldsymbol{v}_0+\boldsymbol{v})\tau\right]} &= \exp\left[-\imath\boldsymbol{k}\cdot\boldsymbol{v}_0\tau\right]\overline{\exp\left[-\imath\boldsymbol{k}\cdot\boldsymbol{v}\tau\right]} \\ &= \exp\left[-\imath\boldsymbol{k}\cdot\boldsymbol{v}_0\tau\right]\exp\left[\frac{\overline{\boldsymbol{v}^2}k^2\tau^2}{6}\right],\end{aligned} \tag{4.93}$$

showing that the two-time energy spectrum originates in a combination of harmonic oscillations induced by the mean field advection and exponential decay due to random

sweeping. The single-time energy spectrum $E(\boldsymbol{k})$ is not modified and is still fully general at this point. One can note that (4.93) is the Fourier transform of a Gaussian distribution with mean velocity $\boldsymbol{v}_0$ and a variance specified by the sweeping velocity $V = \sqrt{\overline{\boldsymbol{v}^2}/3}$.

Therefore, the associated expression wave-number-frequency spectrum spectrum is Wylczek and Narita (2012)

$$E(\boldsymbol{k}, \omega) = \frac{E(\boldsymbol{k})}{\sqrt{2\pi k^2 V^2}} \exp\left(-\frac{(\omega - \boldsymbol{k} \cdot \boldsymbol{v}_0)^2}{2k^2 V^2}\right), \tag{4.94}$$

showing that the mean flow advection induces a Doppler shift in frequency, while random sweeping generates a Doppler broadening of the spectrum in the frequency domain. This model might be further complexified accounting for the Doppler shift induced by the random field $\boldsymbol{v}$. The energy spectrum $E(\boldsymbol{k}, \omega)$ may be anisotropic even in the case of an isotropic $E(k)$ because of the Doppler shift term $\boldsymbol{k} \cdot \boldsymbol{v}_0$.

It is important to note that this model is based on the simplified linear propagator (4.85) which does not account for viscous, pressure and nonlinear effects, allowing for a simple analytical integration. This model is observed to be in satisfactory agreement with DNS data.

A last comment is that these results, including the exponential term due to random sweeping, are recovered considering Taylor series expansions about the isotropic solution (Kaneda 1993; Kaneda et al. 1999). In these references, two-time correlations are obtained computing the coefficient of the time expansion thanks to spectral closures, namely the Lagrangian Renormalized Approximation, which also assumes some degree of Gaussianity for velocity fluctuations.

4.3.5 *Models Two-Point Two-Time Velocity Correlation $R(r, \tau)$*

The longitudinal two-point two-time correlation function $R(r, \tau) = R_{11}(r\boldsymbol{e}_x, \tau)$ is classically approximated via polynomial expansion, which aims at expressing it in terms of the single-time correlation function.

Considering advection by a uniform mean flow with a component u_0 along the x-axis, Taylor's frozen turbulence hypothesis yields the following linear approximation:

$$R(r, \tau) = R(r - u_0 t, 0), \tag{4.95}$$

which is observed to yield bad results, since iso-correlation contours are straight lines in the (x, t) plane that extend up to infinity, which is unphysical since turbulent eddies have finite correlation scales. A more realistic model is obtained considering higher-order expansions. A second-order Taylor series expansion leads to

$$R(r,\tau) = R(0,0) + r\frac{\partial R}{\partial r}(0,0) + \tau\frac{\partial R}{\partial \tau}(0,0) + \frac{r^2}{2}\frac{\partial^2 R}{\partial r^2}(0,0) + \frac{\tau^2}{2}\frac{\partial^2 R}{\partial \tau^2}(0,0) + r\tau\frac{\partial^2 R}{\partial \tau \partial r}(0,0) + O(r^3, \tau^3, r^2\tau, r\tau^2). \tag{4.96}$$

Statistical isotropy and stationarity imply

$$\frac{\partial R}{\partial r}(0,0) = \frac{\partial R}{\partial \tau}(0,0) = 0.$$

Such an expansion was proposed by Kaneda in a series of papers, e.g. Kaneda (1993), Kaneda et al. (1999), to predict both Lagrangian and Eulerian correlation tensors in isotropic turbulence. In Kaneda et al. (1999) a Padé approximation is used to recover the fact that $R(r, \tau \to +\infty) = 0$, an asymptotic behavior that a simple short-time Taylor series expansion is unable to recover.

A second-order model coined as the *Elliptic model* or the *scale-similarity model* is obtained considering an isocontour $R(r,\tau) = C$ (He et al. 2009; Zhao and He 2009). This isocontour intercepts the space separation axis at the point $(r_c, 0)$, leading to

$$R(r,\tau) = R(r_c, 0) = C. \tag{4.97}$$

Now inserting the second-order expansion (4.96), one obtains

$$r_c^2 = (r - U_c\tau)^2 + V_c^2\tau^2, \tag{4.98}$$

where

$$U_c = -\frac{\partial^2 R}{\partial \tau \partial r}(0,0)\left(\frac{\partial^2 R}{\partial r^2}(0,0)\right)^{-1} \tag{4.99}$$

$$V_c^2 = -\frac{\partial^2 R}{\partial \tau^2}(0,0)\left(\frac{\partial^2 R}{\partial r^2}(0,0)\right)^{-1} - U_c^2 \tag{4.100}$$

leading to the final model

$$R(r,\tau) = R\left(\sqrt{(r - U_c\tau)^2 + V_c^2\tau^2}, 0\right). \tag{4.101}$$

Correlation isocontours are self-similar ellipses, with aspect ratio A and angle with the horizontal axis α given by the following formula:

$$\tan^2\alpha = 4U_c^2\left(\sqrt{(1 + U_c^2 - V_c^2)^2 + 4U_c^2V^2} + (1 + U_c^2 - V_c^2)\right)^{-2} \tag{4.102}$$

$$A^2 = 4V_c^2 \left(\sqrt{(1 + U_c^2 - V_c^2)^2 + 4U_c^2 V_c^2} + (1 + U_c^2 - V_c^2) \right)^{-2}. \tag{4.103}$$

The elliptic model is observed to yield very accurate results for small scales within the inertial range, and yields very satisfactory prediction of Taylor and integral scales. Addition of higher-order terms is not observed to yield significant improvement of the results. It is worth noting that the elliptic approximation is not accurate for pressure fluctuations (see Sect. 4.9).

This model accounts for both advection (at velocity U_c) and random sweeping (with characteristic velocity V_c) phenomena. It is compatible with the model two-time two-point energy spectrum (4.94), and can be extended to shear flows (see Sect. 9.6.2.1).

As a matter of fact, an exact relation between $R(r, \tau)$ and the two-time energy spectrum is

$$R(r, \tau) = 2 \iiint E(\boldsymbol{k}, \tau) e^{\imath k_x r} d^3\boldsymbol{k}. \tag{4.104}$$

Now inserting the model (4.92) and accounting for (4.93), one obtains in the isotropic case (and using notation of the preceding section)

$$R(r, \tau) = 2 \int E(k) \frac{\sin(k(r - u_0\tau))}{(k(r - u_0\tau))} \exp\left(-\frac{1}{2} k^2 V^2 \tau^2 \right) dk, \tag{4.105}$$

which should also be equal to (using the elliptic model)

$$R(r, \tau) = 2 \int E(k) \frac{\sin(kr_c)}{kr_c} dk. \tag{4.106}$$

A second order expansion yields the following identification

$$r_c^2 = (r - u_0\tau)^2 + 3V^2\tau^2, \tag{4.107}$$

leading to the following identifications: $U_c = u_0$ and $V_c = \sqrt{3}V$. The formula above show that the random sweeping by large scales results in an exponential decay of the correlations at small scales, without introducing the viscous damping effect. The elliptic model is reported to be in very satisfactory agreement with DNS data also at relatively large scales for which the truncated Taylor series expansions should not hold. It has not be assessed at very large scales.

The velocities U_c and V_c may be measured and evaluated thanks to relations (4.99) and (4.100). They can also be evaluated thanks to dedicated models to recover a predictive model. In the isotropic case, one has

$$\frac{\partial^2 R}{\partial r^2}(0,0) = -\iiint k_x^2 \hat{R}_{ii}(\boldsymbol{k},0)d^3\boldsymbol{k} = -\frac{1}{3}\iiint k^2 \hat{R}_{ii}(\boldsymbol{k},0)d^3\boldsymbol{k}$$
$$= -\frac{2}{3}\int_0^{+\infty} k^2 E(k)dk = -\frac{\varepsilon}{3\nu} \tag{4.108}$$

along with

$$\frac{\partial^2 R}{\partial \tau \partial r}(0,0) = \frac{2}{3}u_0 \int_0^{+\infty} k^2 E(k)dk = u_0 \frac{\varepsilon}{3\nu} \tag{4.109}$$

and

$$\frac{\partial^2 R}{\partial \tau^2}(0,0) = -\frac{2}{3}\left(u_0^2 + v^2\right)\int_0^{+\infty} k^2 E(k)dk = -\left(u_0^2 + v^2\right)\frac{\varepsilon}{3\nu}, \tag{4.110}$$

where the random sweeping velocity is approximated as $v^2 = 2\int_0^{k_c} E(k)dk$, k_c the largest wave number associated to large scales. As a first approximation one can take $v^2 = \mathcal{K}$, leading to

$$U_c = u_0, \quad V_c^2 = \mathcal{K}. \tag{4.111}$$

This elliptic model, being coherent with the spectrum model discussed in the preceding section, does not account for viscous, pressure and straining effects. The relative influence of straining and sweeping can be analyzed considering the scale-by-scale evolution of the correlation time.

Defining the two-time correlation coefficient at wavenumber k as

$$C(k,\tau) = \frac{\overline{\hat{u}_i(k,t)\hat{u}_i(k,t+\tau)}}{\overline{\hat{u}_i(k,t)\hat{u}_i(k,t)}}, \tag{4.112}$$

the correlation time at wave number k is defined as $\tau_D(k) = \int_0^{\infty} C(k,\tau)d\tau$. Depending on the dominant mechanisms, one should have in the inertial range

$$\tau_D(k) \simeq \begin{cases} (E(k)k^3)^{-1/2} \simeq (\epsilon k)^{-2/3} & \text{dominant straining} \\ (V_c k)^{-1} & \text{dominant random sweeping} \end{cases}. \tag{4.113}$$

Favier et al. (2010) observed in DNS that $\tau_D(k)$ switch slowly from dominant straining at large scales to dominant sweeping at smaller scales within the inertial range.

4.4 Free Decay Theories: Self-similarity, Self-preservation, Symmetries and Invariants

We now address the issue of free decay of isotropic turbulence, which is assumed to correspond to grid turbulence in wind tunnels. Specific issues related to this flow can be identified, the most popular one being the prediction of decay of the turbulent kinetic energy $\mathcal{K}(t)$. Tremendous efforts have been devoted to this question since the early 20th century, but a fully satisfactory theory is still lacking. Several related questions have been raised during the past 100 years, among which one must mention:

(i) Does freely decaying isotropic turbulence exhibits self-similar solutions?
(ii) Does kinetic energy follow an algebraic decay law, i.e. $\mathcal{K}(t) \propto t^{-n}$?
(iii) Is there a universal decay regime such that $\mathcal{K}(t) \propto t^{-1}$?

These questions have been controversial issues during the last decades, and definitive answers are still to be found in many cases.

4.4.1 Self-similarity, Self-preservation and Partial Self-preservation

The very definition of self-similarity, self-preservation or partial self-preservation has been debated during decades, yielding several misunderstanding and controversies. In the present book, the following definitions are selected:

(i) A solution will be said to be *exactly self-preserving* iff the full solution at any time and any scale can be described using a single length scale $\ell(t)$ and a single velocity scale $v(t)$, leading to $\overline{u'(r,t)u'(0,t)} = v^2(t)F(r/\ell(t))$ and $E(k,t) = v^2(t)\ell(t)G(k\ell(t))$ where $F(x)$ and $G(x)$ are dimensionless shape functions for the velocity correlation function and energy spectrum, respectively. The very concept of self-preservation (also referred to as the *von Karman hypothesis* in Monin and Yaglom 1975) was pioneered by Taylor (1935), von Karman and Howarth (1938) and von Karman and Lin (1949).
(ii) A solution will be said to be *partially self-preserving* if self-preservation is observed over a limited range of scales and not at all scales.
(iii) A solution will be said to be *self-similar*, according to George's definition (sometimes referred to as *extended self-similarity hypothesis*) George (1992), if Lin equation (or equivalently the Karman–Howarth equation) admits a self-similar solution such as $E(k,t) = E_s(t,\star)\,\psi(k\ell(t),\star)$, $T(k,t) = T_s(t,\star)\,\varphi(k\ell(t),\star)$, where E_s and T_s are time-dependent amplitude terms and ψ and φ shape functions, respectively. Here, $\star$ denotes a possible dependency on initial conditions. This definition is more flexible than pre-existing self-similarity theory, according to which $E(k,t) = v^2(t)\ell(t)\,\psi(kl(t),\star)$ and $T(k,t) = v^3(t)\,\varphi(k\ell(t),\star)$. The difference lies in the fact that no a priori choice is made on both E_s and T_s in the former case, while amplitude scalings are fixed in the later.

The self-similarity theories aim at analyzing the statistical structure of the turbulent field, but they also allow for the prediction of the evolution laws of global physical quantities such as kinetic energy $\mathcal{K}(t)$, turbulent dissipation rate $\varepsilon(t)$, integral length scale $L_f(t)$ and Taylor microscale $\lambda_f(t)$.

The present section is organized as follows. First, symmetry-based analysis of Navier–Stokes equations is discussed in Sect. 4.4.2 along with consequences dealing with the existence of self-similar solutions. The link between symmetry analysis, existence of invariant quantities and algebraic decay of kinetic energy is presented in Sects. 4.4.3 and 4.4.4. Then, the dimensional analysis based Comte-Bellot–Corrsin theory, which bridges between the decay exponent and the features of the initial conditions, is introduced in Sect. 4.4.5. The presentation ends with George's extended self-similarity theory in Sect. 4.4.6, that starts from the full evolution equations to obtain the two important results: (i) self-similar solutions may exist and (ii) the associated decay exponent depends on features of the initial condition. The results of these theoretical analyses are summarized in Sect. 4.4.7, while the most recent results based on numerical simulations, experimental data and EDQNM analysis are presented in Sect. 4.5

4.4.2 *Symmetries of Navier–Stokes Equations and Existence of Self-similar Solutions*

Let us first recall that a physical law $F(x, t; u_1, \ldots, u_N)$ (where x and t denote the space and time, respectively, and $u_i, i = 1, N$ are physical quantities) is said to be invariant under the transformation $F \longrightarrow F^*, x \longrightarrow x^*, t \longrightarrow t^*, u_i \longrightarrow u_i^* (i = 1, N)$ if and only if

$$F(x, t; u_1, \ldots, u_N) = F(x^*, t^*; u_1^*, \ldots, u_N^*), \tag{4.114}$$

i.e. the physical law is not modified by the change of variables. The Navier–Stokes equations for an incompressible fluid in an unbounded domain (i.e. without boundary conditions) are known to admit the following one-parameter set of symmetries[9] (which has the mathematical structure of a Lie group):

- Time translation:

$$(t, \boldsymbol{x}, \boldsymbol{u}, p) \longrightarrow (t + t_0, \boldsymbol{x}, \boldsymbol{u}, p) \tag{4.115}$$

- Pressure translation:

$$(t, \boldsymbol{x}, \boldsymbol{u}, p) \longrightarrow (t, \boldsymbol{x}, \boldsymbol{u}, p + \zeta(t)) \tag{4.116}$$

- Rotation (with $\mathbf{Q}$ a constant rotation matrix):

[9] Other symmetries, such as the mirror symmetry, exist but are not one-parameter symmetries.

$$(t, \boldsymbol{x}, \boldsymbol{u}, p) \longrightarrow (t, \mathbf{Q}\boldsymbol{x}, \mathbf{Q}\boldsymbol{u}, p) \tag{4.117}$$

- Generalized Galilean transformation:

$$(t, \boldsymbol{x}, \boldsymbol{u}, p) \longrightarrow (t, \boldsymbol{x} + \boldsymbol{v}(t), \boldsymbol{u} + \dot{\boldsymbol{v}}(t), p - \rho \boldsymbol{x} \cdot \ddot{\boldsymbol{v}}(t)) \tag{4.118}$$

- Scaling I:

$$(t, \boldsymbol{x}, \boldsymbol{u}, p) \longrightarrow (\alpha^2 t, \alpha \boldsymbol{x}, \alpha^{-1} \boldsymbol{u}, \alpha^{-2} p) \tag{4.119}$$

- Scaling II:

$$(t, \boldsymbol{x}, \boldsymbol{u}, p, \nu) \longrightarrow (t, \alpha \boldsymbol{x}, \alpha \boldsymbol{u}, \alpha^2 p, \alpha^2 \nu) \tag{4.120}$$

where α is an arbitrary strictly positive real parameter.

It is important noting that these symmetries are identified conducting an exact mathematical analysis of the incompressible Navier–Stokes equations, without introducing any hypothesis or modelling assumptions.[10]

Boundary conditions may eventually decrease the number of symmetries, but cannot introduce new symmetries. It is worth noting that scalings I and II are particular forms (taking $h = -1$ and $h = 1$) of the even more general rescaling given below

$$(t, x, u, p, \nu) \rightarrow (\alpha^{1-h} t, \alpha x, \alpha^h u, \alpha^{2h} p, \alpha^{1+h} \nu). \tag{4.124}$$

We now focus on isotropic turbulence. In this case, symmetries such as rotation invariance, Galilean invariance, pressure and time translation are implicitly met. Therefore, the emphasis is to be put on the scaling symmetries and look at the statistical moments of the turbulent velocity field. Let r and f be the correlation distance and the normalized two-point double velocity correlation, respectively (see Sect. 4.2.1 for a detailed description). In the limit of very large Reynolds numbers (i.e. vanishing molecular viscosity), these quantities are transformed as follows (Oberlack 2002)

---

[10] This analysis is performed considering the following one-parameter (Lie-group) transformation:

$$T_a : \boldsymbol{y} \rightarrow \hat{\boldsymbol{y}} = \hat{\boldsymbol{y}}(\boldsymbol{y}, a), \quad \boldsymbol{y} = (t, \boldsymbol{x}, \boldsymbol{u}, p, \nu) \tag{4.121}$$

which depends continuously on the real parameter a. Let us write formally the Navier–Stokes equations as $\mathcal{NS}(\boldsymbol{y}) = 0$. T_a is said to be a symmetry of the Navier–Stokes equations iff

$$\mathcal{NS}(\boldsymbol{y}) = 0 \Longleftrightarrow \mathcal{NS}(\hat{\boldsymbol{y}}) = 0. \tag{4.122}$$

The set of symmetries constitutes a local one-parameter Lie Group, referred to as a symmetry group of the Navier–Stokes equations. Assuming that the neutral element of this group (i.e. the identity transformation) corresponds to $a = 0$, the group is characterized by the variation of $\boldsymbol{y}$ under T_a around $a = 0$, which is represented by the *infinitesimal generator* $\boldsymbol{X}$:

$$\boldsymbol{X} \equiv \left. \frac{\partial \hat{\boldsymbol{y}}}{\partial a} \right\|_{a=0} = \sum_i \xi_i \frac{\partial}{\partial y_i}, \quad \xi_i \equiv \left. \frac{\partial \hat{y}_i}{\partial a} \right\|_{a=0}. \tag{4.123}$$

Once $\boldsymbol{X}$ is known, all elements of the symmetry group T_a can be calculated.

$$t^* = \alpha_2 t, \quad r^* = \alpha_1 r, \quad \overline{u'^2}^* = (\alpha_1/\alpha_2)^2 \overline{u'^2}, \quad f^* = f. \tag{4.125}$$

In the case of finite Reynolds number, the only possible solution is $\alpha_2 = \alpha_1^2$. A set of invariants $\breve{r}$, $\breve{f}$, $\breve{u}$, $\breve{p}$ can be defined:

$$\breve{r} = \frac{r}{t^{\frac{2}{\sigma+3}}}, \quad \breve{f} = \frac{\overline{u'^2} f}{t^{-2\frac{\sigma+1}{\sigma+3}}}, \quad \breve{u} = \frac{u}{t^{-\frac{\sigma+1}{\sigma+3}}}, \quad \breve{p} = \frac{p}{t^{-2\frac{\sigma+1}{\sigma+3}}}, \tag{4.126}$$

where

$$\sigma = 2\frac{\ln \alpha_2}{\ln \alpha_1} - 3. \tag{4.127}$$

It is worth noting that, in the finite Reynolds number case, $\sigma = 1$ is the only possible value. It can be shown, still considering the high Reynolds number limit, that the parameter σ is related to the spatial decay of the two-point correlations and the shape of the kinetic energy spectrum at low wave number:

$$E(k \to 0) \sim k^{\sigma}. \tag{4.128}$$

It is important noticing that the constants involved in these scaling laws are assumed to be independent of time, corresponding to the so-called *Permanence of Large Eddies (PLE) hypothesis*.

We now show that the existence of self-similar solutions for the isotropic decay problem can be deduced from the symmetry analysis (and not assumed a priori). To this end, let us consider the following one-parameter sub-group of transformation (Clark and Zemach 1998)

$$t^* = \alpha(t + t_0) - t_0, \quad \boldsymbol{x}^* = \alpha^{\gamma} \boldsymbol{x}, \tag{4.129}$$

where α is an arbitrary real parameter. This sub-group is labeled by γ and t_0, which are two real parameters. We are now looking for turbulent flows such that the shape of the kinetic energy spectrum $E(k, t)$ is invariant under the transformation (4.129). Simple dimensional analysis yields:

$$\alpha^{3\gamma-2} E(k, t) = E(\alpha^{-k} k, \alpha(t + t_0) - t_0). \tag{4.130}$$

The above property holds for all group elements if it holds for the *infinitesimal element*, i.e. for the group element $\alpha = 1 + \delta\alpha$, with $\delta\alpha \ll 1$. To this end, one differentiates (4.130) with respect to α and then takes $\alpha = 1$. The result is the following *determining equation*:

$$(3\gamma - 2)E(k, t) = -\gamma k \frac{\partial E}{\partial k} + (t + t_0)\frac{\partial E}{\partial t} \tag{4.131}$$

which can be solved by the method of characteristics in the spectral space. The right-hand side of Eq. (4.131) leads to the following characteristic line equation:

$$\frac{d}{dt}k(t) = -\frac{\gamma}{t+t_0}k(t) \tag{4.132}$$

and therefore the wavenumber k evolves as

$$k(t) = \left(1+\frac{t}{t_0}\right)^{-\gamma} k(0) \tag{4.133}$$

along the characteristic line spanned by $k(0)$. Along this line, the kinetic energy spectrum evolution is given by the following relation:

$$\frac{d}{dt}E(k(t),t) = \frac{\partial E}{\partial k}\frac{dk}{dt} + \frac{\partial E}{\partial t} = \frac{3\gamma-2}{t+t_0}E(k(t),t) \tag{4.134}$$

leading to the following solution:

$$\begin{aligned} E(k(t),t) &= \left(1+\frac{t}{t_0}\right)^{3\gamma-2} E_0(k(0)) \\ &= \left(1+\frac{t}{t_0}\right)^{3\gamma-2} E_0\left(k(t)\left(1+\frac{t}{t_0}\right)^{\gamma}\right). \end{aligned} \tag{4.135}$$

Introducing the lengthscale $\ell(t)$ and the energy scale $v'^2(t)$ such that

$$\ell(t) = \ell_0\left(1+\frac{t}{t_0}\right)^{\gamma}, \quad v'^2(t) = v_0'^2\left(1+\frac{t}{t_0}\right)^{2\gamma-2} \tag{4.136}$$

one obtains

$$E(k,t) = v'^2(t)\ell(t)F(k\ell(t)) \tag{4.137}$$

in which the non-dimensional shape function F is such that

$$F(\xi) = \frac{E_0(\xi/\ell_0)}{v_0'^2\ell_0}. \tag{4.138}$$

Therefore, *the solution obeys a self-similar decay regime*.[11] The important conclusion is that (4.137) is not postulated as in early studies like those of Karman and Howarth in the late 1930's, but deduced as being a consequence of the symmetries of the governing equations in the limit of very high Reynolds number.

[11] An adequate choice for $v_0'^2$ yields $v'^2(t) = \mathcal{K}(t)$.

4.4.3 Algebraic Decay Exponents Deduced from Symmetry Analysis

The symmetry analysis introduced in the previous section can also be used to recover some information about the time evolution of the solution. This is done finding the values of σ in Eq. (4.127) or γ in Eq. (4.129).

Time scaling laws for the turbulent kinetic energy $\mathcal{K}(t)$, turbulent dissipation $\varepsilon(t)$, integral lengthscale $L_f(t)$ and turbulent Reynolds number Re_L are deduced from relation (4.126) in a straightforward way:

$$L_f(t) = \int_0^{+\infty} f(r,t)dr = t^{\frac{2}{\sigma+3}} \int_0^{+\infty} f(r^*)dr^* \sim t^{\frac{2}{\sigma+3}}, \tag{4.139}$$

$$\mathcal{K}(t) \sim t^{-2\frac{\sigma+1}{\sigma+3}}, \tag{4.140}$$

$$Re_L(t) = \frac{L_f(t)\sqrt{2\mathcal{K}(t)/3}}{\nu} \sim t^{-\frac{\sigma-1}{\sigma+3}}, \tag{4.141}$$

$$\varepsilon(t) \sim \frac{d}{dt}\mathcal{K}(t) \sim t^{-\frac{3\sigma+5}{\sigma+3}}. \tag{4.142}$$

It is seen that the time evolution exponents of these global turbulent parameters are explicit functions of σ. Since σ is also related to the shape of the kinetic energy spectrum at very large scales (see Eq. (4.128)), this leads to the conclusion that the self-similar decay regime is governed by the very large scales of turbulence.

Different values for σ have been proposed during the past decades, which are now briefly surveyed (corresponding time evolution exponents are displayed in Table 4.10). A value of σ is associated to the existence of an invariant quantity which will remain constant during the decay (see below). In some cases the existence and the physical meaning of this invariant quantity are easily handled, while some controversies exist in other cases. The most popular values for the parameter σ are:

- $\sigma = 4$. According to the Loitsyansky-Landau theory, it was hypothesized by Loitsyansky in 1939 that the following integral quantity (referred to as the *Loitsyansky integral* or the *Loitsyansky invariant*)

$$\mathfrak{I} = -\int r^2 \overline{\boldsymbol{u}'(\boldsymbol{x}) \cdot \boldsymbol{u}'(\boldsymbol{x}+\boldsymbol{r})} d^3\boldsymbol{r} = 8\pi u'^2 \int_0^{+\infty} r^4 f(r)dr \tag{4.143}$$

  is invariant in time during the decay phase. The corresponding time evolution exponents where derived by Kolmogorov in 1941. The associated form the kinetic energy spectrum is referred to as the *Batchelor spectrum*:

$$E(k) = \frac{\mathfrak{I}}{24\pi^2} k^4 + \cdots \quad (kL_f \ll 1) \tag{4.144}$$

The time invariance of $\mathfrak{I}$ is a controversial issue since it depends on the decay rate of velocity two-point correlation at long range. It is constant if velocity long-range interactions decay fast enough, which is not obvious since the pressure fluctuations may induce stronger long-range interactions.[12] The controversy was initiated by Proudman and Reid in 1954, followed by Batchelor and Proudman in 1956, who advocated that long-range interactions are strong enough to render $\mathfrak{I}$ time dependent. Since that time, $\mathfrak{I}$ has been observed to be time-dependent in many numerical simulations, in agreement with predictions of many two-point closures like EDQNM. This issue was very recently revisited by Davidson and coworkers (Davidson 2004; Ishida et al. 2006), who observed that $\mathfrak{I}$ becomes time independent after a transient phase in high-resolution DNS, provided that the domain size is much larger that the turbulent integral scale (they considered a ratio up to 80) and that the Reynolds number is larger than 100. Therefore, time dependency observed in previous simulations was an artefact due to spurious long-range correlations induced by the insufficient domain size and periodic boundary conditions. The fact that pressure fluctuations do not lead to a strong long-range coupling may be attributed to a *screening effect* in fully developed turbulence: long-range correlations are weakened by opposite cancelling effects of the very intricate turbulent vorticity field.

- $\sigma = 2$. This second value was proposed in 1954 by Birkhoff, who made the hypothesis that the following integral quantity is invariant (referred to as the *Birkhoff integral* but also as the *Saffman integral*):

$$\mathfrak{S} = \int \overline{\boldsymbol{u}'(\boldsymbol{x}) \cdot \boldsymbol{u}'(\boldsymbol{x}+\boldsymbol{r})} d^3\boldsymbol{r} = 4\pi u'^2 \int_0^{+\infty} r^2 \left(3f + rf'(r)\right) dr. \qquad (4.145)$$

The corresponding time behavior of the solution was derived by Saffman in 1967, after he argued that the Loitsyansky integral is diverging in isotropic turbulence. For that purpose, Saffman revised the approach introduced by Comte-Bellot and Corrsin in 1966 to investigate the connection between the energy spectrum and the energy decay. The associated spectrum shape (the *Saffman spectrum*) at large scales is

$$E(k) = \frac{\mathfrak{S}}{4\pi^2} k^2 \ldots \quad (kL_f \ll 1). \qquad (4.146)$$

- $\sigma = 1$. This value was proposed by Oberlack (2002), who emphasizes that this is the only value of σ which allows for the full similarity of the Karman–Howarth equation (see Eq. (4.17) and the corresponding subsection) at finite Reynolds number. A noticeable feature of this solution is that the decay occurs at constant turbulent Reynolds number.

[12] This point is easily understood looking at the Green function solution given by Eqs. (2.53) and (2.54), which show that the pressure fluctuations caused by an eddy at a distance r from this eddy have an intensity $p' \sim r^{-3}$ for large r.

Table 4.10 Time evolution exponents in self-similar decay of isotropic turbulence deduced from symmetry analysis, assuming the PLE hypothesis holds

	$\sigma = 1$	$\sigma = 2$	$\sigma = 4$	$\sigma = +\infty$
$L_f(t) \sim$	$t^{1/2}$	$t^{2/5}$	$t^{2/7}$	Const.
$\mathcal{K}(t) \sim$	t^{-1}	$t^{-6/5}$	$t^{-10/7}$	t^{-2}
$Re_L(t) \sim$	Const.	$t^{-1/5}$	$t^{-3/7}$	t^{-1}
Invariant name	Re_L	Birkhoff	Loitsyansky	$L_f(t)$
Invariant definition	$L\sqrt{\mathcal{K}}/\nu$	Eq. (4.145)	Eq. (4.143)	$\int_0^{+\infty} f(r)dr$
Associated spectrum		Saffman	Batchelor	

- $\sigma = +\infty$. This solution was also proposed by Oberlack in 2002. It corresponds to a decay with constant integral scale.

4.4.4 Time Variation Exponent and Inviscid Global Invariants

The direct physical interpretation of the value of the decay parameter σ is unclear in some cases. It is possible to get a deeper insight into the related physics looking at the links that exist between the choice of a value for σ and the conservation of exact invariants of inviscid flows.

Following Oberlack (2002), let us first recall that, for an inviscid flow in an unbounded domain V, the following non-local conservation laws are exact:

$$\frac{d}{dt}\int_V \boldsymbol{u}\cdot\boldsymbol{u}d^3\boldsymbol{x} = 0 \quad \text{(kinetic energy conservation)}, \tag{4.147}$$

$$\frac{d}{dt}\int_V \boldsymbol{x}\times\boldsymbol{u}d^3\boldsymbol{x} = 0 \quad \text{(angular momentum conservation)}, \tag{4.148}$$

$$\frac{d}{dt}\int_V \boldsymbol{u}\cdot(\nabla\times\boldsymbol{u})d^3\boldsymbol{x} = 0 \quad \text{(linear impulse or helicity conservation)}. \tag{4.149}$$

Now using the change of variable based on the invariants introduced in Eq. (4.126), the three conservation laws can be rewritten as follows:

$$(\sigma-2)\int_V \breve{\boldsymbol{u}}\cdot\breve{\boldsymbol{u}}d^3\breve{\boldsymbol{x}} = 0 \quad \text{(kinetic energy conservation)} \tag{4.150}$$

$$(\sigma - 7) \int_V \breve{\boldsymbol{x}} \times \breve{\boldsymbol{u}} d^3\breve{\boldsymbol{x}} = 0 \quad \text{(angular momentum conservation)} \tag{4.151}$$

$$(\sigma - 1) \int_V \breve{\boldsymbol{u}} \cdot (\breve{\nabla} \times \breve{\boldsymbol{u}}) d^3\breve{\boldsymbol{x}} = 0 \quad \text{(linear impulse or helicity conservation).} \tag{4.152}$$

The kinetic energy is strictly positive in a turbulent flow, while the sign and the absolute value of angular momentum and the helicity are not a priori known. Since a choice for σ can enforce only one of the three conservation laws given above, it makes sense to assume that the total linear momentum and helicity are identically null, while the kinetic energy is preserved, yielding $\sigma = 2$. Therefore, the Birkhoff-Saffman theory is coherent with the preservation of kinetic energy at infinite Reynolds number.

Another interpretation is possible (Davidson 2004) since both Loitsyansky and Birkhoff integral quantities are related to exact dynamical invariants of inviscid motion in an unbounded domain. The first one is the *linear impulse*, $\mathfrak{I}_{\mathrm{LI}}$, and the second is the *angular momentum*, $\mathfrak{I}_{\mathrm{AM}}$, with

$$\mathfrak{I}_{\mathrm{LI}} = \frac{1}{2} \int_V (\boldsymbol{x} \times \mathrm{curl}\boldsymbol{u}) dV, \tag{4.153}$$

$$\mathfrak{I}_{\mathrm{AM}} = \int_V (\boldsymbol{x} \times \boldsymbol{u}) dV. \tag{4.154}$$

Considering a volume V filled by isotropic turbulence with a characteristic length much larger that the integral length scale of the turbulent motion, the following relations hold

$$\frac{\langle \mathfrak{I}_{\mathrm{LI}}^2 \rangle}{V} \simeq \mathfrak{I}, \tag{4.155}$$

$$\frac{\langle \mathfrak{I}_{\mathrm{AM}}^2 \rangle}{V} \simeq \mathfrak{S}. \tag{4.156}$$

If turbulent eddies have a finite, non-negligible linear momentum, then $\mathfrak{S} \neq 0$ and therefore the spectrum will be of Saffman type and $\sigma = 2$. If their linear momentum is very small but their angular momentum is finite, then $\mathfrak{S} \simeq 0$ and $\mathfrak{I} \neq 0$, yielding a Batchelor-like spectrum and $\sigma = 4$.

Let us just note that, if the two-point correlations fall sufficiently rapidly to ensure that all integrals are convergent, the following Taylor series expansion holds at small wave numbers:

$$E(k) = \frac{\mathfrak{S}}{4\pi^2} k^2 + \frac{\mathfrak{I}}{24\pi^2} k^4 + \cdots \quad (kL_f \ll 1). \tag{4.157}$$

4.4.5 Comte-Bellot – Corrsin Theory

The theory proposed by G. Comte–Bellot and S. Corrsin for high-Reynolds decay regime relies on dimensional analysis and the following model spectrum

$$E(k,t) = \begin{cases} C_\sigma k^\sigma & kL(t) \leq 1, \quad 1 \leq \sigma \leq 4 \\ K_0 \varepsilon^{2/3} k^{-5/3} & kL(t) \geq 1 \end{cases} \tag{4.158}$$

where $[C_\sigma] = [L]^{\sigma+3}[T]^{-2}$ is a parameter. The *Permanence of Large Eddies* hypothesis consists in assuming that it is time-independent. The scale $L(t)$ is related to the integral scale and characterizes the energy spectrum peak. This model is an exactly self-preserving solution.

Assuming that the Permanence of Large Eddies hypothesis holds, simple dimensional analysis and spectrum continuity at $kL = 1$ lead to

$$\frac{dL}{dt} \propto C_\sigma^{1/2} L^{-(\sigma+1)/2} \quad \Longrightarrow \quad L(t) = L(0)\left(1 + \frac{t}{t_0}\right)^{2/(3+\sigma)}. \tag{4.159}$$

Turbulent kinetic energy can then be approximated as

$$\mathcal{K}(t) \sim \frac{1}{L(t)} E(1/L(t)) = \frac{1}{L(t)} C_\sigma L(t)^{-\sigma}, \tag{4.160}$$

from which one obtains the following time-evolution law:

$$\mathcal{K}(t) = \mathcal{K}(0)\left(1 + \frac{t}{t_0}\right)^{-2(\sigma+1)/(3+\sigma)}. \tag{4.161}$$

An algebraic decay law that depends on the initial condition via σ is recovered, in accordance with the idea that exact self-preservation leads to algebraic deacy laws. The breakdown of Permanence of Large Eddies hypothesis, i.e. the dependency of C_σ may be taken into account replacing σ in the expressions for the time exponent by $(\sigma - p)$ where the correction factor p is to be determined experimentally of using a more complex model. Results are summarized in Table 4.11.

The theoretical analysis based on the EDQNM closure shows that C_σ is constant in time and $p = 0$ for $\sigma \leq 3$, while $p \simeq 0.5$ for $\sigma = 4$. Therefore, one has $n = -6/5$ for $\sigma = 2$ and $n = -1.38$ for $\sigma = 4$. Neglecting the time variation of C_4, one recovers the Kolmogorov value of $n = -10/7 \simeq -1.43$ for $\sigma = 4$.[13]

[13] The value $n = -1.38$ for $\sigma = 4$ is associated to a time varying Loitsyanski integral: $\mathfrak{I} \sim t^{0.16}$. This results conflicts the most recent DNS results Ishida et al. (2006). This can be understood looking at the expansion of the nonlinear transfer term mediated by strongly non-local triadic interactions in the limit of very small wave numbers retrieved from two-point closures (e.g. EDQNM):

$$T(k \to 0) = \partial E/\partial t \sim Ak^4 - 2\nu_{turb} k^2 E,$$

Table 4.11 Analytical formulas for the prediction of the power-law exponents of the decay of the main statistical quantities given by the Comte-Bellot – Corrsin theory. σ denotes the slope of $E(k)$ at small wave numbers and p is the correction for breakdown of the Permanence of Large Eddies hypothesis

	$\mathcal{K}$	ε	L	λ	η	Re_L	Re_λ
High Re_λ	$-2\frac{\sigma-p+1}{\sigma-p+3}$	$-\frac{3(\sigma-p)+5}{\sigma-p+3}$	$\frac{2}{\sigma-p+3}$	$\frac{1}{2}$	$\frac{3(\sigma-p)+5}{4(\sigma-p+3)}$	$\frac{1-(\sigma-p)}{(\sigma-p+3)}$	$\frac{1}{2}\frac{1-\sigma+p}{\sigma-p+3}$
Saturated high Re_λ	-2	-3	0	$\frac{1}{2}$	$\frac{3}{4}$	-1	$-\frac{1}{2}$
Low Re_λ	$-\frac{\sigma+1}{2}$	$-\frac{\sigma+3}{2}$	$\frac{1}{2}$	$\frac{1}{2}$	$\frac{\sigma+3}{8}$	$\frac{1-\sigma}{4}$	$\frac{1-\sigma}{4}$

Typical numerical results (obtained using simplified numerical models, since these data cannot be obtained by experimental means and are out of range of available supercomputing facilities) are displayed in Fig. 4.7. Turbulent flows with an initial small wave-number slope higher than 4 are observed to relax towards the $\sigma = 4$ solutions at large scales.

All results displayed above in this section are related to the initial stage of decay, i.e. the asymptotic high-Reynolds regime, which is governed by non linear interactions. They are observed to be very accurate, since the error on the exponents of the different quantities compared with EDQNM simulations is within 1% in all cases for all quantities (Meldi et al. 2011; Meldi and Sagaut 2012, 2013a). The previous analysis can be extended to asymptotically low-Reynolds numbers, i.e. to the final stage of decay. Before doing that, it is worth reminding that neglecting convective terms the exact solution to the Lin equation reads

$$E(k,t) = E(k,0)e^{-2\nu k^2 t}, \tag{4.162}$$

which is not well suited for quick algebraic manipulation. Assuming that at very low Reynolds number wave number larger than $1/L$ have a negligible kinetic energy, one can write

$$\mathcal{K}(t) \sim \int_0^{1/L(t)} C_\sigma k^\sigma dk. \tag{4.163}$$

Assuming that dynamics is governed by viscous effects, dimensional analysis leads to $L(t) = \gamma\sqrt{\nu t}$, where γ is a dimensionless parameter[14] and therefore

$$\mathcal{K}(t) \sim \int_0^{1/(\gamma\sqrt{\nu t})} C_\sigma k^\sigma dk = \frac{C_\sigma}{\sigma+1}\left(\frac{1}{\gamma\sqrt{\nu}}\right)^{(\sigma+1)/2} t^{-(\sigma+1)/2} \tag{4.164}$$

where ν_{turb} is an eddy viscosity. An error on the constant A may yield an error on the energy balance at very small wave numbers, inducing a spurious time-evolution of $\mathfrak{I}$.

[14] One recognizes here $\sqrt{\nu t}$ which is the similitude variable that appears in the dimensional analysis of the diffusive problems.

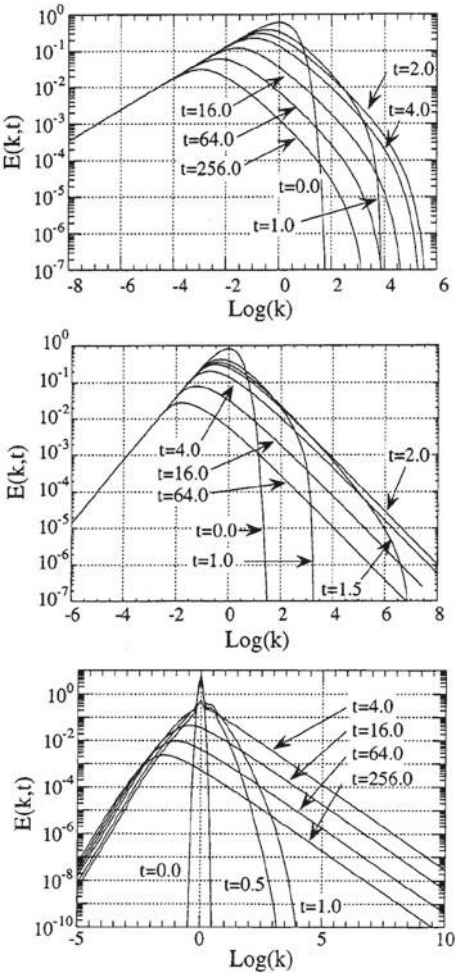

Fig. 4.7 Evolution of the kinetic energy spectrum in the initial stage decay. Top: emergence of self-similarity and validation of the PLE hypothesis for k^1 scaling at low wave number. Middle: emergence of self-similarity and validation of the PLE hypothesis for k^2 scaling at low wave number. Bottom: emergence of self-similarity with a k^4 behavior for initial Gaussian-shaped spectrum, and PLE hypothesis breakdown for the k^4 spectrum. From Clark and Zemach (1998) with permission of AIP

and

$$\mathcal{K}(t) = \mathcal{K}(0)\left(1+\frac{t}{t_0}\right)^{-(\sigma+1)/2}, \quad Re_L(t) = Re_L(0)\left(1+\frac{t}{t_0}\right)^{(1-\sigma)/4}. \quad (4.165)$$

Results are summarized in Table 4.11. They are observed to be as accurate when compared to EDQNM results as in the high-Reynolds number case. Breakdown of PLE hypothesis at very low Reynolds number has never been studied or even reported, therefore no correction is added here to power-law exponents.

Long-time evolution of the kinetic energy spectrum computed with an EDQNM closure is displayed in Fig. 4.8. It is observed that a self-similar final stage of decay

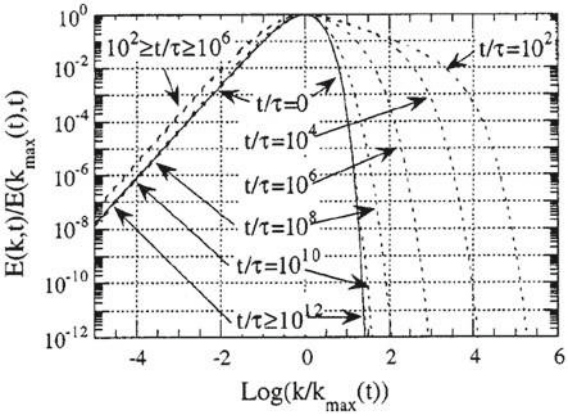

Fig. 4.8 Evolution of the kinetic energy spectrum with transition from the initial stage decay to the final stage of decay. From Clark and Zemach (1998) with permission of AIP

is reached at very long time. Here τ denotes the eddy turnover time scale associated with the peak of the spectrum at the initial time: $\tau = (k_{\max}^3(0)E(k_{\max}, 0))^{-1/2}$. It is also noticed that, in the final viscous decay stage, the PLE holds, even in the present case in which $E(k, 0) \sim k^4$ at very large scales.

It is worth noting that $\sigma = 1$ is related to a singular regime, since decay occurs at constant Re_L along with $\mathcal{K}(t) \propto t^{-1}$, for both high-Reynolds and low-Reynolds decay regimes.

An interesting problem is the time needed to reached the final stage of decay starting from a high-Reynolds number solution initially governed by a non linear initial decay stage. The time evolution of the effective time decay exponent $n(t)$ defined as

$$n^{-1}(t) = -\frac{\partial}{\partial t}\left(\frac{\mathcal{K}(t)}{\partial \mathcal{K}(t)/\partial t}\right) \tag{4.166}$$

is displayed in Fig. 4.9 for different values of the spectrum low-wave-number power-law exponent.

It is observed that in all cases a very long time is needed before the solution reach the final stage of decay, i.e. $n = const$. The turbulence quickly reaches a cascade-dissipation equilibrium for the k^1 spectrum.[15] For other spectrum shapes, the transition is too long to be observed (Clark and Zemach 1998). Considering a wind tunnel with air and a mean flow velocity equal to 20 $\mathrm{m\,s^{-1}}$, a grid-generated turbulence such that $\mathcal{K}(0) = 20\ \mathrm{m^2\,s^{-2}}$ and the initial turbulent Reynolds number is equal to $Re_L = 3000$, the wind tunnel length required to reach the final stage is of the order of 10^{16} m (about one light-year, or about one-third the distance to the nearest star!) for k^2-shaped spectrum, and 5.10^6 m (almost an Earth radius!) for k^4 spectra.

[15]This is consistent with the fact that it is the only solution which is fully consistent with the symmetry analysis at finite Reynolds number.

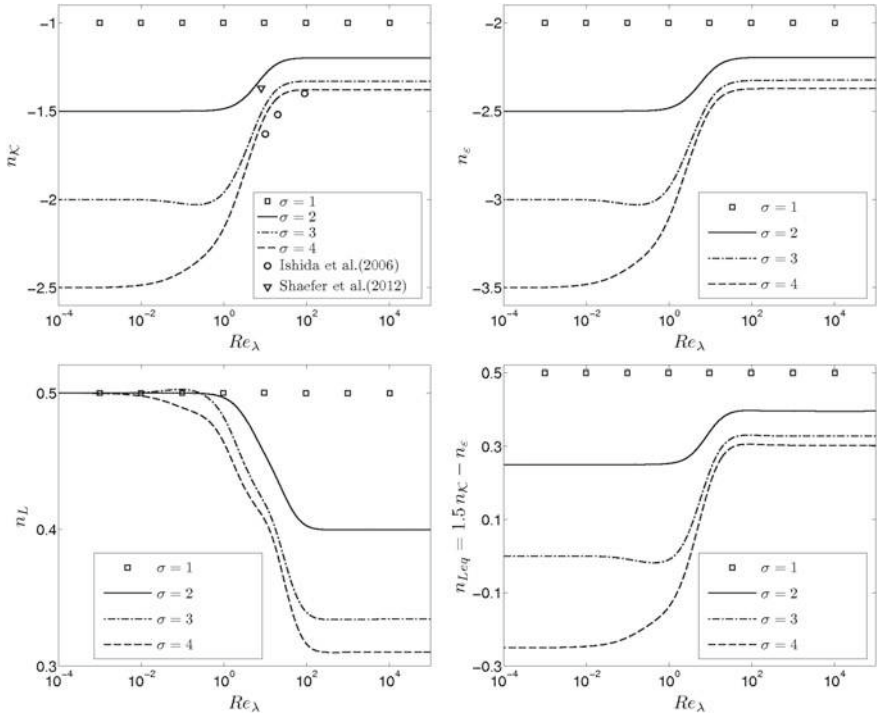

Fig. 4.9 Evolution of the free decay exponents of kinetic energy (top-left), dissipation (top-right), integral velocity scale L (bottom-left) and length scale $\mathcal{K}^{3/2}/\varepsilon$ versus Re_λ for large-scale spectrum slope $\sigma = 1, 2, 3, 4$. $\sigma = 1$ is discontinuous, since Re_λ is constant in time for that solution. From Meldi and Sagaut (2013a) with permission of Taylor & Francis

Previous analyses can be extended to account for more physical phenomena. Skbrek and Stalp introduced a small scale cutoff to account for the very fast damping at scales smaller than the Kolmogorov scale η and a low-wavenumber cutoff to account for possible saturation effects. Saturation occurs if turbulence evolves in a finite-size box. Since $L(t)$ is growing in time in all cases, it will reach the size of the box in a finite time. After that time, $L(t)$ becomes time-independent and no scale larger than L can exist. This can be modeled in a smart and simple way setting $\sigma = +\infty$ in the high-Reynolds regime formula, yielding $\mathcal{K}(t) \propto t^{-2}$ after saturation, whatever was σ at initial time. Saturation is therefore associated to a bifurcation in the flow dynamics and a change in the time exponents of all quantities. Both analytical developments and EDQNM simulations show that introducing the small scale cutoff does not change the classical results.

It is important noting that the Comte-Bellot–Corrsin theory is compatible with the symmetry-based analysis discussed in Sect. 4.4.3, i.e. its results encompass those found in previous section. Decay exponents are the same in cases that can be addressed by symmetry analysis, but this theory is also more general since it allows to include more physics (cutoff at small scales, saturation effects, arbitrary values of σ).

One can also identify invariant quantities during the decay using exponents displayed in Table 4.11. Taking $\mathcal{K}(t)$, $L(t)$ and $\eta(t)$ as independent variables, one can built two invariants $I_L(\sigma) \equiv \mathcal{K}^\alpha L$ and $I_\eta(\sigma) \equiv \mathcal{K}^\beta \eta$ where

$$\alpha = \frac{1}{\sigma - p + 1}, \quad \beta = \frac{1}{8}\frac{3(\sigma - p) + 5}{\sigma - p + 1} \tag{4.167}$$

at high Reynolds number ($Re_\lambda \geq 200$ in practice). The Saffman invariant and the Loitsyansky's invariant are recovered as $I_L(2)$ and $I_L(4)$, respectively. In the later case, one must observe that the p correction is not taken into account in the original theory, yielding slow drift of that quantity.

In the low-Reynolds number asymptotic regime ($Re_\lambda \leq 0.1 - 0.01$ in practice), one as

$$\alpha = \frac{1}{\sigma + 1}, \quad \beta = \frac{1}{4}\frac{\sigma + 3}{\sigma + 1}. \tag{4.168}$$

The differences in the expressions of α and β at low- and high-Reynolds number show that it is impossible to define exact Reynolds-independent quantities that may remain invariant over arbitrary long times, i.e. during the transition between the two regimes. The only case in which such exact invariants may be defined is $\sigma = 1$, in which $\alpha = \beta = 1/2$ in both regimes and there is only one independent invariant, which is proportional to the Reynolds number since $I_L(1) \propto I_\eta(1) \propto Re_\lambda \propto Re_L$. But it is important to note that some "finite-but-long-time" invariant quantities may be encountered as long as the Reynolds number is high enough or once it has reached the low-Re asymptotic regime. In these cases, both $I_L(\sigma)$ and $I_\eta(\sigma)$ will be almost constant and can be considered as invariant quantities. It is important to notice that, in these cases, any function depending only on these two quantities will be invariant, showing that an infinite number of invariants can be defined.

4.4.6 Georges' Extended Self-similarity Theory

George (1992), George and Wang (2000) proposed a theory for the decaying homogeneous isotropic turbulence in which self-preserving solutions of the Lin equation for $E(k)$ are found. The new feature with respect to older self-similarity theories is that both the spectrum and the nonlinear transfer terms are not assumed a priori to scale with a single length and velocity scale.

The starting point is to express the energy spectrum $E(k)$ and the spectral transfer function $T(k)$ under the following the self-preserving forms:

$$E(k,t) = E_s(t,\star)\psi(\xi,\star), \quad T(k,t) = T_s(k,\star)\varphi(\xi,\star), \tag{4.169}$$

with $\xi = k\ell$ where $\ell = \ell(t, \star)$ is a characteristic length scale to be determined. The argument $\star$ denotes a possible dependence on initial conditions. Differentiating Eq. (4.169) leads to

$$\frac{\partial E}{\partial t} = \left[\frac{dE_s}{dt}\right]\psi(\xi, \star) + \left[\frac{E_s}{\ell} \cdot \frac{d\ell}{dt}\right]\xi\psi'(\eta, \star) \ , \tag{4.170}$$

where the prime denotes the differentiation with respect to ξ. Substituting into the Lin equation and dividing by $\nu E_s/\ell^2$ to obtain a dimensionless equation, one obtains

$$\left[\frac{\ell^2}{\nu E_s} \cdot \frac{dE_s}{dt}\right]\psi + \left[\frac{\ell}{\nu} \cdot \frac{d\ell}{dt}\right]\xi\psi' = \left[\frac{T_s\ell^2}{\nu E_s}\right]\varphi - [1]\,2\xi^2\psi \ , \tag{4.171}$$

where the dependency on t, ξ and $\star$ have been suppressed for the sake of simplicity. Bracketed terms are independent dimensionless parameters. George's analysis relies on that equation. In practice, self-similar solutions are sought keeping all terms (i.e. considering all physical mechanisms) or neglecting some of them. Observing that the coefficient of the last term is time independent, self-preserving solutions exist iff all other bracketed terms are also time independent.

Keeping all terms in the dimensionless Lin equation (4.171), one get

$$\left[\frac{\ell^2}{\nu E_s} \cdot \frac{dE_s}{dt}\right] = const, \left[\frac{\ell}{\nu} \cdot \frac{d\ell}{dt}\right] = const, \left[\frac{T_s\ell^2}{\nu E_s}\right] = const. \tag{4.172}$$

The second condition straightforwardly leads to

$$\ell^2(t) = 2A\nu(t - t_0), \tag{4.173}$$

where integration factor was taken equal to $2A$ for the sake of convenience and t_0 can be eliminated by an adequate choice of time origin. Then, hereafter t_0 will assumed to be zero without loss of generality. Combining the first and the third condition one get

$$\frac{t}{E_s} \cdot \frac{dE_s}{dt} = p \ , \tag{4.174}$$

where p is a constant. By integrating one obtains the following power-law decay

$$E_s = E_s(t_0)\left(\frac{t}{t_0}\right)^p \ , \tag{4.175}$$

The third condition in Eq. (4.172) is satisfied iff

$$T_s \sim \frac{\nu E_s}{\ell^2} \sim \frac{E_s}{t} \ . \tag{4.176}$$

One has

$$\mathcal{K} = \frac{3}{2}u'^2 = \int_0^\infty E(k,t)dk = \left[\frac{E_s}{\ell}\right]\int_0^\infty \psi(\zeta,\star)d\zeta \ , \tag{4.177}$$

where the integral term is time independent, leading to

$$E_s \sim u'^2\ell \ . \tag{4.178}$$

Equations (4.173), (4.175) and (4.178) lead to the following algebraic evolution law

$$\frac{u'^2}{u_0'^2} \sim \left[\frac{t}{t_0}\right]^p \left[\frac{\ell_0}{\ell}\right] \sim \left[\frac{t}{t_0}\right]^{p-1/2} \ , \tag{4.179}$$

then

$$\mathcal{K}(t) \propto u'^2(t) \propto t^n \ , \tag{4.180}$$

with $n = p - 1/2$, where p or n must be determined using experimental data or more complex theories.

Now considering the dissipation rate ε, one obtains

$$\varepsilon = \nu\int_0^\infty k^2 E(k,t)dk = \left[\frac{\nu E_s}{\ell^3}\right] 2\int_0^\infty \zeta^2 f(\zeta)d\zeta \sim \nu\frac{u'^2}{\ell^2} \ . \tag{4.181}$$

Now recalling that the energy dissipation $\varepsilon(t)$ in isotropic turbulence reads

$$\varepsilon = 15\nu\overline{\left[\frac{\partial u'}{\partial x}\right]^2} = 15\nu\frac{u'^2}{\lambda_f^2} \ , \tag{4.182}$$

and comparing Eq. (4.181), the characteristic length ℓ is observed to scale as the Taylor microscale λ_f, i.e.:

$$\ell \sim \lambda_f \ .$$

Therefore, relation (4.173) yields the following result

$$\lambda_f^2 = 2A\nu t \ , \tag{4.183}$$

showing that $\lambda_f(t) \propto \sqrt{t}$, in agreement with the Comte-Bellot – Corrsin theory. The coefficient A can be related to the decay law exponent n using the kinetic energy equation

$$\frac{d}{dt}\left(\frac{3}{2}u'^2\right) = -\varepsilon$$

and Eq. (4.182). Thus one obtains

$$\lambda_f^2 = -\frac{10}{n}\nu t \ , \tag{4.184}$$

which is the result obtained by von Karman and Howarth (1938). As a consequence the Taylor-based Reynolds number evolves as

$$Re_\lambda(t) = \frac{u'\lambda_f}{\nu} \propto t^{\frac{n+1}{2}} \ . \tag{4.185}$$

The transfer function amplitude T_s can now be evaluated using $\lambda \sim \ell$ in a straightforward way:

$$T_s \sim \nu\frac{u'^2}{\ell} = \nu\frac{u'^3}{Re_\lambda} \propto t^{n-\frac{1}{2}} \ . \tag{4.186}$$

Among the main conclusions of George's theory, one can mention that the Lin equation admits self-preserving solutions with the following characteristics

- The characteristic length scale for the entire spectrum is the Taylor microscale λ_f which evolves as $\lambda_f \sim t^{1/2}$. As a consequence, the Reynolds number characterizing the turbulent motion is Re_λ.
- The energy follows a an algebraic decay law, i.e. $\mathcal{K}(t) \propto t^n$, where n is a parameter to be determined.
- The constant of proportionality and the exponents are fixed by the initial conditions and are flow-dependent.

All these results are coherent with those issued from the Comte-Bellot–Corrsin theory. Introducing additional assumptions makes it possible to obtain new decay regimes. In practice, this is done assuming that one or several bracketed terms in Eq. (4.171) are identically zero. As an example, the famous Kolmogorov "local equilibrium" similarity solution is recovered considering that the two first bracketed terms are zero. A very interesting extension of these results dealing with the possibility of non-algebraic, exponential decay laws for $\mathcal{K}(t)$ was obtained by George (2000).

Assuming that decay occurs with a time-independent characteristic length, i.e. taking $d\ell/dt = 0$ and $\ell = \ell_0$ and setting the second bracketed term equal to zero, integrating the first bracketed term yields

$$E_s(t) = E_{s0}\exp\left[\nu(t-t_0)/\ell_0^2\right] \ , \tag{4.187}$$

along with

$$\mathcal{K}(t) = \mathcal{K}(0)\exp\left[-10\nu(t-t_0)^2/\lambda_0^2\right] \ . \tag{4.188}$$

This result is important, since this is the unique case in which a non-algebraic decay law is predicted. George's extended self-similarity is the only one able to predict such a behavior.

4.4.7 Sum of Results

All theories for isotropic turbulence decay yield coherent results, which can be summarized as follows:

(i) Self-similar solutions might exist and are tied to the existence of invariant quantities. The existence of such solutions is further discussed in Sect. 4.5.2. Arbitrary values of the decay exponent of kinetic energy, i.e. $\mathcal{K}(t) \sim t^{-n}$ with $n \geq -1$, may be obtained by arbitrarily neglecting some terms in the equations and prescribing some invariant quantities as found by von Karman and Howarth (1938), or in an equivalent way according to Noether's theorem, enforcing a symmetry in the problem (Clark and Zemach 1998; Oberlack 2002). As an example, neglecting the nonlinear term yields an approximation for the low-Reynolds final period of decay, while neglecting the viscous term is classically done to analyze the initial high-Reynolds period of decay.

(ii) Kinetic energy exhibits an algebraic decay whose time exponent depends on the initial condition, more precisely on the shape of the spectrum at very large scales. This spectrum shape can also be related to some integral invariant quantities (each spectrum shape is related to specific invariants) or equivalently to some symmetries.

(iii) The Taylor microscale evolves independently of the Reynolds number and the initial condition with $\lambda_f(t) \propto \sqrt{t}$.

(iv) In the general case, two asymptotic decay regimes are identified, the first one at very high Re_λ and the second one at very low Re_λ.

(v) Assuming exact self-preservation and inserting associated expressions for two-point velocity correlation and energy spectrum in Eqs. (4.17) and (4.38), one finds that there is a unique solution when keeping all terms in these two equations: $\ell(t) = \lambda_f(t) \sim t^{1/2}$ and $\mathcal{K}(t) \sim t^{-1}$, as recognized since the pioneering works on the subject, e.g. Dryden (1943) and Batchelor (1948).

(vi) The case $E(k) \propto k$ at very large scales (i.e. $\sigma = 1$) is a singular case, since decay occurs at constant Re_λ along with $\mathcal{K}(t) \propto t^{-1}$. In this very unique regime all length scales (integral scale, Taylor scale, Kolmogorov scale) have the same growth exponent $1/2$.

4.5 Recent Results About Decay Regimes

4.5.1 Power-Law Exponent in the Transitional Decay Regime

Most theoretical predictions of the power-law exponents given in the preceding section originate in asymptotic high- or low-Reynolds developments. This is not explicitly mentioned in the Comte-Bellot–Corrsin analysis, but this is implicitly assumed when chosing the simplified spectrum model for $E(k)$. Therefore, a theory

that bridges between the two asymptotic regimes to describe turbulence decay at finite Reynolds number[16] would be very useful, since it would correspond to the majority of existing experiments and Direct Numerical Simulations.

A proposal was recently made by Djenidi and Antonia (2015), Djenidi et al. (2015) who developed a theoretical analysis for partially self-preserving decay of isotropic turbulence. Considering the Karman–Howarth equation for the second-order structure function (4.33) equipped with the closure $S_3 = SS_2^{3/2}$, where S is the skewness given in Eq. (4.46), and performing an analysis similar to George's one, these authors proved that the decay exponent n of $\mathcal{K}(t)$ obeys the following relation:

$$n = -1 + 2(t - t_0)\frac{1}{Re_\ell}\frac{dRe_\ell}{dt} \tag{4.189}$$

where $\ell(t)$ denotes the (unique) length scale for which self-preservation is obtained at all scales. It has been seen above that exact self-preservation is obtained in the sole case $\sigma = 1$. Therefore, to extend that result to more realistic cases in which only partial self-preservation exist, the authors propose to take the Taylor scale as a characteristic scale, i.e. $\ell = \lambda$, leading to the semi-empirical law

$$n = -1 + 2(t - t_0)\frac{1}{Re_\lambda}\frac{dRe_\lambda}{dt}. \tag{4.190}$$

This formula is consistent with the Comte-Bellot–Corrsin theory whose results are recovered for both high- and low-Reynolds number regimes.

4.5.2 Do Self-similar Solutions Exist?

The physical relevance of self-similar or self-preserving solutions is a non trivial issue, as emphasized by Batchelor (1953, p. 148): "*The assumption of similarity of shape of the statistical functions during decay in the earlier work was principally a mathematical device, used to enable definite results to be obtained ... To find such solutions has been one task; to determine the conditions under which they can and do provide a correct description of turbulence is another. In this latter task which has engaged much attention in the last five years, but even so most of the established results are negative, and our positive results still rest insecurely on vague intuitive arguments (vague for most of us - clear and precise for the inspired few !)*". While exact self-preservation is appealing from a theoretical and mathematical viewpoint, its physical relevance has been questioned very early. As a matter of fact, early experimental results did not support exact self-preservation, while they were in much better agreement with theoretical results based on incomplete self-preservation, leading Hinze to state that (Hinze 1975, p. 162): "*Hence it appears*

[16]Looking at previous results, such a theory should fill the gap that exists for $0.1 - 1 \leq Re_\lambda \leq 100 - 300$.

to be impossible to take one simple characteristic length for the entire wavenumber range to make the energy spectrum self-similar during decay. It is possible to assume only incomplete self similar preservation ... we may do so for the wavenumber of the energy-containing eddies plus the absolute equilibrium range" and Monin and Yaglom (1975) to qualify it as "*definitely incorrect*".

Despite such solutions are the cornerstones of almost all existing theories for isotropic turbulence decay, their existence has been an open issue until the very recent past. The main difficulty is that a direct measurement of the spectrum $E(k)$ at very large scales is almost impossible in both wind tunnel experiments (because of statistical convergence issue and confinement effects) and direct numerical simulations (for grid resolution and computational cost reasons). What is measured in practice is the kinetic energy decay rate, whose relation with the spectrum shape is inverted to recover an estimate for the parameter σ. But in such a procedure one makes two key assumptions: i) self-similar solutions exist whose large-scale behavior is $E(k) \propto k^{\sigma}$ and ii) only self-similar solutions lead to an algebraic decay law $\mathcal{K}(t) \propto t^{-n}$ where the decay exponent $n(\sigma)$ is given by the theories discussed in the preceding section.

It has been shown recently that the both assumptions are wrong the general case and that algebraic decay law can be recovered for non-self-similar solutions.

An exhaustive EDQNM analysis has been carried out by Meldi and Sagaut (2013a), who have shown that in the general case there exist no unique length scale $\ell(t)$ that allow for a description of the solution using a unique time-independent spectrum shape function. The only exception is the case $\sigma = 1$, which is the only one that exhibits complete self-similarity, in agreement with the fact that all length scales have the same time exponent. The same conclusions hold for the transfer function $T(k)$. Typical results are displayed in Figs. 4.10 and 4.11. It is seen that partial self-preservation is observed on $E(k)$ (based on the integral scale for large scales and Kolmogorov scales for very small scales), while no such behaviour appears on the transfer function $T(k)$.

4.5.3 Which Scales Govern the Energy Decay Rate?

Another interesting issue in isotropic turbulence decay theory is to identify which scales govern the decay rate, i.e. determine the value of the decay exponent of kinetic energy. In most existing theories (see Sect. 4.4), the decay exponent is expressed as a function of the parameter σ, which is usually interpreted as the slope of the energy spectrum at asymptotically large scales, i.e. $E(k \to 0) \propto k^{\sigma}$.

This point was recently investigated by Mons and coworkers (Mons et al. 2014), who developed a Variational Data-Assimilation method based on the Lin equation equiped with an EDQNM closure. It is reminded here that Data Assimilation is an iterative optimal control procedure that allows for the optimization of free parameters (in the initial condition definition in the present case) in order to minimize a given cost function. Data Assimilation was used to reconstruct the optimal initial condition

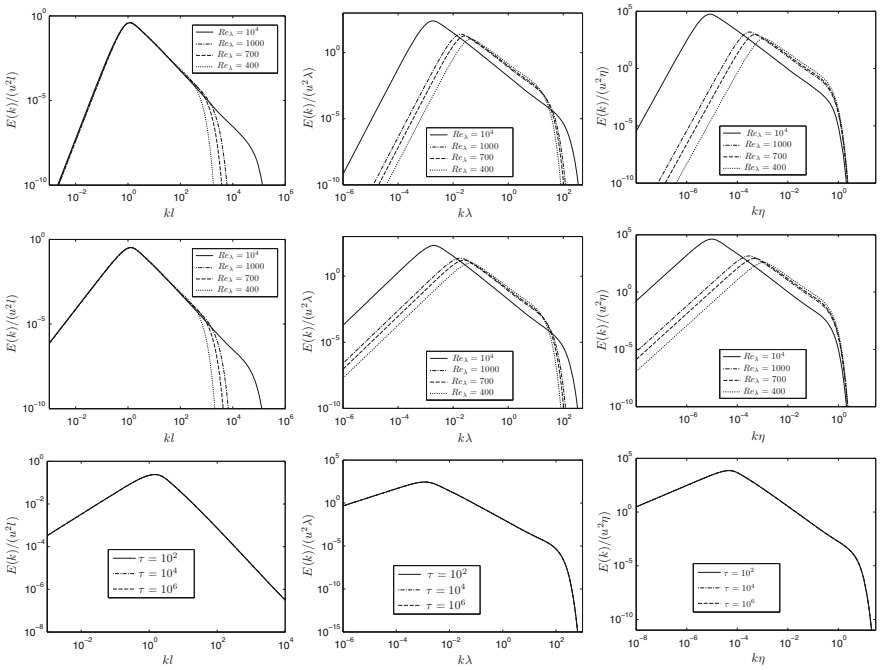

Fig. 4.10 Rescaled energy spectrum $E(k)$ at different EDQNM simulation times/Reynolds numbers. Scaling is based on (from left to right) integral scale, Taylor scale and Kolmogorov scale. Initial condition was chosen such that $E(k) \propto k^\sigma$ at large scales with $\sigma = 4$ (top), $\sigma = 2$ (medium) and $\sigma = 1$ (bottom)

that minimizes the differences with an arbitrary prescribed target decay regime. The gradient of the cost function with respect to the initial condition was obtained by Mons solving the adjoint problem associated to the Lin-EDQNM equation. Looking a finite time decay, the conclusion is that a given time t the decay rate mostly influenced by scales in the range $[L_f(t), 10\, L_f(t)]$. This scales are the one at which the sensitivity of the cost function is maximal, indicating that these scales govern the decay rate. Therefore, considering the full decay from initial time t_0 to final time t_f, the history of decay exponent is mostly sensitive to scales ranging from $L_f(t_0)$ to $10\, L_f(t_c)$.

This result may be recovered by considering the expression of the Gâteaux derivative of the power-law exponent n such that $\mathcal{K}(t) \propto t^n$ at a given spectrum $E(k)$ in the direction $F(k)$.[17]

[17]The Gâteaux derivative of a function Ψ at E in the direction F, with both E and F in the space spanned by the energy spectrum, is defined as:

$$\langle \frac{\partial \Psi}{\partial E}(E), F \rangle = \left. \frac{\partial \Psi}{\partial E} \right|_E (F) = \lim_{\epsilon \to 0} \frac{d}{d\epsilon} \Psi(E + \epsilon F).$$

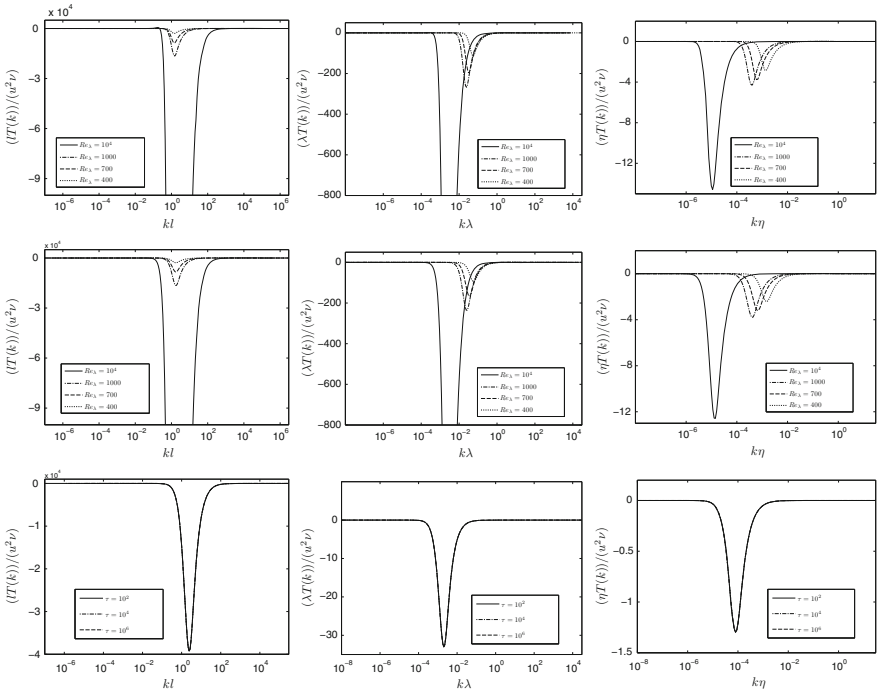

Fig. 4.11 Rescaled transfer function $T(k)$ at different EDQNM simulation times/Reynolds numbers. Scaling is based on (from left to right) integral scale, Taylor scale and Kolmogorov scale. Initial condition was chosen such that $E(k) \propto k^{\sigma}$ at large scales with $\sigma = 4$ (top), $\sigma = 2$ (medium) and $\sigma = 1$ (bottom)

Starting from the classical exact evolution equation for $\mathcal{K}(t)$ in the case of freely decaying HIT:

$$\frac{\partial \mathcal{K}}{\partial t} = -\varepsilon, \tag{4.191}$$

one can deduce the following expression for n:

$$n = -\left(\frac{\partial}{\partial t}\left(\frac{\mathcal{K}}{\varepsilon}\right)\right)^{-1} = \left(1 + \frac{\mathcal{K}}{\varepsilon^2}\frac{\partial \varepsilon}{\partial t}\right)^{-1} \tag{4.192}$$

where the exact expression of $\frac{\partial \varepsilon}{\partial t}$ originating in the Lin equation is:

$$\frac{\partial \varepsilon}{\partial t} = -\int_0^{\infty} 4\nu^2 k^4 E(k) dk + \int_0^{\infty} 2\nu k^2 T(E,k) dk. \tag{4.193}$$

The resulting expression of the Gâteaux derivative of n (in which all quantities are now considered as a functions of the energy spectrum $E(k)$) is

$$\frac{\partial n}{\partial E}\Big|_E(F) = -\frac{n_{\mathcal{K}}(E)^2}{\varepsilon(E)^2}\left[\left(\mathcal{K}(F) - 2\mathcal{K}(E)\frac{\varepsilon(F)}{\varepsilon(E)}\right)\frac{\partial \varepsilon}{\partial t}(E) + \mathcal{K}(E)\frac{\partial}{\partial E}\left(\frac{\partial \varepsilon}{\partial t}\right)\Big|_E(F)\right], \tag{4.194}$$

where the expression of the Gâteaux derivative of the operator $\frac{\partial \varepsilon}{\partial t}$ defined in (4.193) is given by:

$$\frac{\partial}{\partial E}\left(\frac{\partial \varepsilon}{\partial t}\right)\Big|_E(F) = -\int_0^\infty 4\nu^2 k^4 F(k)dk + \int_0^\infty 2\nu k^2 \frac{\partial T}{\partial E}\Big|_E(F,k)dk. \tag{4.195}$$

The expression of $\frac{\partial T}{\partial E}|_E(F,k)$ should be given by a turbulence closure. Using EDQNM, one obtains

$$\begin{aligned}\frac{\partial T}{\partial E}\Big|_E(F,k) = &\iint_{\Delta_k} \theta_{kpq} G_{kpq}\Big[F(q)\big(k^2E(p) - p^2E(k)\big) + F(p)k^2E(q) - F(k)p^2E(q)\Big]dpdq \\ &+ \iint_{\Delta_k} \mathcal{D}_{kpq}\left\{\frac{\int_0^k r^2F(r)dr}{\eta_k} + \frac{\int_0^p r^2F(r)dr}{\eta_p} + \frac{\int_0^q r^2F(r)dr}{\eta_q}\right\}dpdq\end{aligned} \tag{4.196}$$

where the factor $\mathcal{D}_{kpq}$ is defined by:

$$\mathcal{D}_{kpq} = \frac{A^2}{2}\frac{-1 + (\mu_{kpq}t + 1)e^{-\mu_{kpq}t}}{\mu_{kpq}^2} G_{kpq}E(q)\big(k^2E(p) - p^2E(k)\big). \tag{4.197}$$

Expressions for the EDQNM parameters G_{kpq}, μ_{kpq} and θ_{kpq} are given in Sect. 4.8.7. Further algebra yields the following estimate at larger scales

$$\frac{\partial n}{\partial E(k)} \sim -\frac{n^2}{\varepsilon^2}\frac{\partial \varepsilon}{\partial t}k, \tag{4.198}$$

showing that the sensitivity of the power-law exponent vanishes linearly in the limit $k \to 0$. It is important to note that this results is independent of the shape of the spectrum at large scales.

From the physical point of view, this means that the decay rate is mostly governed by the rate at which energetic large scales release their kinetic energy toward small ones via the non-linear kinetic energy cascade, the rate at which it is effectively dissipated being of secondary importance (if it is not too different from the energy cascade rate). This finding is in agreement with a common intuitive picture of the energy cascade process, but it does not fit the interpretation of asymptotic self-similarity theories. More precisely, the asymptotic interpretation of the role of the slope at very large scales such that $k \to 0$ is correct if the energy spectrum exhibits a

range such that $E(k) \propto k^{\sigma}$ in the range $k \in [0, 1/L_f]$. If it exhibits a more complex shape, then the interpretation becomes misleading.

The choice of the integral length scale to characterize the dynamics of energetic eddies is relevant. Since these eddies are expected to govern the decay rate of kinetic energy via tuning of the kinetic energy cascade rate, it is likely to be correct length scale to parameterize the decay regime. This is consistent with the observation that the Comte-Bellot–Corrsin theory, which relies on the sole integral scale, yields very accurate predictions of power-law exponents.

A consequence of that result is that manipulating the shape of the large scales that govern the kinetic energy transfer rate it is possible to prescribe the decay rate during a finite time. Numerical experiments relying on Data Assimilation have also shown that it is possible to enforce unusual decay rate, e.g. very fast decay rate compared with those predicted by classical theories, or even exponential-like decay prescribing unusual initial shape spectrum.

In practice, shape of $E(k)$ at large energetic scales originate in the physical mechanisms responsible for turbulence production. In experiments, this leads to practical difficulties to obtain a fine and explicit control of the decay rate, since there is no available theory that bridges between a grid topology and the induced energy spectrum shape.

4.5.4 *Do All Solutions Converge Toward Self-preserving State in Finite Time?*

Results and conclusions displayed in Sect. 4.5.3 show that scales much larger than the integral length scale may have no influence on the decay rate of kinetic energy during over a finite time window, since only scales up to 10 times larger the final integral length scale have a significant role. Therefore, the decay rate is insensitive to detailed features of $E(k)$ at such large scales, and non-self-preserving solutions may be defined that will lead to self-preserving-like decay regimes identical to those discussed in Sect. 4.4 over finite time. The description of such solutions is now discussed, along with the issue of the possibility of non-self-preserving solutions to be sustained over arbitrary long times.

This issue was raised by Eyink and Thomson (2000) on the grounds of theoretical arguments and later on revisited and extended to more general cases by Meldi and Sagaut (2012) who also performed and exhaustive EDQNM analysis. The idea is to consider non-self-similar initial conditions given by a three-range energy spectrum of the form:

$$E(k, t=0) = \begin{cases} Ak^{\sigma_1} & k \leq 1/\ell_1(t) \\ Bk^{\sigma_2} & 1/\ell_1(t) \leq k \leq 1/\ell_2(t) \\ K_0 \varepsilon^{2/3} k^{-5/3} & k \geq 1/\ell_2(t). \end{cases} \tag{4.199}$$

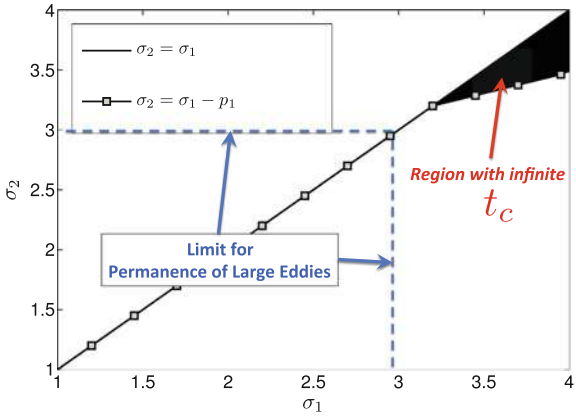

Fig. 4.12 Plot of the region with infinite t_c in the (σ_1, σ_2) plane

and to show that such solutions may exist over arbitrary long evolution times.

A Comte-Bellot–Corrsin type analysis yields

$$\ell_1(t) \propto t^{2p_2/(\sigma_2-\sigma_1+p_1)(\sigma_2-p_2+3)}, \quad \ell_2(t) \propto t^{2/(\sigma_2-p_2+3)}.$$

The solution will recover a self-preserving character if the intermediary spectrum range vanishes in a finite time, i.e. if $\ell_2(t)$ grows faster in time than $\ell_1(t)$. The associated condition is

$$\frac{2p_2}{(\sigma_2-\sigma_1+p_1)(\sigma_2-p_2+3)} < \frac{2}{(\sigma_2-p_2+3)}. \tag{4.200}$$

Therefore the solution will become self-similar at a finite critical time t_c if $(\sigma_2 - \sigma_1 + p_1) < 0$ while the three-range solutions will be sustained over arbitrary long times if $(\sigma_2 - \sigma_1 + p_1) > 0$. These solutions are displayed in the (σ_1, σ_2) plane in Fig. 4.12.

The important point is that in the case of a finite critical time t_c the solution will exhibit a bifurcation at $t = t_c$, switching from decay laws for self-similar solutions with $\sigma = \sigma_2$ to self-similar laws for $\sigma = \sigma_1$. Such a behavior is illustrated in Fig. 4.13. For infinite t_c the solution will obey self-similar decay laws associated with $\sigma = \sigma_2$ over arbitrary long time, without any bifurcation toward another state.

Therefore, measuring the decay exponent for a times smaller than t_c will never allow for identifying the existence of the first spectrum part $E(k) \propto k^{\sigma_1}$, even though this range is sustained over infinite times. That shows that observation of algebraic decay laws predicted by self-similarity/self-preservation theories is not an evidence of the existence of such solutions. Another consequence is that features of the very large turbulent scales cannot be inferred from a measure of power-law exponent of global quantities such as $\mathcal{K}(t)$, $\varepsilon(t)$ or $L(t)$.

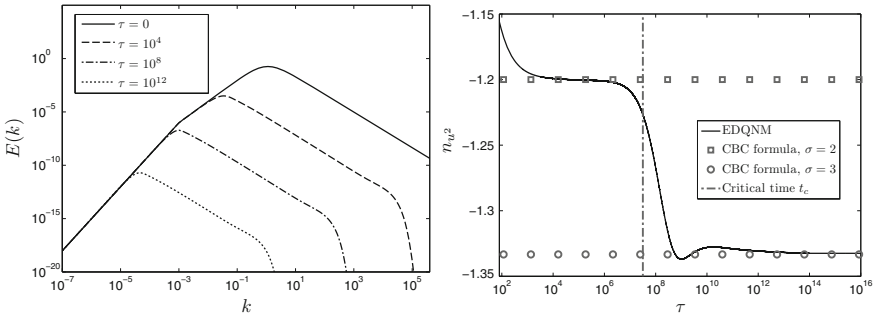

Fig. 4.13 Evolution of an initial non-self-preserving solution with $\sigma_1 = 3$ and $\sigma_2 = 2$. Left: EDQNM-computed $E(k)$ at different times. Right: time-evolution of the decay exponent of $\mathcal{K}(t)$. Evaluation of the critical time t_c is done thanks to a Comte-Bellot–Corrsin-type analysis. Courtesy of M. Meldi and P. Sagaut

This self-similarity breakdown was also observed in one-dimensional Burgers turbulence simulations by Noullez et al. (2005) (see Sect. 4.12.3 for more details about Burgers turbulence).

4.5.5 *Does a Universal Decay Regime with $\mathcal{K}(t) \propto t^{-1}$ Exist?*

The existence of universal solutions describing freely decaying isotropic turbulence is strictly tied to the loss of memory of the initial energy spectrum shape. The possible loss of memory of initial conditions is a highly debated issue, because of its relevance in turbulence statistical description. Very recently, Krogstad and Davidson (2012) stated that "*this ability of the turbulence to largely forget its initial conditions is consistent with numerical studies*", while George stated the same year that "*while there might have been reasons to doubt the role of initial conditions 20 years ago, or even to question the experiments or a new theory, the careful studies of the past two decades have made it clear that theory and experiment are in agreement: initial (and/or upstream) conditions do matter*" George (2012). The later statement is strongly supported by results stemming from self-similarity theories discussed above.

The status of a universal decay regime with $\mathcal{K}(t) \sim t^{-1}$ has been discussed during decades up to a very recent past. It is the sole decay regime associated with exact self-similar/self-preserving solutions keeping all terms in Eqs. 4.17 and 4.38. The interest in that regime as a universal attractor was renewed by Speziale and Bernard (1992), who carried out a fixed point analysis of the evolution equations for kinetic energy and dissipation. The analysis is based on the exact equations for $\mathcal{K}(t)$ and $\varepsilon(t)$ which are recalled here:

$$\frac{d\mathcal{K}}{dt} = -2\nu \int_0^{+\infty} k^2 E(k,t) dk = -\varepsilon(t), \tag{4.201}$$

$$\frac{d\varepsilon}{dt} = -\frac{7}{3\sqrt{15}} S(t) \sqrt{Re_L(t)} \frac{\varepsilon^2(t)}{\mathcal{K}(t)} - \frac{7}{15} G(t) \frac{\varepsilon^2(t)}{\mathcal{K}(t)}. \tag{4.202}$$

Assuming that both the palinstrophy G and the skewness S are time independent, i.e. $G(t) = G_\infty$ and $S(t) = S_\infty$, which amount to assume that exact self-preservation based on the Taylor scale holds, they conclude: "*By a fixed point analysis and numerical integration of the exact one-point equations, it is demonstrated that the* $\mathcal{K} \sim t^{-1}$ *power-law decay is the asymptotically consistent high-Reynolds number solution ... Arguments are provided which indicate that a* t^{-1} *power law decay is the asymptotic decay toward which a complete self-preserving isotropic turbulence is driven at high Reynolds number* " Speziale and Bernard (1992). This means that the $\mathcal{K}(t) \sim t^{-1}$ regime is an attractor, that should be reached starting from any self-similar initial condition. It is worth noting that this asymptotic state is associated with a non-vanishing turbulent Reynolds number: $Re_L \to Re_{L\infty} \neq 0$. This approach was cast in its final form by Ristorcelli and coworkers in a series of papers (Ristorcelli 2003; Ristorcelli and Livescu 2004; Ristorcelli 2006). In the most recent article (Ristorcelli 2006), which displays the final solutions for both kinetic energy decay but also for turbulent mixing, it is stated that: "*Is is emphasized that the constant Reynolds number, asymptotic decay* $\mathcal{K} \sim t^{-1}$, *is a rigorous mathematical consequence of the above Taylor Self-Similarity (TSS) and Kolmogorov Self-Similarity (KSS) scalings.* **We make no claim** *that the* $\mathcal{K} \sim t^{-1}$ *decay is a universal attractor: it is an open question for which there are a number of different results. The TSS and KSS consequences that* $Re_L \to Re_{L\infty}$ *and that* $\mathcal{K} \sim t^{-1}$ *are treated as useful pedagogical approximations*" and that: "*Such* $\mathcal{K} \sim t^{-1}$ *has not been seen experimentally. The speculation has been that the approach to the* t^{-1} *is too slow to be seen experimentally. However the DNS, for example, do all seem to exhibit this behavior when special care has been taken to adjust for virtual origin effects. Using DNS to investigate fixed-point behavior requires long time computations and is a nontrivial problem; the two point correlation begins to approach box size and the energetic modes are at the lowest wavenumber and the largest scales are represented by very few points .... Whether this occurs in practice is another issue and is dependent on the accuracy of the experimental measurements of these quantities.*" The existence of such a regime was also recently revisited in Guo et al. (2013), who proposed an attractive fixed-point solution of a HIT non-linear cascade model, and by Davidson (2011), who discussed possible singularities associated to such a solution which may appear as "*pathological in a number of respects*".

A solution to that question is found looking at results of self-similar decay theories presented in the preceding section and EDQNM results Meldi and Sagaut (2013a). As a matter of fact, it is true that the sole full self-similar solution is associated with $\mathcal{K} \sim t^{-1}$ and that it also corresponds to a decay at constant Reynolds number. But it is associated to a single initial condition, i.e. $E(k, t = 0) \propto k$ at energetic scales and the decay regime is observed from the very beginning of time evolution. Therefore,

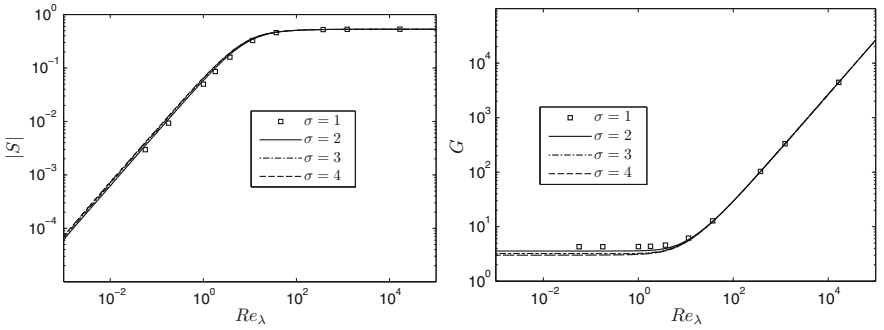

Fig. 4.14 Evolution of the Skewness parameter S (left) and the palinstrophy parameter G versus the Taylor Reynolds number in EDQNM simulations for different initial conditions. It must be kept in mind that $\sigma = 1$ corresponds to decay at constant Reynolds number and therefore to discrete plot with one simulation per value of Re_λ

the wrong part of the initial statement is to hypothesize that it is a universal attractor for long time evolution, but not to say that such a regime may exist.

The flaw in the fixed-point analysis is that authors assume that $S(t) - G(t) = const$, $S(t) = S(0)$ and $G(t) = G(0)$. It can be shown that the skewness and the palinstrophy are tied by the following relation:

$$G = \frac{15}{7}\left(\frac{n-1}{n}\right) - \frac{SRe_\lambda}{2}, \tag{4.203}$$

where n is the decay exponent of kinetic energy, i.e. $\mathcal{K}(t) \propto t^{-n}$. This relation shows that two asymptotic regimes can be expected. At very high Reynolds number one should observed $G/S \propto Re_\lambda$ while G should be nearly constant at vanishing Reynolds number. At medium Re_λ all parameters n, S and Re_λ depend on both time and initial condition. The Skewness S reaches an asymptotic value $S = -0.53$ at very high Reynolds numbers ($Re_\lambda > 5000$ in EDQNM results), while it scales like Re_λ at low Reynolds number. The relation $G = SRe_\lambda/2$ is exact for the full self-similar solution $\sigma = 1$ only. These behaviours are illustrated in Fig. 4.14.

4.5.6 Non-equilibrium State of Isotropic Turbulence: Observations and Theories

4.5.6.1 On Instantaneous Energy Transfers

Most of results presented above dealing with the kinetic energy spectum and the energy transfers (e.g. $E(k)$ and $T(k)$ profile) are related to ensemble-averaged data, and therefore should be interpreted as time-averaged results (providing that the

ensemble-average can be seen as a time-average thanks to the ergodicity theorem) in the forced HIT case.

Direct numerical simulations have provided informations dealing with the main features of the non-averaged, instantaneous energy transfers Kida and Ohkitani (1992a, b) in forced isotropic turbulence. It is observed that both $E(k,t)$ and $T(k,t)$ fluctuate around their mean values, and that the energy transfer function takes both positive and negative values at the same wave number, depending on time. As a consequence, the kinetic energy cascade process is to be understood as an ensemble-averaged concept, which can be difficult to identify in instantaneous fields.

Kida and coworkers observed that the standard deviation of the energy transfer function, $\sqrt{\overline{T(k,t)^2}}$ scales like k^{-1}. By tracking 'blobs' of kinetic energy in the (k,t) plane, they found that the time for energy to be transferred from wave number k_0 to wave number $k = \alpha k_0$ is equal to

$$T_{k_0 \to k} = \left(\frac{\alpha^{2/3}}{\alpha^{2/3} - 1} \right) \left((\bar{\varepsilon} k_0^2)^{-1/3} - (\bar{\varepsilon} k^2)^{-1/3} \right), \tag{4.204}$$

where $\bar{\varepsilon}$ is related to the ensemble-averaged value of the dissipation. The value $\alpha \simeq 1.4$ leads to the best fit of the numerical data, indicating that the net energy transfer is mostly local.

It is worth noting that expression (4.204) has been obtained using the Kolmogorov-type expression for the characteristic time τ_k for the energy to be transferred across the wave number k:

$$\tau_k = \left(\bar{\varepsilon} k^2 \right)^{-1/3}. \tag{4.205}$$

4.5.6.2 Nonlinear Cascade Time Scale, Equilibrium and Dissipation Asymptotics

The possible existence of a universal value of the normalized dissipation rate C_ε in high Reynolds number turbulent flows has been addressed by several authors, and is sometimes referred to as the *zeroth law of turbulence*

This non-dimensional coefficient is defined as

$$C_\varepsilon = \frac{\varepsilon L}{u'^3}, \tag{4.206}$$

where L and $u' = \sqrt{\frac{2}{3}\mathcal{K}}$ are the integral lengthscale (see Sect. 3.4.1) and a turbulent velocity scale, respectively. It appears in commonly used scaling laws related to Kolmogorov's theory, e.g.

$$Re_\lambda = \sqrt{\frac{15}{C_\varepsilon} Re_L}. \tag{4.207}$$

Both experimental data and numerical simulations exhibit a significant scatter in the values of C_ε. The sensitivity on the nature of the flow (freely decaying turbulence or forced turbulence) and on the Reynolds number is observed to be large. A rationale for these discrepancies, based on both EDQNM simulations and an analytical analysis based on a simplified model spectrum, has been proposed in Bos et al. (2007).

The first important conclusion is that the asymptotic value of C_ε explicitly depends on the existence of a turbulence production mechanism at large scales. The key point is that one must distinguish between several characteristic quantities to get an accurate description of kinetic energy dynamics in isotropic turbulence:

- The *production rate*, i.e. the rate at which the turbulent kinetic energy $\mathcal{K}$ is injected at scales of order L. This production rate is characterized by $u'^3(t)/L(t)$. The rate at which kinetic energy leaves the large scales is denoted $\varepsilon_f(t)$, with

$$\varepsilon_f(t) = C_\varepsilon^f \frac{u'^3(t)}{L(t)}, \tag{4.208}$$

  where C_ε^f is the proportionality constant.
- The *cascade time*, T_c, which measures the time it takes for an amount of energy initially injected at scale L to reach the dissipative Kolmogorov scale η. Considering a simplified Kolmogorov inertial range, one obtains $T_c = T(1-\beta^{-2/3})$ where $T = L/u'$ is the integral time scale and $\beta = L/\eta$.
- The *dissipation rate*, $\varepsilon(t)$, which characterizes the transformation of kinetic energy into heat at very small scales.

In forced turbulence with constant injection rate, a statistically stationary state can be reached, in which the production rate is equal to both the cascade transfer rate and the dissipation rate, i.e. $\varepsilon_f(t) = \varepsilon(t)$. The associated value non-dimensional dissipation parameter is denoted $C_\varepsilon = C_\varepsilon^{\text{forced}}$.

In freely decaying turbulence, both u' and L vary in time, yielding time-dependent production and cascade rate. A packet of kinetic energy injected at time t will be dissipated once it as reached the dissipative scales, i.e. at time $t + T_c$. Therefore, the equilibrium equality between $\varepsilon_f(t)$ and $\varepsilon(t)$ found in the forced turbulence case no longer holds, and one must write $\varepsilon_f(t) = \varepsilon(t + T_c) \neq \varepsilon(t)$, or equivalently

$$\varepsilon(t + T_c) = C_\varepsilon^{\text{forced}} \frac{u'^3(t)}{L(t)}. \tag{4.209}$$

Introducing the time decay exponent n such that $\mathcal{K}(t) \propto t^{-n}$ and $\varepsilon(t) \propto nt^{-n-1}$, one has $L(t) \propto t^{1-n/2}$ and $T \propto t$, yielding

$$\varepsilon(t+T_c) = C_\varepsilon^{\text{forced}} \frac{u'^3(t+T_c)}{L(t+T_c)} \left(\frac{t}{t+T_c}\right)^{-n-1} = C_\varepsilon^{\text{decay}} \frac{u'^3(t+T_c)}{L(t+T_c)} \tag{4.210}$$

and therefore

$$\frac{C_\varepsilon^{\text{decay}}}{C_\varepsilon^{\text{forced}}} = \left(1+\frac{T_c}{t}\right)^{n+1} = \left(1+A_c(1-\beta^{-2/3})\right)^{n+1}, \tag{4.211}$$

showing that the normalized dissipation coefficient cannot cannot be the same in forced and freely decaying turbulence. Another important fact is that the decay exponent n is known to be flow-dependent, since it is a function of the kinetic energy spectrum shape at very large scales. For large values of β, i.e. for large values of Re_L, a very good agreement with EDQNM results is obtained taking $A_c = 0.2$.

An expression for $C_\varepsilon^{\text{forced}}$ can be found considering a simplified model spectrum. Using the model

$$E(k) = \begin{cases} Ak^\sigma & kL \le 1 \\ K_0\varepsilon^{2/3}k^{-5/3} & kL \ge, k\eta \le 1 \\ 0 & k\eta > 1 \end{cases}, \tag{4.212}$$

where A is an arbitrary positive parameter, one obtains

$$C_\varepsilon^{\text{forced}} = \frac{\pi\left((3\sigma+5)/5\sigma - \frac{3}{5}\beta^{-5/3}\right)}{2K_0^{3/2}\left((3\sigma+5)/(3\sigma+3) - \beta^{-2/3}\right)^{5/2}}, \tag{4.213}$$

along with

$$Re_L = \frac{\pi K_0^{3/2}\left((3\sigma+5)/\sigma - 3\beta^{-5/3}\right)\left(3\beta^{4/3} - (3\sigma+5)/(\sigma+3)\right)}{20\sqrt{(3\sigma+5)/(3\sigma+3) - \beta^{-2/3}}}. \tag{4.214}$$

Relations (4.213) and (4.214) lead to an implicit expression of $C_\varepsilon^{\text{forced}}$ as a function of Re_L, whose asymptotic value is

$$\lim_{Re_L \longrightarrow +\infty} C_\varepsilon^{\text{forced}} = \frac{\pi(3\sigma+3)^{5/2}}{10K_0^{3/2}\sigma(3\sigma+5)^{3/2}}. \tag{4.215}$$

This asymptotic expression is observed to fit EDQNM results for $Re_L \ge 10^3$. As a general conclusion, let us emphasize that no universal value for C_ε can exist.

In a different context, without using a cascade time-scale nor a production rate, Mazellier and Vassilicos (2008) reach similar conclusions, expressed by the very title of their article: "The turbulence dissipation constant is not universal because

of its universal dependence on large-scale flow topology". The gist of their conclusions can be summarized as follows. A self-similar pattern is one where the small number of large scales is directly reflected in the large number of small scales. Zero-crossings of turbulent velocity correlations form such a pattern and as a result, the averaged distance between consecutive zero-crossings is strongly influenced by a nondimensional parameter C_s' which is some sort of number of large-scale eddies within an integral scale. The "constant" C_ε is then related to the preceding parameter by $C_\varepsilon = f(\log Re_\lambda) C_s'^3$, with the dimensionless function tending to 0.26 in the limit of $\log Re_\lambda \gg 1$. In addition to the variability in terms of moderate Re_λ, the topological structure of large eddies govern the parameter C_s'. Evaluation of this parameter is finally obtained from different physical experiments (regular grid-turbulence, fractal grid-one, "chunk" turbulence at the S_1 wind tunnel in Modane, jet).

4.5.6.3 Energy Spectrum in Non-equilibrium Isotropic Turbulence

As discussed above, the free decay régime corresponds to a non-equilibrium state of turbulence, in which the classical energy spectrum expressions must be modified to account for unsteadiness. Starting from the Lin equation with a production source term $P(k)$

$$\frac{\partial E(k,t)}{\partial t} = -2\nu k^2 E(k) + T(k) + P(k), \tag{4.216}$$

and considering the following small-parameter expansion around a high Reynolds steady-state solution $E_0(k)$ with a $k^{-5/3}$ inertial range associated to a steady injection of energy spectrum $P_0(k)$:

$$E(k,t) = E_0(k) + \delta E_1(k,t) + \delta^2 E_2(k,t) + \cdots \tag{4.217}$$

where the small parameter δ is related to a low-amplitude slow variation of the production term, a multiscale analysis (Woodruff and Rubinstein 2006; Horiuti and Tamaki 2013; Horiuti et al. 2016; Bos and Rubinstein 2017) based on the Heisenberg and Kovasznay differential models for the non-linear transfer term $T(k)$ (see Sect. 4.7.1) leads to

$$\delta \sim \left(\frac{\dot{L}}{L}\right)\left(\frac{\mathcal{K}}{\varepsilon}\right) \ll 1, \tag{4.218}$$

where $\dot{L}$ denotes the time derivative of the integral scale L. The associated expansion of the energy spectrum is

$$E(k,t) = E_0(k) + \frac{2}{3}K_0^2 \frac{\dot{\varepsilon}}{\varepsilon^{2/3}} k^{-7/3} + \frac{1}{3}K_0^3 \left(\frac{\ddot{\varepsilon}}{\varepsilon} - \frac{2}{3}\frac{(\dot{\varepsilon})^2}{\varepsilon^2}\right) k^{-9/3} + \cdots \tag{4.219}$$

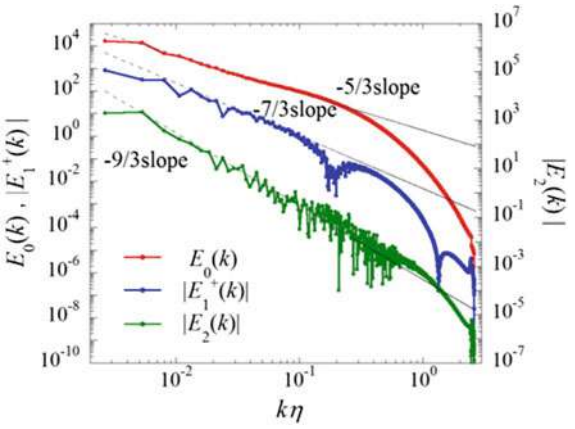

Fig. 4.15 Steady state solution spectrum, $E_0(k) \propto k^{-5/3}$ (red) and first- and second-order perturbations, $E_1(k) \propto k^{-7/3}$ (blue) and $E_2(k) \propto k^{-9/3}$ (green), respectively. From Horiuti et al. (2016) with permission of IOP

While the exact expressions of the coefficients may be sensitive to the closure used for $T(k)$ in the analytical study, the important point is that the classical, steady-state spectrum with a classical $k^{-5/3}$ inertial range is corrected at first order by $E_1(k) \propto k^{-7/3}$ and by $E_2(k) \propto k^{-9/3}$ at second order. This has been recently assessed by numerical simulations in which these perturbations are very accurately observed, see Fig. 4.15.

The associated expansion of the transfer term in the inertial range is

$$\begin{aligned} T(k) &= 0 + \delta T_1(k) + \delta^2 T_2(k) + \cdots \\ &= \frac{2}{3} K_0 \frac{\dot{\varepsilon}}{\varepsilon^{1/3}} k^{-5/3} + \frac{2}{3} K_0^2 \left(\frac{\ddot{\varepsilon}}{\varepsilon^{2/3}} - \frac{1}{3} \frac{(\dot{\varepsilon})^2}{\varepsilon^{5/3}} \right) k^{-7/3} + \cdots \end{aligned} \tag{4.220}$$

showing that the net transfer is not zero within the inertial range for the perturbative components $E_1(k)$ and $E_2(k)$.

These expressions can be used to derive non-equilibrium corrections to various integral quantities (Bos and Rubinstein 2017). Writing $E(k) = E_0(k) + E'(k)$, one has by direct integration

$$\mathcal{K} = \mathcal{K}_0 + \mathcal{K}', \ \varepsilon = \varepsilon_0 + \varepsilon', L = L_0 + L'. \tag{4.221}$$

Restricting the expansions to the first-order perturbation, one obtains

$$\frac{\varepsilon'}{\varepsilon_0} \simeq \frac{1}{Re_\lambda} \frac{\mathcal{K}'}{\mathcal{K}_0}, \quad \frac{\mathcal{K}'}{\mathcal{K}_0} \simeq \frac{(\dot{\varepsilon}/\varepsilon)}{\varepsilon^{1/3} L_0^{2/3}} \tag{4.222}$$

and, after some algebra,

$$\frac{Re_\lambda}{Re_{\lambda_0}} \sim \left(1 + \frac{\mathcal{K}'}{\mathcal{K}_0}\right) \tag{4.223}$$

along with

$$\frac{C_\varepsilon}{C_{\varepsilon_0}} \sim \frac{\left(1 + \frac{10}{7}\frac{\mathcal{K}'}{\mathcal{K}_0}\right)}{\left(1 + \frac{\mathcal{K}'}{\mathcal{K}_0}\right)} \sim \left(1 + \frac{\mathcal{K}'}{\mathcal{K}_0}\right)^{-15/14} \tag{4.224}$$

for the dissipation parameter C_ε. Combining these expressions and using $Re_{\lambda_0} \sim \sqrt{Re_{L_0}}$, one finds

$$C_\varepsilon(t) \propto \left(\frac{\sqrt{Re_{L_0}}}{Re_\lambda(t)}\right)^{15/14}, \tag{4.225}$$

which agrees with the analysis carried out in Sect. 4.5.6.2 on the conclusion that C_ε is a time-dependent parameter in decaying isotropic turbulence.

Time decay of an initially perturbed isotropic turbulence can be analyzed using previous expressions. On should distinguished between two stages: a first transient phase during which the previous expressions holds (with a time-independent base flow $E_0(k)$), and a second one corresponding to decaying base flow with a stabilized non-equilibrium. The second phase is assumed to correspond to an algebraically decaying turbulence such that $\mathcal{K}(t) \propto t^{-n}$, the decay exponent being described by classical theories discussed in Sect. 4.4. Taking into account the fact that $\dot{\varepsilon}/\varepsilon = (-n+1)/t$ and $\varepsilon/\mathcal{K} = n/t$, and evaluating these quantities as

$$\mathcal{K}(t) = \mathcal{K}_0(t) + \mathcal{K}'(t) = \sim \int_{1/L}^{1/\eta} (E_0(k,t) + E'(k,t))dk \tag{4.226}$$

$$\varepsilon(t) = \varepsilon_0(t) + \varepsilon'(t) \sim 2\nu \int_{1/L}^{1/\eta} k^2 (E_0(k,t) + E'(k,t))dk \tag{4.227}$$

one obtains, after some algebra:

$$\frac{\mathcal{K}'}{\mathcal{K}_0} = -\frac{2}{9}\frac{n+1}{n}, \quad \frac{C_\varepsilon}{C_{\varepsilon_0}} \approx \left(\frac{9n}{7n-2}\right)^{15/14}, \tag{4.228}$$

and

$$\frac{Re_\lambda}{Re_{\lambda_0}} \approx \frac{9n}{7n-2}, \quad \frac{\lambda/L}{\lambda_0/L_0} = \left(\frac{Re_\lambda}{Re_{\lambda_0}}\right)^{1/14}. \tag{4.229}$$

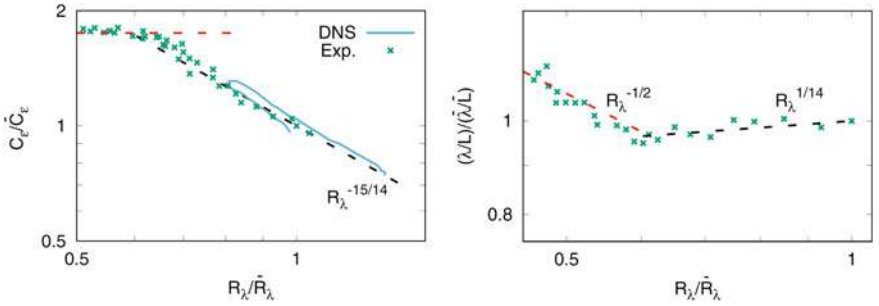

Fig. 4.16 Comparison of Bos-Rubinstein theoretical prediction (dashed lines) with experimental data (symbols) and DNS data (solid line) for non-equilibrium decaying turbulence. From Bos and Rubinstein (2017) with permission of APS

It is seen that during this second stage the ratio of the two components of kinetic energy and the one of the dissipation parameter are time-independent, showing that solution does not relax toward an true equilibrium state. As a matter of fact, self-similar decay is not related to equilibrium but to a state in which the non-equilibrium part is a constant fraction of kinetic energy.

Such a behavior has been reported first in fractal grid experiments since the mid-2000's by C. Vassilicos and his group at Imperial College, and more recently by other groups (see Vassilicos 2015 for a survey). These authors proposed the following relation by data-fitting

$$\varepsilon(t) \sim \frac{Re_0^{p/2}}{Re_\lambda^q(t)} \frac{u'^3(t)}{L(t)}, \quad p \sim q \sim 1, \tag{4.230}$$

where Re_0 is a global time-independent Reynolds number characterizing initial or inlet conditions, which leads to the following scaling law for the dissipation parameter proposed by Vassilicos and colleagues:

$$C_\varepsilon(t) = \frac{\varepsilon(t)L(t)}{u'^3(t)} \propto \frac{\sqrt{Re_0}}{Re_\lambda(t)}, \tag{4.231}$$

which is very close to the relation (4.225). The theory proposed in Bos and Rubinstein (2017) exhibits a very good agreement with experimental and DNS data for both transient stages, as shown in Fig. 4.16 and is presently the best available explanation. A remarkable results is that (4.231) has been reported to agree with experimental data associated to more complex flows, such as wakes of fractal bluff bodies.

4.5.7 *Anomalous Decay Regimes: Very Fast Algebraic Decay and Exponential Decay*

Some recent experimental results dealing with grid turbulence exhibit decay rate that are much higher than those expected looking at classical theories discussed in Sect. 4.4. Most of them have been obtained considering grids with fractal topology by Vassilicos and colleagues from the Imperial College group (Vassilicos 2015). Similar results have been obtained via DNS (Goto and Vassilicos 2015) and EDQNM simulations (Meldi et al. 2014), showing that these anomalous decay regimes are not governed by the breakdown of isotropy or homogeneity.

Despite these phenomena are still not fully understood, some hypotheses about the underlying physical phenomena can be proposed. Two main possibilities are identified:

- *Scenario I: anomalous fast decay régimes are free-decay phenomena due to uncommon initial energy spectrum* $E(k)$. Fractal grids induce turbulence production on a range of scales much wider than classical grids with only one rod diameter and grid cell size. Typical fractal grid topologies correspond to 2 to 4 iterations of fractal duplication of the original pattern, leading to a ratio between the largest and the smallest grid scales about 10. Therefore one can expect that such grids will lead to a massive injection of energy within about 1 decade of turbulent scales. If the production rate is much larger than the kinetic energy turbulence cascade rate, the energy will pile-up at large-scales, leading to the existence of kinetic energy spectra with non-classical shape at large energetic scales at the end of the formation region. According to that hypothesis, the non-classical very fast decay régimes would be a free-decay transient effect associated to the relaxation of a non-classical energy spectrum toward a more classical one, due to the initial non-equilibrium of large scales. This explanation is consistent with the analysis of the intensity of triadic energy transfers presented in Sect. 4.8.4: a bump in the energy spectrum $E(k)$ at energetic scales will induce an increase in the kinetic energy cascade rate and therefore the dissipation rate until this bump will have been smoothed and a classical decay rate recovered. The possibility to obtain kinetic energy spectrum with a non-classical peak shape characterized by a bump at energetic scales using a fractal isotropic forcing term was assessed using EDQNM (Meldi et al. 2014), see Fig. 4.17. The existence of a very fast decay régimes with decay rate such that $\mathcal{K}(t) \propto t^{-3}$ during a finite time before relaxing toward a classical decay régime starting from such an initial solution was reported (Meldi et al. 2014; Goto and Vassilicos 2015). DNS results dealing with non-classical decay also exhibit such a non-classical initial spectrum (Goto and Vassilicos 2015) as displayed in Fig. 4.17. A very nice piece of evidence supporting the idea of a pure initial solution effect are the initial spectra obtained using Data Assimilation by Mons and Sagaut (unpublished). Prescribing very fast decay rates during a fixed finite time window, initial solutions $E(k, 0)$ with a bump at energetic scales were obtained (see Fig. 4.17).

- *Scenario II: anomalous fast decay régimes are forced-decay phenomena due to long-lasting production phenomena originating in fractal grid wake shear*. The key idea is that fractal object wakes generate long-lasting multiscale shear effects downstream the grid with associated turbulence production effects. Therefore, the turbulence experiences decay in the presence of an evolving forcing term. Here, the possibility to generate non-classical decay rate is trivially recovered, since the Lin equation if modified as follows

$$\frac{\partial E(k)}{\partial t} + 2\nu k^2 E(k) = T(k) + f(E(k), k, t), \tag{4.232}$$

  where the forcing term $f(E(k), k, t)$ depends a priori on the spectrum $E(k)$, the scale k, time but also on geometrical features of the grid. Models for this forcing term have been proposed for both DNS and EDQNM simulations (Mazzi and Vassilicos 2004; Meldi et al. 2014). Playing with $f(E(k), k, t)$ one can manipulate the time-evolution of $\mathcal{K}(t)$ in an arbitrary way, from growth to rapid decay. Time evolution of decay exponent of kinetic energy obtained using EDQNM with different time-vanishing fractal forcing term that mimic turbulent kinetic production in the wake is illustrated in Fig. 4.18.

These two scenarii can also be combined, since underlying mechanisms (unusual spectrum shape, long-lasting forcing term) are not contradictory.

The question of the exact form of the anomalous fast decay régime is still an open question. The possibility of an exponential free decay reminiscent of the one predicted by George and Wang (2000) (see Sect. 4.4.6) in the free decay with a constant characteristic length scale has been advocated by some authors, but anomalous decay is usually observed on transient time that are too short to distinguish between exponential and algebraic laws.

4.6 Reynolds Stress Tensor and Analysis of Related Equations

For decaying Homogeneous Isotropic Turbulence (HIT), the Reynolds stress tensor reduces to a spherical form, as the dissipation tensor, so that

$$\overline{u_i' u_j'} = 2\mathcal{K}\frac{\delta_{ij}}{3}, \quad \varepsilon_{ij} = 2\varepsilon\frac{\delta_{ij}}{3},$$

while Eqs. (2.73) and (2.74) simplify as

$$\frac{d\mathcal{K}}{dt} = -\varepsilon \tag{4.233}$$

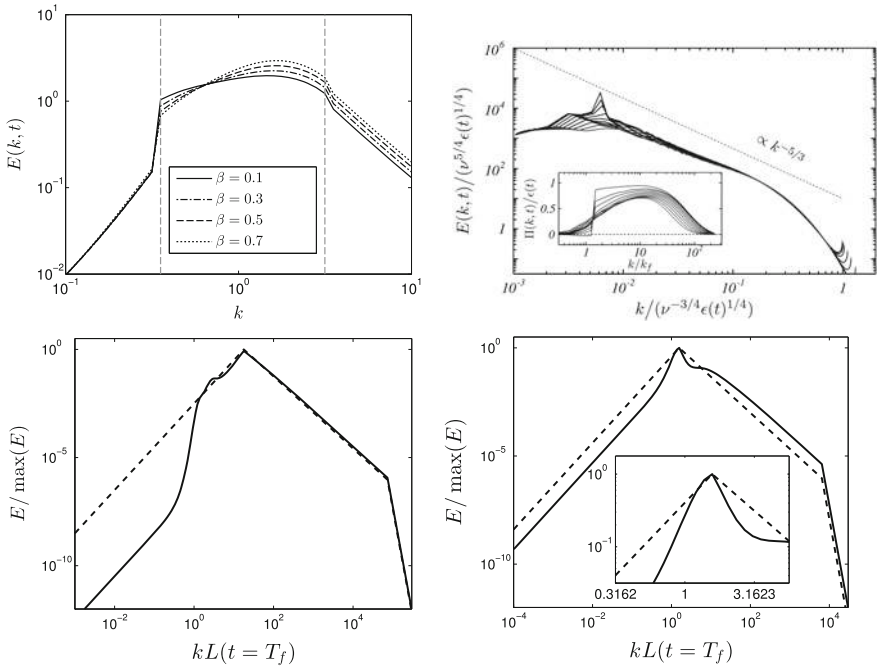

Fig. 4.17 Initial kinetic energy spectrum $E(k,t)$ leading to anomalous decay régime. Top-left: solution obtained via EDQNM with fractal forcing (enlarged view of the peak region), from Meldi et al. (2014) with permission of CUP; Top-right: solution obtained via DNS with initial anisotropic vortical forcing, from Goto and Vassilicos (2015) with permission of AIP; Bottom-left: solution (solid line) obtained via Data Assimilation with EDQNM enforcing $\mathcal{K}(t) \propto t^{-1.5}$, dashed line is the initial guess of the Data Assimilation procedure; Bottom-right: solution (solid line) obtained via Data Assimilation with EDQNM enforcing $\mathcal{K}(t) \propto t^{-3}$, dashed line is the initial guess of the Data Assimilation procedure

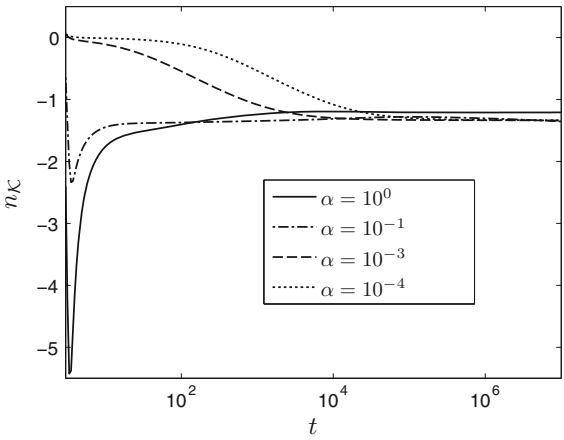

Fig. 4.18 Time evolution of the kinetic energy decay exponent n such that $\mathcal{K}(t) \propto t^n$ in EDQNM with vanishing fractal forcing. α is related to the decay rate of the forcing term, with $\alpha = 10^{-4}$ and $\alpha = 1$ corresponding to very slowly and very quickly decaying forcing, respectively. From Meldi et al. (2014) with permission of CUP

and

$$\frac{d\varepsilon}{dt} = -C_{\epsilon 2}\frac{\varepsilon^2}{\mathcal{K}}. \tag{4.234}$$

In the absence of production due to the uniformity of the mean flow, the first equation is exact. But is important to notice that the second equation for the dissipation rate is a rough approximation since the exact equation (4.44) yields the following expression for the parameter C_{ε_2}:

$$C_{\varepsilon_2} = \frac{7}{15}\left(\frac{1}{2}S(t)Re_\lambda(t) + G(t)\right). \tag{4.235}$$

Therefore, assuming that C_{ε_2} is a constant parameter is wrong in the general case looking at conclusions given in Sect. 4.5.5, in which it was shown that this quantity depends on the Reynolds number and that it exhibits two different asymptotic values, at asymptotically large and small Reynolds numbers.

Assuming that C_{ε_2} is constant and using the logarithmic derivatives, the system (4.233)–(4.234) can be simply solved. It admits power law solutions of the form

$$\mathcal{K}(t) = \mathcal{K}(0)\left(1 + \frac{t}{t_0}\right)^{-n}, \quad \varepsilon(t) = n\frac{\mathcal{K}(0)}{t_0}\left(1 + \frac{t}{t_0}\right)^{-n-1}, \tag{4.236}$$

with

$$t_0 = n\frac{\mathcal{K}(0)}{\varepsilon(0)}, \quad C_{\epsilon 2} = -\frac{d(\log\varepsilon)}{d(\log\mathcal{K})},$$

yielding

$$C_{\epsilon 2} = \frac{n+1}{n}. \tag{4.237}$$

Accordingly, a direct link of $C_{\epsilon 2}$ to the exponent of the decay law is given. Following the results summarized in Table 4.11, one obtains $\sigma = 2, n = 6/5$ and $C_{\epsilon 2} = 11/6$ for a Saffman spectrum and $\sigma = 4, n = 1.38$ and $C_{\epsilon 2} = 1.72$ for a Batchelor spectrum. The analysis of the initial decay stage given in the previous section emphasized that the decay exponent is directly tied to the power-law behavior of the kinetic energy spectrum at low-wavenumber. Therefore, $C_{\epsilon 2}$ can also be recast as a function of the spectrum shape at large scales that govern the decay rate. Using the Comte-Bellot–Corrsin theory, one obtains

$$C_{\epsilon 2} = 1 + \frac{\sigma+3}{2(\sigma+1)}, \quad \text{with} \quad E(k) \sim k^\sigma, \quad (kL \ll 1). \tag{4.238}$$

A direct consequence is that there is no really universal value for $C_{\epsilon 2}$, and that a $\mathcal{K} - \varepsilon$ model with fixed parameters is not able to capture the subtle changes in the decay rate of $\mathcal{K}$ which may occur.

The special form of Eq. (4.236) implies that kinetic energy and dissipation rate (or similarly kinetic energy and Taylor microscale) are known simultaneously in the initial stage with time t_0. In an actual experiment, t_0 corresponds to an "initial section" at a distance (e.g. $x/M \sim 40$ in CBC) pretty far downstream the grid. This is in contrast with the conventional law $\mathcal{K} \sim (t - \tau^*)^{-n'}$, sought using a *virtual origin* τ^*, that is empirically adjusted for obtaining the longest power law. In an actual grid-turbulence experiment, the virtual origin corresponds to a cross-section upstream the grid; accordingly, the resulting perceived exponent $-n'$ takes into account all stages of decay from the close vicinity of the grid. In a preliminar study, Claude Rey (private communication) began to compare n, obtained by simultaneously measuring $\mathcal{K}$ and ε according to Eq. (4.236), and n' adjusted in connection with a virtual origin. Decays of both kinetic energy and scalar variance (heated grid) were considered. A very large scattering of the perceived exponent n' was found, in contrast with a very weak variability of n, around 1.25. These results suggest that the very large scattering of decay exponents, shown in Fig. 4.4, could be drastically reduced, and is probably dependent on the adjustment of the virtual origin in experiments.

All these developments hold for large values of the Reynolds number only, i.e. in the case in which the parameter C_{ε_2} takes its asymptotic high-reynolds value. At lower Reynolds number finite Reynolds number effects occur and more complex expressions for $C_{\epsilon 2}$ must be found. Since the high Reynolds number asymptotic analysis can no longer be used, only empirical expressions are available. Most of them rely on an exponential interpolation between asymptotic values. As an example, let us mention the model proposed by Coleman and Mansour (1991):

$$C_{\epsilon 2}(Re_L) = 1. - 0.222 \exp(-0.1677\sqrt{Re_L}), \tag{4.239}$$

where the turbulent Reynolds number Re_L is defined as $Re_L = \mathcal{K}^2/\nu\varepsilon$. A limitation of this model, which is shared by almost all other models, is that it does not take into account other parameters, like the initial condition. Considering a fully linear evolution, the turbulent kinetic energy spectrum evolves as

$$E(k,t) = E(k,0)e^{-2\nu k^2 t}. \tag{4.240}$$

For small wave numbers, one obtains

$$E(k,t) \sim k^{\sigma} e^{-2\nu k^2 t}, \tag{4.241}$$

which leads to $\mathcal{K}(t) \propto t^{-(\sigma+1)/2}$. Available experimental data, in which non-linear effects are small but not identically zero, lead to $\sigma \simeq 3$. In the strictly linear limit, one expects to recover either the Batchelor solution ($\sigma = 2$, $C_{\epsilon 2} = 1.67$) or the Saffman solution ($\sigma = 4$, $C_{\epsilon 2} = 1.4$).

The analysis can be further extended to account for the influence of the skewness of velocity gradients. This point will not be discussed here (see Piquet 2001 for a detailed discussion of the modeling issues related to the free decay case).

It is clear that the main trends of high-Reynolds dynamics of decaying HIT can be predicted by the simplest $\mathcal{K}-\varepsilon$ model, if the initial conditions are taken into account, including the initial spectrum shape. But the discussion presented above also shows that, even for a very simple turbulent flow such as HIT, several physical mechanisms escape the formalism of the $\mathcal{K}-\varepsilon$ model defined by Eqs. (4.233)–(4.234). The very reason why is that the turbulent decay depends on both the large and the small scales, and that most turbulence models written in the physical space are not able to account for spectral features of turbulence.

It is also worth emphasizing that *prediction is not explanation* and that our knowledge of HIT remains elusive. Internal intermittency which is reflected in the scaling of high order moments is an open problem; formation of micro-structures like worms is shown in physical and numerical experiments but not really explained from the analysis of Navier–Stokes equations.

4.7 Differential Models for Energy Transfer

This section is devoted to local closures for the Lin and Karman–Howarth equations based on eddy-diffusivity or eddy-viscosity paradigm. These closures are sometimes referred to has *classical closures*. It is important noting that closures have been developed independently in Fourier and physical space, so that closures for the Karman–Howarth equation are not explicitly tied to those proposed for the Lin equation.

4.7.1 Closures for the Lin Equation in Fourier Space

The Lin equation (4.38) for the time evolution of the three-dimensional energy spectrum $E(k)$ is among the cornerstones of the theory of turbulence since solving it yields the capability to describe accurately time evolution of kinetic energy of turbulence $\mathcal{K}(t)$. A first class of models developed to close that equation gathers all models based on a differential closure. Assuming that $T(k)$ is regular enough so that there exists a function $F(k)$ such that

$$F(k)=\int_0^k T(p)dp \quad \Longleftrightarrow \quad T(k)=-\frac{\partial F(k)}{\partial k}, \tag{4.242}$$

where it is assumed that $F(0)=0$, an hypothesis which is assessed by existing data and advanced spectral closures (see Sect. 4.8), one obtains

$$\frac{\partial E(k,t)}{\partial t}+2\nu k^2 E(k,t)=\frac{\partial F(k)}{\partial k}. \tag{4.243}$$

The global conservation property $\int_0^k T(p)dp = 0$ yields $F(0) = F(k \to +\infty) = 0$. The function $F(k)$ can be interpreted as the total energy flux exchanged by scales larger than $1/k$ with scales smaller than $1/k$. This is observed looking at the kinetic energy budget of scales larger than $1/k$, i.e. by integrating (4.243) between 0 and k:

$$\frac{\partial}{\partial t}\int_0^k E(p,t)dp + 2\nu\int_0^k p^2 E(p,t)dp = F(k). \tag{4.244}$$

In the case viscous dissipation can be neglected, the equation simplifies as

$$\frac{\partial}{\partial t}\int_0^k E(p,t)dp = F(k), \tag{4.245}$$

showing that large scale kinetic energy decay is driven by non linear cascade mechanisms.

This differential form of Lin equation can be closed expressing the flux function $F(k)$ as an explicit function of the kinetic energy spectrum $E(k)$. A large number of closures have been proposed since the 1940s, some of which are displayed in Table 4.12. It is worth noting that many of them have been designed to allow for an analytical expression for $E(k)$ by exact integration of (4.243) rather than representing the real energy flux. The closure problem consists then in determining $F(k)$. The first constraint used to build a model is $F(0) = 0$. Another common constraint consists in using the relation $F(k) = \varepsilon$, and then $T(k) = 0$, in the statically isotropic stationary turbulence at very large Reynolds number in the inertial range where $E(k) = K_0\varepsilon^{2/3}k^{-5/3}$. A last relation is that the model should ideally be able to recover the steady-state equilibrium solution of the truncated Euler equations, i.e. $E(k) \propto k^2$, yielding $F(k) = 0$ in this case.

The main models are given in the Table 4.12. We can distinguish several model families

- The Oboukhov model (1941) and its variant given by Ellison (1961). Starting from a **spectral equilibrium hypothesis**, one assumes that the kinetic energy production at large scale, the dissipation at small scales and the energy transfer between large and small scales are the same. We can then write (in the inertial range of the kinetic energy spectrum)

$$R_{ij}\frac{\partial \bar{u}_i}{\partial x_j} = -\varepsilon = F(k). \tag{4.246}$$

Dimensional analysis yields

$$R_{ij} = \int_k^{+\infty} E(p)dp, \quad \frac{\partial \bar{u}_i}{\partial x_j} = \left(\int_0^k p^2 E(p)dp\right)^{1/2}, \tag{4.247}$$

leading to the original Oboukhov's model.

Table 4.12 Model for the spectral density of energy flux $T(k) = -\dfrac{\partial F(k)}{\partial k}$. The asterisk denotes the models which lead to an analytical form for the spectral density of kinetic energy $E(k)$ by integrating the Lin equation

Model	$F(k)$
Oboukhov (1941)*	$\alpha_O \left(\int_k^{+\infty} E(p)dp\right)\left(\int_0^k p^2 E(p)dp\right)^{1/2}$
Ellison (1961)*	$\alpha_E k E(k)\left(\int_0^k p^2 E(p)dp\right)^{1/2}$
Heisenberg (1948)*	$\alpha_H \left(\int_k^{+\infty} \sqrt{p^{-3}E(p)}dp\right)\left(\int_0^k p^2 E(p)dp\right), \quad \alpha_H = \dfrac{16}{9}K_0^{-3/2}$
Stewart-Towensend (1951)	$\alpha_{ST}\left(\int_k^{+\infty} p^{-(1+1/2c)}E^{1/2c}(p)dp\right)^c \left(\int_0^k p^2 E(p)dp\right)$
Ogura-Miyakoda (1953)	$\alpha_{OM}\dfrac{1}{k}\left(\int_k^{+\infty} E(p)dp\right)^{1/2}\left(\int_0^k p^2 E(p)dp\right)$
von Karman (1948)	$\alpha_{VK}\left(\int_k^{+\infty} p^m E^n(p)dp\right)\left(\int_0^k p^{1/2-m}E^{3/2-n}(p)dp\right)$
Goldstein (1951)	$\alpha_G\left(\int_k^{+\infty} p^m E^n(p)dp\right)^\lambda \left(\int_0^k p^{m'}E^{n'}(p)dp\right)^{\lambda'}$ $(m+1)\lambda + (m'+1)\lambda' = 5/2, \quad n\lambda + n'\lambda' = 3/2$
Malfliet (1974)	$\alpha_M\left(\int_k^{+\infty}\sqrt{pE(p)}dp\right)\left(\int_k^{+\infty}E(p)dp\right), \quad \alpha_M = \dfrac{4}{9}K_0^{-3/2}$
Rubinstein-Clark (2004)	$\alpha_M\left(-\int_0^k q^4 dq\int_k^{+\infty}\dfrac{E^2(p)}{p^2}\Theta(p,q)dp\right.$ $\left.+\int_0^k q^2 E(q)dq\int_k^{+\infty}\Theta(p,q)E(p)dp\right)$ $\Theta^{-1}(p,q) = \theta^{-1}(p) + \theta^{-1}(q), \theta(k) = \left(\int_0^k p^2E(p)dp\right)^{-1/2}$
Kovasznay (1948)*	$\alpha_K k^{5/2}E^{3/2}(k), \quad \alpha_K = K_0^{-3/2}$
Pao (1965)*	$\alpha_P \varepsilon^{1/2}k^{5/3}E(k)$
Tenekes (1968), Yaglom (1969)	$\alpha_{TY}\varepsilon^{1-2n/3}k^{5n/3}E^n(k), \quad n>0$
Yaglom (1969) Panchev (1969) Panchev (1969), Lin (1972)	$\alpha_Y\varepsilon^{1-2n/3}k^{5n/3}E^n(k)\varphi(k\eta), \quad n>0$ $\varphi(0)=1, \lim_{x\to+\infty}\varphi(x)\propto x^\alpha, \alpha\le 4/3$ $n=1, \quad \varphi(x) = x^{4/3}$ $n=1, \quad \varphi(x) = (1+cx^{2/3})^{-1}$
Leith (1967)	$-\alpha_L k^{13/2}\dfrac{\partial}{\partial k}\left(k^{-3}E^{3/2}(k)\right), \quad \alpha_L = \dfrac{2}{11}K_0^{-3/2}$
Clark (1999)	$-\alpha_L\left(\int_0^k p^2E(p)dp\right)^{1/2}k^4\dfrac{\partial}{\partial k}\left(\dfrac{E(k)}{k^2}\right)$
Connaughton-Nazarenko (2003)	$-\dfrac{1}{8}k^{11/2}\sqrt{E(k)}\dfrac{\partial}{\partial k}\left(\dfrac{E(k)}{k^2}\right)$

- **Spectral eddy viscosity models** This approach, initially suggested by von Weizsäcker in 1948, has been concretized by Heisenberg the same year[18] under the spectral eddy viscosity model. The underlying physical paradigm is that the energy transfer from large toward small scales (energy cascade) can be viewed as an energetic drainage of the large scales by a dissipative mechanism. This approach can be seen as an analogy with kinetic gas theory, in which the movement at the molecular scale is the mechanism which generates the viscosity at larger macroscopic scales. If the eddy viscosity hypothesis seems to be efficient to represent the interactions between very different scales, it seems however to be very contestable for describing the interactions between scales of the same order. the problem, encountered in this theory, is that a turbulent flows contains a continuity of scales which are dynamically active, and that the hypothesis of a scale separation is not valid.
  Numerous versions and generalizations have been proposed. The generic form of these models is
  $$F(k) = 2\nu_t(k) \int_0^k p^2 E(p) dp, \tag{4.248}$$
  where $\nu_t(k)$ is the spectral turbulent viscosity. The original proposal of Heisenberg is
  $$\nu_t(k) = \frac{8}{9} K_0^{-3/2} \int_k^{+\infty} \sqrt{p^{-3} E(p)} dp. \tag{4.249}$$
  This relation has been extended to the general case by Stewart and Townsend in 1951, under the following relation
  $$\nu_t(k) = \left(\int_k^{+\infty} p^{-(1+1/2c)} E^{1/2c}(p) dp \right)^c, \tag{4.250}$$
  where $c > 0$ is an arbitrary constant. Moreover $c = 1/2$ lead to a simple expression, used in particular by Howells en 1960 and Monin in 1962. This last relation can itself be generalized in a new more general expression as
  $$\nu_t(k) = \sum_i a_i \left(\int_k^{+\infty} p^{-(1+1/2c_i)} E^{1/2c_i}(p) dp \right)^{c_i}, \tag{4.251}$$
  with $a_i > 0$ and $c_i > 0, \forall i$.
- **Spectral diffusion models**, following the approach initiated by Leith in 1961. The transfer is represented by a diffusive term in the wave-number space. One advantage of this model, compared to those presented above is its local character in the Fourier space which greatly improves its use. The generic form of a diffusion model is
  $$F(k) = -D \frac{\partial Q}{\partial k} \tag{4.252}$$

[18] Weizsäcker and Heisenberg did not know the works of Oboukhov at this time.

where D is a diffusion coefficient and Q a potential. The dimensional analysis leads to $DQ = [L][T]^{-3}$. Several improved models have been proposed, e.g. by Clark (1999) and Connaughton and Nazarenko (2003).

- **Local models based on the dimensional analysis**, e.g. models proposed by Kovasznay and Pao. Such models may allow for the derivation of exact solutions of the equation for $E(k)$, mostly considering a steady state solution without forcing (which is unphysical in the general case but may be considered as relevant at small scales in some cases).
- **Non-local models** based on the Von Karman hypothesis, use the following generic expression

$$F(k) = \int_k^{+\infty} \int_0^k P(k', k'')dk'dk'' \tag{4.253}$$

where $P(k', k'')dk'dk''$ is the kinetic energy amount produced by the wavenumbers $[k', k' + dk']$ toward the wave numbers $[k'', k'' + dk'']$ by time unit. The detailed conservation property of the energy leads to $P(k', k'') = -P(k'', k')$, which is a constraint that the spectral fluxes models have to satisfy. The expression given by Von Karman in 1948 reads

$$P(k', k'') = \alpha_{VK}(k')^m(k'')^{1/2-m}\left(E(k')\right)^n\left(E(k'')\right)^{3/2-n} \tag{4.254}$$

for $k' > k''$. The spectral viscosity given by Heisenberg is obtained by taking $m = -3/2$ and $n = 1/2$. Moreover, the values $(m = 0, n = 1)$ give formula close to the expression given by Oboukhov and the values $(m = 0, n = 3/2)$ close to the expression given by Kovasznay. Finally, the expression was generalized by Goldstein (1951), whose model admits the models by Von Karman, Oboukhov, Heisenberg and Stewart-Townsend as particular cases. It is worth noting that both Leith and Kovazsnay models can be interpreted as limits of the Heisenberg model in the case of distant interactions.

The ability of these models to lead to relevant unsteady solutions of Lin equation has not been systematically investigated. Some models have been designed to find steady analytical solutions of Lin equation, e.g. Pao's model, but not to close the dynamical equations.

A recent analysis was carried out by Clark et al. (2009), in which several models were tested. The following criteria were used to assess the models:

(i) *Capability of predicting the existence of a dissipation range with exponentially decaying* $E(k)$. Heisenberg and Kovasznay models fail in predicting such a range, while Leith model and Ellison model are able to recover such a behavior (but with different exponentially decaying functions).

(ii) *Capability of capturing the bottleneck phenomenon*. This phenomenon is characterized by a kink in the compensated energy spectrum between the inertial and dissipation ranges. It originates in the fact that due to very high viscous damping, scales in the dissipative range cannot drain the energy of scales located at the very end of the inertial range at the same rate at which these scales are fed

by the nonlinear energy cascade, resulting in a weak pile-up of energy. None of Leith, Heisenberg, Kovazsnay models is able to capture that phenomena, since they are to crude to account for the modification of the cascade rate by viscous damping. But more sophisticated models, such as the Rubinstein-Clark model (which is a generalized Heisenberg model) perform well here.

(iii) *Capability to predict the existence of a thermalized tail in the inviscid case*. In the ideal case of an inviscid fluid the equilibrium solution is $E(k) \propto k^2 \ \forall k$. Before reaching that state, transient solution exhibit an inertial range with $E(k) \propto k^{-5/3}$ followed by the thermalized tail $E(k) \propto k^2$. Thermalized small scales play the role of molecular motion, and give rise to an efficient viscosity that acts on larger scales. Therefore, a small pseudo-dissipative range should be observed between the end of the inertial range and the thermalized range. Both the Kovasznay and the Heisenberg fail in predicting that behavior since they don't yield vanishing fluxes at equipartition, i.e. when $T(k) = 0$ when $E(k) \propto k^2$, while the Leith and the Rubinstein-Clark models succeed. The later model also recover the existence of the pseudo-dissipative range.

(iv) *Capability to prevent unphysical overshoot of kinetic energy in transient solutions of Lin equation*. Considering the transient evolution of a turbulence submitted to a steady forcing toward a steady state solution, it appears that some models may lead to unphysical overshoot in $\mathcal{K}(t)$. It is observed that no form of Leith or Kovasznay models lead to such a spurious behavior, while Heisenberg and Rubinstein-Clark models suffer from that weakness.

4.7.2 Closures for the Karman–Howarth Equation in Physical Space

While closing the Lin equation has been paid a lot of attention during the last 70 years, only very few works have addressed the issue of closing its counterpart in physical space, i.e. the Karman–Howarth equation. Existing closures are local closures, mostly differential closures, which will be discussed hereafter.

A first series of works addressed the evolution equation for the longitudinal correlation function $f(r)$, whose evolution equation (4.17) can be rewritten as

$$\frac{\partial}{\partial t} f = \frac{K}{u'^2} + 2\nu \left(\frac{\partial^2}{\partial r^2} + \frac{4}{r} \right) f - 10\nu \frac{\partial^2 f}{\partial r^2}(0) f, \tag{4.255}$$

where

$$K(r) = u'^3 \left(\frac{\partial}{\partial r} + \frac{4}{r} \right) k(r).$$

Eddy-viscosity closures are defined for this equation setting

$$k(r) = 2\frac{D_t(r)}{u'}\frac{\partial f}{\partial r} \tag{4.256}$$

where the turbulent diffusion parameter $D_t(r)$ is expressed as

$$D_t(r) = \begin{cases} \alpha_1 u' r & \text{Millionshtchikov (1969)} \\ \alpha_2 u' r\sqrt{1-f(r)} & \text{Oberlack \& Peters (1993)} \end{cases} \tag{4.257}$$

where α_1 and α_2 are arbitrary parameters. Numerical experiments show that Millionshtchikov's model yields a poor representation of the kinetic energy cascade process and unphysical results, while the second model leads to good representation of the inertial range with an ad hoc tuning of α_2. De Divitiis (2016) recently proposed the sole closure that does not rely on an eddy-viscosity paradigm. Starting from a Lyapunov analysis of the statistics of the velocity increment, he proposed

$$K(r) = u'^3\sqrt{\frac{1-f(r)}{2}}\frac{\partial f}{\partial r}, \tag{4.258}$$

which does not involve second-order derivatives of f, and therefore is not a diffusive model. This model is observed to yields accurate results for isotropic turbulence decay.

Another group of closures have been derived for the second-order structure function based Karman–Howarth equation (4.33), which can be recast in the following compact form:

$$3\frac{\partial S_2}{\partial t} = \frac{1}{r^4}\frac{\partial}{\partial r}\left[r^4\left(6\nu\frac{\partial}{\partial r}S_2 - S_3\right)\right] - 4\varepsilon. \tag{4.259}$$

Some proposed models are based on the eddy-viscosity assumption

$$S_3 = -6\nu_t\frac{\partial}{\partial r}S_2. \tag{4.260}$$

The most general model was proposed by Thiesset et al. (2013), which reads

$$\frac{\nu_t}{\nu} = \frac{Sr^{*2}}{12\sqrt{15}(1+\gamma r^{*2})^{1/3}}, \quad r^* = r/\eta, \tag{4.261}$$

where S is the velocity skewness. This model is observed to yield very good results for decaying isotropic turbulence, including finite Reynolds number effects, setting $S = 0.424$ and $\gamma = 1/625$, corresponding to a crossover the inertial and the dissipative range at $r^* = 25$, see Fig. 4.19. This model is an extension of the one proposed by Domoradzki and Mellor in 1984 based on inertial range scaling:

$$\frac{\nu_t}{\nu} = \frac{1}{5C}r^{*4/3}, \quad C = 2, \tag{4.262}$$

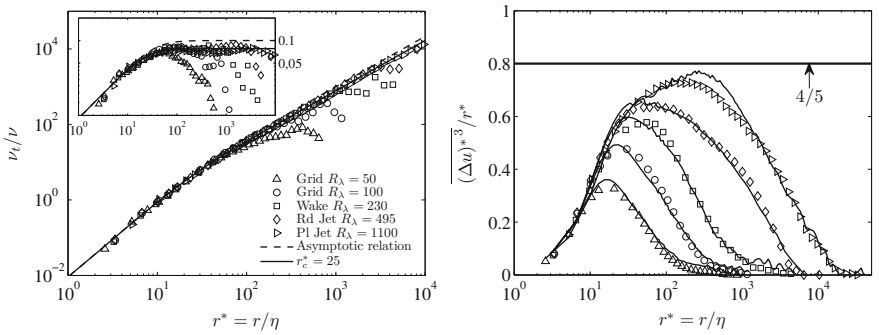

Fig. 4.19 Eddy-viscosity closure for the Karman–Howarth equation. Left: a priori ratio of eddy-viscosity to molecular viscosity in several turbulent flows deduced from experimental data. Right: predicted (lines) versus experimental (symbols) evolution of the normalized third-order structure function, showing Finite Reynolds Number effects on Kolmogorov's 4/5th law. Courtesy of L. Danaila. From Thiesset et al. (2013) with permission of APS

which is observed to poorly capture viscous effects, and the one based on dissipative range scaling

$$\frac{\nu_t}{\nu} = \frac{S}{12\sqrt{15}} r^{*2} \tag{4.263}$$

which is not well suited for inertial range physics.

Simpler models have been proposed to obtain analytical solutions of the steady problem within the inertial and dissipative range. Assuming a constant velocity skewness, one can recover Obukhov's closure (1949)

$$S_3(r) = S S_2(r) \sqrt{|S_2(r)|} \tag{4.264}$$

which is consistent with inertial range scaling. More accurate analytical solutions in the range $r/\eta = O(1)$ with a capture of the bottleneck phenomenon are obtained using a non-constant expression of the skewness, $S = S_3(r)(S_2(r))^{-3/2}$, but details of the dissipative range are still lost.

4.7.3 Why Do Classical Closures Work? A Systematic Approach

The local differential closures, at least some of them, are observed to yield a satisfactory qualitative recovery of a significant number of exact solution features. While most of them have been derived in a pretty heuristic way, it is possible to get a better understanding of the reason why they work, yielding also a better view at physical mechanisms which are at play in turbulence dynamics (Clark et al. 2009).

It can be shown (see Sect. 4.8) that the non-linear term in the Lin equation is equal to

$$T(k,t) = \int d\boldsymbol{p}dvq\delta(\boldsymbol{k}-\boldsymbol{p}-\boldsymbol{q})S(\boldsymbol{k},\boldsymbol{p},\boldsymbol{q},t), \tag{4.265}$$

where $S(\boldsymbol{k},\boldsymbol{p},\boldsymbol{q},t)$ is related to triple correlations by

$$S(\boldsymbol{k},\boldsymbol{p},\boldsymbol{q},t) = \frac{\iota}{2}P_{imn}(\boldsymbol{k})\overline{u_m(\boldsymbol{q})u_n(\boldsymbol{q})u_i(-\boldsymbol{k})}. \tag{4.266}$$

Therefore, the flux term $F(k)$ defined in Eq. (4.242) is excatly defined as

$$F(k,t) = \int_{k'<k}\int_{p,q>k'} d\boldsymbol{p}d\boldsymbol{q}\delta(\boldsymbol{k}-\boldsymbol{p}-\boldsymbol{q})S(\boldsymbol{k},\boldsymbol{p},\boldsymbol{q},t). \tag{4.267}$$

Introducing a time scale $\Theta(k,p,q)$ for the triadic interaction, the integrand can be developed as

$$\begin{aligned} S(\boldsymbol{k},\boldsymbol{p},\boldsymbol{q},t) = {} & P_{imn}(\boldsymbol{k})P_{irs}(\boldsymbol{k})P_{mr}(\boldsymbol{p})P_{ns}(\boldsymbol{q})E(p)E(q)\Theta(k,p,q) \\ & -P_{rmn}(\boldsymbol{k})P_{mrs}(\boldsymbol{p})P_{ns}(\boldsymbol{q})E(k)E(q)\Theta(k,p,q) \\ & -P_{rmn}(\boldsymbol{k})P_{mrs}(\boldsymbol{q})P_{ns}(\boldsymbol{p})E(k)E(p)\Theta(k,p,q) \end{aligned} \tag{4.268}$$

The next step consists in considering *distant interactions only*. Selecting $\boldsymbol{q}$ as the large scale, one now assumes that $0 \sim q \ll p \sim k$ along with $E(q) \gg E(p), E(k)$. Neglecting small terms and introducing the Taylor series expansion

$$E(\|\boldsymbol{k}-\boldsymbol{q}\|) \simeq E(k) - q_i\frac{\partial E}{\partial k}\frac{k_i}{k} + \frac{1}{2}q_iq_j\frac{\partial}{\partial k_j}\left(\frac{\partial E}{\partial k}\frac{k_i}{k}\right) + \cdots \tag{4.269}$$

one find, after integrating over sphere $\|k'\| = const$ and evaluating angular integrals,

$$\begin{aligned} F(k,t) = {} & -c\left(\int_0^k q^2E(q)\theta(k,q,q)dq\right)k^4\frac{\partial}{\partial k}\left[\frac{E(k)}{k}\right] \\ & -c'\left(\int_0^k q^2E(q)dq\right)\left(\int_k^{+\infty}\theta(k,p,p)p^3\frac{\partial}{\partial p}\left[\frac{E(p)}{p}\right]dp\right), \end{aligned} \tag{4.270}$$

where values of parameters c and c' are given by the integration procedure. It is seen that the first term appears as a local diffusion term that is a general extension of Leith's model, showing that local differential closures can be interpreted as restrictions of more general non-local closures to distant interactions that lead to local energy transfer. Therefore, these closures can recover some non-trivial features of turbulence dynamics governed by such interactions.

Several closures can be recovered by chosing a model for the time scales $\theta(k, p, p)$ and $\theta(k, q, q)$, which are observed to depend on two wave number only, and are therefore "pair" relaxation times. As an example, taking $\theta(k, p) = (k^3 E(k))^{-1/2}$ one obtains classical closures of Kovasznay, Heisenberg and Leith.

4.8 Advanced Analysis of Energy Transfers in Fourier Space

4.8.1 The Background Triadic Interaction

The equation introduced in the previous chapter

$$\frac{\partial \hat{u}_i}{\partial t}(\boldsymbol{k}, t) = \imath \underbrace{P_{imn}(\boldsymbol{k}) \sum_{\Delta} \hat{u}_m^*(\boldsymbol{p}, t) \hat{u}_n^*(\boldsymbol{q}, t)}_{s_i} \tag{4.271}$$

with

$$P_{imn} = \frac{1}{2} \left(k_m P_{in}(\boldsymbol{k}) + k_n P_{im}(\boldsymbol{k}) \right) \tag{4.272}$$

is now detailed. Viscous effects are omitted and the symbol $\sum_{\Delta}$ for summation over triads is used in a generic way, in order to avoid distinguishing between the discrete and the continuous formulation from the beginning. The use of complex conjugates for the Fourier coefficients in the sum (or integral) is consistent with a fully symmetric relationship for the triad, i.e.

$$\boldsymbol{k} + \boldsymbol{p} + \boldsymbol{q} = 0 \tag{4.273}$$

instead of $\boldsymbol{p} + \boldsymbol{q} = \boldsymbol{k}$ coming from the convolution product.

A slightly different form of the nonlinear coupling term is found replacing the term $\frac{\partial u_i u_j}{\partial x_j}$ in physical space by $\epsilon_{ijn} \omega_j u_n$. The corresponding form in Fourier space is $\imath s_i = P_{im} \epsilon_{mjn} \sum_{\Delta} \hat{\omega}_j(\boldsymbol{p}, t) \hat{u}_n(\boldsymbol{q}, t)$, which can be shown to be the same as the previous one, using the Ricci relationship and a symmetric form with respect to $\boldsymbol{p}$ and $\boldsymbol{q}$. This formulation is more convenient when using the helical modes basis.

In terms of the helical modes, Eq. (4.271) has the generic form

$$\frac{\partial \xi_s(\boldsymbol{k})}{\partial t} = \imath \sum_{\Delta} \underbrace{M_{ss's''}(\boldsymbol{k}, \boldsymbol{p})}_{I} \underbrace{\xi_{s'}^*(\boldsymbol{p}, t) \xi_{s''}^*(\boldsymbol{q}, t)}_{II} \tag{4.274}$$

using $\xi_s(\boldsymbol{k}) = (1/2) \hat{\boldsymbol{u}} \cdot \boldsymbol{N}(-s\boldsymbol{k})$ and $\hat{\boldsymbol{u}}(\boldsymbol{p}) = \sum_{s'} \xi_{s'} \boldsymbol{N}(s'\boldsymbol{p})$. The signs s, s', s'', or *polarities*, take the values ± 1 only. It is worth noting that, in Eq. (4.274), term I

is only related to the topology of the triad (i.e. is a purely geometric factor), while term II depends only on the amplitude of the modes, i.e. on the turbulent field itself. From Eq. (4.271) it is found that (e.g. Cambon and Jacquin 1989)

$$M_{ss's''}(\boldsymbol{k},\boldsymbol{p}) = \frac{1}{2}\left((\boldsymbol{N}(-s\boldsymbol{k})\cdot\boldsymbol{N}(-s'\boldsymbol{p}))(\boldsymbol{k}\cdot\boldsymbol{N}(-s''\boldsymbol{q})) + (\boldsymbol{N}(-s\boldsymbol{k})\cdot\boldsymbol{N}(-s'\boldsymbol{q}))(\boldsymbol{k}\cdot\boldsymbol{N}(-s''\boldsymbol{p}))\right). \tag{4.275}$$

The second formulation, using $\boldsymbol{\omega}\times\boldsymbol{u}$ as the basic nonlinearity (Waleffe 1992, 1993), yields

$$M_{ss's''}(\boldsymbol{k},\boldsymbol{p}) = \frac{1}{2}(s'p - s''q)\boldsymbol{N}(-s\boldsymbol{k})\cdot(\boldsymbol{N}(s'\boldsymbol{p})\times\boldsymbol{N}(s''\boldsymbol{q})) \tag{4.276}$$

using the additional relationship

$$\boldsymbol{\omega}(\boldsymbol{p}) = p\sum_{s'} s'\xi_{s'}(\boldsymbol{p},t)\boldsymbol{N}(s'\boldsymbol{p}) \tag{4.277}$$

and the antisymmetry of the triple scalar product.

The use of helical modes allows for an optimal factorization of the coupling terms in terms of the moduli k, p, q and the angular variables: the former depend only on the geometry of the triangle while the latter also depend on the orientation of its plane. For further analysis, it is better to start from Eq. (4.276) since it appears more symmetric than (4.275) in terms of the three vectors of the triads, involving a *triple scalar product*, without need for additional calculations.

For instance, Eqs. (4.274) and (4.276) can be rewritten as

$$\frac{\partial\xi_s(\boldsymbol{k})}{\partial t} = \sum_{s's''}\sum_{\Delta}(s'p - s''q)K(s\boldsymbol{k},s'\boldsymbol{p},s'\boldsymbol{q})\xi^*_{s'}(\boldsymbol{p},t)\xi^*_{s''}(\boldsymbol{q},t) \tag{4.278}$$

with

$$K(s\boldsymbol{k},s'\boldsymbol{p},s''\boldsymbol{q}) = \frac{i}{4}\boldsymbol{N}(-s\boldsymbol{k})\cdot(\boldsymbol{N}(-s'\boldsymbol{p})\times\boldsymbol{N}(-s''\boldsymbol{q}). \tag{4.279}$$

The principle of triad instability stated by Waleffe (see Sect. 4.8.4) takes advantage of the full symmetry of the coupling coefficient K with respect to any simultaneous permutation of vectors and polarities within a given triad.

A last set of equations allows us to express K (and other related coefficients in statistical closures) in terms of the parameters of the triad. The idea is to turn from local reference frames (or helical modes) defined with respect to a fixed polar axis to their counterparts defined with respect to the normal unit vector of the triad (or almost equivalently with respect to a fixed $\boldsymbol{k}$, if $\boldsymbol{p}$ and $\boldsymbol{q}$ are under consideration). The unit normal vector is defined as

$$\boldsymbol{\gamma} = \frac{\boldsymbol{k} \times \boldsymbol{p}}{|\, \boldsymbol{k} \times \boldsymbol{p} \,|}, \tag{4.280}$$

and unit vectors in the plane spanned by the triad, normal to $\boldsymbol{k}, \boldsymbol{p}, \boldsymbol{q}$, respectively are

$$\boldsymbol{\beta} = \frac{\boldsymbol{k}}{k} \times \boldsymbol{\gamma}, \quad \boldsymbol{\beta}' = \frac{\boldsymbol{p}}{p} \times \boldsymbol{\gamma}, \quad \boldsymbol{\beta}'' = \frac{\boldsymbol{q}}{q} \times \boldsymbol{\gamma}. \tag{4.281}$$

'Triadic' helical modes are defined by

$$\boldsymbol{W}(s) = \boldsymbol{\beta} + \imath s \boldsymbol{\gamma}, \quad \boldsymbol{W}(s') = \boldsymbol{\beta}' + \imath s' \boldsymbol{\gamma}, \quad \boldsymbol{W}(s'') = \boldsymbol{\beta}'' + \imath s'' \boldsymbol{\gamma}, \tag{4.282}$$

and they are related to the original ones by

$$\boldsymbol{N}(s\boldsymbol{k}) = e^{\imath s \lambda} \boldsymbol{W}(s), \quad \boldsymbol{N}(s'\boldsymbol{p}) = e^{\imath s' \lambda'} \boldsymbol{W}'(s'), \quad \boldsymbol{N}(s''\boldsymbol{q}) = e^{\imath s'' \lambda''} \boldsymbol{W}''(s''), \tag{4.283}$$

where λ, λ' and λ'' are angles which characterize the rotation of the plane of the triad around $\boldsymbol{k}, \boldsymbol{p}, \boldsymbol{q}$ respectively (see also Chap. 17).

The advantage of the $\boldsymbol{W}(s)$, $\boldsymbol{W}'(s')$, $\boldsymbol{W}''(s'')$ with respect to $\boldsymbol{N}(s\boldsymbol{k})$, $\boldsymbol{N}(s'\boldsymbol{p})$, $\boldsymbol{N}(s''\boldsymbol{q})$ is that any invariant combination (double or triple scalar product) of the former will only rely on the geometry of the triad, and therefore can be expressed in terms of the moduli k, p, q only. As a first useful application, the coefficient K can be expressed as

$$K = \frac{i}{4} e^{-\imath(s\lambda + s'\lambda' + s''\lambda'')} \boldsymbol{W}(s) \cdot (\boldsymbol{W}'(s') \times \boldsymbol{W}''(s'')).$$

The triple scalar product involves the sines of the internal angles of the triad

$$\boldsymbol{W}(s) \cdot (\boldsymbol{W}'(s') \times \boldsymbol{W}''(s'')) = \imath (s's'' \sin\alpha + ss'' \sin\beta + ss' \sin\gamma).$$

These sines are connected to the lengths of the triangle through

$$\frac{\sin\alpha}{k} = \frac{\sin\beta}{p} = \frac{\sin\gamma}{q} = C_{kpq}, \tag{4.284}$$

so that

$$K(s\boldsymbol{k}, s'\boldsymbol{p}, s''\boldsymbol{q}) = e^{-\imath(s\lambda + s'\lambda' + s''\lambda'')} \frac{ss's''}{4} (sk + s'p + s''q) C_{kpq}, \tag{4.285}$$

with

$$C_{kpq} = \frac{\sqrt{2k^2p^2 + 2p^2q^2 + 2q^2k^2 - k^4 - p^4 - q^4}}{2kpq}, \tag{4.286}$$

which appears in EDQNM models (see Sect. 4.8.7).

As a second application, the system of dependent variables $\boldsymbol{k}$, p, q, λ is well suited for representing the triadic interactions. If the symbolic operator $\sum_{\Delta}$ is replaced by the integral

$$\iiint S(\boldsymbol{k}, \boldsymbol{p}, t) d^3\boldsymbol{p},$$

where $S(\boldsymbol{k}, \boldsymbol{p}, t)$ originates from $T = (1/2)T_{ii}$ using Eqs. (2.101) and (2.103). Its general expression in terms of triple velocity correlations (see also Eq. (4.288) below) is not important here, since only the change of dependent variables at fixed $\boldsymbol{k}$ (switching from $((p_1, p_2, p_3))$ to (p, q, λ)) is considered, for any integrand S.

If $\boldsymbol{q}$ is expressed as $-\boldsymbol{k} - \boldsymbol{p}$ in S, then the factors p, q and λ can replace p_1, p_2, p_3, yielding

$$\iiint S(\boldsymbol{k}, \boldsymbol{p}, t) d^3\boldsymbol{p} = \iint_{\Delta_k} \frac{pq}{k} dp dq \int_0^{2\pi} S(\boldsymbol{k}, p, q, \lambda) d\lambda. \tag{4.287}$$

The coefficient pq/k is the Jacobian of the change of integration variables, and Δ_k is the domain of p, q, so that k (fixed), p, q are the lengths of the sides of a triangle.

Finally the other angular variables in Eq. (4.285), λ' and λ'', also can be expressed as functions of $\boldsymbol{k}$, p, q and λ.

4.8.2 Nonlinear Energy Transfers and Triple Correlations

The transfer term $T(k)$ in Eq. (4.38) involves triple velocity correlations under summation on triads. We now address closure for triple correlations at three points. They are developed in Fourier space for the sake of mathematical convenience. A third order spectral tensor can be defined as

$$< \hat{u}_i(\boldsymbol{k}) \hat{u}_j(\boldsymbol{p}) \hat{u}_n(\boldsymbol{q}) >= \imath S_{ijn}(\boldsymbol{k}, \boldsymbol{p}, t) \delta(\boldsymbol{k} + \boldsymbol{p} + \boldsymbol{q}), \tag{4.288}$$

which corresponds to the general definition given in Chap. 2, up to a factor $\imath$. The transfer tensor which incorporates their contribution in the equation for the second order spectral tensor is given by

$$T_{ij}(\boldsymbol{k}) \delta(\boldsymbol{k} + \boldsymbol{p}) =< s_i(\boldsymbol{p}) \hat{u}_j(\boldsymbol{k}) > + < \hat{u}_i(\boldsymbol{p}) s_j(\boldsymbol{k}) >,$$

or

$$T_{ij}(\boldsymbol{k}) = \tau_{ij}(\boldsymbol{k}) + \tau^*_{ji}(\boldsymbol{k}) \tag{4.289}$$

with

$$\tau_{ij}(\boldsymbol{k}) = P_{imn} \int S_{jmn}(\boldsymbol{k}, \boldsymbol{p}) d^3\boldsymbol{p}. \tag{4.290}$$

Two contributions can be distinguished in T_{ij}. The first one is given by

$$\frac{1}{2}\left(k_n \int (S_{jin} + S^*_{jin}) d^3\boldsymbol{p} + k_m \int (S_{jmi} + S^*_{imj}) d^3\boldsymbol{p}\right)$$

and corresponds to a true transfer tensor with zero integral. The complementary contribution

$$\frac{1}{2}\frac{k_m k_n}{k^2}\left(k_i \int S_{jmn} d^3\boldsymbol{p} + k_j \int S^*_{imn} d^3\boldsymbol{p}\right)$$

gives by integration the 'slow' pressure strain-tensor Π^s_{ij} introduced in Sect. 2.3.1.

Of course, we are only interested in

$$T(k) = 2\pi k^2 T_{ii} = 2\pi k^2 (\tau_{ii} + \tau^*_{ji})$$

in HIT but it is necessary to address the equation for S_{ijn} to derive a consistent closure.

Similarly to the equation for the second order spectral tensor, the equation which governs S_{ijn} is found as:

$$\left[\frac{\partial}{\partial t} + \nu(k^2 + p^2 + q^2)\right] S_{ijn}(\boldsymbol{k}, \boldsymbol{p}) = T_{ijn}(\boldsymbol{k}, \boldsymbol{p}) + T_{jni}(\boldsymbol{p}, \boldsymbol{q}) + T_{nij}(\boldsymbol{q}, \boldsymbol{k}).$$

The first term (the other ones are derived by circular permutations) in the right-hand-side is exactly expressed as

$$\begin{aligned}\delta(\boldsymbol{k} + \boldsymbol{p} + \boldsymbol{q}) T_{ijn} &= \imath < s_i(\boldsymbol{k}) \hat{u}_j(\boldsymbol{p}) \hat{u}_n(\boldsymbol{q}) > \\ &= \int_{k=r+s} P_{irs}(\boldsymbol{k}) < \hat{u}_r(\boldsymbol{r}) \hat{u}_s(\boldsymbol{s}) \hat{u}_j(\boldsymbol{p}) \hat{u}_n(\boldsymbol{q}) > d^3\boldsymbol{r}, \end{aligned} \tag{4.291}$$

and involves fourth-order correlations.

4.8.3 Global and Detailed Conservation Properties

Some global conservation properties of the Navier–Stokes equations in the limit of vanishing molecular viscosity can be easily recast in the Fourier space, providing some useful constraints on the triadic non-linear transfer term.

We will consider here the conservation of the global kinetic energy and the global helicity (in an unbounded domain and in the absence of external forcing):

$$\frac{\partial}{\partial t} \int \boldsymbol{u}(\boldsymbol{x}) \cdot \boldsymbol{u}(\boldsymbol{x}) d^3\boldsymbol{x} = 0, \tag{4.292}$$

$$\frac{\partial}{\partial t}\int \boldsymbol{u}(\boldsymbol{x})\cdot\boldsymbol{\omega}(\boldsymbol{x})d^3\boldsymbol{x}=0 \quad \boldsymbol{\omega}=\mathrm{curl}(\boldsymbol{u}). \tag{4.293}$$

The global kinetic energy invariance property can be recast in the Fourier space as

$$\int_0^{+\infty} T(k)dk=0, \tag{4.294}$$

where $T(k)$ is defined by Eq. (4.39).

These two relations illustrate the fact that the non-linear term redistribute energy and helicity among the different modes. As shown by Kraichnan, these global conservation properties can be supplemented by other ones, which hold at the level of each triad, leading to *detailed conservation properties*.

Let us consider a triad ($\boldsymbol{k}$, $\boldsymbol{p}$,$\boldsymbol{q}$) which satisfies the constraint (4.273). Using the helical mode decomposition and rewriting relation (4.278) for the single triad under consideration, one obtains

$$\frac{\partial\xi_s(\boldsymbol{k})}{\partial t}=(s'p-s''q)K(s\boldsymbol{k},s'\boldsymbol{p},s'\boldsymbol{q})\xi^*_{s'}(\boldsymbol{p},t)\xi^*_{s''}(\boldsymbol{q},t), \tag{4.295}$$

$$\frac{\partial\xi_{s'}(\boldsymbol{p})}{\partial t}=(s''q-sk)K(s\boldsymbol{k},s'\boldsymbol{p},s'\boldsymbol{q})\xi^*_{s}(\boldsymbol{k},t)\xi^*_{s''}(\boldsymbol{q},t), \tag{4.296}$$

$$\frac{\partial\xi_{s''}(\boldsymbol{q})}{\partial t}=(sk-s'p)K(s\boldsymbol{k},s'\boldsymbol{p},s'\boldsymbol{q})\xi^*_{s}(\boldsymbol{k},t)\xi^*_{s'}(\boldsymbol{p},t). \tag{4.297}$$

It is obvious from these equations that

$$\dot{\xi}_s(\boldsymbol{k})\xi^*_s(\boldsymbol{k})+\dot{\xi}_{s'}(\boldsymbol{p})\xi^*_{s'}(\boldsymbol{p})+\dot{\xi}_{s''}(\boldsymbol{q})\xi^*_{s''}(\boldsymbol{q})=0,$$

since $(s'p-s''q)+(s''q-sk)+(sk-s'p)=0$, all the other terms being perfectly symmetric in terms of $(s\boldsymbol{k},s'\boldsymbol{p},s''\boldsymbol{q})$, as the factor K is. Here,

$$e=(1/2)\xi_s(\boldsymbol{k})\xi^*_s(\boldsymbol{k})=(1/2)\hat{\boldsymbol{u}}(\boldsymbol{k})\cdot\hat{\boldsymbol{u}}^*(\boldsymbol{k}) \tag{4.298}$$

denotes the spectral density of energy. In other words, examination of the very simplified form for $M_{ss's''}$ given in Eqs. (4.295) to (4.297) immediately shows that

$$M_{ss's''}(\boldsymbol{k},\boldsymbol{p})+M_{s's''s}(\boldsymbol{p},\boldsymbol{q})+M_{s''ss'}(\boldsymbol{q},\boldsymbol{k})=0, \tag{4.299}$$

using the same nomenclature as for the non-linear terms as in Sect. 4.8.1, so that the detailed conservation of energy is found in an optimal way.

Detailed conservation of helicity is an even more striking result, due to the optimal modal decomposition, with

$$sk\dot{\xi}_s(\boldsymbol{k})\xi^*_s(\boldsymbol{k})+s'p\dot{\xi}_{s'}(\boldsymbol{p})\xi^*_{s'}(\boldsymbol{p})+s''q\dot{\xi}_{s''}(\boldsymbol{q})\xi^*_{s''}(\boldsymbol{q})=0, \tag{4.300}$$

resulting from $sk(s'p - s''q) + s'p(s''q - sk) + s''q(sk - s'p) = 0$, which implies

$$skM_{ss's''}(\boldsymbol{k},\boldsymbol{p}) + s'pM_{s's''s}(\boldsymbol{p},\boldsymbol{q}) + s''qM_{s''ss'}(\boldsymbol{q},\boldsymbol{k}) = 0. \tag{4.301}$$

The spectral density of helicity is given by

$$h \sim \sum_{s=\pm 1} \imath sk\xi_s(\boldsymbol{k})\xi_s^*(\boldsymbol{k}) = (1/2)\hat{\boldsymbol{u}}^*(\boldsymbol{k}) \cdot \hat{\boldsymbol{\omega}}(\boldsymbol{k}). \tag{4.302}$$

The related interesting result is

$$\frac{M_{ss's''}(\boldsymbol{k},\boldsymbol{p})}{s''q - s'p} = \frac{M_{s's''s}(\boldsymbol{p},\boldsymbol{q})}{sk - s''q} = \frac{M_{s''ss'}(\boldsymbol{q},\boldsymbol{k})}{s'p - sk} = -\imath K(s\boldsymbol{k}, s'\boldsymbol{p}, s''\boldsymbol{q}). \tag{4.303}$$

Equations (4.299) and (4.301) show that the non linear interactions among modes within a given triad conserve both kinetic energy and helicity. A look at Eqs. (4.295)–(4.297) also shows that two modes with the same wave number and the same polarity do not force the third one in the triad. In the previous example, one has $\partial\xi_{s''}(\boldsymbol{q})/\partial t = 0$ if $k = p$ and $s = s'$.

4.8.4 *Advanced Analysis of Triadic Transfers and Waleffe's Instability Assumption*

The analysis of triadic interactions can be further refined distinguishing between the three following types of interactions:

- **local interactions**, which correspond to triads $(\boldsymbol{k},\boldsymbol{p},\boldsymbol{q})$ such that $k \simeq p \simeq q$. A usual definition is that $\max(k, p, q)/\min(k, p, q) \leq 2 - 3$.
- **distant interactions**, which are such that $\max(k, p, q)/\min(k, p, q) \geq 7 - 10$.
- **non-local interactions**, which correspond to all others cases.

It is important to stress that the detailed conservation of energy can be shown in terms of primitive variables, $\hat{\boldsymbol{u}}$, with some consequences on the triadic transfers discussed firstly below, but new properties of these transfers are displayed using helical modes and taking advantage of the formal analogy of Eqs. (4.295)–(4.297) with the Euler problem for the angular momentum of a solid body (see Sect. 4.8.5).

Brasseur coworkers addressed the question of the relative intensity of the transfers associated to each type of triadic interaction (Brasseur and Wei 1994) at large wave numbers contained in the inertial range of the energy spectrum. Considering the triad $(\boldsymbol{k},\boldsymbol{p},\boldsymbol{q})$, the non-linear term which appears in the evolution equation of $e(\boldsymbol{k}) = \hat{\boldsymbol{u}}^*(\boldsymbol{k}) \cdot \hat{\boldsymbol{u}}(\boldsymbol{k})$ associated to this single triad is

$$\dot{e}(\boldsymbol{k})_{\mathrm{NL}} = -\imath\left(\left(\hat{\boldsymbol{u}}(\boldsymbol{k}) \cdot \hat{\boldsymbol{u}}(\boldsymbol{p})\right)\left(\boldsymbol{k} \cdot \hat{\boldsymbol{u}}(\boldsymbol{q})\right) + \left(\hat{\boldsymbol{u}}(\boldsymbol{k}) \cdot \hat{\boldsymbol{u}}(\boldsymbol{q})\right)\left(\boldsymbol{k} \cdot \hat{\boldsymbol{u}}(\boldsymbol{p})\right)\right) + c.c. \tag{4.304}$$

in terms of primitive variables, instead of

$$\dot{e}(\boldsymbol{k})_{\mathrm{NL}} = \imath M_{ss's''}(\boldsymbol{p},\boldsymbol{q})\xi_s^*(\boldsymbol{k})\xi_{s'}^*(\boldsymbol{p})\xi_{s''}^*(\boldsymbol{q}),$$

using helical modes. In any case, the detailed energy conservation implies

$$\dot{e}(\boldsymbol{k})_{\mathrm{NL}} + \dot{e}(\boldsymbol{p})_{\mathrm{NL}} + \dot{e}(\boldsymbol{q})_{\mathrm{NL}} = 0. \tag{4.305}$$

Numerical simulations have shown that distant interactions play a very important role in the dynamics of small scales. This observation can be explained as follows.

First, let us consider a distant triad which couples a low wave number $\boldsymbol{k}$ to two high wave numbers $\boldsymbol{p}$ and $\boldsymbol{q}$, and let us introduce the small parameter $\delta = k/p \simeq k/q$. One obtains from Eq. (4.304) the following scaling laws:

$$\dot{e}(\boldsymbol{k})_{\mathrm{NL}} = O(\delta), \tag{4.306}$$

$$\dot{e}(\boldsymbol{p})_{\mathrm{NL}} = -\dot{e}(\boldsymbol{q})_{\mathrm{NL}} = -\imath\left(\left(\hat{\boldsymbol{u}}(\boldsymbol{p})\cdot\hat{\boldsymbol{u}}(\boldsymbol{q})\right)\left(\boldsymbol{p}\cdot\hat{\boldsymbol{u}}(\boldsymbol{k})\right)\right) + c.c. + O(\delta), \tag{4.307}$$

which show that energy transfers take place between the two high number modes, leading to the existence of a local energy transfer associated to a distant interaction. In the asymptotic limit $\delta \longrightarrow 0$, one can see that no energy is exchanged between large and small scales: the low wave number mode acts only as a catalyst. But it is important to note that small and larger wave number modes are coupled through the distant interactions, even if no energy is exchanged between them, since distant interactions can propagate low-wave number (i.e. large scale) anisotropy at small scales.

The magnitude of the rate of energy exchange of a high wave number mode $\boldsymbol{k}$ ($k \gg 1$) due to distant interactions can be evaluated as

$$\dot{e}(\boldsymbol{k})_{\mathrm{NL}} \propto e(\boldsymbol{k})k\sqrt{e(\boldsymbol{p})} \quad \text{(distant interactions)}, \tag{4.308}$$

where $\boldsymbol{p}$ is the energy-containing mode (i.e. the low wave number mode of the distant triad), while, for the local interactions, one obtains

$$\dot{e}(\boldsymbol{k})_{\mathrm{NL}} \propto e(\boldsymbol{k})k\sqrt{e(\boldsymbol{k})} \quad \text{(local interactions)}. \tag{4.309}$$

These evaluations show that the distant interactions induce a much larger energy transfer than the local ones, since the energy of the low-wave number mode in the distant triad, $e(\boldsymbol{p})$, is much higher than $e(\boldsymbol{k})$. As a consequence, the effect of distant interactions is important at large wave numbers. The relative importance of transfers associated with distant triads with respect to those associated to local triads is an increasing function of the ratio of the energy contained is the small and high wave number modes.

Direct numerical simulations have also shown that:

- The energy transfer from large to small scales (i.e. the kinetic energy cascade) is local across the spectrum.
- For energetic scales (i.e. wave numbers located near the peak of the spectrum), the kinetic energy transfer towards the smaller scales is mainly due to local interactions
- For small scales (i.e. high wave number located within the inertial range), the energy transfer is governed by distant interactions involving one mode in the energy containing range.

A finer analysis of numerical databases also reveals that all distant interactions do not contribute in same way to the energy transfer towards smaller scales, i.e. that distant triads do not redistribute kinetic energy in the same way among the three interacting modes. To explain this and to provide a detailed analysis of all possible transfers within a single distant triad, Waleffe developed a theory based on the *instability assumption* (Waleffe 1992, 1993).

The first step in Waleffe's analysis is to consider the stability of the system (4.295)–(4.297) around its steady solutions. There are three steady solutions. Considering the steady solution given by (the two others can be deduced by simple permutations)

$$\frac{\partial \xi_s(\boldsymbol{k})}{\partial t} = A, \quad \frac{\partial \xi_{s'}(\boldsymbol{p})}{\partial t} = \frac{\partial \xi_{s''}(\boldsymbol{q})}{\partial t} = 0, \tag{4.310}$$

one obtains

$$\frac{\partial^2 \xi_{s'}(\boldsymbol{p})}{\partial t^2} = (s''q - sk)(sk - s'p)|K(s\boldsymbol{k}, s'\boldsymbol{p}, s'\boldsymbol{q})|^2 |A|^2 \xi^*_{s'}(\boldsymbol{p}) \tag{4.311}$$

where the modulus of the complex parameters are defined as follows

$$|K(s\boldsymbol{k}, s'\boldsymbol{p}, s'\boldsymbol{q})|^2 \equiv K(s\boldsymbol{k}, s'\boldsymbol{p}, s'\boldsymbol{q}) K^*(s\boldsymbol{k}, s'\boldsymbol{p}, s'\boldsymbol{q}), \quad |A|^2 \equiv AA^*. \tag{4.312}$$

The disturbance in $\xi^*_{s'}(\boldsymbol{p})$ will grow exponentially if $(s''q - sk)(sk - s'p) > 0$. This happens if sk is intermediate between $s''q$ and $s'p$, leading to a stability criterion based on the intermediate mode. Now combining the energy detailed conservation relation (4.299) and the trivial geometric relation

$$(s''q - sk) + (sk - s'p) + (s'p - s''q) = 0 \tag{4.313}$$

one can see that the unstable mode is the mode whose coefficient $M_{ss's''}$ has a sign opposite to the two others, with the highest absolute value. From this observation it follows that:

- The mode associated to the largest wave number can never be unstable.
- The mode associated with the smallest wave number is unstable if the two larger wave number modes have opposite polarities (i.e. helicities of opposite sign).

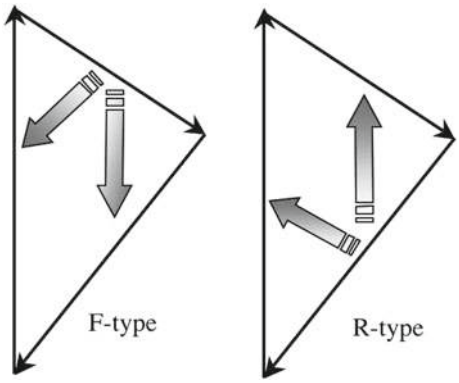

Fig. 4.20 Schematic view of kinetic energy transfers according to Waleffe's instability assumption among modes within a single triad. The two types of interactions are represented. Thick arrows denote the energy transfers

- The mode associated to the intermediate wave number is unstable if it has the same polarity as the mode asssociated to the largest wave number.

The *instability assumption* advocated by Waleffe is that *the mode which releases energy towards the two others within a single triad is the instable mode*.

The combination of the two possible polarities for the three wave vectors leads to the existence of eight possible triadic interactions, which can be grouped in two classes according to the resulting kinetic energy transfer (see Fig. 4.20):

- The *forward interactions* (F-type in the parlance of Waleffe), for which the two smallest wave numbers have opposite polarities. In this case, the above analysis show that the energy is released by the smallest wave number (i.e. the largest scale), leading to a forward energy cascade.
- The *reverse interactions* (R-type), for which the smallest wave vectors have the same polarity. In this case, the intermediate mode can be the unstable one, leading to a transfer of energy towards both a larger (backward energy cascade) and a smaller scale (forward energy cascade).

Let us now focus on the distant interactions, which are of particular importance in the large wave number mode dynamics. Let $(\boldsymbol{k},\boldsymbol{p},\boldsymbol{q})$ be a distant triad with $|\boldsymbol{q}-\boldsymbol{p}| < k \ll p \simeq q$. The triad-related geometrical factor that appears in the definition of $M_{ss's''}$ scales like $(sk+s'p+s''q)$. As a consequence, the energy transfer scales like $\pm k \pm (p-q)$ for distant F-type interactions and like $\pm k \pm (p+q)$ for distant R-type interactions. Therefore, on the average, distant triads mostly induce energy transfers of the R-type, yielding a local energy transfer between the largest wave vectors.

Among the four possible R-type triadic interactions, two contributes in the mean to the backward energy cascade from the large wave number modes towards the small wave number modes. The direction of the cascade associated with the two others depends on the value of the ratio between the smallest and the intermediate wave numbers.

On the average, within the inertial range, the net effect of the R-type interactions is a backward energy transfer toward the small wave number modes, the direct

energy cascade being due to F-type interactions. Consequently, the net energy transfer within the inertial range is a direct energy cascade due to large local energy transfer associated to distant interactions.

Even a more quantitative evaluation of the different energy fluxes were performed in Waleffe (1992, 1993) using additional statistical assumptions about self-similarity, or a statistical closure as EDQNM (or TFM, which is almost identical to EDQNM for 3D Homogeneous Isotropic Turbulence). EDQNM allows to reach much higher Reynolds numbers than DNS, and it may be more accurate in terms of spectral discretization, avoiding errors of cancellation *since it can be developed in terms of helical modes too, separating the eight different kinds of triads in exact agreement with detailed conservation of energy and helicity*.

4.8.5 Further Discussions About the Instability Assumption

We now discuss some analogies that exists between the instability principle and other problems.

As stated by Waleffe in his seminal paper (Waleffe 1992), the instability principle presented in the previous section is formally similar to the problem of the instability of a rigid body rotating around one of its principal axes of inertia. Let first note that the system (4.295)–(4.297) can be recast in the following compact form

$$\frac{d\boldsymbol{\xi}}{dt} = K(s\boldsymbol{k}, s'\boldsymbol{p}, s''\boldsymbol{q})(\mathbf{D}\boldsymbol{\xi}^*) \times \boldsymbol{\xi}^* \tag{4.314}$$

where $\boldsymbol{\xi} = (\xi_s(\boldsymbol{k}), \xi_{s'}(\boldsymbol{p}), \xi_{s''}(\boldsymbol{q}))^T$ and

$$\mathbf{D} = \begin{pmatrix} sk & 0 & 0 \\ 0 & s'p & 0 \\ 0 & 0 & s''q \end{pmatrix}. \tag{4.315}$$

Detailed conservation laws of energy and helicity within the triad yield

$$\frac{d}{dt}(\boldsymbol{\xi} \cdot \boldsymbol{\xi}^*) = \frac{d}{dt}(\boldsymbol{\xi} \cdot \mathbf{D}\boldsymbol{\xi}^*) = 0. \tag{4.316}$$

Let us consider a solid body in rotation, with $\boldsymbol{L}$ and $\boldsymbol{\omega}$ its angular momentum and angular velocity vectors, respectively. The Euler equations which describe this motion are

$$\frac{d\boldsymbol{L}}{dt} = \boldsymbol{L} \times \boldsymbol{\omega}. \tag{4.317}$$

Now introducing the tensor of inertia of the solid, denoted $\mathbf{I}$, one can write the angular momentum as the product of $\mathbf{I}$ with the rotation vector $\mathbf{I}\boldsymbol{\omega}$. The problem (4.317) can be rewritten in the principal axes of the inertia matrix as follows

$$I_1\dot{\omega}_1 = (I_2 - I_3)\omega_2\omega_3, \tag{4.318}$$

$$I_2\dot{\omega}_2 = (I_3 - I_1)\omega_3\omega_1, \tag{4.319}$$

$$I_3\dot{\omega}_3 = (I_1 - I_2)\omega_1\omega_2. \tag{4.320}$$

Therefore, the first conservation law is for the rotational kinetic energy $I_1\omega_1^2 + I_2\omega_2^2 + I_3\omega_3^2$ (equivalent to the triadic kinetic energy conservation law - (4.299)), and the second one for the norm of the angular momentum $(I_1\omega_1)^2 + (I_2\omega_2)^2 + (I_3\omega_3)^2$ (equivalent to triadic helicity conservation law - (4.301)). The systems (4.314) and (4.317) are mathematically similar, $\mathbf{D}$ and $\boldsymbol{\xi}$ playing the role of $\mathbf{I}$ and $\boldsymbol{L}$, respectively. It is known that there exist three steady state solutions for the problem of the rotating solid, which correspond to rotation around any one of the principal axes of inertia. Rotation around the axis of middle inertia is unstable, while the two other cases are stable solutions. This implies that the smallest wave number is unstable if the two largest wave numbers have helicities of opposite sign, and that the medium wave number is unstable otherwise. Therefore, it is seen that the analogy enable to recover the results of the previous section. But it is worth to remark that components of $\mathbf{D}$ can exhibit negative values.

The second point discussed by Waleffe is the link between the F-type interactions and the elliptical instability. Let us first recall that the elliptical instability is the three-dimensional instability of flows with locally elliptical streamlines. The unstable modes are resonant inertial waves associated with the uniform background rotation (see Sect. 7.5). These waves are helical modes of opposite polarities and eigenfrequencies, say f^+ and f^-. A detailed analysis (see Waleffe 1992 for technical details) show that the elliptical instability corresponds to a F-interaction: the two modes with eigenfrequency f^+ and f^- have opposite polarities and are coupled with the mean flow, which is associated to a zero frequency. It can also be shown that there exists a low-wave-number cutoff: the wave number of the perturbation must remain higher than effective wave number of the elliptic background flow for the instability to develop. Therefore, the elliptical instability originates in an interaction that leads to the instability of the smallest wave number mode in a triad through interactions with two larger wave number modes of opposite polarities.

4.8.6 Principle of Quasi-normal Closures

The previous equations for $\hat{\boldsymbol{u}}_i$, $\hat{R}_{ij}$ and S_{inj} illustrate the infinite hierarchy of open equations, which is usually formally written like

$$\frac{\partial}{\partial t}u = uu,$$

$$\frac{\partial}{\partial t} < uu > = < uuu >,$$

$$\frac{\partial}{\partial t} < uuu >=< uuuu >,$$

$$\cdots = \cdots$$

A common feature of triadic closures, from EDQNM (Orszag 1970) to the most sophisticated Kraichnan's theories, is a quasi-normal relationship. Any technique which aims at expressing high order moments as products of low order ones is a good candidate for closing the above mentioned infinite hierarchy of open equations. Instead of moments, cumulants directly express the difference of moments with respect to their factorized expression in terms of lower order ones, so that classical closures rely on small estimates of cumulants. Historically, the assumption of vanishing fourth-order cumulant for the turbulent velocity fluctuations, i.e.

$$\begin{aligned} < u^a u^b u^c u^d > - < u^a u^b >< u^c u^d > - < u^a u^c >< u^b u^d > \\ - < u^a u^d >< u^b u^c >= 0, \end{aligned} \tag{4.321}$$

was first proposed by Milionschikov (1941), then by Tatsumi (1957). In the above equation, different superscripts are used to distinguish different velocity modes, possibly in physical space with four different positions and for different components, finally in Fourier space for mathematical convenience. The assumption of vanishing fourth-order cumulant is usually referred to as the *Quasi-Normal approximation* (QN), but not as Normal (or Gaussian) approximation since nothing is said about third order cumulants (or third-order moments since there is no contribution from $< u >< uu >$). Of course, an estimate for third-order moments is sought, so that a pure Gaussian relationship, which removes them, is meaningless (except in some Rapid Distortion limit, which will be addressed in a subsequent chapter). In addition, a Quasi-Normal assumption can be supported mathematically and physically in the weak turbulence theory of Wave-Turbulence, as illustrated by Benney and Newell (1969) and Zakharov et al. (1992) (this approach will be revisited in Chap. 7).

Starting from the exact definition for T_{ijn}, the QN assumption yields:

$$\begin{aligned} \delta(\boldsymbol{k}+\boldsymbol{p}+\boldsymbol{q})T_{ijn} = P_{irs}(\boldsymbol{k}) \int_{-\boldsymbol{k}+\boldsymbol{r}+\boldsymbol{s}=0} d^3\boldsymbol{p} \times \big[< \hat{u}_r(\boldsymbol{r})\hat{u}_s(\boldsymbol{s}) >< \hat{u}_j(\boldsymbol{p})\hat{u}_n(\boldsymbol{q}) > \\ + < \hat{u}_r(\boldsymbol{r})\hat{u}_j(\boldsymbol{p}) >< \hat{u}_s(\boldsymbol{s})\hat{u}_n(\boldsymbol{q}) > \\ + < \hat{u}_r(\boldsymbol{r})\hat{u}_n(\boldsymbol{q}) >< \hat{u}_j(\boldsymbol{p})\hat{u}_s(\boldsymbol{s}) > \big]. \end{aligned} \tag{4.322}$$

Using $< \hat{u}_r(\boldsymbol{r})\hat{u}_s(\boldsymbol{s}) >= \hat{R}_{rs}(\boldsymbol{s})\delta(\boldsymbol{r}+\boldsymbol{s})$, the contribution from the first term is found to be zero since $\hat{R}_{rs}(\boldsymbol{k}=0)=0$, so that

$$T_{ijn}^{QN}(\boldsymbol{k},\boldsymbol{p}) = P_{ir}k_s \left[\hat{R}_{rj}(\boldsymbol{p})\hat{R}_{sn}(\boldsymbol{q}) + \hat{R}_{rn}(\boldsymbol{q})\hat{R}_{sj}(\boldsymbol{p}) \right] \tag{4.323}$$

or equivalently

$$T_{ijn}^{QN}(\boldsymbol{k},\boldsymbol{p}) = P_{irs}\hat{R}_{rj}(\boldsymbol{p})\hat{R}_{sn}(\boldsymbol{q}). \tag{4.324}$$

Finally, one obtains the following *Quasi-Normal closure*

$$\left[\frac{\partial}{\partial t}+\nu(k^2+p^2+q^2)\right]S_{ijn}(\boldsymbol{k},\boldsymbol{p})=T_{ijn}^{QN}(\boldsymbol{k},\boldsymbol{p})+T_{jni}^{QN}(\boldsymbol{p},\boldsymbol{q})+T_{nij}^{QN}(\boldsymbol{q},\boldsymbol{k}). \tag{4.325}$$

Eventhough the Quasi-Normal closure was proposed a long time ago, the resolution of the corresponding Lin equation requires significant numerical ressources. First numerical solutions obtained in the early 1960s (Ogura 1963; O'Brien and Francis 1963) exhibited an incorrect behaviour for long-time evolution. A negative zone appeared at small k in the energy spectrum, because of a too strong energy transfer from largest structures. This lack of realizability was shown to result from a too high estimate of the right-hand-side of the equation given above. In order to cure this problem, Orszag (1970) proposed to add an *Eddy-Damping term* (ED), so that

$$T_{ijn}(\boldsymbol{k},\boldsymbol{p},t)-T_{ijn}^{QN}(\boldsymbol{k},\boldsymbol{p},t)=-\underbrace{\eta(\boldsymbol{k},t)S_{ijn}(\boldsymbol{k},\boldsymbol{p},t)}_{\text{Damping term}}.$$

Similar relationships are obtained for other wave vector pairs by permuting the wave vectors of the triad. The special form of the linear relationship between fourth-order and third-order cumulants was partly suggested by the Kraichnan's Direct Interaction Approximation (DIA) theory. The left-hand-side represents the contribution from fourth-order *cumulants* and the right-hand-side deals with third-order cumulants. The Eddy Damping coefficient plays the role of an extra-dissipation, reinforcing the dissipative laminar effect, which is not sufficient to ensure realizability in the primitive QN closure. Gathering the dissipative terms into a single one

$$\mu_{kpq}=\theta_{kpq}^{-1}=\nu(k^2+p^2+q^2)+\eta(k,t)+\eta(p,t)+\eta(q,t), \tag{4.326}$$

the EDQN counterpart of Eq. (4.325) is easily obtained from it replacing $\nu(k^2+p^2+q^2)$ by θ_{kpq}^{-1}. The solution of the latter equation is found as

$$S_{ijn}(\boldsymbol{k},\boldsymbol{p},t)=\exp\left(-\mu_{kpq}(t-t_0)\right)S_{ijn}(\boldsymbol{k},\boldsymbol{p},t_0)$$
$$+\int_{t_0}^{t}\exp\left(-\int_{t'}^{t}\mu_{kpq}(t'')dt''\right)\left(T_{ijn}^{QN}(\boldsymbol{k},\boldsymbol{p},t')+\ldots\right)dt'. \tag{4.327}$$

Conventionaly, the last procedure called *Markovianization* yields neglecting the intrinsic history of T_{ijn}^{QN}, or equivalently the one of $\hat{R}_{ij}$, in the time integral. In other words $\hat{\mathbf{R}}$ and T^{QN} are considered as slowly varying quantities, so that one can take $t'=t$ in them, whereas the exponential term is considered as rapidly varying. Ignoring the initial data for triple correlations, consistently with large $t-t_0$, the simplest *EDQNM closure* (in the absence of complex additional linear terms) is:

$$S_{ijn}(\boldsymbol{k},\boldsymbol{p},t)=\theta_{kpq}\left[T_{ijn}^{QN}(\boldsymbol{k},\boldsymbol{p},t)+T_{jni}^{QN}(\boldsymbol{p},\boldsymbol{q},t)+T_{nij}^{QN}(\boldsymbol{q},\boldsymbol{k},t)\right]. \tag{4.328}$$

The latter equation illustrates an instantaneous relationship between third and second order correlations, but nonlocality in spectral space and triadic structure is preserved.

The tensor τ_{ij} defined in Eq. (4.290) is then expressed as follows

$$\begin{aligned}\tau_{ij}=\int\theta_{kpq}P_{jnm}(\boldsymbol{k})\Big(&P_{irs}(\boldsymbol{k})\hat{R}_{rn}(\boldsymbol{p})\hat{R}_{sm}(\boldsymbol{q})+P_{nrs}(\boldsymbol{p})\hat{R}_{rm}(\boldsymbol{q})\hat{R}_{si}(\boldsymbol{k})\\&+P_{mrs}(\boldsymbol{q})\hat{R}_{rm}(\boldsymbol{k})\hat{R}_{sn}(\boldsymbol{p})\Big)\,d^3\boldsymbol{p}\end{aligned} \tag{4.329}$$

in which the characteristic time θ_{kpq} is given by relation (4.326). Permuting $\boldsymbol{p}$ and $\boldsymbol{q}$ in the last term, the simplified form

$$\tau_{ij}=P_{jnm}(\boldsymbol{k})\int\theta_{kpq}\hat{R}_{sm}(\boldsymbol{q})\Big(P_{irs}(\boldsymbol{k})\hat{R}_{rn}(\boldsymbol{p})+2P_{nrs}(\boldsymbol{p})\hat{R}_{ri}(\boldsymbol{k})\Big)\,d^3\boldsymbol{p} \tag{4.330}$$

is finally obtained.

4.8.7 EDQNM for Isotropic Turbulence. Final Equations and Results

Three-dimensional isotropy yields dramatic simplifications, as

$$\hat{R}_{rj}(\boldsymbol{p})=\mathcal{E}(p)P_{rj}(\boldsymbol{p})$$

in Eq. (4.324), and

$$T^{(\mathcal{E})}(k)=\tau_{ii}(k)$$

from (4.290). The transfer term $T^{(\mathcal{E})}$ is therefore found as

$$T^{(\mathcal{E})}(k,t)=\iiint 2kp\theta_{kpq}\mathcal{E}(q,t)\left(A(k,p,q)\mathcal{E}(p,t)-B(k,p,q)\mathcal{E}(k,t)\right)d^3\boldsymbol{p} \tag{4.331}$$

with

$$P_{inm}(\boldsymbol{k})P_{sm}(\boldsymbol{q})P_{irs}(\boldsymbol{k})P_{rn}(\boldsymbol{p})=k^2A(k,p,q)$$

and

$$2P_{inm}(\boldsymbol{k})P_{sm}(\boldsymbol{q})P_{nrs}(\boldsymbol{p})P_{ri}(\boldsymbol{k})=2kpB(k,p,q).$$

Since $kpB(k,p,q)+kqB(k,q,p)=k^2A(k,p,q)$, $A(k,p,q)$ can be replaced by $B(k,p,q)$ in the above equation. In addition, it is simpler to express this unique

coefficient in terms of the cosines of the internal angles of the triangle of sides $k,\ p, q$

$$x = \cos\alpha = \frac{p^2+q^2-k^2}{2pq}, \quad y = \cos\beta = \frac{q^2+k^2-p^2}{2qk},$$

$$z = \cos\gamma = \frac{k^2+p^2-q^2}{2kp}. \tag{4.332}$$

Another relevant geometric term is C_{kpq}, which was already found in Eq. (4.286).

Since $C^2 B(k,\ p, q) = kp - q^2 z$, $B(k,\ p, q) = \sin\alpha \sin\beta - z\sin^2\gamma, = xy + z - z(1 - z^2)$ and finally

$$B(k,\ p, q) = xy + z^3,$$

the simplified expression follows

$$T^{(\mathcal{E})} = \iiint 2kp\theta_{kpq}(xy + z^3)\mathcal{E}(q,\ t)\left(\mathcal{E}(p,\ t) - \mathcal{E}(k,\ t)\right) d^3\boldsymbol{p}, \tag{4.333}$$

It is now possible to use the integration variables p, q and λ as in Eq. (4.287). Since the integrand depends only on $k,\ p, q$ and not on λ, the λ-integral reduces to a multiplication by 2π, so that

$$T^{(\mathcal{E})} = \iint_{\Delta_k} 4\pi p^3 q^2 \theta_{kpq}(xy + z^3)\mathcal{E}(q,\ t)\left(\mathcal{E}(p,\ t) - \mathcal{E}(k,\ t)\right)\frac{dpdq}{pq}. \tag{4.334}$$

A last equation is found reintroducing $E(k) = 4\pi k^2\mathcal{E}(k)$ and $T(k) = 4\pi k^2 T^{(\mathcal{E})}(k)$ as

$$T(k,\ t) = \iint_{\Delta_k} \theta_{kpq}(xy + z^3)E(q,\ t)\left(E(p,\ t)pk^2 - E(k,\ t)p^3\right)\frac{dpdq}{pq}. \tag{4.335}$$

This is the conventional form of isotropic EDQNM. Instead of deriving this equation from (4.271), it is also possible to start from (4.274). The "*byzantine use of projectors*" (Leaf Turner) is the classical way to calculate geometric coefficients, but the same result can be obtained in terms of helical modes and related amplitudes.

Isotropic turbulence allows for dramatic simplifications for all statistical theories or models, and therefore is one of the most interesting canonical flow of reference. For instance, all classical two-point triadic closure theories have the same structure, since they express $T(k)$ as a nonlocal function of $E(k)$.

Different versions of statistical theories only differ from the expression of the damping factor η in (4.326), which add nonlinear readjustment of the response function.

As shown by Orszag Orszag (1970), the use of

$$\eta(k,\ t) \sim k\sqrt{kE(k,\ t)}$$

yields a satisfactory behaviour of E when solving numerically the Lin equation, with the establishment of a Kolmogorov inertial zone. Another variant Pouquet et al. (1975) is

$$\eta(k,t) = A\sqrt{\int_0^k p^2 E(p,t)dp}, \tag{4.336}$$

which amounts to choose η as the inverse of the Corrsin time-scale, the constant A André and Lesieur (1977) being fixed by a given value of the Kolmogorov constant.

Results of the EDQNM model in pure decaying (unforced) HIT are presented below.

4.8.7.1 Well Documented Experimental Data, Moderate Reynolds number

Comparisons with Comte-Bellot and Corrsin (1966) experimental data by Vignon and Cambon (1980), Cambon et al. (1981) illustrate the relevance of EDQNM at moderate Reynolds number (see Fig. 4.21)). The experimental data are very comprehensive, with access to $E(k,t)$ at different sections downstream the grid (the downstream distance $x - x_0$ divided by the mean advection velocity U is equivalent to an elapsed time), the energy spectrum is calculated from its one-dimensional counterpart assuming isotropy. In addition, the dissipation spectrum is derived, and finally even the transfer term $T(k,t)$ is captured, comparing measures at two close sections for estimating $\Delta E/\Delta t$.

4.8.7.2 Transfer Term at Increasing Reynolds Number

Increasing the Reynolds number, a large inertial zone is easily constructed for the energy spectrum, but somewhat surprisingly, the zone of zero transfer term is much shorter, as shown in Fig. 4.22. Particularly, the flat zone of zero transfer appears only for huge values of Re_λ (typically $Re_\lambda \geq 10^4$), while a significant inertial zone appears in the energy spectrum for $10^2 < Re_\lambda < 10^3$. This result is consistent with experimental studies, in which the 4/5-Kolmogorov law for the third-order structure function was recovered only at unexpectedly high Re_λ. Therefore, it is seen that the definition of the inertial range deserves more discussion. All wave numbers located within the inertial range in the energy spectrum do not have a vanishing $T(k)$, and are therefore dynamically sensitive to production and/or dissipation. Modes which are not directly sensitive to production and viscous effects, i.e. modes which are governed by the sole triadic non-linear transfer terms, are modes with wave numbers such that $T(k) = 0$. This dynamical definition is much more stringent than the one based on the existence of a self-similar zone in the kinetic energy spectrum.

These observations that EDQNM can be used to obtain additional results about statistics in physical space, as second and third order structure functions, using

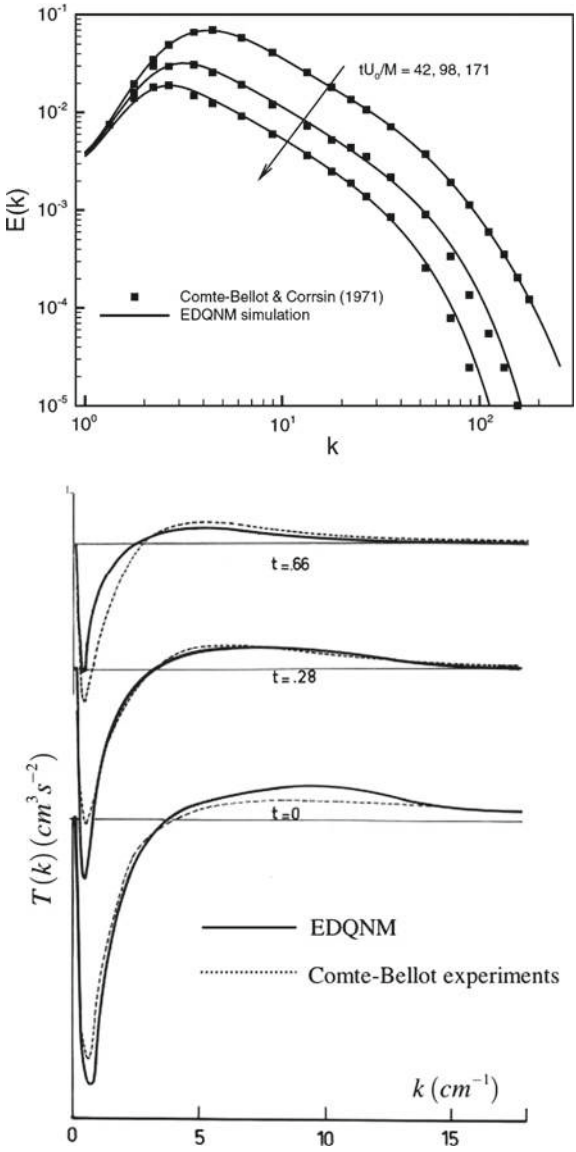

Fig. 4.21 Comparaisons of EDQNM and experimental data in decaying homogeneous isotropic turbulence. Top: turbulence kinetic energy spectrum $E(k)$ at three different locations/elapsed times (reproduced from Park and Mahesh 2007 with permission of Elsevier). Bottom: spectral energy transfer function $T(k)$ at three different locations/elapsed times (from Cambon et al. 1981)

isotropic relationship, which is well documented in Mathieu and Scott (2000), since many recent experiments focused on these statistics. However, it should be borne in mind that $E(k)$ and $T(k)$ are very informative, since they allow to compute various statistics, and they are accurately predicted by EDQNM at almost any Reynolds number. In Fig. 4.22, the transfer term is multiplied by k, in order to preserve the zero value of the integral when k is expressed in logarithmic scale, according to the

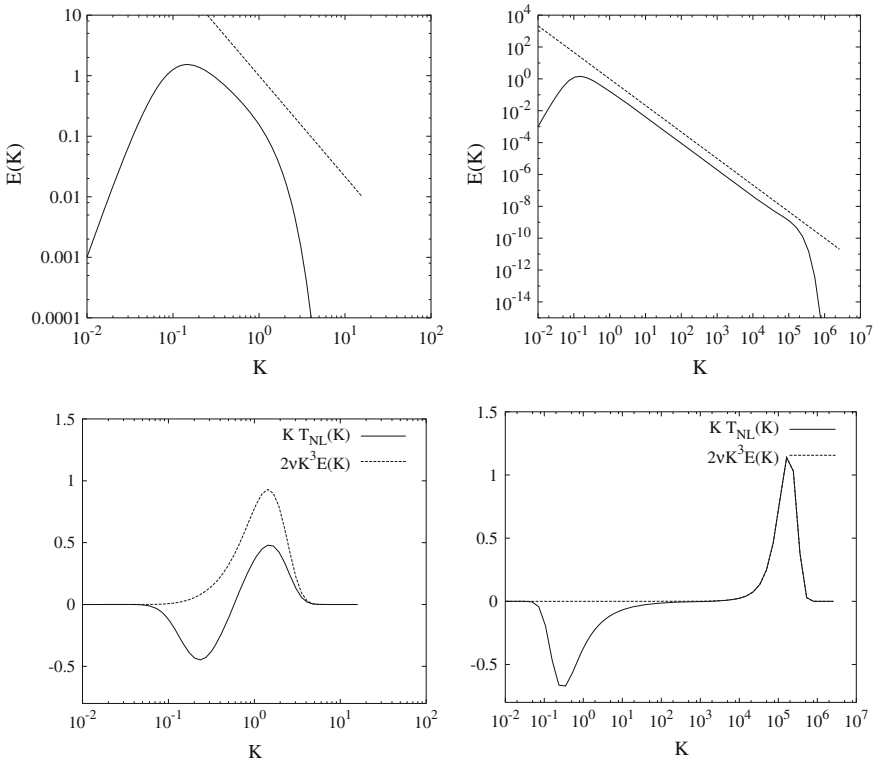

Fig. 4.22 Typical spectra (top), nonlinear transfer and viscous dissipation (bottom) in isotropic turbulence at $Re_\lambda = 30$ (left) and $Re_\lambda = 10^5$ (right). x and y scales are chosen arbitrarily. The straight lines are related to the Kolmogorov $-5/3$ slope

relation

$$kT(k)d(Lnk) = T(k)dk.$$

For the sake of clarity, the enstrophy (or dissipation up to a factor 2ν) spectrum is also multiplied by k. The positive part of the transfer and the dissipation spectrum are observed to coincide only when the transfer function exhibits a significant plateau.

4.8.7.3 Towards an Infinite Reynolds Number

EDQNM calculations can be started with zero molecular viscosity, initializing the Lin equation with a narrow-band energy spectrum. In this case, the inertial zone well develops and extends towards larger and larger k. It is conjectured that the inertial zone could reach an infinite wavenumber, say $k_{max} = \infty$, in a *finite* time, yielding a finite dissipation rate at zero viscosity: this is sometime called the 'energetic catastro-

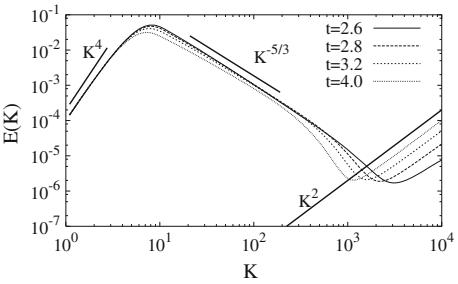

Fig. 4.23 Time evolution of the kinetic energy spectrum in the purely inviscid case using classical EDQNM. Courtesy of W. Bos and J.P. Bertoglio

phe' in the turbulence community. Unfortunately, this cannot be completely proven, because, in practice, the Lin equation closed by EDQNM cannot be solved analytically, so that a numerical solution, with discretized k and finite k_{max} is needed. Nevertheless, very large k_{max}, related to a constant logarithmic step $\Delta k/k = Constant$, can be used, without possible counterpart in DNS. As a very classical behaviour, at least in DNS, spectral energy tends to accumulate near the cut-off wave-number k_{max}, so that a viscous term ought to be introduced in order to avoid an energy peak at the highest wave-vector. The only advantage of EDQNM with respect to DNS in this case is the huge value of k_{max} related with a huge (but not infinite) Reynolds number, which can be reached with modest computational ressources.

Very recently, following a calculation of truncated inviscid Euler equations by Brachet and coworkers (Cichowlas et al. 2005; Bos and Bertoglio 2006a) used the conventional EDQNM model to study the accumulation of spectral energy at a given (very high) k_{max} with zero viscosity. As a nice result, both a thermalized[19] tail following a k^2 law and a large inertial range with $k^{-5/3}$ behavior arise, separated by a sink, as shown in Fig. 4.23.

This sink induces a kind of conventional dissipative range —but at zero laminar viscosity—, probably mediated by the non-local eddy viscosity (Kraichnan 1971, 1976; Lesieur and Schertzer 1978), and is even clearer in EDQNM than in inviscid truncated DNS. Here, the smallest scales act as the molecular motion in real viscous flows, giving a nice illustration of the turbulent eddy viscosity concept.

4.8.7.4 Recent Improvements

A recent improvement, which renders EDQNM closer to a self-consistent theory, consists of evaluating the eddy damping $\mu(k, t)$ using an additional dynamical equation for a velocity-displacement cross correlation Bos and Bertoglio (2006b). As shown in Fig. 4.24, a realistic value of the Kolmogorov constant $K_0 \sim 1.73$ is derived, without need to specify it a priori in the model for μ, as in Eq. (4.336) via A.

[19] Thermalized is used here by analogy with the random molecular motion in which the macroscopic quantities such as temperature and pressure originate.

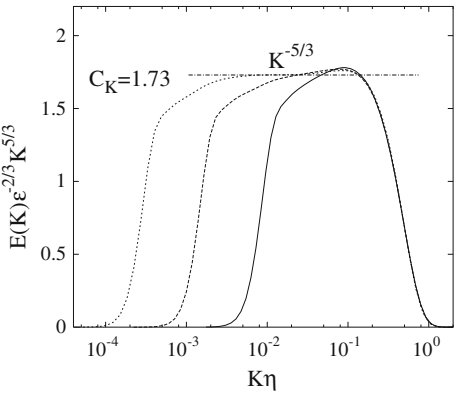

Fig. 4.24 Compensated spectrum $E(k)\varepsilon^{-2/3}k^{5/3}$ in isotropic turbulence computed using EDQNM with self-consistent eddy damping. The plateau correspond to the value of the Kolmogorov constant K_0 (denoted C_K in the figure). Courtesy of W. Bos and J.P. Bertoglio

It is also interesting to calculate by the EDQNM procedure, not only the contribution of triple correlations to the transfer term (a typical cubic moment at two point), which also generates the third order structure function, but more complex cubic statistics in three points, which are very difficult to obtain from experiments or even from DNS/LES (very noisy terms). For instance, triple vorticity (not only velocity) correlations at three-point (which is related to their detailed distribution in terms of triads) can be calculated in a systematic way, only from the given energy spectrum. Applications to the statistics of vorticity, with an answer from statistical theory to the problem of cyclonic/anticyclonic asymmetry in rotating turbulence, is presented in Chap. 7.

4.9 Pressure Field: Spectrum, Scales and Time Evolution

4.9.1 Physical Space Analysis

Statistical moments of the fluctuating pressure field p' are tied to those of the fluctuating velocity field u'. This topic has been extensively studied by the scientific community, from seminal contributions by Batchelor (1951) and Heisenberg (1948) to recent contributions, e.g. Lesieur et al. (1999), Donzis et al. (2012), Meldi and Sagaut (2013b). Following Batchelor's work, pressure fluctuations can be analyzed by the use of the Poisson equation, which is obtained by taking the divergence of Navier-Stokes equations for an incompressible flow. In incompressible isotropic turbulence one obtains:

$$\frac{1}{\rho}\nabla^2 p' = -\frac{\partial u_i}{\partial x_j}\frac{\partial u_j}{\partial x_i} = \frac{\partial^2}{\partial x_i \partial x_j}(u_i u_j) \tag{4.337}$$

whose solution is

$$\frac{1}{\rho}p'(\boldsymbol{x},t) = -\int \frac{\partial^2}{\partial y_i \partial y_j}\left(u_i u_j - \overline{u_i u_j}\right) G(\boldsymbol{x},\boldsymbol{y}) d^3\boldsymbol{y} \tag{4.338}$$

with $G(\boldsymbol{x},\boldsymbol{y}) = 1/4\pi|\boldsymbol{x}-\boldsymbol{y}|$ the Green function associated to the Laplacian operator in unbounded three-dimensional domains. The two-point single-time pressure correlation $R_{pp}(\boldsymbol{x},\boldsymbol{x}') = \overline{p'(\boldsymbol{x},t)p'(\boldsymbol{x}',t)}$ is obtained in a straightforward way:

$$\frac{1}{\rho^2}R_{pp}(\boldsymbol{x},\boldsymbol{x}') = \iint \left(\frac{\partial^4 \overline{u_i u_j u'_l u'_m}}{\partial y_i \partial y_j \partial y'_l \partial y'_m} - \frac{\partial^2 \overline{u_i u_j}}{\partial y_i \partial y_j}\frac{\partial^2 \overline{u'_l u'_m}}{\partial y'_l \partial y'_m}\right) G(\boldsymbol{x},\boldsymbol{y})G(\boldsymbol{x}',\boldsymbol{y}')d^3\boldsymbol{y}d^3\boldsymbol{y}' \tag{4.339}$$

where primed quantities are evaluated at position $\boldsymbol{y}'$, which can be rewritten accounting for isotropy as

$$\frac{1}{\rho^2}R_{pp}(\boldsymbol{\xi}) = \iint \frac{\partial^4 R_{ij,lm}(\boldsymbol{r})}{\partial r_i \partial r_j \partial r_l \partial r_m} G(\boldsymbol{x},\boldsymbol{y})G(\boldsymbol{x}+\boldsymbol{\xi},\boldsymbol{y}+\boldsymbol{r})d^3\boldsymbol{y}d^3\boldsymbol{r} \tag{4.340}$$

with

$$R_{ij,lm}(\boldsymbol{r}) = \overline{u_i(\boldsymbol{y})u_j(\boldsymbol{y})u_l(\boldsymbol{y}+\boldsymbol{r})u_m(\boldsymbol{y}+\boldsymbol{r})} - \overline{u_i(\boldsymbol{y})u_j(\boldsymbol{y})}\ \overline{u_l(\boldsymbol{y}+\boldsymbol{r})u_m(\boldsymbol{y}+\boldsymbol{r})},$$

where $\boldsymbol{y}' = \boldsymbol{y}+\boldsymbol{r}$. The fourth-order two-point correlations $R_{ij,lm}(\boldsymbol{r})$ can be expressed as a linear combination of products of second-order two-point correlations $R_{ij}(\boldsymbol{r}) = \overline{u_i(\boldsymbol{y})u_j(\boldsymbol{y}+\boldsymbol{r})}$ thanks to the Quasi-Normal hypothesis (see Batchelor 1951), leading to a closed expression. Using the isotropic expression of $R_{ij}(\boldsymbol{r})$ in terms of the longitudinal velocity correlation function $f(r)$:

$$R_{ij}(\boldsymbol{r}) = \frac{2}{3}\mathcal{K}\left(\left[f(r) + \frac{1}{2}rf'(r)\right]\delta_{ij} - \frac{1}{2}f'(r)\frac{r_i r_j}{r^2}\right) \tag{4.341}$$

one obtains

$$R_{pp}(r,t) = 2\left(u'^2\right)^2 \int_r^{+\infty}\left(y - \frac{r^2}{y}\right)\left[f'(y)\right]^2 dy. \tag{4.342}$$

The pressure fluctuation variance is then computed as

$$\frac{1}{\rho^2}\overline{p'^2} = R_{pp}(0,t) = 2\left(u'^2\right)^2 \int_0^{+\infty} y\left[f'(y)\right]^2 dy. \tag{4.343}$$

A similar relation was obtained by Heisenberg for the fluctuating pressure gradient variance:

$$\frac{1}{\rho^2}\overline{(\nabla p')^2} = -3\left.\frac{\partial^2 R_{pp}}{\partial r^2}\right|_{r=0} = 12\left(u'^2\right)^2 \int_0^{+\infty}\frac{1}{y}\left[f'(y)\right]^2 dy. \tag{4.344}$$

4.9.2 Fourier Space Analysis

Dual expressions can be obtained in Fourier space. Introducing the pressure spectrum $E_{pp}(k,t)$ which is defined as the Fourier transform of the pressure correlation $R_{pp}(r,t)$, one has

$$\frac{1}{\rho^2}\overline{p'^2} = \int_0^\infty E_{pp}(k,t)dk, \tag{4.345}$$

$$\frac{1}{\rho^2}\overline{(\nabla p')^2} = \int_0^\infty k^2 E_{pp}(k,t)dk. \tag{4.346}$$

Thanks to the Poisson equation and the Quasi-Normal hypothesis, the pressure spectrum can be written as a function of the energy spectrum:

$$E_{pp}(k) = \frac{k^2}{4\pi}\int_{p+q=k} E(p)E(q)\frac{\sin^4\beta}{p^4}dq \tag{4.347}$$

where β is the angle facing k in the triangle formed by the three vectors k, p, q. Heisenberg (1948) also derived an expression for the pressure gradient variance:

$$\frac{1}{\rho^2}\overline{(\nabla p')^2} = \int_0^\infty\int_0^\infty E(p,t)E(q,t)\frac{sin^4\beta}{(p-q)^2}dpdq. \tag{4.348}$$

An integral lengthscale L_p for pressure fluctuations is also defined as

$$L_p = \frac{\pi}{2\overline{p'^2}}\int_0^{+\infty}\frac{E_{pp}(k)}{k}dk. \tag{4.349}$$

Some interesting comments should be done here. First, it is important to note that the Quasi-Normal approximation yields physical results when deriving an expression for the pressure correlations, while it is known to yield unphysical results when closing equations for the energy spectrum. This may be at least partially understood reminding that pressure is a non-local, integral quantity (according to the integral solution of the Poisson equation) which is expected to be smoother than the velocity field and therefore less sensitive to intermittency effects that a responsible for the breakdown of Gaussianity. Second, the shape of the pressure spectrum at very large scales is independent of the slope of the energy spectrum at these scales, i.e. it is independent of the parameter σ. As a matter of fact, one can show that the infrared pressure spectrum behaves as

$$E_{pp}(k\to 0,t) \sim A_p(t)k^2, \quad A_p(t) = \frac{8}{15}\int_0^\infty \frac{E^2(q,t)}{q^2}dq. \tag{4.350}$$

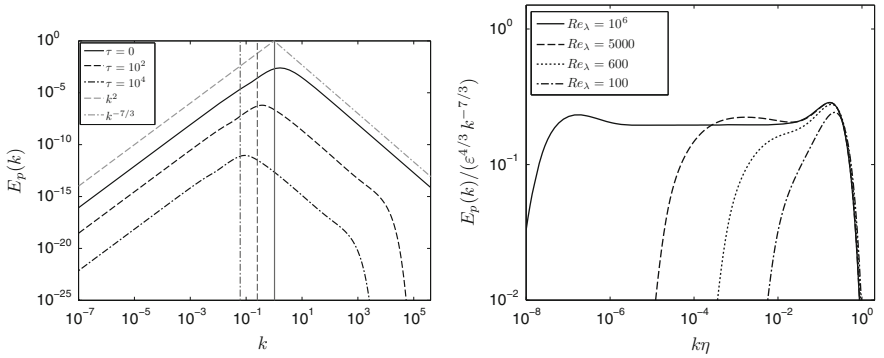

Fig. 4.25 Pressure spectrum $E_{pp}(k)$ (left) and compensated pressure spectrum $\varepsilon^{-4/3}k^{7/3}E_{pp}(k)$ (right) from EDQNM simulations. From Meldi and Sagaut (2013b) with permission of CUP

Third, at high Reynolds number, $E_{pp}(k)$ exhibits an inertial range at small scales, with

$$E_{pp}(k,t) = \varepsilon^{4/3}k^{-7/3} \quad kL_p \gg 1 \quad \text{(inertial range)}. \tag{4.351}$$

The existence of this $-7/3$ inertial range is supported by both theoretical analysis, EDQNM results and a few numerical simulations and experiments. It is much harder to observed than the $-5/3$ inertial range on the energy spectrum, since Finite Reynolds Number effects are stronger on pressure fluctuations. They lead to the existence of a strong bottleneck effect on $E_{pp}(k)$, which can mask the inertial range. This can be understood reminding that pressure spectrum is related to two-points fourth-order velocity correlations while the energy spectrum depends on two-points second-order correlations. EDQNM results show that $Re_\lambda \geq 10^4$ is necessary to observe a clean plateau on the compensated pressure spectrum associated to the inertial range, as shown in Fig. 4.25.

4.9.3 Time Evolution in Freely Decaying Isotropic Turbulence

Time evolution of pressure-related statistical quantities can be investigated in the same ways as for the velocity-related statistical quantities. The Comte-Bellot–Corrsin theory can be extended in a straigthforward way considering an idealized high-Reynolds initial condition such that

$$E(k,t) = \begin{cases} C(t)k^\sigma & kL(t) \leq 1 \\ \varepsilon^{2/3}k^{-5/3} & kL(t) \geq 1 \end{cases}, \quad E_{pp}(k,t) = \begin{cases} A_p(t)k^2 & kL(t) \leq 1 \\ \varepsilon^{4/3}k^{-7/3} & kL(t) \geq 1 \end{cases}, \tag{4.352}$$

Table 4.13 Analytical formulas for the prediction of the power-law exponents of the decay of the main pressure-related statistical quantities given by the Comte-Bellot–Corrsin theory. σ denotes the slope of $E(k)$ at small wave numbers and p is the correction for breakdown of the Permanence of Large Eddies hypothesis

$\overline{p'^2}$	$\overline{(\nabla p')^2}$	L_p	A_p
$-4\dfrac{(\sigma-p+1)}{(\sigma-p+3)}$	$-\dfrac{9(\sigma-p)+15)}{2(\sigma-p+3)}$	$\dfrac{2}{(\sigma-p+3)}$	$3-7\dfrac{(\sigma-p+1)}{(\sigma-p+3)}$

where it is assumed that $E(k)$ and $E_{pp}(k)$ have a peak at the same wavenumber, as observed in DNS and LES by Lesieur et al. (1999). Main results dealing with time exponents of pressure-related quantities are summarized in Table 4.13. These predictions are in very good agreement with EDQNM results. Looking at predicted exponents, one recovers the well known fact that pressure fluctuations decay much faster than velocity fluctuations, since the decay exponent of $\overline{p'^2}$ is exactly twice that of $\mathcal{K}(t)$. The same observation holds for gradients, since $\overline{(\nabla p')^2}$ decays 1.5 times faster than ε.

4.10 Topological Analysis, Coherent Events and Related Dynamics

As mentioned above, it has been known since the direct observations by Siggia (1981) that coherent structures exist in isotropic turbulence.[20] A typical instantaneous snapshot obtained via a high-resolution 4096^3 DNS of isotropic turbulence at $Re_\lambda = 732$ performed by Kaneda an colleagues is displayed in Fig. 4.26. Small elongated worm-like vortices are observed, which are grouped in larger-scale coherent packets. Large empty volumes are also observed, showing the spatial intermittent character of vorticity.

These coherent structures may divided grouped into two classes: *vortex tubes* (also referred to as *worms* or *vortex filaments*) and *vortex sheets*. The former are identified as elongated, tubelike vortices mainly subjected to an axial strain, while the latter are related to vorticity sheets that experience a plain strain.

The existence of these events raises several important questions for both the analysis of isotropic turbulence study and the general turbulence theory:

(i) How to define these events, or, more precisely, how to define them unequivocally?
(ii) What is the dynamics of these events: how are they generated? What is their life cycle ? Do they exhibit some universal features?

[20] While the observation of these structure is recent, it is worth noting that the idea that turbulent dissipation can be tied to a random distribution of vortex tubes and vortex sheets goes back to Townsend in 1951.

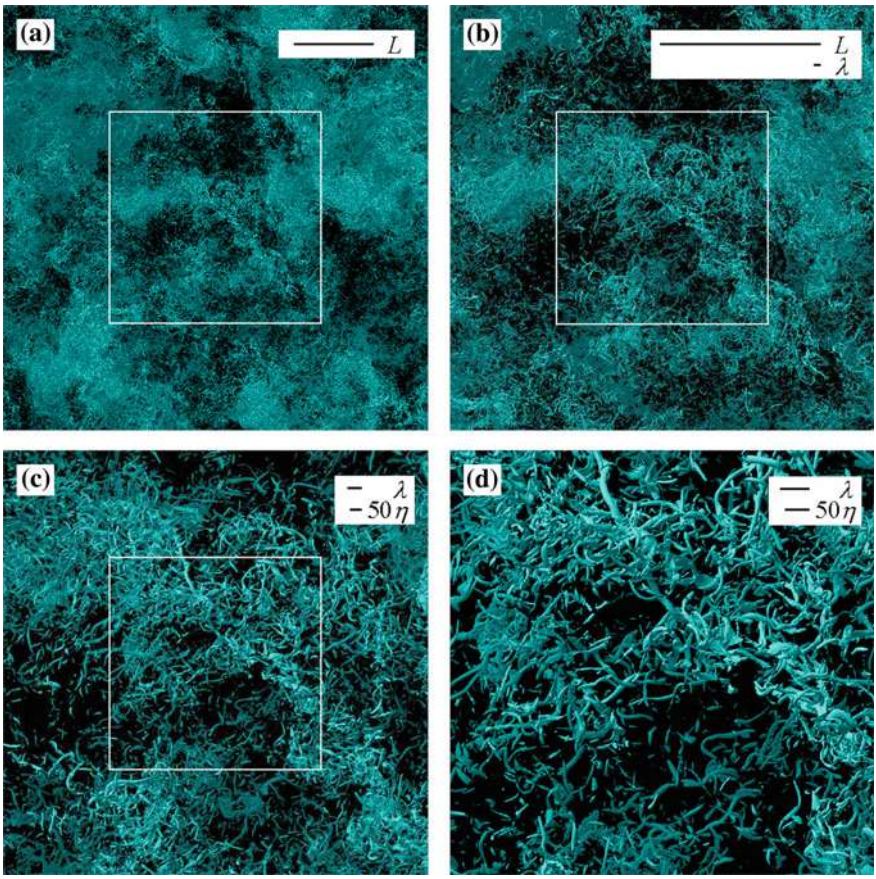

Fig. 4.26 Instantaneous vorticity contours in high-resolution DNS of isotropic turbulence at $Re_\lambda = 732$ at different zoom levels. The domain size (in Kolmogorov length units) is $(5984^2 \times 1496)\eta^3$ **a** Full-domain view; **b** Zoom of the central region with size $(2992^2 \times 1496)\eta^3$ of (**a**) bounded by the white rectangular line; **c** New of the central region of (**b**) in a domain equal to $1496^3\eta^3$; **d** New zoom of the central region of (**c**) in a $(748^2 \times 1496)\eta^3$ volume. Courtesy of Y. Kaneda, Nagoya University, Japan

(iii) What is their role in the isotropic turbulence dynamics? How are they related to well known features such as the kinetic energy cascade, the turbulent kinetic energy dissipation and the internal intermittency?

Recent results dealing with these issues will be surveyed below. But let us emphasize here that, despite the impressive amount of efforts devoted to the analysis of isotropic turbulence, a global complete theory for the coherent events it contains is still lacking.

4.10.1 Topological Analysis of Isotropic Turbulence

The topological analysis of isotropic turbulence first brings in the problem of defining the various coherent events. A huge amount of works has been devoted to this problem. The proposed techniques can be divided roughly into the following two classes.

The first approach consists in projecting the instantaneous turbulent field onto objects (sometimes referred to as the 'cartoons of turbulence') whose definitions are given analytically. It involves a local tuning the control parameters that appear in the analytical model to obtain the best fit with the local turbulent field, leading to the definition of a pattern tracking algorithm. A complete survey of analytical solutions for an isolated viscous vortex has recently be performed by Rossi (2000). Two useful analytical models, namely the Burger's vortex and the Burger's vortex sheet models, are given below.

The *Burgers' vortex* is a model for an axially stretched viscous vortex. Denoting z the direction of the vortex axis, Γ its circulation, α the time-independent rate of strain and ν the viscosity, the cylindrical velocity component are given by

$$u_z = 2\alpha z, \quad u_r = -\alpha r, \quad u_\theta = \frac{\Gamma}{2\pi r}\left(1 - e^{-\zeta}\right), \tag{4.353}$$

where $\zeta = r^2/4\delta^2$ and

$$\delta^2 = \frac{\nu}{\alpha} + \left(\delta_0^2 - \frac{\nu}{\alpha}\right) e^{-\alpha t} \tag{4.354}$$

with $\delta(0) = \delta_0$ and t denotes the time. The axial vorticity is found to be equal to (other component are identically zero):

$$\omega_z = \frac{\Gamma}{\pi\delta^2} e^{-\zeta}. \tag{4.355}$$

The induced kinetic energy dissipation field is

$$\varepsilon = 12\nu\alpha^2 + \frac{\nu\Gamma^2}{16\pi^2\delta^4}\left(e^{-\zeta} - \frac{1 - e^{-\zeta}}{\zeta}\right)^2. \tag{4.356}$$

An asymptotic equilibrium solution is found for large times, i.e. for $\delta^2 = \nu/\alpha$. For this solution, diffusion and convection are balanced and the total dissipation is found to be independent of the viscosity ν. It is worth noting that the dissipation is negligible outside a circular area of order δ^2, while its peak is proportional to $\nu\Gamma^2/\delta^4$. The total rate of vortex-induced dissipation par unit length scales as $\nu\Gamma^2/\delta^2$.

The *Burgers' vortex sheet* is defined as the superposition of a plane potential flow and a plane shear layer. It corresponds to a diffusing vortex sheet with stretched vortex lines. Let us consider the case in which the shear layer vorticity is along the z axis and varies in the y direction. The Cartesian components of potential flow field are given by

$$u_p = 0, v_p = -\alpha y, \quad w_p = \alpha z. \tag{4.357}$$

The vorticity field of the Burgers' vortex sheet is given by

$$\omega_z = -\frac{4}{\sqrt{\pi}} \frac{\Delta U}{\delta} e^{-y^2/\delta^2}, \tag{4.358}$$

where ΔU is the velocity jump across the shear layer and δ is defined as

$$\delta^2 = \frac{2\nu}{\alpha} \left(1 - e^{-2\alpha t}\right). \tag{4.359}$$

The equilibrium solution corresponds to $\delta^2 = 2\nu/\alpha$.

Both Burgers' vortex model and Burgers' vortex sheet model have been observed to compare favorably with local features of simulated turbulent field, and can therefore be used as theoretical models to describe turbulence dynamics.

Before discussing other definitions, let us first recall some results dealing with the topological analysis of instantaneous incompressible isotropic turbulent fields. Most analyses rely on the relation that exists between the vorticity vector and the eigenvectors of the strain rate tensor $\mathbf{S}$. Let us note $\hat{\boldsymbol{e}}_i (i = 1, 2, 3)$ the three eigenvectors of $\mathbf{S}$ and $\hat{\lambda}_i$ the corresponding eigenvalues. In the following, the eigenvalues are reordered so that $\hat{\lambda}_1 \geq \hat{\lambda}_2 \geq \hat{\lambda}_3$. The incompressibility constraint yields

$$\hat{\lambda}_1 + \hat{\lambda}_2 + \hat{\lambda}_3 = 0, \tag{4.360}$$

meaning that there is at least one positive ($\hat{\lambda}_1$) and one negative ($\hat{\lambda}_3$) eigenvalue. The intermediate eigenvalue $\hat{\lambda}_2$ can be either negative or positive. Both numerical and experimental data show that the vorticity vector is preferentially aligned with $\hat{\boldsymbol{e}}_2$. Lund and Rogers (1994) defined the following non-dimensional parameter

$$\hat{\lambda}^* = -\frac{3\sqrt{6}\hat{\lambda}_1\hat{\lambda}_2\hat{\lambda}_3}{\left(\hat{\lambda}_1^2\hat{\lambda}_2^2\hat{\lambda}_3^2\right)^{3/2}}, \tag{4.361}$$

which has the remarquable property that it ranges from -1 to 1 and that its p.d.f. is uniform for a Gaussian random velocity field. This parameter is a measure of the local deformations caused by the strain-rate tensor. Axisymmetric extension and axisymmetric contraction occur when $\hat{\lambda}^* = 1$ and $\hat{\lambda}^* = -1$, respectively, while plane shear corresponds to $\hat{\lambda}^* = 0$. Lund and Rogers observed in DNS data that the most probable case in isotropic turbulence is axisymmetric extension, and that this state is well correlated with region of high dissipation.

The preferential alignement of $\boldsymbol{\omega}$ with $\hat{\boldsymbol{e}}_2$ is a pure kinematic effect. Jimenez Jimenez (1992) showed that in the vicinity of a vortex whose maximum vorticity is large with respect to that in the background flow the vorticity is automatically aligned with the intermediate eigenvector. It can also be shown Horiuti 2001, Andreotti 1997,

Nomura and Post 1998 that this alignement is the result of the crossover of the eigenvalues at a certain distance from the vortex center in Burgers analytical vortex model.[21]

The second approach for finding reliable definitions of coherent events relies on the local analysis of the velocity gradient tensor $\nabla \boldsymbol{u} = \mathbf{S} + \mathbf{W}$, intuition telling us that a vortex will be a region where the vortical part dominates over the irrotational part of the strain.

The first general, Galilean-invariant three-dimensional vortex criterion was proposed by Hunt and coworkers (Hunt et al. 1988). This criterion, referred to as the *Q-criterion*, defines a vortex as a spatial region where the second invariant of the velocity gradient tensor is positive:

$$Q = \frac{1}{2}\left(|\mathbf{W}|^2 - |\mathbf{S}|^2\right) = -\frac{1}{2}\mathrm{tr}\left(\mathbf{S}^2 + \mathbf{W}^2\right) > 0, \tag{4.364}$$

where $|\mathbf{W}|$ and $|\mathbf{S}|$ are Euclidian norms. The *Q-criterion* can be related to the pressure field, since Q has the same sign as the Laplacian of the pressure field. Using this criterion is equivalent to say that vortices are regions where $\nabla^2 p < 0$. It is worth noting that, in two-dimensional flows, this criterion is equivalent to the Okubo-Weiss criterion derived independently by Okubo in 1970 and Weiss in 1991. Tanaka and Kida (1993) observed that the criterion given by Eq. (4.364) does not allow to distinguish between vortex tube cores and curved vortex sheets (discussed below). To isolate vortex tube cores, they used the threshold $|\mathbf{W}|^2 > 2|\mathbf{S}|^2$.

Another three-dimensional criterion is the $\Delta - criterion$ (Chong et al. 1990). Here, a vortex is a region where

$$\Delta = \left(\frac{Q}{3}\right)^2 + \left(\frac{\det(\nabla \boldsymbol{u})}{2}\right)^2 > 0. \tag{4.365}$$

The *swirling length* criterion defined by Zhou and coworkers (Zhou et al. 1999) is an extension of the $\Delta - criterion$. It relies on the observation that in regions where the tensor ∇u has two complex conjugate eigenvalues $\tilde{\lambda}_{cr} \pm i\tilde{\lambda}_{ci}$ and a real eigenvalue $\tilde{\lambda}_c$, $\tilde{\lambda}_{ci}$ and $\tilde{\lambda}_r$ can be interpreted has a measure of the local swirling rate inside the vortex (in the plane defined by the eigenvectors associated with the complex eigenvalues) and a local stretching/compression strength along the last eigenvector. A vortex tube is defined as a region satisfying the $\Delta - criterion$ and in which $\tilde{\lambda}_{ci}$ is above an arbitrary threshold.

---

[21] This can be directly seen looking at the analytical expressions of the eigenvalues obtained for the Burgers vortex:

$$\hat{\lambda}_{\pm} = \frac{\alpha}{2}\left(-1 \pm Re_\Gamma\left(\frac{4\nu}{\alpha r^2}\left(1 - e^{-\alpha r^2/4\nu}\right) - e^{-\alpha r^2/4\nu}\right)\right), \tag{4.362}$$

$$\hat{\lambda}_z = \alpha, \tag{4.363}$$

where $Re_\Gamma = \Gamma/4\pi\nu$ is the circulation-based Reynolds number. If Re_Γ is high enough, the crossover between $\hat{\lambda}_+$ and $\hat{\lambda}_z$ occurs, i.e. there exists a region with $\hat{\lambda}_+ \geq \hat{\lambda}_z$.

This idea of using the local frame associated with the eigenvectors of the velocity gradient tensor was further developed by Chakraborty and coworkers (Chakraborty et al. 2005), who proposed the *enhanced swirling strength criterion*. Following this criterion, a vortex is region where

$$\tilde{\lambda}_{ci} \geq \epsilon \quad \text{and} \quad -\delta' \leq \frac{\tilde{\lambda}_{cr}}{\tilde{\lambda}_{ci}} \leq \delta, \tag{4.366}$$

where ϵ, δ and δ' are positive threshold values.

Another popular criterion, referred to as the $\lambda_2 - criterion$, was proposed by Jeong and Hussain (1995). According to this criterion, a vortex is defined as a region where the intermediate eigenvalue (noted λ_2 if the eigenvalues are reordered in decreasing order) of the symmetric matrix $\mathbf{S}^2 + \mathbf{W}^2$ is negative:

$$\lambda_2 < 0. \tag{4.367}$$

A more recent criterion was proposed by Horiuti (2001), which can be seen as an improvement of the λ_2 criterion. The three eigenvalues of the tensor $\mathbf{S}^2 + \mathbf{W}^2$ are renamed as λ_z, λ_+ and λ_-, where λ_z corresponds to the eigenvector which is the most aligned with the vorticity vector, and λ_+ and λ_- are the largest and smallest remaining eigenvalues, respectively. Using these definitions, Horiuti defines a vortex as region where

$$0 > \lambda_+ \geq \lambda_-. \tag{4.368}$$

This criterion isolates vorticity-dominated region similar to a core region of a Burgers' vortex tube.

While these criterion perform similarly well in simple flows, their use in turbulent shear flows and flows submitted to strong rotation is more problematic, since there are not always able to separate the mean flow contribution from the turbulent one.

The case of vorticity sheets seems to be more difficult to handle and received less attention than the vortex case. A reason for that is certainly that these structures are more disorganized and less stable than vortex tubes. Therefore, their observation is more difficult. Another difficulty is that the category of vortex sheets encompasses different objects. Horiuti (2001) makes the distinction between *flat sheets* similar to Burgers' vortex layer and *curved sheets* that exist in the circumference of the core region of a vortex tube. These two kinds of vorticity sheets may have different dynamical features, since both vorticity and strain are dominant in flat sheets, while strain is predominant is curved sheets. The flat sheets are also referred to as *strong vortex layer* by Tanaka and Kida (1993), who defined them as regions where both vorticity and strain rate take large comparable values.[22] The criterion used by Tanaka and Kida is

$$\frac{1}{2} < \frac{|\mathbf{W}|^2}{|\mathbf{S}|^2} < \frac{4}{3}. \tag{4.369}$$

[22]These authors also define a *strong vortex tube* as a region with large vorticity and small strain rate.

Based on the same reordering of the eigenvalues of the symmetric tensor $\mathbf{S}^2+\mathbf{W}^2$ as for the vortex tube definition given in Eq. (4.368), Horiuti (2001) defines curved sheets as regions where

$$\lambda_+ \geq \lambda_- > 0, \tag{4.370}$$

whereas flat sheet definition is

$$\lambda_+ \geq 0 \geq \lambda_-. \tag{4.371}$$

This definition is observed to educe vortex sheets, but also vortex tube cores in some cases. To get a more accurate definition, Horiuti and Takagi (2005) propose a new definition based on the eigendecomposition of the symmetric second-order velocity gradient tensor $\mathbf{SW}+\mathbf{WS}$. Denoting λ^s_z, λ^s_+ and λ^s_- the eigenvalue associated with the eigenvector which is maximally aligned with the vorticity vector, the largest and the smallest remaining eigenvalue, respectively, it is observed that vortex sheets can be educed using the criterion

$$\lambda^s_+ > \epsilon, \tag{4.372}$$

where ϵ is an arbitrary positive threshold. The vortex sheet normal vector is accurately computed as $\nabla\lambda^s_+$.

4.10.2 Vortex Tube: Statistical Properties and Dynamics

Vortex tube-like structures have been extensively analyzed using both Direct Numerical Simulations and laboratory experiments Jimenez et al. (1993). Probability density functions of vortex tube main features are displayed in Figs. 4.27, 4.28, 4.29 and 4.30. These data were obtained by Jimenez and Wray from Direct Numerical Simulations Jimenez and Wray (1998) of isotropic turbulence for Taylor-scale-based Reynolds numbers Re_λ ranging from 37 to 168 using a vortex-tracking method which relies on the projection of the instantaneous field onto the Burgers' vortex model. It is worth noting that while the normalized peak values are Reynolds-number independent (showing that the vortex tubes exhibit some universal features), the p.d.f. tails is sometimes observed to be sensitive to the Reynolds number (showing that some extreme events do not hae the same dependency with respect to the Reynolds number as the 'mean' vortex tubes).

The main conclusions of Jimenez and coworkers are the following:

- The equilibrium Burgers' vortex model is adequate to describe vortex tubes found in isotropic turbulence, as shown by the peak in the pdf displayed in Fig. 4.28. This point is also supported by results dealing with joint p.d.f.s of stretching and radius and of radius and azimuthal velocity.
- The radius of a vortex tube scales like the Kolmogorov scale η, a typical value being $R \simeq 4-4.2\eta$.

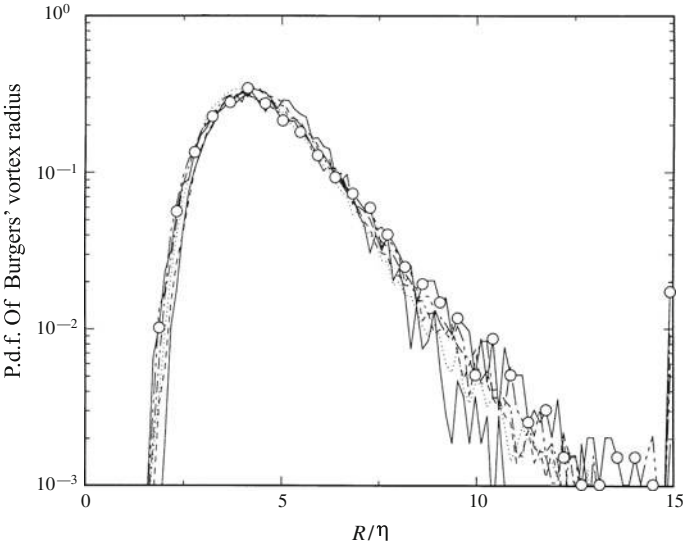

Fig. 4.27 P.d.f. of the radius R of the vortex tube normalized with the Kolmogorov scale η. Different lines and symbols are related to different values of the Reynolds number. From Jimenez and Wray (1998) with permission of CUP

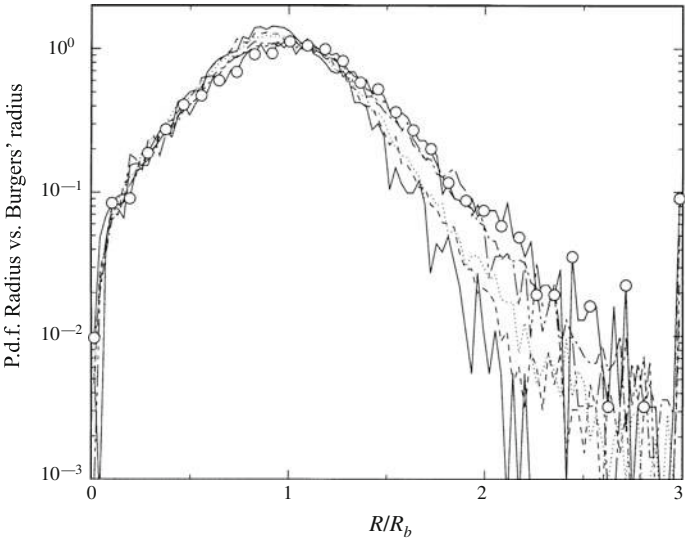

Fig. 4.28 P.d.f. of the radius R of the vortex tube normalized with the local equilibrium Burgers' radius R_b. Burgers' radius is defined as $R_b = 2\sqrt{\nu/\alpha}$, where ν is the viscosity and α the local axial stretching. Different lines and symbols are related to different values of the Reynolds number. From Jimenez and Wray (1998) with permission of CUP

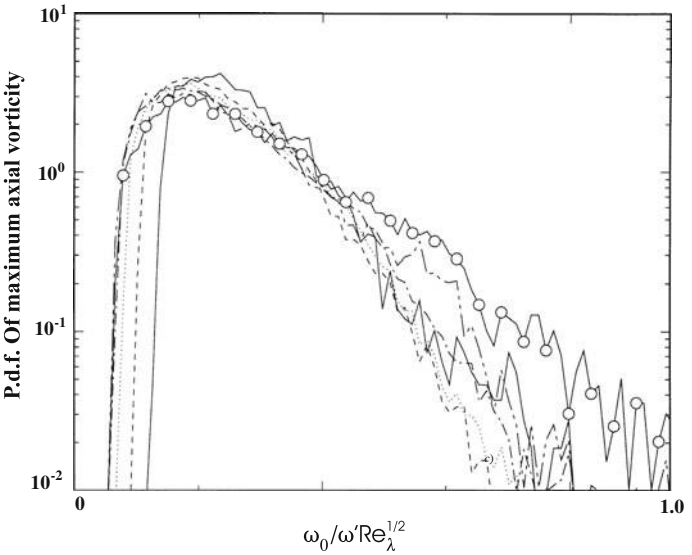

Fig. 4.29 P.d.f. normalized maximum axial vorticity of the vortex tube. Different lines and symbols are related to different values of the Reynolds number. From Jimenez and Wray (1998) with permission of CUP

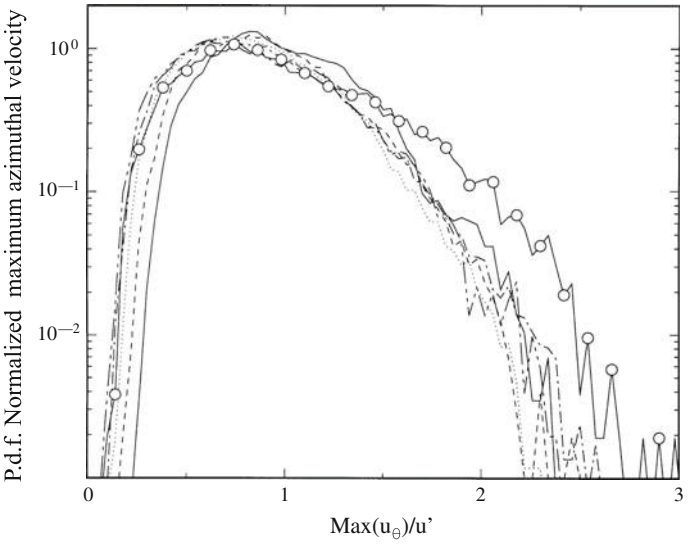

Fig. 4.30 P.d.f. maximum azimuthal velocity u_0 of the vortex tube. Assuming that the vorticity profile is Gaussian, one has $u_0 = 0.319 R\omega_0$. Different lines and symbols are related to different values of the Reynolds number. From Jimenez and Wray (1998) with permission of CUP

- The mean stretching experienced by the vortex tubes scales with ω' independently of Re_λ. The statistics of the stretching along the vortex tube axis are the same as in the background turbulent flow, showing that the later is responsible for the main part of vortex stretching.
  The maximum of the axial strain felt by the vortices scales like $O(\omega' Re_\lambda^{1/2})$. Since it is Reynolds number-dependent, it is believed to be due to self-stretching.[23]
- The maximum vorticity in the vortex tube core scales like $O(\omega' Re_\lambda^{1/2})$. This is in agreement with the idea that vortex tube are more intense at higher Reynolds number.
- The azimuthal velocity, or equivalently the azimuthal velocity increment Δu across the vortex tube diameter scales with the turbulent intensity u'. Since u' is associated with large-scale energy containing scales, this scaling law is inconsistent with Kolmogorov scaling, which states that the velocity increment across distances of $O(\eta)$ should be $O(u' Re_\lambda^{-1/2})$. A Re_λ-independent upper bound for the azimuthal velocity is approximately $2.5u'$, this limit being reached by vortex tubes with the smallest radii. A rationale for that is given below.
- The circulation-based Reynolds number of the vortices observed in Jimenez and Wray (1998) is about $20 Re_\lambda^{1/2}$.
- The vortex tube length, defined in terms of the autocorrelation of some vortex tube property ϕ as

$$L_\phi = \int_0^{s_0} \frac{\overline{\phi(s'+s)\phi(s')}}{\overline{\phi^2(s')}} ds, \tag{4.373}$$

  where s_0 denotes the point where the autocorrelation first vanishes, depends on the quantity ϕ. Results show that two groups must be distinguished. The lengths based on vortex radius and axial vorticity are $O(\eta Re_\lambda^{1/2})$, i.e. scale with the Taylor microscale λ, while the one based on the axial stretching varies like the Kolmogorov scale η.
  The fact that the correlation length of axial stretching is of the order of the vortex tube diameter (i.e. of the Kolmogorov scale, which is also the correlation length of the velocity gradient in the whole flow) shows that the main stretching experienced by the vortex tubes originates in the background flow.
  The existence of the second scale λ can be understood as follows. Let us consider a vortex tube of length $l \ll \lambda$. The line integral of the vorticity stretching is given by

$$\underbrace{\int_0^l \boldsymbol{t}.\mathbf{S}\boldsymbol{t} dl}_{O(\omega' L)} = \boldsymbol{u}\cdot\boldsymbol{t}\|_0^l - \underbrace{\int_0^l \frac{\boldsymbol{u}\cdot\boldsymbol{n}}{\mathcal{R}} dl}_{O(Lu'\mathcal{R}^{-1})}, \tag{4.374}$$

  where $\boldsymbol{n}$, $\boldsymbol{t}$, $\boldsymbol{u}$, $\mathbf{S}$ and $\mathcal{R}$ are the unit normal vector and tangent vector, the velocity vector, and the local radius of curvature. To enforce homogeneity between the left and right hand side of Eq. (4.374), one must have $\mathcal{R} = O(u'/\omega') = O(\lambda)$.

[23] Another possible physical process for this scaling law, the interactions between vortex tubes, is shown to be much weaker than self-stretching.

The physical consequence is that vortex tube must be geometrically complex over length larger than the Taylor microscale.
A higher upper bound for the vortex length is found using a vortex tube-tracking algorithm: the length of the most intense tubes is of the order of the velocity integral scale defined as L_ϵ, where ϵ is the dissipation. The difference between the tube length and the axial length of the vortex properties (radius, ...) can be explained by the existence of axial Kelvin waves driven by the pressure fluctuation along the vortex axis.

- The total volume fraction filled by the vortex tubes decreases as Re_λ^{-2}, corresponding to a total length which increases as Re_λ, leading to a increasing intermittency.

The fact that this upper bound depends on large-scale scale quantities only while the maximum vorticity depends on $Re_\lambda^{1/2}$ is not consistent by the classical dynamical scheme of a stretched vortex with fixed circulation. A possible explanation, based on the stability analysis of a columnar vortex, is that there exists a natural limit beyond which a vortex tube of finite length cannot be stretched without becoming unstable. This instability induces axial currents which counteract the external stretching. This mechanism, studied in the case of the Burgers' vortex by Jimenez and coworkers, limits the maximum azimuthal velocity to be of the same order as the straining velocity differences applied along the vortex axes. The straining field being induced by the background turbulent flow, one recovers a $O(u')$ upper limit. As a consequence, the vorticity can be amplified by the stretching while in the same time the maximum azimuthal velocity remains bounded. This implies that the length of the vortex tube with a azimuthal velocity close to u' must be large enough to have an edge-to-edge velocity difference of that order, i.e. it must be of the order of the velocity integral scale L_ϵ, in agreement with the numerical data.

The dynamics of vortex tubes formation is another fundamental issue. A first point is that the vortex tubes are part of the $O(\omega')$ background vorticity, and therefore must be seen as particular extreme cases of a more general population of weaker vortical structures. The latter have been observed in numerical simulation to originate in the roll-up of vortex sheets due to Kelvin-Helmholtz-type instabilities. In the absence of a mean flow gradient, vortex tubes are created by straining of the weaker vorticity structures. Dimensional analysis shows the large-scale strain u'/L_ϵ yield the creation of Burgers' vortices with an equilibrium radius of the order of the Taylor microscale λ, while the small-scale strain, which is equal to the inverse of the Kolmogorov timescale and to the r.m.s. vorticity $\omega' = \sqrt{\varepsilon/\nu}$, generates Burgers' vortices with a radius of the order of the Kolmogorov length η. One can the see that the classical dynamical picture, which is in agreement with the Kolmogorov scaling. The existence of high-intensity vortex tubes which escape the Kolmogorov scaling is discussed in the next section.

The creation of vortex tubes with a length of the order of the integral scale can not be explained by the usual vortex stretching mechanism. Jimenez made the hypothesis that they originate in the connection of shorter precursors. It has also been shown Verzicco et al. 1995, Jimenez and Wray 1998 that infinitely-long vortices can be maintained by axially inhomogeneous locally compressive strains. Since similar axial

fluctuations of the vorticity have been observed in vortex tubes, this mechanism may explain that these very long vortex tubes are sustained in isotropic turbulence over long times.

4.10.3 Bridging with Turbulence Dynamics and Intermittency

The internal Reynolds number of the vortex tubes being of order $O(Re_\lambda^{1/2})$, these vortices can be unstable at high Reynolds number. The numerical data suggest that the maximum strain felt by the vortices, which scales like $O(\omega' Re_\lambda^{1/2})$, originates in the first sage of this instability process which leads to vortex tube deformation and the creation of small pinched segments whose length is of the order of the diameter of the parent vortex.

This vortex instability lead Jimenez and coworkers to suggest the existence of a *coherent* Δu *cascade*. According to that theory, the vortex instability yields the existence of a hierarchy of coherent stretched vortices, the circulation being preserved while the upper bound $\Delta u \sim O(u')$ holds at each level. Using the Burgers' vortex as a model, two consecutive levels n an $n-1$ are related by

$$\alpha_n \sim \frac{u'}{R_{n-1}}, \quad l_n \sim R_{n-1}, \quad R_n \sim \sqrt{\frac{\nu}{\alpha_n}} \sim \sqrt{\frac{\nu R_{n-1}}{u'}}, \tag{4.375}$$

where l_n, R_n and α_n denote the length, radius and axial strain of the vortex tubes at the nth level of the coherent cascade. The limit of the cascade is obtained as the asymptote $n \longrightarrow \infty$:

$$\alpha_\infty \sim \frac{u'^2}{\nu} \sim \omega' Re_\lambda, \quad l_\infty \sim R_\infty \sim \frac{\nu}{u'} \sim \eta Re_\lambda^{-1/2}. \tag{4.376}$$

The limit value of the circulation-based Reynolds number is 1. An interesting feature of the preceding physical scheme is that it involves scales smaller than the Kolmogorov scale η. Since they originate in vortex tube instabilities, the structures at a given level of the cascade are not space-filling but are concentrated in small volumes, leading to a natural interpretation of the internal intermittency of turbulence at small scales.

It is also worth noting that strong vortex tubes with $\Delta u = O(u')$ must be subject to a more complex instability mechanisms, which will be compatible with the fact that the circulation Γ is invariant and that the velocity increment $\Delta u \sim \Gamma/R$ is upper-bounded. A possible mechanism (compatible with both numerical and experimental observations) is that when a vortex is so strained that its azimuthal velocity would become higher than the driving axial velocity difference, vorticity is expelled into a cylindrical vorticity sheet. The thickness of this sheet is equal to the Burgers' length

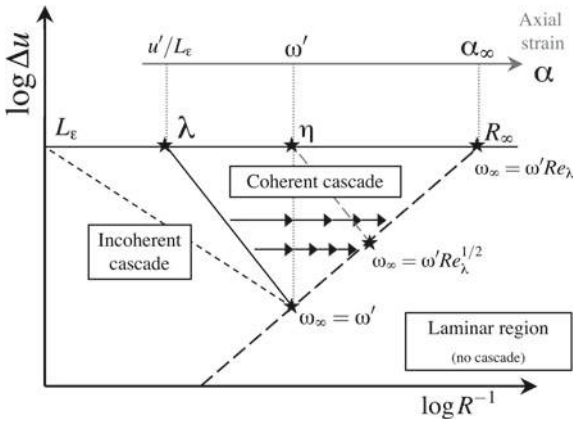

Fig. 4.31 Schematic representation of the two turbulent cascade mechanisms. Adapted from Jimenez and Wray (1998)

of the driving strain. It is unstable, and Kelvin–Helmholtz type instabilities will to its breakup and the formation of longitudinal vortices whose circulation and radius will be such that the global circulation is equal to that of the parent vortex.

The full global dynamical scheme proposed by Jimenez and coworkers consists of two different cascade mechanisms (see Fig. 4.31):

- the *incoherent cascade* associated to space-filling structures such that $\Delta u/R < \omega'$ (i.e. incoherent structures) that fulfill the Kolmogorov scaling $\Delta u = O(R^{1/3})$. The key physical mechanism is at play here is the stretching of non-coherent structures by the background vorticity.
- *the coherent* Δu*cascade* described above, which is associated with vortex tubes that are not space-filling. The governing physical mechanism is the dynamic response of the vortex tubes to the stretching they experience.

The global physical picture is the following. Large-scale uncoherent vortical structures[24] are stretched by the background vorticity, leading to the existence of smaller structures and the kinetic energy cascade. Once the cumulated stretching is strong enough, coherent vortex tubes arise, with typical radius ranging from the Taylor micro scale to the Kolmogorov scale. Each coherent vortex tube is then subject to the coherent Δu cascade mechanism, leading to the generation of a hierarchy of thinner and thinner tubes. The dynamical scheme described above do not account for possible interactions between vortex hierarchies generated by the coherent cascades. Some exchanges are a priori possible, *via* phenomena such as vortex connection or imperfect braiding.

Numerical data reveal that the $O(\omega')$ background vorticity is concentrated in large-scale vortex sheets which separate the energy-containing eddies at the integral scales. This background vorticity is observed to be responsible for almost 80% of

[24]Uncoherent structures are defined here as structures with a characteristic vorticity weaker than the background vorticity ω'.

the total turbulent dissipation in existing numerical simulations, while it fills only 25 % of the total volume of the flow.

The vortex tube are not responsible for the global dynamics of the flow, and play almost no role in global physical mechanisms like the kinetic energy cascade in the inertial range or the turbulent dissipation. This point will be further discussed in Sect. 4.11. Previous scaling laws show that their total energy scales like $O(Re_\lambda^{-2})$, while they induced a kinetic energy dissipation which decreases like $O(Re_\lambda^{-1})$. They are possibly responsible for the intermittency observed on higher-order statistics and for extreme values found in the tails of p.d.fs of many turbulent quantities. It is to be noted that no satisfactory link between coherent event dynamics and inertial range intermittency has been established up to now. Vortex tubes are certainly a source of intermittency, but mostly at small scales. The trend of vortex tubes to form large-scale clusters reported by Moisy and Jimenez (2004) might be a source for large-scale intermittency, but no definitive evidence is available at present time. Other mechanisms, like the persisting long-range coupling between large and small scales, may also contribute to the inertial range intermittency.

4.11 Non-linear Dynamics in the Physical Space

4.11.1 On Vortices, Scales, Wave Numbers and Wave Vectors - What are the Small Scales?

The analysis of isotropic turbulence dynamics, as done in this chapter, is usually carried out concurrently in both Fourier and physical space, a very difficult issue being to bridge between these two different approaches.

It is important to emphasize here that several shortcomings are usually done, which are misleading. The Fourier analysis is based on the use of *wave vectors*, which are not equivalent to *scales*, since a wave vector also carry an information dealing with orientation. The associated *wave number*, defined as a Euclidian norm of the wave vector, has the dimension of the inverse of a length. A large part of the information is now lost, such as the mode polarity in the helical mode decomposition denoted by the parameter s in Eq. (2.104).

Another problem is to switch from the scale concept to classical objects of fluid dynamics like *vortices*. Small scales are very often understood as 'small vortices', which is wrong. The two reasons for that are:

(i) Neither the Fourier analysis, which introduces the wave vectors, nor the scale-dependent analysis in the physical space (based on structure functions, scale-dependent increments, ...) involve the concept of coherent events such as a vortex. It is worth noting that none of the recent definitions of a vortex or a vortex sheets (see Sect. 4.10.1) is based on the scale concept.

(ii) Modes in the Fourier space are non-local in space, while the very concept of vortex is intrinsically local in the physical space since it is associated to a given object.
(iii) As seen in Sect. 4.10.2, three-dimensional vortices (as defined according one the available definitions) can not be defined using a single lengthscale. This is obviously the case of vortex tubes, whose axial length is much higher than their typical diameter.

Therefore, one must be very cautious when 'translating' or 'extrapolating' results coming from Fourier analysis in the physical space (and vice versa).

What definition of *small scales* can be used in the physical space ? Such a definition should rely on the flow dynamics. It is commonly agreed that most of the kinetic energy dissipation ε occurs at modes with high wave numbers[25] since it is equal to

$$\varepsilon = 2\nu \int_0^{+\infty} k^2 E(k) dk \tag{4.377}$$

and that scales dominated by viscous effects are the small scales. Since the r.h.s. of Eq. (4.377) is proportional to the square of the L_2 norm of the velocity gradient ∇u, one can see that *small scales of turbulence in the physical space should be defined as scales associated to large gradients of the velocity field*. On the opposite, *large scales in the physical space are the ones which carry most of the turbulent kinetic energy*. Since

$$\mathcal{K} = \int_0^{+\infty} E(k) dk \tag{4.378}$$

and that $E(k) \geq 0, \forall k$, one can see that modes with dominant contributions to $\mathcal{K}$ and ε are not the same, the latter having larger wave numbers than the former at high Reynolds number. In this sense, one can establish a link between wave numbers and scales in the physical space.

Let us conclude this section by emphasizing that velocity gradients, from which one can define the small scales in the physical space, include both symmetric and anti-symmetric parts, i.e. both turbulent strain $\mathbf{S}$ and vorticity $\boldsymbol{\omega}$.

It is worthy noting that the true exact local expression for the dissipation in the physical space is $\varepsilon = 2\nu S_{ij} S_{ij}$, i.e. dissipation is a function of strain, not vorticity. Introducing the vorticity, one obtains

$$\varepsilon(x,t) \equiv 2\nu S_{ij} S_{ij} = \nu \omega_i \omega_i + \nu \frac{\partial^2}{\partial x_i \partial x_j}(u_i u_j), \tag{4.379}$$

showing that, in unbounded or periodic domain, the following usual volume or statistical averaged relations hold:

[25] High is to be understood as a relative notion, the reference being the wave numbers at which turbulent kinetic energy is injected/created by external forcing or hydrodynamic instabilities.

$$\varepsilon \equiv 2\nu\overline{S_{ij}S_{ij}} = \nu\overline{\omega_i\omega_i}. \tag{4.380}$$

Therefore, mean dissipation can be tied to the mean enstrophy through a purely kinematic relation in isotropic turbulence. But such a relation is meaningless from a local point of view, leading to the conclusion that the strain field is the right quantity to describe the dissipation process.

4.11.2 Is There an Energy Cascade in the Physical Space?

While the kinetic energy energy cascade is a well-established result in the Fourier space and in ensemble-averaged sense, its 'translation' in the physical space is not straightforward. The Navier–Stokes equations just tell us that momentum and kinetic energy are transported in the physical space, the global kinetic energy being invariant in a fully periodic domain in the absence of viscous effects and external forcing. Exact equivalences between terms appearing in Fourier and physical space formulations are only global, non-local expressions, which do not make it possible to have a direct access to single-wave-vector-related informations in the physical space. Therefore, *the energy cascade concept is not relevant in the physical space from a rigorous viewpoint*. It is directly related to the projection of the Navier–Stokes equations onto basis functions which intrinsically bear the information related to the scale dependency (such as Fourier, but also wavelets, *hp* bases in finite-element methods...). This point was emphasized a long time ago by von Neumann and Onsager in 1949.

A very common picture deals with the kinetic energy cascade being the results of a hierarchy of vortex breakdown phenomena, each vortex generating smaller vortices. This phenomenological picture, very often presented as the Richardson cascade, is wrong: experimental and numerical results show that vortices observed in isotropic turbulence do not behave this way, and that the transfer of kinetic energy does not originate in the instability of the vortices. As emphasized by Tsinober (2001) this flawed physical picture originates in a too rapid reading of the famous sentence written by Richardson in 1922 "*We thus realize that: big whirls have little whirls that feed on their velocity, and little whirls have lesser whirls and so on to viscosity - in the molecular sense*". It is to be noticed that Richardson never made further use this picture, and that the term cascade was coined by Onsager two decades latter in the 1940s.

Therefore, the question arise of the existence of a mechanism in the physical space which can be interpreted as the counterpart of the turbulent kinetic energy cascade in the Fourier space. In the physical space, one observes that the injection of turbulent kinetic energy at a given scale yields the generation of velocity gradients and turbulent kinetic energy dissipation. Using the definition given above for the small scales in the physical, one can see that *the turbulent kinetic cascade in the Fourier space must be replaced by the generation of velocity gradients (i.e. both vorticity and strain) in the physical space*.

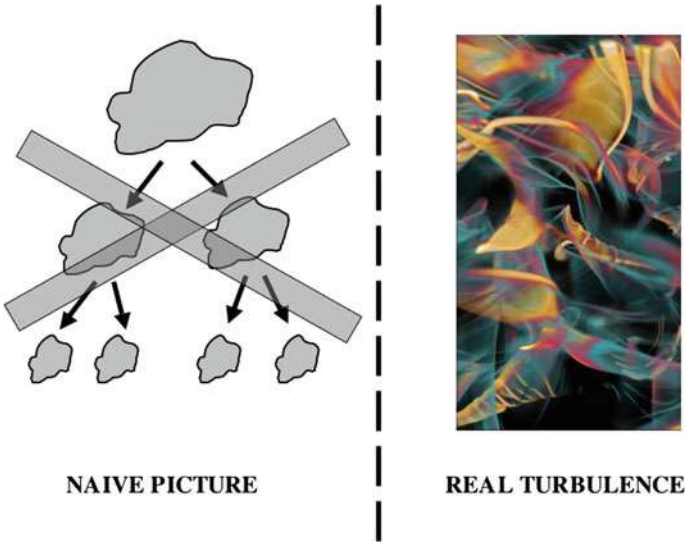

Fig. 4.32 Unphysical simplified view of the turbulent kinetic cascade in the physical space (left) and true structure of the instantaneous vorticity field computed via high-resolution numerical simulation (right). It is seen that the simplified picture based on hierarchical break up process has no physical ground. Right picture reproduced with courtesy of LCSE

It is also important noting that some over-simplified pictures of the cascade which illustrates this process as a hierarchical breakup of structures in smaller ones in the physical space is misleading (see Fig. 4.32). A much more realistic picture is gained looking at the true topology of the turbulent field, revealing that the basic mechanisms are vorticity stretching, vortex sheet folding/rolling up, vortical blobs reconnection …

4.11.3 Self-amplification of Velocity Gradients

In agreement with the definition of the small scales in physical space given above and the observation that the kinetic energy cascade picture does not hold in the physical space, the dynamics of turbulence should be investigated looking at the dynamics of velocity gradients. Therefore, strain and vorticity fields should be privileged to describe turbulence dynamics. Another reason is that they are much more sensitive to internal intermittency that velocity and kinetic energy. Historically, Taylor pointed out the importance of vorticity in 1937, while the role of strain was emphasized by Kolmorogov in 1941. These two quantities must be considered in parallel, since they are weakly correlated in isotropic turbulence and that they are tied by a strongly non-local relation.

Starting from Eqs. (2.39)–(2.40) and restricting the analysis to isotropic turbulence, the evolution of mean enstrophy and mean total strain are governed by the following equations:

$$\frac{1}{2}\frac{\partial \overline{\omega^2}}{\partial t} = \overline{\omega_i \omega_j S_{ij}} + \nu \overline{\omega_i \nabla^2 \omega_i}, \tag{4.381}$$

$$\frac{1}{2}\frac{\partial \overline{S^2}}{\partial t} = -\overline{S_{ik} S_{kj} S_{ij}} - \frac{1}{4}\overline{\omega_i \omega_j S_{ij}} + \nu \overline{S_{ij} \nabla^2 S_{ij}}. \tag{4.382}$$

Two of the most distinctive features of three-dimensional turbulence are:

(i) Enstrophy production via vortex stretching is positive in the mean

$$\overline{\omega_i \omega_j S_{ij}} > 0, \tag{4.383}$$

as hypothesized by Taylor in 1938. Using Lin's equation (4.38) for the evolution of $E(k)$, it is seen that this term is exactly equal to $\int_0^\infty k^2 T(k) dk$.
Numerical simulations show that this term is by two order of magnitude larger than other terms that appear in the r.h.s. of Eq. (4.381). It is important to note that this term happens to take negative values locally. The positive mean value comes from the fact that its p.d.f. is strongly positively skewed. More details about the entrophy production will be given later on in this section, but let us emphasize here that the positivity on the mean of enstrophy production can not be explained considering vortex lines as material lines. This is a misconception, since material line and vorticity line have very different behavior, due to the fact that vorticity is not a passive scalar (it reacts back on the velocity field). These discrepancies are exhaustively discussed in Tsinober (2001).

(ii) Total strain production is positive in the mean. Using the non-local kinematic equality

$$\overline{\omega_i \omega_j S_{ij}} = -\frac{4}{3}\overline{S_{ik} S_{kj} S_{ij}}, \tag{4.384}$$

one observes that the characteristic feature of turbulence is that

$$-\overline{S_{ik} S_{kj} S_{ij}} > 0. \tag{4.385}$$

This term is observed to be larger by two order of magnitude than the viscous term in the balance equation for $\overline{S^2}$.

A few important observations can be drawn from Eqs. (4.381) and (4.382):

(i) Enstrophy production results from the *interaction of vorticity with the strain field*, while the production of total strain mainly comes from *self-amplification of the strain field*. This is illustrated in Fig. 4.33.

(ii) In regions where $\omega_i \omega_j S_{ij} > 0$ the production of total strain is decreased since the two terms have opposite sign (see Eq. (4.384)), i.e. vortex stretching tends

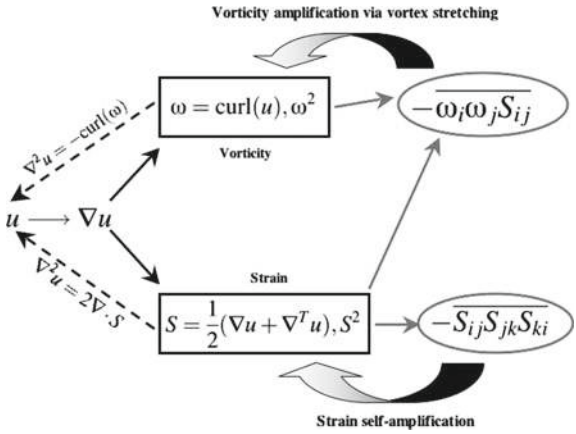

Fig. 4.33 Schematic view of the velocity gradients self-amplification process in isotropic turbulence

to suppress production of strain, at least in a direct way. On the opposite, vortex compression (i.e. regions where $\omega_i \omega_j S_{ij} < 0$) aids the production of total strain. Now identifying the dissipation and its production as the counterpart of the kinetic energy cascade in the physical space, one arrives at the conclusion that *turbulence dynamics in the physical space is associated with predominant production of the rate of strain via strain self-amplification and vortex compression rather than with vortex stretching. The latter is observed to resist the production of dissipation, and therefore to decrease the intensity of the turbulent non-linear dynamics in some sense*.

Direct Numerical Simulations provided a deep insight into the dynamics of the generation of total strain and vorticity. Among other results, they make it possible to identify the regions of space and the physical events responsible for the production mechanisms presented above. As in Sect. 4.10.1, let us denote $\hat{\boldsymbol{e}}_i (i = 1, 2, 3)$ the three eigenvectors of $\mathbf{S}$ and $\hat{\lambda}_i$ the corresponding eigenvalues. Simple algebra yields

$$- S_{ik} S_{kj} S_{ij} = -(\hat{\lambda}_1^3 + \hat{\lambda}_2^3 + \hat{\lambda}_3^3) = -3\hat{\lambda}_1 \hat{\lambda}_2 \hat{\lambda}_3. \tag{4.386}$$

One knows that $\hat{\lambda}_1 > 0$. Numerical simulation show that $\hat{\lambda}_2$ is positively skewed, yielding $\overline{\hat{\lambda}_2^3} > 0$, and that $\hat{\lambda}_3$ is negatively skewed, ensuring the positive production in Eq. (4.385). Typical values are displayed in Table 4.14. Therefore, the *non-linear dynamics, understood as the generation of dissipation and small scales, is directly associated with regions in which* $\hat{\lambda}_3 < 0$, *i.e. with regions of vortex compression*.

The vortex stretching term can be rewritten as follows:

$$\omega_i \omega_j S_{ij} = \omega^2 \hat{\lambda}_i \cos^2(\boldsymbol{\omega}, \hat{\boldsymbol{e}}_i). \tag{4.387}$$

Numerical data reveal that the largest contribution to positive enstrophy production comes from regions where $\boldsymbol{\omega}$ tends to align with $\hat{\boldsymbol{e}}_1$ (see Table 4.14, in which

Table 4.14 Individual contributions of eigenmodes of the strain tensor $\mathbf{S}$ to the production of velocity gradient. Ranges of variations are taken from Tsinober (2001), from $Re_\lambda = 75$ (direct numerical simulation) to $Re_\lambda = 10^4$ (measurements in the atmospheric boundary layer). There is no summation over repeated indices here

Non-linear term	$i = 1$	$i = 2$	$i = 3$
$\overline{\hat{\lambda}_i^3}$	1.2–1.62	0.05	$-2.67 - 2.25$
$\overline{\omega^2 \hat{\lambda}_i^2 \cos^2(\boldsymbol{\omega}, \hat{\boldsymbol{e}}_i)}$	0.52–0.53	0.12–0.15	0.32–0.36

typical values of the contributions to $|\boldsymbol{\omega}\mathbf{S}|^2$ are displayed). But, as mentioned in Sect. 4.10.1, it is known that, in vortex tubes, $\boldsymbol{\omega}$ is mainly aligned with $\hat{\boldsymbol{e}}_2$. This result indicates that *vortex tubes are not responsible for the main part of enstrophy production, which originates in regions with larger strain than enstrophy, and with large curvature of vorticity lines*. In the latter, enstrophy production is maximal and is much larger than viscous destruction. On the contrary, vortex tubes are axial structures with low curvature and maximal enstrophy. In these tubes, modeled as Burgers-like vortices, one observes an approximate equilibrium between enstrophy production and viscous effects. Since their vorticity field is mostly concentrated on the axial component, they are not able to react back on the strain field which stretch them. In this sense, the non-linearity is reduced in these objects, yielding a long lifetime.

It is important noting that enstrophy production mainly originates in strain-dominated regions. Two types of such regions are found:

- *Strain-dominated regions with small curvature of vorticity lines*. These regions are mostly located around vorticity-dominated regions (vortex tubes), in which the vorticity lines wrap around the vortices, leading to a preferential alignement of $\boldsymbol{\omega}$ with $\hat{\boldsymbol{e}}_2$. These regions are not associated with the maximal enstrophy production.
- *Strain-dominated regions with large curvature of vorticity lines*. In these regions, large enstrophy production is associated with large magnitude of $\hat{\lambda}_3$ and large negative values of the enstrophy production rate $\hat{\lambda}_i^2 \cos^2(\boldsymbol{\omega}, \hat{\boldsymbol{e}}_i)$. Predominant mechanisms are vortex compressing and vortex tilting (change of orientation).

4.11.4 Further Investigating Gradient Dynamics: Pressure Effects

Velocity gradient dynamics and related small scales of turbulence can be further investigated looking at the role of the pressure Hessian $\mathbf{H}$ which induces both non-linear and non-local effects (Meneveau 2011). It is worth recalling that the isotropic part of the pressure Hessian preserves incompressiblity, while the deviatoric part $\mathbf{H}^p$ induces couplings between distant points in the velocity gradient field.

It is observed that the evolution equation (2.32) for $\mathbf{A}$ is unclosed due to the presence of the pressure Hessian term in the right-hand side. The role of the viscous term and $\mathbf{H}^p$ can be first investigated by just neglecting them, leading to the *Restricted Euler system*. The mathematical analysis of this system has been carried out in the early 1980 s by several researchers, among which Vieillefosse, who proved that this system exhibits finite-time singularity for all non-null initial conditions. This short-time singularity is due to gradient self-amplification, which is not balanced by viscous and pressure effects. The Restricted Euler solutions also exhibit a preferential alignment of the vorticity vector with the principal axes of $\mathbf{S}$, as the Navier-Stokes solutions do, showing that this phenomenon is due to the local non-linear mechanisms (first two terms in the right-hand side of Eq. (2.37)).

A famous result obtained by Vieillefosse within the Restricted Euler system framework is the following set of coupled ordinary differential equations for Q and R:

$$\frac{dQ}{dt} = -3R, \quad \frac{dR}{dt} = \frac{2}{3}Q^2. \tag{4.388}$$

A remarkable result stemming from the use of the Cayley-Hamilton theorem is that the quantity $\frac{27}{4}R^2 + Q^3$ is time-independent. This leads to the definition of the so-called *Vieillefosse tail* defined as $Q = -\frac{3}{2^{2/3}}R^{2/3}$ in the (R, Q) plane, along which experimental data and DNS results show an increased probability of points where $R > 0$ and $Q < 0$. The associated Restricted Euler equations for the three remaining invariants are

$$\frac{dQ_S}{dt} = -2R_S - R, \quad \frac{dR_S}{dt} = \frac{2}{3}QQ_S + \frac{1}{4}V^2, \quad \frac{dV^2}{dt} = -\frac{16}{3}(R_S - R)Q. \tag{4.389}$$

An analytical solution for $\mathbf{A}$ has been found by Cantwell (1992), which is very complex and that will not be reproduced here for the sake of brevity.

An interesting result is that the finite-time singularity cannot be removed for all initial conditions by just adding a linear damping of the form $-\frac{1}{\tau}\mathbf{A}$ to the Restricted Euler system (which is a reasonable surrogate for the viscous term effect, at least for Gaussian fluctuations), showing that the pressure term plays a significant role in the gradient dynamics.

To alleviate this problem many models for the pressure Hessian or its deviatoric part have been proposed since the early 1990s, most of them being designed in a Lagrangian framework (see Meneveau 2011 for a review). The use of a Lagrangian framework is due to the fact that is provides an interesting way to define closures for both the pressure Hessian and the viscous term in Eq. (2.32). Reminding that a fluid particule obeys $\frac{d}{dt}\boldsymbol{x} = \boldsymbol{u}(\boldsymbol{x}, t)$, one obtains the following exact relation

$$\frac{dF_{ij}}{dt} = A_{ik}F_{kj}, \tag{4.390}$$

where $F_{ij}(\boldsymbol{X},t) = \frac{\partial x_i}{\partial X_j}$ is the Lagrangian deformation tensor, from which the Cauchy-Green tensor $\mathbf{C}$ can be straightforwardly deduced since $\mathbf{C} = \mathbf{F}\mathbf{F}^T$.

The finite-time singularity can be prevented using a Lagrangian Linear Diffusion Model, as proposed by Martin et al. (1998):

$$\frac{dA_{ij}}{dt} + \left(A_{ik}A_{kj} - \frac{1}{3}A_{lk}A_{kl}\delta_{ij}\right) = -\frac{Tr(\mathbf{C}^{-1})}{3\tau_L}\left(1 - \frac{\epsilon_s}{A_{mn}A_{mn}}\right), \tag{4.391}$$

where the Cauchy-Green tensor is obtained solving Eq. (4.390). The parameters τ_L and ϵ_s are related to an arbitrary relaxation time and a prescribed equilibrium value for $A_{mn}A_{mn}$, respectively. This pressure-free model shows that pressure is not necessary to prevent singularities, but its results suffer several flaws. The most important one is that solutions are too much concentrated along the Vieillefosse tail in the (R, Q) plane, showing that pressure has important nonlinear effects that lead to a spreading of the solution in the phase space.

Pressure effects have been modeled in several ways, among which the Tetrad model Chertkov et al. (1999) based on the Lagrangian description of the evolution of a group of four fluid particles and the Recent Fluid Deformation Approximation model (Martins-Afonso and Meneveau 2010), which can be interpreted as a simplified version of the Tetrad model. In the Tetrad model, the description of the displacement of the four particles makes it possible to estimate the local deformation of a small control volume and therefore to estimate $\mathbf{A}$ since four non-aligned points (which are the tetrad) are enough to generate a basis in 3D. The model requires to solve coupled sets of six equations, resulting in an heavy model that will not be given here for the sake of conciseness. It is worth noting that the evolution equation for the Tetrad model is close to the one for the conformation tensor of polymer molecules in the study of visco-elastic turbulence using the FENE-P rheological model discussed in Chap. 5. In the second model, the viscous term is approximated as

$$\nu\frac{\partial^2 A_{ij}}{\partial x_k \partial x_k} = -\frac{Tr(\mathbf{C}^{-1})}{3T}A_{ij}, \quad T = \lambda_f^2/\nu. \tag{4.392}$$

Using the Eulerian-Lagrangian change of variables, one obtains

$$\frac{\partial^2 p(\boldsymbol{x},t)}{\partial x_i \partial x_j} = \frac{\partial X_m}{\partial x_i}\frac{\partial X_n}{\partial x_j}\frac{\partial^2 p(\boldsymbol{x},t)}{\partial X_m \partial X_n} + \frac{\partial^2 X_m}{\partial x_i \partial x_j}\frac{\partial p(\boldsymbol{x},t)}{\partial X_m}. \tag{4.393}$$

Neglecting the spatial gradients of the deformation tensor $\mathbf{F}$ and assuming that pressure loses memory of the initial condition, on can use an isotropic expression for the Lagrangian pressure Hessian, yielding

$$\frac{\partial^2 p(\boldsymbol{x},t)}{\partial x_i \partial x_j} \sim \frac{\partial X_m}{\partial x_i}\frac{\partial X_n}{\partial x_j}\frac{\delta_{mn}}{3}\frac{\partial^2 p}{\partial X_k \partial X_k} \tag{4.394}$$

$$= -\frac{Tr(\mathbf{A}^2)}{Tr(\mathbf{C}^{-1})}(\mathbf{C}^{-1})_{ij} = \frac{2Q}{Tr(\mathbf{C}^{-1})}(\mathbf{C}^{-1})_{ij}. \tag{4.395}$$

The Cauchy-Green tensor can be obtained integrating the corresponding evolution equation. In practice, Chevillard et al. (2008) propose to use a kind Markovianized approximation:

$$\mathbf{C} = \exp\left(\tau_\eta \mathbf{A}\right)\exp\left(\tau_\eta \mathbf{A}^T\right), \tag{4.396}$$

where τ_η is the Kolmogorov time scale. This model (and some variants) leads to very interesting results. At low- to moderate Reynolds number, it is observed to allow for the recovery of important features of Navier-Stokes solutions that were lost considering the Restricted Euler solutions. Exhaustive comparisons with DNS data at Re_λ were performed by Chevillard et al. (see Fig. 4.34), who report a very good recovery of pdf isocontours in the (R, Q) plane, showing that the model is able to capture the predominance of the enstrophy-enstrophy production quadrant ($R < 0$, $Q > 0$) and the dissipation-dissipation quadrant ($R > 0$, $Q < 0$), leading to the tear pattern along the Vieillefosse tail. A good prediction of the pdfs of the angles between $\boldsymbol{\omega}$ and eigenvectors of $\mathbf{S}$ was also observed. Nevertheless, some weaknesses are also observed in specific regions of the flow, especially in those in which the vorticity vector is contracted. But the main problem is that both the accuracy and the stability of the model are observed to rapidly decrease when increasing the Reynolds number.

Several proposals have been made to obtain robust models for high Reynolds flows. Multiscale models have been proposed. These models aim at stabilizing the model by defining a hierarchy of embedded shells that are coupled via non-linear terms to mimic the Richardson cascade, the smaller shell being subjected to very strong dissipative mechanisms. Eventhough stability, i.e. bounded solutions are obtained this way, the quality of the results is not fully satisfactory, since pressure effects are not accurately taken into account. Another closure based on a Gaussian random field modelling was also recently proposed (Wilczek and Meneveau 2014). The main interest of such an approach is that all terms can be closed in a very clean way. The weakness is that parameters should be tuned in an ad hoc way to recover physical results, and robustness for arbitrary Reynolds number is not yet obtained.

Despite the fact that a fully robust, accurate fully general closure for the velocity gradient equation is still to be found, the development of these models emphasized the role of the pressure effects. It is observed that pressure effects play an important role in the control of the gradient amplitude, contributing to the attenuation of self-amplification mechanisms, and that pressure Hessian is also involved in many geometrical features of the vorticity and strain fields.

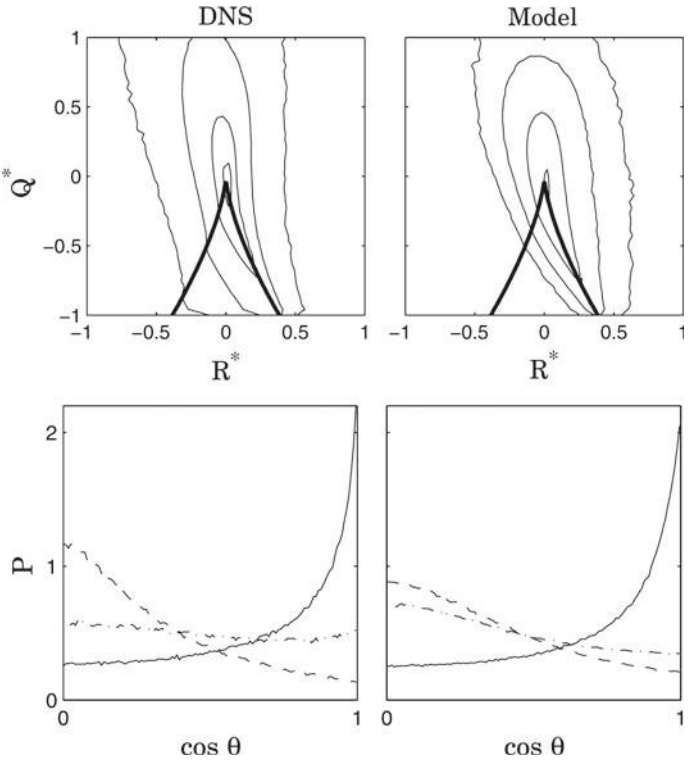

Fig. 4.34 Top: Joint statistics in the normalized (R, Q) plane, with $R^* = R/(\overline{S_{ij}S_{ij}})^{3/2}$ and $Q^* = Q/(\overline{S_{ij}S_{ij}})$. Left: DNS at $Re_\lambda = 150$; Right: Recent Fluid Deformation Model. Bottom: pdf of the cosine between $\boldsymbol{\omega}$ and eignevectors of $\mathbf{S}$: most negative (dashed line), intermediate (solid line) and most positive (das-dotted line). Left: DNS at $Re_\lambda = 150$; Right: Recent Fluid Deformation Model. Reproduced from Chevillard et al. (2008) with permission of AIP

4.11.5 Non-gaussianity and Depletion of Non-linearity

The non-Gaussian character of turbulence, pointed out in Sect. 4.1.2, is intrinsically tied to dynamics of turbulence. This is understood looking at enstrophy and total strain production processes, which can be seen as the counterpart of the turbulent energy cascade in the physical space. A striking feature is that production terms in Eqs. (4.381) and (4.382) are third-order moments, which should be identically zero if the turbulent field was a Gaussian random field. Production of enstrophy and total strain are non-Gaussian features of turbulence. Therefore, non-Gaussianity originates in the very dynamics of turbulence dictated by the Navier–Stokes equations.

The strategy which consists in describing Navier–Stokes turbulence by comparing it with the properties of a Gaussian random velocity field is appealing, since many theoretical results are available for the latter. Kraichnan and Panda (1988) suggested comparing the values of several key non-linear terms which are involved in the

description of the non-linear dynamics in the physical space, and introduced the notion of *depletion of nonlinearity*. This term was coined to account for the fact that some even moments related to nonlinear mechanisms are larger in the Gaussian case than in Navier–Stokes turbulence, e.g. the ratio

$$\frac{\langle \boldsymbol{u}\nabla\boldsymbol{u} + \nabla p\rangle_{\text{Navier–Stokes}}}{\langle \boldsymbol{u}\nabla\boldsymbol{u} + \nabla p\rangle_{\text{Gaussian}}} \simeq 0.5 - 0.6 \tag{4.397}$$

is infered from available numerical data. This results could be interpreted as a sign that the nonlinearities are depleted in Navier–Stokes turbulence. Of course, this idea must be considered with care, since, looking at odd moments, the Navier–Stokes turbulence appears to be infinitely more non-linear than its Gaussian approximation.

As mentioned above, it is also observed that both enstrophy and strain production are reduced in regions dominated by enstrophy with respect to strain dominated regions. Accordingly, vorticity dominated regions, and more specifically vortex tubes, are regions in which the non-linear effects are less intense and can be considered as locally depleted.

4.12 What Are the Proper Features of Three-Dimensional Navier–Stokes Turbulence?

We will now address the following question: among all the features of turbulence presented above, which are the ones which are proper characteristics of three-dimensional Navier–Stokes incompressible turbulence in the sense that they are not shared by other systems?

4.12.1 Influence of the Space Dimension: Introduction to d-Dimensional Turbulence

A first question deals with the influence of the space dimension on turbulence dynamics. While one-dimensional incompressible turbulence does not exist,[26] the dynamics of isotropic turbulence in two (see Lesieur 1997 for a detailed discussion of two-dimensional turbulence), three and even four dimensions has been investigated, both theoretically (Fournier and Frisch 1978) and numerically (Suzuki et al. 2005). Main results are summarized below:

- Turbulent kinetic energy spectrum exhibits an inertial range at small scales if the Reynolds number is high enough. But is worth noting that the spectrum shape

[26] In the one-dimensional case, the divergence-free constraint simplifies into a null space derivative constraint, leading to uniform solutions in space.

depends upon the space dimension. In two-dimensional turbulence, two inertial ranges are detected. A first inertial range with $E(k) \propto k^{-5/3}$ is followed by a second one at higher wave numbers, in which $E(k) \propto k^{-3}$. On the contrary, a single inertial range with $E(k) \propto k^{-5/3}$ is observed in three- and higher dimensions.

- A kinetic energy cascade is observed in all cases, even in the two-dimensional case where the vortex stretching term in the vorticity equation is identically zero. But, in agreement with Waleffe's instability assumption (see Sect. 4.8.4), since F-type distant interactions are almost absent, the net ensemble-averaged dominant mechanism is a reverse energy cascade from large to small wave number modes. In the two-dimensional case, this reverse cascade is easily interpreted in terms of vortex dynamics, since vortices are observed to merge, generating larger and larger structures. In both three- and four-dimensional case, the forward energy cascade is observed dominant at large wave numbers. Theoretical analyses show that two-dimensional turbulence is a singular point, and that the forward cascade is dominant in spaces with dimension $d \geq 3$.
- Self-similar decay regimes exist in all dimensions. An extension of the analysis presented in Sect. 4.1.3 shows that a self-similar decay regime in the d-dimensional case exists if the kinetic energy spectrum at small wave number behaves like

$$E(k, t) \propto C^{(d)}(t) k^{d+1} \quad \text{(small wave numbers)}. \tag{4.398}$$

  Assuming that $C^{(d)}(t)$ is constant (i.e. assuming that the Permanence of Large Eddies assumption holds), one obtains the following law for the decay of the turbulent kinetic energy

$$\mathcal{K}(t) \propto t^{-n}, \quad n = \frac{2(d+2)}{(d+4)}, \quad d \geq 2. \tag{4.399}$$

  The decay coefficient n is a increasing function of the space dimension d. This fact is interpreted by Suzuki as an evidence that energy transfer is more efficient in higher dimension.
- Comparisons between three- and four-dimensional isotropic turbulence (Suzuki et al. 2005) show that the total dissipation is less and less intermittent while intermittency is stronger on velocity increment as the dimension increase. The reason is a change in balance between pressure and convection terms as the dimension d increases. The role of pressure and incompressibility becomes weaker in higher dimension, since the system as more degrees of freedom. As a consequence, the velocity field is less constrained and a larger intermittency can exist. The enhanced energy transfer in higher dimension is also tied to this weakening of the pressure influence: since more persistent straining of the small scales by the large scale strain is allowed, the energy transfer towards small scale is enhanced.
- The role of coherent vortices in kinetic energy cascade is less an less important, as the dimension d is increased.

4.12.2 Pure 2D Turbulence and Dual Cascade

Two-dimensional turbulence without forcing can be characterized by the following kinetic energy spectrum

$$E(k) = C\omega^2 k^{-3},$$

in which ω^2 is the total enstrophy, and k holds for the wavenumber component in the waveplane normal to the direction of the missing velocity component. Two-dimensional turbulence is often considered in the presence of some forcing, for instance with spectral energy injected at a wavenumber k_0, and two situations must be distinguished: the previous law is valid for $k > k_0$, whereas a conventional $k^{-5/3}$ law prevails for $k < k_0$. In addition, 2D turbulence can be seen as an limit case of 3D axisymmetric turbulence, so that the relation above corresponds to

$$\mathcal{E}(\boldsymbol{k}) = \frac{E(k_\perp)}{2\pi k_\perp}\delta(k_\parallel), \tag{4.400}$$

where the Dirac is related to the invariance of the velocity field with respect to the coordinate $x_\parallel$ in physical space. If two-dimensionality is related to the latter invariance only, the Fourier component of the velocity may consists of both components $u^{(1)}$ and $u^{(2)}$ in the Craya-Herring reference frame in the Fourier space, but restricted to $k_\parallel = 0$ (horizontal wave-plane). In this case, $u^{(1)}$ corresponds to the horizontal vortical component, and $u^{(2)}$ to the vertical 'jetal' velocity component. Classical 2D-2C turbulence (two-dimensional two-component) is only characterized by $u^{(1)}$-related velocity.[27] The counterpart of 3D isotropic equations for a single triad is (Fjortoft 1953; Kraichnan 1967; Waleffe 1992)

$$\dot{u}_k^{(1)} = (p^2 - q^2)\frac{\imath s}{2} C_{kpq} u_p^{(1)*} u_q^{(1)*}, \tag{4.401}$$

$$\dot{u}_p^{(1)} = (q^2 - k^2)\frac{\imath s}{2} C_{kpq} u_q^{(1)*} u_k^{(1)*}, \tag{4.402}$$

$$\dot{u}_q^{(1)} = (k^2 - p^2)\frac{\imath s}{2} C_{kpq} u_k^{(1)*} u_p^{(1)*}, \tag{4.403}$$

where C_{kpq} is given by Eq. (4.286). The sign s is equal to $+1$ for any even permutation of the vectors $\boldsymbol{k}, \boldsymbol{p}, \boldsymbol{q}$ of the triad and -1 for an odd permutation. It is clear that each interaction independently conserves energy and enstrophy. Without further quantitative statistical analysis, it is immediately shown that only (R) triads are concerned. Compared with the instability principle expressed in terms of helical modes for 3D isotropic turbulence, the analogy with the Euler stability problem of a solid rotating around its principal axes of inertia, is even more striking, replacing I_1, I_2, I_3 by k^2, p^2, q^2 in Eqs. (4.318)–(4.320). Only positive terms are involved, without need for looking at signs (i.e. polarities of helical modes) as before.

[27] Exact relations are $u^{(1)} = -\hat{\omega}_\parallel / k$ and $u^{(2)} = -\hat{u}_\parallel$ in the horizontal wave plane ($k_\parallel = 0$).

A last important result is that the triad instability principle is found consistent with the concept of *dual cascade* observed in two-dimensional turbulence, i.e. a dominant inverse cascade for energy from large to small wavenumbers, and a direct enstrophy cascade from small to large wave numbers.

4.12.3 Role of Pressure: A View at Burgers Turbulence

We will use here the results dealing with the turbulence-like solutions of the Burgers equations, also referred to as Burgers turbulence or 'Burbulence', to discuss in the role of the pressure. This model

$$\frac{\partial \boldsymbol{u}}{\partial t} + \boldsymbol{u}\nabla\boldsymbol{u} = \nu\nabla^2\boldsymbol{u} \tag{4.404}$$

can be interpreted as an asymptotic model for hydrodynamics, in which pressure has no feedback on the velocity field. Since it is the pressure gradient which enforces the incompressiblity, the Burgers equations corresponds to an infinitely compressible fluids. It is worth noting that the vorticity equation obtained applying the $curl$ operator to Eq. (4.404) is similar to usual one derived from the Navier–Stokes equations. But vorticity will remain identically zero for irrotational initial conditions and ad hoc boundary condition, since a velocity potential exists.

Extensive analysis of both forced and decaying isotropic Burgers turbulence have been carried out, with different space dimensions (Girimaji and Zhou 1995; Noullez and Pinton 2002; Noullez et al. 2005). The main observations are:

- The Burgers velocity field is composed of planar viscous shocks (see Fig. 4.35) and does not exhibit vortices as in the Navier–Stokes case. This important fact put the emphasis on the role of pressure, which is responsible for the existence of coherent vortices (as defined in Sect. 4.10.1). A consequence is that the analysis of the sole vorticity equation is not relevant to characterize Navier–Stokes turbulence. It is also to be noted that this observation if coherent with the one dealing with the weakening of both pressure effects and vortices role in d-dimensional Navier–Stokes turbulence for increasing d (see the preceding section).
- At high Reynolds numbers, Burgers turbulence exhibits an inertial range in the kinetic energy spectrum. Both theoretical and numerical results agree on a $E(k) \propto k^{-2}$ behavior (see Fig. 4.36). The difference from the $E(k) \propto k^{-5/3}$ behavior of the Navier–Stokes turbulence originates in the nature of the small scales events. While in the Navier–Stokes case the small scales are completely characterized by the molecular viscosity ν and the dissipation rate ε, they are determined by the velocity jump across the shock $[[u]]$ and the characteristic shock separation length L in the Burgers case. The dissipation rate is therefore estimated as

$$\varepsilon = \frac{[[u]]^3}{24L}. \tag{4.405}$$

Since $[[u]] \sim \sqrt{12\mathcal{K}}$ and L is approximately equal to the velocity auto-correlation length scale, it is seen that, in Burgers turbulence, small scales are determined by large scale parameters.

- As in Navier–Stokes turbulence, the dominant mechanism within the inertial range is a kinetic energy cascade toward the high wave numbers and a reverse cascade drives the small wave number dynamics. Within the inertial range, the energy transfer is local in spectral space. The triadic interactions causing the most energetic transfers are distant ones, while most of the net kinetic energy transfer is induced by local triadic interactions. Therefore, the global picture is close to the one found in Navier–Stokes turbulence, despite the very important difference in the topology of the velocity field, showing that the spectral features of Navier–Stokes dynamics mentioned above are not intrinsically due to pressure effects and the existence of vortices.
- Burgers turbulence exhibits intermittency, as Navier–Stokes turbulence: tails of the velocity fluctuation p.d.fs have the same non-Gaussian behavior, while velocity increment p.d.fs exhibit strong departure from the Normal distribution. This shows that intermittency, as a general phenomenon, is not a consequence of the existence of coherent vortices in Navier–Stokes turbulence, neither a pressure effect. It is due to the non-linearity of the governing equations and to the existence of strong non-local interactions in the Fourier space.

4.12.4 *Sensitivity with Respect to Energy Pumping Process: Turbulence with Hyperviscosity*

We now address the influence of the energy pumping process on the self-similar decay ad the inertial range behavior of isotropic turbulence. This question was investigated by Borue and Orszag (1995a, b), who performed some simulations in the three-dimensional case using the following hyper-viscous generalization of the Navier–Stokes equations:

$$\frac{\partial \boldsymbol{u}}{\partial t} + \boldsymbol{u}\nabla\boldsymbol{u} = -\nabla p + \nu_p \nabla^{2p}\boldsymbol{u}, \tag{4.406}$$

$$\nabla \cdot \boldsymbol{u} = 0, \tag{4.407}$$

where ν_p is an hyper-viscosity. The usual Navier–Stokes equations are recovered setting $p = 1$. Borue and Orszag used $p = 8$. Their results, in both forced and freely decaying isotropic turbulence, suggest that inertial-range dynamics may be independent of the particular mechanism that governs dissipation at high wave numbers. The usual inertial range behavior was recovered, along with main features of intermittency and non-Gaussianity. But, since the dissipation induced by the hyperviscosity is concentrated at higher wave number than the physical one, the inertial range is observed to be larger in the former case than in the latter. A generalized hyperviscous

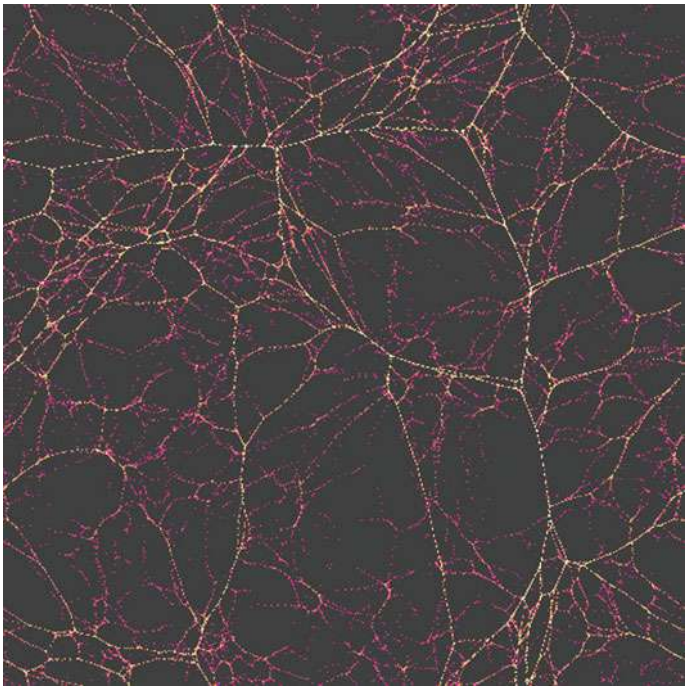

Fig. 4.35 Instantaneous 'turbulent' solution of the two-dimensional Burger's equations. Shocks are observed. Reproduced from Noullez and Vergassola (1994) with permission of PPC

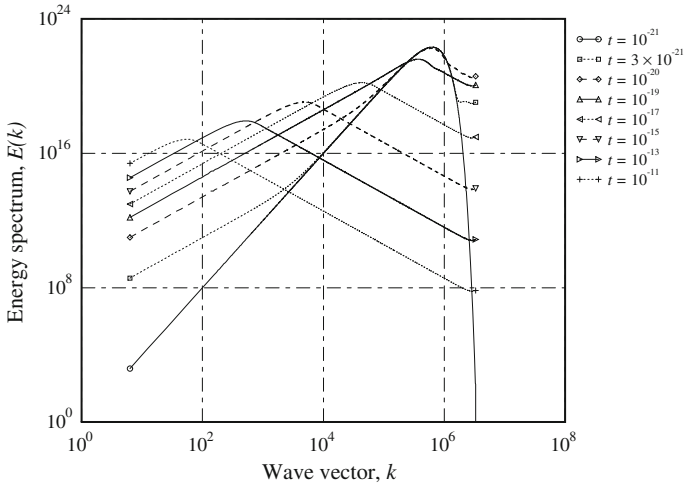

Fig. 4.36 Time evolution of the turbulent kinetic energy spectrum in freely decaying two-dimensional Burger's turbulence. The occurence of a self-similar solution with a k^{-2} inertial range is observed. Reproduced from Noullez et al. (2005) with permission of APS

Kolmogorov length η_p can be defined as

$$\eta_p = \left(\frac{\nu_p^3}{\varepsilon}\right)^{1/(6p-2)}. \tag{4.408}$$

This point was further investigated by Lamorgese et al. (2005) who considered both $p = 2$ and $p = 8$. A novel finding is that the bottleneck effect, i.e. the bump observed on the compensated spectrum $\varepsilon^{-2/3}k^{5/3}E(k)$ at the end of the intertial range, is amplified in the case of hyperviscous simulations. The bottleneck effect originates in the fact that scales in the dissipative region of $E(k)$ are exponentially damped by viscosity, leading to a decrease in the energy cascade rate and then to a small energy pile-up at the end of the inertial range. Since hyperviscosity yields a dissipation of the form

$$\varepsilon = \nu_p \int_0^\infty k^{2p} E(k) dk \tag{4.409}$$

the damping of small scales in the dissipative region is an increasing function of p. Therefore, an amplification of the bottleneck is expected when increasing p. The amplitude of the bottleneck is observed to be a growing function of p and a decreasing function of the Reynolds number in DNS results. A modified spectrum model was proposed by Lamorgese to account for hyperviscous effects, in which the small scale shape function is expressed as (see Sect. 4.3 for a definition of f_η)

$$f_\eta(x) = \left(1 + \frac{\alpha_1}{2}\left[1 + \mathrm{erf}\left\{(1.1 + 0.3\alpha_2 x)\log(\alpha_2 x)\right\}\right]\right) e^{-\alpha_3 x^p} \tag{4.410}$$

where arbitrary parameters α_i are determined on the grounds of DNS data via a least-square procedure. These parameters are strongly p-dependent, since α_1 is found equal to 2.1 for $p = 2$ and 4.2 for $p = 8$, α_2 is found equal to 3.9 for $p = 2$ and 1.2 for $p = 8$, while α_3 is found equal to 2.3 for $p = 2$ and 1.2 for $p = 8$. It is worth noting that this model spectrum is strictly empirical and based on data interpolation. It is observed to recover the main hyperviscosity effects on $E(k)$ at small scales, including p-effects and Reynolds number effects. But it yields unsatisfactory results when trying to recover asymptotic features of Navier-Stokes turbulence (taking $p = 1$) in the limit of infinite Reynolds number.

References

André, J.-C., Lesieur, M.: Influence of helicity on the evolution of isotropic turbulence at high Reynolds number. J. Fluid Mech. **81**, 187–207 (1977)

Andreotti, B.: Studying Burgers' models to investigate the physical meaning of the alignments statistically observed in turbulence. Phys. Fluids **9**, 735–742 (1997)

Antonia, R.A., Burattini, P.: Approach to the 4/5 law in homogeneous isotropic turbulence. J. Fluid Mech. **550**, 175–184 (2006)

Bass, J.: Sur les bases mathématiques de la théorie de la turbulence. Comptes Rendus Acad. Sci. **228**(3), 228–229 (1949)
Batchelor, G.K.: Energy decay and self-preserving correlation functions in isotropic turbulence. Q. Appl. Math. **6**, 97 (1948)
Batchelor, G.K.: Pressure fluctuations in isotropic turbulence. Proc. Camb. Philos. Soc. **47**, 359–374 (1951)
Batchelor, G.K.: The Theory of Homogeneous Turbulence. Cambridge University Press, Cambridge (1953)
Benney, D.J., Newell, A.C.: Random wave closure. Stud. Appl. Math. **48**, 29–53 (1969)
Borue, V., Orszag, S.A.: Self similar decay of three-dimensional homogeneous turbulence with hyperviscosity. Phys. Rev. E **51**(2), R856–R859 (1995a)
Borue, V., Orszag, S.A.: Forced three-dimensional homogeneous turbulence with hyperviscosity. Europhys. Lett. **29**(9), 687–692 (1995b)
Bos, W.J.T., Bertoglio, J.-P.: Dynamics of spectrally truncated inviscid turbulence. Phys. Fluids **18**, 071701 (2006a)
Bos, W.J.T., Bertoglio, J.-P.: A single-time two-point closure based on fluid particle displacements. Phys. Fluids **18**, 031706 (2006b)
Bos, W.J.T., Rubinstein, R.: Dissipation in unsteady turbulence. Phys. Rev. Fluids **2**, 022601(R) (2017)
Bos, W.J.T., Shao, L., Bertoglio, J.P.: Spectral imbalance and the normalized dissipation rate of turbulence. Phys. Fluids **19**, 045101 (2007)
Brasseur, J.G., Wei, C.H.: Interscale dynamics and local isotropy in high Reynolds number turbulence within triadic interactions. Phys. Fluids **6**(2), 842–870 (1994)
Cambon, C., Jacquin, L.: Spectral approach to non-isotropic turbulence subjected to rotation. J. Fluid Mech. **202**, 295–317 (1989)
Cambon, C., Jeandel, D., Mathieu, M.: Spectral modelling of homogeneous non-isotropic turbulence. J. Fluid Mech. **104**, 247–262 (1981)
Cantwell, B.J.: Exact solution of a restricted Euler equation for the velocity gradient tensor. Phys. Fluids A **4**, 782–793 (1992)
Chakraborty, P., Balachandar, S., Adrian, R.J.: On the relationships between local vortex identification schemes. J. Fluid Mech. **535**, 189–214 (2005)
Chandrasekhar, S.: The theory of statistical and isotropic turbulence. Phys. Rev. **76**(5), 896–897 (1949)
Chertkov, M., Pumir, A., Shraiman, B.I.: Lagrangian tetrad dynamics and the phenomenology of turbulence. Phys. Fluids **11**, 2394–2410 (1999)
Chevillard, L., Meneveau, C., Biferale, L., Toschi, F.: Modeling the pressure Hessian and viscous Laplacian in turbulence: comparisons with direct numerical simulation and implications on velocity gradient dynamics. Phys. Fluids **20**, 101504 (2008)
Chong, M.S., Perry, A.E., Cantwell, B.J.: A general classification of three-dimensional flow fields. Phys. Fluids **2**, 765–777 (1990)
Cichowlas, C., Bonati, P., Debbasch, F., Brachet, M.: Effective dissipation and turbulence in spectrally truncated Euler flows. Phys. Rev. Lett. **95**, 264502 (2005)
Clark, T.T., Zemach, C.: Symmetries and the approach to statistical equilibrium in isotropic turbulence. Phys. Fluids **31**, 2395–2397 (1998)
Clark, T.T., Rubinstein, R., Weinstock, J.: Reassessment of the classical turbulence closures: the Leith diffusion model. J. Turbul. **10**(35), 1–23 (2009)
Coleman, G.N., Mansour, N.N.: Modeling the rapid spherical compression of isotropic turbulence. Phys. Fluids **3**, 2255–2259 (1991)
Comte-Bellot, G., Corrsin, S.: The use of a contraction to improve the isotropy of grid-generated turbulence. J. Fluid Mech. **25**, 657–682 (1966)
Davidson, P.A.: Turbulence. An Introduction for Scientists and Engineers. Oxford University Press, Oxford (2004)
Davidson, P.A.: The minimum energy decay rate in quasi-isotropic grid turbulence. Phys. Fluids **23**, 085108 (2011)

De Divitiis, N.: von Karman-Howarth and Corrsin equations closure based on Lagrangian description of the fluid motion. Ann. Phys. **368**, 296–309 (2016)
Djenidi, L., Antonia, R.A.: A general self-preservation analysis for decaying homogeneous isotropic turbulence. J. Fluid Mech. **773**, 345–365 (2015)
Djenidi, L., Kamruzzaman, Md, Antonia, R.A.: Power-law exponent in the transition period of decay in grid turbulence. J. Fluid Mech. **779**, 544–555 (2015)
Donzis, D.A., Sreenivasan, K.R., Yeung, P.K.: Some results on the Reynolds number scaling of pressure statistics in isotropic turbulence. Phys. D **241**, 164–168 (2012)
Dryden, J.L.: A review of the statistical theory of turbulence. Q. Appl. Math. **1**, 7–42 (1943)
Eyink, G.L., Thomson, D.J.: Free decay of turbulence and breakdown of self-similarity. Phys. Fluids **12**(3), 477–479 (2000)
Favier, B., Godeferd, F.S., Cambon, C.: On space and time correlations of isotropic and rotating turbulence. Phys. Fluids **22**, 015101 (2010)
Falkovich, G., Lebedev, V.: Single-point velocity distribution in turbulence. Phys. Rev. Lett. **79**(21), 4159–4161 (1997)
Fjortoft, R.: On the changes in spectral distributions on kinetic energy for two-dimensional, nondivergent flow. Tellus **5**, 225–230 (1953)
Fournier, J.D., Frisch, U.: *d*-dimensional turbulence. Phys. Rev. A **17**(2), 747–762 (1978)
Frisch, U.: Turbulence: The Legacy of A. N. Kolmogorov. Cambridge University Press, Cambridge (1995)
George, W.K.: The decay of homogeneous turbulence. Phys. Fluids A **4**(7), 1492–1509 (2000)
George, W.K.: Asymptotic effect of initial and upstream conditions on turbulence. ASME J. Fluids Eng. **134**, 061203 (2012)
George, W.K., Wang, H.: The exponential decay of homogeneous isotropic turbulence. Phys. Fluids **21**, 025108 (2000)
Girimaji, S.S., Zhou, Y.: Spectrum and energy transfer in steady Burgers turbulence. ICASE Report No. 95–13 (1995)
Goto, S., Vassilicos, J.C.: Energy dissipation and flux laws for unsteady turbulence. Phys. Lett. A **379**, 1144–1148 (2015)
Guo, H., Li, C., Qu, Q., Liu, P.: Attractive fixed-point solution study of shell model for homogeneous isotropic turbulence. Appl. Math. Mech. **34**, 259–268 (2013)
He, G.W., Jin, G., Zhao, X.: Scale-similarity model for Lagrangian velocity correlations in isotropic and stationary turbulence. Phys. Rev. E **80**, 066313 (2009)
Heisenberg, W.: Zur statistischen theorie der turbulenz. Zeitschrift fur Physik **124**, 628–657 (1948)
Hinze, J.O.: Turbulence. McGraw-Hill Series in Mechanical Engineering. McGraw-Hill, New York (1975)
Horiuti, K.: A classification method for vortex sheet and tube structures in turbulent flows. Phys. Fluids **13**(12), 3756–3774 (2001)
Horiuti, K., Takagi, Y.: Identification method for vortex sheet structures in turbulent flows. Phys. Fluids **17**, 121703 (2005)
Horiuti, K., Tamaki, T.: Nonequilibrium energy spectrum in the subgrid-scale one-equation model in large-eddy simulation. Phys. Fluids **25**, 125104 (2013)
Horiuti, K., Yanagihara, S., Tamaki, T.: Nonequilibrium state in energy spectra and transfer with implications for topological transitions and SGS modeling. Fluid Dyn. Res. **48**, 021409 (2016)
Hunt, J.C.R., Wray, A.A. Moin, P.: Eddies, stream, and convergence zones in turbulent flows. Center for Turbulence Research Report CTR-S88, pp. 193–208 (1988)
Ishida, T., Davidson, P.A., Kaneda, Y.: On the decay of isotropic turbulence. J. Fluid Mech. **564**, 455–475 (2006)
Ishihara, T., Kaneda, Y., Yokokawa, M., Itakura, K., Uno, A.: Energy spectrum in the near dissipation range of high resolution DNS of turbulence. J. Phys. Soc. Jpn. **74**(5), 1464–1471 (2005)
Jeong, J., Hussain, F.: On the identification of a vortex. J. Fluid Mech. **285**, 69–94 (1995)
Jimenez, J.: Kinematic alignment effects in turbulent flows. Phys. Fluids **4**, 652–654 (1992)
Jimenez, J., Wray, A.: On the characteristics of vortex filaments in isotropic turbulence. J. Fluid Mech. **373**, 255–285 (1998)

Jimenez, J., Wray, A., Saffman, P.G., Rogallo, R.: The structure of intense vorticity in isotropic turbulence. J. Fluid Mech. **255**, 65–90 (1993)
Kaneda, Y.: Lagrangian and Eulerian time correlations in turbulence. Phys. Fluids A **5**(11), 2835–2845 (1993)
Kaneda, Y., Ishihara, T., Gotoh, K.: Taylor expansions in powers of time of Lagrangian and Eulerian two-point two-time velocity correlations in turbulence. Phys. Fluids **11**, 2154–2166 (1999)
Kida, S., Ohkitani, K.: Spatiotemporal intermittency and instability of a forced turbulence. Phys. Fluids **4**, 1018–1027 (1992a)
Kida, S., Ohkitani, K.: Fine structure of energy transfer in turbulence. Phys. Fluids **4**, 1602–1604 (1992b)
Kovasznay, L.S.G.: The spectrum of locally isotropic turbulence. Phys. Rev. **73**(9), 1115–1116 (1948)
Kraichnan, R.H.: The structure of isotropic turbulence at very high Reynolds numbers. J. Fluid Mech. **5**(4), 497–543 (1959)
Kraichnan, R.H.: Inertial ranges in two-dimensional turbulence. Phys. Fluids **10**, 1417–1423 (1967)
Kraichnan, R.H.: Inertial-range transfer in two- and three-dimensional turbulence. J. Fluid Mech. **47**, 525–535 (1971)
Kraichnan, R.H.: Eddy-viscosity in two and three dimensions. J. Atmos. Sci **33**, 1521–1536 (1976)
Kraichnan, R.H., Panda, R.: Depression of nonlinearity in decaying isotropic turbulence. Phys. Fluids **31**, 2395–2397 (1988)
Krogstad, P.A., Davidson, P.A.: Near-field investigation of turbulence produced by multi-scale grids. Phys. Fluids **24**, 035103 (2012)
Lamorgese, A.G., Caughey, D.A., Pope, S.B.: Direct numerical simulation of homogeneous turbulence with hyperviscosity. Phys. Fluids **17**, 015106 (2005)
Lesieur, M.: Turbulence in fluids, 3rd edn. Kluwer Academic Publishers, Dordrecht (1997)
Lesieur, M., Schertzer, D.: Amortissement auto-similaire d'une turbulence à grand nombre de Reynolds. J. Méc. **17**, 609–646 (1978). (in french)
Lesieur, M., Ossia, S., Metais, O.: Infrared pressure spectra in two- and three-dimensional isotropic incompressible turbulence. Phys. Fluids **11**, 1535–1543 (1999)
Lindborg, E.: Correction to four-fifths law due to variations of the dissipation. Phys. Fluids **11**(3) , 510–512 (1999)
Llor, A., Soulard, O.: Comment on "Energy spectra at low wavenumbers in homogeneous incompressible turbulence" (Phys. Lett. A **375**, 2850 (2011)). Phys. Lett. A **377**, 1157–1159 (2013)
Lund, T.S., Rogers, M.M.: An improved measure of strain rate probability in turbulent flows. Phys. Fluids **6**, 1838–1847 (1994)
Lundgren, T.S.: Kolmogorov two-thirds law by matched asymptotic expansions. Phys. Fluids **14**, 638–642 (2002)
Lundgren, T.S.: Kolmogorov turbulence by matched asymptotic expansion. Phys. Fluids **15**, 1074–1081 (2003)
Manley, O.P.: The dissipation range spectrum. Phys. Fluids **4**(6), 1320–1321 (1992)
Martins-Afonso, M., Meneveau, C.: Recent fluid deformation closure for velocity gradient tensor dynamics in turbulence: timescale effects and expansions. Phys. D **239**, 1241–1250 (2010)
Mazzi, B., Vassilicos, J.C.: Fractal-generated turbulence. J. Fluid Mech. **502**, 65–87 (2004)
Mathieu, J., Scott, J.: An Introduction to Turbulent Flow. Cambridge University Press, Cambridge (2000)
Martin, J., Dopazo, C., Valino, L.: Dynamics of velocity gradient invariants in turbulence: restricted Euler and linear diffusion models. Phys. Fluids **10**, 2012–2025 (1998)
Mazellier, N., Vassilicos, J.C.: The turbulence dissipation constant is not universal because of its universal dependence on large-scale flow topology. Phys. Fluids **20**, 015101 (2008)
Meldi, M., Sagaut, P.: On non-self similar regimes in homogeneous isotropic turbulence decay. J. Fluid Mech. **711**, 364–393 (2012)
Meldi, M., Sagaut, P.: Further insights into self-similarity and self-preservation in freely decaying isotropic turbulence. J. Turbul. **14**(8), 24–53 (2013a)

Meldi, M., Sagaut, P.: Pressure statistics in self-similar freely decaying isotropic turbulence. J. Fluid Mech. **717**, R2-1–R2-12 (2013b)
Meldi, M., Sagaut, P.: Turbulence in a box: quantification of large-scale resolution effects in isotropic turbulence free decay. J. Fluid Mech. **818**, 697–715 (2017)
Meldi, M., Sagaut, P., Lucor, D.: A stochastic view of isotropic turbulence decay. J. Fluid Mech. **668**, 351–362 (2011)
Meldi, M., Lejemble, H., Sagaut, P.: On the emergence of non-classical decay regimes in multi-scale/fractal generated isotropic turbulence. J. Fluid Mech. **756**, 816–843 (2014)
Meneveau, C.: Lagrangian dynamics and models of the velocity gradient tensor in turbulent flows. Ann. Rev. Fluid Mech. **43**, 219–245 (2011)
Meyers, J., Meneveau, C.: A functional form for the energy spectrum parametrizing bottleneck and intermittency effects. Phys. Fluids **20**(6), 065109 (2008)
Millionschikov, M.D.: Theory of homogeneous isotropic turbulence. Dokl. Akad. Nauk. SSSR **32**, 22–24 (1941)
Mohamed, M.S., Larue, J.C.: The decay power law in grid-generated turbulence. J. Fluid Mech. **219**, 195–214 (1990)
Moisy, F.: Kolmogorov equation in a fully developed turbulence experiment. Phys. Rev. Lett. **82**(20), 3994–3997 (1999)
Moisy, F., Jimenez, J.: Geometry and clustering of intense structures in isotropic turbulence. J. Fluid Mech. **513**, 111–133 (2004)
Monin, A.S., Yaglom, A.M.: Statistical Fluid Mechanics, vol. 1. MIT Press, Cambridge (1975)
Mons, V., Chassaing, J.C., Gomez, T., Sagaut, P.: Is isotropic turbulence decay governed by asymptotic behavior of large scales? An eddy-damped quasi-normal Markovian-based data assimilation study. Phys. Fluids **26**, 115105 (2014)
Nomura, K.K., Post, G.K.: The structure and the dynamics of vorticity and rate of strain in incompressible homogeneous turbulence. J. Fluid Mech. **377**, 65–97 (1998)
Noullez, A., Pinton, J.F.: Global fluctuations in decaying Burgers turbulence. Eur. Phys. J. B. **28**, 231–241 (2002)
Noullez, A., Vergassola, M.: A fast Legendre transfrom algorithm and applications to the adhesion model. J. Sci. Comput. **9**(3), 259–281 (1994)
Noullez, A., Wallace, G., Lempert, W., Miles, R.B., Frisch, U.: Transverse velocity increments in turbulent flow using the RELIEF technique. J. Fluid Mech. **339**, 287–307 (1997)
Noullez, A., Gurbatov, S.N., Aurell, E., Simdyankin, S.I.: Global picture of self-similar and non-self-similar decay in Burgers turbulence. Phys. Rev. E **71**, 056305 (2005)
Oberlack, M.: On the decay exponent of isotropic turbulence. Proc. Appl. Math. Mech. **1**, 294–297 (2002)
O'Brien, E.F., Francis, G.C.: A consequence of the zero fourth cumulant approximation. J. Fluid Mech. **13**, 369–382 (1963)
Ogura, Y.: A consequence of the zero fourth cumulant approximation in the decay of isotropic turbulence. J. Fluid Mech. **16**, 33–40 (1963)
Orszag, S.A.: Analytical theories of turbulence. J. Fluid Mech. **41**, 363–386 (1970)
Park, N., Mahesh, K.: Analysis of statistical errors in large-eddy simulation using statistical closure theory. J. Comput. Phys. **222**(1), 194–216 (2007)
Pao, Y.M.: Structure of turbulent velocity and scalar fields at large wavenumbers. Phys. Fluids **8**(6), 1063–1075 (1965)
Piquet, J.: Turbulent flows. Models and Physics, 2nd edn. Springer, Berlin (2001)
Pope, S.B.: Turbulent Flows. Cambridge University Press, Cambridge (2000)
Pouquet, A., Lesieur, M., André, J.-C., Basdevant, C.: Evolution of high Reynolds number two-dimensional turbulence. J. Fluid Mech. **75**, 305–319 (1975)
Qian, J.: Universal equilibrium range of turbulence. Phys. Fluids **27**(9), 2229–2233 (1984)
Qian, J.: Slow decay of the finite Reynolds number effect of turbulence. Phys. Rev. E **60**(3), 3409–3412 (1999)
Ristorcelli, J.R.: The self-preserving decay of isotropic turbulence: analytic solutions for energy and dissipation. Phys. Fluids **15**, 3248–3250 (2003)

Ristorcelli, J.R.: Passive scalar mixing: analytic study of time scale ratio, variance, and mix rate. Phys. Fluids **18**, 075101 (2006)
Ristorcelli, J.R., Livescu, D.: Decay of isotropic turbulence: fixed points and solutions for nonconstant $G \sim R_\lambda$ palinstrophy. Phys. Fluids **16**, 3487–3490 (2004)
Rossi, M.: Of vortices and vortical layers: an overview. In: Maurel, A., Petitjeans, P. (eds.) Vortex Structure and Dynamics. Lecture Notes in Physics, pp. 40–123. Springer, Berlin (2000)
Saffman, P.G.: On the fine scale structure of vector fields convected by a turbulent fluid. J. Fluid Mech. **16**(4), 545–572 (1963)
Siggia, E.D.: Numerical study of small scale intermittency in three dimensional turbulence. J. Fluid Mech. **107**, 375–406 (1981)
Skrbek, L., Stalp, S.R.: On the decay of homogeneous isotropic turbulence. Phys. Fluids **12**(8), 1997–2019 (2000)
Speziale, C.G., Bernard, P.S.: The energy decay in self-preserving isotropic turbulence revisited. J. Fluid Mech. **241**, 645–667 (1992)
Sreenivasan, K.R.: On the universality of the Kolmogorov constant. Phys. Fluids **7**, 2778–2784 (1995)
Suzuki, E., Nakano, T., Takashi, N., Gotoh, T.: Energy transfer and intermittency in four-dimensional turbulence. Phys. Fluids **17**, 081702 (2005)
Tanaka, M., Kida, S.: Characterization of vortex tubes and sheets. Phys. Fluids **5**(9), 2079–2082 (1993)
Tatsumi, T.: The theory of decay process of incompressible isotropic turbulence. Proc. R. Soc. Lond. A **239**, 16 (1957)
Taylor, G.I.: Statistical theory of turbulence. Proc. R. Soc. Lond. A **151**, 421–444 (1935)
Tchoufag, J., Sagaut, P., Cambon, C.: A spectral approach to finite Reynolds number effects on Kolmogorov's 4/5 law in isotropic turbulence. Phys. Fluids **24**, 015107 (2012)
Thiesset, F., Antonia, R.A., Danaila, L., Djenidi, L.: Karman-Howarth closure equation on the basis of a universal eddy viscosity. Phys. Rev. E **88**, 011003 (2013)
Tsinober, A.: An Informal Introduction to Turbulence. Kluwer Academic Publishers, Dordrecht (2001)
Vassilicos, J.C.: Dissipation in turbulent flows. Ann. Rev. Fluid Mech.**47**, 95–114 (2015)
Verzicco, R., Jimenez, J., Orlandi, P.: Steady columnar vortices under local compression. J. Fluid Mech. **299**, 367–388 (1995)
Vignon, J.-M., Cambon, C.: Thermal spectral calculation using eddy-damped quasi-normal Markovian theory. Phys. Fluids **23**, 1935–1937 (1980)
Von Karman, T., Howarth, L.: On the statistical theory of isotropic turbulence. Proc. R. Soc. A **164**, 192–215 (1938)
Von Karman, T., Lin, C.C.: On the concept of similarity in the theory of isotropic turbulence. Rev. Mod. Phys. **21**(3), 516–519 (1949)
Waleffe, F.: The nature of triad interactions in homogeneous turbulence. Phys. Fluids **4**, 350–363 (1992)
Waleffe, F.: Inertial transfers in the helical decomposition. Phys. Fluids **5**, 677–685 (1993)
Wilczek, M., Meneveau, M.: Pressure Hessian and viscous contributions to velocity gradient statistics based on Gaussian random fields. J. Fluid Mech. **756**, 191–225 (2014)
Woodruff, S.L., Rubinstein, R.: Multiplescale perturbation analysis of slowly evolving turbulence. J. Fluid Mech. **565**, 95–103 (2006)
Wylczek, M., Narita, Y.: Wave-number?frequency spectrum for turbulence from a random sweeping hypothesis with mean flow. Phys. Rev. E **86**, 066308 (2012)
Zakharov, V.E., Lvov, V., Falkowitch, G.: Wave Turbulence. Springer, Berlin (1992)
Zhao, X., He, G.W.: Space-time correlations of fluctuating velocities in turbulent shear flows. Phys. Rev. E **79**, 046316 (2009)
Zhou, J., Adrian, R.J., Balachandar, S., Kendall, T.M.: Mechanisms for generating coherent packets of hairpin vortices. J. Fluid Mech. **387**, 353–396 (1999)

Chapter 5
Isotropic Turbulence with Coupled Microstructures. I: Visco-Elastic Turbulence

5.1 Introduction to Turbulence in Dilute Polymer Solutions

Turbulence in dilute polymers suspensions may exhibit some very new interesting features due to the non-Newtonian character of the mixture. Polymers are macromolecules appearing as long chains of monomers which have a complex mechanical behavior. In a turbulent flow, they experience unsteady random forcing and, depending on the ratio of their intrinsic time and length scales with those of turbulence, they will interact with turbulence in a passive or active way. In the latter case, deep modifications of turbulence physics may occur, leading to the definition of several physical turbulent régimes.

The present chapter is restricted to isotropic turbulence in dilute polymer solutions, in which mean shear effects are not present and direct interactions between polymer molecules are negligible. Such a configuration is a very good illustration of turbulence coupled to heterogeneous microstructural physics, since it allows for the analysis of modifications of turbulence non-linear mechanisms without coupling to changes in turbulence production mechanisms.

5.2 Governing Equations

5.2.1 Models for Polymer Physics: FENE, FENE-P and Beyond

Many rheological models for polymers have been proposed, with different degrees of complexity and realism. An interesting discussion is found in Jin and Collins (2007). The emphasis is put here on the Finetely Extensible Non-linear Elastic model (FENE) closed using the Peterlin approximation (FENE-P), since it is used in most published numerical simulations. It is a good trade-off between physical complexity

P. Sagaut and C. Cambon, *Homogeneous Turbulence Dynamics*,
https://doi.org/10.1007/978-3-319-73162-9_5

and numerical cost. Therefore, the FENE-P model will be discussed below, along with the results obtained using it. It is worth noting that direct comparisons with laboratory experiments carried out with real polymers can be done in a qualitative way only, since exact rheological models for realistic polymer modes are still missing. The same restriction also holds for comparisons between experimental data obtained using different polymer solutions.

5.2.1.1 FENE-P Model for Dilute Polymers

In Brownian dynamics approach, a polymer is modeled as a sequence of N beads connected by elastic springs and the deformation of the bead-spring chain is followed along the trajectory of its center of mass. The FENE model corresponds to N = 2, i.e. to a simplified dumbbell model.

At equilibrium a polymer molecule coils up into a ball-like shape with characteristic radius R_0. In dilute suspensions, the influence of the equilibrium size of the polymers has a negligible effect on the solvent rheological behavior. In turbulent flows, the condition is that it is much smaller than the Kolmogorov scale, $R_0 \ll \eta$. When immersed in a non-uniform flow, a molecule experiences a shear and is deformed into an elongated structure characterized by its end-to-end vector $\boldsymbol{R}$. In a flow with constant velocity gradient, this vector evolves according to the FENE model equation:

$$\frac{\partial R_i}{\partial t} = R_j \frac{\partial u_i}{\partial x_j} - \Gamma \frac{\partial E}{\partial R_j} + \xi_i \tag{5.1}$$

where the terms in the right-hand side are related to the stretching by solvent velocity gradient, the resistance to elongation and the forcing by the thermal noise. E and Γ are related to the free energy of the molecule and its kinetic coefficient, respectively. The latter is modeled as a random forcing whose auto-correlation tensor is given by

$$\overline{\xi_i(t)\xi_j(t')} = 2Tk_B\Gamma\delta_{ij}(t - t') \tag{5.2}$$

where k_B is the Boltzmann constant. Denoting R_{max} the maximum elongation of the molecule, the latter can be described using elasticity theory when $R \ll R_{max}$, its free energy being expressed as $E = KR^2/2$ where K denotes the Hook modulus. Thus, R_0 can be estimated from the condition $E \propto k_B T$ as $R_0 \sim \sqrt{k_B T/K}$. The associated equation is

$$\frac{\partial R_i}{\partial t} = R_j \frac{\partial u_i}{\partial x_j} - R_i\tau + \xi_i(t) \tag{5.3}$$

where $\tau = (\Gamma K)^{-1}$ is the molecular relaxation time. In the general case τ is a function of R, since the relaxation mechanism depends on non-linear interactions between monomers. In the Finitely Extensible Non-linear Elastic (FENE) approximation, one takes

$$\tau = \tau_p \phi(R^2) = \tau_p \left(1 - \frac{R^2}{R_{max}^2}\right), \tag{5.4}$$

where τ_p is the characteristic relaxation time scale toward in the absence of flow proposed by Zimm and $R = \|\boldsymbol{R}\|$. Zimm's time scale is usually computed using Fleury's formula:

$$\tau_p = \frac{\mu_s R_g^3}{k_B T}, \quad R_g = N^{3/5} a, \tag{5.5}$$

where μ_s, R_g, N and a denote the solvent viscosity, the equilibrium radius of gyration, the number of monomers per molecule and the length of a monomer, respectively.

The polymer conformation tensor is defined as $C_{ij} = \langle R_i R_j \rangle_\xi$, where $\langle R_i R_j \rangle_\xi$ denotes a statistical average of thermal noise realizations.

Rewritting Eq. (5.3) as

$$\frac{\partial R_i}{\partial t} = R_j \frac{\partial u_i}{\partial x_j} - \phi(R^2) R_i \tau_p + \sqrt{\frac{R_0^2}{\tau_p}} \xi_i(t), \tag{5.6}$$

one obtains by application of the Itô formula

$$\begin{aligned} \frac{\partial}{\partial t}(R_i R_j) &= \frac{\partial R_i}{\partial t} R_j + \frac{\partial R_j}{\partial t} R_i + \frac{R_0^2}{\tau_p} \delta_{ij} \\ &= \frac{\partial u_i}{\partial x_k} R_k R_j + \frac{\partial u_j}{\partial x_k} R_k R_i - \frac{\phi(R^2)}{\tau_p} R_i R_j \\ &\quad + \frac{R_0^2}{\tau_p} \delta_{ij} + \sqrt{\frac{R_0^2}{\tau_p}} \left(R_j \xi_i + R_i \xi_j\right). \end{aligned} \tag{5.7}$$

Now averaging over realizations of thermal noise and reminding that $< R_j \xi_j >_\xi = 0$, one obtains the following time evolution equation for the FENE model:

$$\frac{\partial}{\partial t} C_{ij} = \frac{\partial u_i}{\partial x_k} C_{kj} + \frac{\partial u_j}{\partial x_k} C_{ki} - \frac{1}{\tau_p} \left(\langle \phi(R^2) R_i R_j \rangle_\xi - R_0^2 \delta_{ij}\right). \tag{5.8}$$

This equation describes the evolution of the polymer conformation tensor along the Lagrangian trajectory of its center of mass. This model is not closed since $\langle \phi(R^2) R_i R_j \rangle_\xi$ is not known. The Peterlin approximation is

$$\langle \phi(R) R_i R_j \rangle_\xi \simeq \phi(R^2) \langle R_i R_j \rangle_\xi = \phi(\mathrm{Tr}(\mathbf{C})) C_{ij}, \tag{5.9}$$

leading to the definition of the FENE-P model. This model can be rewritten normalizing $\mathbf{C}$ so that $\mathbf{C} = \mathbf{I}$ at equilibrium, i.e. taking $C_{ij} = \langle R_i R_j \rangle_\xi / R_0^2$, yielding

$$\frac{\partial}{\partial t}C_{ij} = \frac{\partial u_i}{\partial x_k}C_{kj} + \frac{\partial u_j}{\partial x_k}C_{ki} - \frac{1}{\tau_p}\left(f(C_{kk})C_{ij} - \delta_{ij}\right), \tag{5.10}$$

where the renormalized Peterlin function is

$$f(C_{kk}) = \frac{R_0^2 - 3}{R_0^2 - C_{kk}}. \tag{5.11}$$

The corresponding polymer elastic energy stored by unit volume is

$$K_\ell = \frac{\nu_p}{2\tau_p}\ln[f(C_{ii})] + P_0 \tag{5.12}$$

where P_0 is the reference energy and ν_p denotes the zero-shear viscosity of the polymer.

This model is the most common one in numerical simulations of turbulence, since it is observed to be sufficient to describe the sationnary physics of both the extension and the orientation of the polymer molecules in isotropic turbulence. Because it is limited to a single pair of beads, the characteristic time τ_p is related to the largest time scale of the molecule dynamics.

It is worth noting that the FENE-P model is a model for the conformation tensor, which is a statistical quantity. It is therefore less general that the FENE model (5.1), which is based on an equation for the vector $\boldsymbol{R}$. Several authors have analyzed the main drawbacks of Peterlin's closure, and reported that Vincenzi et al. (2015): (i) steady state p.d.f. of large R are overestimated, (ii) predicted alignment of polymers with eigenvectors of the velocity gradient tensor and the vorticity is weaker than with the FENE model and (iii) correlation time of both extension and orientation of polymer molecules is underestimated. As a conclusion, FENE-P model is expected to be less relevant when velocity gradient is much larger than τ_p.

A few simulations of turbulent flows have been performed using more complex models, e.g. Horiuti et al. (2013), Jin and Collins (2007).

Some authors, e.g. Berti et al. (2006), Casciola and De Angelis (2007), use a further simplified model, which is well suited for *mild elongations*. For such cases, one has $f(C_{ii}) \simeq 1$ and $\|\mathbf{C}\| \gg 1$, leading to the simplified linear equation

$$\frac{\partial}{\partial t}C_{ij} = \frac{\partial u_i}{\partial x_k}C_{kj} + \frac{\partial u_j}{\partial x_k}C_{ki} - \frac{C_{ij}}{\tau_p}. \tag{5.13}$$

According to Sect. 2.5.7, and assuming that polymer molecules have no inertia so that they are advected along fluid trajectories at fluid velocity, the Lagrangian solution to Eq. (5.13) is (Balkovsky et al. 2001; Fouxon and Lebedev 2003)

$$\mathbf{C}(\boldsymbol{x}(t), t) = \mathbf{F}(t, t_0)\mathbf{C}(\boldsymbol{x}_0, t_0)\mathbf{F}^T(t, t_0)e^{-(t-t_0)/\tau_p}, \tag{5.14}$$

where the Green function tensor $\mathbf{F}(t, t_0)$ is the Cauchy matrix given by relation (2.5) which is solution of

$$\dot{\mathbf{F}} = (\nabla \boldsymbol{u})\mathbf{F}, \quad \mathbf{F}(t_0, t_0) = \mathbf{I}. \tag{5.15}$$

In the case of a statistically steady solution, one can show that (5.14) has to be uniaxial, i.e. $\mathbf{C} = \boldsymbol{B} \otimes \boldsymbol{B}$ where the vector $\boldsymbol{B}(\boldsymbol{x}, t)$ characterizes the direction and the strength of the polymer molecule elongations weighted by their contribution into the stress tensor. The vector is given by

$$\mathbf{B}(\boldsymbol{x}(t), t) = \mathbf{W}(t, t_0)\mathbf{B}(\boldsymbol{x}_0, t_0)e^{-(t-t_0)/2\tau_p} \tag{5.16}$$

and is solution of the Eulerian equation

$$\frac{\partial}{\partial t}B_i + u_j \frac{\partial B_i}{\partial x_j} = B_j \frac{\partial u_i}{\partial x_j} - \frac{B_i}{\tau_p}, \tag{5.17}$$

which is similar to the one found for the magnetic field in MagnetoHydroDynamics (MHD, see Chap. 12) with τ_p in place of the magnetic resistivity, as discussed in Fouxon and Lebedev (2003). Similarly to the magnetic field, one can see that $\boldsymbol{B}$ is solenoidal, i.e. $\nabla \cdot \boldsymbol{B} = 0$. Note that the analogy with MHD is not only based on the similarity of Eq. (5.17) with the induction equation: this similarity holds for the vorticity equation and the equation for a passively transported bi-point vector as well. In addition, the last term in the modified Navier–Stokes Eq. (5.20) behaves as the Lorentz force, so that *coupled* equations (5.17) and (5.20) do correspond to MHD equations. Therefore, all methods and tools developed for the equivalent MHD model can be used in a straightforward way, the Alfven waves being replaced by elastic waves.

5.2.2 Navier–Stokes Equations for Polymer Solutions

In the case of incompressible flows, only the momentum equation for the solvent must be modified to account for the polymer effects since mass conservation is assumed to be left unchanged. The polymer molecules are assumed to have a negligible inertia and therefore they move as passive tracer. As a consequence, the Eulerian hydrodynamic model associated to (5.8) is

$$\frac{\partial}{\partial t}C_{ij} + \underbrace{u_k \frac{\partial}{\partial x_k}C_{ij}}_{\text{advection}} = \underbrace{\frac{\partial u_i}{\partial x_k}C_{kj} + \frac{\partial u_j}{\partial x_k}C_{ki}}_{\text{vortex stretching action}} \underbrace{-\frac{1}{\tau_p}\left(f(C_{ii})C_{ij} - \delta_{ij}\right)}_{\text{visco-elastic effects}} + \underbrace{\chi \frac{\partial^2}{\partial x_k^2}C_{ij},}_{\text{molecular diffusion}} \tag{5.18}$$

where χ denotes the solvent velocity and diffusivity, respectively. The diffusivity term is usually neglected. The additional stress T_{ij} originating in the action of the polymer on the fluid is

$$T_{ij}^p = \frac{\nu_p}{\tau_p}\left(f(C_{ii})C_{ij} - \delta_{ij}\right) = \frac{(1-\beta)\nu}{\tau_p}\left(f(C_{ii})C_{ij} - \delta_{ij}\right), \tag{5.19}$$

where ν_p is the zero-shear-viscosity of the polymer, $\nu = \nu_s + \nu_p$ is the total viscosity, with ν_s the solvent viscosity, and $\beta = \nu_s/\nu$ leading to the following momentum equation

$$\frac{\partial u_i}{\partial t} + u_j\frac{\partial u_i}{\partial x_j} = -\frac{\partial p}{\partial x_i} + \beta\nu\frac{\partial^2 u_i}{\partial x_i \partial x_i} + \frac{\partial T_{ij}^p}{\partial x_j}. \tag{5.20}$$

5.3 Description of Turbulence with FENE-P Model

The hydrodynamic model for polymer dilute suspensions appears as a modified momentum equation (5.20) in which a visco-elastic stress is added, coupled to an evolution equation for the polymer conformation tensor (5.18), along with $\nabla \cdot \boldsymbol{u} = 0$. Starting from this set of equations, all sequel relations dealing with kinetic energy, vorticity, enstrophy, dissipation ... discussed in Chap. 2 in the case of a Newtonian fluid can be extended. For the sake of brevity, all equations will not be repeated here, the emphasis being put on those which will enlight physical discussion. The procedure to derive them starting from the Navier–Stokes-FENE-P governing equations is identical to the one used in the Newtonian case, and therefore details will not be given.

5.3.1 Quantities and Related Equations in Physical Space

The evolution equation for turbulent kinetic energy becomes, in the isotropic case in the absence of external forcing term

$$\frac{\partial \mathcal{K}}{\partial t} = -\varepsilon_s - G, \quad G = \overline{\frac{\partial u_i'}{\partial x_j}T_{ij}^p}, \tag{5.21}$$

where the definition of the kinetic energy dissipation rate ε_s is the same as for Newtonian fluids, while the mean elastic energy stored by the polymer molecules evolves as

$$\frac{\partial \bar{K}_\ell}{\partial t} = G - \varepsilon_p, \quad \varepsilon_p = \frac{1}{2\tau_p}\overline{f(C_{ii})T_{ii}^p}. \tag{5.22}$$

Here, G and ε_p denote the energy transfer term between kinetic and elastic energy due to visco-elastic stress and the elastic energy dissipation rate (transformation of elastic energy into heat), respectively. It is seen that polymers may accelerate the decay of kinetic energy when $G > 0$ (molecules pump energy from the fluid, converting kinetic energy into elastic energy), or act as a source term by restoring some kinetic energy when $G < 0$.

The total mean free energy of the system, $\bar{K}_{tot} = \mathcal{K} + \bar{K}_\ell$, is governed by

$$\frac{\partial \bar{K}_{tot}}{\partial t} = -\varepsilon_s - \varepsilon_p = -\varepsilon, \tag{5.23}$$

where ε is related to the total dissipation rate. The equation for the evolution of the instantaneous total strain (2.40) and vorticity (2.39) are modified as

$$\frac{1}{2}\frac{\partial S^2}{\partial t} + u_j \frac{\partial S^2}{\partial x_j} = -S_{ik}S_{kj}S_{ij} - \frac{1}{4}\omega_i\omega_j S_{ij} - S_{ij}\frac{\partial^2 p}{\partial x_i x_j} + \nu_s S_{ij}\nabla^2 S_{ij} + \frac{\partial^2}{\partial x_k \partial x_j}\left(T^p_{ik}S_{ij}\right) \tag{5.24}$$

and

$$\frac{1}{2}\frac{\partial \omega^2}{\partial t} + u_j \frac{\partial \omega^2}{\partial x_j} = \omega_i\omega_j S_{ij} + \nu_s \omega_i \nabla^2 \omega_i + \epsilon_{nji}\omega_i \frac{\partial^2 T^p_{mj}}{\partial x_m \partial x_n}. \tag{5.25}$$

For isotropic turbulence, the associated equation for the variance total strain and variance of vorticity are

$$\frac{1}{2}\frac{\partial \overline{S'^2}}{\partial t} = -\overline{S'_{ik}S'_{kj}S'_{ij}} - \frac{1}{4}\overline{\omega'_i\omega'_j S'_{ij}} + \nu_s \overline{S'_{ij}\nabla^2 S'_{ij}} + \overline{\frac{\partial^2}{\partial x_k \partial x_j}\left(T^p_{ik}S'_{ij}\right)} \tag{5.26}$$

and

$$\frac{1}{2}\frac{\partial \overline{\omega'^2}}{\partial t} = \overline{\omega'_i\omega'_j S'_{ij}} + \nu_s \overline{\omega'_i \nabla^2 \omega'_i} + \epsilon_{nji}\overline{\omega'_i \frac{\partial^2 T^p_{mj}}{\partial x_m \partial x_n}}, \tag{5.27}$$

respectively.

5.3.2 *Quantities and Related Equations in Fourier Space*

The Lin equation for the three-dimensional kinetic energy spectrum $E(k)$ is transformed into

$$\frac{\partial E(k,t)}{\partial t} + 2\nu_s k^2 E(k) = T(k,t) + T^{[p]}(k,t), \tag{5.28}$$

where the new term $T^{[p]}(k,t)$ represents the net exchange at wave number k between kinetic and elastic energy. It is defined as

$$T^{[p]}(k,t) = 4\pi k^2 \iint_{\|\boldsymbol{k}\|=const} \overline{\left(\hat{S}^*_{ij}(\boldsymbol{k})\hat{T}^{p}_{ij}(\boldsymbol{k}) + \hat{S}_{ij}(\boldsymbol{k})\hat{T}^{p^*}_{ij}(\boldsymbol{k})\right)} d^2\boldsymbol{k}, \tag{5.29}$$

where the $\hat{\phi}(\boldsymbol{k})$ denotes the Fourier transform of $\phi(\boldsymbol{x})$ and S_{ij} is the symmetric part of the velocity gradient tensor.

Integration of the extended Lin equation and term-by-term identification with (5.21) lead to

$$\int_0^{+\infty} T^{[p]}(k,t)dk = -G, \tag{5.30}$$

which is not zero in the general case, showing that $T^{[p]}(k,t)$ is not a true transfer term like $T(k,t)$.

An spectral equation for the 3D elastic energy spectrum, $E_\ell(k,t)$, which is defined so that

$$\bar{K}_\ell(t) = \int_0^{+\infty} E_\ell(k,t)dk \tag{5.31}$$

can also be obtained. Since its exact expression in the general case directly deduced from (5.18) and (5.12) is complex due to the non-linear character of the Peterlin function, it will not be displayed here. The important fact is that it appears as (neglecting the effect of fluid diffusivity)

$$\frac{\partial E_\ell(k,t)}{\partial t} = T^{[p]}_{adv}(k,t) + T^{[p]}_{p}(k,t) + T^{[p]}_{visc}(k,t), \tag{5.32}$$

where terms in the right-hand side originate in the advection term, the vortex stretching term and the visco-elastic term, respectively. By integration over k and identification with (5.22), one observe that

$$\int_0^{+\infty} T^{[p]}_{adv}(k,t)dk = 0, \int_0^{+\infty} T^{[p]}_{p}(k,t)dk = G, \int_0^{+\infty} T^{[p]}_{visc}(k,t)dk = -\varepsilon_p. \tag{5.33}$$

The term $T^{[p]}_{adv}(k,t)$ is associated to the *elastic kinetic energy cascade*, and $T^{[p]}_{p}(k,t)$ to the *elastic-to-kinetic energy cascade*. It is important to keep in mind that $T^{[p]}_{p}(k,t)$ and $T^{[p]}(k,t)$ are related by the integral relation

$$-\int_0^{+\infty} T^{[p]}(k,t)dk = \int_0^{+\infty} T^{[p]}_{p}(k,t) = G, \tag{5.34}$$

but that there is no a priori scale-by-scale balance, i.e. $T^{[p]}(k,t) + T^{[p]}_{p}(k,t) \neq 0$.

Now introducing the 3D spectrum $E_{tot}(k,t) = E(k,t) + E_\ell(k,t)$ of total energy $\bar{K}_{tot}$, one obtains summing (5.40) and (5.35)

$$\frac{\partial E_{tot}(k,t)}{\partial t} = \underbrace{T^{[p]}(k,t) + T^{[p]}_{adv}(k,t) + T^{[p]}_{p}(k,t)}_{T_{tot}(k,t)} + T^{[p]}_{visc}(k,t) - 2\nu_s k^2 E(k) \tag{5.35}$$

with

$$\int_0^{+\infty} T_{tot}(k,t)dk = 0. \tag{5.36}$$

5.4 Turbulence Régimes in Dilute Polymer Solution

5.4.1 *On the Existence of Different Physical Turbulent Régimes*

As said above, the coupling between turbulent fluctuations and visco-elastic mechanisms can lead to the occurence of several physical régimes, which are discussed in the present section.

A first condition for a strong interaction to occur is that turbulent scales can stretch polymer molecules in an efficient way. One can hypothesize that polymer molecules are affected only by turbulent eddies whose time scales is smaller than polymer relaxation time τ_p. Considering small molecules such that the elongation $R = \sqrt{C_{ii}}$ is smaller than the Kolmogorov length scale η, the typical velocity gradient experienced by the molecules is measured by the inverse of Kolmogorov time scale, τ_η (see Sect. 4.2.1).

Therefore, a *necessary condition* for the polymers being stretched is

$$Wi = \frac{\tau_p}{\tau_\eta} \geq 1, \tag{5.37}$$

where Wi denotes the *Weissenberg number*. For $Wi < 1$, the polymer molecules relax more quickly compared to the turbulent forcing. The Weissenberg number measures the relative influence of the relaxation toward equilibrium and the stretching induced by the smallest scales, i.e. at the highest frequency generated by turbulence. Therefore they remain coiled and are passively advected without any visco-elastic effect. The fluid can be considered as a Newtonian fluid with a modified viscosity $\nu = (\nu_s + \nu_p)$. Switching from $Wi < 1$ to $Wi > 1$ therefore results in a dramatic change in flow physics, often referred to as the *coil-stretch transition*. The transition condition can also be expressed in terms of length scales (Xi et al. 2013). In a fully developed turbulent flow, one may expect that scales small enough for their characteristic time scale $\tau(k)$ is such that $\tau_p \geq \tau(k)$ will experience some viscoelastic effects, while larger scales will not. Therefore, there should be a scale, referred to as the *Lumley scale*, r_*, at which the coil-stretch transition occurs. Taking the classical scaling $\tau^{-1}(k) \propto \sqrt{k^3 E(k)}$ and assuming that the Kolmogorov scaling $E(k) = K_0 \varepsilon_s^{2/3} k^{-5/3}$ holds, the *local Weissenberg number*, $Wi(k) = \tau_p/\tau(k)$,

is equal to $Wi(k) = \sqrt{K_0}\tau_p\varepsilon_s^{1/3}k^{2/3}$. Therefore, the transition occurs at the Lumley wave number $k_* = (\tau_p\sqrt{K_0}\varepsilon_s^{1/3})^{-3/2}$, yielding

$$r_* = 1/k_* = (\tau_p\sqrt{K_0}\varepsilon_s^{1/3})^{3/2}. \tag{5.38}$$

It is worth noting that the Weissenberg number can be expressed as a function of the Reynolds number (Ouellette et al. 2014). Reminding that the Taylor-scale-based Reynolds number Re_λ is equal to $\sqrt{15}\tau_u/\tau_\eta$, with τ_u the turbulence time integral scale, one has

$$Re_\lambda = \sqrt{15}\frac{Wi}{De}, \quad De = \tau_p/\tau_u, \tag{5.39}$$

where De is referred to as the *Deborah number*. It measures the respective influence of the polymer relaxation toward the equilibrium coil state and the stretching imposed by the large energetic scale, τ_u being also interpreted as a characteristic time scale for non-linear cascade.

The criterion $r < r_L$ is not sufficient to ensures the coil-stretch transition, since the fluid response is also sensitive to the polymer concentration (Sreenivasan and White Sreenivasan et al. 2000). As a matter of fact, visco-elastic effects cannot be observed if the concentration of polymer molecules is too low. Accounting for this new criterion amounts to define a second length scale r_{**}. Three criteria have been proposed to define r_{**}:

- A criterion based on the ratio between elastic and kinetic energy proposed by Tabor and de Gennes in 1986, that states that transition occurs at scales such that their elastic energy is equal to their kinetic energy.
- A criterion based on the equality of polymeric viscoelastic stresses and solvent stresses at the transition scale, proposed by Balkovsky et al. (2001).
- A more recent criterion according to which transition takes place at scales at which the elastic energy flux is equal to the turbulent energy flux (Xi et al. 2013).

In practice, it is chosen in the following to discuss the different régimes reported in the literature in the (Wi, De) plane. The threshold values are given here for the sake of clarity, but it must be kept in mind that they are not exactly known, since results may depend on the Reynolds number and the rheological model selected for the polymer.

These régimes are:

- *Pseudo-Newtonian turbulence* observed for $Wi < 1$ or $De < 0.2$, in which visco-elastic elastic effects are negligible, and the fluid behaves as a Newtonian fluid with modified viscosity (see Sect. 5.4.2).
- *Elasto-inertial turbulence* observed for $Wi >$ and $De > 0.2$, in which both kinetic energy and elastic energy cascade exist, along with a possible elastic-to-kinetic energy cascade in some cases (see Sect. 5.4.3).
- *Elastic turbulence* observed for $De \ll 1$ at very low Reynolds number, in which the fluid is almost laminar and turbulence is made of elastic waves due to visco-elastic mechanisms (see Sect. 5.4.4).

5.4.2 Pseudo-Newtonian Turbulence

In this régime, the effect of polymer molecules is almost identical to those of passive particules, and the results reported for dilute particule-ladden flows are recovered. The fluid behaves as a classical Newtonian fluid with modified viscosity $\nu = \nu_s + \nu_p$. The two dissipation mechanisms are almost independent, and the ratio of ε_s and ε_p is proportional to β. Main results discussed for Newtonian isotropic turbulence are valid, and the reader is referred to Chap. 4.

5.4.3 Elasto-Inertial Turbulence

5.4.3.1 Energy Cascade(s) in Visco-Elastic Turbulence

This régime corresponds to strong interactions between fluid turbulence and visco-elasticity. Dynamics of the flow exhibits strong changes when increasing the Deborah number at constant Weissenberg number. Evolution of normalized polymer and solvent dissipations with respect to De obtained in high resolution DNS of forced turbulence (Valente et al. 2014, 2016) are displayed in Fig. 5.6 along with the normalized power input. It is observed that for De increasing from 0.2 to approximately 1, the fraction of the total dissipation stemming from the solvent is decreasing, the polymer elastic dissipation ε_p becoming dominant about $De \sim 0.4$. At $De = 1$ about 80–90% of the total dissipation comes from ε_s. This is observed to originate in two phenomena: an increase of the total dissipation and a depletion of ε_s. Keeping increasing the Deborah number for values larger than one, the trends are observed to be inverted. The solvent dissipation becomes dominant again for $De \geq 6$, along with a decrease of the total dissipation and an increase of ε_s (Fig. 5.1).

This behavior is understood looking at Fig. 5.2, which displays the integral spectral fluxes for different values of Wi and De. Here, spectral fluxes are defined integrating terms in the Lin equation (5.40) between 0 and k:

$$D(k) = 2\nu_s \int_0^k p^2 E(p)dp, \quad \Pi(k) = \int_0^k T(p)dp, \quad \Pi^{[p]}(k) = \int_0^k T^{[p]}(p)dp. \tag{5.40}$$

In statistically steady turbulence, one should have

$$F(k) = \Pi(k) + \Pi^{[p]}(k) + D(k) \quad \forall k, \tag{5.41}$$

where $F(k)$ denotes the integrated flux associated to the forcing term used to obtain statistical stationarity. It is observed that for $(Wi, De) = (0.5, 0.1)$ turbulence exhibits a nearly classical character, since it is dominated by either energy cascade flux $\Pi(k)$ or dissipation term $D(k)$ at all scales, the total kinetic-to-elastic energy transfer being small. This dynamics is schematized in Fig. 5.4. This picture

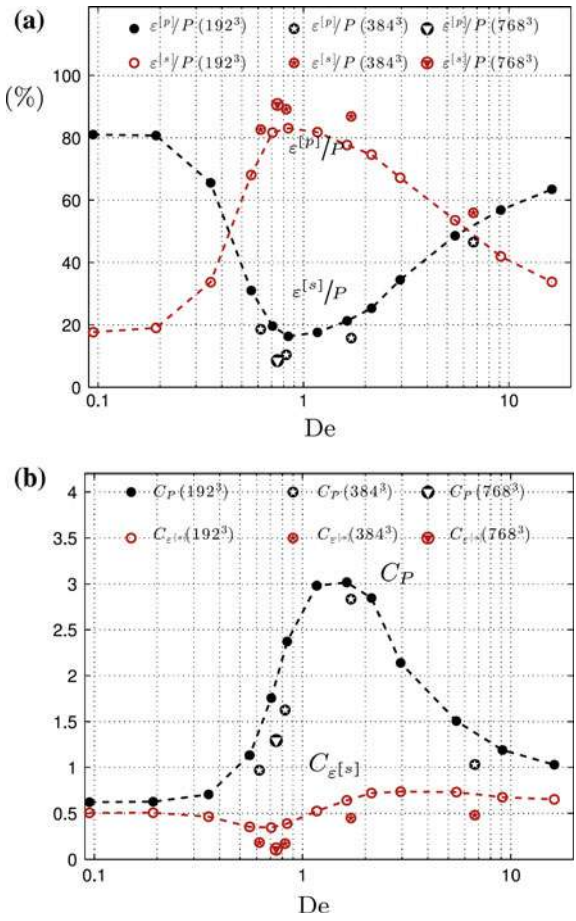

Fig. 5.1 Top: Evolution of the normalized solvent dissipation ε_s/P and normalized polymer dissipation ε_p/P versus the Deborah number, in DNS of forced isotropic turbulence with power input P; Bottom: evolution of normalized power input $C_P \sim PL/\mathcal{K}^{3/2}$ and normalized solvent dissipation $C_P \sim PL/\mathcal{K}^{3/2}$ versus De. Several grid resolutions are shown. From Valente et al. (2016) with permission of AIP

is deeply modified at higher Deborah numbers, since $\Pi^{[p]}(k)$ is observed to be the dominant mechanism at all scales at $De = 0.71$. In such cases, the kinetic-to-elastic energy transfer becomes the most important physical mechanisms responsible for loss of kinetic energy. The flux associated to the classical energy cascade is observed to almost vanish at large De (Fig. 5.3). Therefore, the depletion of ε_s is due to the fact that large scale kinetic energy is pumped by elastic modes along with a decrease of the kinetic energy cascade intensity. A deeper analysis reveals that the depletion of the cascade is not due to a decrease of nonlinearities, but to the fact that the modification of the topology of vortical structures by visco-elastic effects induces a large increase of the backward kinetic energy cascade from small to large scales, resulting in a vanishing net kinetic energy flux across scales.

For large De, it is observed that $\Pi^{[p]}(k)$ tends to decrease at very small scales, a phenomena that becomes very important for $De \geq 4-5$. This phenomena is associated to a change in the sign of the kinetic-to-elastic transfer function $T^{[k]}$ at small

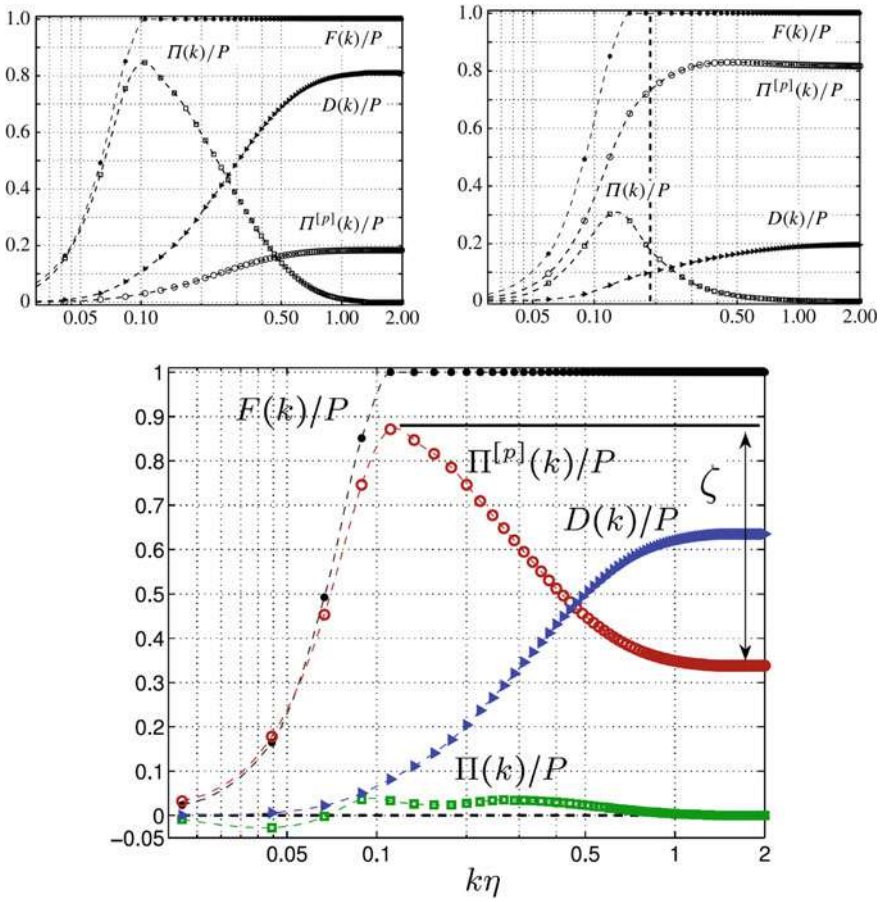

Fig. 5.2 Evolution of integral spectral fluxes appearing in the budget of turbulent kinetic energy versus normalized scale $k\eta$. All quantities are normalized by the power input P. Top-left: $(Wi, De) = (0.5, 0.1)$; Top-right: $(Wi, De) = (2.7, 0.71)$; Bottom: $(Wi, De) = (80.9, 16.2)$, where ζ denote the amplitude of the *elastic-to-kinetic energy cascade*. From Valente et al. (2016) with permission of AIP and Valente et al. (2014) with permission of CUP

scales. This indicates that polymer molecules give some energy back to small turbulent eddies, leading to the definition of an *elastic-to-kinetic energy cascade*: kinetic energy is pumped at large scales by elastic modes, then transferred to small scales by elastic mechanisms associated to an *elastic energy cascade* and finally transferred to small eddies. The amplitude of the integrated flux associated to this new cascade is measured by ζ in Fig. 5.2. It is observed to become as large as $\Pi^{[p]}(k)$ at $De \sim 16$, and this mechanisms is at play at all scales. The increase of the solvent dissipation ε_s at increasing De is therefore due the fact that turbulent eddies are fed more and more efficiently by the *elastic-to-kinetic energy cascade*, which remains the sole

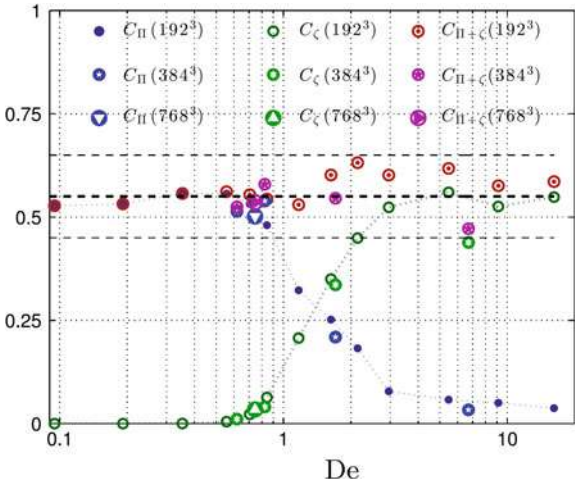

Fig. 5.3 Evolution of the maximum of normalized integral spectral flux $\Pi(k)$ and the amplitude of the *elastic-to-kinetic energy cascade*, ζ, appearing in the budget of turbulent kinetic energy versus De in DNS of forced turbulence. All quantities are normalized by the large scale factor $L/\mathcal{K}^{3/2}$. From Valente et al. (2016) with permission of AIP

mechanism that enforces a transfer of kinetic energy toward small scales at large De. This case is illustrated in Fig. 5.4.

The amplitude of the elastic-to-kinetic energy cascade is displayed in Fig. 5.3, in which the evolution of ζ is compared to the maximum of $\Pi(k)$. A first observation is that $\max(\Pi(k)) + \zeta = const$, showing that the amplitude of total transfer of kinetic energy toward small scales remains almost constant, since depletion of the kinetic energy cascade is balanced by the growth of the elastic-to-kinetic energy cascade. The second observation is that $\max(\Pi(k)) \leq \zeta$ for $De \geq 1$, showing that the most efficient kinetic energy cascade mechanisms is the elastic-to-kinetic energy cascade for Deborah numbers larger than unity.

5.4.3.2 Kinetic Energy Spectrum: Results and Model

The kinetic energy spectrum is observed to also dramatically change in the elasto-inertial régime, according to the value of the Deborah number (see Fig. 5.6). In the pseudo-Newtonian régime or at very low-De, the spectrum is almost identical to those found in isotropic Newtonian turbulence, and a Kolomogorov inertial range with $E(k) \propto \varepsilon_s^{2/3} k^{-5/3}$ is recovered. Increasing the Deborah number, one can observe in DNS results a continuous switch toward a range with $E(k) \propto k^{-3}$ for $0.6 \leq De \leq 1$, followed by a return to a régime such that $E(k) \propto k^{-5/3}$.

The existence of a spectral range such that $E(k) \propto k^{-3}$ can be predicted in a heuristic way. Assuming that the main effect of polymer molecules is to damp the local strain by absorbing kinetic energy of eddies whose characteristic time scale $\tau(k)$ is smaller than τ_p, one see that they ideally bound the local $Wi(k) = \tau_p/\tau(k)$ to one. Taking $\tau(k) = \sqrt{k^3 E(k)}$, it follows that

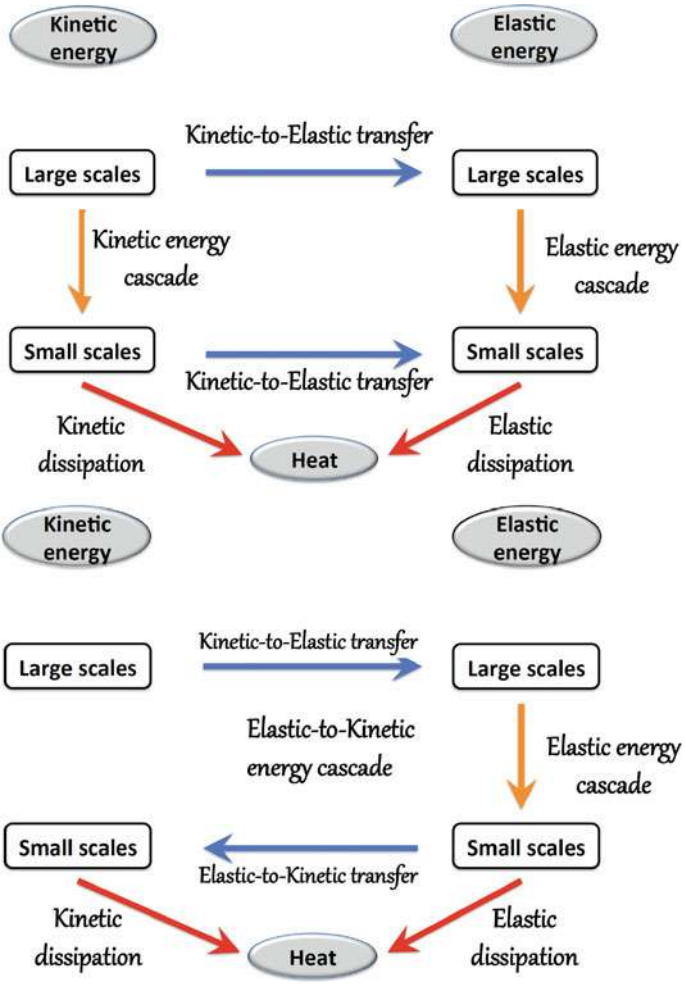

Fig. 5.4 Schematic illustrations of flow dynamics in (top) the pseudo-Newtonian régime or low-De elasto-inertial régime with negligible elastic-to-kinetic energy transfers at small scales and (bottom) the elasto-inertial régime at high Deborah number

$$\sqrt{k^3 E(k)} = \tau_p \quad \Longrightarrow E(k) \propto k^{-3}. \tag{5.42}$$

This *inertio-elastic range* should be observed for scales smaller than the Lumley wave number k_*. At very high Reynolds number, one should observed a classical inertial range with $E(k) \propto k^{-5/3}$ at larger scales, i.e. for $k < k_*$. A range with a k^{-3} has been observed in both DNS (Valente et al. 2016) and grid turbulence of Polyethylene oxide in water (Vonlanthen and Monkewitz Vonlanthen et al. 2013). It

is also supported by theoretical analysis of a linearized model derived from the mild elongation model (Fouxon and Lebedev 2003).[1]

The switch observed for increasing De up to 1 can be understood on the same grounds, since it corresponds to a growing efficiency of the kinetic-to-elastic transfer mechanisms at all active scales. For $De > 1$, the energy drained by the polymer molecules at large scales becomes larger than the energy they dissipate, and the extra energy is injected back to turbulent eddies leading to the rise of the *elastic-to-kinetic cascade mechanism*. As a consequence, the smoothing power of visco-elastic stresses on the local strain is saturated, and the local strain rate $\tau(k)$ is no longer bounded to one. At large De the amount of energy provided back to turbulence is large, since $\max(\Pi(k)) \ll \zeta$, and the -3 slope cannot be maintained. The fact that the spectrum relaxes toward a solution with a Kolmogorov-like spectrum may be explained reminding that, in the classical theory, dimensional analysis that leads to $E(k) \propto \varepsilon_s^{2/3} k^{-5/3}$ assumes that ε_s is the flux of kinetic energy across scales. As a matter of fact, one has $\Pi(k) = \varepsilon_s$ in the inertial range in steady fully developed Newtonian turbulence. In the present case, the total flux of energy across scales is not equal to $\Pi(k)$, since the elastic-to-kinetic energy cascade must be taken into account. Therefore, using dimensional analysis, a relevant scaling law should be (Valente et al. 2016)

$$E(k) \propto (\max(\Pi(k)) + \zeta)^{2/3} k^{-5/3}, \quad De \ll 1, \tag{5.43}$$

which is observed to be in satisfactory agreement with DNS data (Fig. 5.5).

A spectrum model was proposed by Vonlanthen and Monkewitz (2013) to extend expression (4.60) to the case of high Reynolds number with both Kolmogorov inertial and inertio-elastic ranges. Using equilibrium statistical equilibrium assumption, it reads

$$E(k) = K_0 \varepsilon_0 k^{-5/3} \left(1 - \Gamma + \Gamma(1 + \tilde{k}^{\gamma})^{-2/\gamma}\right)^{2/3} f_L(kL) f_\eta(k\eta_0, \tilde{k}), \quad \tilde{k} = k/k_* \tag{5.44}$$

where $0 \leq \Gamma \leq 1$ is an empirical parameter that accounts for concentration, molecular weight, degree of dilution and polymer type. The parameter γ governs the rounding between the inertial and the inertio-elastic range. ε_0 and η_0 are computed using the Kolmogorov range values. The large scale shape function $f_L(kL)$ can be taken identical to those for the Newtonian case. On the contrary, the small scale shape function is deeply modified as

[1] This model is formally equivalent to a linearized model for MagnetoHydroDynamics, Aflven waves being replaced by elastic waves. It also predicts equipartition of kinetic and elastic energy, which is not reported in non linear DNS results. This equilibrium shares many features of the equilibrium between kinetic and acoustic energy found in linearized theory for weakly compressible isentropic turbulence, see Sect. 13.2.2.

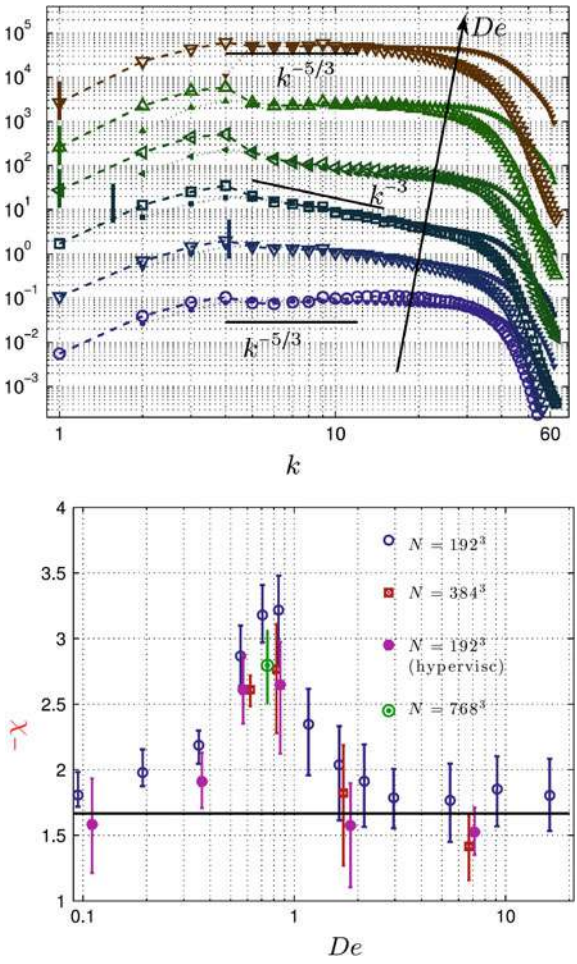

Fig. 5.5 Top: Evolution of the premultiplied turbulent kinetic energy spectrum versus De in DNS of forced turbulence. Bottom: Evolution of computed slope within the inertial range versus De, with uncertainty bars displayed. From Valente et al. (2016) with permission of AIP

$$\ln f_\eta(k\eta_0, \tilde{k}) = -\left\{5.2\left[(k\eta_0)^4 + 0.4^4\right]^{1/4} - 2.08\right\} \frac{\left(1 - \Gamma + \Gamma(1 + \tilde{k}^\gamma)^{-2/\gamma}\right)^{2/3}}{\left(1 - \Gamma + \frac{3}{2}\Gamma(1 + \tilde{k}^\gamma)^{-2/\gamma}\right)}. \tag{5.45}$$

The elastic energy spectrum $E_\ell(k)$ has been much less investigated that the kinetic energy spectrum. In the absence of strong interaction with the velocity field, Tabor and de Gennes proposed the following inertial range expression:

$$E_\ell(k) = n_p k_B T \left(\frac{k}{k_*}\right)^{5n/2}, \tag{5.46}$$

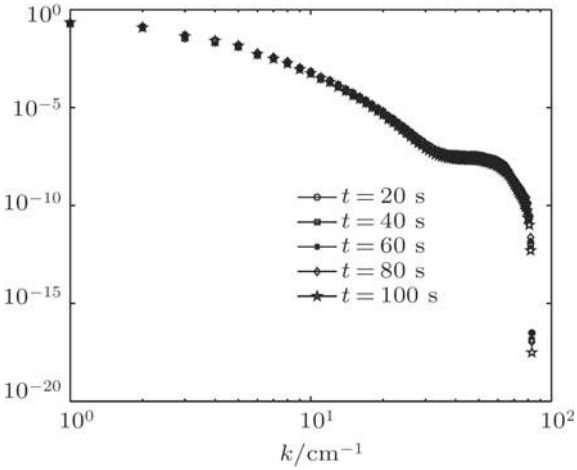

Fig. 5.6 Elastic energy spectrum $E_\ell(k)$ in DNS of low-Reynolds number isotropic turbulence with elastic-to-kinetic energy cascade. From Li et al. (2012) with permission of Chinese Phys. J. via IOP

where n_p, k_B, T, k_* and n denote the number of polymer molecules per unit volume, the Boltzmann constant, the temperature, the Lumley wave number and an exponent related to the average stretching of the local flow field, respectively. Experimental results lead to $n = 1 \pm 0.2$ for Polyacrylamide in water, for a concentration up to 10 ppm (parts per million by weight) (Xi et al. 2013).

In the case of strong interaction with the fluid at Deborah numbers such that the transfers of energy between polymer and turbulent eddies are strong, the picture may be different, as illustrated in Fig. 5.6 which displays the elastic energy spectrum computed in a low-Reynolds DNS in a case with significant elastic-to-kinetic energy cascade. A plateau is observed at very small scales, which corresponds to a pile-up of elastic energy at very small scales.

5.4.4 Elastic Turbulence

Elastic turbulence has been analyzed theoretically (Balkovsky et al. 2001) and observed in laboratory experiments at very low Reynolds number (Groisman and Steinberg 2000). In this régime one has $De \gg 1$, meaning that all scales are dominated by visco-elastic effects. The polymer stress tensor can reach a universal state. The underlying physics is similar to the one found in the inertio-elastic range discussed in the preceding section, i.e. one observes elastic waves propagating at a speed close to $\sqrt{C_{ii}}$. The kinetic energy spectrum is expected to be $E(k) \propto k^{-3}$, but there is no results available at present time to assess that hypothesis.

5.5 Visco-Elastic Effects on Flow Topology

Equations (5.26) and (5.27) show that visco-elastic stresses may have a deep effect on flow topology, since they appear in the budget equations of both fluctuating strain and vorticity, which are at the core of turbulence non linear dynamics (see Sect. 4.11.3). The modification in the kinetic energy cascade due to the growth of the backward energy cascade discussed above is the footprint of dramatic changes in velocity gradient topology and dynamics, since velocity gradient self-amplification mechanisms govern Newtonian isotropic turbulence dynamics.

Typical modifications of flow topology are illustrated in Fig. 5.7. It is observed that viscoelastic effects result in a strong depletion all types of small scales structures, e.g. Cai et al. (2010), Cai et al. (2011), Horiuti et al. (2013), Valente et al. (2014), Valente et al. (2016). Tube-like vortices that are observed in the Newtonian case can be almost completely inhibited at large De, while vortex sheets are flattened and smoothed. A fine analysis of associated p.d.fs shows that large extreme values of fluctuating strain and vorticity are severely damped in dilute polymer solutions after the coil-stretch transition.

As discussed in Sect. 4.11, the main mechanisms are the self-amplification of strain in the generation of irrotational strain (term $-\overline{S'_{ik}S'_{kj}S'_{ij}}$ in Eq. (5.26)), and generation of vorticity by vortex stretching (term $\overline{\omega'_i\omega'_j S'_{ij}}$ in Eq. (5.27)).

The analysis of low-to-medium Reynolds number DNS (De Angelis et al. 2005; Cai et al. 2010, 2011; Li et al. 2012; Perlekar et al. 2006, 2010; Valente et al. 2014, 2016) provides some insight into the way that visco-elasticity modifies the flow dynamics, at least for cases in which the elastic-to-kinetic energy cascade does not completely overwhelms other mechanisms. The main observations are the following:

- Depletion of strain is due to a reduction of strain generation. The detailed analysis of the results show that polymer-induced term in (5.26) is mainly negative, and in opposite sign with the self-amplification term when the later is negative. The two terms have similar amplitude, showing the importance of the visco-elastic effect. Therefore, two effects are at play that inhibit the generation of strain: (i) the existence of a visco-elastic term that preferentially reduces the strain generation and (ii) the fact that the self-amplification mechanism itself is not intrinsically modified but weakened since the strain amplitude is reduced and that it scales as $\|\mathbf{S}\|^3$. From the phenomenological viewpoint, the polymer effects inhibit the generation of vortex sheets.
- Depletion of vorticity is not due to a significant modification of the vortex stretching mechanism, since angles between the vorticity vector and the eigenvectors of the strain tensor are almost the same as in the Newtonian case. The vorticity vector is observed to be preferentially aligned with the first and intermediate eigenvectors of the conformation tensor $\mathbf{C}$ and in the two directions along which the polymer molecules are mostly stretched. Analysis of the p.d.f.s shows that the visco-elastic term in (5.27) is mainly opposed to the vortex stretching term and then appears as a sink term for vorticity. As for the strain case, depletion of vorticity originates in several factors: (i) the existence of a visco-elastic force that counteracts the vortex

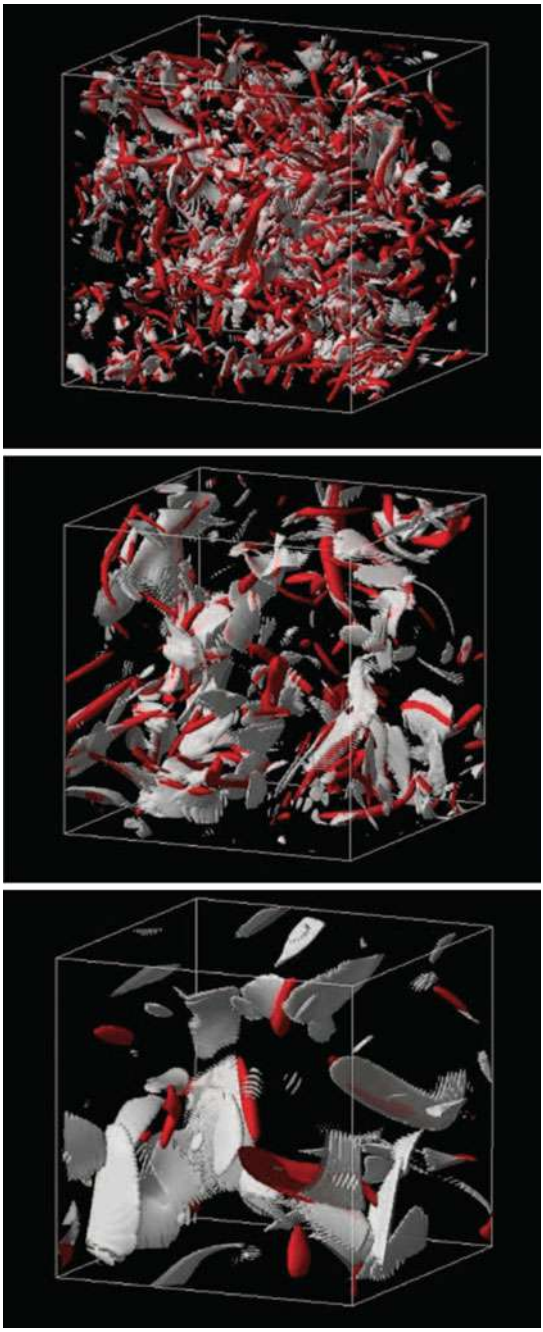

Fig. 5.7 Instantaneous flow topology in Newtonian fluid (top), visco-elastic turbulence (middle), visco-elastic turbulence with very strong vorticity depletion effect (bottom). Red: vortex structures; Grey: vortex sheets. From Horiuti et al. (2013) with permission of AIP

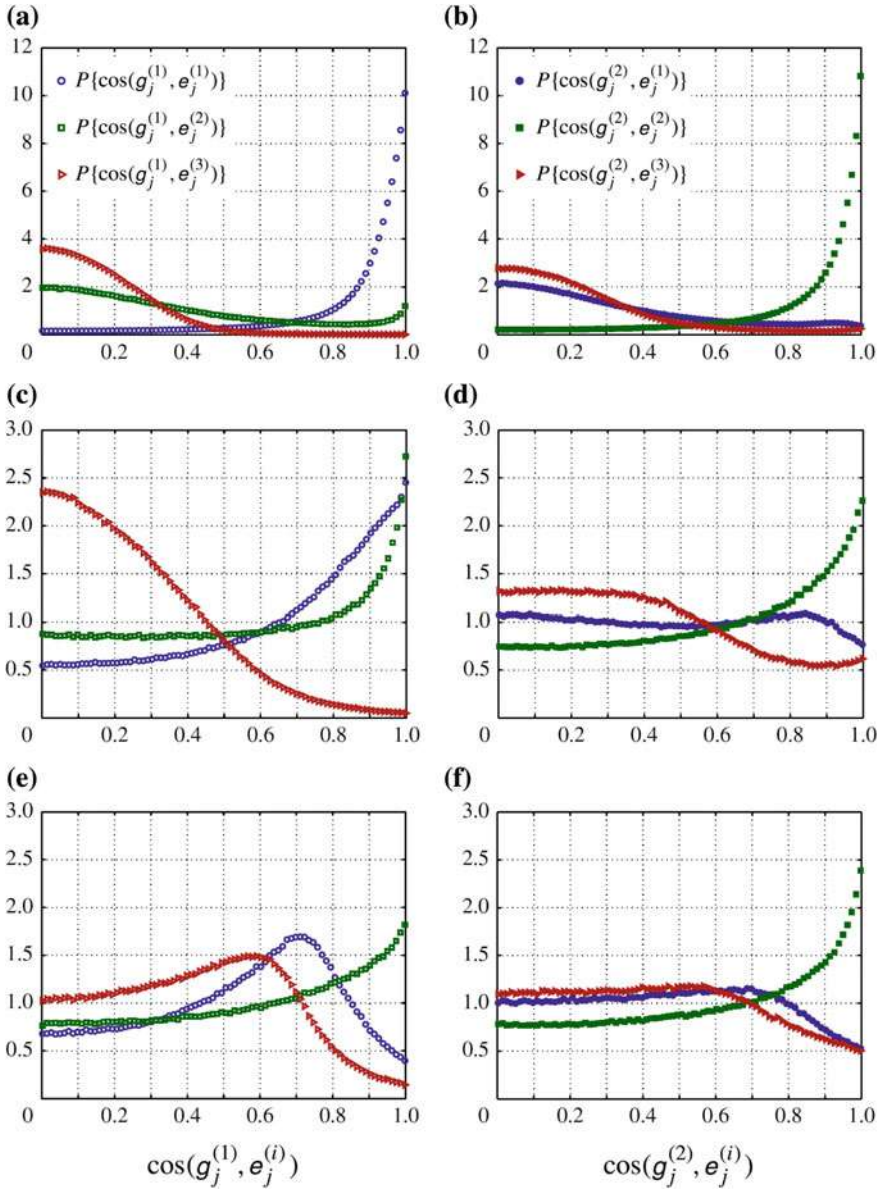

Fig. 5.8 Evolution of the p.d.f. of the alignment of the principal axes of $\mathbf{C}$ with those of the strain-rate tensor $\mathbf{S}$. Left column: eigenvector associated with the largest eigenvalue; Right column: intermediary eigenvalue: Top: $De = 0.19$, Middle: $De = 0.56$, Bottom: $De = 2.14$. From Valente et al. (2014) with permission of CUP

stretching mechanisms, (ii) the reduction of the vortex stretching term because of the damping of strain and (iii) the reduction of the vortex stretching term because of the decrease of vorticity.

The occurence of the elastic-to-kinetic energy cascade is tied to the sign of the term $\frac{\partial u_i'}{\partial x_j} T_{ij}^p$. Elastic energy is converted into kinetic energy if it is negative, while the inverse transfer occurs when it is positive.

This tensor product can be rewritten as

$$\frac{\partial u_i'}{\partial x_j} T_{ij}^p = \lambda_i \xi_j \cos^2(e_k^{(i)}, g_k^{(i)}), \tag{5.47}$$

where $\boldsymbol{e}^{(i)}$ and λ_i, $i = 1, 3$ denote the eigenvectors and eigenvalues of the strain tensor $\mathbf{S}$ and $g^{(i)}$ and ξ_i are related to those of $\mathbf{T}^p$. These terms are sorted in the order of decreasing eigenvalues. The p.d.f.s of the cosine of the angle between the eigenvectors at different Deborah numbers is displayed in Fig. 5.8. In all cases, $g^{(2)}$ is preferentially aligned with $\boldsymbol{e}^{(2)}$. On the contrary, the $g^{(1)}$ exhibits a strong dependency on the Deborah number. At low De it is mainly aligned with $\boldsymbol{e}^{(1)}$, leading to a net drain of kinetic energy by polymer molecules. At high De, it is preferentially aligned with $\boldsymbol{e}^{(2)}$, but with alternative preferred directions with angles of 45 and 55 with $\boldsymbol{e}^{(1)}$ and $\boldsymbol{e}^{(3)}$, respectively. The latter can lead to negative values of the contraction of the two tensor, and then to the elastic-to-kinetic energy cascade. At medium De, $g^{(1)}$ can be aligned with either $\boldsymbol{e}^{(1)}$ or $\boldsymbol{e}^{(2)}$, leading to both elastic-to-kinetic and kinetic-to-elastic transfers.

References

Balkovsky, E., Fouxon, A., Lebedev, V.: Turbulence of polymer solutions. Phys. Rev. E **64**, 056301 (2001)

Berti, S., Bistagnino, A., Boffetta, G., Celani, A., Musacchio, S.: Small-scale statistics of viscoelastic turbulence. Europhys. Lett. **76**, 63–69 (2006)

Cai, W.H., Li, F.C., Zhang, H.N.: DNS study of decaying homogeneous isotropic turbulence with polymer additives. J. Fluid Mech. **665**, 334–356 (2010)

Cai, W.H., Li, F.C., Zhang, H.N.: DNS study of the interaction between the polymer effect and velocity gradient tensor in decaying homogeneous isotropic turbulence. Chin. Phys. B **20**, 124702 (2011)

Casciola, C.M., De Angelis, E.: Energy transfer in turbulent polymer solutions. J. Fluid Mech. **581**, 419–436 (2007)

De Angelis, E., Casciola, C.M., Benzi, R., Piva, R.: Homogeneous isotropic turbulence in dilute polymer solutions. J. Fluid Mech. **531**, 1–10 (2005)

Dubief, Y., Terrapon, V.E., Soria, J.: On the mechanism of elasto-inertial turbulence. Phys. Fluids **25**, 110817 (2013)

Fouxon, A., Lebedev, V.: Spectra of turbulence in dilute polymer solutions. Phys. Fluids **15**, 2060–2072 (2003)

Groisman, A., Steinberg, V.: Elastic turbulence in a polymer solution flow. Nature **405**(6872), 53–55 (2000)

Horiuti, K., Matsumoto, K., Fujiwara, K.: Remarkable drag reduction in non-affine viscoelastic turbulent flows. Phys. Fluids **25**, 015106 (2013)
Jin, S., Collins, L.R.: Dynamics of dissolved polymer chains in isotropic turbulence. New J. Physics **9**, 360 (2007)
Li, F.C., Cai, W.H., Zhang, H.N., Wang, Y.: Influence of polymer additives on turbulent energy cascading in forced homogeneous isotropic turbulence studied by direct numerical simulations. Chin. Phys. B **21**, 114701 (2012)
Liberzon, A., Guala, M., Kinzelbach, W., Tsinober, A.: On turbulent kinetic energy production and dissipation in dilute polymer solutions Phys. Fluids **18**, 125101 (2006)
Lumley, J.L.: Turbulence in NonNewtonian fluids. Phys. Fluids **7**, 335–337 (1964)
Ouellette, N.T., Xu, H., Bodenschatz, E.: Bulk turbulence in dilute polymer solutions. J. Fluid Mech. **629**, 375–385 (2014)
Perlekar, P., Mitra, D., Pandit, R.: Manifestations of drag reduction by polymer additives in decaying, homogeneous, isotropic turbulence. Phys. Rev. Lett. **97**, 264501 (2006)
Perlekar, P., Mitra, D., Pandit, R.: Direct Numerical Simulations of statistically steady, homogeneous, isotropic fluid turbulence with polymer additives. Phys. Rev. E **82**, 066313 (2010)
Sreenivasan, K., White, C.M.: The onset of drag reduction by dilute polymer additives, and the maximum drag reduction asymptote. J. Fluid Mech. **409**, 149–164 (2000)
Valente, P.C., da Silva, C.B., Pinho, F.T.: The effect of viscoelasticity on the turbulent kinetic energy cascade. J. Fluid Mech. **760**, 39–62 (2014)
Valente, P.C., da Silva, C.B., Pinho, F.T.: Energy spectra in elasto-inertial turbulence. Phys. Fluids **28**, 075108 (2016)
Vincenzi, D., Perlekar, P., Biferale, L., Toschi, F.: Impact of the Peterlin approximation on polymer dynamics in turbulent flows. Phys. Rev. E **92**, 053004 (2015)
Vonlanthen, R., Monkewitz, P.A.: Grid turbulence in dilute polymer solutions: PEO in water. J. Fluid Mech. **730**, 76–98 (2013)
Xi, H.D., Bodenschatz, E., Xu, H.: Elastic energy flux by flexible polymers in fluid turbulence. Phys. Rev. Lett. **111**, 024501 (2013)

Chapter 6
Isotropic Turbulence with Coupled Microstructures. II: Quantum Turbulence

6.1 Introductory Phenomenology to Quantum Turbulence

Quantum Turbulence is a relatively recent field of research compared with classical turbulence, since this terminology was coined in 1982 by C. Barenghi in his PhD thesis. It encompasses a wide range of turbulent phenomena observed at ultra-low temperature below a critical fluid-dependent temperature T_c in superfluid Helium (superfluid phase of liquid ^{4}He and ^{3}He-B) and Bose–Einstein atomic condensates (dilute atomic alkalis gas such as lithium or rubidium vapor, in practice), some of which having been studied since the 1950s. Typical values of T_c are displayed in Table 6.1. The present chapter is restricted to the case of isotropic turbulence in such fluids, the emphasis being put on main differences and common features with isotropic turbulence in classical Newtonian fluids, as discussed in Chap. 4. Here, the purpose is to discuss features of turbulence when the very structure of small scales is radically different from the one found in classical fluids. Therefore, the emphasis will be put on the aspects related to fluid mechanics of superfluid turbulence, introducing only the minimum amount of quantum physics. Historical perspectives and issues related to experimental techniques will not be detailed here, and the reader is referred to recent review articles, e.g. Vinen and Niemela (2002), Vinen (2006, 2010), Tsubota (2009, 2013), Skrbek and Sreenivasan (2012), Nemirovskii (2013), Barenghi et al. (2014), Tsatos et al. (2016), Tsubota et al. (2017).

The most striking feature of superfluids is that, as anticipated by Onsager and Feynman in the late 1940s and the early 1950s respectively, superfluids at zero temperature behave as inviscid fluids in which circulation and vorticity are quantized. More precisely, all vorticity is concentrated in discrete filament vortices with radius r_c and fixed vorticity (see Table 6.1 and Sect. 6.3 for details about the properties of quantized vortices and their dynamics), and superfluid turbulence consists of a disordered tangle of such vortices. A typical tangle is shown in Fig. 6.1. An important fact is that the vortex radius is fluid-dependent and may vary with pressure and temperature, but it is not governed by the flow. The quantum of circulation associated to each vortex is $\hbar/m$, where $\hbar = 6.6260\,10^{-34}$ m^2 kg/s is the Planck constant and m

P. Sagaut and C. Cambon, *Homogeneous Turbulence Dynamics*,
https://doi.org/10.1007/978-3-319-73162-9_6

Table 6.1 Main features of the three levels of description of Quantum turbulence

	^{4}He	^{3}He-B	Bose–Einstein atomic condensates
Transition temperature at saturated vapor pressure T_c	2.17 K	1 mK	O(nK)
Threshold for pure superfluid behavior	$T < 0.3 - 1$ K	$T < 200\,\mu$K	
State	Liquid	Liquid	Gas (alkalis)
Quantized vortex radius r_c	~ 1 Å $= 10^{-10}$ m	$\sim$800 Å	10^{-7} m (10^5 atoms of ^{87} Rb)
Inter-vortex spacing ℓ	$\sim 10^{-5}$ m	$\sim 10^{-5}$ m	$\sim r_c$
Typical $\Lambda = \log(\ell/r_c)$	$\uparrow$ 12–14	$\uparrow$ 4	$\sim$1–2
Circulation quantum $\kappa = \hbar/m$	$9.997\,10^{-8}$ m^2/s ($m = m_4$)	$6.65\,10^{-8}$ m^2/s ($m = 2m_3$)	
Kelvin-wave weak turbulence (small scales)	Yes	Yes	Yes
Pseudo-Kolmogorov turbulence (large scales)	Yes	No (high normal fluid viscosity)	Yes (in DNS)
Compressibility effects on turbulence	Weak	Weak	Strong

the mass of the particule given by quantum physics theory (1 atom in ^{4}He, 2 atoms in ^{3}He-B). Superfluid flows are characterized by two microscopic length scales: the quantized vortex radius, r_c, and the mean inter-vortex distance, ℓ. At scales smaller or of the order of ℓ, superfluid flows are governed by quantized vortex dynamics and exhibit a very particular dynamics not found in classical fluids.

Key elements of quantized vortex dynamics are reconnection, i.e. interaction with neighbouring vortices yielding the creation of new vortices, oscillations due to Kelvin waves excited by reconnection phenomena, and dissipation of energy via emission of phonons (i.e. acoustic waves in the parlance of classical fluid mechanics, see Sect. 3.2) in ^{4}He or quasi-particules trapped in vortex core in ^{3}He-B. A very important fact is that quantized vortex vorticity depends on the fluid, the temperature and the pressure, and that all vortices have the same vorticity. Therefore, they are not sensitive to the vortex stretching mechanism which is a leading mechanism in vorticity dynamics in classical fluids. As a matter of fact, quantized vortices in superfluids are not classical vortices, and their name may be misleading. Looking at microscopic physical theories stemming from quantum physics, they corresponds to topological defects of a state vector which induce a quantum of circulation, than can be tied to an equivalent quantum of vorticity thanks to Kelvin's circulation theorem.

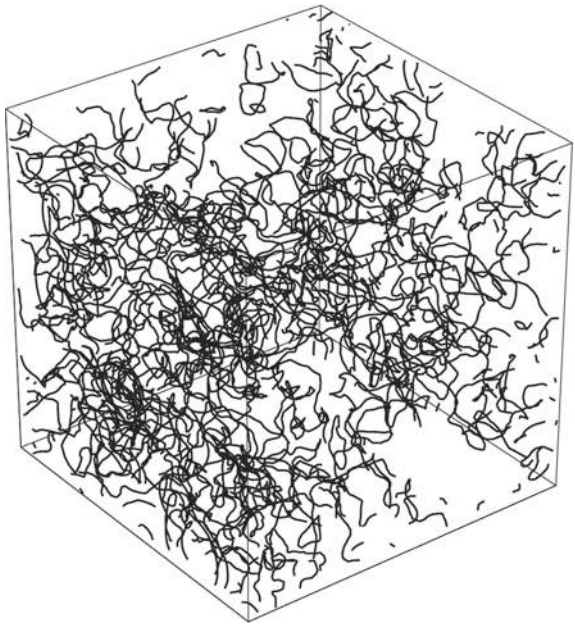

Fig. 6.1 Typical view of a vortex filament tangle in a numerical simulation of counterflowing ^{4}He based on the Biot–Savart filament vortex model. From Baggaley et al. (2014) with permission of APS

At scales much larger than ℓ classical hydrodynamics phenomena can be observed under some circumstances, leading to so-called *quasi-classical* régimes. In the case fluctuating kinetic energy is injected, e.g. using a grid, at scales much larger than ℓ, a flow can develop at hydrodynamics scales that shares many features with classical turbulence, as observed in ^{4}He. The fact that all vortices have the same radius and that vortical structures whose typical size is several order of magnitude larger than r_c can occur is not paradoxical. As a matter of fact, large vortical hydrodynamic scales correspond to pockets of fluids in which quantized vortices are partially or totally polarized, yielding a non-zero coherent vorticity at large scales. Such pockets are often referred to as *vortex bundles*. It is important noting that large-scales features are very dependent on both the superfluid under consideration and the way that turbulence is injected, e.g. via mechanical forcing or thermal forcing. Key elements of Quantum Turbulence in the limit of zero-temperature are displayed in Sect. 6.4. A schematic view based on actual knowledge of superfluid dynamics, mostly based on counterflowing ^{4}He turbulence theory is displayed in Fig. 6.2.

Superfluid flows at non-zero temperature are more complex, since thermal effects come into play. A powerful paradigm to describe these effects is the two-fluid hydrodynamic model, proposed by Tisza and Landau. According to this model, a superfluid flow at non-zero temperature can be described as the combination of a superfluid flow and a classical viscous fluid flow, the two fluids being tied by a *mutual friction force*. This mutual friction force is a paradigm to account for interactions between quantized vortices and quasi-particules that constitute the normal fluid component (more precisely scattering of phonons and rotons on the vortex core). In a macroscopic

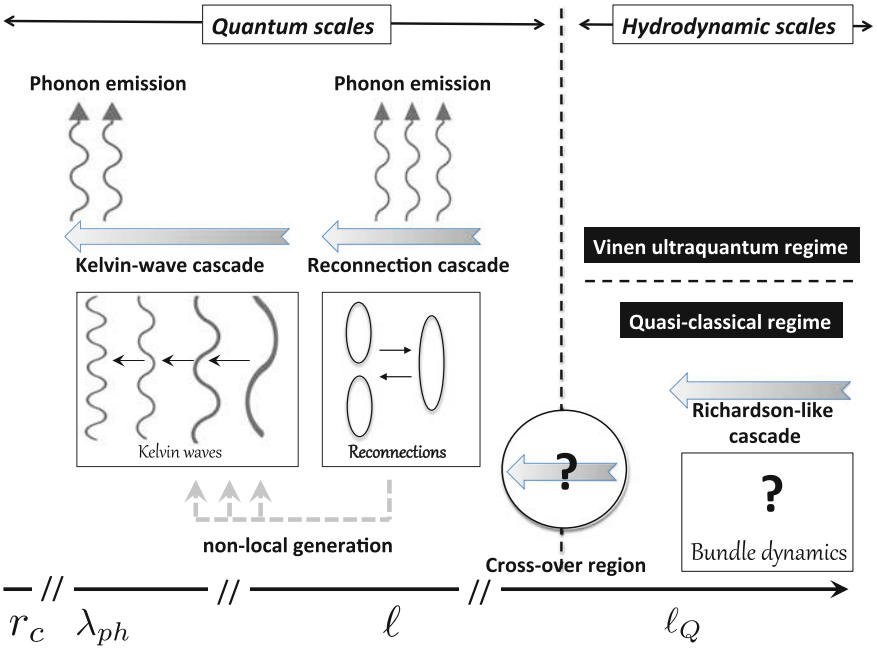

Fig. 6.2 Schematic view of Quantum Turbulence dynamics, mostly relevant for counterflowing ^{4}He turbulence. r_c: quantized vortex radius; λ_{ph}: cutoff length of the Kelvin wave cascade due to phonon emission; ℓ: mean inter-vortex distance; ℓ_Q: cutoff length scale of the pseudo-Kolmogorov inertial range at large hydrodynamic scales. Kelvin wave cascade is likely not to occur in ^{3}He-B and Bose–Einstein condensates, due to the low value of the ratio ℓ/r_c. Phonon radiation must be replaced by quasi-particule radiation in ^{3}He-B

description, these interactions are represented by forces exerted on quantized vortices, e.g. a drag force, and the reciprocal force experienced by the normal fluid. Despite this model is mostly an empirical model that does not derive rigorously from finer microscopic models, it appears to be a meaningful and powerful model to describe large-scale hydrodynamic features of turbulence in some cases, especially liquid superfluid helium. In this model, the mass fraction of both superfluid and normal fluid are tabulated as functions of temperature. The viscosity of the normal fluid is strongly dependent on the nature of the superfluid under consideration: while the normal component of ^{4}He exhibits a very low viscosity, ^{3}He-B is a very viscous fluid whose viscosity behaves as $1/T^2$. Consequently, hydrodynamic large scales may exhibit very different dynamics depending on the fluid. As an example, let us mention that quasi-classical turbulence has been reported at scales much larger than the inter-vortex distance ℓ in ^{4}He, while the normal fluid component is almost at rest due to its very high viscosity in existing experimental realization of turbulence in ^{3}He-B. Mutual friction makes it possible to account for several effects such has the lock-on between superfluid and normal fluid at large hydrodynamic scales, damping

of Kelvin waves, but also production of turbulence in counterflowing turbulence. Physical origin and models for the mutual friction are discussed in Sect. 6.6.

The case of dilute gas Bose–Einstein condensates is different, since these gas have ultra-low densities (in practice, experimental realizations deal with $O(10^3)$ - $O(10^7)$ trapped atoms of alkalis gas at adequate temperature and pressure). Here, the range of scales is much smaller than in superfluid liquid helium, and ad hoc models must be found. An interesting point is that quantized vortex radius is much larger than in superfluid helium, allowing for highly improved experimental observations. Another point is that, due to their very low-density, compressibility effects are more important so that an adequate two-fluid model should incorporate many features of weakly compressible turbulence (see Sect. 13.2).

Quantum turbulence is generic term that encompass a huge number of physical phenomena that occur on a dramatically broad range of scales, from atomic scale to large scales of turbulence such as the integral length scale. It is also observed that the nature of the fluid, liquid for superfluid helium of gas for atomic Bose–Einstein condensates, also plays a great role. Therefore, several models have been developed to represent Quantum Turbulence dynamics at different scales in a efficient way, each model being optimized to account for a set of physical mechanisms occuring over a fixed range of scales. These models are described in Sect. 6.2.

6.2 The Three Levels of Description and Physical Modelling

There are three main models (with multiple variants and ad hoc corrections to account for specific additional phenomena not captured in the original models):

- The Gross–Pitaevskii Equation, also referred to as the nonlinear Schrödinger equation, which is well suited to describe physics in weakly interacting Bose gas at zero temperature from the atomic scale to the typical inter-vortex distance ℓ, and which accounts for almost all phenomena related to single quantized vortex dynamics (see Sect. 6.2.1).
- The filament vortex model based on the Biot–Savart law, in which quantized vortices are represented as incompressible vortex filaments with zero radius obeying the incompressible Euler equations for an inviscid fluid (see Sect. 6.2.2).
- Two-fluid hydrodynamic model which is build to describe coarse-grained physics at scale much larger than the inter-vortex distance (see Sect. 6.2.3). This can be interpreted as a kind of homogenized model, keeping in mind that it is note derived from finer models using a rigorous homogenization procedure.

Their main features and limitations are displayed in Table 6.2.

Table 6.2 Main features of the three levels of description of Quantum turbulence

	Gross–Pitaevskii equation	Biot–Savart vortex line model	Two-fluid hydrodynamic model
Liquid superfluid helium	Limited accuracy (ultra-low density assumption violated)	Yes	Yes
Atomic Bose–Einstein condensates	Yes	A priori poorly accurate (incompressibility assumption)	No
Quantized vortex internal dynamics	Yes	No	No
Quantized vortex reconnection	Yes	With ad hoc empirical model only	No
Kelvin waves and Kelvin cascade	Yes	Yes	No
Large-scale hydrodynamics (vortex bundles)	A priori loss of accuracy (single-state assumption may be violated)	LIA not accurate due to importance of non-local effects	Yes
Dissipative mechanisms	Yes (phonon emission)	No	Yes (equivalent macroscopic viscosity)
Finite temperature/mutual friction effects	No (zero-temperature assumption, but some ad hoc models exist)	With ad hoc empirical model only with ad hoc empirical model only	Yes, ad hoc models with tabulated $\rho_n(T)$ and $\rho_s(T)$
Dilatational effects	Yes	No	No

6.2.1 Gross–Pitaevskii Model for Superfluid Dynamics

6.2.1.1 The Gross–Pitaevskii Equation

The Gross–Pitaevskii equation, also referred to as the nonlinear Schrödinger equation, was derived in 1961 to describe quantized vorticity in a Bose gas at ultra-low temperature and density (Tsubota 2009, 2013; Nemirovskii 2013; Tsatos et al. 2016). This is a mean-field theory, in which it is assumed that all bosons are in the same quantum state, so that the whole system can be described thanks to a single particule state $\psi(\boldsymbol{x}, t)$, which is a complex-valued function. With such a simplification, the particule density ρ is given by $|\psi|^2$, i.e. the number of particules N is equal to

$$N = \iiint |\psi(\boldsymbol{x})|^2 d^3\boldsymbol{x}. \tag{6.1}$$

The Gross–Pitaevskii evolution equation for a system of N particules of mass m is

$$\imath\hbar\frac{\partial}{\partial t}\psi(\boldsymbol{x},t)=\left(-\frac{\hbar^2}{2m}\nabla^2+V_{trap}+g|\psi(\boldsymbol{x},t)|^2\right)\psi(\boldsymbol{x},t), \tag{6.2}$$

where $\hbar$, V_{trap} and g are related to the Planck constant, the confining external potential[1] and the strength of the particule interactions, respectively. The interaction between particules is here assumed to be weak thanks to the hypotheses of (i) ultra-low temperature and (ii) very low-density, leading to the use of the term $|\psi(\boldsymbol{x},t)|^2$. It is assumed to consist of weak s-wave scattering that can be modeled by a two-body contact potential. The amplitude term g is taken proportional to the s-wave scattering length r_s, yielding $g=4\pi r_s\hbar^2/m$.

Using the classical polar expression for complex numbers $\psi(\boldsymbol{x},t)=f(\boldsymbol{x},t)e^{\imath S(\boldsymbol{x},t)}$, the macroscopic fluid velocity $\boldsymbol{u}_s$ and momentum $\rho_s\boldsymbol{u}_s$ are recovered as

$$\boldsymbol{u}_s=\frac{\hbar}{m}\nabla S,\quad \rho_s=f^2 \tag{6.3}$$

and relation (6.2) is rewritten as the following system

$$\frac{\partial f^2}{\partial t}=-\frac{\hbar}{m}\nabla\cdot(f^2\nabla S), \tag{6.4}$$

$$-\hbar\frac{\partial S}{\partial t}=-\frac{\hbar^2}{2m}\nabla^2 f+\frac{1}{2}m\|\boldsymbol{u}_s\|^2+V(\boldsymbol{x})+gf^2. \tag{6.5}$$

For an infinite time independent system, the quantized vortex radius can be evaluated as being equal to the *healing length* r_c, i.e. the distance over which the perturbation of the base state due to the vortex is non-negligible. Therefore, it is estimated as the length scale over which the interaction term balances kinetic energy, i.e.

$$\frac{\hbar^2}{2m}|\nabla\psi|^2\sim g|\psi|^4\implies\frac{\hbar^2}{2m}\frac{|\psi|^2}{r_c^2}=g|\psi|^4\implies r_c=\frac{\hbar}{\sqrt{2mg\rho_0}}, \tag{6.6}$$

where ρ_0 is the density of the uniform base state. Typical values are $r_c\sim 10^{-10}$ m in ^{4}He and $r_c\sim 10^{-8}$ m in ^{3}He-B, respectively.

6.2.1.2 Equivalent Hydrodynamic Equations

The equation for mass conservation appears to be exactly the same as for classical fluids, i.e.

$$\frac{\partial\rho_s}{\partial t}+\nabla\cdot(\rho_s\boldsymbol{u}_s)=0. \tag{6.7}$$

[1] It must be kept in mind that experiments related to quantum turbulence are all performed in closed configurations, which leads to the use of a potential to account for the confinement appartus.

The associated hydrodynamic momentum equation can be obtained taking the gradient of Eq. (6.5), yielding the *quantum Euler equations* also referred to as the *Madelung equations*:

$$\frac{\partial \boldsymbol{u}_s}{\partial t} = -\frac{1}{m\rho_s}\nabla p_s - \frac{1}{2}\nabla u_s^2 + \frac{1}{m}\nabla\left(\frac{\hbar}{2m\sqrt{\rho_s}}\nabla^2\sqrt{\rho_s}\right) - \frac{1}{m}\nabla V_{trap}, \tag{6.8}$$

where $\rho_s = f^2$ and $p_s = \rho_s^2 g/2$ are the density and the pressure, respectively. The third term in the right-hand side is known as the *quantum pressure*. It is non-negligible only in regions in which the density varies rapidly, i.e. in the core of the quantized vortices in which it is dominant over the pressure. Therefore, this term can be neglected outside quantized vortex cores. The classical Euler equations for an irrotational compressible flow of inviscid fluid are recovered as a limit considering $\hbar \to 0$. The associated speed of sound for small perturbations (see below Sect. 6.2.1.4) obeying linearized equations is $a_s = \sqrt{\frac{1}{m}\frac{\partial p_s}{\partial \rho_s}}$.

The above equations are exact in the limit of an infinite number of particles at zero temperature. They a priori cannot account for mutual friction and other finite temperature effects. They can describe important phenomena for quantized vortex dynamics, including Kelvin waves and vortex reconnection. It is worth noting that they rely on the assumption that all particules are in the same state. Such an approximation may be not realistic when handling a huge number of quantized vortices subjected to partial or total polarization in subdomains, i.e. when considering large-scale phenomena associated with Kolmogorov-like turbulence at scales much larger than the separation length. Another point is that they are derived assuming very-low densities, i.e. for gas, and their use to describe liquid superfluid helium is not assessed a priori. Only qualitative features must be sought for in this case.

6.2.1.3 Energy of Fluctuations

Solutions to the Gross–Pitaevskii equation have a total energy E_{tot} defined as

$$E_{tot}(\boldsymbol{x}, t) = \left(\frac{\hbar^2}{2m}|\nabla\psi(\boldsymbol{x}, t)|^2 + V_{trap}|\psi(\boldsymbol{x}, t)|^2 + \frac{1}{2}g|\psi(\boldsymbol{x}, t)|^4\right), \tag{6.9}$$

which can also be split as $E_{tot} = E_K + E_v + E_I + E_Q$ where the kinetic energy, E_K, potential energy, E_v, interaction energy, E_I and quantum energy, E_Q are defined as

$$E_K(\boldsymbol{x}, t) = \frac{m}{2}\rho_s(\boldsymbol{x}, t)\|\boldsymbol{u}_s(\boldsymbol{x}, t)\|^2, \quad E_v(\boldsymbol{x}, t) = \rho_s(\boldsymbol{x}, t)V_{trap}(\boldsymbol{x}, t),$$

$$E_I(\boldsymbol{x}, t) = \frac{1}{2}g\rho_s^2(\boldsymbol{x}, t), \quad E_Q(\boldsymbol{x}, t) = \frac{\hbar^2}{2m}|\nabla\sqrt{\rho_s(\boldsymbol{x}, t)}|^2.$$

It is worth noting that the velocity field $\boldsymbol{u}_s(\boldsymbol{x}, t)$ is not solenoidal. Therefore, it can be split into a solenoidal and a dilatational components as in the case of compressible Navier–Stokes equations, e.g. using the Helmholtz decomposition, see Sect. 2.1.5.

6.2.1.4 Small Amplitude Waves

The dynamics of small disturbances can be analyzed using linearized Gross–Pitaevskii equations. Considering a base state $e^{-\imath\mu t/\hbar}\psi_0(\boldsymbol{x})$ along with a small disturbance of the form $e^{-\imath\mu t/\hbar}[u(\boldsymbol{x})e^{-\imath\omega t} + v^*(\boldsymbol{x})e^{\imath\omega t}]$ and inserting this solution into (6.2), one obtains at the leading order for the perturbation

$$\hbar\omega u(\boldsymbol{x}) = \left(-\frac{\hbar^2}{2m}\nabla^2 - \mu + V_{trap} + 2g\psi_0(\boldsymbol{x})\right)u(\boldsymbol{x}) + g\psi_0^2(\boldsymbol{x})v(\boldsymbol{x}), \tag{6.10}$$

$$-\hbar\omega v(\boldsymbol{x}) = \left(-\frac{\hbar^2}{2m}\nabla^2 - \mu + V_{trap} + 2g\psi_0(\boldsymbol{x})\right)v(\boldsymbol{x}) + g\psi_0^2(\boldsymbol{x})u(\boldsymbol{x}). \tag{6.11}$$

The solution found by Bogoliubov in 1947 considering a plane wave perturbation with wave vector $\boldsymbol{k}$ is

$$(\hbar\omega(\boldsymbol{k}))^2 = \left(\frac{\hbar^2k^2}{2m}\right)\left(\frac{\hbar^2k^2}{2m} + 2g\rho_s\right), \tag{6.12}$$

where $\hbar\omega(\boldsymbol{k})$ is the energy of the perturbation. At large momenta, i.e. $k \gg 1$, one has $\omega(\boldsymbol{k}) \sim \hbar k^2/2m$, corresponding to free-particule solutions. At low momenta ($k \ll 1$), one obtains

$$\omega(\boldsymbol{k}) = a_s k, \quad a_s = \sqrt{\frac{g\rho_s}{m}}, \tag{6.13}$$

which corresponds to an acoustic wave propagating at the speed of sound a_s in the macroscopic interpretation. It is interesting to observe that this speed of sound coincides with the hydrodynamic definition $a_s^2 = \frac{1}{m}\frac{\partial p_s}{\partial \rho_s}$ for a fluid with equation of state $p_s = g\rho_s^2/2$. This solution shows that there is a continuous transition from free-particules to phonons (and therefore acoustic waves using the macroscopic hydrodynamical interpretation) in the small disturbance solution. It is worth noticing that the Gross–Pitaevskii model does not contain short-wave disturbances such as rotons, i.e. perturbations are associated to irrotational velocity fields. Therefore the solution is made of an inviscid superfluid component and a gas of quasi-particules (phonons, i.e. an acoustic field). The acoustic waves can interact because of non-linear effects, leading to an equilibrium state corresponding to the local Planck distribution of phonons.

6.2.1.5 Accounting for Thermal Dissipation

The Gross–Pitaevskii equation discussed above is valid in the limit of zero temperature, and does not account for thermal effects, which are responsible for the existence of mutual friction. It is important noticing that no concept exists in the theory of atomic Bose–Einstein condensates that explains dissipation or mutual friction of quantized vortices. Some dissipation can be added in an heuristic way (Kobayashi and Tsubota 2006, 2007; Tsubota 2013) considering that both energy and particules are exchanged with a particule reservoir. The latter is assumed to acts in such a way that the chemical potential of the system, μ, relaxes toward that of the reservoir, μ_r. Accounting for this relaxation phenomenon by a complex relaxation term $\gamma(\mu - \mu_r)$ into the evolution equation for the renormalized state function $\psi_\mu(\boldsymbol{x}, t) = \psi(\boldsymbol{x}, t)e^{-\imath\mu t}$, one obtains the following modified Gross–Pitaevskii equation

$$\imath\hbar\frac{\partial}{\partial t}\psi_\mu(\boldsymbol{x}, t) = \left(-\frac{\hbar^2}{2m}\nabla^2 + g|\psi_\mu(\boldsymbol{x}, t)|^2 - \imath\gamma(\mu - \mu_r)\right)\psi_\mu(\boldsymbol{x}, t). \tag{6.14}$$

The parameter γ is a relaxation frequency. Using the approximation

$$\imath\hbar\frac{\partial}{\partial t}\psi_\mu(\boldsymbol{x}, t) \simeq \mu\psi_\mu(\boldsymbol{x}, t), \tag{6.15}$$

and $\mu \simeq \mu_r$, one obtains

$$(\imath - \gamma)\hbar\frac{\partial}{\partial t}\psi_\mu(\boldsymbol{x}, t) = \left(-\frac{\hbar^2}{2m}\nabla^2 + g|\psi_\mu(\boldsymbol{x}, t)|^2 + \imath\gamma\mu\right)\psi_\mu(\boldsymbol{x}, t). \tag{6.16}$$

The associated equation for the state function $\psi(\boldsymbol{x}, t)$ is

$$(\imath - \gamma)\hbar\frac{\partial}{\partial t}\psi(\boldsymbol{x}, t) = \left(-\frac{\hbar^2}{2m}\nabla^2 + g|\psi(\boldsymbol{x}, t)|^2 - \mu\right)\psi(\boldsymbol{x}, t). \tag{6.17}$$

It is important noticing that the introduction of this relaxation term yields a loss of the conservation of both energy and number of particules. To recover a constant number of particules, one should use a time-dependent chemical potential μ_r.

The hydrodynamic mass and momentum equations associated to (6.17), sometimes referred to as *quantum Navier–Stokes equations*, are

$$\frac{\partial\rho_s}{\partial t} + \nabla\cdot(\rho_s\boldsymbol{u}_s) = \gamma\left(\frac{\hbar\sqrt{\rho_s}\nabla^2\sqrt{\rho_s}}{m} - \frac{m\rho_s u_s^2}{\hbar} - \frac{2(g\rho_s - \mu)\rho_s}{\hbar}\right), \tag{6.18}$$

$$\frac{\partial\boldsymbol{u}_s}{\partial t} = -\frac{1}{m\rho_s}\nabla p_s - \frac{1}{2}\nabla u_s^2 + \frac{1}{m}\nabla\left(\frac{\hbar}{2m\sqrt{\rho_s}}\nabla^2\sqrt{\rho_s}\right) - \nu_q\nabla^2\boldsymbol{u}_s, \tag{6.19}$$

with the effective kinematic viscosity $\nu_q = \hbar\gamma/2m$, where γ is an arbitrary real parameter. Introducing a reference length D, one can define the *effective quantum Reynolds number* $Re_q = L\boldsymbol{u}_s/\nu_q = 2mL\boldsymbol{u}_s/\hbar\gamma$.

This approach can be refined coupling the Gross–Pitaevskii equation for the condensate to an auxiliary equation for thermal disturbances, whose wave length is smaller than the vortex core radius, r_c. Such perturbations are emitted during vortex reconnection, by high frequency Kelvin waves and small quantized vortex disappearance. Introducing the decomposition

$$\psi(\boldsymbol{x}, t) = \psi_0(\boldsymbol{x}, t) + \zeta(\boldsymbol{x}, t) \tag{6.20}$$

where $\psi_0(\boldsymbol{x}, t)$ and $\zeta(\boldsymbol{x}, t)$ denote the base condensate state and the (small) thermal noise excitation, respectively, one couples the Gross–Pitaevskii supplemented by a thermal forcing term for the condensate to a Bogoliubov – de Gennes equation for the excitation:

$$\imath\hbar\frac{\partial}{\partial t}\psi_0(\boldsymbol{x}, t) = \left(-\frac{\hbar^2}{2m}\nabla^2 - \mu + g\left[|\psi_0(\boldsymbol{x}, t)|^2 + 2\overline{\zeta^\dagger\zeta}\right] + \imath\boldsymbol{u}_e\cdot\nabla\right)\psi_0(\boldsymbol{x}, t) + g\overline{\zeta^2}\psi_0^* \tag{6.21}$$

$$\imath\hbar\frac{\partial}{\partial t}\zeta(\boldsymbol{x}, t) = \left(-\frac{\hbar^2}{2m}\nabla^2 - \mu + g|\psi_0(\boldsymbol{x}, t)|^2 + \imath\boldsymbol{u}_e\cdot\nabla\right)\zeta(\boldsymbol{x}, t) + g\psi_0^2(\boldsymbol{x}, t)\zeta^\dagger \tag{6.22}$$

where the term $\imath\boldsymbol{u}_e\cdot\nabla$ has been added to account for advection effect by the velocity field $\boldsymbol{u}_e$. This advection term is useful when analyzing the origin of the mutual friction term that is present in hydrodynamic two-fluid models of superfluid flows. The dissipation in (6.21) is given by the imaginary term

$$g\Im\left(\frac{\overline{\zeta^2}\psi_0^*}{\psi_0}\right). \tag{6.23}$$

6.2.2 Biot–Savart Model for Vortex Tangle Dynamics

6.2.2.1 Vortex Filament Kinematics

Modelling of quantized vortices as vortex filaments obeying the Biot–Savart law was popularized by Schwarz in 1985 to perform numerical simulation of vortex tangle dynamics (Schwarz 1985, 1988; Nemirovskii 2013; Tsubota et al. 2017). Using that approximation, fine details of superfluid physics are neglected and quantized vortices are represented as inviscid vortex filaments with zero radius that obey the vorticity evolution equation (2.36) in which the viscous term is removed and where the velocity field is computed thanks to the Biot–Savart law discussed in Sect. 2.1.8.

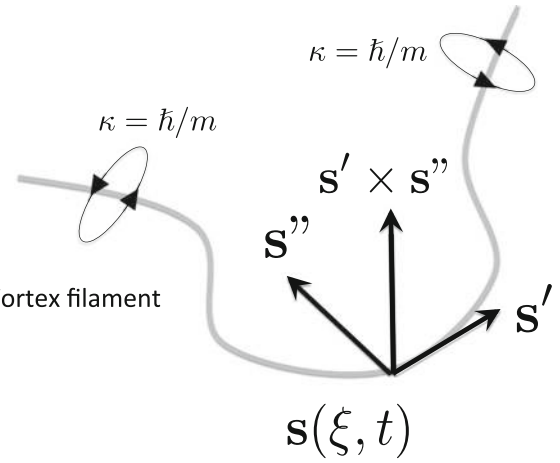

Fig. 6.3 Sketch of the vortex filament

In the case of several filaments, it can be seen that each filament is submitted to self-induction if it is not exactly straight and the force exerted by other filaments since the velocity field originates in two sources.

Considering a single vortex filament L parametrized by ξ, the vorticity field $\boldsymbol{\omega}$ is given by

$$\boldsymbol{\omega}(\boldsymbol{x}, t) = \kappa \int_L \boldsymbol{s}'(\xi, t)\delta\left(\boldsymbol{x} - \boldsymbol{s}(\xi, t)\right) d\xi \tag{6.24}$$

where $\boldsymbol{s}$, $\boldsymbol{s}' = \frac{\partial \boldsymbol{s}}{\partial \xi}$ and $\boldsymbol{s}'' = \frac{\partial^2 \boldsymbol{s}}{\partial \xi^2}$ denote the unit radius vector, the unit tangent vector along the filament at position $\boldsymbol{s}(\xi, t)$ and the principal normal vector at $\boldsymbol{s}$ with magnitude $1/R$, with R the local radius of curvature (see Fig. 6.3). Here $\kappa = \hbar/m$ is related to the quantum of vorticity associated to each quantized vortex, as discussed in the preceding section.

Introducing (6.24) into the Biot–Savart relation (2.42), one obtains the following expression for the induced velocity field $\boldsymbol{u}_{BS}$:

$$\boldsymbol{u}_{BS}(\boldsymbol{x}, t) = \frac{\kappa}{4\pi} \int_L \frac{\boldsymbol{s}'(\xi, t) \times [\boldsymbol{x} - \boldsymbol{s}(\xi, t)]}{\|\boldsymbol{x} - \boldsymbol{s}(\xi, t)\|^3} d\xi. \tag{6.25}$$

It is observed that this expression diverges when trying to compute the induced velocity at a location $\boldsymbol{s}_0 = \boldsymbol{s}(\xi_0, t)$ located on the vortex line, since the integrand becomes singular as $\boldsymbol{s} \to \boldsymbol{s}_0(\xi, t)$. This problem is treated expanding $\boldsymbol{s}(\xi)$ around $\boldsymbol{s}_0 = \boldsymbol{s}(\xi_0)$

$$\boldsymbol{s} = \boldsymbol{s}_0 + \boldsymbol{s}'\xi + \frac{1}{2}\boldsymbol{s}''\xi^2 + \cdots \tag{6.26}$$

Inserting this expansion into (6.25) and introducing an upper cutoff parameter ξ_* on the order of the curvature radius at point $\boldsymbol{s}_0$, one obtains

$$\boldsymbol{u}_{BS}(\boldsymbol{s} \to \boldsymbol{s}_0) = \frac{\kappa}{8\pi} \boldsymbol{s}' \times \boldsymbol{s}'' \int_{-\xi_*}^{+\xi_*} \frac{d\xi}{|\xi|} + \text{regular part.} \tag{6.27}$$

The singular part can be evaluated reminding that the Kelvin–Helmholtz theorem states that each elementary piece of the vortex line should move with a velocity equal to the velocity of the net motion of a small contour surrounding that element. Reminding that the Biot–Savart formula holds only for $|\xi| > r_c$ and that the part of the vortex line with $|\xi| \ll r_c$ has a negligible contribution to the net motion on the small contour, one has

$$\lim_{\xi_* \to 0} \int_{-\xi_*}^{+\xi_*} \frac{d\xi}{|\xi|} = 2 \ln(\xi_*/r_c), \tag{6.28}$$

leading to the following expression for the induced velocity:

$$\boldsymbol{u}_{BS}(\boldsymbol{x}, t) = \underbrace{\frac{\kappa}{4\pi} \ln\left(\frac{R}{r_c}\right) \boldsymbol{s}' \times \boldsymbol{s}''}_{\text{local part}} + \underbrace{\frac{\kappa}{4\pi} \int_{L/[\xi-R,\xi+R]} \frac{\boldsymbol{s}'(\xi, t) \times [\boldsymbol{x} - \boldsymbol{s}(\xi, t)]}{\|\boldsymbol{x} - \boldsymbol{s}(\xi, t)\|^3} d\xi}_{\text{non-local part}} \tag{6.29}$$

where ξ_* has been fixed equal to the radius of curvature R.

Let us note that conservation of kinetic energy and momentum are expressed respectively as

$$\frac{d}{dt} \int \frac{d\boldsymbol{s} \cdot d\boldsymbol{s}_0}{\|\boldsymbol{s} - \boldsymbol{s}_0\|} = 0 \tag{6.30}$$

and

$$\frac{d}{dt} \int \boldsymbol{s} \times d\boldsymbol{s} = 0. \tag{6.31}$$

Using this approximation, one can study the dynamics of vortex tangles in the absence of vortex reconnection and mutual friction. Ad hoc models have been proposed by some authors for these purposes (Schwarz 1985; Tsubota and Adachi 2011; Baggaley 2012; Zuccher et al. 2012; Kondaurova et al. 2014). Since they are purely empirical models they will not be discussed here for the sake of brevity. But it should be kept in mind that they lead to interesting but model-sensitive qualitative results. It is also worth noting that dissipative mechanisms that occur at very small scale (emission of phonos) are not taken into account. Compressibility-induced mechanisms are also neglected, e.g. interaction between acoustic waves and quantized vortices. Such phenomena are expected to be very weak in most configurations.

6.2.2.2 Local Induction Approximation

The previous estimation shows that in the absence of huge increase of non-local interactions associated to polarization of the vortex tangle (i.e. in the absence of large-scale vortical motion at scale much larger than the filament spacing scale ℓ),

the vortex line motion is dominated by the local self-induced singular contribution. Therefore, one can simplifies Eq. (6.29) keeping the later term only, defining the *Local Induction Approximation* (LIA):

$$\boldsymbol{u}_{BS} \sim \frac{\kappa}{4\pi} \ln(R/r_c)\boldsymbol{s}' \times \boldsymbol{s}'' \tag{6.32}$$

where R denotes a characteristic curvature radius taken as a constant parameter. This approximation is valid in the absence of very strong local curvature effects for which the Taylor series expansion may become meaningless, i.e. in the presence of singularities like cusps associated to vortex reconnection. LIA is very attractive for numerical simulation, since it is a purely local model that does not involve expensive non-local integral terms. It can be shown that (6.32) exactly preserves filament length and then filament energy, along with momentum. It also preserves more integral invariants, such as the square of the curvature radius:

$$\frac{d}{dt} \int \|\boldsymbol{s}''\|^2 d\xi = 0. \tag{6.33}$$

The link with Schrödinger equation can be established following the works by Betchov in 1965 and Hasimoto in 1972. Rewriting (6.32) in terms of intrinsic variables of the vortex line, namely the curvature ζ and the torsion τ, and than introducing the complex variable $\psi(\xi, t)$ such that

$$\zeta = |\psi|, \quad \tau = \frac{\partial \Phi}{\partial \xi}, \tag{6.34}$$

where Φ is the phase of ϕ, then (6.32) is equivalent to the 1D nonlinear Schrödinger equation

$$\imath \frac{\partial \psi}{\partial t} = -\frac{\partial^2 \psi}{\partial \xi^2} - \frac{1}{2}|\psi|^2 \psi. \tag{6.35}$$

This equation, and consequently the LIA equation (6.32) is an integrable system with an infinite number on invariants I_n:

$$I_n = \int_{-\infty}^{+\infty} a_n(\xi) d\xi, \; a_1 = \frac{1}{4}|\psi|, \; a_{n+1} = \psi \frac{d}{d\xi}\left(\frac{a_n}{\psi}\right) + \sum_{p+q=n} a_p a_q. \tag{6.36}$$

6.2.2.3 Forces Exerted on a Vortex Line and Dynamical Equations

We now address the issue of finding a dynamical evolution equation for the vortex filament. Considering that the vortex filament moves at velocity $\boldsymbol{u}_L$ in the laboratory frame in a superfluid with density ρ_s and velocity $\boldsymbol{u}_s$, it is subjected to the Magnus

force,[2] which is expressed as (per unit length)

$$\boldsymbol{f}_M = \rho_s \kappa \boldsymbol{s}' \times (\boldsymbol{u}_L - \boldsymbol{u}_T) \tag{6.37}$$

where $\boldsymbol{u}_T = \boldsymbol{u}_s + \boldsymbol{u}_{BS}$ is related to the total velocity of the superfluid in the vicinity of the vortex filament in the laboratory frame.

The existence of *mutual friction* between the superfluid and the normal fluid component originates in the scattering of quasi-particules that form the normal fluid component (rotons, phonons) by the quantized vortex core and the neighboring region in which $\boldsymbol{u}_s$ is large. Denoting $\boldsymbol{u}_n$ the velocity of the normal fluid component, it is heuristically modeled as a *drag force acting on the vortex filament*, which is expressed as (where underscript $\perp$ denotes the component perpendicular to the vortex line)

$$\boldsymbol{f}_D = \rho_s \kappa \left[\alpha' (\boldsymbol{u}_n - \boldsymbol{u}_{BS})_\perp - \alpha \boldsymbol{s}' \times (\boldsymbol{u}_n - \boldsymbol{u}_{BS}) \right] \tag{6.38}$$

or equivalently

$$\boldsymbol{f}_D = -\rho_s \kappa \left[\alpha' \boldsymbol{s}' \times [\boldsymbol{s} \times (\boldsymbol{u}_n - \boldsymbol{u}_{BS})] + \alpha \boldsymbol{s}' \times (\boldsymbol{u}_n - \boldsymbol{u}_{BS}) \right] \tag{6.39}$$

where α and α' two empirical parameters proportional to ρ_n/ρ, where ρ_n is the normal fluid density and $\rho = \rho_n + \rho_s$ the total density. A detailed discussion of the mutual friction model and its variants, along with the link with microscopic theories is displayed in Sect. 6.6. Therefore, the second law of Newton yields:

$$m_{eff} \frac{d^2 \boldsymbol{s}}{dt^2} = \boldsymbol{f}_M + \boldsymbol{f}_D \tag{6.40}$$

where $m_{eff} \propto \rho_s r_c^2$ is the effective mass of the filament per unit length. Since it is very small, inertia effects can be neglected, leading to $\boldsymbol{f}_M + \boldsymbol{f}_D = 0$. Considering this equilibrium relation and remembering that a $\boldsymbol{f}_D$ induces a velocity field equal to $\frac{1}{\rho_s \kappa} \boldsymbol{s}' \times \boldsymbol{f}_D$, Schwarz proposed in 1985 the following formula in is seminal paper related to numerical simulation of vortex filament dynamics (Schwarz 1985):

$$\dot{\boldsymbol{s}} = \boldsymbol{u}_{BS} + \boldsymbol{u}_D = \boldsymbol{u}_{BS} + \alpha \boldsymbol{s}' \times (\boldsymbol{u}_n - \boldsymbol{u}_{BS}) - \alpha' \boldsymbol{s}' \times \left[\boldsymbol{s}' \times (\boldsymbol{u}_n - \boldsymbol{u}_{BS}) \right]. \tag{6.41}$$

This formula can be enriched to account for the possible existence of a base flow in the superfluid component with velocity $\boldsymbol{u}_s$ (e.g. a superfluid stream induced by a temperature gradient), by operating the substitution $\boldsymbol{u}_{BS} \rightarrow \boldsymbol{u}_T = \boldsymbol{u}_{BS} + \boldsymbol{u}_s$, leading to

$$\dot{\boldsymbol{s}} = \boldsymbol{u}_{BS} + \boldsymbol{u}_s + \alpha \boldsymbol{s}' \times (\boldsymbol{u}_n - \boldsymbol{u}_s - \boldsymbol{u}_{BS}) - \alpha' \boldsymbol{s}' \times \left[\boldsymbol{s}' \times (\boldsymbol{u}_n - \boldsymbol{u}_s - \boldsymbol{u}_{BS}) \right]. \tag{6.42}$$

[2] The Magnus force arises when a body with non-zero circulation moves into a flow. The circulation induces an asymmetry in the velocity and pressure distribution along the body surface, yielding a non-zero force.

This formula can be upgraded to account for boundary conditions and reconnection between vortices and more additional physical phenomena. Evaluation of parameters α and α' and bridging with microscopic theories are discussed in Sect. 6.6.

6.2.2.4 Hamiltonian Representation, Kelvin Waves and Weak Wave Turbulence

Dynamics of Kelvin waves that develop on quantized vortices, including induced weak wave turbulence generated by resonant interactions, can be captured using the vortex filament model. An elegant way to do that is to use the Hamiltonian mechanics framework when neglecting all normal fluid effects, i.e. in the limit of zero temperature. The key elements of the resulting analysis are given below, technical details being omitted for the sake of brevity. The reader is referred to original papers for more details, e.g. Kozik and Svistunov (2004), L'vov et al. (2007), Kozik and Svistunov (2009), L'vov and Nazarenko (2010), Laurie et al. (2010), Nemirovskii (2013).

It is assumed that a vortex line can be parametrized in Cartesian coordinates expressing its x and y coordinates as functions of z, i.e. the vortex filament is parametrized as $(x(z), y(z), z)$. Let's introduce the position vector $\boldsymbol{r}(z,t) = (x(z,t), y(z,t))$. Then, time derivatives of $\boldsymbol{r}$ and $\boldsymbol{s}$ are tied by the following relation

$$\frac{\partial \boldsymbol{r}}{\partial t} = \frac{\partial \boldsymbol{s}}{\partial t} - \left(\boldsymbol{e}_z \cdot \frac{\partial \boldsymbol{s}}{\partial t}\right)\left(\boldsymbol{e}_z + \frac{\partial \boldsymbol{r}}{\partial z}\right). \tag{6.43}$$

Then using expression for the time derivative of $\boldsymbol{s}$ and replacing $\boldsymbol{r}(z,t)$ by the complex variable $w(z,t) = x(z,t) + \imath y(z,t)$, one arrives at the following Hamiltonian Biot–Savart equation for vortex line motion:

$$\imath \dot{w} = \frac{\delta H\{w, w^*\}}{\delta w^*} \tag{6.44}$$

where * denotes complex conjugation and $w' = dw/dz$, with

$$H\{w, w^*\} = \frac{\kappa}{4\pi} \iint \frac{[1 + \Re(w'^*(z_1)w'(z_2)]}{\sqrt{(z_1 - z_2)^2 + |w(z_1) - w(z_2)|^2}} dz_1 dz_2. \tag{6.45}$$

This Hamiltonian is singular as $z_1 \to z_2$ and then requires to be regularized. This can be done introducing a intermediary scale r_* such that $r_c \ll r_* \ll \lambda$, where r_c and λ denotes the quantized vortex core radius and the typical wave length of Kelvin waves, respectively. The Hamiltonian can then be expanded as the sum of a singular local part, H_{loc} and a regular non-local part, H_{nloc}, i.e.

$$H\{w, w^*\} = H_{nloc}\{w, w^*\} + H_{loc}\{w, w^*\} + O(r_*/\lambda) \tag{6.46}$$

$$H_{nloc}\{w, w^*\} = \frac{\kappa}{4\pi} \iint_{|z_1-z_2|>r_*} \frac{[1 + \Re(w'^*(z_1)w'(z_2)]}{\sqrt{(z_1 - z_2)^2 + |w(z_1) - w(z_2)|^2}} dz_1 dz_2 \tag{6.47}$$

$$H_{loc}\{w, w^*\} = 2\beta \int \sqrt{1 + |w'(z)|^2} dz, \quad \beta = \frac{\kappa}{2\pi} \ln(r_*/a_*) \tag{6.48}$$

where the auxiliary scale $a_* \sim r_c$ is introduced to remove a factor of the order of unity in the logarithm. Tuning r_* such that $\ln(r_*/r_c) \gg \ln(\lambda/r_*)$, one can take

$$\beta \simeq \frac{\kappa}{2\pi} \ln(\lambda/r_c), \tag{6.49}$$

which leads to a satisfactory approximation of the leading local term.

Further simplification originates in the fact that H_{loc} vanishes taking $r_* = a_*$. In this case, one obtains the pseudo-Hamiltonian approximation:

$$H\{w, w^*\} \simeq \frac{\kappa}{4\pi} \iint_{|z_1-z_2|>a_*} \frac{[1 + \Re(w'^*(z_1)w'(z_2)]}{\sqrt{(z_1 - z_2)^2 + |w(z_1) - w(z_2)|^2}} dz_1 dz_2. \tag{6.50}$$

Kelvin waves are found linearizing the pseudo-Hamiltonian function, i.e. assuming that disturbances have small amplitudes and that

$$\alpha(z_1, z_2) = \frac{|w(z_1) - w(z_2)|}{|z_1 - z_2|} \ll 1. \tag{6.51}$$

At the leading order, the Hamiltonian Biot–Savart equation leads to

$$\imath \dot{w} = \frac{\delta H_2\{w, w^*\}}{\delta w^*}, \tag{6.52}$$

with

$$H_2\{w, w^*\} = \frac{\kappa}{8\pi} \iint_{|z_1-z_2|>a_*} \left(2\Re(w'^*(z_1)w'(z_2)) - \alpha^2(z_1, z_2)\right) \frac{dz_1 dz_2}{|z_1 - z_2|}. \tag{6.53}$$

The subscript 2 denotes the fact that $H_2\{w, w^*\}$ is a quadratic term that represents the scattering of 1 wave into 1 wave. Considering a vortex filament of length L with periodic boundary conditions and the Fourier mode decomposition $w(z) = L^{-1/2} \sum_k w_k(t) e^{\imath kz}$, the linearized pseudo-Hamiltonian simplifies as

$$H_2\{w, w^*\} = \frac{\kappa}{4\pi} \sum_k \Omega(k) w_k^* w_k. \tag{6.54}$$

Solving that problem, the dispersion law for Kelvin waves is found to be

$$\Omega(k) = \frac{\kappa}{4\pi}k^2\left(\ln\frac{1}{ka_*} + C_0 + O((ka_*)^2)\right), \quad C_0 \simeq -2.077, \tag{6.55}$$

in agreement with results discussed in Sect. 6.3.2. Terms $O((ka_*)^2)$ should be omitted, since they do not correspond to the range of validity of the pseudo-Hamiltonian.

Higher-order expansion of the Hamiltonian yields a wave-turbulence model which represents the Kelvin-wave cascade of energy toward smaller scales, i.e. writing

$$H\{w, w^*\} = H_2\{w, w^*\} + H_4\{w, w^*\} + H_6\{w, w^*\} + \cdots \tag{6.56}$$

where $H_4\{w, w^*\}$ is a quartic term that accounts for scattering of 2 interacting waves into 2 waves and $H_6\{w, w^*\}$ a sixth-order term representing a 3-to-3 Kelvin wave scattering, and so on. Nonlinear wave interactions responsible for the Kelvin cascade are mediated by terms higher than $H_2\{w, w^*\}$. A very heavy technical algebra yields the conclusion that the 4-wave interaction term $H_4\{w, w^*\}$ does not contribute to the cascade, and that weak turbulence made of interacting Kelvin waves is governed by the 6-wave term $H_6\{w, w^*\}$. The full expression of $H_6\{w, w^*\}$ contains 73 terms among which 72 are related to the contribution of two-by-two combinations of 4-wave interactions leading to 6-wave scattering, the last one representing direct 6-wave scattering phenomena, as illustrated in Fig. 6.4. These 73 terms involves about 20,000 individual contributions, showing the complexity of the problem.

Thanks to a canonical change of variable $(w, w^*) \to (b, b^*)$, the problem can be recast as

$$\imath\dot{b} = \frac{\delta H_{eff}\{b, b^*\}}{\delta b^*} \tag{6.57}$$

where, in Fourier space representation

$$H_{eff}\{b, b^*\} = \sum_k \omega_k b_k b_k^* + \frac{1}{36}\sum_{i+j+p=l+m+n} \mathcal{W}_{i,j,p}^{l,m,n} b_i b_j b_p b_l^* b_m^* b_n^* \tag{6.58}$$

where $\mathcal{W}_{i,j,p}^{l,m,n}$ is related to the nonlinear interactions of modes (i, j, p) resulting in the generation of modes (l, m, n).

A controversy exists dealing with the estimate of the magnitude of $\mathcal{W}_{i,j,p}^{l,m,n}$. On the one hand, Laurie, L'vov, Nazarenko and Rudenko propose

$$\mathcal{W}_{i,j,p}^{l,m,n} \sim -\frac{3}{4\pi\kappa}k_i k_j k_p k_l k_m k_n, \tag{6.59}$$

where k_q denotes the wave number of mode q, while, on the other hand, Kosik and Sistunov have the different scaling in their original proposition

$$\mathcal{W}_{i,j,p}^{l,m,n} \propto k_i^2. \tag{6.60}$$

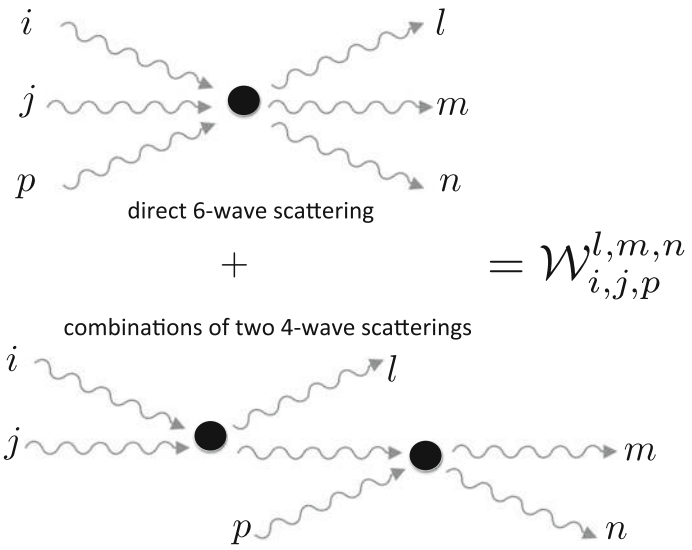

Fig. 6.4 Sketch of multiple wave scattering phenomena that contribute to the Kelvin-wave cascade

The main difference between the two scalings comes from the fact that the latter theory is based on a locality assumption in wave number space (i.e. only wave vectors with close amplitude yield significant interactions), while in the former it is hypothesized that main interactions involve two wave vectors (on the same side: incident or scattered) with amplitude $O(\ell)$, i.e. two Kelvin waves with large wave length.

This difference yields different estimations of the slope of the energy spectrum associated to Kelvin wave, which will be discussed later on. But let us emphasize here that there is no direct experimental measure of the Kelvin wave spectrum, and that numerical simulations do not allow for a definitive conclusion at present time due to a lack of spatial resolution. This point will be further discussed in Sect. 6.4.2.

6.2.3 Two-Fluid Model for Coarse-Grained Hydrodynamics

We now address *two-fluid models* for quantum turbulence, which where pioneered by Tisza (1938) and Landau (1941). Such models, sometimes referred to as *coarse-grained* models, are empirical models built to represent motion at scales much larger than the quantized vortex separation length ℓ, i.e. they are valid in the range of hydrodynamic scales, see Vinen and Niemela (2002), Tsubota (2013), Nemirovskii (2013). Therefore, they are a priori unable to describe smaller scale physics, such as Kelvin wave dynamics and quantized vortex reconnection. Consequently, the normal

and superfluid velocity fields, $\boldsymbol{u}_n$ and $\boldsymbol{u}_s$, used in this macroscopic theory should be understood as locally averaged values of those found in the two previous theories over control volumes with typical diameter much larger than ℓ.

The possibility to account for the existence of normal fluid effects in superfluid momentum equation is understood in the following way. The effective energy per atom is equal to $m\mu$ where μ is the chemical potential per unit mass. Therefore the condensate state function is equal to $\psi(\boldsymbol{x}, t) = \sqrt{\rho(\boldsymbol{x}, t)}\exp(-\imath m\mu t/\hbar)$, yielding

$$\frac{\partial \boldsymbol{u}_s}{\partial t} = -\nabla\mu \tag{6.61}$$

Now introducing $\mu_0 = \mu - u_s^2/2$ the chemical potential in a frame at rest with the superfluid, one has the classical thermodynamical relation (with s the entropy of the fluid per unit mass):

$$d\mu_0 = -sdT + \frac{1}{\rho}dp - \frac{\rho_n}{\rho}(\boldsymbol{u}_n - \boldsymbol{u}_s)\cdot d(\boldsymbol{u}_n - \boldsymbol{u}_s), \tag{6.62}$$

and therefore

$$\frac{\partial \boldsymbol{u}_s}{\partial t} + \nabla\left(\frac{u_s^2}{2}\right) = s\nabla T - \left(\frac{1}{\rho}\right)\nabla p + \frac{\rho_n}{\rho}\nabla(\boldsymbol{u}_n - \boldsymbol{u}_s)^2. \tag{6.63}$$

It is similar to the Euler equation for inviscid fluids, with two additional term. The entropic term, which shows that superfluid current can be induced using temperature gradient, and the last one, which accounts for the difference between superfluid and normal velocity.

This simple model can be extended writing a companion equation for the normal fluid component and inserting a *mutual friction term* as proposed by Gorter and Mellink in 1949 that accounts for the drag force exerted of quantized vortices, leading to the Hall–Vinen–Bekarevich–Khalatnikov model[3]:

$$\rho_s\left(\frac{\partial \boldsymbol{u}_s}{\partial t} + \boldsymbol{u}_s\nabla\boldsymbol{u}_s\right) = -\frac{\rho_s}{\rho}\nabla p + \rho_s s\nabla T + \frac{\rho_s\rho_n}{2\rho}\nabla(\boldsymbol{u}_n - \boldsymbol{u}_s)^2 - \boldsymbol{f}_{ns}, \tag{6.64}$$

$$\rho_n\left(\frac{\partial \boldsymbol{u}_n}{\partial t} + \boldsymbol{u}_n\nabla\boldsymbol{u}_n\right) = -\frac{\rho_n}{\rho}\nabla p - \rho_s s\nabla T - \frac{\rho_s\rho_n}{2\rho}\nabla(\boldsymbol{u}_n - \boldsymbol{u}_s)^2 + \boldsymbol{f}_{ns} + \mu_n\nabla^2\boldsymbol{u}_n, \tag{6.65}$$

where μ_n is the normal fluid viscosity, along with

$$\nabla\cdot\boldsymbol{u}_s = 0, \quad \nabla\cdot\boldsymbol{u}_n = 0. \tag{6.66}$$

[3]The original HVBK model was not design for turbulence but equations used to describe quantum turbulence are formally the same.

The sake of coherence with the estimate for the drag force exerted on a single rectilinear quantized vortex given by Eq. (6.39) yields

$$\boldsymbol{f}_{ns} = -\frac{\rho_n \rho_s}{2\rho}\left(B\hat{\boldsymbol{\omega}} \times [\boldsymbol{\omega} \times (\boldsymbol{u}_s - \boldsymbol{u}_n)] + B'\hat{\boldsymbol{\omega}} \times (\boldsymbol{u}_s - \boldsymbol{u}_n)\right), \tag{6.67}$$

where $\boldsymbol{\omega}$ denotes the vorticity and $\hat{\boldsymbol{\omega}} = \boldsymbol{\omega}/\|\boldsymbol{\omega}\|$ is the associated unit vector. More details about this model and its relation to other mutual friction terms defined in the vortex filament model and the Gross–Pitaevskii equation are given in Sect. 6.6.3.

Mutual friction modifies the propagation of *second sound* in superfluids. This fact is important, since coefficients B and B' are often tabulated measuring the damping of second sound waves in laboratory experiments. Denoting $\boldsymbol{u}_{sn} = \boldsymbol{u}_s - \boldsymbol{u}_n$, the modified wave equation for second sound disturbances is

$$\ddot{\boldsymbol{u}}_{sn} + (2 - B')(\boldsymbol{\omega} \times \dot{\boldsymbol{u}}_{sn}) - B\hat{\boldsymbol{\omega}} \times (\boldsymbol{\omega} \times \dot{\boldsymbol{u}}_{sn}) = a_{s,2}^2 \nabla(\nabla \cdot \boldsymbol{u}_{sn}), \tag{6.68}$$

where $a_{s,2}$ is the speed of second sound waves in the absence of mutual friction.

These two-fluid equations can be further extended to account for anisotropy of quantized vortex tangles, boundary conditions, inhomogeneity …Such extensions are beyond the scope of the present book, and the reader is referred to original publications, e.g. Lipniacki (2011), Jou et al. (2011).

6.3 Quantized Vortices and Kelvin Waves: Facts and Models

Quantized vortices observed in laboratory experiments or in numerical solutions of the Gross–Pitaevskii equation, appear as vortex filaments and vortex rings. Corresponding dynamics and kinematics can be described in a meaningful way using models discussed above.

6.3.1 Quantized Vortex Kinematics

Quantized vortices are represented as vortex lines and/or vortex rings with quantized circulation. Denoting Γ the circulation along a closed path $\mathcal{L}$ one has

$$\Gamma = \oint_{\mathcal{L}} \boldsymbol{u}_s \cdot \boldsymbol{t} dl = \frac{\hbar}{m} \oint_{\mathcal{L}} \nabla S \cdot \boldsymbol{t} dl \tag{6.69}$$

where $\boldsymbol{t}$ is the tangential unit vector to $\mathcal{L}$. It is assumed that the typical radius of $\mathcal{L}$ is much larger than the healing length r_c, i.e. than the quantized vortex radius. In the case that $\mathcal{L}$ encompass n quantized vortices with the same vorticity sign, one has

$$\Gamma = n\kappa = n\frac{\hbar}{m}, \tag{6.70}$$

where κ is the *quantum of circulation*, i.e. the circulation induced by a single vortex. The velocity field induced by a single vortex ($n = 1$) outside the vortex core region consists of an azimuthal velocity component v_ϕ:

$$u_\phi(r > r_c) = \frac{\kappa}{2\pi r}. \tag{6.71}$$

The energy per unit length of the quantized vortex, E_{QV}, is equal to the kinetic energy of the entrained superfluid. Considering a cylindrical domain with radius $b > r_c$ centered on the vortex line, one has

$$E_{QV} = \int_{r_c}^{b} \pi\rho_s u_\phi^2 r dr = \frac{\rho_s \kappa^2}{4\pi} \ln\left(\frac{b}{r_c}\right). \tag{6.72}$$

Several models for the vortex core have been proposed based on semi-empirical rationale, none of them being fully satisfactory. Therefore, they will not be discussed here.

6.3.2 Kelvin Waves Using the Vortex Filament Model

Quantized vortices can be considered as vortex filaments described by classical fluid mechanics. Classical analytical solutions for velocity and pressure distribution in a cylindrical vortex will not be reproduced here for the sake of brevity, since they are available in many textbooks. Therefore, as shown by Lord Kelvin in the analysis of the stability of Rankine vortex, a small amplitude oscillation of the vortex with wave length $\lambda = 2\pi/k$ will give birth to an helical perturbation that rotates at angular velocity $\Omega(k)$ and propagates along the vortex line at phase velocity $\Omega(k)/k$, with

$$\Omega^{\pm}(k) = \frac{\kappa}{2\pi r_c^2}\left(1 \pm \sqrt{1 + kr_c \frac{Y_0(kr_c)}{Y_1(kr_c}}\right) \tag{6.73}$$

where $Y_n(x)$ denotes the Bessel function of second kind of order n of imaginary argument. The solution exhibits two branches, namely fast waves with angular velocity $\Omega^+(k)$ and slow waves with $\Omega^-(k)$. Since on expects the Kelvin waves to be intrinsically polarized and to rotate in a sense opposite to the direction of the superfluid velocity circulation, the fast wave must be discarded, therefore $\Omega(k) = \Omega^-(k)$. In the long wavelength limit, asymptotic expansion yields

$$\Omega(k) \simeq -\frac{\kappa}{2\pi r_c^2} k^2 \left[\ln(2/kr_c) - A\right], \tag{6.74}$$

where A is a constant of the order of the unity, which depends on the detailed radial profiles of velocity and density inside the vortex core. A common value is $A = \gamma_E + 3/2$, where $\gamma_E = 0.5772$ is the Euler–Tricomi constant.

The energy of the wave is given by the relation $E_{KW}(k) = \hbar\Omega(k)$.

6.3.3 Kelvin Waves in the Gross–Pitaevskii Model

Another solution is to describe vortex lines and Kelvin waves using the Gross–Pitaevskii equation. Considering a steady straight vortex line defined in cylindrical coordinates as

$$\psi_0(r, z, \phi, t) = e^{-\imath\mu t} e^{\imath\phi} f(r) \tag{6.75}$$

and inserting this solution into Eq. (6.2), one obtains the following ordinary differential equation:

$$-\frac{\hbar^2}{2m}\frac{1}{r}\frac{d}{dr}\left(r\frac{df}{dr}\right) + \frac{\hbar^2}{2mr^2} f - \mu f + g f^3 = 0 \tag{6.76}$$

which can be solved numerically. One can show that $f(r) \to 0$ when $r \to 0$ and $f(r) \to const$ when $r \to +\infty$.

Kelvin waves are recovered considering small disturbances of the state function ψ about ψ_0 of the form

$$\psi(r, z, \phi, t) = e^{\imath(\phi - \mu t/\hbar)} b_l(k, r) e^{\imath(kz + l\phi)}. \tag{6.77}$$

Pitaevskii recovered the same expression (6.74) for the angular velocity as in the classical fluid dynamics solution. A very interesting result is that the solution associated to (6.77) is not restricted to the vortex core, so that it also describes waves emitted by the Kelvin waves. As seen in Sect. 6.2.1.4, this field is made of phonons, i.e. Kelvin waves radiate an acoustic field. This phenomena is discussed in Sect. 6.3.7.

6.3.4 Kelvin Waves: Finite Amplitude Effects

Kelvin waves described in previous sections where assumed to be small disturbances obeying linearized equations. Finite amplitude perturbations can also be analyzed (Barenghi et al. 1985). To this end, the energy of a wave with wave number k is split into the sum of the kinetic energy of the vibrating vortex core, E_c, and the potential energy caused the increase of the length of the vortex, E_v. Assuming that $E_c + E_v$ is equal to the energy of a single wave, $E_{KW}(k)$, times the mean number of excitations, one obtains

$$E_c + E_v = \frac{\hbar\Omega(k)}{\exp\left(\frac{\hbar\Omega(k)}{k_B T}\right) - 1}, \tag{6.78}$$

with k_B and T the Boltzmann constant and the temperature, respectively. Defining z as the axis of the (unperturbed) vortex and noting $x(z)$ and $y(z)$ the location of the disturbed vortex at a given z, the kinetic energy per unit length is

$$\rho_s \frac{\pi r_c^2}{2}(\dot{x}^2 + \dot{y}^2) \tag{6.79}$$

where ρ_s is a mean density in the vortex core. Considering a rectilinear vortex with initial length $2\pi R$ in its undisturbed state, along with a discrete set of modes, the total kinetic energy associated with mode n is

$$E_c(n) = \pi^2 r_c^2 \rho_s A_n^2 \Omega^2(k_n) R \tag{6.80}$$

where A_n and $k_n = n/R$ denote the amplitude and the wave number of the mode, respectively. The potential energy for mode n is approximated as $E_{QV}\Delta l(n)$, where the energy per unit length of the quantized vortex is given by relation (6.72) and the variation of the length of the vortex is computed as

$$\Delta l(n) = \int_0^{2\pi R} \left(\sqrt{1 + k_n^2 A_n^2} - 1\right) dz. \tag{6.81}$$

The amplitude A_n is found solving Eq. (6.78) supplemented by relations (6.80) and (6.81). Numerical solution reveals that in realistic cases finite wave amplitude is about a few r_c in ^{4}He and ^{3}He-B. It may be larger in dilute atomic gases, at least for low-order modes. The increase of the quantized vortex length may be as large as 50% near the critical temperature.

6.3.5 *Mutual Friction Effects on Kelvin Waves*

Another issue deals with the modification of Kelvin wave features by mutual friction force (Barenghi et al. 1985). Considering a case in which there is no mean superfluid or normal velocity current, the equilibrium between the Magnus force and the drag force for a massless vortex filament reads (see Sect. 6.2.2.3)

$$\rho_s \kappa \boldsymbol{s}' \times (\boldsymbol{u}_L - \boldsymbol{u}_{BS}) - \gamma_0 \boldsymbol{u}_L - \gamma_0' \boldsymbol{s}' \times \boldsymbol{u}_L = 0, \tag{6.82}$$

where γ_0 and γ_0' are the compact notations of the coefficients of the two component of the mutual friction drag force. Considering the same geometrical configuration as in the previous section devoted to finite amplitude effect, i.e. a displacement in the

(x, y) plane, and projecting the previous equations onto the two axes in this plane, one has

$$-\rho_s\kappa\dot{y} - \gamma_0\dot{x} + \gamma_0'\dot{x} + T_0\frac{d^2x}{dz^2} = 0, \tag{6.83}$$

$$\rho_s\kappa\dot{x} - \gamma_0\dot{y} - \gamma_0'\dot{y} + T_0\frac{d^2y}{dz^2} = 0. \tag{6.84}$$

Here, the term $-\rho_s\kappa\boldsymbol{s}'\times\boldsymbol{u}_{BS}$ has been replaced by an equivalent tension force with amplitude T_0. Assuming that the displacement is proportional to $\exp[\imath(\Omega(k)t - kz)]$, one obtains the system

$$\imath\Omega(k)(\gamma_0' - \rho_s\kappa)y - (\imath\Omega(k)\gamma_0 + T_0k^2)x = 0, \tag{6.85}$$

$$\imath\Omega(k)(\gamma_0' - \rho_s\kappa)x + (\imath\Omega(k)\gamma_0 + T_0k^2)y = 0, \tag{6.86}$$

whose solution is

$$\Omega(k) = \frac{2\imath\gamma_0T_0k^2 \pm \left\{-4\gamma_0^2T_0^2k^4 + 4T_0^2k^4[\gamma_0^2 + (\gamma_0' - \rho_s\kappa)^2]\right\}}{2[\gamma_0^2 + (\gamma_0' - \rho_s\kappa)^2]}. \tag{6.87}$$

The real and imaginary parts of $\Omega(k)$ are

$$\Re(\Omega(k)) = \frac{T_0k^2}{\rho_s\kappa}\frac{\gamma_0"(\rho_s\kappa - \gamma_0')}{\gamma_0\rho_s\kappa} \sim \Omega^-(k)\frac{\gamma_0"(\rho_s\kappa - \gamma_0')}{\gamma_0\rho_s\kappa}, \tag{6.88}$$

$$\Im(\Omega(k)) = \frac{T_0k^2\gamma_0"}{\rho_s^2\kappa^2} \sim \Omega^-(k)\frac{\gamma_0"}{\rho_s\kappa}, \tag{6.89}$$

where $\Omega^-(k)$ is the asymptotic solution of the slow mode solution given by Eq. (6.74) and

$$\gamma_0" = \frac{\gamma_0\rho_s^2\kappa^2}{\gamma_0^2 + (\rho_s\kappa - \gamma_0')^2}.$$

Looking at these results, it is seen that the mutual friction has two effects on Kelvin waves: (i) a frequency shift and (ii) an amplitude damping. A numerical analysis of these parameters shows that the modifications can be neglected unless the temperature is very close to the critical temperature T_c associated with the transition to the classical hydrodynamic régime (see Table 6.1).

6.3.6 Normal Fluid Effects on Kelvin Waves: Donnelly–Glaberson Instability

Frequency shift and damping of Kelvin waves induced by mutual friction are not the only effects of the presence of the normal fluid component on Kelvin waves, even in the case of a uniform normal fluid velocity with amplitude u_n. If u_n is large enough, it can destabilize Kelvin waves via the Donnelly–Glaberson instability, which is associated to the transformation of normal fluid kinetic energy into superfluid vortex length, i.e. into superfluid energy, circulation and vorticity. In such a case, the amplitude of the Kelvin wave $A(t)$ with wave number k evolves as

$$A(t) = A(0)e^{\sigma t}, \quad \sigma = \alpha(ku_n - \nu' k^2) \tag{6.90}$$

where the efficient viscosity is defined as $\nu' = \frac{\kappa}{4\pi}\ln(1/kr_c)$. The mode that undergoes the most rapid growth is $k_{max} = u_n/2\nu'$ with the amplification rate $\sigma_{max} = \alpha u_n^2/4\nu'$, which is a very long wave length compared with typical vortex length since $2\pi/k_{max} \geq \ell$, where ℓ is the mean intervortex spacing.

This instability yields large deformations of quantized vortices which can be stopped by vortex reconnection. A rough estimate shows that in thermally driven flows the amplitude of perturbations can grow to approximately ℓ before reconnections dominate the behavior of the vortex tangle. In mechanically driven cases the picture is different since perturbations along the vortices can be more amplified and modify the topology of the vortex tangle before being dominated by reconnections.

6.3.7 Sound Radiation from a Kelvin Wave

As discussed above, Kelvin waves are associated to emission of phonons outside the vortex core, i.e. they radiate an acoustic field. This phenomena can be efficiently analyzed considering vortex filament model and calculating the emitted field using classical models for vortex noise developed in the classical quasi-incompressible flow aeroacoustic framework.

A first estimate was proposed by Vinen (2000, 2001, 2002), who considered a Kelvin wave with wave length $\tilde{k}$ and angular frequency $\Omega(\tilde{k})$ propagating over a quantized vortex/vortex filament with undisturbed length $2l$ aligned with direction z. Each element of the vortex displaced by the wave acts a sound source, whose amplitude is denoted $f(z) = f_0 e^{\imath\tilde{k}z}$. The total amplitude of the radiated pressure field at wave number k at an angle β to the plane normal to the length of the undisturbed vortex, $p_s(q)$, where $q = k\sin\beta$, is equal to

$$p_s(q) = \frac{B}{2}\int_{-l}^{+l} f(z)e^{-\imath qz}dz = Bf_0 l\frac{\sin[(\tilde{k}-q)l]}{(\tilde{k}-q)l}, \tag{6.91}$$

where B and f_0 are constants. The case $\tilde{k} = 0$ corresponds to a straight vortex line moving in a circle with radius b equal to the Kelvin wave amplitude at constant angular velocity. The total radiated power by the Kelvin wave is

$$\Pi(\tilde{k}) \simeq \frac{2B^2 f_0^2 k}{\tilde{k}^2}, \quad \Pi(0) \simeq \pi B f_0^2 l, \tag{6.92}$$

from which it is easily seen that

$$\frac{\Pi(\tilde{k})}{\Pi(0)} \sim \frac{2}{\pi}\frac{1}{\tilde{k}l}\frac{k}{\tilde{k}}, \quad \tilde{k} \gg k. \tag{6.93}$$

Classical aeroacoustic results for a line of dipolar sources yield

$$\Pi(0) = \frac{\rho_s \kappa^2 b^2 \omega^3}{8a_s^2}. \tag{6.94}$$

Combination of these two results yields the following estimate for the power radiated by a Kelvin wave with amplitude b on a vortex line per length l via acoustic wave emission:

$$\Pi(\tilde{k}) = \frac{\rho_s \kappa^3 b^2 \Omega^3(\tilde{k}) b^2}{16\pi^2 a_s^3 l} \ln\left(\frac{1}{\tilde{k}r_c}\right) \propto \tilde{k}^6. \tag{6.95}$$

This approximation corresponds to a dipolar source, and vanishes as $l \to \infty$ due to cancellation of sound waves in phase opposition. A quadrupolar model would lead to a non-vanishing contribution.

Such a quadrupolar estimate was proposed by Kozik and Svistunov (2004, 2005b, 2009), who derived an estimate based on the analysis of the Hamiltonian equation for the occupation number[4] of Kelvin waves, $n(k)$, where k denotes the wave number. According to their model

$$\Pi(\tilde{k}) \simeq \frac{\kappa^2 \rho_s}{a_s^5 \tilde{k}} \varepsilon_{KW}^6(\tilde{k}) b^2(\tilde{k}) b^2(-\tilde{k}) \simeq \frac{\tilde{k}\varepsilon_{KW}^6(\tilde{k})}{a_s^5 \rho_s} n(\tilde{k}) n(-\tilde{k}) \simeq -\varepsilon_{KW}(\tilde{k}) \dot{n}(\tilde{k}), \tag{6.96}$$

where $\varepsilon_{KW}(\tilde{k}) \sim \tilde{k} r_c \Omega(\tilde{k})$ and

$$\dot{n}(\tilde{k}) = -\frac{(\kappa/2\pi)^5}{15\pi\rho_s} \left(\ln\left(\frac{1}{kr_c}\right) + C_0\right)^5 \left(\frac{\tilde{k}}{a_s}\right)^5 k^5 n^2(\tilde{k}) \tag{6.97}$$

leading to

$$\Pi(\tilde{k}) \simeq \ln^6\left(\frac{\ell}{r_c}\right) \frac{\kappa^8 \rho_s k^{11} b^2(\tilde{k})}{a_s^5}, \tag{6.98}$$

[4]This number denotes the number of Kelvin waves with wave number k.

where $b(\tilde{k})$ is the spectrum of the amplitude of the Kelvin waves. It is important noticing that there is no available direct measure of $\Pi(\tilde{k})$, so that none of these formula can be definitively assessed.

6.4 Quantum Turbulence Dynamics at Zero or Nearly-Zero Temperature

This section is devoted to dynamics of Quantum Turbulence at (ideally) zero temperature or nearly zero temperature, i.e. in configurations in which mutual friction effects are not dominant. Main dynamical features are discussed below in separated subsections, a separation being made between scales smaller than the mean vortex separation length ℓ and larger scales. The dynamics of the former is governed by physical mechanisms that are associated to the very nature of quantized vortices and which are absent in classical Navier–Stokes turbulence. The later can, in some cases, exhibit features that are similar to Navier–Stokes turbulence, leading to the quasi-classical régime.

6.4.1 Dynamics at Small Scales. I: Quantized Vortex Reconnection

6.4.1.1 Generals and Dimensional Analysis

Reconnection is related to the interaction between two quantized vortices, during which they connect and exchange tails as schematized in Fig. 6.6, leading to a change in the topology of the vortex tangle. This phenomenon has been observed directly in experiments dealing with dilute gas Bose–Einstein condensates (Tsatos et al. 2016) and in numerical simulations based on the Gross–Pitaevskii equation, see Ogawa et al. (2002), Zuccher et al. (2012), Tsubota (2013), Rorai et al. (2016), Tsubota et al. (2017). It escapes simulations based on hydrodynamic two-fluid models, and may be incorporated thanks to ad hoc models in vortex filament methods (Schwarz 1985, 1988; Tsubota and Adachi 2011; Baggaley 2012; Kondaurova et al. 2014). It has been indirectly observed in liquid helium and can therefore be considered as universal in the sense that is present in all types of quantum turbulence.

Quantized vortex reconnection occurs when two vortices get close enough to trigger the reconnection mechanisms. A quantitative criterion is that the distance between the two vortices should be smaller than a critical distance estimated as $R/\ln(R/r_c)$, where R and r_c are the radius of curvature of the vortex filament and the vortex radius, respectively. The duration of a reconnection is very small. The typical associated time scale is r_c/a_s, leading to $r_c/a_s \sim 10^{-12}$ s in ^{4}He. This mechanisms is

very important, since it is the only one that allows for the creation of new quantized vortices in the absence of external forcing and boundary condition effects.

Direct numerical simulations based on the Gross–Pitaevskii equations have shown that the reconnection is a compressible phenomenon, during which a rarefaction wave is emitted that induces both acoustic waves and thermal excitations (Ogawa et al. 2002; Tsubota 2009, 2013; Rorai et al. 2016; Zuccher et al. 2012). The typical wave length of emitted acoustic waves is of the order of the vortex radius. Vortex reconnection is one of the most important small scale mechanisms, whose main effects are[5]:

- Emission of phonons
- Decrease of the length of the vortices
- Generation of Kelvin waves on the quantized vortices
- Change in the topology of the vortex tangle by changing the p.d.f. of the length of the quantized vortices present in the flow.

The first two mechanisms lead to a decay of kinetic energy, while the third one induces both a direct cascade of energy toward small scales and a backward cascade toward large scales (see Fig. 6.6). Generation of Kelvin waves can be understood in a simple way. During reconnection, singularities or very sharp kinks are generated on vortices, which have a non-local spectrum in Fourier space. Therefore a reconnection should excite Kelvin waves on a wide range of wave numbers. The generation of Kelvin waves by reconnections in a simple ring vortex configuration is illustrated in Fig. 6.5, in which both the initial generation and induced the Kelvin-wave cascade are observed. Both the large amplitude of the deformations and the kinky character of the vortex lines at the last time must be noticed. It is also worth noticing that DNS of the Gross–Pitaevskii equations have shown that Kelvin wave can be triggered by the interaction between vortex lines and a strong acoustic/rarefaction waves, like those generated during reconnections (Berloff 2004).

A first issue is to evaluate the reconnection rate per unit volume. This parameter can be evaluated in the following heuristic way (Leadbeater et al. 2001; Ogawa et al. 2002; Barenghi et al. 2002, 2004) in the case of superfluid helium. Let's first introduce the *vortex line density* L_0, defined as the total vortex length $\mathcal{L}$ per unit volume V. The dimension of L_0 is m^{-2}. Observed values can be as large as $L_0 \simeq 10^7\,\mathrm{cm}^{-2}$ and $L_0 \simeq 10^6\,\mathrm{cm}^{-2}$ in ^{4}He and ^{3}He-B, respectively. The characteristic inter-vortex distance is often evaluated as $\ell \propto L_0^{-1/2}$ along with the characteristic radius of curvature of vortices, R, leading to $\ell \sim L_0^{-1/2} \sim R$. A vortex segment with length equal to l moving at speed U during a time Δt sweeps a volume $\mathcal{V} = \Delta t U l^2$ in which it interacts with m other vortices. The later is roughly estimated as the number of vortex line per unit volume, n, times $\mathcal{V}$ times a geometrical prefactor equal to 2/3 which accounts for the fraction of vortex segments that are perpendicular to the moving vortex: $m = \frac{2}{3} n \mathcal{V}$. The number of vortex lines per unit volume, n, is taken

[5]It is important noticing that the most advanced theories for reconnection deals with the case of Bose–Einstein condensates, which are often extrapolated for liquid helium for which no such theory exists and only indirect measurements of vortex line length are possible.

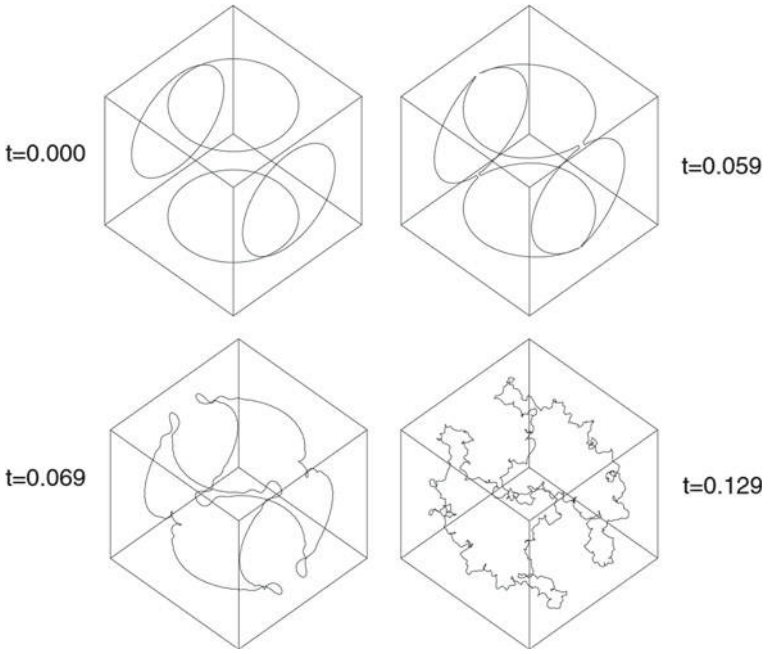

Fig. 6.5 Generation of Kelvin waves by vortex reconnections at zero temperature in a numerical simulation based on the Biot–Savart vortex filament model. The original non-local generation is observed at time $t = 0.069$. A much wider spectrum of disturbances originating in the Kelvin-wave cascade is seen at $t = 0.129$. From Kivotides et al. (2001) with permission of APS

equal to the total vortex line length in $\mathcal{V}$, $\mathcal{L}$, divided by l, leading to $n = (\mathcal{L}/\mathcal{V})/l = L_0/l$. Therefore, the number of collisions/reconnections experienced by a single vortex line is $m = \frac{2}{3}L_0 l U \Delta t$. The number of reconnections per unit time per unit volume, i.e. the reconnection rate per unit volume is

$$f = mn/\Delta t = \frac{2}{3}UL_0^2. \tag{6.99}$$

The kinetic energy transformed in acoustic energy per unit time per unit volume is

$$\frac{\Delta E_c}{V\Delta t} = f\delta_E, \tag{6.100}$$

where δ_E is the energy transformed into a sound burst by a single reconnection. There is no exact theory to estimate δ_E, but numerical simulations show that it depends on vortex topology and how the vortices reconnect (Leadbeater et al. 2001; Ogawa et al. 2002; Barenghi et al. 2002, 2004). A rough approximation is $\delta_E \sim 3r_c E_{QV}$, i.e. the released energy corresponds to a decrease of $3r_c$ of the quantized vortex length. A

typical order of magnitude is $\delta_E \sim 10^{-15}$ erg in liquid helium. Much larger values can be obtained for Bose–Einstein condensates in which r_c is much bigger.

Another important parameter is the vortex line density lost per unit time. It is evaluated as

$$\frac{\Delta L_0}{\Delta t} = \frac{\Delta \mathcal{L}}{V \Delta t} = \frac{\Delta \mathcal{L}}{\Delta E_c} \frac{\Delta E_c}{V \Delta t} = \frac{\delta_E f}{E_{QV}} \tag{6.101}$$

where E_{QV} is the quantized vortex kinetic energy per unit length given by Eq. (6.72).

The last open question in this semi-empirical approach is the evaluation of the characteristic velocity U. In the case the self-induced velocity is dominant, the Local Induction Approximation (6.32) yields

$$U = \|\boldsymbol{u}_{BS}\| \simeq \frac{\kappa L_0^{1/2}}{4\pi} \ln\left(\frac{L_0^{-1/2}}{r_c}\right) \tag{6.102}$$

leading to

$$f = \frac{\kappa}{6\pi} L_0^{5/2} \ln\left(\frac{L_0^{-1/2}}{r_c}\right) \sim \kappa L_0^{5/2} = \kappa \ell^{-5}, \tag{6.103}$$

where the logarithmic dependence has been omitted, and

$$\frac{\Delta L_0}{\Delta t} \simeq \frac{2}{3} \frac{\delta_E}{\kappa \rho_s} L_0^{5/2}. \tag{6.104}$$

The corresponding rate of energy loss per unit volume due to reconnections is therefore

$$\varepsilon_{reconnection} = \kappa \ell^{-5} 3 r_c E_{QV} \sim \frac{3\kappa^3 \ell^{-5} r_c \rho_s}{4\pi} \ln\left(\frac{\ell}{r_c}\right). \tag{6.105}$$

In the case in which the counterflow velocity is dominant, then $U \sim \alpha |\boldsymbol{u}_{ns}|$, leading to

$$f = \frac{2}{3} \alpha |\boldsymbol{u}_{ns}| L_0^2 \tag{6.106}$$

along with

$$\frac{\Delta L_0}{\Delta t} \simeq \frac{4}{3} \alpha |\boldsymbol{u}_{ns}| L_0^2. \tag{6.107}$$

The associated dissipation rate is

$$\varepsilon_{reconnection} = 2\alpha |\boldsymbol{u}_{ns}| L_0^2 r_c E_{QV} \simeq \frac{1}{2\pi} \alpha \rho_s \kappa^2 r_c \Lambda L_0^2. \tag{6.108}$$

Therefore, two types of decay régimes in which the dissipation is driven by reconnections can be identified, with different evolution laws for the vortex line density

L_0: $dL_0/dt = -\beta L_0^{\gamma}$, with $\gamma = 5/2$ (type II) in the absence of counterflow and $\gamma = 2$ (type I) if counterflow velocity is dominant, whose general solution is

$$L_0(t) = \left[L_0^{1-\gamma}(0) - \beta(1-\gamma)t\right]^{1/(1-\gamma)}. \tag{6.109}$$

The two predicted decay exponents have been observed in numerical simulations based on the Biot–Savart vortex filament method mimicking decaying ^{4}He turbulence, e.g. Schwarz (1988), Tsubota (2013), Kondaurova et al. (2014).

6.4.1.2 Random Quantized Vortex Loops and Rings: Model and Results

More detailed and rigorous theories have been proposed to study the kinetics of quantized vortex rings and loops (Nemirovskii 2013). A powerful theory can be built modeling the quantum turbulence structure as an ensemble of interacting vortex rings and vortex loops, each one being strongly deformed by reconnections and Kelvin waves. These deformations are modelled assuming that vortex loops composing the vortex tangle have a random walk structure that can be described thanks to a generalized Wiener distribution. The topology of the vortex tangle is described introducing $n(l,t)$ defined as the number of vortex loops with lengths in the range $[l, l+dl]$ per unit volume at time t. One can easily see that there are two mechanisms at play in the evolution of distribution function $n(l,t)$: the fusion of two loops into a single larger loop and the breakdown of a vortex loop into two smaller loops. The former is associated to a inverse energy cascade toward larger scales, while the latter leads to a direct cascade of energy toward small scales. Denoting $A(l,l_1,l_2)$ the intensity of the first mechanisms and $B(l,l_1,l_2)$ those of the second one, one obtains the following kinetic equation for the rate of change of $n(l,t)$

$$\begin{aligned}\frac{\partial n(l,t)}{\partial t} + \frac{\partial\left(n(l,t)\dot{l}\right)}{\partial t} = &\underbrace{\iint A(l_1,l_2,l)n(l_1)n(l_2)\delta(l-l_1-l_2)dl_1dl_2}_{l_1+l_2\to l}\\ &-\underbrace{\iint A(l_1,l,l_2)n(l_1)n(l)\delta(l_2-l_1-l)dl_1dl_2}_{l_1+l\to l_2}\\ &-\underbrace{\iint A(l_2,l,l_1)n(l_2)n(l)\delta(l_1-l_2-l)dl_1dl_2}_{l_2+l\to l_1}\\ &-\underbrace{\iint B(l,l_1,l_2)n(l)\delta(l-l_1-l_2)dl_1dl_2}_{l\to l_1+l_2}\end{aligned}$$

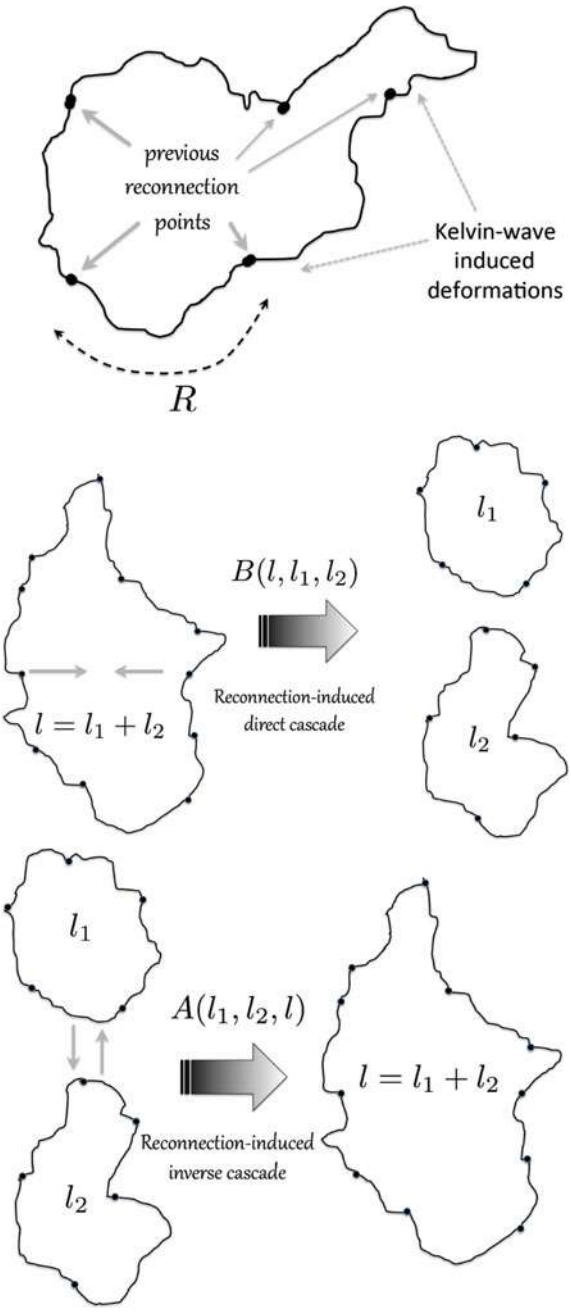

Fig. 6.6 Schematic view of quantized vortex reconnection. Top: schematic view of simple line reconnection; Middle: Vortex ring reconnection yielding a direct cascade toward small scales; Bottom: Vortex ring reconnection yielding an inverse cascade toward large scales

$$+\underbrace{\iint B(l_1,l_2,l)n(l_1)\delta(l_1-l_2-l)dl_1dl_2}_{l_1\to l+l_2}$$
$$+\underbrace{\iint B(l_2,l_1,l)n(l_2)\delta(l_2-l_1-l)dl_1dl_2}_{l_2\to l_1+l}. \tag{6.110}$$

Each term in this equation can be evaluated analytically if an adequate model for the vortex loop structure is used. The assumption of a Brownian nature of the vortex loop structure allows for such an evaluation. After some very long algebra, one obtains

$$A(l_1,l_2,l)=b_mUl_1l_2,\quad B(l,l_1,l-l_1)=b_sU\frac{l}{(Rl_1)^{3/2}}, \tag{6.111}$$

where $b_m=1/\sqrt{18}$, $b_s=\sqrt{3/64}\,\pi^{-9/4}$ and where R is the parameter of the generalized Wiener distribution, taken to be of the order of typical curvature of the vortex line, which is also the step in the random walk. As in the empirical calculations displayed above, the characteristic velocity U can be computed considering that self-induction is dominant, leading to $U=c_v\kappa/R$, where c_v is a constant parameter.

Some particular analytical solutions can be found. Among them, a stationnary solution of (6.110) neglecting the second term in the left-hand side is $n(l)=c_nl^{-5/2}$, where c_n is a constant parameter.

Further insight into this solution can be gained introducing the length density in space of sizes l, $L(l,t)=n(l,t)l$, which corresponds the total length in vortex loops of size l per unit volume. The total vortex line length per unit volume L_0, i.e. the vortex line density, is recovered as $L_0(t)=\int L(l,t)dl$. This last quantity is conserved by vortex reconnection if dissipation via acoustic wave radiation is omitted, i.e. $dL_0/dt=0$, which leads to

$$\frac{\partial L(l,t)}{\partial t}+\frac{\partial P(l,t)}{\partial l}=0, \tag{6.112}$$

where $P(l,t)$, i.e. the flux of vortex length in space of sizes of the loops, can be evaluated from $A(l,l_1,l_2)$ and $B(l,l_1,l_2)$. After some long algebra, one obtains

$$P=P^+-P^-=\frac{12.555}{2}c_n^2b_mU-\frac{5.545}{2R^{3/2}}c_nb_sU. \tag{6.113}$$

Here, P^+ and P^- correspond to the inverse cascade toward large scales and the direct cascade, respectively. This direct cascade mechanisms associated to reconnections of vortex loops was anticipated by Feynman in 1955. It has been debated, since a cascade based on undisturbed circular vortex rings in place of Gaussian vortices

used here would lead to violation of physical conservation laws. More precisely, considering circular vortex rings does not allow for the conservation of both energy and momentum, while more complex shapes, such has the randomized Gaussian vortex model allow for the recovery of conservation laws.

Since both P^+ and P^- are large quantities and that P is comparatively small, a first-order approximation yields $P^+ \simeq P^-$, leading to

$$c_n = \frac{5.545}{12.555}\frac{b_s}{b_m}\frac{1}{2R^{3/2}} = c_n^{'}\frac{1}{2R^{3/2}}, \tag{6.114}$$

along with

$$n(l) = \frac{c_n^{'}}{2R^{3/2}} l^{-5/2}. \tag{6.115}$$

A very interesting results if found considering the total length per unit volume L_0:

$$L_0 = \int_R^{+\infty} n(l) l dl = \frac{2c_n^{'}}{R^2} \quad \Longrightarrow \quad R = \sqrt{2c_n^{'}} L_0^{-1/2}, \tag{6.116}$$

from which one can deduce that the inter vortex spacing $\ell \simeq L_0^{-1/2}$ is of the order of the mean radius of curvature R. Reintroducing this relation into the evaluation of the of the net flux (6.113), one obtains that both P^+ and P^- scale as L_0^{-2}, yielding

$$\frac{dL_0}{dt} \propto -L_0^{-2}. \tag{6.117}$$

The full rate of reconnection is recovered from relation (6.110) giving a plus sign to all terms. Therefore the total number of reconnection n_{tot} evolves as

$$\dot{n}_{tot} = \frac{1}{3}\frac{\kappa c_n^{'}(b_s + b_m^2)}{R^5} = c_n^{''}\kappa L_0^{5/2} = f, \tag{6.118}$$

where $c_n^{''}$ is a constant of the order of the unity. It is remarkable that the scaling law found in the empirical approach is recovered.

It is worth noting that the cascades associated to the quantized vortex length distribution $n(l,t)$ induces both direct and inverse kinetic energy cascade, since the energy of quantized vortices with length l per unit volume is equal $n(l)lE_{QV}$. This point is discussed below.

6.4.1.3 Reconnection-Driven Cascades

As mentioned above, reconnections induce several cascade phenomena:

- A direct energy cascade via breakdown of large vortex loops/rings into smaller ones

- An inverse energy cascade via merging of small vortex loops/rings into larger ones
- Injection of kinetic energy into small scales by direct nonlocal excitation of Kelvin waves on quantized vortices due to the singular nature reconnections, which are associated as a cusp with non local spectral signature at reconnection points.
- Indirect triggering of Kelvin wave cascades, which are discussed in Sect. 6.4.2.

Reconnections and induced cascades and dissipation are, in almost all existing theories, considered as the dominant phenomena at scales of the order of the vortex interspacing scale ℓ, and possibly at scales larger or smaller than ℓ within a few decades of scales. Both direct and inverse reconnection-driven energy cascades have been reported in simulations based on the Biot–Savart vortex filament method, e.g. Baggaley et al. (2014). A careful analysis that the net effect is a forward energy cascade toward small scales, due to the fact the splitting-type reconnections have higher probability than merging-type ones. This asymmetry has been repeatedly reported in simulations mimicking ^{4}He turbulence, e.g. Kondaurova and Nemirovskii (2012), Kondaurova et al. (2014), Baggaley et al. (2014).

A theoretical analysis of the dynamics of scales dominated by reconnections has been proposed by Kozik and Svistunov (2008a, b, 2009). Considering a case in which the superfluid is mechanically forced injecting kinetic energy at a rate ε_p at scales much larger than ℓ in such a way that quantized vortices are organized into polarized bundles, these authors developed a model in which several ranges of scales must be distinguished. The key assumptions of this analysis are that: (i) the energy flux associated to the reconnection-driven energy cascade is conserved at all scales and (ii) the quantity of energy transferred to a smaller scale after one reconnection of vortex line at wave number k can be estimated as

$$\varepsilon(k) \sim f(\theta)\Lambda\rho_s\kappa^2 k^{-1}, \quad \Lambda \equiv \ln\left(\frac{\ell}{r_c}\right) \tag{6.119}$$

where θ denotes the angle at which the vortex lines cross, $\theta = 0$ being associated to parallel lines. The dimensionless function $f(\theta)$ behaves asymptotically as $f(\theta \to 0) \propto \theta^2$, showing that the efficiency of energy transfer vanishes quickly for nearly parallel vortices. The three proposed ranges of scales are:

- Scales dominated by reconnections of bundles, $r_0^{-1} \leq k \leq \lambda_b^{-1}$, where r_0 is the size of the smallest classical eddies observed at hydrodynamic scales (i.e. the Kolmogorov scale in classical fluids), which is also interpreted as the characteristic size of the quantized vortex bundles. It is related to the interspacing length by $r_0 \simeq \Lambda^{1/2}\ell > \ell$, while $\ell \simeq (\Lambda\kappa^3/\varepsilon_p)^{1/4}$. At such large scales there is no direct coupling between quantized vortices inside a given bundle, and the reconnections occur between vortex bundles. More precisely, crossing of bundles trigger reconnections between all their quantized vortices. This picture is coherent with numerical simulations based on both the Gross–Pitaevskii equations and the vortex filament model. Dimensional analysis and phenomenological arguments yield the following estimation of the energy flux per unit mass in this régime, which is assumed to be equal to ε_p:

$$\varepsilon_p = \left(\frac{k}{\rho_s b^2(k)}\right) N_k \varepsilon(k) \tau_k^{-1}, \tag{6.120}$$

where the correlation volume of the reconnection is $\frac{k}{\rho_s b^2(k)}$, $N_k \sim (b(k)/\ell)^2$ is the number of vortex lines involved in the reconnection and $\tau_k^{-1} \sim \kappa \Lambda k^2$ is the rate at which the bundles cross. The associated solution for spectrum for the amplitude of the deformation of vortex lines is

$$b(k) \simeq r_0^{-1} k^{-2}. \tag{6.121}$$

The scale λ_b is defined as the scale at which the amplitude of the deformation is of the order of the inter-vortex spacing, i.e. $b(k) = \ell$. Using the previous estimation, one obtains $\lambda_b = \Lambda^{1/4}\ell$. At smaller scales the notion of bundle is meaningless, and reconnections between adjacent vortices become dominant.

- Scales dominated by reconnections of adjacent quantized vortices in the same bundle, $\lambda_b^{-1} \leq k \leq \lambda_c^{-1}$. Here, the rate of reconnection per each line element with length k^{-1} and the energy transferred by a single collision are estimated as Λk^2 and $\Lambda b^2(k)k$, respectively, leading to

$$b(k) \propto \ell(\lambda_b k)^{-1/2}. \tag{6.122}$$

The scale λ_c is determined as the scale at which the curvature of the quantized vortices is large-enough to allow for self-reconnections of a quantized vortices. The curvature being estimated as $kb(k)$, the condition for self-reconnections to take place is $kb(k) \simeq 1$, leading to $\lambda_c \sim= \Lambda^{-1/4}\ell$.

- Scales dominated by self-reconnections of quantized vortices, $\lambda_c^{-1} \leq k \leq \lambda_*^{-1}$. Self-reconnections govern the cascade for scales in this range, resulting in the production of vortex rings/loops of typical size λ_*. The rate of production per unit time in a control volume ℓ^3 is approximated as $\kappa\Lambda^{1/2}/\ell^2$. It is worth noting that in the absence of vortex bundles, i.e. in a random superfluid turbulence without large-scale polarization, the self-reconnection rate was estimated by Svistunov as $\kappa\Lambda^2/\ell^2$. Conservation of the energy flux ε_p yields

$$b(k) \propto k^{-1}. \tag{6.123}$$

The scale $\lambda_* \sim \ell/\Lambda^{1/2}$ is the scale at which self-reconnection ceases and the Kelvin wave cascade becomes dominant.

This phenomenological picture has not been presently assessed by either numerical simulation or experiments. It is worth noting that in ^{4}He and ^{3}He-B one has $\Lambda = 12-15$ and $\Lambda = 1-2$ in existing realizations of atomic gas Bose–Einstein condensates, leading to almost undistinguishable spectrum range in experimental data or numerical simulations. Nevertheless, the different mechanisms (bundle reconnections, adjacent vortex reconnections and self-reconnections) should be at play in practical cases. In the case of quantum turbulence without vortical hydrodynamic

scales, i.e. random distribution of quantized vortices, bundle reconnection does not exist.

6.4.2 *Dynamics at Small Scales. II: Kelvin-Wave Cascade and Weak Wave Turbulence*

The nonlinear Kelvin-wave cascade that takes place at scales smaller than λ_* has been investigated by many authors, since it is presently considered as the main physical mechanisms responsible for transfer of kinetic energy to smaller scales at which dissipation becomes significant. The cascade is usually considered to end at the scale λ_{ph} at which the dissipation via emission of phonons (at least in ^{4}He) is equal to the energy transfer rate via the cascade. It is worth noting that such cascade is not observed directly in laboratory experiments because of the smallness of the involved scales, and that other mechanisms, such that the direct nonlocal production of Kelvin waves by reconnections may also play a role, as advocated by Vinen. Another remark is that in some cases in which the dissipation occurs at scales that are not very small compared with the vortex inter spacing scale, i.e. $\lambda_{ph} \sim \ell$ (e.g. in experimental realizations of dilute atomic gas Bose–Einstein condensates), such a cascade is likely not to build up.

Several methods have been used to predict the solution associated to the Kelvin wave cascade: phenomenological approach coupled to dimensional analysis (Vinen 2000), weak turbulence theory derived from Hamiltonian representation of the vortex filament dynamics as discussed in Sect. 6.2.2.4 (Kozik and Svistunov 2004, 2005a; Kozik and Svistunov 2009; L'vov et al. 2007; L'vov and Nazarenko 2010; Laurie et al. 2010; Boué et al. 2011; Nemirovskii 2013). Weak wave turbulence at small scales as also been analyzed considering the Gross–Pitaevskii equations, including numerical simulations (Nemirovskii 2013; Tsubota et al. 2017), extension of Kraichnan's Direct Interaction Approximation (Yoshida and Arimitsu 2013) for both strong and weak turbulence régimes and classical approaches for wave turbulence (Proment et al. 2009; Fujimoto and Tsubota 2015; Tsubota et al. 2017).

An important point is that theoretical analyses that use relation (6.74) to evaluate the frequency of the Kelvin waves implicitly assume that these waves are small amplitude disturbances propagating along quantized vortices, since this relation originates in a linear theory based on a small parameter expansion. Waves with large amplitudes should a priori not be referred to as Kelvin waves, and there is presently no detailed theory for them. Numerical simulations based on both the Biot–Savart vortex filament model and the Gross–Pitaevskii equations have been performed, e.g. Kivotides et al. (2001), Vinen et al. (2004). It is important noting that acoustic wave radiation is not taken into account in the former, in which numerical resolution errors are assumed to play the role of an implicit dissipation. Artificial dissipation is also sometimes added to the Gross–Pitaevskii simulations to prevent energy pile-up at smallest resolved scales.

6.4.2.1 Empirical Theories

A first approach was developed by Vinen (Vinen and Niemela 2002) on the ground of dimensional analysis. The evaluation of the Kelvin cascade is based on the upper bound for the cascade rate, which is taken equal to the estimated production of cascade rate by reconnections. Evaluating the reconnection rate as $\kappa\ell^{-5}$ per unit volume, and assuming that each reconnection lead to the generation of a length of line of order ℓ associated to an injection of energy into Kelvin waves equal to $\rho_s\kappa\ell$, the rate of injection of energy into Kelvin wave per unit mass of superfluid is

$$\varepsilon_p = G\kappa^3\ell^{-4} = G\kappa^3\tilde{L}_0^2, \tag{6.124}$$

where G is a constant of the order of unity and $\tilde{L}_0$ is not the vortex line density introduced in Sect. 6.4.1.1 but a smoothed vortex length per unit volume based on the length of vortex line per unit volume after the excited Kelvin waves have been removed. The corresponding rate of energy injection by reconnection per unit smoothed length of vortex line is $G\rho_s\kappa^3\ell^{-2}$.

The maximum spectral intensity is estimated assuming that the maximum amplitude for a wave with wave number k is proportional to k^{-1}, leading to (via dimensional analysis)

$$E_{KW}(k) = A\rho_s\kappa^2 k^{-1} \tag{6.125}$$

where A is a constant. It should be kept in mind that this is an upper bound estimation, since the analysis carried out in Sect. 6.3.4 shows that displacements associated to finite amplitude Kelvin waves are restricted to a few vortex cores.

The wave number $k_{ph} \sim 1/\lambda_{ph}$ at which the Kelvin wave cascade vanishes due to dissipation by phonon emission is found assuming that $E_{KW}(k)$ has a sharp cut-off wave number at k_{ph}. The characteristic time associated to phonon emission for a Kelvin wave with wave number k and amplitude $b(k)$, $\tau_{ph}(k)$, is computed as the ratio of the energy of the Kelvin wave per unit length E_{QV} over the power radiated per unit length $\Pi(k)$ discussed in Sect. 6.3.7. Evaluating the increase of vortex length due to the Kelvin wave by its amplitude $b(k)$, the energy per unit length is equal to

$$E_{QV}b^2(k) = \frac{\rho_s\kappa^2}{4\pi}\ln\left(\frac{1}{kr_c}\right)k^2b^2(k), \tag{6.126}$$

where E_{QV} is given by (6.72), and using Vinen's evaluation for $\Pi(k)$, one has

$$\tau_{ph}(k) = \frac{4\pi a_s^3\ell k^2}{\kappa\Omega^2(k)}. \tag{6.127}$$

Equalizing the dissipation rate and the production rate yields

$$\int_{1/\ell}^{k_{ph}} \frac{E_{KW}(k)}{\tau_{ph}(k)}dk = \varepsilon_p = G\rho_s\kappa^3\ell^{-2} \quad \Longrightarrow \quad k_{ph}\ell \simeq \left(\frac{16\pi G a_s^3\ell^3}{A\kappa^3}\right)^{1/4} \tag{6.128}$$

in which it has been assumed that $k_{ph} \gg 1$ and $\ln(1/kr_c) \simeq 4\pi$. For a typical vortex tangle in ^{4}He with $\ell = 10\,\mu$m, one has $\lambda_{ph} \simeq 2\,$nm, which is much larger than the vortex core radius $r_c \approx 0.1\,$nm. The corresponding frequency is $\Omega(k_{ph}) \simeq 4\,$GHz. A generalized estimation is $\lambda_{ph} \sim 100 r_c$ in ^{4}He.

6.4.2.2 Weak Turbulence Theories Based on Hamiltonian Biot–Savart Vortex Filament Model

Previous analyses based on dimensional analysis do not yield univocal results, depending on the empirical ingredients used to recover expressions for the energy flux and associated spectra. It is now commonly accepted that Kelvin-wave cascade can be described by weak wave-turbulence theory and that dominant interactions are three-to-three wave scattering discussed in Sect. 6.2.2.4.

The key element is the derivation of an evolution equation for the *wave action* defined as

$$n(k,t) = \frac{\mathcal{L}}{2\pi}\overline{b(k,t)b^*(k,t)}, \tag{6.129}$$

where $b(k,t)$ denotes here the canonical variable that appears in the Hamiltonian formulation (6.57). The Kelvin wave kinetic energy and kinetic energy spectrum are recovered from the wave action via the following relations:

$$\mathcal{K}_{KW} = \int_{-\infty}^{+\infty} \Omega(k)n(k)dk = \int_0^{+\infty} \Omega(k)N(k)dk = \int_0^{+\infty} E_{KW}(k)dk \tag{6.130}$$

where $N(k) = n(k) + n(-k)$ and the Kelvin wave frequency $\Omega(k)$ is given by (6.74) and

$$E_{KW}(k) = \Omega(k)N(k) = \frac{\Lambda\kappa}{4\pi}k^2N^2(k). \tag{6.131}$$

The amplitude of Kelvin wave is recovered as $b^2(k) \simeq kN(k)$. The equation evolution derived from the Hamiltonian problem (6.57), commonly referred to as the *kinetic equation*, is usually written as

$$\frac{dn(k,t)}{dt} = St(k, n(k,t)), \tag{6.132}$$

where the *collision integral* $St(k, n(k,t))$ is equal to

$$St(k,n(k,t)) = \frac{\pi}{12}\iiint\!\!\iint |\mathcal{W}^{3,4,5}_{k,1,2}|^2 n_k n_1 n_2 n_3 n_4 n_5 \delta^{3,4,5}_{k,1,2}\delta\Omega^{3,4,5}_{k,1,2} \times \left(\frac{1}{n_k} + \frac{1}{n_1} + \frac{1}{n_2} - \frac{1}{n_3} - \frac{1}{n_4} - \frac{1}{n_5}\right) d\boldsymbol{k}_1 d\boldsymbol{k}_2 d\boldsymbol{k}_3 d\boldsymbol{k}_4 d\boldsymbol{k}_5, \tag{6.133}$$

where $n_i = n(k_i)$ and

$$\delta^{3,4,5}_{k,1,2} = \delta(\boldsymbol{k} + \boldsymbol{k}_1 + \boldsymbol{k}_2 - \boldsymbol{k}_3 - \boldsymbol{k}_4 - \boldsymbol{k}_5)$$

along with

$$\delta\Omega^{3,4,5}_{k,1,2} = \delta(\Omega(k) + \Omega(k_1) + \Omega(k_2) - \Omega(k_3) - \Omega(k_4) - \Omega(k_5)).$$

A pseudo-Lin equation can be derived for $E_{KW}(k)$

$$\frac{\partial}{\partial t} E_{KW}(k) = T_{KW}(k) = \frac{\partial}{\partial k} F_{KW}(k), \tag{6.134}$$

where the energy flux term is given by

$$F_{KW}(k) = \int_0^k St(p, n(p,t))\Omega(p)dp \tag{6.135}$$

that can be approximated as

$$F_{KW}(k) = k\dot{N}(k)\Omega(k). \tag{6.136}$$

The Kelvin wave cascade is observed to conserve two global quantities in the absence of phonon emission: the total energy $\mathcal{K}_{KW}$ and the total wave action $\mathcal{N}_{KW} = \int_0^{+\infty} N(k)dk$. Therefore, it is expected that two cascades will take place, one direct cascade toward small scales and one inverse cascade toward large scales. Corresponding solutions for $n(k)$ exhibiting a constant non-zero flux in some inertial ranges are referred to as Kolmogorov–Zakharov solutions in the field of wave turbulence. There is one additional remarkable solution that corresponds to the thermodynamical equipartition of energy and wave action, namely the Rayleigh–Jeans distribution given by

$$n(k) = \frac{T}{\Omega(k) + \mu}, \tag{6.137}$$

where T and μ are the temperature and the chemical potential, respectively.

The direct cascade if found observing that kinetic equation (6.132) has scale-invariant solutions of the form $N(k) \sim k^{-m}$. Two main values for m have been obtained depending on the assumed degree of locality of the Kelvin wave scattering. Using the local approximation, one obtains via dimensional analysis $\dot{N}(k) \sim k^{14}N^5(k)$, yielding $F_{KW}(k) \sim k^{15}N^5(k)$. Mimicking the analysis of the classical Kolmogorov inertial range in isotropic turbulence in classical fluids, it is hypothesized that there is an inertial range within the Kelvin wave cascade with a constant energy flux, leading to $N(k) \sim k^{-17/5}$. The non-local approximation yields more tedious manipulations, which are not reproduced here. The two solutions are

$$N(k) \sim \begin{cases} 4\pi\varepsilon^{1/3}\Psi^{2/3}k^{-11/3} & \text{L'vov–Nazarenko (non-local approx.)} \\ k^{-17/5} & \text{Kozik–Svistunov (local approx.)} \end{cases} \tag{6.138}$$

where $\Psi = 8\pi\mathcal{K}_{KW}/\Lambda\kappa^2$. Therefore, the Kelvin wave energy spectrum is equal to

$$E_{KW}(k) \sim \begin{cases} \frac{\Lambda\kappa\varepsilon^{1/3}}{\Psi^{2/3}}k^{-5/3} & \text{L'vov–Nazarenko (non-local approx.)} \\ \Lambda\kappa^{7/5}\varepsilon^{1/5}k^{-7/5} & \text{Kozik–Svistunov (local approx.)} \end{cases}. \tag{6.139}$$

The cut-off wave number k_{ph} is evaluated in the same way as for the empirical approaches, i.e. by finding the wave number at which the rate of dissipation via phonon emission is equal to the energy cascade rate.

Using their estimate for the phonon emission rate and cascade rate, Kozik and Svistunov propose two evaluations, one for cases with polarized vortex bundles and another one for random vortex distribution:

$$\lambda_{ph} \sim \begin{cases} \Lambda^{27/31}(\kappa/a_s\ell)^{25/31}\ell & \text{(with polarized bundles)} \\ \Lambda^{24/31}(\kappa/a_s\ell)^{25/31}\ell & \text{(random distribution)} \end{cases}. \tag{6.140}$$

The inverse cascade is found applying the same reasoning to the flux of wave action $F^{(n)}_{KW}(k)$, defined as

$$F^{(n)}_{KW}(k) = \int_0^k \dot{n}(p)dp = \int_0^k St(p, n(p))dp. \tag{6.141}$$

Dimensional analysis yields $F^{(n)}_{KW}(k) \sim k^{15}n^5(k)$, and constant flux assumption leads to $n(k) \sim k^{-3}$, showing that there is a second inertial range associated to a cascade of wave action. According to the Fjørtoft argument, this cascade is an inverse cascade toward large scales.

The most recent theoretical works (Laurie et al. 2010; Boué et al. 2011) are in favor of the non-local theory proposed by L'vov and Nazarenko. There is of course no available direct measurement of such small scales, precluding strong assessment by experiments. Most available numerical simulations based on the Biot–Savart vortex filament methods yield results that are not accurate enough to draw a final conclusions. As an example, Baggaley and Barenghi (2011) reported $N(k) \sim k^{-3.1}$, which is close to both $-11/3 = -3.7$ and $-17/5 = -3.4$. But a very recent simulation based on the full Biot–Savart equation (Baggaley and Laurie 2014) yielded results in clear agreement with the non-local theory, giving the first numerical evidence that the local model should be discarded, at least in the case of Kelvin waves developing on an ideal straight vortex line. In these simulations, an inertial range with both a constant energy flux and the expected spectrum slope was observed.

6.4.2.3 About the 3D Energy Spectrum Generated by Kelvin Waves Propagating along a Vortex Line

All theories mentioned above deal with the energy spectrum of Kelvin waves, which are 1D waves that propagate along an idealized vortex. Therefore, the evaluation of the associated 3D energy spectrum $E(k)$ of the velocity field induced in the fluid must be carried out to bridge with classical turbulence theory.

The general method to reconstruct $E(k)$ is to compute the statistical average of the spectrum generated by a single vortex element (line, loop, ring, …) corrugated by Kelvin waves with a given spectrum E_{KW}. In such a calculation, one must prescribe (i) the type of vortex element, (ii) the distribution function of the vortex elements and (iii) the spectrum of Kelvin waves, showing that their is a large degree of empiricism.

For a single vortex element with length L, one obtains the following general formula:

$$E(k) = \frac{\rho_s \kappa^2}{(2\pi)^2} \int_0^L \int_0^L \boldsymbol{s}'(\xi_1) \cdot \boldsymbol{s}'(\xi_2) \frac{\sin(k|\boldsymbol{s}(\xi_1) - \boldsymbol{s}(\xi_2)|)}{k|\boldsymbol{s}(\xi_1) - \boldsymbol{s}(\xi_2)|} d\xi_1 d\xi_2. \tag{6.142}$$

Applying that formula, one obtains the following results for typical vortex elements without Kelvin waves (Nemirovskii 2013):

- For a straight vortex line with zero radius:

$$E(k) \propto k^{-1}. \tag{6.143}$$

- For a circular vortex ring with radius R:

$$E(k) \propto \begin{cases} k^{-2} & kR \ll 1 \\ k^{-1} & kR \gg 1 \end{cases}. \tag{6.144}$$

- For random loops/rings with Gaussian distribution and with fractal Hausdorff dimension H_D and characteristic size L:

$$E(k) \propto \begin{cases} k^2 & kL \ll 1 \text{ (far field)} \\ k^{-2+H_D} & kL \gg 1 \end{cases}. \tag{6.145}$$

The disturbance in the energy spectrum induced by Kelvin waves, $\delta E(k)$, is obtained in the same way accounting for the corrugation of the vortex line in the integrand in relation (6.142). Considering Kelvin waves with mean amplitude a and spectrum $E_{KW}(p) \propto p^{2-s}$, one obtains

$$\delta E(k) \propto a^2 k^{2-s} \tag{6.146}$$

The fact that E_{KW} and $\delta E(k)$ exhibit the same exponent should not be generalized into $E(k) \sim E_{KW}(p)$, since the amplitude factor a^2 is very small for waves described by the weak turbulence theories discussed above.[6]

Therefore, the energy spectrum $E(k)$ is mostly governed by the large scale topology and distribution of vortex filaments, the Kelvin-wave-induced part $\delta E(k)$ being mostly a small-amplitude correction.

Most existing numerical simulations dealing with vortex tangle dynamics based on the Biot–Savart vortex filament model exhibit $E(k) \propto k^{-1}$ at small scales, i.e. much smaller than the inter vortex distance ℓ, in agreement with the fact that at such small scales vortex filament curvature effects are small and that the straight vortex line should dominate. It is worth noting that in such simulations the dissipation related to compressible mechanisms associated to acoustic wave radiation is not accounted for.

6.4.2.4 Concluding Remarks

Some caveats must be mentioned at this point:

- Kelvin waves are small amplitude waves. Therefore, huge deformations of order ℓ of quantized vortices observed in numerical simulations a priori escape this theory and miss to be theoretically described.
- Kelvin waves propagate along dynamically bent vortex filaments. In the theoretical approaches discussed above curvature effects, which may be non-negligible for long waves, are neglected.
- Quantized vortices experience reconnections at random points at a non-negligible rate, the effect of which are not taken into account. Two effects should be taken into account: "kinematic" non-local generation of Kelvin waves over a wide range of scales by the singular topological character of the reconnection (without any cascade-like process) and destruction of vortex filaments by reconnections.
- Kelvin wave theory is developed considering infinite vortex lines, and finite length effects that must take place on real quantized vortices are not taken into account.
- All developments contain some degree of empiricism to identify the governing part of the Hamiltonian term $\mathcal{W}_{k,i,j}^{m,p,q}$. There is no rigorous mathematical proof here, and comparison with the few existing DNS data is the only available validation.
- Numerical experiments have shown that quantitative results obtained thanks to Biot–Savart-based vortex filament methods are very sensitive to details of the numerical algorithms when the Local Interaction Approximation is used (Adachi and Tsubota 2010; Baggaley 2012). Therefore mostly qualitative conclusions should be drawn from these simulations.

The relevance of the Kelvin-wave-induced cascade to explain transfer of kinetic energy toward small scales remains to be assessed in realistic cases, despite it has been addressed in a large number of theoretical studies. The issue here is twofold. First,

[6]The shortcoming relation $E(k) = E_{KW}(k)$ is misleading and should be avoided.

the idealized vortex filament model with null radius is mostly relevant to describe superfluid ^{4}He dynamics, while it is less appropriate to describe phenomena in ^{3}He-B and Bose–Einstein condensates, in which the quantized vortex radius is much larger, restricting the range of scales over which a Kelvin-wave cascade may take place. Second, there is a competition between reconnection-induced cascade and Kelvin-wave induced cascade, the later being overwhelmed by the former in many cases. This is illustrated by the following example given by Nemirovskii. Considering a typical experiment in superfluid Helium with counterflowing velocity of 1 cm/s and a fluid volume of 1 cm^3, the interline space $\ell \propto L_0^{-1/2}$ is about 10^{-2} cm. The associated full rate of reconnection is of the order of 10^7 collisions per second per unit volume and the rate of reconnection per unit length of the vortex filaments is about 10^3 1/cm $\cdot$ s. Therefore, a vortex loop with length $\sim 10\ell$ will experience about 100 reconnections per second. Now considering signal propagation along the same vortex loop, one can find that the characteristic propagation time is about $\ell^2/\kappa \simeq 10$ s. One can see that Kelvin wave dynamics is a much slower process that reconnection, since its characteristic time is nearly 100 times larger than the life time of the vortex loop, at least for large-scale Kelvin waves. The two characteristic times become similar for wave with period of the order of ℓ, and Kelvin wave cascade should exist only at scale much smaller than ℓ.

Therefore, Kelvin wave dynamics is an important topic from a theoretical viewpoint considering the nonlinear wave framework, but with restricted relevance for Quantum Turbulence, since Kelvin waves are responsible for a limited part of the full dynamics in practice, when they exist. According to Nemirovskii (2013), the two main issues that may be addressed using Kelvin wave theory in the field of Quantum Turbulence are (i) the decay of a vortex tangle and (ii) the 3D energy spectrum generated by vortex lines with Kelvin waves excited on them.

6.4.3 Small Scales Dynamics. III: Turbulent Cascades Using Gross–Pitaevskii Equations

6.4.3.1 Generals

A last set of theoretical results comes from the theoretical analysis of the Gross–Pitaevskii equations in the non-linear régime. An important difference with previous results is that the these results are not restricted to the incompressible velocity field or to waves propagating along ideal vortex filaments. As mentioned in Sect. 6.2.1, the fluctuations of the state field $\psi(\boldsymbol{x}, t)$ may represent fluctuations in the condensate, phonons/acoustic waves or a mix of them. Therefore, a direct univoque correspondance between previous results dealing with Kelvin waves and fluctuations described in the present section should not be expected, but useful qualitative comparisons can be done. An important point is that the Gross–Pitaevskii equation is a reliable model

for dilute cold atomic gas at small to medium scales, and that the mean field assumption may be violated at scales larger than ℓ.

In the absence of external source/sink term, the Gross–Pitaevskii equation exhibits three invariants. The two first invariants of motion are the number of particules per unit volume, $\bar{N}$, and the total energy per unit volume E_{tot}, where it is recalled that $\psi = \sqrt{n}e^{\imath S}$, with $\rho_s = mn$ where m is the mass of the particule. The total number of particules is computed as

$$\bar{N} = \frac{1}{V}\int_V |\psi(\boldsymbol{x},t)|^2 d^3\boldsymbol{x}, \tag{6.147}$$

while the total energy per unit volume is evaluated as the sum of the kinetic energy and interaction energy

$$E_{tot} = E_K + E_I = \frac{1}{V}\int_V \frac{\hbar^2}{2m}|\psi(\boldsymbol{x},t)|^2 d^3\boldsymbol{x} + \frac{1}{V}\int_V \frac{g}{2}|\psi(\boldsymbol{x},t)|^4 d^3\boldsymbol{x}. \tag{6.148}$$

The third one is the momentum per unit volume

$$\mathcal{M} = \frac{1}{2}\imath\frac{1}{V}\int_V (\psi(\boldsymbol{x},t)\nabla\psi^*(\boldsymbol{x},t) - \psi^*(\boldsymbol{x},t)\nabla\psi(\boldsymbol{x},t))d^3\boldsymbol{x}, \tag{6.149}$$

which can be taken equal to zero in isotropic turbulence.

Most of the analyses rely on the Fourier transform of the Gross–Pitaevskii equation, from which the following irreversible exact kinetic equation for the particule number spectrum $\hat{n}(k)$ is derived

$$\begin{aligned}\frac{\partial}{\partial t}\hat{n}(k) = St(k) = 4\pi\iiint |T(k,k_1,k_2,k_3)|^2\delta(\boldsymbol{k}+\boldsymbol{k}_1-\boldsymbol{k}_2-\boldsymbol{k}_3)\delta(\omega_k+\omega_1-\omega_2-\omega_3)\\ \times(n_1n_2n_3 + n_kn_2n_3 - n_kn_1n_2 - n_kn_1n_3)d\boldsymbol{k}_1 d\boldsymbol{k}_2 d\boldsymbol{k}_3\end{aligned} \tag{6.150}$$

where $\omega_k = \omega(k)$, $\omega_i = \omega(k_i)$ denote the Bogoliubov frequency given by Eq. (6.12) and $n_i = \hat{n}(k_i)$. $T(k,k_1,k_2,k_3)$ is a non-linear cubic geometrical interaction term which originates in the very structure of the governing equations. It can be approximated in different ways, according to the dominant physical mechanisms at play: different approximations are used for strong turbulence, weak turbulence developing about a strong condensate and weak wave turbulence about a weak condensate.

The energy spectrum is obtained as $E(k) = \hat{n}(k)\omega(k)$, and the associated kinetic equation is

$$\frac{\partial}{\partial t}E(k) = \omega(k)St(k). \tag{6.151}$$

This equation plays the role of the Lin equation (4.38) for classical fluids described via the Navier–Stokes equations, in which the non-linear transfer term $T(k)$ is replaced by $\omega(k)St(k)$. It is important noting that the present equation exhibits no dissipative viscous term.

The global quantities are recovered as

$$\bar{N} = \int_0^{+\infty} \hat{n}(k)dk, \quad E_K = \int_0^{+\infty} \hat{n}(k)\omega(k)dk, \tag{6.152}$$

and their conservation in the absence of source/sink term lead to

$$\int_0^{+\infty} St(k)(k)dk = 0, \quad \int_0^{+\infty} St(k)\omega(k)dk = 0, \tag{6.153}$$

showing that there should exist cascade mechanisms associated to the globally conservative non-linear transfer terms. The first cascade is related to the particule number and is governed by $St(k)$. The second one is an energy cascade driven by $St(k)\omega(k)$.

These cascades are classically characterized by their associated fluxes:

$$\Pi_K(k) = \frac{\partial}{\partial t}\int_0^k St(p)\omega(p)dp, \quad \Pi_n(k) = \frac{\partial}{\partial t}\int_0^k St(p)dp \tag{6.154}$$

A fine analysis shows that, as for the classical Navier–Stokes turbulence, conservation of global invariants originates in local conservation properties. Considering a quartet of interacting waves with amplitudes A_i, wave vectors $\boldsymbol{k}_i$ and frequencies $\omega_i = \omega(k_i)$, one can show that quartic interactions conserve both energy and particule number, i.e.

$$|A_1|^2 + |A_2|^2 + |A_3|^2 + |A_4|^2 = const. = N \tag{6.155}$$

and

$$\omega_1|A_1|^2 + \omega_2|A_2|^2 + \omega_3|A_3|^2 + \omega_4|A_4|^2 + 2(A_1^*A_2^*A_3A_4 + A_1A_2A_3^*A_4^*) + N^2 \\ -\frac{1}{2}(|A_1|^4 + |A_2|^4 + |A_3|^4 + |A_4|^4) = const. \tag{6.156}$$

where it is recalled that $\overline{A_k A_p^*} = \hat{n}(k)\delta(\boldsymbol{k} - \boldsymbol{p})$.

6.4.3.2 Weak Wave Turbulence Solutions

Weak turbulence theory has been applied to the Gross–Pitaevskii equation to characterize some physical régimes governed by resonant interactions between small amplitude waves. The relevance of such solutions depends strongly on the properties of the dispersion relation and the nonlinear interaction term $T(k, k_1, k_2, k_3)$, since weak turbulence analysis holds when quadratic terms dominate over the quartic ones. As an example, the applicability of weak wave turbulence results depends also on the wave number: in the limit of vanishing k (very large scales), one has $T(k, k_1, k_2, k_3)/\omega(k) \to +\infty$ and a genuinely non linear model is required.

Weak-turbulence solutions are also expected to be valid over a limited time (in finite domain without extra source/sink term), since the inverse cascade of particule number yields an accumulation at very large scales that may trigger modulation instabilities of the condensate and the rise of collapsing filaments, whose structure is strongly non-linear. Nevertheless, if a damping term is added to prevent such an accumulation, weak turbulence solutions may hold over long times.

Generally speaking, most wave-turbulence results obtained for quantum turbulence have been derived in the absence of condensate, i.e. for a null mean state. The presence of a condensate does not prevent the weak wave turbulence to occur, but it modifies the results in a very deep way since one has to study fluctuations about a non-zero mean state. One of the main effects is the change in the dispersion relation from a four-wave relation to a three-wave resonant process of decay type.

As a general picture, weak-wave turbulence in the Gross–Pitaevskii equation is mostly concerned with the coexistence of resonant interactions between quartets of waves with nearly-gaussian statistics and a condensate field made of randomly occuring collapsing filaments.

A first way consists of applying the same dimensional-analysis-based approach as for classical turbulence to identify inertial ranges, which are defined as ranges of scales with constant cascade fluxes. A first solution is the Rayleigh–Jeans solution associated to thermodynamic equilibrium, i.e. zero fluxes of both particule number and energy:

$$\hat{n}(k) = \frac{T}{\mu + \omega(k)}, \tag{6.157}$$

where μ is the chemical potential and T the temperature.

The turbulent constant-Π_n and null energy flux Kolmogorov-like inertial range solution obtained via dimensional analysis is

$$\hat{n}(k) \sim |\Pi_n|^{1/3} \omega^{-1-\gamma/3}(k). \tag{6.158}$$

The second pseudo-Kolmogorov inertial range associated to a constant energy flux Π_K and zero particule number flux is

$$\hat{n}(k) \sim |\Pi_K|^{1/3} \omega^{-(4+\gamma)/3}(k), \tag{6.159}$$

where the parameter γ depends on the linear dispersion relation and features of $T(k, k_1, k_2, k_3)$. Analysis of quartic terms yields in 3D turbulence

$$\hat{n}(k) \sim \begin{cases} k^{-3} & (\Pi_K \neq 0, \Pi_n = 0) \\ k^{-7/3} & (\Pi_K = 0, \Pi_n \neq 0) \end{cases}. \tag{6.160}$$

A deeper analysis shows that, if excitations are injected at wave number k_0 in a wide-enough domain, a direct energy cascade (i.e. $\Pi_K > 0$) toward small scales

($k > k_0$) will take place, along with an inverse cascade of particule number (i.e. $\Pi_n < 0$) toward small scales ($k < k_0$).

In a bounded domain, the system is expected to converge toward the equilibrium solution over long time.

6.4.3.3 Results from Two-Point Two-Time Spectral Closure

Yoshida and Arimitsu (2013) analyzed the cascade phenomena thanks to a closed form of Eq. (6.2) written in Fourier space. The associated unknowns are now the 1D spectra $\Psi(k) = 4\pi k^2 \hat{n}(k)$ and $\Psi_n(k)$ which are such that

$$\bar{N} = \int_0^{+\infty} \Psi(k)dk, \quad E_K = \int_0^{+\infty} \frac{k^2}{2m}\Psi(k)dk, \quad E_I = \left(\int_0^{+\infty} \Psi_n(k)dk + \bar{N}^2\right). \tag{6.161}$$

The proposed closure is an extension of Kraichnan's Direct Interaction Approximation, whose details will not be discussed here for the sake of brevity. Thanks to this closure, inertial range solutions for the spectrum $\Psi(k)$ considering both energy cascade and particule-number cascade can be obtained, in a way similar to what is done for energy and helicity cascade in classical fluid isotropic turbulence. Introducing the energy flux $\Pi_K(k)$ and the particule-number flux $\Pi_n(k)$

$$\Pi_K(k) = \frac{\partial}{\partial t}\int_0^k \left(\frac{k^2}{2m}\Psi(p) + \frac{g}{2}\Psi_n(p)\right)dp, \quad \Pi_n(k) = \frac{\partial}{\partial t}\int_0^k \Psi(p)dp, \tag{6.162}$$

and assuming that they are constant, i.e. independent of the wave number k, within devoted inertial ranges, the two following inertial range solutions are obtained for the energy cascade

$$\Psi(k) \sim \begin{cases} \sqrt{2m}g^{-1/2}\Pi_K^{1/2}k^{-2} & k_0 \ll k \ll \min(k_*, k_1) \quad \text{(strong turbulence)} \\ g^{-2/3}\Pi_K^{1/3}k^{-1}\ln^{-1/3}\left(\frac{k}{\max(k_0,k_*)}\right) & \max(k_*, k_0) \ll k \ll k_1 \quad \text{(weak wave turbulence, type I)} \\ g^{-1}\bar{N}^{-1/2}\Pi_K^{1/2}k^{-1} & \max(k_*, k_0) \ll k \ll k_1 \quad \text{(weak wave turbulence, type II)} \end{cases} \tag{6.163}$$

where k^* is the wave number at which the characteristic time scale for linear effect, $\tau_L(k) \sim 2\,mk^{-2}$ is equal to the one of the non-linear terms, $\tau_{NL} \sim 1/g\bar{N}$, i.e. $k_* = \sqrt{2mg\bar{N}}$. For $k < k_*$ the dynamics will be dominated by non-linear effects, yielding a strong turbulence régime, while in the opposite linear effects are more important, leading to a weak wave turbulence dynamics. Here, k_0 and k_1 are the bounds of the inertial range region in which both production effects by external forcing and dissipative effects are negligible. Type I weak wave turbulence at small scales occurs if $\bar{N}$ is mostly associated to low wave numbers in the range $k_0 \ll k \ll \min(k_*, k_1)$ and type II to the opposite case in which small scales are the main contributors. Analytical developments show that $\Pi_K > 0$ at all scales, characterizing a direct energy cascade

towards small scales in both inertial ranges. For the particule-number cascade, one has

$$\Psi(k) \sim \begin{cases} g^{-1/2}|\Pi_n|^{1/2}k^{-1} & k_0 \ll k \ll \min(k_{*n}, k_1) \quad \text{(strong turbulence)} \\ (2m)^{-1/3}g^{-2/3}|\Pi_n|^{1/3}k^{-1/3} & \max(k_{*n}, k_0) \ll k \ll k_1 \quad \text{(weak wave turbulence)} \end{cases} \tag{6.164}$$

where the characteristic time of non-linear terms is $\tau_{NL,n} = (g\|\Pi_n\|)^{-1/2}$, yielding equality of linear and non linear effects at $k_{*n} = \sqrt{2m}(g\|\Pi_n|)^{1/4}$. Detailed analysis shows that $\Pi_n > 0$ in the strong turbulence inertial range while $\Pi_n < 0$ in the weak wave turbulence régime. This corresponds to the existence of a direct particule-number cascade at large scales and an inverse cascade at small scales governed by the weak wave turbulence régime.

The link with previous developments dealing with Kelvin wave weak turbulence is not straightforward, since Gross–Pitaevskii solutions are space-filling solutions that do not separate quantized vortex oscillations and induced near- and far-fields of acoustic and non-acoustic nature. But the important results are that: (i) a weak turbulence dynamics should occur at small scales while large ones exhibit a strong turbulence dynamics associated to a direct energy cascade and (ii) an inverse cascade associated to the second global conserved quantity is likely to occur at small scales.

6.4.3.4 Numerical Results and Conclusions

Several pseudo-Direct Numerical Simulations of Quantum Turbulence based on the Gross–Pitaevskii equations have been published in the recent past, including high-resolution 5760^3 simulations (Yepez et al. 2009). A typical view of instantaneous solution at several zoom level is displayed in Fig. 6.7. The existence of vortex loops and vortex rings at very small scale is observed, in agreement with theoretical statements. The organization of the flow in large-scale packets of small objects is also observed. This picture is reminiscent of the one found in classical isotropic Navier–Stokes turbulence, in which small-scale vortex tubes and vortex sheets organized in large-scale coherent clusters are detected (see Sect. 4.10).

Numerical simulations have allowed to see, on very simplified two-filament configurations, the emission phonons under the form of a rarefaction wave that can be approximated as an acoustic wave during vortex reconnection, proving that this mechanisms is at the heart of Quantum Turbulence dynamics. Another striking fact is the dispersion of results dealing with the slope of the energy spectrum $E(k)$.

First, it must be reminded that the total energy, which is constant in the absence of boundary condition of thermal noise, is the sum of several contributions, namely the kinetic energy, the potential energy, the interaction energy and the quantum energy (see Sect. 6.2.1). Since the Gross–Pitaevskii equation is related to a compressible equivalent Navier–Stokes-like equation, the kinetic energy (and other components too) can be split into a compressible and an incompressible component thanks to the Helmholtz decomposition discussed in Sect. 2.1.5. Only very few numerical results dealing with both components of the velocity fields are available, and such data escape

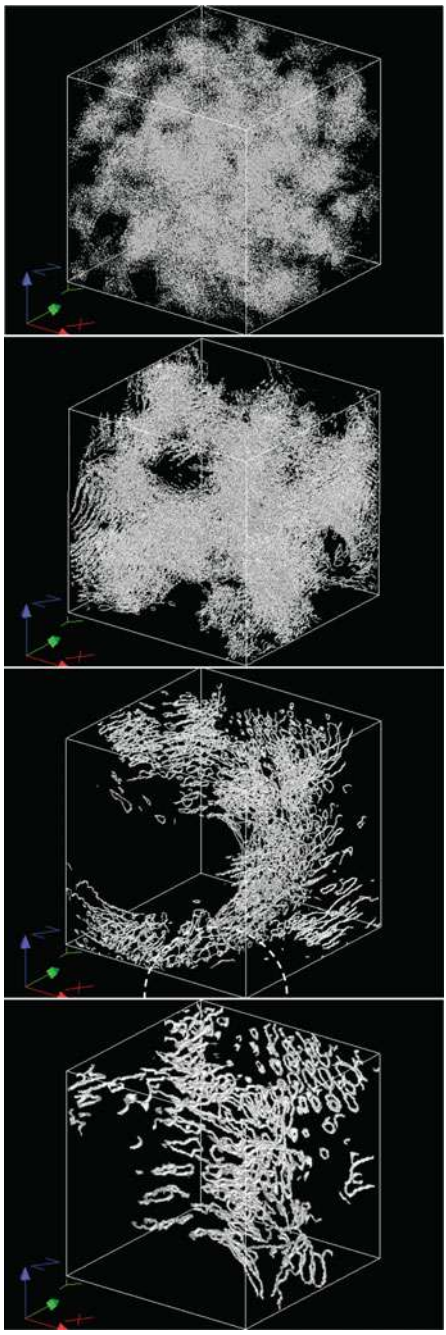

Fig. 6.7 Instantaneous view of DNS solution of the Gross–Pitaevskii equation at increasing zoom level. From Sasa and Machida (2011) with permission

direct measurements in Bose–Einstein condensates. Most related simulations deal with 2D quantum turbulence, and therefore characteristic features of 3D turbulence, which is the scope of the present book, remain to be investigated. Existing results show that the incompressible kinetic energy is converted into compressible one during the emission of acoustic waves, as in classical isotropic compressible turbulence. The existence of possible weak and strong equilibrium states between the solenoidal and the compressible components similar to those found in compressible Navier–Stokes quasi-isentropic turbulence (see Sect. 13.2.2) has not been investigated up to now. Such equilibrium states in Quantum Turbulence should exist, as they do in Quasi-Static MHD turbulence and viscoelastic turbulence. They should depend on the features of the forcing term in stationary turbulence or those of the initial condition in freely decaying turbulence.

The existence of an inertial range at small scales, i.e. scales smaller than the average inter vortex spacing ℓ, has been reported by several authors, but with a large dispersion on the slope value. In their pioneering low-resolution simulation, Nore et al. (1997) reported a trend toward $E(k) \propto k^{-1}$, while a -3 slope is observed in much more recent high resolution simulations by Tsubota et al. (2017) and by Yepez et al. (2009). Inertial-range-type solution is not observed in the simulation by Sasa et al. (Sasa et al. 2011; Sasa and Machida 2011), in which a more complex solution made of a $E(k) \propto k^2$ range followed by a $E(k) \propto k^0$ and then a rapidly decaying region is reported. The k^{-1} solution found in Biot–Savart-vortex filament simulation is not observed, showing the importance of the compressible dissipative effects on the solution at small scales. At present time, no definitive conclusion about the slope value can be drawn due to the very limited amount of available independent solutions, but it seems that the most probable solution is $E(k) \propto k^{-3}$.

Another very interesting result coming from DNS of the dynamics of vortex rings and vortex filaments (Berloff 2004) is that Kelvin wave generation can be triggered by the interaction between vortex lines and acoustic waves, and not only directly during vortex reconnection. This purely dilatational effect escapes simulations based on the Biot–Savart filament vortex approach, and represents a feedback of the acoustic field on the vorticity field whose effect in a full vortex tangle remains to be modeled and quantified.

6.4.4 Dynamics at Small Scales. IV: Dissipative Mechanisms and Vortex Heating

It has been seen in previous sections that dissipation at zero temperature is due to the emission of quasi-particules (phonons in ^{4}He, trapped quasi-particules in ^{3}He-B) during vortex reconnections or displacements and deformations of quantized vortices (Vinen 2000, 2001; Leadbeater et al. 2001, 2004; Ogawa et al. 2002; Berloff 2004; Kozik and Svistunov 2005b; Barenghi 2008; Hänninen 2013). The later mechanisms can be interpreted as a generalization of the vortex sound

phenomenon in classical fluids, and available theories predict that high frequency Kelvin-waves may yield a significant dissipation in ^{4}He at very low temperature. Quasi-particule emission due to large-amplitude large-scale deformations of vortex filaments is still to be analyzed theoretically and numerically, but there is no evidence that this phenomena is always negligible compared to other mechanisms. Therefore, one can theoretically distinguish between three dissipative mechanisms, namely the reconnection-induced decay, the large-scale vortex noise decay and the small scale vortex noise decay associated to Kelvin waves. According to many authors inspired by the Richardson energy cascade in classical fluid turbulence, the last dissipative mechanisms is mediated by the Kelvin-wave cascade, which is assumed to be the main way of transfer of energy from low-frequency Kelvin waves to high-frequency ones, low-frequency waves being generated by reconnections. This scenario is appealing because it mimics in some sense the classical turbulence dynamics, but it is worth noting that there is presently no available direct measurement or clear numerical evidence for it in realistic configurations.[7]

The respective part of each mechanisms in the total dissipation in realistic 3D isotropic realizations of Quantum Turbulence remains to be measured and analyzed theoretically. One can expect that the relative importance of each mechanisms will be case-dependent, with significant differences between Bose–Einstein condensates, ^{4}He and ^{3}He-B. Vinen (Vinen 2005; Vinen and Niemela 2002) emphasizes that in ^{3}He-B, due to the large radius of the quantized vortex,[8] high frequency Kelvin waves potentially responsible for dissipation by phonon emission can not be generated as in ^{4}He. As a consequence, this dissipative mechanisms can not exist, but it is replaced by another one, namely the damping of Kelvin waves (and other vortex deformations) by interaction between bound quasi-particules in the vortex core and Kelvin waves.

At higher temperature mutual friction induces a new direct dissipation mechanisms, but also indirectly modify the other dissipative mechanisms by influencing the vortex reconnection and Kelvin wave dynamics (Vinen 2005). A smoothing of the vortex filaments by mutual friction has been reported in vortex-filament-based simulations, which lead to a damping of Kelvin wave and a regularization of the kink induced by vortex reconnection. The later phenomena induces a decrease of the non-local generation of Kelvin waves.

A side-effect of emission of phonons is the increase of the temperature of the superfluid, a phenomenon referred to has *vortex heating* (Samuels and Barenghi 1998). Denoting $\Delta\mathcal{K}$ the amount of kinetic energy transformed into dilatational energy, the difference between the initial temperature T_{init} and the final one T_{final} can be computed by integrating the usual relation $dE = c_v dT$. For helium II below 0.6K, considering only the specific heat of phonons, i.e. taking

[7] As a matter of fact, most existing results dealing on Kelvin wave cascade have been obtained on very simplified configurations with one or very few vortex filaments.

[8] At low temperatures, the quantized vortex core radius is about 77 nm in ^{3}He-B, to be compared to 0.1 nm in ^{4}He.

$$c_v = \left(\frac{2\pi^5 k_B^4 V}{15\hbar a_s^3}\right) T^3, \tag{6.165}$$

where $a_s \sim 2.4 \times 10^2$ m/s, k_B and V denote the speed of first sound, the Boltzmann's constant and the volume of fluid under consideration, respectively, Samuels and Barenghi obtained

$$T_{final}^4 = T_{init}^4 + \frac{30\hbar^3 a^3}{\pi^5 k_B^4} \frac{\Delta \mathcal{K}}{V}. \tag{6.166}$$

A important remark is that vortex heating may result in a significant increase of the temperature and of related mutual friction effects, and then significant changes in Quantum Turbulence dynamics. A detailed analysis of the resulting temperature and velocity field in isotropic turbulence with frictional heating, similar to what has been done for classical fluids (see Sect. 13.3.4) remains to be done.

6.4.5 Coarse-Grained Dynamics. I: Generals

Preceding sections where devoted to small scale dynamics, i.e. to physical phenomena that occur at scales of the order or smaller than the inter-vortex spacing ℓ. It has been seen that small scale physics is dominated by quantized vortex dynamics, and has no counterpart in classical fluid turbulence. But it appears that in some configurations fluctuations at scales much larger than ℓ may occur, which may exhibit many features of classical isotropic turbulence, leading to the so-called *quasi-classical Kolmogorov régime*, see Sect. 6.4.6. In this state, large scale vortical eddies are detected along with a direct cascade of kinetic energy. But another large scale state has been identified, namely *Vinen's Ultra-Quantum turbulence* in which no large scale vortical eddies are present (see Sect. 6.4.7). The existence of these two states has been historically identified thanks to the fact that they are associated to significantly different decay rate of kinetic energy in freely decaying grid turbulence. This point is discussed in Sect. 6.5. Quasi-classical Kolmogorov and Vinen Ultra-Quantum states have been mostly addressed considering counterflowing superfluid helium (both experimentally and numerically, using either Biot–Savart-vortex-filament framework or two-fluid hydrodynamic models), but they have also been reported in numerical solutions of the Gross–Pitaevskii equation.

The existence of these large-scale régimes raises many presently unsolved issues. Among them, one should mention the role of the mutual friction term and the possibility for them to exist at zero temperature, the identification of the mechanisms responsible for the large-scale organization and dynamics, the role of external forcing and the quantized vortex nucleation process, the very nature of the large scale eddies …These issues are further discussed below.

6.4.6 *Coarse-Grained Dynamics. II: Quasi-classical Kolmorogov Turbulence*

In this régime, the energy spectrum at scales much larger than ℓ is observed to exhibit the classical Kolmogorov inertial range scaling, i.e. $E(k) \propto k^{-5/3}$. It has been reported in numerical solutions based on both Gross–Pitaevskii equation, e.g. Kobayashi and Tsubota (2005), Yepez et al. (2009), Sasa et al. (2011), Tsubota (2013), Tsubota et al. (2017), and Biot–Savart vortex filament models, e.g. Baggaley et al. (2012a, 2014), see Figs. 6.8 and 6.12. It has also been reported in numerical simulations based on the two-fluid model, e.g. Roche et al. (2009), Tchoufag and Sagaut (2010). It is worth noting that in Gross–Pitaevskii simulations, this result is obtained looking at the kinetic energy of the solenoidal part of the velocity field only. This robustness indicates that this large-scale organization is not very sensitive to details of small scale physics and dissipation. But such a spectrum has not been directly measured in experiments, even in Bose–Einstein condensates which allow very interesting direct measurements of density fluctuations. As a matter of fact, it is only indirectly inferred in experiments from data dealing with energy decay in superfluid helium. It is worth noting that the classical turbulence in Newtonian fluids is also observed to exhibit some degree of independence to details of the dissipative mechanisms, as proved by numerical experiments based on hyperviscosity (see Sect. 4.12.4) and by large-eddy simulation results (Sagaut 2005), in which the physical Navier–Stokes dissipative term is replaced or supplemented by a dramatically different nonlinear term. In these simulations, the classical $E(k) \propto k^{-5/3}$ is recovered if both the Reynolds number and the grid resolution are large enough.

Large vortical eddies are observed, whose nature and dynamics are not fully understood. The commonly adopted model for them relies on the concept of large scale bundles of quantized vortex filaments, whose non-zero large-scale vorticity comes from the total or partial polarization of the vortex lines inside the bundle. The intensity of the vorticity can also be a function of the number threads/vortex filaments trapped in the bundle. This schematic picture is a cornerstone of many theoretical developments, but it is worth noting that bundles have never been directly observed in experiments. It can be seen as a kind of extrapolation of what is observed in laminar superfluid helium flow subjected to solid body rotation. In this case, quantized vortices are organized as parallel, polarized vortex lines. First clear views of large-scale organization of isotropic Quantum Turbulence have been obtained only very recently thanks to high-resolution numerical simulations of the Gross–Pitaevskii equation. But there are only very few of them, precluding definitive conclusions. These results are illustrated in Fig. 6.7. It is seen small scales are mostly made of loops and rings, which are clustered in large scale pockets. At the maximum zoom level, a tendency of the rings and loops to be organized in a coherent way is seen. More precisely, vortex loops/rings tend to be located in parallel planes, opening the possibility for the generation of a coherent motion at larger scales. Therefore, a more realistic picture might be to define quantized vortex bundles as clusters of (partially)

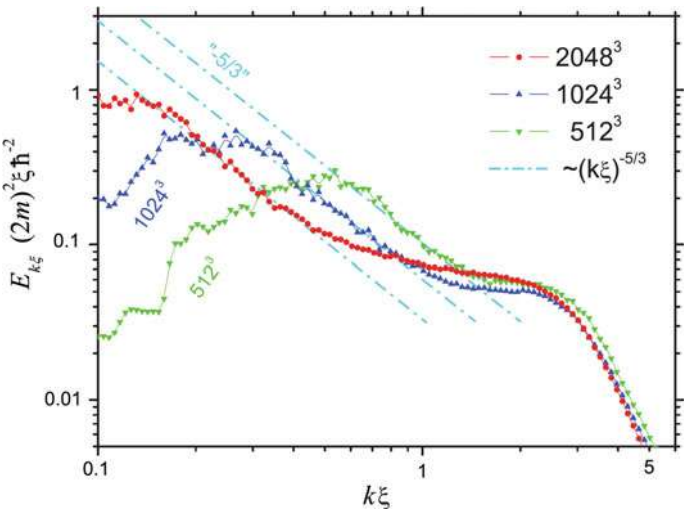

Fig. 6.8 Kinetic energy spectrum of the solenoidal velocity field $E(k)$ computed using the Gross–Pitaevskii equation at different grid resolutions. From Sasa et al. (2011) with permission

coherently distributed quantized vortex loops/rings. This qualitative model shares some features with large-eddies in classical turbulence, which appear as clusters of small-scale worm-like elongated vortex tubes, as seen in Fig. 4.26.

How such large-scale coherent packets can be generated in superfluids with quantized vortices and how they can sustain a Richardson-like cascade are still open problems. At this point, it is worth noting that a direct cascade of kinetic energy toward small scales (but still larger than ℓ) has been repeatedly reported in numerical simulations, and therefore such a mechanisms should be at play in the quasi-classical turbulent régime. It has been seen in Sects. 4.11.2 and 4.11.3 that key features of isotropic turbulence dynamics in classical fluids in physical space are (i) the production of enstrophy by the interaction of vorticity with the strain field and (ii) the self-amplification of strain by vortex compression. Another important finding is that small-scale vortex tube dynamics, including the effects of vortex stretching on them, is not a key element in the kinetic energy cascade in Newtonian fluid turbulence. Therefore, there is a possibility that classical turbulence and Quantum Turbulence, while exhibiting very different dynamics at the smallest scales, may have similar dynamics at scales much larger than ℓ. Nevertheless, two key questions remain to be answered: (i) how a local velocity gradient can induce changes in the organization of quantized vortices inside a bundle and (ii) how the rate of reconnection inside a bundle is modified by a local shear. This first question may be (at least partially) answered looking at kinematics of frozen vortex rings subjected to an homogeneous shear. An expected result is that vortex rings with the same polarization will have the same equilibrium orientation, giving a possible explanation for the local coherence in flow regions with locally homogeneous of slowly-varying shear.

The pseudo-Kolmogorov inertial range is not limited by viscous effects as in classical fluids at zero temperature, but it may develop only at scales that are not affected by typical quantum effects such as reconnection. Therefore, an empirical estimate for the high-wavenumber cutoff is $k_c \sim 2\pi/\ell$. Skbrek et al. (2001) introduced another cutoff length scale, by analogy of the definition of the Kolmogorov scale in classical turbulence. Using dimensional analysis, they define the *characteristic quantum wave number* $k_Q = (\varepsilon/\kappa^3)^{1/4}$ and the associated *quantum length scale* $\ell_Q = 2\pi/k_Q$. Here, ε is the rate of transfer of kinetic energy mediated by the kinetic energy cascade, and it is assumed to be constant across the inertial range, as in classical turbulence. Duplicating the classical Kolmogorov-like dimensional analysis for the energy spectrum, one finds

$$E(k) = C\varepsilon^{2/3}k^{-5/3}\varphi(k_Q^4 k^{-4}), \tag{6.167}$$

where φ is the dimensionless shape function at small hydrodynamic scales. They propose $\varphi(x) = x^\alpha$, where $\alpha = 1/3$ to optimize the fit with some experimental data dealing with the energy decay rate. Therefore, one has $E(k) = C\varepsilon\kappa^{-1}k^{-3}$ for small hydrodynamic scales such that $k_Q \ll k \ll \ell^{-1}$.

At very low but non-zero temperature, the existence of a normal fluid component yields a more complex dynamical picture, because of mutual friction effects. In the case of dominant mutual friction effects, the two-fluid macroscopic dynamical system simplifies as

$$\frac{\partial \boldsymbol{u}_s}{\partial t} \simeq -\frac{\gamma_0 \ell}{\rho_s}(\boldsymbol{u}_s - \boldsymbol{u}_n), \quad \frac{\partial \boldsymbol{u}_n}{\partial t} \simeq -\frac{\gamma_0 \ell}{\rho_n}(\boldsymbol{u}_n - \boldsymbol{u}_s) \tag{6.168}$$

leading to

$$\frac{\partial}{\partial t}(\boldsymbol{u}_s - \boldsymbol{u}_n) \simeq -\frac{1}{\tau_\gamma}(\boldsymbol{u}_s - \boldsymbol{u}_n), \quad \tau_\gamma = \frac{\rho_n}{\alpha\rho\kappa\ell}, \tag{6.169}$$

showing that the two velocity fields will be locked by the mutual friction. Therefore, if a classical turbulence is induced on the normal fluid at large scales by external mechanical forcing or initial conditions, the enslaved superfluid component will exhibit similar features. This analysis can be refined reminding that the eddy turnover time at wave number k can be estimated as $\tau(k) = (ku(k))^{-1}$, where $u(k) \sim \sqrt{kE(k)}$ is the characteristic velocity at this scale and $E(k)$ the energy spectrum. Therefore, the two fields will be locked at wave number k is the following condition is satisfied:

$$\frac{\tau_\gamma}{\tau(k)} = \frac{\rho_n k u(k)}{\alpha\rho\kappa\ell} \ll 1. \tag{6.170}$$

Now assuming that $E(k) = K_0\varepsilon^{2/3}k^{-5/3}$, one has $u(k) \sim \sqrt{K_0}\varepsilon^{1/3}k^{-1/3}$ and the criterion becomes

$$\frac{\tau_\gamma}{\tau(k)} = \frac{\rho_n\sqrt{K_0}\varepsilon^{1/3}k^{2/3}}{\alpha\rho\kappa\ell} \ll 1. \tag{6.171}$$

Looking at experimental values for ℓ, α and κ, it is seen than lock-on may occur at almost all large scales in realistic superfluid helium flows. A quasi-perfect lock-on over a wide range of scales is observed in two-fluid-based numerical simulations (Roche et al. 2009; Tchoufag and Sagaut 2010). This analysis can be refined to evaluate the possibility of the existence of a viscous cutoff due to the normal fluid viscosity on the superfluid kinetic energy cascade because of the mutual-friction-induced lock-on. To this end, Vinen and Niemela assumed that the Kolmogorov spectrum matches "smoothly" the one derived considering the vortex filament model at scales of the order of the inter vortex spacing ℓ. Assuming that at such scales the flow is made of a random tangle of quantized vortex lines, one has

$$u^2(\ell^{-1}) = \frac{\beta\kappa^2}{\ell^2} \tag{6.172}$$

where the parameter β depends on details of the tangle topology. Equalizing the two expressions for the fluid velocity at scale ℓ, one finds the following expression for the kinetic energy cascade rate:

$$\varepsilon = \left(\frac{\beta}{K_0}\right)^{3/2} \kappa^3 \ell^{-4} = \left(\frac{\beta}{K_0}\right)^{3/2} \kappa^3 L_0^2 \tag{6.173}$$

where L_0 denotes the length of vortex line per unit volume. Using this estimate for ε, the velocity within the inertial range can be expressed as

$$u^2(k) = \beta \left(\frac{\kappa^2}{\ell^2}\right) (k\ell)^{-2/3} \tag{6.174}$$

and criterion (6.171) becomes

$$\frac{\tau_\gamma}{\tau(k)} = \frac{\rho_n \beta^{1/2}}{\alpha\rho} (k\ell)^{2/3} \ll 1, \tag{6.175}$$

which is satisfied at large scales such that $k\ell \ll 1$. Viscous effects can be taken into account introducing the following viscous time scale, which has two different values depending the fact that normal and superfluid components are fully coupled or fully decoupled

$$\tau_\nu(k) = \left(\nu_\star k^2\right)^{-1}, \quad \nu_\star = \begin{cases} \mu_n/\rho_n & \text{(fully decoupled case)} \\ \mu_n/\rho & \text{(fully coupled case)} \end{cases} \tag{6.176}$$

where μ_n is the normal fluid viscosity. Viscous effects will significantly damp velocity fluctuations if

$$\frac{\tau_\nu(k)}{\tau(k)} < 1 \iff \frac{\beta^{1/2}\kappa}{\nu_\star} (k\ell)^{-4/3} < 1. \tag{6.177}$$

Looking at physical values of the parameters in ^{4}He, these expressions show that dissipation is always negligible in the range $k\ell < 1$ at temperatures above 1 K, but that it becomes important for smaller scales such that $k\ell \geq 1$. As a consequence, at least in ^{4}He, the pseudo-Kolmogorov inertial range may develop down to scales of the order of ℓ. In ^{3}He-B the normal fluid viscosity is much higher, and viscous damping effects may preclude the occurence of a Kolmogorov-like inertial range in the normal fluid component, and consequently also in the superfluid component. Only very few experimental realizations of turbulence in ^{3}He-B have been reported up to now, but one can extrapolate the preceding reasoning defining a viscous cutoff length scale for the normal fluid, l_ν, which will be of the order of the Kolmogorov scale $\eta = (\nu_n^3/\varepsilon)^{1/4}$ if it is turbulent (Vinen 2005). In the case $l_\nu \geq \ell$, the inertial range, if any, may develop down to scales of the order of l_ν.

The question of the shape of the energy spectrum at hydrodynamic scales smaller than the cut-off scale of the $-5/3$ inertial range has been the matter of several controversies, and is still an open issue. Considering the two-fluid model, one can see that this is a two-field problem with two-way couplings, that shares some features with the problem of classical isotropic turbulence coupled to an active scalar field. Neglecting the feedback of superfluid velocity on the normal component to get a one-way coupling mode (e.g. L'vov et al. 2004), a weak analogy with possible states exhibited by a passive scalar field depending of the Prandtl number and the production mechanisms (e.g. Briard et al. 2015; Briard and Gomez 2015) indicates that a systematic analysis would reveal a significant number of possible turbulent states for both normal and superfluid components, parametrized by the temperature. The hypothetical ranges that may exist could therefore be understood as some kind of extensions of the inertio-convective, inertio-conductive and inertio-balanced ranges found in the passive scalar case. Accounting for the two-way coupling increases the number of possible states.

Several theories have been proposed, based on different physical assumptions and tools. The emphasis is put here on the approach proposed in L'vov et al. (2004, 2006), Vinen (2005), Skbrek (2006), and other authors, which is the most popular one. It relies on Lin-type equations for both superfluid and normal kinetic energy spectra, denoted $E_s(k)$ and $E_n(k)$, respectively:

$$\frac{\partial E_n(k,t)}{\partial t} - T_n(k,t) = \hat{F}_{s\to n}(k,t) \tag{6.178}$$

$$\frac{\partial E_s(k,t)}{\partial t} + \nu_n k^2 E_s(k,t) - T_s(k,t) = \hat{F}_{n\to s}(k,t) \tag{6.179}$$

where T_s, T_n, $\hat{F}_{n\to s}$ and $\hat{F}_{n\to s}$ are related to the nonlinear inertial transfer terms for the superfluid and the normal component, and to the spectrum of the mutual friction terms, respectively. Different states are then identified searching for steady solutions of the set of coupled equations via fixed-point methods or analytical integration. The system is closed using a differential model for the non-linear transfer terms T_s and

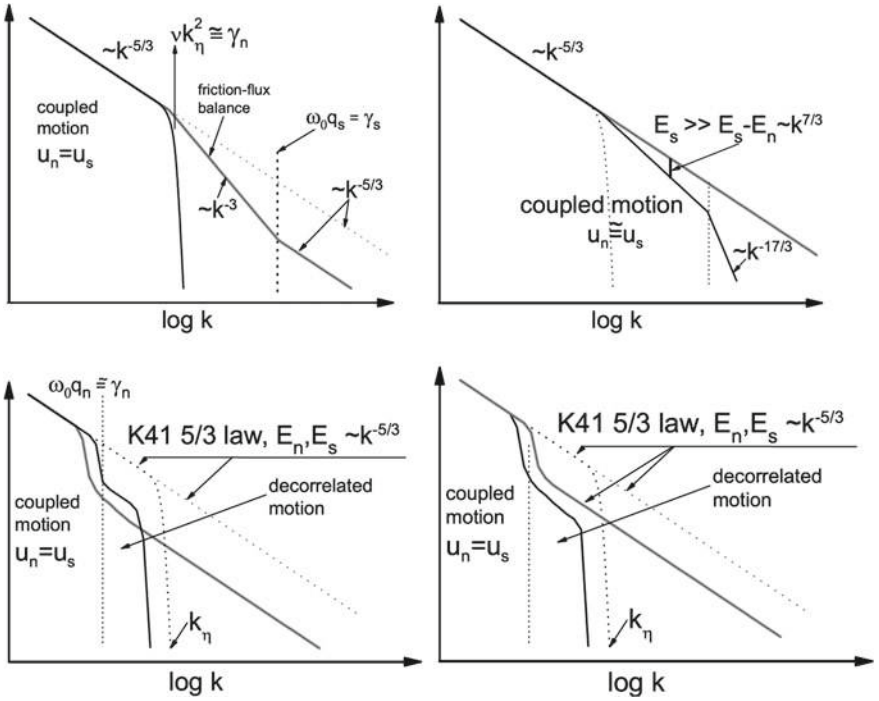

Fig. 6.9 Schematic view of incompressible kinetic energy spectra of the normal fluid component ($E_n(k)$, solid black line) and the superfluid component ($E_n(k)$, solid grey line) corresponding to four possible asymptotic states at hydrodynamic scales. Dotted lines are related to Kolmogorov spectra obtained when mutual friction effects are removed. Top: large mutual friction effects; Bottom: low mutual friction effects; Left: large normal fluid density ρ_n; Right: small normal fluid density ρ_n. From L'vov et al. (2006) with permission

T_n (Kovasznay or Leith models in practice, see Sect. 4.7.1), and an ad hoc model for the mutual friction terms (see L'vov et al. 2006; Vinen 2005 for details).

Depending on the amplitude of the normal fluid density ρ_s and the intensity of the mutual friction, at least four possible states have been suggested in L'vov et al. (2006), which are illustrated in Fig. 6.9. New possible spectral ranges with slopes equal to -3 and $-17/3$ are predicted. These results have been confirmed solving dynamical equations for $E_s(k)$ and $E_n(k)$ using an EDQNM closure for T_s and T_n in place of differential models (Tchoufag and Sagaut 2010). This agreement demonstrates the robustness of the prediction versus the locality of the energy transfer responsible for the pseudo-Richardson energy cascade at hydrodynamic scales. But since the same model for the mutual friction was used, one cannot draw definitive conclusions about the existence of the four solutions displayed in Fig. 6.9. Another point is that these states must be considered as asymptotic solutions, which would only be observable when clear scale separation between the different cutoff length scales occurs, something that may be out of reach of realistic experimental configurations.

The preceding analyses were restricted to hydrodynamic scales that can be represented by the two-fluid models, i.e. scales much larger than the inter vortex distance ℓ. Some proposals have been made to extend them to investigate the *cross-over region*, in which the hydrodynamic solution is expected to match smoothly the one dominated by typical mechanisms related to quantized vortices, namely reconnections, quasi-particule radiation and Kelvin wave dynamics (L'vov et al. 2007, 2008; Kozik and Svistunov 2008a). In this spectral region, the energy flux is assumed to be transferred from the large-scale hydrodynamic motion to quantum mechanisms. A key assumption shared by the existing approaches is the continuity of the flux across scales during this transition. Two main theories have been proposed, which lead to different results.

The first one relies on an extension of the model discussed above to scales smaller than ℓ. A new Lin-type equation is proposed to compute the energy spectrum of Kelvin waves E_{KW} at non-hydrodynamic scales and a coupling term between E_n, E_s and E_{KW}, e.g. Boffetta et al. (2009), L'vov et al. (2006, 2007, 2008) is added to account for the energy transfer between hydrodynamic and non-hydrodynamic scales. Ad hoc local differential models are used to close the equation for E_{KW}, modeling several physical mechanisms, namely the Kelvin-wave cascade, the loss of energy by phonon emission, the production by vortex reconnection and the damping of Kelvin wave by mutual friction at high temperature. Results are then obtained seeking for fixed-point solutions or numerical solutions of the set of coupled equations. Among the main outputs of these models, one must mention the existence of a possible bottleneck in the energy spectrum in the cross-over range, as illustrated in Fig. 6.10 which displays the total energy spectrum $E_s(k) + E_{KW}(k)$ (where E_{KW} is here to be understood as the kinetic energy spectrum induced by the 1D Kelvin-wave spectrum, see Sect. 6.4.2.3). The predicted bottlneck is characterized by a k^2 range, which is interpreted as a range of thermalized scales in which the energy transferred from large scales pile-up. A fairly good comparison with numerical solution of the Gross-Pitaesvkii equation is obtained, tuning the parameter $\Lambda = \log(\ell/r_c)$ to 2, while physical values are within the range 12–15 in superfluid helium. Here, it is important to note that this comparison is the unique available piece of validation for the model. But it should be kept in mind that the model was originally developed for superfluid helium turbulence, in which the crossover region and Kelvin wave cascade are likely to exist. The comparison with Gross–Pitaevskii solution should therefore be considered with care, since this equation is not adequate for superfluid helium. The decrease of Λ from 12–15 to 2 is coherent with the fact that this quantized vortices have a much larger radius r_c in atomic Bose–Einstein condensates than in superfluid helium. This is also coherent with the absence of k^2 region in the numerical results. Consequently, more results are certainly needed to assess this crossover model, especially in the case of superfluid helium.[9]

[9] As quoted by Nemirovskii (2013), it is also important to note that the idea underlying the pile-up of kinetic energy at scales about the inter-vortex distance ℓ is that the Kelvin wave energy at such scales is much smaller than the one given by the Kolmogorov spectrum, leading to a mismatch between the two spectra and the associated cascade rate. This corresponds to the flawed equality

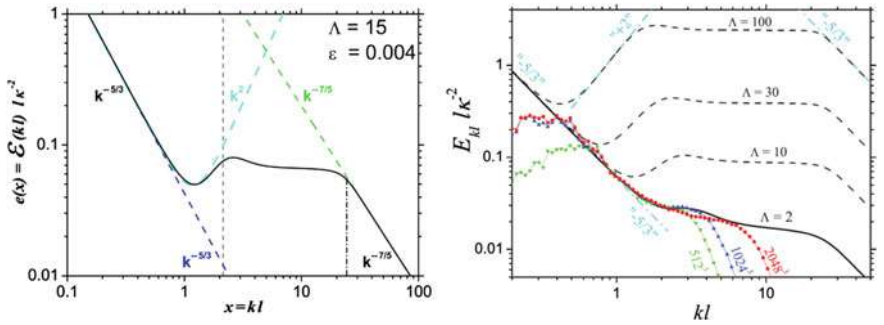

Fig. 6.10 Total kinetic energy spectrum in the cross-over region predicted by the L'vov–Nazarenko–Rudenko model. Left: schematic view (from L'vov et al. 2008 with permission); Right: comparison with large-scale simulation of the Gross–Pitaevskii equation at different grid resolutions (from Sasa et al. 2011 with permission)

The second approach developed in Kozik and Svistunov (2008a, b, 2009) relies on the detailed analysis of the different dynamical ranges of scales associated to reconnection of bundles and quantized vortices discussed in Sect. 6.4.1.3. This model predicts the existence of several ranges with associated slopes but without bottleneck. It is illustrated in Fig. 6.11, which displays the schematic spectrum of Kelvin wave amplitude, along with comparison with experimental data obtained in superfluid helium (taking $\Lambda = 13$) for the evolution of associated vortex line density versus the temperature-dependent mutual friction parameter $\alpha(T)$. A very good agreement with experimental data is observed, but it should be borne in mind that the model exhibits 7 tunable parameters, and that the comparison deals with the vortex line density, leading to an indirect validation only.

A few additional comments should be made to close this section:

- The existence of vortex bundles, as defined or described in most existing theories for Quantum Turbulence, is still to be assessed by experiments. Only very few numerical data show a trend to a large-scale organization of quantized vortices. There is also no theoretical rigorous proof that such objects can be generated, and their dynamics remains almost unknown.
- Bridging between kinematics and dynamics at scales larger than ℓ is still unclear. More precisely, physical mechanisms that govern kinetic energy cascade at these scales in Quantum Turbulence have not been investigated with the same completness and accuracy as in classical Newtonian fluid turbulence.
- Most existing theoretical developments presented above that deal with the quasi-Kolmogorov inertial range are based on heuristics and dimensional analysis, not on a detailed analysis of either Gross–Pitaevskii or two-fluid model equations, and it must be kept in mind that such small scales escape direct measurements

$E(k) = E_{KW}(k)$, as discussed in Sect. 6.4.2.3. As a matter of fact, if the correct kinetic energy, i.e. the one of the velocity fluctuations induced by quantized vortices and Kelvin waves is taken into account, the mismatch and the need for a bottlneck disappear.

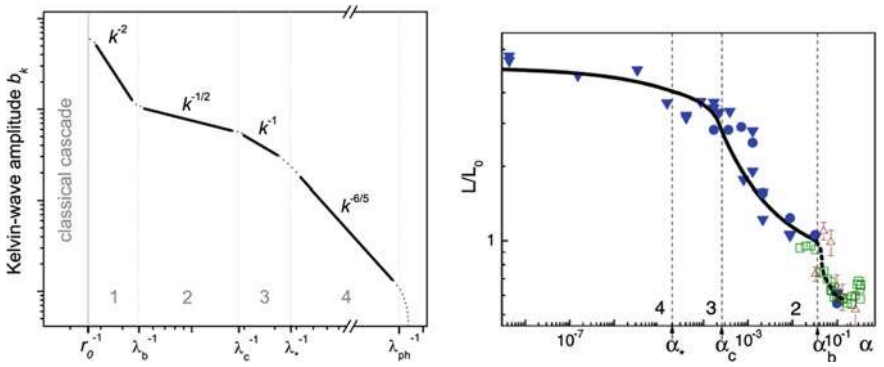

Fig. 6.11 Model for the cross-over region predicted by the Kozick and Svistunov. Left: schematic view of the Kelvin wave spectrum (from Kozik and Svistunov 2009 with permission). The different ranges are discussed in Sect. 6.4.1.3; Right: comparison of the associated normalized vortex line density (solide line) versus the temperature-dependent mutual friction parameter $\alpha(T)$ with experimental data (symbols) (from Kozik and Svistunov 2008b with permission)

in experiments. Existing theories dealing with spectrum shape at small scales at the edge of the inertial range are mostly speculative and exhibit a wide dispersion of results, and have received almost no assessment from experiments or direct simulations. Therefore, it is almost impossible to draw conclusions on that issue at present time.

- Most attention was paid to the solenoidal velocity field when analyzing solutions of the Gross–Pitaevskii equation. Therefore, the structure of the dilatational part of the solution, along with those of the density and the pressure fields, remain to be analyzed. Possible similarities with results found in compressible isotropic turbulence, especially in the quasi-isentropic régime (see Sect. 13.2) have not been investigated up to now.

6.4.7 Coarse-Grained Dynamics. III: Vinen's Ultra-Quantum Turbulence

A second state, referred to as Ultra-Quantum turbulence, has been reported in several experiments performed in superfluid Helium. It is characterized by a different kinetic energy decay rate when compared to the quasi-Kolmogorov régime. There is no direct experimental investigation of the topology of large scales in this régime, but the most commonly admitted picture is that it is characterized by the absence of vortical energetic eddies at scales larger than the intervortex distance ℓ. This picture is supported by numerical results obtained using the Biot–Savart filament vortex model (Baggaley et al. 2012a, b), which exhibit decay régimes very close to experimental data in both classical and ultra-quantum turbulence. The difference is illustrated

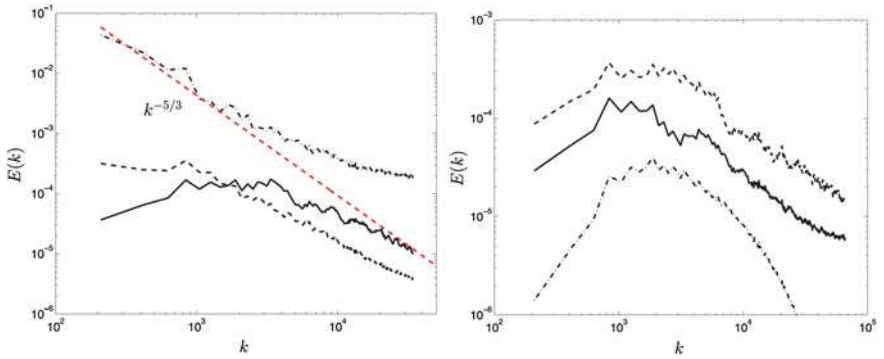

Fig. 6.12 Kinetic energy spectrum $E(k)$ at different times in Biot–Savart vortex filament model simulations. Left: classical quasi-Kolmogorov state; Right: Vinen's ultra-quantum state. From Baggaley et al. 2012a with permission of APS

in Fig. 6.12, which displays the kinetic energy spectrum $E(k)$ at different times. The difference at wave numbers $k\ell > 1$ clearly shows the absence of energetic hydrodynamic vortical eddies in the ultra-quantum régime.

Numerical experiments show that the ultra-quantum régime is obtained if the kinetic energy injection (i) has a moderate intensity and duration and (ii) occurs at scales larger but not very large compared to ℓ. In these conditions, the kinetic energy cascade cannot build-up with enough efficiency to give rise to a Kolmogorov-like inertial range, preventing the occurence of the quasi-classical régime.

A qualitative rationale for the possibility of the existence of the two régimes mentioned above has been suggested by Volovik (2003, 2004) on the grounds of dimensional analysis, considering the case of isotropic turbulence in a counterflow with uniform normal velocity U in a channel with characteristic diameter D. Starting from the macroscopic equation for the superfluid velocity issued from two-fluid models and writing it in the reference frame moving with the normal fluid counterflow, i.e. taking $\boldsymbol{u}_n = 0$ in Eq. (6.64), one obtains the following equation for the macroscopic superfluid velocity $\boldsymbol{u}_s$

$$\frac{\partial \boldsymbol{u}_s}{\partial \tilde{t}} + \nabla \tilde{\mu} = \boldsymbol{u}_s \times \boldsymbol{\omega} + q \frac{\boldsymbol{\omega}}{\|\boldsymbol{\omega}\|} \times (\boldsymbol{\omega} \times \boldsymbol{u}_s) \tag{6.180}$$

where $\boldsymbol{\omega} = \nabla \times \boldsymbol{u}_s$ is the vorticity of the coarse-grain superfluid velocity. The dimensionless temperature-dependent parameter q is defined as

$$q = \frac{\alpha}{1 - \alpha'} \tag{6.181}$$

and where $\tilde{t} = (1 - \alpha')t$ is a renormalized time unit. Expressions and physical meaning of coefficients α and α' are given in Sect. 6.6. This equation is to be compared to the classical momentum equation for a Newtonian incompressible fluid:

$$\frac{\partial \boldsymbol{u}}{\partial t} + \nabla \mu = \boldsymbol{u} \times \boldsymbol{\omega} + \nu \nabla^2 \boldsymbol{u}. \tag{6.182}$$

It is seen that $1/q$ is a measure of the ratio of inertial to coupling effects, and plays the role of a kind of Reynolds number since it tunes the dissipation rate of the superfluid kinetic energy $\mathcal{K}_s$, ε_s:

$$\varepsilon_s = -\overline{\left(\boldsymbol{u}_s \cdot \frac{\partial \boldsymbol{u}_s}{\partial \tilde{t}}\right)} = -q\overline{\left[\boldsymbol{u}_s \cdot \left(\frac{\boldsymbol{\omega}}{\|\boldsymbol{\omega}\|} \times (\boldsymbol{\omega} \times \boldsymbol{u}_s)\right)\right]}. \tag{6.183}$$

The amplitude of the dissipation can be roughly estimated as

$$\varepsilon_s \simeq q\omega U_s^2, \tag{6.184}$$

where U_s is related to the mean value of the large-scale superfluid velocity. It is taken equal to the velocity difference $|\boldsymbol{u}_{ns}|$ in the case of counterflowing superfluid helium turbulence. One can see that turbulence may occur at large scales iff $q \ll 1$, i.e. if the dissipation induced by mutual friction is small enough to allow for an energy cascade to take place. Another condition is that the quantum Reynolds number $Re_s = UD/\kappa$ is very large, which is a necessary condition for the two-fluid model to hold.

Let us first consider the quasi-classical régime. The inertial range with $E(k) \propto \varepsilon^{2/3}k^{-5/3}$ is assumed to range from $k_D \sim 1/D$ to $k_c \sim 1/l_c$. The energy flux ε is assumed to be constant across the scales within this range. Using classical dimensional analysis, local velocity and vorticity are given by $u(r) \sim \varepsilon^{1/3}r^{1/3}$ and $\omega(r) = u(r)/r \sim \varepsilon^{1/3}r^{-2/3}$. Now assuming that the energy flux is continuous at the cutoff scale l_c, one obtains

$$\varepsilon \sim q\omega(l_c)U_s^2 \sim qU_s^2 u(l_c)/l_c = qU_s^2\varepsilon^{1/3}r^{-2/3} = U_s^3/D, \tag{6.185}$$

from which one can deduce the following scaling laws:

$$l_c \sim q^{3/2}D, \quad u(l_c) \sim q^{1/2}U_s, \tag{6.186}$$

which are valid if $\ell \ll l_c < D$ and $u(l_c) < U_s$. It is important noting that there is one important underlying hypothesis in the above developments: the circulation is assumed to be the one of turbulent large eddies, so that it must be much larger than the one of a quantized vortex, leading to $u(l_c)l_c \ll \kappa$. Since $u(l_c)l_c = q^2U_sD = q^2\kappa Re_s$, this last condition yields the following criterion for the existence of the quasi-classical régime:

$$Re_s > q^{-2} \gg 1. \tag{6.187}$$

The utra-quantum state is therefore obtained in the case

$$q^{-2} > Re_s \gg 1. \tag{6.188}$$

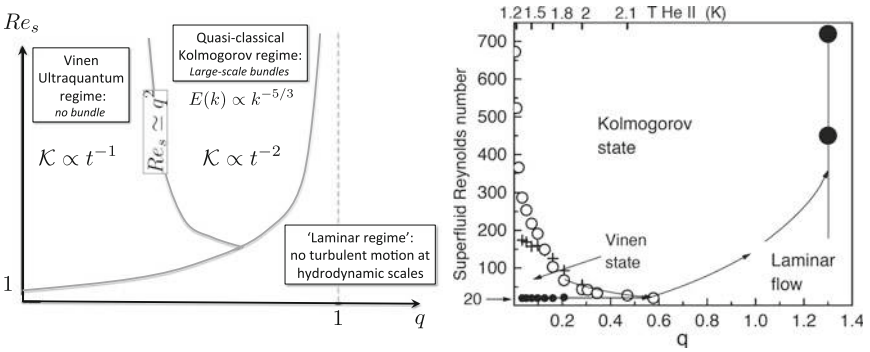

Fig. 6.13 Phase diagram for quasi-classical and ultra-quantum turbulence as suggested by Volovik. Left: schematic phase diagram (adapted from Volovik 2003); Right: compilation of experimental data (from Skbrek 2004 with permission)

In this state, the characteristic circulation is $\kappa = \hbar/m$, where m is the mass of the particule associated to the superfluid. Dimensional analysis yields also different expressions for the vortex line density per unit volume, L_0:

$$L_0 \propto \begin{cases} \dfrac{u(l_c)}{\kappa l_c} \simeq \dfrac{U_s}{q\kappa D} = \dfrac{1}{D^2}\dfrac{Re_s}{q^2} & \text{(Quasi-classical Kolmogorov regime)} \\ \ell^{-2} \sim \lambda^2 \dfrac{U_s^2}{\kappa^2} = Re_s^2 \dfrac{\lambda^2}{D^2} & \text{(Ultra-Quantum regime)} \end{cases}, \tag{6.189}$$

where λ is the dimensionless parameter such that $\ell = \lambda\kappa/U_s$. The corresponding phase diagram proposed by Volovik is shown in Fig. 6.13.

6.5 The Decay of Isotropic Quantum Turbulence

6.5.1 Quasi-classical and Ultra-Quantum Decay Régimes

The decay of grid turbulence in superfluid is among the leading topic in the field of superfluid turbulence theory, and a striking difference with the dual topic in classical fluids is that only very few accurate quantitative experiments have been carried out, e.g. Gao et al. (2016), the first one dealing grid turbulence in ^{4}He having been carried out in 2007. It should be borne in mind, reading the section below, that the main available data deal with decay of kinetic energy, which is most often interpreted as the evolution of the total quantized vortex length $\mathcal{L}$ and the corresponding vortex line density L_0. The main result is that two decay régimes have been identified, which are assumed to be tied to two different flow dynamics. It is further hypothesized that they are tied to the two different hydrodynamic scale topologies discussed in

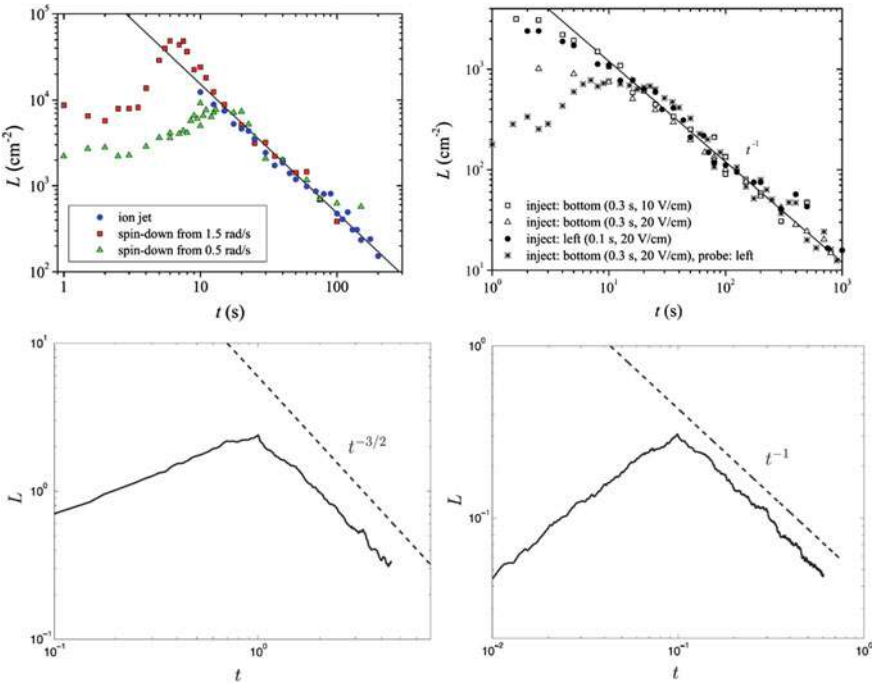

Fig. 6.14 Decay of vortex line density L_0 for quasi-classical (left) and ultra-quantum (right) turbulence. Top: experimental data obtained in ^{4}He (from Walmsley and Golov 2008; Golov and Walmsley 2009 with permission of APS). Bottom: numerical results computed using the Biot–Savart vortex filament model (from Baggaley et al. 2012a with permission of APS)

Sects. 6.4.6 and 6.4.7. In the first one, referred to as the quasi-classical Kolmogorov régime, the commonly reported decay law is $\mathcal{K}(t) \propto t^{-2}$ and $L_0(t) \propto t^{-3/2}$. In the second one, namely the Vinen ultra-quantum state, one observes $\mathcal{K}(t) \propto t^{-1}$ and $L_0(t) \propto t^{-1}$. These results have been obtained in both superfluid helium experiments and numerical simulations based on the Biot–Savart vortex filament method, see Fig. 6.14.

The existence of these two decay rates can be handled in a heurisitc way. The starting point is the evolution equation for the turbulent kinetic energy in isotropic turbulence without forcing:

$$\frac{d\mathcal{K}}{dt} = -\varepsilon \tag{6.190}$$

where the dissipation rate ε gathers all existing dissipative mechanisms (mutual friction, emission of phonons, …) that occur at all scales. By analogy with turbulence in classical fluids, many authors introduce an associated *effective viscosity* ν' and a mean superfluid vorticity $\bar{\omega}_s$ such that $\varepsilon = \nu' \bar{\omega}_s^2$, where it is *assumed* that $\bar{\omega}_s^2 \sim \kappa^2 L_0^2$ in grid turbulence. It is important to emphasize that the last relation is mainly derived

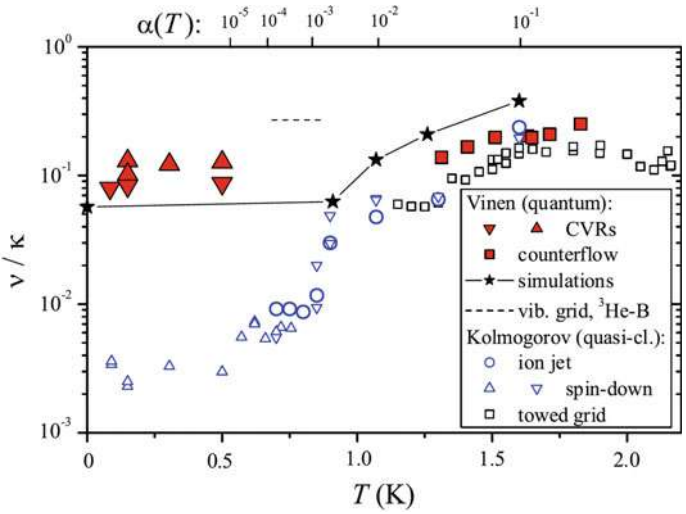

Fig. 6.15 Effective viscosity deduced from experimental data, in both quasi-classical and ultra-quantum régimes. From Walmsley and Golov 2008 with permission

by analogy with classical isotropic turbulence and dimensional analysis, and that ν' is nothing but an artifact used for modelling purpose.

The $\mathcal{K}(t) \propto t^{-2}$ law is obtained in a straightforward way thanks to the Comte–Bellot-Corrsin analysis in the saturated case (see Sect. 4.4.5), the large-scale saturation being very rapidly reached in experiments due to the very small diameter of vessels used to deal with superfluid helium (Skrbek and Stalp 2000). The main assumption here is that kinetic energy is mainly beared by scales with size about the vessel diameter D, i.e. $\mathcal{K} \sim K_0 \varepsilon^{2/3} D^{2/3}$ and that the dissipation can be expressed as $\varepsilon \sim \kappa^3 \ell^{-4}$. Plugging this relation into (6.190), one obtains the result immediately by integration of the resulting relation. Combining the two above expressions, one obtains the following expression for the turbulent kinetic energy: $\mathcal{K} \sim K_0 D^{2/3} \kappa^2 L_0^{4/3}$.

The second régime is recovered now assuming that turbulent kinetic energy and characteristic vorticity are not associated to hydrodynamic large scales, but to very small scales dominated by quantum phenomena. This new assumption leads to $\mathcal{K} \sim \rho_s \frac{\kappa^2}{4\pi} \Lambda L_0$, $\bar{\omega} \sim \kappa L_0$ and $\nu' \propto \kappa$, with $\Lambda = \log(\ell / r_c)$. Inserting these relations into (6.190), one recovers the expected results. It is worth noting that the turbulent kinetic energy exponent in terms of L_0 is not the same in the two régimes.

Values of ν' have been deduced from experimental data using the above reasoning. Typical results are displayed in Fig. 6.15. A good approximation for temperature above 1 K in superfluid Helium is $\nu' \simeq q\kappa$ (Skbrek 2010).

More sophisticated expressions for the effective viscosity ν' can be obtained in a few idealized cases (Vinen and Niemela 2002). Let's first address the case in which dissipation mainly originates in mutual friction. If there is no large-scale hydrodynamic vortical eddies, the evolution equation deduced from the two-fluid model is

$$\frac{d\mathcal{K}}{dt} = -\alpha\rho_s\kappa|\boldsymbol{u}_{ns}|^2 L_0. \tag{6.191}$$

Assuming that $\boldsymbol{u}_n = 0$ and that the superfluid velocity is dominated by the self-induction mechanisms, i.e. $|\boldsymbol{u}_s| \simeq \kappa\Lambda/4\pi\ell$, one obtains

$$\frac{d\mathcal{K}}{dt} = -\underbrace{\left(\frac{\alpha\rho_s\kappa c_2^2\Lambda^2}{16\pi^2}\right)}_{\nu'_{friction}}(\kappa L_0)^2, \tag{6.192}$$

where the self-similarity hypothesis $\ell^{-2} = c_2^2 L_0$ was used. In the presence of large hydrodynamic scales, the effective viscosity is modified as follows

$$\nu'_{friction} = \sigma\left(\frac{\alpha\rho_s\kappa c_2^2\Lambda^2}{16\pi^2}\right), \tag{6.193}$$

where $0 < \sigma < 1$ is a parameter that accounts for the partial polarization of vortex lines that induces a decrease in the rate of destruction of vortex lines. In both cases, one has $\nu'_{friction} \propto \kappa$, in agreement with Skrbek's experimental fit. It is worth noting that the existence of two different decay régimes when reconnection-dissipation is dominant can also be derived from the two evolution régimes for the vortex line density L_0 in Sect. 6.4.1.1, since

$$\frac{1}{\mathcal{V}}\frac{d\mathcal{K}}{dt} = E_{QV}\frac{dL_0}{dt} \tag{6.194}$$

where $\mathcal{V}$ and E_{QV} denote the unit volume and the energy per unit length of quantized vortex, respectively.

We now address the case of superfluid helium at zero-temperature at which mutual friction vanishes, and neglecting the emission of phonons due to reconnections. Within the Biot–Savart vortex filament framework, the variation of kinetic energy is directly proportional to the change in total vortex line length. Now assuming that the dissipation is due to the damping of Kelvin wave kinetic energy by radiation of phonons, it is convenient to express the normalized Kelvin wave kinetic energy as:

$$\frac{L_0 - \tilde{L}_0}{\tilde{L}_0} = \frac{\tilde{\mathcal{K}}_{KW}}{\rho_s\kappa^2} = \frac{1}{\rho_s\kappa^2}\int_{1/\ell}^{+\infty} E_{KW}(k)dk \tag{6.195}$$

where L_0 and $\tilde{L}_0$ are related to the total and the smoothed vortex line lengths (i.e. without Kelvin-wave-induced corrugation), respectively. Using (6.125) for E_{KW} and integrating from $1/\ell$ to the cutoff wave number k_{ph} given by (6.128), one obtains

$$\frac{L_0 - \tilde{L}_0}{\tilde{L}_0} \sim A\ln(k_{ph}\ell) \tag{6.196}$$

Now using Vinen's estimate for the phonon radiation (see Sect. 6.3.7), the rate of dissipation of energy via phonon emission by Kelvin waves per unit mass of helium is

$$\varepsilon_{ph} \simeq \frac{G\kappa^3 L_0^2}{[1 + A \ln(k_{ph}\ell)]^2}. \tag{6.197}$$

The associated effective kinematic viscosity ν' is obtained writing

$$\varepsilon_{ph} = \nu'_{ph}\kappa^2 L_0^2, \tag{6.198}$$

leading to

$$\nu'_{ph} \simeq \frac{G\kappa}{[1 + A \ln(k_{ph}\ell)]^2}, \tag{6.199}$$

where the injection rate of energy in the Kelvin-wave cascade by vortex reconnections is taken equal to $G\kappa^3\ell^{-4} \sim G\kappa^3 L_0^2$. Other formulas can be obtained using different estimates for the phonon emission rate. In the case of reconnection-dissipation in ^{4}He, (Vinen and Niemela 2002) evaluate the rate of reconnection per unit volume as $\kappa\ell^{-5}$ and the energy loss per reconnection as $\rho_s\kappa r_c/4\pi$, leading to a dissipation rate per unit mass equal to

$$\varepsilon_{reconnection} = \underbrace{\frac{1}{4\pi}\kappa\left(\frac{r_c}{\ell}\right)}_{\nu'_{reconnection}}(\kappa^2 L_0^2) \tag{6.200}$$

The factor r_c/ℓ is very small in ^{4}He, supporting the hypothesis made above that Kelvin-wave-induced dissipation is dominant in this case.

Another source of dissipation, referred to as quantized vortex diffusion (Nemirovskii 2013), can also be taken into account when considering a fixed control volume in a statistically unsteady flow. In such a configuration, there are non-zero influx and outflux of quantized vortices which are not in balance, leading possibly to a decrease of the total vortex length and the related kinetic energy within the control volume.

The link between the measured decay exponent of $\mathcal{K}$ and the details of the flow topology and physics is an important question, since no direct measurements of energy spectrum and similar flow details are available in superfluid grid turbulence. At present time, the main pieces of evidence that bridge between decay rates and large-scale topology are the few existing vortex-filament based simulations that recover the quasi-classical and the ultra-quantum régime. In the classical régime analysis, the only assumption is that flow physics is dominated by large scales which are not directly governed by vortex reconnection and quasi-particule emission. Dimensional analysis does not allow for a deep insight of underlying physics. Therefore, one can only conclude that the $\mathcal{K}(t) \propto t^{-2}$ régime is coherent with what is found for a saturated classical turbulence, but there is no direct evidence that large scales in

that régime exhibit exactly the same dynamics as in Newtonian fluids. In the ultra-quantum régime, the main assumption is that energetic scales are of the order of the inter vortex distance. Once again, dimensional analysis yields no knowledge about detailed dynamics at these scales. The weakness of the conclusions drawn from these results has been quoted by several authors, e.g. Vinen (2010), Nemirovskii (2013).

6.5.2 Vinen's Equation

The equation for the time evolution vortex line density L_0 proposed by Vinen in 1957 is among the cornerstone of the theory of turbulence in superfluids, since it has been used as a framework in a huge number of papers. Following the phenomenological scheme proposed by Feynman, who proposed the idea of a vortex-ring-induced energy cascade, Vinen proposed the following empirical relation:

$$\frac{dL_0}{dt} = \mathcal{P}_{L_0}(t) - \mathcal{D}_{L_0}(t), \tag{6.201}$$

where the first and second terms in the right-hand side denote production and destruction rates, respectively. The key issues are then to close that expression by finding appropriate models for the mechanisms that contribute to these two global effects. The discussion about the nature of dissipation and the three different mechanisms that contribute to it, along with the fact that they are fluid- and temperature-dependent, shows that universal models are not likely to be derived. As a matted of fact, case-dependent detailed models should be sought for.

In the case of turbulence in ^{4}He generated by a thermal counterflow, mutual friction generates vortex lines. Assuming that the production term depends only on the instantaneous vortex line density $L_0(t)$, the quantized circulation κ and the mutual friction force modulus $|\boldsymbol{f}_{ns}|$, Vinen found via dimensional analysis

$$\mathcal{P}_{L_0} \sim \kappa L_0^2 \varphi\left(\frac{|\boldsymbol{f}_{ns}|}{\rho_s \kappa L_0^{1/2}}\right), \tag{6.202}$$

where φ is a dimensionless function of a dimensionless input. Extrapolating the results obtained by Hall for the growth of a single vortex ring put transversally with a uniform counterflow, he proposed

$$\mathcal{P}_{L_0} = \chi_1 |\boldsymbol{u}_{ns}| L_0^{3/2}, \tag{6.203}$$

where χ_1 is a tunable parameter which a priori depends on the mutual friction parameter α that appears in the two-fluid model (and consequently on temperature T) and $\boldsymbol{u}_{ns} = \boldsymbol{u}_n - \boldsymbol{u}_s$.

The destruction term is evaluated by analogy with dimensional analysis theory of classical turbulence, in which $\varepsilon \propto u'^3/L$. Taking $L = \ell \simeq L_0^{-1/2}$ and defining u' as the velocity generated by an infinite straight vortex line at a distance ℓ, i.e. $u' = \kappa/2\pi\ell = L_0^{1/2}\kappa/2\pi$,[10] Vinen's original model is

$$\mathcal{D}_{L_0} = \chi_2 \frac{\kappa}{2\pi} L_0^2, \tag{6.204}$$

where χ_2 is another adjustable parameter, leading to the famous Vinen equation:

$$\frac{dL_0}{dt} = \underbrace{\chi_1 |\boldsymbol{u}_{ns}| L_0^{3/2}}_{Production} - \underbrace{\chi_2 \frac{\kappa}{2\pi} L_0^2}_{Destruction} \tag{6.205}$$

whose steady-state solution is

$$L_0 = \left(\frac{\chi_1}{\chi_2} \frac{2\pi}{\kappa} \right)^2 |\boldsymbol{u}_{ns}|^2 = \gamma(T) |\boldsymbol{u}_{ns}|^2. \tag{6.206}$$

This equilibrium solution has been observed in the case of counterflowing ^{4}He up to $T = 1.95\,\mathrm{K}$ in numerical simulations based on the vortex filament method, e.g. Schwarz (1988), Adachi and Tsubota (2010), Tsubota and Adachi (2011), Kondaurova et al. (2014), and in experiments (Babuin et al. 2012). A good qualitative agreement on the evolution of the parameter γ with respect to the temperature is reported.

Bridging between the empirical Feynman–Vinen theory illustrated by Eq. (6.205) and more recent ones, refining it and extending it to other flow configurations has been the subject of many research works. Among them, one must notice the pioneering work by Schwarz (1988, 1991) dealing with the recovery of Vinen's equation starting from the Biot–Savart vortex filament model discussed in Sect. 6.2.2. This is possible because macroscopic quantities related to vortex tangle topology can be recovered via statistical averaging over vortex filaments contained in a control volume $\mathcal{V}$. As a matter of fact, the vortex line density is recovered summing over all vortex filaments within the control volume:

$$L_0 = \frac{1}{\mathcal{V}} \overline{\sum_j \int |\boldsymbol{s}'_j(\xi_j)| d\xi_j}. \tag{6.207}$$

The macroscopic time evolution of a dummy quantity $\Phi(\boldsymbol{s}_j(\xi_j, t))$ defined along vortex filaments is obtained thanks to the following exact relation:

[10] It is worth noting that this model for the destruction term corresponds to the type I decay discussed in Sect. 6.4.1.1. Another version of Vinen's equation must be formulated for the type II régime, in which counterflow velocity is small with respect to the self-induced velocity and the destruction term scales as $L_0^{5/2}$.

$$\frac{\partial}{\partial t}\overline{\Phi(\boldsymbol{s}_j(\xi_j,t))} = \overline{\sum_i \int \frac{\delta\Phi(\boldsymbol{s}_j(\xi_j,t))}{\delta \boldsymbol{s}_i(\xi_i',t)} \frac{\partial \boldsymbol{s}_i(\xi_i',t)}{\partial t} d\xi_i'}. \tag{6.208}$$

To retrieve an equation for the vortex line density L_0, one must first consider the equation for the rate of change of an elementary vortex filament element with length δl. Writing $\delta l = |\boldsymbol{s}'|\delta\xi$, one has

$$\frac{\partial}{\partial t}\delta l = \frac{\partial}{\partial t}(|\boldsymbol{s}'|\delta\xi) = \boldsymbol{s}' \cdot \frac{d\boldsymbol{s}'}{dt}\delta\xi. \tag{6.209}$$

Now using the Local Interaction Approximation to compute $d\boldsymbol{s}'/dt$, one obtains

$$\frac{\partial}{\partial t}\delta l = \left(\alpha(\boldsymbol{s}' \times \boldsymbol{s}'') \cdot \boldsymbol{u}_{ns} - \alpha\beta(\boldsymbol{s}' \times \boldsymbol{s}'')^2\right)\delta\xi. \tag{6.210}$$

Now integrating over the arc length and averaging over the control volume, one recovers the following equation:

$$\frac{\partial}{\partial t}L_0 = \alpha \boldsymbol{u}_{ns} \int \overline{(\boldsymbol{s}' \times \boldsymbol{s}'')} d\xi - \alpha\beta \int \overline{|\boldsymbol{s}''|^2}\delta\xi. \tag{6.211}$$

The terms in the right hand side can be further developed, introducing some topological parameters associated to the vortex tangle. These indicators were historically introduced by Schwarz to characterize the anisotropy of a vortex tangle generated in a vessel with axis $\boldsymbol{e}_z$ in counterflowing ^{4}He in the steady state case. The *polarization indicator* I_l is defined as

$$\overline{\frac{1}{\mathcal{V}L_0^{3/2}} \sum_j \int \boldsymbol{s}_j'(\xi_j) \times \boldsymbol{s}_j''(\xi_j) d\xi_j} = I_l \boldsymbol{e}_z \tag{6.212}$$

leading to

$$\overline{\boldsymbol{s}_j'(\xi_j) \times \boldsymbol{s}_j''(\xi_j)} = I_l L_0^{1/2} \boldsymbol{e}_z. \tag{6.213}$$

The second term can be expressed using the assumption that the mean curvature of the vortex tangle should be of the order of the intervortex distance ℓ:

$$\overline{\frac{1}{\mathcal{V}L_0} \sum_j \int \boldsymbol{s}_j''(\xi_j) \cdot \boldsymbol{s}_j''(\xi_j) d\xi_j} = \ell, \tag{6.214}$$

whose local counterpart is

$$\overline{\boldsymbol{s}_j''(\xi_j) \cdot \boldsymbol{s}_j''(\xi_j)} = c_2^2 L_0, \tag{6.215}$$

where the dimensionless parameter c_2^2 is of the order of the unity. Combining Eqs. (6.211), (6.213) and (6.215) one recovers an expression for the empirical terms

that appears in the original expression given by Vinen:

$$\frac{\partial}{\partial t}L_0 = \alpha I_l |\boldsymbol{u}_{ns}| L_0^{3/2} - \alpha\beta c_2^2 L_0^2. \tag{6.216}$$

It is important to note that this last equation is valid assuming a very slow evolution, i.e. a quasi steady-state in which the coefficients that appear in the right-hand side are nearly constant, i.e. if they relax toward equilibrium much faster than $L_0(t)$. An important remark is that the previous Vinen equation and steady-state solution can be recovered looking for self-similar expressions (Schwarz 1988). Such solutions are found introducing the scaling parameter λ and considering the transformation

$$x^* \to \lambda x^* = x, \quad t^* \to \lambda^2 t^* = t, \tag{6.217}$$

and looking for symmetry-preserving solutions. Assuming that L_0 depends only on the counterflow velocity amplitude, one immediately finds

$$L_0(u_{ns}) = L_0(u_{ns}^* \lambda^{-1}) = \lambda^{-2} L_0^*(u_{ns}^*), \tag{6.218}$$

whose solution is $L_0 \propto u_{ns}^2$, which is the steady-state solution (6.206).

The role of the anisotropy of the vortex tangle can be further emphasized looking for more general expressions of Vinen equation. Such extensions are beyond the scope of the present chapter, and the reader is referred to original articles, e.g. Lipniacki (2011), Jou et al. (2011), Nemirovskii (2013).

The Vinen equation can also be inferred from theoretical models, e.g. the Gaussian random vortex loop model discussed in Sect. 6.4.1.2 (Nemirovskii 2013). Starting from the identity

$$L_0 = \int_R^{+\infty} n(l) l dl, \tag{6.219}$$

one obtains in a straightforward way

$$\frac{\partial L_0}{\partial t} = -\int \frac{\partial}{\partial t}(n(l,t)\dot{l}) l dl = \int n(l,t)\dot{l} dl - P \tag{6.220}$$

where the net flux of the length in l-space due to vortex loop/ring reconnections, P is given by Eq. (6.113). The first term in the right-hand side is related to the change in L_0 due to the mutual friction, which can be evaluated thanks to the relation (6.210) for the evolution of the length of an elementary line element δl. The Gaussian vortex loop model allows for some analytical integrations:

$$\overline{\boldsymbol{s}' \times \boldsymbol{s}''} = \frac{I_l}{\sqrt{2} c_2 R} \frac{\boldsymbol{u}_{ns}}{|\boldsymbol{u}_{ns}|}, \quad \overline{(\boldsymbol{s}' \times \boldsymbol{s}'')^2} = \overline{(\boldsymbol{s}'')^2} = \frac{1}{2R^2}, \tag{6.221}$$

leading to

$$\int n(l,t)\dot{l}dl = \left(\alpha\frac{I_l|\boldsymbol{u}_{ns}|}{\sqrt{2}c_2R} - \alpha\beta\frac{1}{2R^2}\right)\int n(l,t)ldl = \left(-\alpha\frac{I_l\sqrt{2}|\boldsymbol{u}_{ns}|}{c_2R} + \alpha\beta\frac{1}{R^2}\right)L_0 \tag{6.222}$$

which can be rewritten, using the relation $R \propto L_0^{-1/2}$ and taking $c_2 = \sqrt{2}$ as

$$\int n(l,t)\dot{l}dl = \alpha I_l|\boldsymbol{u}_{ns}|L_0^{3/2} - \alpha\beta c_2^2 L_0^2. \tag{6.223}$$

As mentioned in Sect. 6.4.1.2, the net flux can be approximated as $P = |c_F|\kappa L_0^2$ where c_F is a temperature-dependent parameter, leading to

$$\frac{\partial L_0}{\partial t} = \alpha I_l|\boldsymbol{u}_{ns}|L_0^{3/2} - \alpha\beta c_2^2 L_0^2 - |c_F|\kappa L_0^2. \tag{6.224}$$

The physical meaning of the term in the right-hand side are: production of vortex lines by mutual friction, destruction of vortex lines by mutual friction and decrease of vortex line density due to random collisions of quantized vortices which induce a transfer toward small scales at which dissipative mechanisms take place.

6.6 Mutual Friction: Microscopic Origin and Models

6.6.1 Mutual Friction on Vortex Filaments

The mutual friction exerted on a quantized vortex per unit length can be heuristically modeled in different ways, e.g. see Barenghi et al. (1983), Swanson et al. (1987), Idowu et al. (2000). The most popular expressions used within the vortex filament framework are

$$\boldsymbol{f}_D = \begin{cases} -\gamma_0\boldsymbol{s}'\times[\boldsymbol{s}'\times(\boldsymbol{u}_n-\boldsymbol{u}_L)] + \gamma_0'\kappa\boldsymbol{s}'\times(\boldsymbol{u}_n-\boldsymbol{u}_L) \\ -\alpha\rho_s\boldsymbol{s}'\times[\boldsymbol{s}'\times(\boldsymbol{u}_n-\boldsymbol{u}_s)] + \alpha'\kappa\boldsymbol{s}'\times(\boldsymbol{u}_n-\boldsymbol{u}_s) \\ -B\frac{\rho_n\rho_s}{2\rho}\boldsymbol{s}'\times[\boldsymbol{s}'\times(\boldsymbol{u}_n-\boldsymbol{u}_s)] + B'\frac{\rho_n\rho_s}{2\rho}\kappa\boldsymbol{s}'\times(\boldsymbol{u}_n-\boldsymbol{u}_s) \\ -D\boldsymbol{s}'\times[\boldsymbol{s}'\times(\boldsymbol{u}_R-\boldsymbol{u}_L)] + D_t\boldsymbol{s}'\times(\boldsymbol{u}_R-\boldsymbol{u}_L) \end{cases} \tag{6.225}$$

where $\boldsymbol{u}_n, \boldsymbol{u}_s, \boldsymbol{u}_L, \boldsymbol{u}_R$ denote the normal fluid velocity, the superfluid velocity, the vortex line velocity and the normal fluid mean drift velocity, respectively, all measured in the laboratory frame. The drift velocity $\boldsymbol{u}_R$ accounts for the fact that the normal fluid is dragged by a vortex line, so that its velocity is not equal to $\boldsymbol{u}_n$ in the surrounding of the vortex. Coefficients of the different expressions of the mutual friction drag force can be written as functions of each others. One obviously has

$$\alpha = B\rho_n/2\rho, \quad \alpha' = B'\rho_n/2\rho, \tag{6.226}$$

and, by elimination,

$$\gamma_0 = \frac{\rho_n\rho_s}{2\rho}\kappa\frac{B}{(1-B'\rho_n/2\rho)^2 + B^2\rho_n^2/4\rho^2}, \tag{6.227}$$

$$\gamma_0' = \frac{\rho_n\rho_s}{2\rho}\kappa\frac{B^2\rho_n/2\rho - B'(1-B'\rho_n/2\rho)}{(1-B'\rho_n/2\rho)^2 + B^2\rho_n^2/4\rho^2}. \tag{6.228}$$

Hall and Vinen introduced in 1956 the complex parameter E such that

$$\boldsymbol{u}_n - \boldsymbol{u}_R = \frac{1}{E}\boldsymbol{f}_N, \tag{6.229}$$

where $\boldsymbol{f}_N$ is the force exerted on the excitation gas by a quantized vortex on a cylinder of radius $r_c + L \simeq L$, where L is the mean free path of the quasi-particules that are scattered by the vortex. Here, the normal fluid is treated as a classical viscous fluid with a correction to account for the mean free path of the quasi-particules that form it, i.e. mainly rotons in ^{4}He for $T > 1$ K, with $L \sim 10^{-6}$ cm. The parameter E is estimated in the asymptotic case of low-amplitude large-wave length (compared with the quantized vortex radius r_c) rotons interacting with the vortex core. It can be expressed as

$$E = -\frac{4\pi\nu_n}{\Re(M)}, \quad M = \ln(l/2\delta) + 1 + \imath\pi/4, \tag{6.230}$$

where $l = 3\nu_n/\rho_n v_G$ is the roton mean free path, $\delta = \sqrt{\nu_n/\rho_n\sigma}$ is the viscous penetration depth, ν_n the normal fluid viscosity, $v_G = \sqrt{2k_BT/\pi m_r}$ the roton group velocity, m_r the roton mass and σ the angular frequency of the counterflow oscillation.

Using relation (6.229), one obtains

$$\alpha = \frac{a}{\rho_s\kappa(a^2+b^2)}, \quad \alpha' = \frac{b}{\rho_s\kappa(a^2+b^2)}, \tag{6.231}$$

with

$$a = \frac{1}{E} + \frac{D}{D^2+D_t^2}, \quad b = \frac{1}{\rho_s\kappa} - \frac{D_t}{D^2+D_t^2}, \tag{6.232}$$

and

$$D = \frac{c}{(c^2+d^2)}, \quad D_t = -\frac{d}{(c^2+d^2)}, \tag{6.233}$$

where

$$c = \frac{\alpha}{\rho_s\kappa(\alpha^2+\alpha'^2)} - \frac{1}{E}, \quad d = \frac{\alpha'}{\rho_s\kappa(\alpha^2+\alpha'^2)} - \frac{1}{\rho_s\kappa}. \tag{6.234}$$

Combination of previous results yields

$$\gamma_0 = \frac{E[D(D+E)+D_t^2]}{(D+E)^2+D_t^2}, \quad \gamma_0' = \frac{D_t E^2}{(D+E)^2+D_t^2}. \tag{6.235}$$

6.6.2 Bridging with Microscopic Theories

A first link between mutual friction drag force in the vortex filament model and microscopic theories can be established in the following way. In a microscopic theory, one should relate the mutual friction to the scattering and absorption of quasi-particules of the normal fluid by the vortex. Such an interaction results in a change of momentum of the quasi-particules.

The force exerted on the vortex line per unit length due to scattering and absorption is

$$\boldsymbol{f}_{ex} = D(\boldsymbol{u}_R - \boldsymbol{u}_L) + D'\boldsymbol{s}' \times (\boldsymbol{u}_R - \boldsymbol{u}_L), \tag{6.236}$$

where parameters are related to the scattering lengths $\sigma_\parallel$ and $\sigma_\perp$ by

$$D = \rho_n v_G \sigma_\parallel, \quad D' = \rho_n v_G \sigma_\perp. \tag{6.237}$$

The scattering lengths could in principle be calculated from fundamental physics of vortex-quasi-particule interaction. This is not possible in practice because there exist no realistic model for the quantized vortex core. Therefore, these parameters are tabulated from experimental data or DNS based on the modified Gross–Pitaevskii equations (6.17) or (6.21) and (6.22), keeping in mind that such simulations are not fully relevant for liquid superfluids. This is illustrated in Fig. 6.16, in which coefficients α and α' are computed solving the latter model. Some analytical formula can be derived in a few very simplified cases. This is illustrated below by the derivation of model based on the Biot–Savart theory for vorticity-induced velocity field starting from the more fundamental Gross–Pitaevski model. Expressing a line vortex with radius r_c as

$$\psi(r,t) = \sqrt{\rho_s} e^{\imath\phi} f(r/r_c), \tag{6.238}$$

where ϕ and $f(x)$ denote the azimutal angle about the axis and the radial shape function, respectively. One has $f(0) = 0$ and $f(x \to +\infty) = 1$. Therefore, the vortex line model is recovered identifying the line such that $\psi(\boldsymbol{x}, t) = 0$, which can be parametrized as $\psi(\boldsymbol{s}(\xi, t), t) = 0$. Following the chain rule, one obtains

$$\frac{\partial \psi(\boldsymbol{r},t)}{\partial t} = \int_\Gamma \frac{\delta \psi(\boldsymbol{r},t)}{\delta \boldsymbol{s}(\xi',t)} \cdot \frac{\partial \boldsymbol{s}(\boldsymbol{\xi}',t)}{\partial t} d\xi'. \tag{6.239}$$

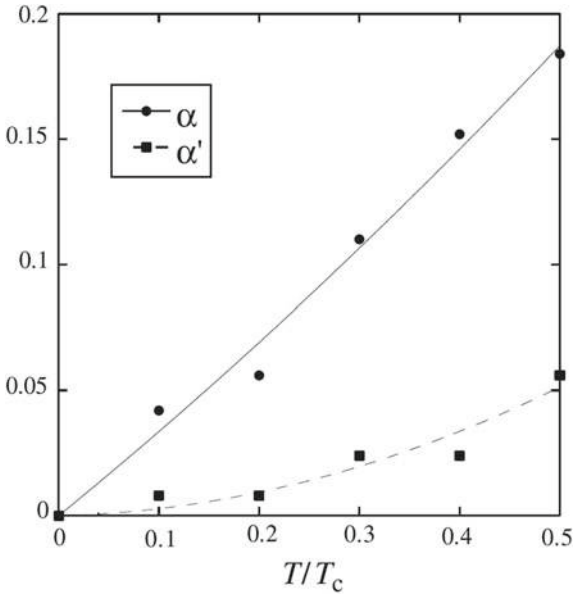

Fig. 6.16 Evolution of mutual friction force coefficients α and α' versus normalized temperature T/T_c computed solving a coupled Gross–Pitaevskii–Bogoliubov-de Gennes system for a single quantized vortex in a thermal bath with an imposed velocity field. Symbols: DNS data; lines: best fits. From Kobayashi and Tsubota (2006) with permission of APS

Rewriting the Gross–Pitaevski equation including thermal noise source term as

$$\frac{\hbar}{m}\frac{\partial\psi}{\partial t} = -(\Lambda + \imath)\frac{\delta H(\psi)}{\delta\psi^*} + \zeta(\boldsymbol{x}, t) \tag{6.240}$$

where ζ is related to the thermal noise, Λ is related to the thermal noise excitation $\zeta(\boldsymbol{x}, t)$ by (with T the temperature and k_B the Boltzmann constant)

$$\overline{\zeta(\boldsymbol{x}, t)\zeta^*(\boldsymbol{x}', t')} = \frac{2k_B T\Lambda}{m/\hbar}\delta(\boldsymbol{x} - \boldsymbol{x}')\delta(t - t') \tag{6.241}$$

and $H(\psi)$ is the Ginzburg–Landau free energy functional:

$$H(\psi) = \int\left(\frac{\hbar^2}{2m^2}|\nabla\psi|^2 - \frac{\mu}{m}|\psi|^2 + \frac{V}{2m}|\psi|^4\right)d\boldsymbol{x}^3 \tag{6.242}$$

after some cumbersome algebra (see Nemirovskii 2013 for details), one recovers the following expression for the line velocity $\dot{\boldsymbol{s}}$ at point ξ_0 one the vortex line:

$$\dot{\boldsymbol{s}}(\xi_0) = \frac{1 + \Lambda^2}{1 + \Lambda^2\sigma^2}\boldsymbol{u}_{BS}(\xi_0) + \frac{(1 + \Lambda^2)\Lambda\sigma}{1 + \Lambda^2\sigma^2}\boldsymbol{s}'(\xi_0) \times \boldsymbol{u}_{BS} + \frac{m}{\hbar}\boldsymbol{\zeta}(\xi_0, t), \tag{6.243}$$

where $\sigma = \log(R/r_c)$ (with R the local radius of curvature of the vortex line), and the induced velocity $\boldsymbol{u}_{BS}$ is given by Eq. (6.25). In the case of null macroscopic normal

and superfluid velocities, i.e. $\boldsymbol{u}_n = \boldsymbol{u}_s = 0$, the two coefficients appearing in relation (6.41) are identified as

$$\alpha = \frac{(1+\Lambda^2)\Lambda\sigma}{1+\Lambda^2\sigma^2}, \quad \alpha' = \frac{\Lambda^2(\sigma^2-1)}{\sigma^2\Lambda^2+1}. \tag{6.244}$$

Data shows that these coefficients strongly depend on the temperature, the pressure and the fluid nature. Tabulated values and expressions based on data fitting are available in the literature.

The condition for the balance of the force on the vortex line is

$$\boldsymbol{f}_N + \boldsymbol{f}_{ex} + \boldsymbol{f}_I = 0, \tag{6.245}$$

where $\boldsymbol{f}_I$ denotes the *Iordanskii force* (per unit length), with

$$\boldsymbol{f}_I = -\rho_n \kappa \boldsymbol{s}' \times (\boldsymbol{u}_R - \boldsymbol{u}_L). \tag{6.246}$$

This extra-force originates in the fact that the normal fluid component in the two-fluid model cannot be exactly identified with the fluid formed from the gas of thermal excitations. This is understood observing that the momentum of the normal fluid is $\rho_n \boldsymbol{u}_n$, while the one carried by thermal excitations is $\rho_n(\boldsymbol{u}_n - \boldsymbol{u}_s)$. Therefore, the total momentum is obtained by adding that of the superfluid, $\rho_s \boldsymbol{u}_s$, to $\rho_n \boldsymbol{u}_n$, or by adding that of the background fluid, $\rho \boldsymbol{u}_s$, to that of thermal excitations.

Since the total force on the superfluid must balance that on the normal fluid, one has $\boldsymbol{f}_N = \boldsymbol{f}_M$ (i.e. the Magnus force is equal to $\boldsymbol{f}_N$), leading to

$$\rho_s \kappa \boldsymbol{s}' \times (\boldsymbol{u}_s - \boldsymbol{u}_L) = D(\boldsymbol{u}_R - \boldsymbol{u}_L) + D_t \boldsymbol{s}' \times (\boldsymbol{u}_R - \boldsymbol{u}_L), \tag{6.247}$$

where D_t is the transverse diffusion coefficient.

6.6.3 Bridging with Hydrodynamic Two-Fluid Model

The mutual friction term $\boldsymbol{f}_{ns}$ that appears in the momentum equations of the two-fluid macroscopic models (6.64) and (6.65) is a force per unit volume that is the same as the Magnus force per unit volume on the superfluid,

$$\boldsymbol{F}_M = \frac{1}{V} \iiint_{\mathcal{L} \in V} \boldsymbol{f}_M(\boldsymbol{x}) d^3\boldsymbol{x} = L_0 \bar{\boldsymbol{f}}_M. \tag{6.248}$$

where the integral is computed over all vortex filaments $\mathcal{L}$ present in the control volume V. Here, $L_0 = 2\|\boldsymbol{\omega}\|/\kappa$ denotes the *effective length of quantized vortex per unit volume* and $\boldsymbol{f}_M$ is given by (6.37) and $\bar{\boldsymbol{f}}_M$ denotes the averaged value per unit length within the control volume. Since all quantized vortices are not polarized and

parallel in the control volume in the general case, the L_0 is smaller than real total vortex line length inside V.

The macroscopic mutual friction force can therefore be written as

$$\boldsymbol{f}_{ns} = -L_0 \bar{\boldsymbol{f}}_M = -\frac{2\|\boldsymbol{\omega}\|}{\kappa} \bar{\boldsymbol{f}}_M, \tag{6.249}$$

The equilibrium condition on quantized vortices between Magnus force and the mutual friction drag discussed in Sect. 6.2.2.3, $\boldsymbol{f}_M + \boldsymbol{f}_D = 0$, shows that the averaged Magnus force $\bar{\boldsymbol{f}}_M$ may be replaced by the averaged value of the mutual friction drag force $\bar{\boldsymbol{f}}_D$.

It is often chosen to use an expression for the macroscopic volumic force that mimics the microscopic force per quantized vortex unit length, and to introduce adjustable parameters to account for the degree of polarization of quantized vortices, yielding

$$\boldsymbol{f}_{ns} = -\frac{\bar{\rho}_n \bar{\rho}_s}{2\bar{\rho}} \left(B\hat{\boldsymbol{\omega}} \times [\boldsymbol{\omega} \times (\bar{\boldsymbol{u}}_s - \bar{\boldsymbol{u}}_n)] + B'\hat{\boldsymbol{\omega}} \times (\bar{\boldsymbol{u}}_s - \bar{\boldsymbol{u}}_n) \right), \tag{6.250}$$

where bar symbol denotes the averaged value over the control volume V. This symbol is omitted for the sake of brevity when manipulating the equations of the two-fluid model. The coefficients B and B' are tabulated experimentally considering damping of second sound waves.

It is worth noticing that some simplified expressions are sometimes used, mainly to allow for analytical works or to accelerate numerical simulations. An example is

$$\boldsymbol{f}_{ns} = B \frac{\rho_n \rho_s}{2\rho} \|\nabla \times \boldsymbol{u}_s\| (\boldsymbol{u}_n - \boldsymbol{u}_s). \tag{6.251}$$

References

Adachi, H., Tsubota, M.: Numerical studies of counterflow turbulence. Velocity distribution of vortices. J. Low Temp. Phys. **158**, 422–427 (2010)

Babuin, S., Stammeier, M., Varga, E., Rotter, M., Skrbek, L.: Quantum turbulence of bellows-driven ^{4}He superflow: steady state. Phys. Rev. B **86**, 134515 (2012)

Baggaley, A.W.: The sensitivity of the vortex filament method to different reconnection models. J. Low Temp. Phys. **168**, 18–30 (2012)

Baggaley, A.W., Barenghi, C.F.: Spectrum of turbulent Kelvin-wave cascade in superfluid helium. Phys. Rev. B **83**, 134509 (2011)

Baggaley, A.W., Barenghi, C.F., Sergeev, Y.A.: Quasiclassical and ultraquantum decay of superfluid turbulence. Phys. Rev. B **85**, 060501(R) (2012)

Baggaley, A.W., Barenghi, C.F., Sergeev, Y.A.: Three-dimensional inverse energy transfer induced by vortex reconnections. Phys. Rev. E **89**, 013002 (2014)

Baggaley, A.W., Laurie, J.: Kelvin-wave cascade in the vortex filament model. Phys. Rev. B **89**, 014504 (2014)

Baggaley, A.W., Sherwin, L.K., Barenghi, C.F., Sergeev, Y.A.: Thermally and mechanically driven quantum turbulence. Phys. Rev. B **86**, 104501 (2012)
Barenghi, C.F.: Is the Reynolds number infinite in superfluid turbulence? Physica D **237**, 2195–2202 (2008)
Barenghi, C.F., Donnelly, R.J., Vinen, W.F.: Friction on quantized vortices in helium II. A review. J. Low Temp. Phys. **52**, 189–247 (1983)
Barenghi, C.F., Donnelly, R.J., Vinen, W.F.: Thermal excitation of waves on quantized vortices. Phys. Fluids **28**, 498–504 (1985)
Barenghi, C.F., Samuels, D.C., Kivotides, D.: Superfluid vortex reconnections. J. Low Temp. Phys. **126**, 271–279 (2002)
Barenghi, C.F., Samuels, D.C., Kivotides, D.: Scaling laws of vortex reconnections. J. Low Temp. Phys. **136**, 281–293 (2004)
Barenghi, C.F., Skrbek, L., Sreenivasan, K.R.: Introduction to quantum turbulence. Proc. Natl. Acad. Sci. USA **111**, 4647–4652 (2014)
Berloff, N.G.: Interactions of vortices with rarefaction solitary waves in a Bose–Einstein condensate and their role in the decay of superfluid turbulence. Phys. Rev. A **69**, 053601 (2004)
Boffetta, G., Celani, A., Dezzani, D., Laurie, J., Nazarenko, S.: Modeling Kelvin wave cascades in superfluid helium. J. Low Temp. Phys. **156**, 193–214 (2009)
Boué, L., Dasgupta, R., Laurie, J., L'vov, V., Nazarenko, S., Procaccia, I.: Exact solution for the energy spectrum of Kelvin-wave turbulence in superfluids. Phys. Rev. B **84**, 064516 (2011)
Briard, A., Gomez, T., Sagaut, P., Memari, S.: Passive scalar decay laws in isotropic turbulence: prandtl number effects. J. Fluid Mech. **784**, 274–303 (2015)
Briard, A., Gomez, T.: Passive scalar convective-diffusive subrange for low Prandtl numbers in isotropic turbulence. Phys. Rev. E **101**, 011001(R) (2015)
Fujimoto, K., Tsubota, M.: Bogoliubov-wave turbulence in Bose–Einstein condensates. Phys. Rev. A **91**, 053620 (2015)
Gao, J., Guo, W., L'vov, V.S., Pomyalov, A., Skrbek, L., Varga, E., Vinen, W.F.: Decay of counterflow turbulence in superfluid ^{4}He. JETP Lett. **103**, 648–652 (2016)
Golov, A.I., Walmsley, P.M.: Homogeneous turbulence in superfluid ^{4}He in the low-temperature limit: experimental progress. J. Low Temp. Phys. **156**, 51–70 (2009)
Hänninen, R.: Dissipation enhancement from a single vortex reconnection in superfluid helium. Phys. Rev. B **88**, 054511 (2013)
Idowu, O.C., Kivotides, D., Barenghi, C.F., Samuels, D.C.: Equation for self-consistent superfluid vortex line dynamics. J. Low Temp. Phys. **120**, 269–280 (2000)
Jou, D., Mongiovi, M.S., Sciacca, M.: Hydrodynamic equations of anisotropic, polarized and inhomogeneous superfluid vortex tangles. Physica D **240**, 249–258 (2011)
Kivotides, D., Vassilicos, J.C., Samuels, D.C., Barenghi, C.F.: Kelvin-wave cascade in superfluid turbulence. Phys. Rev. Lett. **86**, 3080–3083 (2001)
Kobayashi, M., Tsubota, M.: Kolmogorov spectrum of superfluid turbulence: numerical analysis of the Gross–Pitaevskii equation with small-scale dissipation. Phys. Rev. Lett. **94**, 065302 (2006)
Kobayashi, M., Tsubota, M.: Thermal dissipation in quantum turbulence. Phys. Rev. Lett. **97**, 145301 (2006)
Kobayashi, M., Tsubota, M.: Dissipation of Gross–Pitaevskii turbulence coupled with thermal excitations. J. Low Temp. Phys. **148**, 275–279 (2007)
Koundaurova, L., L'vov, V., Pomyalov, A., Procaccia, I.: Structure of a quantum vortex tangle in ^{4}He counterflow turbulence. Phys. Rev. B **89**, 014502 (2014)
Koundaurova, L., Nemirovskii, S.K.: Numerical study of decay of vortex tangles in superfluid helium at zero temperature. Phys. Rev. B **86**, 134506 (2012)
Kozik, E.V., Svistunov, B.V.: Kelvin-wave cascade and decay of superfluid turbulence. Phys. Rev. Lett. **92**, 035301 (2004)
Kozik, E.V., Svistunov, B.V.: Scale-separation scheme for simulating superfluid turbulence: Kelvin-wave cascade. Phys. Rev. Lett. **94**, 025301 (2005a)
Kozik, E.V., Svistunov, B.V.: Vortex-phonon interaction. Phys. Rev. B **72**, 172505 (2005b)

Kozik, E.V., Svistunov, B.V.: Kolmogorov and Kelvin-wave cascades of superfluid turbulence at T = 0: what lies between. Phys. Rev. B **77**, 060502(R) (2008a)
Kozik, E.V., Svistunov, B.V.: Scanning superfluid-turbulence cascade by its low-temperature cutoff. Phys. Rev. Lett. **100**, 195302 (2008b)
Kozik, E.V., Svistunov, B.V.: Theory of decay of superfluid turbulence in the low-temperature limit. J. Low Temp. Phys. **156**, 215–267 (2009)
Landau, L.: The theory of superfluidity of helium II. J. Phys. – USSR **5**, 71–90 (1941)
Laurie, J., L'vov, V.S., Nazarenko, S., Rudenko, O.: Interaction of Kelvin waves and nonlocality of energy transfer in superfluids. Phys. Rev. B **81**, 104526 (2010)
Leadbeater, M., Samuels, D.C., Barenghi, C.F., Adams, C.S.: Decay of superfluid turbulence via Kelvin-wave radiation. Phys. Rev. A **67**, 015601 (2004)
Leadbeater, M., Winiecki, T., Samuels, D.C., Barenghi, C.F., Adams, C.S.: Sound emission due to superfluid vortex reconnections. Phys. Rev. Lett. **86**, 1410–1413 (2001)
Lipniacki, T.: Dynamics of superfluid ^{4}HE: two-scale approach. Eur. J. Mech. B/Fluids **25**, 435–458 (2011)
L'vov, V.S., Nazarenko, S.: Spectrum of Kelvin-wave turbulence superfluid. JETP Lett. **91**, 428–434 (2010)
L'vov, V.S., Nazarenko, S.V., Rudenko, O.: Bottleneck crossover between classical and quantum superfluid turbulence. Phys. Rev. B **76**, 024520 (2007)
L'vov, V.S., Nazarenko, S.V., Rudenko, O.: Gradual eddy-wave crossover in superfluid turbulence. J. Low Temp. Phys. **153**, 140–161 (2008)
L'vov, V.S., Nazarenko, S.V., Skrbek, L.: Energy spectra of developed turbulence in helium superfluids. J. Low Temp. Phys. **145**, 125–142 (2006)
L'vov, V.S., Nazarenko, S., Volovik, G.E.: Energy spectra of developed super uid turbulence. JETP Lett. **80**, 479–483 (2004)
Nemirovskii, S.K.: Quantum turbulence: theoretical and numerical problems. Phys. Rep. **524**, 85–202 (2013)
Nore, C., Abid, M., Brachet, M.E.: Kolmogorov turbulence in low temperature superflows. Phys. Rev. Lett. **78**, 3896–3899 (1997)
Ogawa, S., Tsubota, M., Hattori, Y.: Study of reconnection and acoustic emission of quantized vortices in superfluid by the numerical analysis of the Gross–Pitaevskii equation. J. Phys. Soc. Jpn. **71**, 813–821 (2002)
Proment, D., Nazarenko, S., Onorato, M.: Quantum turbulence cascades in the Gross–Pitaevskii model. Phys. Rev. A **80**, 051603(R) (2009)
Roche, P.E., Barenghi, C.F., Leveque, E.: Quantum turbulence at finite temperature: the two-fluid cascade. EPL **87**, 54006 (2009)
Rorai, C., Skipper, J., Kerr, R.M., Sreenivasan, K.R.: Approach and separation of quantised vortices with balanced cores. J. Fluid Mech. **808**, 641–667 (2016)
Sagaut, P.: Large-Eddy Simulation of Incompressible Flows - An Introduction, 3rd edn. Springer, Berlin (2005)
Samuels, D.C., Barenghi, C.F.: Vortex heating in superfluid helium at low temperature. Phys. Rev. Lett. **81**, 4381–4383 (1998)
Sasa, N., Kano, T., Machida, M.: Large scale numerical simulation of superfluid turbulence. Phys. Rev. B **84**, 054525 (2011)
Sasa, N., Kano, T., Machida, M., L'vov, V.S., Rudenko, O., Tsubota, M.: Energy spectra of quantum turbulence: large-scale simulation and modeling. Prog. Nucl. Sci. Technol. **2**, 609–612 (2011)
Schwarz, K.W.: Three-dimensional vortex dynamics in superfluid ^{4}He: line-line and line-boundary interactions. Phys. Rev. B **31**, 5782–5804 (1985)
Schwarz, K.W.: Three-dimensional vortex dynamics in superfluid ^{4}He: homogeneous superfluid turbulence. Phys. Rev. B **38**, 2398–2417 (1988)
Schwarz, K.W.: Anomalous decay of turbulence in ^{4}He. Phys. Rev. Lett. **66**, 1898–1901 (1991)

Skbrek, L.: Flow phase diagram for the helium superfluids. In: IUTAM Symposium on Elementary Vortices and Coherent Structures: Significance in Turbulence Dynamics. Book Series: Fluid Mechanics and Its Applications, vol. 79, pp. 361–366 (2004)
Skbrek, L.: Energy spectra of quantum turbulence in He II and ^{3}He-B: a unified view. JETP Lett. **83**, 127–131 (2006)
Skbrek, L.: A simple phenomenological model for effective kinematic viscosity of helium superfluids. J. Low. Temp. Phys. **161**, 555–560 (2010)
Skbrek, L., Niemela, J.J., Sreenivasan, K.R.: Energy spectrum of grid-generated He II turbulence. Phys. Rev. E **64**, 067301 (2001)
Skrbek, L., Sreenivasan, K.R.: Developed quantum turbulence and its decay. Phys. Fluids **24**, 011301 (2012)
Skrbek, L., Stalp, S.R.: On the decay of homogeneous isotropic turbulence. Phys. Fluids **12**(8), 1997–2019 (2000)
Swanson, C.E., Wagner, W.T., Donnelly, R.J., Barenghi, C.F.: Calculation of frequency- and velocity-dependent mutual friction parameters in helium II. J. Low Temp. Phys. **66**, 263–276 (1987)
Tchoufag, J., Sagaut, P.: Eddy-damped quasinormal Markovian simulations of superfluid turbulence in helium II. Phys. Fluids **22**, 125103 (2010)
Tisza, L.: The viscosity of liquid helium and the Bose-Einstein statistic. Comptes Rendus hebdomadaires des séances de l'Acad. des Sci. **207**, 1186–1189 (1938)
Tsatos, M.C., Tavares, P.E.S., Cidrim, A., Fritsch, A.R., Caracanhas, M.A., dos Santos, F.E.A., Barenghi, C.F., Bagnato, V.S.: Quantum turbulence in trapped atomic Bose–Einstein condensates. Phys. Rep. **622**, 1–52 (2016)
Tsubota, M.: Quantum turbulence - from superfluid helium to atomic Bose–Einstein condensates. J. Phys. Condens. Matter. **21**, 164–207 (2009)
Tsubota, M.: Quantum hydrodynamics. Phys. Rep. **522**, 191–238 (2013)
Tsubota, M., Adachi, H.: Simulation of counterflow turbulence by vortex filaments. Statistics of vortex reconnections. J. Low Temp. Phys. **162**, 367–374 (2011)
Tsubota, M., Fujimoto, K., Yui, S.: Numerical studies of quantum turbulence. J. Low Temp. Phys. **188**, 119–189 (2017)
Vinen, W.F.: Classical character of turbulence in a quantum liquid. Phys. Rev. B **61**, 1410–1420 (2000)
Vinen, W.F.: Decay of superfluid turbulence at a very low temperature: the radiation of sound from a Kelvin wave on a quantized vortex. Phys. Rev. B **64**, 134520 (2001)
Vinen, W.F.: Theory of quantum grid turbulence in superfluid ^{3}He-B. Phys. Rev. B **71**, 024513 (2005)
Vinen, W.F.: An introduction to quantum turbulence. J. Low Temp. Phys. **145**, 7–24 (2006)
Vinen, W.F.: Quantum turbulence: achievements and challenges. J. Low Temp. Phys. **161**, 419–444 (2010)
Vinen, W.F., Niemela, J.J.: Quantum turbulence. J. Low Temp. Phys. **128**, 167–231 (2002)
Vinen, W.F., Tsubota, M., Mitani, A.: Kelvin-wave cascades in turbulent superfluid ^{4}He at very low temperatures. J. Low Temp. Phys. **134**, 457–462 (2004)
Volovik, G.E.: Classical and quantum regimes of the superfluid turbulence. JETP Lett. **78**, 533–537 (2003)
Volovik, G.E.: On developed superfluid turbulence. J. Low Temp. Phys. **136**, 309–327 (2004)
Walmsley, P.M., Golov, A.I.: Quantum and quasiclassical types of superfluid turbulence. Phys. Rev. Lett. **100**, 245301 (2008)
Yepez, J., Vahala, G., Vahala, L., Soe, M.: Superfluid turbulence from quantum Kelvin wave to classical Kolmogorov cascades. Phys. Rev. Lett. **103**, 084501 (2009)
Yoshida, K., Arimitsu, T.: Inertial-range structure of Gross–Pitaevskii turbulence within a spectral closure approximation. J. Phys. A: Math. Theor. **46**, 335501 (2013)
Zuccher, S., Caliari, M., Baggaley, A.W., Barenghi, C.F.: Quantum vortex reconnections. Phys. Fluids **24**, 125108 (2012)

Chapter 7
Incompressible Homogeneous Anisotropic Turbulence: Pure Rotation

7.1 Physical and Numerical Experiments

Rotation of the reference frame is an important factor in certain mechanisms of flow instability, and the study of rotating flows is interesting from the point of view of turbulence modelling in fields as diverse as engineering (e.g. turbomachinery and reciprocating engines with swirl and tumble), geophysics and astrophysics. Effects of mean curvature or of advection by a large eddy can be tackled using similar approaches. In this chapter, the emphasis is put to the dynamics of turbulence subjected to a solid body rotation with constant angular velocity. Considering rotation with angular velocity Ω around the axis $\boldsymbol{e}_3$, the mean flow gradient matrix and mean flow displacement gradient matrix are given by the following expressions (see Sect. 2.1.9):

$$\mathbf{A} = \begin{pmatrix} 0 & -\Omega & 0 \\ \Omega & 0 & 0 \\ 0 & 0 & 0 \end{pmatrix}, \quad \mathbf{F} = \begin{pmatrix} \cos \Omega t & -\sin \Omega t & 0 \\ \sin \Omega t & \cos \Omega t & 0 \\ 0 & 0 & 1 \end{pmatrix}. \tag{7.1}$$

This expression for $\mathbf{A}$ is obtained setting $S = 0$ in Eq. (2.69).

Some commonly agreed statements have been drawn from several experimental, theoretical and numerical studies, in which rotation is suddenly applied to homogeneous turbulence. The main results are summarized below:

- Rotation inhibits the energy cascade, so that the dissipation rate is reduced (Bardina et al. 1985; Jacquin et al. 1990). This is illustrated in Fig. 7.1.
- The initial three-dimensional (3D) isotropy is broken, so that a moderate anisotropy, consistent with a transition from a 3D to a 2D state, can develop. Anisotropy is more reflected in integral lengthscales with various components than in Reynolds stresses (Jacquin et al. 1990; Cambon et al. 1997). Typical results are shown in Fig. 7.2.
- Elongated vortical structures are generated, with an asymmetry in terms of cyclonic and anticyclonic axial vorticity (Bartello et al. 1994; Morize et al. 2005; Biferale et al. 2016), structures with cyclonic vorticity being observed to be dominant.

P. Sagaut and C. Cambon, *Homogeneous Turbulence Dynamics*,
https://doi.org/10.1007/978-3-319-73162-9_7

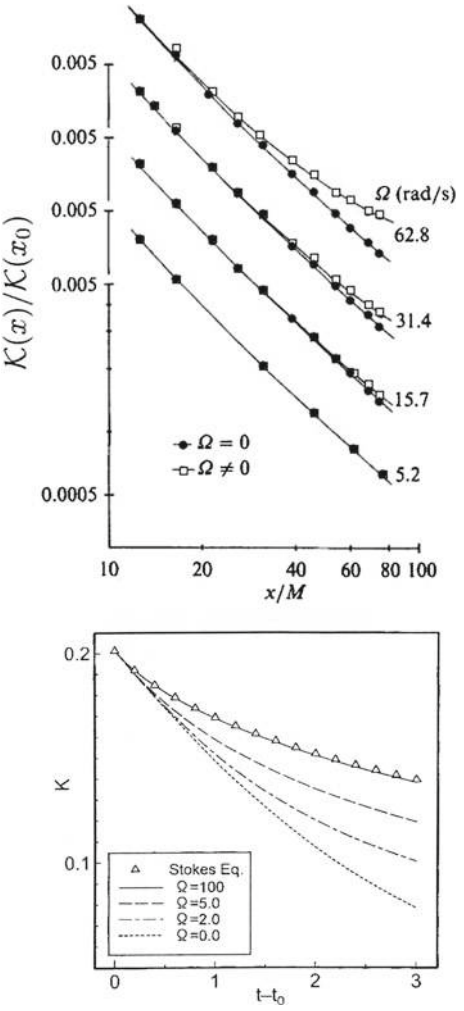

Fig. 7.1 Time evolution of the turbulent kinetic energy in initially isotropic turbulence submitted to solid body rotation. Top: experimental data from Jacquin et al. (1990), with permissions of CUP; Bottom: DNS data from Morinishi et al. (2001), with permissions of AIP. The decay rate is observed to be a decreasing function of the rotation rate Ω. At very high rotation rate, DNS results perfectly match the decay recovered considering the linear Stokes equations, showing that the non-linear mechanisms are totally inhibited. The rotation rate Ω is not expressed in the same units in the two plots

Cyclonic eddies are characterized by a positive fluctuating vorticity in the axial direction $\omega_{\parallel} = \omega_i n_i > 0$ ($= \omega_3$ with a particular choice of frame), seen in the rotating frame: they correspond to eddies rotating with the same sense as system vorticity. Negative axial vorticity characterizes *anti-cyclonic eddies* in the same conditions.

- If the turbulence is initially anisotropic, the "rapid" effects of rotation (i.e. the linear dynamics described by the RDT approach) conserve a part of the anisotropy (called *directional anisotropy* $b_{ij}^{(dir)}$) and damp the other part (called *polarization anisotropy* $b_{ij}^{(pol)}$), resulting in a spectacular change of the anisotropy b_{ij} of the Reynolds Stress tensor (Cambon et al. 1992; Kassinos et al. 2001).

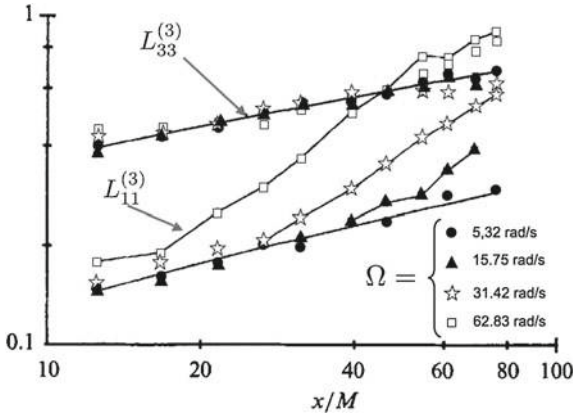

Fig. 7.2 Time evolution of the turbulence integral lengthscales in initially isotropic turbulence submitted to solid body rotation. Experimental data from Jacquin et al. (1990), with permissions of CUP

These effects, which are not at all taken into account by current one-point second order closure models (from $\mathcal{K} - \varepsilon$ to $\overline{u_i' u_j'} - \varepsilon$ models), have motivated new single-point modelling approaches by Cambon et al. (1992), Mansour et al. (1991), and to a lesser extent by Kassinos et al. (2001) for linear (or "rapid") effects only. It is worth noticing that the modification of the dynamics by the rotation ultimately comes from the presence of inertial waves (Greenspan 1968). Inertial waves have an anisotropic dispersion law. They are capable of changing the initial anisotropy of the turbulent flow and also can affect the non-linear dynamics. This explains the relevance of spectral theory to study HAT (Homogeneous Anisotropic Turbulence) with mean flow rotation.

7.1.1 Brief Review of Experiments, More or Less in the Configuration of Homogeneous Turbulence

A first class of experiments consists of decaying grid turbulence in a wind tunnel, in which a rotation generator creates a constant angular velocity in the streamwise direction. In the experiment by Traugott (1958), the rotation was imposed in the annular region between two coaxial rotating discs. This study is mentioned for our record, but very few information can be obtained, because of the non-uniformity of the mean flow and the very short length of the duct. The experiment by Wigeland and Nagib (1978) introduced a much better rotation generator. In this setup, solid body rotation was enforced thanks to a cylindrical rotating honey comb, with the grid just behind and attached to the rotating cylinder. This rotating device was successfully used by Jacquin et al. (1990) (see Fig. 7.3) but in a much larger wind tunnel, fulfilling homogeneity with an excellent accuracy and yielding reliable results about kinetic energy decay, Reynolds stress components, integral lengthscales and one-dimensional energy spectra. The results can be analyzed as in a conventional

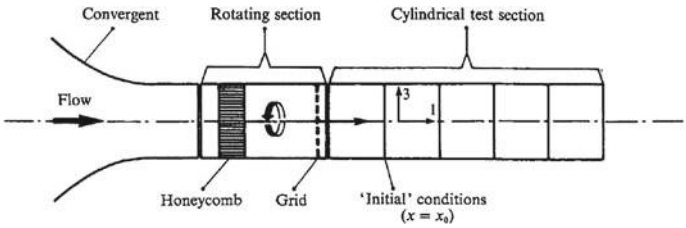

Fig. 7.3 ONERA's experimental setup for initially decaying isotropic turbulence submitted to solid body rotation. Courtesy of O. Leuchter

grid-generated turbulence experiment, the streamwise spatial coordinate playing the role of the elapsed time. A large range of "initial" (in the first transverse section chosen closely downstream to the grid) Rossby numbers was covered. The only drawback of this experiment was the initially moderate value, and monotonic decrease, of the Reynolds number, as usual in grid-generated turbulence.

A second class of experiments were carried out in a rotating tank, a diffusive turbulence being created by an oscillating grid (Hopfinger et al. 1982; Dickinson and Long 1984) near the bottom of the tank. The turbulence is essentially inhomogeneous in the vertical, axial, direction, and statistically steady. The steady state is different in different horizontal sections, moving away from the grid. In the experiment by Ibbetson and Tritton (1975), an unsteady turbulence was created by the initial motion of perforated plates in a rotating torical annulus with square section.

Another interesting experiment was carried out by Mc Ewan (1976). A radially uniform, small-scale mixing pattern without advection in the radial plane, was obtained in a rotating transparent cylinder by injecting and pumping fluid from the perforated plane-ended bottom. Polystyrene beads were suspended in the fluid and illuminated by a stroboscope to visualise the flow motion. Without rotation, the jets caused randomly shape wiggly particle paths, whereas intense vortices, always cyclonic, were observed in the presence of rotation.

The development of Particle Image Velocimetry (PIV) measurements was beneficial to these types of experiments, with renewed interest for the spatial structure of the rotating flow. The experiment by Baroud et al. (2003) used a very special forcing by jets in an annulus in the rotating tank. Despite specific non-homogeneity and anisotropy are generated by the forcing process, in a way difficult to control and to compare with the sole effect of rotation, useful conclusions about scaling laws were drawn from the experimental results. Some of these results being consistent with those of the experiment by Simand (2002) dealing with turbulence near the core of a strong vortex, they will be discussed at the end of this chapter (see Sect. 7.7.6). Another experiment by Praud et al. (2006), carried out in the Coriolis platform in Grenoble, deserves attention. It will be discussed in Chap. 11, since it combined solid body rotation and vertical stable stratification. In addition, the use of a rake instead of a grid yielded a preferential forcing of the horizontal motion.

The experiment by Morize et al. (2005) has something to do with the experiment by Ibbetson & Tritton, with the grid being moved only in a first phase, before studying the free decay in a rotating tank. This experiment aimed at reproducing initially homogeneous isotropic turbulence suddenly set into solid body rotation, but at higher Reynolds number than in Jacquin's experiment, and using modern PIV anemometry. Non-homogeneity and anisotropic forcing are prevented, as far as possible, by moving the grid, only in the phase of generation of initial turbulence, in the whole vertical extend of the tank. Another experimental study by Staplehurst et al. (2008) appears to fulfil even better homogeneous conditions than the latter one, especially in removing some mean flow spurious components.

Detailed results of these experiments are not discussed in this section. Results dealing with quasi-homogeneous turbulence will be emphasized and discussed throughout this chapter, inhomogeneous effects being briefly considered in Sects. 7.7 and 7.8.

7.2 Governing Equations

7.2.1 Generals

The problem of turbulence subjected to solid-body rotation can be directly related to the case of turbulence in the presence of a mean flow with space-uniform gradients, provided a purely antisymmetric mean velocity gradient matrix is chosen, i.e. $A_{ij} = \epsilon_{ikj}\Omega_k$, where $\boldsymbol{\Omega}$ is the angular velocity, in agreement with Eq. (7.1). But it is simpler to work with a coordinate system and velocity vectors defined in the steadily rotating frame. In this *non-Galilean* frame, rotation of the frame only introduces inertial forces, namely centrifugal and Coriolis forces. Since the former can be incorporated in the pressure term, only the latter has to be explicitly taken into account when writing the Navier–Stokes equations in the rotating frame:

$$\frac{\partial \boldsymbol{u}}{\partial t} + 2\boldsymbol{\Omega} \times \boldsymbol{u} + \boldsymbol{\nabla} p = \nu \nabla^2 \boldsymbol{u} - \mathbf{u} \cdot \boldsymbol{\nabla} \boldsymbol{u}. \tag{7.2}$$

As usual in incompressible fluid dynamics, the pressure term is completely determined by the solenoidal condition $\boldsymbol{\nabla} \cdot \boldsymbol{u} = 0$. Taking the Divergence and the Curl of these equations yields

$$\nabla^2 p - 2\boldsymbol{\Omega} \cdot \boldsymbol{\omega} = -\frac{\partial u_j}{\partial x_i}\frac{\partial u_i}{\partial x_j} \tag{7.3}$$

and

$$\frac{\partial \omega_i}{\partial t} + u_j \frac{\partial \omega_i}{\partial x_j} - 2\Omega_l \frac{\partial u_i}{\partial x_l} = \omega_l \frac{\partial u_i}{\partial x_l} + \nu \nabla^2 \omega_i. \tag{7.4}$$

In all the equations given above, nonlinear and viscous terms are gathered on the right-hand-side.

7.2.2 *Important Non-dimensional Numbers. Particular Régimes*

Using a reference velocity scale U and a reference length scale L, so that $u_i = \tilde{u}_i U$, $x_i = \tilde{x}_i L$, $\boldsymbol{\nabla} = \tilde{\boldsymbol{\nabla}} \frac{1}{L}$, Eq. (7.2) becomes

$$\frac{\partial \tilde{\boldsymbol{u}}}{\partial \tilde{t}} + \frac{1}{Ro} \boldsymbol{n} \times \tilde{\boldsymbol{u}} - \frac{1}{Re} \tilde{\nabla}^2 \tilde{\boldsymbol{u}} + \frac{L}{U^2} \boldsymbol{\nabla} p = -\tilde{\boldsymbol{u}} \cdot \tilde{\boldsymbol{\nabla}} \tilde{\boldsymbol{u}}, \tag{7.5}$$

in which only non-dimensional quantities appear (except in the pressure term, which is further discussed below). The unit vector $\boldsymbol{n}$ is chosen so that $\boldsymbol{\Omega} = \boldsymbol{n}\Omega$. In addition to the Reynolds number Re, the Rossby number

$$Ro = \frac{U}{2\Omega L} \tag{7.6}$$

is displayed. In the latter equation, the time scale was taken equal to L/U. Another possibility is to choose $1/2\Omega$ as the time scale, leading to $t = 2\Omega \tilde{t}$,[1] and

$$\frac{\partial \tilde{\boldsymbol{u}}}{\partial \tilde{t}} + \boldsymbol{n} \times \tilde{\boldsymbol{u}} - \frac{Ro}{Re} \tilde{\nabla}^2 \tilde{\boldsymbol{u}} + \frac{1}{2\Omega U} \boldsymbol{\nabla} p = -Ro \tilde{\boldsymbol{u}} \cdot \tilde{\boldsymbol{\nabla}} \tilde{\boldsymbol{u}}, \tag{7.7}$$

so that the Rossby number only affects the nonlinear term. The term Ro/Re is the inverse of the Ekman number. The linear inviscid limit is recovered by discarding the right-hand-side, assuming very low Rossby number and very high Ekman number. The pressure term is not so easy to treat. Following Eq. (7.3), it must be split into a linear part and a nonlinear part which scale as $\frac{1}{Ro} U^2/L$ and U^2/L, respectively.

Applying the same scaling to Eq. (7.4) yields:

$$\frac{\partial \tilde{\omega}_i}{\partial \tilde{t}} - \frac{1}{Ro} n_l \frac{\partial \tilde{u}_i}{\partial \tilde{x}_l} = \tilde{\omega}_l \frac{\partial \tilde{u}_i}{\partial \tilde{x}_l} + \frac{1}{Re} \tilde{\nabla}^2 \tilde{\omega}_i \tag{7.8}$$

in the first case, and

$$\frac{\partial \tilde{\omega}_i}{\partial \tilde{t}} - n_l \frac{\partial \tilde{u}_i}{\partial \tilde{x}_l} = Ro \tilde{\omega}_l \frac{\partial \tilde{u}_i}{\partial \tilde{x}_l} + \frac{Ro}{Re} \tilde{\nabla}^2 \tilde{\omega}_i \tag{7.9}$$

in the second case. The *Proudman theorem* is conventionally derived from Eq. (7.8), in the limit of zero Rossby number, so that

[1] Possible slightly different scalings are $t = \tilde{t} \frac{\Omega}{2\pi}$ and $t = \tilde{t} \frac{2\Omega}{2\pi}$.

$$n_j \frac{\partial \tilde{u}_i}{\partial \tilde{x}_j} = 0 \tag{7.10}$$

characterizes a 2D state, in the sense that the dependency of velocity upon the axial coordinate $x_\parallel = \boldsymbol{x}\cdot\boldsymbol{n}$ vanishes at high rotation rate. Accordingly, the velocity equation reduces to the *geostrophic balance* in the same conditions, or

$$\tilde{\nabla}\tilde{p} = \boldsymbol{n} \times \tilde{\boldsymbol{u}}. \tag{7.11}$$

On the other hand, choosing Ω^{-1} as the time scale, the zero-Rossby limit only leads to the linear regime, i.e.

$$\frac{\partial \tilde{\boldsymbol{u}}}{\partial \tilde{t}} + \boldsymbol{n} \times \tilde{\boldsymbol{u}} + \tilde{\nabla}\tilde{p} = 0 \tag{7.12}$$

$$\tilde{\nabla}^2 \tilde{p} - \boldsymbol{n}\cdot\tilde{\boldsymbol{\omega}} = 0 \tag{7.13}$$

$$\frac{\partial \tilde{\omega}_i}{\partial \tilde{t}} - n_l \frac{\partial \tilde{u}_i}{\partial \tilde{x}_l} = 0. \tag{7.14}$$

It is important to note that the conditions for having a complete two-dimensionalization are very stringent, since both linear and steady limits must be reached at the same time. Taylor columns were found in beautiful historical experiments of rotating laminar flows (Taylor 1921), for instance when Taylor *slowly* pushed a coin in the bottom of his rotating tank. In a rapidly rotating turbulent flow, it is clear that these conditions are not fulfilled at small but nonzero Rossby number, since nonlinear effects, even weak at a given time, can accumulate over a long time and induce a modified cascade, which is not necessarily the conventional 2D cascade. Anyway, the transition from 3D to 2D structure is essentially an unsteady —transition requires evolution !— and nonlinear process, as will be seen below. The linear régime consists of unsteady wave motion, which becomes steady (zero dispersion frequency) only in the 2D limit. Consequently, the Taylor–Proudman theorem (Proudman 1916; Taylor 1921) will be used in a restricted sense here: the steady mode of the motion is the 2D mode in the linear régime of rapidly rotating flow. Non-dimensional equations will no longer be used in this chapter, but the choice of relevant scales, L, U and Ω, remains an important issue, allowing to define different, e.g. macro and micro, Rossby and Reynolds numbers.

7.3 Advanced Analysis of Energy Transfer via DNS

The striking decrease in the dissipation rate of kinetic energy has been intensively investigated using Direct Numerical Simulation. The main findings are summarized below, before being analyzed in the rest of this chapter through linear and non-linear theories.

Main observations are the following:

- Rotation induces a deep modification of the kinetic energy transfer function $T(k)$. Spherically averaged profiles of $T(k)$ are displayed in Fig. 7.4. Both its shape and amplitude are drastically modified, resulting in a dramatic reduction of the kinetic energy cascade.
- Both the forward and the reverse energy cascade are affected by rotation. They both vanish, as illustrated in Fig. 7.5.
- This modification is due to the so-called *phase scrambling* phenomenon,[2] which originates in the fact that the transfer function $T(k)$ is generated by triadic contributions which are differentially affected by oscillations, depending on the angle θ between the wave vector $\boldsymbol{k}$ and the rotation vector $\boldsymbol{\Omega}$, not to mention similar effects on the other vectors of each triad. This is illustrated in Fig. 7.6, which displays $T(k, \cos\theta)$ for different values of Ω. The usual dynamical picture is recovered in the case $\Omega = 0$, while in the cases $\Omega \neq 0$, regions with negative/positive values of $T(k)$ are more and more mixed, leading to a weakening of the kinetic energy cascade.
- The effect of rotation is visible for a certain range of Rossby number only. Very small rotation rate yields a negligible influence of rotation, while very high rotation rates lead to an almost complete inhibition of the non linear kinetic energy cascade, resulting in a "frozen" field submitted to linear viscous effects. Partial two-dimensionalization and two-componentalization, resulting from fully nonlinear dynamics, is illustrated in Fig. 7.7, which presents the evolution of directional anisotropy component $b_{33}^{(dir)}$ and the polarization anisotropy coefficient $b_{33}^{(pol)}$ (firstly defined in Chap. 2) as a function of the Rossby number. The meaning and the behavior of these descriptors will be rediscussed at length throughout this chapter.

Of course, present DNS results are limited in terms of Reynolds numbers and elapsed time, and very long evolution time Ωt is required to capture nonlinear effects at very low Rossby numbers. This explains some of the discrepancies observed between DNS, LES and statistical theory, as discussed later on. Fortunately, a very consistent core of agreed statements arises from this threefold approach, not to mention experimental data.

7.4 Balance of RST Equations. A Case Without "Production". New Tensorial Modelling

The Reynolds stress equations for HAT submitted to the solid body rotation defined by Eq. (7.1) are

[2]This effect could be perhaps better denoted as phase-mixing, in connection with the very angle-dependent dispersion relation of inertial waves, as we will discuss on the ground of basic equations.

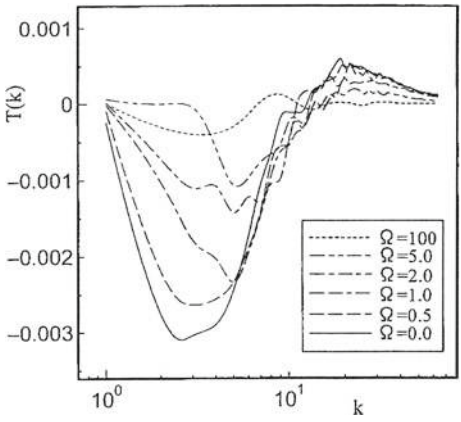

Fig. 7.4 Spherically averaged energy transfer function $T(k)$ in initially decaying isotropic turbulence submitted to solid body rotation, for different rotation rates. From Morinishi et al. (2001) with permission of American Institute of Physics

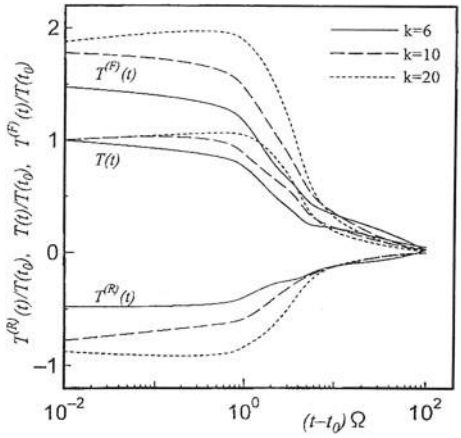

Fig. 7.5 Time evolution of the full transfer function $T(k)$, the forward transfer function $T^{(F)}(k)$ and the backward transfer function $T^{(R)}(k)$ in initially decaying isotropic turbulence submitted to solid body rotation, for different rotation rates. One has $T(k) = T^{(F)}(k) + T^{(R)}(k)$. Different values of k are considered. From Morinishi et al. (2001) with permission of American Institute of Physics

$$\frac{\partial \overline{u_i' u_j'}}{\partial t} + \overline{u}_k \frac{\partial \overline{u_i' u_j'}}{\partial x_k} = -\Omega \begin{pmatrix} -2\overline{u_1' u_2'} & \overline{u_1' u_1'} - \overline{u_2' u_2'} & -\overline{u_2' u_3'} \\ \overline{u_1' u_1'} - \overline{u_2' u_2'} & 2\overline{u_1' u_2'} & \overline{u_1' u_3'} \\ -\overline{u_2' u_3'} & \overline{u_1' u_3'} & 0 \end{pmatrix} + \Pi_{ij} - \varepsilon_{ij}. \tag{7.15}$$

A careful examination of Eq. (7.15) reveals that the production term is identically zero if the turbulent field is isotropic at the initial time. Therefore explicit coupling between the mean flow and the turbulent field is not responsible for the triggering of the departure from isotropy; pressure effects are responsible for this.

Considering only the most relevant Reynolds stress components (this is more general than specifying initial isotropy or initial anisotropy), so that $\overline{u_\alpha' u_3'} = \overline{u_3' u_\alpha'} = 0$, $\alpha = 1, 2$, the system (7.15) simplifies as

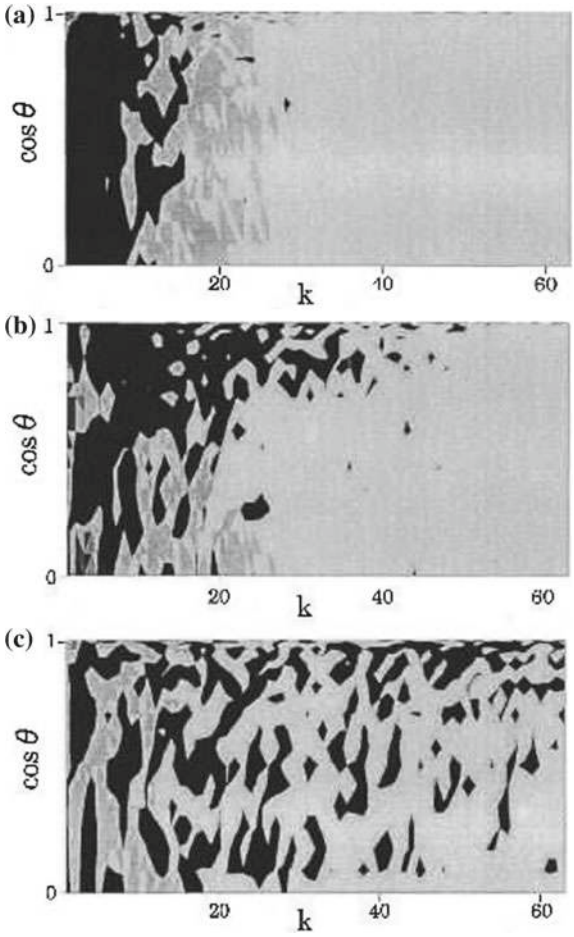

Fig. 7.6 Instantaneous plot of the transfer function $T(k)$ as a function of k and θ, which is defined has the angle between $\boldsymbol{k}$ and $\boldsymbol{\Omega}$. Top: no rotation ($\Omega = 0$), middle: medium rotation rate, bottom: strong rotation rate. Dark region corresponds to negative value, and the other regions to positive values. From Morinishi et al. (2001) with permission of American Institute of Physics

$$\begin{cases} \dfrac{d\overline{u_1'u_1'}}{dt} = +2\Omega\overline{u_1'u_2'} & +\Pi_{11} \; -\varepsilon_{11} \\ \dfrac{d\overline{u_2'u_2'}}{dt} = -2\Omega\overline{u_1'u_2'} & +\Pi_{22} \; -\varepsilon_{22} \\ \dfrac{d\overline{u_3'u_3'}}{dt} = & \Pi_{33} \; -\varepsilon_{33} \\ \dfrac{d\overline{u_1'u_2'}}{dt} = \Omega(\overline{u_2'u_2'} - \overline{u_1'u_1'}) & +\Pi_{12} \; -\varepsilon_{12} \end{cases} . \tag{7.16}$$

The different couplings are illustrated in Fig. 7.8.

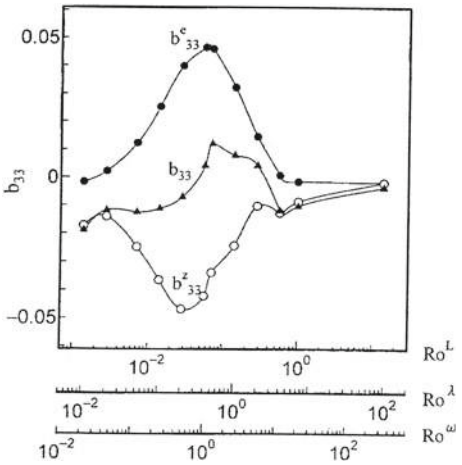

Fig. 7.7 Evolution of the directional anisotropy component $b_{33}^{(dir)}$ (denoted $b_{33}^{(e)}$ on the figure) and the polarization anisotropy component $b_{33}^{(pol)}$ (denoted $b_{33}^{(z)}$ on the figure) as a function of the Rossby number. Three Rossby numbers are shown: the macro-Rossby number $Ro^L = \sqrt{\mathcal{K}}/2\Omega L$, the Taylor micro-Rossby number $Ro^\lambda = \sqrt{\mathcal{K}}/2\Omega\lambda$, and the micro-Rossby number $Ro^\omega = \omega'/2\Omega$, in which $L = \mathcal{K}^{3/2}/\varepsilon$ and ω' denotes the rms vorticity fluctuation. From Morinishi et al. (2001) with permission of American Institute of Physics

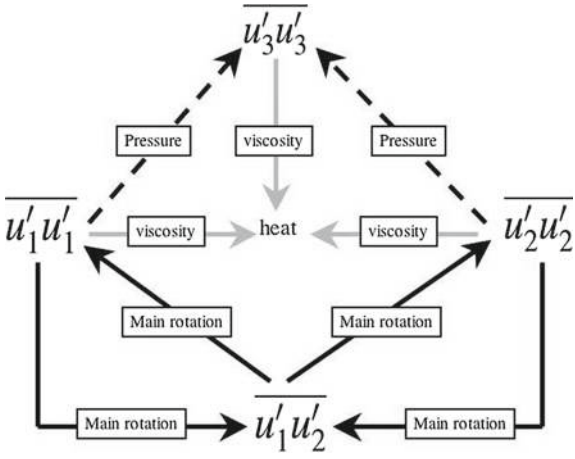

Fig. 7.8 Couplings between the different non-vanishing Reynolds stresses in the pure rotation case. Arrows indicate the production process, their color being related to the physical quantity at play (mean strain, pressure, viscosity)

These equations can be rearranged in order to diagonalize the production term, introducing the three deviatoric components (Cambon et al. 1992)

$$A = \overline{u_3'u_3'} - \frac{1}{2}(\overline{u_1'u_1'} + \overline{u_2'u_2'}); \quad B = \frac{1}{2}\overline{(u_1' + \imath u_2')^2}.$$

The above system of equations results in

$$\begin{cases} \dfrac{d\mathcal{K}}{dt} = & -\varepsilon \\ \dfrac{dA}{dt} = & \Pi_A^{(r)} + \Pi_A^{(s)} \\ \dfrac{dB}{dt} = & 4\iota\Omega B + \Pi_B^{(r)} + \Pi_B^{(s)} \end{cases}, \tag{7.17}$$

in which pressure-strain and dissipation-rate components are derived in a trivial way, following the rules for deriving $\mathcal{K}$, A, B from the Reynolds stress original components. For convenience, pressure-strain rate contributions are split into a "rapid" linear (superscript $^{(r)}$) and a "slow" nonlinear (superscript $^{(s)}$) contribution. Possible deviatoric contributions from the dissipation tensor are included in the "slow" term.

Almost all the principles for single-point modelling are questioned in the case of rotating turbulence. Looking at the turbulent kinetic energy, the exact $\mathcal{K} - \varepsilon$ equations do not include any explicit additional term with respect to the isotropic non-rotating case, since the Coriolis force produces no work (as evidenced from the first equation of (7.17)). The only way to take into account alteration of the kinetic energy decay is to modify the $C_{\epsilon 2}$ constant in the evolution equation for the turbulent dissipation (4.234). Empirical ways to render this constant sensitive to the Rossby number (Bardina et al. 1985; Aupoix et al. 1983) are discussed in Cambon et al. (1992).

A more rational way consists of modeling the inbalance between the production (non-linear gradient self-amplification) and the destruction (dissipation) in the ε-equation, as reported in Cambon et al. (1997). Using results of Sect. 4.11.3, the exact equation for the dissipation rate is

$$\frac{d\varepsilon}{dt} = 2\nu\overline{\omega_i'\omega_j' u_{i,j}'} - 2\nu^2\overline{\omega_{i,j}'\omega_{i,j}'},$$

in rotating and non-rotating homogeneous turbulence, without any *explicit* contribution from the Coriolis force. Using an adequate scaling, the velocity derivative skewness S_k is linked to the enstrophy-production term by the following relation

$$S_k = \frac{6\sqrt{15}}{7}\nu\overline{\omega_i'\omega_j' u_{i,j}'}\frac{\mathcal{K}}{\varepsilon^2}Re^{-1/2},$$

in which Re is a macro-Reynolds number and the numerical prefactor comes from the conventional definition of the skewness used by experimentalists in isotropic turbulence. A second non-dimensional parameter was defined by Mansour et al. (1991) to account for the departure of the enstrophy-destruction term from its conventional evaluation in the non-rotating case

$$G = \frac{3\sqrt{15}}{7}\left(2\nu^2\overline{\omega_{i,j}'\omega_{i,j}'} - C_{\varepsilon 2}(Re)\frac{\varepsilon^2}{\mathcal{K}}\right)\frac{\mathcal{K}}{\epsilon^2}Re^{-1/2}.$$

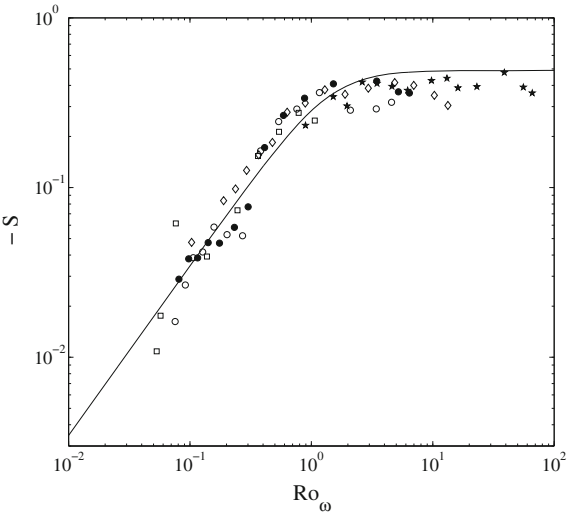

Fig. 7.9 Experimental measurements of velocity derivative skewness S_k, denoted $-S$ on the figure, plotted in terms of the micro Rossby number Ro_ω. Symbols: experimental data; Solid line: Eq. (7.19). From Morize et al. (2005) with permission of AIP

A modified ε-equation is then recovered

$$\frac{d\varepsilon}{dt} = \left(\frac{7}{3\sqrt{15}} (S_k - G) Re^{1/2} - C_{\varepsilon 2}(Re) \right) \frac{\varepsilon^2}{\mathcal{K}}, \tag{7.18}$$

where S_k is the only term which accounts for triple correlations directly affected by rotation. The non-rotating case is simply recovered taking $S_k = G$, whereas a four-equations model (whose unknowns are $\mathcal{K}$, ε, S and G) was proposed by Mansour et al. (1991) in the rotating case. This model was supported by EDQNM and full DNS in Cambon et al. (1997), with the following asymptotic model for the velocity gradient skewness

$$S_k = \frac{S_k(0)}{\sqrt{1 + 2/Ro_\omega^2}}, \quad Ro_\omega = \frac{\omega'}{2\Omega} \tag{7.19}$$

where Ro_ω is the micro Rossby number, and $S_k(0) \sim -0.49$ is the asymptotic value in isotropic turbulence without rotation. An almost perfect collapse onto this curve was also recovered in the experimental study by Morize et al. (2005), as shown in Fig. 7.9.

The accuracy of description and/or prediction provided by conventional single-point models is even worse regarding the anisotropy. In spite of the strong anisotropy evidenced in two-point (or spectral) descriptions which is mainly reflected by the integral lengthscales in physical space, the deviatoric part of the Reynolds stress tensor is a very poor indicator. The condition of statistical axisymmetry implies

$$b_{ij} = -\frac{3}{2} b_{in} n_i n_j \left(\frac{\delta_{ij}}{3} - n_i n_j \right), \tag{7.20}$$

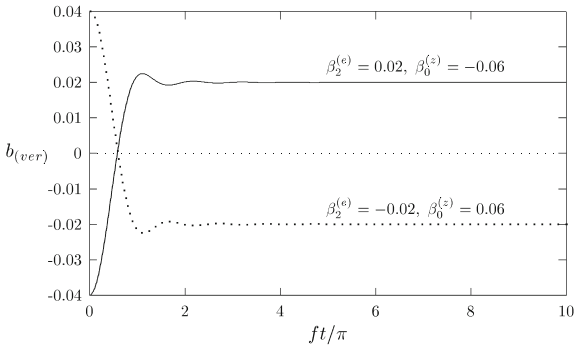

Fig. 7.10 Linear evolution of b_{33} ($= b_{(ver)}$) under rapid rotation. $\beta_2^{(e)} = b_{33}^{(dir)}(0)$, $\beta_0^{(z)} = b_{33}^{(pol)}$. Reproduced from Salhi and Cambon (2007) with permission of AIP

so that a single component $b_{ij}n_in_j$ (b_{33} in the present case, proportional to A in Eq. (7.17)) is enough to describe the full anisotropy tensor (and therefore the corresponding line in the Lumley's map is only needed). A similar relationship is valid for any trace-free single-point tensor. Restricting our attention to the linear régime, rapid rotation applied to an initially anisotropic flow yields conservation of directional anisotropy $b_{ij}^{(dir)}$ and rapid damping of polarization anisotropy $b_{ij}^{(pol)}$. This effect is completely missed in any conventional single-point closure model, in which only b_{ij} is used. The latter effect was called "rotational randomization" by Kassinos et al. (2001), but can be more physically related to anisotropic phase-mixing induced by dispersive inertial waves (e.g. Cambon et al. 1992; Kaneda and Ishida 2000). As an illustration, the case of axisymmetric initial anisotropy is shown in Fig. 7.10.

The rapid change of the relevant anisotropy ratio corresponds to the evolution from the initial state in which $b_{33}^{(dir)}(0) = -\frac{1}{2}b_{33}(0)$ and $b_{33}^{pol}(0) = \frac{3}{2}b_{33}(0)$ (e.g. as in the flow generated by an axisymmetric duct) to a final state in which $b_{33} = b_{33}^{(dir)}(0) = -\frac{1}{2}b_{33}(0)$, due to the conservation of $b_{33}^{(dir)}$ and rapid (about a quarter of a revolution) damping of $b_{33}^{(pol)}$. In the same "rapid" limit, no Reynolds stress model, even the most sophisticated one, yields an evolution of anisotropy. As a matter of fact, the initial anisotropy is conserved, since there is no production and any conventional closure of the rapid pressure strain tensor as a function of the sole Reynolds stress tensor yields a zero contribution in rotating axisymmetric homogeneous turbulence.

For instance, in the axisymmetric case, only the first two equations of (7.17) are relevant, and all classical closure models yield $\Pi_A^{(r)} = 0$, with $\Pi_A^{(s)} = 0$, in the rapid inviscid limit. Some improvements were independently proposed by Cambon et al. (1992) and Kassinos et al. (2001), using an implicit splitting in terms of directional and polarization anisotropy. Finally, the role conventionally attributed in Reynolds stress models to "rapid" and "slow" pressure-strain tensors is completely wrong in rotating turbulence: in the true rotating homogeneous turbulence case, the rapid (linear) part contributes to a partial return to isotropy (i.e. a damping of $b_{33}^{(pol)}$), whereas the slow (non-linear) part must generate a mild anisotropy associated with the component b_{33} (or equivalently A in Eq. (7.17)) indirectly connected to the transition from 3D to 2D structure.

7.5 Inertial Waves. Linear Régime

7.5.1 Analysis of Deterministic Solutions

Linearized inviscid equations, written in a non-dimensional form at the end of Sect. 7.2, are revisited here for velocity, pressure and vorticity. Equations are rewritten in dimensional form for physical discussions:

$$\frac{\partial \boldsymbol{u}}{\partial t} + 2\boldsymbol{\Omega} \times \boldsymbol{u} + \nabla p = 0, \qquad \nabla \cdot \boldsymbol{u} = 0 \tag{7.21}$$

$$\nabla^2 p - 2\Omega \boldsymbol{n} \cdot \boldsymbol{\omega} = 0 \tag{7.22}$$

$$\frac{\partial \omega_i}{\partial t} - 2\Omega \frac{\partial u_i}{\partial x_\parallel} = 0. \tag{7.23}$$

Since the Coriolis force is not divergence-free, the pressure term has a nontrivial contribution to enforce the incompressibility constraint. A closed sub-system of equations can be used for $u_\parallel = \boldsymbol{u} \cdot \boldsymbol{n}$, p and $\omega_\parallel = \boldsymbol{\omega} \cdot \boldsymbol{n}$. Eliminating the axial components of velocity and vorticity in the latter subsystem, the following closed equation is found for p:

$$\partial_t^2 \left(\nabla^2 p \right) + 4\Omega^2 \nabla_\parallel^2 p = 0, \tag{7.24}$$

with $\nabla_\parallel^2 = \frac{\partial^2}{\partial x_\parallel^2}$. Even if the primitive Poisson equation $\nabla^2 p = f$ is an elliptic one, Eq. (7.24) admits propagating wave solutions. Very surprising properties of these inertial waves are illustrated by the St Andrew-cross shaped structures observed in experiments by Mc Ewan (1970) and Mowbray and Rarity (1967) (see Fig. 7.11). If a local harmonic forcing with frequency σ_0 takes place in a tank rotating at angular velocity Ω, simplified solutions can be sought using a normal mode decomposition. Considering normal modes of the form $p = e^{\imath \sigma_0 t} \mathcal{P}$, the spatial part is governed by

$$[\sigma_0^2 \nabla_\perp^2 + (\sigma_0^2 - 4\Omega^2) \nabla_\parallel^2] \mathcal{P} = 0.$$

which shows the possible transition from an elliptic to a hyperbolic problem when σ_0 crosses the threshold 2Ω by decreasing values. This transition explains the sudden appearance of the cross-shaped structures for $\sigma_0 < 2\Omega$. In spite of the rather complex geometry, one can assume, in addition, that the disturbances are plane waves, i.e. $p \sim e^{\imath(\boldsymbol{k} \cdot \boldsymbol{x} - \sigma_k t)}$. Injecting this solution into Eq. (7.24), the classical dispersion law of inertial waves is recovered

$$\sigma_k = \pm 2\Omega \frac{k_\parallel}{k} = \pm 2\Omega \cos\theta. \tag{7.25}$$

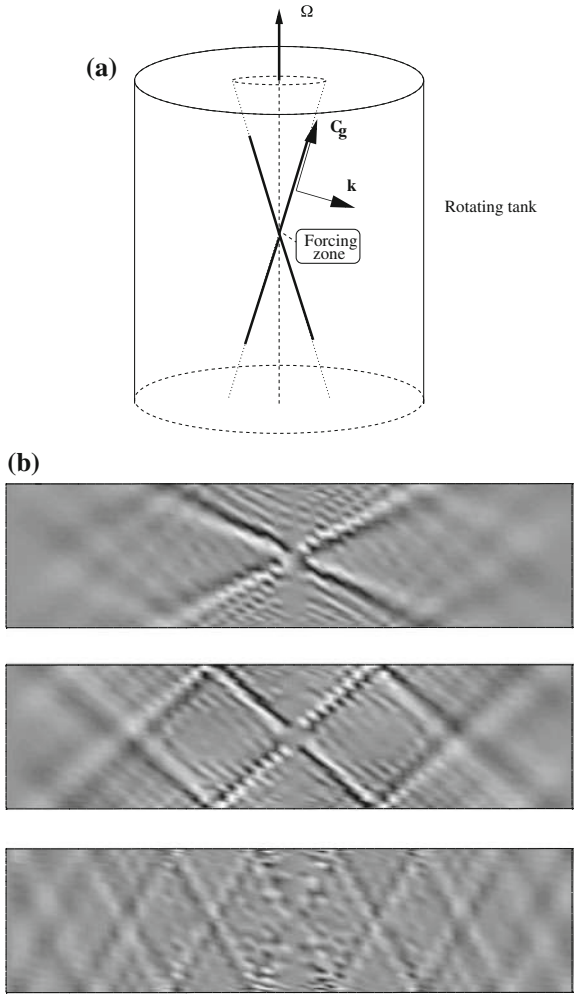

Fig. 7.11 Saint Andrew's Cross shaped structures in a rotating flow, **a** sketch of the experiments by Mc Ewan and Mowbray & Rarity, **b** results from DNS in a plane channel, rotating around the vertical axis. From top to bottom $2\Omega/\sigma_0 = 1.10, 1.33, 2$. Reproduced from Godeferd and Lollini (1999) with permission of CUP

The phase and group velocity of these inertial waves, denoted $\boldsymbol{C}_p(\boldsymbol{k})$ and $\boldsymbol{C}_g(\boldsymbol{k})$, respectively, are given by:

$$\boldsymbol{C}_p(\boldsymbol{k}) = 2\frac{\Omega\cos\theta}{k^2}\boldsymbol{k} = \frac{\sigma_k}{k^2}\boldsymbol{k} \tag{7.26}$$

$$\boldsymbol{C}_g(\boldsymbol{k}) = (\nabla\sigma_k)\cdot\boldsymbol{k} = \frac{2}{k^3}\boldsymbol{k}\times(\boldsymbol{\Omega}\times\boldsymbol{k}) = 2\frac{\Omega\sin\theta}{k}\boldsymbol{e}^{(2)} \tag{7.27}$$

where $\boldsymbol{e}^{(2)}$ is the vector of the local Craya–Herring frame in the Fourier space defined in Eq. (2.86).

If one interprets the rays emanating from the small forcing zone in the figure as traces of isophase surfaces, so that the wave vector is normal to them, Eq. (7.25) with $\sigma_k = \sigma_0$ gives the angle θ (defined as the angle between $\boldsymbol{k}$ and the rotation axis) in excellent agreement with the directions of the rays.

It is important to note that if pressure effects are omitted (leading to the definition of a pressure-released problem) only the horizontal part of the flow is affected by the circular periodic (with constant frequency 2Ω) motion, but propagating waves cannot occur. Hence, fluctuating pressure (through its linkage with the incompressibility constraint) is responsible both for anisotropic dispersivity and horizontal-vertical coupling.

Going back to velocity, an equation similar to (7.24) can be found for both poloidal and toroidal potentials defined in Eq. (2.25). Without forcing and boundary conditions, the specific initial-value linear problem takes the form

$$\frac{\partial \hat{u}_i}{\partial t} + 2\Omega P_{in}\epsilon_{n3j}\hat{u}_j = 0. \tag{7.28}$$

This equation is simpler than the generic one for the RDT problem addressed in the next chapter, since $\boldsymbol{x}$ and $\boldsymbol{u}$ in physical space are projected onto the rotating frame, so that there is no advection by the mean flow, and therefore no time shift in the wave vector.[3] Given the incompressibility constraint $\hat{\boldsymbol{u}}\cdot\boldsymbol{k} = 0$, it is easier to project the equation onto the local frame $(\boldsymbol{e}^{(1)}, \boldsymbol{e}^{(2)})$ normal to $\boldsymbol{k}$ defined by Eq. (2.86). The solution expresses that the initial Fourier component $\hat{\boldsymbol{u}}(\boldsymbol{k}, 0)$ is rotated about the axis $\boldsymbol{k}$ by an angle $2\Omega t k_\parallel/k = \sigma_k t$. The linear solution for the two-component velocity vector $u^{(\alpha)}$, $\alpha = 1, 2$ is

$$\begin{pmatrix} u^{(1)}(\boldsymbol{k}, t) \\ u^{(2)}(\boldsymbol{k}, t) \end{pmatrix} = \begin{pmatrix} \cos\sigma_k(t-t') & -\sin\sigma_k(t-t') \\ \sin\sigma_k(t-t') & \cos\sigma_k(t-t') \end{pmatrix} \begin{pmatrix} u^{(1)}(\boldsymbol{k}, t') \\ u^{(2)}(\boldsymbol{k}, t') \end{pmatrix}. \tag{7.29}$$

The corresponding linear solution in the fixed frame of reference for the initial value problem is

$$\hat{u}_i(\boldsymbol{k}, t) = G_{ij}(\boldsymbol{k}, t, t')\hat{u}_j(\boldsymbol{k}, t'), \tag{7.30}$$

in which the Green's function is expressed as a function of the two complex eigenvectors $\boldsymbol{N} = \boldsymbol{e}^{(2)} - \imath\boldsymbol{e}^{(1)}$ and $\boldsymbol{N}^* = \boldsymbol{N}(-\boldsymbol{k}) = \boldsymbol{e}^{(2)} + \imath\boldsymbol{e}^{(1)}$ in the plane normal to $\boldsymbol{k}$

$$G_{ij}(\boldsymbol{k}, t, t') = \sum_{s=\pm 1} N_i(s\boldsymbol{k})N_j(-s\boldsymbol{k})e^{\imath s\sigma_k(t-t')}. \tag{7.31}$$

[3] Of course, a strictly equivalent problem is defined by the equations of Sect. 2.1 written in a Galilean frame of reference, for a pure antisymmetric gradient matrix $A_{ij} = \Omega\epsilon_{i3j}$, with $\boldsymbol{k}(\Omega t)$ following the solid-body rotating motion.

The diagonal decomposition is particularly useful in the context of pure rotation, since $\boldsymbol{N}$ and $\boldsymbol{N}^*$ more generally generate the eigenmodes of the Curl operator, and directly appear in the $(\mathcal{E}, Z, \mathcal{H})$ decomposition (see Eq. (2.128)).

The main features of the inertial waves are summarized below. An inertial wave is:

(i) *a plane wave* which propagates along $\boldsymbol{k}$,
(ii) *a transverse wave*, since $\hat{\boldsymbol{u}}(\boldsymbol{k}, t) \perp \boldsymbol{k}$,
(iii) *a dissipative wave*. The damping factor associated with $\hat{\boldsymbol{u}}(\boldsymbol{k}, t)$ is equal to $e^{-\nu k^2 t}$, as deduced from a trivial extension of the inviscid linear analysis discussed above.

Complete linear solutions are often referred to as RDT solutions. Even if the above mentioned Green's function is a particular case of the ones defined in the general RDT theory, the terminology RDT is misleading in the case of rotating turbulence. First, there is no space-distortion: even in the Galilean frame of reference, strictly circular characteristic lines (i.e. mean trajectories) are found in physical space. This is easily seen writing the equation for these lines: $x_i = Q_{ij}(\Omega t) X_j$. A similar result is obtained in the spectral space, since $k_i = Q_{ij}(\Omega t) K_j$, where Q, which is equal to $\mathbf{F}$ in Eq. (7.1), is an orthogonal matrix. Therefore, the transformation has isometric properties. Second, the linear solution can be valid for a very long time, since the appearance of a significant nonlinear cascade is delayed with respect to the non-rotating case. The occurrence of phase mixing due to interactions between dispersive inertial waves is the best explanation for this depletion of non-linearity (recall that nonlinear effects do vanish in some DNS results, but keeping in mind limitations in terms of Reynolds number and in terms of elapsed time Ωt).

The linear régime of inertial waves has interesting properties, which can be discussed independently of any statistical treatment:

- the dispersion frequency is modulated by the angle-dependent term $\cos\theta$. This modulation reflects the role of fluctuating pressure in connection with $\boldsymbol{k}\cdot\hat{\boldsymbol{u}} = 0$, with a variation of σ_k from 0 (wave plane normal to $\boldsymbol{\Omega}$) to 2Ω (wave vector parallel to $\boldsymbol{\Omega}$). This wide range of dispersion frequencies allows for parametric resonances, either for linear processes (as for elliptical flow instability with weak additional strain discussed in Chap. 11) or for weakly nonlinear interactions (e.g. the wave-turbulence approximation, discussed in Sect. 7.6).
- the zero frequency is found for the wave plane normal to $\boldsymbol{\Omega}$: this illustrates the fact that the sole steady mode (i.e. zero frequency mode) is the two-dimensional mode ($k_\parallel = 0$ corresponds to $\partial/\partial x_\parallel = 0$ in the physical space), in agreement with (our restricted use of) the Taylor–Proudman theorem.
- the fact that the dispersion frequency depends on the orientation but not on the modulus of the wave vector is a very particular situation, encountered in other cases of *purely transverse pressure and vorticity waves*, like the internal gravity waves

addressed in Chap. 10. As a consequence, phase velocity and group velocity are orthogonal to each others. In the same way, the group velocity is found maximal and in the axial direction, when the phase velocity is near zero, close to the waveplane normal to $\boldsymbol{\Omega}$.

7.5.2 *Analysis of Statistical Moments. Phase-Mixing and Low Dimensional Manifolds*

Linear equations can be used to compute various statistical moments of the solution. For instance, the linear solution for the second-order spectral tensor equation is

$$\mathcal{E}(\boldsymbol{k},t)=\mathcal{E}(\boldsymbol{k},t_0),\quad \mathcal{H}(\boldsymbol{k},t)=\mathcal{H}(\boldsymbol{k},t_0),\quad Z(\boldsymbol{k},t)=e^{4\imath\sigma_k(t-t_0)}Z(\boldsymbol{k},t_0) \tag{7.32}$$

As a first consequence, an initially anisotropic flow is altered, with $b_{ij}^{(dir)}$ and $b_{ij}^{(pol)}$ being conserved and damped, respectively, as illustrated in Fig. 7.10. In counterpart, these equations yield no evolution for isotropic initial data, with $Z=\mathcal{H}=0$.

The concept of *phase-mixing* can be understood from Eqs. (7.30) and (7.31) in which the initial data term $\hat{\boldsymbol{u}}(\boldsymbol{k},t')$ could be replaced by a new slow time-evolving variable, $\mathcal{U}(\boldsymbol{k},\epsilon t,t')$. The impact of the basic Green's function, for instance in breaking 3D isotropy, depends on the order and on the degree of complexity of statistical moments (purely initial values or slowly evolving ones) to which it is applied.

Throughout this book, *manifold* means a sub-space of the spatial configuration space. The configuration space is defined in the 3D Fourier space for mathematical convenience. For instance, the *2D manifold* (also referred to as the *slow manifold* because $\sigma_k=0$ for modes belonging to this manifold) corresponds to the waveplane $k_\parallel=0$ embedded in 3D Fourier space (all $\boldsymbol{k}$). The *manifold of resonant triads* represents the subspace defined by $(\pm\sigma_k\pm\sigma_p\pm\sigma_q=0,\boldsymbol{k}+\boldsymbol{p}+\boldsymbol{q}=0)$, which is embedded in the space of all triads $(\boldsymbol{k}+\boldsymbol{p}+\boldsymbol{q}=0)$ in 6D (all $\boldsymbol{k}$, $\boldsymbol{p}$) Fourier space.

7.5.2.1 Single-Time Second-Order Statistics

Looking at single-time second-order statistics, isotropy is essentially conserved in the linear limit, since time dependency can cancel out by multiplying $e^{\imath\sigma_k t}$ by its complex conjugate. This result is often considered as too general, saying that phase information is lost in homogeneous turbulence (Davidson et al. 2006).

A refined analysis can be derived from Eq. (7.32). Both kinetic energy and directional anisotropy $b_{ij}^{(dir)}$ are conserved in the linear inviscid limit, whereas the polarization anisotropy, given by

$$2\mathcal{K}(0)b_{ij}^{(pol)}(t)=\iiint \Re\left(Z(k,x,0)e^{4\imath\Omega xt}N_iN_j\right)d^3\boldsymbol{k}\quad\text{with}\quad x=\cos\theta, \tag{7.33}$$

is essentially damped. This damping is a general effect obtained by summing up terms affected by different oscillations, here from 0 ($x = 0$) to 2Ω ($x = 1$). If initial data are axisymmetric with mirror symmetry, for instance, the relevant integral which illustrates the damping of $b_{ij}^{(pol)}$ is

$$I(k, \Omega t) = \int_0^1 C(k, x) \cos(4\Omega x t) dx,$$

which always tends to zero as the nondimensional time Ωt becomes large ($C(k, x)$ is taken equal to $(1 - x^2)\Re(Z(k, x, 0))$ in Eq. (7.33) for $i = j = 3$). The only exception is found when $C(x)$ has a non-integrable singularity: a simple instance is given by 2D-2C (i.e. two-dimensional two-component) initial data such that $Z(\boldsymbol{k}, 0) = -[E(k)/(2\pi k)]\delta(kx)$. It is clear from our very simple example that the phase-mixing, induced by the x-weighting term in the integrand via the frequency $4\Omega x$, is responsible for damping, whereas $x = 0$ may characterize a low-dimensional manifold which escapes the damping effect if it is singular.

Unexpected behavior of the Reynolds stress tensor results from the selective damping of the initial polarization anisotropy $b_{ij}^{(pol)}$, as shown in Fig. 7.10.

Useful dynamical properties, however, are recovered for two-time (t, t') second order statistics, with interesting applications to Lagrangian diffusivity as discussed in Kaneda and Ishida (2000) and Cambon et al. (2004), since time dependency cannot cancel out when multiplying $e^{\pm 2\imath\Omega x t}$ by $e^{\pm 2\imath\Omega x t'}$. These applications are briefly discussed in Sect. 11.2.5.

7.5.2.2 Single-Time Third Order Statistics

In this case the linear operator generates a product of three phase terms, $e^{\pm 2\imath(k_\parallel/k)\Omega t}$, $e^{\pm 2\imath(p_\parallel/p)\Omega t}$ and $e^{\pm 2\imath(q_\parallel/q)\Omega t}$, which are related to the triad $(\boldsymbol{k}, \boldsymbol{p}, \boldsymbol{q})$.

Triple velocity correlations which govern the nonlinear energy and anisotropy transfers in related Lin-type equations are considered in the next subsection: the effect of phase mixing, considered as linear if applied to triple correlations, is interpreted as nonlinear via the impact of transfer on energy distribution.

Triple correlations undergoing phase mixing can also be studied per se, as the triple vorticity correlations revisited in Sect. 7.8. Let us mention that in any cubic correlation, which is generated from triadic components $\langle \hat{u}_m(\boldsymbol{q}, t)\hat{u}_n(\boldsymbol{k}, t)\hat{u}(\boldsymbol{p}, t)\rangle$ with $\boldsymbol{k} + \boldsymbol{p} + \boldsymbol{q} = 0$, the phase-mixing is induced by the term

$$\exp\left[\imath 2\Omega t\left(s\frac{k_\parallel}{k} + s'\frac{p_\parallel}{p} + s''\frac{q_\parallel}{q}\right)\right],$$

which results from the above-mentioned product of three phase terms, the zero value of its phase corresponding to the manifold of resonant triads.

7.6 Nonlinear Theory and Modeling: Wave Turbulence and EDQNM

7.6.1 Full Exact Non-linear Equations. Wave Turbulence

Simplified equations projected on the local basis of eigenmodes $\boldsymbol{N}$ and $\boldsymbol{N}^*$ can be used for discussing both linear and nonlinear operators, as well as to develop closure theories for rotating turbulence. The starting point is the same as in Chap. 4. Using the associated amplitudes ξ_s, $s = \pm 1$, which are defined by

$$\hat{\boldsymbol{u}}(\boldsymbol{k}, t) = \xi_+(\boldsymbol{k}, t)\boldsymbol{N}(\boldsymbol{k}) + \xi_-(\boldsymbol{k}, t)\boldsymbol{N}(-\boldsymbol{k}), \tag{7.34}$$

one obtains the following evolution equation

$$\left[\frac{\partial}{\partial t} + \nu k^2 - \imath s \underbrace{\left(2\Omega \frac{k_\parallel}{k}\right)}_{\sigma_k}\right] \xi_s = \sum_{s',s''=\pm 1} \int_{k+p+q=0} M_{ss's''}(\mathbf{k}, \mathbf{p}) \xi^*_{s'}(\mathbf{p}, t) \xi^*_{s''}(\mathbf{q}, t) d^3\mathbf{p}, \tag{7.35}$$

in which a diagonal form of the linear operator appears, and the nonlinear term $M_{ss's''}(\mathbf{k}, \mathbf{p})$ is given by Eqs. (4.275) and (4.276). The linear inviscid solution is

$$\xi_s(\mathbf{k}, t) = \exp\left(2\imath s \Omega t \frac{k_\parallel}{k}\right) \xi_s(\mathbf{k}, 0), \quad s = \pm 1.$$

Replacing[4] the initial condition by a new function $\boldsymbol{a}_s$ such that

$$\xi_s(\mathbf{k}, t) = \exp\left(2\imath s \Omega t \frac{k_\parallel}{k}\right) a_s(\mathbf{k}, t), \quad s = \pm 1 \tag{7.36}$$

one obtains an equation for $\boldsymbol{a}_s$ in which linear operators are absorbed in the nonlinear one as integrating factors:

$$\dot{a}_s = \sum_{s',s''=\pm 1} \int_{k+p+q=0} \exp\left[2\imath\Omega\left(s\frac{k_\parallel}{k} + s'\frac{p_\parallel}{p} + s''\frac{q_\parallel}{q}\right)t\right] M_{ss's''}(\boldsymbol{k}, \boldsymbol{p}) a^*_{s'}(\boldsymbol{p}, t) a^*_{s''}(\boldsymbol{q}, t) d^3\mathbf{p}. \tag{7.37}$$

Note that the quantities $\boldsymbol{a}_s$ can be interpreted as *amplitudes of slow variables*, since the contribution of rotation has been removed. This problem can be analyzed

[4] This change of variables is referred to as the Poincaré transform.

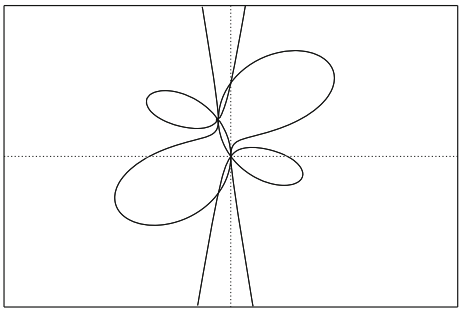

Fig. 7.12 Visualization of resonant surfaces of inertial waves, given by Eq. (7.39), for a given orientation of $\boldsymbol{k}$. The locus of $\boldsymbol{p}$ is seen in the plane $p_2 = 0$, for $\theta_k = 1.1$. Complex loops appear for $\pi/3 < \theta_k < \pi/2$. Courtesy of F. S. Godeferd

using a multiple (two) time-scale technique, by setting $\boldsymbol{a}_s = \boldsymbol{a}_s(\boldsymbol{k}, \epsilon t)$, where ϵ is a (really) small parameter for asymptotic expansion which can be related to a Rossby number. Incidentally, it should be more convenient to consider $\boldsymbol{a}_s = \boldsymbol{a}_s(\boldsymbol{k}, t)$ and the phase as $\exp(2\imath s\Omega \frac{k_\parallel}{k} \frac{t}{\epsilon})$, also in agreement with the theory of Lifschitz and Hameiri discussed in Chap. 17. Such a refined analysis is not needed here, and we will just retain from Eq. (7.37) the importance of resonant triads. These triads are defined by the relation

$$s\sigma_k + s'\sigma_p + s''\sigma_q = 0 \tag{7.38}$$

and correspond to a zero value of the phase term in the right-hand-side of Eq. (7.37), leading to

$$s\frac{k_\parallel}{k} + s'\frac{p_\parallel}{p} + s''\frac{q_\parallel}{q} = 0 \quad \text{with} \quad \boldsymbol{k} + \mathbf{p} + \mathbf{q} = 0. \tag{7.39}$$

These resonant or quasi-resonant triads are found to dominate the nonlinear slow motion, since the effect of the phase term in the left-hand-side of Eq. (7.37) is a severe damping of the nonlinearity by *phase mixing*. The complexity of the resonant surfaces is illustrated by Fig. 7.12. The detailed helicity conservation property yields the following additional relationship for resonant triads:

$$sk\sigma_k + s'p\sigma_p + s''q\sigma_q = 0. \tag{7.40}$$

In that case, why not to obtain a simplified model by solving Eq. (7.37) with an integral restricted to the resonant triads? Because the resonant surfaces are sufficiently complex to require very accurate interpolation, rendering the resulting computation efficient for a smooth distribution of the slow amplitudes a_s in Fourier space only. Such a smooth distribution cannot represent turbulence, so that one has to resort to describing naturally smooth quantities like statistical moments instead of the instantaneous solution. It is not forbidden, however, to try to isolate resonant triads in DNS: some related studies are discussed in Sect. 7.7.

A qualitative analysis of resonant triads (Waleffe 1993) deserves attention, before addressing quantitative issues dealing with statistical moments. Going back to the analysis presented in Sect. 4.8, and introducing the selection rules of resonant triads (7.38) and (7.40), one obtains

$$\frac{\cos\theta_k}{s'q - s''p} = \frac{\cos\theta_p}{s''k - sq} = \frac{\cos\theta_q}{sp - s'k}. \tag{7.41}$$

Applying the instability principle of Waleffe introduced in Sect. 4.8.4, but *restricting the analysis to resonant triads*, the equality (7.41) shows that the transfer of energy always goes from a less slanted leg of the triad (with respect to the rotation vector) to a more slanted one. This result comes from the fact that the unstable mode is also the mode whose pulsation σ_k has the larger amplitude and opposite sign with respect to the two other modes of the triad under consideration. Let us consider the triad $(\boldsymbol{k}, \boldsymbol{p}, \boldsymbol{q})$ and assume that $\boldsymbol{k}$ is the unstable mode. Then, one has $|\sigma_k| > |\sigma_p|, |\sigma_q|$, which leads to $|\cos\theta_k| > |\cos\theta_p|, |\cos\theta_q|$. Accordingly, a drain of energy is predicted towards the wave plane orthogonal to $\boldsymbol{\Omega}$ as illustrated in Fig. 7.13. Waleffe, however, points out that the rate of energy transfer vanishes exactly when the wave vector reaches the equatorial orientation characterized by $\boldsymbol{k}\cdot\boldsymbol{\Omega} = 0$. The latter wave plane is exactly both the slow and the 2D manifold. Its meaning is very different in the discrete case and in the continuous case: for instance, extension of the resonance condition to the exact slow manifold is only valid in the discrete case, and related issues are further discussed in Sect. 7.7.2.

Wave turbulence is a key concept in other fields, e.g. plasmas physics, with a very large literature which influenced the "Russian School", although it also addressed turbulence in classical fluids (Zakharov et al. 1992). Applications can be found even in physics of solids: random weakly interacting acoustic waves are considered as a gas of phonons in the latter case. Several recent studies address vibrating plates

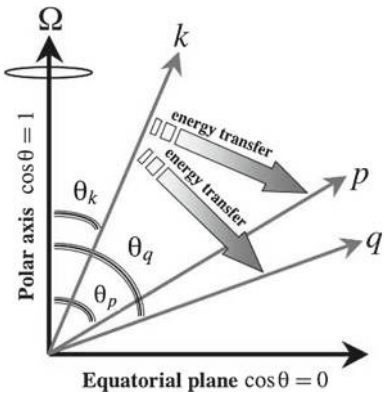

Fig. 7.13 Schematic view of kinetic energy transfer according to Waleffe's instability assumption among resonant modes in rotating turbulence

and surface waves, but much less deal with internal waves. In fluid mechanics, the turbulent flow is seen as a sea of random spatio-temporal wave-modes, whose nonlinear interactions can be considered as weak in the limit of a small parameter. The deterministic ingredient is the dispersion law, which gives a straightforward link of a 'rapid' temporal frequency σ to the spatial wave-vector $\boldsymbol{k}$. All other variables of the flow, such as the amplitudes A of the wave-modes and/or some phase terms φ in any generic wave-mode of motion $a\exp[\imath(\boldsymbol{k}\cdot\boldsymbol{x}-\sigma(\boldsymbol{k})t+\varphi)]$, are treated as random variables. Even $\boldsymbol{k}$ could be considered as random, in some models, ranging from linear Kinematic Simulation (Cambon et al. 2004) to weakly nonlinear ones, e.g. Monte-Carlo methods for solving statistical closures. The possibility of applying a weakly nonlinear theory relies on a time-scale separation: amplitudes a are assumed to slowly evolve in time with respect to the rapid temporal oscillations induced by $\sigma(\boldsymbol{k})t$. Phase-terms φ are removed here, or absorbed in a, such as $ae^{\imath\varphi}\rightarrow A$. In this sense, wave-turbulence is a theory for the evolution of slowly evolving envelopes which modulate high frequency oscillations.

Rapidly rotating turbulence is an almost perfect case to apply such a theory: the inertial wave-modes form a complete basis (they are identical to the helical modes, which are even useful for studying "strong" turbulence), the small parameter which controls the "weak" nonlinearity is not artificial: this is a Rossby number.

In the recent experimental study by Yarom and Sharon (2014), the relevance of the dispersion law is confirmed in wave turbulence for spatio-temporal realizations of a forced, rotating flow, at least for larger scales. For this purpose, spectra in terms of both the wave vector $\boldsymbol{k}$ and the temporal frequency ω are considered, with for instance

$$E^s(\boldsymbol{k},\omega)\propto\frac{1}{2}a_s^*(\boldsymbol{k},\omega)a_s(\boldsymbol{k},\omega),$$

extending the definition of amplitudes from Eq. (7.36). Spectral data are plotted in terms of ω and θ, and are found to collapse on the curves given by the dispersion relation, especially at the largest Rossby numbers and the larger k's.

It is important to notice that to bridge between a small Rossby number and a weak nonlinearity seems to be trivial and tautological at first glance (this argument is used in RDT, for instance, without any refined analysis of the nature of nonlinearity); more important is the fact that the phase-mixing induced by "rapid" oscillations yields a severe damping of nonlinear interactions, so that nonlinearity concentrates on a low-dimension manifold: among all the triads called into play in the absence of waves, only very few survive in the long-term limit, forming quasi-resonant triads. Finally, when transferring the EDQNM (Orszag 1970) machinery from velocity (spatial) Fourier modes to slow amplitudes, in agreement with an exact Poincaré transform (7.36), the limit of wave turbulence (e.g. Benney and Newell 1969) is recovered at vanishing eddy-damping, as we will see in the following subsections.

7.6.2 Second Order Statistics: Identification of Relevant Spectral Transfer Terms

Second-order correlations are entirely generated by the quantities $\mathcal{E}$, Z, $\mathcal{H}$, or equivalently by $\langle a_s^* a_{s'} \rangle$, $s = \pm 1, s' = \pm 1$. Without any assumption, second order correlations are governed by the following system of equations

$$\left(\frac{\partial}{\partial t} + 2\nu k^2 \right) \mathcal{E}(k,t) = T^{(\mathcal{E})}(k,t), \tag{7.42}$$

$$\left(\frac{\partial}{\partial t} + +2\imath\sigma_k + 2\nu k^2 \right) Z(k,t) = T^{(Z)}(k,t), \tag{7.43}$$

$$\left(\frac{\partial}{\partial t} + 2\nu k^2 \right) \mathcal{H}(k,t) = T^{(h)}(k,t), \tag{7.44}$$

in which the nonlinear terms $T^{(\mathcal{E})}(k,t)$, $T^{(Z)}(k,t)$ and $T^{(h)}(k,t)$ are defined starting from the transfer tensor T_{ij} given by Eq. (2.119), as

$$T^{(\mathcal{E})} = \frac{1}{2} T_{ii}, \quad T^{(Z)} = \frac{1}{2} T_{ij} N_i^* N_j^*, \quad T^{(h)} = \frac{-\imath}{2} \epsilon_{ijn} \frac{k_i}{k} T_{jn}$$

in full agreement with $\mathcal{E} = (1/2)\hat{R}_{ii}$, $Z = (1/2)\hat{R}_{ij} N_i^* N_j^*$ and $\mathcal{H} = -\imath(1/2)\epsilon_{ijn}(k_i/k)\hat{R}_{jn}$.

It appears that the Coriolis force does not affect the (linear) left-hand-sides, except for the polarization parameter $Z(k,t)$. Replacing Z by ζ, where ζ is such that

$$Z(\boldsymbol{k},t) = e^{2\imath\sigma_k t} \zeta(\boldsymbol{k},t), \tag{7.45}$$

and $T^{(Z)}(\boldsymbol{k},t)$ by $e^{2\imath\sigma_k t} T^{\zeta}(\boldsymbol{k},t)$, only the left-hand-side terms, which are linked to triple correlations and mediated by nonlinearity, are possibly rotation-dependent. Contribution from triple velocity correlations are therefore gathered into the generalized spectral transfer terms $T^{(\mathcal{E},Z,h)}$, which derives from Eqs. (7.42)–(7.44). If the above system of equations is initialized with 3D isotropic initial data, i.e. by setting $\mathcal{E}(k,0) = E(k)/(4\pi k^2)$ and $Z = \mathcal{H} = 0$ at initial time, then the anisotropy which should reflect the transition towards 2D structure can be created by the nonlinear spectral transfer terms only. This anisotropy consists of axisymmetry without mirror symmetry, leading to $\mathcal{E} = \mathcal{E}(k, \cos\theta = \frac{k_\parallel}{k}, t)$ and $Z = Z(k, \cos\theta = \frac{k_\parallel}{k}, t)$, with $Z = 0$ if $\boldsymbol{k}$ is parallel to the vertical axis, in agreement with the symmetries of rotating Navier–Stokes equations, which ought to be satisfied by the closure theory.

7.6.3 Towards a Rational Closure Using EDQNM

A complete anisotropic EDQN model can be built in terms of the Green function $\mathbf{G}$ and the spectral tensor $\hat{\mathbf{R}}$, using products of $\mathbf{G}$ to solve the linear operators which appear in the equations for third order correlations (Cambon 1982; Cambon and Scott 1999), from the generic Eq. (2.117) in Chap. 2. On the ground of these equations, it is possible to discuss an optimal way to treat the *Markovianisation* procedure, i.e. to simplify the time-dependency in the integrands that connect the transfer term to second order correlations. Closed equations display three kinds of time-dependent terms:

(i) Viscous, or viscous + damping, terms

$$\exp\left(\int_{t'}^{t} \mu dt''\right) \to V(t,t'),$$

(ii) Terms involving the RDT Green's function

$$\mathbf{G}(t,t') \to \exp[\pm\imath\sigma(t-t')],$$

(iii) Terms from the second-order spectral tensor (through quasi-normal assumption)

$$\hat{\mathbf{R}}(t') \to (\mathcal{E}, Z, \mathcal{H})(t').$$

According to the Markovianization procedure in classical EDQNM, we can assume that $V(t,t')$ is so rapidly decreasing in terms of time-separation $\tau = (t-t')$ that it is only concerned by the time integral in the closure equations, whereas the other terms take their instantaneous value, at $t' = t$, so that they are replaced by $\mathbf{G}(t,t)$ and $\hat{\mathbf{R}}(t)$, respectively. In other words, one considers that the only rapid term is $V(t,t')$, the other terms being assumed to be slow ones. This procedure, referred to as EDQNM1, is not relevant for rotating turbulence, since the presence of $\mathbf{G}(t-t')$ in the closure relationship is responsible for the breakdown of the initial isotropy. Using EDQNM1 with isotropic initial data, isotropy is maintained, and no effect of system rotation can appear. It is possible, however, to take into account the effect of rotation in incorporating the rotation rate Ω in the eddy damping term

$$\eta^{\Omega} = A\sqrt{(2\Omega)^2 + \int_0^k p^2 E(p,t)dp} \tag{7.46}$$

in the basic EDQNM for isotropic turbulence, in Chap. 4, from Eq. (4.336). This is consistent with the interpretation of the eddy damping as the turnover time of largest eddies, and had suggested Eq. (7.19), as discussed in Cambon et al. (1997).

A second step, referred to as EDQNM2, consists of simply "freezing" the $(\mathcal{E}, Z, \mathcal{H})$ terms by setting $t' = t$ in them, whereas the complete 'readjusted' response function, with both $V(t, t')$ and $\mathbf{G}(t, t')$ terms, is conserved in the time-integrand with its detailed time-dependency. An interesting result is that the time integral of the three-fold product of response functions yields a generic closure relationship of the form

$$T^{(\mathcal{E},Z,h)} = \sum_{s=\pm1,s'=\pm1,s''=\pm1} \int \frac{S^{ss's''}(\mathcal{E}, Z, \mathcal{H})}{\mu_{kpq} + \imath(s\sigma_k + s'\sigma_p + s''\sigma_q)} d^3\mathbf{p}. \tag{7.47}$$

Results dealing with the rise of directional anisotropy and the description of the transition from 3D isotropy to 2D structure obtained using EDQNM2 are illustrated in Fig. 7.14, in which they are compared with high-resolution (in 1997!) $528 \times 128 \times 128$ Large-Eddy Simulation data. It should be borne in mind that the development of angular dependency in $\mathcal{E}(k, \cos\theta = \frac{k_\parallel}{k}, t)$, which amounts to a concentration of energy towards the 2D slow manifold (sketched in Fig. 7.17), results from nonlinear interactions mediated by $T^{(\mathcal{E})}$ in Eqs. (7.42) and (7.47).

The latter procedure can be questioned, in spite of its excellent numerical results, since it is not completely consistent with the basic rapid-slow decomposition suggested by Eq. (7.36). All the terms in the set $(\mathcal{E}, Z, \mathcal{H})$ which generate $\hat{\mathbf{R}}$ should not be considered as "slow" terms according to the RDT solution (7.32). Therefore, it is necessary to use the decomposition defined by Eq. (7.45), so that only ζ appears as a slow variable, in complete agreement with Eq. (7.36). The resulting optimal procedure, referred to as EDQNM3, yields freezing $\mathcal{E}(t') = \mathcal{E}(t)$, $\mathcal{H}(t') = \mathcal{H}(t)$, $\zeta(t') = \zeta(t)$ while keeping the t' dependency under the integral for $Z(t') = \exp(2\imath\sigma t')\zeta(t)$, $V(t, t')$ and $\mathbf{G}(t, t')$, as before. This EDQNM3 version only slightly differs from EDQNM2, but presents decisive advantages. It is completely consistent with building EDQNM in terms of slow amplitudes using relation (7.36). Another advantage is that an asymptotic expansion can be obtained in the limit $\mu_{kpq} \ll 2\Omega$, which exactly coincides with the Eulerian wave-turbulence theory (see Galtier 2003). It is proved that realizability is enforced in this limit, while it is not in the EDQNM2 version.

7.6.4 *Recovering the Asymptotic Theory of Inertial Wave Turbulence*

Ignoring the $\mathcal{H}$ and ζ contributions for the moment, EDQNM3 (or equivalently EDQNM2 (Cambon and Jacquin 1989; Cambon et al. 1997) since the two versions differ only in treating Z) yields the following closure for the Lin equation:

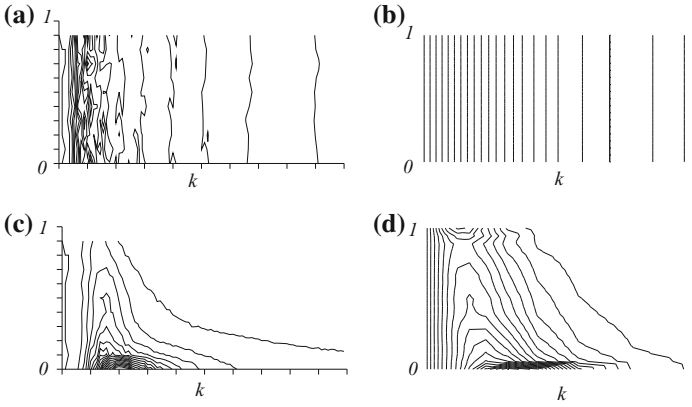

Fig. 7.14 Isolines of kinetic energy $\mathcal{E}(k, \cos\theta, t)$ for $512 \times 128 \times 128$ LES computations (a) at $\Omega = 0$ at time $t/\tau = 427$, (b) EDQNM2 with $\Omega = 0$; (c) LES with $\Omega = 1$ at $t/\tau = 575$; and (d) EDQNM2 calculation with $\Omega = 1$ at time $t/\tau = 148$. The vertical axis bears $\cos\theta_k$ (from 0 to 1 upwards) and the horizontal one the wave number k. Reproduced from Cambon et al. (1997) with permission of CUP

$$T^{(\mathcal{E})} = \sum_{s',s''=\pm 1} \iiint \frac{A(k, s'p, s''q)}{\mu_{kpq} + \imath(\sigma_k + s'\sigma_p + s''\sigma_q)} \times \mathcal{E}(\boldsymbol{q})\,(\mathcal{E}(\boldsymbol{p}) - \mathcal{E}(\boldsymbol{k}))\,d^3\boldsymbol{p}, \tag{7.48}$$

where the exact from of A and μ_{kpq} are given in Chap. 18.

The denominator reflects the time-integration of a product of three 'eddy damped' Green's functions derived from Eq. (7.31).

In the limit of very high rotation rate, or at vanishing Rossby number, the asymptotic version of this equation is obtained using the following Riemann–Lebesgue relationship for distributions (also sometimes referred to as the Plemelj or Sokhotsky formula)

$$\frac{1}{\mu + \imath x} \to \pi\delta(x) - \imath\mathcal{P}\left(\frac{1}{x}\right) \quad \text{when} \quad \mu \to 0,$$

in which $\mathcal{P}$ holds for the principal value in the complete integral expression (such as (7.48)).

The resulting *Asymptotic Quasi-Normal Markovian* (AQNM) closure is expressed as

$$T^{(\mathcal{E})} = \sum_{s',s''=\pm 1} \int \int_{\mathfrak{M}_{s's''}} \pi \frac{A(k, s'p, s''q)}{s'\boldsymbol{C}_g(\boldsymbol{p}) - s''\boldsymbol{C}_g(\boldsymbol{q})} \times \mathcal{E}(\boldsymbol{q})\,(\mathcal{E}(\boldsymbol{p}) - \mathcal{E}(\boldsymbol{k}))\,d^2\boldsymbol{p} \tag{7.49}$$

in which $\mathfrak{M}_{s's''}$ is the family of resonant surfaces and $\boldsymbol{C}_g(\boldsymbol{k})$ the group velocity of inertial waves. The damping factor μ no longer appears in the final equation, while the denominator accounts for the fact that the reduction from a volume to a surface integral brings in the gradient of resonant surfaces, whence the occurrence of the group velocity. The reader is referred to Cambon et al. (2004) for a presentation of the full EDQNM3 equations (without $\mathcal{H}$) and to Bellet et al. (2006) for AQNM equations for $\mathcal{E}, \zeta, \mathcal{H}$.

Starting from isotropic initial data, with a narrow-band energy spectrum, an inertial zone is constructed solving AQNM equation for $\mathcal{E}(k, \theta)$ at vanishing Rossby number and infinite Reynolds number, until the inertial range reaches the maximum wave number. At this stage of the computation, the laminar viscosity is reintroduced,[5] and a self-similar spectrum is obtained. The spherically averaged energy spectrum $E(k)$ is constructed with a k^{-3} slope, as shown in Fig. 7.15, but the prefactor is $E(k) \sim \frac{\Omega}{t} k^{-3}$. Axisymmetric shape, with strong directional anisotropy, is found for the angle-dependent spectrum $4\pi k^2 \mathcal{E}(k, \cos\theta, t)$, as shown in Fig. 7.16. This directional anisotropy, only mediated by nonlinear transfer, is consistent with the sketch displayed in Fig. 7.17, and with all previous theoretical and numerical studies by Cambon and Jacquin (1989), Waleffe (1993), Cambon et al. (1997). That illustrates a transition from a 3D ($\mathcal{E}$ equidistributed on spherical shells) to a 2D structure ($\mathcal{E}$ concentrated on the horizontal wave plane). Nevertheless, the two-dimensionalization is limited to large k, and is never fully achieved. The k^{-3} slope for E results from the averaging of various slopes for $4\pi k^2 \mathcal{E}$, ranging from k^{-2} (for quasi-horizontal wave-vectors) to k^{-5} (for quasi-vertical wave-vectors). The relevance of this asymptotic result is perhaps marginal, since the time τ needed to obtain the inertial zone built via weak wave-turbulence dynamics is very high, since $\Omega\tau \sim O(Ro^{-2})$ at very small Rossby number Ro. In this context, it is interesting to note that a similar result was obtained by a high resolution (512^3) DNS, therefore at moderate Ro, Re and elapsed time, as shown on Fig. 7.18.

7.7 Fundamental Issues: Solved and Open Questions

7.7.1 Eventual Two-Dimensionalization or Not

It is clear that the trends towards two-dimensional structure saturate at very long time, at least in the continuous case. The anisotropic state, which eventually becomes self-similar, is consistent with power-law decay for single-point statistics. The turbulent kinetic energy is observed to decay as $\mathcal{K}(t) \sim t^{-0.86}$ in AQNM. Full

[5] Unfortunately, it is not possible to continue the computation at infinite Reynolds number at this stage, as it was done in the isotropic case without rotation in Chap. 4, because the eddy damping is no longer present in the AQNM equation, and especially because accumulation of spectral energy at k_{max} is no longer possible, due to typical oscillations emanating from largest wavevectors as numerical instabilities.

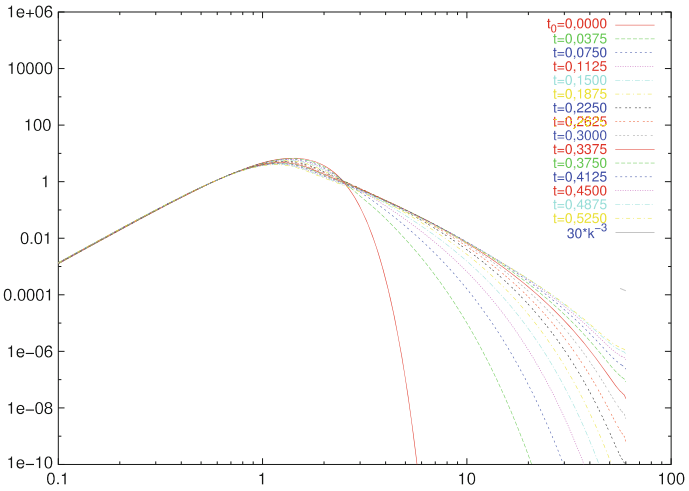

Fig. 7.15 Construction of the spherically averaged spectrum in AQNM. The straight line gives the k^{-3} slope. Reproduced from Bellet et al. (2006) with permission of CUP

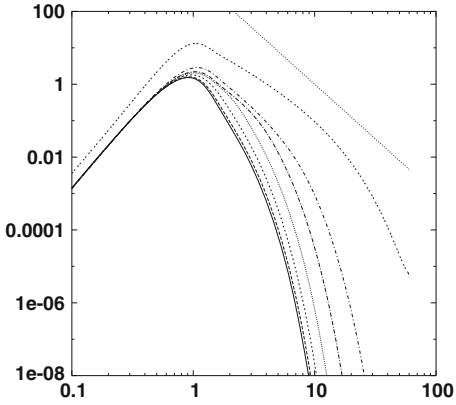

Fig. 7.16 Asymptotic angular dependent spectra from AQNM. Spectral energy density for different angles, from bottom to top, $\theta/(\pi/2) = 1/300$ (what we call the vertical mode), $\theta/(\pi/2) = 51/300$, $\theta/(\pi/2) = 101/300$, $\theta/(\pi/2) = 151/300$, $\theta/(\pi/2) = 201/300$, $\theta/(\pi/2) = 251/300$, and $\theta/(\pi/2) = 299/300$ (the 'horizontal' mode). The straight line gives the k^{-2} slope. Reproduced from Bellet et al. (2006) with permission of CUP

two-dimensionalization requires very strong conditions of axisymmetric angular distribution for $\mathcal{E}$:

$$\mathcal{E}(k_\perp, k_\parallel) = \frac{E(k_\perp)}{2\pi k_\perp}\delta(k_\parallel), \tag{7.50}$$

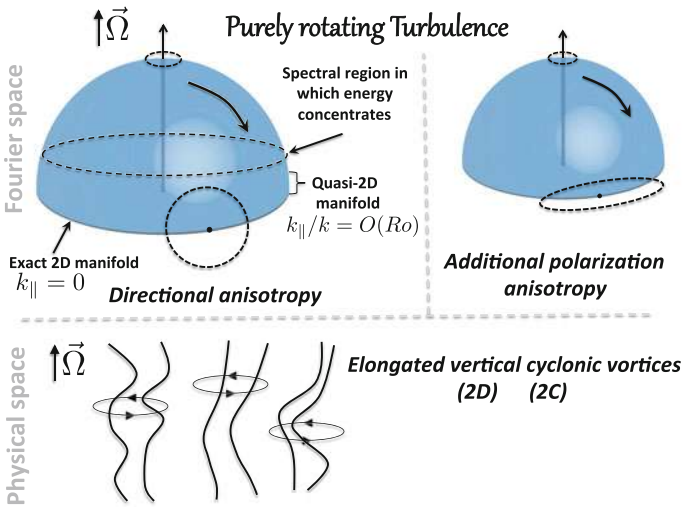

Fig. 7.17 Top: schematic view of the net energy spectral transfers in the pure rotation case. Bottom: sketch of emerging large-scale coherent structures. Notice that the conical region in which the energy concentrates remains finite, even if the size of the quasi-2D manifold tends to zero at vanishing Rossby number

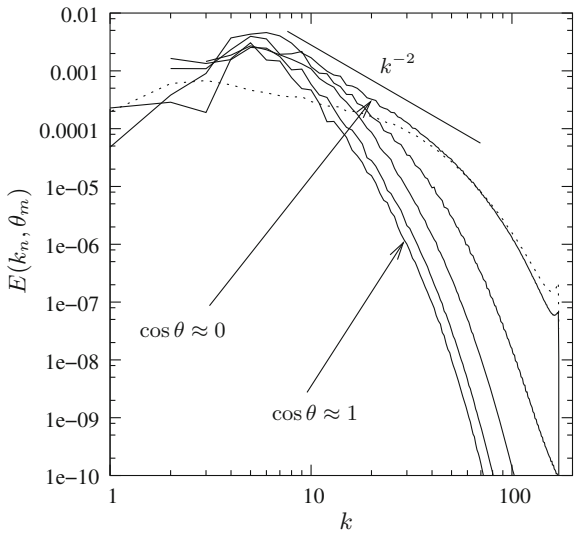

Fig. 7.18 Angular dependent spectra of purely rotating turbulence. A comparable isotropic spectrum of the same quantity is shown as a black dotted line. Data from Liechtenstein et al. (2005)

or equivalent conditions expressed using $k = \sqrt{k_\perp^2 + k_\parallel^2}$ and $\cos\theta = k_\parallel/k$, where δ denotes the Dirac delta function. An additional condition possibly brings in the polarization anisotropy Z, leading to

$$Z(k_\perp, k_\parallel) = -\frac{E(k_\perp)}{2\pi k_\perp}\delta(k_\parallel) \tag{7.51}$$

in order to ensure that the contribution to vertical velocity is identically zero. The first equation characterizes a 2D (two-dimensional) state only, whereas both characterize a 2D-2C state (two-dimensional and two-component) (Cambon et al. 1997). In contrast, the asymptotic state of weak inertial turbulence predicted by AQNM is consistent with an *integrable singularity* at $k_\parallel = 0$ for $\mathcal{E}(k_\perp, k_\parallel)$, and with a zero Z. Near the two-dimensional manifold, the distribution is consistent with

$$\mathcal{E}(k_\perp, k_\parallel) \sim k_\perp^{-7/2} k_\parallel^{-1/2}, \quad \text{or} \quad \mathcal{E}(k, \theta) \sim (\pi/2 - \theta)^{-1/2} k^{-4}, \tag{7.52}$$

as analytically obtained by Galtier (2003). The k^{-4} law at smallest $\cos\theta$'s is consistent with the AQNM result (Fig. 7.16), or k^{-2} slope after multiplication by k^2.

Things can be different in the discrete case, for instance when the velocity field is chosen to be periodic with finite wave length in one, two or three directions. On the one hand, some mathematical theorems can predict decoupled dynamics and eventual dominance of the slow manifold. Such a "nonlinear Proudman theorem" relies on smoothness assumptions about the initial velocity field and emphasizes the role of purely 2D particular resonant triads which are sometimes referred to as *catalytic triads*. On the other hand, some under-resolved DNS or LES (for instance DNS with hyperviscosity) discussed in Sect. 7.7.4 seem to predict two-dimensionalization, in agreement with essentially decoupled dynamics of the slow manifold, in which the energy is eventually concentrated.

7.7.2 Meaning of the Slow Manifold

Both the definition and relative weight of the slow manifold depend on the discretization in conventional pseudo-spectral DNS and LES. In any case, the underlying assumptions of weak turbulence are no longer valid in the domain $k_\parallel/k = O(Ro)$, because the time-scale separation between "slow" amplitudes $a_{\pm 1}$ and "rapid" phases $\exp(\pm 2\Omega t k_\parallel/k)$ no longer holds. In DNS and LES, $k_\parallel/k$ cannot be smaller than a typical mesh-ratio Δ_k/k, so that the apparent thickness of the slow manifold is fixed independently of the Rossby number, which questions any calculation at too small Rossby number (See also Smith and Lee 2005).

Even if EDQNM3 and AQNM equations deal with the continuous case, their numerical resolution needs dicretization in Fourier space, but the angular step can be much smaller than in DNS/LES. The exact limit $k_\parallel = 0$ cannot be afforded by AQNM equations in any case, and the AQNM numerical code is only used until the smallest nonzero value of this parameter.

The consequence is twofold:

(i) The contribution of the neighborhood of $k_\parallel = 0$ is singular. But, since this singularity is integrable, any quantity which involves an integral over the whole angle-dependent wave space can be accurately computed. Examples of such quantities are the spherically averaged energy spectrum $E(k)$ and the Reynolds stress components.

(ii) The system of AQNM equations has to be complemented in order to take into account the slow manifold per se. This is needed to evaluate statistical quantities which only involve the $k_\parallel = 0$ wave plane, as the 2D energy components:

$$\overline{u_3^2} L_{33}^{(3)} = 2\pi^2 \int_0^\infty \left(\mathcal{E}(k_\perp, k_\parallel = 0) + Z(k_\perp, k_\parallel = 0)\right) k_\perp dk_\perp \tag{7.53}$$

and

$$\overline{u_1^2} L_{11}^{(3)} = \overline{u_2^2} L_{22}^{(3)} = \pi^2 \int_0^\infty \left(\mathcal{E}(k_\perp, 0) - Z(k_\perp, 0)\right) k_\perp dk_\perp. \tag{7.54}$$

These quantities are very important. They were measured in Jacquin et al. (1990) and accurately predicted using DNS and EDQNM2 in Cambon et al. (1997). The strong difference in the evolution of these quantities suggests that the polarization anisotropy $Z = \Re Z$ is important in the exact slow manifold $k_\parallel = k_3 = 0$. Generally, $\mathcal{E} + \Re Z$ and $\mathcal{E} - \Re Z$ give the spectral energy of the poloidal and toroidal modes, respectively. In the equatorial wave plane ($k_\parallel = 0$), they contribute to both horizontal and vertical energy. A refined statistical model ought to match AQNM outside the vicinity of the slow manifold, with $Z = 0$, and full EDQNM3 in the vicinity of the 2D manifold (Cambon et al. 2004). An interesting related problem is that the eddy damping cannot be ignored in the vicinity of the slow manifold, as it is in classical wave turbulence theory, so that a fully nonlinear statistical theory is needed.

7.7.3 Wave Turbulence Theory for a Confined Rotating Flow

This recent study by Scott (2014) extends the application of wave turbulence theory to rapidly rotating turbulence confined by two infinite, parallel walls perpendicular to the rotation axis. This flow configuration is similar to the one addressed by Godeferd and Lollini (1999) using DNS if the local forcing is removed. The flow is modeled as a combination of inertial waveguide modes, continuous in the transverse (horizontal) directions and discrete in the axial (vertical) one. This leads to a spectral covariance matrix $M_{mn}(k_\perp, t)$ whose diagonal elements $m = n$ are related to the distribution of energy over modes and whose off-diagonal $m \neq n$ elements represent correlations between modes of different orders. The 2D manifold corresponds to $n = 0$, with $k_\parallel = n\pi/L$ in terms of the distance $2L$ between the walls: It recovers its meaning of

true, non-singular, "vortex" mode, in contrast with wave turbulence in the unbounded case $L \to \infty$. It is shown to evolve as in a classical two-dimensional non-rotating flow, but with wall friction due to Ekman pumping by the boundary layers. As in unbounded wave turbulence theory, energy is transfered between wave modes ($n \neq 0$) via resonant triadic interactions. Energy transfer takes place at times $O(Ro^{-2})$ multiple of the rotational period. Despite playing no role in wave-mode energetics, the two-dimensional mode $n = 0$ induces the decay of the off-diagonal elements of the spectral matrix on a time-scale that is small compared with $O(Ro^{-2})$ rotation periods. Equations for $M_{mn}(k_\perp, t)$ are closed in an analytical way, their numerical solution is in progress, as well as DNS in a rotating channel with unprecedented resolution with respect to Godeferd and Lollini (1999).

7.7.4 Are Present DNS and LES Useful for Theoretical Prediction?

DNS and LES results have also shown the tendency of rotating turbulence to become anisotropic by spectral transfer towards the horizontal waveplane (Cambon et al. 1997; Morinishi et al. 2001), not to mention qualitative results dealing with the development of vortices elongated in the vertical direction (Bartello et al. 1994; Biferale et al. 2016). Nevertheless, it is difficult to decide, based on these results, whether the flow becomes two-dimensional in the long time-limit, for several reasons. Spatial periodicity of the flow, which is assumed in numerical models, implies that the size of the periodic box must be sufficiently large in order to avoid spurious confinement effects. In particular, the turbulent correlation length and $C_g t$ must remain small compared to the box size, where C_g is the inertial wave group velocity given by Eq. (7.27). The latter condition is very stringent for long-time simulations, since the evolution time scales as $Ro^{-2}\Omega^{-1}$ at small Rossby number.

Regarding Reynolds stress tensor anisotropy with directional/polarization splitting, the exact equation

$$2\mathcal{K}(t)b_{33}(t) = \underbrace{\iiint \left(\mathcal{E} - \frac{E}{4\pi k^2}\right)\sin^2\theta d^3\boldsymbol{k}}_{b_{33}^{(dir)}(t)} + \underbrace{\iint \Re\left(\zeta e^{-2\imath\cos\theta t}\right)\sin^2\theta d^3\boldsymbol{k}}_{b_{33}^{(pol)}(t)}, \tag{7.55}$$

along with Eq. (7.42) allows to discuss some results. DNS/LES (Cambon et al. 1997; Morinishi et al. 2001; Yang and Domaradzki 2004) yield results similar to those of AQNM (Bellet et al. 2006) dealing with the time history of $b_{33}^{(dir)}$. A monotonic increase from about 0 (initial isotropy) to a maximum value is observed. This maximum value is never larger than 0.08, and therefore remains far below the theoretical two-dimensional limit which is equal to 1/6 (obtained in injecting Eq. (7.50) in Eq. (7.55) (Cambon et al. 1997)). In AQNM, the $b_{33}^{(pol)}$ term remains equal to zero, so that

$b_{33} = b_{33}^{(dir)}$. The vanishing of $b_{33}^{(pol)}$ seems to be a very general result, also valid in the nonlinear case if ζ evolves slowly and has integrable singularity at $k_\parallel = 0$. In almost all under-resolved DNS (or LES), a rapid evolution of $b_{33}^{(pol)}$ with negative value can yield a strong departure of b_{33} from $b_{33}^{(dir)}$, resulting eventually in a negative value of b_{33} about -0.2. The latter effect, e.g. Bartello et al. (1994), which means that two-componentalization is much more important than two-dimensionalization, is probably due to the numerical confinement (finite-box effect). This discrepancy yields distinguishing the continuous case from the discrete one. In the continuous unbounded case, it is clear that Z can have a physically relevant negative value in the slow manifold, allowing a large increase of the ratio $\overline{u_1^2} L_{11}^{(3)} / \overline{u_3^2} L_{33}^{(3)}$, according to Eqs. (7.53) and (7.54) and Cambon and Jacquin (1989), Jacquin et al. (1990), Cambon et al. (1997), but its integral contribution to $b_{33}^{(pol)}$ must vanish by phase-mixing under the conditions mentioned above on ζ in Eq. (7.55). Finally, Eq. (7.55) illustrates the fact that directional and polarization anisotropy can have opposite effects on the RST anisotropy. Using the terminology introduced by Kassinos et al. (2001), one should say that "dimensionality" (anisotropy of the dimensionality tensor corresponds to $-2b_{ij}^{(dir)}$) and polarization have opposite effects on "componentality" (conventionally measured by b_{ij}).

7.7.5 Is the Pure Linear Theory Relevant?

Restricting the analysis to single-time second-order statistics in homogeneous turbulence, it is clear that anisotropic structuration is only possible through non-linear mechanisms. As pointed out by Davidson et al. (2006), this does not exclude that formation of organized structures can be mediated by linear mechanisms.

On the one hand, single-time second order statistics are particular cases, since phase information is essentially lost when combining $e^{\imath\sigma_k t}$ and its conjugate in the definition of the second order spectral tensor $\hat{\mathbf{R}}$, at least looking at its trace. Phase information is recovered considering more complex correlations, even in the homogeneous case. Not to mention two-times second order statistics with relevant "linear" (so-called RDT) applications (Kaneda and Ishida 2000), third-order correlations are affected by these phase effects. It is because the linear operator has a deep influence on third order correlations that the transfer terms $T^{(\mathcal{E},Z,h)}$ become rotation-dependent and anisotropic in Eq. (7.42), breaking the initial isotropy.

On the other hand, it is suggested that inertial waves propagating from a blob of vorticity can generate elongated structures in the pure linear —but non-homogeneous— case. This illustrates the fact that the lowest frequencies are linked to the fastest group velocity, which is close to the axial direction. In addition, a very interesting analysis of the angular momentum, with different time-scalings depending of the angle of ray propagation, is performed in Davidson et al. (2006). It is also suggested that the strong but transient anisotropy of integral lengthscales observed in the intermediate range of Rossby numbers by Jacquin et al. (1990) reflects this linear mechanism. Incidentally, this intermediate range was very clearly delineated

in the Jacquin's experimental study, as discussed below. First, several parameters were defined to describe the flow dynamics: a macro Rossby number $Ro^L = \frac{u'}{2\Omega L}$ with $L = L_{33}^{(3)}$ and $u' = \sqrt{\overline{u_3^2}}$ (from the observation that the axial components were the less altered by rotation) and a micro Rossby number Ro^λ choosing the axial Taylor lengthscale for λ with $Ro^\lambda \sim \omega'/(2\Omega)$. Second, in the free decay experiments, both Rossby numbers were initialized with $Ro^\lambda > Ro^L > 1$, and then decrease together, so that two transitions were successively observed. The first one is for $Ro^\lambda > Ro^L = 1$ and the second one for $Ro^\lambda = 1 > Ro^L$, respectively. These two transitions delineate the intermediate range of Rossby numbers, in which anisotropy was observed to develop. A very clear collapse of quantities combining Reynolds stresses and integral lengtscales from Figs. 7.1 and 7.2 was found in terms of the macro-Rossby number, showing that anisotropy of these quantities is triggered at a macro-Rossby number close to one. Nevertheless, these features were well reproduced by pure homogeneous EDQNM-type models and DNS/LES, in which RDT for single-time second order statistics give no anisotropy at all, if started with isotropic initial data.

Based on a very large and old experience on rotating flows, we consider that the different viewpoints can be reconciled. Instead of opposing linear to nonlinear dynamics, or homogeneous to inhomogeneous flows, we prefer to say that linear and nonlinear processes interact in a subtle way. As also discussed in the last section, it is more important to specify the order and the nature of the correlations to which the linear operator is applied. The fact that these correlations do or do not exhibit quasi-Gaussian properties is perhaps more important than their degree of statistical inhomogeneity.

7.7.6 *Provisional Conclusions About Scaling Laws and Quantified Values of Key Descriptors*

The kinetic energy decays more slowly in homogeneous rotating turbulence, with an exponent (e.g. -0.86 in AQNM) about one-half of the one observed in the non-rotating case (Squires et al. 2000; Bellet et al. 2006; Morize et al. 2005). This situation seems to correspond to high Reynolds and very low Rossby number limits, so that different decay laws can be found in DNS and experiments, such as a purely viscous decay law linked to negligible nonlinearity. On the other hand, a faster decay can be explained by inhomogeneous effects, dissipation of energy carried by inertial waves near the Ekman boundary layers (Ibbetson and Tritton 1975), and more non local effects of Ekman pumping on organized eddies (Morize et al. 2005). Directional anisotropy reaches a value of about $b_{33}^{(dir)} \sim 0.07-0.08$ (Cambon et al. 1997; Morinishi et al. 2001; Yang and Domaradzki 2004; Bellet et al. 2006), whereas polarization anisotropy $b_{33}^{(pol)}$ remains zero (Bellet et al. 2006), weak (Cambon et al. 1997; Morinishi et al. 2001),or reaches a large negative value, so that $b_{33} \sim -0.2$ (DNS and LES with long elapsed time and low resolution) (Fig. 7.19).

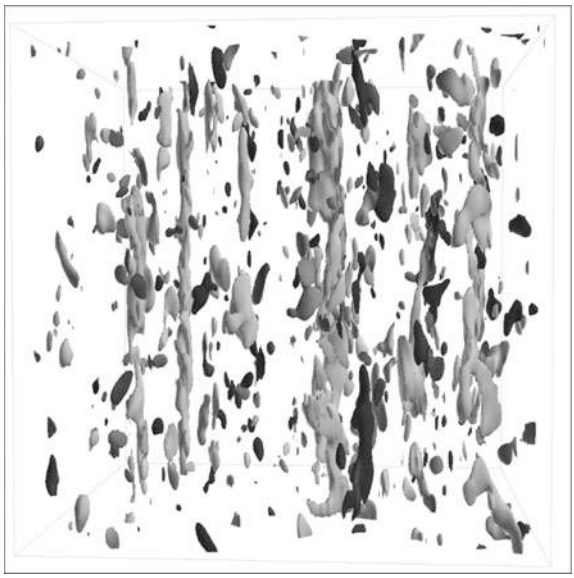

Fig. 7.19 Isovorticity surfaces from high resolution DNS. Dominant cyclonic structures are in gray. Courtesy of L. Liechtenstein

The spherically averaged energy spectrum is assumed to scale as $E(k) \sim \sqrt{\Omega\varepsilon}k^{-2}$ (Zhou 1995), in agreement with an energy transfer scaling as Ω^{-1} but completely ignoring the anisotropy. In the same way, an isotropic scaling of the second order structure function in terms of r (and not $r^{2/3}$ as in the usual Kolmogorov theory) is invoked by Baroud et al. (2003) and directly connected to a k^{-2} energy spectrum. We consider this proposal as not fully consistent, also because the authors claimed that they have quasi-2D dynamics with an inverse energy cascade. More generally, however, the "anomalous" scaling of the nth-order structure function as $r^{n/2}$ seems to be supported by both (Baroud et al. 2003; Simand 2002), see Fig. 7.20.

A complete scaling of $\mathcal{E}(k_\perp, k_\parallel)$ for any wavevector modulus and direction is possible from the AQNM numerical database (Bellet et al. 2006), or even from DNS/LES with convenient post-processing (Cambon et al. 1997; Liechtenstein et al. 2005), but it is not yet available. It may generalize the scaling law (7.52) given in Galtier (2003).

7.7.7 Deriving Effective Diffusivities and Atmospheric Spectra from a QNSE Theory

A promising approach is developed by Sukoriansky and Galperin (2016) (and references therein) in line with QNSE (Quasi-Normal Scale Elimination). In contrast with QNM approaches discussed at length in this chapter, the eddy-damping is not vanishing (asymptotic wave turbulence limit) or empirically fitted as in HIT, but is derived from successive coarsening of a flow domain, only assuming weak rotation. Accordingly, the emphasis cannot be put on the most detailed anisotropic structure,

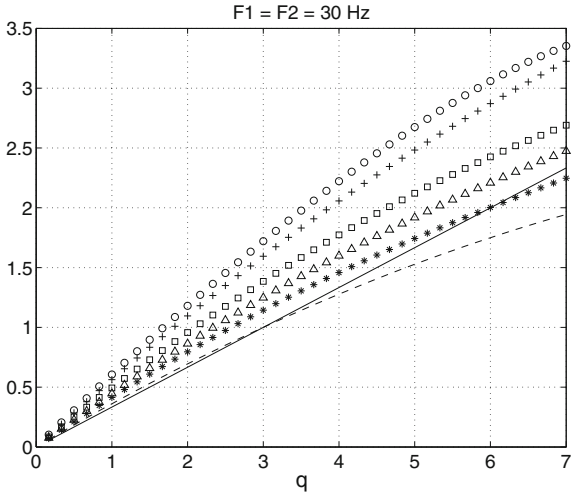

Fig. 7.20 $\zeta_q(q)$ exponents for structure functions at positions d closer and closer to the core of an intense vortex ('French washing machine' with co-rotative discs at 30 Hz): d = 4.5 cm ⋆, d= 3.5 cm △, d= 2.5 cm □, d= 1.5 +, d = 0.5 ∘, K41 model (full line), K62 model (dashed line) (Simand 2002)

but the QNSE theory yields scale-dependent eddy viscosities and diffusivities. These scale-dependent effective viscosities and diffusivities affect both directional anisotropy and polarization anisotropy. Four different viscosities are investigated and one-dimensional energy spectra are calculated. Incidentally, the scale expected for a re-isotropization of the flow, that is the rotational analogue of the Ozmidov scale in stably stratified flows, is recovered as a Woods scale (see Woods 1980.) The related threshold wavenumber, called k_Ω, is given by Eq. (7.62), and its effect on anisotropy is addressed in Sect. 7.9.

On the one hand, these scalings show a combination of k^{-3} and $k^{-5/3}$ slopes for the energy spectrum $E(k)$, that is a result common to different models based on weak anisotropy, e.g. in stratified turbulence, as reported in Chap. 10. More originally, the procedure gives access to a spectral tensor in terms of temporal frequency ω

$$\hat{R}_{ij}(\omega,\boldsymbol{k}) = 2Dk^{-3}\frac{|\mathbf{G}(\omega,\boldsymbol{k}|^2}{|\mathbf{D}(\omega,\boldsymbol{k})|^2}\left[A(\omega,\boldsymbol{k})P_{ij}(\boldsymbol{k}) + B(\omega,\boldsymbol{k})Q_{ij}(\boldsymbol{k}) + C(\omega,\boldsymbol{k})P_{3i}(\boldsymbol{k})P_{3j}(\boldsymbol{k})\right], \tag{7.56}$$

from which it is easy to recover the polarization (related to C) anisotropy and the contribution from helicity (related to B). The reader is referred to Sukoriansky and Galperin (2016) for details. The angle-dependent axisymmetric spectral coefficients derive from renormalized expansions of both the Green tensor (e.g. $\mathbf{G}$) and the solenoidal velocity. The steady ($\omega = 0$) energy spectra obtained in rotating turbulence are:
the k-dependent (spherically-averaged) spectrum

$$E(k) = 1.458\varepsilon^{2/3}k^{-5/3} + 0.564\,f^2k^{-3} = 1.458\varepsilon^{2/3}k^{-5/3}\left(1 + 0.387\left(\frac{k}{k_\Omega}\right)^{-4/3}\right), \tag{7.57}$$

the horizontal 1D (plane-averaged) longitudinal spectrum

$$E_1(k_1) = 0.47\varepsilon^{2/3}k_1^{-5/3} + 0.0926 f^2 k_1^{-3} = 0.47\varepsilon^{2/3}k_1^{-5/3}\left(1 + 0.197\left(\frac{k_1}{k_\Omega}\right)^{-4/3}\right), \tag{7.58}$$

and the horizontal 1D (plane averaged) transverse spectrum

$$E_1(k_2) = 0.62\varepsilon^{2/3}k_2^{-5/3} + 0.240 f^2 k_2^{-3} = 0.62\varepsilon^{2/3}k_2^{-5/3}\left(1 + 0.385\left(\frac{k_2}{k_\Omega}\right)^{-4/3}\right). \tag{7.59}$$

Due to axisymmetry (called horizontal isotropy by the authors) $E_1(k_1) = E_2(k_2)$.

On the other hand, these scalings were recently used by Galperin and Sukoriansky (2017) to revisit the Nastrom–Gage spectra in atmospheric turbulence. This new interpretation completely questions the interpretation by Lindborg, reported in Chap. 10. It is in agreement with the recent analysis from global high-resolution simulation by Skamarock et al. (2014), with two essential points: (i) The scaling of the k^{-3} part of the spectrum is associated with the Coriolis frequency, f in Eq. (7.57), and one recovers the fact that the spectra are latitude-dependent; as said by Skamarock et al. (2014): *Hence, the results do not support recent conjecture that stratified turbulence explains the mesoscale portion of the kinetic energy spectrum.* (ii) Both longitudinal and transverse energy spectra can be computed from the general axisymmetric scaling (7.56). Figure 7.21 from Galperin and Sukoriansky (2017) compares the QNSE spectrum by Eq. (7.58) (red lines) with the "canonical" spectra by Nastrom and Gage (1985). The data are the longitudinal spectra of the zonal and meridional winds. Due to the isotropy in the horizontal plane (axisymmetry of the model), both spectra are very close in the data (the meridional spectrum is shifted one decade to the right in Fig. 7.21) and they coincide in the theory. The canonical spectra were latitudinally averaged between 25 and 50° North thereby masking the dependence on f. The QNSE spectra were computed for 30° North. The factor of 2 difference between the transverse and longitudinal spectra on large scales was considered later (Callies et al. 2014). Other than QNSE, Eqs. (7.58) and (7.59), no other analytical theory so far was able to account for this difference.

7.8 Coherent Structures, Description and Dynamics

Emergence of "cigar-shaped" vortex structures has been observed in several DNS and LES studies. A recent visualization is shown on Fig. 7.19. At least in DNS initialized with conventional "almost Gaussian" realizations with random phase terms, they do not emerge if the nonlinear terms are cancelled. This is consistent with the

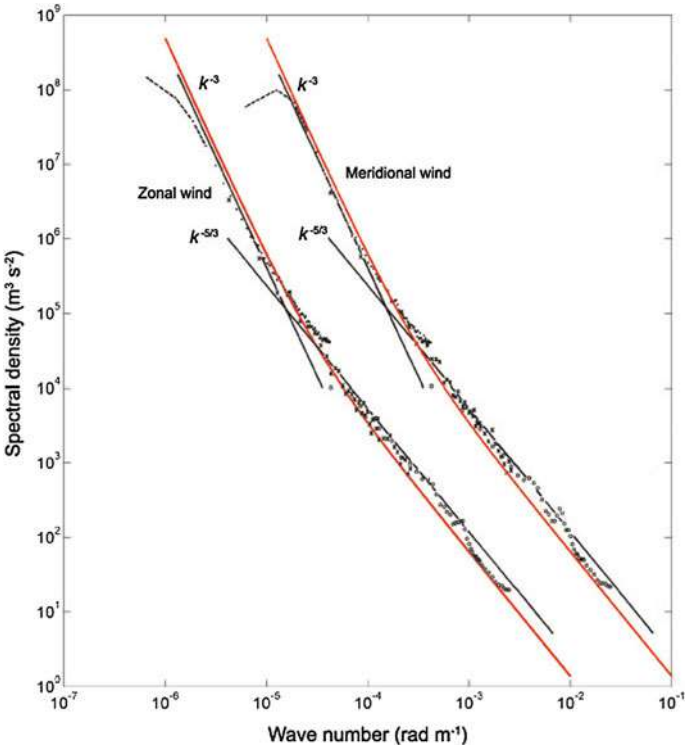

Fig. 7.21 Comparison of the canonical spectra of Nastrom and Gage (1985) with QNSE Eq. (7.58) (red lines). The "canonical"meridional spectrum is shifted one decade to the right. Courtesy of Boris Galperin and Sukoriansky (2017)

hypothesis of "non-linear formation of structures", supported by the anisotropic statistical approach of Cambon's team, but relevant criticisms by Peter Davidson must be accounted for. The appearance of these structures depends on the range of Rossby and Reynolds numbers, and also on the resolution and effective confinement of the numerical simulation.

A more realistic confinement is present in the DNS by Godeferd and Lollini (1999) on a plane channel rotating about the vertical direction. In addition to a realistic numerical approach to vertical confinement (pseudo-spectral Fourier-Fourier-Chebishev code with no-slip boundary conditions), another motivation was to reproduce the main results of the experiment by Hopfinger et al. (1982), briefly introduced in Sect. 7.1.1. Identification of vortices is illustrated in Fig. 7.22 (top) using both horizontal sections of iso-surfaces (noisy spots in the bottom plane of the figure) and isovalue surfaces of a normalized angular momentum, which is defined in the caption. The latter criterion (Normalized Angular Momentum) was suggested by experimentalists (Marc Michard, Lyon) in PIV for obtaining smooth isovalues. Asymmetry in terms of cyclones-anticyclones is mainly induced by the Ekman pumping near the

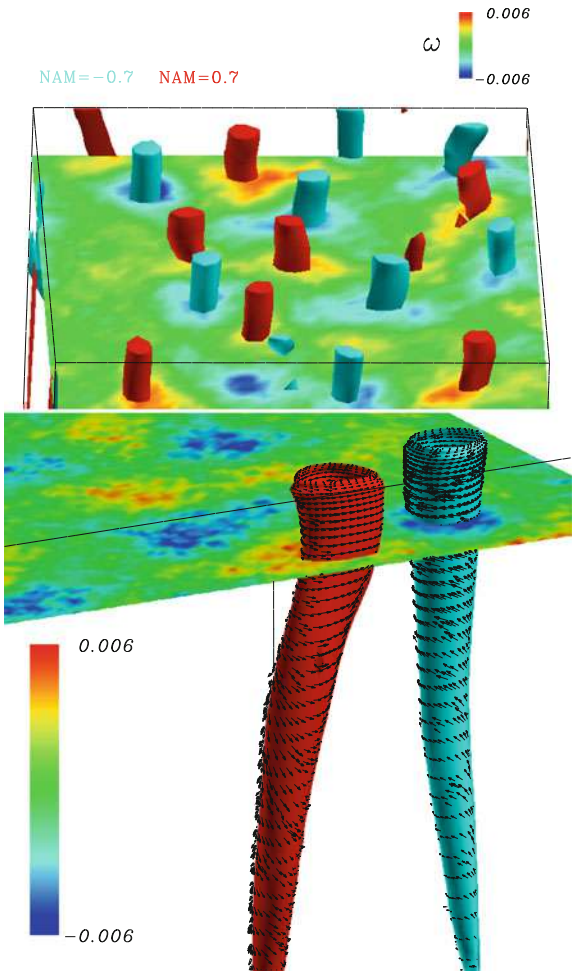

Fig. 7.22 Top: Vortex structures identified by NAM iso-values (tubes) and horizontal cross-section of vorticity iso-values (noisy spots in the bottom plane). NAM value at point M is obtained by averaging $|\,\mathbf{MP}\times\boldsymbol{u}(P)\,|\,/(|\,\mathbf{MP}\,||\,\boldsymbol{u}(P)\,|)$ over point P in a small domain surrounding M. Bottom: Selected pair of cyclonic-anticyclonic eddy structures, identified by NAM = 0.7 isosurfaces. Helical lines along them correspond to instantaneous streamlines in close vicinity of isosurfaces. Reproduced from Godeferd and Lollini (1999) with permission of CUP

solid boundaries, yielding helical trajectories. This is illustrated in Fig. 7.22 (bottom), in which a cyclone-anticyclone pair is isolated. Even if the Ekman pumping generates a three-component motion, the presence of the horizontal walls, and the presence of the forcing in the horizontal plane between them, are essential for enforcing coherent vortices. Nevertheless, and in contrast with the experimental results, no significant asymmetry between cyclonic and anticyclonic structures was observed in terms of number and intensity. In the same way, the typical distance between adjacent vortices is of the same order of magnitude as of their diameter, and the Rossby number in their core is close to one. It was expected that for a given symmetric distribution of more intense and concentrated vortices, the centrifugal and the elliptic instabilities could act in preferentially destabilizing the anticyclones, so that the cyclone could

emerge. It seems that the unsufficiently high Reynolds number is responsible for the lack of intensity and concentration of cigar vortices.

7.8.1 More on Cyclone/Anticyclone Asymmetry

There is now a general agreement about the fact that cyclonic vertical vorticity is dominant, i.e. $\omega_3 > 0$ on the average, at sufficiently high Reynolds number, and in an *intermediate range* of Rossby numbers. The intermediate range is not the same, according to the definitions by Jacquin et al. (1990) or by Bourouiba and Bartello (2007). Anyway, the latter definition only deals with micro-Rossby numbers significantly smaller than 1, as in Bartello et al. (1994).

It is perhaps puzzling that the approach by Bartello et al. (1994), and more recently by Chen et al. (2005), is essentially supported by low resolution LES (not DNS because of hyperviscosity), whereas the dynamics of vorticity is emphasized. It is well known that LES cannot accurately capture the small scales which contribute to the enstrophy, except if a sophisticated subgrid-scale model is used to explicitly represent the continuation of scales. The fact that the skewness of axial vorticity in Bartello et al. (1994) seems to grow with positive value until a reasonable level is reached is corroborated by recent experiments (Morize et al. 2005) (see Fig. 7.23). This suggests that, even if the dimensional value of $\langle \omega_3^3 \rangle$ is likely strongly underestimated in a low resolution LES, the nondimensional ratio

$$S_\omega = \frac{\langle \omega_3^3 \rangle}{\langle \omega^2 \rangle^{3/2}} \tag{7.60}$$

is probably captured with an acceptable order of magnitude.

In addition, the study by Morize et al. (2005) of decaying rotating turbulence shows the relevance of the linear time-scale to compare different cases with the same scaling: the vorticity skewness grows as t^α with $\alpha \in [0.7; 0.75]$ in Fig. 7.23(top). In this figure, the final rapid collapse is attributed to the rise of non-homogeneous mechanisms, such as Ekman pumping. DNS by van Bokhoven et al. (2008) yield similar results (Fig. 7.23(middle)). The late-time collapse in Fig. 7.23(middle) can be interpreted as a final stage of linear "triadic" phase-mixing, because of the absence of strong enough nonlinearity in decaying turbulence at moderate initial Reynolds number.

Since a significant part of the vorticity statistics, informative for the above mentioned issue of asymmetry in terms of cyclonic and anticyclonic axial vorticity, deals with triple correlations, statistical theory can be revisited and confronted to arguments from stability analysis, as discussed below.

Triple vorticity correlations are found as

$$\langle \omega_\parallel^3 \rangle(t) = \sum_{s,s',s''=\pm 1} \int_{R^6} \exp\left[\imath 2\Omega t \left(s\frac{k_\parallel}{k} + s'\frac{p_\parallel}{p} + s''\frac{q_\parallel}{q} \right) \right] T_{ss's''}(\mathbf{k}, \mathbf{p}, \epsilon t) d^3\mathbf{k} d^3\mathbf{p}. \tag{7.61}$$

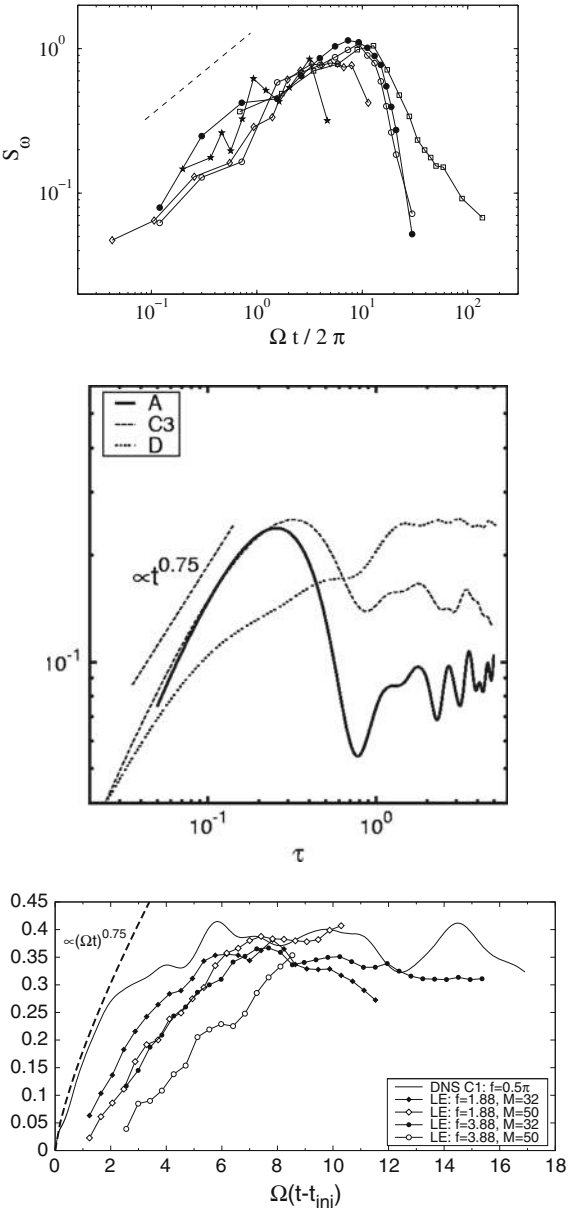

Fig. 7.23 skewness of the vertical vorticity distribution, experiment (top) (Morize et al. 2005), DNS (middle) (van Bokhoven et al. 2008), DNS run at the largest Rossby number plotted with experimental results (bottom) (Staplehurst et al. 2008, with permissions of CUP)

This equation is exact in the linear (RDT) limit, with $\epsilon = 0$ in the contribution from slowly evolving amplitudes denoted $T_{ss's''}$, even if applying RDT to cubic statistical moments is not usual. It exactly reflects the consequence of the Poincaré transform (7.36) at the level of cubic moments if ϵ is not zero.

In order to compute this integral, it is necessary to know the contribution from initial, or slowly evolving, triple correlations for all triads.[6] But the problem is much better documented than in physical space since robust spectral theories such as EDQNM provide a systematic way to express initial, isotropic, $T_{ss's''}$ in terms of the initial scalar energy spectrum $E(k)$. More generally, more advanced EDQNM$_{2,3}$ versions can be used to solve the full nonlinear problem, not only for generating isotropic initial data in Eq. (7.61) with $\epsilon = 0$. Common to the linear and nonlinear formulations, the phase term controlling phase-mixing appears in Eq. (7.61), and is zero when triads are in exact resonance.

As another result of statistical theory, it can be shown that the triple vorticity correlation $\langle\omega_3^3\rangle$ is necessarily produced with a positive value (corresponding to net production of cyclonic vertical vorticity) when 3D isotropic turbulence is suddenly set into solid body rotation (Gence and Frick 2001). This result comes from the Euler equations written in the rotating frame

$$\frac{d}{dt}\langle\omega_3^3\rangle = 3\langle\omega_3^2\omega_j S_{3j}\rangle + 6\Omega\langle\omega_3^2 S_{33}\rangle \quad \text{with} \quad S_{ij} = \frac{1}{2}\left(\frac{\partial u_i}{\partial x_j} + \frac{\partial u_j}{\partial x_i}\right),$$

since the specific rotation-induced "production" term $6\Omega\langle\omega_3^2 S_{33}\rangle$ is essentially positive, as is the classical "nonlinear vortex stretching term" $\langle\omega_i\omega_j S_{ij}\rangle$. The reader is referred to van Bokhoven et al. (2008) for the statistical analysis and its discussion, supported by both DNS and experimental results.

7.8.2 Is Bulk Helicity Everywhere or Nowhere?

Although rotating flows are often considered to be helical, this is not necessarily the case for homogeneous turbulence with supporting arguments based on a rigorous statistical analysis. Of course, patches, or special realizations containing helicity are often observed in several DNS studies of homogeneous rotating turbulence. Nonetheless, the rise of statistically significant helicity spectrum, such as $\mathcal{H}(\boldsymbol{k}, t)$, is never found in the absence of ad hoc initialization or forcing. Even when considering weak turbulence propagating from a local blob, or cloud, of vorticity, coexisting pairs of inertial waves with opposite polarity yield exactly zero helicity. We do not think that there is a mechanism capable of breaking symmetry between helical modes of positive and negative polarity in homogeneous turbulence, and even in unbounded turbulence. On the other hand, net helicity is created near a wall in rotating turbulence, and then could be transported towards the core of the flow. A very good example is given in the DNS database by Godeferd and Lollini (1999), but was hardly mentioned in that article. As illustrated by Fig. 7.22, it is found that the sign of helicity is

[6] Or equivalently, in physical space, for any triple correlation at three points, information which cannot be provided by the third-order structure function alone.

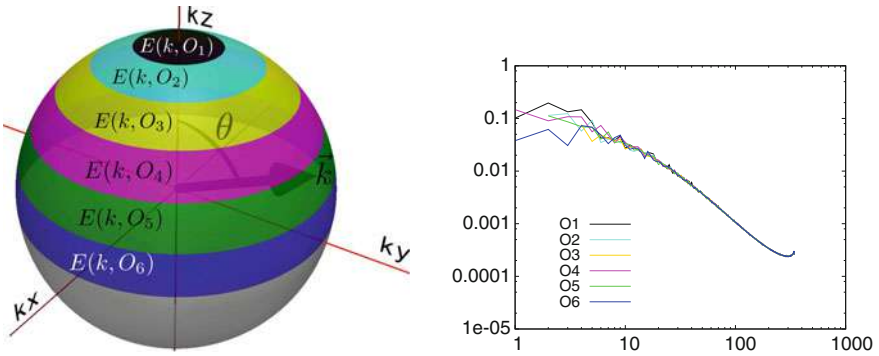

Fig. 7.24 Left: Diagram of angular (ring by ring) energy distribution. Right: Angle-dependent energy spectrum obtained without rotation. Reproduced from Delache et al. (2014) with permission of AIP

correlated with the motion of an eddy with axis normal to the wall and axial motion: helicity of two such eddies, with up and down opposite axial motion is additive.

Breaking of mirror symmetry is induced by solid-body rotation but is not sufficient to create net (in the statistical sense) helicity without boundaries. In the presence of coupled effects, such as in rotating stably stratified turbulence, helicity is not a conserved quantity, and the rise of helicity is expected without artificial forcing, even in homogeneous turbulence. In this case, helicity is linearly coupled with the toroidal buoyancy flux (also related to the correlation of axial vorticity with buoyancy), and both can break mirror symmetry. Unfortunately, no significant statistical value of one quantity or the other can emerge in DNS, at least if strict homogeneity (no finite box effect) is fulfilled. This is rediscussed in Chap. 12, Sect. 12.8.1. The reader is referred to several recent DNS studies with system rotation and artificial helical forcing, such as Mininni et al. (2012).

7.9 Scale-by-Scale Anisotropy

In spite of the peculiarity of purely rotating turbulence, some recent results have confirmed general trends found in other shear-driven or buoyancy-driven flow cases. One of them is the re-isotropization of rotating turbulence for scales smaller than a typical Zeman's, or Hopfinger's scale (Hopfinger et al. 1982; Zeman 1994), anticipated by Woods (1980) as well.

The corresponding threshold wavenumber is defined as

$$k_\Omega = \sqrt{\frac{\Omega^3}{\varepsilon}}, \tag{7.62}$$

with possible variants in multiplying by π or in using 2Ω instead of Ω. Anyway, the phenomenological interpretation of this threshold is not supported by an analytical

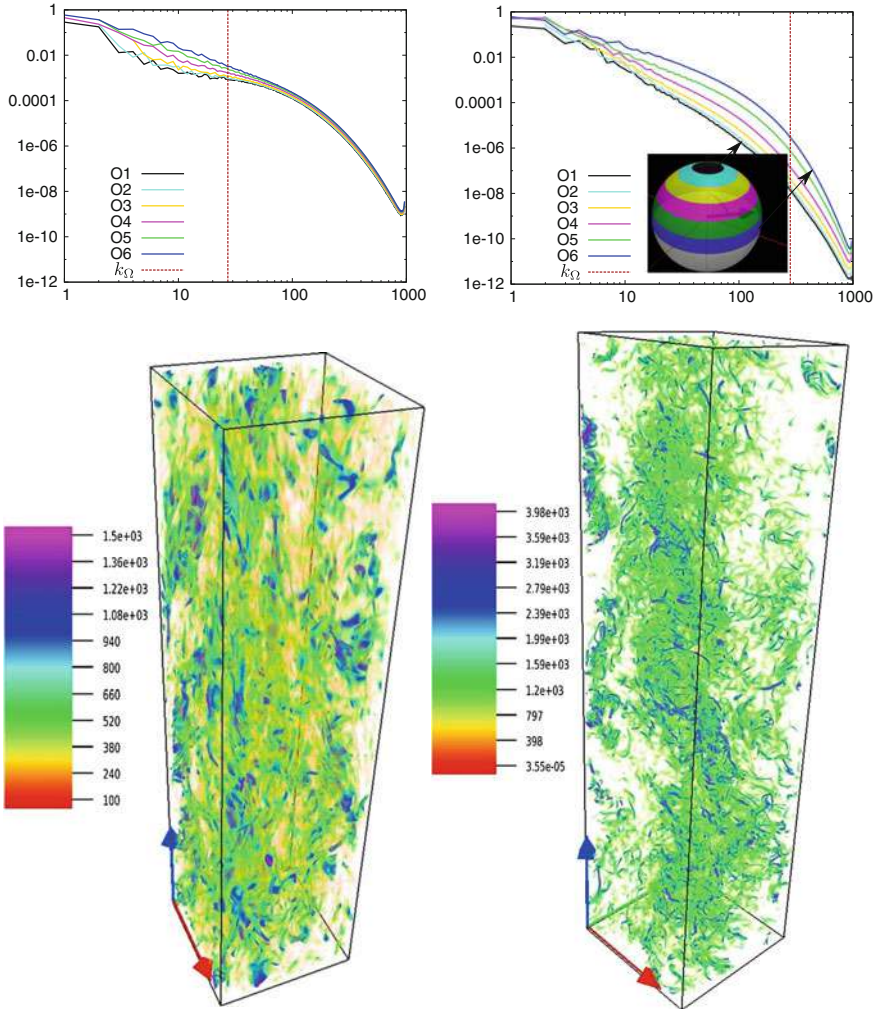

Fig. 7.25 Top: Angle-dependent spectra with rotation, at two different initial large-scale Rossby numbers, $Ro = 0.074$ and $Ro = 0.022$. Bottom: Visualization with vapor of the enstrophy distribution of the computational box. Reproduced from Delache et al. (2014) with permission of AIP

theory. Scale by scale distribution of both directional anisotropy and polarization anisotropy are analysed by Delache et al. (2014). Results are only given for the former, for the sake of simplicity. For this purpose, angle-dependent energy spectra $\mathcal{E}(k, \theta, t)$ are derived from a 6-bands distribution of energy for each (half) spherical shell, as shown in Fig. 7.24. Without rotation, contributions from different bands collapse, except for the smallest wavenumbers, for which angular resolution is very sparse (same figure, right). When rotation is present, as shown in Fig. 7.25, directional

anisotropy develops with the scattering of spectra from different angles at all scales (wavenumbers). We recover that this anisotropy first increases with increasing wavenumber, from the smallest, and that energy concentrates from polar to equatorial bands. This is also consistent with results of Figs. 7.16 and 7.18. But the directional anisotropy reaches a maximum when the wavenumber continues to increase and tends to decrease towards values close to k_Ω. This non-monotonic scale-by-scale distribution of directional anisotropy qualitatively confirms the role of the Zeman's scale, even if a complete re-isotropization is not found for $k > k_\Omega$. The monotonic increase of directional anisotropy with increasing wavenumber means that $k_\Omega \to \infty$ in the limit of wave turbulence, and that k_Ω is larger than the largest wavenumber k_{max} in DNS of Fig. 7.18. All these results are consistent with the experimental analysis of Pierre Philippe Cortet and Frédéric Moisy (private communication). A clear effect of re-isotropization at wavenumbers larger than k_Ω is also found in DNS by Mininni et al. (2012), but the directional anisotropy is monotonically decreasing from the forcing wavenumber. We think that the strong helical forcing used in the latter study imposes the maximum anisotropy at large scale, and that it is not possible in this case to disentangling anisotropic helicity from directional and polarization anisotropies (see also Sect. 7.8.2).

References

Aupoix, B., Cousteix, J., Liandrat, J.: Effects of rotation on isotropic turbulence. In: Bradbury, L.J.S., Durst, F., Launder, B.E., Schmidt, F.W., Whitelaw, J.H. (eds.) Turbulent Shear Flows. Springer, New York (1983)

Bardina, J., Ferziger, J.M., Rogallo, R.S.: Effect of rotation on isotropic turbulence: computation and modelling. J. Fluid Mech. **154**, 321–326 (1985)

Baroud, C.N., Plapp, B.B., Swinney, H.L.: Scaling in three-dimensional and quasi-two-dimensional rotating turbulent flows. Phys. Fluids **15**(8), 2091–2104 (2003)

Bartello, P., Métais, O., Lesieur, M.: Coherent structures in rotating three-dimensional turbulence. J. Fluid Mech. **273**, 1–29 (1994)

Bellet, F., Godeferd, F.S., Scott, J.F., Cambon, C.: Wave-turbulence in rapidly rotating flows. J. Fluid Mech. **562**, 83–121 (2006)

Benney, D.J., Newell, A.C.: Random wave closure. Stud. Appl. Math. **48**, 29–53 (1969)

Biferale, L., Bonaccorso, F., Mazzitelli, I.M., et al.: Coherent structures and extreme events in rotating multiphase turbulent flows. Phys. Rev. X **6**, 041036 (2016)

Bourouiba, L., Bartello, P.: The intermediate Rossby number range and 2D–3D transfers in rotating decaying homogeneous turbulence. J. Fluid Mech. **587**, 131–161 (2007)

Callies, J., Ferrari, R., Buehler, O.: Transition from geostrophic turbulence to inertia-gravity waves in the atmospheric energy spectrum. PNAS **111**(48), 17033–17038 (2014)

Cambon, C.: Etude spectrale d'un champ turbulent incompressible soumis à des effets couplés de déformation et rotation imposés extérieurement. Thèse de Doctorat d'Etat, Université Lyon I, France (1982)

Cambon, C., Jacquin, L.: Spectral approach to non-isotropic turbulence subjected to rotation. J. Fluid Mech. **202**, 295–317 (1989)

Cambon, C., Scott, J.F.: Linear and nonlinear models of anisotropic turbulence. Annu. Rev. Fluid Mech. **31**, 1–53 (1999)

Cambon, C., Jacquin, L., Lubrano, J.-L.: Towards a new Reynolds stress model for rotating turbulent flows. Phys. Fluids A **4**, 812–824 (1992)
Cambon, C., Mansour, N.N., Godeferd, F.S.: Energy transfer in rotating turbulence. J. Fluid Mech. **337**, 303–332 (1997)
Cambon, C., Rubinstein, R., Godeferd, F.S.: Advances in wave-turbulence: rapidly rotating flows. New J. Phys. **6**, 73 (2004)
Cambon, C., Godeferd, F.S., Nicolleau, F., Vassilicos, J.C.: Turbulent diffusion in rapidly rotating flows with and without stable stratification. J. Fluid Mech. **499**, 231–255 (2004)
Chen, Q., Chen, S., Eyink, G.S., Holm, D.D.: Resonant interactions in rotating homogeneous three-dimensional turbulence. J. Fluid Mech. **542**, 139–164 (2005)
Davidson, P.A., Stapelhurst, P.J., Dalziel, S.B.: On the evolution of eddies in a rapidly rotating system. J. Fluid Mech. **557**, 135–144 (2006)
Delache, A., Cambon, C., Godeferd, F.S.: Scale by scale anisotropy in freely decaying rotating turbulence. Phys. Fluids **26**, 025104 (2014)
Dickinson, S.C., Long, R.R.: Oscillating grid-turbulence including effects of rotation. J. Fluid Mech. **126**, 315–333 (1984)
Galperin, B., Sukoriansky, S.: Turbulence in rotating fluids and the Nastrom and Gage spectrum. Invited talk Sixth International Conference Turbulence Mixing and Beyond, ICTP, Trieste (Italy), 14–18 Aug 2017
Galtier, S.: A weak inertial wave-turbulence theory. Phys. Rev. E **68**, 1–4 (2003)
Gence, J.N., Frick, C.: Naissance des corrélations triples de vorticité dans une turbulence statistiquement homogène soumise à une rotation. C. R. Acad. Sci. Paris Série II b **329**(5), 351–356 (2001)
Godeferd, F.S., Lollini, L.: Direct numerical simulations of turbulence with confinment and rotation. J. Fluid Mech. **393**, 257–308 (1999)
Greenspan, H.P.: The Theory of Rotating Fluids. Cambridge University Press, Cambridge (1968)
Hopfinger, E.J., Browand, F.K., Gagne, Y.: Turbulence and waves in a rotating tank. J. Fluid Mech. **125**, 505 (1982)
Ibbetson, A., Tritton, D.: Experiments of rotation in a rotating fluid. J. Fluid Mech. **68**, 639–672 (1975)
Jacquin, L., Leuchter, O., Cambon, C., Mathieu, J.: Homogeneous turbulence in the presence of rotation. J. Fluid Mech. **220**, 1–52 (1990)
Kaneda, Y., Ishida, T.: Suppression of vertical diffusion in strongly stratified turbulence. J. Fluid Mech. **402**, 311–327 (2000)
Kassinos, S.C., Reynolds, W.C., Rogers, M.M.: One-point turbulence structure tensors. J. Fluid Mech. **428**, 213–248 (2001)
Liechtenstein, L., Godeferd, F.S., Cambon, C.: Nonlinear formation of structures in rotating stratified turbulence. J. Turbul. **6**, 1–18 (2005)
Mansour, N.N., Cambon, C., Speziale, C.G.: Single point modelling of initially isotropic turbulence under uniform rotation. Center for Turbulence Research, Stanford University, Annual Research Briefs (1991)
Mc Ewan, A.D.: Inertial oscillations in a rotating fluid cylinder. J. Fluid Mech. **40**, 603–639 (1970)
Mc Ewan, A.D.: Angular momentum diffusion and the initialization of cyclones. Nat. Ser. **260**, 126 (1976)
Mininni, P., Rosenberg, D., Pouquet, A.: Isotropisation at small scales of rotating helically driven turbulence. J. Fluid Mech. **699**, 263–279 (2012)
Morinishi, Y., Nakabayashi, K., Ren, S.K.: Dynamics of anisotropy on decaying homogeneous turbulence subjected to system rotation. Phys. Fluids **13**(10), 2912–2922 (2001)
Morize, C., Moisy, F., Rabaud, M.: Decaying grid-generated turbulence in a rotating tank. Phys. Fluids **17**(9), 095105 (2005)
Mowbray, D.E., Rarity, B.S.H.: A theoretical and experimental investigation of the phase configuration of internal waves of small amplitude in a density stratified liquid. J. Fluid Mech. **28**, 1–16 (1967)

Nastrom, G.D., Gage, K.S.: A climatology of atmospheric wavenumber spectra of wind and temperature observed by commercial aircraft. J. Atmos. Sci. **42**, 950–960 (1985)
Orszag, S.A.: Analytical theories of turbulence. J. Fluid Mech. **41**, 363–386 (1970)
Praud, O., Sommeria, J., Fincham, A.: Decaying grid turbulence in a rotating stratified fluid. J. Fluid Mech. **547**, 389–412 (2006)
Proudman, J.: On the motion of solids in a liquid possessing vorticity. Proc. R. Soc. Lond. A **92**, 408 (1916)
Salhi, A., Cambon, C.: Anisotropic phase-mixing in homogeneous turbulence in a rapidly rotating or in a strongly stratified fluid: an analytical study. Phys. Fluid **19**, 055102 (2007)
Scott, J.F.: Wave turbulence in a rotating channel. J. Fluid Mech. **741**, 316–349 (2014)
Simand, C.: Etude de la turbulence au voisinage d' un vortex, Ph.D. Thesis, Ecole Normale Supérieure de Lyon, defended on 28 Aug 2002 (2002)
Skamarock, W.C., Park, S.-H., Klemp, J.B., Snyder, C.: Atmospheric kinetic energy spectra from global high-resolution nonhydrostatic simulations. J. Atmos. Sci. **71**, 4369–4381 (2014)
Smith, L.M., Lee, Y. : On near resonances and symmetry breaking in forced rotating flows at moderate Rossby number. J. Fluid Mech. **535**, 111–142 (2005)
Squires, K.D., Chasnov, J.R., Mansour, N.N., Cambon, C.: The asymptotic state of rotating homogeneous turbulence at high Reynolds number. In: 74 th Fluid Dynamics Symposium on Application of Direct and Large Eddy Simulation to Transition and Turbulence, Chania, Greece, AGARD CP 551, 4-1– 4-9 (2000)
Staplehurst, P.J., Davidson, P.A., Dalziel, S.B.: Structure formation in homogeneous, freely-decaying, rotating turbulence. J. Fluid Mech. **598**, 81–103 (2008)
Sukoriansky, S., Galperin, B.: QNSE theory of turbulence anisotropization and onset of the inverse energy cascade by solid body rotation. J. Fluid Mech. **805**, 384–421 (2016)
Taylor, G.I.: Experiments on the motion of solid bodies in rotating fluids. Proc. R. Soc. London A **104**, 213 (1921)
Traugott, S.S.: Influence of solid body rotation on screen produced turbulence. NACA Technical Report 4135 (1958)
van Bokhoven, L.J.A., Cambon, C., Liechtenstein, L., Godeferd, F.S., Clercx, H.J.H.: Refined vorticity statistics of decaying rotating three-dimensional turbulence. J. Turbul. **9**, 1–24 (2008)
Waleffe, F.: Inertial transfers in the helical decomposition. Phys. Fluids A **5**, 677–685 (1993)
Wigeland, R.A., Nagib, H.M.: Grid generated turbulence with and without rotation about the stream wise direction. IIT Fluids and Heat Transfer Report R78-1 (1978)
Woods, J.D.: Do waves limit turbulent diffusion in the ocean? Nature **288**, 219–224 (1980)
Yang, X., Domaradzki, J.A.: LES of decaying rotating turbulence. Phys. Fluids **16**(11), 4088–4104 (2004)
Yarom, E., Sharon, E.: Experimental observation of steady inertial wave turbulence in deep rotating flows. Nat. Phys. **10**(7), 510–514 (2014)
Zakharov, V.E., L'vov, V.S., Falkowich, G.: Kolmogoroff Spectra of Turbulence I. Wave Turbulence. Springer Series in Nonlinear Dynamics. Springer, Berlin (1992)
Zeman, O.: A note on the spectra and decay of rotating homogeneous turbulence. Phys. Fluids **6**, 3221 (1994)
Zhou, Y.: A phenomenological treatment of rotating turbulence. Phys. Fluids **7**(8), 2092–2094 (1995)

Chapter 8
Incompressible Homogeneous Anisotropic Turbulence: With Strain

The presence of mean strain allows for a direct production of energy and anisotropy by linear terms, and such a *production* is in contrast with the case of purely rotating turbulence in the previous chapter. But, given its importance in many applications, the particular case of turbulence subjected to pure plane mean shear deserves a dedicated chapter, see Chap. 9. As discussed in Chap. 2, the case of the pure plane shear delineates two classes of mean flows with space-uniform gradients, those dominated by strain with hyperbolic streamlines, and those dominated by (mean) vorticity, with elliptic ones. In addition to the linear regime, which is displayed by the RDT approximation, more details are given on fully nonlinear calculation and modeling. Finally, the dynamics of return-to-isotropy is addressed after relaxation of the strain.

8.1 Main Observations

This chapter is devoted to the dynamics of homogeneous turbulent flows submitted to mean velocity gradients, with pure strain as a first step. More general combination of the effects of mean strain and mean vorticity, or rotational strain, are addressed later in in this chapter. The pure strain case is defined as the case in which the mean velocity gradient matrix $\mathbf{A}$ is symmetric. As discussed in the rest of this chapter, several experimental setups have been designed during the last decades, which lead to different forms for $\mathbf{A}$. Kinematic aspects, from the design of ducts in experiments to a first insight to RDT, are also introduced in the general case in which $\mathbf{A}$ combines a symmetric and an antisymmetric part (mean vorticity), in order to characterize in the simplest way what is the specificity of an irrotational straining process.

Both experiments and numerical simulations lead to the following observations dealing with the dynamics of homogeneous turbulence subjected to pure strain:

- The initially isotropic turbulence becomes anisotropic in the presence of a mean strain, and the principal axes of the Reynolds stress tensor become identical to those of the $\mathbf{A}$, the axis of contraction for $\mathbf{A}$ corresponding to the direction of

P. Sagaut and C. Cambon, *Homogeneous Turbulence Dynamics*,
https://doi.org/10.1007/978-3-319-73162-9_8

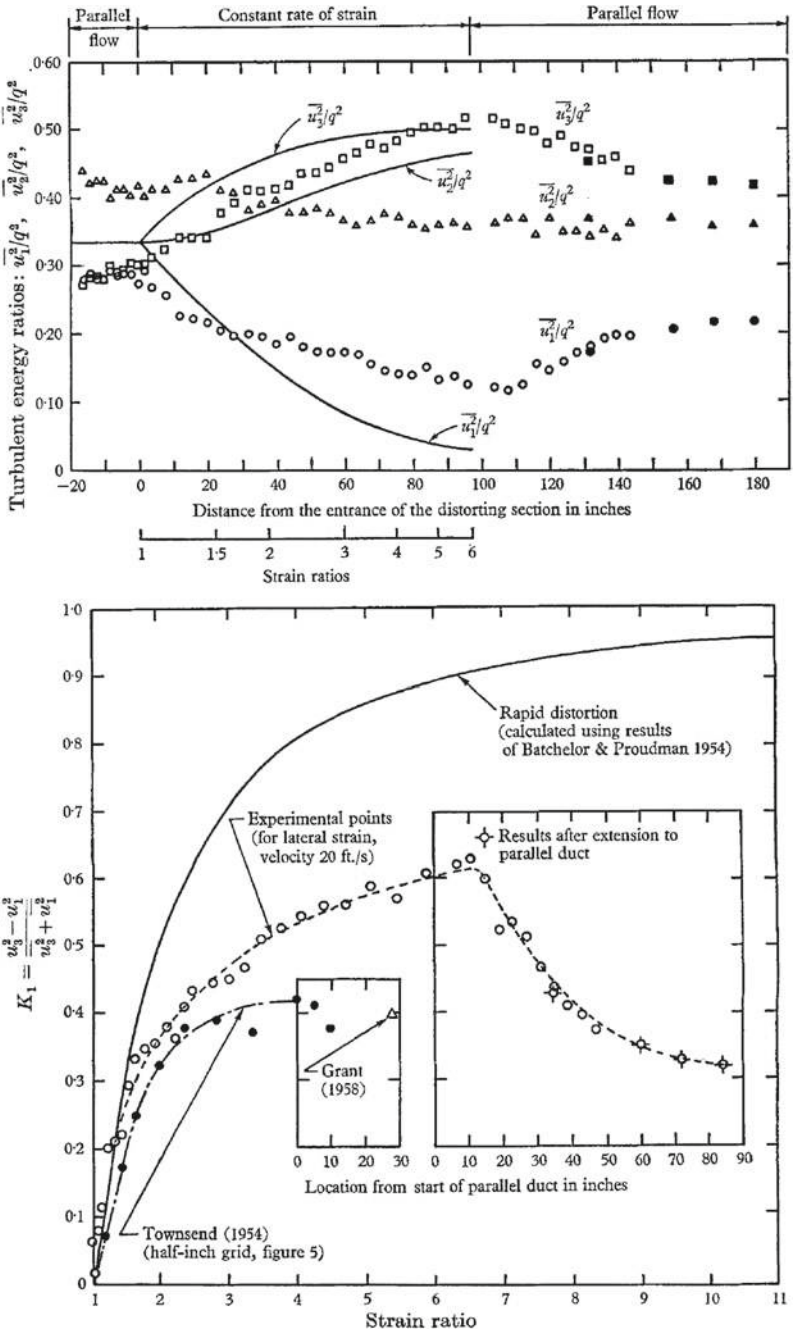

Fig. 8.1 Time evolution of anisotropy in the pure strain case with isotropic initial field. Top: evolution of the three components of the total kinetic energy (solid lines: linear RDT prediction; symbols: experiments). Bottom: evolution of the structural anisotropy indicator in different experiments. Reproduced from Tucker and Reynolds (1968) with permission of CUP

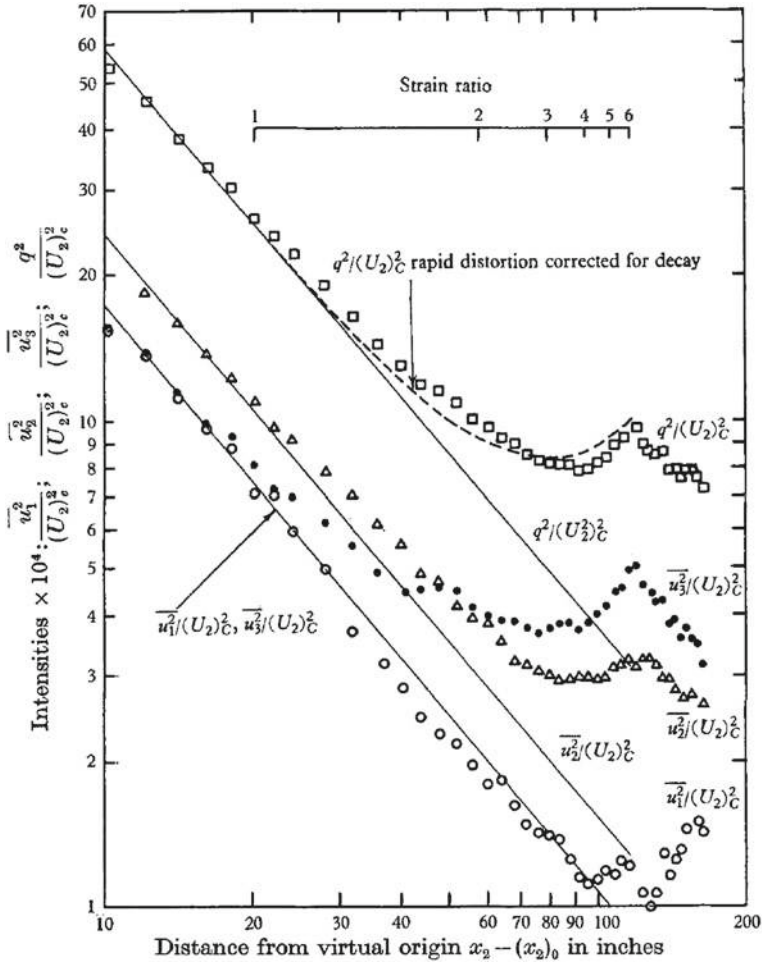

Fig. 8.2 Time evolution of turbulent kinetic energy in the pure strain case with isotropic initial field, illustrating the production phenomenon. The turbulent kinetic energy $\mathcal{K}$ is denoted q^2 here. Reproduced from Tucker and Reynolds (1968) with permission of CUP

maximum amplification for the Reynolds stress tensor. If the strain is applied for a long enough time, anisotropy reaches an asymptotic state. Typical results are displayed in Fig. 8.1.

- The turbulent kinetic energy $\mathcal{K}(t)$ is a growing function of time at large non-dimensional time St (see Fig. 8.2), where S is related to a norm of $\mathbf{A}$. This *production of turbulent kinetic energy* is related to the growth of anisotropy. For initially isotropic turbulence, an initial period of decay is observed, which corresponds to the transient phase during which the anisotropy starts raising from zero.

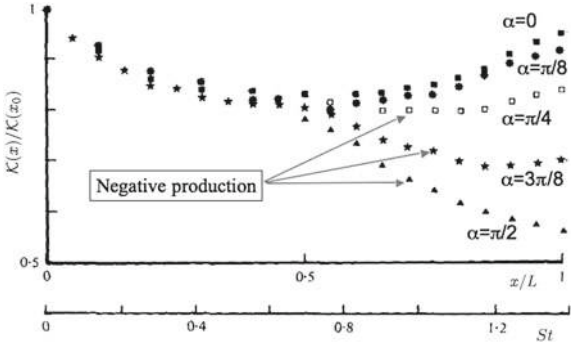

Fig. 8.3 Time evolution of turbulent kinetic energy in the pure strain case with anisotropic initial field, illustrating the negative production phenomenon. α is the angle of rotation between two successive coplanar strains. $\alpha = 0$ corresponds to a constant strain rate without rotation of the strain direction. Reproduced from Gence and Mathieu (1979) with permission of CUP

- *Negative production*, i.e. destruction of $\mathcal{K}(t)$ by the mean flow, can be observed over transient phase for some initially anisotropic turbulent flows (see Fig. 8.3). It is important to note that this phenomenon is not related to a dissipative mechanism involving the molecular viscosity, or nonlinear cascade. It is due to the same physical mechanisms that are responsible for turbulence production in other cases. The negative/positive character of turbulence production by pure strain is determined by the angle between the principal axes of the Reynolds stress tensor and those of $\mathbf{A}$. In addition, the temporal memory of the straining process, identified by the Cauchy matrix $\mathbf{F}$ related to $\mathbf{A}$, plays an essential role for explaining the response of turbulence to time-dependent processes $\mathbf{A}(t)$.

8.2 Experiments for Turbulence in the Presence of Mean Strain. Kinematics of the Mean Flow

In most wind-tunnel experiments, turbulence was generated by a grid and transported along the tunnel by the mean flow. Distorted ducts located downstream the grid were used to impose the desired strain on the initially isotropic turbulence. The principle is the following: The distorted duct is designed so that its internal surface is coincidental with a streamtube surface of the desired mean flow, leading to the imposition of the target mean velocity gradient field. The Lagrangian formalism introduced in Sect. 2.1.9 is particularly useful. It provides a simple and elegant framework to describe the geometry of streamtubes and to recover a kinematic interpretation of the mathematical operators that appear in the Rapid Distortion Theory (RDT). Accordingly, the kinematic description of the mean "distorting flow" makes use of the Lagrangian and mixed Lagrangian/Eulerian formalism introduced in Chap. 2, but

the quantities related to Lagrangian features of the solution, such as the Lagrangian coordinates X_i, the trajectories, and mixed Eulerian/Lagrangian quantities such as the Cauchy matrix F_{ij}, will be restricted to the sole mean flow.

8.2.1 Pure Irrotational Strain, Planar Distortion

The decay of HIT is well reproduced in wind-tunnel experiments, in which turbulence created by a grid is advected downstream without significant distortion (see Sect. 4.1.1). In this case, an equivalent elapsed time is estimated thanks to the Taylor frozen turbulence hypothesis (see Sect. 4.1.1) as $t = \frac{x_3 - x_3^0}{U_0}$, where x_3 denotes the streamwise coordinates. Here, x_3^0 is a typical 'initial' distance from the grid, needed to homogenize the wakes of the rods (about 40 mesh-sizes in practice), and U_0 the mean velocity, which is considered as uniform in the duct, outside the boundary layers.

The additional straining process is obtained using a distorting duct, whose transverse sections have a constant area, in order to conserve U_0, but are more and more elongated as the distance from the grid increases. Rectangular transverse sections were used by Maréchal (1970), Tucker and Reynolds (1968), while elliptical sections were used by Gence and Mathieu (1979). In all cases, the contour lines have an hyperbolic design in order to reproduce a mean strain with constant rate.

As a typical feature of the experiment by Gence and Mathieu, the initial section of the distorting duct is elliptical with its large axis in the vertical direction, so that the aspect ratio of the ellipse first decreases to reproduce a compression in the vertical direction (say x_2) and a dilatation in the spanwise (x_1) direction. Continuation of the process yields recovering an increasing aspect ratio, with elongation of the elliptical section in the spanwise direction. The change from decreasing to increasing the aspect ratio implies that a *circular* section is obtained at a particular downstream position. Accordingly, the distorting duct is split into two parts, before and after the circular section, so that a sudden change of the principal axes of the straining process can be reproduced by only rotating the second part of the duct with respect to the first part from an angle α (see Fig. 8.4). For instance, in the case of the continuous strain, a rotation of $\pi/2$ allows to revert the strain, so that the initial section is exactly recovered at the end of the duct.

Moreover, a duct with constant section can be added at the end of the distorting one, in order to study the expected return-to-isotropy of turbulence, at least when the distortion results in a large anisotropy of the turbulent flow.

All these experiments illustrate the generation of the mean velocity gradients $\mathbf{A}$ in a cross section normal to the uniform streamwise velocity, denoted U_0 and chosen along the direction 3, so that the mean trajectories can be defined by:

$$x_i = F_{ij}(t, t_0) X_j + U_0 t \delta_{i3}. \tag{8.1}$$

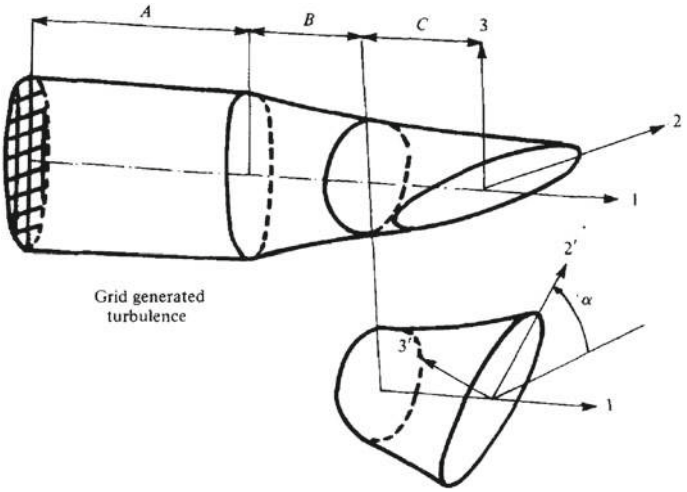

Fig. 8.4 Sketch of the duct used by Gence and Mathieu to obtain plane straining of turbulence. Reproduced from Gence and Mathieu (1979) with permission of CUP

The initial time, t_0, will be omitted or denoted by 0, in the following.

The corresponding mean gradient matrix $\mathbf{A}$ and mean displacement matrix $\mathbf{F}$ are (see. Sect. 2.1.9)

$$\mathbf{A} = \mathbf{A}_0 = \begin{pmatrix} -S & 0 & 0 \\ 0 & S & 0 \\ 0 & 0 & 0 \end{pmatrix}, \quad \text{and} \quad \mathbf{F} = \mathbf{F}_0(t) = \begin{pmatrix} e^{-St} & 0 & 0 \\ 0 & e^{St} & 0 \\ 0 & 0 & 1 \end{pmatrix} \tag{8.2}$$

for a constant straining process, or the first part of the duct in the Gence's experiment, and

$$\mathbf{A} = \tilde{\mathbf{Q}}\mathbf{A}_0\mathbf{Q}, \mathbf{F} = \mathbf{F}_0(t_1) + \tilde{\mathbf{Q}}\mathbf{F}_0(t - t_1)\mathbf{Q} \quad \text{for} \quad t_1 < t < 2t_1 \tag{8.3}$$

with

$$\mathbf{Q} = \begin{pmatrix} \cos\alpha & -\sin\alpha & 0 \\ \sin\alpha & \cos\alpha & 0 \\ 0 & 0 & 1 \end{pmatrix}, \tag{8.4}$$

for the second part of the duct with $t_1 = L/U_0$ corresponding to the location of the circular section at half the length $2L$ of the full Gence's distording duct.

The distorting duct is built by materializing a stream-tube, corresponding to an initial cross-section, chosen rectangular (Maréchal 1970; Tucker and Reynolds 1968)

or elliptical (Gence and Mathieu 1979). True streamlines are expected to be homothetic and to follow the geometry imposed by the duct, in agreement with previous equations, an expectation which appeared to be reasonable in a large part of the duct not too close to solid boundaries.

More recently, the experiment by Chen et al. (2006) used a piston to apply plane straining and destraining on turbulence generated by active grids. The mean-velocity gradient matrix in the experiment is of the form

$$\mathbf{A} = \begin{pmatrix} S(t) & 0 & 0 \\ 0 & -S(t) & 0 \\ 0 & 0 & 0 \end{pmatrix}, \tag{8.5}$$

where the temporal evolution of $S(t)$ is given by the Fig. 8.9. Initially, the mean flow corresponds to plane straining ($S(t) > 0$), until $t/\tau_0 \sim O.5$. After a relaxation phase ($0.5 \leq t/\tau_0 \leq 0.7$), destraining is applied to the turbulence. In this experiment, the Taylor-microscale-based Reynolds number at the beginning of the straining cycle is $Re_\lambda \sim 400$, larger than in previously mentioned experimental facilities. This experiment is re-discussed when the temporal return-to-isotropy is addressed (Sect. 8.7) — because of the presence of a relaxation phase —, with results compared with those of a spectral model.

8.2.2 *Axisymmetric (Irrotational) Strain*

This case presents particular interest since axial symmetry is the simplest anisotropy. The corresponding mean flow can be reproduced by means of an axisymmetric distorting duct, convergent or divergent. As also discussed in the next subsection, the mean velocity is not constant in the streamwise — and axial — direction, and it is not constant in a given cross-section with increasing (divergent duct) or decreasing (convergent duct) surface. Flow separation and specific instabilities can appear, especially in the divergent case, but also in the convergent case (Leclaire 2006). In spite of the complexity of these experimental issues, this flow will be considered as a reference case, at least from a theoretical and numerical viewpoint.

The configuration of axisymmetric strain is approached in convergent and divergent ducts, and only the vicinity of the centerline (axis) is considered for the sake of simplicity. Mean velocity gradient matrix is

$$\mathbf{A} = \begin{pmatrix} -S/2 & 0 & 0 \\ 0 & -S/2 & 0 \\ 0 & 0 & S \end{pmatrix} \tag{8.6}$$

with S possibly time-dependent, $S > 0$ corresponds to the case of axisymmetric convergent duct. As previously, the axial direction is chosen as $n_i = \delta_{i3}$ without lack

of generality, the non-trivial components in the Cauchy matrix are

$$F_{33}(t) = \exp\left(\int_0^t S(t')dt'\right) = C(t), \quad F_{11}(t) = F_{22}(t) = \frac{1}{\sqrt{C(t)}}. \tag{8.7}$$

8.2.3 The Most General Case for 3D Irrotational Case

On the other hand, three-dimensional irrotational strain characterized by **A** having three eigenvalues, S_1, S_2, S_3, with zero sum (incompressibility), and possibly time-dependent, has little interest from the viewpoint of homogeneous turbulence and related experimental approaches. Some specific RDT solutions were initially proposed by Courseau et Loiseau (1978), but can be easily generalized and simplified, using the formalism introduced by Cambon (1982), Cambon et al. (1985), using both a reduced Green's function and the Cauchy matrix. *For any analytical result subsequently given, we will specify if it applies to the 3D general irrotational case or not.*

8.2.4 More General Distortions. Kinematics of Rotational Mean Flows

A different kind of experimental procedure was initially proposed to obtain a pure mean shear flow. For instance in Rose (1966), Champagne et al. (1970), the shear gradient is created in the vertical direction (here x_1) by a pile-up of plates, without distortion of the duct. Even if a constant mean velocity gradient $\partial\overline{u}_2/\partial x_1$ is obtained throughout the duct, the consistency with statistical homogeneity of turbulence is much more problematic than in the experiments for irrotational strain presented in the preceding section. The streamwise velocity is no longer uniform in a cross-section, so that the mean advection time $(x_3 - X_3)/U_3(x_1)$ varies with x_1; it is shorter near the top (largest U_3) than near the bottom (smallest U_3) of the duct. As a consequence, $A_{21} = S$ can be considered as constant in a current cross-section, but not $F_{21} = St$.

In order to obtain a pure shear flow in a more satisfactory way (regarding homogeneity of turbulence), and especially to generalize it to an arbitrary combination of vorticity and strain, a general procedure was defined at ONERA, in close collaboration with the LMFA team (Leuchter et al. 1992). The principle is to generate a solid body rotation in a cylindrical duct, and then to superimpose a convenient irrotational process by a subsequent distorting duct. The Jacquin's experiment (Jacquin et al. 1990) for pure rotation, presented in the previous chapter, was used for this purpose, replacing the cylindrical duct after the rotation generator (a rotating honeycomb) by a duct designed in exact accordance with Eq. (8.1). Current cross-sections of the distorting duct do correspond to a single advection time $(x_3 - X_3)/U_0$.

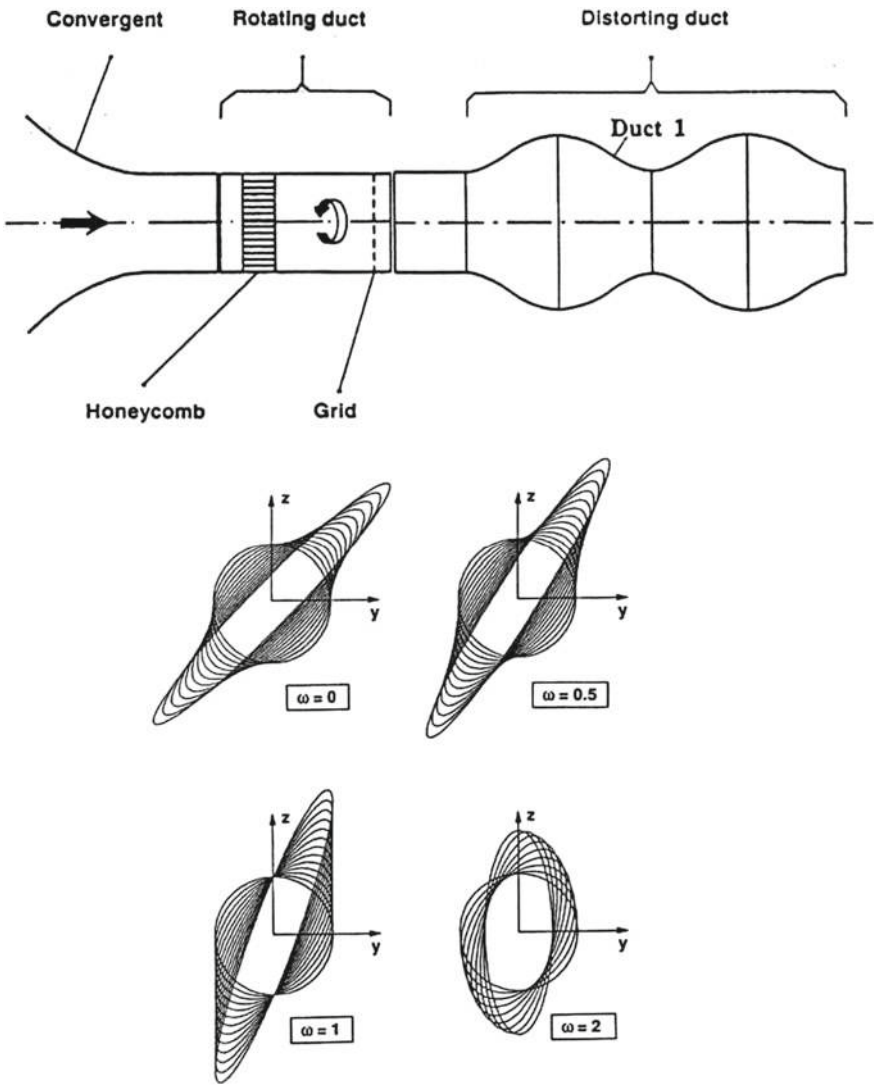

Fig. 8.5 Sketch of the distorting ducts in the experiment by Leuchter et al. (1992). Top: side view of the experimental facilities, 'periodic' case with $\omega = \Omega/S = 2$. Bottom: front view of the duct for different values of $\omega = \Omega/S$

They are ellipses of constant area with both their aspect ratio and the orientation of their axes varying continuously with the streamwise position. In Eq. (8.1), $\mathbf{F}$ (with corresponding $\mathbf{A}$) is easily calculated as follows

$$\mathbf{A} = \begin{pmatrix} 0 & S-\Omega & 0 \\ S+\Omega & 0 & 0 \\ 0 & 0 & 0 \end{pmatrix}, \quad \mathbf{F} = \begin{pmatrix} \cosh\sigma_0 t & (S-\Omega)\frac{\sinh\sigma_0 t}{\sigma_0} & 0 \\ (S+\Omega)\frac{\sinh\sigma_0 t}{\sigma_0} & \cosh\sigma_0 t & 0 \\ 0 & 0 & 1 \end{pmatrix} \tag{8.8}$$

with

$$\sigma_0^2 = S^2 - \Omega^2. \tag{8.9}$$

The hyperbolic case $S > \Omega$ is given here as an example, but the elliptical case $S < \Omega$ is straightforwardly derived by changing σ_0 into $\imath\sigma_0$, yielding a periodic $\mathbf{F}$. The analytical solution $F_{\alpha\beta} = \delta_{\alpha\beta}\cosh\sigma_0 t + A_{\alpha\beta}\frac{\sinh\sigma_0 t}{\sigma_0}$ results from $A_{\alpha\gamma}A_{\gamma\beta} = \sigma_0^2\delta_{\alpha\beta}$, so that $\ddot{F}_{\alpha\beta} = \sigma_0^2 F_{\alpha\beta}$, excluding the value 3 for Greek indices. The particular case of the pure shear $S = \Omega$, whose associated shear rate is equal to $\Omega + S = 2S$, is consistently recovered in the limit $\sigma_0 \to 0$.

Elliptical cross-sections are analytically derived from the initial (circular) section of the distorting duct, i.e. $X_\alpha X_\alpha = R^2$, so that

$$F^{-1}_{\alpha\beta}(t)F^{-1}_{\alpha\gamma}(t)x_\beta x_\gamma = R^2, \quad t = \frac{x_3 - x_3^0}{U_0}. \tag{8.10}$$

Typical streamlines, such as those sketched in Fig. 2.1, are recovered in the plane $(1, 2)$ of the mean distortion as the envelope of the moving ellipses. They are hyperboles for $\sigma_0^2 > 0$, straight lines for $\sigma_0 = 0$, and ellipses for $\sigma_0^2 < 0$. Only in the last case, the duct is periodic, a typical sketch is shown on Fig. 8.5.

8.3 First Approach in Physical Space to Irrotational Mean Flows

8.3.1 Governing Equations, RST Balance and Single-Point Modelling

8.3.1.1 Planar Strain

The evolution equations for Reynolds stresses associated with the gradient matrix $\mathbf{A}$ defined in Eq. (8.2) are

$$\frac{\partial\overline{u_i'u_j'}}{\partial t} + \overline{u}_k\frac{\partial\overline{u_i'u_j'}}{\partial x_k} = S\begin{pmatrix} 2\overline{u_1'u_1'} & 0 & \overline{u_1'u_3'} \\ 0 & -2\overline{u_2'u_2'} & -\overline{u_2'u_3'} \\ \overline{u_1'u_3'} & -\overline{u_2'u_3'} & 0 \end{pmatrix} + \Pi_{ij} - \varepsilon_{ij}. \tag{8.11}$$

The corresponding equation for the turbulent kinetic energy is:

$$\frac{\partial \mathcal{K}}{\partial t} = S\left(\overline{u_1'u_1'} - \overline{u_2'u_2'}\right) - \varepsilon. \tag{8.12}$$

It is seen that the production of kinetic energy by explicit linear effects is due to the anisotropy, and more precisely to the difference between the two diagonal Reynolds stresses $\overline{u_1'u_1'}$ and $\overline{u_2'u_2'}$. This production can be either positive or negative, depending on the signs of S and $\left(\overline{u_1'u_1'} - \overline{u_2'u_2'}\right)$. The possible occurence of a negative production term corresponds to the existence of flows in which the mean irrotational strain will destroy the turbulent kinetic energy. A direct consequence is that the production mechanism escapes the isotropic two-equations turbulence models, in which the differences between the diagonal Reynolds stresses are neglected. The errors committed on turbulent kinetic energy production in the vicinity of stagnation points in non-homogeneous flows are directly related to this problem.

Of course, negative production occurs in the Gence's experiment, and this is further discussed at the end of this section.

8.3.1.2 Axisymmetric Irrotational Strain

For axisymmetric strain with $\mathbf{A}$ given by Eq. (8.6), one has

$$\frac{\partial \overline{u_i'u_j'}}{\partial t} + \overline{u}_k \frac{\partial \overline{u_i'u_j'}}{\partial x_k} = S \begin{pmatrix} \overline{u_1'u_1'} & \overline{u_1'u_2'} & -\frac{1}{2}\overline{u_1'u_3'} \\ \overline{u_1'u_2'} & \overline{u_2'u_2'} & -\frac{1}{2}\overline{u_2'u_3'} \\ -\frac{1}{2}\overline{u_1'u_3'} & -\frac{1}{2}\overline{u_2'u_3'} & -2\overline{u_3'u_3'} \end{pmatrix} + \Pi_{ij} - \varepsilon_{ij}. \tag{8.13}$$

The corresponding equation for the turbulent kinetic energy is:

$$\frac{\partial \mathcal{K}}{\partial t} = \frac{S}{2}\left(\overline{u_1'u_1'} + \overline{u_2'u_2'} - 2\overline{u_3'u_3'}\right) - \varepsilon. \tag{8.14}$$

It is seen that the production mechanisms is still governed by anisotropy in this configuration, but this time it involves the three diagonal Reynolds stresses.

8.3.1.3 More General Rotational Strains

In the general case corresponding to Eq. (8.8), one has

$$\frac{\partial \overline{u_i'u_j'}}{\partial t} + \overline{u}_k \frac{\partial \overline{u_i'u_j'}}{\partial x_k} = -\begin{pmatrix} 2(S-\Omega)\overline{u_1'u_2'} & (S-\Omega)\overline{u_2'u_2'} + (S+\Omega)\overline{u_1'u_1'} & (S-\Omega)\overline{u_2'u_3'} \\ (S-\Omega)\overline{u_2'u_2'} + (S+\Omega)\overline{u_1'u_1'} & 2(S+\Omega)\overline{u_1'u_2'} & (S+\Omega)\overline{u_1'u_3'} \\ (S-\Omega)\overline{u_2'u_3'} & (S+\Omega)\overline{u_1'u_3'} & 0 \end{pmatrix} + \Pi_{ij} - \varepsilon_{ij} \tag{8.15}$$

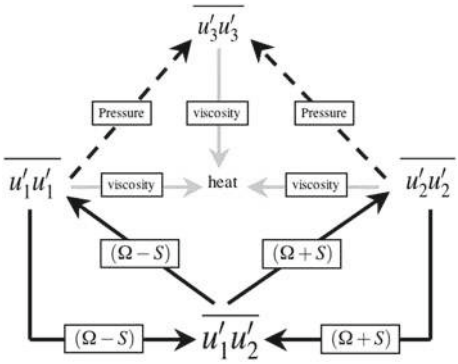

Fig. 8.6 Couplings between the different non-vanishing Reynolds stresses in the general strain case. Arrows indicate the production process, their color being related to the physical quantity at play (mean strain, pressure, viscosity)

and

$$\frac{\partial \mathcal{K}}{\partial t} = 2S\overline{u_1'u_2'} - \varepsilon. \tag{8.16}$$

Considering the case of an initially isotropic field, one has $\overline{u_\alpha'u_3'} = \overline{u_3'u_\alpha'} = 0$, $\alpha = 1, 2$ so that Eq. (8.15) simplifies as

$$\begin{cases} \dfrac{d\overline{u_1'u_1'}}{dt} = 2(\Omega - S)\overline{u_1'u_2'} & +\Pi_{11} \; -\varepsilon_{11} \\ \dfrac{d\overline{u_2'u_2'}}{dt} = -2(\Omega + S)\overline{u_1'u_2'} & +\Pi_{22} \; -\varepsilon_{22} \\ \dfrac{d\overline{u_3'u_3'}}{dt} = & +\Pi_{33} \; -\varepsilon_{33} \\ \dfrac{d\overline{u_1'u_2'}}{dt} = \Omega(\overline{u_2'u_2'} - \overline{u_1'u_1'}) + S(\overline{u_2'u_2'} + \overline{u_1'u_1'}) & +\Pi_{12} \; -\varepsilon_{12} \end{cases}. \tag{8.17}$$

The different couplings are illustrated in Fig. 8.6. This case is rediscussed from the viewpoint of RDT, first in Sect. 8.4.1, then in Chap. 11.

8.3.2 General Assessment of RST Single-Point Closures

The most general irrotational flow case, with time-dependent and even three-dimensional (i.e. with three different nonzero eigenvalues) $\mathbf{A}$ is now considered.

Full Reynolds stress models work satisfactory to predict the effect of irrotational strain. For instance, the Reynolds stress component in the direction of mean compression is shown to increase, the one in the direction of mean dilatation is shown to decrease, so that increasing anisotropy is created by a monotonic strain.

In addition, directional and polarization anisotropies defined in Chap. 2 seem to be closely related, at least at the level of single-point statistics, via:

$$b_{ij}^{(dir)} = -\frac{1}{2} b_{ij}, \quad b_{ij}^{(pol)} = \frac{3}{2} b_{ij}. \tag{8.18}$$

This relationship was quoted in Kassinos et al. (2001) as "*dimensionality*" (measured by $-2b_{ij}^{(dir)}$) *equals to "componentality"* (measured by b_{ij}.) Such relationship will be shown to be consistent with RDT, but only for very short times and starting from isotropic initial data in Sect. 8.7.1.

On the other hand, $\mathcal{K} - \varepsilon$ modelling is questioned if the straining process is time-varying. This can be explained by the fact that even a crude "pressure-released" equation like Eq. (8.21) given in the next subsection is much better for predicting RST anisotropy than the so-called Boussinesq approximation $b_{ij}(t) \propto A_{ij}(t)$. Since the instantaneous Boussinesq relationship used in $\mathcal{K} - \varepsilon$ models, and even in its so-called non-linear variants, cannot take into account the time history of $\mathbf{A}$, they completely miss the quasi-reversible behavior observed in the Gence's experiment. Similar conclusions can be drawn for time-periodic strains (relevant for reciprocating engines, for instance) for both full Reynolds stress models and $\mathcal{K}-\varepsilon$ variants (Hadzic et al. 2001).

8.3.3 *Linear Response of Turbulence to Irrotational Mean Strain*

The role of mean vorticity is easily understood linearizing the vorticity equation:

$$\dot{\omega}_i' = \frac{\partial \overline{u}_i}{\partial x_j} \omega_j' + \frac{\partial u_i'}{\partial x_j} \overline{\omega}_j.$$

Only in the absence of mean vorticity, this equation is similar to Eq. (2.30) in Chap. 2, and admits the solution

$$\omega_i'(\boldsymbol{x}, t) = F_{ij}(\boldsymbol{X}, t, t_0) \omega_j'(\boldsymbol{X}, t_0) \tag{8.19}$$

which is now a true solution, since $\mathbf{F}$ and $\boldsymbol{X}$ are only related to the irrotational mean flow, and therefore are *external given data*. Similarly, a linearized Weber equation can be written, leading to

$$u_i'(\boldsymbol{x}, t) = F_{ji}^{-1}(\boldsymbol{X}, t) u'(\boldsymbol{X}, t_0) + \frac{\partial \phi'}{\partial x_i}. \tag{8.20}$$

The last two equations, which are directly useful in Rapid Distortion Theory, are no longer valid if the mean flow is rotational.

Generalization to rotational mean flows is possible, using Clebsh potentials, but the method is much less tractable; it is touched upon by Hunt (1973), Goldstein (1978) and used by Nazarenko and Zakharov (1994) in the case of pure plane shear flow.

Interpretation of results from experiments of distortion is easy in the irrotational case. From the vorticity equation, with $\mathbf{F}$ given by Eq. (8.2), it is seen that the vorticity component is decreased in the direction of compression (direction x_1 here) and increased in the direction of elongation of the mean constant strain. More generally, the RDT solution for vorticity correlations is

$$\overline{\omega_i'\omega_j'}(t) = F_{im}(t)F_{jn}(t)\overline{\omega_m'\omega_n'}(0).$$

Such a solution is not very realistic, since enstrophy involves the smallest scales, and it is much more constraining than for the RST to exclude nonlinearity in the response of turbulence to the mean strain. The basic process suggested by Eq. (8.19), however, yielded a qualitative argument to interpret the effect of the strain on velocity fluctuations (Gence and Mathieu 1979), as schematized in Fig. 8.7: vorticity is amplified if a vortex tube is elongated, so that it rotates faster and the velocity components are amplified in the two directions *normal to* the axis of the elongated vortex tube. Conversely, a compressed vortex tube rotates slower and the velocity components are decreased in the two directions normal to the axis of the compressed vortex tube. This effect is sketched starting from two similar vortex tubes (a situation which mimics initial isotropy) with axes in directions x_1 and x_2, the first being compressed and the second being elongated. Accordingly, it is suggested that the velocity fluctuation is amplified in the direction of compression, with $\overline{u_1'^2}$ increasing, and is decreased in the direction of elongation, with $\overline{u_2'^2}$ decreasing. Of course,

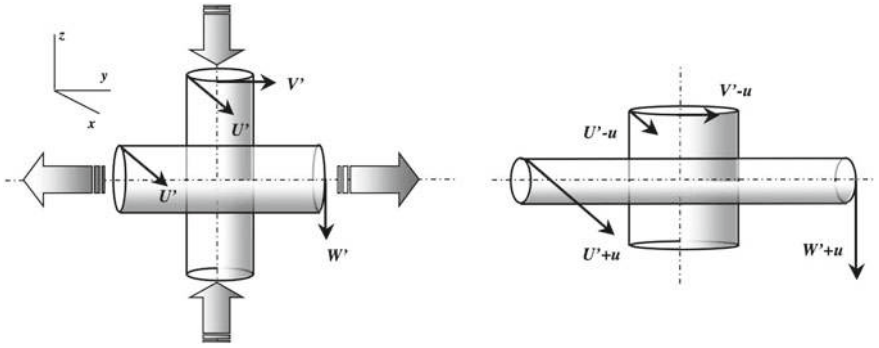

Fig. 8.7 Cartoon using two individual vortices aligned with compression/dilatation axes to predict anisotropic trends induced by a mean strain. Left: Two straight vortices with equal diameters and circulation. Right: vortices after compression/dilatation assuming preservation of (i) volume of each vortex and (ii) angular momentum of each vortex. It is seen that velocity component in the plane normal to the strain is left unchanged, while velocity is increased (resp. decreased) in the direction of the compression (resp. dilatation)

this simple reasoning accounts for the fact that $\mathbf{F}$ is present in Eq. (8.19) whereas its inverse $\mathbf{F}^{-1}$ is present in Eq. (8.20), but does not account for the fact that the linear velocity dynamics is also dependent on a "rapid" pressure effect, mediated by the scalar potential term in Eq. (8.20). However, the qualitative prediction remains correct, and the "pressure-released" equation

$$\overline{u_i' u_j'}(t) = F_{mi}^{-1}(t) F_{nj}^{-1}(t) \overline{u_m' u_n'}(0), \tag{8.21}$$

for the Reynolds stress tensor is consistent with the qualitative development of anisotropy.

If the mean strain is irrotational, but with the principal axes of $\mathbf{A}$ possibly moving with time, as in the Gence's experiments, it is possible to use the previous equations with $\mathbf{F}$ given by Eq. (8.2) for $0 < t < t_1$ and by Eq. (8.3) for $t_1 < 0 < 2t_1$. The quasi-reversibility of the flow anisotropy when $\alpha = \pi/2$, which is associated to $F_{ij}(2t_1) = F_{ij}(0)$, reflects the dominant role of $\mathbf{F}$, which returns to its initial value, as the final elliptical section returns to its initial position. Note that $\mathbf{F}$ is no longer symmetric in the second phase (see Eq. (8.3)), even if $\mathbf{A}$ is, because of the history of $\mathbf{A}$. As a consequence, it is convenient to distinguish between F_{ij} and F_{ji} in the general equations, even for irrotational mean flows. The matrix $\mathbf{F}$ is continuous in time, generating continuous mean trajectories, even if $\mathbf{A}$ is discontinuous due to a sudden change of principal axes. The same reversible behavior might be obtained at the end of the more complex distorting duct in the elliptic flow case, "forgetting" to rotate the honey comb. This experiment is just mentioned here as a "gedanken experiment" since it has never been performed. The design of the distorting duct accounts for a given Ω rate, and makes it possible — in principle — to reproduce the elliptical flow instability at given S, with $S < \Omega$ (see Chap. 11); this possibility appeared as more exciting than producing a new reversible irrotational strain with continuous motion of its principal axes.

8.4 The Fundamentals of Homogeneous RDT

Background for homogeneous RDT is introduced in Chap. 2. The present section aims at providing the key elements of this method which are necessary to understand the physical analysis given below in this chapter.

The simplest multi-point closure consists of dropping all nonlinear terms in Eq. (2.50) before applying the statistical average operator. Also dropping the viscous term, one obtains the Rapid Distortion Theory (RDT), introduced by Batchelor and Proudman (1954). The RDT model is assumed to be a relevant model for the large scales of turbulence, which are not directly governed by viscous effects at very high Reynolds number. This approach was further developed by Townsend (1976), Hunt (1973). Useful reviews were given by Hunt and Carruthers (1990) and more recently by Cambon and Scott (1999). An effort was made in the latter review to bridge between the RDT basic concepts and equations and some studies carried out in the

fields of applied mathematics and hydrodynamic stability by Craik and Criminale (1986), Bayly (1986) and other authors.

In neglecting nonlinearity entirely, the effects of the interaction of turbulence with itself are supposed to be small compared with those resulting from mean-flow distortion of turbulence. One often has in mind flows such as weak turbulence encountering a sudden contraction in a channel or flows around an airfoil. The underlying implicit assumption is that the time required for a significant distortion by the mean flow to develop is short compared with that for the turbulent evolution in the absence of distortion effect. The linear theory can also be relevant, at least over short enough times, if physical influences leading to linear terms in the fluctuation equations dominate turbulent flows, such as in strongly stratified or rotating fluid or a conducting fluid in a strong magnetic field. For such cases, the term 'rapid distortion theory' is probably a little bit misleading.

Thanks to the linearity assumption, the time evolution of u_i' may be formally written as

$$u_i'(\mathbf{x}, t) = \iiint \mathcal{G}_{ij}(\mathbf{x}, \mathbf{x}', t, t') u_j'(\mathbf{x}', t') d^3\mathbf{x}' \tag{8.22}$$

where $\mathcal{G}_{ij}(\mathbf{x}, \mathbf{x}', t, t')$ is a Green's function matrix expressing the evolution from time t' to time t. Whereas u_i' is a random quantity, which varies from one realization to another realization of the flow, $\mathcal{G}_{ij}$ is deterministic and can in principle be calculated for a given $\overline{u}_i(\mathbf{x}, t)$. From $\mathcal{G}_{ij}$ and the initial turbulence, Eq. (8.22) may be used to predict the time evolution.

Another simplifying assumption which is often made is that the size of turbulent eddies, L, is small compared with the overall length scales of the flow, ℓ, which might be the size of a body encountering fine-scale free-stream turbulence (see e.g. Hunt and Carruthers 1990). In that case, one uses a local frame of reference convected with the mean velocity and approximates the mean velocity gradients as uniform, but time-varying. Thus, the mean velocity is approximated by Eq. (2.67) in the moving frame of reference. In the example of fine-scale turbulence encountering a body, one may imagine following a particle convected by the mean velocity, which sees a varying mean velocity gradient, $A_{ij}(t)$, even when the mean flow is steady.

For the sake of simplicity, the following equations are derived in the case of an extensional mean flow, with mean velocity gradients uniform in the whole space.[1] This is referred to 'homogeneous RDT' since statistical homogeneity (invariance by translation of all fluctuating flow statistics) holds for the fluctuating flow, provided some additional conditions of admissibility be imposed to $\mathbf{A}$, as introduced in Chap. 2. Recall that the mean flow is a particular solution of Euler equations and is not itself invariant by translation (only its gradient is). In the linear limit, the fluctuating fields (u_i', p') satisfy the modified Eq. (2.50) with the advection-distortion parts written in terms of $A_{ij}(t)$:

[1] One has to keep in mind that essentially the same equations can be used in more realistic flow cases, following Hunt and coworkers, and Lifschitz and Hameiri (1991).

$$\underbrace{\frac{\partial u'_i}{\partial t} + A_{jk}x_k\frac{\partial u'_i}{\partial x_j}}_{\text{advection}} + A_{ij}u'_j + \frac{\partial p'}{x_i} = 0. \tag{8.23}$$

Its solution is most easily obtained via Fourier analysis, with elementary components of the form

$$u'_i(\boldsymbol{x}, t) = a_i(t)\exp(\imath \boldsymbol{k}(t)\cdot\boldsymbol{x}) \tag{8.24}$$

$$p'(\boldsymbol{x}, t) = b(t)\exp(\imath \boldsymbol{k}(t)\cdot\boldsymbol{x}). \tag{8.25}$$

Evolution equations for both the wavevector and the amplitudes are easily obtained from Eq. (8.23). They can be written as follows, under simple ODE:

$$\frac{dk_i}{dt} + A_{ji}k_j = 0 \tag{8.26}$$

and

$$\frac{da_i}{dt} = -\underbrace{\left(\delta_{in} - 2\frac{k_i k_n}{k^2}\right)A_{nj}}_{M_{ij}}a_j. \tag{8.27}$$

Given the pioneering study of Lord Kelvin, quoted and extended by Keith Moffatt in Moffatt (1967), the two Eqs. (8.26) and (8.27) are referred to as Kelvin-Moffatt equations.

General solutions which are valid for arbitrary initial data are expressed as follows in terms of linear transfer matrices

$$k_i(t) = F^{-1}_{ji}(t, t_0)k_j(t_0), \tag{8.28}$$

$$a_i(t) = G_{ij}(t, t_0)a_j(t_0), \tag{8.29}$$

in which the Cauchy matrix appears under a transposed and inversed form[2] and corresponds to the solution for the gradient of a passive scalar (see Chap. 17). The use of a Green's function $\mathbf{G}$ allows us to get rid of particular initial data for the fluctuating field. In the equations above, it is perhaps clearer to specify the wavevector dependency in $\boldsymbol{a}$ and v, especially if we combine elementary solutions of the form given by Eq. (8.24) via Fourier synthesis. As a consequence, the RDT solution can be expressed as follows:

$$\widehat{u}_i[\boldsymbol{k}(t), t] = G_{ij}(\boldsymbol{k}, t, t_0)\widehat{u}_j[\boldsymbol{k}(t_0), t_0], \tag{8.30}$$

[2]This is a general solution for any Eikonal-type equation, see Eq. (8.26).

in which the Green's function is eventually determined by the (universal, not flow-dependent) initial conditions

$$G_{ij}(\boldsymbol{k}, t_0, t_0) = \delta_{ij} - \frac{K_i K_j}{K^2}, \quad K_i = k_i(t_0). \tag{8.31}$$

At this stage, it may be noticed that homogeneous RDT gathers enough features for solving two problems:

- A deterministic problem, which consists in solving the initial value linear system of equations for a_i, in the most general way. This is done by determining the spectral Green function, which is also the key quantity requested in linear stability analysis.
- A statistical problem which is useful for the prognostic of statistical moments of $\boldsymbol{u}'$ and p'. Interpreting the initial amplitude $\hat{\boldsymbol{u}}(\boldsymbol{k}(t_0), t_0)$ as a random variable with a given dense $\boldsymbol{k}(t_0)$-spectrum, relation (8.30) yields the prediction of statistical moments though products of the basic Green's function.

A useful reduced (using the minimum number of components) Green's function can be used in the Craya–Herring frame of reference, as

$$u^{(\alpha)}(\boldsymbol{k}(t), t) = g_{\alpha\beta}(\boldsymbol{k}, t, t') u^{(\beta)}(\boldsymbol{k}(t'), t'). \tag{8.32}$$

A Green's function is then expressed in terms of only four components, solving the two-component linear system in (2.104). Using helical modes is less useful, except near the limit of pure rotation or purely antisymmetric $\mathbf{A}$.

8.4.1 Qualitative Trends Induced by the Green's Function

Considering a mean flow given by Eq. (8.8), qualitative RDT results are presented below, before being discussed with more details in Chaps. 9 and 11.

Irrotational mean flows, with $A_{ij} = A_{ji}$ yield simple RDT solutions in which both $\mathbf{F}$ and $\mathbf{G}$ display dominant exponential growth (if $\mathbf{A}$ is not time-dependent), reflecting pure stretching of vorticity disturbances, in accordance with the existence of the hyperbolic instability.

Rotational mean flows yield more complicated linear solutions, and only the steady case has received much attention (Craik and Coworkers, Bayly and coworkers performed recent developments in unsteady cases, see e.g. Bayly et al. 1996).

The steady, rotational, case, when axes are chosen appropriately, corresponds to constant $S, \Omega \geq 0$, generating steady plane flows, which combine vorticity 2Ω and irrotational straining S. The related streamfunction is sketched in Fig. 2.1. The problem with arbitrary S and Ω was analysed in Cambon (1982), Cambon et al. (1985) with the purpose of extending classical RDT results, which were restricted to pure strain and pure shear. For $S > \Omega$, the mean flow streamlines are open and

hyperbolic, and RDT results are qualitatively close to those of the pure strain case $\Omega = 0$. For $S < \Omega$, the mean flow streamlines are closed and elliptic about the stagnation point at the origin. This case is the most surprising one, in which $\mathbf{F}$ is periodic in time while $\mathbf{G}$ is capable of generating exponential growth of fluctuations for $\boldsymbol{k}$-directions concentrated about special angles ($k_3/k \sim \pm 1/2$ if $S \ll \Omega$). The Rapid Distortion Theory can therefore be relevant for explaining the mechanism of *elliptical flow instability* (Bayly 1986) (details are discussed in Chap. 11). The limiting case $S = \Omega$ corresponds to pure shearing of straight mean streamlines. The RDT solutions by Moffatt (1967), Townsend (1976) reflect *algebraic growth* in the parlance of stability analysis (see Chap. 9).

8.5 Final RDT Results for Mean Irrotational Strain

8.5.1 General RDT Solution

A complete analytical solution for the velocity in Fourier space can be obtained from its counterpart in term of vorticity, using Eq. (8.19). An easier way is to use the linearized Weber equation (8.20)

$$G_{ij}(\boldsymbol{k}, t, t') = P_{in}(\boldsymbol{k}) F_{jn}^{-1}(t, t'). \tag{8.33}$$

This solution is valid for any irrotational straining process, even three-dimensional and time-dependent. The Cauchy matrix appears as the only explicit time-dependent tensor in the solution; an implicit time-dependency is mediated by $\boldsymbol{k}$, but it is again governed by the Cauchy matrix, according to the Eikonal solution (8.28). Accordingly, this solution is completely time-reversible if the history of $\mathbf{F}$ is. This shows that the complete RDT solution shares qualitative properties with the pressure-released oversimplified one introduced in Sect. 8.3.3. Only the additional viscous factor, which is very easy to add, not to mention nonlinear effects, can break the reversibility of such a solution.

In this case, the use of the Craya–Herring frame does not simplify the solution significantly, except if the straining process is axisymmetric, as considered just below.

8.5.2 Linear Response of Turbulence to Axisymmetric Strain

The mean velocity gradient matrix is given by (8.6), the general equations (8.33) — any irrotational strain — and (8.26) — any RDT case — are valid, and characteristic lines in Fourier space are

$$k_\alpha = K_\alpha C^{1/2}, \quad k_3 = K_3 C^{-1}. \tag{8.34}$$

The parameter C, which is given by Eq. (8.7), is directly related to the contraction ratio of the streamtube, or to the ratio $A(t)/A(0)$ of the area of a current circular section to the initial one in the corresponding axisymmetric duct, since $C^{-2}(t) = A(t)/A(0)$. The linear inviscid solution in the Craya–Herring frame is

$$u^{(\alpha)}(\boldsymbol{k},t) = \underbrace{e_i^{(\alpha)}(\boldsymbol{k})F_{ij}^{-1}(t)e_j^{(\beta)}(\boldsymbol{K})}_{g_{\alpha\beta}}u^{(\beta)}(\boldsymbol{K},0)$$

and finally a very simple form of $g_{\alpha\beta}$ is obtained

$$g_{\alpha\beta} = \begin{pmatrix} C^{1/2} & 0 \\ 0 & C^{-1/2}\frac{K}{k} \end{pmatrix}. \tag{8.35}$$

For instance, solutions for the spectral tensor of double correlations are equal to

$$\Phi^{11}(\boldsymbol{k},t) = C(t)\frac{E(K)}{4\pi K^2}, \quad \Phi^{22}(\boldsymbol{k},t) = C^{-1}(t)\frac{E(K)}{4\pi k^2}, \tag{8.36}$$

starting from isotropic initial data. Only two non-trivial components are needed, Φ^{11} related to toroidal energy and Φ^{22} related to poloidal energy, taking into account simplifications from axisymmetry (with mirror symmetry), yielding

$$\mathcal{E} = \frac{1}{2}\left(\Phi^{11}+\Phi^{22}\right), \quad Z = \frac{1}{2}\left(\Phi^{22}-\Phi^{11}\right)$$

in the expression of the general spectral tensor $\hat{\mathbf{R}}$. As a consequence, toroidal and poloidal contributions to the kinetic energy are found equal to

$$\frac{\mathcal{K}^{(tor)}(t)}{\mathcal{K}(0)} = \frac{3}{2}C(t), \quad \frac{\mathcal{K}^{(pol)}(t)}{\mathcal{K}(0)} = C^{-1}(t)\int_0^1 \frac{K_\perp K^2}{k^4}dx.$$

These results use a minimal number of components for generating RDT solutions, and they are consistent with those of Sreenivasan and Narasimha (1978), Lee (1989), Ribner (1953). In addition, Lee (1989) provided complete useful analytical solutions for the Reynolds stress tensor which has only two non-trivial axial and transverse components:

$$\overline{u_3'^2} = \mathcal{K}(0)\frac{C^{4s/3}}{2(1-C^{2s})}\left[-1+(2-C^{2s})\sigma'\right] \tag{8.37}$$

$$\overline{u_1'^2} = \overline{u_2'^2} = \mathcal{K}(0)\frac{C^{4s/3}}{4(1-C^{2s})}\left[\frac{2-C^{2s}}{C^{2s}} - C^{2s}\sigma'\right], \tag{8.38}$$

with $s = \pm 1$ being the sign of S, and

$$\sigma' = \frac{1}{2\sqrt{1-C^{-2}}} Ln \frac{1+\sqrt{1-C^{-2}}}{1-\sqrt{1-C^{-2}}} \quad \text{if} \quad S > 0,$$

and

$$\sigma' = \frac{arctan(\sqrt{C^2-1})}{\sqrt{C^2-1}} \quad \text{if} \quad S < 0.$$

Expressions for various terms in the RST budget equations can also be found.

8.6 Towards a Fully Nonlinear Approach

A "first loop" of nonlinear iteration was offered by Kevlahan and Hunt (1997) for pure irrotational constant strain.

Issues linked to triadic closures are discussed below, from the general introduction in Chap. 2, from Eqs. (2.116) and (2.117) in Sect. 2.5.7.

Before examining the simplest and most interesting applications of linear and nonlinear theory, it is worthwhile to anticipate the difficulties for passing from (linear) RDT to generalized quasi-normal (nonlinear) closure for homogeneous anisotropic turbulence, in the presence of mean flows given by (8.8).

8.6.1 Qualitative Discussion

In the "hyperbolic" and "elliptic" cases, with $0 \neq S \neq \Omega$ in (8.8), the RDT Green's function can display exponential growth, at least for particular angles of $\boldsymbol{k}$ ($k_3/k \sim 1/2$ in the case $S \ll \Omega$). If the bare zeroth-order response function is only modified by eddy damping, convergence is not ensured for the time integral of the three-fold product $\mathbf{G}^{(NL)}\mathbf{G}^{(NL)}\mathbf{G}^{(NL)}$ in the generic closure relationship (2.117).

A less critical situation occurs when $S = \Omega$ (pure plane shear), since the inviscid RDT Green's tensor yields only algebraic growth, so that the viscous term ensures convergence of the time integral involved in the closure. Nevertheless, it is very cumbersome to develop, and especially to solve numerically with enough accuracy, a complete anisotropic EDQNM model in this case. Recall that even calculation of single-point correlations resulting from viscous RDT at high St is not easy (Beronov and Kaneda, private communication), the asimptotic analysis being even complex for inviscid RDT (Rogers 1991). Direct Numerical Simulations suggest that fully nonlinear effects yield exponential growth for the turbulent kinetic energy, but computations are very sensitive to cumulated errors (remeshing, low angular resolution at small k). Such a transition from algebraic growth (linear dynamics at small time) to exponential growth (nonlinear dynamics) is not completely described and explained, but very simple single-point closure models can mimic it. In addition, interesting scaling laws for possible exponential growth follow from an approach by Julian Scott

(private communication), which is itself a refinement of Oberlack's approach dealing with symmetries of the Navier–Stokes equations. All these issues are addressed in the devoted chapter (Chap. 9).

Only for pure rotation, or $S = 0, \Omega \neq 0$, the most general EDQNM versions were carried out towards complete achievement. In this case, the zeroth order state consists of superimposed oscillating modes of motion, with no amplification and no interaction: they correspond to neutral dispersive inertial waves. Time integral of a three-fold product of Green's functions converges, provided an infinitesimal viscous (or eddy damping) term is added. In the limit of small interactions, two-point closures and theories of wave-turbulence were reconcilied (Chap. 7).

This preliminary discussion justifies, to a certain extent, to discriminate flows dominated by production from flows dominated by waves, a distinction which is revisited in Chaps. 10, 11 and 17. The first class is illustrated by classical shear flows, in which a nonzero "production term" is displayed in the equations governing the Reynolds Stress tensor. This production is often related to growth of instabilities, when stability analysis is addressed. The second class is illustrated in Chaps. 7, 10 and 11, as the more relevant area to apply spectral closures. It is worth noting that the dynamics can be dominated by dispersive waves, which are neutral but for a small part of the configuration space, in which exponential amplification occurs. In the latter case, e.g. for flows with weak ellipticity ($S \ll \Omega$), production of energy is nonzero, but classic single-point closure models are of poor relevance, since only particular orientations in wave-space are subjected to parametric instability.

8.6.2 *Generalized Lin Equation, and Derivation of Simpler Quantitative Models*

Exact Lin-type equations for the set energy -polarization - helicity, which is equivalent to the second-order spectral tensor, are derived from the so-called Craya equation, see Chap. 2. Equations obtained for the state vector $(\mathcal{E}, Z, \mathcal{H})$ are

$$(\dot{k\mathcal{E}}) + 2\nu k^3 \mathcal{E}(\boldsymbol{k}, t) + \Re\left(kZ(\boldsymbol{k}, t) S_{ij} N_i(\boldsymbol{\alpha}) N_j(\boldsymbol{\alpha})\right) = kT^{(\mathcal{E})}(\boldsymbol{k}, t), \tag{8.39}$$

$$(\dot{kZ}) + 2\nu k^3 Z + k\mathcal{E}(\boldsymbol{k}, t) S_{ij} N_i(-\boldsymbol{\alpha}) N_j(-\boldsymbol{\alpha}) - 2\imath kZ(\boldsymbol{k}, t)\left(\frac{1}{2}\boldsymbol{W}\cdot\boldsymbol{\alpha} - \Omega_E\right) = kT^{(Z)}(\boldsymbol{k}, t), \tag{8.40}$$

and

$$\dot{\mathcal{H}} + 2\nu k^2 \mathcal{H} = T^{(H)}, \tag{8.41}$$

in which S_{ij} is the symmetric part of the mean velocity gradient matrix, and $W_i = \epsilon_{ijn} A_{nj}$ refers to its antisymmetric part (mean vorticity vector).

The "overdot" represents the advection operator by the mean flow, inherited from RDT:

$$\dot{(\cdots)} = \frac{\partial}{\partial t} - A_{mn}k_m \frac{\partial}{\partial k_n}. \tag{8.42}$$

The linear term related to mean vorticity in the Z-equation reflects the strophol-ysis effect, identified in structure-based single-point models by Kassinos et al. (2001). Geometric anisotropic coefficients display projection along the already defined helical modes and Ω_E is the rotation vector for switching from the fixed system of coordinates of $\boldsymbol{k}$ to the Craya–Herring one with time-dependent wave vector

$$\Omega_E = -\frac{k}{|\boldsymbol{k} \times \boldsymbol{n}|} A_{mp} n_m e_p^{(1)} - A_{mn} e_m^{(2)} e_p^{(1)} \tag{8.43}$$

(e.g. from Mons et al. 2016.)

Equations (8.39) and (8.40) for $\mathcal{E}$ and Z are presented and discussed in different papers, e.g. Mons et al. (2016), but a special form is used here, in order to absorb the shear-induced diagonal linear terms (left-hand-side, except the strophol-ysis term) as integrating factors, working on a slightly modified state vector $(k\mathcal{E}(\boldsymbol{k}, t), kZ(\boldsymbol{k}, t))$ multiplied by $\boldsymbol{k}$-modulus. We have no general explanation for the fact that the multiplication by k simplifies linear couplings, but at least in the case of pure plane shear addressed in Chap. 9, this is directly related to the relevance of Orr-Sommerfeld-Squires variables, in close connection with toroidal/poloidal decomposition seen in Fourier space. It is worth reminding that $\mathcal{H}$ is not the exact helicity spectrum, but the 3D, possibly angle-dependent, spectrum of helicity divided by k. One recovers that this reduced helicity spectrum is not affected by the mean flow gradient, except a possible advection, represented by the 'overdot'. The helicity spectrum, if initially zero, remains zero, as rediscussed in general for homogeneous turbulence. Accordingly, it will be ignored in the following.

The dedicated contribution from two-point third-order correlations is identified in the left-hand-side of preceding equations for the optimal state vector which represents two-point second-order correlations. $T^{(\mathcal{E})}$ is the generalized energy transfer and is conservative, with zero integral in $\boldsymbol{k}$-space. The generalized polarization transfer $T^{(Z)}$ gathers a conservative part, with zero integral, and the nonlinear contribution from pressure -strain rate correlations. Both parts are disentangled in Mons et al. (2016).

8.6.3 *A Model from EDQNM in Terms of Spherically-Averaged Descriptors Only*

The case of purely rotating turbulence is recovered, by discarding the strain term in Eqs. (8.39) and (8.40), *which only couples their linear parts*, but in the Galilean frame of reference. Fortunately, equations are eventually completely consistent with

the ones of the previous chapter, seen in the rotating frame, and the stopholysis term displays twice the dispersion law in both cases, with $\Omega_E = -(1/2)W_m\alpha_m$ and $W_m = 2\Omega_m$. Is it possible to derive a more flexible and versatile nonlinear model for $T^{(\mathcal{E})}$ and $T^{(Z)}$ in all other cases of turbulence subjected to arbitrary mean velocity matrix A_{ij}, which is not purely antisymmetric? Because energy production exists, the need for a very complex closure for nonlinear transfer and pressure-redistribution terms is less pressing. For such flows, the EDQNM1 version yields a satisfactory level accuracyy, which is sufficient to deal with the complexity of turbulence dynamics. In addition to the fact that the explicit effect of the mean gradient is not essential in the dynamics of triple correlations as it is in purely rotating turbulence, without production, two reasons prevent the use of most complicated EDQNM versions such as EDQNM2 and EDQNM3:

- Such versions render the structure of the EDQNM model much more complicated, via a three-fold product of tensorial Green's functions and explicitly dependent on the type of mean shear, preventing easy further projection of angular harmonics.
- They are not correct when the (direct) linear effect of the mean shear/strain yields exponential growth, with a lack of convergence of the time integral of the above-mentioned three-fold product (Cambon and Scott 1999).

EDQNM1 equations can be written for arbitrary anisotropy, and yield closed expression of generalized transfer terms $T^{(\mathcal{E})}$ and $T^{(Z)}$ (Cambon et al. 1981; Cambon et al. 1997; Mons et al. 2016) in terms of $\mathcal{E}$ and Z, and therefore close Eqs. (8.39) and (8.40). Faced with the high computational cost for solving these equations for all wavevector directions, a second step was applied to restrict the description to spherically averaged descriptors only. This step, purely technical, amounted to replace fully anisotropic $\mathcal{E}$ and Z terms by their following truncated expansion:

$$\mathcal{E}(\boldsymbol{k},t) = \frac{E(k,t)}{4\pi k^2}\left(1 - 15H_{mn}^{(dir)}(k,t)\alpha_m\alpha_n\right) \tag{8.44}$$

and

$$Z(\boldsymbol{k},t) = \frac{5}{2}\frac{E(k,t)}{4\pi k^2}H_{mn}^{(pol)}(k,t)N_m^*(\boldsymbol{\alpha})N_n^*(\boldsymbol{\alpha}). \tag{8.45}$$

These expansions involve the non-dimensional deviatoric tensors $H_{mn}^{(dir)}$ and $H_{mn}^{(pol)}$ which are given by spherically averaging $\hat{R}_{ij}(\boldsymbol{k},t)$, with its three contributions, isotropic, directional anisotropy and polarization anisotropy, so that

$$\varphi_{ij}(k,t) = \iint_{S_k}\hat{R}_{ij}(\boldsymbol{k},t)d^2\boldsymbol{k} = 2E(k,t)\left(\frac{1}{3}\delta_{ij} + H_{ij}^{(dir)}(k,t) + H_{ij}^{(pol)}(k,t)\right). \tag{8.46}$$

On the one hand, it is possible to extract from an arbitrary anisotropic spectral tensor $\hat{R}_{ij}$ the set of spherically-averaged descriptors (E, $H_{ij}^{(dir)}$, $H_{ij}^{(pol)}$), in which directional anisotropy and polarization anisotropy are disentangled. On the other hand, it

is possible to reconstruct a part of the full spectral tensor by means of these descriptors using Eqs. (8.44) and (8.45). Of course, only a part of the anisotropic structure is restored, because angular harmonics of degree larger than 2 are ignored (see also Chap. 2). It is consistent to express the generalized transfer terms using the same truncated expansion, or

$$T^{(\mathcal{E})}(\boldsymbol{k},t) = \frac{T(k,t)}{4\pi k^2}\left(1 - 15\tilde{S}_{mn}^{NL(dir)}(k,t)\alpha_m\alpha_n\right) \tag{8.47}$$

and

$$T^{(Z)}(\boldsymbol{k},t) = \frac{5}{2}\frac{T(k,t)}{4\pi k^2}\tilde{S}_{mn}^{NL(pol)}(k,t)N_m^*(\boldsymbol{\alpha})N_n^*(\boldsymbol{\alpha}). \tag{8.48}$$

Finally, a closed system of equations is found for the set $(E, H_{ij}^{(dir)}, H_{ij}^{(pol)})$, in which linear terms in the left-hand-side of Eqs. (8.39) and (8.40) give contributions S_{ij}^{L}, $S_{ij}^{L(dir)}$ and $S_{ij}^{L(pol)}$, whereas nonlinear contributions yield the above-mentioned T, $\tilde{S}_{ij}^{NL(dir)}$ and $\tilde{S}_{ij}^{NL(pol)}$ terms (more precisely, their dimensional form $S_{ij}^{NL(dir)} = \frac{T}{4\pi k^2}\tilde{S}_{ij}^{NL(dir)}$ and $S_{ij}^{NL(pol)} = \frac{T}{4\pi k^2}\tilde{S}NL(pol)_{ij}$. In short, a model using only spherically-averaged descriptors is exactly derived from the first-step EDQNM1 model in $\boldsymbol{k}$-vector, using second-order truncated expansions.

The simplified model by Mons, Cambon and Sagaut (MCS) is much more flexible, versatile and tractable than the first-step model. Looking at Table 8.1, the first-step nonlinear closure addresses the expression of $T^{(\mathcal{E})}(\boldsymbol{k})$ and $T^{(Z)}(\boldsymbol{k})$ in terms of $\mathcal{E}$ and Z, whereas it reduces in MCS to the expression of $T(k)$, $\tilde{S}_{ij}^{NL(dir)}(k)$ and $\tilde{S}_{ij}^{NL(pol)}(k)$ in terms of E, $H_{ij}^{(dir)}$ and $H^{(pol)}$. Accordingly, its nonlinear part reduces to calculations similar to what is made for isotropic EDQNM, because integration over the direction of the plane of the triads can be performed analytically, and the orientation of the wave vector is eventually removed analytically as well. Final equations are given in Chap. 17, Sect. 17.9. This model began to be validated in Mons et al. (2016) for several flow cases, including effects of irrotational straining processes (A_{ij} symmetric, possibly time-dependent), plane shear, and return-to-isotropy when mean flow gradients are relaxed. On the other hand, the rapid distortion limit, which was preserved in the first-level model by cancelling the nonlinear terms, is no longer

Table 8.1 Description of anisotropy for both second-order spectral tensor and its counterpart for third-order contributions, using $\boldsymbol{k}$-vectors descriptors and their corresponding spherically-averaged contributions

.	Spherically averaged descriptors		
$\boldsymbol{k}$-vectors descriptors	Isotropy	Directional anisotropy	Polarization anisotropy
$\mathcal{E}(\boldsymbol{k},t)$	$E(k,t)$	$H_{ij}^{(dir)}(k,t)$	0
$Z(\boldsymbol{k},t)$	0	0	$H_{ij}^{(pol)}(k,t)$
$T^{(\mathcal{E})}(\boldsymbol{k},t)$	$T(k,t)$	$\tilde{S}_{ij}^{NL(dir)}(k,t)$	0
$T^{(Z)}(\boldsymbol{k},t)$	0	0	$\tilde{S}_{ij}^{NL(pol)}(k,t)$

exact in the MCS model, because the very strong anisotropy induced by RDT calls into play higher degree angular harmonics. For the sake of brevity, we will not report calculation in which the mean strain is sustained, but only results for temporal relaxation of initial anisotropy.

8.7 Return to Isotropy

This general behavior can be understood from two different investigations. In the first one, the mean strain (irrotational or not) is sustained, but we try to delineate a range of scales in which the isotropy is possibly restored. This amounts to explore the degree of penetration of anisotropic structure in the space of scales. In the second approach, the strain is suddenly relaxed, and we look at the further temporal evolution of turbulence statistics, with possible recovery of isotropy.

8.7.1 Scale by Scale Analysis, Towards Recovering an Universal State at Sufficiently Small Scale?

Assuming that weak anisotropy results from a linear response to turbulence perturbated from a fully nonlinear quasi-isotropic state, scaling laws are found by Ishihara et al. (2002), Yoshida et al. (2003). The domain of valididy is given by a very small local interaction parameter, or $k^{2/3}\varepsilon^{1/3}/S \gg 1$, with $S \sim \sqrt{A_{mn}A_{mn}}$ and ε is the dissipation rate. This condition is equivalent to choose the wavenumber k as much larger than the threshold one, inverse of the Corrsin's scale (Corrsin 1958), (which amounts to a Hopfinger's scale, also used by Zeman for purely rotating flow, see Chap. 7.), or $k \gg k_S$, with

$$k_S = \left(\frac{S^3}{\varepsilon}\right)^{1/2}. \tag{8.49}$$

In this wavenumber range, the scalings laws recover the classical Kolmogorov inertial range for the energy spectrum $E(k)$, whereas the anisotropic spherical descriptors defined in Chap. 2 are

$$H_{ij}^{(dir)}(k) = \frac{1}{15}(B-A)\varepsilon^{-1/3}k^{-2/3}S_{ij}, \quad H_{ij}^{(pol)}(k) = \frac{2}{5}A\varepsilon^{-1/3}k^{-2/3}S_{ij}, \tag{8.50}$$

in which A and B are constants, assumed to be universal, with a satisfactory agreement between DNS for pure plane shear flow and LRA. Accordingly, a kind of universality is restored, but in the limit of small scales and vanishing shear (or strain) rate. General solutions only depend on the symmetric part of the mean strain, and therefore are the same for the three different cases (elliptical, hyperbolical, rectilinear), a result which is at odds with our main approach here.

Note also that a direct relationship of anisotropic descriptors to the strain tensor is also recovered from RDT at short time. As recalled in Cambon and Rubinstein (2006), the first significant terms of RDT solution for single-time second-order statistics at short time, started from 3D isotropic initial data, only involve the symmetric part **S** of **A**, yielding

$$\mathcal{E}(\boldsymbol{k},t)=\frac{1}{2}\left[k\frac{\partial\mathcal{E}}{\partial k}|_{t=0}+\mathcal{E}(k,0)\right]tS_{ij}\frac{k_ik_j}{k^2},$$

and

$$Z(\boldsymbol{k},t)=\frac{1}{2}\mathcal{E}(k,0)tS_{ij}N_i^*(\boldsymbol{k})N_j^*(\boldsymbol{k}),$$

with $\mathcal{E}(k,0)=E(k)/(4\pi k^2)$.

Spherical integration gives

$$H_{ij}^{(dir)}(k,t)=-\frac{1}{15}\left(-1+\frac{k}{E}\frac{dE}{dk}\right)S_{ij}t \quad \text{and} \quad H_{ij}^{(dir)}(k,t)=-\frac{2}{5}S_{ij}t,$$

for the spherically averaged spectra of $b_{ij}^{(dir)}$ and $b_{ij}^{(pol)}$, given eventually by

$$b_{ij}^{(dir)}=\frac{2}{15}S_{ij}t, \quad b_{ij}^{(pol)}=-\frac{2}{5}S_{ij}t, \quad b_{ij}=-\frac{4}{15}S_{ij}t.$$

One recovers that "componentality" is equal to "dimensionality" (see Eq. (8.18) and related discussion), but this results does not persists at long time. One can see that the time-scale in short-time RDT is simply the elapsed time t, whereas it is a turbulent time-scale in the linear response theory by the Kaneda's group. Given the values of "constants" A and B, which are evaluated from LRA theory and from DNS data, no simple relationship between $b_{ij}^{(dir)}$ and $b_{ij}^{(pol)}$ similar to Eq. (8.18) is shown.

8.7.2 Temporal Evolution After Relaxation of the Mean Strain

The experiment by Gence and Mathieu is considered again, with its additional duct in which the mean strain is relaxed (Gence and Mathieu 1980). The case of straining without rotation in the second part of the distorting duct ($\alpha = 0$), followed by a relaxation phase, is illustrated here in Fig. 8.8. The MCS model properly captures the evolution of the anisotropy indicators b_{ij} and that of the turbulent kinetic energy, both in the region dominated by linear effects and in the purely nonlinear one.

We now consider the experiment of Chen et al. (2006) where turbulence is subjected to a nonstationary straining-relaxation-destraining cycle. Both linear and

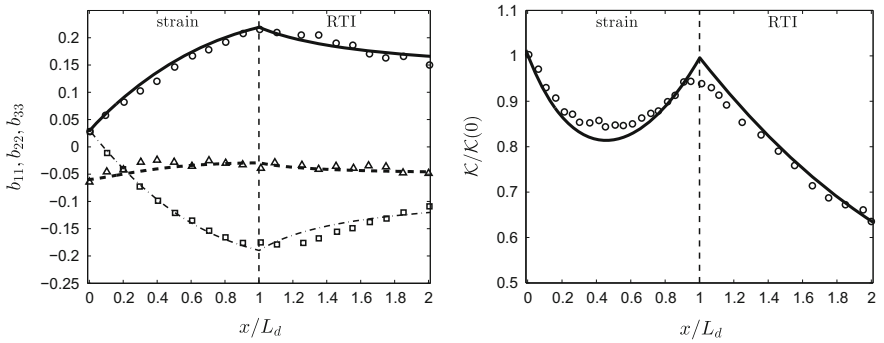

Fig. 8.8 Evolution of (left) the anisotropy indicators b_{11} (△), b_{22} (□) and b_{33} (○) and (right) that of the turbulent kinetic energy $\mathcal{K}$ versus the position in the distorting duct of length L_d for the experiment in Gence and Mathieu (1980) without rotation in the second part of the distorting duct ($\alpha = 0$). Symbols correspond to experimental data and lines are obtained with the system of governing equations. From Mons et al. (2016) with permission of CUP

nonlinear phenomena come into play in the response of turbulence to this particular straining. Figure 8.9 illustrates the temporal evolution of the anisotropy indicator $\tilde{b}_{11}(t)$ defined by

$$\tilde{b}_{11}(t) = \frac{\overline{u_1^2}(t)/\overline{u_1^2}(t_0)}{\overline{u_1^2}(t)/\overline{u_1^2}(t_0) + \overline{u_2^2}(t)/\overline{u_2^2}(t_0)} - \frac{1}{2}, \tag{8.51}$$

where t_0 refers to the time at which strain starts.

Experimental and numerical values obtained with the present model are reported, along with the RDT prediction, provided by Chen et al. (2006), corresponding to the mean flow defined by Eq. (8.5) and Fig. 8.9 (left). The temporal evolution of $\tilde{b}_{11}(t)$ shows good agreement between the experiment and the present model. From the comparison with RDT results, it appears that nonlinear phenomena are significant on a quantitative level. This is partly due to the presence of a relaxation phase in the straining cycle. Thus, the validity of both linear and nonlinear contributions in the system of governing MCS equations can be confirmed by the comparison with this experiment.

The relaxation of an axisymmetric turbulence obtained by applying an axial compression/dilatation over a finite time to an initially isotropic turbulence is analyzed in Mons et al. (2014) thanks to an anisotropic EDQNM model (Cambon et al. 1981). The initial anisotropic state after the release of the strain is characterized by the coefficient γ, which measures the ratio between the axial Reynolds stress and the two other ones:

$$R_{11}(t) = \gamma(t) R_{22}(t) = \gamma(t) R_{33}(t). \tag{8.52}$$

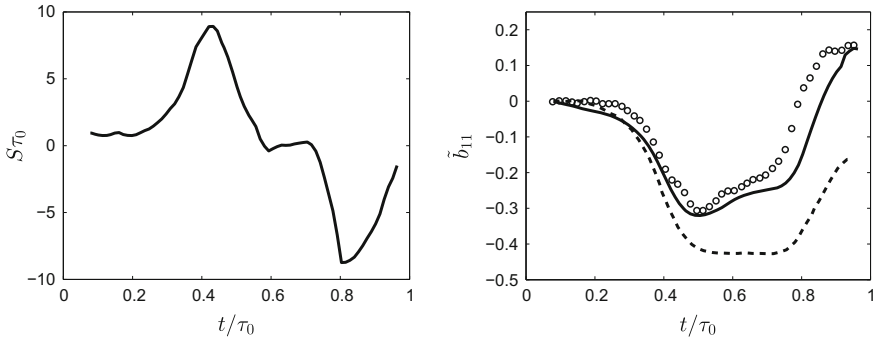

Fig. 8.9 (left) Temporal evolution of the strain $S(t)$ applied to the turbulence; (right) experimental values (∘), numerical values obtained with the present model (solid line) and RDT prediction (dashed line) for the temporal evolution of the anisotropy indicator $\tilde{b}_{11}(t)$ in the experiment of Chen et al. (2006). From Mons et al. (2016), with permission of CUP

Long time evolution of γ starting from an initially very high Reynolds solution is displayed in Fig. 8.10 (left), for different values of the infrared kinetic energy spectrum slope at initial time σ. It is seen that the anisotropy exhibits three stages. In the first one, the anisotropy decreases thanks to the return to isotropy of small scales via non-linear mechanisms, while large scales remain anisotropic. The second stage corresponds to a plateau for $\sigma \neq 4$, which corresponds to the destruction of small isotropic eddies via viscous effects. The last stage consists of a dramatic growth of the anisotropy coefficient, associated to the decay regime at asymptotically low Reynolds number, except for $\sigma = 4$ at which the very large scale have been isotropized thanks to the breakdown of the permanence of large eddies. In other cases, the growth of γ is due to the fact that all small scales have been dissipated and that the field is only

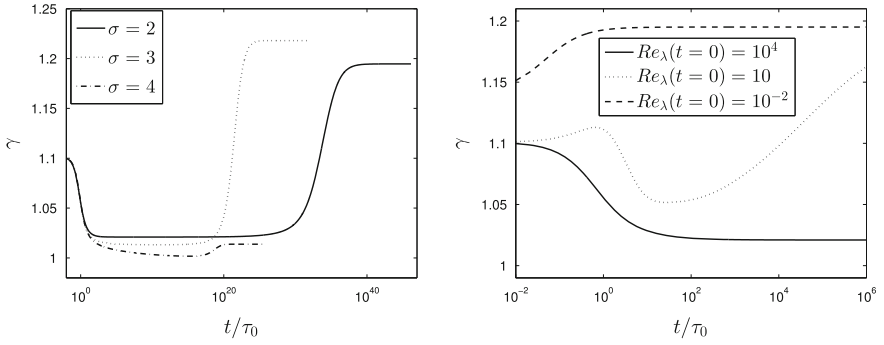

Fig. 8.10 Time evolution of the anisotropy coefficient γ in strain-released axisymmetric turbulence. Left: very long time evolution starting from initially high-Re_λ turbulence for different values of the infrared slope σ. Right: Evolution for $\sigma = 2$ and different initial Re_λ. From Mons et al. (2014) with permission of AIP

made of large anisotropic scales that now obey an almost linear diffusive dynamics. This results show that there is now relaxation toward a fully isotropic state, whatever is the evolution time under consideration and the initial infrared slope σ.

The sensitivity of the evolution of γ to the initial Reynolds number is illustrated in Fig. 8.10 (right). It is observed that at initially low- to very-low Re_λ anisotropy may grow from the very beginning or exhibit a non-monotonic behaviour, due to Finite Reynolds Number effects.

Therefore, the concept of return to isotropy should be taken with care, since it is observed over finite times only and for large initial Reynolds numbers.

8.8 Nonhomogeneous Flow Cases. Coherent Structures in Strained Homogeneous Turbulence

The RDT for irrotational strain can be extended to analyse the vicinity of stagnation points, in connection with the hyperbolic instability. Application to modeling of turbulence impinging on bluff bodies was given by Hunt and coworkers (see Hunt 1973). The mean flow is a potential 2D inviscid flow, hence strictly irrotational, and equations very similar to the ones found in the homogeneous case are recovered following mean flow trajectories for short-wave disturbances.

8.8.1 Strained Turbulence in a von Kármán Flow

Recent unpublished results have been obtained using the experimental setup by Machicoane et al. (2013). It is nicely confirmed that the flow near the stagnation point in a von Kármán flow, with exactly co-rotating discs (see Fig. 8.11), consists of quasi-irrotational strain.

Such a setup allows to reach high Reynolds numbers ($Re_\lambda = 200$ in the present case) and it was often alledged in the past that "quasi-isotropic" turbulence is gener-

Table 8.2 Parameters of the flow. Ω, rotation rate of the discs; ε, dissipation rate obtained from the power consumption of the motors. The rms velocities are obtained at the geometrical centre of the flow using data points situated in a ball with a 1 cm radius. The Taylor-based Reynolds number is estimated as $Re_\lambda = \sqrt{15u'^4/\nu\varepsilon}$ with $u' = \sqrt{({u'_x}^2 + {u'_y}^2 + {u'_z}^2)/3}$. The large scale Reynolds number is $Re = 2\pi R^2\Omega/\nu$. The kinematic viscosity of the water-Ucon^{TM} mixture is $\nu = 8.2\ 10^{-6}$ m^2s^{-1} with a density $\rho = 1000\,kg\ m^{-3}$. Courtesy from Romain Volk

State	Ω	u'_x	u'_y	u'_z	u'	τ_η	η	ϵ	R_λ	Re
–	Hz	$m.s^{-1}$	$m.s^{-1}$	$m.s^{-1}$	$m.s^{-1}$	ms	μm	$W.kg^{-1}$	–	–
x-dominant	5.5	0.58	0.39	0.33	0.45	2.1	130	1.9	200	21200

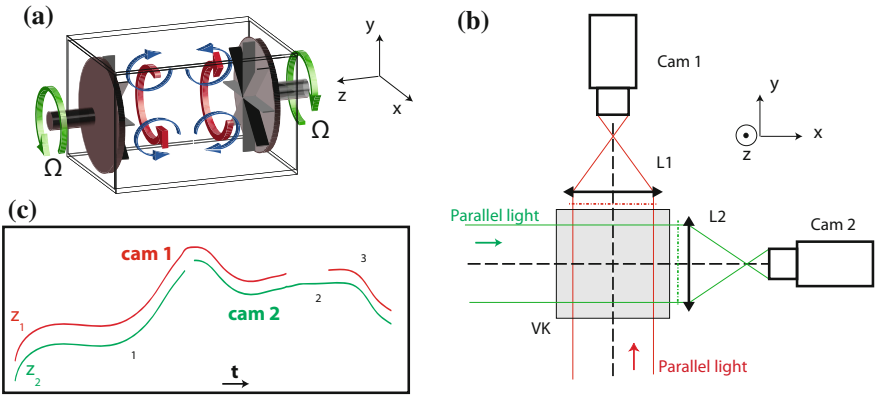

Fig. 8.11 Set-up of the experiment on the von Kármán flow. **a** general facility; **b** optical set-up; **c** Typical trajectories obtained by both cameras (cam1 and cam2). Courtesy from Romain Volk

ated in the center region. Here, the flow is bistable, so that both directions x or y can alternatively characterize the direction of (large-scale) contraction. Results below concern only the case with x related to the axis of contraction. Lagrangian measurements are made in a cubic box around the stagnation point. Parameters of the flow are gathered in Table 8.2. The measured mean velocity gradient, non-dimensionalized with respect to the rotation rate Ω of the discs (see Table 8.2), and the non-dimensional Reynolds stress tensor, are

$$\frac{1}{2\pi\Omega}\mathbf{A} = \begin{pmatrix} -0.90 & 0.18 & 0.00 \\ 0.00 & 0.31 & 0 \\ 0.08 & 0.00 & 0.60 \end{pmatrix} \qquad \frac{1}{3}\delta_{ij} + b_{ij} = \begin{pmatrix} 0.54 & 0.00 & 0.00 \\ 0.00 & 0.27 & 0.02 \\ 0.00 & 0.02 & 0.18 \end{pmatrix}. \tag{8.53}$$

Both are almost diagonal, reflecting a pure straining process, with the principal axes of the mean velocity gradient matrix almost aligned with the (x, y, z) directions of Fig. 8.11. The mean flow is given in two cross-sections in Fig. 8.12; it ressembles the pattern of two impacting jets in x-direction.

8.8.2 Structures in Numerical Studies

A theoretical and numerical study was performed by Leblanc and Godeferd (1999), on the ground of the zonal short-wave analysis introduced by Lifschitz and Hameiri (1991). Further theoretical insight to the hyperbolic instability is found in a "non-homogeneous" case, in which the "mean" flow is a cell of 2D Taylor-Green vortices (the Taylor's four roller mill). Stretching of the vorticity perturbation along the prin-

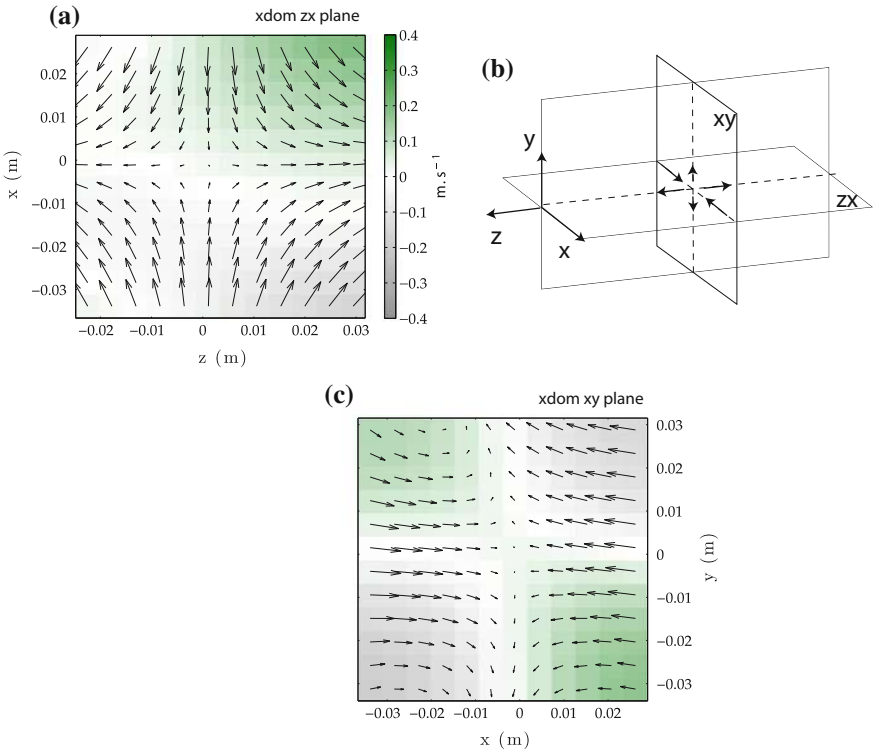

Fig. 8.12 Results from the experiment on the von Kármán flow. Mean flow. Courtesy from Romain Volk

cipal axis of strain leads to the formation of spanwise counter-rotating vortices (also sometimes referred to as ribs or braids) in the irrotational stagnation point region. Beautiful rib (or braid) structures obtained in a DNS with 128^3 grid points are visualized in Fig. 8.13.

Only a very few DNS studies have been devoted to the analysis of coherent structures in homogeneous strained turbulence, since the topology of the flow is simpler than the one observed in other cases (see Chaps. 7 and 9) and that flow dynamics is relatively well understood. Using low-Reynolds DNS, Rogers and Moin (1987) also observed that vorticity tends to be statistically aligned with the direction of positive strain. Vorticity occurs in coherent elongated vortex tubes that are stretched and strengthened by the mean strain. Vortex tubes submitted to a compressive effect buckle rather than decrease in strength. The absence of mean flow rotation is observed to prevent the occurence of hairpin vortices (which are observed in the pure shear case, see Sect. 9.8).

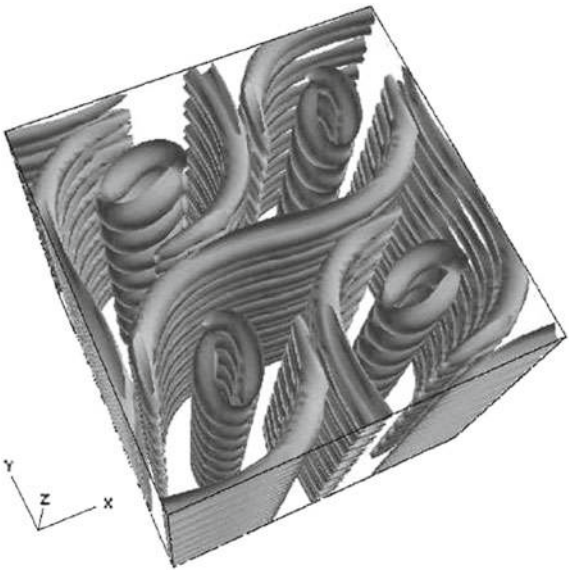

Fig. 8.13 Isosurface of the vorticity magnitude of the perturbed flow in the non-linear regime. Reproduced from Leblanc and Godeferd (1999) with permission of AIP

A look at instantaneous fields yield the following observations:

- Axisymmetric-contraction flows develop elongated vortex tubes in the stretching direction.
- Axisymmetric-expansion flows develop no unique structure, and a number of ring-like structures are observed.
- Plane strain flows exhibit a combination of structures observed in the two previous cases.

References

Batchelor, G.K., Proudman, I.: The effect of rapid distortion in a fluid in turbulent motion. Q. J. Mech. Appl. Maths **2**, 7–83 (1954)

Bayly, B.J.: Three-dimensional instability of elliptical flow. Phys. Rev. Lett. **57**(17), 2160–2163 (1986)

Bayly, B.J., Holm, D.D., Lifschitz, : Three-dimensional stability of elliptical vortex columns in external strain flows. Phil. Trans. R. Soc. Lond. A **354**, 895–926 (1996)

Cambon, C.: Etude spectrale d'un champ turbulent incompressible soumis à des effets couplés de déformation et rotation imposés extérieurement. Université Lyon I, France, Thèse de Doctorat d'Etat (1982)

Cambon, C., Teissèdre, C., Jeandel, D.: Etude d' effets couplés de rotation et de déformation sur une turbulence homogène. Journal de Mécanique Théorique et Appliquée **5**, 629 (1985)

Cambon, C., Mansour, N.N., Godeferd, F.S.: Energy transfer in rotating turbulence. J. Fluid Mech. **337**, 303–332 (1997)

Cambon, C., Jeandel, D., Mathieu, J.: Spectral modelling of homogeneous non-isotropic turbulence. J. Fluid Mech. **104**, 247–262 (1981)

Cambon, C., Scott, J.F.: Linear and nonlinear models of anisotropic turbulence. Ann. Rev. Fluid Mech. **31**, 1–53 (1999)
Cambon, C., Rubinstein, R.: Anisotropic developments for homogeneous shear flows. Phys. Fluids **18**, 085106 (2006)
Champagne, F.H., Harris, V.G., Corrsin, S.J.: Experiments on nearly homogeneous turbulent shear flows. J. Fluid Mech. **41**, 81–139 (1970)
Chen, J., Meneveau, C., Katz, J.: Scale interactions of turbulence subjected to a straining-relaxation-destraining cycle. J. Fluid Mech. **562**, 123–150 (2006)
Corrsin, S.: On local isotropy in turbulent shear flow, *NACA RM* 58B11 (1958)
Courseau, P., Loiseau, M.: Contribution à l' analyse de la turbulence homogène anisotrope. Journal de Mécanique **17**(2) (1978)
Craik, A.D.D., Criminale, W.O.: Evolution of wavelike disturbances in shear flows: a class of exact solutions of Navier–Stokes equations. Proc. R. Soc. Lond. Ser. A **406**, 13–26 (1986)
Gence, J.-N., Mathieu, J.: On the application of successive plane strains to grid-generated turbulence. J. Fluid Mech. **93**, 501–513 (1979)
Gence, J.N., Mathieu, J.: The return to isotropy of an homogeneous turbulence having been submitted to two successive plane strains. J. Fluid Mech.**101**, 555–566 (1980)
Goldstein, M.E.: Unsteady vortical and entropic distortions of potential flows round arbitrary obstacles. J. Fluid Mech. **89**(3), 433–468 (1978)
Hadzic, I., Hanjalic, K., Laurence, D.: Modeling the response of turbulence subjected to cyclic irrotational strain. Phys. Fluid **13**(6), 1739–1747 (2001)
Hunt, J.C.R.: A theory of turbulent flow around two-dimensional bluff bodies. J. Fluid Mech. **61**, 625–706 (1973)
Hunt, J.C.R., Carruthers, D.J.: Rapid distortion theory and the 'problems' of turbulence. J. Fluid Mech. **212**, 497–532 (1990)
Ishihara, T., Yoshida, K., Kaneda, Y.: Anisotropic velocity correlation spectrum at small scale in a homogeneous turbulent shear flow. Phys. Rev. Lett. **88**(15), 154501 (2002)
Jacquin, L., Leuchter, O., Cambon, C., Mathieu, J.: Homogeneous turbulence in the presence of rotation. J. Fluid Mech. **220**, 1–52 (1990)
Kassinos, S.C., Reynolds, W.C., Rogers, M.M.: One-point turbulence structure tensors. J. Fluid Mech. **428**, 213–248 (2001)
Kevlahan, N.K.R., Hunt, J.C.R.: Nonlinear interactions in turbulence with strong irrotational straining. J. Fluid Mech. **337**, 333–364 (1997)
Leblanc, S., Godeferd, F.S.: An illustration of the link between ribs and hyperbolic instability. Phys. Fluids **11**(2), 497–499 (1999)
Leclaire, B. (2006). Etude théorique et expérimentale d' un écoulement tournant dans une conduite, *Ph. D. thesis,* Thèse de l' Ecole Polytechnique, 21 Dec 2006
Lee, M.J.: Distortion of homogeneous turbulence by axisymmetric strain and dilatation. Phys. Fluids A **1**(9), 1541–1557 (1989)
Leuchter, O., Benoit, J. -P., Cambon, C.: . Homogeneous turbulence subjected to rotation-dominated plane distortion. Turb. Shear Flow 4, Delft, The Netherlands (1992)
Lifschitz, A., Hameiri, E.: Local stability conditions in fluid dynamics. Phys. Fluids A **3**, 2644–2641 (1991)
Machicoane, N., Bonaventure, J., Volk, R.: Melting dynamics of large ice balls in a turbulent swirling flow. Phys. Fluids **25**, 12 (2013)
Maréchal, P.: Contribution à l' étude de la déformation plane de la turbulence. Université de Grenoble, France, Doctorat es Sciences (1970)
Moffatt, H.K.: Interaction of turbulence with strong wind shear. In: Yaglom, A.M., Tatarski, V.I. (eds.) Colloquium on Atmospheric Turbulence and Radio Wave Propagation, pp. 139–156. Nauka, Moscow (1967)
Mons, V., Meldi, M., Sagaut, P.: Numerical investigation on the partial return to isotropy of freely decaying homogeneous axisymmetric turbulence. Phys. Fluids **26**, 025110 (2014)

Mons, V., Cambon, C., Sagaut, P.: A spectral model for homogeneous shear-driven anisotropic turbulence in terms of spherically averaged descriptors. J. Fluid Mech. **788**, 147–182 (2016)
Nazarenko, S.V., Zakharov, V.E.: The role of he convective modes and sheared variables in the Hamiltonian-dynamics of uniform-shear-flow perturbations. Phys. Lett. A **191**(5–6), 403–408 (1994)
Ribner, H.S.: Convection of a pattern of vorticity through a shock wave. Technical report 1164, NACA (1953)
Rogers, M.M., Moin, P.: The structure of the vorticity field in homogeneous turbulent flows. J. Fluid Mech. **176**, 33–66 (1987)
Rogers, M.: The structure of a passive scalar field with a uniform mean gradient in rapidly sheared homogeneous turbulent flow. Phys. Fluids A **3**(1), 144–154 (1991)
Rose, W.G.: Results of an attempt to generate a homogeneous turbulent shear flow. J. Fluid Mech. **25**, 97–120 (1966)
Sreenivasan, K.R., Narasimha, R.: Rapid distortion theory of axisymmetric turbulence. J. Fluid Mech. **84**(3), 497–516 (1978)
Townsend, A.A.: The Structure of Turbulent Shear Flow, 2nd edn. Cambridge University Press, Cambridge (1976)
Tucker, H.J., Reynolds, A.J.: The distortion of turbulence by irrotational plane strain. J. Fluid Mech. **32**, 657–673 (1968)
Yoshida, K., Ishihara, T., Kaneda, Y.: Anisotropic spectrum of homogeneous turbulent shear flow in a Lagrangian renormalized approximation. Phys. Fluids **15**(8), 2385–2397 (2003)

Chapter 9
Incompressible Homogeneous Anisotropic Turbulence: Pure Shear

9.1 Physical and Numerical Experiments: Kinetic Energy, RST, Lengthscales, Anisotropy

Mean shear flows are ubiquitous in turbulence. In a real flow, the shear is always created by the no-slip condition on solid walls, except in shear-free boundary layers where there is no tangential velocity thanks to the use of a belt moving with the same velocity as the flow. Shear flows are therefore intimately connected with near wall turbulence dynamics. Nevertheless, many features can be understood in the idealized case of an uniform mean shear in the absence of boundaries, in the context of HAT (Homogeneous Anisotropic Turbulence). The relevance of this idealized model flow was discussed by W.C. Reynolds, among many others. The effect of the wall is to induce a mean shear and to block the vertical motion. The arbitrary imposed uniform shear in the HAT framework is also responsible for a reduction of vertical velocity fluctuation (as we shall see with all details in this chapter). Therefore, the presence of the wall is not mandatory.

The emphasis will be put in this chapter on the departure from isotropy due to the application of a constant shear. The main reasons are that it contains all the physical mechanisms present in homogeneous shear flows and that it is the most extensively analyzed flow in this family. The mean flow $\bar{\boldsymbol{u}} = (Sy, 0, 0)$ is characterized by the following space-uniform mean velocity gradient matrix $\mathbf{A}$ and Cauchy (or displacement gradient) matrix $\mathbf{F}$

$$\mathbf{A} = \begin{pmatrix} 0 & S & 0 \\ 0 & 0 & 0 \\ 0 & 0 & 0 \end{pmatrix}, \mathbf{F}(t) = \begin{pmatrix} 1 & St & 0 \\ 0 & 1 & 0 \\ 0 & 0 & 1 \end{pmatrix} \tag{9.1}$$

and components $i = 1, 2, 3$ classically will be referred to as streamwise, cross-gradient (or vertical) and spanwise directions, respectively. In other chapters, permutation of the indices 2 and 3 will be used, but the intrinsic nomenclature *streamwise/cross-gradient/spanwise* will be kept unchanged.

P. Sagaut and C. Cambon, *Homogeneous Turbulence Dynamics*,
https://doi.org/10.1007/978-3-319-73162-9_9

It is important noticing that the shear rate S in Eq. (9.1) is equal to twice the rotation rate Ω and the strain rate S defined in Eq. (8.8), since the pure shear rate is defined as $\Omega = S$. Therefore, in the present chapter, the rotation rate and the strain rate are equal to $S/2$.

9.1.1 Experimental and Numerical Realizations

Many experiments were designed to reproduce the mean flow gradient given in Eq. (9.1) while preserving a quasi-homogeneous turbulent state. The experimental setups combining a piling-up of plates in the vertical direction and grid-generated turbulence are the most known and documented (Rohr et al. 1988; De Souza et al. 1995). As discussed in Chap. 8, in which older experimental studies are also mentioned, they suffer the significant drawback that they do not ensure uniformity of the Cauchy matrix in the whole cross-section, or in a simpler way they do not to ensure the uniformity of the mean streamwise velocity. As a consequence, the equivalent elapsed time St is not uniform in a cross section, yielding spurious diffusion effects. The specific experimental facility developed at ONERA by Leuchter and coworkers (see Chap. 8), which combines a mean rotation generator with an angular velocity $S/2$ in the direction normal to the plane of the shear and an additional distorting duct to create the additional straining process in the cross-sections is much more satisfactory, but the length of the distorting duct severely limits the maximum elapsed time $St \sim 1.5$. Finally, some relevant experiments aim at reproducing a planar Couette flow, using a moving belt, but 'initial' turbulence cannot be created independently, so that such experiments are more devoted to study hydrodynamic stability than developed turbulence dynamics. They will be touched upon in Chap. 11, when the rotating shear will be addressed.

Some relevant DNS have been performed. Most of them were based on the Rogallo (1981) method, which uses a pseudo-spectral scheme to evaluate nonlinear terms and the mean-Lagrangian system of coordinates to capture the linear effects in an optimal way. Among these numerical studies, many useful results and analyses can be found in the rather old study by Lee et al. (1990), whereas the numerical study by Brethouwer (2005) provides one of the most reliable and accurate database for both homogeneous rotating and non-rotating shear flows, at least for single-point statistics. Additional spectral information was recently obtained by Salhi et al. (2014), as discussed in Sect. 9.4 (Fig. 9.1).

9.1.2 Main Observations

Looking at the time-development of Reynolds stresses, physical and numerical experiments provide a consistent picture which consists in three phases (see Figs. 9.2 and 9.14):

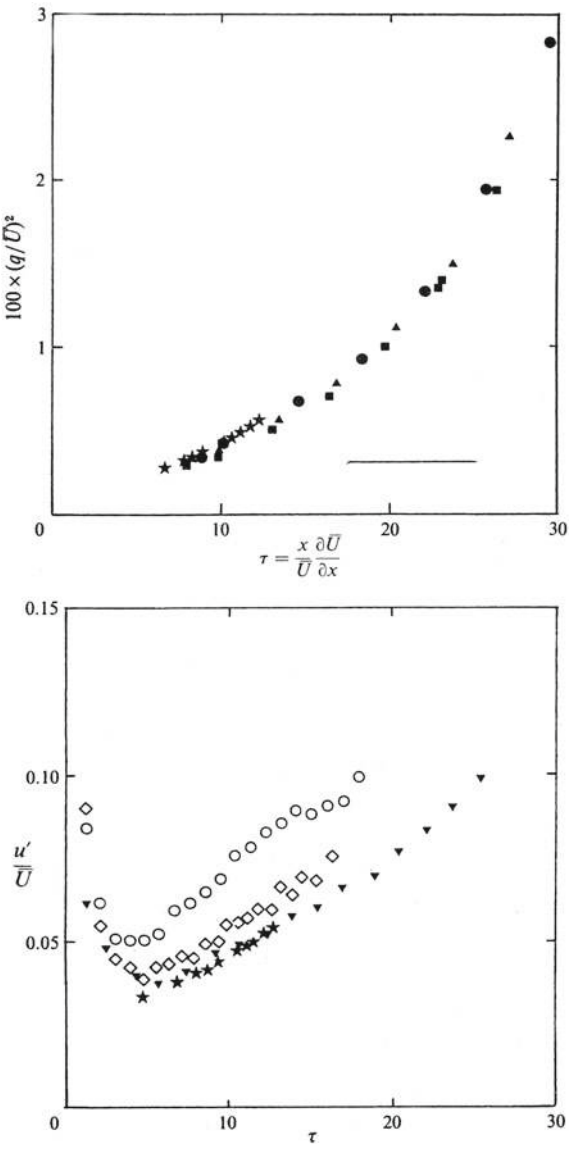

Fig. 9.1 Evolution of turbulent kinetic energy, $\mathcal{K}$ (top) and streamwise turbulence intensity (bottom), measured in different laboratory experiments. In all cases, the production phenomenon is clearly observed after the initial decay phase. Reproduced from Rohr et al. (1988) with permission of CUP

(i) Initial data, or upstream data in a grid-generated turbulence, being quasi isotropic, the Reynolds stress tensor is nearly spherical with no significant cross-correlation $\overline{u_1' u_2'}$, so that the first phase of the evolution is close to the decay of unsheared turbulence.

(ii) In a second phase anisotropy develops, so that the production of turbulent kinetic energy (which is proportional to $\overline{u_1' u_2'}$) becomes larger than its dissipation rate, and turbulent kinetic energy begin to increase. It is worth noting that, if the initial turbulent kinetic energy is too low, the viscous damping may be so high

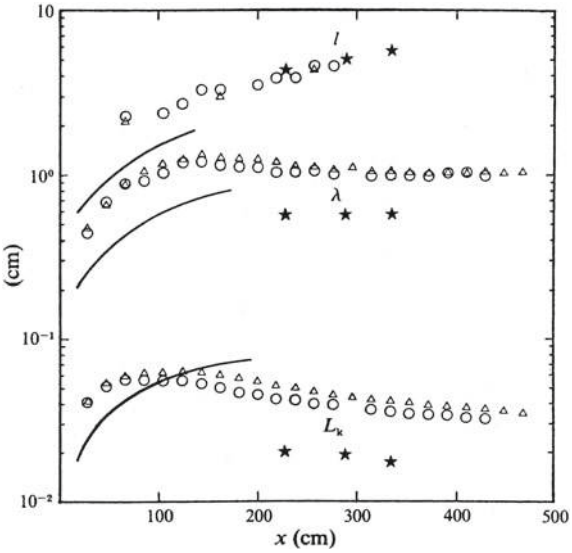

Fig. 9.2 Evolution of turbulence characteristic scales in different experiments. Top part: integral scale, medium part: Taylor scale, bottom part: Kolmogorov scale. The ratio L/η is observed to increase, showing that the spectrum is filled by the production mechanism. Solid lines are related to isotropic decay. Reproduced from Rohr et al. (1988) with permission of CUP

that the flow will be dominated by linear viscous effects, resulting in a monotone decay until all fluctuations have been suppressed.

(iii) In the final stage, an asymptotic régime is reached, in which the turbulent kinetic energy growth rate can become exponential, but this point is more subtle than it is generally admitted. The exponential growth is associated to constant values of the components of the anisotropy tensor, b_{ij}. Both numerical and experimental data indicate that the following non-dimensional quantities exhibit constant (but flow-dependent!) values in the asymptotic régime:

$$\frac{S\mathcal{K}}{\varepsilon}, \quad \frac{S\overline{u_1' u_2'}}{\varepsilon}$$

which are the *shear rapidity* (which compares the nonlinear time scale $\tau_{NL} = \mathcal{K}/\varepsilon$ to the shear time scale S^{-1}) and the ratio of the production of turbulent kinetic energy to the dissipation rate. Combining these two quantities, one finds that $\overline{u_1' u_2'}/\mathcal{K}$ is also constant. There is no universal value of the exponential growth coefficient. Typical values are reported in Table It is worth noting that the exponential growth régime can not be sustained for arbitrary long times, since turbulent kinetic energy must remain finite in physical systems. The kinetic energy growth can be estimated as Rohr et al. (1988)

$$\mathcal{K}(t) = \mathcal{K}(0) e^{\sigma S t}, \quad \sigma = \left(-\frac{\overline{u_1' u_2'}}{\mathcal{K}} \right) \left(1 - \frac{S\overline{u_1' u_2'}}{\varepsilon} \right) \tag{9.2}$$

where the damping factor σ is constant, flow-dependent and positive. Typical values reported in the literature are displayed in Table 9.1.

Table 9.1 Summary of measured global quantities in existing DNS and experiments for shear flows, classified by date. For experiments, $Re_\lambda(0)$ and $(S\mathcal{K}/\varepsilon)(0)$ refer to estimated values throughout the measurements. When two results from the same work are presented, they correspond to lowest shear and highest shear cases

Authors	Type	$Re_\lambda(0)$	$(S\mathcal{K}/\varepsilon)(0)$	$(S\mathcal{K}/\varepsilon)(final)$	b_{12}	σ	$(St)_{\max}$
Tavoularis and Corrsin (1981)	Exp	245	12.5	/	−0.14	0.12	11.6
Shirani et al. (1981)	DNS	20	3.3	16.328	−0.147	/	7
Tavoularis and Karnik (1989)	Exp	160	5.6	/	−0.149	0.08	8
Tavoularis and Karnik (1989)	Exp	310	8.4	/	−0.165	0.09	8
Lee et al. (1990)	DNS	40	33.5	36.2	−0.1	/	12
Clark and Zemach (1995)	Spectral model					0.3	
De Souza et al. (1995)	Exp	1050	11.9	/	−0.121	0.07	12
De Souza et al. (1995)	Exp	1010	21.8	/	−0.093	0.10	9
Ferchichi and Tavoularis (2002)	Exp	253	/	/	/	0.0846	23
Schumacher (2004)	DNS	55	0.8	8.2	/	/	10
Brethouwer (2005)	DNS	32	36	/	−0.14	0.178	12
Isaza and Collins (2009)	DNS	26	3	26.6	−0.165	0.10	9
Isaza and Collins (2009)	DNS	26	27	10.3	−0.126	0.18	9
Sukheswalla et al. (2013)	DNS	50	3	7.14	−0.19	0.12	20
Sukheswalla et al. (2013)	DNS	50	27	21.43	−0.135	0.13	20
Weinstock (2013)	Spectral model					0.17	
Briard et al. (2016)	EDQNM					0.33	

This expression is very useful: it shows that St is not the only parameter which describes the flow and that σ must be taken into account, and that, for low values of σSt, a first-order Taylor series expansion makes it possible to recover the turbulent kinetic energy linear growth rate (see Sect. 9.3) reported by some authors.

We now discuss the asymptotic régime in more details. Anisotropy of the Reynolds stress tensor develop too, with the streamwise component becoming largely dominant with respect to the two other diagonal ones, and the vertical one being the smallest. Exact values of the components of the anisotropy tensor b_{ij} are difficult to infer from available data, since a non-negligible dispersion among data is observed. Plausible target values given by Piquet (2001) are displayed in the first column of Table 9.2. It is worth noting that the asymptotic value of b_{12} is observed to be flow-dependent, but that the true asymptotic value may be equal to 0. Other values may be in fact intermediate plateau values found in experiments and numerical simulation at moderate St.

It is worth noting that b_{ij} is only one descriptor of anisotropy among many others. Interesting anisotropy indicators also are provided by the integral lengthscales $L_{ij}^{(n)}$, which are defined as follows:

Table 9.2 Asymptotic behavior of homogeneous shear turbulence for large St. The asymptotic value given between parentheses for b_{12} in the first column is the one given in Piquet (2001), which is a plateau value observed for a finite range of St, while zero is presumably the true asymptotic value for $St \gg 1$

Quantity	DNS and experiments	RDT	Pressure-released RDT
$\mathcal{K}(St \gg 1)/\mathcal{K}(0)$	$\propto e^{\sigma St}$	$\propto St$	$\propto (St)^2$
$b_{11}(St \gg 1)$	0.203	2/3	2/3
$b_{22}(St \gg 1)$	–0.143	–1/3	–1/3
$b_{33}(St \gg 1)$	–0.06	–1/3	–1/3
$b_{12}(St \gg 1)$	0. (–0.15)	0	0

$$\overline{u_i' u_j'} L_{ij}^{(n)} = \int \overline{u_i'(\boldsymbol{x}) u_j'(\boldsymbol{x} + r\boldsymbol{a}^{(n)})} dr \quad \text{with} \quad a_m^{(n)} = \delta_{mn}, \tag{9.3}$$

with no summation over repeated i, j subscripts, $i, j, n = 1, 3$.[1]

The longitudinal integral scale $L_{11}^{(1)}$ becomes very large and dominates all other components at large St. Among various components, the (large) ratio $L_{11}^{(1)}/L_{11}^{(3)}$ is particularly informative since it is directly linked to the aspect ratio (streamwise length to spanwise spacing) streak-like structures (this point will be further developed in Sect. 9.3.2). Incidentally, one can notice that appearance of streaks is found in the homogeneous shear case, even if their dynamics and topology is significantly different from the 'true' near-wall streaks. Analysis of structures will be addressed with much more details in Sects. 9.3.2 and 9.9.

9.2 Reynolds Stress Tensor and Analysis of Related Equations

The equation governing the Reynolds stress tensor is

$$\frac{d\overline{u_i' u_j'}}{dt} = -S \begin{pmatrix} 2\overline{u_1' u_2'} & \overline{u_2'^2} & \overline{u_2' u_3'} \\ \overline{u_2'^2} & 0 & 0 \\ \overline{u_2' u_3'} & 0 & 0 \end{pmatrix} + \Pi_{ij} - \varepsilon_{ij}, \tag{9.4}$$

in which the structure of the production term (first term in the right hand side) has been detailed. Reynolds stress components involving the vertical, or cross-gradient, u_2' component are present in this term.

[1] In isotropic turbulence, all these quantities reduce to a single one, say L_f, with $L_{nn}^{(n)} = L_f$ (any n, no summation on it), $L_{ii}^{(n)} = L_f/2$ if $n \neq i$ (no summation on i) and $L_{ij}^{(n)} = 0$ if $i \neq j$. Accordingly, departure from this simple relationship reflects anisotropic structure too.

Now considering the case of an initially isotropic field, this system simplifies as

$$\begin{cases} \dfrac{d\overline{u_1'u_1'}}{dt} = -2S\overline{u_1'u_2'} + \Pi_{11} - \varepsilon_{11} \\ \dfrac{d\overline{u_2'u_2'}}{dt} = \Pi_{22} - \varepsilon_{22} \\ \dfrac{d\overline{u_3'u_3'}}{dt} = \Pi_{33} - \varepsilon_{33} \\ \dfrac{d\overline{u_1'u_2'}}{dt} = -S\overline{u_2'u_2'} + \Pi_{12} - \varepsilon_{12} \end{cases} \tag{9.5}$$

The different couplings are illustrated in Fig. 9.3. The associated evolution equation for the turbulent kinetic energy is

$$\frac{d\mathcal{K}}{dt} = -S\overline{u_1'u_2'} - \varepsilon \tag{9.6}$$

which shows the importance of the cross-correlation $\overline{u_1'u_2'}$ for the kinetic energy growth rate.

Reynolds stress models with conventional closure techniques perform satisfactorily in the shear flow case. One reason is historical and not really rational: adjustable constants in the closure models were fitted with maximum care on this case only! Another reason is that the dynamics is dominated by a simple production to dissipation balance (or partial imbalance), and it is not very sensitive to the modeling of the pressure-strain rate tensor, especially to its rapid part, whose single-point modelling is the most difficult task.

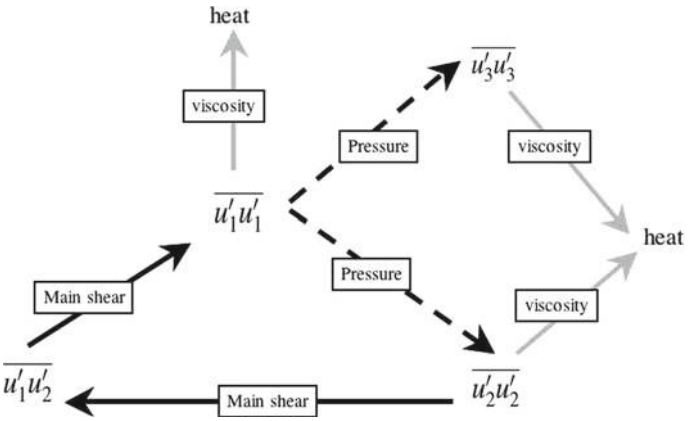

Fig. 9.3 Couplings between the different non-vanishing Reynolds stresses in the pure shear case. Arrows indicate the production process, their color being related to the physical quantity at play (mean strain, pressure, viscosity)

For instance, the exponential growth of turbulent kinetic energy obtained at sufficiently large elapsed time and at large Reynolds number can be predicted, even if not really explained. Equation (9.6) can be rewritten as

$$\frac{1}{S\mathcal{K}}\frac{d\mathcal{K}}{dt} = -\frac{\overline{u_1' u_2'}}{\mathcal{K}} - \frac{\varepsilon}{S\mathcal{K}} \tag{9.7}$$

leading to $\frac{1}{S\mathcal{K}}\frac{d\mathcal{K}}{dt} = Constant$ in the asymptotic régime. A reasonable asymptotic value of the shear rapidity term is obtained from both the previous equation and the modelled corresponding ε equation

$$\frac{1}{S\varepsilon}\frac{d\varepsilon}{dt} = C_{\epsilon 1}(-2b_{12}) - C_{\epsilon 2}\frac{\varepsilon}{S\mathcal{K}} \tag{9.8}$$

provided a correct asymptotic value is assumed for b_{12}. The dependence of the prediction on the two empirical constants will not be discussed here. The reasonable asymptotic value for the nondimensional term $-2b_{12}$ given above is obtained considering the pressure-strain rate modeling and distinguishing between the rapid (or linear) and the slow (or nonlinear) pressure terms, respectively denoted $\Pi_{ij}^{(r)}$ and $\Pi_{ij}^{(s)}$. In the pure shear case, the rapid and slow time scales are S^{-1} and $\mathcal{K}/\varepsilon$, respectively. Assuming that the dissipation is nearly isotropic for the sake of simplicity, the equation for the cross-stress can be rewritten as

$$\frac{d\overline{u_1' u_2'}}{dt} = -S\overline{u_2'^2} + \Pi_{12}^{(r)} + \Pi_{12}^{(s)} \tag{9.9}$$

where $\overline{u_2'^2}$ is governed by

$$\frac{d\overline{u_2'^2}}{dt} = \Pi_{22}^{(r)} + \Pi_{22}^{(s)} - \frac{2}{3}\varepsilon \tag{9.10}$$

It immediately appears that the growth rate of $\overline{u_1' u_2'}$ is firstly driven by the vertical correlation $\overline{u_2'^2}$, this effect being modulated by both rapid and slow pressure strain rate correlations terms. The effect of the linear term $\Pi_{12}^{(r)}$ is modelled to reduce the production, and is perhaps not so important, at least qualitatively. In contrast, the conventional return-to-isotropy effect of the modelled nonlinear term:

$$\Pi_{22}^{(s)} = -C_{(rti)}\varepsilon b_{22} \tag{9.11}$$

is essential for allowing an exponential growth rate in a fully nonlinear régime. Simple explanation can be offered as follows. In the absence of nonlinear terms (and without significant dissipation), Reynolds stress equations, even if they cannot reproduce the RDT behavior (see Sect. 9.3), at least are consistent with an algebraic growth of the turbulent kinetic energy: $\mathcal{K}(St) \propto (St)^n$, $1 \leq n \leq 2$. In this régime, $\overline{u_2'^2}$

remains very small. The presence of the nonlinear pressure-strain rate, modelled in agreement with the return-to-isotropy principle, will redistribute the energy between the diagonal components of the Reynolds stress tensor, therefore feeding the smallest component $\overline{u_2'^2}$. This effect will reinforce the production term $-S\overline{u_2'^2}$ through a strong positive $\Pi_{22}^{(s)}$ term in Eq. (9.10). Even if the term $\Pi_{12}^{(s)}$, being positive, will contribute to damp the growth of $\overline{u_1'u_2'}$, the effect of $\Pi_{22}^{(s)}$ will be the most efficient 'nonlinear' one to enhance $\overline{u_2'^2}$ and therefore to allow a dramatic increase of production, consistent with an eventual exponential growth.

9.3 Rapid Distortion Theory: Equations, Solutions, Algebraic Growth

Linearized inviscid equations in physical space are

$$\frac{\partial u_i'}{\partial t} + Sx_2\frac{\partial u_i'}{\partial x_1} + S\delta_{i1}u_2' = -\frac{\partial p'}{\partial x_i}. \tag{9.12}$$

The pressure (here divided by the mean reference density) term is identified by taking the divergence of the previous equation as

$$\nabla^2 p' = -2S\frac{\partial u_2'}{\partial x_1} \tag{9.13}$$

so that the vertical (cross-gradient) component of the velocity is evidenced as the key component. Combining linearized Navier–Stokes and Poisson equation, it can be easily found that the Laplacian of the vertical velocity fluctuation is simply advected by the mean flow

$$\left(\dot{\nabla^2 u_2'}\right) = \left(\frac{\partial}{\partial t} + Sx_2\frac{\partial}{\partial x_1}\right)\nabla^2 u_2' = 0. \tag{9.14}$$

The fact that $\nabla^2 u_2'$ obeys a decoupled equation, and may be chosen as one of the basic variables to study linear solutions in the presence of mean shear, is not surprising since in the analyses of Orr-Sommerfeld and Squire, $\nabla^2 u_2'$ and ω_2' (vertical vorticity fluctuation) are the two basic variables. Accordingly, it is not too difficult to find complete solutions in physical space for these variables. Nevertheless, these solutions displays non-local operators and involve an integro-differential Green's function in physical space, so that the RDT problem is much more easily solved in Fourier space.

Using the general formalism introduced in Chap. 8, RDT equations can be recast as

$$\dot{\hat{u}}_i + S\left(\delta_{i1} - 2\frac{k_1 k_i}{k^2}\right)\hat{u}_2 \tag{9.15}$$

and

$$\dot{k}_i + Sk_1\delta_{i2} = 0. \tag{9.16}$$

The latter equation generates the following characteristic lines in Fourier space

$$k_1 = K_1, \quad k_2 = K_2 - StK_1, \quad k_3 = K_3 \tag{9.17}$$

which are related to the mean trajectories in physical space

$$x_1 = X_1 + X_2 St, \quad x_2 = X_2, \quad x_3 = X_3. \tag{9.18}$$

It is worth noting that Eqs. (9.17) and (9.18) are a special case of the solution of the Eikonal equation, $k_i = F_{ji}^{-1}(t)K_j$, and the mean trajectory equation, $x_i = F_{ij}(t)X_j$, using Eq. (9.1). Taking advantage of the decoupling of the equation for $\hat{u}_2$

$$\dot{\hat{u}}_2 - 2S\frac{k_1 k_2}{k^2}\hat{u}_2 = 0 \tag{9.19}$$

and using $\dot{k}_i k_i = \dot{k}k = -Sk_1 k_2$ from Eq. (9.16), one obtains

$$\frac{D}{Dt}(k^2\hat{u}_2) = 0 \tag{9.20}$$

which is the exact counterpart of Eq. (9.14). The solution is

$$\hat{u}_2(\boldsymbol{k}, t) = \frac{K^2}{k^2}\hat{u}_2(\boldsymbol{K}, 0). \tag{9.21}$$

Finally, the full solution is expressed as (e.g. Townsend 1976; Piquet 2001)

$$\begin{pmatrix} \hat{u}_1(\boldsymbol{k}, t) \\ \hat{u}_2(\boldsymbol{k}, t) \\ \hat{u}_3(\boldsymbol{k}, t) \end{pmatrix} = \begin{pmatrix} 1 & G_{12} & 0 \\ 0 & \frac{K^2}{k^2} & 0 \\ 0 & G_{32} & 1 \end{pmatrix} \begin{pmatrix} \hat{u}_1(\boldsymbol{K}, 0) \\ \hat{u}_2(\boldsymbol{K}, 0) \\ \hat{u}_3(\boldsymbol{K}, 0) \end{pmatrix} \tag{9.22}$$

where the two extra-diagonal terms are given by

$$G_{12} = -S\int\left(1 - 2\frac{K_1^2}{k^2}\right)\frac{K^2}{k^2}dt, \quad G_{32} = 2S\frac{K_1 K_3}{K^2}\int\frac{K^4}{k^4}dt, \tag{9.23}$$

in which the time dependency is induced by $k^2(t)$ following Eq. (9.17). Analytical integration is not difficult but rather tedious (a whole page would be needed only to write the analytical solutions with various algebraic and $\tan^{-1}$ terms), see Townsend (1976), Piquet (2001).

For $K_1 = 0$, the solution drastically simplifies, leading to $K/k = 1$, $G_{12} = -St$ and $G_{32} = 0$.

This solution can be found with the minimum number of components in the Craya-Herring frame of reference, from Eq. (2.86). Choosing the polar axis of the decomposition $\boldsymbol{n}$ in the vertical direction, the two modes $u^{(1)}$ and $u^{(2)}$ are related to vertical vorticity and Laplacian of vertical velocity, respectively. Therefore, they appear to be the spectral normalized counterparts of Orr-Sommerfeld-Squire variables which are commonly used within the linear instability theory framework. The resulting system of two equations is

$$\dot{u}^{(\alpha)} + S e_1^{(\alpha)} e_2^{(\beta)} u^{(\beta)}, \quad \alpha, \beta = 1, 2 \tag{9.24}$$

since the terms $\dot{e}_i^{(\alpha)} e_i^{(\beta)}$ identically vanish, although $\boldsymbol{k}$ itself if time-dependent.

As for the solution in the fixed frame of reference, the equation for the poloidal component $u^{(2)}$ is decoupled from the one for the toroidal component, since

$$\dot{u}^{(2)} - S \frac{k_1 k_2}{k^2} u^{(2)} = 0$$

The evolution equation for the toroidal component $u^{(1)}$ reduces to

$$\dot{u}^{(1)} + S \frac{K_3}{k} u^{(2)} = 0$$

so that the complete solution is

$$\begin{pmatrix} u^{(1)}(\boldsymbol{k}, t) \\ u^{(2)}(\boldsymbol{k}, t) \end{pmatrix} = \begin{pmatrix} 1 & g_{12} \\ 0 & \frac{K}{k} \end{pmatrix} \begin{pmatrix} u^{(1)}(\boldsymbol{K}, 0) \\ u^{(2)}(\boldsymbol{K}, 0) \end{pmatrix}, \tag{9.25}$$

in which the unique extra-diagonal term is

$$g_{12} = -S \frac{K_3}{K} \int \frac{K^2}{k^2} dt = \frac{K K_3}{K_1 K_\perp} \left(\tan^{-1} \frac{k_2}{K_\perp} - \tan^{-1} \frac{K_2}{K_\perp} \right) \tag{9.26}$$

with

$$K_\perp = \sqrt{K_1^2 + K_3^2} \tag{9.27}$$

so that a complete solution (e.g. in Salhi and Cambon 1997) is generated, which is much simpler than the Townsend's one in the fixed frame of reference. As before, the particular case $K_1 = 0$ yields $K/k = 1$ and $g_{12} = -St \frac{k_3}{k}$.

9.3.1 Some Properties of RDT Solutions

The role of fluctuating pressure is clearly to reduce the vertical velocity component, and therefore to diminish the production of turbulent kinetic energy. This point is illustrated looking at the growth rates reported in the first line of Table 9.2. Ignoring the pressure term in the linearized equation, the vertical velocity component is just advected. More generally the *pressure-released RDT* solution is

$$u_2'(\boldsymbol{x},t) = u_2'(\boldsymbol{X},0),\ u_3'(\boldsymbol{x},t) = u_3'(\boldsymbol{X},0),\ u_1'(\boldsymbol{x},t) = u_1'(\boldsymbol{X},0) - St\,u_2'(\boldsymbol{X},0). \tag{9.28}$$

Of course, this oversimplified solution is not divergence-free. The pressure-released RDT solution for the departure from isotropy problem is

$$\overline{u_1'u_1'}(t) = \frac{2}{3}\mathcal{K}(0)\left(1+(St)^2\right), \tag{9.29}$$

$$\overline{u_2'u_2'}(t) = \overline{u_3'u_3'}(t) = \frac{2}{3}\mathcal{K}(0), \tag{9.30}$$

$$\overline{u_1'u_2'}(t) = -\frac{2}{3}St\mathcal{K}(0), \tag{9.31}$$

yielding a quadratic $(St)^2$ growth rate for the kinetic energy. Corresponding asymptotic values of the anisotropy tensor components are presented in Table 9.2.

But it must be borne in mind that this is the Laplacian of the vertical velocity component that is advected in the full RDT solution, so that

$$\frac{\partial^2 u_2'(\boldsymbol{x},t)}{\partial x_i \partial x_i} = \frac{\partial^2 u_2'(\boldsymbol{X},0)}{\partial X_i \partial X_i},$$

leading to a decrease of the vertical component. This effect is quantified in Fourier space by the factor $K^2/k^2(t)$, which tends to zero at large St if K_1 is nonzero. For instance

$$\overline{u_2'^2} = \iint \frac{K^4}{k^4}\hat{R}_{22}(\boldsymbol{K},0)d^3\boldsymbol{k},$$

which can be evaluated from isotropic initial data

$$\hat{R}_{ij}(\boldsymbol{K},0) = \frac{E(K)}{4\pi k^2}\left(\delta_{ij} - \frac{K_iK_j}{K^2}\right),$$

with $d^3\boldsymbol{k} = d^3\boldsymbol{K}$ coming from incompressibility constraint,[2] so that

[2] It is recalled that in this case one has $\det \mathsf{F} = 1$.

$$\overline{u_2'^2} = \frac{2\mathcal{K}(0)}{3}\frac{1}{4\pi}\iint_{|\boldsymbol{K}|=1}\frac{K^2K_\perp^2}{k^4}d^2\boldsymbol{K}, \tag{9.32}$$

where the surface integral on the initial wave-number $\boldsymbol{K}$ has to be performed on a spherical shell of radius unity. A system of polar-spherical coordinates can be used for further calculations. The decay with time of the integral results from the growth of $k^4(t)$ for almost all $\boldsymbol{K}$-directions, except $K_1 = 0$.

All the Reynolds stresses can be obtained in a similar way. Let us just mention the general solution for the kinetic energy, as

$$\overline{u_i'u_i'} = \iiint \hat{R}_{ii}(\boldsymbol{k}, t)d^3\boldsymbol{k}$$

and

$$\hat{R}_{ii}(\boldsymbol{k}, t) = \frac{E(K)}{4\pi K^2}g_{\alpha\beta}(\boldsymbol{k}, t)g_{\alpha\beta}(\boldsymbol{k}, t)$$

if the initial field is isotropic. Finally, the RDT amplification rate of kinetic energy is found as

$$\frac{\mathcal{K}(t)}{\mathcal{K}(0)} = \frac{1}{2}\frac{1}{4\pi}\iint_{|\boldsymbol{K}|=1} |\,\mathsf{g}\,|^2\, d^2\boldsymbol{K}, \tag{9.33}$$

where the integral of the square of the norm of g has to be calculated on a spherical shell of radius unity, for the initial wavevector.

Despite the simplicity of the latter integral and the fact that $g_{\alpha\beta}$ is analytically expressed from Eqs. (9.25), (9.26), the final derivation of the kinetic energy history is not an easy task. The problem comes from the existence of two different solutions, one for $K_1 = 0$ and one for $K_1 \neq 0$, even if continuity holds. An expansion for high values of St yields a result which is not uniformly valid over the angular domain in $\boldsymbol{k}$: a substantial contribution to the integral comes from a narrow region of thickness $O[(St)^{-1}]$ near $K_1 = 0$ as St increases. This difficulty yielded Rogers (1991) to use matched asymptotic expansions to recover the large St behavior of the turbulent kinetic energy. Only the final result is discussed here for the sake of brevity: the growth rate is linear $\mathcal{K}(St)/\mathcal{K}(0) \sim St$. Such a linear growth rate is satisfactorily recovered in the DNS of Brethouwer (2005), discarding nonlinear terms. More generally, large-time contributions were derived for all Reynolds stress components as

$$\frac{\overline{u_1'u_2'}}{2\mathcal{K}(0)} \to -\ln 2, \tag{9.34}$$

$$\frac{\overline{u_1'^2}}{2\mathcal{K}(0)} \to (2\ln 2)St, \tag{9.35}$$

$$\frac{\overline{u_2'^2}}{2\mathcal{K}(0)} \to 4(St)^{-1}\ln(4St), \tag{9.36}$$

$$\frac{\overline{u_3'^2}}{2\mathcal{K}(0)} \to \frac{\pi^2}{8}\ln(St) - 1.419. \tag{9.37}$$

The corresponding asymptotic values of the components of the anisotropy tensor are given in Table 9.2.

As a last result, it is interesting to calculate some statistical quantities with very simple RDT solutions.

Let us first consider statistical quantities which are defined looking at the sole plane $K_1 = 0$ This plane corresponds to 2D (two-dimensional) structures averaged in the streamwise direction, so that $\overline{u_i'u_j'}L_{ij}^{(1)}$ (without summation over repeated indices) are immediately found from a RDT integral restricted to $K_1 = 0$, e.g.

$$\overline{u_1'^2}L_{11}^{(1)} = \frac{2\mathcal{K}(0)}{3}L_f\left(1 + \frac{(St)^2}{3}\right).$$

The plane $K_3 = 0$ corresponds to two-dimensional structures averaged in the spanwise direction, and similarly simple RDT solutions can be derived for $\overline{u_i'u_j'}L_{ij}^{(3)}$

$$\overline{u_1'^2}L_{11}^{(3)} = \frac{2\mathcal{K}(0)}{3}\frac{L_f}{2} = Constant.$$

The ratio of the two latter quantities illustrates the fact that a simple RDT analysis can predict an increasing streaky aspect ratio $L_{11}^{(1)}/L_{33}^{(3)}$. The idea of evaluating the integral lengthscales, or more precisely their product by related Reynolds stresses referred to as "2D energy components" by Cambon and Salhi, was introduced by Townsend but only applied to RDT for irrotational mean strain. Applications to pure shear and to rotating shear cases are reported in Salhi and Cambon (1997). The Fig. 9.4 shows the excellent agreement between RDT predictions and DNS results if the shear rate is high enough.

9.3.2 *Relevance of Homogeneous RDT*

RDT can predict qualitative trends, and even quantitative ones for single and two-point statistical quantities, which are often dimensionless and characterize anisotropy. Most usual quantities are Reynolds Stress components $\overline{u_i'u_j'}$, with nondimensional deviatoric tensor b_{ij}, and integral lengthscales $L_{ij}^{(n)}$ for different velocity components (subscripts i and j) and different directions of two-point separation (superscript n) for them. The anisotropy reflected in the latter lengthscales can be very different from the Reynolds Stress anisotropy, and therefore cannot be derived from the knowledge of b_{ij}. Qualitative relevance of RDT solutions can appear even for particular realizations (snapshots) of the fluctuating velocity field, when compared to full DNS. This is illustrated in Fig. 9.5, which compares instantaneous velocity

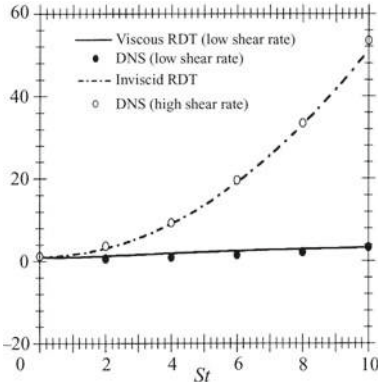

Fig. 9.4 Inviscid and viscous RDT compared to high shear rate and low shear rate DNS. DNS came from a joint exploitation by C. Cambon and M. J. Lee of the CTR database in 1990 (the same database was used by Lee et al. 1990). Time history of the streamwise two-dimensional energy components $\overline{u_1'^2} L_{11}^{(1)}$ are plotted. Reproduced from Salhi and Cambon (1997) with permission of CUP

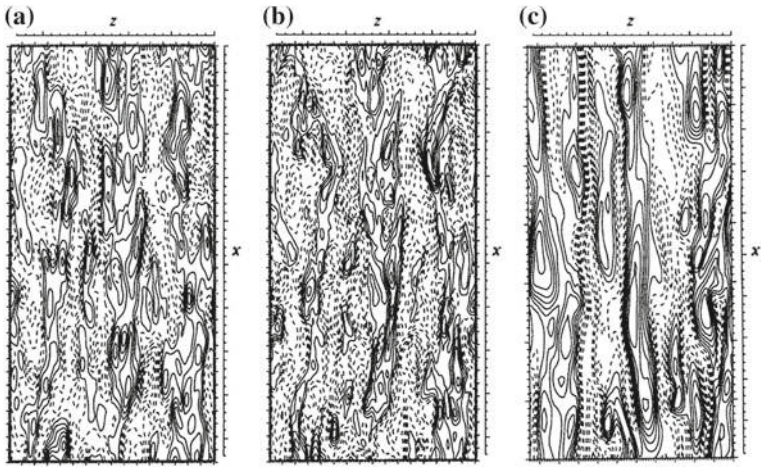

Fig. 9.5 Contours of streamwise fluctuating velocity from **a** direct numerical simulation (DNS), and **b** rapid distortion theory (RDT) calculations for uniformly sheared homogeneous turbulence, and **c** direct numerical simulation of plane channel flow near a wall horizontal plane $y^+ \sim 10$. The streamwise elongation of turbulent structures resulting from shear appears clearly, as does the strong similarity between RDT and DNS results. From Lee et al. (1990) with permission of CUP

fields obtained in the case of pure plane shear and plane channel flow near the wall. It is concluded that the tendency to create elongated streaky structures by a strong mean shear is inherent to this "homogeneous RDT" operator, independently of the presence of a wall and non linear effects.

A detailed analysis of the vortical structures dynamics will be given in Sect. 9.8. We will just summarize here the results of Iida et al. (2000), who performed a detailed analysis of subtle discrepancies which exist between vortex tubes predicted by RDT and those observed in DNS for a medium shear $0 \leq St \leq 6$.

Direct numerical simulations reveal that these longitudinal vortices are inclined in the (x, y) plane and tilted in (x, z) plane. Vortices with positive (resp. negative) longitudinal vorticity tend to tilt at a positive (resp. negative) angle, while they are all inclined at a positive angle. An important result is that RDT is able to predict the inclination of longitudinal vortices, but not their tilting. Therefore, the tilting appears to be a non-linear phenomenon. This subtle kinematical difference on the vortices topology has a very large impact on the non-linear dynamics. To measure this effect, Iida and coworkers have computed non-linear terms using both DNS and RDT velocity field as an input. Their main observations are the following:

- In DNS, the kinematics of longitudinal vortices is deeply affected by the instantaneous strain rate tensor. They are stretched in the streamwise and spanwise direction, and compressed in the vertical direction. These local strains yield the existence of spiral streamlines in the streamwise direction and the production of non-zero instantaneous local Reynolds stress $u'_2u'_3$. The streamwise fluctuations generated at the sides of the longitudinal vortex are wrapped around it, leading to the existence of negative values of the local fluctuating strain $(\partial u'_1/\partial x_2 + \partial u'_2/\partial x_1)$ inside the vortex. This phenomenon, referred to as *vortex wrapping*, is absent in RDT fields.
- The vortex wrapping phenomenon and its effect on the kinematics of longitudinal vortices have a strong impact on nonlinear energy transfers. RDT fields lead to a vanishing transfer function in the Fourier space for the vertical Reynolds stress $\overline{u'_2u'_2}$, while it contributes to an inverse energy cascade in the DNS field. RDT fields also yield to an underestimation of the forward energy cascade associated with the non-linear transfers of $\overline{u'_1u'_1}$ and $\overline{u'_3u'_3}$. This underestimation is tied to the misprediction of the instantaneous values of $u'_2u'_3$.

9.4 Nonlinear Spectral Analysis, Simplified Closure and Self-similarity

Some attempts exist to reproduce both linear and fully nonlinear régimes by an unified spectral theory. Anisotropic EDQNM approach by Cambon et al. (1981) was limited to moderate anisotropy, and was unable of covering a very large St domain. Theoretical derivations from LRA by Ishihara et al. (2002) are even more limited to weak anisotropy and small structures. The general formalism, called EDQNM(1-2-3), is valid in principle, but no complete solution, with arbitrary degree of anisotropy, was numerically computed. Recently the model by Mons et al. (2016) (referred to as MCS model, in order to distinguish several versions of anisotropic EDQNM) presented

in Chap. 8 offered a way to calculate second-order statistics of any homogeneous shear-driven turbulent flow, as illustrated in the next subsection.

A different approach was proposed by Nazarenko and Zakharov (1994), who use a kind of "first loop" for evaluating the impact of nonlinearity. On the one hand, this approach includes an interesting formalism relying Clebsh potentials, allowing to derive a Hamiltonian operator.[3] On the other hand, the basic RDT solution is completely missed, since the authors consider that the asymptotic value of kinetic energy is a non-zero constant in inviscid RDT, ignoring all the subtle effects correctly accounted for by Rogers (1991). This last point unfortunately invalidates their main result, which is that turbulent kinetic energy grows as $(St)^2$ in their particular nonlinear régime.

Simple results for the coexistence of linear and nonlinear effects can be inferred from the numerical and theoretical study of Salhi et al. (2014), as shown in Fig. 9.6. The evolution of the radial energy spectrum $E(k)$ is shown in left. Large scales contribution (small wavenumber range) continuously evolve, whereas small scale reach an almost steady state after a transient phase of viscous decay ($St \leq 3$). Looking at viscous RDT, the behavior of largest scales is almost the same as the DNS one, whereas smallest scales continue to evolve and never reach a steady state. It is possible to analyse separate terms in the equation for $E(k,t)$

$$\frac{\partial E}{\partial t} + T^L(k,t) - P(k,t) = T(k,t) - 2\nu k^2 E(k,t), \tag{9.38}$$

in which T^L denotes the linear transfer by mean shear advection, P corresponds to the radial spectrum of production, whereas $T(k)$ and $2\nu k^2 E(k)$ holds for the nonliner transfer term and the dissipation spectrum, inherited from the Lin equation for THI. Looking at Fig. 9.6-right, it is confirmed that the quasi-steady shape of the energy spectrum at large scale corresponds to an almost balance, k by k, of positive nonlinear transfer term and dissipation spectrum, with an almost zero contribution of the right-hand-side of Eq. (9.38), together with a negligeable contribution from the linear terms ($T^L - P$) to the unsteadiness of E in this range. *This situation is very close to what happens in decaying HIT at very high Reynolds number, in connection with the asymptotic recovery of the* 4/5 *Kolmogorov law.* It is found, however, at moderate Reynolds numbers permitted by DNS.

9.4.1 Results in Term of Spherically-Averaged Descriptors

The model by Mons et al. (2016) gives direct access to the 11 independent spherically averaged descriptors (energy spectrum, 2 trace-free symmetric deviatoric spectral tensors for directional anisotropy and polarization anisotropy). They are governed by closed equations, in which a truncated expansion in terms of angular harmonics of

[3] Hamiltonian formalism is also very important in the "Russian" school of wave turbulence theory.

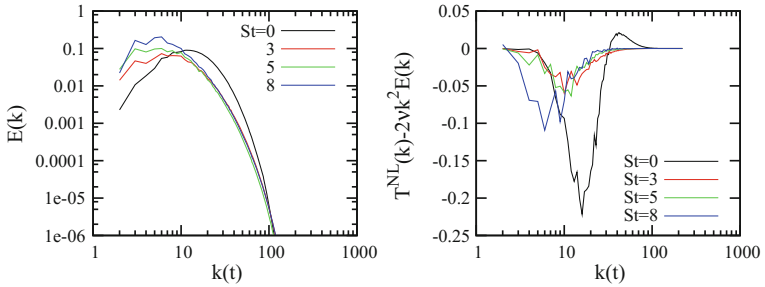

Fig. 9.6 Left: Time-development of radial energy spectrum $E(k,t)$ by DNS in pure shear case. Right: Time-development of the term $T(k) - 2\nu k^2 E(k)$. The initial time ($St = 0$) corresponds to a shearless precomputation (full line). Adapted from Salhi et al. (2014) with permission of APS

$\boldsymbol{k}$-vector spectra is injected in both linear terms (inherited from RDT) and nonlinear ones from EDQNM1. From the Eq. (8.46)

$$\varphi_{ij}(k,t) = 2E(k,t)\left(\frac{1}{3}\delta_{ij} + H_{ij}^{(dir)}(k,t) + H_{ij}^{(pol)}(k,t)\right),$$

valid for any anisotropic flow subjected to mean velocity gradients $\mathbf{A}$, four components are nonzero in the case of pure plane shear with isotropic initial data. The spherically averaged spectrum φ_{12} — with $P = S\varphi_{12}$ in Eq. (9.38) — of the off-diagonal Reynolds stress component obtained at $St = 20$ is plotted on Fig. 9.7, with its two contributions, in log-log coordinates (to show the slopes, left) and in linear-log coordinates (to show the change of sign of the directional anisotropy term, right). The rise of a $-7/3$ slope, as suggested by several authors since Lumley (1967), is found for wavenumbers larger than the threshold wavenumber (recalled below) with an inprecedented range, permitted by the high Reynolds number. Given the weak value of anisotropy at larger wavenumbers, the ratio $H_{12}^{(dir)}/H_{12}^{(pol)}$ is plotted in Fig. 9.9.

Looking at the diagonal streamwise component φ_{11}, similar results are found, but a better plateau is recovered for the abovementioned ratio, with a positive value of about 0.6. In addition to the $-7/3$ slope for both $EH_{11}^{(dir)}$ and $EH_{11}^{(pol)}$, the classical Kolmogorov slope is recovered for the total contribution, because of the dominance of the energy spectrum E.

9.4.2 Local Isotropy in Homogeneous Shear Flows

A threshold wavenumber was identified in both rotating turbulence (Zeman's scale, also referred to as Hopfinger's scale or Woods' scale) and stratified turbulence (Ozmidov scale). In the shear case, one has the Corrsin's scale (Corrsin 1958) whose associated wavenumber is

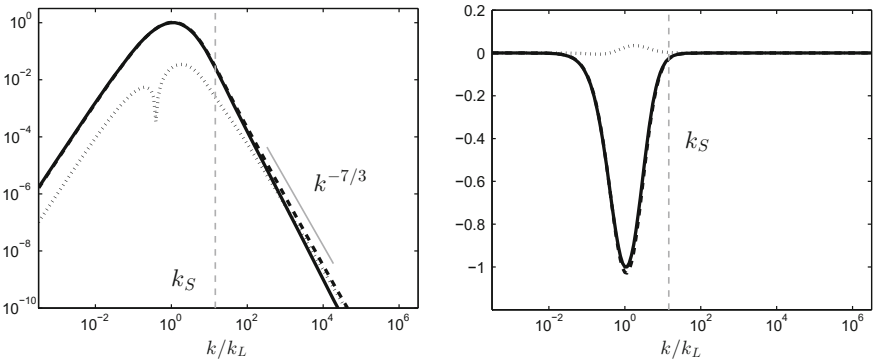

Fig. 9.7 Spectral contributions to the off-diagonal component φ_{12} in log-log (left) and log-linear (right) representation: Total (full line), directional $2EH_{12}^{(dir)}(k)$ (dotted line) and polarization $2EH_{12}^{(dir)}(k)$ (dashed line) contributions. Courtesy from Vincent Mons

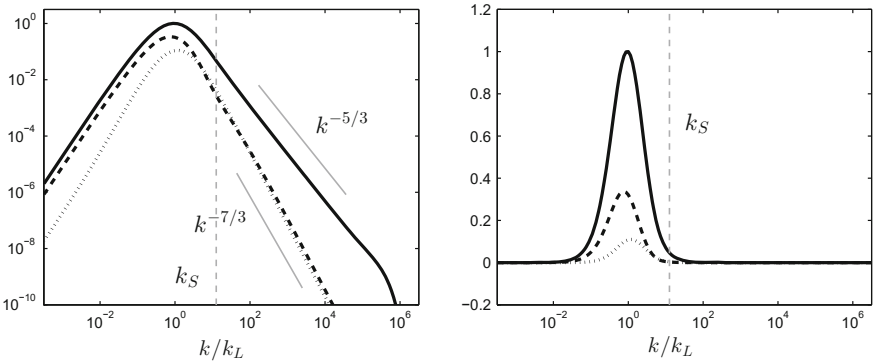

Fig. 9.8 Spectral contributions to the diagonal (streamwise) component φ_{11} in log-log (left) and log-linear (right) representation: Total (full line), directional $2EH_{11}^{(dir)}(k)$ (dotted line) and polarization $2EH_{11}^{(dir)}(k)$ (dashed line) contributions. Courtesy from Vincent Mons

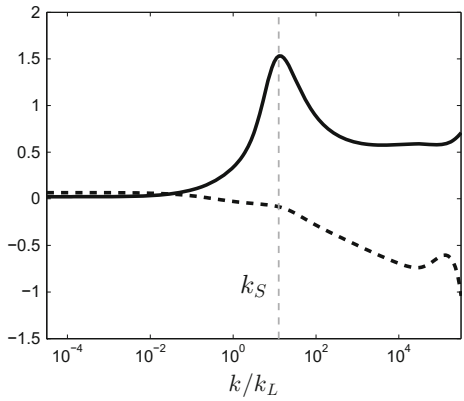

Fig. 9.9 Ratios $H^{(dir)}/H^{(pol)}$ for both off-diagonal (dashed line) and diagonal (full line) components. Log-linear plotting. Courtesy from Vincent Mons

$$k_S = \sqrt{\frac{S^3}{\varepsilon}}. \tag{9.39}$$

As a general result for any shear-driven turbulent flow, S is the shear rate here, but could be proportional to the norm of an arbitrary $\mathbf{A}$ mean flow gradient matrix, or $S = \sqrt{A_{ij}A_{ij}}$ as well. The trend to restore isotropy for wavenumbers larger than k_S (or scales smaller than the Corrsin's lengthscale k_S^{-1}) is shown in Figs. 9.7, 9.8 and 9.9 for both the off-diagonal component φ_{12} and the streamwise one φ_{11}.

The existence of a threshold wavenumber is not so obvious in turbulence without production. On the other hand, it is expected that in flows with production, the maximum anisotropy induced by linear RDT operators will be found at largest scales/smallest wavevectors, whereas it can only decay monotonically as the wavenumber increases, until a classical quasi-isotropic Kolmogorov range is recovered.

The question of the validity of Kolmogorov's local isotropy hypothesis in homogeneous shear flows has been addressed by several authors, using both experimental and simulation data. A first observation is that, as expected, the mean shear induces a breakdown of global isotropy. Looking at p.d.fs of velocity increments (see Fig. 9.10), one can see that the effect of the shear is scale-dependent. Its influence on small scale anisotropy is strong, leading to a noticeable departure from the isotropic turbulence case, while the effects at larger scales is weaker. There is no contradiction with the expected scale-by-scale distribution of anisotropy: Departure from Gaussianity is weaker in the largest scales, anisotropic and dominated by RDT, than in the smallest scales, dominated by intrinsic nonlinearity.

In addition, experimental data suggest that the threshold wavenumber k_S given by Eq. (9.39) delineates two ranges for the energy spectrum $E(k)$, with k^{-1} and $k^{-5/3}$ slopes, as follows

$$E(k) \propto \begin{cases} k^{-1} & k < k_S \\ k^{-5/3} & k > k_S \end{cases} \tag{9.40}$$

As a crude interpretation, one can say that for scales larger than $L_S = k_S^{-1}$ the dynamics is dominated by linear shear effects, while scales much smaller than L_S should be governed by nonlinear effects. Local isotropy may hold for the latter range of scales.

The subtle but straightforward linear RDT analysis of Hanazaki and Hunt (2004) confirms the rise of the k^{-1} slope. This slope can be found in near wall turbulence as well, with a rather recent experimental evidence by Nickels et al. (2005). Such a slope cannot be seen in Fig. 9.8, because the spectral range between the peak of the energy spectrum and the k_S wavenumber is too small. This is a generic remark for other cases of spectral distribution given in this book: No information for a Bolgiano range in stably stratified turbulence, no information for a spectrum "nothing like" the Kolmogorov spectrum in unstably stratified turbulence. Only when k_S is far larger than the wavenumber of the peak, slopes very different from Kolmogorov's one are observed, as in rapidly rotating or in strongly stratified turbulence.

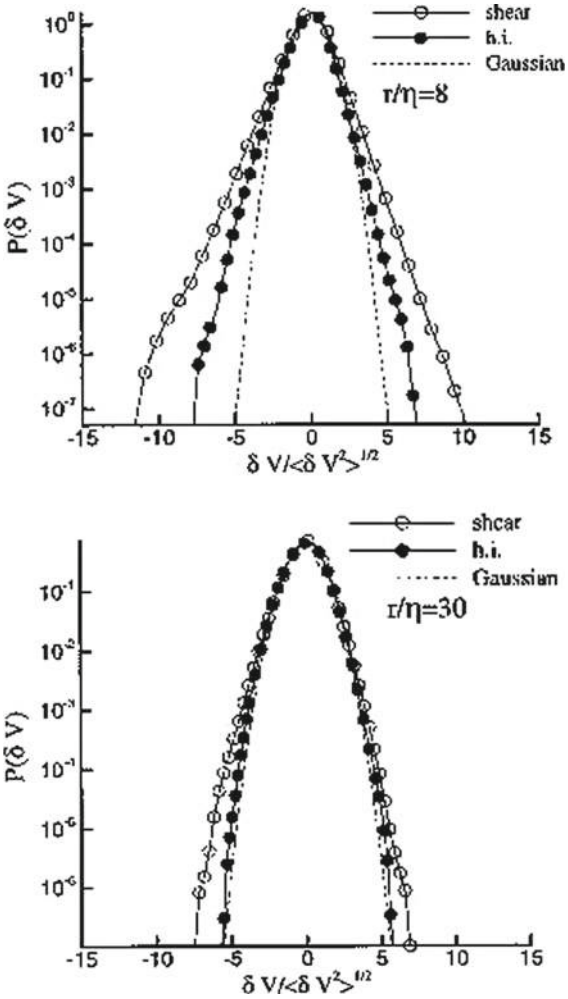

Fig. 9.10 Probability density function of the velocity increment in isotropic turbulence (black circle) and homogeneous shear turbulence (white circle) for $r/\eta = 8$ (top) and $r/\eta = 30$ (top), where η is the Kolmogorov scale. The dashed line is related to the Gaussian distribution. Reproduced from Gualtieri et al. (2002) with permission of AIP

Experimental data suggest that the bifurcation between the two "inertial" ranges (but probably the range at largest scales is not inertial) occurs for $kL_S \sim 0.5-1$. Such a transition in the slope of $E(k)$ can be hardly identified in Fig. 9.11, in which the spectrum computed thanks to the anisotropic EDQNM model detailed in Sect. 17.9 in the pure shear case at very high Reynolds number.

The above criterion is not sufficient to account for the full complexity of the problem, since viscous effects are neglected and that these effects can preclude the occurence of the quasi-isotropic inertial range. One needs to define two non-dimensional parameters, S_i and S_d, to describe the full problem. The first one measures the relative importance of nonlinear inertial mechanisms and linear shear effects:

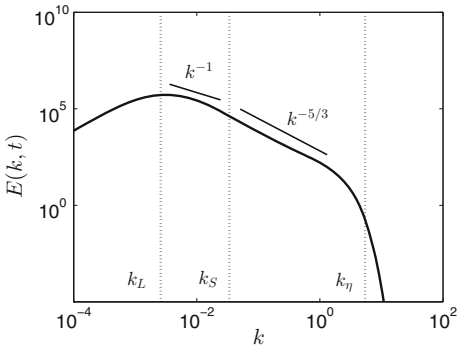

Fig. 9.11 Energy spectrum in the homogeneous pure shear case computed via anisotropic EDQNM (MCS model). Courtesy of V. Mons and A. Briard

$$S_i = \frac{2S\mathcal{K}}{\varepsilon} = \left(\frac{l}{L_S}\right)^{2/3}, \quad l = \frac{(2\mathcal{K})^{3/2}}{\varepsilon} \tag{9.41}$$

The second one is defined as the ratio of the dissipative and shear effects:

$$S_d = S\sqrt{\frac{\nu}{\varepsilon}} = \left(\frac{\eta}{L_S}\right)^{2/3} \tag{9.42}$$

One can expect to observe a pseudo-isotropic inertial range for small values of S_d only. For large values of S_i, most of the scales in the inertial range are dominated by the mean shear effects, precluding the existence of scales compatible with local isotropy. A consequence is that true local isotropy, if it exists, can be recovered at very high Reynolds number only. Such high values have not been reached up to now, and available data only makes it possible to identify trends. Available results suggest that, increasing the Reynolds number, small scales in homogeneous turbulence come closer to isotropy, but that some anisotropy persists, even at $Re_\lambda = 660$ (Ferchichi and Tavoularis 2000). An open issue is the existence, even at very high Reynolds number, of a pseudo-isotropic state of the small scales, in which some anisotropy would remain.

9.4.3 Exponential Growth from Self-similarity

Exponential growth is reproduced by the model (Mons et al. 2016), but with a rate probably overestimated. Even single-point closures satisfactorily work for that, provided that constants are appropriately chosen, as discussed in Sect. 9.2.

We will discuss now how to introduce a self-similar argument in the spectral theory, following a very relevant approach proposed by Julian Scott (private communication) as follows. A reminiscent approach applied to the Lin equation was proposed in George and Gibson (1992).

Large-scale self-similarity can be expressed very similarly as in Eq. (4.137) for the shearless flow case, as

$$\hat{R}_{ij}(\boldsymbol{k}, t) = u^2 L^3 \Psi_{ij}(\boldsymbol{k}L), \tag{9.43}$$

where $u(t)$ and $L(t)$ are velocity and length scales characterizing the self-similar evolution of turbulence, respectively, and Ψ_{ij} is a dimensionless tensor. The Reynolds stress tensor is therefore given by

$$\overline{u_i' u_j'} = u^2 \iiint \Psi_{ij}(\boldsymbol{q}) d^3\boldsymbol{q}, \tag{9.44}$$

showing that its different components are proportional to the same function, u^2, of time. Thus, the ratio of different components is constant, as observed asymptotically. Using Eq. (9.43), the Craya's equation (2.102) becomes

$$\begin{aligned} \alpha_2 \left(q_m \frac{\partial \Psi_{ij}}{\partial q_m} + 3\Psi_{ij} \right) - \alpha_1 \Psi_{ij} + \\ \alpha_3 \left(M_{im}\Psi_{mj} + M_{jm}\Psi_{im} - A_{lm} q_l \frac{\partial \Psi_{ij}}{\partial q_m} \right) = \Xi_{ij}, \end{aligned} \tag{9.45}$$

where $\boldsymbol{q} = \boldsymbol{k}L$ is the similarity variable, $T_{ij} = u^2 L^3 \Xi(\boldsymbol{q})$, and the quantities α_1, α_2 and α_3 are given by

$$\alpha_1(t) = \frac{L}{u^3}\frac{du^2}{dt}, \quad \alpha_2(t) = \frac{1}{u}\frac{dL}{dt}, \quad \alpha_3 = \frac{L}{u}. \tag{9.46}$$

Given the fact that we are concerned with the large scales, the viscous term in Eq. (2.102) is dropped out. From Eq. (9.46), it follows that the α_i are related by

$$\frac{d\alpha_3}{dt} = \alpha_2 + \frac{1}{2}\alpha_1. \tag{9.47}$$

Presuming that the given mean flow does not permit self-similar solutions of RDT (which is the case for the pure plane shear, but also for all but the pure rotation case), the only possible large-scale self-similarity, allowing for nonlinearity, has constant α's. From Eq. (9.46) this implies the following exponential behaviour

$$u(t) \sim \exp\left(\frac{\alpha_2}{\alpha_3} t\right), \quad L(t) \sim \exp\left(\frac{\alpha_2}{\alpha_3} t\right), \tag{9.48}$$

using $\alpha_1 = -2\alpha_2$. A positive value of α_2/α_3 is consistent with experimental and numerical DNS results.

Of course, we have not shown that large-scale self-similarity occurs, merely that, if it does, it must respect (9.48). The previous analysis has something to do with the Oberlack's approach, in the sense that no closure theory is needed, but the discussion of the admissible values for the constants α's relies on a very subtle analysis of asymptotic RDT (not reported here for the sake of brevity).

We also take from Julian Scott the following remark. Exponential growth of L means that, in practice, the large scales in turbulence increase rapidly in size until they encounter inhomogeneities or boundaries of the flow, at which point the above model, assuming homogeneous turbulence in an infinite domain, no longer holds.

Finally, the exponential growth appears as generic for shear-driven flows dominated by production, in which $\mathbf{A}$ is not purely antisymmetric, but may result from different histories. For strain-dominated flows, exponential growth is first induced by linear effects of vortex-stretching-type; then nonlinear dynamics can reduce the growth rate but cannot saturate the hyperbolic instability, so that the linear exponential growth is eventually altered but not suppressed. In the case of pure shear flow only, the exponential growth does not result from the linear (algebraic) growth, but needs a complex interplay between linear and nonlinear effects.

9.5 Return to Isotropy in Shear-Released Homogeneous Turbulence

The return to isotropy of homogeneous shear turbulence is classically addressed considering an initially isotropic turbulence experiencing an homogeneous constant shear during a finite. Anisotropy growths during the first stage, and then evolves freely in a second time.

A typical evolution of the anisotropy tensor b_{ij} is displayed in Fig. 9.12. It is observed that the solution doesn't converge toward an isotropic final state, but toward a state with constant b_{ij}. This is due to the fact that anisotropy at very large scales is almost frozen, the decay of anisotropy observed just after the shear-release time being due to the return of isotropy of small scales. The scale-by-scale structure of anisotropy during the final stage of evolution is illustrated in Fig. 9.13, which displays both polarization and directional component of anisotropy during the final stage of evolution. It is observed that small scales are fully isotropic, while very large scales are not: the shear-induced anisotropy at such scales remains unchanged by the nonlinear cascade mechanisms. The relaxation of very large scales is observed to be sensitive to the infrared slope of the initial kinetic energy spectrum σ such that $E(k \to 0, t = 0) \propto k^{\sigma}$. In the case $\sigma = 4$ (initial Batchelor turbulence), the permanence of large eddies is broken by inverse cascade mechanisms and large scales exhibits a significant evolution associated to a reduction of anisotropy. For smaller values of σ (e.g. Saffman turbulence with $\sigma = 2$) large scales and their associated anisotropy are almost frozen.

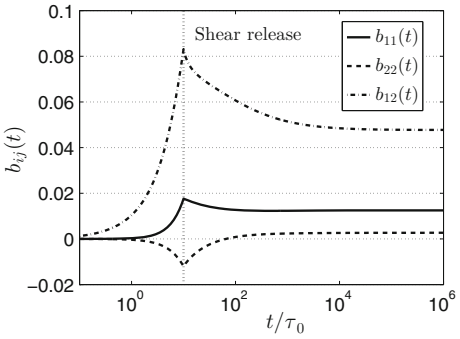

Fig. 9.12 Time history of anisotropy tensor component $b_{ij}(t)$ in homogeneous shear-released turbulence computed via anisotropic EDQNM (MCS model). Shear release time is shown by the vertical dashed line. The positive value of b_{12} corresponds to inverting the sign of S, consistently with the fact that 2 and 3 axes are permutated with respect to the original publication. Adapted from Briard et al. (2016). Courtesy of A. Briard

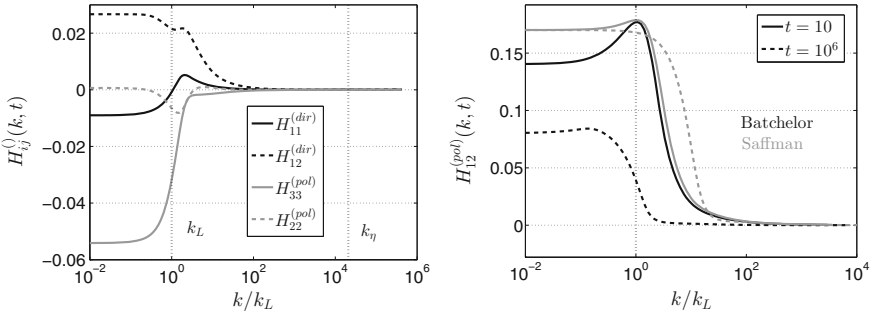

Fig. 9.13 Scale-by-scale decomposition anisotropy in homogeneous shear-released turbulence during final stage of evolution computed via anisotropic EDQNM. Left: poloidal and toroidal components. Right: influence of the infrared kinetic energy spectrum slope at initial time. Same remark on the sign of the off-diagonal component as in Fig. 9.12. Adapted from Briard et al. (2016). Courtesy of A. Briard

Decay laws for integral quantities such as kinetic energy, $\mathcal{K}(t)$, and the non-zero extra-diagonal Reynolds stress R_{12} can be obtained using an extended version of the Comte-Bellot – Corrsin theory. The analysis performed in Briard et al. (2016) shows that the decay exponent of kinetic energy is the same as in the pure isotropic case, i.e.

$$\mathcal{K}(t) \propto t^n, \quad n = \frac{\sigma - p + 1}{\sigma - p + 3}, \quad p = \begin{cases} 0 & 1 \le \sigma \le 3 \\ 0.55 & \sigma = 4 \end{cases}$$

while $R_{12}(t)$ exhibits the following algebraic decay law:

$$R_{12}(t) \propto t^m, \quad m = \frac{\sigma - p_S + 1}{\sigma - p + 3}, \quad p = \begin{cases} 0 & 1 \le \sigma \le 3 \\ 0.279 & \sigma = 4 \end{cases} \tag{9.49}$$

where p is the same as for $\mathcal{K}(t)$. Values of p and p_S are tuned thanks to anisotropic EDQNM results, leading to a very good agreement in all cases.

9.6 Models for Space- and Space-Time Correlations

9.6.1 Models for Single-Time Velocity Spectral Tensor

This section is devoted to explicit models for the spectral tensor $\hat{\mathbf{R}}(\boldsymbol{k})$.

Most existing models are based on the use of the Rapid Distorsion Theory has been used to develop models for the velocity spectral tensor. A hierarchy of models with increasing complexity and theoretical consistency can be identified:

- Models based on inviscid RDT, e.g. Mann (1994). The key idea is to use the analytical solution given by RDT for the time-evolution of the spectral tensor starting from an initially isotropic field, and to assume that eddies cannot be stretched over a duration larger than their lifetime. The spectral tensor is therefore defined as a kind of equilibrium value reached at a time equal to the lifetime, for which linear RDT effects are counterbalanced by nonlinear effects. It is important to emphasize here that such models are time-independent, which is not fully consistent with the fact that homogeneous shear turbulence is an genuinely unsteady flow that does not exhibit a steady state. As a matter of fact, these models are mostly used to predict the spectral tensor in turbulent parallel or quasi-parallel shear flows (jet, mixing layer, boundary layer, channel flow ...) at equilibrium or close to equilibrium. A weak time-dependency is still present thanks to the fact that such model scalar inputs, e.g. turbulent kinetic energy $\mathcal{K}(t)$ are time-evolving quantities. Therefore, the use of such models should be restricted to the exponential growth phase in which anisotropy is assumed to have reach en equilibrium state.
- An improvement of previous models, in which (i) damping or saturation of anisotropy via non-linear effects is taken into account continuously modifying the RDT Green function in an ad hoc way and (ii) the generation of new eddies via the mean shear at all times is taken into account (De Mare and Mann 2016).
- Models with full modelling of non-linear effects and pressure effects, models being defined in such a way that analytical integration can be carried out, yielding explicit models that can be rewritten in a formalism close to the one of RDT, being based on a Green function. A recent example was given by Weinstock (2013).

We first illustrate the first class of models, i.e. models associated to a steady state. Denoting $\hat{R}_{ij}^{eq}(\boldsymbol{k})$ the associated solution, one takes $\hat{R}_{ij}^{eq}(\boldsymbol{k}) = \hat{R}_{ij}(\boldsymbol{k}, \tau_{life}(k))$, where $\tau(k)$ is the lifetime of the eddy with characteristic size $1/k$. Several estimates have been proposed, which are summarized in Table 9.3. The important point is that all the scale-dependent models lead to $\tau_{life}(k) \propto k^{-2/3}$ for small scales located within the inertial range. Results obtained using atmospheric boundary layer data seems to show that Mann's expression is the most accurate one. It is worth noting that taking

Table 9.3 Models for the eddy lifetime to be used in the expression for the velocity spectral tensor in incompressible homogeneous shear flows. S denotes the mean shear. Asymptotics are obtained considering the von Karman model spectrum for $E(k)$

Source	$\tau_{life}(k)$	$\tau_{life}(kL \ll 1)$	$\tau_{life}(kL \gg 1)$
Maxey (1982)	$\sim 1/S$	$\sim 1/S$	$\sim 1/S$
Mann (1994)	$\sim k^{-1}\left(\int_0^{+\infty} E(p)dp\right)^{-1/2}$	$\sim k^{-1}$	$\sim k^{-2/3}$
Comte-Bellot and Corrsin (1971)	$\sim k^{-2}\left(\int_0^{+\infty} p^2 E(p)dp\right)^{-1/2}$	$\sim k^{-2}$	$\sim k^{-2/3}$
Lesieur (1987)	$\sim \left(k^3 E(k)\right)^{-1/2}$	$\sim k^{-7/2}$	$\sim k^{-2/3}$

a scale independent lifetime as in Maxey's model yields a failure in the prediction in the slope of the non-zero velocity cross-spectra in the inertial range.

The resulting model expressed in the classical frame of reference is (a compact form can also be written using the local frame used in Sect. 9.3):

$$\hat{R}_{ij}^{eq}(\boldsymbol{k}) = \hat{R}_{ij}(\boldsymbol{k}(\tau_{life}(k)), \tau_{life}(k)) = G_{im}^{(0)}(\boldsymbol{k}, \tau_{life}(k), t_0) G_{jn}^{(0)}(\boldsymbol{k}, \tau_{life}(k), t_0) \hat{R}_{mn}(\boldsymbol{K}, t_0) \tag{9.50}$$

where $\mathbf{G}^{(0)}$ denotes the Green function of the inviscid pure shear problem, $\boldsymbol{k} = (k_1, k_2, k_3)$, $\boldsymbol{K} = (K_1 = k_1, K_2 = k_2, K_3 = k_3 + \beta(k)k_1)$ and with $\beta(k) = S\tau_{life}(k)$, and $\hat{\mathbf{R}}(\boldsymbol{K})$ is the isotropic spectral tensor used as an initial condition at time t_0. In the present case, the spectral tensor can be written in the following explicit form:

$$\hat{R}_{11}^{eq}(\boldsymbol{k}) = \frac{E(K)}{4\pi K}(K^2 - k_1^2 - 2k_1K_3\xi_1 + (k_1^2 + k_2^2)\xi_1^2) \tag{9.51}$$

$$\hat{R}_{22}^{eq}(\boldsymbol{k}) = \frac{E(K)}{4\pi K}(K^2 - k_2^2 - 2k_2K_3\xi_2 + (k_1^2 + k_2^2)\xi_2^2) \tag{9.52}$$

$$\hat{R}_{33}^{eq}(\boldsymbol{k}) = \frac{E(K)}{4\pi k^4}(k_1^2 + k_2^2) \tag{9.53}$$

$$\hat{R}_{12}^{eq}(\boldsymbol{k}) = \frac{E(K)}{4\pi K^4}(-k_1k_2 - k_1K_3\xi_2 - k_2K_3\xi_1 + (k_1^2 + k_2^2)\xi_1\xi_2) \tag{9.54}$$

$$\hat{R}_{13}^{eq}(\boldsymbol{k}) = \frac{E(K)}{4\pi K^2k^2}(-k_1K_3 + (k_1^2 + k_2^2)\xi_1) \tag{9.55}$$

$$\hat{R}_{23}^{eq}(\boldsymbol{k}) = \frac{E(K)}{4\pi K^2k^2}(-k_2K_3 + (k_1^2 + k_2^2)\xi_2) \tag{9.56}$$

along with

$$\xi_1 = \left(C_1 - \frac{k_2}{k_1}C_2\right), \quad \xi_2 = \left(C_2 + \frac{k_2}{k_1}C_1\right) \tag{9.57}$$

and

$$C_1 = \frac{\beta(k)k_1^2(K^2 - 2K_3^2 + \beta(k)k_1K_3)}{k^2(k_1^2 + k_2^2)} \tag{9.58}$$

$$C_2 = \frac{k_2K^2}{(k_1^2 + k_2^2)^{3/2}} \arctan\left(\frac{\beta(k)k_1(k_1^2 + k_2^2)^{1/2}}{K^2 - K_3k_1\beta(k)}\right). \tag{9.59}$$

This model is observed to accurately predict the velocity spectra and cross-spectra in neutral atmospheric boundary layer when supplemented by an ad hoc term to account for wall effects and local, altitude-dependent tuning of the energy spectrum.

The extension of this model to account for both continuous nonlinear eddy damping and generation of new eddies proposed in De Mare and Mann (2016) leads to

$$\hat{R}_{ij}^{eq}(\boldsymbol{k}) = \int_{-\infty}^{t} G_{im}(\boldsymbol{K}, t - t')G_{jn}(\boldsymbol{K}, t - t')\frac{1}{\tau_{life}(K)}\hat{R}_{mn}(\boldsymbol{K})dt', \tag{9.60}$$

where $\mathbf{G}$ is the modified Green function given by:

$$\mathbf{G}(\boldsymbol{K}, t - t') = \exp\left(-(\Omega(\boldsymbol{K}, t - t') - \Omega(\boldsymbol{K}, 0))\right)\mathbf{G}^{(0)}(\boldsymbol{k}, S(t - t'), t'), \tag{9.61}$$

where $\mathbf{G}^{(0)}$ is the original RDT Green function mentioned above and $\Omega(\boldsymbol{K}, t - t')$ accounts for the continuous damping effect. The latter is solution of the following equation:

$$\frac{\partial}{\partial t}\Omega(\boldsymbol{K}, t - t') = \frac{1}{2\tau_{life}(\boldsymbol{k}(t))}. \tag{9.62}$$

The model by Weinstock (2013) is based on an actual closure of the Craya equation, in which nonlinear effects are present via spectral transfer terms and pressure-strain rate spectral tensor. With respect to the general Equations. (8.39) and (8.40) under their most compact form, the nonlinear closure amounts to

$$T^{(\mathcal{E})}(\boldsymbol{k}, t) = \frac{T(k, t)}{4\pi k^2} - \varphi^{RTI}(k, t)\left(\mathcal{E}(\boldsymbol{k}, t) - \frac{E(k, t)}{4\pi k^2}\right), \quad T^{(Z)}(\boldsymbol{k}, t) = -\varphi^{RTI}(k, t)Z(\boldsymbol{k}, t).$$

This closure combines purely isotropic (conservative) energy transfer $T(k, t)$ and explicit return-to-isotropy term, as a spectral Rotta's effect, that is mediated by the

relaxation coefficient $\varphi^{RTI}(k,t)$. It is perhaps useful to report the original equations, component by component, in the Cartesian frame:

$$\begin{aligned}
&\left[\frac{\partial}{\partial t} - k_1 S\frac{\partial}{\partial k_2} + 2\nu k^2 + \varphi(k,t)\right]\hat{R}_{ij}(\boldsymbol{k},t) \\
&= -S\left[\left(\delta_{i1} - 2\frac{k_i k_1}{k^2}\right)\hat{R}_{j2}(\boldsymbol{k},t) + \left(\delta_{j1} - 2\frac{k_1 k_j}{k^2}\right)\hat{R}_{i2}(\boldsymbol{k},t)\right] \\
&\quad + \frac{2\pi^2}{k^2}\left[T(k,t) + \varphi^{RTI}(k,t)E(k,t)\right]P_{ij}(\boldsymbol{k}),
\end{aligned} \tag{9.63}$$

up to a strange factor $1/(8\pi^2)$ in the definitions of E and T versus the definitions used in the rest of the book, where $T(k,t)$ is closed by isotropic EDQNM, see Sect. 4.8.7. The relaxation coefficient used to model return-to-isotropy effects due to pressure effects is given by[4]

$$\varphi^{RTI}(k,t) = \frac{1}{5\pi}\int_0^{+\infty} p^2 dp \int_0^{\pi} \theta_{kpq}\frac{k^4 E(p,t)E(q,t)}{p^2 q^2 E(k,t)}\left(1 - \frac{(\boldsymbol{k}\cdot\boldsymbol{q})^2}{k^2 q^2}\right)\sin\theta_p d\theta_p. \tag{9.64}$$

The expression for the characteristic time θ_{kpq} is the same as for isotropic EDQNM, see Sect. 4.8.7. In the inertial range, it is expected that $\varphi(k,t) = 2\eta(k,t) \sim k^{2/3}\varepsilon^{2/3}$. The formal explicit solution to the previous equation is found as in the integral form of the Craya equation in Eq. (2.116) with mean-flow Lagrangian approach already described for modified RDT. It appears as the sum of a damped RDT solution and a fully nonlinear contribution:

$$\begin{aligned}
\hat{R}_{ij}(\boldsymbol{k},t) &= \hat{R}_{ij}^{RDT}(\boldsymbol{k},t)\exp\left(-\int_0^t \varphi(k(t'),t-t')dt'\right) \\
&\quad + \frac{2\pi^2}{k^2}\int_0^t A_{ij}(\boldsymbol{k},t")\left[T(k(t"),t-t") + \varphi(k(t"),t-t")E(k(t"),t-t")\right] \\
&\quad \times \exp\left(-\int_0^{t"} dt'\left[\nu k^2(t') + \varphi(k(t'),t-t')\right)\right)dt".
\end{aligned} \tag{9.65}$$

The expressions of the dimensionless coefficients $A_{ij}(\boldsymbol{k},t")$ are very cumbersome and will therefore not be reported here for the sake of brevity. The full equations were never solved numerically in the original paper, because of the very complex

[4]Confusing notations in the original paper have been corrected here, as far as possible; the EDQNM-like integral uses a polar-spherical system of coordinates for $\boldsymbol{p}$ with polar axis $\boldsymbol{k}$. Formulation in terms of the bipolar system of coordinates (as in Chap. 4) is easily recovered from

$$\iiint (...)d^3\boldsymbol{p} = 2\pi\int_0^{\infty} p^2 dp\int_0^{\pi}(...)sin\theta_p d\theta_p = 2\pi\iint_{\Delta_k}\frac{pq}{k}(...)dpdq.$$

computation of the sole EDQNM equations for $T(k,t)$ and $\varphi^{RDT}(k,t)$. Assuming simplified given forms of these terms, however, numerical integration yields a satisfactory agreement with existing DNS and experimental results (within 15% errors about Reynolds stresses and anisotropy). It is observed to recover the existence of a regime with exponential growth of kinetic energy Since the full solution appears as a pretty complex ones, it dramatically simplifies looking at large wave number asymptotics, i.e. inertial range scales:

$$\hat{R}_{ij}(\boldsymbol{k},t) = \hat{R}_{ij}^{(iso)}(\boldsymbol{k},t) - \frac{2S\pi^2}{k^2}\left[\left(\delta_{j1} - 2\frac{k_1k_j}{k^2}\right)P_{i2}(\boldsymbol{k}) + \left(\delta_{i1} - 2\frac{k_ik_1}{k^2}\right)P_{j2}(\boldsymbol{k})\right]\frac{E(k,t)}{2\nu k^2 + \varphi(k,t)}. \tag{9.66}$$

The effect of the mean shear appears as a perturbation of the isotropic solution $\hat{R}_{ij}^{(iso)}(\boldsymbol{k},t)$. The predicted inertial range spectrum for the extra-diagonal term obtained via spherical integration is

$$\varphi_{12}(k,t) = -\frac{4}{15}S\frac{E(k,t)}{2\nu k^2 + \varphi(k,t)} \simeq -\frac{1}{2}S\varepsilon^{1/3}(t)k^{-7/3}, \tag{9.67}$$

in agreement with EDQNM and DNS results, where the molecular viscous term νk^2 has been neglected and the following approximation have been made: $E(k,t) = 1.5\varepsilon^{2/3}(t)k^{-5/3}$ and $\varphi(k,t) = 0.8\varepsilon^{1/3}(t)k^{2/3}$.

9.6.2 Models for Space-Time Correlations

9.6.2.1 Elliptic Model for Space-Time Longitudinal Correlation

The Elliptic model discussed in Sect. 4.3.5 can be extended to shear flows (Zhao and He 2009). Restricting the analysis to the longitudinal correlation function computed along the direction of the mean velocity, i.e. $R(r,\tau) = \overline{u(\boldsymbol{x},t)u(\boldsymbol{x}+r\boldsymbol{e}_x,t+\tau)}$ in the present case in which the mean flow is given by $\bar{\boldsymbol{u}} = Sy\boldsymbol{e}_x$, the second-order expansion (4.96) still holds, but the expression of the non-zero coefficients need to be adapted.

These new expressions are found inserting the full Navier–Stokes equations in the definition of the coefficients[5] and assuming that higher-order statistics are nearly isotropic, i.e. coefficients will be evaluated considering isotropic expressions for the spectral tensor $\hat{R}_{ij}(\boldsymbol{k})$. Such an approximation can be understood as a weak anisotropy

[5] A similar procedure is used in Kaneda (1993), Kaneda et al. (1999) to compute coefficients of the Taylor-series expansion of both Lagrangian and Eulerian velocity correlations.

restriction at all scales, or a small scale analysis with arbitrary anisotropy at large scales.

One has

$$\begin{aligned}\frac{\partial^2 R}{\partial r^2}(0,0) &= \overline{u(\boldsymbol{x},t)\frac{\partial^2 u}{\partial x \partial x}(\boldsymbol{x},t)} = -\overline{\frac{\partial u}{\partial x}(\boldsymbol{x},t)\frac{\partial u}{\partial x}(\boldsymbol{x},t)} \\ &= -\int k_1^2 \hat{R}_{11}(\boldsymbol{k},t)d^3\boldsymbol{k} \\ &= -\frac{2}{3}\int_0^{+\infty} k^2 E(k)dk, \end{aligned} \tag{9.68}$$

which is identical to the expression found in the isotropic case. The mixed derivative term leads to

$$\begin{aligned}\frac{\partial^2 R}{\partial r \partial t}(0,0) &= \overline{u(\boldsymbol{x},t)\frac{\partial^2 u}{\partial x \partial t}(\boldsymbol{x},t)} = -\overline{\frac{\partial u}{\partial x}(\boldsymbol{x},t)\frac{\partial u}{\partial t}(\boldsymbol{x},t)} \\ &= \frac{2}{3}\bar{u}\int_0^{+\infty} k^2 E(k)dk + \imath S \int \left(\delta_{i1} - 2\frac{k_i k_1}{k^2}\right) k_1^2 \hat{R}_{1i}(\boldsymbol{k},t)d^3\boldsymbol{k} \\ &= \frac{2}{3}\bar{u}\int_0^{+\infty} k^2 E(k)dk \end{aligned} \tag{9.69}$$

and

$$\begin{aligned}\frac{\partial^2 R}{\partial t \partial t}(0,0) &= \overline{u(\boldsymbol{x},t)\frac{\partial^2 u}{\partial t \partial t}(\boldsymbol{x},t)} = -\overline{\frac{\partial u}{\partial t}(\boldsymbol{x},t)\frac{\partial u}{\partial t}(\boldsymbol{x},t)} \\ &= -\frac{2}{3}\bar{u}^2\int_0^{+\infty} k^2 E(k)dk - \frac{2}{3}S^2\int_0^{+\infty} E(k)dk - \frac{2}{3}v_0^2\int_0^{+\infty} k^2 E(k)dk, \end{aligned} \tag{9.70}$$

where $v_0^2 = 2\int_0^k E(k)dk$ is the energy of the large scales responsible for the random sweeping phenomenon.

Substitution into the Elliptic model relation

$$R(r,\tau) = R\left(\sqrt{(r - U_c\tau)^2 + V_c^2\tau^2}, 0\right) \tag{9.71}$$

makes it possible to identify the convection velocity U_c and the diffusion velocity V_c:

$$U_c = \bar{u}, \quad V_c^2 = S^2\lambda^2 + v_0^2, \tag{9.72}$$

where λ is the Taylor microscale. Looking at the model, it appears that the main effect of the shear is to increase the diffusion velocity. The Elliptic model has been reported to yield accurate results in a wide class of free shear flows and wall bounded flows at steady equilibrium state. An estimate for the wave-number longitudinal frequency

spectrum is obtained inserting this new expression for V_c into Eq. (4.94), leading to an y-dependent expression:

$$E(\boldsymbol{k},\omega,y)=\frac{E(\boldsymbol{k})}{\sqrt{2\pi k^2 V_c^2}}\exp\left(-\frac{(\omega-\boldsymbol{k}\cdot\bar{u}(y)\boldsymbol{e}_x)^2}{2k^2V_c^2}\right). \tag{9.73}$$

Such an expression has recently been proposed for turbulent boundary layers, e.g. Wilczek et al. (2015).

It is worth pointing out that these models are a priori well suited for turbulent shear flows once an equilibrium steady state has been reached. There relevance to described the unsteady development of homogeneous shear turbulence has not been definitely assessed up to now.

9.6.2.2 A Model for the Two-Point Two-Time Spectral Tensor

A model for the full two-point two-time spectral tensor was proposed by De Mare and Mann (2016), by modifying (9.60) to account for random sweeping by large scales. The resulting model is:

$$\hat{R}_{ij}^{eq}(\boldsymbol{k},\tau)=\int_{-\infty}^{t}e^{-\frac{1}{2}\Theta^2(\boldsymbol{k},\tau)}G_{im}(\boldsymbol{K},t-t_0)G_{jn}(\boldsymbol{K},t-t_0)\frac{1}{\tau(K)}\hat{R}_{mn}(\boldsymbol{K})dt_0. \tag{9.74}$$

The exponential form of the random sweeping term arise from the hypothesis that this mechanisms can be considered as a Gaussian process, as for the Linear Random Advection model and the resulting Elliptic model. The key idea here is to model an eddy at wave number k as a sphere of radius $R_k\sim 1/k$ in which the fluid has a uniform velocity $\boldsymbol{u}^{R_k}(\boldsymbol{x},t)$ defined as the mean value of velocity within this sphere. The standard deviation of the velocity of the eddies with radius R_k in the direction $\boldsymbol{k}$ is therefore

$$\sigma(\boldsymbol{k})=\left(\overline{\frac{k_ik_j}{k^2}u_i^{R_k}u_i^{R_k}}\right)^{1/2} \tag{9.75}$$

and the resulting random sweeping effect is characterized in the Lagrangian framework by

$$\Theta(\boldsymbol{k},\tau)=\int_t^{t+\tau}\sigma(\boldsymbol{k}(t'))k(t')dt', \tag{9.76}$$

which is assumed to obey a Normal distribution.

9.7 Pressure Field: Theory and Models

9.7.1 Exact Expression for Fluctuating Pressure and Its Two-Point Correlations

The pressure field associated to homogeneous sheared turbulence can be analyzed extending the analysis displayed in Sect. 4.9 for the isotropic case. Removing the mean flow contribution, the Poisson equation for the fluctuating pressure is

$$\frac{1}{\rho}\nabla^2 p' = -\frac{\partial U_i}{\partial x_j}\frac{\partial u_j}{\partial x_i} - \frac{\partial u_i}{\partial x_i}\frac{\partial u_j}{\partial x_j}, \tag{9.77}$$

where $\boldsymbol{u}$ and $\boldsymbol{U}$ denote the fluctuating and the mean velocity field, respectively, for the sake of simplicity. The solution is expressed as

$$\begin{aligned}\frac{1}{\rho}p'(\boldsymbol{x},t) = &-\int\left(\frac{\partial U_i}{\partial y_j}\frac{\partial u_j}{\partial y_i}+\frac{\partial U_j}{\partial y_i}\frac{\partial u_i}{\partial y_j}\right)G(\boldsymbol{x},\boldsymbol{y})d^3\boldsymbol{y}\\ &-\int\frac{\partial^2}{\partial y_i\partial y_j}\left(u_iu_j-\overline{u_iu_j}\right)G(\boldsymbol{x},\boldsymbol{y})d^3\boldsymbol{y},\end{aligned} \tag{9.78}$$

where $G(\boldsymbol{x},\boldsymbol{y}) = 1/4\pi|\boldsymbol{x}-\boldsymbol{y}|$ denotes the three-dimensional Green function associated to the Poisson equation in unbounded domains. The first term in the right hand side is related to the interaction between the mean flow gradient (which vanishes in the isotropic case) while the second one arise from self-interactions between velocity fluctuations. The two-point single-time pressure correlation $R_{pp}(\boldsymbol{x},\boldsymbol{x}') = \overline{p'(\boldsymbol{x},t)\,p'(\boldsymbol{x}',t)}$ in a general free shear flow is given by

$$\begin{aligned}\frac{1}{\rho^2}R_{pp}(\boldsymbol{x},\boldsymbol{x}') = &\iint\left(\frac{\partial U_i}{\partial y_j}\frac{\partial U_l'}{\partial y_m'}\frac{\partial^2\overline{u_ju_m'}}{\partial y_i\partial y_l'}+\frac{\partial U_i}{\partial y_j}\frac{\partial U_m'}{\partial y_l'}\frac{\partial^2\overline{u_ju_l'}}{\partial y_i\partial y_m'}+\frac{\partial U_j}{\partial y_i}\frac{\partial U_l'}{\partial y_m'}\frac{\partial^2\overline{u_iu_m'}}{\partial y_j\partial y_l'}\right.\\ &\left.+\frac{\partial U_j}{\partial y_i}\frac{\partial U_m'}{\partial y_l'}\frac{\partial^2\overline{u_iu_l'}}{\partial y_j\partial y_m'}\right)G(\boldsymbol{x},\boldsymbol{y})G(\boldsymbol{x}',\boldsymbol{y}')d^3\boldsymbol{y}d^3\boldsymbol{y}'\\ &+\iint\left(\frac{\partial U_i}{\partial y_j}\frac{\partial^3\overline{u_ju_l'u_m'}}{\partial y_i\partial y_l'\partial y_m'}+\frac{\partial U_j}{\partial y_i}\frac{\partial^3\overline{u_iu_l'u_m'}}{\partial y_j\partial y_l'\partial y_m'}\right.\\ &\left.+\frac{\partial U_l'}{\partial y_m'}\frac{\partial^3\overline{u_m'u_iu_j}}{\partial y_l'\partial y_i\partial y_j}+\frac{\partial U_m'}{\partial y_l'}\frac{\partial^3\overline{u_l'u_iu_j}}{\partial y_m'\partial y_i\partial y_j}\right)G(\boldsymbol{x},\boldsymbol{y})G(\boldsymbol{x}',\boldsymbol{y}')d^3\boldsymbol{y}d^3\boldsymbol{y}'\\ &+\iint\left(\frac{\partial^4\overline{u_iu_ju_l'u_m'}}{\partial y_i\partial y_j\partial y_l'\partial y_m'}-\frac{\partial^2\overline{u_iu_j}}{\partial y_i\partial y_j}\frac{\partial^2\overline{u_l'u_m'}}{\partial y_l'\partial y_m'}\right)G(\boldsymbol{x},\boldsymbol{y})G(\boldsymbol{x}',\boldsymbol{y}')d^3\boldsymbol{y}d^3\boldsymbol{y}',\end{aligned} \tag{9.79}$$

where primed quantities are evaluated at position $\boldsymbol{y}'$. The first two terms in the right-hand side are related to second- and third-moment interactions between the mean shear and the fluctuating field, while the third arise from non-linear self-interactions of the fluctuating field.

In the case of a constant-mean-shear homogeneous turbulence with $\boldsymbol{U} = (Sy, 0, 0)$, and taking $\boldsymbol{y}' = \boldsymbol{y} + \boldsymbol{r}$ the above expression simplifies as

$$\begin{aligned}\frac{1}{\rho^2} R_{pp}(\boldsymbol{\xi}) = 4S^2 \iint \frac{\partial^2 R_{22}(\boldsymbol{r})}{\partial r_1^2} G(\boldsymbol{x}, \boldsymbol{y}) G(\boldsymbol{x}+\boldsymbol{\xi}, \boldsymbol{y}+\boldsymbol{r}) d^3\boldsymbol{y} d^3\boldsymbol{r} \\ + 2S \iint \frac{\partial^3}{\partial r_1 \partial r_l \partial r_m} \left(R_{2lm}(-\boldsymbol{r}) - R_{2lm}(\boldsymbol{r})\right) G(\boldsymbol{x}, \boldsymbol{y}) G(\boldsymbol{x}+\boldsymbol{\xi}, \boldsymbol{y}+\boldsymbol{r}) d^3\boldsymbol{y} d^3\boldsymbol{r} \\ + \iint \frac{\partial^4 R_{ij,lm}(\boldsymbol{r})}{\partial r_i \partial r_j \partial r_l \partial r_m} G(\boldsymbol{x}, \boldsymbol{y}) G(\boldsymbol{x}+\boldsymbol{\xi}, \boldsymbol{y}+\boldsymbol{r}) d^3\boldsymbol{y} d^3\boldsymbol{r}, \end{aligned} \tag{9.80}$$

where the following notations have been used for the velocity correlations:

$$R_{ij}(\boldsymbol{r}) = \overline{u_i(\boldsymbol{y}) u_j(\boldsymbol{y}+\boldsymbol{r})}, \; R_{ilm}(\boldsymbol{r}) = \overline{u_i(\boldsymbol{y}) u_l(\boldsymbol{y}+\boldsymbol{r}) u_m(\boldsymbol{y}+\boldsymbol{r})}$$

along with

$$R_{ij,lm}(\boldsymbol{r}) = \overline{u_i(\boldsymbol{y}) u_j(\boldsymbol{y}) u_l(\boldsymbol{y}+\boldsymbol{r}) u_m(\boldsymbol{y}+\boldsymbol{r})} - \overline{u_i(\boldsymbol{y}) u_j(\boldsymbol{y})} \; \overline{u_l(\boldsymbol{y}+\boldsymbol{r}) u_m(\boldsymbol{y}+\boldsymbol{r})}.$$

The associated exact expression for the pressure spectrum $E_{pp}(\boldsymbol{k}) = \frac{1}{(2\pi)^3} \iiint \exp(\imath \boldsymbol{k} \cdot \boldsymbol{r}) R_{pp}(\boldsymbol{r}) d^3\boldsymbol{r}$ is

$$\begin{aligned}\frac{1}{\rho^2} E_{pp}(\boldsymbol{k}) = S^2 \left(\frac{k_1^2}{k^4} \hat{R}_{22}(\boldsymbol{k})\right) + \frac{S}{2} \imath \frac{k_1 k_l k_m}{k^4} \left(\hat{R}^*_{2lm}(\boldsymbol{k}) - \hat{R}_{2lm}(\boldsymbol{k})\right) \\ + \frac{k_i k_j k_l k_m}{k^4} \hat{R}_{ij,lm}(\boldsymbol{k}), \end{aligned} \tag{9.81}$$

where the hat symbol denotes the Fourier transform. The term on the right hand side are commonly referred to as the second-moment turbulence-shear interaction, the third moment turbulence-shear interaction and the turbulence-turbulence interaction, respectively.

The three-dimensional spectrum is then obtained by integrating $E_{pp}(\boldsymbol{k})$ over sphere with radius k, yielding

$$E_{pp}(k) = E^{s2}_{pp}(k) + E^{s3}_{pp}(k) + E^{t}_{pp}(k), \tag{9.82}$$

where the three components are related to the three terms in Eq. (9.81).

9.7.2 Inertial Range Scalings and Models

The three components of $E_{pp}(k)$ can be easily estimated using dimensional analysis, keeping S, ε and k as analysis parameters, yielding:

$$\frac{E_{pp}^{s2}(k)}{\rho^2} \propto S^2\varepsilon^{2/3}k^{-11/3}, \quad \frac{E_{pp}^{s3}(k)}{\rho^2} \propto S\varepsilon k^{-3}, \quad \frac{E_{pp}^{t}(k)}{\rho^2} \propto \varepsilon^{4/3}k^{-7/3}. \tag{9.83}$$

The last expression is identical to the one found for isotropic turbulence, see Sect. 4.9.2. These expressions are assumed to be valid within the inertial range, if the Reynolds number is large enough to allow for the existence of such a range.

The components of the pressure spectrum can be further analyzed assuming that, in the inertial range, the kinetic energy spectrum is almost isotropic. Assuming that the third-moment shear-turbulence interaction term is negligible,[6] the shear-turbulence interaction simplifies as

$$S^2\left(\frac{k_1^2}{k^4}\hat{R}_{22}(\boldsymbol{k})\right) = \frac{1}{\pi}S^2\frac{k_1^2}{k^6}E(k)\left(1-\frac{k_2^2}{k^2}\right) \tag{9.84}$$

yielding

$$E_{pp}^{s2}(k) = \rho^2\frac{16}{15}S^2\frac{E(k)}{k^2}, \quad E_{pp}^{s3}(k) = 0. \tag{9.85}$$

The turbulence-turbulence term expression is the same as in the isotropic case. Therefore, invoking the Quasi-Normal hypothesis the evaluate the fourth-order moment terms, one obtains:

$$\frac{k_ik_jk_lk_m}{k^4}\hat{R}_{ij,lm}(\boldsymbol{k}) = \frac{1}{8\pi^2}\int E(\boldsymbol{k}')E(\boldsymbol{k}-\boldsymbol{k}')\frac{\sin^4\phi}{|\boldsymbol{k}-\boldsymbol{k}'|^4}d^3\boldsymbol{k}', \tag{9.86}$$

where ϕ is the angle between $\boldsymbol{k}$ and $\boldsymbol{k}'$, along with $E_{pp}^{t}(k) \propto \rho^2\varepsilon^{4/3}k^{-7/3}$ by spherical integration.

The scalings for the amplitude of each component was evaluated in George et al. (1984) via analytical integration using a model spectrum for $E(k)$. The main results is that the amplitude of the turbulence-shear terms scales as $S^2\ell^3\mathcal{K}$, where $\ell = \mathcal{K}^{3/2}/\varepsilon$, while the turbulence-turbulence term amplitude is proportional to $\mathcal{K}^2\ell$. The net pressure spectrum results from the combination of the three components, whose relative weights depends on both the wave number and the ratio $S\ell/\sqrt{\mathcal{K}}$. The turbulence-

[6] Such a simplification can be obtained in several ways. First, assuming that velocity fluctuations are nearly Gaussian, third-order moments are identically null. Second, looking at the structure of this term, it is seen that the difference between the two third-moment terms vanishes in isotropic turbulence. Then, assuming that we are dealing with weak departure from isotropy in the inertial range, this term can be assumed to be small in front of the other ones.

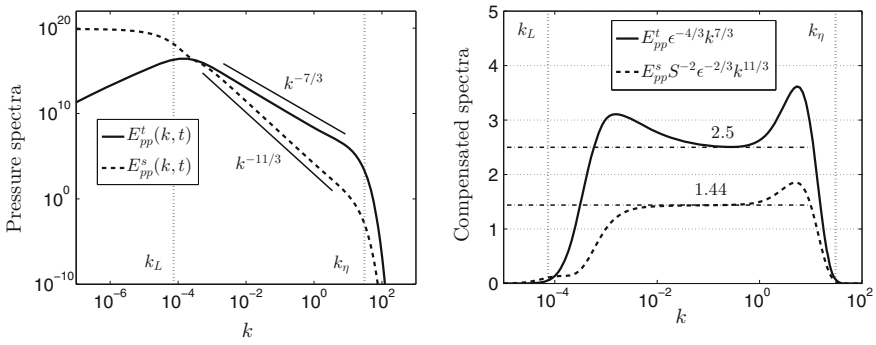

Fig. 9.14 Components of the pressure spectrum in homogeneous shear turbulence computed via anisotropic EDQNM. Adapted from Briard et al. (2017). Courtesy of A. Briard and T. Gomez. Left: spectra in log-log scales; Right: compensated spectra

shear term is expected to dominate at large scales, i.e. at largest scales in the inertial range, while the turbulence-turbulence term will dominate at smaller scales. The transition between the two solutions takes place at a wave-number which depends on the ratio mentioned above.

Both $E^{s2}_{pp}(k)$ and $E^{t}_{pp}(k)$ can be computed thanks to the anisotropic EDQNM model developed by Mons et al. (2016) (see Sect. 17.9 for details). The expression for the isotropic part associated to self-interactions of turbulent velocity fluctuations is exactly the same as for the pure isotropic case. It is therefore given by Eq. (4.347). For the shear-turbulence component, one obtains (Briard et al. 2017) using the anisotropic decomposition of the spectral tensor introduced in Sect. 2.6.1 the following expression:

$$E^{s2}_{pp}(k) = 4\frac{E(k)}{k^2}\left(\frac{1}{5}A^+_{ij}A^+_{ij} + \frac{1}{3}A^-_{ij}A^-_{ij} - H^{(\mathrm{dir})}_{il}(k)\Big[\frac{6}{7}A^+_{ij}A^+_{jl} + 2A^-_{ij}(A^-_{lj} + 2A^+_{lj})\Big]\right) + 8\frac{E(k)}{k^2}H^{(\mathrm{pol})}_{il}(k)\Big[\frac{3}{7}A^+_{ij}A^+_{lj} + A^-_{ij}\left(A^-_{lj} - \frac{2}{3}A^+_{lj}\right)\Big], \tag{9.87}$$

where $\mathbf{A}^+$ and $\mathbf{A}^-$ denote the symmetric and anti-symmetric part of the mean flow velocity gradient tensor $\mathbf{A}$, respectively. The reader is referred to Sect. 2.6.1 for exact definitions components of $\hat{R}(\boldsymbol{k})$, $H^{(\mathrm{dir})}_{ij}(k)$ and $H^{(\mathrm{pol})}_{ij}(k)$. Results are displayed in Fig. 9.14. It is observed that George's theoretical predictions dealing are perfectly recovered.

9.7.3 Physical Space Analysis

Scaling laws for both pressure fluctuation variance and fluctuating pressure gradient variance can be obtained from previous results.

Pressure variance can be split into two contributions:

$$\overline{p'^2} = \overline{p_s'^2} + \overline{p_t'^2} = \int_0^{+\infty} (E_{pp}^{s2}(k) + E_{pp}^{s3}(k))dk + \int_0^{+\infty} E_{pp}^{t}(k)dk, \tag{9.88}$$

where $\overline{p_s'^2}$ and $\overline{p_t'^2}$ are the shear-turbulence and the turbulence-turbulence parts, respectively. Direct integration using the von Karman model for $E(k)$ leads to George et al. (1984)

$$\overline{p_s'^2} = \frac{1}{3}\rho^2 S^2 \ell^2 \mathcal{K}, \quad \overline{p_s'^2} = 0.42\rho^2 \mathcal{K}^2. \tag{9.89}$$

A similar work leads to

$$\overline{(\nabla p')^2} = \overline{(\nabla p')_s^2} + \overline{(\nabla p')_t^2} = \int_0^{+\infty} k^2 (E_{pp}^{s2}(k) + E_{pp}^{s3}(k))dk + \int_0^{+\infty} k^2 E_{pp}^{t}(k)dk \tag{9.90}$$

and, for high-Reynolds number flows,

$$\overline{(\nabla p')_s^2} = \frac{8}{5}\rho^2 S^2 \mathcal{K}, \quad \overline{(\nabla p')_t^2} = 214\nu \frac{\mathcal{K}^{3/2}}{\lambda^3}\left(1 - \frac{16.94}{Re_\lambda}\right), \tag{9.91}$$

where λ is the Taylor microscale.

It is worth noting that all models presented in this section are still to be validated in the case of strict homogeneity. Satisfactory qualitative agreement has been observed in free shear flows such as jets and mixing layers.

9.8 Vortical Structures Dynamics in Homogeneous Shear Turbulence

The statistical behavior of homogeneous shear turbulence described above can be explained as being the consequence of the growth and collapse of vortical structures. It is worth noting here that these structures govern the dynamics of the flow, while it has been seen in Sect. 4.10 that their influence on the dynamics of isotropic turbulence is weak.

Using numerical simulations, Kida and Tanaka (1994) identify the following scenario for the departure from isotropy:

(i) Uncoherent vorticity blobs initially present in isotropic turbulence are transformed into coherent elongated vortex tube by the imposed mean shear via the vortex stretching process. This linear mechanism, well recovered by the Rapid Distortion Theory, yields the formation of *longitudinal vortex tubes*. These structures are aligned with the directions of maximal extension of the mean shear flow (i.e. they are inclined at 45°–225° to the downstream direction). The distance between the longitudinal vortex tubes is determined by the initial field and has not been observed to depend on the mean shear rate.

(ii) Longitudinal vortex tubes experience the mean shear, and are inclined more and more toward the streamwise direction with further increase in their vorticity. This two trends are easily understood considering a rectilinear vortex filament which makes an angle θ with the streamwise axis and with axial vorticity Ω. Neglecting viscous effects and assuming that the vortex filament remains rectilinear, one obtains (Brasseur and Wang 1992)

$$\frac{d\Omega}{dt} = \frac{1}{2} S\Omega \sin(2\theta) \tag{9.92}$$

$$\frac{d\theta}{dt} = -S \sin^2(\theta). \tag{9.93}$$

Due to non-linear effects, vorticity vectors inside the longitudinal vortex tubes are less inclined (by about 10°) than the vortex tubes themselves, leading to the *vortex wrapping phenomenon*.

(iii) Longitudinal vortex tubes induce a swirling motion which leads to the formation of *vortex sheets* with a spanwise component. These sheets are generated in planes nearly parallel both to the longitudinal vortex tube axes and to the spanwise axis.

(iv) The vortex sheets are linearly unstable and roll up through the Kelvin–Helmholtz instability, leading to the growth of vortex tubes in the spanwise direction. These new vortex tubes are usually referred to as *lateral vortex tubes*.

(v) Lateral vortex tubes are subject to the mean shear effect in the presence of fluctuations, yielding the generation of *hairpin-like vortices*, whose legs correspond to streamwise vortices.

(vi) All vortical structures present in the flow interact and are subjected to the mean shear, and break down into a disordered field with weak enstrophy.

(vii) The continuous action of the mean shear leads to the occurence of a large *oblique stripe structure*, which inclines at $10° - 15°$ with the downstream direction. The growth of this structure leads to a very large decrease of vertical velocity and vorticity fluctuations.

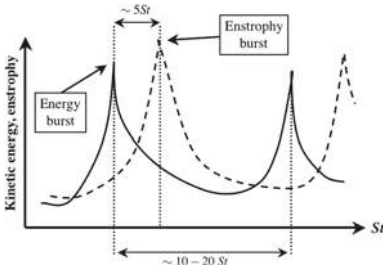

Fig. 9.15 Schematic view of the time histories of global turbulent kinetic energy and enstrophy in DNS of homogeneous shear turbulence. One cycle of the self-sustaining process is shown

9.9 Self-sustaining Turbulent Cycle in Quasi-homogeneous Sheared Turbulence

The asymptotic long-time behavior of homogeneous shear turbulence discussed above in this chapter can not be sustained for arbitrary long-time, since turbulent kinetic energy and characteristic length scales must remain bounded. The very-large St behavior of homogeneous sheared turbulence is usually not observed in wind-tunnel experiments, due to experimental set-up characteristics.

Some calculations in tri-periodic box were performed in successive phases: In the first phase, some elongated structures reach the size of the box, and therefore collapse; after their collapse, a new phase of growth takes place, and so on. Accordingly, there is violation of statistical homogeneity in this process, in which the finite size of the box is essential. A cyclic behavior of global turbulent kinetic energy and enstrophy associated to a kind of unsteady equilibrium solution has been observed in such numerical simulations at very large St (typically for $St \geq 30$) (Pumir 1996; Gualtieri et al. 2002). This turbulent cycle involves the existence of a *self-sustaining turbulent mechanism* (also referred to as *self-regenerating* or *autonomous* cycle, or *self-sustaining process*). Typical evolution of global turbulent kinetic energy and enstrophy are displayed in Fig. 9.15. A typical cycle is composed of a spike of energy followed by a spike of enstrophy. These global quantities are observed to exhibit very large relative fluctuations within 40–50%. The period of the cycle is observed to be of the order of 10–20 S^{-1}.

As stated by Pumir (1996), let us first note that an additional arbitrary lenghthscale must be prescribed in the simulation to allow for the existence of an equilibrium solution.[7] From Eq. (9.7), it is seen that a steady statistical equilibrium is reached if

$$-S\overline{u_1' u_2'} = \varepsilon. \tag{9.94}$$

Now using the usual scaling laws $\varepsilon \propto \mathcal{K}^{3/2}/L$ and $\overline{u_1' u_2'} \propto \sqrt{\mathcal{K}}$, where L is a characteristic lengthscale, one sees that an equilibrium is possible if and only if $\mathcal{K} \propto SL$, leading to the constraint that L must be finite. In very-large St simulations,

[7] It is recalled here that an external length scale, other than those related to the fluctuating flow statistics, is missing in strictly homogeneous turbulence.

the lengthscale L is imposed by the size of the computational domain, which is always finite and represent an upper bound for the large-scale size. But is worth noting that in such simulations large-scales interact with themselves via the periodic boundary conditions, resulting in a breakdown of ergodicity.

Numerical simulations have shown that the kinetic energy production is mainly governed by the interaction of the mean shear with the spanwise mode $\boldsymbol{k}_S = (0, 0, \pm 1)$. The energy extracted by this mode from the mean flow is then transferred to other modes by the non-linear kinetic energy cascade process, the frequency of the cycle being determined by the dynamical balance between these two processes. Due to the incompressibility constraint, the associated velocity field is $\hat{\boldsymbol{u}}(\boldsymbol{k}_S) = (\hat{u}, \hat{v}, 0)$. The linear interaction mechanism is described by the following system:

$$\frac{d\hat{u}}{dt} = -S\hat{v} - \nu k_S^2 \hat{u} \tag{9.95}$$

$$\frac{d\hat{v}}{dt} = -\nu k_S^2 \hat{v}. \tag{9.96}$$

The vertical component $\hat{v}$ is monotonically damped by the viscous effects, while the streamwise component $\hat{u}$ is amplified if

$$S\left(\mathrm{Re}(\hat{u})\mathrm{Re}(\hat{v}) + \mathrm{Im}(\hat{u})\mathrm{Im}(\hat{v})\right) < 0. \tag{9.97}$$

The corresponding physical scheme is the following: the growth of energy results from the one of streamwise velocity fluctuations, which is due to the advection of fluid blobs of high streamwise velocity toward regions of lower velocity by the normal

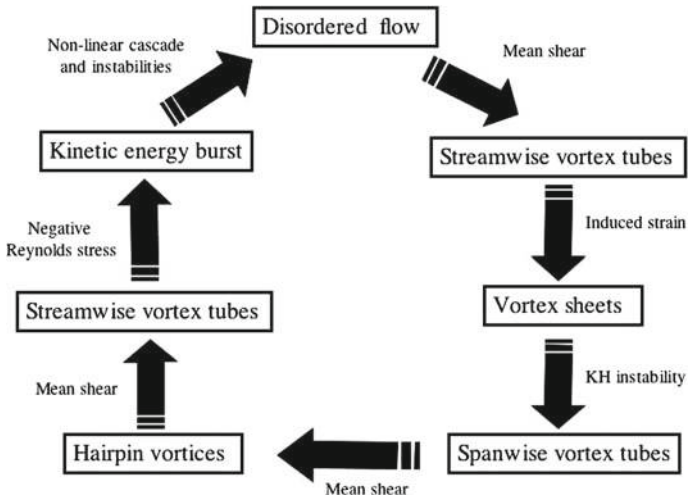

Fig. 9.16 Sketch of the self-sustaining turbulent cycle in homogeneous shear flows

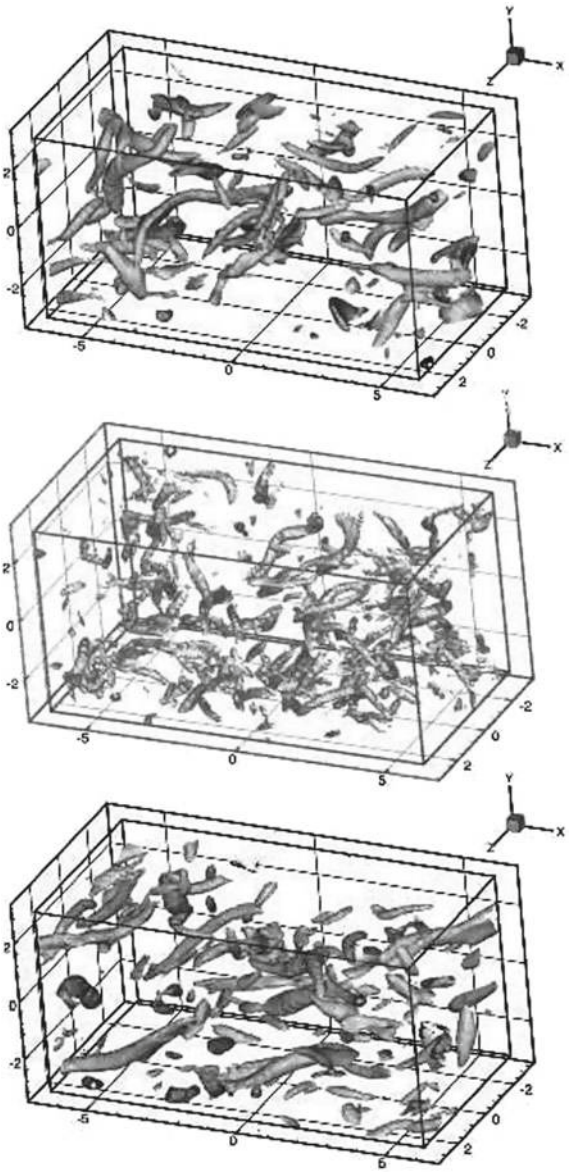

Fig. 9.17 Vortical structures at different stages of self-sustaining turbulent cycle in homogeneous shear flows. Top: during the kinetic energy growth phase; Middle: after the energy burst; Bottom: when kinetic energy reaches a minimum before a new burst. Reproduced from Gualtieri et al. (2002) with permission of AIP

velocity v. This scenario is reminiscent of the *ejection/sweep* mechanism observed in turbulent boundary layers.

The different phases of the self-sustaining cycle are fully compatible with the vortical structure dynamics observed by Kida and Tanaka (1994) and described in the previous section. The energy burst is observed to occur when the legs of the hairpin vortices (i.e. longitudinal vortex tubes) interact with large negative Reynolds

stresses, while the minimum of kinetic energy is observed at the beginning of the cycle when randomly distributed vorticity blobs experience the mean shear action. A sketch of the full cycle is displayed in Fig. 9.16. Typical vortical structures at different stages of the cycle are displayed in Fig. 9.17.

Recent studies keep using this *quasi*-homogeneous way of simulating bursts, e.g. Cardesa et al. (2015), Sekimoto et al. (2016). A less empirical approach could result from the explosive transient growth permitted by RDT solution, with its non-modal property related to time-dependent wave-vector, combined with regeneration mechanisms ensured by nonlinearity. The reader is referred to the discussion in Chap. 11, more precisely sections dealing with the seminal analysis by Chagelishvili et al. (2003) devoted to transient growth and bypass transition to turbulence in Keplerian disc (see also Orr 1909.)

9.10 Self-sustaining Processes in Non-homogeneous Sheared Turbulence: Exact Coherent States and Travelling Wave Solutions

The *self-sustaining process* (SSP) in homogeneous shear flows described in the preceding section has been identified in numerical simulations only. It existence seems to rely on a numerical trick, namely the possibility to enforce an upper bound for the turbulent integral scale via the use of periodic boundary conditions in the simulation. In these simulations, the length scale which is missing because of the homogeneity assumption is recovered defining the computational box. Nevertheless, previous results show that some self-sustaining processes may exist in turbulent shear flows. This phenomenon is found in the inner region of turbulent boundary layers, and modern analyses dealing with turbulence control and turbulent drag reduction in these flows rely on the SSP concept.

Because of the huge importance of shear flows in all fields of application, recent theoretical results dealing with self-sustaining processes in wall-bounded shear flows will be briefly surveyed in this section. The main goal here is to characterize the near-wall turbulence in terms of nonlinear exact solutions to incompressible Navier–Stokes equations for Couette, Poiseuille and Couette-Poiseuille flows. All these solutions look qualitatively similar: a wavy low-velocity streak flanked by staggered streamwise vortices of alternating signs. According to Jimenez and coworkers (2005), these solutions, which correspond to permanent stationary or travelling waves and to limit cycles in autonomous flows, can be classified into upper- and lower branch families. The upper branch family consists of weak streaks with strong streamwise vortices, while the lower branch solutions have much stronger streaks and weaker vortices.

The emphasis will be put on the theory proposed by Waleffe and coworkers (see Hamilton et al. 1995; Waleffe 1996, 2003 and references given therein), since it is fully consistent and closed from the theoretical point of view and that its results

correlate satisfactorily with wind tunnel experiments and numerical simulation. The main discrepancy with the self-sustaining turbulent cycle in homogeneous shear flows discussed in the previous section is that the SSP in non-homogeneous shear flows involve a local change in the mean flow due to a feedback of the fluctuating field. It is worth recalling here that such a feedback is by definition precluded in homogeneous turbulent flows.

The original purpose of Waleffe and coworkers was to explain the regeneration of turbulent structures observed in the near wall region in turbulent wall bounded flow. An important finding is that the results discussed below have been proved to hold for a large variety of shear flows: Couette flow, Poiseuille flow and the continuum of Couette–Poiseuille solutions. Since the theoretical analysis reveal that the SSP is not sensitive to the boundary conditions imposed on the fluctuations (either free-slip or no-slip conditions can be used), it can be conjectured that the main role of the solid boundary is to sustain a mean shear, and that similar SSP might develop in free shear flows.

Waleffe's SSP theory is essentially a weakly nonlinear theory of a three-dimensional process about a base shear flow that has an $O(1)$ spanwise modulation $U(y, z)$, but it is not weakly nonlinear about a one-dimensional laminar base flow $U(y)$. It relies on *exact traveling wave solutions* of the incompressible Navier–Stokes equations of the form $\boldsymbol{u}(\boldsymbol{x}, t) = \boldsymbol{u}(\boldsymbol{x} - ct\boldsymbol{e}_x, 0)$, where c and $\boldsymbol{e}_x$ are the constant wave velocity and the unit vector in the streamwise direction, respectively. The full velocity field, including the base shear flow, is decomposed via a Fourier transform in the streamwise direction, leading to

$$\boldsymbol{u}(\boldsymbol{x}, t) = \boldsymbol{u}_0(y, z) + \left(e^{\imath\alpha\zeta}\boldsymbol{u}_1(y, z) + c.c.\right) + \ldots \tag{9.98}$$

where $\boldsymbol{u}_0(y, z) = (u_0(y, z), v_0(y, z), w_0(y, z))$ is the base shear flow and $\zeta = x - ct$. The base shear flow can be decomposed as the sum of a one dimensional mean shear flow $\overline{u}(y)$ (defined as the streamwise velocity averaged over the periodic x and z directions) and streaky structures responsible for the modulation $\boldsymbol{u}_0(y, z) - \overline{u}(y)$. These streaky structures are assumed to represent elongated streamwise blobs of rapid and slow fluid observed in the near wall region of turbulent wall-bounded flows. They are modeled via streamwise rolls, which are longitudinal vortices with alternating streamwise vorticity sign and low $O(Re^{-1})$ amplitude. The SSP theory consists of three main steps (see Fig. 9.18):

(i) **Formation of the streaky flow**. The existence of weak streamwise rolls $(0, v_0(y, z), w_0(y, z))$ redistribute the streamwise momentum, leading to large spanwise fluctuations in the streamwise velocity, $(u_0(y, z), 0, 0)$. If the rolls are strong enough, an inflexional streamwise velocity profile can be generated.

(ii) **Instability of the streaky flow**. The existence of a locally inflexional streamwise velocity profile lead to wake-like instability in which a three-dimensional disturbance develops.

(iii) **Nonlinear feedback on the rolls**. The *streak eigenmode* $\left(e^{\imath\alpha\zeta}\boldsymbol{u}_1(y, z) + c.c.\right)$ is the first harmonic in the streamwise direction of the disturbance. Its quadratic

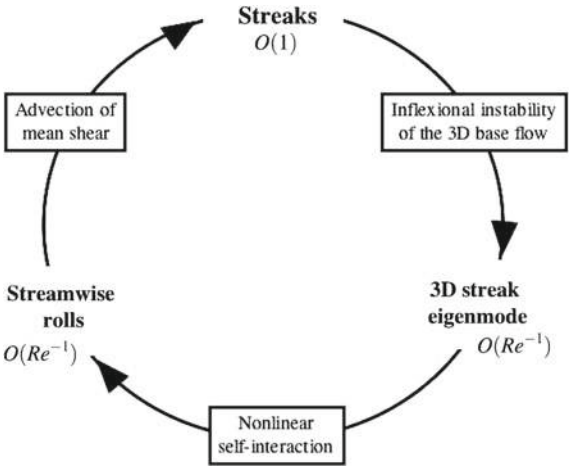

Fig. 9.18 Schematic representation of Waleffe's self-sustaining process (SSP) in non-homogeneous shear flows

self-interaction $\left(e^{2\imath\alpha\zeta}\boldsymbol{u}_1(y,z)\boldsymbol{u}_1(y,z)+\boldsymbol{u}_1^*(y,z)\boldsymbol{u}_1(y,z)+c.c.\right)$ generates a second harmonic $\left(e^{2\imath\alpha\zeta}\boldsymbol{u}_2(y,z)+c.c.\right)$. But, more importantly, the nonlinear self-interaction term $\boldsymbol{u}_1^*(y,z)\boldsymbol{u}_1(y,z)$ is observed to extract energy from the streak and to reenergize the original streamwise rolls, leading to the definition of a closed nonlinear feedback loop.

Therefore, the three necessary ingredients of the SSP are: streamwise rolls, streaks and streak eigenmode. An additional element is the mean shear, which provides the overall energy. It is worth noting that the streak instability extracts energy from the streaks, and then cannot directly sustain them. It sustains the rolls, which sustain the streaks. The destruction of one of these key elements would lead to a breakdown of the SSP, and therefore to a possible deep modification of turbulence, as done in several turbulent drag reduction strategies.

References

Brasseur, J.G., Wang, Q.: Structural evolution of intermittency and anisotropy at different scales analyzed using three-dimensional wavelet transforms. Phys. Fluids **4**, 2538–2554 (1992)

Brethouwer, G.: The effect of rotation on rapidly sheared homogeneous turbulence and passive scalar transport. Linear theory and direct numerical simulation. J. Fluid Mech. **542**, 305–342 (2005)

Briard, A., Gomez, T., Mons, V., Sagaut, P.: Decay and growth laws in homogeneous shear turbulence. J. Turbul. **17**(7), 699–726 (2016)

Briard, A., Iyer, M., Gomez, T.: Anisotropic spectral modeling for unstably stratified homogeneous turbulence. Phys. Rev. Fluids **2**, 044604 (2017)

Cambon, C.: Contribution to single and double point modelling of homogeneous turbulence, Annual Research Briefs, Stanford University and NASA Ames, Center for Turbulence Research (1990)

Cambon, C., Jeandel, D., Mathieu, M.: Spectral modelling of homogeneous non-isotropic turbulence. J. Fluid Mech. **104**, 247–262 (1981)
Cardesa, J.I., Vela-Martin, A., Dong, S., Jiménez, J.: The temporal evolution of the energy flux across scales in homogeneous turbulence. Phys. Fluids **27**, 111702 (2015)
Chagelishvili, G.D., Zahn, J.P., Tevzadze, A.G., Lominadze, J.G.: On hydrodynamic shear turbulence in Keplerian discs: via transient growth to bypass transition. A & A **402**, 401–407 (2003)
Clark, T.T., Zemach, C.: A spectral model applied to homogeneous turbulence. Phys. Fluids **7**, 1674–1694 (1995)
Corrsin, S.: On local isotropy in turbulent shear flow. NACA RM 58B11 (1958)
De Mare, M., Mann, J.: On the space-time structure of sheared turbulence. Boundary-Layer Meteorol. **160**, 453–474 (2016)
De Souza, F.A., Nguyen, V.D., Tavoularis, S.: The structure of highly sheared turbulence. J. Fluid Mech. **303**, 155–167 (1995)
Ferchichi, M., Tavoularis, S.: Reynolds number effects on the fine structure of uniformly sheared turbulence. Phys. Fluids **12**, 2942–2953 (2000)
Ferchichi, M., Tavoularis, S.: Scalar probability density function and fine structure in uniformly sheared turbulence. J. Fluid Mech. **461**, 155–182 (2002)
Garg, S., Warhaft, Z.: On the small scale structure of simple shear flow. Phys. Fluids **10**, 662–673 (1998)
George, W.K., Beuther, P.D., Arndt, R.E.A.: Pressure spectra in turbulent shear flows. J. Fluid Mech. **148**, 155–191 (1984)
George, W.K., Gibson, M.M.: The self-preservation of homogeneous shear flow turbulence. Exp. Fluids **13**, 229–238 (1992)
Gualtieri, P., Casciola, C.M., Benzi, R., Amati, G., Piva, R.: Scaling laws and intermittency in homogeneous shear flows. Phys. Fluids **14**, 583–596 (2002)
Hamilton, J.M., Kim, J., Waleffe, F.: Regeneration mechanisms of near-wall turbulence structures. J. Fluid Mech. **287**, 317–348 (1995)
Hanazaki, H., Hunt, J.C.R.: Linear processes in unsteady stably stratified shear turbulence with mean shear. J. Fluid Mech. **507**, 1–42 (2004)
Isaza, J.C., Collins, L.R.: On the asymptotic behaviour of large-scale turbulence in homogeneous shear flow. J. Fluid Mech. **367**, 213–239 (2009)
Ishihara, T., Yoshida, K., Kaneda, Y.: Anisotropic velocity correlation spectrum at small scale in a homogeneous turbulent shear flow. Phys. Rev. Lett. **88**(15), 154501 (2002)
Jimenez, J., Kawahara, G., Simens, M.P., Nagata, M., Shiba, M.: Characterization of near-wall turbulence in terms of equilibrium and bursting solutions. Phys. Fluids **17**, 015105 (2005)
Iida, O., Iwatsuki, M., Nagano, Y.: Vortical turbulence structure and transport mechanism in a homogeneous shear flow. Phys. Fluids **12**, 2895–2905 (2000)
Kaneda, Y.: Lagrangian and Eulerian time correlations in turbulence. Phys. Fluids A **5**(11), 2835–2845 (1993)
Kaneda, Y., Ishihara, T., Gotoh, K.: Taylor expansions in powers of time of Lagrangian and Eulerian two-point two-time velocity correlations in turbulence. Phys. Fluids **11**, 2154–2166 (1999)
Kida, S., Tanaka, M.: Dynamics of vortical structures in a homogeneous shear flow. J. Fluid Mech. **274**, 43–68 (1994)
Lee, M.J., Kim, J., Moin, P.: Structure of turbulence at high shear rate. J. Fluid Mech. **216**, 561–583 (1990)
Lumley, J.L.: Similarity and the turbulent energy spectrum. Phys. Fluids **10**(4), 855–858 (1967)
Mann, J.: The spatial structure of neutral surface-layer turbulence. J. Fluid Mech. **273**, 141–168 (1994)
Mons, V., Cambon, C., Sagaut, P.: A spectral model for homogeneous shear-driven anisotropic turbulence in terms of spherically averaged descriptors. J. Fluid Mech. **788**, 147–182 (2016)
Nazarenko, S.V., Zakharov, V.E.: The role of he convective modes and sheared variables in the Hamiltonian-dynamics of uniform-shear-flow perturbations. Phys. Lett. A **191**(5–6), 403–408 (1994)

Nickels, T.B., Marusic, I., Hafez, S., Chong, M.S.: Evidence of a k^{-1} law in a high-Reynolds-number turbulent boundary layer. Phys. Rev. Lett. **95**, 074501 (2005)
Orr, W.M.F.: The stability or instability of the steady motions of a perfect liquid. In: Proceedings of the Royal Irish Academy. Section A: Mathematical and Physical Sciences, vol. 27, pp. 9–68 (1909)
Piquet, J.: Turbulent flows. Models and Physics, 2nd edn. Springer, Berlin (2001)
Pumir, A.: Turbulence in homogeneous shear flows. Phys. Fluids **8**, 3112–3127 (1996)
Pumir, A., Shraiman, B.I.: Persistent small scale anisotropy in homogeneous shear flows. Phys. Rev. Lett. **75**(17), 3114–3117 (1995)
Rogallo, R.S.: Numerical experiments in homogeneous turbulence. Technical Memorandum NASA-TM-81315 (1981)
Rogers, M.: The structure of a passive scalar field with a uniform mean gradient in rapidly sheared homogeneous turbulent flow. Phys. Fluids A **3**(1), 144–154 (1991)
Rohr, J.J., Itsweire, E.C., Helland, K.N., Van Atta, C.W.: An investigation of the growth of turbulence in a uniform-mean-shear flow. J. Fluid Mech. **187**, 1–33 (1988)
Salhi, A., Cambon, C.: An analysis of rotating shear flow using linear theory and DNS and LES results. J. Fluid Mech. **347**, 171–195 (1997)
Salhi, A., Jacobitz, F., Schneider, K., Cambon, C.: Nonlinear dynamics and anisotropic structure of rotating sheared turbulence. Phys. Rev. E **89**, 013020 (2014)
Schumacher, J.: Relation between shear parameter and reynolds number in statistically stationary turbulent shear flows. Phys. Fluids **16**, 3094–3102 (2004)
Sekimoto, Dong, Jiménez.: DNS of statistically stationary and homogeneous shear turbulence and its relation to other shear flows. Phys. Fluids **28**, 035101 (2016)
Shirani, E., Ferziger, J.H., Reynolds, W.C.: Mixing of a passive scalar in isotropic and sheared homogeneous turbulence. Tech. Rep. NASA-CR-164938 Tf-15. Stanford (CA): Department of Mechanical Engineering, Stanford University (1981)
Sukheswalla, P., Vaithianathan, T., Collins, L.R.: Simulation of homogeneous turbulent shear flows at higher reynolds numbers: numerical challenges and a remedy. J. Turbulence **14**, 60–97 (2013)
Tavoularis, S., Corrsin, S. J.: Experiments in nearly homogenous turbulent shear flow with a uniform mean temperature gradient. Part 1. J. Fluid Mech. **10**, 311–347 (1981)
Tavoularis, S., Karnik, U.: Further experiments on the evolution of turbulent stresses and scales in uniformly sheared turbulence. J. Fluid Mech. **204**, 457–478 (1989)
Townsend, A.A.: The Structure of Turbulent Shear Flow, 2nd edn. Cambridge University Press, Cambridge (1976)
Waleffe, F.: On a self-sustaining process in shear flows. Phys. Fluids **9**, 883–900 (1996)
Waleffe, F.: Homotopy of exact coherent structures in plane shear flows. Phys. Fluids **15**, 1517–1534 (2003)
Weinstock, J.: Analytical theory of homogeneous shear turbulence. J. Fluid Mech. **727**, 256–281 (2013)
Wilczek, M., Stevens, R., Meneveau, C.: Spatio-temporal spectra in the logarithmic layer of wall turbulence: large-eddy simulations and simple models. J. Fluid Mech. **769**(1–11), R1 (2015)
Zhao, X., He, G.W.: Space-time correlations of fluctuating velocities in turbulent shear flows. Phys. Rev. E **79**, 046316 (2009)

Chapter 10
Incompressible Homogeneous Anisotropic Turbulence: Buoyancy Force and Mean Stratification

10.1 Observations, Propagating and Non-propagating Motion. Collapse of Vertical Motion and Layering

Turbulent flows can transport passive scalars, such as temperature or concentration. In important applications, such scalar (e.g. temperature, salinity) fluctuations generate a buoyancy force in the presence of gravity, which directly affects the velocity field. In addition, the transport of such "active" scalars by turbulence is altered by a mean density gradient — intimately related to a mean scalar gradient — in many applications, especially in atmospheric and oceanic research.

A first sketch of what stable and unstable stratification are can be understood from a simple displaced-particle argument, as follows. Considering a vertical negative mean density gradient (the heaviest flow is at the bottom), as in the scheme in Fig. 10.1, if a fluid particle is displaced upward, keeping its density and initially in hydrostatic equilibrium, it must experience a lighter fluid environment : the imbalance between (smaller) buoyancy — or Archimedean — force and (same) weight will result in a downward force. The opposite situation occurs if the particle is moved downward, the imbalance buoyancy/weight will result in a upward force. Accordingly, the buoyancy force acts as a restoring force in this situation of negative mean density gradient. Vertical oscillations with a typical frequency N (rediscussed below) are expected.

The same reasoning holds for explaining unstable stratification. The mean velocity gradient is now positive: a particle which is displaced upward will experience a heavier fluid environment, so that the buoyancy will result in a upward force, forcing the particle to continue to move up. This case of unstable stratification, which includes important instances of thermal convection, makes it possible to integrate RDT for linear dynamics and fully nonlinear generalized EDQNM. In addition, some clues are offered to go beyond the strict statistical homogeneity restricted to fluctuations, and to address a more realistic mixing layer. More generally, the simplest sketch of Fig. 10.1-left can be more complex and more general, if the displaced particle is affected by other mechanisms, such as moisture, weak compressibility, and other effects, ignored in our simplified context of Boussinesq approximation. For more

P. Sagaut and C. Cambon, *Homogeneous Turbulence Dynamics*,
https://doi.org/10.1007/978-3-319-73162-9_10

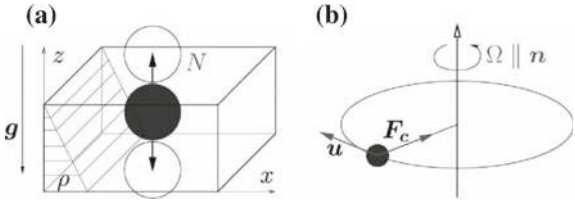

Fig. 10.1 Sketch of basic oscillations, vertical displacement in stable stratification (left), horizontal displacement in rotating flow case (right)

general applications, the gravitational acceleration can be replaced by, or superimposed to, an acceleration related to a whole convective motion of the mixing layer. The typical stratification frequency, or Brunt–Wäisälä frequency in the stable case, is directly connected to the mean density gradient in our sketch, as

$$N^2 = -\frac{g}{\rho_0}\frac{\partial \overline{\rho}}{\partial x_3}, \tag{10.1}$$

with g the modulus of gravitationnal acceleration and $\overline{\rho} = \rho_0 + \frac{\partial \overline{\rho}}{\partial x_3} x_3$ the mean density gradient. Slightly different definitions in terms of other mean buoyancy gradients are recalled in this chapter.

Stable stratification is first considered in this chapter. This situation is common in the ocean, except in a neutral mixing layer located near the surface. All cases, stable, unstable and neutral, are encountered in the atmosphere, with persistent case of the inversion of temperature gradient which yields a stable case in the tropopause and low stratosphere.

The above-mentioned vertical oscillations are the simplest mechanism for generation of internal gravity waves. Gravity waves have strong analogy with inertial waves introduced in Chap. 7. On the one hand, since the velocity field remains divergence-free, pressure fluctuations are responsible for both anisotropic dispersivity and vertical/horizontal interchange of motion by the gravity waves, in a way very similar to what occurs for inertial waves. Similar "Saint-Andrew" cross-shaped structures are found in both rotating and stratified cases. On the other hand, it is possible to define a potential energy for gravity waves only, as we will see further: the wave kinetic energy is essentially the poloidal kinetic energy, whereas the potential energy is proportional to the variance of density or buoyancy fluctuations. In this sense, buoyant flows with stable stratification illustrate another case of *flow dominated by wavy effects* with *zero energy production*, as introduced in Chap. 7. For pure rotating turbulence, there is zero production of kinetic energy and for stratified and stratified rotating turbulence there is *zero production of total energy*, the latter being defined as the sum of kinetic energy and potential energy.

The essential difference between the rapidly rotating case and the strongly stratified one is the existence of an important non-propagating mode of motion in the latter case. The toroidal part of the motion is unaffected by the gravity waves in the linear limit of small Froude number. It is perhaps useful to recall the definition of Froude numbers, which are very similar to macro-Rossby numbers in Chap. 7, only

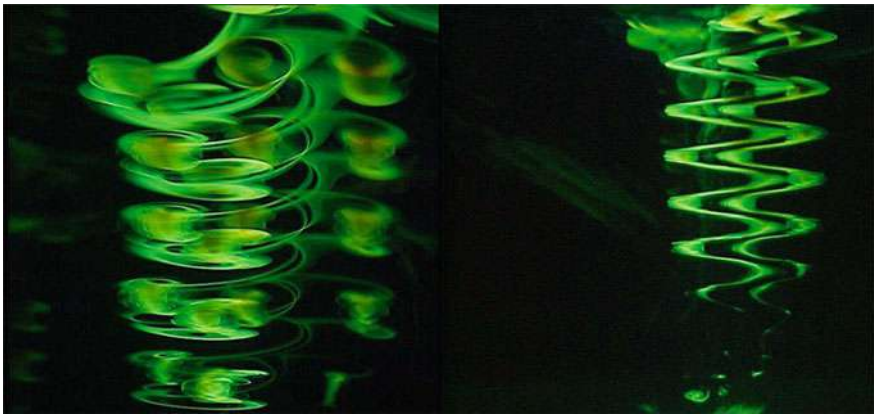

Fig. 10.2 Experimental illustrations of the zig-zag instability. Courtesy from J.-M. Chomaz and P. Billant

replacing 2Ω by N, e.g. in Eq. (10.1), and using either large horizontal $L_\perp$ or vertical $L_\parallel$ lengthscales

$$Fr_\perp = \frac{u'}{NL_\perp}; \quad Fr_\parallel = \frac{u'}{NL_\parallel}. \tag{10.2}$$

More generally, the Ertel theorem yields a nonlinear definition of the non-propagating mode which will be rediscussed in Chap. 11, in agreement with general definition of potential vorticity. In the geophysical community, this mode is referred to as the *quasi-geostrophic (QG) mode* which is generally defined in the presence of additional Coriolis effects (see Chap. 11). Many wave-vortex decompositions exist in the literature, which are often neither intrinsic nor general, so that a particular care will be put in this book on the very definition of the modes of motion. For instance the wave-vortex decomposition by Riley and coworkers (1981) is only meaningful in the absence of additional rotation. The same decomposition was recently coined "vortical-divergent" by Brethouwer et al. (2007): this terminology is more confusing than the former, because the whole velocity field is divergence-free. It would be relevant, however, in connection with the true Helmholtz decomposition for compressible flows introduced in Sect. 2.1.5. The "vortex" (Riley et al. 1981) or "vortical" (Brethouwer et al. 2007) mode is better qualified as the toroidal one anyway.

The main effect of stable stratification is to inhibit the vertical motion. Nevertheless, this stabilizing effect is not necessarily true for the horizontal motion, as recently shown in several studies devoted to the *zig-zag instability*, following Billant and Chomaz (2000). Considering vertical columnar vortices, strong stratification partly inhibits elliptical and/or centrifugal instabilities (touched upon in Chap. 11) but breaks the vertical coherence of the columns by creating alternate, tangling, horizontal motion via zig-zag instability (Fig. 10.2).

This instability is even invoked to explain the horizontal layering of strongly stratified flows: we think that this is only a part of the full answer. In the same way, the scaling of the vertical length scale as U/N, where U (or u' in Eq. (10.2)) is a typical horizontal velocity scale and N the gravity wave typical frequency, is suggested by the zig-zag instability (Billant and Chomaz 2001) but also by many other arguments disconnected from it.

Finally, the morphology of a strongly stratified flow is essentially a pilling-up of velocity and density horizontal "pancakes" which can be observed in Fig. 10.6. A similar topology was reported looking at instantaneous iso-vorticity surfaces by Kimura and Herring (1996).

The flow is really quasi-horizontal but far from being two-dimensional. Even with a random forcing of two-dimensional modes, DNS by Herring and Métais (1989) exhibit a clear tendency of forming horizontal layers, with a limited vertical thickness.

Gravity waves are present in the layered flow, but perhaps only in the limit of low frequencies (low dispersion frequency at given high frequency N is obtained in the limit of quasi-vertical wave-vectors, forming a *Vertically Sheared Horizontal Flow* —VSHF from Smith and Waleffe 2002 — mode, as shown below). A clear analysis of such flows cannot be made without a rigorous terminology, avoiding the confusion between horizontal, 2D and toroidal motions. In addition to an accurate description of the morphology, dynamical arguments must be discussed: what is the mechanism which controls the thickness of the "pancakes"?

In addition to the mathematical/numerical decomposition by Riley et al. (1981), another related aspect are the scaling arguments for small (horizontal) Froude number, which supports the idea of almost vertically decorrelated thin horizontal pancake layers. The scaling by Riley et al. (1981) seems to hold for laboratory experiments, for internal waves (since the vertical scale of U/N is generally not of importance), and possibly for larger-scale flows (if their dynamics are not controlled by the vertical scale U/N). Note that strongly stratified flows (low Froude numbers in either sense) can exhibit waves over a broad range of frequencies. They are not limited by scaling or dynamical arguments to vertical scales of order U/N. There can be significant vertical motion associated with the waves.

Applications are very important for flows in the atmosphere and the ocean, in which the stable stratification limits the vertical motion and makes the flow mainly horizontal. The problem of the sense of the kinetic energy cascade (forward or backward) in such flows is still controversial, even if a global consensus is now emerging against the idea of a classical 2D inverse cascade. On the one hand, the analogy between quasi-geostrophic and 2D dynamics, with conservation of potential vorticity, was investigated by Charney (1971); this analogy was revisited by Bartello (1995) with a refined analysis of pure QG interactions, also in the line of the Waleffe's instability principle. Regarding applications, Lilly (1983) has proposed that the kinetic energy spectra observed in the atmosphere at mesoscales (i.e. very low wave numbers) are a manifestation of this two-dimensional mechanism. In spite of this questionable speculation about upscale energy transfer, Lilly (1983) was probably the first to suggest that vertical layering and instabilities would result from strong stratification (at low Froude number). At the bottom of page 755 and the top of page

756 of his paper he states: "*the second and more difficult problem is concerned with the continuing validity of the RMW* (Riley et al. 1981) *scale analysis over a long period of time. The predicted decoupling of the dynamics at adjacent vertical levels can be maintained only as long as the local Richardson number is large. Both the inherent instability of turbulent flows and the existence of any mean vertical shear will decorrelate the vertical flow structure and produce locally small Richardson numbers. The subsequent regeneration of small-scale three-dimensional turbulence then modifies the stratified turbulence evolution to a yet uncertain degree.*"

Recently, Lindborg and Cho (2001), Cho and Lindborg (2001) deduced from analysis of third order statistical moments that the energy cascade is in the direct sense, i.e. from small to large wave numbers. This observational evidence was further supported by a dimensional analysis related to the zig-zag instability (Billant and Chomaz 2001), showing that the vertical scale is necessary limited by a local buoyancy length scale $L_B = U/N$, where U is the horizontal velocity scale and N the Brunt–Väisälä frequency. Several DNS (or rather LES because of the use of an hyperviscosity instead of the classical molecular viscosity) were carried out by Lindborg and coworkers to investigate such a forward cascade. In these computations, the 2D-2C modes, and only them, are randomly forced, and the horizontal lengthscales are a priori chosen much larger than the vertical ones, using flattened boxes. Even if these studies present interest for atmospheric flows, their contribution to a better conceptual understanding of turbulence is limited by both geometric constraints and artificial forcing: no refined analysis of the anisotropy of the flow is performed, as it was done in the case of rotating turbulence. Even more importantly, no new mechanism of triad interactions is derived from such LES.

10.2 Simplified Equations, Using Navier–Stokes and Boussinesq Approximations, with Uniform Density Gradient

Navier–Stokes equations, with buoyancy force $\boldsymbol{b} = b\boldsymbol{n}$ within the Bousinesq assumption, are given below in the presence of a uniform mean density (more generally buoyancy) gradient. For the sake of simplicity, the mean flow is restricted to a "stabilizing" uniform vertical gradient of density, whose strength is given by N, the Brunt–Väisälä frequency:

$$(\partial_t + \boldsymbol{u}\cdot\boldsymbol{\nabla})\,\boldsymbol{u} + \boldsymbol{\nabla} p - \nu\nabla^2\boldsymbol{u} = b\boldsymbol{n} \tag{10.3}$$

$$(\partial_t + \boldsymbol{u}\cdot\boldsymbol{\nabla})b - \kappa\nabla^2 b = -N^2\boldsymbol{n}\cdot\boldsymbol{u} \tag{10.4}$$

$$\boldsymbol{\nabla}\cdot\boldsymbol{u} = 0. \tag{10.5}$$

Dependent variables are the fluctuating velocity $\boldsymbol{u}$, the pressure p divided by a mean reference density, and the buoyancy force $\boldsymbol{b}$. The vector $\boldsymbol{n}$ denotes the vertical unit upward direction aligned with the gravitational acceleration $\boldsymbol{g} = -g\boldsymbol{n}$. The Boussinesq approximation (Boussinesq 1876) (the reader is referred to the large literature in geophysics) preserves the solenoidal property for the velocity, but allows the density to fluctuate. In the basic continuity equation $\dot{\rho} + \rho u_{i,i} = 0$, it amounts to consider separately $\dot{\rho} = 0$ and $u_{i,i} = 0$. The first condition generates the b-equation (10.4), while only the right-hand-side of the momentum equation (10.3) calls b into play.

Since a large literature is devoted to the turbulent transport of the passive scalar, a short discussion of this case cannot be avoided. Let us consider first that the fluctuating concentration of a passive scalar, say c, is addressed, instead of b, and that a vertical mean gradient $(\partial C/\partial x_3)\boldsymbol{n}$ exists for scalar concentration. The classical advection-diffusion equation, with additional 'mean production' is

$$(\partial_t + \boldsymbol{u} \cdot \boldsymbol{\nabla})c - \kappa \nabla^2 c + \frac{\partial C}{\partial x_3} \boldsymbol{u} \cdot \boldsymbol{n} = 0, \tag{10.6}$$

which is the same as Eq. (10.4). The only difference with the passive scalar equation is the presence of the right-hand-side in (10.3) which reflects an "active" feed-back from scalar concentration to velocity field.

The use of the buoyancy variable b allows us to have the same equations, with the unique frequency N, for a liquid or for a gas. For a liquid, $b = g\rho'/\rho_0$, where ρ' denotes a small fluctuation and ρ_0 is the mean reference density. The definition $N = \sqrt{g\Gamma/\rho_0}$, see Eq. (10.1), with Γ the absolute value of the mean vertical gradient of density, presents a strong analogy with the frequency of a pendulum, $(\Gamma/\rho_0)^{-1}$ playing the role of the length of the pendulum. For a gas, b is proportional to the fluctuating potential temperature τ, as $b = \beta g \tau$, with β the thermometric expansivity. Accordingly one has $N = \sqrt{g\beta\gamma}$ with γ the mean vertical gradient of temperature.

Finally, the different flow cases are only discriminated by the diffusivity coefficient for b. Since there is no meaning for a diffusive density, κ must be considered as the diffusivity of the stratifying agent, for instance the temperature for a gas —κ/ν is a Prandtl number— or the salinity for a liquid — κ/ν is a Schmidt number—. Without loss of generality the fixed frame of reference is chosen below such that $n_i = \delta_{i3}$. Therefore, u_3 is the vertical velocity component.

10.2.1 Reynolds Stress Equations with Additional Scalar Variance and Flux

As for the case of a passive scalar, single-point second-order correlations include not only the Reynolds stress tensor $\overline{u_i u_j}$ (there is no mean velocity here, so that $\boldsymbol{u} = \boldsymbol{u}'$), but also the scalar variance $\overline{b^2}$ and the scalar flux $\overline{bu_i}$. Transport equations for the

latter correlations are standard passive scalar in the presence of a mean gradient of passive scalar of magnitude N^2. The Reynolds stress equations must be affected by the *active* buoyancy term, yielding

$$\frac{d\overline{u_i u_j}}{dt} = \overline{bu_j}\delta_{i3} + \overline{bu_i}\delta_{j3} + \Pi_{ij}^{(s)} + \Pi_{ij}^{(r)} - \varepsilon_{ij}.$$

All Reynolds stresses with a vertical component are therefore altered by buoyancy fluxes. Buoyancy fluxes $\overline{bu_i}$ are themselves governed by

$$\frac{d\overline{u_i b}}{dt} = N^2\overline{u_i u_3} + \Pi_{ib}^{(r)} + \Pi_{ib}^{(s)} - \epsilon_{ib},$$

whereas the buoyancy variance $\overline{b^2}$ satisfies

$$\frac{d\overline{b^2}}{dt} = 2N^2\overline{bu_3} - \epsilon_b.$$

Similarly to the pressure terms appearing the equations for the Reynolds stress tensor discussed in Chap. 2, $\Pi_{ib}^{(s)}$ and $\Pi_{ib}^{(r)}$ denote the linear "rapid" and nonlinear "slow" pressure-buoyancy gradient cross-correlations, respectively. In the absence of mean velocity gradient, the "slow" term $\Pi_{ij}^{(s)}$ remains in the equation for the Reynolds stress tensor, and a similar "rapid" one, $\Pi_{ij}^{(r)}$ is now related to two-point pressure-buoyancy correlations. These equations immediately result from combining basic equations (10.3) and (10.4). They can be found in Craft and Launder (2002) up to slightly different notations, with additional nonhomogeneous diffusive terms, and replacing d/dt by D/Dt (i.e. considering full convective term). Even in strictly homogeneous turbulence, some additional contributions from triple correlations, neglected in conventional modelling, may appear. They result from the fact that conservation laws (with zero contribution of related nonlinear transfer terms) are valid for separately considered toroidal and wave (poloidal + potential) energies, but not for horizontal, vertical and potential energies (those which are only tractable in RSM framework, with potential energy proportional to $\overline{b^2}$). This will appear looking at generalized Lin equations in Sect. 10.5.

Craft and Launder (2002) developed one of the most sophisticated full Reynolds-Stress Model, whose details are not given here for the sake of brevity, with application in the Two-Component Limit, *which must not be confused with 2D limit*. This Two-Component model is relevant here, but also (for different reasons) for near-wall turbulence. In particular cases, such as the pure decay of homogeneous stably-stratified turbulence, the model mimics the damping of oscillations induced by gravity waves, without significant dissipation (see Fig. 10.3). The damping effect results from phase-mixing of dispersive waves, and this physical effect cannot be directly incorporated in a single-point closure model: The correct behavior of the model is even more surprising, and is probably due to the high complexity of the linear pressure-strain rate

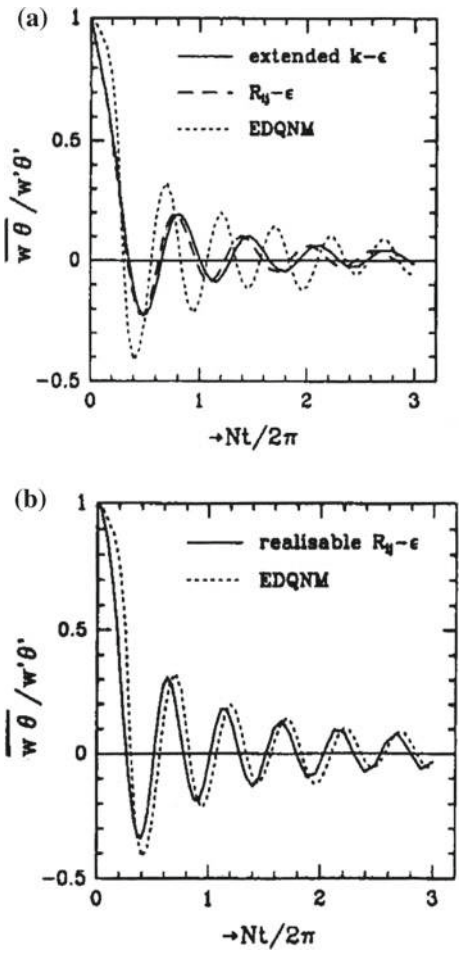

Fig. 10.3 Normalized vertical buoyancy flux $\overline{u_3 b}$. Realizable $R_{ij} - \epsilon$ means the sophisticated Two-Component Limit model. EDQNM is essentially RDT here, the damping of oscillations reflects the phase mixing due to anisotropic dispersivity of gravity waves. Courtesy of L. Van Haren

tensors, such as $\Pi_{3b}^{(r)}$, along with strong constraints imposed, such as realizability. It is important to remind that in similar conditions, all single-point closure models miss the effects of inertial waves.

10.2.2 First Look at Gravity Waves

Analysis of the linear limit, mathematical treatment of equations in terms of eigenmodes, and closure methods for statistics in homogeneous anisotropic turbulence, can be developed as in the case of pure rotation discussed in Chap. 7.

In the absence of pressure fluctuations, the additional buoyancy and stratification terms yield oscillations for vertical velocity and buoyancy term at frequency N. This

simple motion shows that the buoyancy force acts as a restoring force in the case of stable stratification. As for the case of pure rotation, the pressure term in (10.3) is needed to satisfy (10.5), and its role in the complete linear solution consists of coupling vertical and horizontal motion and of generating dispersive inertia-gravity waves.

The counterpart of Eq. (7.24) for inertial waves is

$$\frac{\partial^2}{\partial t^2}\left(\nabla^2 p\right) + N^2 \nabla_\perp^2 p = 0. \tag{10.7}$$

It is only needed to replace 2Ω by N and to replace the vertical component $\nabla_\parallel$ of the Laplacian operator by its horizontal $\nabla_\perp$ counterpart. The same treatment (i.e. normal mode decomposition and derivation of the dispersion relation) shows that the threshold value to trigger Saint-Andrew-cross shaped structures with a local harmonic forcing σ_0 (Mowbray and Rarity 1967) is $\sigma_0 = N$. The dispersion frequency in an unbounded domain is defined as

$$\sigma_k = N\frac{k_\perp}{k} = N \sin\theta. \tag{10.8}$$

As for the case of rapid rotation, a zero frequency mode exists for gravity waves, but it corresponds to the vertical wavevector direction, forming the *one-dimensional* VSHF mode, instead of the two-dimensional Taylor-Proudman mode linked to $k_\parallel = 0$ for inertial waves. As said before, another even more important difference with the rotating flow case is that a part of the horizontal motion remains steady in the linear limit, and therefore decoupled from 3D wave motion.

10.3 Eigenmode Decomposition. Physical Interpretation

In the unbounded case, or for periodic boundary conditions, the different modes, wavy and steady, are easily found in Fourier space, and a tractable RDT solution is found in terms of them. Pressure fluctuation is removed from consideration in the Fourier-transformed equations by using the local Craya-Herring frame of reference in the plane normal to the wave vector, taking advantage of Eqs. (10.5) and (2.86), or

$$\hat{\boldsymbol{u}}(\boldsymbol{k}, t) = u^{(1)}(\boldsymbol{k}, t)\boldsymbol{e}^{(1)}(\boldsymbol{\alpha}) + u^{(2)}(\boldsymbol{k}, t)\boldsymbol{e}^{(2)}(\boldsymbol{\alpha}), \quad \boldsymbol{\alpha} = \boldsymbol{k}/k,$$

so that the problem with five components (u_1, u_2, u_3, p, b) in physical space is reduced to a problem with three components in Fourier space, namely two solenoidal velocity components $(u^{(1)}, u^{(2)})$ and a component for $\hat{b}$. The three-component set $(u^{(1)}, u^{(2)}, \hat{b})$ is not a true vector, and this can complicate further mathematical developments in terms of its eigenmodes and statistical correlations. So it is more convenient to gather these three components into a new vector $\hat{v}$, whose inverse 3D

Fourier transform, $\boldsymbol{v}$, is real. $\hat{\boldsymbol{v}}$, can be written as[1]

$$\hat{\boldsymbol{v}} = \hat{\boldsymbol{u}} + \imath \frac{1}{N} \widehat{b} \frac{\boldsymbol{k}}{k} \tag{10.9}$$

so that its three components are $u^{(1)}$, $u^{(2)}$, and $u^{(3)} = \imath \frac{1}{N} \hat{b}$ in the Craya-Herring frame, using also its third direction $\boldsymbol{e}^{(3)} = \boldsymbol{k}/k$, even if it is more usually related to a divergent part of the velocity flow. The scaling of the contribution of the buoyancy force allows one to define twice the total spectral energy density as

$$\widehat{v_i^* v_i} = \widehat{u_i^* u_i} + N^{-2} \widehat{b^* b} \tag{10.10}$$

Linear inviscid equation are easily found as

$$\begin{pmatrix} \dot{u}^{(1)} \\ \dot{u}^{(2)} \\ \dot{u}^{(3)} \end{pmatrix} = \begin{pmatrix} 1 & 0 & 0 \\ 0 & 0 & -N \frac{k_\perp}{k} \\ 0 & N \frac{k_\perp}{k} & 0 \end{pmatrix} \begin{pmatrix} u^{(1)} \\ u^{(2)} \\ u^{(3)} \end{pmatrix}. \tag{10.11}$$

Linear — improperly called RDT — solutions are easily found, with constant $u^{(1)}$ and oscillating $u^{(2)}$-$u^{(3)}$. In any orthonormal frame of reference, linear solutions can be found in terms of the three eigenmodes

$$\hat{\boldsymbol{v}} = \xi^{(0)} \boldsymbol{N}^{(0)} + \xi^{(1)} \boldsymbol{N}^{(1)} + \xi^{(-1)} \boldsymbol{N}^{(-1)}, \tag{10.12}$$

or

$$\hat{\boldsymbol{v}} = \sum_{s=0,\pm 1} a_s(\boldsymbol{k}, t) \exp(\imath s \sigma_k t) \boldsymbol{N}^{(s)}, \tag{10.13}$$

in which the eigenmodes $\boldsymbol{N}^{(s)}$, $s = 0, \pm 1$ are simple linear combinations of the vectors in the Craya-Herring frame of reference. ($\boldsymbol{N}^{(0)}$ reduces to the toroidal mode $\boldsymbol{e}^{(1)}$ here.) The reader is referred to Chap. 11 and to Cambon (2001) for a more general QG-AG decomposition, also valid in the presence of additional rotation. Essentially the same decomposition was introduced by Bartello (1995) in the geophysical context. Of course, the a_s are constants given by initial data in the strict linear limit. A Green's function similar to (7.31) is derived as

$$G_{ij}(\boldsymbol{k}, t, t_0) = \sum_{s=0,\pm 1} N_i^s(\boldsymbol{k}) N_j^{-s}(\boldsymbol{k}) \exp[\imath s \sigma_k (t - t_0)], \tag{10.14}$$

and the nonlinear equations can be expressed in terms of the eigenmodes, as in Chap. 7, if time-dependency is re-introduced in the a_s, $s = 0, \pm 1$, as in the more

[1] The term $\imath \boldsymbol{k} \hat{b}$ corresponds to the *gradient* of the fluctuating buoyancy term in physical space. As in other studies dealing with the passive scalar, it can be better to use the scalar gradient than the scalar itself, e.g. Gonzalez (2009).

general version of (10.13). The new element, with respect to (7.37) is the presence of a "strong" nonlinearity, related to a term $M_{(000)}$, which does not reduce to "weak" wave-turbulence, as the other coupling terms such as $M_{(00\pm1)}$, $M_{(0\pm1\pm1)}$ and $M_{(\pm1\pm1\pm1)}$ (only the latter being present in rotating turbulence). Because of the form of the eigenvectors and of the dispersion law, the structure of $\mathbf{G}$ in (10.14) is consistent with axisymmetry around the axis of reference (chosen vertical here), with mirror symmetry, and where $k_\parallel$ and $k_\perp$ hold for axial (along the axis) and transverse (normal to the axis) components of $\boldsymbol{k}$, respectively.

Anisotropy can be significantly broken through axisymetrical response function for triple correlations only, or possibly for two-time second order statistics (whose analysis is beyond the scope of this book, except the new subsection in Chap. 11), but the linear limit exhibits no interesting creation of structural anisotropy in classic RDT for predicting second order single-point statistics. However, in practice there is a partial two-dimensionalization in rotating turbulence and a horizontal layering tendency in the stably stratified case. In other words, RDT only alters phase dynamics and exactly conserves the spectral density of typical modes, namely full kinetic energy for the rotating case and total energy and toroidal energy for the stably stratified case, so that two-dimensionalization or 'two-componentalization' (horizontal layering), which affect the distribution of this energy, are pure nonlinear effects.

Nevertheless, the eigenmodes of the linear regime form a useful basis for expanding the fluctuating velocity-buoyancy field, even when nonlinearity is present, and nonlinear interactions can be evaluated and discussed in terms of triadic interactions between these eigenmodes. Accordingly, the complete anisotropic description of two-point second order correlations, can be related to spectra and cospectra of these eigenmodes.

Finally, it is important to recall that the spectral mode related to the first vector $\boldsymbol{e}^{(1)}$ of the Craya-Herring frame of reference is linked to the toroidal mode in physical space, only if the wavevector direction differs significantly from $\boldsymbol{n}$. This mode matches the VSHF mode if $\boldsymbol{k}$ is vertical. The same property holds for the second vector $\boldsymbol{e}^{(2)}$, which corresponds essentially to poloidal motion but also matches the VSHF mode for vertical $\boldsymbol{k}$. The VSHF mode, or $u_\perp(x_\parallel, t)$ in physical space, is not really a wavy mode, even if it corresponds to the zero frequency limit of gravity waves. In addition, the coupling with buoyancy, which is the main characteristic of linear gravity waves (poloidal velocity coupled with buoyancy) vanishes for this mode, so that b is again a passive scalar in the VSHF limit, and strong departure from equipartition in terms of kinetic and potential wave-energy is possible. Regarding vorticity, the VSHF mode has no contribution to vertical vorticity and contributes to horizontal vorticity, while the toroidal mode (sometime called 'vortex' or 'vortical' mode) generates the vertical vorticity component. The Craya-Herring decomposition allows us to incorporate in a very tractable geometrical way the toroidal/poloidal decomposition, with very different limits given by 2D Taylor-Proudman modes (horizontal wavevectors) and 1D VSHF modes (vertical wavevectors). Near the 2D limit, the toroidal mode corresponds to horizontal velocity and vertical vorticity, and vice-versa for the poloidal mode. More generally, toroidal velocity corresponds to poloidal vorticity

and vice-versa (the Craya-Herring frame is also a useful cyclic basis, see Eq. (10.17) below). Only near the VSHF limit, both vorticity and velocity are quasi-horizontal.

The main nonlinear mechanism in quasi-homogeneous unsteady stratified flows consists of concentrating energy towards more and more vertical wave-vectors, as shown in the cartoon from Godeferd and Cambon (1994) in Fig. 10.5. This anti-2D (compared to the case of rotation, see Fig. 7.17 in Chap. 7) trend can be explained by the toroidal cascade, independently of wave-turbulence "weak" nonlinearity, and without invoking specific instabilities to preexisting and/or forced coherent vertical vortices.

10.4 The Toroidal Cascade as a Strong Nonlinear Mechanism Explaining the Layering

Looking at the velocity equation, under the slightly different form (the inviscid case is considered for the sake of simplicity),

$$\frac{\partial \boldsymbol{u}}{\partial t} + \boldsymbol{\omega} \times \boldsymbol{u} + \nabla \left(p + \frac{1}{2} u^2 \right) = b\boldsymbol{n}, \tag{10.15}$$

projection onto the $\boldsymbol{e}^{(1)}$-mode removes both the "divergent" term (total pressure here), because of solenoidal property, and the b-term because it is vertical. The toroidal (or toroidal + VSHF) equation is therefore

$$\frac{\partial u^{(1)}}{\partial t} + \boldsymbol{e}^{(1)} \cdot \widehat{\boldsymbol{\omega} \times \boldsymbol{u}} = 0,$$

and it is possible to extract the pure toroidal contribution in the nonlinear term as

$$\frac{\partial u^{(1)}(\boldsymbol{k}, t)}{\partial t} + \imath \frac{k}{2} \sum_{\Delta} \boldsymbol{e}^{(1)}(\boldsymbol{k}) \cdot \left(\boldsymbol{e}^{(2)}(\boldsymbol{p}) \times \boldsymbol{e}^{(1)}(\boldsymbol{q}) + \boldsymbol{e}^{(2)}(\boldsymbol{q}) \times \boldsymbol{e}^{(1)}(\boldsymbol{p}) \right) u^{(1)*}(\boldsymbol{p}, t) u^{(1)*}(\boldsymbol{q}, t) + CCC, \tag{10.16}$$

using

$$\hat{\boldsymbol{u}} = u^{(1)} \boldsymbol{e}^{(1)} + u^{(2)} \boldsymbol{e}^{(2)}, \quad \hat{\boldsymbol{\omega}} = \imath k \left(u^{(1)} \boldsymbol{e}^{(2)} - u^{(2)} \boldsymbol{e}^{(1)} \right). \tag{10.17}$$

The "CCC" term denotes the contribution of other quadratic terms, those which correspond to $u^{(1)*} u^{(2)*}$ and to $u^{(2)*} u^{(2)*}$. Some are identically zero because, for instance, the triple scalar product in terms of $\boldsymbol{e}^{(1)}$ for $\boldsymbol{k}, \boldsymbol{p}, \boldsymbol{q}$ is zero ($\boldsymbol{e}^{(1)}$ being always horizontal). More generally the decomposition in terms of eigenmodes shows that any $u^{(2)}$ contribution in "CCC" involves a "rapid" phase factor $e^{\imath \sigma t}$, as seen from Eq. (10.13). These rapid factors result in an efficient damping of the nonlinearity

by anisotropic phase mixing, except if their time-dependency is cancelled out via resonance conditions. Accordingly, in the limit of strong stratification, "CCC" terms survive only through "weak" resonant wave interactions, exactly as for rotating turbulence in Chap. 7. The new fact is that all triads involving $u^{(1)}$ only have a non-vanishing contribution without any wave resonance constraint. On the other hand, resonant wave interactions represent a low dimensional manifold, so that magnitude of the "CCC" contributions can be considered as being of the order of the Froude number. Discarding "CCC" terms is therefore relevant if the Froude number is very small (but with very high Reynolds number in order to allow significant nonlinearity, purely toroidal here) and the elapsed time not too high, with in addition a special care to investigate the VSHF limit.

The relevance of pure toroidal cascade, or of pure QG cascade revisited in Chap. 11, deserves further discussion in the geophysical context. But let us note that this study can be almost disconnected from the context of geophysical applications, since it deals with the basic nonlinearity of Euler equations, seen via triad interactions in 3D Fourier space. Given the success of the Waleffe's triad instability principle for predicting the energy cascades, a similar approach is now applied to Eq. (10.16) neglecting the "CCC" term.

Restricting this equation to a single triad, one obtains

$$\dot{u}_k^{(1)} = (p_\perp^2 - q_\perp^2) G u_p^{(1)*} u_q^{(1)*}, \tag{10.18}$$

$$\dot{u}_p^{(1)} = (q_\perp^2 - k_\perp^2) G u_q^{(1)*} u_k^{(1)*}, \tag{10.19}$$

$$\dot{u}_q^{(1)} = (k_\perp^2 - p_\perp^2) G u_k^{(1)*} u_p^{(1)*}, \tag{10.20}$$

where

$$G = \frac{\imath}{2} C_{kpq} \frac{kpq}{k_\perp p_\perp q_\perp} \frac{\boldsymbol{k} \times \boldsymbol{p}}{\mid \boldsymbol{k} \times \boldsymbol{p} \mid} \cdot \boldsymbol{n} \tag{10.21}$$

and

$$C_{kpq} = \frac{\mid \sin \widehat{(\boldsymbol{p}, \boldsymbol{q})} \mid}{k} = ...sym(k, p, q). \tag{10.22}$$

New detailed conservation laws can be identified in the present case. The factor G is invariant with respect to any even permutation of the vectors $\boldsymbol{k}$, $\boldsymbol{p}$, $\boldsymbol{q}$ of the triad and changes its sign for an odd permutation. Therefore, it is clear that triadic interactions within a single triad conserves toroidal energy, since $\dot{u}_k^{(1)} u_k^{(1)*} + \dot{u}_p^{(1)} u_p^{(1)*} + \dot{u}_q^{(1)} u_q^{(1)*} = 0$ and vertical contribution to toroidal enstrophy, since

$$k_\perp^2 \dot{u}_k^{(1)} u_k^{(1)*} + p_\perp^2 \dot{u}_p^{(1)} u_p^{(1)*} + q_\perp^2 \dot{u}_q^{(1)} u_q^{(1)*} = 0. \tag{10.23}$$

The analogy with the 2D case is very strong (see also Waleffe 1992, and especially his Appendix A, and pioneering papers by Fjortoft 1953 and Kraichnan), but it must be noticed that 2D-2C limit requires the additional condition that $k_\parallel = p_\parallel = 0$ in Eq. (10.20). Without further quantitative statistical analysis (next section), it is

immediately shown that only (R) triads are concerned, but in terms of $k_\perp$ only. Compared with the instability principle expressed in terms of helical modes for 3D isotropic or rapidly rotating turbulence, the analogy of (10.20) with the stability of a solid rotating around its principal axes of inertia (Euler problem), is even more striking. In contrast with the helical case, in which terms $sk, s'p, s''q$ play the role of (positive) principal inertia moments I_1, I_2, I_3, with the additional difficulty linked to various signs (polarities of helical modes $s = \pm 1, s' = \pm 1, s'' = \pm 1$), now really positive terms $(k_\perp^2, p_\perp^2, q_\perp^2)$ play these roles.

In short, the presence of only reverse interactions could suggest an inverse cascade, at least in term of $k_\perp$ wavevector components and therefore in terms of cylinders. Strong anisotropy allows for very rich modalities of cascade, with various senses depending on shell-to-shell (direct), cylinder-to-cylinder or angle-to-angle (see Fig. 10.10) spectral energy transfer. Statistical theory is needed to derive such informations in a quantitative way.

10.5 The Viewpoint of Modelling and Theory: RDT, Wave-Turbulence, EDQNM

The case of stably stratified turbulence is different from the one of pure rotation, even if the gravity waves present strong analogies with inertial waves. An additional element is the presence of the toroidal mode, which is steady and decoupled from gravity wave modes, at least in the linear limit.

As for the case of rotating turbulence, exact generalized Lin equations are easily found:

$$\left(\frac{\partial}{\partial t} + 2\nu k^2\right) \mathcal{E}^{(tor)} = T^{(tor)}, \tag{10.24}$$

$$\left(\frac{\partial}{\partial t} + 2\nu k^2\right) \mathcal{E}^{(w)} = T^{(w)}, \tag{10.25}$$

$$\left(\frac{\partial}{\partial t} + 2\nu k^2 + 2\imath N \frac{k_\perp}{k}\right) Z' = T^{(z')}, \tag{10.26}$$

in which abridged definitions

$$\mathcal{E}^{(tor)} = \frac{1}{2} u^{(1)} u^{(1)*}, \quad \mathcal{E}^{(pol)} = \frac{1}{2} u^{(2)} u^{(2*)}, \quad \mathcal{E}^{(pot)} = \frac{1}{2} u^{(3)} u^{(3)*} \tag{10.27}$$

are sufficient for recovering the structure of the system (10.24)–(10.26), but ought to be replaced by more rigorous relationship (e.g. for the closure of the right-hand-sides) such as

$$\frac{1}{2} \langle u^{(1)*}(\boldsymbol{p}, t) u^{(1)}(\boldsymbol{k}, t) \rangle = \mathcal{E}^{(tor)}(\boldsymbol{k}, t) \delta^3(\boldsymbol{k} - \boldsymbol{p}),$$

and so on, as in the whole book.

The total energy of gravity waves (in the linear limit of the eigenmode decomposition) is given by

$$\mathcal{E}^{(w)}(\boldsymbol{k},t) = \mathcal{E}^{(pol)}(\boldsymbol{k},t) + \mathcal{E}^{(pot)}(\boldsymbol{k},t). \tag{10.28}$$

The Z' term quantifies the imbalance between the kinetic contribution to gravity waves ($\mathcal{E}^{(pol)}$) and their potential contribution ($\mathcal{E}^{(pot)}$) as

$$Z'(\boldsymbol{k},t) = (1/2)(\mathcal{E}^{(pot)}(\boldsymbol{k},t) - \mathcal{E}^{(pol)})(\boldsymbol{k},t) + \imath\,\Psi(\boldsymbol{k},t),$$

in which the poloidal buoyancy flux Ψ is given by

$$\langle u^{(2)*}(\boldsymbol{p},t)u^{(3)}(\boldsymbol{k},t)\rangle = \Psi(\boldsymbol{k},t)\delta^3(\boldsymbol{k}-\boldsymbol{p}). \tag{10.29}$$

Because of mirror symmetry, all cross-correlations among the set $(u^{(1)}, u^{(2)}, u^{(3)})$ are not present: The toroidal buoyancy flux related to $\langle u^{(1)*}u^{(3)}\rangle$ remains zero, as the helicity spectrum (More details are given in Godeferd and Cambon 1994; Godeferd and Staquet 2003).

EDQNM closure for the transfer terms (rhs of Eqs. (10.24)–(10.26)) are found in terms of the basic set of abovementioned spectra, depending on both $k_\perp$ and $k_\parallel$ (or on k and $\cos\theta_k = k_\parallel/k$) in the simplest statistical way consistent with the symmetries (axisymmetry with mirror symmetry) of the dynamical basic equations. As an example, the contribution to $T^{(tor)}$, which is related to purely toroidal triple correlations $\langle u^{(1)}(\boldsymbol{k},t)u^{(1)}(\boldsymbol{p},t)u^{(1)}(\boldsymbol{q},t)\rangle$ under an integral, involve a term $\theta_{kpq}\mathcal{E}^{(tor)}(\boldsymbol{q},t)(a(\boldsymbol{k},\boldsymbol{p})\mathcal{E}^{(tor)}(\boldsymbol{p},t) - b(\boldsymbol{k},\boldsymbol{p})\mathcal{E}^{(tor)}(\boldsymbol{k},t))$ once closed by the anisotropic EDQNM procedure.

In order to bridge shear-driven flows and buoyancy-driven flows with the most unified formalism, the previous equations can be recast as:

$$\left(\frac{\partial}{\partial t} + 2\nu k^2\right)\mathcal{E}(\boldsymbol{k},t) + 2N\frac{k_\perp}{k}\Psi = T^{(\mathcal{E})}(\boldsymbol{k},t), \tag{10.30}$$

$$\left(\frac{\partial}{\partial t} + 2\nu k^2\right)Z + 2N\frac{k_\perp}{k}\Psi = T^{(Z)}(\boldsymbol{k},t), \tag{10.31}$$

$$\left(\frac{\partial}{\partial t} + 2\nu k^2\right)\mathcal{E}^{(pot)}(\boldsymbol{k},t) - 2N\frac{k_\perp}{k}\Psi = T^{(pot)}(\boldsymbol{k},t), \tag{10.32}$$

$$\left(\frac{\partial}{\partial t} + 2\nu k^2\right)\Psi(\boldsymbol{k},t) + N\frac{k_\perp}{k}\left(\frac{1}{2}(\mathcal{E}+Z) - \mathcal{E}^{(pot)}\right) = T^{(F)}(\boldsymbol{k},t). \tag{10.33}$$

With respect to Lin equations for shear-driven flows, the problem is simplified because axisymmetry with mirror symmetry can be consistently applied, resulting in an angular dependence of spectra and co-spectra restricted to the polar angle only,

denoted θ_k from now on, and no imaginary part for the polarization term Z, nor helicity $\mathcal{H}$. On the other hand, second-order statistics involve two new terms: The spectrum of (buoyancy) scalar variance, resulting in potential energy $\mathcal{E}^{(pot)}$, and the co-spectrum of poloidal buoyancy flux Ψ from Eq. (10.29).

About global and detailed conservation laws, it is important to stress that Eqs. (10.24) and (10.25) are always exact, provided that their r-h-s are properly expressed from two-point triple correlations. The total energy (kinetic + potential), is conserved in the inviscid limit, so that $T^{(\mathcal{E})} + T^{(pot)}$ has zero integral. On the other hand, *detailed conservation laws per triad, for both toroidal kinetic energy and for vertical enstrophy are valid only if the poloidal contribution to the velocity field is discarded.* Removal of poloidal components in the detailed triadic budget for the toroidal mode amounts to neglect weak gravity-wave turbulence with respect to strong turbulence, a conjecture which is reasonable at very small Froude number and moderate elapsed time.

Discarding the rhs in the above system of equations (and viscosity, even if it is easily accounted for) yields the so-called RDT limit for second-order single-time statistics. Integrating the spectra and co-spectra over Fourier space, toroidal energy is strictly conserved, as is $\mathcal{E}^{(tor)}$ at any $\boldsymbol{k}$, whereas poloidal and potential energy components asymptotically equilibrate after a transient phase made of damped oscillations with opposed phases (see, e.g. Salhi and Cambon 2007 for details, and Fig. 10.4). The damping originates in phase mixing, since the integral of Z' over the polar angle $\sin\theta = k_\perp/k$ tends towards zero because of the weighting factor $e^{2\imath Nt\sin\theta}$ coming from RDT.

Detailed equations and DNS/EDQNM comparisons, including the angle-dependent spectra, are given in Godeferd and Staquet (2003). More details are provided in Sect. 10.7.7. The EDQNM2 model in Godeferd and Cambon (1994) yielded the angular drain of energy which condenses the energy towards vertical wavevectors, in agreement with collapse of vertical motion and layering (see the sketch on Fig. 10.5). Recall that, because of the incompressibility constraint ($\boldsymbol{k}\cdot\hat{\boldsymbol{u}} = 0$), both contributions to velocity and vorticity become almost horizontal if the spectral density of energy is concentrated near the vertical wavevectors. In terms of directional and polarization anisotropy, polarization becomes marginal and all anisotropic features depend on the sole directional anisotropy, including the collapse of vertical motion.

The latter effect is reflected in physical space by a pancake structure, sketched in Fig. 10.5-(bottom) and illustrated in Fig. 10.6, in which isovalues of velocity gradients are obtained from a snapshot of instantaneous DNS data. This layering can be statistically quantified by the development of two different integral length scales, as shown in Fig. 10.7 (from EDQNM2) and Fig. 10.8 (from DNS), with excellent agreement. The integral lengthscale related to horizontal velocity components and horizontal separation $L_{11}^{(1)}$ is shown to develop similarly to isotropic unstratified turbulence, whereas the one related to vertical separation $L_{11}^{(3)}$ is blocked. In the same conditions, with initial equipartition of potential and wave energy, linear calculation (RDT) exhibits no anisotropy, i.e. $L_{11}^{(1)} = 2L_{11}^{(3)}$.

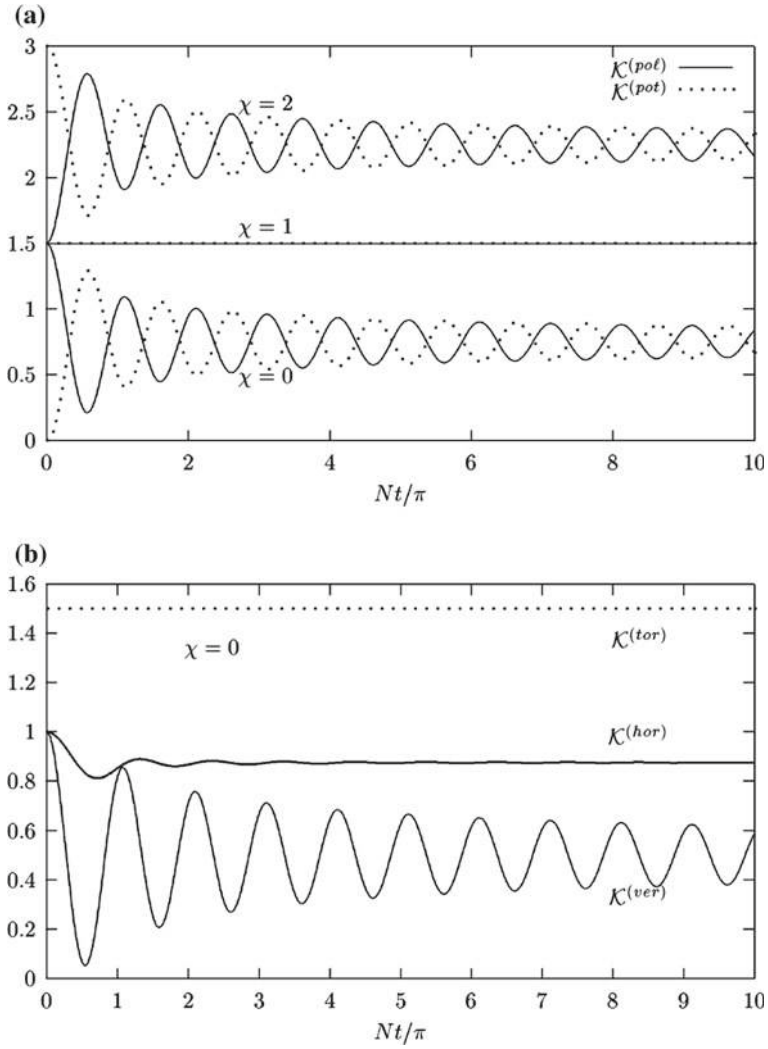

Fig. 10.4 Stable stratification, purely linear inviscid calculation, isotropic initial data with initially unbalanced poloidal/potential energy of ratio χ; The toroidal component remains constant and equal to the initial poloidal component. Reproduced from Salhi and Cambon (2007) with permission of APS

The EDQNM2 procedure was made as simple as possible in Cambon et al. (2007), in order to focus on pure toroidal interactions and to reach very high Reynolds numbers R_e, at low Froude numbers F_r and long elapsed times, a range of parameters not presently accessible to DNS. More details on the equation governing three-point third-order correlations are given in Sect. 10.7.7.

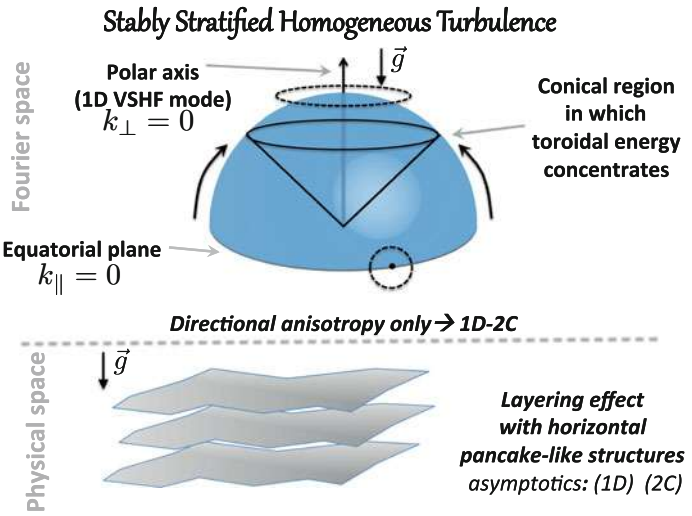

Fig. 10.5 Stable stratification, sketch of the nonlinear cascade (top, angular drain in Fourier space) and (bottom) corresponding layering effect in physical space

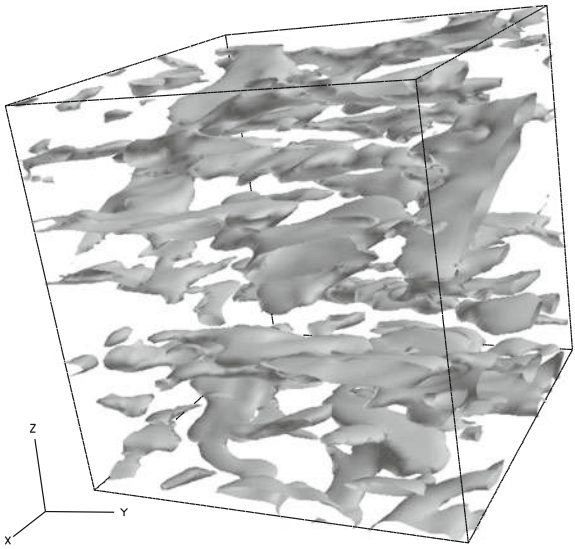

Fig. 10.6 Isovalues of vertical gradient of horizontal velocity fluctuation. Pure stratification. DNS with 256^3 grid points and isotropic initial data. Reproduced from Godeferd and Staquet (2003) with permission of CUP

A typical shape of strongly anisotropic transfer related to $T^{(tor)}(k, \cos\theta)$ in Eq. (10.26) is shown in Fig. 10.9.

Cartoons for different type of interactions, and related cascades, are displayed for sphere-to-sphere and cylinder-to-cylinder energy transfers in Fig. 10.10. Our analysis may suggest an apparent inverse cascade in terms of purely transverse ($k_\perp$) wave vectors, but the fact that the cascade is globally direct is ascertained from different

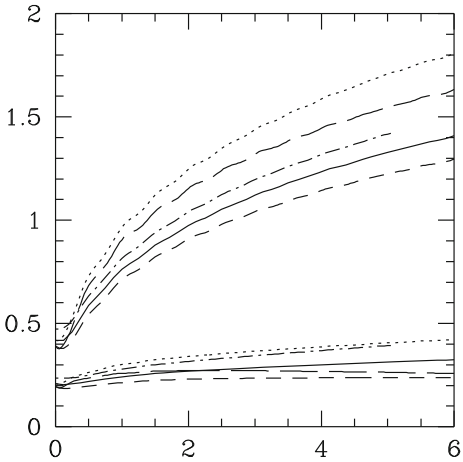

Fig. 10.7 Development of typical integral lengthscales from EDQNM2. $L_{11}^{(1)}$ (top) and $L_{11}^{(3)}$ (bottom), where indices 1 and 3 denote horizontal and vertical directions, respectively. (Initial) isotropy implies $L_{11}^{(1)} = 2L_{11}^{(3)}$. Reproduced from Godeferd and Staquet (2003) with permission of CUP

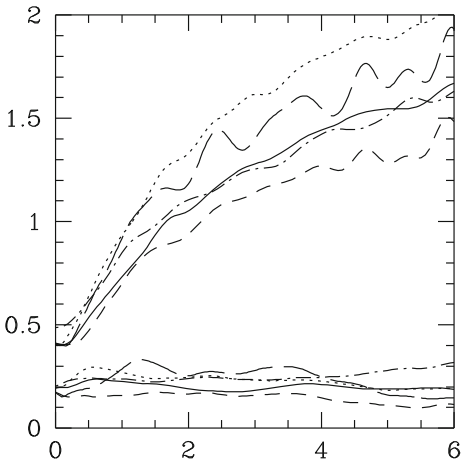

Fig. 10.8 Same as Fig. 10.7, from DNS with 256^3 grid points. Reproduced from Godeferd and Staquet (2003) with permission of CUP

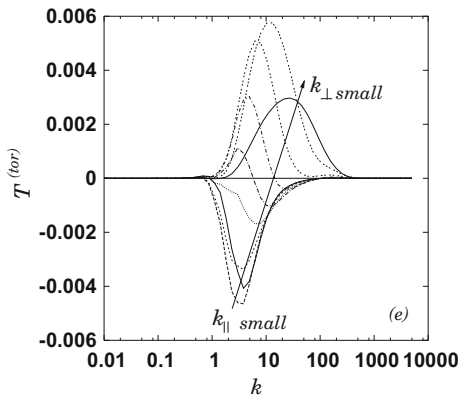

Fig. 10.9 Angle-dependent toroidal transfer term. Each figure displays its k-dependence at a given polar angle $\theta = \widehat{(\boldsymbol{k}, \boldsymbol{n})}$. EDQNM2 results in stably stratified decaying turbulence at initial $Re_\lambda = 145$. Data taken from Cambon et al. (2007)

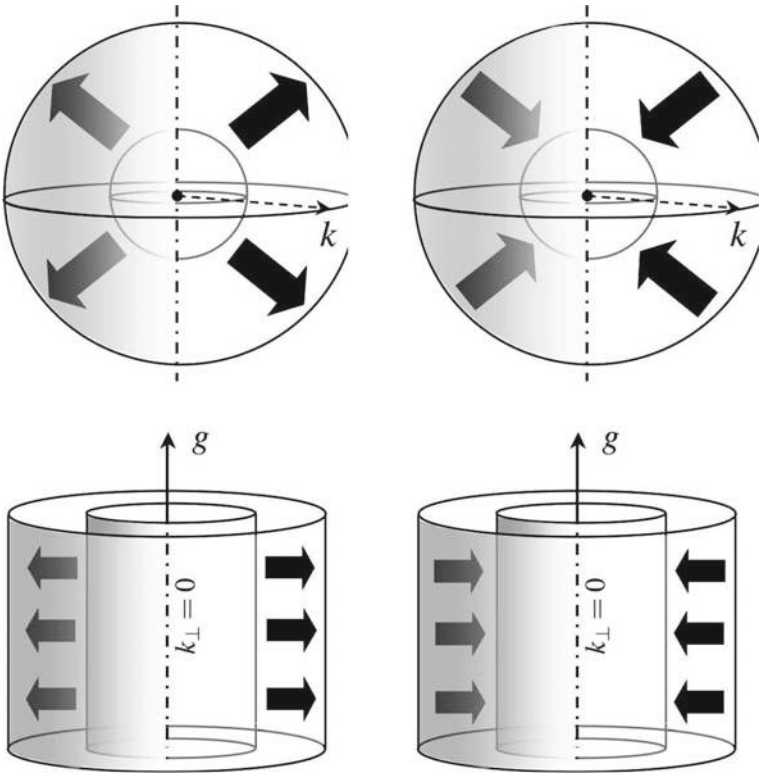

Fig. 10.10 Top: isotropic energy drain in spectral space. Direct (left) and inverse (right) cascade. Bottom: cylinder to cylinder cascade

studies. A similar result was recently supported by forced DNS (Marino et al. 2014) and is further discussed in Chap. 11. Finally, the nonlinear energy transfer in stably-stratified turbulence reconciles the three cartoons: The angular drain in Fig. 10.5, the sketch of "isotropized" cascade in Fig. 10.10-top-left, and the sketch of apparently inverse cascade for horizontal wave vectors in Fig. 10.10-bottom-right.

10.6 Coherent Structures: Dynamics and Scaling of the Layered Flow, "Pancake" Dynamics, Instabilities

10.6.1 Simplified Scaling Laws

Ignoring the detailed anisotropy of the flow, simplified scaling laws seem to be valid looking at results of various numerical and physical experiments. For instance, Lindborg (2006) reported a conventional scaling in DNS/LES in flattened boxes with

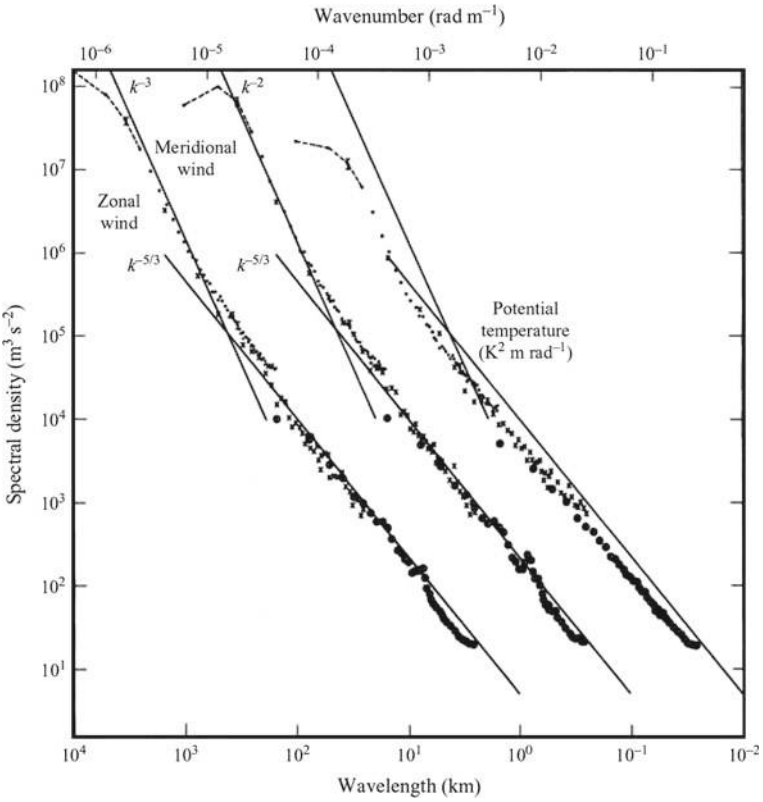

Fig. 10.11 Spectral scalings in (presumably) stratified flows. Reproduced from Nastrom and Gage (1985) and Lindborg (2006) with permission of CUP

the strongest stratification for both horizontal kinetic and potential energy spectra:

$$E_\perp(k_\perp) = C_1 \varepsilon^{2/3} k_\perp^{-5/3}, \quad E^{(pot)}(k_\perp) = C_2 \varepsilon_p \varepsilon^{-1/3} k_\perp^{-5/3}, \tag{10.34}$$

where ε and ε_p are the dissipation rate of kinetic and potential energy, respectively. These scaling laws are consistent with a vertical Froude number close to the unity, equipartition in terms of potential and kinetic energy,[2] and classical estimates by Taylor for lengthscales, as in isotropic flows without stratification. The spectral scalings are apparently consistent with the ones by Nastrom and Gage (1985), as shown in Fig. 10.11. This interpretation was recently radically questioned by high-resolution global DNS (Skamarock et al. 2014), and Coriolis-dependent related scalings by Galperin and Sukoriansky (2017), as discussed in Sect. 7.7.7 in Chap. 7.

[2]The equipartition of kinetic and potential energy is not imposed by dynamical equations, except for linear internal waves.

Keeping the focus on stratified flows only, the numerical method can be questioned, because of under-resolution in the vertical direction (use of a hyperviscosity) and artificial forcing of purely 2D horizontal modes, but the very different simulation by Riley (2003), rediscussed in the next subsection, gives a similar scaling. Such a scaling was expected but not observed in a recent experiment by Praud et al. (2005), — Adam Fincham attributes this to the Reynolds number being too low — carried out in the large Coriolis tank filled of salted water (without rotation here, the cases with additional rotation are addressed in the next chapter), turbulence being generated by a moving rake.

10.6.2 Pancake Structures, Zig-Zag and Kelvin–Helmholtz Instabilities

The fact that conventional scaling laws are recovered, in a very similar way to what is found in isotropic turbulence without stratification, seems to contradict the highly anisotropic organisation of the strongly stratified flow. This anisotropic organisation can be quantified using various statistical indicators, from single-point correlations to two-component spectra such as the ones presented in Godeferd and Staquet (2003), Liechtenstein et al. (2005). It is linked to anisotropic structures which are identified in DNS snapshots, via iso-velocity-gradient surfaces. Pancake structures were identified from a long time in pseudo-spectral DNS (Kimura and Herring 1996). More recently, it was shown that the horizontal layering with pancake structures essentially modifies the toroidal part of the flow, whereas the poloidal part remained apparently almost isotropic, regarding its angular dependence. Angle-dependent spectra $\mathcal{E}^{(tor)}(k, \cos\theta)$ and $\mathcal{E}^{(pol)}(k, \cos\theta)$ calculated from DNS give a consistent, more quantitative, information. The whole result, in both physical (see Fig. 10.13) and spectral space (see Fig. 10.12), confirms the cartoon displayed in Fig. 10.5, but restricted to the sole toroidal component of the flow.

It is worth noting that in actual flows internal waves would not be expected to be isotropic. The reason why is that some of them are generated by the adjustment of the toroidal modes (cyclostrophic adjustment), some can be affected by the toroidal shear, while others can undergo the resonant wave/vortex interaction (see Lelong and Riley 1991). The latter was reported to be important in numerical simulations in Bartello (1995).

Another type of more specific structures results from the zig-zag instability. Such instabilities were firstly identified in the presence of vertical columnar structures moving horizontally in a stratified tank. A typical tangling motion develops in the horizontal direction perpendicularly to the main motion of eddies, with typical velocity U, breaking their vertical coherence with a typical length scale U/N. In addition to the case of a pair of counter-rotating eddies, advancing with almost constant velocity due to mutual induction, the case of co-rotating eddies was investigated (Otheguy et al. 2006). In the latter case, mutual induction results in circular motion and tangling

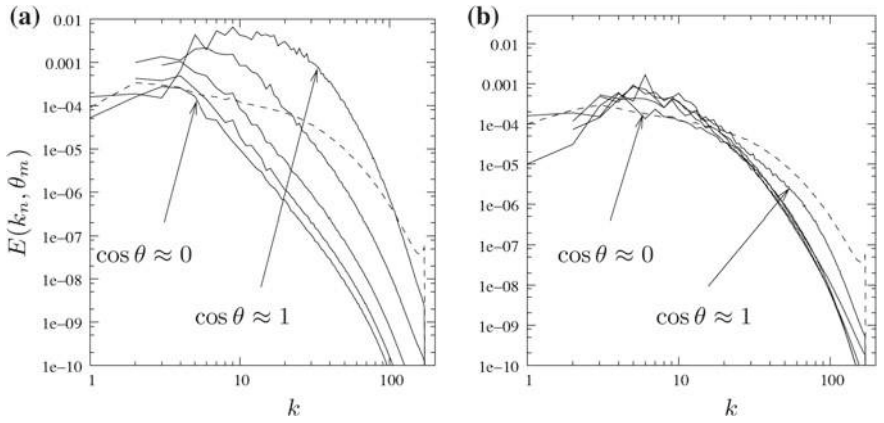

Fig. 10.12 Angle-dependent spectra, toroidal (left) and poloidal (right) energy. High resolution DNS of strongly stratified flow. Courtesy of L. Liechtenstein

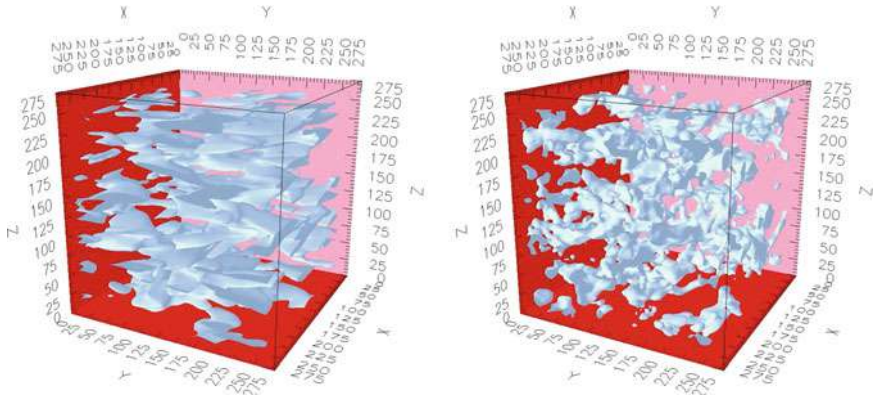

Fig. 10.13 Iso-enstrophy surfaces (snapshot), using only the toroidal (left) and the poloidal (right) contribution from the fluctuating velocity field. High resolution DNS of strongly stratified flow. Courtesy of L. Liechtenstein

zig-zag motion develops in the radial direction. This instability was proposed as a generic mechanism to create the layering with an universal scaling U/N in strongly turbulent stratified flow (Billant and Chomaz 2001). This assumption is probably too simple. On the one hand, the zig-zag instability requires the presence of prexisting coherent vortices with vertical length much larger than U/N: in some experiments, in which a moving rake favours 2D structuring, the zig-zag motion is recovered (Praud et al. 2005), but it is not found in other ones with smaller dimension (Peter Davidson, experimental study in progress), in which turbulence is generated by a grid with not a too large mesh. On the other hand, even in the presence of an array of vertical 2D vortices, significant horizontal velocity U must result from translational or rotational motion of eddies: for instance, the zig-zag instability is inhibited if the base flow is

the 2D Taylor-Green flow, or Taylor's "four rollers mill", in which all degrees of freedom are blocked by mutual induction of vortices.

A more promizing type of instability is of Kelvin–Helmholtz type and can result from the intense vertical shearing between pancake layers. Such structures do not appear in the fully 3D DNS (in cubic boxes) of decaying stratified turbulence by Liechtenstein et al. (2005) because the moderate Reynolds number probably limits the shearing process. For a different reason, because of the unsufficient vertical resolution, they hardly appear in the DNS/LES with flattened computational domains (Lindborg 2006).

Only in the DNS by Riley and coworkers, significant occurence is found for such Kelvin–Helmholtz instabilities, as shown in Fig. 10.14.

The resolution of these DNS (which can be considered as really 3D) is comparable to the ones by Liechtenstein et al. (2005), but largest structures are initialized by a network of 3D Taylor-Green vortices, allowing for a much larger Reynolds number.

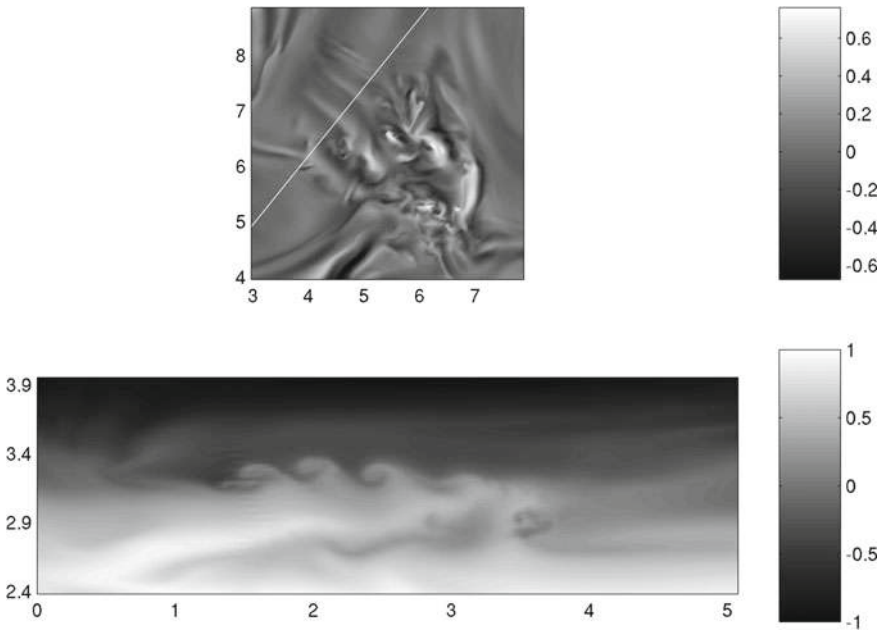

Fig. 10.14 Top panel shows part of a horizontal slice through the w field. The white dashed line gives the orientation of a vertical slice through the horizontal plane. The bottom panel shows ρ_T on that vertical slice. Reproduced from Riley (2003) with permission of AIP

It has been suggested for a long time that a stability criterion, such as the one of Miles (1961), i.e. $R_i = N^2/S^2 \sim 1/4$, can control the "efficient" local shear S. More generally, Riley (2003) introduced the nondimensional number

$$R_b = F_r^2 Re,$$

referred to as the *buoyancy efficiency parameter*, to identify a régime of strongly turbulent and strongly stratified flows characterized by $R_b > 1$, capable of developing strong inter-layer shearing. The latter threshold was recently rediscovered by Brethouwer et al. (2007), with relevant application to their DNS, even if probably under-resolved in the vertical direction. In Fig. 10.15, several DNS results are plotted on a diagram in terms of both Reynolds number and inverse of the horizontal Froude number from Eq. (10.2).

The parameter R_b is almost equivalent to the parameter $\epsilon/(\nu N^2)$, which is called the *activity parameter* or the *buoyancy Reynolds number* by oceanographers. Bill Smyth and Jim Riley (private) suggest that this parameter must be greater than about 20 for the flow to sustain turbulence.

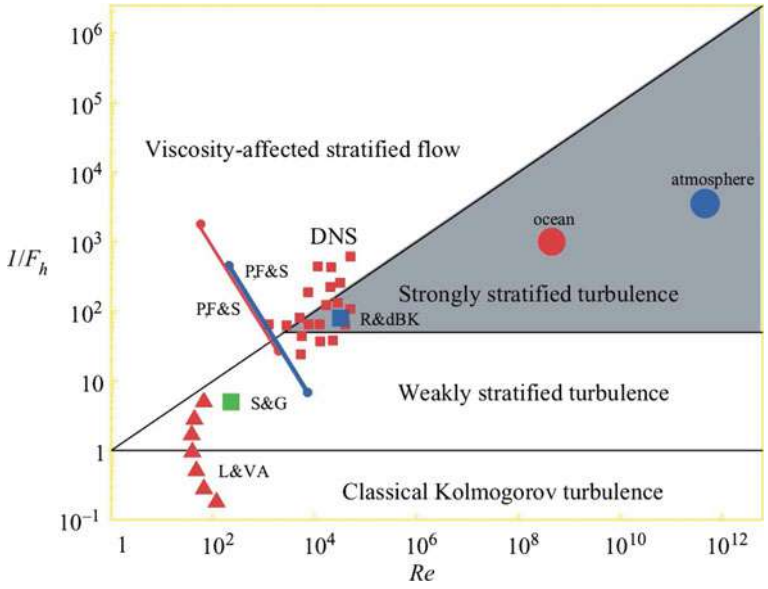

Fig. 10.15 Different domains for weakly statified and strongly stratified turbulent flows, in term of the Reynolds number (horizontal axis) and the inverse of the vertical Froude number (vertical axis). F_h on the figure denotes the horizontal Froude number, or $Fr_\perp$ in Eq. (10.2). Scheme adapted from Brethouwer et al. (2007). Courtesy from Alex Delache

10.7 Unstable Stratified Homogeneous Turbulence

10.7.1 Generals

10.7.1.1 From Stable to Unstable Quasi-homogeneous Turbulence

There are several studies of stable stratification with geophysical applications, and less in the unstable case. The context of baroclinic instability can be found with a stabilizing mean buoyancy gradient, but, as revisited in Chap. 11, the presence of combined effects of rotation and mean shear can yield an additional horizontal mean buoyancy gradient: In this case the mean isopycnes are no longer horizontal and their tilting induces an exponential instability, called baroclinic- or symmetric-instability depending on the context. But the simplest pattern for the unstable stratification is obtained with horizontal isopycnes in changing the sign of the vertical mean buoyancy gradient, e.g. in Fig. 10.1-left. This configuration is found in the turbulent mixing layer resulting from the Rayleigh–Taylor instability, when a heavy fluid is suddenly placed above a light one. The development of such a mixing zone is illustrated by DNS in Fig. 10.16. In other words, mean horizontal isopycnes are recovered after a complete turnover of the mean flow pattern (vs. the stable case), corresponding to a tilting of 180 degrees, whereas a rather low tilting angle (vs. horizontal direction) is sufficient for triggering a baroclinic-type instability.

The multiform physical context is illustrated by different observations and applications: Atmospheric context, local convection under mammatus clouds; astrophysical context, with collapse of star and supernova (Cook and Cabot 2006); oceanographic

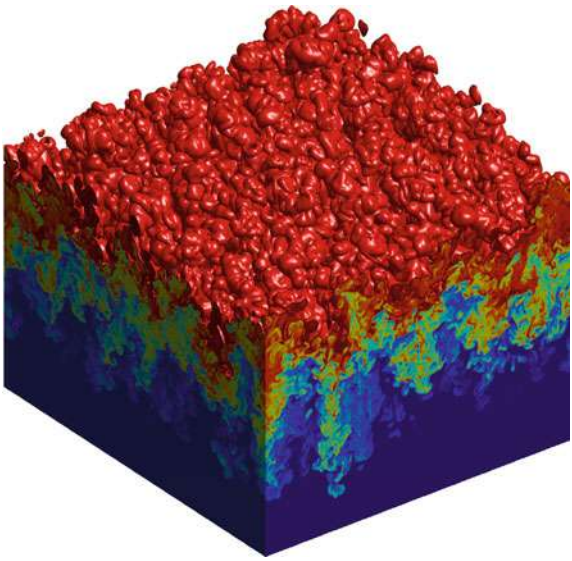

Fig. 10.16 Visualization of the instantaneous mixing layer from R-T instability, by iso-concentration surfaces. DNS from the TRICLADE numerical code. Reproduced from Cambon and Gréa (2013) with permission of T and F

context, with sinking of cold waters in thermo-hyaling circulation; nuclear fusion by inertial confinement. A good overview is given by Sharp (1984).

10.7.1.2 The Framework of Unstably Stratified Homogeneous Turbulence, at Fixed N

Basic equations for velocity, buoyancy and reduced pressure fluctuations are derived from Eqs. (10.3) and (10.4), by only changing the sign of the square of the stratification parameter N. As for the stable case, only the Prandtl or Schmidt number χ/ν distinguishes cases with different stratifying agents (density, temperature, salinity): it will be taken equal to 1 in the following. Equations for two-point second-order correlations are derived for a state vector in four components, by virtue of axisymmetry with mirror symmetry: The second-order spectral tensor of velocity correlations reduces to toroidal $\frac{1}{2}(\mathcal{E} - Z)$) and poloidal $\frac{1}{2}(\mathcal{E} + Z)$ energy spectra, Z being purely real, the spectrum of the buoyancy variance reduces to a spectrum of potential energy $\mathcal{E}^{(pot)}$, and the cross-correlation between velocity and buoyancy reduces to a co-spectrum of poloidal buoyancy flux Ψ.

Equations (10.30), (10.31), (10.32) and (10.33) are modified in the unstable case by changing the sign of N in the first two ones and in changing the sign of the poloidal term $\frac{1}{2}(\mathcal{E} + Z)$ in the latter. Examples of evaluation of N in geophysical flows are obtained by changing the sign of the mean gradient, be density (liquid) or temperature (gas). A very recent application of USHT (Unstably Stratified Homogeneous Turbulence) addressed the dynamics of the mixing zone induced by Rayleigh–Taylor instability, when turbulence is sufficiently developed to permit a quasi-homogeneous approach, with a given value of N (Burlot et al. 2015a). As in the stable case, N is still called stratification frequency, even if temporal oscillations are replaced by an exponential growth. The buoyancy variance, divided by N^2, is again coined as potential energy, even if this terminology is less obvious than in the stable case. In the linear inviscid limit, it is found that both poloidal and potential energy spectra are affected by the same exponential growth $\exp(2Nt\frac{k_\perp}{k})$. Even if the total energy is not conservative, we conserve the zero integral over $\boldsymbol{k}$ of the sum $T^{(\mathcal{E})} + T^{(pot)}$. The nonlinear flux term $T^{(F)}$ has not zero integral; it is possible, however, to disentangle in it a conservative part (with zero integral) and a part of pressure-strain rate type, as for $T^{(Z)}$ in the shear-driven flow case.

10.7.1.3 Dynamical Trends, Dominant Modes

Development of two-dimensional structures is very different of what it is found in rotating or in quasi-static Magnetohydrodynamics flows, because the velocity field is organized into up and down vertical "jettal" (as a crude sketch), rather than vertical "vortical" structures, in the mixing zone. More precisely, these structures have vorticity, but it is rather horizontal than vertical. Density structures are elongated

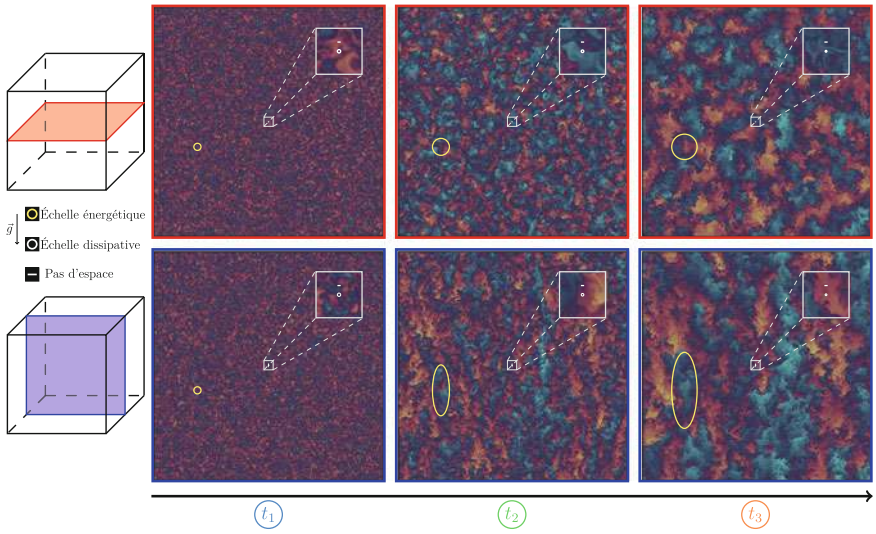

Fig. 10.17 Visualization of results from 2048^3 pseudo-spectral DNS in tri-periodic box with constant N at three different elapsed times, started with isotropic initial data. Top: Cross-section in an horizontal plane, showing apparent isotropy (axisymmetry) and growth of structures. Bottom: Cross-section on a vertical plane, showing the increasing elongation of structures in the vertical direction. Details of DNS (but without this figure) are in Gréa et al. (2016). Courtesy from Benoît-Joseph Gréa and Alan Burlot

in the vertical direction as well. They consist in physical space of "spikes" for the downward heavy fluid and "bubbles" for the upward light fluid. Asymmetry between spikes and bubbles is only significant at large Atwood numbers (see Sect. 10.8). In our homogeneous approach (USHT), velocity structures are shown in Fig. 10.17, from high resolution DNS, with a dramatic growth of the large-scale Reynolds number, from about 20 initially to about 5000 at the final time. Their typical anisotropic signature is reflected by dominant poloidal component rather concentrated at small $k_\parallel/k$ spectral directions, at largest scales. Directional anisotropy is therefore qualitatively similar to what is found in rotating or in Quasi-Static Magnetohydrodynamics flow cases, but polarization anisotropy is opposite, as shown in Fig. 10.18.

This corresponds to the two spectral sketchs of Fig. 2.5 giving a "cigar" contribution to the Reynolds stress tensor, and is quantified by Fig. 10.23 for directional anisotropy.

10.7.2 Description and Modelling of Anisotropic USHT

All the rest of the present Sect. 10.7 is devoted to results from statistical models matching RDT and EDQNM. USHT gives the best illustration of the strategy by

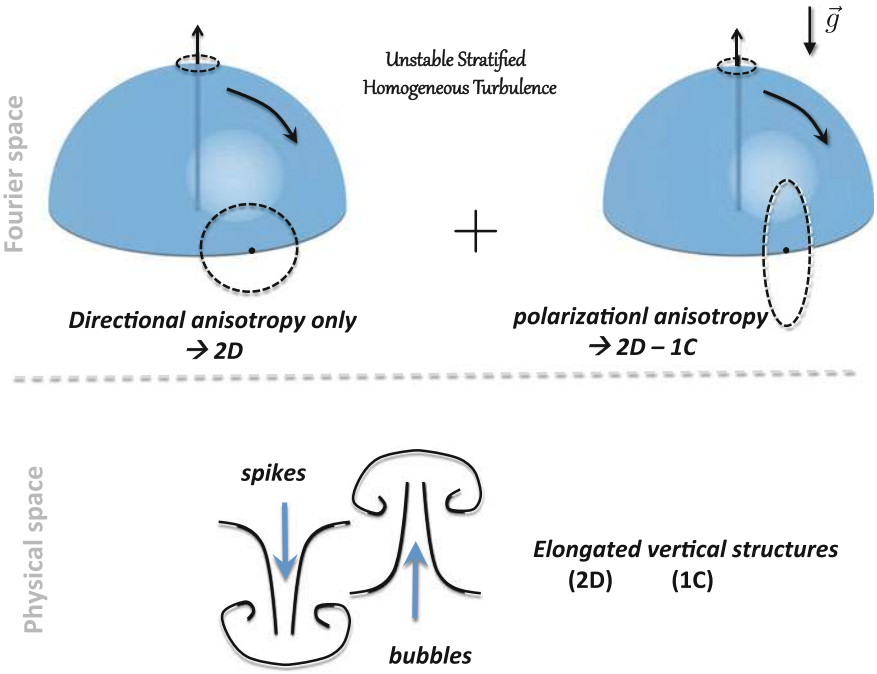

Fig. 10.18 Sketch of the anisotropy created in USHT for the velocity field. A similar trend is found for the scalar field, but only directional anisotropy (top-left) is relevant

Table 10.1 Description of anisotropy at the velocity, scalar and scalar flux levels, using $\boldsymbol{k}$-vectors descriptors and their corresponding spherically-averaged contributions.

	Spherically averaged descriptors		
$\boldsymbol{k}$-vectors descriptors	Isotropy	Directional anisotropy	Polarization anisotropy
$\mathcal{E}(\boldsymbol{k},t)$	$E(k,t)$	$H_{ij}^{(dir)}(k,t)$	0
$Z(\boldsymbol{k},t)$	0	0	$H_{ij}^{(pol)}(k,t)$
$\mathcal{E}^{(pot)}(\boldsymbol{k},t)$	$E^{(pot)}(k,t)$	$H_{ij}^{(pot)}(k,t)$	0
$F_i(\boldsymbol{k},t)$	0	0	$E_i^{(F)}(k,t)$

Burlot et al. (2015a), Burlot et al. (2015b), that is to cross-validate DNS and generalized EDQNM at the highest Reynolds numbers permitted by DNS, and then to use only EDQNM at far higher Reynolds numbers and elapsed times. The problem of anisotropic description of two-point second-order statistics is addressed at two different levels of description, as recalled in the Table 10.1. The anisotropic description of shear-driven flows and the one of buoyancy-driven flows are unified, following (Cambon et al. 2017).

This table extends the preceding one for the velocity (2.5) to the coupled flow case with scalar, passive (e.g. Briard et al. 2016) to active (buoyancy Briard et al. 2017).

For any angle-dependent potential energy spectrum $\mathcal{E}^{(pot)}$ and related scalar flux, it is possible to extract the related spherically-averaged descriptors $E^{(pot)}$, $H_{ij}^{(pot)}$ and E_i^F.

$$\iint_{S_k} \mathcal{E}^{(pot)}(\boldsymbol{k},t)d^2\boldsymbol{k} = E^{(pot)}(k,t), \tag{10.35}$$

$$\iint_{S_k} \sin^2\theta \mathcal{E}^{(pot)}(\boldsymbol{k},t)d^2\boldsymbol{k} = \frac{2}{3}E^{(pot)}(k,t) + 2E^{(pot)}(k,t)H_{33}^{(pot)}(k,t), \tag{10.36}$$

and

$$\int_{S_k} F_3(\boldsymbol{k},t)d^2\boldsymbol{k} = E_3^F(k,t). \tag{10.37}$$

Conversely, it is possible to reconstruct a part of the fully anisotropic spectral tensors by means of these spherically-averaged descriptors, with

$$\mathcal{E}^{(pot)}(\boldsymbol{k},t) = \frac{E^{(pot)}(k,t)}{4\pi k^2}\left(1 - \frac{15}{2}\left(3\cos^2\theta - 1\right)H_{33}^{(pot)}(k,t)\right). \tag{10.38}$$

Note that polarization has no meaning for a scalar, so that $H_{33}^{(pot)}$ only characterizes directional anisotropy. Finally, a similar expansion applied to the flux term yields

$$F_3(\boldsymbol{k},t) = -\sin\theta\Psi(\boldsymbol{k},t) = \frac{3}{2}\sin^2\theta E_3^F(k,t), \tag{10.39}$$

in which F_3 denotes the vertical component of the buoyancy flux, in agreement with a general (non-axisymmetric) scalar flux vector F_i used in Briard et al. (2016) as well.

Only the axisymmetric case is considered in former expansions, that are truncated in terms of the first relevant angular harmonics, because their application will be restricted to USHT consistent with axisymmetry. For the sake of completeness, their counterpart is given for $\mathcal{E}$ and Z as follows (see Eqs. (8.44) and (8.45) for more general non-axisymmetric expansions).

$$\mathcal{E}(\boldsymbol{k},t) = \frac{E(k,t)}{4\pi k^2}\left(1 - \frac{15}{2}\left(3\cos^2\theta - 1\right)H_{33}^{(dir)}(k,t)\right) \tag{10.40}$$

and

$$Z(\boldsymbol{k},t) = \frac{15}{4}\frac{E(k,t)}{4\pi k^2}\sin^2\theta H_{33}^{(pol)}(k,t), \tag{10.41}$$

from $H_{ij} = \frac{1}{2}\left(3\delta_{i3}\delta_{j3} - \delta_{ij}\right) H_{33}$, with θ the polar angle of $\boldsymbol{k}$ versus the vertical direction, referred to index 3.

About closure strategy, two successive models were applied. The first one is applied to the system of equations for $\mathcal{E}$,Z, $\mathcal{E}^{(pot)}$, Ψ, without assumption on the angular dependence of spectra and co-spectra. As in the system of Eqs. (10.30)–(10.33), their linear left-hand-sides are exact, and their nonlinear contributions are closed by the generalized EDQNM1 model, with details in Sect. 10.7.7. This model is referred to as USHT-EDQNM (Burlot et al. 2015a). In line with the strategy by Mons et al. (2016), a simpler model (with reduced cost and memory-size) in terms of the spherically-averaged descriptors only is readily derived by reinjecting Eqs. (10.38)–(10.41) in the previous model. This model is referred to as USHT-EDQNM-S (S for spherically-averaged descriptors). To do justice to the model by Briard et al. (2017), it can extend the one by Mons et al. (2016), incorporating effects of mean velocity gradients as well, and it is not restricted to axisymmetry, even though only shearless axisymmetric applications will be considered in the present Sect. 10.7.

10.7.3 Time-Evolution of Global Quantities and Exponential Growth Régime

Both DNS and generalized EDQNM at the highest Reynolds numbers predict the existence of a régime characterized by an exponential growth of turbulent kinetic energy, as in the pure shear case (Burlot et al. 2015a). The transient stage before this regime is reached depends on the initial condition. Typical time evolution of the turbulent kinetic energy $\mathcal{K}(t)$, the Froude number $Fr(t) = \varepsilon(t)/N\mathcal{K}(t)$ and the mixing parameter $\Lambda(t) = \mathcal{K}^{(pot)}(t)/\mathcal{K}(t)$ are displayed in Fig. 10.19. The rise of the expected self-similar state is clearly seen, and a very good agreement between DNS and anisotropic EDQNM is observed. Much more results are found in Burlot et al. (2015b), including a parametric analysis of the influence of the infrared slope

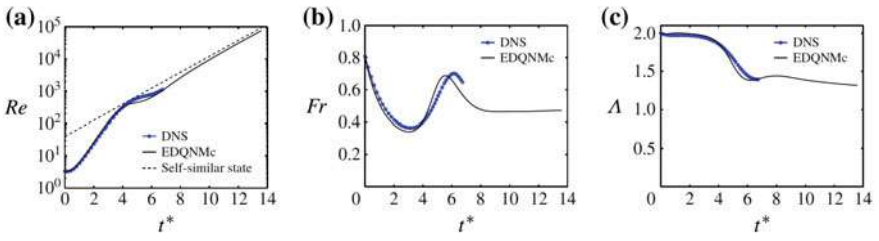

Fig. 10.19 Time evolution of turbulent kinetic energy $\mathcal{K}(t)$, Froude number $Fr(t)$, and ratio of kinetic to potential energy, from DNS and USHT-EDQNM using the N-correction of Eq. (10.57), denoted EDQNMc. Reproduced from Burlot et al. (2015a) with permission of CUP

σ of the initial energy spectrum ($E(k \to 0, t = 0) \sim k^{\sigma}$). The simple relationship by Soulard et al. (2014) for the corrected exponential growth $e^{\alpha' Nt}$ of the kinetic energy is

$$\alpha' = \frac{\log \mathcal{K}(t)}{Nt} = \frac{4}{\sigma + 3}. \tag{10.42}$$

It is worth noting that, even though both homogeneous shear turbulence and unstable stratified homogeneous turbulence exhibit an asymptotic exponential growth of turbulent kinetic energy, there is an important difference between these two cases. The exponential growth rate does not depend on the infrared slope σ in the former, it is governed by this parameter in the later.

Both the Froude number and the mixing coefficient converge toward constant asymptotic values during the exponential growth regime, whose values depend on the infrared slope σ. It is observed that an increase in σ leads to an increase in Fr and a decrease in Λ and in the growth rate α'. Asymptotic values of these parameters do not depend on N.

10.7.4 Spectra in the Exponential Growth Régime

Universal inertial ranges appear in spectra during the exponential growth regime if the Reynolds number is large enough. Typical results are displayed in Fig. 10.24 for the turbulent kinetic energy spectrum $E(k, t)$, the scalar variance spectrum $E^{(pot)}(k, t)$ (scaled as a potential energy) and the vertical buoyancy flux spectrum $F_3(k, t)$.

Both $E(k)$ and $E^{(pot)}(k)$ exhibit an inertial range with a –5/3 slope, while a –7/3 slope is detected for the cospectrum $F_3(k)$. These results are in agreement with a classical Kolmogorov-type analysis. An interesting result is that the peaks of the three spectra evolve as k^{-3} with increasing Nt (Briard et al. 2016, 2017). This can be recovered using the following heuristic rationale. Denoting $E_{max}(t)$ the maximum value of $E(k, t)$, dimensional analysis yields $E_{max}(t) \sim \mathcal{K}(t)L(t)$ along with $L(t) \sim \mathcal{K}^{3/2}(t)/\varepsilon(t)$. In the asymptotic exponential growth regime, one has $\mathcal{K}(t) \propto \exp(\alpha' Nt)$ and $\varepsilon(t) \propto \exp(\alpha' Nt)$, leading to $L(t) \propto \exp(\alpha' Nt/2)$. Therefore one obtains $E_{max}(t) \propto \exp(3\alpha' Nt/2)$. Now assuming that $E_{max}(t)$ occurs at wave number $k_L \sim 1/L$, time t can be eliminated since $t \sim -2\log(k_L)/\alpha' N$, yielding

$$E_{max}(t) \sim k_L^{-3}.$$

The slope of spectrum of the polarization-induced anisotropic correction to the vertical Reynolds stress spectrum $\hat{R}_{33}(k)$ is still controversial. Both –3 and –7/3 values have been proposed in Burlot et al. (2015b) and Briard et al. (2017), respectively. DNS results are still not accurate enough to make a final conclusion (Fig. 10.20).

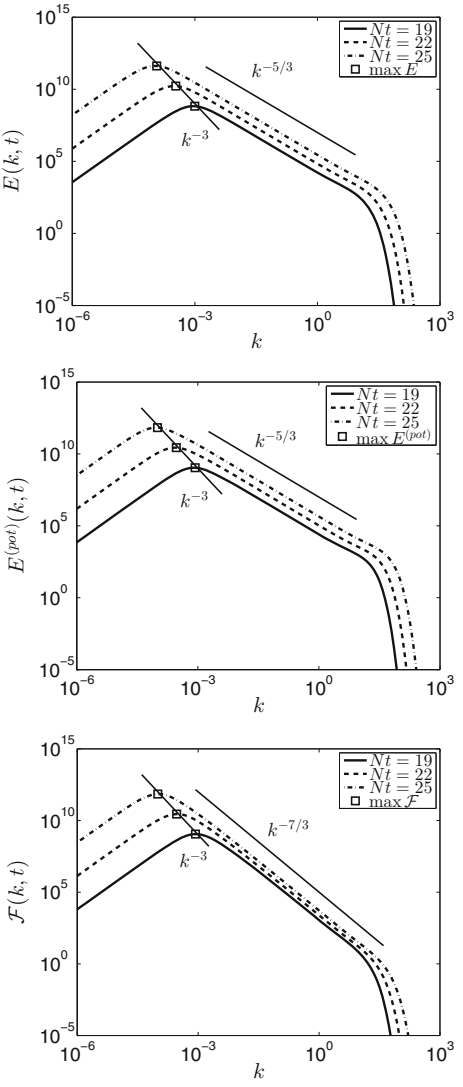

Fig. 10.20 Spectra in high-Reynolds Unstable Stratified Homogeneous Turbulence at different times. Top: kinetic energy spectrum $E(k,t)$ represented via the turbulent Reynolds number $Re = \mathcal{K}^2/\nu\varepsilon$; Middle: scalar variance spectrum $E^{(pot)}(k,t)$; bottom: vertical buoyancy flux cospectrum $\mathcal{F}(k,t) = F_3(k,t)$. USHT-EDQNM-S model. Reproduced from Briard et al. (2017) with permission of APS

10.7.5 Anisotropy in the Exponential Growth Régime

Anisotropy can be first investigated looking at Reynolds stress anisotropy b_{33} and the scalar anisotropy indicator $b_{33}^{(pot)}$, where $b_{ij}^{(pot)}(t)$ is defined as

$$b_{ij}^{(pot)}(t) = \frac{1}{\mathcal{K}^{(pot)}} \int_0^{+\infty} E^{(pot)}(k,t) H_{ij}^{(pot)}(k,t) dk. \tag{10.43}$$

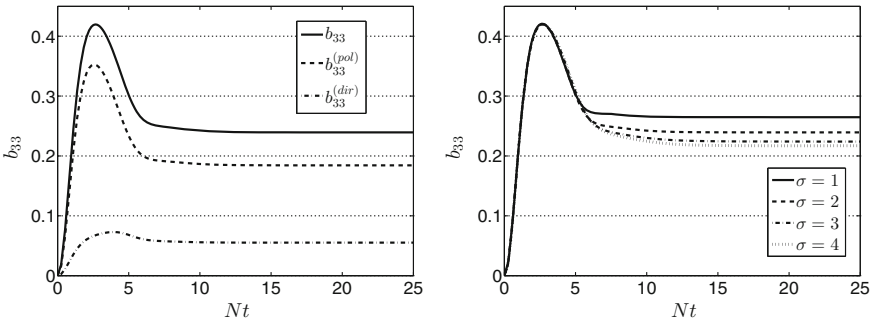

Fig. 10.21 Vertical Reynolds stress anisotropy b_{33} in high-Reynolds Unstable Stratified Homogeneous Turbulence. Left: time evolution of $b_{33}(t)$, its polarization component $b_{33}^{(pol)}(t)$ and its directional component $b_{33}^{(dir)}(t)$; Right: Time evolution of $b_{33}(t)$ for different values of the initial infrared slope σ of $E(k, t = 0)$. USHT-EDQNM-S model. Adapted from Briard et al. (2017) with permission of APS. Courtesy of A. Briard

It is worth noting again that $H_{ij}^{(pot)}(k, t)$ reflects directional anisotropy only (Table 10.1). Results dealing with b_{33} and its polarization and directional components are displayed in Fig. 10.21. The large-scale anisotropy is contributed by large positive polarization and directional component, which is the footprint of vertically elongated structures with a dominance of the vertical velocity component. Such structures can be referred to as vertical jets or vertical plumes. It is observed that b_{33} converges toward a constant value during the exponential growth stage, which is dominated by the polarization anisotropy and whose exact value depends on the kinetic energy spectrum infrared slope σ. Similar results are obtained for $b_{33}^{(pot)}$: an asymptotic constant value is observed, that depends on the features of the initial condition at very large scales. As a matter of fact, asymptotic values of both b_{33} and $b_{33}^{(pot)}$ are decreasing values of σ and are not sensitive to N.

A deeper insight can be gained looking at scale-by-scale anisotropy. This is first done looking at the spectral anisotropy descriptors $H_{ij}^{(pol)}$ and $H_{ij}^{(dir)}$. It is reminded that

$$\varphi_{ij}(k, t) = \iint_{S_k} \hat{R}_{ij}(\boldsymbol{k}, t) d^2\boldsymbol{k} = 2E(k, t) \left(\frac{\delta_{ij}}{3} + H_{ij}^{(pol)}(k, t) + H_{ij}^{(dir)}(k, t) \right).$$

Results for $H_{33}(k, t) = H_{33}^{(pol)}(k, t) + H_{33}^{(dir)}(k, t)$ and its two components are displayed in Fig. 10.22. It is seen that anisotropy is governed by polarization anisotropy at all scales, and is almost null for scales smaller than the Taylor microscale. Anisotropy at the Ozmidov scale (further Eq. (10.47)) is very small, but not negligible.

Fully directional anisotropy can be better understood considering the scale-by-scale distribution of directional parameters, using the angle-dependent USHT-EDQNM model. Directional anisotropy for the fluctuating velocity field is

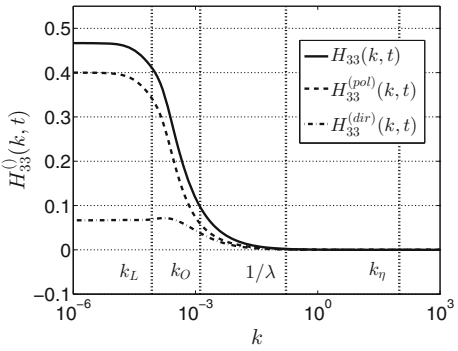

Fig. 10.22 Spectral decomposition of scale-by-scale anisotropy of the vertical Reynolds stress anisotropy in high-Reynolds Unstable Stratified Homogeneous Turbulence. Adapted from Briard et al. (2017) with permission of APS. USHT-EDQNM-S model. Courtesy of A. Briard

characterized by the global angular coefficient (to be compared to the angular term by Moreau or Shebalin in MHD, see Chap. 12)

$$\sin^2\gamma_u = \frac{\iiint \sin^2\theta_k \mathcal{E}(\boldsymbol{k},t)d^3\boldsymbol{k}}{\iiint \mathcal{E}(\boldsymbol{k},t)d^3\boldsymbol{k}}. \tag{10.44}$$

Its scale-by-scale distribution, expressed as $\sin^2\gamma_u(k)$, exactly corresponds to

$$\sin^2\gamma_u(k,t) = \frac{2}{3} + 2H_{33}^{(dir)}(k,t). \tag{10.45}$$

A similar parameter is calculated for the directional anisotropy of the scalar spectrum of the variance of concentration,

$$\sin^2\gamma = \frac{\iiint \sin^2\theta_k \mathcal{E}^{(pot)}(\boldsymbol{k},t)d^3\boldsymbol{k}}{\iiint \mathcal{E}^{(pot)}(\boldsymbol{k},t)d^3\boldsymbol{k}}, \tag{10.46}$$

with its scale by scale distribution calculated as well.

The asymptotic values for the directional parameter, $\sin^2\gamma_u$ or $\sin^2\gamma$, is 1 for 2D structure, 0 for 1D structure (as for the VSHF mode that is the relevant limit for the stable case, see also Fig. 10.5), and 2/3 for 3D isotropy.

Typical results, at very high Reynolds number unreachable by DNS at their highest resolution 2048^3 and highest elapsed time are plotted in Fig. 10.23 for various values of infrared slope of the initial energy spectrum, σ. The role of the Ozmidov wavenumber

$$k_O = 2\pi\sqrt{\frac{N^3}{\varepsilon}}, \tag{10.47}$$

as a threshold for restoring isotropy (dashed line, right) at smallest scales is confirmed, especially for the velocity. Note that the complete re-isotropization shown in top-right is found only at huge Reynolds numbers, whereas anisotropy persists for wavenumbers larger than k_O at smaller (but large anyway) Reynolds numbers, with

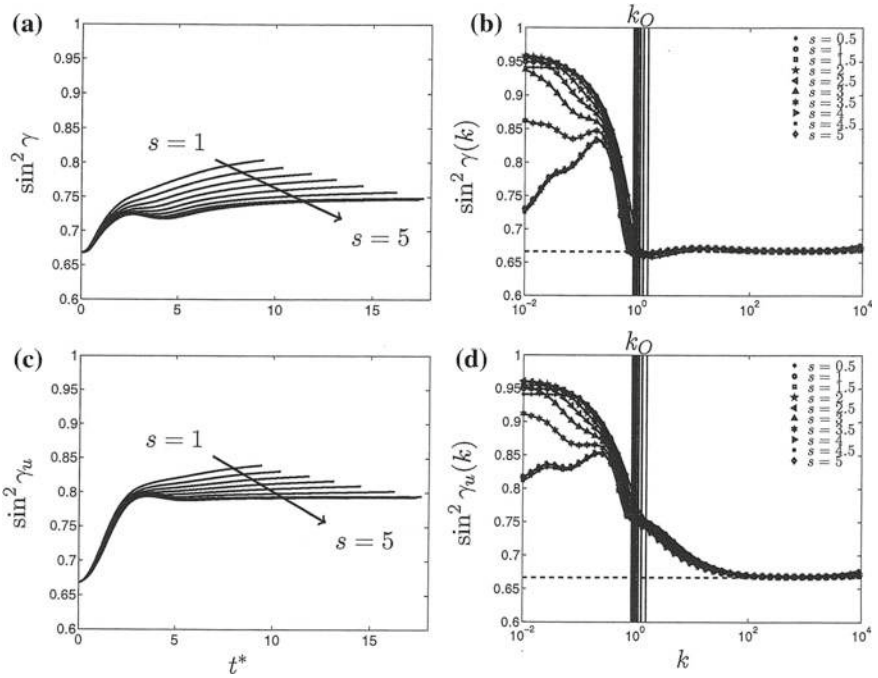

Fig. 10.23 Distribution of the parameter of directional anisotropy for both velocity and concentration. Left: Temporal evolution of the global parameter $\sin^2\gamma$ (top) and $\sin^2\gamma_u$ (bottom). Right: scale-by-scale distribution. Reproduced from Burlot et al. (2015b) with permission of AIP

complete accordance between DNS and EDQNM. The persistence of anisotropy for the velocity at k's larger than the Ozmidov's threshold, and not the buoyancy, is not completely explained. On the other hand, the dependence with respect to s and the distribution of largest scales is completely consistent for velocity (bottom) and buoyancy (top). The tendency to reach the 2D limit is found for the large scales, only for the smallest σ, in agreement with a dominant effect of RDT. In the other cases, especially with non-monotonic distribution of largest scales, nonlinear effects, probably of backscatter-type, compete with RDT mechanisms.

10.7.6 Pressure Field

The pressure field can be computed in the same was as for previous incompressible flows cases, e.g. the homogeneous shear case discussed in Sect. 9.7, i.e. starting from the Poisson equation derived from the momentum equation. In the present case, it reads

$$-\nabla^2 p' = \frac{\partial^2}{\partial x_i \partial x_j}(u_i u_j) + \lambda_i \frac{\partial c}{\partial x_i}, \tag{10.48}$$

where $\lambda_i = \frac{\partial C}{\partial x_i}$ denotes the mean scalar gradient, as in Eq. (10.6). Following the same procedure as in Sect. 9.7 and still using the Quasi-Normal hypothesis to close the fourth-order velocity correlation term, one obtains for the three-dimensional pressure spectrum defined as

$$\mathcal{E}_p(\boldsymbol{k}, t)\delta(\boldsymbol{k} - \boldsymbol{p}) = \overline{\hat{p}(\boldsymbol{k}, t)\hat{p}^*(\boldsymbol{p}, t)}, \tag{10.49}$$

which appears as the sum of an isotropic and an anisotropic component (Briard et al. 2017)

$$\mathcal{E}_p(\boldsymbol{k}, t) = \underbrace{2\frac{k_i k_j k_l k_m}{k^4} \iint\!\!\!\int_{\boldsymbol{k}=\boldsymbol{p}+\boldsymbol{q}} \hat{R}_{im}(\boldsymbol{p}, t)\hat{R}_{jl}(\boldsymbol{q}, t)d^3\boldsymbol{p}}_{\text{isotropic}} + \underbrace{\frac{k_i k_j}{k^4}\lambda_i\lambda_j\mathcal{E}_b(\boldsymbol{k}, t)}_{\text{anisotropic}}, \tag{10.50}$$

where $\mathcal{E}_b(\boldsymbol{k}, t)$ denotes the scalar variance spectrum (or $N^2\mathcal{E}^{(pot)}(\boldsymbol{k}, t)$. It is not rescaled as an energy spectrum here, as it should be for a special choice of λ_i). The isotropic part is identical to the one found in the pure incompressible isotropic case discussed in Sect. 4.9.2. The associated spherically-averaged pressure spectrum is

$$\begin{aligned} E_p(k, t) &= \underbrace{16\pi^2 \iint_{\Delta_k} kpq(1 - y^2)(1 - z^2)\mathcal{E}_0(p, t)\mathcal{E}_0(q, t)dpdq}_{\text{isotropic}} \\ &\quad + \underbrace{E_b(k, t)\frac{\lambda_i\lambda_j}{k^2}\left(\frac{\delta_{ij}}{3} - 2H_{ij}^{(pot)}(k, t)\right)}_{\text{anisotropic}} \\ &= E_{pp}^t(k, t) + E_{pp}^N(k, t), \end{aligned} \tag{10.51}$$

where the domain of integration Δ_k, the cosines y and z of the triangle formed by the triad, and the rescaled energy spectra $\mathcal{E}_0(k) = \frac{E(k)}{4\pi k^2}$ are defined consistently with the rest of the book. Dimensional analysis yields $E_{pp}^t(k, t) \propto k^{-7/3}$ and $E_{pp}^N(k, t) \propto k^{-11/3}$ in inertial ranges at very large Reynolds number during the exponential growth regime, in very good agreement with EDQNM results displayed in Fig. 10.24.

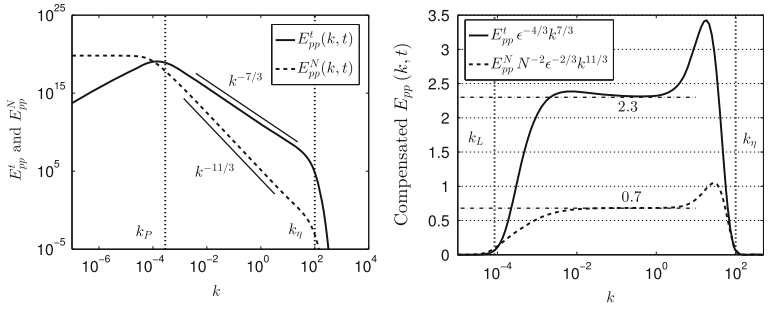

Fig. 10.24 Pressure spectra in high-Reynolds Unstable Stratified Homogeneous Turbulence. Left: isotropic and anisotropic components in log-log scales; Right: compensated spectra. Adapted from Briard et al. (2017) with permission of APS. Courtesy of A. Briard

10.7.7 Generalized EDQNM Approach with both Linear and Nonlinear Dynamics, from Stable Case to Unstable One

In this section, the most general equations to be closed and the crucial assumptions are given for the most elaborate (angle-dependent spectra) EDQNM-SSHT (stable case with internal waves) and EDQNM-USHT (unstable case without waves) procedures.

As for the shear-driven flow case, the generalized transfer terms $T^{(\mathcal{E})}$, $T^{(Z)}$, $T^{(pot)}$, $T^{(F)}$ are not directly expressed in terms of the state-vector $(\mathcal{E}, Z, \mathcal{E}^{(pot)}, \Psi)$, but the triadic closure is performed at the level of three-point third-order correlations.

Because the full equations for three-point third-order correlations were not discussed above, we go back on them *for both the stable case and the unstable one*. In the stable case, the general EDQN equation for three-point third-order correlations is

$$\begin{aligned} S_{ss's''}(\boldsymbol{k},\boldsymbol{p},t) = \exp\Big[&-\nu(k^2+p^2+q^2)(t-t_0) \\ &+\imath N\left(s\frac{k_\perp}{k}+s'\frac{p_\perp}{p}+s''\frac{q_\perp}{q}\right)(t-t_0)\Big] S_{ss's''}(\boldsymbol{k},\boldsymbol{p},t_0) \\ &+\int_{t_0}^{t}\exp\left[-\int_{t_0}^{t'}\mu_{kpq}(t'')dt''+\imath N\left(s\frac{k_\perp}{k}+s'\frac{p_\perp}{p}+s''\frac{q_\perp}{q}\right)(t-t')\right] \\ &\times\tau^{(QN)}_{ss's''}(\boldsymbol{k},\boldsymbol{p},t')dt'. \end{aligned} \tag{10.52}$$

For the sake of mathematical convenience, a diagonal form of the RDT Green's function in Eq. (10.14) is used, projecting the correlation tensor on the eigenmodes of the linear regime, mixing toroidal ("vortex") mode and gravity wave modes. This equation corresponds to the generic equation in Chap. 2 for shear-driven flows: The spectral tensor of three-point third-order correlations is given by

$$\langle\xi^{(s'')}(\boldsymbol{q},t)\xi^{(s)}(\boldsymbol{k},t)\xi^{(s')}(\boldsymbol{p},t)\rangle = \imath S_{ss's''}(\boldsymbol{k},\boldsymbol{p},t)\delta^{(3)}(\boldsymbol{k}+\boldsymbol{p}+\boldsymbol{q}), \tag{10.53}$$

in terms of the eigenmodes in Eq. (10.12). Accordingly, the signs s, s', s'' take not only the value ± 1, for waves (gravity waves here), as in purely rotating turbulence, but also the zero value, for the toroidal mode. Another difference with the case of purely rotating flow is that the explicit linear operator in the previous equation involves the dispersion frequency of gravity waves (10.8) instead of the dispersion frequency of inertial waves. The contribution from three-point fourth-order correlations, that is called into play by quadratic nonlinearity in the equation governing $S_{ss's''}$, or

$$\tau_{ss's''}(\boldsymbol{k}, \boldsymbol{p}, t) = \tau^{(QN)}_{ss's''}(\boldsymbol{k}, \boldsymbol{p}, \boldsymbol{q}, t) + \tau^{(IV)}_{ss's''}(\boldsymbol{k}, \boldsymbol{p}, t), \tag{10.54}$$

is split as the sum of its quasi-normal counterpart, $\tau^{(QN)}_{ss's''}(\boldsymbol{k}, \boldsymbol{p}, t)$, expressed in terms of sums of products of second-order correlations as for a normal law (symbolically $\langle uuuu\rangle^{(QN)} = \sum\langle uu\rangle.\langle uu\rangle$), and the contribution from fourth-order *cumulants* $\tau^{(IV)}_{ss's''}(\boldsymbol{k}, \boldsymbol{p}, t)$ that originates in the departure from Gaussianity at this level of three-point fourth-order statistics. The detailed expression of $S^{(QN)}_{ss's''}$ is not given here for the sake of brevity. On the other hand, we recall that the only physical problem of closure is the replacement of the "bare" Green's tensor by a "dressed", or renormalized version, that accounts for the departure from Gaussianity via $\tau^{(IV)}_{ss's''}$. The extension of the original procedure by Orszag (1970), with an eddy-damping coefficient added to the purely viscous term, yields the damping term μ_{kpq}. As a last reminder, two levels of Markovianization are eventually applied: EDQNM1 if only the exponential damping term is considered as "rapid", so that the temporal integral is applied to it only, and all the other terms are fixed at their instantaneous value, forcing $t' = t$ in the integral, as for a fading memory; EDQNM2 if both the damping term and the explicit linear term (in N here) are considered as rapid. A third version, EDQNM3, in which "rapid" and "slow" terms are distinguished in $\tau^{(QN)}_{ss's''}$ may be used for recovering the strict asymptotic limit of wave turbulence theory, as in Chap. 7, but it does not yield significant improvement for quantitative results. In the stable (SSHT) case, EDQNM2, in which the linear N-operator, which reflects the three-fold product of inviscid RDT Green's function, is much more suited than the EDQNM1 version, in which this term is neglected, with $t' = t$ (Godeferd and Cambon 1994; Godeferd and Staquet 2003).

Passing from stable case to unstable one, the EDQN equation is now

$$\begin{aligned} S_{ss's''}(\boldsymbol{k}, \boldsymbol{p}, t) = \exp\Big[&-\nu(k^2+p^2+q^2)(t-t_0) \\ &-N\left(s\frac{k_\perp}{k} + s'\frac{p_\perp}{p} + s''\frac{q_\perp}{q}\right)(t-t_0)\Big] S_{ss's''}(\boldsymbol{k}, \boldsymbol{p}, t_0) \\ &+\int_{t_0}^{t} \exp\left[-\int_{t_0}^{t'} \mu_{kpq}(t'')dt'' - N\left(s\frac{k_\perp}{k} + s'\frac{p_\perp}{p} + s''\frac{q_\perp}{q}\right)(t-t')\right] \\ &\times \tau^{(QN)}_{ss's''}(\boldsymbol{k}, \boldsymbol{p}, t')dt'. \end{aligned} \tag{10.55}$$

The essential difference with the stable case is now the presence of real terms, instead of purely imaginary ones, that account for the explicit effect of N. Accordingly, as

expected in Cambon and Scott (1999), the EDQNM2 version cannot be applied as in the stable case, because the temporal integral of the term with N factor diverges at large $t - t'$. Consequently, a strict EDQNM1 version, which amounts to making $N = 0$ in the above integral, was first checked when the full numerical code used in the stable case has been adapted to the unstable one.

The related model and numerical code adapted to USHT gave satisfactory results compared to high resolution DNS, but the accumulated energy transfers appeared a bit overestimated with respect to their DNS counterpart. Much more accurate EDQNM1/DNS agreement was finally obtained by reintroducing N in a global quasi-isotropic way. This procedure is consistent with a heuristic way to close of the EDQN Eq. (10.55) for USHT:

$$-\tau^{(IV)}_{ss's''}(\boldsymbol{k},\boldsymbol{p},t) - N\left(s\frac{k_\perp}{k} + s'\frac{p_\perp}{p} + s''\frac{q_\perp}{q}\right) S_{ss's''}(\boldsymbol{k},\boldsymbol{p},t) =$$

$$= \left(\eta^N(k,t) + \eta^N(p,t) + \eta^N(q,t)\right) S_{ss's''}(\boldsymbol{k},\boldsymbol{p},t), \quad s,s',s'' = 0,\pm 1, \quad (10.56)$$

with

$$\eta^N(k,t) = a_0\left(\int_0^k p^2 E(p,t)dp\right)^{1/2} + a_1 N. \quad (10.57)$$

Burlot et al. (2015a) provide no justification that the additional term in Eq. (10.57) represents a global isotropized estimate of the explicit linear anisotropic N-term in EDQN equations, or a specific contribution from fourth-order cumulants $\tau^{(IV)}_{ss's''}$. However, it is possible to show that a reasonable fitting of the constant a_1 gives excellent overall results, as shown in Fig. 10.25.

Interestingly, the analogy with similar adjustments in wave turbulence, as in Eq. (7.46) for purely rotating turbulence, is not really convincing. It is sure that the effect of interacting dispersive waves results in a global damping of triple correlations. On the other hand, we cannot explain why the explicit linear operator related to N yields amplification of second-order correlations, but seems to induce opposite global damping of triple correlations. Two perspectives can help us for a rational explanation and perhaps an improved modelling:

(i) As done long time ago in rotating turbulence (e.g. Fig. 11 in Cambon and Jacquin 1989), it is possible to calculate the impact of the transient term, first line, in Eq. (10.55), which gives the rapid distortion of triple correlations from the initial value problem. For consistency, initial isotropy can be assumed at $t = t_0$. This transient contribution was not calculated in almost all related EDQNM versions, whenever the versions, because either t_0 was taken at its far past value or the initial contribution of third-order correlations was neglected, in order to isolate the secular term only (second line in Eq. (10.55). The optional calculation of the transient term, which is present in EDQNM2 codes for both rotation and stable stratification, can be reactivated in the USHT code, derived from the EDQNM2 SSHT one.

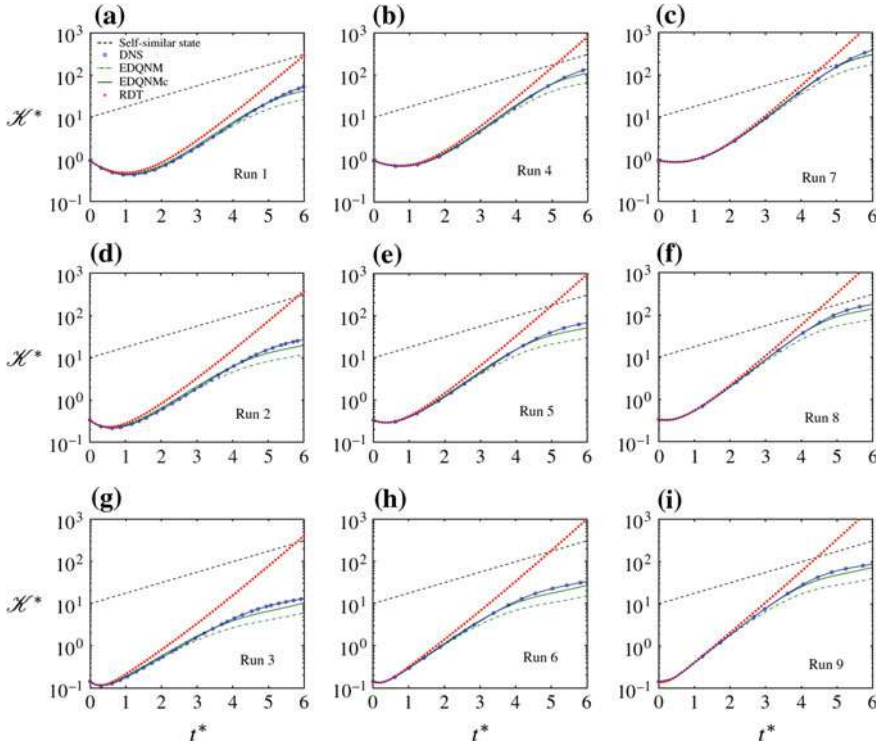

Fig. 10.25 Kinetic energy evolution for different runs from DNS, and EDQNM with (denoted EDQNM-c) and without N correction from Eq. (10.57). Reproduced from Burlot et al. (2015a) with permission of CUP

(ii) As suggested by Julian Scott (private communication), the problem of the lack of convergence of the temporal integral for a three-fold product of Green's functions with possible exponential growth, can be treated using a temporal integral *from past to future*, with *non-causal* Green's function.

10.8 Extension to the Mixing Zone Resulting from Rayleigh–Taylor Instability and Beyond

The USHT with its modeling by generalized EDQNM is a useful canonical model for the mixing zone resulting from the Rayleigh–Taylor instability (Rayleigh 1882; Taylor 1950), once turbulence is well developed, but strict homogeneity cannot describe a realistic unsteady growth rate of the mixing zone.

The Rayleigh–Taylor instability is the interfacial instability which develops when the heavy fluid, with density ρ_2, is suddenly placed above the light fluid, with density ρ_1 (see, e.g. Chandrasekhar 1981). The dispersion frequency of this instability is

$$\sigma_{RT}^2 = -\mathcal{A}gk, \tag{10.58}$$

in terms of the gravitational acceleration g, the wavenumber k, and the Atwood number

$$\mathcal{A} = \frac{\rho_2 - \rho_1}{\rho_2 + \rho_1}. \tag{10.59}$$

Exponential instability is then found for positive Atwood numbers, and its strength is proportional to k, so that small scales are preferentially instable. Incidentally, the stable case is recovered for negative Atwood numbers, and disturbances consist of surface gravity waves at the interface.

Accordingly, the first stage of the development of the mixing zone crucially depends on the form of the initial perturbation of the surface, with high sensitivity to small scale corrugations. We no longer consider this stage here, in order to address a sufficiently thick mixing zone, in which turbulence is well developed. In the following, Rayleigh–Taylor Turbulence (RTT) illustrates such a developed turbulence. It is worth noting that its development can keep a memory of the initial stage of the Rayleigh–Taylor instability, via initial modes with moderate growth rate but with very slow saturation in time.

10.8.1 Simple Models for the Growth Rate of the Mixing Layer

In the strict context of statistical homogeneity restricted to fluctuations, a mean flow with space-uniform gradients is a priori given, it includes a time-scale, N, as well as the inverse of the shear rate for shear-driven turbulence but no lengthscale. The typical vertical lengthscale of the mixing zone, denoted $L(t)$, is the first unsteady "mean" quantity to be predicted.

Useful definitions allow us to bridge between Rayleigh–Taylor turbulence (RTT) and USHT. The buoyancy parameter is chosen as the concentration C, that is linked to the density of the mixture by

$$\frac{1}{\rho} = \frac{C}{\rho_1} + \frac{1 - C}{\rho_2}, \tag{10.60}$$

in which ρ_1 and ρ_2 denote the density of the light fluid and the one of the heavy fluid respectively. C is split into a mean contribution $\overline{C}$ obtained by horizontal averaging, and a fluctuating one denoted c. The frequency N and the fluctuating buoyancy term b used in USHT are given by

$$N = \sqrt{-2\mathcal{A}g\frac{d\overline{C}}{dx_3}} \quad \text{and} \quad b = 2\mathcal{A}gc, \tag{10.61}$$

where the Atwood number $\mathcal{A}$ is assumed to be small.

When the mixing zone becomes fully turbulent, it is expected that its typical width L eventually reaches an asymptotic self-similar state (Youngs 1984)

$$L = 2\alpha\mathcal{A}gt^2. \tag{10.62}$$

No definite value, other than the order of magnitude, was found for the semi-empirical nondimensional parameter α, in spite of a wealth of numerical (DNS,LES) and experimental data. In turn, a way to define a time-dependent α is

$$\alpha(t) = \frac{\dot{L}^2}{8\mathcal{A}gL}. \tag{10.63}$$

A popular *buoyancy-drag* model equation was proposed for the temporal evolution of $L(t)$ as

$$\ddot{L} = \underbrace{-C_d\frac{\dot{L}^2}{L}}_{\text{drag}} + \underbrace{C_b\mathcal{A}g}_{\text{buoyancy}}, \tag{10.64}$$

with two arbitrary parameters, C_b and C_d, to be tuned. The two terms represent physical effects, with a kind of "ballistic" inter-penetration of the heavy and light fluid for the latter, and a turbulent friction between up and down jettal structures for the former. To which extent is it possible to replace tuned constants by terms related to the anisotropic structure of the mixing zone? An answer was given by Gréa (2013), with

$$C_b = \sin^2\gamma(1-\Theta) \quad \text{and} \quad C_d = 2/C_b, \tag{10.65}$$

where the dimensionality parameter $\sin^2\gamma$ quantifies the angular structure, or directional analysis, of the spectrum of concentration variance and Θ is the global molecular mixing introduced by Youngs (1994)

$$\Theta = \frac{\int_{-\infty}^{+\infty}\overline{C(1-C)}dx_3}{\int_{-\infty}^{+\infty}\overline{C}.\overline{(1-C)}dx_3}, \tag{10.66}$$

where the overbar holds for horizontal averaging (see also Poujade and Peybernes 2010 for the second relationship.)

The crucial equation which represents a feedback from fluctuating flow to mean flow, ignored in the strict homogeneous context is

$$\frac{\partial \overline{C}}{\partial t} + \frac{\partial \overline{u_3 c}}{\partial x_3} = \nu \frac{\partial^2 \overline{C}}{\partial x_3^2}. \tag{10.67}$$

The vertical concentration flux $\overline{u_3 c}$ plays the role of the Reynolds stress tensor in shear-driven flows, with its gradient affecting the mean flow. If we do not retain all the information from the vertical dependence of averaged quantities, considered as slowly varying in the vertical direction, a simplified quasi-homogeneous model can be derived from an explicit linkage of N to L, from

$$\frac{d\overline{C}}{dx_3} = \beta / L, \tag{10.68}$$

with the parameter β specified below. A unique value of the vertical mean concentration gradient is evaluated at the center of the mixing zone for practical applications.

Some essential features of the inhomogeneous RTT case are first gathered in Fig. 10.26, from DNS, before addressing typical statistical models. Evolution from the α parameter is shown (bottom) from the initial case, in which a simple interface separates heavy (top) fluid and light one (bottom) to the quasi-steady, quasi-homogeneous, flow case. At initial time, both α and Θ given Eq. (10.66) are taken equal to zero. During the quasi-steady state, a clear inertial $-5/3$ slopes are recovered (top of the figure.) This is in complete agreement with all numerical calculations for USHT, from DNS and EDQNM extended towards very high Reynolds numbers. The recovery of Kolmogorov law is controversial, however, from the study of Poujade (2006): To be more careful, all calculations presented here in USHT and RTT support the Kolmogorov law, but at rather small scales; nothing excludes a different, a bit steeper, law in the spectral domain delineated by the peak of the energy spectrum and the Ozmidov's wavenumber, domain which is not very large in the these simulations.

In addition, the scale by scale parameter of directional anisotropy is extracted: With respect to the "isotropic" value, $\sin^2 \gamma = 2/3$, the higher value which characterizes largest scales is similar to what is found in USHT, as the signature of a trend towards two-dimensionalization. The value slightly smaller than $2/3$ found in smallest scales is not completely interpreted, due to remaining explicit inhomogeneity or numerical artefact.

10.8.2 A Rapid Acceleration Model and Beyond

The RAM (Rapid Acceleration Model) by Gréa (2013) used all the definitions and concepts for RTT in the previous subsection. It illustrates *a system approach to turbulence*, in which a Reynolds decomposition is used, with three characteristics, related to three following interactions:

(i) Mean-to-fluctuating: The linear operator that expresses the action of the mean flow on the fluctuating one is not calculated as a disturbance to a given particular

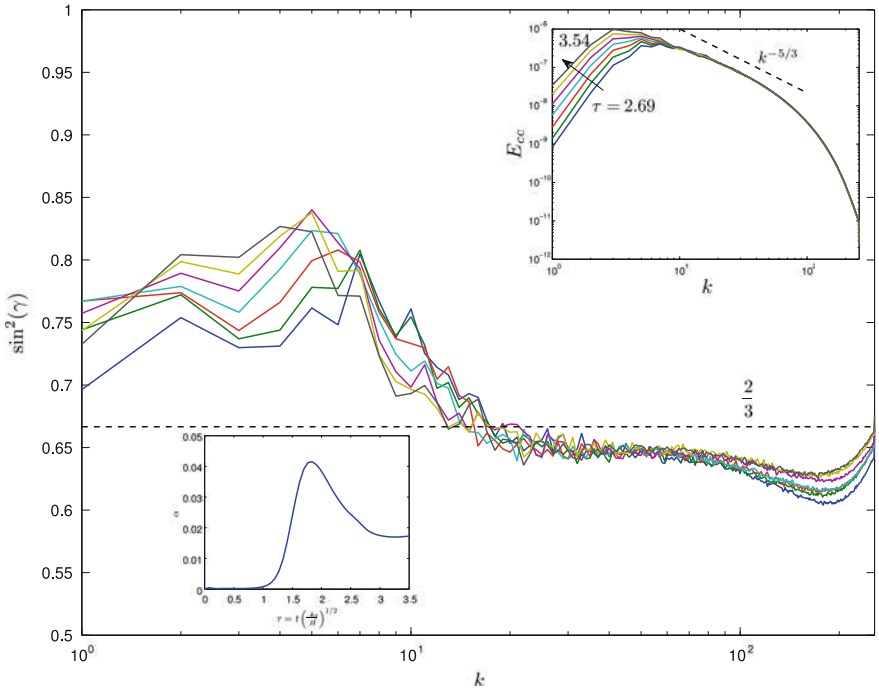

Fig. 10.26 Numerical DNS results for RTT. Spherically averaged (radial, in k) spectrum of the dimensionality parameter $\sin^2\gamma$. Top: Related development of the radial spectrum of the variance of concentration. Bottom: Development of the α parameter. Reproduced from Cambon and Gréa (2013) with permission of T and F

solution of basic equations, as it is done in conventional linear stability analysis (and in homogeneous RDT). This linear operator takes into account the fact that the mean flow is not a priori known, because it is subjected to the feed-back from the fluctuating flow via generalized Reynolds stresses. No approximation of "weak" disturbance, with respect to the given base flow, is needed.

(ii) Fluctuating-to-mean: The above-mentioned feed-back is accurately accounted for.

(iii) Fluctuating-to-fluctuating: This effect is generally considered as less important than the preceding two ones. It is ignored, or mimiced by effective diffusivities, that replace laminar diffusivities.

This approach extends the conventional stability analysis. It is also much more elaborate than the RANS modeling, even if RANS addresses the three interactions as well, because a spectral, multiscale or multimodal description of the fluctuating flow is sought, and/or its dominant modes are investigated.

In the RAM, the mean flow is characterized by an unsteady $N(t)$ stratification frequency, directly related to the thickness $L(t)$ of the unsteady mixing layer by Eq. (10.68). The two-way coupling between the mean field and the fluctuating one,

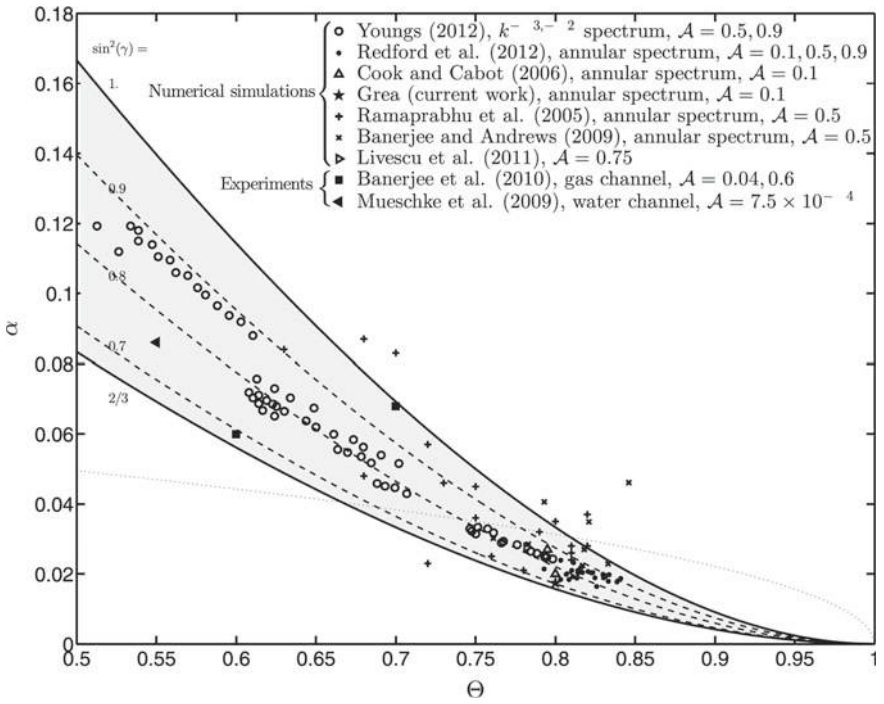

Fig. 10.27 α parameter in terms of the global molecular mixing Θ, and parameterized by the directional anisotropy term $\sin^2\gamma$, from the RAM. Several results from DNS and experiments are plotted. The gray zone is delineated by the two extreme values, $\sin^2\gamma = 1$ (2D) and $\sin^2\gamma = 2/3$ (3D isotropic). Reproduced from Gréa (2013) with permission of AIP

with the feedback given by the vertical gradient of the vertical buoyancy flux, yields new eigenmodes and new eigenvalues, different from the ones of the basic linear solution at constant N. Starting from the complete state-vector $(\mathcal{E}, Z, \mathcal{E}^{(pot)}, \Psi)$ in both k and θ_k, that describes the fluctuating flow, one conserves the angle-dependence, whereas the scale-dependence is removed from consideration by averaging over k (Fig. 10.27).

10.8.3 Towards a Fully Nonlinear, Very High Reynolds Model

Models that illustrate the system approach to turbulence with the abovementioned characteristics were developed in very different contexts. Examples can be given for calculations of the global planetary circulation, in which the mean flow is obtained by zonal averaging, and thus reduces to a profile of meridional velocity, only depending on the latitude. Another promising context is near-wall turbulence, with classical Reynolds averaging for extracting the mean flow. A detailed survey of these models

is outside the scope of this book, and we will only refer to Beverley McKeon and Brian Farrell as internationally well-known specialists of this domain. Because it is geometrically much simpler, the case of RTT permits one of the most elaborate treatment: It is possible to combining the strategy of RAM and the fully anisotropic EDQNM-type model for USHT. Unsteady $N(t)$ and feed-back from the gradient of the vertical buoyancy flux is now implemented in both pseudo-spectral DNS and generalized EDQNM. Accordingly, the fully nonlinear model is rendered consistent with a realistic calculation of the α coefficient, towards a plateau. The model can even reproduce alternance of unstable phases and stable phases, in which the sign of N^2 is changed. With respect to the RAM approach and with respect to the system approach to planetary circulation or to wall turbulence, the new ingredient is a complex model for nonlinear fluctuation-to-fluctuation coupling. It is possible to extend the value of a typical large-scale Reynolds number, say 5000 in 2048^3 DNS, to values of 10^9 in generalized EDQNM (B.-J. Gréa, private communication).

References

Bartello, P.: Geostrophic adjustment and inverse cascades in rotating stratified turbulence. J. Atmos. Sci. **52**(24), 4410–4428 (1995)

Billant, P., Chomaz, J.M.: Experimental evidence for a new instability of a vertical columnar vortex pair in a strongly stratified fluid. J. Fluid Mech. **418**, 167–188 (2000)

Billant, P., Chomaz, J.M.: Self-similarity of strongly stratified inviscid flows. Phys. Fluids **13**, 1645–1651 (2001)

Boussinesq, J: Théorie analytique de la chaleur, mise en harmonie avec la thermodynamique et la théorie mécanique de la lumière, Paris, Gauthier-Villars (two vols.) (1876)

Brethouwer, G., Billant, P., Lindborg, E., Chomaz, J.M.: Scaling analysis and simulation of strongly stratified turbulent flows. J. Fluid Mech. **585**, 343–368 (2007)

Briard, A., Gomez, T., Cambon, C.: Spectral modeling for passive scalar dynamics in homogeneous anisotropic turbulence. J. Fluid Mech. **799**, 159–199 (2016)

Briard, A., Iyer, M., Gomez, T.: Anisotropic spectral modeling for unstably stratified homogeneous turbulence. Phys. Rev. Fluids **2**, 044604 (2017)

Burlot, A., Gréa, B.-J., Godeferd, F.S., Cambon, C., Griffond, J.: Spectral modelling of high Reynolds number unstably stratified homogeneous turbulence. J. Fluid Mech. **765**, 17–44 (2005)

Burlot, A., Gréa, B.-J., Godeferd, F.S., Cambon, C., Soulard, O.: Large Reynolds number self-similar states of unstably stratified homogeneous turbulence. Phys. Fluids **27**, 065114 (2005)

Cambon, C., Jacquin, L.: Spectral approach to non-isotropic turbulence subjected to rotation. J. Fluid Mech. **202**, 295–317 (1989)

Cambon, C., Scott, J.F.: Linear and nonlinear models of anisotropic turbulence. Annu. Rev. Fluid Mech. **31**, 1–53 (1999)

Cambon, C.: Turbulence and vortex structures in rotating and stratified flows. Eur. J. Mech. B (fluids) **20**, 489–510 (2001)

Cambon, C., Godeferd, F.S., Kaneda, Y.: Phase-mixing and toroidal cascade in rotating and stratified flows. Congrès Français de Mécanique, Grenoble, August 27–31 (2007)

Cambon, C., Gréa, B.-J.: The role of directionality on the structure and dynamics of strongly anisotropic turbulent flows. J. Turbul. **14–1**, 50–71 (2013)

Cambon, C., Mons, V., Gréa, B.-J., Rubinstein, R.: Anisotropic triadic closures for shear-driven and buoyancy-driven turbulent flows. Comput. Fluids **151**, 73–84 (2017)

Chandrasekhar, S.: Hydrodynamic and Hydromagnetic Stability. Dover Publications, inc, New York (1981)
Charney, J.G.: Geostrophic turbulence. J. Atmos. Sci. **28**, 1087–1095 (1971)
Cho, J. Y. N., Lindborg, E.: Horizontal velocity structure functions in the upper troposphere and lower stratosphere 1. Observations. J. Geophys. Res., **106** (D–10), 10223–10232 (2001)
Cook, A., Cabot, W.: Reynolds number effects on Rayleigh-Taylor instability with possible implications for type-ia supernovae. Nat. Phys. **2**, 562–568 (2006)
Craft, T.J., Launder, B.E.: Application of TCL modelling to stratified flows. In: Launder B., Sandham N. (eds.) Closure strategies for Turbulent and Transitional Flows. Cambridge University Press, Cambridge (2002)
Fjortoft, R.: On the changes in the spectral distribution of kinetic energy for two-dimensional, non-divergent flows. Tellus **5**, 225–230 (1953)
Galperin, B., Sukoriansky, S.: Turbulence in rotating fluids and the Nastrom and Gage spectrum. In: Invited talk Sixth International Conference Turbulence Mixing and Beyond, ICTP, Trieste (Italy), 14–18 August (2017)
Godeferd, F.S., Cambon, C.: Detailed investigation of energy transfers in homogeneous stratified turbulence. Phys. Fluids **6**, 2084–2100 (1994)
Godeferd, F.S., Staquet, C.: Statistical modelling and direct numerical simulations of decaying stably stratified turbulence. Part 2. Large-scale and small-scale anisotropy. J. Fluid Mech. **486**, 115–159 (2003)
Gonzalez, M.: Kinematic properties of passive scalar gradient predicted by a stochastic Lagrangian model. Phys. Fluids **21**, 055104 (2009)
Gréa, B.-J.: The rapid acceleration model and growth rate of a turbulent mixing zone induced by Rayleigh-Taylor instability. Phys. Fluids **25**, 015118 (2013)
Gréa, B.-J., Burlot, A., Godeferd, F.S., Soulard, O., Griffond, J., Cambon, C.: Dynamics and structure of unstably stratified homogeneous turbulence. J. Turbul. **17**, 651–663 (2016)
Herring, J.R., Métais, O.: Numerical experiments in forced stably-stratified turbulence. J. Fluid Mech. **25**, 505–534 (1989)
Kimura, Y., Herring, J.R.: J. Fluid Mech. **328**, 253–269 (1996)
Lelong, M.P., Riley, J.J.: Internal wave-vortical mode interactions in strongly stratified flows. J. Fluid Mech. **232**, 1–19 (1991)
Liechtenstein, L., Godeferd, F.S., Cambon, C.: Nonlinear formation of structures in rotating stratified turbulence. J Turbul. **6**, 1–18 (2005)
Lilly, D.K.: Stratified turbulence and the mesoscale variability of the atmosphere. J. Atmos. Sci. **40**, 749–761 (1983)
Lindborg, E.: The energy cascade in a strongly stratified fluid. J. Fluid Mech. **550**, 207–242 (2006)
Lindborg, E., Cho, J.Y.N.: Horizontal velocity structure functions in the upper troposphere and lower stratosphere 2. Theoretical considerations. J. Geophys. Res., **106**(D–10), 10233–10241 (2001)
Marino, R., Mininni, P.D., Rosenberg, D.L., Pouquet, A.: Large-scale anisotropy in stably stratified rotating flows. Phys. Rev. E **90**, 023018 (2014)
Miles, J.W.: On the stability of heterogeneous shear flows. J. Fluid Mech. **10**, 496–508 (1961)
Mons, V., Cambon, C., Sagaut, P.: A spectral model for homogeneous shear-driven anisotropic turbulence in terms of spherically averaged descriptors. J. Fluid Mech. **788**, 147–182 (2016)
Mowbray, D.E., Rarity, B.S.H.: A theoretical and experimental investigation of the phase configuration of internal waves of small amplitude in a density stratified liquid. J. Fluid Mech. **28**, 1–16 (1967)
Nastrom, G.D., Gage, K.S.: A climatology of atmospheric wavenumber spectra of wind and temperature observed by commercial aircraft. J. Atmos. Sci. **42**, 950–960 (1985)
Orszag, S.A.: Analytical theories of turbulence. J. Fluid Mech. **41**, 363–386 (1970)
Otheguy, P., Billant, P., Chomaz, J.M.: Effect of the planetary rotation on the zig-zag instability of co-rotating vortices in a stratified fluid. J. Fluid Mech. **553**, 273–281 (2006)
Pedlowsky, J.: Geophysical Fluid Dynamics, Springer, Berlin (1987)

Poujade, O.: Rayleigh-Taylor turbulence is nothing like Kolmogorov turbulence in the self-similar regime. Phys. Rev. Lett. **97**, 185002 (2006)
Poujade, O., Peybernes, M.: Growth rate of Rayleigh-Taylor turbulent mixing layers with the foliation approach. Phys. Rev. E **81**, 016316 (2010)
Praud, O., Fincham, A.M., Sommeria, J.: Decaying grid turbulence in a strongly stratified fluid. J. Fluid Mech. **522**, 1–33 (2005)
Praud, O., Sommeria, J., Fincham, A.M.: Decaying grid turbulence in a rotating stratified fluid. J. Fluid Mech. **547**, 389–412 (2006)
Rayleigh, L.: Investigation of the character of the equilibrium of an incompressible heavy fluid of variable density. Proc. Lond. Math. Soc. **s1–14**(1), 170–177 (1982)
Riley, J.J., deBruynKops.: Dynamics of turbulence strongly influenced by buoyancy. Phys. Fluids **15**, 2047–2059 (2003)
Riley, J.J., Metcalfe, R.W., Weissman, M.A.: Proceedings of the AIP Conference on Nonlinear Properties of Internal Waves (Ed. B.J. West), 72–112 (1981)
Salhi, A., Cambon, C.: Anisotropic phase-mixing in homogeneous turbulence in a rapidly rotating or in a strongly stratified fluid: an analytical study. Phys. Fluids **19**, 055102 (2007)
Sharp, D.H.: An overview of Rayleigh-Taylor instability. Physica D: Nonlinear phenomena **12**(1-3), 3–18 (1984)
Skamarock, W.C., Park, S.-H., Klemp, J.B., Snyder, C.: Atmospheric kinetic energy spectra from global high-resolution nonhydrostatic simulations. J. Atmos. Sci. **71**, 4369–4381 (2014)
Smith, L.M., Waleffe, F.: Generation of slow large scales in forced rotating stratified turbulence. J. Fluid Mech. **451**, 145–168 (2002)
Soulard, O., Griffond, J., Gréa, B.-J.: Large-scale analysis of self-similar unstably stratified homogeneous turbulence. Phys. Fluids **26**, 015110 (2014)
Taylor, G.I.: The instability of liquid surfaces when accelerated in a direction perpendicular to their planes. I. Proc. R. Soc. Lond. A **201**(1065), 192–196 (1950)
Waleffe, F.: The nature of triad interactions in homogeneous turbulence. Phys. Fluids A **4**(2), 350–363 (1992)
Youngs, D.L.: Numerical simulation of turbulent mixing by Rayleigh-Taylor instability. Physica D **12**(1–3), 32–44 (1984)
Youngs, D.L.: Numerical simulation of mixing by Rayleigh-Taylor and Richtmeyer-Meshkov instabilities. Laser Part. Beams **12**, 725 (1994)

Chapter 11
Coupled Effects: Rotation, Stratification, Strain and Shear

Combination of system rotation and stable stratification is essential for geophysical applications, even if the former effect is significantly smaller than the latter in 3D flows, e.g. for scales much smaller than the *synoptic* ones in the atmosphere. As for pure rotating turbulence in Chap. 7 and purely *stably* stratified turbulence in Chap. 10, linear analysis, i.e. RDT (Rapid Distortion Theory), describes neutral stability and will lead to the definition of both the wave-vortex eigenmode decomposition and dispersion frequencies of inertia-gravity waves in the present chapter. Prediction of statistics by RDT in this case with waves without production is poorly accurate for single-time second-order correlations, but is more relevant for two-time statistics, as discussed in Sect. 11.2.5, and, of course, for triple correlations. On the other hand, nonlinear dynamics is pivotal, and allows us to revisit a *quasi-geostrophic cascade*, which generalizes the toroidal cascade discussed in Chap. 10 with additional Coriolis effects.

Other coupled effects investigated in this chapter, after the first section, can generate linear instabilities which can be analyzed within the RDT framework. These instabilities are associated to turbulence production mechanisms, which are the main striking new physical phenomena when compared to other flows discussed in this book. In the presence of mean shear, *barotropic instabilities* occur, with a strong analogy between the rotating shear flow case and the stratified shear flow. A special case combining the three ingredients, namely the mean shear, system rotation and stable stratification is shown to give a new insight into the *baroclinic instability.* Finally, the very important *elliptical flow instability* is investigated, which results from a coupled effect of mean vorticity with weak additional mean strain. This instability can trigger nonlinear cascade and turbulence in physical systems with large strained vortices.

A general conclusion about linear stability theory is provided at the end of the chapter, in order to delineate the domain of relevance of homogeneous RDT, and of its natural extension via WKB (Wentzel–Kramer–Brillouin) RDT.

The present Chapter includes recent results on nonlinear mechanisms and quantification of cascades, mainly from DNS. In addition to applications to geophysics, atmosphere or ocean far from topography, and engineering, astrophysics is addressed, with the dynamics of accretion discs. We illustrate the fact that the rotating shear

P. Sagaut and C. Cambon, *Homogeneous Turbulence Dynamics*,
https://doi.org/10.1007/978-3-319-73162-9_11

flow, as a simple model for turbomachinery, is also a model for an accretion disc via the *shearing sheet approximation*. Finally, the case of rotating flow with precession gives a special occurrence of elliptical flow instability coming from shear-rotation interaction.

11.1 Governing Equations for the Dynamics of Coupled Effects

We consider in the present Chapter homogeneous turbulent flows subjected to various, possibly coupled, external effects, with the three parameters N (for stratification frequency, as in Chap. 10), S (for the mean shear rate, as in Chap. 9) and f, or 2Ω (system vorticity as in Chap. 7.) In addition, for elliptical flow instability, we consider an additional strain rate D or a precessing system vorticity $2\Omega^C$. Accordingly, it is useful to give, or remind, basic equations, that are used in the different sections, in order to show how the chapter is organized at a glance (Table 11.1).

Within the Boussinesq approximation framework, the equation for the solenoidal velocity field $\boldsymbol{u}(\boldsymbol{x}, t)$ in a rotating frame displays two additional terms, reflecting both Coriolis and buoyancy forces, the intensity of the latter being denoted b.

Table 11.1 N-S-f framework at a glance

	.	Parameters for linear stability/typical nonlinear structuring		
	External $N-S-f$ parameters	Stable	Linearly unstable (exponential growth)	Typical structures
Chapter 7	f (or 2Ω)	Inertial wave	None	2D - 2C state
Chapter 10	N ($N^2 > 0$)	Gravity wave and toroidal	None	1D - 2C (VSHF mode)
Chapter 10	N ($N^2 < 0$)	Toroidal	Poloidal and potential	2D - 1C (jettal)
Section 11.2	N and f	See Table 11.2	None	Inverse QG cascade if $f/N \sim 1$
Chapter 9	S	Algebraic	None	2D-1C (streaks)
Section 11.3.1	f and S	If $B \geq 0$	If $B < 0$	Many types
Section 11.3.2	N and S	If $R_i = \frac{N^2}{S^2} \geq 0$	If $R_i < 0$	Many types
Section 11.4.1	N and S and spanwise-f	R_i, $R = \frac{f}{S}$	See Fig. 11.13	Many types
Section 11.4.1	N and S and vertical-f	R_i, $\epsilon = \frac{Sf}{N^2}$	Baroclinic	Many types

$$\boldsymbol{F}_b = 2\boldsymbol{\Omega} \times \boldsymbol{u} - b\boldsymbol{n} \tag{11.1}$$

The use of the buoyancy scalar b allows us to get rid of the different formulations in terms of temperature or density. Let us just recall that b is related to the density ρ by the relation $b = \rho g/\rho_0$ in a liquid, where g is the gravitational acceleration and ρ_0 the constant density of reference (its definition for a gaz is given in Chap. 10, for instance in terms of potential temperature and thermal expansivity). The vector $\boldsymbol{n}$ is the vertical unit upward vector such that $g = -g\boldsymbol{n}$. Before splitting the field into mean and fluctuating components, the momentum equation is recast as follows

$$\frac{\partial u_i}{\partial t} + u_j \frac{\partial u_i}{\partial x_j} + 2\Omega_n \epsilon_{inj} u_j = -\frac{1}{\rho_0}\frac{\partial p}{\partial x_i} + b n_i \tag{11.2}$$

and the mass conservation equation $\dot{\rho} + \rho \frac{\partial u_i}{\partial x_i} = 0$ yields

$$\frac{\partial b}{\partial t} + u_j \frac{\partial b}{\partial x_j} = 0, \quad \frac{\partial u_i}{\partial x_i} = 0. \tag{11.3}$$

Except for the case without mean motion (in addition to the sole solid-body rotation) discussed in Sect. 11.2, specific notations from the Reynolds decomposition, i.e. $\overline{\boldsymbol{u}}$ for mean velocity and $\boldsymbol{u}'$ for fluctuations, will be used in the following. A similar distinction will be made for the buoyancy scalar, introducing $\overline{b}$ and b'.

The extensional mean flow, with uniform gradients, is given by

$$\overline{u}_i = A_{ij} x_j + \overline{u}_0, \quad \overline{b} = B_i x_i + \overline{b}_0, \tag{11.4}$$

in which $\overline{u}_0$ has no effect and can be removed from consideration, due to Galilean invariance, and $\overline{b}_0$ is generally related to a mean density of reference, denoted ρ_0. Equations for fluctuating quantities are

$$\frac{\partial u_i'}{\partial t} + A_{mn} x_n \frac{\partial u_i'}{\partial x_m} + A_{ij} u_j' + u_j \frac{\partial u_i}{\partial x_j} + 2\Omega_n \epsilon_{inj} u_j + \nu \nabla^2 \boldsymbol{u} = -\frac{1}{\rho_0}\frac{\partial p}{\partial x_i} + b'\boldsymbol{n}, \tag{11.5}$$

for u', and

$$\frac{\partial b'}{\partial t} + A_{mn} x_n \frac{\partial b'}{\partial x_m} + u_j' \frac{\partial b'}{\partial x_j} - \nu P_r \nabla^2 b' = -B_i u_i', \tag{11.6}$$

for b', reintroducing the diffusivity of the stratifying agent for generality, via the Prandtl (or Schmidt) number Pr.

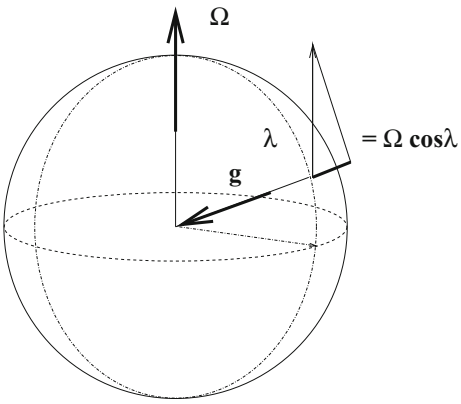

Fig. 11.1 Definition and meaning of the Coriolis parameter f in geophysics

11.2 Rotating Stratified Turbulence

In the absence of mean shear, it is possible to consider that both the system angular velocity and the mean buoyancy gradient are vertical in Eq. (11.4), yielding

$$2\Omega_i = 2\Omega n_i = 2\Omega\delta_{i3}, \quad B_i = N^2\delta_{i3}, \tag{11.7}$$

so that the Brunt–Väisälä frequency N appears as the characteristic frequency of buoyancy-stratification. The vertical mean vorticity can be replaced by the Coriolis parameter

$$f = 2\Omega\cos\lambda, \tag{11.8}$$

where λ is the *co-latitude* (see Fig. 11.1).[1]

With respect to general Eqs. (11.5) and (11.6) used throughout this chapter, we have $A_{ij} = 0$ along with Eq. (11.7), so that we will keep $\boldsymbol{u} = \boldsymbol{u}'$ and $b' = b$ in this first section only, for the sake of simplicity.

Only neutral stability can be described using inviscid RDT in this case, from linearized equations, as in the cases of purely rotating and purely stratified flows, separately considered. The linear inviscid solution for velocity/buoyancy fluctuations consists of superimposed steady and oscillating modes, as for the purely stratified flow case. The former corresponds to the *Quasi-geostrophic mode* (which is equal

[1] Projecting the angular velocity onto the local vertical axis, which yields the angle-dependent factor $\cos\lambda$, is analogous with projecting the angular velocity on the wave-vector direction, which yields the angle-dependent dispersion frequency of inertial waves with $\cos\theta$. This projection reflects a dominant role of the Coriolis force in the tangent plane of the rotating spheroid (our Earth), whereas it reflects pure solenoidal motion looking at a sphere in 3D Fourier space. In the geophysical community, the angle of latitude is commonly used, and therefore a sine often appears instead of a cosine.

to the toroidal mode in the absence of rotation) and the latter, referred to as the *AGeostrophic modes*, are related to inertia-gravity waves. This decomposition is commonly referred to as the QG/AG decomposition (e.g. Pedlowsky 1987.) RDT yields very simple behavior, in which single-time velocity/buoyancy correlations are possibly affected by damped oscillations, the damping resulting from the dispersivity of wave motion. The poloidal-toroidal-like decomposition, closely related to the QG/AG one, was shown to simplify the RDT prediction. For instance, the total turbulent kinetic energy is conserved in pure rotation, and damped oscillations yield an asymptotic equidistribution of poloidal and toroidal turbulent kinetic energy. In pure stable stratification, both total (kinetic + potential) and toroidal kinetic energy are conserved, whereas poloidal kinetic and potential energies asymptotically reach equilibrium after damped oscillations (see Fig. 10.4). In these cases, linear dynamics — if restricted to single-time, two- or single-point correlations — are of poor interest, since relevant structuring effects result only from the nonlinear terms. In the present case, RDT suggests to build a full nonlinear model in terms of the slowly varying amplitudes of QG/AG modes, which are constant in the pure linear inviscid limit.

As for the purely stratified case (see Eq. (10.13)), a single vector $\boldsymbol{w}$ can gather both velocity and buoyancy fluctuations, with the following decomposition

$$\hat{\boldsymbol{w}} = \sum_{s=0,\pm1} \underbrace{a^{(s)}(\boldsymbol{k},t)\exp(s\imath\sigma_{rs}(\boldsymbol{k})t)}_{\xi^{(s)}(\boldsymbol{k},t)} \boldsymbol{N}^{(s)}(\boldsymbol{k}), s = 0, \pm1, \tag{11.9}$$

It is important to note that both the eigenmodes $\boldsymbol{N}^{(s)}$, $s = 0, \pm1$ and the (unsigned) dispersion frequency of inertia-gravity waves

$$\sigma_{rs}(\boldsymbol{k}) = \sqrt{N^2 \sin^2\theta + f^2\cos^2\theta} \tag{11.10}$$

are explicit functions of the ratio f/N (Pedlowsky 1987; Cambon 2001). Here, $s = 0$ is related to the QG mode, which is also referred to as the non-propagating mode, while $s = \pm1$ corresponds to the AGeostrophics modes, which are propagating inertia-gravity waves.

As shown in Fig. 11.2, the QG/AG (or wave-vortex) decomposition is dependent on f/N: the inertia-gravity wave contribution to the velocity field is the poloidal part of the flow without rotation, and includes an increasing part of the toroidal component when the rotation (via the ratio f/N) increases. In the case of pure rotation, the inertial wavemode includes the entire velocity field, and the non-propagating (QG) part of the flow identically vanishes.

When the QG mode, with amplitude $a^{(0)}$ in Eq. (11.9), has a significant contribution, the cascade related to triadic interactions including QG modes only can be expected to be dominant with respect to the other resonant or quasi resonant wave interactions. It is recalled that using the nomenclature used in other chapters these pure QG triadic interactions are denoted $(0, 0, 0)$. This purely QG cascade is discussed in the next subsection.

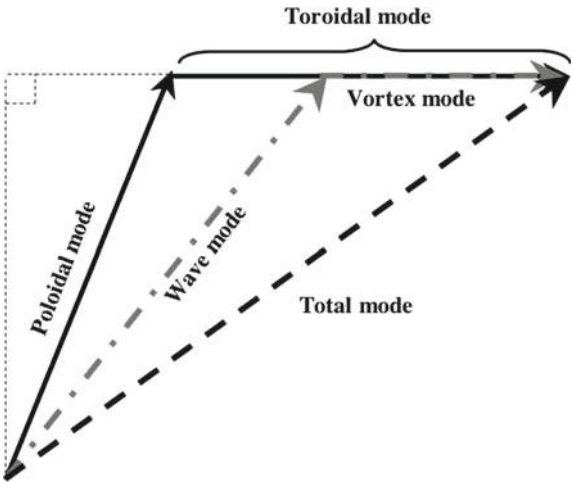

Fig. 11.2 Cartoon of the 'wave-vortex' (or linear QG-AG) decomposition from the Craya–Herring decomposition, or related toroidal-poloidal one in physical space. The toroidal mode is the part of the horizontal velocity fluctuation with zero divergence in terms of horizontal coordinates; it corresponds to (velocity contribution to) the QG mode only without rotation; (velocity contribution to) the QG mode is only a fraction of this toroidal mode at a given f/N ratio, and identically vanishes at $N = 0$ (pure rotation)

Discarding a priori the QG mode, it can be shown that resonant inertia-gravity waves can play a role in concentrating energy towards larger scales and quasi-VSHF (Vertically Sheared Horizontal Flow) mode, at least if f/N is small. This was found by Smith and Waleffe (2002), for instance, by forcing isotropically the small scales without putting energy at large scale at the initial time.

At least two radically different mechanisms of concentration of energy towards the VSHF mode are thus possibly present:

- the *toroidal cascade*, already investigated in Chap. 10 for the pure stratification case; toroidal mode is the limit of the QG mode in the absence of system rotation. This mechanism plays a dominant role and leads to a rapid layering of the flow if a significant large-scale toroidal part of the flow exists initially and if f/N is not too large.
- the *transfers induced by the resonant inertia-gravity waves*.

The relevance of the quasi-geostrophic model was expected by Smith and Waleffe (2002) to prevail when $1/2 < N/f < 2$, since triadic 'wave' resonances are forbidden in this range of parameter, as seen looking at the dispersion law (11.10).

11.2.1 Basic Triadic Interaction for Quasi-geostrophic Cascade

If the flow is described in a rotating frame of reference with angular velocity $(f/2)\boldsymbol{n}$, f being the Coriolis parameter for geophysical applications, only the basic momentum equation for $\boldsymbol{u}$ is affected by the additional Coriolis force $f\boldsymbol{n}\times\boldsymbol{u}$. The associated evolution equation for b is identical to the one obtained in the pure stratification case, see Eq. (10.4). In agreement with Eq. (11.9) and with the cartoon displayed in Fig. 11.2, the non-propagating mode now combines toroidal kinetic energy and potential energy

$$\xi^{(0)} = a^{(0)} = \frac{\sigma_s}{\sigma_{rs}} u^{(1)} + \frac{\sigma_r}{\sigma_{rs}} u^{(3)}, \tag{11.11}$$

with

$$\sigma_s = N\frac{k_\perp}{k}, \quad \sigma_r = f\frac{k_\parallel}{k}, \quad \sigma_{rs} = \sqrt{\sigma_r^2 + \sigma_s^2}. \tag{11.12}$$

and where $\xi^{(0)}$ is related to the *quasi-geostrophic energy*. The two other terms $\xi^{(\pm 1)}$ deal with inertia-gravity waves whose dispersion frequency σ_{rs} is given by Eq. (11.10). All details are gathered in Table 11.2.

Let us now investigate detailed properties of the interactions within a single isolated triad. Following the same procedure as for the toroidal cascade in Chap. 10, i.e. removing all nonlinear interactions involving wave modes in order to retain only the quasi-geostrophic ones, one obtains a set of equations similar to (10.20).

Table 11.2 Linear eigenmodes, vortex-wave-type and dispersion law for different flow cases. The case of the acoustic regime, addressed in Sect. 13.2, is added to contrast very different waves effects; of course $u^{(3)}$ is a true dilatational mode in the latter case, coupled with the pressure mode $u^{(4)}$, whereas it is a buoyancy mode in this chapter, as in Chap. 10

.	Propagating/non-propagating modes		
Flow configuration	Non-propagating mode(s)	Wave mode(s)	Dispersion law
Purely rotating	None	$\underbrace{u^{(2)} \pm \imath u^{(1)}}_{\text{inertial w.}}$	$\sigma_r = f\frac{k_\parallel}{k}$
Purely stratified	$\underbrace{u^{(1)}}_{\text{toroidal}}$	$\underbrace{u^{(3)} \pm \imath u^{(2)}}_{\text{gravity w.}}$	$\sigma_s = N\frac{k_\perp}{k}$
Rotating and stratified	$\underbrace{\frac{\sigma_s}{\sigma_{rs}} u^{(1)} + \frac{\sigma_r}{\sigma_{rs}} u^{(3)}}_{\text{quasi-geostrophic}}$	$\underbrace{-\frac{\sigma_r}{\sigma_{sr}} u^{(1)} + \frac{\sigma_s}{\sigma_{sr}} u^{(3)} \pm \imath u^{(2)}}_{\text{inertia-gravity w.}}$	$\sigma_{rs} = \sqrt{\sigma_r^2 + \sigma_s^2}$
Weakly compressible	$\underbrace{u^{(1)}, u^{(2)}}_{\text{solenoidal}}$	$\underbrace{u^{(4)} \pm \imath u^{(3)}}_{\text{acoustic w.}}$	$\sigma_c = c_0 k$

$$\dot{\xi}_k^{(0)} = (p^2\sigma_{rs}^2(\boldsymbol{p}) - q^2\sigma_{rs}^2(\boldsymbol{q}))G'\xi_p^{(0)*}\xi_q^{(0)*}, \tag{11.13}$$

$$\dot{\xi}_p^{(0)} = (q^2\sigma_{rs}^2(\boldsymbol{q}) - k^2\sigma_{rs}^2(\boldsymbol{k}))G'\xi_q^{(0)*}\xi_k^{(0)*}, \tag{11.14}$$

$$\dot{\xi}_q^{(0)} = (k^2\sigma_{rs}^2(\boldsymbol{k}) - p^2\sigma_{rs}^2(\boldsymbol{p}))G'\xi_k^{(0)*}\xi_p^{(0)*}, \tag{11.15}$$

which involves a modified factor $G'(\boldsymbol{k}, \boldsymbol{p}, \boldsymbol{q})$. This new geometrical factor is fully symmetric in terms of $(\boldsymbol{k}, \boldsymbol{p}, \boldsymbol{q})$ (Cambon et al. 2007). One finds from this system of equations that detailed conservation holds for both quasi-geostrophic energy and potential enstrophy, i.e.

$$\dot{\xi}_k^{(0)}\xi_k^{(0)*} + \dot{\xi}_p^{(0)}\xi_p^{(0)*} + \dot{\xi}_q^{(0)}\xi_q^{(0)*} = 0$$

and

$$k^2\sigma_{rs}^2(\boldsymbol{k})\dot{\xi}_k^{(0)}\xi_k^{(0)*} + p^2\sigma_{rs}(\boldsymbol{p})p^2\dot{\xi}_p^{(0)}\xi_p^{(0)*} + q^2\sigma_{rs}^2(\boldsymbol{q})\dot{\xi}_q^{(0)}\xi_q^{(0)*} = 0,$$

These two detailed conservation laws are analogous to those for toroidal energy and vertical enstrophy associated with the pure toroidal cascade for purely stratified flows and to those for the total energy and total enstrophy in two dimensional isotropic turbulence. The linkage to *potential enstrophy* comes from

$$\frac{k^2\sigma_{rs}^2(\boldsymbol{k})}{N^2}\xi^{(0)}\xi^{(0)*} = \kappa_\perp^2 u^{(1)}u^{(1)*} + \left(\frac{f}{N}k_\parallel\right)^2 u^{(3)}u^{(3)*}, \tag{11.16}$$

using Eq. (11.11). This result is to be compared to vertical enstrophy, which is recovered if $f = 0$. These two conservations laws were already quoted by Bartello (1995), his eigenmode decomposition being essentially the same[2] as the one deduced from Craya–Herring decomposition, and its geometric factor $N^{(000)}$ is similar to the above one (but it does not display the factor $p^2\sigma_{rs}^2(\boldsymbol{p}) - q^2\sigma_{rs}^2(\boldsymbol{q})$ explicitly).

An important remark must be made here. Equation (11.16) gives the spectral density of the variance of the *linearized absolute potential vorticity* (APV). The fluctuating linearized APV can be defined as

$$\boldsymbol{n}\cdot\boldsymbol{\omega} + \frac{f}{N^2}\frac{\partial b}{\partial x_\parallel}, \tag{11.17}$$

in the physical space, and as

$$\imath k_\perp u^{(1)} + \imath\frac{f}{N}k_\parallel u^{(3)}, \tag{11.18}$$

[2]The geometrical decomposition used in Godeferd and Cambon (1994), Cambon (2001) has the only advantage that a true pseudo-compressible vector can be defined in physical space, by inverse Fourier transformation of the single 'true' vector $\hat{\mathbf{w}} = \hat{\boldsymbol{u}} + \imath(\boldsymbol{k}/k)(\hat{b}/N) = \sum_{i=1,3} u^{(i)}\boldsymbol{e}^{(i)} = \sum_{s=0,\pm1}\xi^{(s)}\boldsymbol{N}^{(s)}$ with all related simplifications due to orthonormality. Mixing a true vector $\hat{\boldsymbol{u}}$ and a scalar $\hat{b}$ is less tractable in general.

also equal to $\imath \frac{k\sigma_{rs}}{N} \xi^{(0)}$ from Eq. (11.11) and Table 11.2, in Fourier space. Its fully nonlinear counterpart is defined as the scalar product of the absolute vorticity (mean $f\boldsymbol{n}$ + fluctuating $\boldsymbol{\omega}$) by the gradient of buoyancy (mean $N^2\boldsymbol{n}$ + fluctuating $\boldsymbol{\nabla} b$), and is eventually divided by N^2 for keeping the dimension of vorticity

$$\frac{1}{N^2} (f\boldsymbol{n} + \boldsymbol{\omega}) \cdot \left(N^2\boldsymbol{n} + \boldsymbol{\nabla} b\right). \tag{11.19}$$

In short, from the above equation, one can derive an additive threefold decomposition in terms of

- a 'mean' contribution f,
- the linearized fluctuation given by Eq. (11.17),
- a *nonlinear quadratic* contribution $\boldsymbol{\omega}\cdot(\boldsymbol{\nabla} b/N^2)$.

11.2.2 About the Case with Small but Non-negligible f/N Ratio

Especially in oceanography, one encounters f/N ratios of the order $10^{-1}-10^{-2}$ at mesoscales. Nevertheless, even with such a weak f/N ratio, the effect of the Coriolis force cannot be ignored. The dominant structures are pancake structures, as in strongly stably stratified turbulence without rotation, but their scaling and dynamics are influenced by the Coriolis force. For instance, the contribution from gravity wave dispersion frequency ($\sigma_s = N \sin\theta$) is assumed to be of the same order as the contribution from the inertial wave frequency, or

$$N\frac{k_\perp}{k} \sim f\frac{k_\parallel}{k}. \tag{11.20}$$

The latter relation is consistent with a Burger number,

$$Bu = \left(\frac{f}{N}\frac{L_h}{L_v}\right)^2,$$

close to one, if the ratio of typical vertical L_v and horizontal L_h lengthscales, is related to the inverse of the ratio $k_\parallel/k_\perp$.

11.2.3 The QG Model Revisited. Discussion

The QG model discussed by Charney (1971) was already touched upon in Chap. 10. Conservation of full nonlinear absolute potential vorticity defined by Eq. (11.19) is a direct consequence of the Ertel theorem (see also Staquet and Riley 1989).

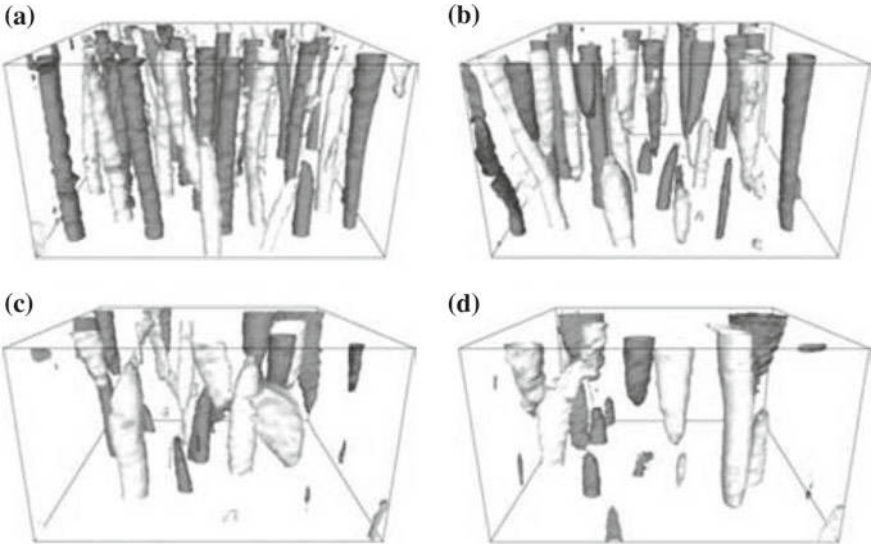

Fig. 11.3 Visualization by PIV of vortex structures, $N/f = 1.2$, from Praud et al. (2006) with permission of CUP

Roughly speaking, this amounts to replace the vertical direction by the local normal to isopycnal surfaces in the toroidal/poloidal decomposition, the QG motion being along these surfaces and AG motion being across them.

Of course, if these surfaces are weakly undulated and therefore close to horizontal surfaces, linearization of APV is physically justified.

Too strong properties are often attributed to QG motion, in an analogous way to the unjustified use of the Proudman theorem to explain the transition toward a two-dimensional state, yielding some wrong statements:

- QG motion is analogous to 2D motion, with dual energy cascades, so that a direct cascade is expected for APV and an inverse cascade is for QG energy,
- In spite of the strong anisotropy of QG motion, a simple rescaling in terms of f/N can restore an apparent isotropy.

The experimental study by Praud et al. (2006), which made use of the very large Coriolis platform in Grenoble, contributed to support this point of view, at least for values of f/N ranging from 0.8 to 1.2. Beautiful cigar vortices are created just behind a moving rake, looking very similar to 2D structures, and then evolve towards less elongated structures (Fig. 11.3), in the rotating tank full of brine. The use of the PIV technique allowed almost 3D velocity and vorticity measurements.

In principle, vertical variability is captured in this experimental study. Even if the horizontal dimension greatly exceeds the vertical dimension of the layer, this does not reduces to the shallow water case in which "2D", "QG" and "horizontal motion" concepts collapse. On the other hand, *the use of a rake with only vertical*

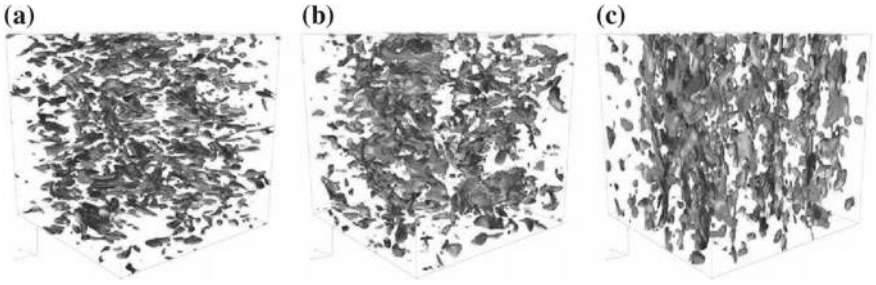

Fig. 11.4 Enstrophy isosurfaces **a** $f/N = 0.1$, **b** $f/N = 1$, **c** $f/N = 10$. 256^3 unforced DNS results from Liechtenstein et al. (2005) with permission of T and F

sticks favours and even generates pure 2D motion, with respect to the use of a square grid.

In a DNS without any forcing, it is possible to switch from "pancake" to "cigar" structures by increasing the ratio f/N, as shown in Fig. 11.4, for instance. Incidentally, the fact that an apparently isotropic structure is found for $f/N = 1$ is possibly misleading: this case is very different from pure isotropic turbulence. It is also worthwhile to note that "structures", identified by iso-vorticity surfaces in high resolution DNS, are much more scrambled than the ones visualized by PIV techniques in physical experiments: cigars are very different from smooth Taylor columns in such DNS ! A bit paradoxically, under-resolved DNS and LES can show apparently smoother structures, but this is a numerical artefact.

Neglecting wall effects and anisotropic forcing, a more subtle QG model could be written for the new Lin equation

$$\left(\frac{\partial}{\partial t} + 2\nu k^2\right) \mathcal{E}^{(QG)}(k_\parallel, k_\perp, t) = T^{(QG)}(k_\parallel, k_\perp, t), \tag{11.21}$$

with

$$\frac{1}{2}\langle \xi^{(0)*}(\boldsymbol{p}, t)\xi^{(0)}(\boldsymbol{k}, t)\rangle = \mathcal{E}^{(QG)}(\boldsymbol{k}, t)\delta^{(3)}(\boldsymbol{k} - \boldsymbol{p}) \tag{11.22}$$

extending Eqs. (10.24)–(10.26) for the toroidal cascade in purely stratified flows to various f/N ratios. The generalized transfer term $T^{(QG)}(k_\parallel, k_\perp, t)$ can be constructed from triadic contributions strictly preserving detailed conservation of both QG energy and (linearized) APV. Depending of f/N, a very complex and multiform anisotropic cascade is expected in terms of the full distribution of the transfer term expressed as a function of $k_\perp$ and $k_\parallel$. As for the model of toroidal cascade in Chap. 10 for $f/N = 0$, the strong dependence of the term G' in Eq. (11.13) with respect to $k_\parallel$ can induce a dynamical cascade process very different from the one observed in 2D turbulence, in spite of the conservation of APV. Only the case of pure rotation cannot be recovered this way, since the QG mode vanishes in this case and that only inertial wave-turbulence is relevant. Nevertheless, the case of pretty large f/N ratios — as

the highest ratios addressed by Praud et al. (2006)— remains of interest. Note that Herring (1980) proposed a first QG model based on a Lin equation with a transfer term closed by an EDQNM technique, but its relevance was limited by additional quasi-isotropic assumptions.

A very different angle of attack is to try to generalize the Kolmogorov 4/5 law using both velocity and APV increments for building third order structure functions (Kurian et al. 2006). The advantage of working on structure functions in physical space is avoiding a too strict limitation to quadratic nonlinearity (a fully nonlinear APV variable can be used), whereas cubic and quartic nonlinearities are very difficult to handle in Fourier space (even the classical convolution product mediated by quadratic nonlinearity is not so simple!). A drawback is that a complete solenoidal description, with exact removal of explicit pressure terms from the very beginning, is very complicated in physical space; removal of mixed pressure-velocity terms in the 4/5 Kolmogorov law is a very marginal case, for instance.

Of course, a more complete analysis may be developed on the ground of the most general set of spectra and cospectra consistent with axisymmetry without mirror symmetry. In this more general case, another Lin equation is written for the spectrum of total (kinetic + potential) inertia-gravity wave energy, $\mathcal{E}^{(w)}$, defining an other "true" *conservative* transfer term[3] $T^{(w)}$. The system must be supplemented by two additional terms similar to Z in Eq. (10.26) characterizing the imbalance between potential and kinetic energy of waves, together with poloidal and toroidal buoyancy fluxes exchanged between them. Only these Z-terms are affected by linear (rapid) factors $\imath\sigma_{rs}(\boldsymbol{k})t$, and they are not associated to global conservation laws. This is a complete generalization of the $(\mathcal{E}, Z)$ system for pure rotation, and the system $(\mathcal{E}^{(tor)}, \mathcal{E}^{(pol+pot)}, Z')$ for pure stratification, see Eq. (10.26).

It is important to note that the vanishing integral for $T^{(QG)} + T^{(w)}$ reflects global conservation laws, whereas the *detailed conservation of both QG energy and potential vorticity is only found when discarding inertia-gravity wave modes in triads*. Such a removal can be made a priori, or invoking the physical context of very small Rossby and Froude numbers.

11.2.4 Quantification of the Inverse Cascade for Rotating Stratified Turbulence

A wealth of conventional pseudo-spectral DNS in tri-periodic boxes were published in the recent past for stably-stratified flows with and without rotation, and for purely rotating flows. We prefer not to list all of them, because they often suffer from classical drawbacks of these numerical studies: under-resolution with respect to the concept of homogeneous turbulence, with finite-box effects, lack of angular resolution at

[3] Let us recall that a nonlinear term in a Lin-type equation is referred to as a *true* transfer term if its integral over all wavenumbers is zero, i.e. if it is associated with a global conservation law.

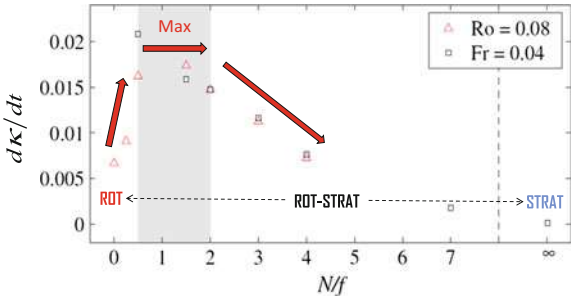

Fig. 11.5 Quantification of the inverse cascade by means of the growth rate of the kinetic energy $d\mathcal{K}/dt$ in DNS of rotating stratified flows with different N/f, including the purely statified case ($N/f \sim \infty$). The gray band highlights runs in which the kinetic energy growths faster. Adapted from Marino et al. (2013)

smallest wavenumbers, artificial forcing of largest scales, and so on. Among them, the quantification of the inverse cascade at various N/f by Marino et al. (2013) is a useful complementary study to the theoretical study of quasi-geostrophic cascade.

With a similar forcing of large scales, the rapid growth of kinetic energy is related to the growth of largest scales, as an indicator of dramatic inverse cascade of energy. This effect is "rapid" in terms of a time scale $\tau_{NL} = \sqrt{k_F E(k_F)}$, where k_F is the forcing wavenumber: After an initial adjusting phase, the inverse cascade is observed after $t/\tau_{NL} \sim 5$ in DNS of rotating stratified flows forced at small scale, with the growth rate of kinetic energy $d\mathcal{K}/dt$ being maximal in the range $1/2 \leq N/f \leq 2$ (see Fig. 11.5).

A dual cascade of kinetic energy is thereby ascertained in this case of rotating and stratified turbulence by Marino et al. (2015). It has also been shown that the following scaling relationship in terms of both Rossby and Froude numbers

$$R_\Pi \sim (F_r Ro)^{-1} \tag{11.23}$$

holds for the ratio of the inverse to the direct kinetic energy transfer rate in simulations forced at intermediate scales, see Fig. 11.6. Incidentally, all these results at largest N/f are consistent with the vanishing of inverse cascade for purely (stably) stratified turbulence, as discussed in Chap. 10, with recent investigation by Marino et al. (2014). On the other hand, the inverse cascade in purely rotating flows, if it exists, is confirmed to be very small, or appearing at much larger t/τ_{NL} times than for N/f close to one. The reader is referred to the active debate on the inverse cascade in purely rotating turbulence in Chap. 7.

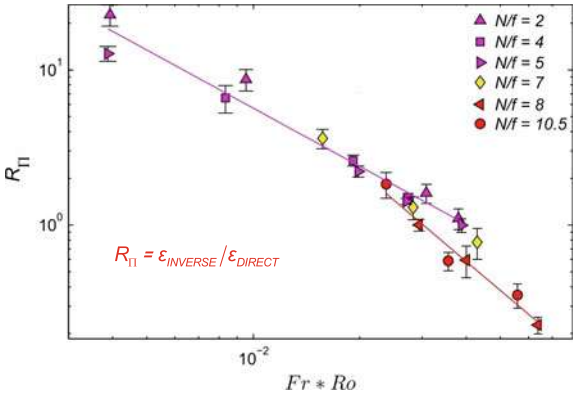

Fig. 11.6 Scatter-plot of R_Π as a function of $Fr.Ro$ in log-log coordinates. Points refer to high-resolution DNS of rotating stratified flows (forced at intermediate scales) where a dual cascade of kinetic energy is observed. A linear scaling prediction holds for each group of points with the same color (thus similar values of f/N) indicating that the scaling is modulated by N/f. Adapted from Marino et al. (2015)

11.2.5 Lagrangian Diffusion in Rotating Stably Stratified Turbulence

It is possible to use purely linear dynamics, as emphasized in the beginning of the present Chapter, but either to use RDT for two-time correlations or to address the equation for a passive scalar advected by the rotating stratified fluid. For instance, in Cambon et al. (2004), two methods were used to predict the single-particle displacement, or absolute Lagrangian diffusion, in addition to DNS.

11.2.5.1 RDT for Two-Time Velocity and Buoyancy Correlations

The method originates from Kaneda (2000). Mean square Lagrangian displacement, or

$$\Delta^2_{ij}(t,t') = \langle x_i(\boldsymbol{X},t)x_j(\boldsymbol{X},t')\rangle \tag{11.24}$$

is obtained by time-integrating the two-point velocity correlation matrix $\langle \hat{u}_i^*(\boldsymbol{k},t)\,\hat{u}_j(\boldsymbol{k},t')\rangle$ derived by inviscid RDT from isotropic initial data. In addition to the assumption of purely linear motion, a simplified Corrsin hypothesis amounts to identify Lagrangian two-time velocity correlations to their Eulerian counterparts. In Cambon et al. (2004), RDT calculations for $\langle \hat{\boldsymbol{w}}^*(\boldsymbol{k},t)\otimes\hat{\boldsymbol{w}}(\boldsymbol{k},t')\rangle$ in rotating and stratified flows derive from Eq. (11.9). A sketch of the displacement vector $\boldsymbol{\Delta}(\boldsymbol{X},t,t') = \boldsymbol{x}(\boldsymbol{X},t') - \boldsymbol{x}(\boldsymbol{X},t)$ is shown in Fig. 11.7. Results from two-time RDT are shown in Fig. 11.8, left. To give a single analytical result among many other ones, the vertical mean square displacement is found as

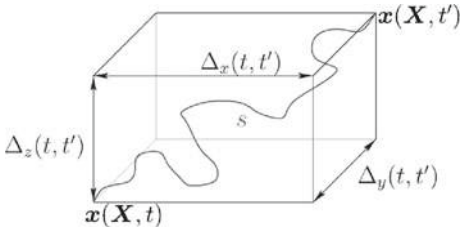

Fig. 11.7 Sketch of a particular trajectory and related displacement $\boldsymbol{\Delta}$, three directions. Reproduced from Liechtenstein et al. (2005) with permission of T and F

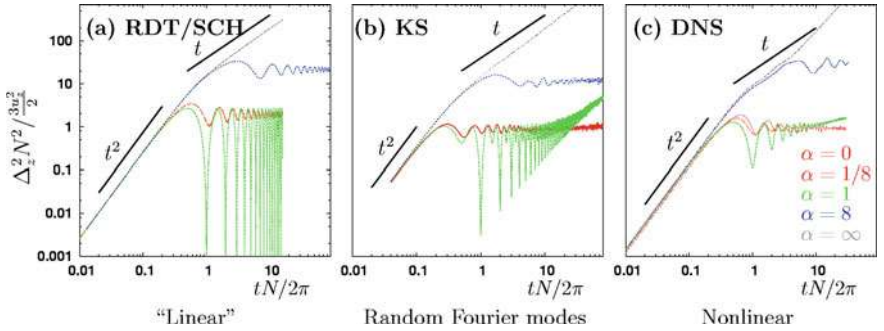

Fig. 11.8 Vertical mean square displacement for single particle diffusion, for rotating and stratified turbulence, $\alpha = f/N$. From RDT using SCH (Simplified Corrsin Hypothesis) (left), KS (center) and DNS (right). Reproduced from Liechtenstein et al. (2005) with permission of T and F

$$\Delta_{33}^2(0,t) = 2\mathcal{K}(t=0)\int_0^1 \left(1-x^2\right)\frac{1-\cos(\sigma_{rs}(x)t)}{\sigma^2(x)}dx, \tag{11.25}$$

with $x = \cos\theta_k = \frac{k_\parallel}{k}$, so that the vertical diffusivity is found as a functional of the dispersion law of dispersive inertia-gravity waves.

11.2.5.2 Kinematic Simulation Incorporating RDT

Kinematic Simulation is very briefly introduced in Chap. 2. For solenoidal velocity fields, it is better formalized using. The Craya Herring frame of reference for the synthetic field, chosen as

$$\boldsymbol{u}^{(KS)}(\boldsymbol{x},t) = \sum_{\alpha=1,2}\left(\sum_{nm} a_{mn}^{(\alpha)}(\boldsymbol{k}_m)\exp\left(\imath\left(\boldsymbol{k}_m\cdot\boldsymbol{x}-\omega_n t\right)\right)\right)\boldsymbol{e}^{(\alpha)}(\boldsymbol{k}_n). \tag{11.26}$$

Under this form, this is only a discretization in terms of spatial Fourier modes (discrete wave vectors $\boldsymbol{k}_m$) and temporal Laplace frequencies ω_n, but the summation

is done over a very large number of randomly chosen spatio-temporal $(\boldsymbol{k}_m, \omega_n)$ parameters, and the amplitudes $a_{mn}^{(s)}$ can be seen as random variables. In this sense, generalized KS is a Lagrangian stochastic model, but very different from the classical Langevin stochastic models, touched upon in Chap. 2.

Trajectories are calculated from

$$\dot{x}_i = u_i^{(KS)}(\boldsymbol{x}, t), \tag{11.27}$$

as for any Lagrangian model, in which "particles" are fluid elements.

From Eq. (11.9), it is easy to move from the general KS model for $\boldsymbol{u}$ to the one for $\boldsymbol{w}$ with additional buoyancy mode, in exactly incorporating linear wave effects, by means of

$$\boldsymbol{w}^{(KS)}(\boldsymbol{x}, t) = \sum_{s'=0,\pm 1} \left(\sum_{mn} a_{nm}^{(s)}(\boldsymbol{k}_m) \exp\left(\imath(\boldsymbol{k}_m \cdot \boldsymbol{x} - [s'\sigma_{rs}(\boldsymbol{k}_n) + \omega_n]t)\right) \right) \boldsymbol{N}^{(s)}(\boldsymbol{k}_n). \tag{11.28}$$

Accordingly, the total frequency $s'\sigma_{rs}(\boldsymbol{k}_m) + \omega_n$ appears as a sum of the deterministic dispersion law (for $s' = \pm 1$) and the random one.

KS results are found in performing statistics from a huge number of realizations for Eq. (11.27) (in which $\boldsymbol{u}_i^{(KS)}$ is the contribution of $\boldsymbol{w}_i^{(kS)}$ removing the spectral component along $\boldsymbol{k}$), and Eq. (11.28). Typical results are shown in Fig. 11.8, center.

11.2.5.3 Discussion of Typical Results

In isotropic turbulence (HIT), the RDT method only recovers the ballistic régime $\Delta^2 \sim t^2$, resulting from a constant velocity correlation matrix. The KS method recovers a correct transition from the ballistic régime, at smaller times, to the Brownian régime $\Delta^2 \sim t$, at larger times. The advantage of KS lies in the model of "turbulent" trajectories, using both Eq. (11.27) and a simplified form of Eq. (11.26) in which a phenomenological scaling of ω_n is incorporated to mimic nonlinear decorrelation. In rotating stratified flows, the operators that reflect dispersive waves give a dramatic change in both two-time RDT and KS. A ballistic t^2 law is found again at small time, but isotropy is broken and new scalings appear at a threshold time close to one period of wave motion: A plateau is found for horizontal mean square displacement in the purely stably stratified case; it is delayed but it persists at larger f/N ratios, as soon as N is nonzero. In the same conditions, the horizontal mean square displacement continue to grow, hence an increasing anisotropy is found. Because the plateau for vertical diffusion can be predicted from simpler phenomenological arguments in flows dominated by stable stratification, the most surprizing result is found in the case of pure rotation: An apparent $\sim t$ Brownian law is found after the ballistic $\sim t^2$ one, but the threshold is found at a much smaller time than the classical transition from ballistic law to "nonlinear" Brownian law. Finally the most striking

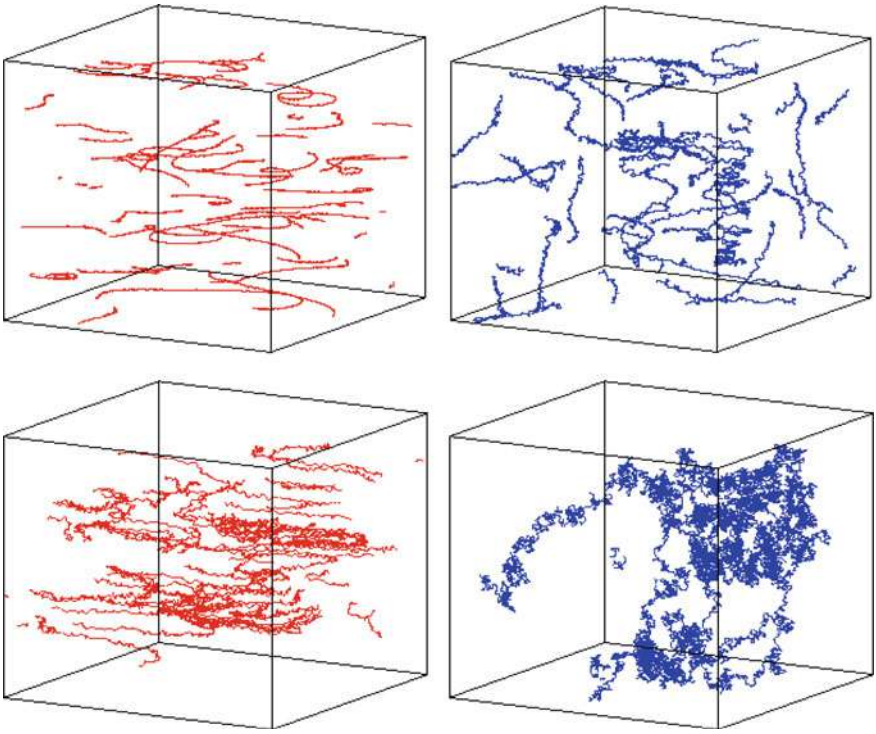

Fig. 11.9 Typical trajectories obtained by DNS (top) and KS (bottom), for purely (stably) stratified (left) and purely rotating (right) flows. Courtesy of L. Liechtenstein

results are given by the analytical law from Eq. (11.25) and a similar one for horizontal diffusion. KS and DNS, as shown in Fig. 11.8, give some refinements but do not question the results from two-time RDT. As a final remark, we have a clear illustration that RDT, even if poorly relevant for predicting single-time second-order statistics, is useful for predicting two-time statistics. Indeed, the phase term $e^{\imath\sigma t}$ cancels out when multiplied by its complex conjugate (single-time case), whereas the product of $e^{\imath\sigma t}$ by $e^{-\imath\sigma t'}$ alters the dynamics in terms of $t - t'$. A similar reasoning can be made for the prediction of third-order correlations, in which the linear wave operator $e^{\imath(\pm\sigma_k \pm\sigma_p \pm\sigma_q)t}$ alter all triads and suggest the role of resonant ones (Fig. 11.9).

11.3 Rotation or Stratification with Mean Shear

From now on, turbulence is subjected to a mean motion as well. The mean buoyancy gradient is vertical as before, and the mean velocity gradient matrix in Eq. (11.4) is given by

$$A_{ij} = S\delta_{i1}\delta_{j3},$$

where the indices 1, 2, 3 refer to streamwise, spanwise and vertical directions of the pure plane shear mean motion, respectively, with $n_i = \delta_{i3}$, as in Fig. 11.14c.

This mean flow is an exact solution of Eqs. (11.2) and (11.3) *if the system rotation axis is in the spanwise direction* i.e. $\Omega_i = \Omega\delta_{i2}$. In this case, Eqs. (11.5) and (11.6) become

$$\frac{\partial b'}{\partial t} + Sx_3\frac{\partial b'}{\partial x_1} + u'_j\frac{\partial b'}{\partial x_j} - \nu P_r\nabla^2 b' = -N^2 u'_3,$$

and

$$\frac{\partial u'_i}{\partial t} + Sx_3\frac{\partial u'_i}{\partial x_2} + S\delta_{i1}u'_3 + u_j\frac{\partial u_i}{\partial x_j} + 2\Omega^s_n\epsilon_{inj}u_j + \nu\nabla^2\boldsymbol{u} = -\frac{1}{\rho_0}\frac{\partial p}{\partial x_i} + b'n_i, \tag{11.29}$$

In the absence of the mean buoyancy gradient, i.e. if $N = 0$, one can get rid of b' and the rotating mean shear flow is a particular solution of the Euler equations in the rotating frame.

The main RDT results are now revisited in the presence of pure plane mean shear, system rotation and/or mean density stratification/buoyancy.

Equations for the fluctuating fields are written in Fourier space. The corresponding variables are denoted $\hat{\boldsymbol{u}}$ and $\hat{b}$ as before, the 'prime' being omitted since there is no ambiguity with the mean flow, never considered in Fourier space.

In all cases addressed below, including the baroclinic context, the linear advection process is only induced by a mean shear, so that the time dependency of the wave vector is always

$$k_1 = K_1, \quad k_2 = K_2, \quad k_3 = K_3 - K_1 St, \tag{11.30}$$

choosing $S = \partial\overline{u}_1/\partial x_3$. In a polar-spherical system of coordinates for the initial wavevector $\mathbf{K}$ in Eq. (11.30), the polar angle, θ, and the azimutal angle, φ, are defined by

$$\sin\theta = \sqrt{k_1^2 + k_2^2}/K, \ \cos\varphi = k_1/\sqrt{k_1^2 + k_2^2}, \tag{11.31}$$

using the usual relationship

$k_1 = K_1 = K\sin\theta\cos\phi, \quad k_2 = K_2 = K\sin\theta\sin\phi, \quad K_3 = K\cos\theta.$

Inviscid RDT governing equations are

$$\frac{d\hat{u}_i}{dt} = -\underbrace{\left[S\delta_{j3}\left(\delta_{i1} - 2\frac{k_i k_1}{k^2}\right) + 2\Omega P_{in}\epsilon_{n2j}\right]}_{M_{ij}}\hat{u}_j + P_{i3}\hat{b}, \tag{11.32}$$

in which contributions from pure shear, Coriolis force and buoyancy effects are taken into account, and

$$\frac{d\hat{b}}{dt} = -N^2 \hat{u}_3. \tag{11.33}$$

As in previous RDT studies, a system of equations is derived in the Craya–Herring frame of reference

$$\begin{pmatrix} \dot{u}^{(1)} \\ \dot{u}^{(2)} \\ \dot{u}^{(3)} \end{pmatrix} = \begin{pmatrix} 0 & (2\Omega + S)\frac{k_2}{k} & 0 \\ -2\Omega\frac{k_2}{k} & S\frac{k_1 k_3}{k^2} & -N\frac{k_\perp}{k} \\ 0 & N\frac{k_\perp}{k} & 0 \end{pmatrix} \begin{pmatrix} u^{(1)} \\ u^{(2)} \\ u^{(3)} \end{pmatrix}, \tag{11.34}$$

with $k_\perp = \sqrt{k_1^2 + k_2^2}$. One can recover easily the terms identified in the pure shear (with S factor), pure rotation (with the dispersion frequency $2\Omega k_2/k$) and in pure stratification (with the dispersion frequency $Nk_\perp/k$) cases. But the main difficulty remains the time dependency of k_3, also reflected on k, which is induced by the pure shear according to Eq. (11.30).

11.3.1 The Rotating Shear Flow Case

The rotating shear flow, with angular velocity aligned with the spanwise direction ($i = 2$ here) and without stratification ($N = 0$) is well documented. The homogeneous case was studied by single-point closure methods, RDT and DNS/LES. Competition between linear and nonlinear effects is analysed by DNS in Salhi et al. (2014) from a multiscale (spectral) anisotropic viewpoint, with many references.

11.3.1.1 Engineering Context

The mechanisms of stabilization and destabilization by rotation, identified in the homogeneous case, can explain what happens in rotating channels and blade cascades in turbomachinery. As a general result, the production of turbulence increases near the pressure-driven (or intrados) wall, in agreement with an anticyclonic rotation with respect to the rotation induced by the mean shear. On the opposite side, the turbulence is damped (relaminarization is even possible) near the succion side (or extrados) wall, in agreement with a cyclonic rotation. Near the middle of the channel, the flat profile corresponds almost exactly to *zero absolute vorticity* for the mean flow, with the anticyclonic constant shear rate S, with vorticity $-S$ in this system of coordinates, balancing the system vorticity 2Ω. (permutating axes 2 and 3, as in all the equations here, S is the mean vorticity (Fig. 11.10).)

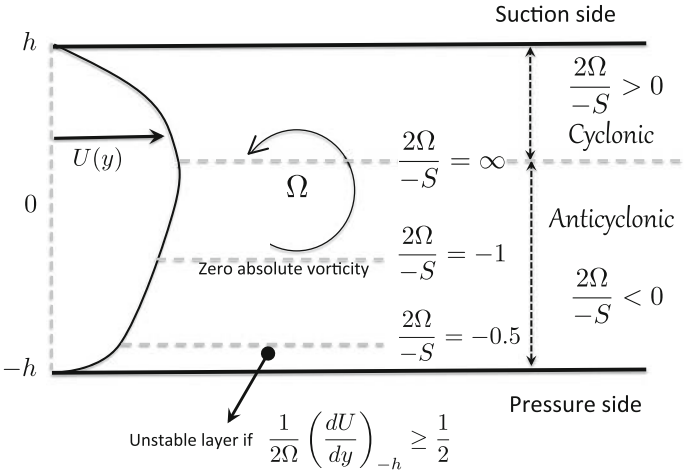

Fig. 11.10 Scheme of the stabilizing/destabilizing effect of rotation in a rotating channel

The asymmetry in terms of cyclonic and anticyclonic spanwise system rotation is not reproduced by a basic $k-\epsilon$ model, which completely misses the Coriolis force effects. It could be recovered, however, by some more sophisticated "nonlinear" versions, which are close to Algebraic Stress Models. Any RSM model can work more satisfactorily, the key-point being to have an exact "production" tensor. The basic effect of production can be understood thanks to the very simple analysis based on a particle-displacement argument introduced by Bradshaw (1969) and revisited in a slightly different way by Tritton (1992).

The starting point is the following system of equations for the planar fluctuating flow, which corresponds to oversimplified *pressure-released* inviscid RDT

$$\frac{d}{dt}u_1' + (S+2\Omega)u_3' = 0, \quad \frac{d}{dt}u_3' + 2\Omega u_1' = 0, \tag{11.35}$$

the spanwise component u_2' being constant in the same conditions. The dynamical behavior of this system is governed by the *Bradshaw number* (or *rotational Richardson number*, in order to avoid a confusion with the "true" Richardson number introduced in the stably-stratified shear case)

$$B = \frac{2\Omega}{S}\left(1+\frac{2\Omega}{S}\right), \tag{11.36}$$

An exponential growth is obtained for $B<0$, and exponential damping for $B>0$ and a neutral behavior is recovered for $B=0$.

This effect of the Bradshaw number is confirmed by much more sophisticated analyses, such as RDT and even "non-homogeneous" stability analyses in more

complex flows. One of the most popular is the one by Pedley (1969), which deals with rapidly rotating pipes.

As pointed out by J. Riley (private communication, see also Yanase et al. 1992), this was almost fortuitously that this oversimplified analysis based on Eq. (11.35) gave the same criterion of instability as the rigorous stability analysis performed by Pedley. A relevant explanation was given by Leblanc and Cambon (1997): in the simplified system (11.35), u_1' and u_3' must be replaced by the amplitudes of *solenoidal* disturbance modes with very high spanwise wavenumber, which are naturally pressure-less, and are not the primitive fluctuating velocity components in the mean shear plane. The term "very high spanwise wave number" is related to modes such that $k_2 \gg 1/L$, where L is a typical lengthscale of the horizontal motion and k_2 is the wavenumber of the disturbance in the direction normal to the plane of the 2D base flow.

Such modes, like $\boldsymbol{v} = \boldsymbol{A}(\boldsymbol{x})e^{\sigma t}e^{\imath k_2}$, with vectors $\boldsymbol{A}$ and $\boldsymbol{x}$ lying in the plane of the base flow, have dominant contributions to exponential instability with respect to all other modes. This result is valid for the stability of any 2D base flow in a rotating frame subjected to 3D disturbances. The system (11.34) gives a simple illustration in "homogeneous" RDT, where $u^{(1)}$ (toroidal mode) and $u^{(2)}$ (poloidal mode) satisfy the same system as the two-component pressure-less one if $k_1 = k_3 = 0, k_2 = k$. In contrast, the pure 2D contribution (no variability in the spanwise direction) is recovered at vanishing k_2, for which the Coriolis force has no contribution.[4] A related point is that only exponential instability is governed by the Bradshaw number B whereas different dynamics are given for the parameters $R = 2\Omega/S$ and $-(1 + R)$, having the same B, as investigated by Salhi and Cambon (1997). The simplest example is the case without rotation and the case with zero absolute vorticity ($R = -1$), which are very different despite they both correspond to $B = 0$.

Looking more closely at RDT solutions, an Ince equation (1956) can be written for both the poloidal and toroidal velocity components. The simplest way is to start from the first two equations in (11.34), so that

$$\frac{1}{S^2}\frac{d}{dt}\left[k^2(t)\frac{du^{(1)}}{dt}\right] + k_2^2 B u^{(1)} = 0 \tag{11.37}$$

$$\frac{1}{S}\frac{du^{(1)}}{dt} = \left(1 + \frac{2\Omega}{S}\right)\frac{k_2}{k(t)}u^{(2)}. \tag{11.38}$$

The first one gives the typical Ince equation, and displays only the Bradshaw (or rotational Richardson) number.

Typical RDT results for the turbulent kinetic energy are shown on Fig. 11.19, and rediscussed in Sect. 11.5.

[4] The mode of planar motion, which is relevant for explaining the stabilizing/destabilizing effect of rotation, is very close to the VSHF mode emphasized in stably stratified turbulence, replacing the vertical direction by the spanwise direction; as the VSHF mode, it is completely different from a 2D mode.

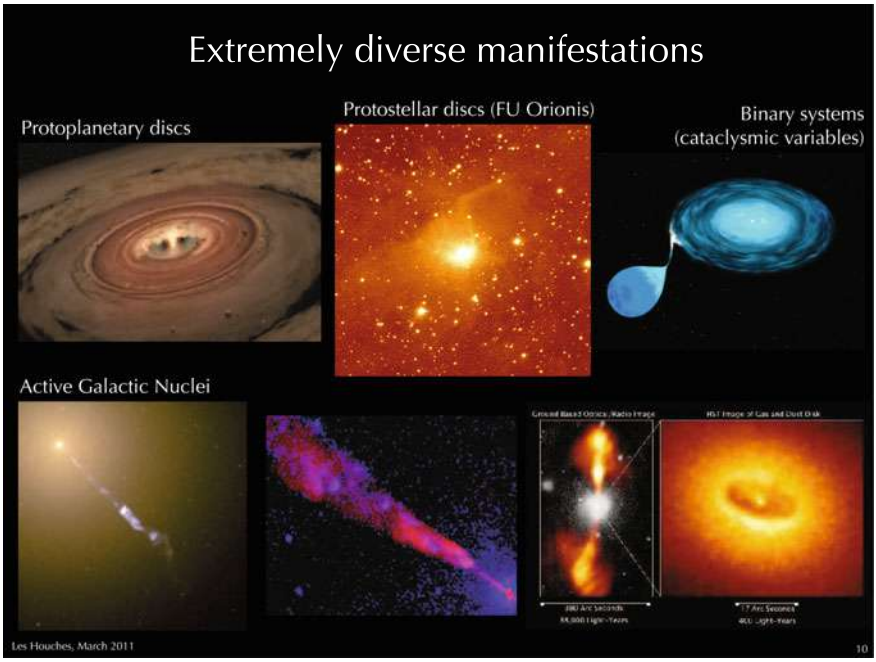

Fig. 11.11 Illustration of accretion discs. Courtesy from François Rincon

11.3.1.2 Astrophysical Context

The homogeneous case of rotating shear flow is used as a toy-model for the dynamics of accretion discs, with an apparently different viewpoint.

The accretion disc, with several examples illustrated by Fig. 11.11, is considered as a cylindrical Taylor–Couette flow, with circular streamlines and *differential* rotation. A typical distribution of the radial rotation rate is $\Omega(r) \sim r^{-q}$. The classical Rayleigh stability criterion for circulation extremum can be written

$$\frac{d\left(r^2\Omega(r)\right)}{dr} < 0 \quad \text{with} \quad \Omega = \Omega_0 \left(\frac{r}{r_0}\right)^{-q} \tag{11.39}$$

for (centrifugal) instability, and yields $2 - q < 0$.

The differential rotation rate yields a radial shear, or $S(r) = r d\Omega(r)/dr$, so that

$$\frac{S(r)}{2\Omega(r)} = -\frac{2}{q} \quad \text{with} \quad \Omega = \Omega_0 \left(\frac{r}{r_0}\right)^{-q}. \tag{11.40}$$

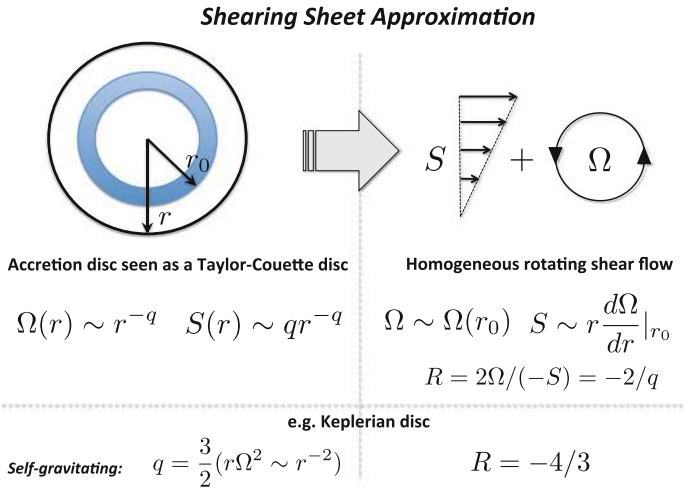

Fig. 11.12 Sketch for the SSA

The abovementioned Bradshaw -Richardson criterion amounts to

$$B = \frac{2\Omega}{S}\left(1 + \frac{2\Omega}{S}\right) = \frac{2}{q^2}(2 - q),$$

therefore the same criterion of instability as the Rayleigh's one is found.

About nomenclature, the approaches by the engineering community and by the astrophysical one, even if they use similar concepts, seem at first glance almost disconnected, especially from their terminology and the fact that they are published in different journals. But all can be reconciled, of course (Fig. 11.12).

The *Shearing Sheet Approximation* (SSA), introduced by Balbus and Hawley (1998), consists of considering a single circular sheet in the rotating disc around $r = r_0$. Once "unrolled", the rectilinear band resulting from the circular band corresponds to a fluid domain with constant $S = S(r_0)$ and constant $\Omega = \Omega(r_0)$. The peripheral direction yields the streamwise direction x_1, the axial direction holds for the spanwise one x_2, and the radial one holds for the cross-gradient, or vertical, one. This explains why the mode $k_1 = 0$, or two-dimensional manifold in the streamwise direction, is called the (axi)symmetric mode in the astrophysical community. In addition, the frequency $\sqrt{2\Omega(2\Omega - S)}$, equal to $S\sqrt{B}$ (in terms of the Bradshaw number, e.g. chosen positive), is called the epicyclic frequency. Finally, the numerical method by Rogallo was recovered by Lesur in 2005, resulting in a "Snoopy" numerical code, very popular among astrophysicists.

11.3.2 The Stratified Shear Flow Case

This case is less documented than the previous one, but a good survey of available results can be found in Hanazaki and Hunt (2004) along with RDT analyses. The analogy between the two cases, rotating and stratified shear flows, was discussed by Bradshaw (1969), but only on the ground of very simple arguments. This analysis suggested a quasi-complete analogy between the number in Eq. (11.36) (called Richardson number in Bradshaw 1969 !) and the *true Richardson number*, which is defined by

$$R_i = \frac{N^2}{S^2} \tag{11.41}$$

in the stratified shear flow case.

In this case, RDT equations yield the following Ince equation for b found by Hanazaki and Hunt (2004)

$$k^2(t)\frac{d^2\hat{b}}{dt^2} - 2Stk_1k_3(t)\frac{d\hat{b}}{dt} + (k_1^2 + k_2^2)N^2\hat{b} = 0, \tag{11.42}$$

which suggested new analytical solutions based on Legendre functions of complex order. Without shear, the time-dependency of the coefficients vanishes in Eq. (11.42), and the periodic solutions are immediately recovered, with a frequency equal to the dispersion frequency of gravity waves: $\sigma_s = N \sin\theta$. Of course, since this equation corresponds to the last one in Eq. (11.34), it can be rewritten as

$$\frac{1}{S^2}\frac{d}{dt}\left[k^2(t)\frac{d\hat{b}}{dt}\right] + (k_1^2 + k_2^2)R_i\hat{b} = 0, \tag{11.43}$$

which displays the Richardson number.

About nonlinear effects, a comprehensive DNS study was given by Jacobitz et al. (1997). The case of homogeneous stratified shear is stable, from linear analysis, for any positive Richardson number. Note that negative Richardson numbers correspond to $N^2 < 0$, that yield unstably stratified turbulence, with exponential growth, in the second part of Chap. 10. The domain of stability with threshold $R_i = 0$ in the linear limit, is shown to extend to $R_i \sim 0.1$ in the DNS, looking at a marginally constant turbulent kinetic energy.

11.3.3 Analogies and Differences Between the Two Cases

When $k_1 = 0$[5] the time dependency of the wave vector vanishes, and RDT solutions with exponential growth (if $B < 0$ or $R_i < 0$) or periodic behavior (if $B > 0$ or $R_i > 0$) are immediately recovered. In the latter case, the typical frequency is the dispersion frequency of gravity waves in the stratified shear case, $\sigma_s = N \sin\theta$, and the dispersion frequency of inertial waves in the rotating shear case, $\sigma_r = 2\Omega \cos\theta$. In the general case ($k_1 \neq 0$), the solutions of the g_{ij}-equations were found in terms of hypergeometric functions (Salhi and Cambon 1997), and then in terms of Legendre functions of complex order (Salhi 2002), generalizing the solutions given by Hanazaki and Hunt (2004). This complex order was denoted μ in the rotating case and γ in the stratified shear case (Salhi 2002), where

$$\begin{aligned} \mu &= \frac{1}{2}(-1 + \sqrt{1 - 4B\tan^2\varphi}\,), \\ \gamma &= \frac{1}{2}(-1 + \sqrt{1 - 4R_i/\cos^2\varphi}\,). \end{aligned} \tag{11.44}$$

According to these new RDT solutions, it can be confirmed that the exponential instability is only governed by the Bradshaw (or rotational Richardson) number, or by the Richardson number, with detailed analogy between rotating and buoyant/stratified cases. Algebraic instability, however, does not scale with neither the Bradshaw nor the Richardson number alone, as stated above by comparing the rotating shear cases at $R = 2\Omega/S$ and at $R = -(1 + 2\Omega/S)$.

11.4 Shear, Rotation and Stratification. Approach to Baroclinic Instability

Two cases with the three nonzero external parameters N, S and f (or 2Ω) are considered in this section. The first one is a natural combination of rotating shear and stratified shear, already addressed separately. The second case yields a toy model for baroclinic instability, introduced by Salhi and Cambon (2006), when considering the angular velocity of the rotating frame aligned with the vertical (cross-gradient) direction of the shear, instead of the spanwise one.

[5]This mode corresponds to an infinite streamwise wavelength, or 2D manifold in the streamwise direction, or symmetric mode in astrophysics.

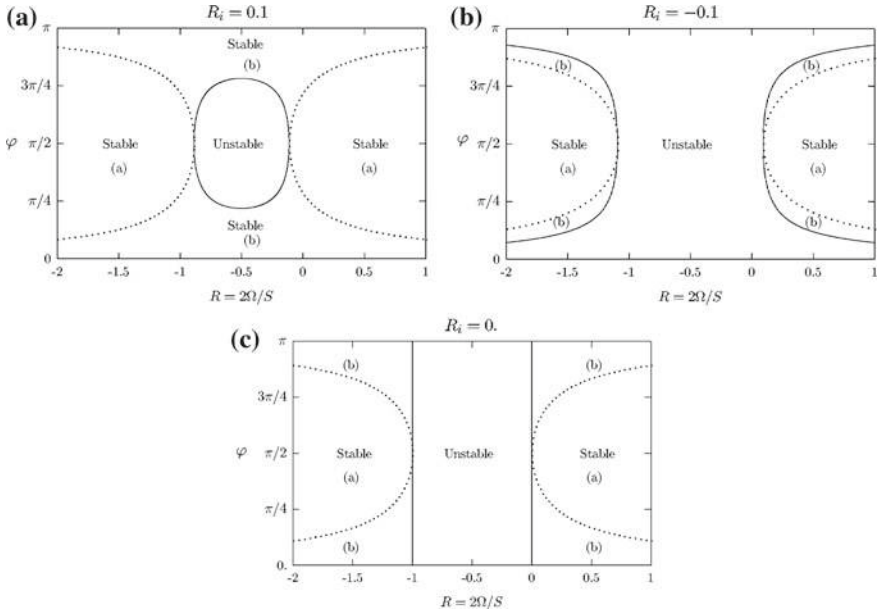

Fig. 11.13 Stability diagram in the (R, ϕ) plane, for three values of the Richardson number. The angle φ in the plane of the mean shear flow is given by Eq. (11.31). The region indexed by **b** corresponds to the stable modes that undergo a power law decay, while the region indexed by **a** corresponds to the stable modes that exhibit a damped oscillatory behavior. The neutral limit is given by the full line, with recovery **c** of the classical case of rotating shear without stratification. Reproduced from Salhi and Cambon (2010) with permission of APS

11.4.1 Case with Spanwise System Rotation and Vertical Mean Stratification

The general RDT solutions are generalized to the shear case with both spanwise system rotation and vertical stratification by Salhi and Cambon (2010), and at least the solutions at $k_1 = 0$ were addressed by Kassinos et al. (2006). Typical results for linear stability are shown in Fig. 11.13. The case of rotating shear without mean stratification is found at $R_i = 0$, whereas it is shown how the unstable domain is extended at $R_i = -0.1$ and reduced at $R_i = 0.1$.

11.4.2 Physical Context, the Mean Flow for Baroclinic Instability

We now consider the same homogeneous turbulent shear flow having mean velocity in the x_1 direction in a Cartesian reference frame, but rotating with angular velocity Ω about the x_3 (vertical) axis (see Fig. 11.14). The absolute mean vorticity is

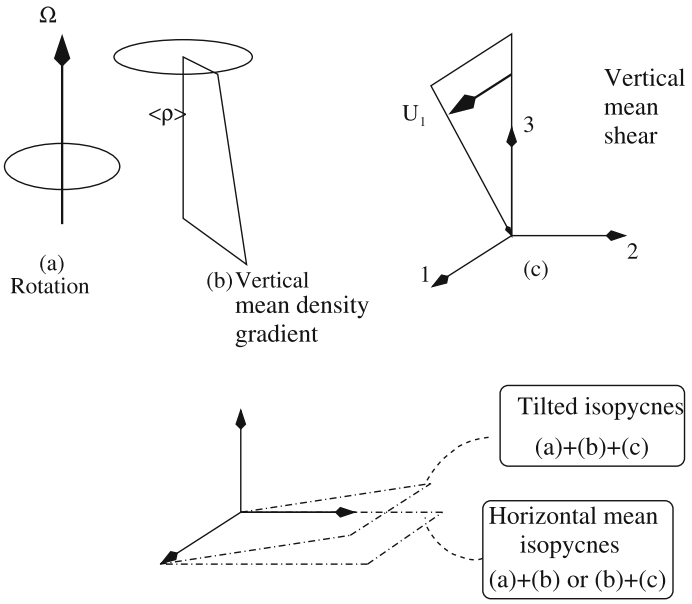

Fig. 11.14 Sketch of the mean flow, including system vorticity (**a**), vertical stable stratification (**b**) and mean shear (**c**). Tilting of isopycnal surfaces can trigger the baroclinic instability, if **a–b–c** are simultaneously present

$$\Omega_i^a = S\delta_{i2} + f\delta_{i3} \tag{11.45}$$

with $f = 2\Omega$. As in the previous section, the mean flow is subject to a vertical stratification, with uniform density gradient

$$\overline{\rho} = \rho_0 - S_\rho x_3, \tag{11.46}$$

where ρ_0 is a constant reference density. S_ρ is chosen positive in the stabilizing case. Equivalently, one has

$$\overline{b} = -N^2 x_3. \tag{11.47}$$

This mean flow is not an exact solution of the Euler equations, which reduces to

$$\frac{\partial \overline{u}_i}{\partial t} + \overline{u}_j \frac{\partial \overline{u}_i}{\partial x_j} + f\epsilon_{i3j}\overline{u}_j = -\frac{1}{\rho_0}\frac{\partial \overline{p}}{\partial x_i} + \overline{b}\delta_{i3} \tag{11.48}$$

The corresponding equation for the vorticity is found by taking the *Curl* of this equation, leading to

$$\frac{dW_i}{dt} + \overline{u}_j \frac{\partial W_i}{\partial x_j} - \frac{\partial \overline{u}_i}{\partial x_j}(W_j + f\delta_{j3}) = -\epsilon_{ij3}\frac{\partial \overline{b}}{\partial x_j} \tag{11.49}$$

This equation is satisfied by Eq. (11.45) in both vertical and spanwise directions, but not in the streamwise direction, for which

$$\frac{dW_1}{dt} - Sf = -\frac{\partial \overline{b}}{\partial x_2}. \tag{11.50}$$

Without an additional spanwise component of the mean density (or buoyancy) gradient, mean vorticity is created in the streamwise direction. Accordingly, in order to remove W_1, the following density gradient component ought to be accounted for

$$\frac{\partial \overline{b}}{\partial x_2} = Sf = -\underbrace{\frac{Sf}{N^2}}_{\epsilon}\frac{\partial \overline{b}}{\partial x_3} \quad \text{with} \quad N^2 = S_\rho \frac{g}{\rho_0}. \tag{11.51}$$

In other words, the tendency for the horizontal density gradient $\frac{\partial \overline{b}}{\partial x_2}$ to generate vorticity, see Eq. (11.50), in the streamwise direction is exactly balanced by twisting the background vorticity associated to the Sf term. This is often called the *geostrophic adjustment of fronts* in the geophysical community (Drazin and Reid 1981).

With respect to the case of *unstable stratification* addressed in Chap. 10, our toy-model consistent with homogeneous turbulence restricted to fluctuations is a first step towards linearly unstable buoyancy-driven flows. The tilting angle ϵ, often small, is replaced by an angle of 180 degree when the sign of the vertical mean buoyancy gradient is changed, from stable to unstable, recovering again mean horizontal isopycnes.

Then, the linearisation of mass and momentum conservation equations yields

$$\frac{\partial u'_i}{\partial t} + \underbrace{Sx_3\frac{\partial u'_i}{\partial x_1} + S\delta_{i1}u_3}_{Shear} + f\epsilon_{i3j}u'_j + \frac{1}{\rho_0}\frac{\partial p}{\partial x_i} = b'\delta_{i3} \quad ; \quad \frac{\partial u'_i}{\partial x_i} = 0 \tag{11.52}$$

$$\frac{\partial b'}{\partial t} + \underbrace{Sx_3\frac{\partial b'}{\partial x_1}}_{Shear} = -N^2\left(u'_3 - \underbrace{\epsilon u'_2}_{HDG}\right). \tag{11.53}$$

Viscous/diffusive terms are ommitted for the sake of brevity: in the b-equation, the diffusivity $\kappa\nabla^2 b$ would be related to the kinematic diffusivity κ of the *stratifying agent*, salt or temperature in an experimental or observational case (of course, diffusion of ρ has no sense in the mass conservation equation). New terms induced by the shear are underlined. They consist of direct distortion terms (Shear) and horizontal density gradient (HDG) effects. Equation (11.50) is a consequence of the basic flow admissibility constraint, which requires that the mean flow must be a particular solution of Euler or Helmholtz equations, as the admissibility condition ($d\mathbf{A}/dt + \mathbf{A}^2$ symmetric) in the pure kinematic non-buoyant case with arbitrary $A_{ij}(t)$. The slope

$\epsilon = \overline{b}_{,2}/\overline{b}_{,3}$ of the mean isopycnal (constant density) surfaces with respect to the horizontal direction is due to the coupling between shear and rotation since $\epsilon = 0$ without shear or without the Coriolis force (the latter cases were addressed in the previous section).

The mean flow with three parameters S, f and N is shown on Fig. 11.14. Two independent non-dimensional numbers can be chosen among the Rossby number, the Richardson number and the baroclinic coefficient

$$Ro = \frac{S}{f}, \quad Ri = \frac{N^2}{S^2}, \quad \epsilon = \frac{Sf}{N^2}. \tag{11.54}$$

Let us emphasize that the present case with nonzero ϵ, which corresponds to the baroclinic instability, can be considered as a model for an important problem in meteorology that is the large-scale instability of the westerly winds in mid-latitudes (Drazin and Reid 1981).

11.4.3 Advanced RDT Equations in Fourier Space

The equation for the velocity Fourier mode is derived from (11.32), only changing $2\Omega\epsilon_{n3j}$ into $f\epsilon_{n2j}$, whereas the new equation for $\hat{b}$ is found as

$$\frac{d\hat{b}}{dt} = -N^2\left(-\epsilon\hat{u}_2 + \hat{u}_3\right). \tag{11.55}$$

For the sake of convenience, a new scaling is used to define the third buoyancy-related mode, keeping unchanged the two solenoidal modes: $u^{(3)} = (S/N^2)\hat{b}$. After some tedious algebra, a new system of equations, very similar to (11.34) is obtained:

$$\begin{pmatrix} \dot{u}^{(1)} \\ \dot{u}^{(2)} \\ \dot{u}^{(3)} \end{pmatrix} = \begin{pmatrix} 0 & \frac{k_2+\epsilon R_i k_3}{k} & 0 \\ -\epsilon R_i \frac{k_3}{k} & \frac{k_1 k_3}{k^2} & -R_i \frac{k_\perp}{k} \\ -\epsilon \frac{k_1}{k_\perp} & \frac{k_\perp}{k} + \epsilon \frac{k_2 k_3}{k k_\perp} & 0 \end{pmatrix} \begin{pmatrix} u^{(1)} \\ u^{(2)} \\ u^{(3)} \end{pmatrix} \tag{11.56}$$

A possible viscous factor modified only by mean shear at $Pr = 1$ (Prandtl number) is not recalled for the sake of brevity (see Salhi and Cambon 1997; Hanazaki and Hunt 2004; Salhi 2002.)

Simple analytical solutions of the system (11.56) are obtained when considering the $k_1 = 0$ mode that corresponds to an infinite streamwise wavelength. In this case, the wave vector is no longer time-dependent, since the shear advection vanishes. Accordingly, the coefficients of the system of RDT are constant, and analytical solutions are easily found.

For $k_1 = 0$, on obtains

$$\dot{u}^{(1)} = \frac{k_2 + \epsilon R_i k_3}{k} u^{(2)} \tag{11.57}$$

$$\dot{u}^{(2)} = R_i \left(\frac{\epsilon k_3}{k} u^{(1)} - \frac{k_\perp}{k} u^{(3)} \right) \tag{11.58}$$

$$\dot{u}^{(3)} = \left(\frac{k_\perp}{k} + \epsilon \frac{k_2 k_3}{k k_\perp} \right) u^{(2)} \tag{11.59}$$

leading to the following equation for the poloidal component

$$\ddot{u}^2 + \underbrace{R_i \left((\epsilon \frac{k_3}{k} + \frac{k_2}{k})^2 - (1 - R_i)\epsilon^2 \frac{k_3^2}{k^2} \right)}_{\sigma_0^2} u^{(2)} = 0 \tag{11.60}$$

These solutions exhibit an oscillating behaviour (stable case) when $\sigma_0^2 > 0$, an exponential growth (unstable case) whenever $\sigma_0^2 < 0$, and a linear (algebraic) growth if $\sigma_0 = 0$, where

$$\sigma_0^2 = \left[\left(\frac{\cos\theta}{R_0} + \sin\theta \right)^2 - (1 - R_i) \sin^2\theta \right]. \tag{11.61}$$

Neutral curves drawn in the $(R_i, \theta = \widehat{(\boldsymbol{k}, \boldsymbol{n})})$ plane for $k_1 = 0$ for different values of Ro (left) and ϵ (right) are displayed in Fig. 11.15. For the latter case, a zoom is made on small values of ϵ, which are more relevant for geophysical applications.

It is shown that the threefold coupling between shear, rotation and stratification allows to extend the band of instability until $R_i = 1$. Without system rotation, the instability essentially concerns negative values of the Richardson number, and is limited by rather small positive values of R_i: $R_i \sim 0.1$ from DNS (Jacobitz et al. 1997) and LES studies, while $Ri = 1/4$ is recovered from the analysis of Miles (1961)[6]

About the occurence of baroclinic instability in the geophysical context, the pionering approach by Eady (1949) seems to be radically different at first glance, but numerical solution of the general RDT equations at $k_1 \neq 0$ yields amplification rates which are comparable to those found by Eady for small values of the parameter ϵ (such values are illustrated in the left part of Fig. 11.15). Typical DNS results, carried out for extending the RDT results are shown in Fig. 11.16. Another recent approach by Mamatsashvili et al. (2010) yields extension of the analysis by Salhi and Cambon (2006) towards transient growth. More details are given in Sect. 11.7.1.

[6]The stability analysis of Miles, however, is different, since it accounts for a possible inflexion point of the mean shear profile for an horizontal slab limited by two horizontal walls.

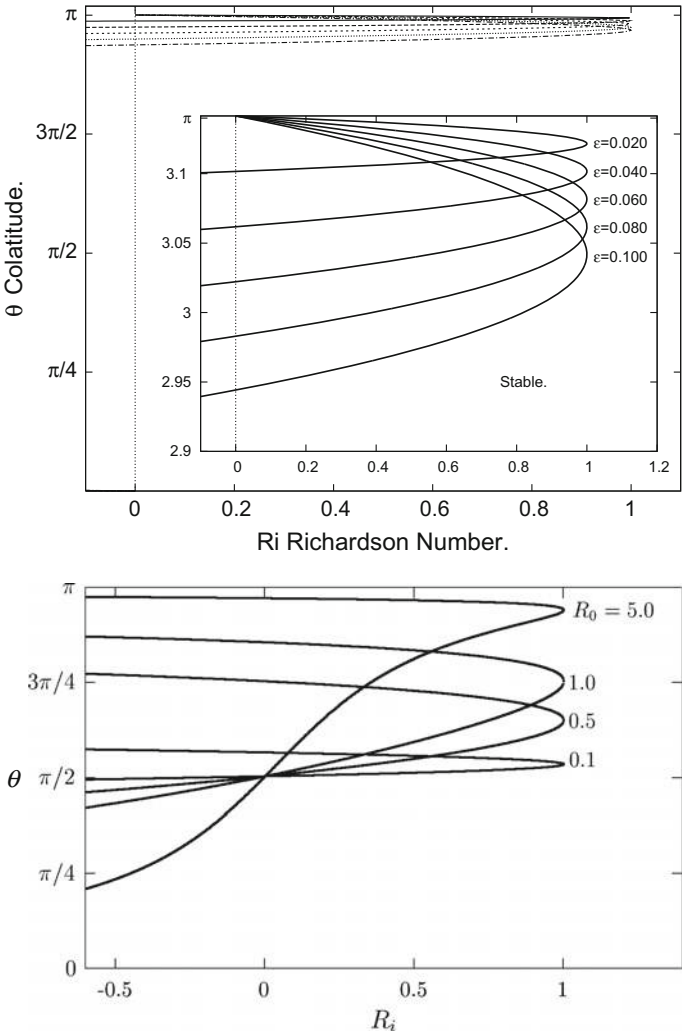

Fig. 11.15 Neutral curves (exponentially instable zone are in the part of the surface delineated by the concave side of the curve), or $\sigma_0 = 0$, for $k_1 = 0$, at different values of ϵ (top) and Ro (bottom)

The particular approach to baroclinic instability with extensional shear flow and statistical homogeneity restricted to fluctuations, was continued by a comprehensive linear analysis of the role of potential vorticity (Pieri et al. 2012), then by DNS (Pieri et al. 2013). The latter study contributes to disentangle what is called "symmetric instability", only induced by the presence of negative background potential vorticity, from the general baroclinic context.

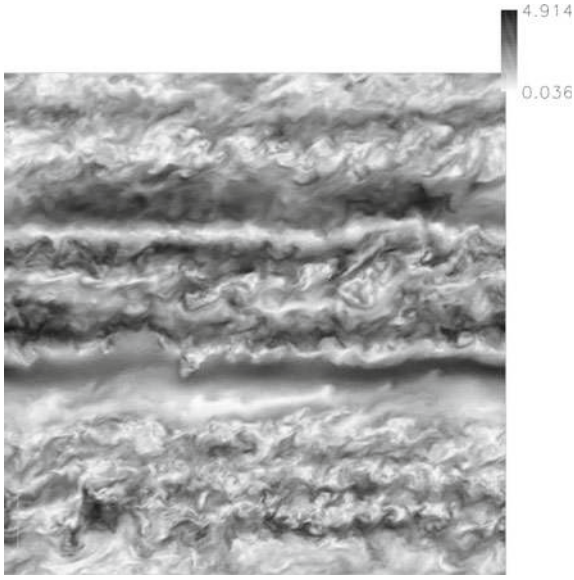

Fig. 11.16 Isosurfaces for the buoyancy fluctuation in the zonal spanwise-vertical plane, from DNS. $\epsilon = 0.2$, $Ri = 0.99$, $Re_\lambda(t = 0) = 66$. Courtesy of Guillaume Simon

11.5 The Elliptical Flow Instability from "Homogeneous" RDT

11.5.1 General Case, Rotation Coupled with Additional Small Strain

This instability is very generic and occurs in many flow configurations. The reader is referred to Kerswell (2002) for a detailed review. A sudden interest arised when Pierrehumbert discovered its characteristic properties by a conventional normal mode analysis approach, whereas at the same time (Bayly 1986) found the same results using a much simpler and more elegant method, which is essentially equivalent to RDT (e.g. Cambon 1982; Cambon et al. 1985).

Ellipticity in the core of large vortices is very general. It can originate in mutual interaction of adjacent vortices, whereas an isolated vortex can remain circular. As proposed by the authors previously mentioned, it is not necessary to study the stability of a pair of vortices, but to study the stability of a single vortex, getting rid of the mutual-interaction origin of the ellipticity.[7] One just has to assume, in addition, that the typical wavelength of the instability is small with respect to the dimension of the core of the vortex. In this sense, elliptical instability is a local instability in actual flows, in contrast with cooperative instabilities (e.g. the Crow instability in a vortex pair) which involve the whole pattern of adjacent eddies.

[7] A similar reasoning is made when the mean shear is considered a priori, getting rid of its origin, like solid wall effects.

Going back to RDT, one has to imagine that the mean flow given by Eq. (8.8) with $S < \Omega$ represents an infinite elliptical eddy. In this case, no mean lengthscale may appear, and dynamics of initial disturbances depends only on the orientation, but not on the modulus, of their wave-vector. The effect of a viscous cut-off in viscous RDT can be easily accounted for, but it will not be discussed here for the sake of brevity. Of course, it is more realistic to consider that the elliptic core has a finite size, and that RDT (or WKB RDT, or short-wave asymptotics) is only valid for disturbances with wavelengths much smaller than this size, but equations are essentially the same.

RDT calculations carried out by Cambon (1982), Cambon et al. (1985) for $S < \Omega$ foreshadowed the Bayly's analysis. Such calculations contributed to motivate the experimental study by Leuchter and coworkers, with the design of a very complex distorting duct capable of reproducing an elliptical flow case with $S = \Omega/2$, as discussed in Chap. 8. Observation of a clear elliptical flow instability was problematic, given the limited length of the duct. The emphasis was put on the complex evolution of Reynolds stress components, related spectra and integral lengthscales, for statistical modelling purpose. In order to avoid confusion with the notations used in this chapter, the strain rate will be called D (and not S, kept for the shear rate only) and the vorticity of the elliptical eddy will be called W (and not 2Ω, kept for the system vorticity in the rotating frame). Expressed in terms of the solenoidal modes $u^{(1)}$ and $u^{(2)}$, the general RDT equations are

$$\begin{pmatrix} \dot{u}^{(1)} \\ \dot{u}^{(2)} \end{pmatrix} = \begin{pmatrix} 2aD & -\frac{k_3}{k}(W+2\Omega) \\ 2bD + \frac{k_3}{k}(W+2\Omega) & \frac{\dot{k}}{k} - aD \end{pmatrix} \begin{pmatrix} u^{(1)} \\ u^{(2)} \end{pmatrix}, \tag{11.62}$$

with $a = e_1^{(1)} e_1^{(1)}$ and $b = e_1^{(2)} e_2^{(1)} + e_2^{(2)} e_1^{(1)}$ (Cambon 1982; Cambon et al. 1994), choosing the axial vector $\boldsymbol{n}$ along the direction of mean vorticity ($\boldsymbol{n}$ normal to the plane of the 2D mean flow here). Choosing $\boldsymbol{n}$ in the (cross-gradient) direction of the shear is interesting too, but not discussed here (see Salhi et al. 1997). For more generality, and anticipating the study by Craik (1989), an additional Coriolis effect is accounted in the previous equation, the case of the basic elliptical instability in a Galilean frame being recovered for $\Omega = 0$ and $D < W/2$. As a very simple term, *the matrix exhibits the projection of the absolute vorticity* $2\boldsymbol{\Omega} + \boldsymbol{W}$ *onto the wave vector, as the unique contribution from rotational terms*.

Solving analytically this system of two equations is difficult because $\boldsymbol{k}$ is periodic in time according to the Eikonal equation (17.28), so that all coefficients a, b and $\dot{k}/k$ are periodic as well. Computation of the Green's functions $g_{\alpha\beta}$ and $\mathbf{G}$ must therefore be performed through numerical integration. The main result is displayed in Fig. 11.17.

This figure has the merit to suggest the mechanism of *resonant amplification* by a periodic forcing, which is more accurately captured by Bayly (1986) using a Floquet analysis.

The Floquet analysis takes advantage of the fact that the coefficients in the linear system of equations are periodic with a frequency

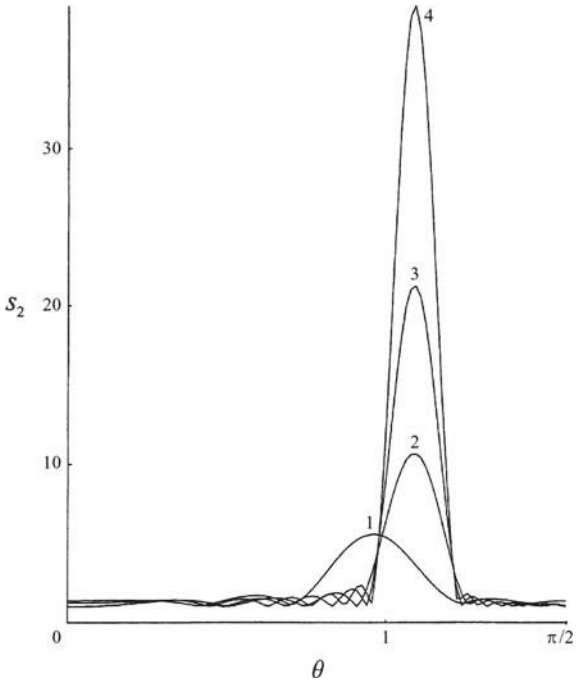

Fig. 11.17 Figure reproduced from Cambon's thesis (1982) in Godeferd et al. (2001): Maximum eigenvalue of the symmetric Green's function $\mathbf{G}\tilde{\mathbf{G}}$ as a function of the direction θ of the wavevector measured from the polar axis (Taken at a period $t = 2\pi/\sigma_0$, this eigenvalue differs only from the actual Floquet parameter because of the use of a symmetric form of the Green's matrix). Curves labelled 1, 2, 3, 4, are obtained at times $t/T = 1.3, 2, 2.5, 3$ in terms of the period $T = 2\pi/\sigma_0$, $W/(2D) = 3$

$$\sigma_0 = \sqrt{\left(\frac{W}{2}\right)^2 - D^2}. \tag{11.63}$$

It is therefore possible to compute the Green's function only for a single period $T = 2\pi/\sigma_0$, and to extract its eigenvalues once for all. The Green's function given by an arbitrary number p of periods is obtained by simply calculating the power p of the one-period matrix. Exponentiation of the one-period matrix amounts to exponentiation of its eigenvalues, so that the amplification rate is easily calculated from a single-period run.

The instability band was found to correspond to

$$W\frac{k_3}{k} \sim \pm W/2,$$

at very small D: one recovers in the left-hand side the intrinsic frequency of inertial waves, which is also the dominant term in Eq. (11.62) at small D, whereas the right-hand side is the frequency of the external forcing following mean elliptical streamlines at small D. One can imagine a scheme where the wave-vector direction describes a periodic trajectory (with frequency $W/2$ at vanishing D), whereas the Fourier component rotates in the plane normal to it with frequency $W\cos\theta = Wk_3/k$: resonance is found when $\cos\theta = \pm 1/2$. The subharmonic conditions with $\cos\theta$ given

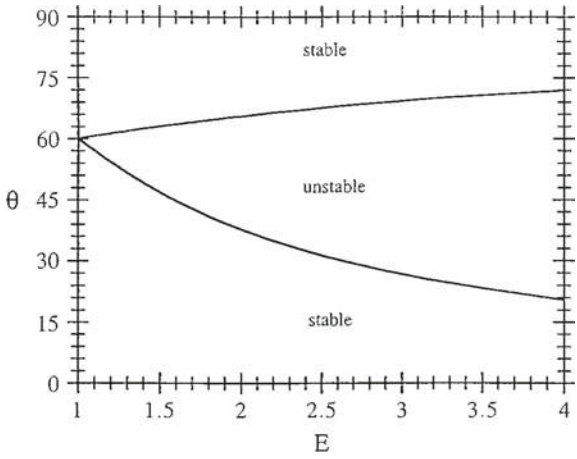

Fig. 11.18 Typical instability band in the θ- e plane, $e = (W/2 - D)/(W/2 + D)$ being the ellipticity. Reproduced from Salhi et al. (1997) with permission of AIP

by a rational number other than $\pm 1/2$ yield no significant amplification here. The location of the instability peak near $\frac{k_3}{k} = \cos\theta = \pm 1/2$ in Fig. 11.17 is therefore explained. The maximum growth rate at the leading order in terms of D/W is found as

$$\sigma = \frac{9}{16} D,$$

for the particular wavenumber orientation $\cos\theta = 1/2$. On time-average, this means that the vorticity $\hat{\omega}$ aligns itself with the underlying stretching direction.

Using the rigorous Floquet analysis, it is shown how the instability band, which emanates from the point $\theta = \pi/3$ at vanishing ellipticity, expands at larger ellipticities (see Fig. 11.18).

Among a lot of results not given here for the sake of brevity, one can mention the analytical study of an Ince equation by Waleffe (1990). Such an equation can be obtained by deriving a single second-order ordinary differential equation from the system (11.62), as we have seen other examples in the previous sections. Transition to turbulence was further investigated using LES/DNS by Lundgren and Mansour (1996) (Fig. 11.19).

Let us also mention the shift of the instability band when the elliptical flow is seen in a reference frame rotating at angular velocity Ω (Craik 1989): it is simply found using

$$(2\Omega + W)\frac{k_3}{k} \sim \pm W/2.$$

This illustrates that the system vorticity and the relative (mean) vorticity do not act in the same way: they are simply added in the left-hand side, displaying the absolute vorticity in the dispersion frequency, but W is kept in the right-hand side. Typical results from inviscid and viscous RDT for the rotating elliptical flow are shown in Fig. 11.20. As shown by Cambon et al. (1994), Salhi et al. (1997), four flow cases

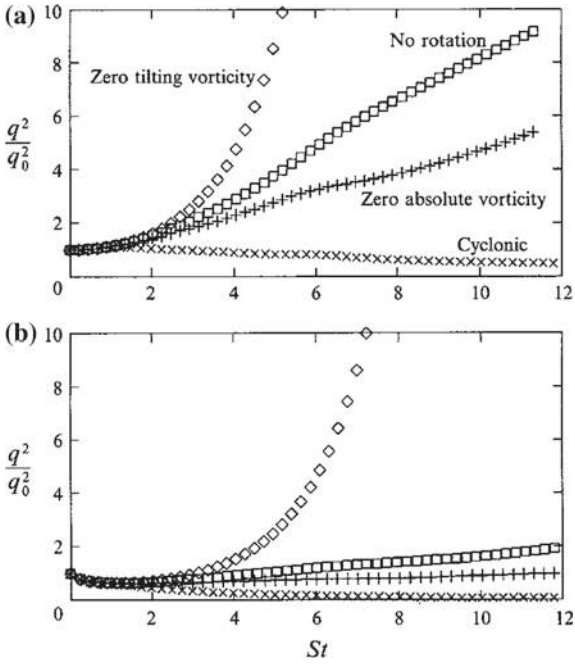

Fig. 11.19 Inviscid (**a**) and viscous (**b**) RDT results for the four cases $R = 2\Omega/W$, pure shear flow in the rotating frame. Reproduced from Cambon et al. (1994) with permission of CUP

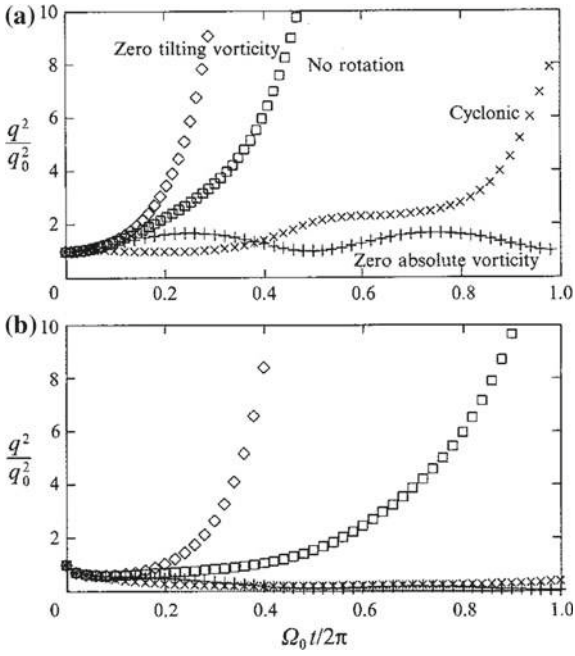

Fig. 11.20 Inviscid (**a**) and viscous (**b**) RDT results for the four cases, $R = 2\Omega/W$, elliptical flow case with $D = W/4$ in the rotating frame. Reproduced from Cambon et al. (1994) with permission of CUP

are very relevant among all possible 2D mean flows with rectilinear $D = W/2$, hyperbolical $D > W/2$, or elliptical $D < W/2$ streamlines in the frame rotating with angular velocity Ω:

- the reference case without system rotation,
- the case with zero mean *tilting vorticity*, $2\Omega + W/2 = 0$, which gives always the most destabilizing one,
- the case with zero mean absolute vorticity, $2\Omega + W = 0$ which is always the only unconditionally stable one, even if subject to some algebraic growth. (see also Craik 1989),
- a cyclonic case, with $2\Omega = W/2$.

Viscous RDT is only given here as a reference, in order to show the effect of a viscous cut-off, and therefore to select only the most robust exponential growths.

11.5.2 Precessing Rotational Flows with Additional Shear

The case of precessing rotational flow offers an example of elliptic instability, in which the ellipticity of mean trajectories results from an additional mean shear. In our simplified context of extensional mean flow and homogeneity restricted to fluctuations (Salhi and Cambon 2009), the additional shear is induced by the gyroscopic torque, that results from the misalignment of a main rotation and a secondary one, treated as an external Coriolis force.

We consider a flow subjected to pure solid-body rotation, of angular velocity $\boldsymbol{\Omega}$, and seen in a frame rotating with an additional angular velocity $\boldsymbol{\Omega}^c$. As for the baroclinic case, the mean flow only given by solid body rotation is no longer a solution of Euler equations if Ω and Ω^c are not aligned. The mean vorticity is not conserved due to the term $\boldsymbol{\Omega} \times \boldsymbol{\Omega}^c$. It is suggested from the general analysis of Kerswell, who revisited the Poincaré's study of spheroidal container, that the effect of an additional mean shear flow can exactly balance the abovementioned gyroscopic torque. This additional mean shear flow scales with the Poincaré number, or Ω^c/Ω, denoted ϵ. Of course, this parameter is very small in the geophysical context ($\sim 10^{-7}$, known from Ptolemeus!), but significant values up to 0.2 are displayed in typical experimental studies to trigger instability and turbulence.

Considering the case in which $\boldsymbol{\Omega}$ and $\boldsymbol{\Omega}^C$ are perpendicular, superposition of solid-body rotation and additional shear yield two cases

$$\boldsymbol{U} = \Omega \begin{pmatrix} 0 & -1 & 0 \\ 1 & 0 & 0 \\ 0 & -2\epsilon & 0 \end{pmatrix} \boldsymbol{x} \quad \text{and} \quad \boldsymbol{U} = \Omega \begin{pmatrix} 0 & -1 & 0 \\ 1 & 0 & -2\epsilon \\ 0 & 0 & 0 \end{pmatrix} \boldsymbol{x}, \tag{11.64}$$

with $\Omega_i = \Omega\delta_{i3}$ and $\Omega_i^C = \epsilon\Omega\delta_{i1}$. Both cases corresponds to planar elliptic trajectories, but in a different plane. The first one corresponds to the analysis of Mahalov, and is referred to as MBF (Mahalov Base Flow) (Mahalov 1993), and the second one

is KBF (Kerswell Base Flow) (Kerswell 1993). In addition to details to be found in Mahalov (1993), Kerswell (1993), Salhi and Cambon (2009), new instability tongues are presented in Chap. 12 for magnetized precessing flow.

11.6 Axisymmetric Strain with Rotation

Axial strain, as the one obtained near the centerline of a convergent axisymmetric duct, was addressed in Chap. 8. An interesting case was obtained by Leuchter and Dupeuble (1993), when adding an axisymmetric convergent duct after the generator of rotation illustrated in Fig. 7.3. In close connection with what was observed when rapid rotation is suddenly applied to axisymmetric initial data (see Fig. 7.10), the anisotropy of the flow is dramatically modified. This effect is completely missed by any RSM model, since it is linked to the selective rapid damping of polarization anisotropy by phase-mixing, the directional anisotropy being conserved. This linear effect can be reproduced by the structure-based model of Kassinos and Reynolds, as discussed in Cambon and Scott (1999).[8]

A more sophisticated study was carried out by Leuchter and Cambon (1997), with access to both linear and subtle nonlinear effects of rotation in the straining geometry, using RDT, DNS and EDQNM-2. The anisotropy parameter $A/(2\mathcal{K})$, with

$$A = b_{33} - (b_{11} + b_{22})/2,$$

is plotted in Figs. 11.21 and 11.22. This parameter is the unique one needed to characterize b_{ij} with axial symmetry, since b_{ij} is diagonal with $b_{11} = b_{22} = -b_{33}/2$. A RSM model can reproduce the rise of A with negative value due to the axisymmetric strain, reflecting the rise of a 'pancake-type' Reynolds stress tensor $b_{11} = b_{22} > 0$, but not the effect of additional rotation, which partly counterbalances this production.

The case of axial compression with rotation can be considered as another case of "compressed", not compressible, turbulence, as discussed in Sect. 14.3 of Chap. 14. If the compression is periodic — this could be illustrated in a reciprocating engine with swirl – specific instabilities can be shown using homogeneous RDT, very closely to the elliptical flow case. After a first numerical RDT computation by C. Cambon, a complete Floquet's analysis was performed by Mansour and Lundgren (1990), showing different bands of instability similar to the one displayed in Fig. 11.18. A mechanism of parametric resonance of inertial waves by the external periodic compression is displayed. This mechanism was further investigated in the more realistic configuration of an axially rotating cylindrical vessel, with small-amplitude periodic compression (Duguet et al. 2005).

[8]The damping of polarization anisotropy was referred to as 'rotational randomization' in the structure-based model.

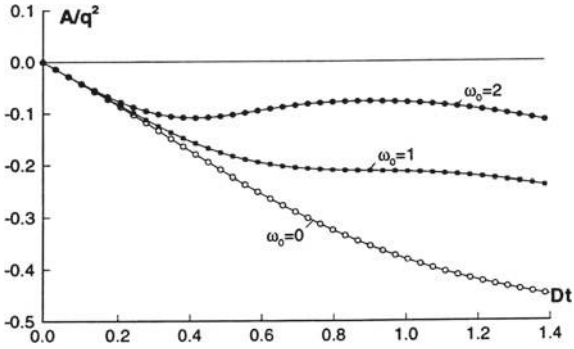

Fig. 11.21 A-parameter (which characterizes the RST anisotropy in the case of axial symmetry) with $q^2 = 2\mathcal{K}$. ω_0 is the rotation-to-strain-rate ratio. RDT calculation, data taken from Leuchter and Cambon (1997). Courtesy of O. Leuchter

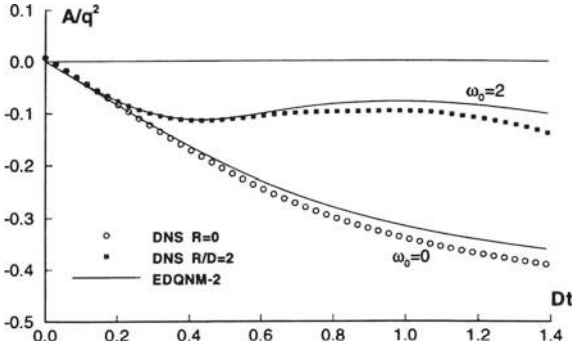

Fig. 11.22 Same quantities and parameters as in Fig. 11.21. DNS and EDQNM-2 results, data taken from Leuchter and Cambon (1997). Courtesy of O. Leuchter

11.7 Relevance of RDT and WKB RDT Variants for Analysis of Transient Growth and Exponential Instabilities

Recent literature on algebraic instability, consistent with transient growth of disturbances, offers a modern continuation of what was called "RDT" in Cambridge. Applications address the dynamics of accretion discs. Going back to the toy-model derived from the Taylor–Couette flow in Sect. 11.3.1, the case of self-gravitating disc, or Keplerian disc, is particularly important. In this case the gravitational force balances the centrifugal force, or $\Omega^2(r)r \sim r^{-2}$, resulting in $q = 3/2$. According to the simple stability criterion, from Rayleigh or from Bradshaw via the shearing sheet approximation, the Keplerian disc is stable ($S/(2\Omega) = -4/3 < -1$). From the observation that a Keplerian disc is probably turbulent, several alternative explanations were proposed. Recourse to exponential instability, as the Magneto-Rotational Instability (MRI) is well known for magnetized discs (see Chap. 12). Additional density stratification, possibly both in axial and radial direction, as in Salhi et al. (2013), is invoked as well. Among them, one of the most promising approach is the role of transient growth, that can trigger a transition to turbulence. Transient growth, connected to algebraic instability, is addressed by a non-normal or nonmodal linear

analysis (Schmid 2007), usually looking at the continuous spectrum of temporal complex amplification rates in classical hydrodynamic stability analysis. Because linear RDT can address algebraic growth as well, it is the simplest model to be used. In all the simplified mean flows considered from now on in this chapter, transient growth is induced by modes $k_1 \neq 0$, for which the wave vector is time-dependent, from Eq. (11.30).

Another useful variant of homogeneous RDT is its extension to inhomogeneous flows, for zonal analysis, via a WKB approximation.

11.7.1 Transient Growth and Generalized Wave-Vortex Dynamical Analysis

Linear stability of the extensional pure shear flow offers the guidelines for explaining strong algebraic growth of disturbances. In the language of astrophysicists who rediscovered RDT, the Fourier modes with possibly time-dependent wave vector are called SFH (Spatial Fourier Harmonics) or Kelvin modes, but the latter nomenclature is confusing (two many Kelvin's modes and Kelvin's waves!). The $k_1 = 0$ mode, or 2D mode in the streamwise direction, is called the symmetric (or axisymmetric) mode, and particular emphasis is put on the asymmetric mode $k_1 \neq 0$, which generates the time-dependent $k_3(t)$ wavenumber in the cross-gradient direction, which is the key for the simplest analysis of the non-normal (or nonmodal, see Schmid 2007) stability. Following Chagelishvili et al. (2003), several publications are now dedicated to transient growth and bypass transition to turbulence in sheared flows. A simple scheme of the bypass scenario in Keplerian disc flow is given in the wavenumber plane ($k_x(= k_3), k_y(= k_1)$) of the mean shear in Fig. 11.23. Viscous dissipation can be neglected in an "active domain" of sufficiently low value of $k = \sqrt{k_1^2 + k_3^2}$. The point 1 in the figure corresponds to $k_3/k_1 < 0$: According to Eq. (11.30), the velocity Fourier mode drifts in the direction marked by the arrows. Initially, as $\mid k_3 \mid$ decreases, the energy of the velocity Fourier mode grows. this grows lasts until the wave vector crosses the line $k_3 = 0$ (point 2). Then, while undergoing attenuation, the velocity Fourier mode continues its drift until it reaches the point 3, where it is dissipated through viscous friction. The same will occur with all other Fourier modes. Consequently, if the nonlinear interaction between different Fourier modes is inefficient, the perturbation disappears eventually. Permanent extraction of shear energy by the perturbations is necessary for their maintenance, which is possible when quadrants II and IV where $k_3/k_1 < 0$ are being repopulated through nonlinear interactions between Fourier modes of quadrants I and III that have reached sufficient amplitude. An example of triadic nonlinear process $\boldsymbol{k}_1 + \boldsymbol{k}_2 \rightarrow \boldsymbol{k}$ is presented in the Fig. 11.23, process that contributes to the regeneration of a velocity Fourier mode in the amplification area, transferring perturbation energy to it from the attenuation areas.

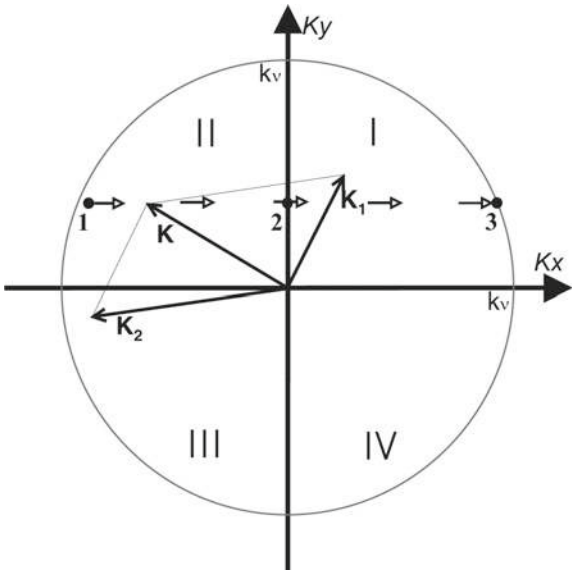

Fig. 11.23 Sketch of the bypass scenario applied to Keplerian disc flows, in the wave vector plane of the mean shear. Here, k_x (for k_3) is the wavenumber in the radial direction (or cross-gradient using SSA) and k_y (for k_1) in the azimuthal direction (or streamwise using SSA). The wave vector $\boldsymbol{k}(t)$ of the velocity Fourier mode $\hat{\boldsymbol{u}}(\boldsymbol{k}, t)$ drifts from its initial position 1, $\hat{\boldsymbol{u}}(\boldsymbol{k}, t)$ is amplified in quadrant II, reaches maximum amplitude in 2, is attenuated in quadrant I, and undergoes viscous dissipation in 3. But the amplification quadrant II is repopulated through nonlinear interaction from velocity Fourier modes located in the attenuation quadrants I and III (see text for more details). Reproduced from Chagelishvili et al. (2003), with permission of A and A

The following conclusions are drawn from this preliminary 2D analysis of Chagelishvili et al. (2003):

- the onset of turbulence and the turbulent state itself in smooth spectrally stable shear flows is supported energetically by the linear transient growth of vortex mode perturbations;
- nonlinear processes do not contribute to any energy growth, but *regenerate vortex mode perturbations that are able to extract shear flow energy;*
- the non-orthogonal nature of linearized Navier–Stokes equations is the formal basis of the transient growth;
- the non-orthogonal nature increases with increasing Reynolds number; thus the operators are highly nonnormal for the huge Reynolds number of Keplerian discs ($Re > 10^{10}$).

A second important ingredient for a simpler analytical treatment is the use of invariants, as linear combinations of the components of disturbances. The rank of the linear system of equations can be reduced, leading to nonhomogeneous differential equations. This is called generalized wave-vortex decomposition in the astrophysical community, following Chagelishvili et al. (1997). The first example discussed below

is the case of rotating stratified shear flows, in which the linearized potential vorticity is the invariant and provides the "vortex" mode of the decomposition.

In the presence of mean shear, the linearized APV mode given be Eq. (11.18) is extended as

$$k_\perp u^{(1)} + \frac{f+S}{N} k_2 u^{(3)}. \tag{11.65}$$

This amounts to replace the system vorticity f by the total absolute vorticity $f + S$, with the mean shear vorticity. From Eqs. (11.18)–(11.65), the possible change of wavenumber direction comes from the fact that system vorticity is along x_3 in the former equation and along x_2 in the latter.

Accordingly, the linear system of rank 3, for toroidal- poloidal - buoyancy -type modes $(u^{(1)}, u^{(2)}, u^{(3)})$ in Eq. (11.34) reduces to a system of two equations.

11.7.2 Zonal Variant of RDT for More Complex Inhomogeneous Base Flows

The short-wave asymptotic theory introduced by Lifschitz and Hameiri (1991) is presented in Chap. 17. It can be seen as a WKB (Wentzel–Kramer–Brillouin) variant of RDT. It is used in the following for identifying localized elliptic, centrifugal and hyperbolic instabilities (Godeferd et al. 2001).

The Coriolis force alters the stability of 2D vortex flows subjected to 3D disturbances. As an illustration, it is possible to consider 2D base flows more complex than those of homogeneous RDT illustrated in Fig. 2.1. For instance, the Taylor–Green flow in a rectangular cell (see Fig. 11.24) has an elliptic point in the core of each eddy, and an hyperbolic point in the corner of the four cells. The Stuart flow (see Fig. 11.25) is elliptic in the core region with hyperbolic points inserted between adjacent vortices (only a single vortex is shown, but one has to consider periodicity in the horizontal direction). The stability of these flows can be revisited in a rotating frame, using the

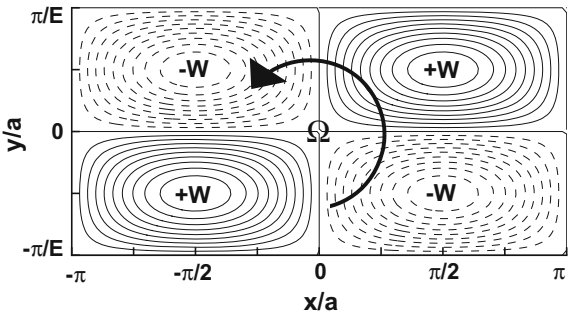

Fig. 11.24 The Taylor–Green flow: iso-values of the vorticity. Case E = 2. Reproduced from Sipp et al. (1999) with permission of AIP

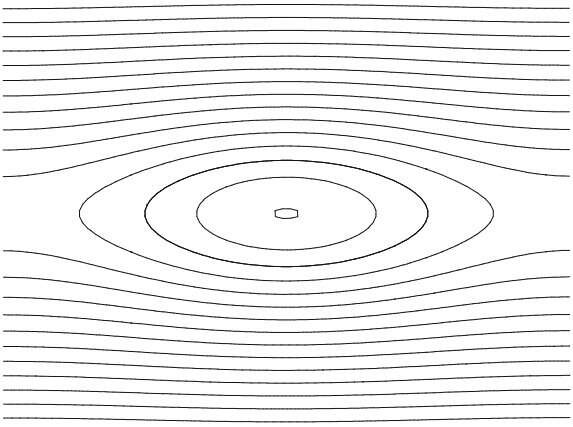

Fig. 11.25 The Stuart flow. Isovalues of the streamfunction. Core ellipticity parameter $\rho = 1/3$

short wave WKB theory developed by Lifschitz and Hameiri (1991), which amounts to a zonal RDT analysis. Such an analysis allows for the identification of the role of elliptic and hyperbolic points in 3D instabilities altered by system rotation, but also to capture the centrifugal instability that may affect anticyclonic vortices (Sipp et al. 1999; Godeferd et al. 2001). The three kinds of instability and their possible competition were studied by solving the Townsend (or Kelvin–Townsend) equations along different trajectories. For each closed trajectory, a temporal Floquet parameter can be calculated from the zonal RDT Green's function. This parameter, denoted $\sigma(x_0, \theta)$, depends on both the space coordinate x_0, that labels the trajectory, and on the angle θ which gives the orientation of the wave-vector. A typical pattern of $\sigma(x_0, \theta)$ in the case of the rotating Stuart flow is shown in Fig. 11.26. The dominant instability is the centrifugal one in the particular anticyclonic case illustrated here. In addition, a typical elliptical instability branch emanates from the core (left part of the figure). One should point out that the local WKB RDT for short wave disturbances can provide real insight into the nature of instabilities – e.g. elliptical, hyperbolic, and centrifugal – that occur in non-parallel flow, with and without system rotation. Classical massive eigenvalue problems provide little or no such insight. In such studies, for instance by Peltier and coworkers, different kinds of instabilities, called "core", "braid" and "edge", were identified, but the local analysis allowed to substitute "elliptical", "hyperbolical" and "centrifugal" to this terminology.

Finally, it is perhaps worthwhile to mention the instabilities which cannot be captured by RDT (possibly extended towards WKB RDT). A very important one is the inflexional shear instability. Even if every point of a linear profile is an inflexional point, the case of change of concavity cannot be recognized by RDT as such. The reason is that only the gradient of the mean velocity is accounted for in the local theory, but not the curvature. A related point is that the inflexional instability in actual flows is not a short-wave, very local, one.

The case of the baroclinic instability is more subtle and surprizing. On the one hand, the baroclinic instability is a long-wave instability in many geophysical

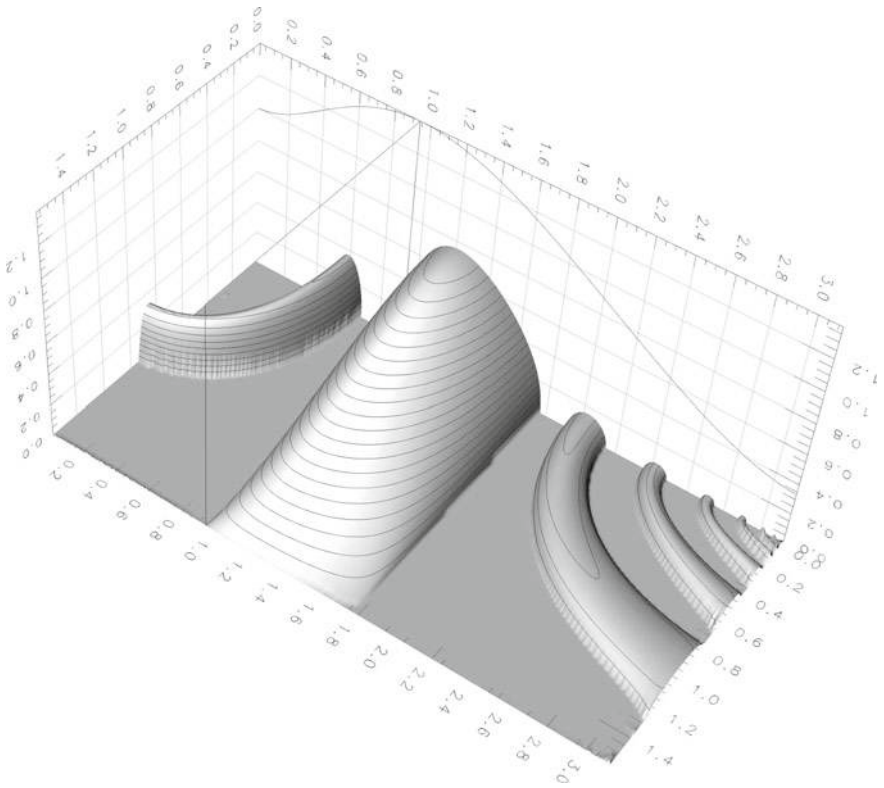

Fig. 11.26 Floquet amplification parameter σ (plotted onto the vertical axis) as a function of the trajectory, indexed by the position x_0 (on the left), and the orientation θ (on the right) of the local wavevector to the spanwise (normal to the plane of the base flow) axis. x_0 varies from 0 (core) to π (periphery), and θ varies from 0 (pure spanwise modes) to $\pi/2$ (pure two-dimensional modes). Anticyclonic system rotation: the dimensionless vorticity at the core ($x_0 = 0$) of a Stuart cell is -7 and the related Rossby number is -5. Reproduced from Godeferd et al. (2001) with permission of CUP

contexts; on the other hand, we hope that the specific section in this chapter could show a possible relevance of homogeneous and WKB RDT, and at least will generate a debate in the geophysical community.

References

Balbus, S.A., Hawley, J.F.: Instability, turbulence, and enhanced transport in accretion discs. Rev. Mod. Phys. **70**(1), 1 (1998)

Bartello, P.: Geostrophic adjustment and inverse cascades in rotating stratified turbulence. J. Atmos. Sci. **52**(24), 4410–4428 (1995)

Bayly, B.J.: Three-dimensional instability of elliptical flow. Phys. Rev. Lett. **57**, 2160–2163 (1986)

Bradshaw, P.: The analogy between streamline curvature and buoyancy in turbulent shear flow. J. Fluid Mech. **36**, 177–191 (1969)
Cambon, C.: Etude spectrale d'un champ turbulent incompressible soumis à des effets couplés de déformation et rotation imposés extérieurement. Université Lyon I, France, Thèse de Doctorat d'Etat (1982)
Cambon, C.: Turbulence and vortex structures in rotating and stratified flows. Eur. J. Mech. B (Fluids) **20**, 489–510 (2001)
Cambon, C., Scott, J.F.: Linear and nonlinear models of anisotropic turbulence. Annu. Rev. Fluid Mech. **31**, 1–53 (1999)
Cambon, C., Teissèdre, C., Jeandel, D.: Etude d' effets couplés de rotation et de déformation sur une turbulence homogène. Journal de Mécanique Théorique et Appliquée **5**, 629 (1985)
Cambon, C., Godeferd, F.S., Kaneda, Y.: Phase-mixing and toroidal cascade in rotating and stratified flows, In: 18 th Congrès Français de Mécanique, International Session on stratied rotating flows, Grenoble, 27–31 August 2007 (AFM Symposium)
Cambon, C., Benoit, J.P., Shao, L., Jacquin, L.: Stability analysis and LES of rotating turbulence with organized eddies. J. Fluid Mech. **278**, 175–200 (1994)
Cambon, C., Godeferd, F.S., Nicolleau, F., Vassilicos, J.C.: Turbulent diffusion in rapidly rotating flows with and without stable stratification. J. Fluid Mech. **499**, 231–255 (2004)
Chagelishvili, G.D., Tevzadze, A.G., Bodo, G., Moiseev, S.S.: Phys. Rev. Lett. **79**, 3178 (1997)
Chagelishvili, G.D., Zahn, J.-P., Tevzadze, A.G., Lominadze, J.G.: On hydrodynamic shear turbulence in Keplerian discs: via transient growth to bypass transition. Astron. Astrophys. **402**, 401–407 (2003)
Charney, J.G.: Geostrophic turbulence. J. Atmos. Sci. **28**, 1087–1095 (1971)
Craik, A.D.D.: The stability of unbounded two- and three-dimensional flows subject to body forces: some exact solutions. J. Fluid Mech. **198**, 275–292 (1989)
Drazin, P.G., Reid, W.H.: Hydrodynamic Stability. Cambridge University Press, Cambridge (1981)
Duguet, Y., Scott, J.F., Le Penven, L.: Instability inside a rotating gas cylinder subject to axial periodic strain. Phys. Fluids **17**, 114103 (2005)
Eady, E.T.: Long waves and cyclonic waves. Tellus **1**, 33–52 (1949)
Godeferd, F.S., Cambon, C.: Detailed investigation of energy transfers in homogeneous stratified turbulence. Phys. Fluids **6**, 2084–2100 (1994)
Godeferd, F.S., Cambon, C., Leblanc, S.: Zonal approach to centrifugal, elliptic and hyperbolic instabilities in Suart vortices with external rotation. J. Fluid Mech. **449**, 1–37 (2001)
Hanazaki, H., Hunt, J.C.R.: Linear processes in unsteady stably stratified sheared turbulence with mean shear. J. Fluid Mech. **507**, 1–42 (2004)
Herring, J.R.: Statistical theory of quasi-geostrophic turbulence. J. Atmos. Sci. **37**, 969–977 (1980)
Jacobitz, F.G., Sarkar, S., van Atta, C.W.: J. Fluid Mech. **342**, 231 (1997)
Kaneda, Y.: Single-particle diffusion in strongly stratified and/or rapidly rotating turbulence. J. Phys. Soc. Jpn. **69**, 3847–3852 (2000)
Kassinos, S.C., Akylas, E., Langer, C.A.: Rapidly sheared homogeneous stratified turbulence in a rotating frame. Phys. Fluids **19**, 021701 (2006)
Kerswell, R.R.: The instability of precessing flow. Geophys. Astrophys. Fluid Dyn. **72**, 107–144 (1993)
Kerswell, R.R.: Elliptical instability. Annu. Rev. Fluid Mech. **34**, 83–113 (2002)
Kurian, S., Smith, L., Wingate, B.: On the two-point correlation of potential vorticity in rotating and stratified turbulence. J. Fluid Mech. **555**, 131–140 (2006)
Leblanc, S., Cambon, C.: On the three-dimensional instabilities of plane flows subjected to Coriolis force. Phys. Fluids **9**(5), 1307–1316 (1997)
Leuchter, O., Cambon, C.: EDQNM and DNS predictions of rotation effects in strained axisymmetric turbulence. In: Proceedings of 11th International Symposium Turbulent Shear Flow, Grenoble (1997)

Leuchter, O., Dupeuble, A.: Rotating homogeneous turbulence subjected to an axisymmetric contraction. In: Proceedings of 9th International Symposium Turbulent Shear Flow, vol. 137, pp. 1–6. Kyoto (1993)
Liechtenstein, L., Godeferd, F.S., Cambon, C.: Nonlinear formation of structures in rotating stratified turbulence. J. Turbul. **6**, 1–18 (2005)
Lifschitz, A., Hameiri, E.: Local stability conditions in fluid dynamics. Phys. Fluids A **3**, 2644–2641 (1991)
Lundgren, T.S., Mansour, N.N.: Transition to turbulence in an elliptic vortex. J. Fluid Mech. **307**, 43–62 (1996)
Mahalov, A.: The instability of rotating fluid columns subjected to a weak external Coriolis force. Phys. Fluids A **5**, 891–900 (1993)
Mamatsashvili, G.R., Avsarkisov, V.S., Chagelishvili, G.D., Chanishvili, R.G., Kalashnik, M.V.: Transient dynamics on nonsymmetric perturbations versus symmetric instability in baroclinic zonal shear flows. J. Atmos. Sci. **67**, 2972–2989 (2010)
Mansour, N.N., Lundgren, T.S.: Three-dimensional instability of rotating flows with oscillating axial strain. Phys. Fluids A **2**, 2089–2091 (1990)
Marino, R., Pouquet, A., Rozenberg, D.: Resolving the paradox of oceanic large-scale balance and small-scale mixing. Phys. Rev. Lett. **114**, 114504 (2015)
Marino, R., Mininni, P.D., Rozenberg, D., Pouquet, A.: Inverse cascades in rotating stratified turbulence. Eur. Phys. Lett. **102**, 44006 (2013)
Marino, R., Mininni, P.D., Rozenberg, D., Pouquet, A.: Large-scale anisotropy in stably stratified rotating flows. Phys. Rev. E **90**, 023018 (2014)
Miles, J.W.: On the stability of heterogeneous shear flows. J. Fluid Mech. **10**, 496–508 (1961)
Pedley, T.J.: On the stability of viscous flow in a rapidly rotating pipe. J. Fluid Mech. **35**, 97–115 (1969)
Pedlowsky, J.: Geophysical Fluid Dynamics. Springer, New York (1987)
Pieri, A.B., Cambon, C., Godeferd, F.S., Salhi, A.: Linearized potential vorticity mode and its role in transition to baroclinic instability. Phys. Fluids **24**, 076603 (2012)
Pieri, A.B., Godeferd, F.S., Cambon, C., Salhi, A.: Non-geostrophic instabilities of an equilibrium baroclinic state. J. Fluid Mech. **734**, 535–566 (2013)
Praud, O., Sommeria, J., Fincham, A.: Decaying grid turbulence in a rotating stratified fluid. J. Fluid Mech. **547**, 389–412 (2006)
Salhi, A.: Similarities between rotation and stratification effects on homogeneous shear flow. Theor. Comput. Fluid Dyn. **15**, 339–358 (2002)
Salhi, A., Cambon, C.: An analysis of rotating shear flow using linear theory and DNS and LES results. J. Fluid Mech. **347**, 171–195 (1997)
Salhi, A., Cambon, C.: Advance in rapid distortion theory: from rotating shear to the baroclinic instability. J. Appl. Mech. **73**, 449–460 (2006)
Salhi, A., Cambon, C.: Precessing rotating flows with additional shear: stability analysis. Phys. Rev. E **79**, 036303 (2009)
Salhi, A., Cambon, C.: Stability of rotating stratified shear flow: an analytical study. Phys. Rev. E **81**, 026302 (2010)
Salhi, A., Cambon, C., Speziale, C.G.: Linear stability analysis of plane quadratic flows in a rotating frame. Phys. Fluids **9**(8), 2300–2309 (1997)
Salhi, A., Lehner, T., Godeferd, F., Cambon, C.: Wave-vortex mode coupling in astrophysical accretion discs under combined radial and vertical stratification. Astrophys. J. **771**, 103 (2013)
Salhi, A., Jacobitz, F.G., Schneider, K., Cambon, C.: Nonlinear dynamics and anisotropic structure of rotating sheared turbulence. Phys. Rev. E **89**, 013020 (2014)
Schmid, P.J.: Nonmodal stability theory. Annu. Rev. Fluid Mech. **39**, 129–162 (2007)
Sipp, D., Lauga, E., Jacquin, L.: Vortices in rotating systems: centrifugal, elliptic and hyperbolic type instabilities. Phys. Fluids **11**, 3716–3728 (1999)
Smith, L.M., Waleffe, F.: Generation of slow, large scales in forced rotating, stratified turbulence. J. Fluid Mech. **451**, 145–168 (2002)

Staquet, C., Riley, J.J.: On the velocity field associated to potential vorticity. Dyn. Atmos. Ocean. **14**, 93–123 (1989)
Tritton, D.J.: Stabilization and destabilization of turbulent shear flow in a rotating fluid. J. Fluid Mech. **241**, 503–523 (1992)
Waleffe, F.: On the three-dimensional instability of strained vortices. Phys. Fluid A **2**, 76–80 (1990)
Yanase, S., Flores, C., Métais, O., Riley, J.J.: Rotating free shear flow I: linear stability analysis. Phys. Fluids A **5**, 2725–2737 (1992)

Chapter 12
Incompressible Homogeneous Anisotropic Turbulence: Magnetohydrodynamic Turbulence

12.1 Generalities, Analogies and Differences with Respect to the Purely Hydrodynamic Case

Magnetohydrodynamic (MHD) turbulence is present in electrically-conducting fluids, both in industrial devices and in the core of the earth, and is ubiquitous in heliophysics and astrophysics. MHD is also the first step to address the physics of plasmas, with recent studies motivated by the ITER project. Interactions of velocity and magnetic (or induction) fields yield new coupled effects. These effects can be mainly described and modelled in our context of homogeneous turbulence, because the Lorentz (or Laplace) force is a body force, as are the Coriolis force (Chap. 7) and the buoyancy force (Chap. 10). Limits of our incompressible and "homogenized" approach are touched upon at the end of this chapter. Incompressibility is not questioned in a turbulent liquid metal, but it is not suited in many astrophysical situations, so that we will explore the limits of this approximation as well, and look at some extensions using the anelastic approximation, or magnetosonic modes.

Analogies and differences with the "hydro" (hydrodynamic hereinafter) case can be first discussed in the presence of a mean magnetic field, which can appear as a mean Alfvén velocity using a simple rescaling. Without strong diffusion and in the presence of a dominant mean field $\boldsymbol{B}_0$, Alfvén waves are easily identified from background coupled equations, observations, experiments and numerical simulations. With respect to the other wave régimes presented in this book in the "hydro" case, these plane waves are not dispersive (sometime called semi-dispersive), the dispersion law displays a typical mean-velocity-scale (the Alfvén velocity) and not a typical frequency (Coriolis parameter, stratification frequency). In contrast with the Coriolis force and the buoyancy force (at least within the Boussinesq approximation), that are linear, *the Lorentz force is quadratic*, so that it yields cubic correlations in the equations for kinetic energy and total energy, as for nonlinear transfer terms. Accordingly, Alfvén waves are well identified in the presence of a dominant external magnetic field, when the Lorentz force is linearized, but they do exist without mean magnetic field.

P. Sagaut and C. Cambon, *Homogeneous Turbulence Dynamics*,
https://doi.org/10.1007/978-3-319-73162-9_12

As another new feature, the basic wave régime is strongly altered when velocity field and magnetic field are affected by very different values of diffusivity: This is the case for a liquid metal, with a very low value of the Prandtl magnetic number (ratio of kinematic viscosity ν to magnetic diffusivity η); a very special *quasi-static* régime can be predicted and observed, in which the waves are not only modulated and selectively damped by viscous effects, but are discarded.

Strong differences appear because the interpretation of the magnetic field, be entirely fluctuating or with a dominant mean contribution, as an Alfvén velocity, is only a useful convenience to homogeneize dimensions. The magnetic field is governed by an equation closer to the one of vorticity than the one of velocity; it corresponds to a transported vector, but not a passive vector, as should be a bi-point: It is active via the feed-back of the Lorentz force on the momentum (Navier–Stokes-type) equations.

As an important consequence, there is no principle equivalent to Galilean invariance applied to the Alfvén "velocity". For instance, the first version of DIA theory, recognized as wrong because it violates random Galilean invariance and yields a $-3/2$ spectral slope for the energy spectrum (instead of $-5/3$), is possibly valid when MHD is considered, replacing the rms "true" velocity by the rms "Alfvén velocity". This issue, addressed by Iroshnikov (1964) and Kraichnan (1965), remains controversial and merits more thinking. Another related point is that in "hydro" the (space-uniform) mean velocity itself is not relevant, so that only its gradients yield interesting linear effects, which are emphasized in RDT if considered alone, with a complex interplay with basic nonlinearity (here Chaps. 7–11). On the other hand, the mean magnetic field has relevant structuring effects with no need to account for its gradients. Only in some problems of plasma physics, not considered here, the dynamics induced by mean magnetic gradients are important.

Wave turbulence is particularly relevant from MHD to plasmas physics, as illustrated by the spectrum of magnetic fluctuations in Fig. 12.1 from Kiyani et al. (2016). As a final general consideration, the development of anisotropy, be a general statistical mechanism or the reflect of coherent structures, is considered as different in "hydro" and MHD cases. Re-isotropization of small scales, with a threshold lengthscale close to Corrsin's (mean shear), Ozmidov's (mean stratification) or Hopfinger's / Zeman's (rotation) scale is well supported in the hydro case (this scale-by-scale anisotropy is better discussed in the new edition of this book from recent results). On the other hand, a dominant anisotropy at small scales is often expected in MHD, in connection with the nonlinearity of the Lorentz force: This yields some Alfvén wave packets at small scale, driven by the magnetic field at largest scale. This asks the problem of fully anisotropic subgrid scale model in LES, with the recent review by Miesch et al. (2015).) A typical structure in MHD is the layering of current sheets, which presents only some qualitative analogy with the layering in stably stratified turbulence (Chap. 10).

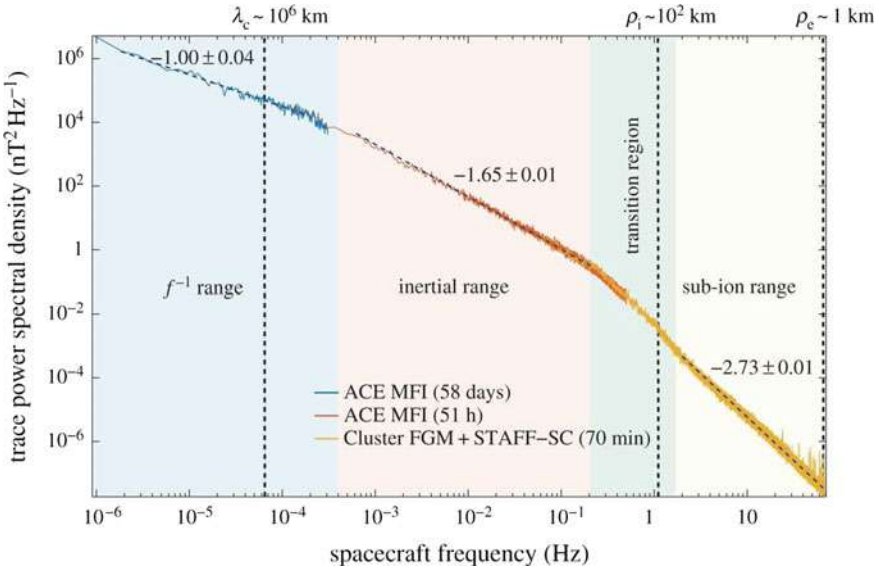

Fig. 12.1 Canonical power spectral density of the magnetic field fluctuations of a plasma in the ecliptic solar wind, from Kiyani et al. (2016)

12.2 Governing Equations

12.2.1 Basic Equations for Ideal MHD

The magnetic field $\boldsymbol{b}(\boldsymbol{x}, t)$ is an *active vector field*, transported by the velocity $\boldsymbol{u}(\boldsymbol{x}, t)$: It is governed by the following equation (the induction equation), which is the same as the one for a material bipoint, or for the vorticity, up to a specific diffusion term, with magnetic diffusivity η.

$$\frac{\partial \boldsymbol{b}}{\partial t} - \boldsymbol{\nabla} \times (\boldsymbol{u} \times \boldsymbol{b}) = \eta \nabla^2 \boldsymbol{b}, \quad \boldsymbol{\nabla} \cdot \boldsymbol{b} = 0. \tag{12.1}$$

This vector is active, having feedback on the velocity field via the Lorentz force, which is the new term $\boldsymbol{j} \times \boldsymbol{b}$ in the modified Navier–Stokes equation

$$\frac{\partial \boldsymbol{u}}{\partial t} + \omega \times \boldsymbol{u} - \underbrace{(\boldsymbol{\nabla} \times \boldsymbol{b})}_{\boldsymbol{j}} \times \boldsymbol{b} = -\nabla(p + u^2/2) + \nu \nabla^2 \boldsymbol{u}, \quad \boldsymbol{\nabla} \cdot \boldsymbol{u} = 0, \tag{12.2}$$

in which p is the pressure fluctuation divided by a reference density ρ_0, and $\boldsymbol{j}(\boldsymbol{x}, t)$ is the current density. The generality of MHD equations is only restricted by the choice of the simplified equation for the current density $\boldsymbol{j}$, here $\boldsymbol{j} = \boldsymbol{\nabla} \times \boldsymbol{b}$ (simplified

Ohm equation). The explicit inclusion of typical physical coefficients is avoided in the preceding equations by scaling $\boldsymbol{b}$ as a velocity ($\boldsymbol{b} \to \boldsymbol{b}/\sqrt{\mu_0 \rho_0}$ where μ_0 is the magnetic permeability and ρ_0 is the density). The basic quadratic nonlinearity $\boldsymbol{u}\cdot\nabla\boldsymbol{u}$ in Navier–Stokes equations is replaced by the Lamb vector $\boldsymbol{\omega} \times \boldsymbol{u}$, adding to the pressure fluctuation term p its dynamical part $(1/2)u^2$. Conversely, the Lorentz force $(\nabla \times \boldsymbol{b}) \times \boldsymbol{b}$ could be replaced by $\boldsymbol{b} \cdot \nabla \boldsymbol{b}$, adding $b^2/2$ to the pressure fluctuation. Accordingly, Eq. (12.2) can be written

$$\frac{\partial \boldsymbol{u}}{\partial t} + \boldsymbol{u}\cdot\nabla\boldsymbol{u} - \boldsymbol{b}\cdot\nabla\boldsymbol{b} = -\nabla(p + b^2/2) + \nu\nabla^2\boldsymbol{u}. \tag{12.3}$$

Similarly, the analogy of the induction equation with the classical form of the Helmholtz equation for vorticity (e.g. in Chap. 2) is complete when rewritting the left-hand-side of Eq. (12.1) as

$$\frac{\partial \boldsymbol{b}}{\partial t} + \boldsymbol{u}\cdot\nabla\boldsymbol{b} - \nabla\boldsymbol{u}.\boldsymbol{b} = \eta\nabla^2\boldsymbol{b}, \tag{12.4}$$

in which $\boldsymbol{u}\cdot\nabla\boldsymbol{b}$ is the advection term and $-\nabla\boldsymbol{u}.\boldsymbol{b}$ is similar to the nonlinear vortex stretching term.

As in the purely hydro case, the solenoidal (divergencefree) constraint for both $\boldsymbol{u}$ and $\boldsymbol{b}$ yields an explicit form of the pressure fluctuation, and this amounts to take the solenoidal projection of both the nonlinear advection term and the Lorentz force, *which are not divergencefree*, in Eq. (12.2). Taking the divergence of Eq. (12.3) gives the following new Poisson equation:

$$\nabla^2 p = -\frac{\partial u_i}{\partial x_j}\frac{\partial u_j}{\partial x_i} + \frac{\partial b_i}{\partial x_j}\frac{\partial b_j}{\partial x_i}. \tag{12.5}$$

In our set of basic equations, it is convenient to rewrite the Helmholtz equation for vorticity, taking the Curl of Eq. (12.2) or (12.3) (For the sake of complementarity: The Poisson equation corresponds to the projection of Navier–Stokes-type equation on the dilatational subspace, and the vorticity equation gives the projection on the solenoidal subspace.)

$$\frac{\partial \boldsymbol{\omega}}{\partial t} + \boldsymbol{u}\cdot\nabla\boldsymbol{\omega} + \boldsymbol{b}\cdot\nabla\boldsymbol{j} - \nabla\boldsymbol{j}.\boldsymbol{b} - \nabla\boldsymbol{u}.\boldsymbol{\omega} = \nu\nabla^2\boldsymbol{\omega}. \tag{12.6}$$

The Lorentz force has two contributions in the latter equation, $\boldsymbol{b}\cdot\nabla\boldsymbol{j}$, that expresses the advection of $\boldsymbol{j}$ by $\boldsymbol{b}$, and the term $\nabla\boldsymbol{j}.\boldsymbol{b}$, which has the same structure as the nonlinear vortex stretching term, replacing $\boldsymbol{\omega}$ by $\boldsymbol{j}$ and replacing $\boldsymbol{b}$ by $\boldsymbol{\omega}$.

Our last basic equation makes use of the (Elsaesser 1950) variables, that can be introduced from the very beginning, taking advantage of the symmetry of equations for $\boldsymbol{u}$ and $\boldsymbol{b}$.

$$\boldsymbol{z}^s = \boldsymbol{u} + s\boldsymbol{b}, \quad s = \pm 1, \quad \boldsymbol{u} = \frac{1}{2}\left(\boldsymbol{z}^s + \boldsymbol{z}^{-s}\right), \quad \boldsymbol{b} = \frac{s}{2}\left(\boldsymbol{z}^s - \boldsymbol{z}^{-s}\right). \tag{12.7}$$

Combining the left hand side of Eqs. (12.3) and (12.4), one obtains

$$\left(\frac{\partial}{\partial t} + \boldsymbol{u}\cdot\boldsymbol{\nabla}\right)\boldsymbol{z}^s(\boldsymbol{x},t) - s\boldsymbol{b}\cdot\boldsymbol{\nabla}\boldsymbol{z}^s,$$

which is also equal to

$$\left(\frac{\partial}{\partial t} + \boldsymbol{z}^{-s}\cdot\boldsymbol{\nabla}\right)\boldsymbol{z}^s(\boldsymbol{x},t).$$

Finally, the equation in terms of Elsaesser variables is

$$\left(\frac{\partial}{\partial t} + \boldsymbol{z}^{-s}\cdot\boldsymbol{\nabla}\right)\boldsymbol{z}^s(\boldsymbol{x},t) = \boldsymbol{\nabla}(p+b^2/2) + \frac{1}{2}\nabla^2\left((\nu+\eta)\boldsymbol{z}^s + (\nu-\eta)\boldsymbol{z}^{-s}\right), \tag{12.8}$$

with $s = \pm 1$. Except for the pressure term and the dissipation term (if the magnetic Prandtl number ν/η is very different from one), the dynamical MHD equations are dramatically simplified.

12.2.1.1 First Approach to Energies. Single-Point Statistics

Equations for kinetic energy and magnetic energy are easily found from scalar product of Eqs. (12.3) and (12.4) by $\boldsymbol{u}$ and $\boldsymbol{b}$, respectively. The kinetic energy $(1/2)u^2 = (1/2)\boldsymbol{u}\cdot\boldsymbol{u}$ is governed by

$$\frac{1}{2}\frac{\partial u^2}{\partial t} + \frac{\partial}{\partial x_j}\left(u^2 u_j\right) + \frac{\partial}{\partial x_j}\left(u_i b_i b_j\right) - \frac{\partial u_i}{\partial x_j} b_i b_j = -\frac{\partial}{\partial x_i}\left(u_i(p + b^2/2)\right) + \nu\boldsymbol{u}\cdot\nabla^2\boldsymbol{u},$$

using $\boldsymbol{\nabla}.\boldsymbol{u} = 0$.

Now performing statistical averaging, one obtains

$$\frac{d\mathcal{K}}{dt} - \left(\overline{\frac{\partial u_i}{\partial x_j} b_i b_j} - \underbrace{\frac{\partial}{\partial x_j}\overline{(u_i b_i b_j)}}_{=0}\right) + \underbrace{\frac{\partial}{\partial x_j}\overline{(u_i u_i u_j)}}_{=0} = -\varepsilon. \tag{12.9}$$

Of course, statistical homogeneity yields zero value for all gradient terms, but they are conserved in the above equations in order to anticipate the origin of true, or conservative, spectral transfer terms: The (zero) contribution of the advection term is related to a spectral transfer with zero integral. The contribution from the Lorentz force to energy is twofold, with a conservative part $\frac{\partial}{\partial x_j}\overline{(u_i b_i b_j)}$ (zero value here, zero

integral for its spectral counterpart) and a non-conservative part $-\overline{\frac{\partial u_i}{\partial x_j} b_i b_j}$. Similarly, the equation for magnetic energy $\mathcal{K}^M = (1/2)\overline{b^2}$ is written as

$$\frac{d\mathcal{K}^M}{dt} + \overline{\frac{\partial u_i}{\partial x_j} b_i b_j} + \underbrace{\frac{\partial}{\partial x_j}\overline{(b_i b_i u_j)}}_{=0} = -\varepsilon^M, \tag{12.10}$$

in which ε^M is the magnetic dissipation rate. The term $\overline{\frac{\partial u_i}{\partial x_j} b_i b_j}$ is non-zero in general and appears with opposite sign in the equations for kinetic energy and magnetic energy.

12.2.1.2 Equations in Fourier Space

Solving the pressure term, so that it no longer appears in equations consistent with solenoidal constraint, is particularly simple in Fourier space. Rewriting the basic equations in spectral space, one has

$$\left(\frac{\partial}{\partial t} + \nu k^2\right)\hat{u}_i(\boldsymbol{k}, t) - \imath\, P_{im}(\boldsymbol{k}) k_j \widehat{\left(b_m b_j\right)} = -P_{ij}(\boldsymbol{k})\widehat{(\boldsymbol{\omega} \times \boldsymbol{u})}_j, \tag{12.11}$$

and

$$\left(\frac{\partial}{\partial t} + \eta k^2\right)\hat{b}_i - \imath k_j \widehat{\left(u_i b_j\right)} = \imath k_j \widehat{\left(u_j b_i\right)}. \tag{12.12}$$

In these equations, as in the whole book, the overhat denotes a three-dimensional Fourier transform — possibly in the sense of the theory of distributions — $\boldsymbol{k}$ is the wave vector, and $P_{ij} = \delta_{ij} - \frac{k_i k_j}{k^2}$ is the projection operator. Divergence-free properties amount to $\boldsymbol{k}\cdot\hat{\boldsymbol{u}} = 0$ and $\boldsymbol{k}\cdot\hat{\boldsymbol{b}} = 0$.

In order to separate conservative and non-conservative terms in energy-equations, quadratic nonlinearity in the equation for velocity is split into the solenoidal contribution from the Lorentz force and the advection term. It is important to stress again that, with respect to body forces already considered, Coriolis force or buoyancy force, the Lorentz force is nonlinear (quadratic) from the very beginning.

In Eq. (12.11), the right-hand side can be replaced by $-\imath\, P_{imn}(\boldsymbol{k})\widehat{u_m u_n}$, using the symmetrized Kraichnan's projector used in the classical hydrodynamic case. This type of nonlinearity is recovered for the compact form of both equations in terms of Elsaesser variables as:

$$\frac{\partial}{\partial t}\hat{z}_i^s(\boldsymbol{k}, t) = -\imath k_m P_{in}(\boldsymbol{k})\widehat{z_m^{-s} z_n^s} - \frac{1}{2}k^2\left((\nu+\eta)\hat{z}_i^s + (\nu-\eta)\hat{z}_i^{-s}\right), \tag{12.13}$$

with $\widehat{z_m^{-s} z_n^s}(\boldsymbol{k},t) = \iiint_{k=p+q} z_m^{-s}(\boldsymbol{p},t) z_n^s(\boldsymbol{q},t) d^3\boldsymbol{p}$, and possible symmetrization in terms of $\boldsymbol{p}$ and $\boldsymbol{q}$, as for $\widehat{u_m u_n}$.

12.2.1.3 Reduced Basis of Solenoidal Modes, Craya-Herring, Helical and Elsaesser

Finally, it is possible to project both $\hat{\boldsymbol{u}}$ and $\hat{\boldsymbol{b}}$ onto the basis of helical modes, itself related to the Craya–Herring frame of reference via

$$\hat{\boldsymbol{u}}(\boldsymbol{k},t) = u^{(1)}(\boldsymbol{k},t)\boldsymbol{e}^{(1)}(\boldsymbol{k}) + u^{(2)}(\boldsymbol{k},t)\boldsymbol{e}^{(2)}(\boldsymbol{k}) = u_+(\boldsymbol{k},t)\boldsymbol{N}(\boldsymbol{k}) + u_-(\boldsymbol{k},t)\boldsymbol{N}(-\boldsymbol{k}), \tag{12.14}$$

with all definition from Cambon and Jacquin (1989), rediscussed in Chap. 2. The same decompositions are applied to the magnetic field as

$$\hat{\boldsymbol{b}}(\boldsymbol{k},t) = b^{(1)}(\boldsymbol{k},t)\boldsymbol{e}^{(1)}(\boldsymbol{k}) + b^{(2)}(\boldsymbol{k},t)\boldsymbol{e}^{(2)}(\boldsymbol{k}) = b_+(\boldsymbol{k},t)\boldsymbol{N}(\boldsymbol{k}) + b_-(\boldsymbol{k},t)\boldsymbol{N}(-\boldsymbol{k}). \tag{12.15}$$

Both decompositions can be applied to the Elsaesser variables in Fourier space. Considering helical Elsaesser variables, one has to use two different types of signs: The superscript refers to Elsaesser combination of $\boldsymbol{u}$ and $\boldsymbol{b}$, whereas the index, called s_k and not s in order to avoid confusion, denotes the polarity of the helical mode:

$$z^s_{s_k}(\boldsymbol{k},t) = u_{s_k}(\boldsymbol{k},t) + s b_{s_k}(\boldsymbol{k},t), \quad s = \pm 1, \quad s_k = \pm 1. \tag{12.16}$$

It is recalled that $N_i(-\boldsymbol{k}) = N_i^*(\boldsymbol{k})$ (Hermitian property), $N_i N_i = 0$ and $k_i N_i = 0$. Both linearized and fully nonlinear dynamical equations will be rewritten in terms of this reduced basis of solenoidal modes in the following sections. An optimal description of two-point second order statistics is derived in the next section, in line with what was done for the "hydro" case.

12.2.2 Fully Anisotropic Second-Order Statistics, with Cross-Spectra

We consider velocity $\boldsymbol{u}$ and magnetic field $\boldsymbol{b}$ fluctuations, both solenoidal.

The spectral tensor of velocity correlations is written as in (Cambon and Jacquin 1989)

$$\hat{R}_{ij}(\boldsymbol{k},t) = \mathcal{E}(\boldsymbol{k},t)P_{ij}(\boldsymbol{k}) + \Re[Z(\boldsymbol{k},t)N_i(\boldsymbol{k})N_j(\boldsymbol{k})] + \mathrm{i}\epsilon_{ijn}\frac{k_n}{2k^2}\mathcal{H}(\boldsymbol{k},t), \tag{12.17}$$

and the scalar spectra are expressed as

$$\mathcal{E} = \frac{1}{2}\hat{R}_{ii} \;\leftrightarrow\; \frac{1}{2}\langle u_+^* u_+ + u_-^* u_- \rangle, \tag{12.18}$$

$$Z = \frac{1}{2}\hat{R}_{ij}(\boldsymbol{k},t) N_i^* N_j^* \;\leftrightarrow\; 2\langle u_+^* u_- \rangle, \tag{12.19}$$

$$\mathcal{H} = \frac{1}{2}\epsilon_{nij} k_n \hat{R}_{ij} \;\leftrightarrow\; \frac{1}{2}\langle u_+^* u_+ - u_-^* u_- \rangle, \tag{12.20}$$

as discussed at length in Chap. 2. To be consistent with the definitions mainly used in MHD, the kinetic helicity spectrum slightly differs from the one introduced in Cambon and Jacquin (1989) with Eq. (2.128), in order to recover $\langle \boldsymbol{u}\cdot\boldsymbol{\omega}\rangle = \iiint \mathcal{H}(\boldsymbol{k},t) d^3\boldsymbol{k}$, without a prefactor $2k$.

It is clear that the spectral tensor related to $\langle \hat{b}_i^* \hat{b}_j \rangle$, denoted $R_{ij}^M(\boldsymbol{k},t)$ hereinafter, has exactly the same structure as $\hat{R}_{ij}$, or

$$R_{ij}^M = \mathcal{E}^M P_{ij} + \Re[Z^M N_i N_j] + \mathrm{i}\epsilon_{ijn}\frac{k_n}{2k^2}\mathcal{H}^M, \tag{12.21}$$

in which the quantities with superscript M are the "magnetic" counterparts of the "kinetic" ones (energy, polarization, helicity.) The term related to magnetic helicity, with spectrum $\mathcal{H}^M(\boldsymbol{k},t)$ deserves an additional discussion as follows, with respect to classical litterature: Magnetic helicity is usually defined from the scalar product of the magnetic field $\boldsymbol{b}$ with the potential vector of induction, $\boldsymbol{a}$, instead of the Curl of $\boldsymbol{b}$ itself. From the relationship $\boldsymbol{b} = \boldsymbol{\nabla}\times\boldsymbol{a}$, and applying a Gauge condition which renders $\boldsymbol{a}$ divergencefree, it is found $\boldsymbol{\nabla}\times\boldsymbol{b} = -\nabla^2\boldsymbol{a}$ (this relationship is similar to the one between palinstrophy and velocity.) Accordingly, the term $\mathcal{H}^M(\boldsymbol{k},t)$ called into play in Eq. (12.22) is proportional to the spectrum of classical magnetic helicity, via a k^2 factor. The reader is referred to the seminal study by Matthaeus and Goldstein (1982) for the context of magnetic helicity in homogeneous turbulence.

The kinetic/magnetic cross-spectral tensor $C_{ij}(\boldsymbol{k},t)$ is related to $\langle b_i u_j \rangle$ and its structure derives from $\hat{u}_i^* \hat{b}_j$. Starting from the decomposition of $\hat{\boldsymbol{b}}$ and $\hat{\boldsymbol{u}}$ in terms of $\boldsymbol{N}$ and $\boldsymbol{N}^*$ in Eqs. (12.14) and (12.15), one finds

$$C_{ij} = \frac{1}{2}\mathcal{H}^C P_{ij} + Z^1 N_i N_j + Z^2 N_i^* N_j^* + \frac{1}{2}\epsilon_{inj}\frac{k_n}{k}\mathcal{C}\,, \tag{12.22}$$

with four pseudo-scalars, probably all complex-valued, except the first one: $\mathcal{H}^C(\boldsymbol{k},t)$ is the spectrum of cross-helicity. Another relevant term is the vector spectrum of the averaged electromotive force $\langle \boldsymbol{u}\times\boldsymbol{b}\rangle$; it is given by $\epsilon_{imn}C_{mn}$, which reduces to $\epsilon_{imn}\epsilon_{mnj}\frac{k_j}{k}\mathcal{C}$, so that $\frac{\boldsymbol{k}}{k}\mathcal{C}$ is the vectoral spectrum of $\langle \boldsymbol{u}\times\boldsymbol{b}\rangle$. Accordingly

$$\langle \boldsymbol{u}\cdot\boldsymbol{b}\rangle = \iiint \mathcal{H}^C(\boldsymbol{k}) d^3\boldsymbol{k}, \quad \langle \boldsymbol{u}\times\boldsymbol{b}\rangle = \iiint \frac{\boldsymbol{k}}{k}\mathcal{C}(\boldsymbol{k}) d^3\boldsymbol{k}. \tag{12.23}$$

It is unfortunately not possible to attribute to the "cross-polarization" complex pseudo-scalars Z^1 and Z^2 more specific physical meaning. Z^1 corresponds to $\langle u_-^* b_+ \rangle$,

and Z^2 to $\langle u_+^* b_- \rangle$ in term of helical modes. On the other hand, it is clear that all the information for second-order two-point statistics can be generated by the following list:

$$(\mathcal{E}, Z, \mathcal{H}, \mathcal{E}^M, Z^M, \mathcal{H}^M, \mathcal{H}^C, Z^1, Z^2, \mathcal{C}) \tag{12.24}$$

The decomposition above was initially proposed by Cambon et al. (2012); another, less general, decomposition can be found by Oughton et al. (1997) in line with Chandrasekkhar and restricted to axisymmetry, but it does not involve the helical modes, and does not address the dynamical equations for the two-point second-order statistics.

12.3 Alfvén Waves and Ohmic Damping Linear Régime

Basic equations are first linearized around a mean magnetic field $\boldsymbol{B}_0$, without mean motion, and diffusivities are neglected, so that:

$$\frac{\partial \boldsymbol{u}}{\partial t} - \boldsymbol{B}_0 \cdot \nabla \boldsymbol{b} + \nabla p = 0 \tag{12.25}$$

$$\frac{\partial \boldsymbol{b}}{\partial t} - \boldsymbol{B}_0 \cdot \nabla \boldsymbol{u} = 0. \tag{12.26}$$

Because the linearized Lorentz force remains divergencefree, with space-uniform $\boldsymbol{B}_0$, the pressure term can be cancelled in the first equation. In view of the symmetric role played by $\boldsymbol{u}$ and $\boldsymbol{b}$, their combination under the form of Elsaesser variables, or $\boldsymbol{z}^{\pm} = \boldsymbol{u} \pm \boldsymbol{b}$ yields a simpler diagonal solution, with

$$\left(\frac{\partial}{\partial t} - \boldsymbol{B}_0 \cdot \nabla \right) \boldsymbol{z}^+ = 0, \left(\frac{\partial}{\partial t} + \boldsymbol{B}_0 \cdot \nabla \right) \boldsymbol{z}^- = 0.$$

As the well-known dynamics of non-dispersive waves, one recovers apparent advection of basic variables by the Alfvén velocity, but the existence of two different directions with opposite signs is a crucial difference with a simple effect of advection.

Finally expressed in terms of Fourier coefficients, the linear solution is written as

$$\left(\hat{\boldsymbol{u}} + s\hat{\boldsymbol{b}} \right) (\boldsymbol{k}, t) = \exp(\imath s \boldsymbol{B}_0 \cdot \boldsymbol{k} t) \left(\hat{\boldsymbol{u}} + s\hat{\boldsymbol{b}} \right) (\boldsymbol{k}, 0), s = \pm 1. \tag{12.27}$$

The dispersion frequency of Alfvén waves is found as

$$\sigma_a = \boldsymbol{B}_0 \cdot \boldsymbol{k} = V_a k_{\parallel}, \tag{12.28}$$

where $k_\parallel$ is the component of the wave vector along the mean magnetic field, whose magnitude, scaled as a velocity, is the Alfvén velocity V_a.

The important case of liquid metal, or any case with magnetic Prandtl number very far from one, is now addressed, so that we reintroduce different values of the kinematic viscosity ν and of the magnetic diffusivity η. Linear solutions with diffusivities were investigated by Moffatt (1967), using a classical description in Fourier space, taking advantage of the solenoidal property of both velocity and magnetic field fluctuations. A slightly different method is used here, introducing the two solenoidal components of $\boldsymbol{b}$, $b^{(1)}$ and $b^{(2)}$, in the Craya–Herring frame of reference, as for the velocity vector. In terms of the four dependent variables, the linearized system of Eqs. (12.25) and (12.26) with added diffusivities is rewritten as

$$\frac{\partial}{\partial t}\begin{pmatrix} u^{(\alpha)} \\ b^{(\alpha)} \end{pmatrix} + \begin{pmatrix} \nu k^2 & -\imath\sigma_a \\ -\imath\sigma_a & \eta k^2 \end{pmatrix}\begin{pmatrix} u^{(\alpha)} \\ b^{(\alpha)} \end{pmatrix} = \begin{pmatrix} 0 \\ 0 \end{pmatrix}, \tag{12.29}$$

with $\alpha = 1, 2$. The dispersion law (Eq. 12.28) σ_a of Alfvén waves appears in the off-diagonal term of this matrix, so that, without diffusivity, a classical wave-equation is recovered for $u^{(\alpha)} \pm b^{(\alpha)}$, $\alpha = 1, 2$, corresponding to Elsaesser's variables. The differential diffusivity (difference of the diagonal terms) is responsible for a very important effect: Waves are not only modulated by a diffusive effect, as they would if $\nu = \eta$, they are completely suppressed outside the specific dumbell-like spectral subdomain shown in Fig. 12.2. Indeed, diagonalizing the matrix in the preceding linear system yields a complete analytical solution, with eigenvalues

$$\sigma_{\pm 1} = \frac{\nu + \eta}{2}k^2 \pm \sqrt{\left(\frac{\nu - \eta}{2}k^2\right)^2 - \sigma_a^2}, \tag{12.30}$$

so that the circles (spheres in this axisymmetric pattern) corresponds to the zero value of the term inside the square-root of Eq. (12.30).

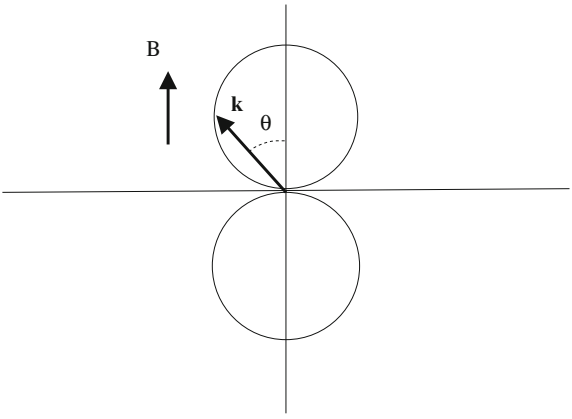

Fig. 12.2 Domain in Fourier space for delineating wave effects (inside the circles) and pure Ohmic damping without waves (outside the circles), in the $(k_\parallel = k\cos\theta_k, k_\perp = k\sin\theta_k))$ plane. The circles are of diameter K_0 and correspond to equation $k^2 = 4K_0^2\cos^2\theta_k$, with $K_0 = V_a/(\eta - \nu)$, from Eq. (12.30.) Adapted from Moffatt (1967)

The quasi-static limit is found when the magnetic Reynolds number is small, so that the induction equation reduces to $\boldsymbol{B}_0 \cdot \nabla \boldsymbol{u} = \eta \nabla^2 \boldsymbol{b}$. An explicit form of $\boldsymbol{b}$ in terms of $\boldsymbol{u}$ is thereby found, and readily closes the Lorentz force, linearized around the mean magnetic field. Consequently, the Lorentz force amounts to a sole, highly anisotropic, Ohmic damping, as follows:

$$\hat{\boldsymbol{F}}(\boldsymbol{k}, t) = -\eta^{-1} B_0^2 \cos^2 \theta_k \hat{\boldsymbol{u}}(\boldsymbol{k}, t) = -M_0^2 \cos^2 \theta_k \hat{\boldsymbol{u}}(\boldsymbol{k}, t), \tag{12.31}$$

under an algebraic form using Fourier transform, where θ_k is the angle between the wave vector and $\boldsymbol{B}_0$. Vertical (axial) Fourier modes, aligned with the imposed magnetic field, are rapidly dissipated whereas horizontal (transverse) ones remain unchanged.

12.4 The Quasi-static Régime, from Linear to Nonlinear Dynamics

The very low value of the Prandtl magnetic number $Pr_M = \nu/\eta$ (e.g. $Pr_M = 10^{-7}$ in liquid sodium) allows us to consider that only the velocity field is turbulent, with possibly very high (kinetic) Reynolds number, while the magnetic Reynolds number is small (usually smaller than one). In this limit, the contribution to dynamics inside the dumbell diagram of Fig. 12.2 can be ignored. Accordingly, we can get rid of the induction equation and the Lorentz force reduces to the explicit (in terms of velocity) form (12.31) given above.

Homogeneous quasi-static MHD was investigated by Moreau (1968), who introduced the angle that characterizes directional anisotropy, via

$$\cos^2 \gamma_u = \frac{\iiint \cos^2 \theta_k \mathcal{E}(\boldsymbol{k}) d^3\boldsymbol{k}}{\iiint \mathcal{E}(\boldsymbol{k}) d^3\boldsymbol{k}}, \tag{12.32}$$

in complete accordance with the parameter $\sin^2 \gamma_u$ ($= 1 - cos^2 \gamma_u$) used in USHT (Unstably Stratified Homogeneous Turbulence, Eq. (10.44, Chap. 10.) A similar angle, introduced later, is known as Shebalin's angle, but it is related to smaller structures, replacing $\mathcal{E}$ by $k^2\mathcal{E}$, or energy by enstrophy, in Eq. (12.32). An experimental approach followed with the seminal studies in mercury tank (e.g. Capéran et Alemany 1985.) Quasi-static MHD gives an excellent toy-model to study the full transition from three-dimensional to two-dimensional structure, as recently revisited and investigated by Favier et al. (2011a) using pseudo-spectral DNS and generalized EDQNM, following the first anisotropic EDQNM approach to QS-MHD by Cambon (1991).

Two-point second-order velocity correlations are governed by

$$\left(\frac{\partial}{\partial t} + 2\nu k^2 + M_0^2 \cos^2\theta_k\right) \mathcal{E}(\boldsymbol{k}, t) = T^{(\mathcal{E})}(\boldsymbol{k}, t), \tag{12.33}$$

and

$$\left(\frac{\partial}{\partial t} + 2\nu k^2 + M_0^2 \cos^2\theta_k\right) Z(\boldsymbol{k}, t) = T^{(Z)}(\boldsymbol{k}, t), \tag{12.34}$$

that only differ from their right-hand-sides, spectral transfer contributions mediated by triple velocity correlations.

Some basic mechanisms can be unterstood on the ground of single-point statistics, possibly introducing structure-based modeling. The equation for kinetic energy is

$$\frac{d\mathcal{K}}{dt} + M_0^2 \cos^2\gamma_u \mathcal{K} = -\varepsilon. \tag{12.35}$$

12.4.1 Linear Dynamics

In the linear, or viscous RDT limit, the basic spectra $\mathcal{E}$ and Z, which describe two-point second-order velocity correlations evolve as

$$\mathcal{E}(\boldsymbol{k}, t) = \exp\left(-\nu k^2 t - M_0^2 \cos^2\theta_k t\right) \frac{E(k, 0)}{4\pi k^2}, \quad Z = 0, \tag{12.36}$$

from isotropic initial data.

The inviscid time development of all single-point statistical quantities is derived analytically, in terms of the error function erf. The dominant terms in the evolution yield the following simple scalings: The kinetic energy decays as $M_0^2\Gamma(\infty)(2t)^{-1/2}$, as well as the Reynolds stress components, integral length scales with axial separation behave as $M_0 L_0 t^{1/2}$. Upon introduction of viscosity in the integrands, the viscous RDT solution is found, but this time depending on the explicit shape of the initial energy spectrum $E(k, 0)$ in Eq. (12.36). For example, the viscous RDT evolution leads to a linear evolution, in t, instead of $t^{1/2}$, for the abovementioned integral length scales.

It is clear that the spectral energy is more and more concentrated towards the transverse waveplane $k_\parallel = 0$, and without any polarization, by the linear solution. This yields asymptotically a 2D-3C state, characterized by

$$b_{33}^{(dir)} = \frac{1}{6}, \quad b_{33}^{(pol)} = 0, \quad b_{33} = \frac{1}{6},$$

for the relevant (axial) components of the deviatoric part of the Reynolds stress tensor in axisymmetric configuration. Counter-intuitively, this state corresponds to $\overline{u^2}_\parallel/\overline{u^2}_\perp = 2$, or the axial Reynolds stress component *larger than, twice,* the transverse one (see also Moffatt 1967.) The same ratio is found for the components of vorticity correlations, as $\overline{\omega^2}_\parallel/\overline{\omega^2}_\perp = 2$. This behavior is related to the fact that a relative depletion of energy around $\boldsymbol{k}$ in the axial direction, where velocity contribution is transverse ($\hat{\boldsymbol{u}} \perp \boldsymbol{k}$), means relative reduction of transverse (versus axial) Reynolds stress component, in the absence of polarization.

It is well known, however, from experiments and DNS, that the typical state of Quasi-Static MHD is 2D-2C, with the ratio $\overline{u^2}_\parallel/\overline{u^2}_\perp$ tending to zero. Accordingly, the nonlinearity is crucial for altering both componentality and dimensionality, using the parlance of Kassinos et al. (2001), or directional and polarization anisotropy, both considered throughout this book.

For a slightly different approach, we can consider the following equation for transverse vorticity fluctuation:

$$\boldsymbol{\omega}_\perp = \boldsymbol{\nabla} u_\parallel - \frac{\partial \boldsymbol{u}}{\partial x_\parallel}. \tag{12.37}$$

Hence, the two trends $u_\parallel \to 0$ (2C) and $\frac{\partial \boldsymbol{u}}{\partial x_\parallel} \to 0$ (2D) have to be found simultaneously in order to ensure the 2D-2C state, seen as a one-component state for vorticity (only axial).

12.4.2 Fully Nonlinear Dynamics for Quasi-Static MHD

As shown by DNS and generalized EDQNM, the nonlinear dynamics, through spectral transfer terms in the right-hand-side of Eqs. (12.33) and (12.34), moderately reduce the directional anisotropy, and *create a crucial polarization anisotropy.* This polarization anisotropy is particularly relevant in the 2D manifold, or $k_\parallel \sim 0, \cos\theta_k \sim 0$, in favoring the transverse mode of velocity with respect to the axial mode. The nondimensional magnetic interaction parameter

$$N_m = \frac{B_0^2 \ell_0}{\eta u_0}, \tag{12.38}$$

compares the magnetic time scale to a turnover time scale ℓ_0/u_0 in MHD; it is equal to $M_0^2 \ell_0/u_0$ in the quasi-static limit.

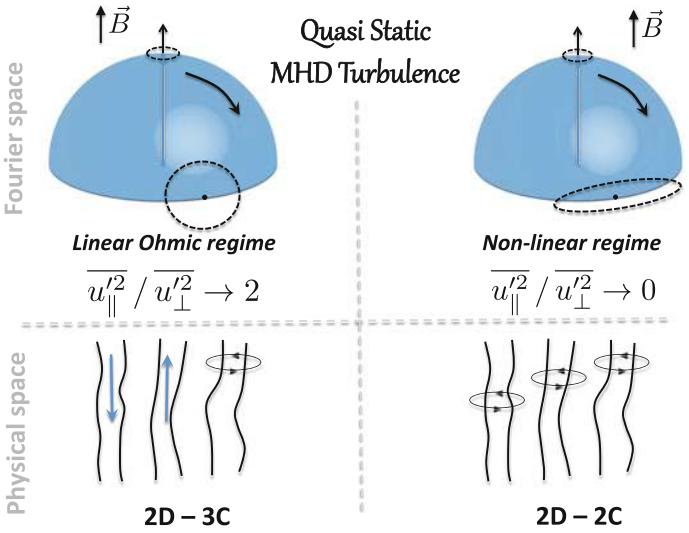

Fig. 12.3 Sketch of the creation of anisotropy and 2D-2C eventual structure in QS-MHD

A scenario of complete two-dimensionalization is ascertained: In a first stroke, almost linear, the spectral energy is more and more concentrated towards the 2D manifold, but this effect is less and less efficient as $\cos^2 \gamma_u$ in Eq. (12.32) is closer and closer to zero. In a second stroke, almost nonlinear, the flow state is close to a purely 2D flow for the transverse mode of velocity (or toroidal mode in the 2D limit) and to a passively advected scalar for the axial mode of velocity (or poloidal mode in the 2D limit). Accordingly, the energy of the axial velocity mode is rapidly damped by the direct cascade, as for a scalar advected by a 2D flow, whereas the energy of the transverse flow is enhanced by the classical inverse energy cascade. A sketch of this scenario is given on Fig. 12.3. It was recently recovered by the mathematical analysis of Gallet and Doering (2015).

Note that this scenario was invoked for more complex flow cases, as purely rotating turbulence. We think that it is erroneous, or at least oversimplified, when the dynamics are purely nonlinear. Here, the linear "forcing" via anisotropic Ohmic dissipation is both simple and efficient to create the 2D-3C state (two-dimensional three-components), from which classical 2D nonlinear dynamics naturally moves from 2D-3C to 2D-2C (second stroke above).

This transition from 3D isotropic turbulence to a 2D-3C state, then to a 2D-2C one, is reflected by single-point statistical descriptors as follows.

Looking at the Reynolds stress anisotropy, the growth of $b_{33}^{(dir)}$ is monotonic from 0 to the 2D value 1/6, and the curves satisfactorily collapse in terms of the linear time scale $M_0^2 t$. Meanwhile, $b_{33}^{(pol)}$ departs from zero after a delay and becomes more and more negative, when the polarization induced by nonlinear dynamics becomes dominant, so that it is found asymptotically

$$b_{33}^{(dir)} = \frac{1}{6}, \quad b_{33}^{(pol)} = -\frac{1}{2}, \quad b_{33} = -\frac{1}{3},$$

The latter value corresponding to 2C axisymmetric flows. Meanwhile, the evolution of the ratio $\overline{u_\parallel^2}/\overline{u_\perp^2}$ is not monotonic, first increasing, as in the linear regime, and then decreasing towards 0.

It is possible to extract (dir) and (pol) contributions in the Reynolds stress tensor from DNS or from two-point or spectral closure models, but not from experiments. On the other hand, two statistical quantities are measurable and quantify the polarization really restricted to the 2D manifold. There are

$$\overline{u_3^2} L_{33}^{(3)}, \quad \text{and} \quad \overline{u_1^2} L_{11}^{(3)} + \overline{u_2^2} L_{22}^{(3)}, \tag{12.39}$$

or two-dimensional energy components, for axial direction (index 3) and transverse direction, respectively. Because the integral length scales $L_{ij}^{(3)}$ are related to axial separation (superscript (3)), the quantities in Eq. (12.39) quantify the 2D-1C mode and the 2D-2C mode, respectively. Their difference, or

$$\zeta(t) = \left(\overline{u_1^2} L_{11}^{(3)} + \overline{u_2^2} L_{22}^{(3)}\right) - \overline{u^2}_3 L_{33}^{(3)} = -4\pi^2 \int_0^\infty Z(k, \cos\theta_k = 0) k dk, \tag{12.40}$$

therefore quantifies the polarization in the 2D manifold. It is initially zero, as in 3D isotropic turbulence, and remains exactly zero in linear (RDT) evolution. Its strong increase in DNS and EDQNM quantifies the nonlinear stoke, with decrease and eventual vanishing of $\overline{u_3^2} L_{33}^{(3)}$ and increase of $\left(\overline{u_1^2} L_{11}^{(3)} + \overline{u_2^2} L_{22}^{(3)}\right)$.

We conclude this section by a direct quantitative comparison between DNS and EDQNM results. In Favier et al. (2011a), both EDQNM1 and EDQNM2 versions are used in order to close $T^{(\mathcal{E})}$ and $T^{(Z)}$ in Eqs. (12.33) and (12.34) in terms of $\mathcal{E}$ and Z. The EDQNM2 model was derived from the one used in purely rotating turbulence (Cambon and Jacquin 1989; Cambon et al. 1997) (see also Chap. 7) by replacing the triadic, purely imaginary, term $2\imath\Omega(s\frac{k_\parallel}{k} + s'\frac{p_\parallel}{p} + s''\frac{q_\parallel}{q})$, with $s, s', s'' = \pm 1$ by $M_0^2(\frac{k_\parallel}{k})^2 + (\frac{p_\parallel}{p})^2 + (\frac{q_\parallel}{q})^2)$. The angle-dependent structure of spectral energy is shown in Fig. 12.4. We note a very good overall agreement between DNS and EDQNM2. Results from DNS are very scrambled and inaccurate in the "infrared range" of smallest wavenumbers, due to the sparsity of angular discretization. Energy is systematically underestimated in EDQNM with respect to DNS in the highest wavenumbers. These characteristics are generic of all quantitative EDQNM/DNS comparisons surveyed in this book.

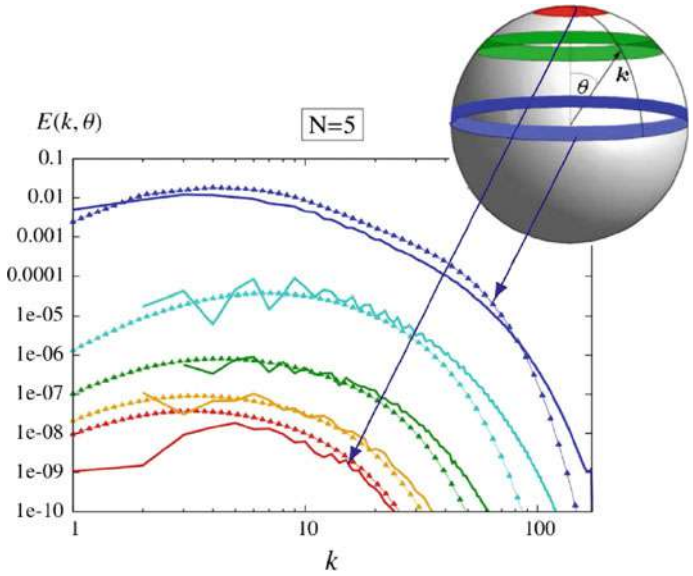

Fig. 12.4 Angular energy spectra for $N_m = 5$ (N on the figure). Comparison of DNS to EDQNM2 results. Adapted from Favier et al. (2011a) by Alexandre Delache

12.5 A First Statistical Approach, Kolmogorov–Monin Laws, Without Mean Magnetic Field

From the equations of incompressible ideal MHD, it is possible to derive a Kármán–Howarth equation for the two-point counterpart of total (kinetic + magnetic) energy as

$$\frac{1}{2}\frac{\partial}{\partial t}\underbrace{\langle u_i(\boldsymbol{x},t)u_i(\boldsymbol{x}+\boldsymbol{r},t)+b_i(\boldsymbol{x},t)b_i(\boldsymbol{x}+\boldsymbol{r},t)\rangle}_{R_{ii}(\boldsymbol{r},t)+R^M_{ii}(\boldsymbol{r},t)} =$$

$$= \frac{1}{4}\nabla_r\cdot\langle(\delta\boldsymbol{u}\cdot\delta\boldsymbol{u}+\delta\boldsymbol{b}\cdot\delta\boldsymbol{b})\,\delta\boldsymbol{u}\rangle - \frac{1}{2}\nabla_r\cdot\langle(\delta\boldsymbol{u}\cdot\delta\boldsymbol{b})\,\delta\boldsymbol{b}\rangle$$

$$+\frac{\partial}{\partial r_k\partial r_k}\langle\nu u_i(\boldsymbol{x},t)u_i(\boldsymbol{x}+\boldsymbol{r},t)+\eta b_i(\boldsymbol{x},t)b_i(\boldsymbol{x}+\boldsymbol{r},t)\rangle, \tag{12.41}$$

in which the contributions from triple correlations are recast in terms of third-order structure functions, with two-point increments for velocity $\delta\boldsymbol{u} = \boldsymbol{u}(\boldsymbol{x}+\boldsymbol{r},t)-\boldsymbol{u}(\boldsymbol{x},t)$ and magnetic field $\delta\boldsymbol{b} = \boldsymbol{b}(\boldsymbol{x}+\boldsymbol{r},t)-\boldsymbol{b}(\boldsymbol{x},t)$ (Galtier 2013).

Of course, the $\boldsymbol{x}$-dependence vanishes by statistical homogeneity, as does the explicit contribution from pressure fluctuation by incompressibility, and the contri-

bution from the Lorentz force. The Fourier-transform of this equation with respect to $\boldsymbol{r}$ gives the Lin equation for total energy $\mathcal{E}(\boldsymbol{k},t)+\mathcal{E}^M(\boldsymbol{k},t)$ (see Eq. (12.24).)

Assuming a global forcing for the sake of steadyness and a mean rate of injection for total (kinetic + magnetic) energy ε^T, the following relationship is proposed by Galtier (2013) for high Reynolds steady turbulence in the core of the inertial range ($\boldsymbol{r}$ much larger than dissipative scales and much smaller than the largest scale)

$$\frac{1}{4}\boldsymbol{\nabla}_r\cdot\langle(\delta\boldsymbol{u}\cdot\delta\boldsymbol{u}+\delta\boldsymbol{b}\cdot\delta\boldsymbol{b})\,\delta\boldsymbol{u}\rangle-\frac{1}{2}\boldsymbol{\nabla}_r\cdot\langle(\delta\boldsymbol{u}\cdot\delta\boldsymbol{b})\,\delta\boldsymbol{b}\rangle=-\varepsilon^T. \tag{12.42}$$

The so-called "4/3 exact law for MHD" (Politano and Pouquet 1998) is then derived as

$$-\frac{4}{3}\varepsilon^T r=\langle(\delta\boldsymbol{u}\cdot\delta\boldsymbol{u}+\delta\boldsymbol{b}\cdot\delta\boldsymbol{b})\,\delta u_L\rangle-2\langle(\delta\boldsymbol{u}\cdot\delta\boldsymbol{b})\,\delta b_L\rangle, \tag{12.43}$$

in which δu_L and δb_L denote the longitudinal increments, i.e. projected along the direction of the $\boldsymbol{r}$-vector. Due to the symmetry of Elsaesser variables $\boldsymbol{z}^{\pm}=\boldsymbol{u}\pm\boldsymbol{b}$, a more compact form is found as

$$-\frac{4}{3}\varepsilon^{\pm}r=\langle\left(\delta\boldsymbol{z}^{\pm}\cdot\delta\boldsymbol{z}^{\pm}\right)\delta z_L^{\pm}\rangle. \tag{12.44}$$

We consider that the role of external forcing together with the introduction of ε^T may be somewhat misleading. The rate ε^T is already implicitly present in Eq. (12.41), via

$$\lim_{r\to 0}\frac{1}{2}\left(R_{ii}(\boldsymbol{r},t)+R_{ii}^M(\boldsymbol{r},t)\right)=\mathcal{K}(t)+\mathcal{K}^M,$$

so that

$$\varepsilon^T=\lim_{r\to 0}\frac{\partial}{\partial r_k\partial r_k}\langle\nu u_i(\boldsymbol{x},t)u_i(\boldsymbol{x}+\boldsymbol{r},t)+\eta b_i(\boldsymbol{x},t)b_i(\boldsymbol{x}+\boldsymbol{r},t)\rangle. \tag{12.45}$$

One recovers the same duality as for ε in "hydro", that is both the injection rate of kinetic energy and the "true" dissipation rate. As for the "hydro" case, we recommend to avoid external forcing and external injection rate, and to derive from Eq. (12.41) an isotropic equation with both instationary term and dissipation rate. As shown in Chap. 4, in the hydro case, it is possible to recover such a law without forcing, and to evaluate the conditions for which the unsteady term in Kármán–Howarth or in Lin equation becomes negligeable: The Reynolds number is really huge, as $R_\lambda\sim 5.10^4$. In astrophysics, we are sure that these conditions are fulfilled. An interesting application is to evaluate ε^T in the solar wind: There is no possible direct evaluation, but third-order structure functions can be estimated.

12.6 Refined Analysis: Triadic Interactions in MHD Without Mean Magnetic Field

Isotropic EDQNM model was applied to MHD for a quantitative prediction, after the use of DIA by Kraichnan (1965), and a good survey is given by Biskamp (2003). More insight to the nature of triadic interaction can be found using helical modes, from hydro to MHD turbulence, as done in Chaps. 2 and 7.

12.6.1 Isotropic, or "isotropized" Models Using EDQNM

From the general set of statistical descriptors for two-point second-order correlations (12.24), polarization-type terms vanish in isotropic turbulence, whereas helicity-type terms can be kept, provided that isotropy be considered without mirror symmetry. The relevant set to be considered in MHD-HIT is therefore $E(k,t)$, $E^M(k,t)$, $H(k,t)$, $H^M(k,t)$. The spectrum of the electromotive force is not considered in general.

MHD equations were proposed in HIT by Pouquet et al. (1976) and Grappin et al. (1982); Grappin et al. (1983). The role of cross-helicity, even in an "isotropized" study, $H^C(k,t)$ was found very important by Grappin et al. (1983).

The new technical aspect with respect to the "hydro" case is to incorporate the vector $\hat{\boldsymbol{b}}$ in third-order and fourth-order correlations, with a more tedious calculation of quasi-normal terms; very simple and compact relationship is found, however, in using Elsaesser variables. But the most important new phenomenological aspect is to generalize the eddy damping term in the presence of magnetic field. The proposal by Pouquet et al. (1976) is

$$\tilde{\nu}(k,t) = (\nu+\eta)k^2 + \\ + a_s\left(\int_0^k p^2\left(E(p,t)+E^M(p,t)\right)dp\right)^{1/2} + a_A k\left(2\int_0^k E^M(p,t)dp\right)^{1/2}. \tag{12.46}$$

(η being the magnetic diffusivity in this chapter, the new notation $\tilde{\nu}$ from Biskamp (2003) is used for the Eddy–Damping term, denoted η from Chap. 4.) The first term comprises the laminar collisional dissipation effects. The second term represents the nonlinear eddy-distortion rate analogous to the eddy damping used in HIT. The third term corresponds to the Alfvén effect, which leads to relaxation of the triple correlations within an Alfvén time due to propagation of Alfvén waves along the large-scale field. As in the "hydro" case, a_S is related to the Kolmogorov constant, while an explicit calculation of the triple correlations for a Gaussian large-scale field gives $a_A = 1/\sqrt{3}$. The EDQNM closure model consists of the equations for the five quantities $E(k,t)$ $E^M(k,t)$, the kinetic and magnetic helicities $H(k,t)$ and $H^M(k,t)$, and the cross-helicity $H^C(k,t)$.

Stationary spectra E and E^M are found by numerically solving EDQNM equations in forcing the kinetic energy at large scale. Both spectra exhibit the $k^{-3/2}$ law in the inertial range. While the kinetic energy is larger in the forcing range, there is a slight excess of magnetic energy in the inertial range.

The isotropic Iroshnikov–Kraichnan (IK) energy spectrum is therefore recovered as

$$E(k) = C_{IK}\sqrt{\varepsilon v_A}k^{-3/2}, \tag{12.47}$$

with the constant C_{IK} of order one. The phenomenology invoked is the decorrelation effect of small-scale Alfvén wave packets propagating in the opposite sense along lines of almost constant (large-scale) magnetic field. In the isotropic EDQNM model, the IK scaling mainly results from the third term in Eq. (12.46).

Solutions of EDQNM equations with injection of both H and H^M in large scales yield an inverse cascade for the magnetic helicity with a slope close to k^{-2} for wave numbers smaller than the forcing one.

12.6.2 On the 2D Limit

Some analogies between rotating turbulence and MHD turbulence may be invoked, but the 2D limit is very different. The effect of the Coriolis force vanishes in this limit. On the other hand, the Lorentz force is always present in the 2D MHD case and profoundly affects the vortex dynamics.

In the 2D limit, all variables become independent of one coordinate, say $x_\parallel$. The vectors $\boldsymbol{\omega}$ and $\boldsymbol{j}$ reduce to $\omega = \omega_\parallel$ and $j = j_\parallel$. More precisely, in the more restricted 2D-2C limit, there is no axial, space-uniform, component for $\boldsymbol{u}$ and $\boldsymbol{b}$, and purely transverse velocity vector and the magnetic field vector derive from scalar streamfunctions

$$\boldsymbol{u} = \boldsymbol{n} \times \nabla\phi, \quad \boldsymbol{b} = \boldsymbol{n} \times \nabla\psi, \tag{12.48}$$

which are 2D (independent of $x_\parallel$) toroidal potentials as well (see Chap. 2). ψ is minus the axial component of the vector potential, or (magnetic) flux function. Accordingly

$$\omega = \omega_\parallel = \nabla^2\phi, \quad j = j_\parallel = \nabla^2\psi.$$

The two relevant equations for 2D MHD are

$$\left(\frac{\partial}{\partial t} + \boldsymbol{u}\cdot\nabla\right)\omega - \boldsymbol{b}\cdot\nabla j = \nu\nabla^2\omega, \tag{12.49}$$

which, with respect to its 3D counterpart Eq. (12.6), is without vortex stretching (by velocity) term and without stretching of $\boldsymbol{b}$ by $\boldsymbol{j}$, and

$$\left(\frac{\partial}{\partial t}+\boldsymbol{u}\cdot\boldsymbol{\nabla}\right)\psi=\eta\nabla^2\psi. \tag{12.50}$$

Note incidentally that these equations represent a physical case, e.g. for elongated toroidal modes in the cross-section of an annular tore in a idealized tokamak, in the presence of a strong axial magnetic field of intensity B_0, referred to as the "lowest order reduced MHD equations" (Kadomtsev and Pogutse 1974; Biskamp 2003)

$$\left(\frac{\partial}{\partial t}+\boldsymbol{u}\cdot\boldsymbol{\nabla}\right)\omega-\boldsymbol{b}\cdot\boldsymbol{\nabla}j=B_0\frac{\partial j}{\partial x_\parallel}+\nu\nabla^2\omega,\quad \left(\frac{\partial}{\partial t}+\boldsymbol{u}\cdot\boldsymbol{\nabla}\right)\psi=B_0\frac{\partial\phi}{\partial x_\parallel}+\eta\nabla^2\psi. \tag{12.51}$$

We will no longer consider the case with mean magnetic field in this section, and only use the system of 2D MHD equations (12.48, 12.6 and 12.50.) With respect to the hydro case, the contribution of the Lorentz force is crucial in the vorticity equation. It can amplify the enstrophy even in the absence of nonlinear vortex stretching. This system has three quadratic ideal invariants, the total energy, the cross-helicity and the mean-square magnetic potential, with corresponding k-spectra given here by

$$E(k)+E^M(k)\leftarrow\frac{1}{2}k^2\left(\langle\hat{\phi}(\boldsymbol{k})\hat{\phi}^*(\boldsymbol{k})+\hat{\psi}(\boldsymbol{k})\hat{\psi}^*(\boldsymbol{k})\rangle\right),\ H^C(k)\leftarrow k^2\langle\hat{\phi}(\boldsymbol{k})\hat{\psi}^*(\boldsymbol{k})\rangle,$$

and

$$A(k)\leftarrow k^2\langle\hat{\psi}(\boldsymbol{k})\hat{\psi}^*(\boldsymbol{k})\rangle. \tag{12.52}$$

The abridged notation, with $\leftarrow$, is used to avoid the full notation with Dirac distributions, as $k^2\langle\hat{\psi}(\boldsymbol{k})\hat{\psi}^*(\boldsymbol{p})\rangle=A(k)\delta^{(2)}(\boldsymbol{k}-\boldsymbol{p})$ for the latter equation.

At first glance, the results of DNS and EDQNM seem not to be different from the 3D case. The IK spectrum with Eq. (12.47) is recovered for the total energy spectrum, with $C_{IK}\sim 1.8$, and a direct cascade. An inverse cascade is found for the mean-square potential $A(k)$ as it is found for the magnetic helicity in 3D. For wavenumbers larger than the forcing one, a law $A(k)\sim\varepsilon_A^{2/3}k^{-7/3}$ prevails, whereas a law in $k^{-7/2}$ corresponds to $A(k)\sim k^{-2}E(k)$ for smaller wavenumbers.

12.6.3 Anisotropic Equations. Triadic Interactions in Terms of Helical Modes

Lin equations for both kinetic and magnetic energy are

$$\left(\frac{\partial}{\partial t}+2\nu k^2\right)\mathcal{E}(\boldsymbol{k},t)+\mathcal{L}(\boldsymbol{k},t)=T^{(\mathcal{E})}(\boldsymbol{k},t) \tag{12.53}$$

and

$$\left(\frac{\partial}{\partial t}+2\eta k^2\right)\mathcal{E}^M(\boldsymbol{k},t)+\mathcal{S}(\boldsymbol{k},t)=T^{(\mathcal{E}^M)}(\boldsymbol{k},t). \tag{12.54}$$

We recover the exact spectral counterpart of Eq. (12.41) for the sum $\mathcal{E}+\mathcal{E}^M$. Triple correlations appear in $\mathcal{L}$ via $-\langle\hat{\boldsymbol{u}}(\boldsymbol{k})\cdot\widehat{(\boldsymbol{j}\times\boldsymbol{b})}\rangle$ (or $k_j\langle\hat{u}_i^*\widehat{(b_ib_j)}\rangle$, $\langle ubb\rangle$-type), and in $T^{(\mathcal{E})}$ via $-\langle\hat{\boldsymbol{u}}(\boldsymbol{k})\cdot\widehat{(\boldsymbol{\omega}\times\boldsymbol{u})}\rangle$ (or $k_j\langle\hat{u}_i^*\widehat{(u_iu_j)}\rangle$, $\langle uuu\rangle$-type). Triple correlations appear in $\mathcal{S}$ via $k_j\langle\hat{b}_i^*\widehat{(u_ib_j)}\rangle$ and in $T^{(\mathcal{E}^M)}$ via $-k_j\langle\hat{b}_i^*(\boldsymbol{k})\cdot\widehat{(u_jb_i)}\rangle$ (or $\langle ubb\rangle$-type). The equation for the kinetic energy spectrum is not conservative: Only $T^{(\mathcal{E})}$ has zero integral, but not the cubic contribution $\mathcal{L}$ from the Lorentz force. In accordance with Eq. (12.9)

$$\iiint\mathcal{L}(\boldsymbol{k},t)d^3\boldsymbol{k}=-\overline{\frac{\partial u_i}{\partial x_j}b_ib_j}-\underbrace{\frac{\partial}{\partial x_j}\overline{(u_ib_ib_j)}}_{=0}. \tag{12.55}$$

Conversely, in the equation for the magnetic energy spectrum, only $T^{(\mathcal{E}^M)}$ has zero integral, but not $\mathcal{S}$ which is similar to the nonlinear vortex stretching term in enstrophy equation, in the "hydro" case. In accordance with Eq. (12.10), one has

$$\iiint\mathcal{S}(\boldsymbol{k},t)d^3\boldsymbol{k}=\overline{\frac{\partial u_i}{\partial x_j}b_ib_j}. \tag{12.56}$$

On the other hand, the total energy is conservative, so that the sum $\mathcal{L}+\mathcal{S}$ has zero integral. This is consistent with the fact that only the gradient of cubic correlations is present in the Kármán–Howarth equation (12.41) for the two-point contribution to total energy.

Helical modes are particularly suited to express the basic nonlinear equations. They are derived from $\hat{\boldsymbol{u}}$ as

$$u_s(\boldsymbol{k},t)=\frac{1}{2}\hat{\boldsymbol{u}}(\boldsymbol{k},t)\cdot\boldsymbol{N}(-s\boldsymbol{k}),\ s=\pm1,$$

so that Eq. (12.11) is rewritten as

$$\left(\frac{\partial}{\partial t}+\nu k^2\right)u_s(\boldsymbol{k},t)-\frac{1}{2}\boldsymbol{N}(-s\boldsymbol{k})\widehat{(\boldsymbol{j}\times\boldsymbol{b})}=-\frac{1}{2}\boldsymbol{N}(-s\boldsymbol{k})\widehat{(\boldsymbol{\omega}\times\boldsymbol{u})}, \tag{12.57}$$

and the basic nonlinear terms are expressed with the same variables, so that

$$\widehat{(\boldsymbol{\omega}\times\boldsymbol{u})}=\sum_{s',s''=\pm1}\iiint_{p+q=k}s'pu_{s'}(\boldsymbol{p},t)u_{s''}(\boldsymbol{q},t)\boldsymbol{N}(s'\boldsymbol{p})\times\boldsymbol{N}(s''\boldsymbol{q})d^3\boldsymbol{p},$$

using $\imath\,\boldsymbol{p}\times\boldsymbol{N}(s'\boldsymbol{p})=s'p\boldsymbol{N}(s'\boldsymbol{p})$ (the helical modes diagonalize the Curl operator). The Lorentz force is expressed in the same way, as

$$\widehat{(\boldsymbol{j}\times\boldsymbol{b})}=\sum_{s',s''=\pm1}\iiint_{p+q=k}s'pb_{s'}(\boldsymbol{p},t)b_{s''}(\boldsymbol{q},t)\boldsymbol{N}(s'\boldsymbol{p})\times\boldsymbol{N}(s''\boldsymbol{q})d^3\boldsymbol{p}.$$

Finally, the nonlinearity in the induction equation is written as

$$\widehat{(\boldsymbol{u}\times\boldsymbol{b})}=\sum_{s',s''=\pm1}\iiint_{p+q=k}u_{s'}(\boldsymbol{p},t)b_{s''}(\boldsymbol{q},t)\boldsymbol{N}(s'\boldsymbol{p})\times\boldsymbol{N}(s''\boldsymbol{q})d^3\boldsymbol{p}.$$

In the convolution products, there is the same triadic coefficient $\imath g=\frac{1}{2}\boldsymbol{N}(s\boldsymbol{k})\cdot\big(\boldsymbol{N}(s'\boldsymbol{p})\times\boldsymbol{N}(s''\boldsymbol{q})\big)$. This product comes from Eq. (2.107), and from the relationship

$$\frac{1}{2}\boldsymbol{N}(-s\boldsymbol{k})\cdot\Big(\imath\boldsymbol{k}\times\widehat{(\boldsymbol{u}\times\boldsymbol{b})}\Big)=\frac{1}{2}sk\boldsymbol{N}(-s\boldsymbol{k})\cdot\widehat{(\boldsymbol{u}\times\boldsymbol{b})}$$

in the induction equation.

This coefficient is simplified by means of the last change of local frames

$$\underbrace{\boldsymbol{e}^{(2)}(\boldsymbol{k})-s\imath\boldsymbol{e}^{(1)}(\boldsymbol{k})}_{\boldsymbol{N}(s\boldsymbol{k})}=e^{\imath s\lambda}\underbrace{(\boldsymbol{\beta}+s\imath\boldsymbol{\gamma})}_{\boldsymbol{W}(s)},\tag{12.58}$$

$$\underbrace{\boldsymbol{e}^{(2)}(\boldsymbol{p})-s'\imath\boldsymbol{e}^{(1)}(\boldsymbol{p})}_{\boldsymbol{N}(s'\boldsymbol{p})}=e^{\imath s'\lambda'}\underbrace{\big(\boldsymbol{\beta}'+s'\imath\boldsymbol{\gamma}\big)}_{\boldsymbol{W}'(s')},\tag{12.59}$$

$$\underbrace{\boldsymbol{e}^{(2)}(\boldsymbol{q})-s''\imath\boldsymbol{e}^{(1)}(\boldsymbol{q})}_{\boldsymbol{N}(s''\boldsymbol{q})}=e^{\imath s''\lambda''}\underbrace{\big(\boldsymbol{\beta}''+s\imath\boldsymbol{\gamma}\big)}_{\boldsymbol{W}''(s'')}.\tag{12.60}$$

The three helical modes $\boldsymbol{W}$, $\boldsymbol{W}'$ and $\boldsymbol{W}''$ related to $\boldsymbol{k}$, $\boldsymbol{p}$ and $\boldsymbol{q}$ are now defined with respect to a unit polar vector which is the unit vector normal to the plane of the triad, instead of a fixed one. Accordingly, $\boldsymbol{\gamma}$ is normal to the plane of the triad, and the three unit vectors $\boldsymbol{\beta}$, $\boldsymbol{\beta}'$, $\boldsymbol{\beta}''$ are all located in the (same) plane of the triad. It is found

$$\imath g=\boldsymbol{W}(s)\cdot\big(\boldsymbol{W}(s')\times\boldsymbol{W}(s'')\big)e^{\imath(s\lambda+s'\lambda'+s''\lambda'')}=\imath(s\sin\alpha+s'\sin\beta+s''\sin\gamma)e^{\imath(s\lambda+s'\lambda'+s''\lambda'')},$$

and using the triangle equality

$$C_{kpq}=\frac{\sin\alpha}{k}=\frac{sin\beta}{p}=\frac{\sin\gamma}{q},$$

$$2\imath g=\boldsymbol{N}(s\boldsymbol{k})\cdot\big(\boldsymbol{N}(s'\boldsymbol{p})\times\boldsymbol{N}(s''\boldsymbol{q})\big)=\imath C_{kpq}\big(sk+s'p+s''q\big)e^{\imath(s\lambda+s'\lambda'+s''\lambda'')}.\tag{12.61}$$

Changing the sign of $\boldsymbol{p}$ and $\boldsymbol{q}$ in the convolution integrals in order to recover the completely symmetric relationship $\boldsymbol{k}+\boldsymbol{p}+\boldsymbol{q}=0$, and symmetrizing these integrals in terms of $\boldsymbol{p}$ and $\boldsymbol{q}$, one finds

$$\left(\frac{\partial}{\partial t}+\nu k^2\right)u_s(\boldsymbol{k},t)=\imath\sum_{s',s''=\pm1}\iint_{k+p+q=0}\left(s'p-s''q\right)g(s\boldsymbol{k},s'\boldsymbol{p},s''\boldsymbol{q})\times$$

$$\times\left(u^*_{s'}(\boldsymbol{p},t)u^*_{s''}(\boldsymbol{q},t)-b^*_{s'}(\boldsymbol{p},t)b^*_{s''}(\boldsymbol{q},t)\right)d^3\boldsymbol{p},\ s=\pm1, \tag{12.62}$$

and

$$\left(\frac{\partial}{\partial t}+\nu k^2\right)b_s(\boldsymbol{k},t)=\imath\sum_{s',s''=\pm1}\iint_{k+p+q=0}(-sk)\,g(s\boldsymbol{k},s'\boldsymbol{p},s''\boldsymbol{q})\times$$

$$\times\left(u^*_{s'}(\boldsymbol{p},t)b^*_{s''}(\boldsymbol{q},t)-b^*_{s'}(\boldsymbol{p},t)u^*_{s''}(\boldsymbol{q},t)\right)d^3\boldsymbol{p},\ s=\pm1. \tag{12.63}$$

One recovers the single-triad expression of Waleffe (1992), extended to the ideal MHD (Lessines et al. 2009).

The latter authors used this system of equations to improve helical shell models, but much more work can be done. For instance it is possible to display all reduced set of triple correlations for the whole set of second-order correlations in Eq. (12.24), in line with Eqs. (12.17), (12.21) and (12.22). Anisotropic EDQNM could be derived by calculating the exact quasi-normal counterpart of all these sets of triple correlations, so that the role of a semi-empirical eddy-damping, as in Eq. (12.46), could be reduced with respect to isotropic EDQNM models. It is worth reminding that the eddy-damping term can vanish in the limit case of wave turbulence theory.

But two difficulties are found when trying to further mimic Waleffe's analysis of triadic interactions performed in the hydrodynamic case.

Firstly, it is not possible to derive in general the sense of cascade from a single triad, as done by Waleffe (1992), using his triad instability principle. Indeed, it is not possible to disentangle $\langle uuu\rangle$-type contributions from $\langle ubb\rangle$-type ones, for instance in contributions to energy, $u^*_s u_s$, $u^*_{s'}u_{s'}$, $u^*_{s''}u_{s''}$. A much more complicated analysis of stability must be done.

A second difficulty comes from the possible use of Elsaesser variables. It is possible in principle to use compact variables such as

$$z^s_{s_k}(\boldsymbol{k},t)=u_{s_k}(\boldsymbol{k},t)+sb_{s_k}(\boldsymbol{k},t),\ s_k=\pm1,\ s=\pm1,$$

in which two different signs are used: s_k (index) holds for the polarity of helical modes in terms of $\boldsymbol{k}$, denoted s in the equations above, and s (superscript) holds for the Elsaesser combination. Notations can be extended to dependence in terms of $\boldsymbol{p}$ and $\boldsymbol{q}$, as $z^{s'}_{s_p}(\boldsymbol{p},t)$ and $z^{s''}_{s_q}(\boldsymbol{q},t)$. This should allow to have a more diagonal form, combining re-arrangement in terms of Curl operators and basic symmetry in terms of $\boldsymbol{u}$ and $\boldsymbol{b}$. The relationship

$$z_n^{-s}\frac{\partial z_i^s}{\partial x_n}=z_n^{-s}\frac{\partial z_n^s}{\partial x_i}-\epsilon_{ijn}(\boldsymbol{\nabla}\times\boldsymbol{z}^s)_j z_n^{-s},$$

allows to display the term $-(\nabla \times z^s) \times z^{-s}$, well suited for expression in terms of helical Elsaesser modes, but the second term cannot be expressed as a purely gradient term, eventually removed with the pressure term, because of the different signs s and $-s$. Only for a symmetric form, $z^{-s}\cdot\nabla z^s + z^s\cdot\nabla z^{-s}$ can be replaced by $-(\nabla \times z^z) \times z^{-s} - (\nabla \times z^{-z}) \times z^s$, because the second term amounts to a pure gradient $\nabla(z^{-s}\cdot z^s)$, ... but only the kinetic equation (12.62) is recovered. Incidentally, we recommend to use Ricci relationship in order to address the latter calculations, as in all calculations in which it is dangerous to use ∇ as a "true" vector.

12.7 MHD Turbulence and Interactions with Other Body Forces and Mean Gradients

We will first survey the case in which a mean velocity magnetic field is present, with $\boldsymbol{b} \to \boldsymbol{B}_0 + \boldsymbol{b}$. A new case of wave turbulence theory is found when $|\boldsymbol{u}|, |\boldsymbol{b}| \ll |\boldsymbol{B}_0|$. Then more complex cases are defined considering combination with other (linear) body forces, namely Coriolis and buoyancy effects, i.e. extending results discussed in Chap. 11 The next step consists of introducing of mean shear in addition to the above body forces, yielding a simple model for magnetized accretion discs, with the Magneto Rotational Instability (MRI) and beyond.

12.7.1 Wave Turbulence in the Presence of a Dominant Mean Magnetic Fluid

As done in purely rotating turbulence, wave turbulence theory is relevant when dominant Alfvén waves are generated by an external, constant, magnetic field $\boldsymbol{B}_0$, whereas weak nonlinearity is considered. Isotropy is broken and axisymmetry (around $\boldsymbol{B}_0$) is the simplest statistical symmetry to be fulfilled. Accordingly, spectra depend on two coordinates: $\mathcal{E}(k_\parallel, k_\perp)$ using cylindrical coordinates (as in Fig. 12.2) or $\mathcal{E}(k, \theta_k)$ using a polar-spherical system of coordinates. The phenomenological argument used for deriving the Iroshnikov–Kraichnan energy spectrum is adapted in the presence of the dominant magnetic field, yielding

$$\mathcal{E}(k_\parallel, k_\perp) \sim \sqrt{\varepsilon B_0} k_\perp^{-4} k_\parallel^{-1/2}.$$

Because of its definition, multiplied by k^2, the related contribution in Galtier (2013) is $k_\perp^{-2}$. This law seems to recover the same integrable singularity at $k_\parallel = 0$ near the 2D manifold, as in inertial wave turbulence. But the role of the 2D manifold is very different in rotating turbulence and in Alfvénic MHD turbulence, as shown in Sect. 12.6.2, and eventually only the scaling for the transverse component of the wave vector is confirmed by the rigorous application of wave turbulence theory by

Galtier et al. (2000), discussed below. As for rotating turbulence in Chap. 7, a purely nonlinear equation for the "slow" amplitudes of Alfvén waves is found:

$$\frac{\partial a_i^s}{\partial t} = -\imath k_m P_{in}(\boldsymbol{k}) \iiint_{\boldsymbol{p}+\boldsymbol{q}=\boldsymbol{k}} a_m^{-s}(\boldsymbol{q},t) a_n^s(\boldsymbol{p},t) \exp(-\imath s t(\sigma_a(\boldsymbol{k}) - \sigma_a(\boldsymbol{p}) + \sigma_a(\boldsymbol{q}))d^3\boldsymbol{p}, s = \pm 1, \tag{12.64}$$

with σ_a given by Eq. (12.28), and

$$z^s(\boldsymbol{k},t) = \boldsymbol{a}^s(\boldsymbol{k},t)\exp[\imath s\sigma_a(\boldsymbol{k})]. \tag{12.65}$$

Discussion of slightly different forms using more symmetrization in terms of $\boldsymbol{p}$ and $\boldsymbol{q}$ is unimportant. The most important difference with rotating turbulence is the fact that only one sign is displayed (the full phase term $s\sigma_r(\boldsymbol{k}) + s'\sigma_r(\boldsymbol{p}) + s''\sigma_r(\boldsymbol{q})$ is called into play in the rotating case, in terms of the polarities of interacting helical modes.) At this stage, there is no assumption, and the use of amplitudes $\boldsymbol{a}^s$ instead of variables $\boldsymbol{z}^s$ is only a way to render implicit the explicit linear effects of Alfvén waves induced by $\boldsymbol{B}_0$.

Only when considering the asymptotic limit of really slow amplitudes, or instead really rapid phases (see the discussion in Chap. 7 and Bellet et al. 2006), with

$$z^s(\boldsymbol{k},t) = \boldsymbol{a}^s(\boldsymbol{k},t)\exp[\frac{1}{\epsilon}\imath s\sigma_a(\boldsymbol{k})]$$

where ϵ is an arbitrarily small parameter, the wave turbulence theory holds, so that the effective nonlinearity reduces to the three-wave resonant condition

$$k_\parallel = p_\parallel - q_\parallel \quad \text{with} \quad \boldsymbol{k} = \boldsymbol{p} + \boldsymbol{q}.$$

The simple constraint

$$q_\parallel = 0 \tag{12.66}$$

is derived, with $\boldsymbol{k}_\perp = \boldsymbol{p}_\perp + \boldsymbol{q}_\perp$. This means that the weakly nonlinear cascade is restricted to transverse wave vectors. At last, the complete calculation yields the following expression for the energy spectrum $E^s(k_\parallel)$ without helicity and in the limit $k_\parallel \ll k_\perp$:

$$E^s(k_\perp) = C\sqrt{\Pi B_0}k_\perp^{-2}. \tag{12.67}$$

This result raises the question of what happens with the dependence in terms of $k_\parallel$. The sole solution is $E^s(k_\parallel, k_\perp) = E^s(k_\perp)g^s(k_\parallel)$, in which g^s is an arbitrary function, whose form is for instance given by initial data.

12.7.2 Rotating MHD

There have been only few studies on rotating MHD since the seminal theoretical studies by Lehnert (1954, 1955), and Moffatt (1970), but impressive experimental facilities have been developed to get a better understanding of the geodynamo (Schmitt et al. 2008 in Grenoble, Stefani et al. 2006; Ruediger et al. 2014 in Dresden). This topic is illustrated here by simple analytical results on linear dynamics, with combination of inertial and Alfvén waves, leading to magneto-inertia, or Magneto-Coriolis (MC), waves. In addition, recent DNS results give a first insight into nonlinear dynamics.

In the absence solid-body rotation, it is not necessary to use the Craya–Herring frame for studying the linear solutions for Alfvén waves. On the contrary, when rotation is present, the Coriolis force breaks the symmetry between poloidal and toroidal velocity components, so that a fourth-order linear system is required:

$$\frac{\partial}{\partial t}\begin{pmatrix} u^{(1)} \\ u^{(2)} \\ \imath b^{(1)} \\ \imath b^{(2)} \end{pmatrix} + \begin{pmatrix} \nu k^2 & \sigma_r & \sigma_a & 0 \\ \sigma_r & \nu k^2 & 0 & -\sigma_a \\ -\sigma_a & 0 & \eta k^2 & 0 \\ 0 & \sigma_a & 0 & \eta k^2 \end{pmatrix} \begin{pmatrix} u^{(1)} \\ u^{(2)} \\ \imath b^{(1)} \\ \imath b^{(2)} \end{pmatrix} = 0. \tag{12.68}$$

where the contributions from the magnetic field are multiplied by $\imath$ with respect to the linear system (12.29), as done in Salhi et al. (2012). This allows for the recovery of a real matrix (e.g., $\imath\sigma_a$ in Eq. (12.30) becomes σ_a), that is more tractable, whereas the components $b^{(\alpha)}$ being probably complex-valued anyway, are not significantly more complicated. The superposition of rotation and an imposed magnetic field leads to a competition between Coriolis and Lorentz forces. Note that without rotation, the poloidal and toroidal components of both velocity and magnetic fields are independent. The corresponding dispersion law is

$$\sigma_{mc}^2 = \frac{1}{2}\sigma_r^2 + \sigma_a^2 \pm \sqrt{\left(\frac{1}{2}\sigma_r^2 + \sigma_a^2\right)^2 - \sigma_a^4}, \tag{12.69}$$

in the absence of diffusivities. Looking at Fig. 12.5, the very different shapes of wavepackets are shown, from purely Alfvén waves (left) to purely inertial waves (right), with intermediate cases of magneto-inertia waves.

Both linear and nonlinear dynamics have been investigated by Favier et al. (2011b) using pseudo-spectral DNS without forcing, starting from isotropic initial data. Relevant non-dimensional numbers are the magnetic interaction number N_m, already introduced in the particular case of Quasi-Static MHD, and the Rossby number R_o. Their product defines the Elsaesser number Λ

$$N_m = \frac{B_0^2 \ell_0}{\eta u_0}, \quad R_0 = \frac{u_0}{2\Omega \ell_0}, \quad \Lambda = \frac{B_0^2}{2\Omega\eta}, \tag{12.70}$$

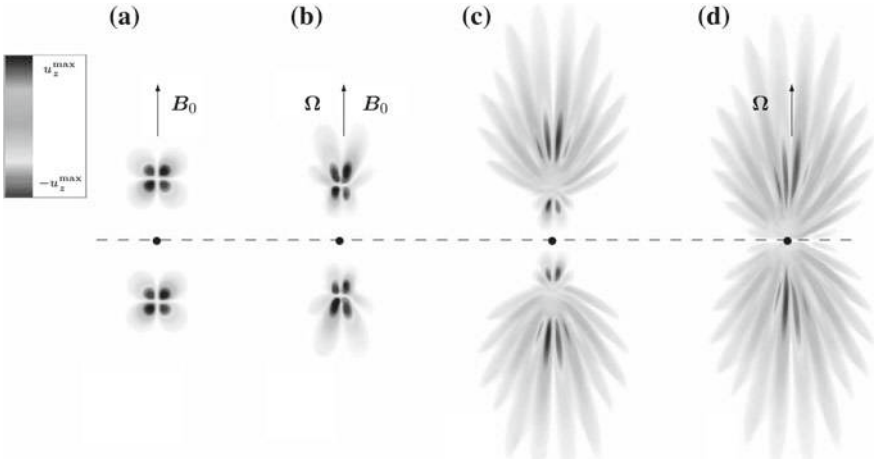

Fig. 12.5 Visualization of magneto-inertia wave packets. Reproduced from Favier et al. (2011b) with permission of IOP

in which ℓ_0/u_0 is a typical turnover time. The increasing effect of rotation is quantified by the decreasing Elsaesser number. It is found that the development of magnetic energy is more and more inhibited as Λ decreases, as shown in Fig. 12.6.

The dramatic breakdown of equipartition is related to a re-orientation of velocity fluctuations with respect to magnetic field fluctuations. The normalized probability density function of the cross-correlation parameter

$$\rho(\boldsymbol{x}) = \frac{2(\boldsymbol{u}(\boldsymbol{x})\cdot\boldsymbol{b}(\boldsymbol{x}))}{\boldsymbol{u}^2(\boldsymbol{x}) + \boldsymbol{b}^2(\boldsymbol{x})} \tag{12.71}$$

is plotted on Fig. 12.7a. Without rotation, the pdf is very flat, whereas it is symmetrically peaked at $\rho = \pm 1$ in the linear régime of pure Alfvén waves, meaning alignment of $\boldsymbol{u}$ and $\boldsymbol{b}$. As the Elsaesser number decreases, the pdf becomes more and more peaked at $\rho = 0$, indicating a trend toward orthogonality of $\boldsymbol{u}$ and $\boldsymbol{b}$ fluctuations. The large scale fluctuations are dominated by inertial waves so that Alfvénic fluctuations (characterized by an equipartition between kinetic and magnetic energies, and by $\rho \sim \pm 1$) are damped. On Fig. 12.6b, one can see that the horizontal component of the magnetic field is dominant and less Gaussian in rotating cases than in non-rotating case.

The last result chosen to illustrate rotating MHD deals with nonlinear transfer spectra obtained from DNS. With respect to nonlinear equations (12.9) and (12.10) for kinetic energy and magnetic energy, additional second-order linear terms account for the linearized Laplace force, which are equal to $\overline{\boldsymbol{u}\cdot((\nabla\times\boldsymbol{b})\times\boldsymbol{B}_0)}$ in Eq. (12.9) and $\overline{\boldsymbol{b}\,(\nabla\times(\boldsymbol{u}\times\boldsymbol{B}_0))}$ in Eq. (12.10), respectively. The Coriolis force, that produces no energy, has no explicit contribution in Eq. (12.9). Similarly, second-order terms with $\boldsymbol{B}_0$ are added to spectral equations (12.53) and (12.54). Important cubic terms

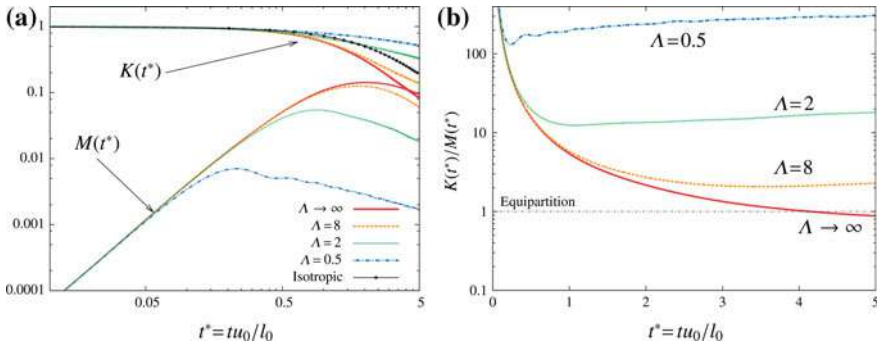

Fig. 12.6 **a** Development of kinetic energy $\mathcal{K}$ (denoted K) and magnetic energy $\mathcal{K}^M$ (denoted M) versus dimensionless time $t^* = tu_0/\ell_0$. **b** ratio $\mathcal{K}(t^*)/\mathcal{K}^M(t^*)$. Reproduced from Favier et al. (2011b) with permission of IOP

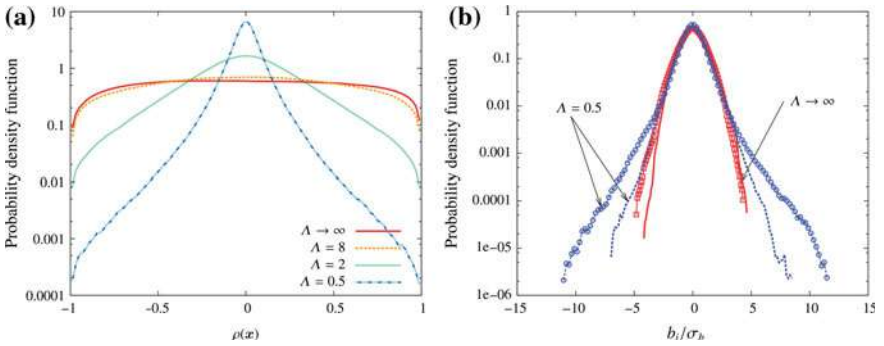

Fig. 12.7 **a** Normalized pdf of the correlation coefficient $\rho(\boldsymbol{x})$ at $t^* + 5$. **b** Normalized pdf of $\boldsymbol{b}/\sigma_b$, where σ_b is the variance of $\boldsymbol{b}$. The symbols correspond to horizontal components, and solid lines to vertical ones. Reproduced from Favier et al. (2011b) with permission of IOP

in these equations are now related to nonlinear transfer spectra. The kinetic energy spectrum in Fig. 12.8a corresponds to spherically averaging $T^{(\mathcal{E})}(\boldsymbol{k}, t)$ in Eqs. (12.9) and (12.10), and the total transfer term in Fig. 12.8b corresponds to $T^{(\mathcal{E})} + T^{(\mathcal{E}^M)}$. Given the fact that the figures are plotted in semi-log scale, the spectra are multiplied by k in Fig. 12.8, in order to display zero-integral-property, when it holds (according to $\int kT(k)d\ln k = \int_0^\infty T(k)dk = 0$). Both kinetic energy transfer and total, kinetic + magnetic, transfer, are plotted: We note that the property of zero integral is well reproduced, and that the effect of rotation significantly reduces the strength of the transfer spectrum. The whole contribution of cubic nonlinearity to the magnetic energy equation yields the last spectrum plotted in Fig. 12.8c, that corresponds to spherically integrating $T^{(\mathcal{E}^M)} - \mathcal{S}$ in Eq. (12.10). This term is no longer a true interscale transfer term, and its integral is equal to the term $-\overline{\frac{\partial u_i}{\partial x_j} b_i b_j}$. It is however also reduced by rotation.

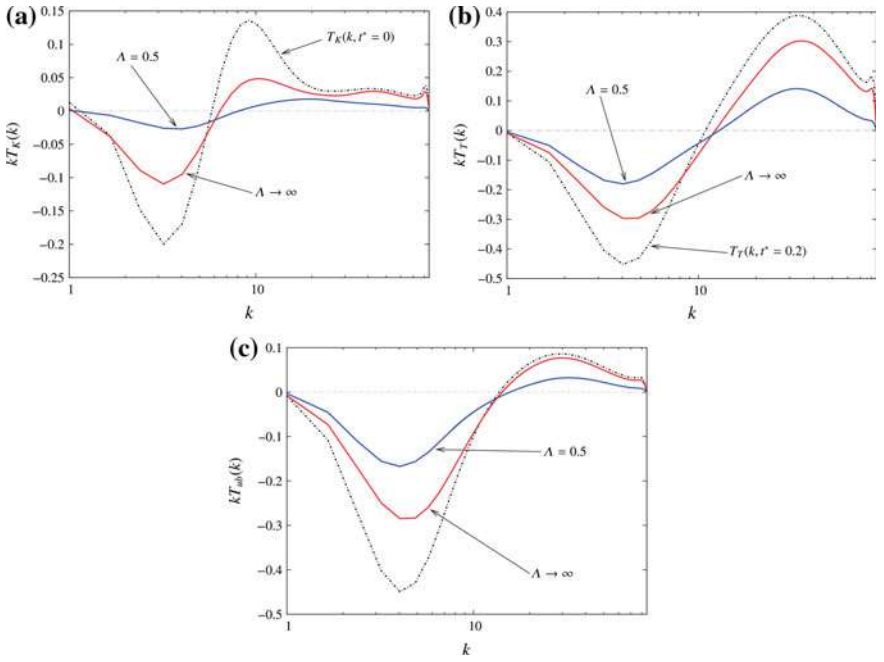

Fig. 12.8 **a** Shell-averaged kinetic energy transfer spectrum $T(k, t^*)$; the dashed thick line corresponds to the initial ($t^* = 0$) energy transfer spectrum after isotropic precomputation (without rotation, without mean magnetic field); solid lines correspond to energy transfer at the final time $t^* = 2$, with ($\Lambda = 0.5$) and without ($\Lambda = \infty$) rotation. **b** Total, kinetic + magnetic, shell-averaged energy transfer spectrum. **c** Shell-averaged spectrum of the $\boldsymbol{b}\cdot\boldsymbol{q}$ part of the magnetic transfer. In both (**b**) and (**c**), the dashed line corresponds to the spectrum at $t^* = 2$, whereas solid lines correspond to spectra at $t^* = 2$. Reproduced from Favier et al. (2011b) with permission of IOP

12.7.3 Magneto-Archimedes-Coriolis (MAC) Waves

MAC waves are ubiquitously present in several geophysical and astrophysical systems, like the Earth core, Sun's interior, solar corona, astrophysical accretion disks. In this Chapter only, the buoyancy scalar is denoted b_u from now on, not to be confused with the norm of the magnetic field.

It is possible to find a linear system of equations very similar to (12.68) for the five-rank vector $u^{(1)}, u^{(2)}, b^{(1)}, b^{(2)}, u^{(3)}$, in which the three individual dispersion frequencies are displayed: σ_r, σ_a, and σ_s.

But the five components are not independent. The linearized potential vorticity is no longer an invariant in the presence of the Lorentz force, as it is in coupled effects surveyed in Chap. 11. But another invariant of Boussinesq-MHD equations is present: The so-called induction potential scalar introduced by Salhi et al. (2012), which is defined as the scalar product of the magnetic field with the gradient of buoyancy. Reintroducing a Reynolds decomposition, with $\overline{\boldsymbol{b}}$ (formerly $\boldsymbol{B}_0$) and $\boldsymbol{b}'$, $\overline{b_u}$ and b'_u,

ω^M has three contributions, as the absolute potential vorticity in non-magnetized fluids (see Eq. (11.9)

$$\omega^M = \overline{\boldsymbol{b}}\cdot\overline{\nabla b_u} + \left(\overline{\boldsymbol{b}}\cdot\nabla b'_u + \boldsymbol{b}'\cdot\overline{\nabla b_u}\right) + \boldsymbol{b}'\cdot\nabla b'_u. \tag{12.72}$$

The first term is the mean contribution, the second term comprises mean- fluctuating contribution, and the third term holds for fluctuating - fluctuating one. Conservation of linearized induction potential scalar allows us to express the buoyancy mode $u^{(3)}$ in terms of the poloidal magnetic mode $b^{(2)}$ and the invariant $\pi^{(0)}$. Without diffusivities, the following system of equations is found

$$\frac{\partial}{\partial t}\begin{pmatrix} u^{(1)} \\ u^{(2)} \\ \imath b^{(1)} \\ \imath b^{(2)} \end{pmatrix} + \begin{pmatrix} 0 & \sigma_r & \sigma_a & 0 \\ -\sigma_r & 0 & 0 & -\frac{\sigma_a^2+\sigma_s^2}{\sigma_a} \\ -\sigma_a & 0 & 0 & 0 \\ 0 & \sigma_a & 0 & 0 \end{pmatrix}\begin{pmatrix} u^{(1)} \\ u^{(2)} \\ \imath b^{(1)} \\ \imath b^{(2)} \end{pmatrix} + \begin{pmatrix} 0 \\ \pi^{(0)} \\ 0 \\ 0 \end{pmatrix} = 0. \tag{12.73}$$

In line with the study of coupled effects in Chap. 11, the rank of the linear system is reduced using the invariant, here from 14 components in physical space (three-component velocity and magnetic fields, one for pressure fluctuation, one for the buoyancy scalar), 5 in Fourier space using solenoidal modes, down to 4 in the system of equations above. Solutions of this system can be studied as in the generalized "wave-vortex" decomposition, but such a study is richer in the presence of a mean shear, because it allows a non-modal approach to transient growth.

12.7.4 The Magneto-Rotational Instability (MRI) and Beyond

In Chap. 11, it is shown how the simple model of rotating shear flow can be used for studying some aspects of accretion discs in astrophysics, using the Shearing Sheet Approximation (SSA). It is discussed how a turbulent behavior or a bypass transition to turbulence is predicted, even if the Keplerian disc is stable under Rayleigh criterion or Bradshaw / Tritton analysis, with $R = 2\Omega/S = -4/3$. Extension of the domain of instability under MHD is sketched on Fig. 12.9, with a simple model of the MRI (e.g. Balbus and Hawley 1991). Experimental approaches are performed by Stefani et al. (2006), Ruediger et al. (2014).

As for all cases with pure plane shear flows, the simplest spectral linear solution for disturbances is found for the zero value of the streamwise component k_1 of the wave vector. This mode corresponds to the so-called symmetric mode in astrophysics using SSA.

With a mean magnetic field in the spanwise direction (or axial direction before using SSA), the linear system for $\hat{\boldsymbol{b}}$ and $\hat{\boldsymbol{u}}$ yields the equation for the dispersion frequency as

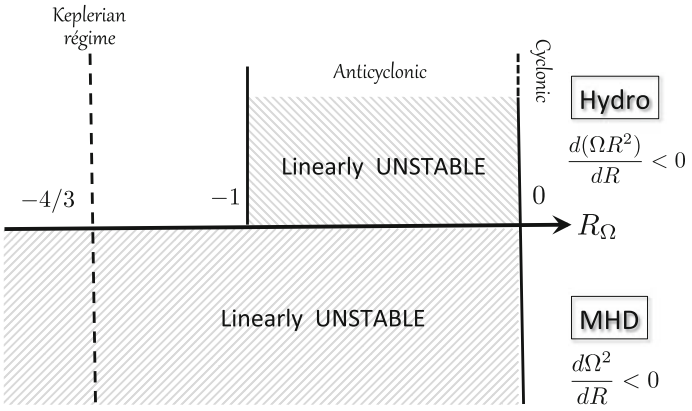

Fig. 12.9 Scheme of magnetized Shearing Sheet Approximation. Courtesy of François Rincon

$$\sigma^4 - \left(\alpha^2 S^2 B + 2k_3^2 B_0^2\right)\sigma^2 - k_3^2 B_0^2 \left(2\Omega S\alpha^2 - k_3^2 B_0^2\right) = 0. \tag{12.74}$$

One recovers the dispersion frequency of inertial waves, $2\Omega\alpha$, with $\alpha = k_3/(k_2^2+k_3^2)$ the cosine of the angle of the wave vector with the spanwise direction, along with the one of Alfvén waves $B_0 k_3$. With respect to the case of rotating shear without MHD discussed in Chap. 11, one recovers the square of the epyciclic frequency, or $2\Omega(2\Omega + S)$, also equal to $S^2 B$, with B the Bradshaw number. The solution is

$$\sigma_s^2 = k_3^2 B_0^2 + \frac{1}{2}\alpha^2 S^2 B + \frac{s}{2}\sqrt{\alpha^4 S^4 B^2 + 16 k_3^2 B_0^2 \Omega^2 \alpha^2}, s = \pm 1. \tag{12.75}$$

For $s = -1$, this solution reveals a typical exponential instability, with $\sigma_{-1}^2 < 0$. Stability is found for $kB_0 > 2\Omega S$. Accordingly, a strong magnetic field yields stabilization, but a rather weak magnetic field can induce the typical MRI, especially at small k. If attention is restricted to the case of the Keplerian disc, or $2\Omega/S = -4/3$, $B = 4/9$, the maximum growth rate is found for $kB_0 = \sqrt{5/12}S$, $\alpha = 1$, as $\gamma = \sqrt{-\sigma_{-1}^2} = S/2$. To give an order of magnitude, over a period of rotation, the amplification is $\exp(\gamma.2\pi/\Omega) = \exp(3\pi/2)$, or a bit more than 110.

It is possible to extend these results towards a more complete spectral linear analysis, with $k_1 \neq 0$ modes as well. A study gathering all the effects surveyed above, mean magnetic field, system rotation, mean buoyancy gradient with (Boussinesq) buoyancy fluctuation, and mean shear is given by Salhi et al. (2012). In order to avoid a too exhaustive review of all effects, with their detailed combination, we prefer to finish this section on external effects by an illustration of magnetized rotating and precessing sheared flows.

Stability of precessing flows is briefly discussed in Chap. 11 without magnetic field. It is shown how the gyroscopic torque induced by the misalignment of the

"precessing" system rotation of rate Ω^c, or $f = 2\Omega^c$, and the background rotation of rate Ω can be balanced by an additional mean shear, so that purely circular mean trajectories (if $\Omega^C = 0$) are rendered elliptic. A special form of the generic "elliptical flow instability" is thereby triggered. Two different cases for the additional mean shear are found when $\boldsymbol{\Omega}^C$ and $\boldsymbol{\Omega}$ are perpendicular, say $\Omega_i^C = \epsilon\Omega\delta_{i1}$ and $\Omega_i = \Omega\delta_{i3}$, referred to as the Mahalov base flow (MBF) and the Kerswell base flow (KBF). Admissibility conditions simply mean that the mean flow ought to be a particular solution of background equations, invoking either consistency with statistical homogeneity restricted to fluctuations (in line with Craya) or consistency with stability analysis (in line with Craik and Criminale). When the additional mean magnetic field is added, with dominant component along the system vorticity, these conditions are fulfilled for

$$B_{0i} = B_0\delta_{i3} + 2\epsilon B_0\delta_{i1}, \quad W_i = 4\epsilon\Omega, \tag{12.76}$$

in the KBF case, in which $\boldsymbol{W}$ holds for the mean absolute vorticity. They are

$$B_{0i} = B_0\delta_{i3}, \quad W_i = 2\Omega, \tag{12.77}$$

in the MBF case. From this viewpoint, the magnetized KBF case is more complicated, because an additional (horizontal, component 1) component of the mean magnetic field is generated by the interaction between the horizontal plane shear and the vertical (component 3) mean magnetic field. The stability problem depends on three parameters, the Poincaré number $\epsilon = \Omega^C/\Omega$, the characteristic angle α and a parameter η given by

$$\chi = \cos\alpha = \frac{k_0}{\sqrt{k_0^2 + k_p^2}}, \quad \eta = \frac{B_0}{\Omega_0}\sqrt{k_0^2 + k_p^2}. \tag{12.78}$$

Specific values of k_0 and k_p derive from the eikonal equation for the periodic time-dependent wave vector, and are different for MBF and KBF cases. The parameter η (not to be confused with magnetic diffusivity, ignored here) is very similar to a specific Lehnert number.

As for the basic elliptical flow instability surveyed in Chap. 11, instability tongues emanate from resonance conditions at typical angles of the time-periodic wave vector and vanishing ellipticity. They appear similar but much more subtle and detailed in the magnetized precessing case, as show in Fig. 12.10. Both KBF and MBF cases should coincide at very small ϵ. The comparison is made for harmonic resonance until the order $O(\epsilon^4)$. The comparison made for several values of η shows that the hydrodynamic and magnetic harmonic instability bands are larger in the MBF case than in the KBF one.

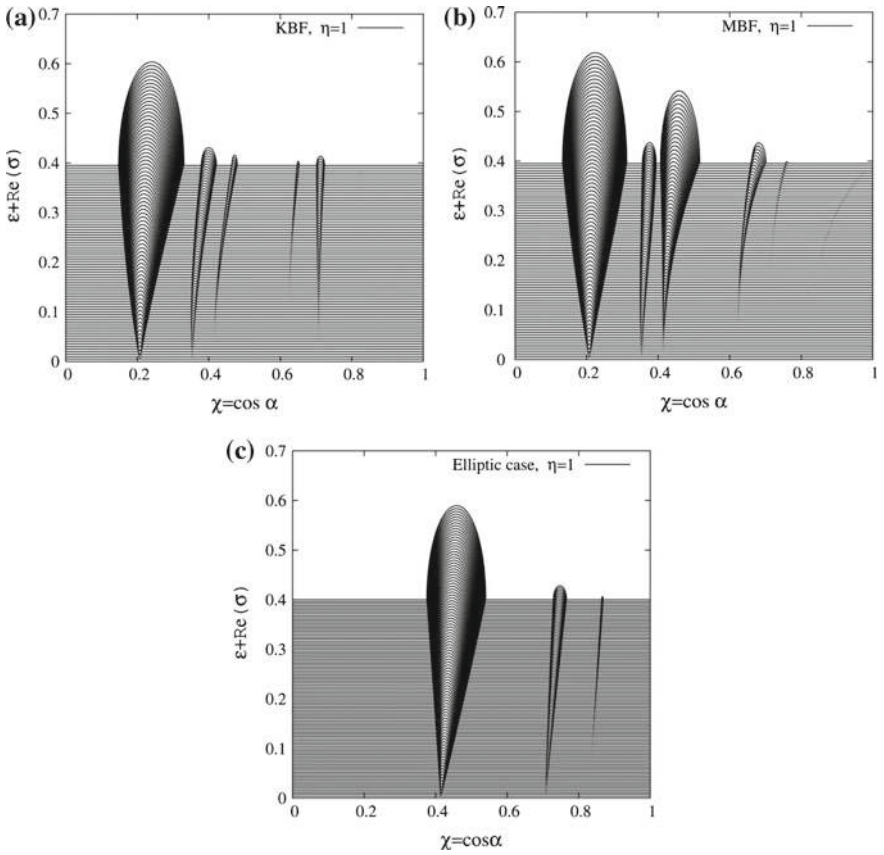

Fig. 12.10 Magnetized precessing flows. Variation of the growth rate (rescaled Floquet's parameter) in terms of the angular parameter $\chi = \cos\alpha$, for $0 \leq \epsilon \leq 0.4$ and $\eta = 1$ (from Eq. (12.78.) **a** The KBF case, **b** the MBF case, **c** a case with geometric ellipticity (hydrodynamic resonance only.) Reproduced from Salhi et al. (2010) with permission of APS

12.8 Homogeneous Incompressible MHD Turbulence and Beyond

Even in the case of purely incompressible and homogeneous MHD, work remains to be done, especially for a better quantitative dynamical and statistical approach to two-point anisotropy (from which the single-point anisotropy is implied). This study exists for the very special case of quasi-static MHD, but this case is closer to hydrodynamics, with additional anisotropic forcing (from Ohmic origin), than to actual MHD. On the one hand, there are several studies on both anisotropy and internal intermittency, but they often rely on visualization of snapshots, and therefore are not really quantified

with reliable statistical tools. Discarding internal intermitency,[1] that is very difficult to integrate in this book, as discussed in Chaps. 1, 4 and 18, and very incidentally otherwise, the anisotropic substructure of MHD can be advocated as follows.

Spectral anisotropy generates a distribution of excitation in wave vector space such that perpendicular wave vectors have more energy in average than parallel wave vectors. This is sometime summarized by $k_\perp > k_\parallel$ in a very abridged way, the dominant direction being the one of a large scale *local* magnetic field, even in the absence of an external one, denoted $\boldsymbol{B}_0$ here. it is expected that the degree of anisotropy becomes greater at smaller scales, so, for example, the anisotropy of $\boldsymbol{j} = \boldsymbol{\nabla} \times \boldsymbol{b}$ exceeds that of $\boldsymbol{b}$.

Another type of anisotropy that arises in plasma turbulence at MHD scales is polarization anisotropy. In this case one finds that mean square value of each component of the fluctuations perpendicular to the (dominant, large-scale) magnetic field is larger than the mean square parallel component. This condition naturally occurs, e.g., in Reduced MHD treatment around Eq. (12.51).

On the other hand, present quantitative prediction of statistical theory is very limited, in spite of the high potential of QNM closure, possibly extended towards generalized EDQNM. With respect to asymptotic (AQNM) wave turbulence theory in the purely rotating "hydro" case, no result is given about directional anisotropy in "weak" MHD, and only a strongly polarized cascade is suggested around Eq. (12.67). Older EDQNM studies in MHD were carried out in the isotropic, or "isotropized" case only, excluding again the too peculiar case of QS-MHD. It is strongly suggested to write rigorous equations for the two-point state vector with ten components in Eq. (12.24), as a system of Lin equations with given cubic contributions, as done in Eqs. (12.53) and (12.54) for two energy spectra only. Closure of these cubic contributions by generalized EDQNM is possible in principle. Solution of such equations, without $\boldsymbol{B}_0$ (or with very weak one if needed for breaking initial isotropy), could be made for axisymmetry, really breaking isotropy scale-by-scale, towards the smallest ones. This strategy is ambitious, and offers new perspectives, not expected from our previous "success stories" in rotating, stably-stratified, and unstably-stratified, turbulence. The new fact is that the Lorentz force is basically quadratic, as is its counterpart (e.g. yielding the opposite cubic contribution in the spectrum of $\overline{\frac{\partial u_i}{\partial x_j} b_i b_j}$) in the induction equation. In turn, the Coriolis force is linear in purely rotating turbulence, even if anisotropic dynamics (breakdown of 3D isotropy) are relevant only at the level of third-order correlations, in the absence of "production".

We do not survey other important effects, as magnetic reconnection, formation of strong current sheets, because our mold of "homogeneous anisotropic turbulence" addresses only a part of the problem. Some of mechanisms discussed in this Chapter, as various wave effects, play an important role in the dynamo theory, with all effects being present in the Earth's core (see Roberts and Soward 1972 for a survey.) The dynamo effect, however, as the spontaneous breaking of mirror symmetry discussed in the next section, may involve explicit boundaries conditions, so that we prefer not

[1] The reader is referred to books by Biskamp (2003) and Galtier (2013) for conventional approach to internal intermittency in both general "hydro" turbulence and MHD turbulence.

to discuss it more in this book. For instance, interpretation of the results of a recent VKS (Von Kármán Sodium) experimental approach (Monchaux et al. 2007) is not completely clarified, as resulting from a fluid dynamo action or from a *fluid-structure* dynamo action.

12.8.1 More About Helicities, Particularly the So-Called Cross-Helicity

As in rotating turbulence, the role of helicity is expected to be very important. In Sect. 7.8.2, however, it is discussed how kinematic helicity, that is seen everywhere in snapshots, patches or clouds from numerical simulations, cannot yield significant statistical covariance $\langle \boldsymbol{\omega}' \cdot \boldsymbol{u}' \rangle$, with its two-point, or spectral, counterpart $\mathcal{H}(\boldsymbol{k}, t)$, if statistical homogeneity is strictly fulfilled in anisotropic hydrodynamic turbulence (of course in the absence of artificial initialization or, stochastic or deterministic, forcing). Even more, breakdown of mirror symmetry and related net production of helicity covariance needs a wall effect, as illustrated by the role of Ekman layers in rotating turbulence. The situation is different in MHD, particularly for the so-called cross-helicity. In fact, chirality or breaking of mirror symmetry is less subtle for the rise of cross-helicity. Net creation of cross-helicity spectrum can be obtained in purely homogeneous MHD, probably with additional body forces, as suggested by Favier et al. (2011a) in close connection with alignment properties of $\boldsymbol{u}$ and $\boldsymbol{b}$. In the study by Pieri et al. (2014), the purely hydrodynamic case of baroclinic instability, presented in Chap. 11, was revisited to investigate a statistical quantity very close to MHD cross-helicity: Following Gibbon and Holm (2010), an analog of the magnetic field is defined as the cross product between the potential vorticity gradient and the buoyancy gradient. The resulting vector $\mathcal{B}$ is solenoidal and is shown to obey a stretching equation similar to the vorticity equation. Using this cross-helicity $\langle \boldsymbol{u} \cdot \mathcal{B} \rangle$, high-resolution DNS by Pieri et al. (2014) provides a detailed analysis of related pdf. A net preference for positive cross-helicity is shown to be related to a new alignment mechanism.

On the other hand, the very accurate calculation of kinematic helicity exhibits no net creation. This result invalidates the expectation of such a creation in rotating stratified flows, e.g. by Marino et al. (2013b).

12.8.2 Incorporating Acoustics, Then Large Variations in Density

Compressibility is a last effect to be discussed. In line with various dispersion laws in spectral linear analysis investigated in this chapter, there are several solutions with both "fast" and "slow" frequencies, even in the purely incompressible case

or within the quasi-incompressible case consistent with Boussinesq approximation (the velocity remains divergence-free, but the buoyancy can fluctuate). This is the case when the solution for σ^2 is obtained from a second-order algebraic equation, as $\sigma^2_\pm = S \pm \sqrt{S^2 - P^2}$, in which $\pm = +1$ and $\pm = -1$ give "fast" and "slow" frequency, respectively (see Eqs. (12.69), similarly for MAC waves, and (12.75).)

A new useful instance is given by the magnetosonic modes, as nicely introduced, e.g. by Cho and Lazarian (2005). If weak compressibility is accounted for, permitting propagation of acoustic waves in the "hydro" case, the nature of MHD waves is much more complicated. This is because we need to consider three restoring forces: Magnetic tension, magnetic pressure, and gas pressure. For Alfvén waves, magnetic tension is the sole restoring force. For slow and fast *magneto-sonic* waves, all three restoring forces are important. For slow modes, magnetic and gas pressure are out of phase, and, for fast modes, they are in phase. Another dispersion frequency is found again as

$$\sigma^2_{f,s} = S \pm \sqrt{S^2 - P^2},$$

with

$$S = \frac{1}{2}\left(\frac{k^2}{k^2_\parallel}\sigma^2_a + \sigma^2_{ac}\right)$$

and

$$P = \sigma^2_a \sigma^2_{ac},$$

in which the new ingredient is the dispersion frequency of acoustic waves $\sigma^2_{ac} = k^2 c^2$, with c the sonic speed.

Perhaps few words can be said about the anelastic approximation, in the context of MHD for astrophysics and heliophysics. Simple equations and numerical schemes to solve them are given by Lantz and Fan (1999), together with a useful survey (see references therein.) This approximation suppresses, or filters, the acoustic modes, briefly mentioned above. In counterpart, it permits larger simulated time steps to be taken than would be possible in a fully compressible model. Basically, the momentum $\rho \boldsymbol{u}$ is treated as solenoidal (divergencefree), instead of the velocity in the Boussinesq approximation, but the relevance of extended applications depend on what is the ρ, "density", variable in this anelastic approximation. In some cases, ρ can vary other several order of magnitudes, that is useful in solar and stellar convection zones, with no counterpart with the "weak" density variation permitted by the Boussinesq approximation. Variation with depth of the background density is essential in such convection zones. Thus, a nontrivial depth stratification may be incorporated into one's model without resorting to full compressibility. Magnetic nonlinearities may also be incorporated in this model in a straightforward way, provided that the local Alfvén speed is small compared to the speed of sound. Other models of convection, and very different applications, such as to the convection in the Earth's liquid core, are possible (of course at very large scale, strict incompressibility being fulfilled otherwise.)

References

Balbus, S.A., Hawley, J.F.: A powerful local shear instability in weakly magnetized discs. Astrophys. J. **376**, 214–233 (1991)

Bellet, F., Godeferd, F.S., Scott, J.F., Cambon, C.: Wave-turbulence in rapidly rotating flows. J. Fluid Mech. **562**, 83–121 (2006)

Biskamp, D.: Magnetohydrodynamic Turbulence. CUP, Cambridge (2003)

Cambon, C.: Homogeneous MHD turbulence at weak magnetic Reynolds numbers: Approach to angular-dependent spectra. In: Branover, H., Unger, Y. (eds.) in Advances in Turbulence Studies, Progresses in Astronautics and Aeronautics, vol. 149, pp. 131–145, AIAA, Washington, DC (1991). ISBN 1-56347-018-7

Cambon, C., Jacquin, L.: Spectral approach to non-isotropic turbulence subjected to rotation. J. Fluid Mech. **202**, 295–317 (1989)

Cambon, C., Mansour, N.N., Godeferd, F.S.: Energy transfer in rotating turbulence. J. Fluid Mech. **337**, 303–332 (1997)

Cambon, C., Godeferd, F.S., Favier, B. Incorporating linear dynamics and strong anisotropy in KS. Application to diffusion in rotating, stratified, MHD turbulence and to aeroacoustics. In: New Approaches In Modeling Multiphase Flows And Dispersion In Turbulence, Fractal Methods And Synthetic Turbulence, ERCOFTAC Series 18, Springer, New York (2012)

Capéran, P., Alemany, A.: Tuurbulence homogène MHD à faible nombre de Reynolds magnétique : étude de la transition à la phase bidimensionnelle et caractérisation de son anisotropie (in French). J. Méca. Théor. Appl. **4**(2), 175–200 (1985)

Cho, J., Lazarian, A.: Generation of compressible modes in MHD turbulence. Theor. Comput. Fluid Dyn. **19**(2), 127–157 (2005)

Elsaesser, W.M. The hydromagnetic equations. Phys. Rev. E. **79**, 183 (1950)

Favier, B.F.N., Godeferd, F.S., Cambon, C., Delache, A., Bos, W.: Quasi-static magnetohydrodynamic turbulence at high Reynolds number. J. Fluid Mech. **681**, 434–461 (2011a)

Favier, B.F.N., Godeferd, F.S., Cambon, C.: On the effect of rotation on magnetohydrodynamic turbulence at high magnetic Reynolds number. Geophys. Astrophys. Fluid Dyn. **106**, 89–111 (2011b)

Gallet, B., Doering, C.R.: Exact two-dimensionalization of low-magnetic-Reynolds-number flows subject to a strong magnetic field. J. Fluid Mech. **773**, 154–177 (2015)

Galtier, S. *Magnéto-hydrodynamique*. Vuibert (2013)

Galtier, S., Nazarenko, S., Newell, A.C., Pouquet, A.: A weak turbulence theory for incompressible MHD. J. Plasma Phys. **63**, 447–488 (2000)

Gibbon, J.D., Holm, D.D.: The dynamics of the gradient of potential vorticity. J. Phys. A **43**, 172001 (2010)

Grappin, R., Frisch, U., Léorat, J., Pouquet, A.: Alfvénic fluctuations as asymptotic states of MHD turbulence. Astron. Astrophys. **105**, 6–14 (1982)

Grappin, R., Pouquet, A., Léorat, J.: Dependence of MHD turbulence spectra on the velocity-magnetic fluid correlation. Astron. Astrophys. **126**, 51–58 (1983)

Iroshnikov, P.S. Turbulence in a conducting fluid in a strong magnetic field. Sov. Astron. **7**, 566 (1964)

Kadomtsev, B.B., Pogutse, O.P.: Nonlinear helical perturbations of a plasma in a tokamak. Sov. J. Plasma Phys. **I**, 389–391 (1974)

Kassinos, S.C., Reynolds, W.C., Rogers, M.M.: One-point turbulence structure tensors. J. Fluid Mech. **428**, 213–248 (2001)

Kiyani, K.H., Osman, K.T., Chapman, S.C.: Dissipation and heating in solar wind turbulence: from the macro to the micro and back again. Trans. R. Soc. A, Phil (2016). https://doi.org/10.1098/rsta.2014.0155

Kraichnan, R.H. Inertial-range spectrum for hydromagnetic turbulence. Phys. Fluid. **8**, 1385 (1965)

Lantz, S.R., Fan, I.: Anelastic MHD equations for modeling solar and stellar convection zones. Astrophys. J. Suppl. **121**, 247–264 (1999)

Lehnert, B.: Magneto-hydrodynamic waves under the action of the Coriolis force. Astrophys. J. **119**, 647 (1954)
Lehnert, B.: The decay of magneto-turbulence in the presence of a magnetic field and Coriolis force. Quart. Appl. Math. **4**, 321–341 (1955)
Lessines, T., Plunian, F., Carati, D.: Helical shell models for MHD. Theor. Comput. Fluid Dyn. **23**, 439–450 (2009)
Marino, R., Mininni, P.D., Rosenberg, D., Pouquet, A.: Spontaneous emergence of helicity in rotating stratified turbulence. Phys. Rev. E **87**, 033016 (2013)
Matthaeus, W.H., Goldstein, M.L.: Evaluation of magnetic helicity in homogeneous turbulence. Phys. Rev. Lett. **48**(18), 1256–1259 (1982)
Miesch, M., et al.: LES of magnetohydrodynamic turbulence in heliophysics and astrophysics. Space Sci. Rev. (2015). https://doi.org/10.1007/s11214-015-0190-7
Moffatt, H.K.: On the suppression of turbulence by a uniform magnetic field. J. Fluid Mech. **28**, 572–592 (1967)
Moffatt, H.K.: Dynamo action associated with random inertial waves in a rotating conducting fluid. J. Fluid Mech. **44**, 705–719 (1970)
Monchaux, R., Berhanu, M., Bourgoin, M., Moulin, M., Odier, P., Pinton, J.-F., Volk, R., Fauve, S., Mordant, N., Petrelis, F., Chiffaudel, A., Daviaud, F., Dubrulle, B., Gasquet, C., Marié, L., Ravelet, F.: Generation of a magnetic field by dynamo action in a turbulent flow of liquid sodium. Phys. Rev. Lett. **98**(4), 044502 (2007)
Moreau, R. On Magnetohydrodynamic turbulence. In: Proceedings of the Symposium on Fluids and Plasmas, pp. 359–372. Polytechnic Institute of Brooklyn, NY, 16–18 April 1968
Oughton, S., Raedler, K.H., Matthaeus, W.H. Phys. Rev. E. **56**(3), 2875 (1997)
Pieri, A.B., Godeferd, F.S., Cambon, C., Dubrulle, B., Thalabard, S.: Cross-helicity in rotating homogeneous shear-stratified turbulence. Phys. Rev. Lett. **112**, 114501 (2014)
Politano, H., Pouquet, A.: von Kármán-Howarth equation for MHD and its consequences on third-order longitudinal structure and correlation functions. Phys. Rev. E **57**, 21–24 (1998)
Pouquet, A., Frisch, U., Léorat, J.: Strong MHD helical turbulence and the nonlinear dynamo effect. J. Fluid Mech. **77**, 321–354 (1976)
Roberts, P.H., Soward, A.M. Magnetohydrodynamics of the Earth's core. Annu. Rev. Fluid Mech. **4**, 117 (1972)
Ruediger, G., Gellert, M., Schultz, Hollerbach, M., Stefani, F.: Astrophysical and experimental implications from the magnetorotational instability in toroidal fields. Mon. Not. R. Astron. Soc. **438**, 271–277 (2014)
Salhi, A., Lehner, T., Godeferd, F.S., Cambon, C.: Magnetized stratified rotating shear waves. Phys. Rev. E **85**, 026301 (2012)
Salhi, A., Lehner, T., Cambon, C.: MHD instabilities in rotating and precessing sheared flows: An asymptotic analysis. Phys. Rev. E **82**, 016315 (2010)
Schmitt, D., Alboussière, T., Brito, D., Cardin, P., Gagnière, N., Jault, D., Nataf, H.C.: Rotating spherical Couette flow in a dipolar magnetic field: experimental study of magneto-inertial waves. J. Fluid Mech. **604**, 157–197 (2008)
Stefani, F., Gundrum, T., Gerbeth, G., Ruediger, G., Schultz, M., Szklarski, J., Hollerbach, R.: Experimental evidence for magnetorotational instability in a Taylor-Couette flow under the influence of a helical magnetic field. Phys. Rev. Lett. **97**, 184502 (2006)
Waleffe, F.: The nature of triad interactions in homogeneous turbulence. Phys. Fluids, A **4**, 350–363 (1992)

Chapter 13
Compressible Homogeneous Isotropic Turbulence

13.1 Different Régimes in Compressible Turbulence

Numerical experiments and theoretical analyses show that several dynamical régimes exist in isotropic compressible turbulence, even in the free decay case where no external forcing is present. This is a noticeable difference with incompressible decaying turbulence which exhibits a single behavior. A major difficulty is that these régimes are very sensitive to a large number of parameters, such as the turbulent Mach number[1] and the initial conditions (i.e. the relative energy of each mode in the Kovasznay or Helmholtz decomposition). That can be intuitively understood looking at the nonlinear Kovasnay analysis (see Sect. 3.2), which reveals that each physical mode has a very specific dynamics: changing the initial condition might therefore have a strong influence on the development of the flow.

Four main régimes have been identified, according to the influence of compressibility effects on the turbulence dynamics[2]:

- The *low-Mach number quasi-isentropic régime*, in which the turbulent Mach number is low and the interactions between the solenoidal and dilatational components are weak. Moreover, the dilatational component is assumed to obey a quasi-linear acoustic dynamics. A vast majority of available studies are devoted to the case where the dilatational mode is restricted to the acoustic mode. Two kinds of theories will be emphasized below: a purely linear one, which basically predicts that *acoustic equilibrium* holds at all scales, and a more powerful nonlinear one, which shows that *acoustics equilibrium* is restricted to very small wavenumbers only,

[1] Let us recall that the turbulent Mach number is defined as $M_t = \sqrt{\mathcal{K}}/a_0$.

[2] A very low-Mach number régime of compressed — but not really compressible — turbulence, is discussed in Chap. 14. Despite isotropy is assumed for this flow, it is more convenient to include the corresponding discussion in the next chapter, since the isotropic fluctuating flow is subjected to an external mechanism of mean spherical compression-dilatation. This case is revisited as well in Chap. 17.

P. Sagaut and C. Cambon, *Homogeneous Turbulence Dynamics*,
https://doi.org/10.1007/978-3-319-73162-9_13

while another régime, referred to as *pseudo-sound*, is observed at large wavenumbers. This régime is usually observed for $M_t \leq 0.1$, where $M_t = \sqrt{\mathcal{K}}/a_0$ is the turbulent Mach number, if initial conditions and/or external forcing terms are solenoidal.

- The *low-Mach number thermal régime*, which includes thermal effects which are not governed by acoustic phenomena. The base flow is assumed to be solenoidal. The incompressible Navier–Stokes equations for the momentum are supplemented by an energy equation without feedback on the velocity field. Several forms of the energy equations are identified, according to the nature of the heat source.
- The *nonlinear subsonic régime*, in which the turbulent Mach M_t number is still less than one, but the fluctuations of the dilatational mode are strong enough to make non-linear phenomena arising. Two cases are classically identified. In the first case, dilatational effects are weak and have a negligible influence on the global dynamics, which is similar to those of low-Mach number régimes. In the second case, dilatational effects are stronger and play a significant role since some turbulence-induced very small shocks (referred to as *shocklets* or *eddy-shocklets*) are detected. An exact threshold Mach number doesn't seems to exist, since freely decaying and forced compressible turbulence may exhibit different features depending on initial conditions and forcing term. In the case of a statistically steady solenoidal forcing, Jagannathan and Donzis (2016) observed that dilatational effects remain very weak for $M_t \leq 0.3$ and exhibit a very rapid growth at higher M_t. A commonly reported threshold value for the occurrence of shocklets is $M_t = 0.3 - 0.4$.
- The *supersonic régime*, in which the turbulent Mach number is larger than one. In this case, the dilatational mode is of great importance and shocklets have a large impact on the full field. It is important noting that flows with large shock waves may be obtained in theoretically subsonic conditions if a dilatational forcing term is used, e.g. Wang et al. (2013).

13.2 Quasi-isentropic Turbulent Régime

13.2.1 Quasi-isentropic Isotropic Turbulence: Physical and Spectral Descriptions

A simplified model is obtained assuming that turbulent fluctuations are isentropic. The resulting model is widely used to analyze the properties of compressible turbulence in the compressible régime in the absence of significant thermal effects. The associated set of governing equations is

$$\frac{\partial u'_i}{\partial t} + \frac{1}{\bar{\rho}}\frac{\partial p'}{\partial x_i} - \nu\frac{\partial u'_i}{\partial x_k \partial x_k} - \frac{\nu}{3}\frac{\partial}{\partial x_i}\left(\frac{\partial u'_k}{\partial x_k}\right) = -u'_j\frac{\partial u'_i}{\partial x_j} \tag{13.1}$$

$$\frac{\partial}{\partial t}\left(\frac{p'}{\gamma P}\right) + \frac{\partial u'_i}{\partial x_i} = -u'_j\frac{\partial}{\partial x_j}\left(\frac{p'}{\gamma P}\right) \tag{13.2}$$

in which all nonlinear terms have been put on the right hand side, and where

$$\frac{p'}{\gamma P} = \frac{p'}{\bar{\rho} a_0^2} \quad \text{with} \quad a_0^2 = \gamma \frac{P}{\bar{\rho}}, \tag{13.3}$$

in which P and $\bar{\rho}$, which can possibly be time-dependent variables (see Chap. 14), are chosen constant together with the speed of sound in this section. More general quasi-isentropic equations can be derived, as discussed in Chap. 14, but additional assumptions are very useful, such as the low-Mach number assumption, which leads to $\gamma p/P \ll 1$ and the possible removal of the nonlinear term in the last equation for the pressure p.

Viscous terms may be omitted, in agreement with the isentropic assumption, but they have been kept here since they are used in some closure approaches and/or for numerical convenience (hence, the term quasi-isentropic used for this subsection). The second viscous term which involve the divergence of the velocity is consistent with Eq. (2.15) supplemented with the Stokes law $3\lambda + 2\mu = 0$, as well as with Eq. (3.2). Let us also note that the role of viscosity in Kovasznay mode coupling, which has already been introduced in Sect. 3.2.2, will be rediscussed in a simpler way below.

The problem can be recast in a much simpler and useful way using the local Craya basis in the Fourier space.[3] The solenoidal and dilatational part of the velocity field, denoted $\hat{\boldsymbol{u}}_s$ and $\hat{\boldsymbol{u}}_d$, can be decomposed as follows

$$\hat{\boldsymbol{u}}_s(\boldsymbol{k}) = u^{(1)}(k)\boldsymbol{e}^{(1)}(\boldsymbol{k}) + u^{(2)}(k)\boldsymbol{e}^{(2)}(\boldsymbol{k}), \hat{\boldsymbol{u}}_d(\boldsymbol{k}) = u^{(3)}(k)\boldsymbol{e}^{(3)}(\boldsymbol{k}), \tag{13.4}$$

where $\boldsymbol{e}^{(i)}(\boldsymbol{k}), i = 1, 3$ are defined as in the incompressible case (see Eq. (2.86)). Their counterparts in terms of vorticity ($\boldsymbol{\omega}' = \text{curl}(\boldsymbol{u}') = \text{curl}(\boldsymbol{u}_s)$) and divergence ($d = \boldsymbol{\nabla}\cdot\boldsymbol{u} = \boldsymbol{\nabla}\cdot\boldsymbol{u}_d$) are immediately found

$$\widehat{\omega'} = \imath k \left(u^{(2)}\boldsymbol{e}^{(1)} - u^{(1)}\boldsymbol{e}^{(2)}\right) \quad \text{and} \quad \widehat{d} = \imath k u^{(3)}. \tag{13.5}$$

The definition of vorticity in terms of the Craya modes is the same as the one used in the incompressible case. These three velocity modes must be supplemented by a fourth mode, which accounts for the remaining independent thermodynamic quantity.[4] In order to have a problem with homogeneous dimension, the pressure fluctuation can be scaled as a velocity, and considered as a fourth component (Simone et al. 1997):

[3] This projection onto the local reference frame is valid without any assumption dealing with statistical symmetries, such as isotropy. Isotropy allows us to use the projectors $P_{ij}^{\perp}$ and $P_{ij}^{\parallel}$, instead of, or in addition to the Craya–Herring modes, as extensively discussed in Sect. 2.5.2. This is true only because of the equipartition in terms of poloidal and toroidal modes which is imposed by 3D isotropy.

[4] A single additional degree of freedom is enough thanks to the isentropy assumption.

$$u^{(4)} = \imath \frac{\hat{p}}{\bar{\rho} a_0}. \tag{13.6}$$

This scaling is similar to the one used in Eckhoff and Storesletten (1978).

Therefore, the governing equations (13.1) and (13.2) are rewritten in terms of the four variables in the Fourier space as follows:

$$\frac{d}{dt}\begin{pmatrix} u^{(1)} \\ u^{(2)} \\ u^{(3)} \\ u^{(4)} \end{pmatrix} + \begin{pmatrix} \nu k^2 & 0 & 0 & 0 \\ 0 & \nu k^2 & 0 & 0 \\ 0 & 0 & \frac{4}{3}\nu k^2 & -a_0 k \\ 0 & 0 & a_0 k & 0 \end{pmatrix} \begin{pmatrix} u^{(1)} \\ u^{(2)} \\ u^{(3)} \\ u^{(4)} \end{pmatrix} = \begin{pmatrix} T_{NL}^{(1)} \\ T_{NL}^{(2)} \\ T_{NL}^{(3)} \\ T_{NL}^{(4)} \end{pmatrix}, \tag{13.7}$$

where all linear terms have been grouped in the left hand side. The non linear terms are defined as follows:

$$\begin{pmatrix} T_{NL}^{(1)} \\ T_{NL}^{(2)} \\ T_{NL}^{(3)} \\ T_{NL}^{(4)} \end{pmatrix} = \begin{pmatrix} -\boldsymbol{e}^{(1)} \cdot \left(\widehat{\boldsymbol{\omega}' \times \boldsymbol{u}'} \right) \\ -\boldsymbol{e}^{(2)} \cdot \left(\widehat{\boldsymbol{\omega}' \times \boldsymbol{u}'} \right) \\ -\boldsymbol{e}^{(3)} \cdot \widehat{\boldsymbol{\omega}' \times \boldsymbol{u}'} - \frac{1}{2}\imath k \widehat{u'_j u'_j} \\ \imath u_j \widehat{\frac{\partial (p'/(\bar{\rho} a_0))}{\partial x_j}} \end{pmatrix}, \tag{13.8}$$

where the *hat* symbol denotes the Fourier transform, and $\boldsymbol{\omega}' = \mathrm{curl}(\boldsymbol{u}') = \mathrm{curl}(\boldsymbol{u}_s)$. A more advanced closed form of the nonlinear terms of Eq. (13.7) in terms of $u^{(1)}, u^{(2)}, u^{(3)}$ and $u^{(4)}$ is obtained by injecting (13.4) and (13.5) into Eq. (13.8) (Briard et al. 2017).

It is worth noting that since a simplified isentropic model is used, the computed solenoidal and dilatational fields are not identical to those obtained by projecting the solution of the full compressible Navier–Stokes equations. In the present simplified model, only Kovasznay's vortical and acoustic modes (characterized by $(u^{(1)}, u^{(2)})$ and $(u^{(3)}, u^{(4)})$, respectively) are retained, while the entropic mode is (almost) discarded.[5]

Two-point statistical moments are now considered. Because of 3D isotropy, two-point second order statistics are generated by three independent spectra, namely the spectrum of the solenoidal kinetic energy $E_{ss}(k)$, the kinetic energy spectrum of the dilatational component $E_{dd}(k)$ and the pressure spectrum $E_{pp}(k)$

$$< u^{(1)*}(\boldsymbol{p}, t) u^{(1)}(\boldsymbol{k}, t) > = < u^{(2)*}(\boldsymbol{p}, t) u^{(2)}(\boldsymbol{k}, t) > = \frac{E_{ss}(k, t)}{8\pi k^2} \delta^3(\boldsymbol{k} - \boldsymbol{p}), \tag{13.9}$$

$$< u^{(3)*}(\boldsymbol{p}, t) u^{(3)}(\boldsymbol{k}, t) > = \frac{E_{dd}(k, t)}{4\pi k^2} \delta^3(\boldsymbol{k} - \boldsymbol{p}), \tag{13.10}$$

[5] As stressed by Rainer Friedrich, private communication, the related model is not strictly isentropic, because it includes dissipation with $\nu \neq 0$, rather for the sake of further numerical solution. From this viewpoint, a first-order "entropic" Kovasznay's mode is implied.

$$< u^{(4)*}(\boldsymbol{p},t)u^{(4)}(\boldsymbol{k},t) >= \frac{E_{pp}(k,t)}{4\pi k^2}\delta^3(\boldsymbol{k}-\boldsymbol{p}), \tag{13.11}$$

and the cross-spectrum

$$< u^{(3)*}(\boldsymbol{p},t)u^{(4)}(\boldsymbol{k},t) >= \frac{E_{dp}(k,t)}{4\pi k^2}\delta^3(\boldsymbol{k}-\boldsymbol{p}), \tag{13.12}$$

whose imaginary part is neglected, consistently with 3D isotropy with mirror symmetry.

The pressure variance is recovered as follows:

$$\overline{p'p'}(t) = \rho_0^2 a_0^2 \int_0^{+\infty} E_{pp}(k,t)dk, \tag{13.13}$$

while the solenoidal and dilatational kinetic energies, $\mathcal{K}_s$ and $\mathcal{K}_d$, are computed thanks to relation (3.80).

The evolution equations associated to the four spectra are similar to the original Lin equation (4.38) derived in the incompressible case for the kinetic energy spectrum $E(k)$:

$$\frac{d}{dt}\begin{pmatrix} E_{ss} \\ E_{dd} \\ E_{dp} \\ E_{pp} \end{pmatrix} + \begin{pmatrix} 2\nu k^2 & 0 & 0 & 0 \\ 0 & 2\frac{4}{3}\nu k^2 & 2a_0 k & 0 \\ 0 & -a_0 k & \frac{4}{3}\nu k^2 & a_0 k \\ 0 & 0 & -2a_0 k & 0 \end{pmatrix} \begin{pmatrix} E_{ss} \\ E_{dd} \\ E_{dp} \\ E_{pp} \end{pmatrix} = \begin{pmatrix} T_{ss} \\ T_{dd} \\ T_{dp} \\ T_{pp} \end{pmatrix} \tag{13.14}$$

where nonlinear terms have been grouped in the right hand side. As for the cases of rotating and/or stratified turbulence, only the transfer terms related to true energy spectra may have zero integral, i.e. exhibit a global conservation property. This constraint is almost fulfilled at weak Mach number by T_{ss} (solenoidal energy transfer) and $T_{pp} + T_{dd}$ (transfer of total acoustic wave energy) but not by $T_{pp} - T_{dd}$ and T_{dp}, which therefore are not true transfer terms. The non-linear terms are related to the physical mechanisms mentioned in Table 3.2. Neglecting viscous terms, this system can be recast in the following compact form (see also rotating and/or stratified incompressible flow cases):

$$\frac{dE_{ss}(k)}{dt} = T_{ss}(k), \tag{13.15}$$

$$\frac{dE_w(k)}{dt} = T_w(k), \tag{13.16}$$

$$\frac{dZ(k)}{dt} + 2\imath(a_0 k)Z(k) = T_z(k), \tag{13.17}$$

in which

$$E_w(k) = E_{dd}(k) + E_{pp}(k) \tag{13.18}$$

is the *total turbulent acoustic energy spectrum*,[6] and

$$Z(k) = E_{dd}(k) - E_{pp}(k) + 2\imath E_{dp}(k) \tag{13.19}$$

characterizes the inbalance between kinetic and potential energy of waves.

13.2.2 Linear Theory

Theoretical developments for this régime are pivotal from our viewpoint since they all rely on all the basic exact equations of Sect. 13.2.1. Meaning of the term 'exact' must be taken here in the same sense as for exactness of Eq. (13.2). Pure linear theory allows us to recover the essentials of the acoustic equilibrium, which is possibly altered by laminar viscous terms. Regarding nonlinear theories, no less than three versions will be presented, giving very different results even if they rely on the same 'exact' Lin equations and use similar Quasi-Normal closures which have been improved for extra-dissipative terms.

The basic equations of the linear theory for compressible turbulence are obtained in a trivial way, dropping the right hand sides in Eqs. (13.7) and (13.14). It is observed that the solenoidal and the wavy components of the solution are totally decoupled, in agreement with the usual linear acoustic theory. The dilatational and the pressure modes are coupled through acoustic wave dynamics, which induce some exchanges between the dilatational kinetic energy and the turbulent potential energy.

Let us first consider the linear viscous régime. The solenoidal kinetic energy decays exactly as in the incompressible case (see Chap. 4), leading to

$$u^{(\alpha)}(k,t) = e^{-\nu k^2 t} u^{(\alpha)}(k,0), \alpha = 1,2 \quad E_{ss}(k,t) = e^{-2\nu k^2 t} E_{ss}(k,0) \tag{13.20}$$

---

[6] It is recalled (Chu and Apfel 1983) that the *acoustic energy density* is usually defined as

$$\rho_0 \frac{u'^2}{2} + \frac{p'^2}{2\rho_0 a_0^2}$$

in the framework of linear acoustics, where u' and p' denote acoustic velocity and pressure disturbances, respectively. *Acoustic potential energy density* and *acoustic intensity* are defined as

$$\frac{p'^2}{2\rho_0 a_0^2}$$

and

$$p'\boldsymbol{u}'$$

respectively.

The linear system related to acoustic waves simplifies as

$$\frac{d}{dt}\begin{pmatrix} u^{(3)} \\ u^{(4)} \end{pmatrix} + \begin{pmatrix} \frac{4}{3}\nu k^2 & -a_0 k \\ a_0 k & 0 \end{pmatrix}\begin{pmatrix} u^{(3)} \\ u^{(4)} \end{pmatrix} = 0, \tag{13.21}$$

whose solution is governed by the sign of the discriminant

$$D = [(2/3)\nu k^2]^2 - [a_0 k]^2.$$

A cut-off value $k_d = 3a_0/(2\nu)$ is therefore introduced: for $k < k_d$ (i.e. $D < 0$) the eigenvalues of the above linear system of equations are complex conjugates, yielding damped oscillating solutions, whereas only damping without oscillations is found for $k > k_d$ (i.e. $D > 0$) in relation with real eigenvalues. At low Mach number and large Reynolds number, the cutoff value k_d is very large,[7] so that the domain $k > k_d$ is irrelevant, but a renormalized version of this system can be useful, with drastic modification of k_d: this issue is discussed below.

The linear inviscid theory has received much more attention (e.g. Erlebacher et al. 1990; Sarkar et al. 1991; Erlebacher and Sarkar 1993), since it leads to the prediction of possible equilibrium states. It is handled in a very simple way (Cambon et al. 1993; Simone et al. 1997) using both the local Craya–Herring decomposition and the pressure rescaling given by Eq. (13.6)[8] Dropping all nonlinear and viscous terms, one can see that the solenoidal component is frozen, while the following conservation relations hold at all wavenumbers:

$$u^{(3)}(k,t) + s\imath u^{(4)}(k,t) = e^{\imath s a_0 k t}\left(u^{(3)}(k,0) + s\imath u^{(4)}(k,0)\right), s = \pm 1 \tag{13.22}$$

$$E_w(k,t) = E_{ss}(k,t) + E_{dd}(k,t) = E_{ss}(0,t) + E_{dd}(0,t) = E_w(k,0), \tag{13.23}$$

along with

$$\begin{aligned} E_{dd}(k,t) = {} & \frac{1}{2}E_w(k,0) + \frac{1}{2}(E_{dd}(k,0) - E_{pp}(k,0))\cos(2a_0 k t) \\ & - E_{dp}(k,0)\sin(2a_0 k t), \end{aligned} \tag{13.24}$$

$$\begin{aligned} E_{pp}(k,t) = {} & \frac{1}{2}E_w(k,0) - \frac{1}{2}(E_{dd}(k,0) - E_{pp}(k,0))\cos(2a_0 k t) \\ & + E_{dp}(k,0)\sin(2a_0 k t), \end{aligned} \tag{13.25}$$

[7] Considering air at common pressure and temperature, one has $a_0 \simeq 340\,\mathrm{m.s}^{-1}$ and $\nu \simeq 10^{-5}\,\mathrm{m}^2.\mathrm{s}^{-1}$, yielding $k_d \sim 5.10^7\,\mathrm{m}^{-1}$.

[8] It is worth noting that a large number of works dealing with the inviscid linear theory have been carried out in the physical space, using system (13.1) and (13.2). In this case, a multiple scale expansion is needed to operate the splitting between the solenoidal and the dilatational component, while it is trivial in the local spectral frame of reference. It can also yield a premature occurence of non-dimensional parameters and an artificial unnecessary complexification of the problem.

$$E_{dp}(k,t) = \frac{1}{2}(E_{dd}(k,0) - E_{pp}(k,0))\sin(2a_0kt) + E_{dp}(k,0)\cos(2a_0kt). \tag{13.26}$$

The *acoustic equilibrium state* is defined as an equilibrium state in which *the kinetic energy of the dilatational mode is equal to the potential energy of the pressure mode*. One has to distinguish between two variants of the acoustic equilibrium assumption.

The first one, referred here to as the *strong acoustic equilibrium hypothesis*, assumes that this equilibrium holds at all wave number, yielding

$$E_{dd}(k) = \frac{1}{\rho_0^2 a_0^2} E_{pp}(k) \quad \forall k \quad \text{(strong acoustic equilibrium hypothesis).} \tag{13.27}$$

The second variant, namely the *weak acoustic equilibrium hypothesis*, deals with the asymptotic values of global quantities, such as $\mathcal{K}_d(t)$ and $\overline{p'p'}(t)$ at large time. Using the analytical solutions given above, one has

$$\begin{aligned}\lim_{t\to+\infty} \mathcal{K}_d(t) &= \lim_{t\to+\infty} \int_0^{+\infty} E_{dd}(k,t)dk \\ &= \frac{1}{2}\int_0^{+\infty} E_w(k,0)dk = \frac{1}{2}\left(\mathcal{K}_d(0) + \frac{\overline{p'p'}(0)}{\rho^2 a_0^2}\right) \\ &= (\mathcal{K}_d)_\infty, \end{aligned} \tag{13.28}$$

$$\begin{aligned}\lim_{t\to+\infty} \overline{p'p'}(t) &= \rho_0^2 a_0^2 \lim_{t\to+\infty} \int_0^{+\infty} E_{pp}(k,t)dk \\ &= \frac{\rho_0^2 a_0^2}{2}\left(\mathcal{K}_d(0) + \frac{\overline{p'p'}(0)}{\rho^2 a_0^2}\right) = (\overline{p'p'})_\infty, \end{aligned} \tag{13.29}$$

along with

$$\lim_{t\to+\infty} \int_0^{+\infty} E_{dp}(k,t)dk = \lim_{t\to+\infty} \int_0^{+\infty} (E_{pp} - E_{dd})dk = 0. \tag{13.30}$$

The later relation is comes from the relation (13.19), which leads to

$$Z(k,t) = e^{\imath a_0 kt} Z(k,0), \quad \lim_{t\to+\infty} \int_0^{+\infty} Z(k,t)dk = 0. \tag{13.31}$$

This last result is seen to be a consequence of the *phase-mixing phenomenon*. Let us recall that phase-mixing was induced by an angle-dependent factor in the dispersion law for inertia and/or gravity waves, whereas it results from the presence of the factor k in the integrand in the present case.

An important conclusion is that, whatever initial condition is considered, the solution converges toward the following equilibrium state:

$$(\mathcal{K}_d)_\infty = \frac{1}{\rho_0^2 a_0^2}(\overline{p'p'})_\infty \quad \text{(weak acoustic equilibrium hypothesis).} \tag{13.32}$$

It is of course easily seen that strong acoustic equilibrium is a sufficient but not necessary condition for the weak acoustic equilibrium to be satisfied.

The weak acoustic equilibrium solutions can be represented in a very simple and elegant way using the ratio of the mean compressible kinetic energy to the total mean turbulent kinetic energy, $\chi(t)$, and the function $\mathcal{F}(t)$ introduced by Sarkar

$$\mathcal{F}(t) \equiv \rho_0^2 a_0^2 \frac{\mathcal{K}_d(t)}{\overline{p'p'}(t)} = \rho_0^2 a_0^4 M_t^2 \frac{\chi(t)}{\overline{p'p'}(t)}, \tag{13.33}$$

with $\mathcal{K} = \mathcal{K}_s + \mathcal{K}_d$, $M_t = \sqrt{\mathcal{K}}/a_0$ and

$$\chi(t) = \frac{\mathcal{K}_d(t)}{\mathcal{K}_s(t) + \mathcal{K}_d(t)} = \frac{\mathcal{K}_d(t)}{\mathcal{K}_s(0) + \mathcal{K}_d(t)}. \tag{13.34}$$

The equilibrium values can be rewritten as

$$(\overline{p'p'})_\infty = \frac{1}{2}\overline{p'p'}(0)\,(1 + \mathcal{F}(0))\,, \tag{13.35}$$

$$(\mathcal{K}_d)_\infty = \frac{1}{2}\mathcal{K}_d(0)\left(1 + \frac{1}{\mathcal{F}(0)}\right). \tag{13.36}$$

A very interesting result obtained inserting equilibrium values into (13.33) is that the acoustic equilibrium value of Sarkar's function, $\mathcal{F}_\infty$, is equal to unity:

$$\mathcal{F}_\infty = \lim_{t\to\infty} \mathcal{F}(t) = 1. \tag{13.37}$$

This result indicates that at acoustic equilibrium there is an equipartition between the kinetic (numerator of Eq. (13.33)) and the potential component (half the denominator of Eq. (13.33)) of the compressible energy. The relative weights of the incompressible and compressible parts of the kinetic energy are obtained evaluating the acoustic equilibrium value of the parameter χ

$$\chi_\infty = \chi(0)\frac{1 + \mathcal{F}(0)}{2\mathcal{F}(0) + \chi(0)(1 - \mathcal{F}(0))}. \tag{13.38}$$

Main features of the weak acoustic equilibrium state are illustrated in Figs. 13.1 and 13.2. It is clearly seen that a low value of $\mathcal{F}(0)$ yields a very rapid increase of the kinetic energy ratio in terms of $\chi(0)$, meaning that initial strong non-equilibrium

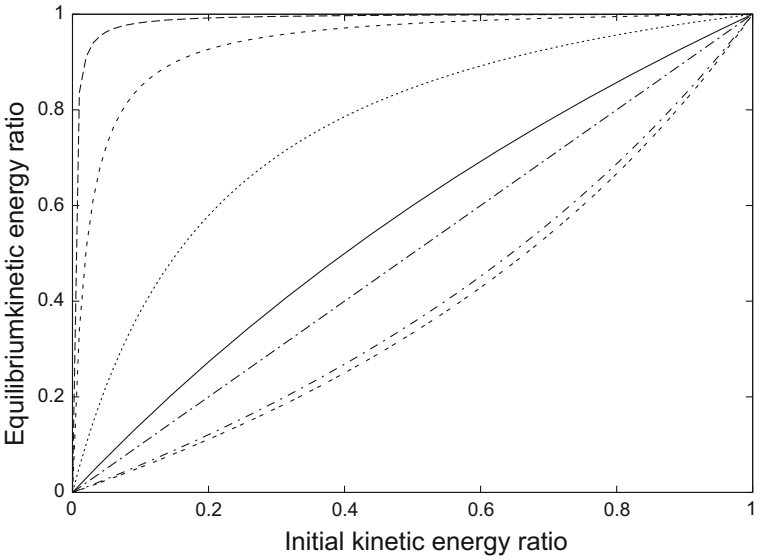

Fig. 13.1 Values of the equilibrium turbulent kinetic energy ratio χ_∞ as a function of $\chi(0)$ and $\mathcal{F}(0)$. Increasing values of $\mathcal{F}(0)$ correspond to decreasing values of χ_∞ at fixed $\chi(0)$. Lines plotted correspond to (from left to right) $\mathcal{F}(0) = 10^{-3}, 10^{-2}, 10^{-1}, 0.5, 1, 10, 10^5$

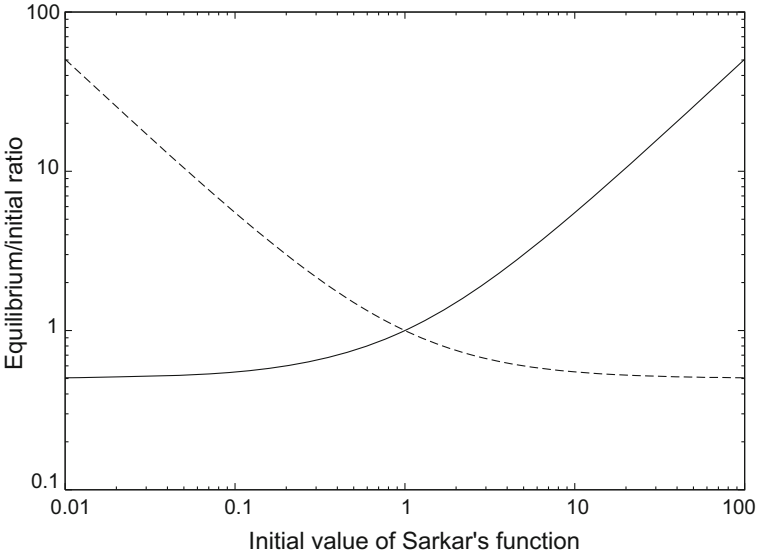

Fig. 13.2 Acoustic equilibrium value referred to the initial value as a function of $\mathcal{F}(0)$. Dashed line: dilatational velocity field; solid line: dilatational pressure

leads to very rapid changes in the solution for $\mathcal{F}(0) \ll 1$. This relaxation is also seen to yield a dramatic change in the repartition of the acoustic energy. An interesting conclusion is that the linear dynamics which corresponds to the pseudo-acoustic régime is compatible with very important changes in the dilatational field.

13.2.3 The Relevant Incompressible Limit for both Spectra of Solenoidal Energy and Pressure Variance

Before modelling the spectra and co-spectra related to dilatational and pressure components, definition of the incompressible reference is the first mandatory task.

At low Mach number, it is possible to neglect the feedback from dilatational and pressure modes in Eq. (13.15), so that the spectrum of the solenoidal mode, $E_{ss}(k)$, is given as in strictly incompressible turbulence. Therefore, a closed form for $T_{ss}(k)$ is obtained by classical isotropic incompressible EDQNM, and $E_{ss}(k)$ exhibits a classical Kolmogorov inertial range at high Reynolds number. This is consistent with a selection among all resonant triads, neglecting all resonant triads involving waves with respect to the pure solenoidal ones (more details are given Chap. 15). In a similar way, neglecting all triads involving at least one wave mode versus pure vortex interactions yields selecting the toroidal cascade in Chap. 10 and the Quasi-Geostrophic cascade in Chap. 11.

Calculation of spectrum of the pure incompressible part of the pressure fluctuation, denoted E_{pp}^{inc}, is performed starting from the Poisson equation and using a Quasi-Normal approximation as in Batchelor's approach.[9] As a result, the following robust model of $E_{pp}^{inc}(k)$ as a function of $E_{ss}(k)$ is obtained

$$E_{pp}^{inc}(k) = \frac{1}{\bar{\rho}^2 a_0^2} \cdot \frac{\bar{\rho}^2}{2} k \iint_{\Delta_k} (1-x^2)(1-y^2) E_{ss}(p) E_{ss}(q) \frac{dpdq}{pq}, \qquad (13.39)$$

using the same notations as for the isotropic incompressible EDQNM transfer term (see Sect. 4.8.7).

The first prefactor $1/(\bar{\rho}^2 a_0^2)$ originates in the pressure scaling (13.3) and can be omitted in order to interpret $E_{pp}^{inc}(k)$ as the spectrum of the pressure variance with its original dimension. Even if the integral above cannot be analytically solved in general, this equation is consistent with a pressure spectrum form at small k and the scaling $kE^2(k) \sim k^{-7/3}$, at larger k, for a Kolmogorov energy spectrum.

[9] The pressure variance is linked to fourth-order velocity correlations via the Poisson equation, and fourth-order correlations are factorized in term of products of second-order ones via Quasi-Normal approximation, see Sect. 4.9.

13.2.4 Quasi-inviscid Limit: Towards an Extended Wave-Turbulence Model

In the low-Mach number case, acoustic perturbations travel at a much higher speed than hydrodynamic fluctuations, and a two-time-scale problem can be defined. Associating the fast time scale to acoustic perturbations and the slow-time scale to hydrodynamic fluctuations, a Wave-turbulence-type problem is obtained, whose governing equations can be expressed in terms of the slow amplitudes $a_\alpha^{(0)}$, $\alpha = 1, 2$ and $a^{(s)}$ which are defined as

$$u^{(\alpha)} = a_\alpha^{(0)}(\boldsymbol{k}, t), \quad \alpha = 1, 2 \tag{13.40}$$

$$u^{(3)} + s u^{(4)} = e^{\imath s a_0 k t} a^{(s)}(\boldsymbol{k}, t), \quad s = \pm 1. \tag{13.41}$$

Here, $\boldsymbol{a}^{(0)}$ denotes the amplitude of the vortical non-propagating mode and $a^{(s)}$, $s = \pm 1$ are related to the amplitudes of wavy acoustic modes. General properties of the associated nonlinear system of equations are discussed in Chap. 17. Nonlinear terms, once expressed as functions of these new variables, still involve convolution products inherited from their quadratic nature. Exact inviscid equation can be written as

$$\dot{a}^{(s)} = \sum_{s'=0,\pm1, s''=0,\pm1} \iiint_{k+p+q=0} N_{ss's''}(\boldsymbol{k}, \boldsymbol{p}) e^{\imath a_0 t (sk + s'p + s''q)} a^{(s')*}(\boldsymbol{p}, t) a^{(s'')*}(\boldsymbol{q}, t) d^3\boldsymbol{p}, \tag{13.42}$$

up to some formal difficulties: since $\boldsymbol{a}^{(0)}$ is a two-component *vector*, the index s no longer refers to the solenoidal part in this particular section, and only the value $s = 0$ is related to the solenoidal mode. The influence matrix $N_{ss's''}$ is derived from (13.8) in a straightforward — but tedious — way. As in the similar cases of rotating (which does not involve any $s = 0$ mode), stratified (in which $s = 0$ would correspond to the toroidal+ VSHF mode) and rotating stratified (in which $s = 0$ would correspond to the QG mode), an interesting feature is that all products $a^{(s')*}(\boldsymbol{p}, t) a^{(s'')*}(\boldsymbol{q}, t)$ present in the convolution integral governing $a^{(s)}(\boldsymbol{k}, t)$ are weighted by the following resonance operator

$$\exp[\imath a_0 t (sk + s'p + s''q)], s, s', s'' = 0, \pm 1, \quad \boldsymbol{k} + \boldsymbol{p} + \boldsymbol{q} = 0. \tag{13.43}$$

Different interactions are only characterized by the set (s, s', s''):

- *pure vortex* (solenoidal here) triadic interactions associated with $(0, 0, 0)$,
- *pure wavy* triadic interactions corresponding to $(\pm 1, \pm 1, \pm 1)$,
- *mixed* triadic interactions with $(0, \pm 1, 0)$ or $(0, \pm 1, \pm 1)$. This last class is assumed to be very weak with respect to pure vortex interactions when modelling the nonlinear transfer term T_{ss}.

The generation of all transfer terms using asymptotic Quasi-Normal Markovian theory readily follows, but the absence of a relevant eddy damping term (with vanishing eddy viscosity) would generate an inertial range with a k^{-2} slope and not a $k^{-5/3}$ one for T_{ss}. The optimal compromise between 'strong' turbulence and 'weak' wave-turbulence theory, is to introduce an eddy damping correction in generating the typical Green's function (or Kraichnan's response function) as follows:

$$\frac{\partial}{\partial t}\begin{pmatrix} u^{(1)} \\ u^{(2)} \\ u^{(3)} \\ u^{(4)} \end{pmatrix} + \begin{pmatrix} \eta & 0 & 0 & 0 \\ 0 & \eta & 0 & 0 \\ 0 & 0 & \epsilon_{acous} & -a_0 k \\ 0 & 0 & a_0 k & \epsilon_{acous} \end{pmatrix} \begin{pmatrix} u^{(1)} \\ u^{(2)} \\ u^{(3)} \\ u^{(4)} \end{pmatrix} = \begin{pmatrix} X^{(1)} \\ X^{(2)} \\ X^{(3)} \\ X^{(4)} \end{pmatrix} \tag{13.44}$$

The arbitrary vector $(X^{(1)}, X^{(2)}, X^{(3)}, X^{(4)})^T$ can be replaced by a Dirac term (impulsional response) in the most general definition of the Green's function, but the same result (identifying the response function once for all) is most easily obtained from the general initial-value problem with $(X^{(1)}, X^{(2)}, X^{(3)}, X^{(4)})^T = (0, 0, 0, 0)^T$ (Cambon and Scott 1999). *It is very important to stress that the above system of equations is only used for generating the nonlinear Green's function, and only for solving corresponding equations for triple correlations needed in the integrands of* T_{dd}, T_{pp}, *and* T_{pp}, *or equivalently for* $T_{pp} + T_{dd}$ *and* $T^{(z)}$. The eddy-damping term η can be chosen as in Sect. 4.8.7, and ϵ_{acous} is a formal small parameter, only used for the sake of mathematical regularization of the resonance operator. Of course, the very high Reynolds number limit allows us to get rid of detail for the laminar viscous terms, which are displayed in the next section.

13.2.5 *Introducing Relevant Eddy-Damping. Main Results*

A first application of EDQNM procedure was performed by Marion coworkers (1998a, b), with some inaccuracies corrected by Bataille (1994), and new numerical results given in Bertoglio et al. (2001). This procedure follows the one proposed by Leslie (1973) and invokes Kraichnan's DIA theory as an intermediate step, using two-point spectral tensors of the form $\hat{\mathbf{R}}_{ij}(\boldsymbol{k}, t, t')$, before deriving EDQNM-type equations.[10] One can reinterpret the system generating the nonlinear response function as

$$\frac{d}{dt}\begin{pmatrix} u^{(1)} \\ u^{(2)} \\ u^{(3)} \\ u^{(4)} \end{pmatrix} + \begin{pmatrix} \eta & 0 & 0 & 0 \\ 0 & \eta & 0 & 0 \\ 0 & 0 & (4/3)\nu k^2 + \eta & -a_0 k \\ 0 & 0 & a_0 k & \eta \end{pmatrix} \begin{pmatrix} u^{(1)} \\ u^{(2)} \\ u^{(3)} \\ u^{(4)} \end{pmatrix} = \begin{pmatrix} X^{(1)} \\ X^{(2)} \\ X^{(3)} \\ X^{(4)} \end{pmatrix}. \tag{13.45}$$

[10] A direct procedure for solving linear operators at the level of triple correlations, however, would probably be more general and more convenient for mathematical analysis, like the one for deriving EDQNM1 to EDQNM3, the latter giving wave-turbulence in the limit of inviscid wave-propagator.

The choice of the eddy-damping term for the compressible nonlinear terms associated to $E_{dd}(k)$, $E_{pp}(k)$ and $E_{dp}(k)$ has a dramatic influence on the results. The choice of the same $\eta(k)$ for all modes amounts to introduce the very simple and unique decorrelation function as $e^{-\eta(t-t')}$. This procedure is not theoretically grounded and must therefore be considered as an empirical closure, since it relies on the direct use of a damping term built for solenoidal modes for the nonlinear interactions involving dilatational modes, which obey a very different physics.

Two main results are obtained: first, the acoustic equilibrium is recovered in a strong sense; second, a typical slope for the pressure spectrum is found, as $-7/2$ (Marion et al. 1998a), then $-11/3$ (Bataille 1994; Bertoglio et al. 2001), but in any case the Batchelor's one $-7/3$ is not recovered in the incompressible limit $M_t \to 0$. Another reported problem is that strong acoustic equilibrium, together with the high level of pressure spectrum in the inertial range yield overestimating the level of E_{dd}.

These results, considered at least as puzzling and somehow unphysical, motivated (Fauchet 1998; Fauchet and Bertoglio 1999a, b) for choosing a new decorrelation function. Mentioning some informal proposal made by Kraichnan, Fauchet and Bertoglio proposed to replace the usual eddy damping factor $-\eta(t-t')$ by $\eta^2(t-t')^2$ for the dilatational and pressure modes. This result can be recast in a more general way. Instead of renormalizing the pure dissipative laminar term, one may try to renormalize the dispersion frequency of acoustic waves, so that the relevant response function would be generated by

$$\frac{\partial}{\partial t}\begin{pmatrix} u^{(1)} \\ u^{(2)} \\ u^{(3)} \\ u^{(4)} \end{pmatrix} + \begin{pmatrix} \eta & 0 & 0 & 0 \\ 0 & \eta & 0 & 0 \\ 0 & 0 & (4/3)\nu k^2 + \epsilon_{acoust} & -a_0 k - r \\ 0 & 0 & a_0 k + r & \epsilon_{acoust} \end{pmatrix} \begin{pmatrix} u^{(1)} \\ u^{(2)} \\ u^{(3)} \\ u^{(4)} \end{pmatrix} = \begin{pmatrix} X^{(1)} \\ X^{(2)} \\ X^{(3)} \\ X^{(4)} \end{pmatrix}. \tag{13.46}$$

In other words, η is not used as an additional nonlinear dissipative effect for dilatational pressure and dilatational modes. It is replaced by a nonlinear correction $r(t)$ for the purely linear acoustic dispersion frequency $a_0 k$. The too simple choice $r \sim \eta$ is not correct, since the decorrelation effect cannot be obtained with a deterministic r, and only a modified resonance operator would be generated in Eq. (13.43), changing $a_0(t-t')$ into $(a_0 + r)(t-t')$. As a more subtle interpretation, r is really a random factor (hence our coining r for random), changing from a realization of $(u^{(3)}, u^{(4)})$ to another one. One must assume that r is a Gaussian process, having zero mean and variance η. A physical rationale for the existence of the random factor r is provided by the *random oscillator* in Sect. 13.2.6. A related scaling of the η term in a Gaussian response function is given by the *randomly swept wave model* discussed in Sect. 13.2.7, in which one assumes that acoustic waves experience random sweeping by large turbulent eddies. Therefore, their propagation speed is $a_0 \pm u'$, where u' is the turbulent velocity, leading to $r = ku'$.

Main results obtained using this improved model are the following (predictions related to the inertial range are gathered in Table 13.1, and a simplified analytical model will be exhaustively discussed in Sect. 13.2.8):

Table 13.1 Two-point closure prediction dealing with inertial range in the low-Mach number régime ($M_t < 0.1$). Left and right columns display results given by EDQNM and the improved Fauchet–Bertoglio model, respectively. $E^{acous}_{p'p'}(k)$ denotes the spectrum of the acoustic pressure fluctuation defined as $p' = p - p_s$, where p_s is the pressure field associated to the solenoidal velocity field $\boldsymbol{u}_s$. The last two lines summarize results dealing ratio of solenoidal/dilatational kinetic energy and dissipation, respectively. Adapted from Fauchet (1998)

Decorrelation function	$\sim \exp[-\eta(k)(t-t')]$	$\sim \exp[-\eta^2(k)(t-t')^2]$
$E_{dd}(k)$	$\propto M_t^2 Re_L^1 k^{-11/3}$	$\propto M_t^4 Re_L^0 k^{-3}$
$E_{pp}(k)$	$\propto M_t^2 Re_L^1 k^{-11/3}$	$\propto M_t^2 Re_L^0 k^{-7/3}$
$E^{acous}_{p'p'}(k)$	$\sim E_{dd}(k)$	$\propto M_t^6 Re_L^0 k^{-11/3}$
$\lim_{M_t \to 0} E_{pp}(k)$	$\neq E^{inc}_{pp}(k)$	$= E^{inc}_{pp}(k)$
$\mathcal{K}_d/\mathcal{K}_s$	$\propto M_t^2 Re_L^1$	$\propto M_t^4 Re_L^0$
$\bar{\varepsilon}_d/\bar{\varepsilon}_s$	$\propto M_t^2 Re_L^0$	$\propto M_t^4 Re_L^{-1} \ln(Re_L)$

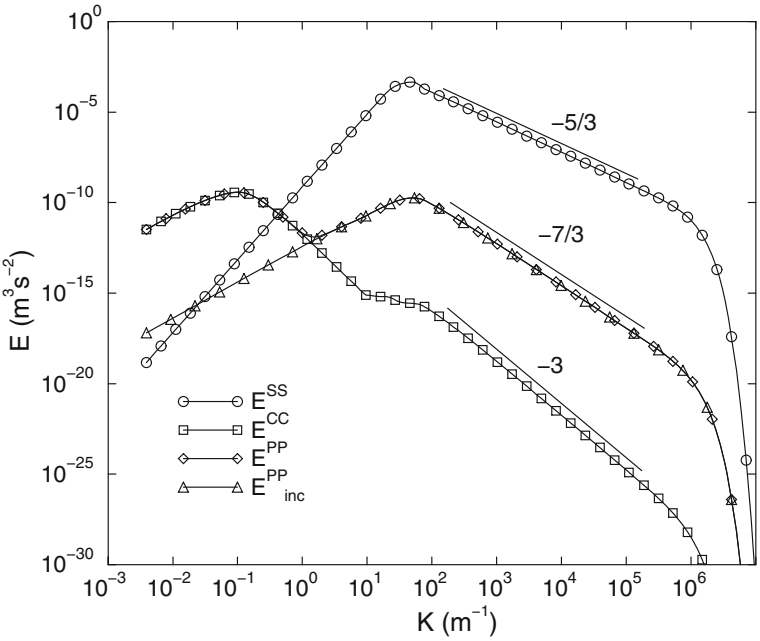

Fig. 13.3 Spectra in the nonlinear equilibrium state predicted using an extended EDQNM-type closure for compressible flows (the dilational energy spectrum is denoted E^{cc} instead of E_{dd}). Courtesy of G. Fauchet and J.B. Bertoglio

- The *strong acoustic equilibrium hypothesis*, which states that $E_{pp}(k) = E_{dd}(k)$, is violated, showing the importance of nonlinear effects. This is seen on Fig. 13.3, which displays computed spectra in the nonlinear equilibrium state.

- Strong acoustic equilibrium is now observed at very small k only (and not over the entire inertial range), at scales really corresponding to acoustic wavelengths that are much larger than the integral velocity lengthscale given by $E_{ss}(k)$.
- In the inertial range, the $E_{pp}(k)(k)$ spectrum almost collapses with its incompressible counterpart $E_{pp}^{inc}(k)$, with related $-7/3$ slope, but $E_{dd}(k)$ is found far below, with a -3 slope. This last result is consistent with a much smaller magnitude of the dilatational motion with respect to the evaluation consistent with strong acoustic equilibrium (which yields the total collapse $E_{pp}^{inc}(k) \sim E_{pp}(k) \sim E_{dd}(k)$). The scaling is now $E_{dd} \sim M_t^4 k^{-3}$ in the inertial range. The corresponding behavior of the compressibility ratio χ defined by Eq. (13.34) as a function of the turbulent Mach number is therefore $\chi \sim M_t^4$, and not $\chi \sim M_t^2$ as suggested by Bataille (1994). The fact that the potential energy of waves, with $E_{pp}(k)$ spectrum, can so greatly exceed their kinetic energy, with $E_{dd}(k)$ spectrum, even questions the very concept of acoustic waves. This observation led many authors, including historical specialists of aeroacoustics, such as Lighthill, to refer to this state as the *pseudo-sound régime* instead of real acoustics. The noise radiated by isotropic turbulence in the quasi-isentropic régime and the related Lighthill analogy are discussed in Sect. 13.2.10.
- It is worth noting that previous results hold in the low-Mach number régime only. For $M_t > 0.1$, the pseudo-sound régime disappears and the k^-3 inertial range is not observed any more on $E_{dd}(k)$. A $k^{-5/3}$ is recovered for M_t close to 1 according to the improved two-point closure, but this result must be considered with care since several assumptions which underly this theory are not satisfied anymore.
- The ratio $\bar{\varepsilon}_d/\bar{\varepsilon}_s$ is observed to scale as M_t^5 for $M_t > 0.2$ instead of M_t^4 at lower Mach numbers (see Fig. 13.4).

13.2.6 Additional Discussion About the Modified Decorrelation Function

The use of the modified decorrelation function $e^{-\eta^2(t-t')^2}$ is the essential improvement brought by Fauchet with respect to earlier developments. Now we will show that the Gaussian form is suggested by the Kraichnan's Linear Random Advection toy-model, rediscussed by Leslie (1973) and Orszag (1977), with an excellent survey given by Kaneda (2007), that was used in Sects. 4.3.4 and 4.3.5 to derive models for two-time velocity statistics in the incompressible case.

The starting point is the following single-mode model:

$$\frac{d}{dt}g(t) = -[\imath(b_0 + b(t)) + \nu_0]g(t), \quad g(0) = 1,$$

in which b_0 holds for the acoustic frequency $a_0 k$, $b(t)$ for a time-dependent *random* contribution to the former taken equal to $b(t) = u'(t)k$ according to the *Randomly*

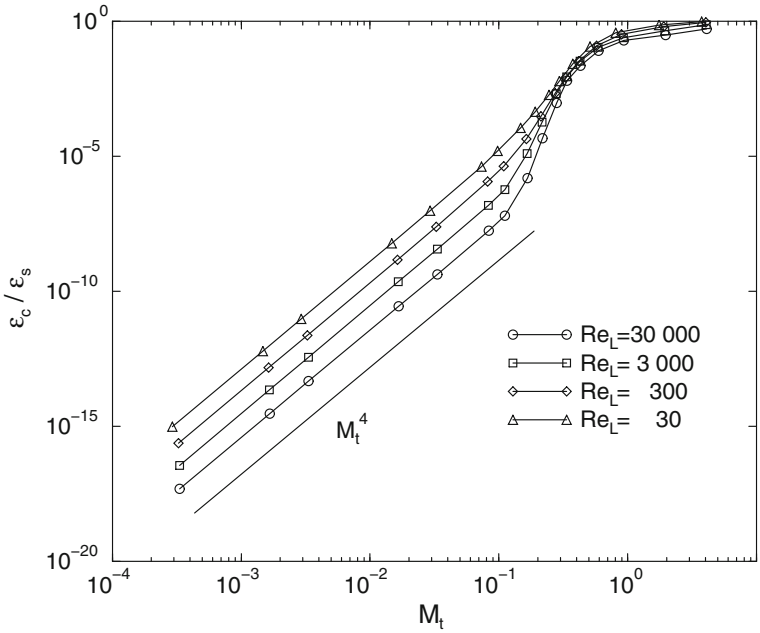

Fig. 13.4 Ratio of the dilatational dissipation (denoted ε^c here) over the solenoidal dissipation (denoted ε^s here) in the nonlinear equilibrium state predicted using an extended EDQNM-type closure for compressible flows, versus the turbulent Mach number for different values of the turbulent Reynolds number. Courtesy of G. Fauchet and J.B. Bertoglio

Swept Wave model and ν_0 for a viscous parameter, e.g. proportional to νk^2. Exact solution of this single-mode equation is

$$g(t) = \exp[-(\nu_0 - \imath b_0)t - \imath \int_0^t b(s)ds],$$

while the solution for its ensemble average is

$$< g(t) >= \exp\left[-(\nu_0 - \imath b_0)t - \frac{1}{2}\iint_0^t < b(s)b(s') > ds'\right].$$

In particular, the latter equation reduces to

$$< g(t) >= \exp\left[-(\nu_0 - \imath b_0)t - \frac{1}{2}\sigma^2 t^2\right],$$

with $\sigma^2 =< b^2 >$, if b is a real time-independent Gaussian process with zero mean. It is recalled that $< \exp(\imath s b) >= \exp(-\sigma^2 t^2/2)$ for such a process.

Of course, $g(t)$ is a scalar function here, but the analogy between its equation and the sub-system ($u^{(3)}$-$u^{(4)}$), with $X^{(3)} = X^{(4)} = 0$ in (13.46) is obvious, considering $u^{(3)} \pm \imath u^{(4)}$ and removing the laminar factor $(4/3)\nu k^2$, with $b(t) = r(t)$.

This simple analysis shows that a Gaussian part of the renormalized response function can be generated by a random contribution added to the mean frequency of linear acoustic waves. Going back to our specific problem of weakly nonlinear compressible turbulence, this suggests that a renormalization of the viscous terms is likely less crucial — and even less adequate — than a renormalization of the dispersion frequency. Main conclusions and semi-open questions are listed below:

- Pure acoustic-wave turbulence, corresponding to triadic interactions without contribution of solenoidal modes, i.e. with $(s = \pm 1, s' = \pm 1, s'' = \pm 1)$, is a marginally relevant model. It probably preserves the acoustic equilibrium, without need to renormalize neither the viscous factors nor the acoustic frequency. One can expect a strong analogy with inertial-wave rotating turbulence from this point of view, since damping terms are only needed to regularize the resonance operators in the high Reynolds number limit.
- Modelling issues not present in pure wave-turbulence occur when strong turbulence (e.g. usual solenoidal turbulence) interacts with wave-turbulence. The concept of waves, which is associated to a balance between potential and kinetic energy, may even become irrelevant since the compressible state can be very far from acoustic equilibrium if k is not too small, yielding $E_{pp}(\text{potential}) \gg E_{dd}(\text{kinetic})$.
- Breakdown of acoustic equilibrium in the closure model seems to be linked to the introduction of a Gaussian factor in the response tensor, possibly resulting from the renormalization of the acoustic-wave frequency, rather than from renormalized viscosity. The Gaussian decorrelation factor can inhibit the time-memory of triple correlations in a more efficient way than the classical exponential term does. As a result, typical oscillations in the resonance operator (13.43) are inhibited too.
- There is no physical explanation for choosing the order of magnitude of the renormalized dispersion frequency as $< r^2 >= \eta^2$ in Eq. (13.46). It is also suggested that the extended wave-turbulence models using (13.44) can be of interest too. The breakdown of the 'strong' acoustic equilibrium is also possible in such a model. This is evidenced by the linearly sheared (with shear rate S) flow model discussed in Chap. 14, in which there is a source term ($\sim Su^{(2)}$ in the shear case, while T_{dd} plays this role in the present case) induced by the coupling with the solenoidal mode in the equation for $u^{(3)}$. Since this source term has no counterpart in the equation for $u^{(4)}$, it can break the acoustic equilibrium at sufficiently large values of the $S/(a_0 k)$ parameter.

To conclude this section, it is important to note that the interpretation of η as the standard deviation of a random acoustic frequency $r(t)$ with zero mean does not imply its scaling as a "straining" or a "sweeping" term. The "straining" scaling is conserved in Fauchet (1998) for instance. On the other hand, recent models suggest the sweeping $u'k$ scaling, as re-discussed in the next section. In fact, we know that the

sweeping choice at all scale yields the flaw in the original DIA version (Kraichnan 1959), but there is now a consensus on a progressive transition from the straining scaling at largest scales to the sweeping scaling at smallest scales. This was illustrated by Favier et al. (2010) using first Kinematic Simulation (see also Favier et al. 2008 for the noise radiated by rotating turbulence) as a linear stochastic model, in line with the abovementioned interpretation of r, with application to two-point two-time statistics and radiated noise. This was confirmed by DNS, so that the scale of transition between "straining" and "sweeping" is given in this study.

13.2.7 Two-Point Two-Time Velocity Correlations and Randomly Swept Wave Model

The two-time two-point velocity correlation tensors can be split using Helmholtz decomposition. Considering the quasi-isentropic linear régime, in which the physics of the solenoidal modes is modified in a negligible way by dilatational effects, all results obtained in Sect. 4.3 can be applied immediately to the solenoidal field $\boldsymbol{u}^s$ and related statistical quantities.

The case of the dilatational component $\boldsymbol{u}^d$ is more difficult since new physical mechanisms are at play. Restricting the analysis to cases in which $\boldsymbol{u}^d$ is associated with acoustic phenomena, the model developed within the incompressible flow framework is not relevant since fast and slow acoustic waves propagate at the speed of sound with respect to the fluid. It must be replaced by a *swept wave model* accounting for random sweeping by large turbulent scales and acoustic wave propagation (Li et al. 2013). The associated extension of (4.85) is

$$\left(\frac{D^2}{Dt^2} - a_0^2\nabla^2\right)\boldsymbol{u}^d = 0, \quad \frac{D}{Dt} = \left(\frac{\partial}{\partial t} + \boldsymbol{v}\cdot\nabla\right) \tag{13.47}$$

where a_0 and $\boldsymbol{v}$ denotes the mean speed of sound and the random sweeping velocity induced by large energetic scales, respectively. The exact wave solution is expressed as

$$\begin{aligned}\boldsymbol{u}^d(\boldsymbol{k},t) = {}& \boldsymbol{u}^+(\boldsymbol{k},0)\exp\left[-\imath(\boldsymbol{k}\cdot\boldsymbol{v})t - \imath k a_0 t\right] \\ & + \boldsymbol{u}^-(\boldsymbol{k},0)\exp\left[-\imath(\boldsymbol{k}\cdot\boldsymbol{v})t + \imath k a_0 t\right]\end{aligned} \tag{13.48}$$

where $\boldsymbol{u}^+(\boldsymbol{k},t)$ and $\boldsymbol{u}^-(\boldsymbol{k},t)$, i.e. the fast and slow acoustic waves, are assumed to be decorrelated. This expression is equivalent to Eq. (2.112), with $G_{ij}^{(0)}(\boldsymbol{k},t,t_0) = \exp\left[-\imath(\boldsymbol{k}\cdot\boldsymbol{v})t - \imath k a_0 t\right]$ for fast acoustic waves and $G_{ij}^{(0)}(\boldsymbol{k},t,t_0) = \exp\left[-\imath(\boldsymbol{k}\cdot\boldsymbol{v})t + \imath k a_0 t\right]$ for slow acoustic waves. Here, nonlinear and viscous effects have been neglected, leading to $\boldsymbol{s}(\boldsymbol{k}(t),t) = 0$ and a simple analytical expression.

Following the same method as in Sects. 4.3.4 and 4.3.5, the two-time correlation for the dilatational velocity field is

$$\begin{aligned}\hat{R}_{ij}^d(\boldsymbol{k},t) &= \overline{u_i^d(\boldsymbol{k},t)u_j^d(-\boldsymbol{k},t+\tau)} \\ &= \overline{u_i^+(\boldsymbol{k},0)u_j^+(-\boldsymbol{k},0)}\ \overline{\exp\left[\imath(\boldsymbol{k}\cdot\boldsymbol{v})\tau+\imath ka_0\tau\right]} \\ &\quad +\overline{u_i^-(\boldsymbol{k},0)u_j^-(-\boldsymbol{k},0)}\ \overline{\exp\left[\imath(\boldsymbol{k}\cdot\boldsymbol{v})\tau-\imath ka_0\tau\right]} \\ &= \hat{R}_{ij}^d(\boldsymbol{k},0)\cos(ka_0\tau)\exp\left[-\frac{1}{2}V^2k^2\tau^2\right], \end{aligned} \tag{13.49}$$

where $3V^2 = \|\boldsymbol{v}\|^2$ and

$$\hat{R}_{ij}^d(\boldsymbol{k},0) = 2\overline{u_i^+(\boldsymbol{k},0)u_j^+(-\boldsymbol{k},0)} = 2\overline{u_i^-(\boldsymbol{k},0)u_j^-(-\boldsymbol{k},0)}$$

This swept wave model is observed to be in very good agreement with DNS data (Li et al. 2013) in the régimes referred to as low-Mach quasi-isentropic régime and subsonic nonlinear régime, in the absence of dilatational forcing and strongly dilatational initial conditions, up to $M_t = \sqrt{3}V/a_0 \simeq 0.4$, i.e. when shocklets do not play a governing role and that dilatational modes are mostly restricted to acoustic waves. Relation (13.49) shows that linear wave propagation induces a sinusoidal modulation, while the random sweeping exponential damping is the same as for the solenoidal mode. The dependency on the turbulent Mach number is illustrated rewritting Eq. (13.49) as

$$\hat{R}_{ij}^d(\boldsymbol{k},t) = \hat{R}_{ij}^d(\boldsymbol{k},0)\cos(\tau_a)\exp\left[-\frac{\tau_a^2M_t^2}{6}\right],\ \tau_a = a_0k\tau \tag{13.50}$$

showing that the random sweeping damping increases rapidly as M_t grows. Again, one can mention that the typical sweeping time is $\tau_a M_t$, whence proportional to $ku'\tau$: this can be indirectly related to the Gaussian response function $\exp -\eta^2\tau^2$ used in Fauchet (1998) ... but not to the fact that a "straining" scaling is still used for η in the latter study.

13.2.8 Analytical Fauchet–Bertoglio Model

In the absence of analytical results from the extended wave-turbulence model discussed above, let us give more details provided by the model proposed in Fauchet (1998). Carrying out an asymptotic analysis in the limit of very low Mach number and very high Reynolds numbers, and considering the following solenoidal kinetic energy spectrum model

$$E_{ss}(k) = \begin{cases} Bk^\sigma & k < k_L \\ K_0\bar{\varepsilon}_s^{2/3}k^{-5/3} & k_L \le k \le k_\eta \\ 0 & k > k_\eta \end{cases} \tag{13.51}$$

where

$$B = K_0 \bar{\varepsilon}_s^{2/3} k_L^{-5/3-\sigma}, \tag{13.52}$$

Fauchet, Bertoglio and J. Scott obtained analytical models for both non-linear transfer terms and related spectra. The analysis is restricted to $T_{dd}(k)$ and $T_{dp}(k)$, since $T_{ss}(k)$ is not modified by compressibility effects and there is no feedback of the dilatational part of the solution on $\boldsymbol{u}_s$. The leading order terms for the local and non-local transfers in $T_{dp}(k)$ are:

$$T_{dp}(k) \simeq \begin{cases} \underbrace{\dfrac{k^{2(1+\sigma)}}{a_0}}_{I} + \underbrace{\dfrac{8}{65}\dfrac{K_0^2}{a_0}\bar{\varepsilon}_s^{4/3}\dfrac{k^3}{k_L^{13/3}}}_{II} & (k < k_L) \\ \underbrace{a_0 k E_{pp}^{inc}(k)}_{III} + \underbrace{\left(\dfrac{k}{k_L}\right)^{4/3} a_0^2 k^2 E_{pp}^{inc}(k)}_{IV} & (k \geq k_L) \end{cases} \tag{13.53}$$

where terms I and III are related to local interactions, while non-local interactions are grouped in contributions II and IV. The exact form of the incompressible pressure spectrum $E_{pp}^{inc}(k)$ is not known at this stage. One just has to know that $E_{pp}^{inc}(k) \propto k^{-7/3}$ in the inertial range. A careful analysis of the relative amplitude of these terms shows that the non-local transfer IV is dominant at small wave numbers such that $k < k_P$, while the local interaction term III is dominant at higher wave numbers $k \geq k_P$. The threshold wave number is evaluated by the formula below:

$$k_P = \left(\frac{65}{16} C_G\right)^{3/13} k_L \simeq 1.47 k_L, \quad C_G \simeq 1.32. \tag{13.54}$$

Now using the relation

$$T_{dp}(k) = a_0 k E_{pp}^{inc}(k) \tag{13.55}$$

and taking $\sigma = 4$ as a slope for the energy spectrum at large scales, one obtains the following expression for the incompressible pressure spectrum:

$$E_{pp}^{inc}(k) = \begin{cases} \frac{8}{65} K_0^2 \bar{\varepsilon}_s^{4/3} \frac{k^2}{a_0^2 k_L^{13/3}} & k < k_P \\ \frac{C_G}{2a_0^2} K_0^2 \bar{\varepsilon}_s^{4/3} k^{-7/3} & k_P \leq k \leq k_\eta \\ 0 & k > k_\eta \end{cases}. \tag{13.56}$$

Therefore, it is seen that the incompressible pressure spectrum and the solenoidal kinetic energy spectrum do not have their maxima at the same wave numbers, since $k_P > k_L$. It is worth noting that the exact expression for $E_{pp}^{inc}(k)$ in the inertial range, i.e. $k \geq k_P$, is not a direct output of the asymptotic analysis which is supplemented by an auxiliary model.

$$T_{dd}(k) \simeq \begin{cases} \underbrace{\frac{4}{3}\nu\frac{k^{(4+3\sigma)}}{a_0^4}}_{V} + \underbrace{\frac{64}{5}\beta^{3/2}\sqrt{2\pi}K_0^{7/2}\frac{\bar{\varepsilon}_s^{7/3}}{a_0^4 k_L^{7/3}}F_p\left(\frac{k}{k_{acous}}\right)}_{VI} \\ \qquad + \underbrace{\frac{64}{15}\beta\frac{4}{3}\nu K_0^3\frac{\bar{\varepsilon}_s^2}{a_0^4 k_L^3}k^2}_{VII} & (k < k_L) \\ \underbrace{12\frac{4}{3}\nu\frac{\beta}{a_0}k^3 E_{ss}(k)E_{pp}^{inc}(k)}_{VIII} + \underbrace{k^{-7/3}\exp(-\beta a_0^2 k^{2/3})}_{IX} \\ \qquad + \underbrace{\frac{4}{3}\nu\frac{k^{-7/3}}{a_0^4}}_{X} & (k \geq k_L) \end{cases} \tag{13.57}$$

with $\beta \simeq 0.2$, where the function F_p in term VI is defined as follows:

$$F_p(x) = \frac{\Gamma(15/4) - \Gamma(15/4, x^2)}{x^7/2} \tag{13.58}$$

The parameter k_{acous} denotes the wave number associated to the peak of the acoustic spectrum. It is evaluated as

$$k_{acous} = \frac{2\sqrt{2\beta}}{C_b}M_t k_L, \quad C_b = \sqrt{\frac{3\sigma+5}{3(\sigma+1)}} \tag{13.59}$$

Here, local interactions are represented by terms V and $VIII$, while other terms are related to non-local contributions.

The analysis of the relative amplitudes reveals the existence of three different spectral zones:

- The *acoustic region*, which corresponds to very small wave numbers such that $k < k_{r1}$, with

$$k_{r1} = \frac{3}{4}(10C_G)^{1/3}k_L \simeq 1.8k_L. \tag{13.60}$$

  In this region, the non-local term VI is dominant. It is therefore interpreted as the production of acoustic wave. The spectrum of acoustic production, $\mathcal{P}_{acous}(k)$, can therefore be rewritten as follows

$$\mathcal{P}_{acous}(k) = (VI) = \frac{256}{15}\frac{\beta}{C_b^7}\sqrt{\frac{\pi\beta}{3}}\mathcal{K}_s^{3/2}M_t^4 F_p\left(\frac{k}{k_{acous}}\right). \tag{13.61}$$

  The total radiated acoustic power, P_{tot} is then equal to

$$P_{tot} = \int_0^{k_\eta} \mathcal{P}_{acous}(k)dk = 4.2C_b^{-5}\bar{\varepsilon}_s M_t^5 \tag{13.62}$$

which is in very good agreement usual estimates found using the acoustic Lighthill analogy (see Sect. 13.2.10). Relation (13.61) does not yield the right estimate for both the value and the location of the peak of the normalized acoustic production spectrum $\mathcal{P}^*_{acous}(k) \equiv \mathcal{P}_{acous}(k)/P$. Using the normalized frequency $\omega^* = a_0 k u'^2/\bar{\varepsilon}_s$, the correct prediction $\max(\mathcal{P}^*_{acous}(\omega^*)) \simeq 0.1$ for $\omega^* = \omega^*_{max} \simeq 3.5$ is recovered using a realistic spectrum shape for $E_{ss}(k)$ instead of (13.51). Doing so, the term VI yields a normalized production spectrum which is very close to the one proposed by Lilley in 1994:

$$\mathcal{P}^*_{acous}(\omega^*) = \frac{8}{3\pi S_t} \frac{\omega^*/(2S_t)^4}{(1+(\omega^*/2S_t)^2)^3}, \quad S_t = 1.24 \tag{13.63}$$

- a *transition region*, in which both non local transfer terms IX and X play an important role, term X having the largest amplitude. This region is defined as $k_{r1} < k < k_{r2}$, where

$$k_{r2} \simeq \frac{2.5}{C_b^{5/11} C_a^{2/11}} M_t^{7/11} Re_L^{2/11} k_L, \quad C_a = \frac{3\sigma+5}{3\sigma} \tag{13.64}$$

- an *inertial range region* for $k > k_{r2}$, in which the local transfer term $VIII$ is now dominant. This inertial range is associated with the *pseudo-sound régime*, in which the dilatational velocity field is in equilibrium with the solenoidal pressure.

This simplified form of $T_{dd}(k)$ enables a detailed analysis of the dilatational energy spectrum $E_{dd}(k)$. To this end, the following expression is derived from Eq. (13.14):

$$2\left(\frac{4}{3}\nu + \nu_t^{acous}(k)\right) k^2 E_{dd}(k) = T_{dd}(k) \tag{13.65}$$

where the eddy-damping term $\nu_t^{acous}(k)$ accounts for cumulated effects of higher-order terms neglected during the derivation of the simplified form of $T_{dd}(k)$ given above. The improved two-point closure suggests that

$$\nu_t^{acous}(k) = \frac{1}{30}\sqrt{\frac{2\pi K_0}{\beta}} \left(\frac{\bar{\varepsilon}_s}{k_L^4}\right)^{1/3} F_\nu\left(\frac{k}{k_{acous}}\right) \tag{13.66}$$

with

$$F_\nu(x) = 5\frac{1-e^{-x^2}}{x^2} - e^{-x^2}. \tag{13.67}$$

The effect of this damping term is to prevent the occurrence of an *acoustic catastrophe* in the limit of infinite Reynolds number, i.e. $E_{dd}(k)$ remains bounded.

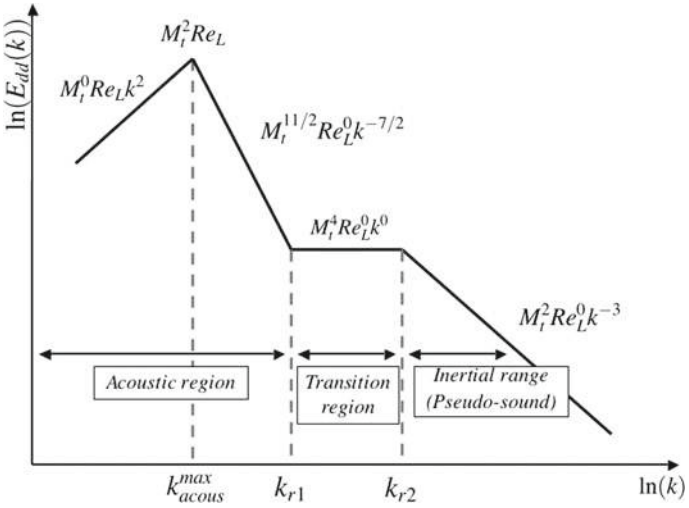

Fig. 13.5 Sketch of the dilatational kinetic energy spectrum $E_{dd}(k)$ in the nonlinear equilibrium state, according to the simplified Fauchet–Bertoglio analytical model derived from the extended two-point closure for compressible flows

A similar term was introduced by Crow in 1967. This damping term is very small for wave number larger than k_{acous}, and will therefore be neglected in both the transition region and the inertial range since it is much smaller than the molecular viscosity at these scales. Combining the equilibrium relation (13.65) with the simplified form of the non-linear transfer term, one obtains (see Fig. 13.5):

$$E_{dd}(k) = \begin{cases} 32\dfrac{\sqrt{2}\beta^{3/2}}{C_b^5 k_{acous}} M_t^3 \mathcal{K}_s F_{acous}\left(\dfrac{k}{k_{acous}}\right) & k < k_{r1} \\ \dfrac{64}{135}\dfrac{\beta}{C_b^6} M_t^4 Re_L^0 \mathcal{K}_s \dfrac{k^0}{k_L} & k_{r1} < k < k_{r2} \\ 2a\dfrac{C_G}{C_b^6} M_t^4 Re_L^0 \mathcal{K}_s k_L^{-1}\left(\dfrac{k}{k_L}\right)^{-3} & k \geq k_{r2} \end{cases} \tag{13.68}$$

where

$$F_{acous}(x) = \frac{1}{x^2}\frac{F_p(x)}{F_\nu(x)}. \tag{13.69}$$

The peak of $E_{dd}(k)$ in the acoustic region observed at $k = k_{acous}^{max} \simeq 1.32\, k_{acous}$, is

$$E_{dd}(k_{acous}^{max}) \simeq \frac{0.046}{C_b^7}\frac{\mathcal{K}_s^{5/2}}{\bar{\varepsilon}_s} M_t^2 Re_L^0. \tag{13.70}$$

In the acoustic region, further analysis shows that

$$E_{dd}(k) \propto \begin{cases} M_t^0 Re_L^0 k^2 & k < k_{r1}, k \ll k_{acous}^{max} \\ M_t^{11/2} Re_L^0 k^{-7/2} & k < k_{r1}, k \gg k_{acous}^{max} \end{cases}. \tag{13.71}$$

This analytical expression for $E_{dd}(k)$ enables a straightforward evaluation of the turbulent acoustic kinetic energy

$$\mathcal{K}_{acous} = \int_0^{+\infty} 32 \frac{\sqrt{2}\beta^{3/2}}{C_b^5 k_{acous}} M_t^3 \mathcal{K}_s F_{acous}\left(\frac{k}{k_{acous}}\right) dk \propto 32 \frac{\sqrt{2}\beta^{3/2}}{C_b^5} M_t^3 \mathcal{K}_s \tag{13.72}$$

which is in perfect agreement with Crow's scaling law for this quantity.

The compressible turbulent kinetic energy contained in the inertial range and the corresponding dilatational dissipation are found to be equal to

$$\mathcal{K}_d = \int_{k \geq k_{r2}} E_{dd}(k) dk = 0.25 C_b^{-6} \mathcal{K}_s M_t^4, \tag{13.73}$$

$$\bar{\varepsilon}_d = \frac{4}{3}\nu \int_{k \geq k_{r2}} k^2 E_{dd}(k) dk = 1.65 C_a C_b^{-5} \bar{\varepsilon}_s M_t^4 \frac{\ln(Re_L)}{Re_L}. \tag{13.74}$$

13.2.9 Numerical Experiments

Isotropic compressible turbulence has been investigated by several research groups via direct numerical simulation of the full compressible Navier–Stokes equations. In most cases, the low-Reynolds number free decay régime is considered. The main results are summarized below

(i) A statistical equilibrium is observed, which corresponds to the *weak acoustic equilibrium hypothesis* with $\mathcal{F}(t) \approx 1 = \mathcal{F}_\infty$. The function $\mathcal{F}$ fluctuates almost periodically around unity. This result is remarkable, since all couplings with internal energy are neglected in the theoretical derivation of the linear model for the pseudo-acoustic régime and that the *strong acoustic equilibrium hypothesis* is shown to be violated by both improved two-point closures and numerical simulations. These slight fluctuations might be explained by an almost periodic energy exchange between the acoustic mode and the entropy mode (i.e. the internal energy). This point is further discussed below.

(ii) This weak equilibrium state is very robust: it is has been observed for a very wide range of turbulent Mach numbers and initial conditions. As a matter of fact, statistical equilibrium states with $\mathcal{F} \approx 1$ have been found for turbulent Mach numbers as high as 0.5 (Sarkar et al. 1991).

(iii) The theoretical prediction (13.38) for χ_∞ was found to be accurate for a large number of cases simulated in Erlebacher et al. (1990).

The energy balance associated with the statistical equilibrium states has been very finely analyzed in both decaying and forced isotropic turbulence (Kida and Orszag 1990a, 1992; Miura and Kida 1995). In these studies, the transfers between the dilatational turbulent kinetic energy $\mathcal{K}_d$, the solenoidal turbulent kinetic energy $\mathcal{K}_s$ and the fluctuating internal energy $\tilde{e}$ have been investigated. The main conclusions dealing with the global energy transfers at the equilibrium state are the following:

(i) In the acoustic equilibrium state, both $\mathcal{K}_d(t)$ and $\tilde{e}(t)$ fluctuate sinusoidally about a constant mean value (see Fig. 13.6). The two signals are in exact phase opposition and have similar amplitude, leading to $\mathcal{K}_d(t) + \tilde{e}(t) \simeq Cst$. This is consistent with the finding that $\mathcal{F}(t)$ is nearly constant.
(ii) The solenoidal kinetic energy $\mathcal{K}_s$ varies slowly with irregular fluctuations of small amplitude, and does exhibit phase locking with either $\mathcal{K}_d(t)$ or $\tilde{e}(t)$.
(iii) The interactions between the solenoidal and compressive components of the turbulent kinetic energy are weaker than self-interactions of the respective components.
(iv) The pressure-dilatation term (term II in Eqs. (3.104) and (3.106)) governs the coupling between $\mathcal{K}_d(t)$ and $\tilde{e}(t)$ (see Fig. 13.7). It is also observed to overwhelm other terms which appears in the evolution equations for $\mathcal{K}_d(t)$, the total mean turbulent kinetic energy $\mathcal{K} = \mathcal{K}_d + \mathcal{K}_s$ and the internal energy $\tilde{e}$. It exhibits a periodic behavior with the same period as $\mathcal{K}_d(t)$ and $\tilde{e}(t)$, and it is due to acoustic pressure fluctuations.

This dynamical picture can be further refined looking at energy exchanges at individual wave numbers. The main findings of Miura and Kida are

(i) The periodic behavior of the compressible kinetic energy and the internal energy is observed at each wave number in the spectra associated to these quantities, $E_{dd}(k,t)$ and $E_e(k,t)$, respectively (see Fig. 13.8). The same observation holds for the compressible pressure spectrum $E_{pp}(k,t)$.
(ii) The period of oscillation $\tau(k)$ depends on the wave number and is the same for the three spectra at each wave number. The measured period corresponds almost exactly with the one associated to acoustic waves:

$$\tau(k) = \frac{\pi}{\omega(k)}, \quad \omega_k \sim \pm a_0 k. \tag{13.75}$$

At every wave number, it is found that the phase of oscillation of $E_{pp}(k,t)$ is in advance those of $E_{dd}(k,t)$ and behind those of $E_e(k,t)$ by a quarter of period.

A schematic view if the energy transfers associated to this régime is displayed in Fig. 13.9.

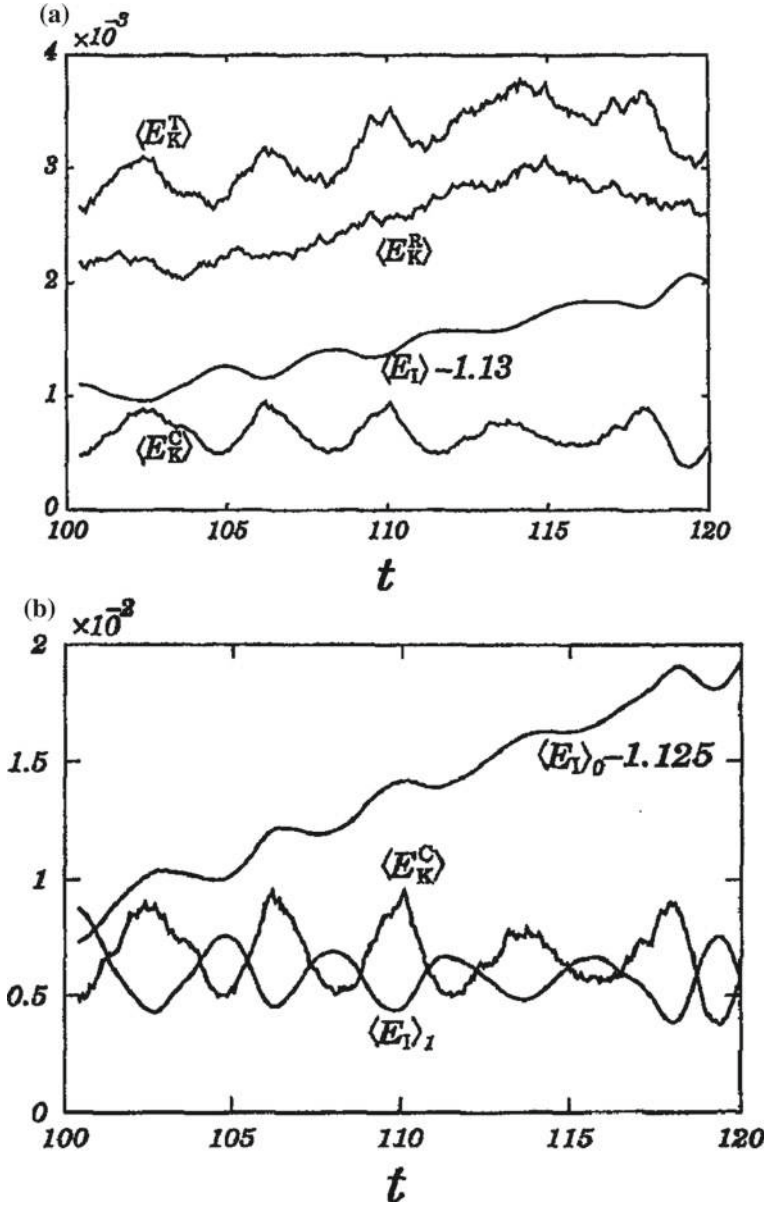

Fig. 13.6 Computed time history of volume-averaged energies in forced compressible isotropic turbulence. $< E_K^T >$, $< E_K^R >$, $< E_K^C >$ and $< E_I >$ are the full turbulent kinetic energy, solenoidal kinetic energy, dilatational kinetic energy and internal energy, respectively. Since a source term is present the mean internal energy undergoes a constant growth, and is split as the sum of a uniform part $< E_I >_0$ and a turbulent part $< E_I >_1$. Reproduced from Miura and Kida (1995) with permission of AIP

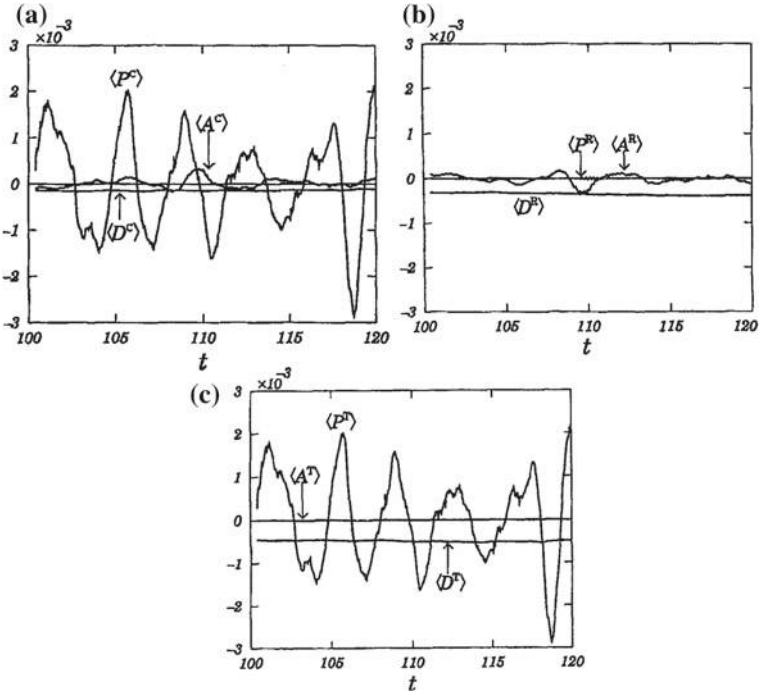

Fig. 13.7 Time histories of the volume-averaged budget terms for the dilatational turbulent kinetic energy **(a)**, the solenoidal turbulent kinetic energy **(b)** and the internal energy **(c)**. Terms A, D and P denote the advection, viscous diffusion and pressure terms, respectively. Reproduced from Miura and Kida (1995) with permission of AIP

13.2.10 Noise Generation by Isotropic Turbulence: Lighthill Analogy

13.2.10.1 Fundamentals and Governing Equations

We now address in a more detailed way the issue of the noise radiated by a volume of fluid, $\mathcal{V}$, filled by quasi-isentropic isotropic turbulence, including effects due to the advection by an uniform mean flow with arbitrary Mach number. Such a case is an example of one-way coupling, kinetic energy of the vorticity mode being transformed into acoustic energy, without feedback. Since noise radiated by turbulence is at the heart of aeroacoustic theories, the present section is devoted to its analysis. The theory developed in the present Section can be interpreted as a first nonlinear statistical extension of the nonlinear Kovasznay decomposition discussed in Sect. 3.2.3.

Lighthill's theory (Lighthill 1952, 1954, 1961) aims at describing the far field noise radiated by a flow, i.e. on the transfer of energy of vortical fluctuations to acoustic modes. It is a seminal fully nonlinear theory, which does not rely on any

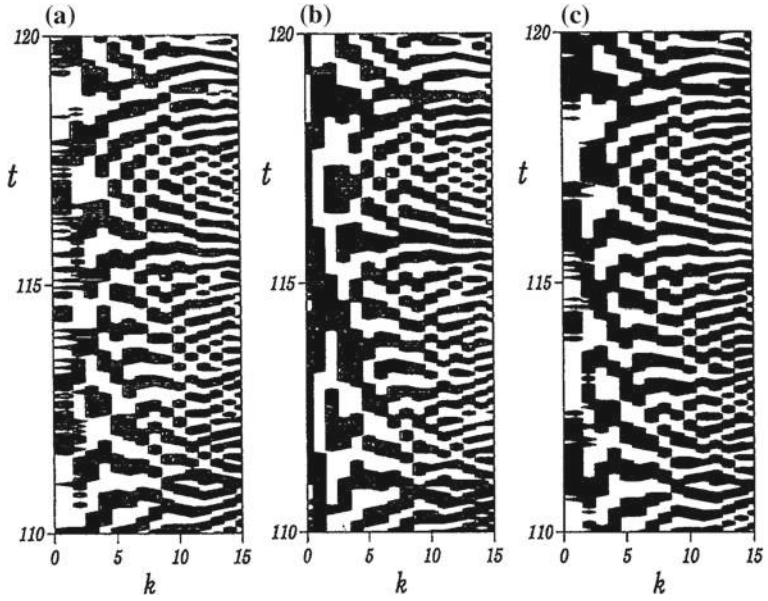

Fig. 13.8 Time histories of the wave number spectra of dilatational turbulent kinetic energy (left), internal energy (middle) and dilatational pressure (right). White (resp. dark) regions are regions where the instantaneous spectrum coefficients are decreasing (resp. increasing) in time. Reproduced from Miura and Kida (1995) with permission of AIP

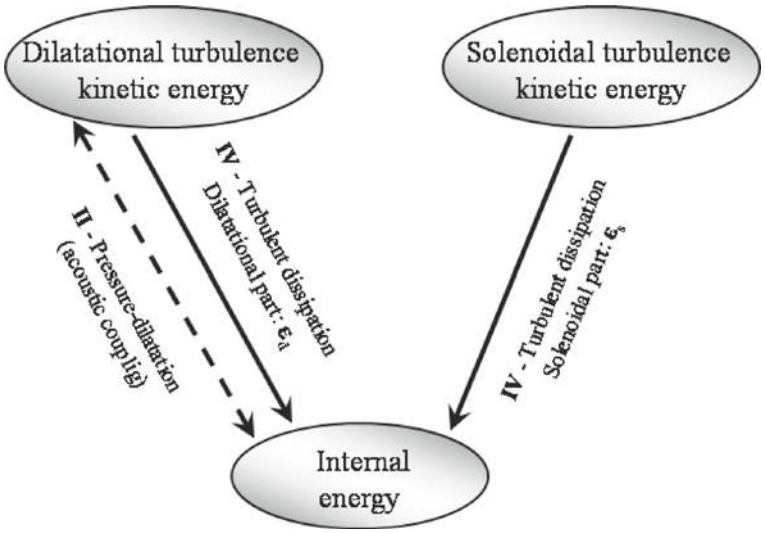

Fig. 13.9 Detailed schematic view of mean energy exchanges in compressible isotropic turbulence in the quasi-acoustic equilibrium state

small parameter expansion. It has been extended to include the role of entropy modes and immersed solid boundaries in noise generation. This theory relies on an analogy: the flow is modeled by an equivalent set of acoustic sources localized in a bounded volume embeded in a homogeneous medium at rest.

The first step consists of deriving an exact governing equation for acoustic wave evolution, which will be simplified in a second step to get an analytical solution. To this end, one subtracts the divergence of the momentum equation from the material derivative of the mass conservation equation, leading to:

$$\frac{\partial^2 \rho}{\partial t^2} - \nabla^2 p = \nabla \cdot \nabla \cdot (\rho \boldsymbol{u} \otimes \boldsymbol{u} - \boldsymbol{\Pi}), \tag{13.76}$$

where $\boldsymbol{\Pi}$ is related to viscous stresses. The D'Alembertian operator for wave propagation appears when subtracting $a_\infty^2 \nabla^2 \rho$ to both sides of the above equation:

$$\frac{\partial^2 \rho}{\partial t^2} - a_\infty^2 \nabla^2 \rho = \nabla \cdot \nabla \cdot (\rho \boldsymbol{u} \otimes \boldsymbol{u} - \boldsymbol{\Pi}) + \nabla^2 (p - a_\infty^2 \rho), \tag{13.77}$$

where a_∞ is related to an arbitrary propagation speed for density waves. This equation is an exact one. The left hand side describes wave propagation operator for acoustic waves with speed of sound a_∞, while the right hand side is interpreted as source terms, i.e. as terms responsible for the existence of acoustic waves. An equivalent equation for pressure waves was proposed by Morfey in 1973 and Lilley in 2008:

$$\frac{1}{a_\infty^2} \frac{\partial^2 p}{\partial t^2} - \nabla^2 p = \nabla \cdot \nabla \cdot (\rho \boldsymbol{u} \otimes \boldsymbol{u} - \boldsymbol{\Pi}) - \frac{\partial^2}{\partial t^2} \left(\rho - \frac{1}{a_\infty^2} p \right). \tag{13.78}$$

Looking at this equation, one can see the Poisson equation (2.18) for pressure obtained in the incompressible case is the asymptotic limit of the full equation when the speed of sound is infinite, i.e. $a_\infty^2 \to +\infty$.

Additional equivalent expressions have been proposed for other variables: $(p + \rho u^2/3)$ (Ffwocs Williams and Hawkings 1969), total enthalpy $(h + u^2/2)$ (Howe 1975) or $\left[(p/p_\infty)^{1/\gamma} - 1\right]$ (Goldstein and He 2001). All these formulations are mathematically equivalent, but each one is best suited to analyze some specific features of noise generation or noise propagation.

Equation (13.77) is often modified to describe the propagation of density fluctuations in a uniform quiescent fluid with temperature T_∞, pressure p_∞, density ρ_∞ and speed of sound $a_\infty = \sqrt{\gamma p_\infty / \rho_\infty}$, leading to the following *exact equation*

$$\left(\frac{\partial^2}{\partial t^2} - a_\infty^2 \nabla^2 \right) (\rho - \rho_\infty) = \nabla \cdot \nabla \cdot \underbrace{\left(\rho \boldsymbol{u} \otimes \boldsymbol{u} + \left[(p - p_\infty) - a_\infty^2 (\rho - \rho_\infty) \right] \mathbf{I} - \boldsymbol{\Pi} \right)}_{\mathbf{T}} \tag{13.79}$$

The source term tensor $\mathbf{T}$ in the right-hand-side is referred to as the *Lighthill tensor*. It is made of three parts, each part being associated to a specific noise generation mechanism:

- $\rho \boldsymbol{u} \otimes \boldsymbol{u}$ is related to acoustic wave generation by nonlinear self-interactions of velocity fluctuations. Since Kovasznay decomposition shows that all modes contribute to fluctuating velocity in viscous flows, this quadratic term accounts for all possible interactions (including self-interactions) between vorticity, acoustic and entropy modes.
- $\left[(p - p_\infty) - a_\infty^2(\rho - \rho_\infty)\right]\mathbf{I}$ accounts for local instantaneous heterogeneities of pressure and density (and temperature, because of the equation of state). One can see here that fluctuations of thermodynamical quantities may generate acoustic waves, in agreement with the nonlinear Kovasznay decomposition discussed in Sect. 3.2.3. Such fluctuations can originate in external forcings or in couplings between entropy and the acoustic field, but also in intense turbulent vortical events. This term is important in high temperature flows, but is often negligible in practical applications if intense heat sources are not present.
- $\boldsymbol{\Pi}$ is related to generation of acoustic waves by viscous effects. Such effects may stem from different physical process, e.g. from temperature-induced viscosity fluctuations.

13.2.10.2 Integral Solution

Exact analytical solutions to (13.79) may be found under the three following assumptions (see also Fig. 13.10):

(i) All acoustic sources are located in a finite bounded domain $\mathcal{V}$, i.e. $\mathbf{T}$ is identically null outside $\mathcal{V}$.

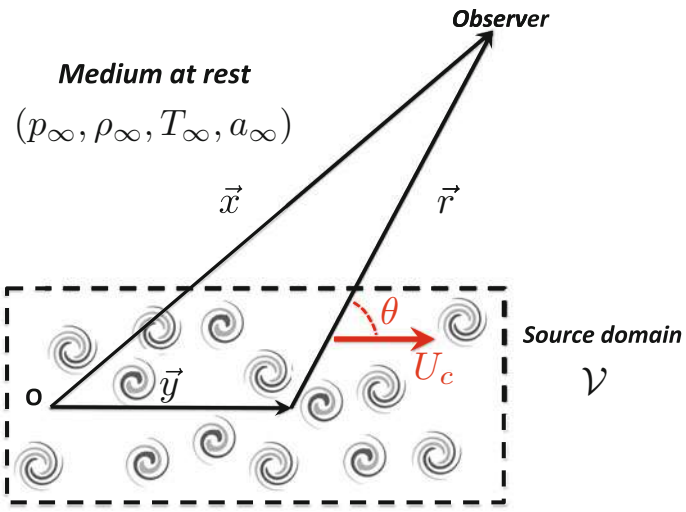

Fig. 13.10 Schematic view of the Lighthill analogy

(ii) The medium is homogeneous and at rest outside $\mathcal{V}$. It is characterized by the temperature T_∞, the pressure p_∞, the density ρ_∞ and the speed of sound $a_\infty = \sqrt{\gamma p_\infty/\rho_\infty}$.
(iii) The observer is located at position $\boldsymbol{x}$ which is outside $\mathcal{V}$.

An analytical solution of Eq. (13.79) is then obtained using the Green function of the d'Alembertian operator in unbounded domain:

$$G(\boldsymbol{x},t) = \frac{1}{4\pi a_\infty^2}\delta\left(t - \frac{x}{a_\infty}\right), \tag{13.80}$$

where $\delta(t)$ denotes the Kronecker symbol and $(t - x/a_\infty)$ is referred to as the *retarded time* that accounts for the finite time needed by acoustic waves to travel from the source to the observer at speed a_∞. The solution is

$$\rho(\boldsymbol{x},t) - \rho_\infty = \frac{1}{4\pi a_\infty^2}\int_{\mathcal{V}} \frac{1}{r}\frac{\partial^2 T_{ij}}{\partial y_i \partial y_j}\left(\boldsymbol{y}, t - \frac{r}{a_\infty}\right) d^3\boldsymbol{y}, \quad r = |\boldsymbol{r}|. \tag{13.81}$$

It can be simplified in several cases.

A first case is related to the *far field approximation*, in which the distance between the observed and the source domain is very large compared to the characteristic size of the source domain. In this case, one can write $|\boldsymbol{x}| \gg |\boldsymbol{y}|$, from which $|\boldsymbol{x}| \simeq r$ and therefore

$$\rho(\boldsymbol{x},t) - \rho_\infty = \frac{1}{4\pi a_\infty^2 r}\int_{\mathcal{V}} \frac{\partial^2 T_{ij}}{\partial y_i \partial y_j}\left(\boldsymbol{y}, t - \frac{r}{a_\infty}\right) d^3\boldsymbol{y}, \quad r = |\boldsymbol{r}|. \tag{13.82}$$

Applying twice the Green formula to this expression, one obtains

$$\begin{aligned}\rho(\boldsymbol{x},t) - \rho_\infty = {} & \frac{1}{4\pi a_\infty^2 r}\int_{\mathcal{S}} \frac{\partial T_{ij}}{\partial y_j}\left(\boldsymbol{y}, t - \frac{r}{a_\infty}\right) n_i dS \\ & + \frac{1}{4\pi a_\infty^2 r}\frac{\partial}{\partial x_j}\int_{\mathcal{S}} T_{ij}\left(\boldsymbol{y}, t - \frac{r}{a_\infty}\right) n_j dS \\ & + \frac{1}{4\pi a_\infty^2 r}\frac{\partial^2}{\partial x_i \partial x_j}\int_{\mathcal{V}} T_{ij}\left(\boldsymbol{y}, t - \frac{r}{a_\infty}\right) d^3\boldsymbol{y},\end{aligned} \tag{13.83}$$

where $\mathcal{S}$ denotes the boundary of $\mathcal{V}$ and $\boldsymbol{n}$ is the outward normal unit vector to $\mathcal{S}$. When $\mathcal{V}$ is chosen to be large enough such that boundary terms vanish, the expression dramatically simplifies to the third term of the right hand side.

An equivalent expression based on time derivatives instead of spatial derivatives can be derived using the convection operator and the relation

$$\frac{\partial f_i(\boldsymbol{y}, t=\tau)}{\partial y_i} = \left(\frac{\partial f_i}{\partial y_i}\right)_\tau + \frac{(x_i - y_i)}{|\boldsymbol{x}-\boldsymbol{y}|}\left(\frac{\partial f_i}{a_\infty \partial \tau}\right), \quad \tau = t - \frac{|\boldsymbol{x}-\boldsymbol{y}|}{a_\infty}. \tag{13.84}$$

The first term in the right hand side leads to surfacic integral terms (thanks to the Green formula) that vanish when the source domain encompasses all acoustic sources. Assuming that surfacic terms are null, one has

$$\rho(\boldsymbol{x}, t) - \rho_\infty = \frac{1}{4\pi a_\infty^2 r}\int_{\mathcal{V}} \frac{\partial^2 T_{rr}}{\partial t^2}\left(\boldsymbol{y}, t - \frac{r}{a_\infty}\right) d^3\boldsymbol{y}, \quad r = |\boldsymbol{r}|, \quad T_{rr} = \frac{x_i x_j}{x^2} T_{ij} \tag{13.85}$$

where T_{rr} denotes the source in the direction of the observer. The expression based on time derivates is observed to be much more accurate in practical applications than the one based on spatial derivatives.

The solution can be further simplified assuming that the source is a *compact source*, which holds when the size of the source domain is small compared with the wavelength of the acoustic signal under consideration. In this case, it is possible to neglect retarded time effects and to consider that the waves emitted by all sources at a given time are received at the same time by the observer. Under this assumption, the solution is expressed as follows

$$\rho(\boldsymbol{x}, t) - \rho_\infty = \frac{1}{4\pi a_\infty^2 r}\int_{\mathcal{V}} \frac{\partial^2 T_{rr}}{\partial t^2}\left(\boldsymbol{y}, t - \frac{r_0}{a_\infty}\right) d^3\boldsymbol{y} \tag{13.86}$$

where r_0 is the mean value of the distance between the sources and the observer.

13.2.10.3 Sound and Pseudo-sound

Pressure fluctuations are not due to the sole acoustic mode, since vortical fluctuations also generate pressure fluctuations. While acoustic waves propagate at the speed of sound with respect to the fluid, hydrodynamic pressure fluctuations are advected at local fluid velocity. Therefore, one must distinguish between acoustic and hydrodynamic pressure fluctuations. The former constitute the *sound* while the later are responsible for the *pseudo-sound*, which is also received by the observer.

A theoretical and practical issue is to find a way to separate them in a fully general and accurate way. By applying a time Fourier transform to (13.85), one can get a deeper insight into the noise generation mechanisms. The resulting expression is

$$\hat{\rho}(\boldsymbol{x}, \omega) = -\frac{\exp(\imath\omega x/a_\infty)}{4\pi a_\infty^4 x}\omega^2 \hat{T}_{rr}\left(\boldsymbol{k} = \frac{\omega}{a_\infty}\frac{\boldsymbol{x}}{x}, \omega\right) \tag{13.87}$$

where the space-time Fourier transform is defined as

$$\hat{f}(\boldsymbol{k}, \omega) = \int f(\boldsymbol{y}, t) e^{-\imath(\boldsymbol{k}\cdot\boldsymbol{y} - \omega t)} d^3\boldsymbol{y} dt. \tag{13.88}$$

This expression emphasizes the fact that acoustic fluctuations are associated to the following *dispersion relation*

$$\omega = ka_\infty, \quad \boldsymbol{k} = k\frac{\boldsymbol{x}}{x}. \tag{13.89}$$

All pairs $(\omega, \boldsymbol{k})$ that do not satisfy this dispersion law are not associated to acoustic wave and therefore contribute to the pseudo-sound.

13.2.10.4 Application to the Noise Radiated by Isotropic Turbulence

This section is devoted to the analysis of the generation of noise by isotropic turbulence using Lighthill's analogy. For the sake of simplicity, the discussion is restricted to the case in which the uniform mean velocity field can be written as $\bar{\boldsymbol{u}} = (U_c, 0, 0)$.

The far field radiated noise is described via the normalized pressure autocorrelation function

$$R_{pp}(\boldsymbol{x}, \tau) = \frac{1}{\rho_\infty a_\infty} \overline{(p(\boldsymbol{x}, t) - p_\infty)(p(\boldsymbol{x}, t+\tau) - p_\infty)}. \tag{13.90}$$

The *acoustic intensity* is defined as $I(\boldsymbol{x}) = R_{pp}(\boldsymbol{x}, 0)$. Reminding that considering the equation of state for a perfect gas the pressure fluctuations, the density fluctuations and the entropy fluctuations are tied by the following relation

$$p' = a_\infty^2 \rho' + \frac{p_\infty}{c_v} s' \tag{13.91}$$

and considering cold flows in which entropy fluctuations are negligible, one obtains $p' = a_\infty^2 \rho'$. In this case, one can also describe radiated sound in an equivalent way using the density autocorrelation function:

$$R_{\rho\rho}(\boldsymbol{x}, \tau) = \frac{1}{\rho_\infty a_\infty^{-3}} \overline{(\rho(\boldsymbol{x}, t) - \rho_\infty)(\rho(\boldsymbol{x}, t+\tau) - \rho_\infty)}. \tag{13.92}$$

Also assuming that the Reynolds number is large and that the viscous acoustic source terms can be neglected, along with density fluctuations, the Lighthill source term simplifies as

$$T_{ij} \simeq \rho_\infty u_i u_j. \tag{13.93}$$

It is worth noting that using this simplification, the problem is now formally similar to the one of modeling the pressure in incompressible isotropic turbulence discussed in Sect. 4.9, the main difference being the change from the Green function of the Laplacian operator in the incompressible case to the one of the d'Alembertian operator in the compressible case with a finite speed of sound. Now using Eq. (13.85), one obtains the following far field approximation

$$R_{\rho\rho}(\boldsymbol{x},\tau)=\frac{\rho_\infty x_i x_j x_k x_l}{16\pi^2 a_\infty^5 x^6}\iint_{\mathcal{V}}\overline{\frac{\partial^2}{\partial t^2}u_i u_j(\boldsymbol{y}',t')\frac{\partial^2}{\partial t^2}u_i u_j(\boldsymbol{y}'',t'')}d^3\boldsymbol{y}'d^3\boldsymbol{y}'' \quad (13.94)$$

with

$$t'=t-\frac{|\boldsymbol{x}-\boldsymbol{y}''|}{a_\infty},\quad t''=t-\frac{|\boldsymbol{x}-\boldsymbol{y}''|}{a_\infty}+\tau. \quad (13.95)$$

For a statistically steady flow, the following equivalent expression can be used

$$R_{\rho\rho}(\boldsymbol{x},\tau)=\frac{\mathcal{A}}{x^2}\frac{\partial^4}{\partial\tau^4}\iiint_{\mathcal{V}}D_{ijkl}\mathcal{R}_{ijkl}(\boldsymbol{y},\boldsymbol{\zeta},t)\delta\left(t-\tau-\frac{\boldsymbol{y}\cdot\boldsymbol{\zeta}}{xa_\infty}\right)d^3\boldsymbol{y}d^3\boldsymbol{\zeta}dt, \quad (13.96)$$

where the directivity tensor D_{ijkl}, the amplitude factor A and the two-time two-point fourth-order velocity correlation tensor $\mathcal{R}_{ijkl}$ are expressed as

$$\mathcal{A}=\frac{1}{16\pi^2 a_\infty^5\rho_\infty},\quad D_{ijkl}=\frac{x_i x_j x_k x_l}{x^4} \quad (13.97)$$

and

$$\mathcal{R}_{ijkl}\left(\boldsymbol{y},\boldsymbol{\zeta},\tau+\frac{\boldsymbol{y}\cdot\boldsymbol{\zeta}}{xa_\infty}\right)\approx\overline{T_{ij}\left(\boldsymbol{y},t-\frac{|\boldsymbol{x}-\boldsymbol{y}|}{a_\infty}\right)T_{kl}\left(\boldsymbol{y}+\boldsymbol{\zeta},t-\frac{|\boldsymbol{x}-\boldsymbol{y}|}{a_\infty}+\tau\right)} \quad (13.98)$$

where the Fraunhofer approximation for retarded time is used:

$$t-\frac{|\boldsymbol{x}-\boldsymbol{y}|}{a_\infty}\simeq t-\frac{x}{a_\infty}+\frac{\boldsymbol{x}\cdot\boldsymbol{y}}{xa_\infty}. \quad (13.99)$$

13.2.10.5 Effects Due to the Advection by the Mean Flow

To further refine the analysis one must account for the advection of the turbulent fluctuations/sources by the mean flow. For the sake of simplicity, we restrict ourselves to the case in which all fluctuations are advected at the same uniform speed $U_c\boldsymbol{e}_x$. Now writing the problem in a frame of reference moving with the large scale fluctuations, one has (FfwocsWilliams 1963):

$$R_{\rho\rho}(\boldsymbol{x},\tau)=\frac{\mathcal{A}}{x^2}\frac{1}{C^5}\iiint_{\mathcal{V}}D_{ijkl}\frac{\partial^4}{\partial t^4}R_{ijkl}(\boldsymbol{y},\boldsymbol{\xi},t)\delta\left(t-\frac{\tau}{C}\right)d^3\boldsymbol{y}d^3\boldsymbol{\xi}dt \quad (13.100)$$

with

$$\mathcal{R}_{ijkl}(\boldsymbol{y},\boldsymbol{\zeta},t)=R_{ijkl}(\boldsymbol{y},\boldsymbol{\zeta}-U_c t\boldsymbol{e}_x,t)=R_{ijkl}(\boldsymbol{y},\boldsymbol{\xi},t). \quad (13.101)$$

The *Doppler factor* is given by:

$$C = C(M_c, \theta) = \sqrt{(1 - M_c \cos\theta)^2 + \alpha^2 M_c^2} \tag{13.102}$$

where $M_c = U_c/a_\infty$ is referred to as the *convective Mach number* defined as the ratio between the advection speed of energetic turbulent large scales and the speed of sound, θ is the angle between the direction of the mean velocity field, $\boldsymbol{e}_x$, and the direction of the observer seen from the source, $\boldsymbol{r} = \boldsymbol{x} - \boldsymbol{y}$, and

$$\alpha^2 M_c^2 = \frac{4\pi L_u^2}{\tau_u^2 a_\infty^2}. \tag{13.103}$$

Here, L_u and τ_u denote an integral length scale and integral time scale of turbulence, respectively.

Equation (13.100) shows that the Doppler $C(M_c, \theta)$ has a very strong influence on the far field radiated noise, since radiated acoustic intensity scales as $1/C^5$. This factor introduces non-uniform *directivity*, i.e. the radiated acoustic intensity depends on the angle θ.

The advection of turbulent sources at speed U_c also induces another phenomenon: the range of scales that contribute to far field acoustic field also depends on θ. This can be understood reminding that acoustic waves received by the observer are characterized by the dispersion relation $\omega = a_\infty k$, which defines the *sonic line* in Fig. 13.11. In spectral space, a non-zero advection velocity U_c leads to the fact that the Lighthill source term is maximum when $\omega = \boldsymbol{k} \cdot U_c \boldsymbol{e}_x = k U_c \cos\theta$, where $U_c \cos\theta$ is the advection speed of fluctuations seen by the observer.

This relation defines the *convection line* in Fig. 13.11, on which $\hat{T}_{rr}(\boldsymbol{k}, \omega)$ is centered.

Therefore, fluctuations that will contribute to the acoustic intensity measured by the observer are those that fulfill both relations at the same time, i.e. when the advection speed seen by the observer is equal to the speed of sound. From a geometrical standpoint, the part of $\hat{T}_{rr}(\boldsymbol{k}, \omega)$ that efficiently contributes to the far field noise is the one located close to the sonic line in the wavenumber-frequency plane (k, ω), as illustrated in Fig. 13.11.

One may distinguish between two cases:

- *The subsonic case* (i.e. $U_c < a_\infty$): the convection line is always located under the sonic line. For all values of θ, radiating sources are mainly large scale turbulent structures and the radiated noise will exhibit a very strong low-frequency component. The maximum contribution of small scale turbulent motion is observed for $\theta = \pi/2$.
- *The supersonic case* (i.e. $U_c \geq a_\infty$): the convection line is above the sonic line for $\theta = \pi/2$. For small values of the angle θ, only large scale coherent fluctuations contribute to the far field noise, in a similar way to the subsonic case. But there exist a critical angle θ_0 such that $\cos\theta_0 = 1/M_c$ for which the convection line and the sonic line are identical. In this case, all coherent turbulent fluctuations at all

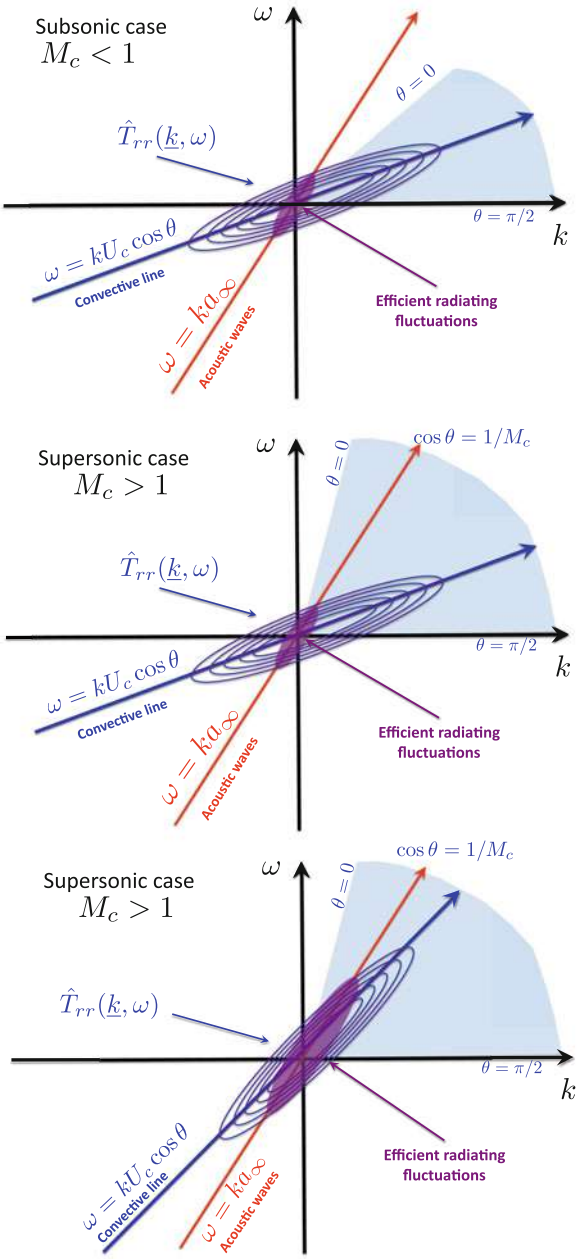

Fig. 13.11 Analysis of the radiated noise in the case where turbulent fluctuations are advocated at the uniform speed U_c with respect to the observer. Top: subsonic case ($U_c < a_\infty$); Middle: supersonic case ($U_c \geq a_\infty$) at an angle far from the critical angle θ_0; Bottom: supersonic case ($U_c \geq a_\infty$) at an angle close to the critical angle $\theta \simeq \theta_0$

scales efficiently radiate acoustic waves, leading to a broadening of the spectrum of the radiated noise. The radiated waves are referred to as *Mach waves*. This also holds for $\theta \sim \theta_0$, with a maximum acoustic radiation at angle θ_0. The directivity phenomenon is more important in the supersonic case than in the subsonic case.

13.2.10.6 Modelling of Turbulent Self-noise

It is necessary to model the fourth-order velocity correlation tensor $R_{ijkl}(\boldsymbol{y}, \boldsymbol{\xi}, t)$ to obtain a fully explicit expression for the radiated noise. The model retained here is exactly the same as for the evaluation of the pressure in the incompressible case discussed in Sect. 4.9. Thanks to the Quasi-Normal hypothesis, the fourth-order correlations are expressed as a combination of two-point two-time second-order correlations. The latter are modeled using the local isotropy hypothesis and also on the assumptions that the flow is statistically steady and that space and time variable can be separated, yielding

$$R_{ij}(\boldsymbol{y}, \boldsymbol{\xi}, \tau) = \frac{2}{3}\mathcal{K}\left(\left[f + \frac{1}{2}\xi\frac{df}{d\xi}\right]\delta_{ij} - \frac{1}{2}\frac{df}{d\xi}\frac{\xi_i\xi_j}{\xi^2}\right)G(\tau), \tag{13.104}$$

where $\mathcal{K}$ denotes the turbulent kinetic energy, f is the longitudinal velocity correlation function and $G(\tau)$ is the velocity time autocorrelation function. It must be emphasized that both f and G are unknown functions, which are open research topics. To obtain a closed reliable expression, it is often assumed that f is a Gaussian function (Ribner 1963):

$$f(\xi) = e^{-\pi\xi^2/L_u^2} \tag{13.105}$$

where L_u is the integral length scale of turbulence. Several expressions have been proposed for $G(\tau)$, among which

$$G(\tau) = \begin{cases} e^{-4\pi^2\tau^2/\tau_u^2} & \text{(Ribner 1963)} \\ \frac{1}{\cosh(2\pi\beta\tau/\tau_u)} & \text{(Bailly et al. 1997)} \end{cases} \tag{13.106}$$

where τ_u denotes the integral time scale of turbulence and $\beta \sim 2/5$ looking at experimental data. It is worth noting that more complex models for space-time velocity correlations $R_{ij}(\boldsymbol{y}, \boldsymbol{\xi}, \tau)$ might be used to evaluate the noise source term, starting from the space-time correlation models discussed in Sects. 4.3.4, 4.3.5 and 13.2.7, but more complex models would prevent a complete analytical integration.

The analytical analysis can be further continued assuming that all statistical quantities related to the turbulent field are uniform in a domain whose volume is equal to L_u^3. Under that assumption the integration with respect to $\boldsymbol{\xi}$ can be performed analytically, yielding the following expression for acoustic intensity:

$$I(\boldsymbol{x}) = \underbrace{\frac{\mathcal{A}\rho_\infty^2}{x^2}\int_{\mathcal{V}} \frac{2L^6\mathcal{K}^2}{9\sqrt{2}C^5}\frac{d^4G^2}{d\tau^4}(0)d^3\boldsymbol{y}}_{\text{self noise}}. \tag{13.107}$$

Dimensional analysis yields the following scaling laws:

$$I(\boldsymbol{x}) \propto \frac{a_\infty^3}{\rho_\infty}\rho_\infty^2\left(\frac{\sqrt{\mathcal{K}}}{a_\infty}\right)^8\left(\frac{L_u}{r}\right)^2 = \rho_\infty M_t^5\sqrt{\mathcal{K}}^3\left(\frac{L_u}{r}\right)^2 \tag{13.108}$$

where $M_t = \sqrt{\mathcal{K}}/a_\infty$ is the turbulent Mach number.

Providing an analytical model for $G(\tau)$ also enables to obtain an expression for the radiated acoustic pressure spectrum. Applying the Fourier transform to (13.100), it comes:

$$\hat{R}_{\rho\rho}(\boldsymbol{x},\omega) = \frac{\mathcal{A}}{x^2}\int_{\mathcal{V}}\hat{S}_{\text{self}}(\boldsymbol{y},\omega)d\boldsymbol{y} \tag{13.109}$$

where, according to Bailly's formula for $G(\tau)$

$$\hat{S}_{\text{self}}(\boldsymbol{y},\omega) = \frac{4\rho_\infty^2L^3\mathcal{K}^2}{9\sqrt{2}\beta\tau_u}\omega^4\frac{C\omega\tau_u/4\beta}{\sinh(C\omega\tau_u/4\beta)}. \tag{13.110}$$

This model is very accurate for subsonic mean flows. Its accuracy diminishes for $\theta \in [\pi/2, \pi]$, i.e. to predict the radiated acoustic intensity in the downstream direction when M_c is close or larger than 1. The main reason for that loss of accuracy is that the Lighthill analogy relies on the hypothesis that acoustic waves propagate in a medium at rest, which is unrealistic is this case. Another weakness is also observed in the supersonic case $M_c > 1$: for θ close to θ_0, further refined hypotheses must be used to account for Mach wave radiations. A last weakness is that the model does not account for the possible existence of shock waves.

13.2.11 Noise Scattering by Isotropic Turbulence

Wave propagation across random and/or turbulent media has been investigated by many authors (e.g. see Tatarski 1967 for a detailed discussion including electromagnetic waves), sound propagation across turbulence being among the most addressed issue. The emphasis is put below on Howe's theory (Howe 1973), which accounts for (i) scattering of sound by spatial fluctuations of turbulence, (ii) spectral broadening of turbulence, also referred to as *turbulent diffusion of sound* induced by time fluctuations of turbulent eddies and (iii) the net transfer of energy from the acoustic field to turbulence.

These phenomena represent new couplings between vortical and acoustic modes. Here, acoustic waves are not generated by turbulence, but they propagate across a

volume filled by isotropic vortical turbulence.[11] This phenomena can be modeled via the Lighthill analogy (Lighthill 1953; Ford and Meecham 1960), considering that velocity, pressure and density fields that appear in the right-hand side of Eqs. (13.79) and (13.81) come from the sum of the contributions of the base flow and the propagating acoustic field. Lighthill's theory for acoustic wave scattering by vortical events is another nonlinear statistical extension of the nonlinear Kovasznay decomposition discussed in Sect. 3.2.3.

13.2.11.1 Lighthill Modelling

Restricting the analysis to a quasi-isentropic turbulence, the main effects arise in the quadratic velocity terms, as for the noise production phenomena. Therefore, the Lighthill tensor can be written as

$$T_{ij} = \rho_0(u_i + v_i)(u_j + v_j) \tag{13.111}$$

where ρ_0, $\boldsymbol{u}$ and $\boldsymbol{v}$ denote the base flow density, the turbulent vortical velocity field and the acoustic wave velocity field, respectively. Quadrupolar source terms $\rho u_i u_j$ and $\rho v_i v_j$ are related to the production of noise by self-interactions of turbulence independently from the propagating acoustic wave (see the preceding section) and self-modification of the sound wave due to finite amplitude effects, respectively. The sound scattering by turbulence is related to cross-terms which can be referred to as scattering quadrupoles. The associated Lighthill tensor considered hereafter is given by

$$T_{ij} = \rho_0(u_i v_j + u_j v_i) \tag{13.112}$$

which can be further refined splitting the turbulent velocity field into its mean and fluctuating components, $u_i = \bar{u}_i + u'_i$:

$$T_{ij} = \rho_0(\bar{u}_i v_j + \bar{u}_j v_i) + \rho_0(u'_i v_j + u'_j v_i) = \bar{T}_{ij} + T'_{ij}. \tag{13.113}$$

The two components $\bar{T}_{ij}$ and T'_{ij} are related to refraction by the mean flow and refraction by turbulent fluctuations, respectively. In isotropic turbulence, one has $\bar{T}_{ij} = 0$.

13.2.11.2 Howe's Theory for Turbulent Multiple Scattering

The associated evolution equation for the density fluctuations associated to the propagating acoustic wave used by Howe is

[11] Self-sound generated by turbulence and incident sound are assumed to have very different frequency domains. As a matter of fact, the typical frequency of aerodynamic turbulent self-sound is $\sim u'/L$, with L the turbulent integral scale, and its wavelength is about L/M, where $M = u'/a_\infty$ denotes the turbulent Mach number.

$$\left(\frac{1}{a_\infty^2}\frac{\partial^2}{\partial t^2}-\nabla^2\right)\rho' = \frac{2\rho_\infty}{a_\infty^2}\frac{\partial^2}{\partial x_j \partial x_j}(u_i' v_j) + \frac{\overline{u_i' u_j'}}{a_\infty^2}\frac{\partial^2 \rho'}{\partial x_j \partial x_j}, \tag{13.114}$$

where the term related to noise generation has been omitted and the second order approximation $u_i' u_j' \rho' \sim \overline{u_i' u_j'}\rho'$ has been used. Based on that equation and using a two-scale decomposition, Howe derived a Lin-type (kinetic) equation for the spectrum $\beta(\boldsymbol{k}, \omega)$ of the Fourier coefficients of the incident acoustic field. This two-scale approach is based on the observation that when acoustic waves propagate across a random medium, non-propagating disturbances are generated whose typical length scale is of the order of the correlation length of the random medium, which is very different from the incident noise wavelength. These fluctuations are correlated with random medium/vortical turbulence fluctuations.

Assuming that

$$\beta(\boldsymbol{k}, \omega) = \mathcal{E}(\boldsymbol{k})\delta(k^2 - \omega^2/a_\infty^2) \tag{13.115}$$

the Lin-like equation reads

$$\left(\frac{\partial}{\partial t} + a_\infty \hat{\boldsymbol{k}}\cdot\nabla_x\right)\mathcal{E}(\boldsymbol{k}) = \frac{4\pi}{a_\infty k^2}\int_{-\infty}^{+\infty}\int \frac{(\boldsymbol{k}\cdot\boldsymbol{p})^2}{p^2} k_i k_j \hat{R}_{ij}(\boldsymbol{k}-\boldsymbol{p}, a_\infty k - \omega) \times \left[k\mathcal{E}(\boldsymbol{p}) - p\mathcal{E}(\boldsymbol{k})\right]\delta(k^2 - \omega^2/a_\infty^2) d^3\boldsymbol{p} d\omega, \tag{13.116}$$

where $\hat{\boldsymbol{k}} = \boldsymbol{k}/k$ and $\hat{R}_{ij}(\boldsymbol{k}, \omega)$ is related to the wave number-frequency spectral correlation tensor of the vortical turbulent fluctuations. It is important to notice that this term frequency-dependent, being interchanges of energy between the acoustic field and the ambient turbulent field can occur. As a consequence, it is not possible to derive an acoustic energy conservation equation in the general case.

The integro-differential equation (13.116) can be simplified to get a diffusion equation, restricting the analysis to short acoustic waves such that $Lk/M \gg 1$. For such waves, the right hand side term in (13.116) can be approximated observing that only terms involving $E(k, a_\infty(k-p))$ will have significant contributions. Expanding the remaining terms about $\boldsymbol{p} = \boldsymbol{k}$, one obtains after cumbersome algebra:

$$\left(\frac{\partial}{\partial t} + a_\infty \frac{\partial}{\partial x_\parallel}\right)\mathcal{E}(\boldsymbol{k}) = \underbrace{-\frac{12Lu'^2}{a_\infty \ell^2}\mathcal{E}(\boldsymbol{k})}_{\text{transfer}} + \underbrace{\frac{12Lku'^2}{a_\infty \ell^2}\frac{\partial}{\partial k_\parallel}\mathcal{E}(\boldsymbol{k})}_{\text{spectral drift}} + \underbrace{\frac{2Lk^2u'^2}{a_\infty \ell^2}\frac{\partial^2}{\partial k_\parallel^2}\mathcal{E}(\boldsymbol{k})}_{\text{broadening}} + \underbrace{\frac{k^2 u'^2}{2a_\infty \Delta}\nabla_\perp^2 \mathcal{E}(\boldsymbol{k})}_{\text{scattering}}, \tag{13.117}$$

where Δ is the turbulence lengthscale defined as

$$\frac{1}{\Delta} = \frac{\pi}{2u'^2}\int_0^{+\infty} kE(k)dk$$

and parallel and perpendicular components are defined with respect to $\boldsymbol{k}$. The lengthscale $\ell = a_\infty \tau$ is related to the two-point correlation time τ which is such that the two-point two-time kinetic energy spectrum of turbulence is given by

$$E(k, \omega \to 0) = \frac{\tau}{2\sqrt{\pi}} E(k) e^{-\omega^2\tau^2/4}. \tag{13.118}$$

The first term in the right hand side of Eq. (13.117) is negative. It represents the transfer of kinetic energy from acoustic waves to vortical turbulence. The second term is related to a steady drift in wavenumber space in the direction of $\boldsymbol{k}$. The last two terms represent the diffusion of acoustic energy in wavenumber space. The coefficient of the first one (parallel diffusion) vanishes in the case of frozen turbulence, i.e. when $\ell \to +\infty$. This term is associated to length dilatation of $\boldsymbol{k}$, i.e. for the spectral broadening of the acoustic spectrum. The second term, related to perpendicular second-order derivatives, describes rotation of vectors in the wavenumber space, i.e. scattering of acoustic waves.

13.2.11.3 Single Scattering Asymptotics

The previous theory is referred to as a *multiple scattering theory*, since it does not rely on any assumption about the loss of coherence of the acoustic waves due to scattering effects. This theory can be simplified if the characteristic size of the volume occupied by turbulence and the correlation scale of inhomogeneities are small compared to the acoustic wave length and that the amplitude of the turbulent fluctuations are small enough. In this case, the coherence of the acoustic waves is preserved, and a single scattering theory can be used (Lighthill 1953; Ford and Meecham 1960).

A first way to simplify multiple scattering theory is to assume that temporal variations of vortical fluctuations are negligible during the time of passage of an incident acoustic wave, leading to the use of the frozen turbulence hypothesis. In that case, one has $\hat{R}_{ij}(\boldsymbol{k}, \omega) = \hat{R}_{ij}(\boldsymbol{k})\delta(\omega)$ and Eq. (13.116) simplifies as

$$\left(\frac{\partial}{\partial t} + a_\infty \hat{\boldsymbol{k}} \cdot \nabla_x\right) \mathcal{E}(\boldsymbol{k}) = \frac{4\pi}{a_\infty k^3} \int (\boldsymbol{k}\cdot\boldsymbol{p})^2 k_i k_j \hat{R}_{ij}(\boldsymbol{k}-\boldsymbol{p}) \times \left[\mathcal{E}(\boldsymbol{p}) - \mathcal{E}(\boldsymbol{k})\right] \delta(p^2 - k^2) d^3\boldsymbol{p}. \tag{13.119}$$

The symmetry of the integrand in the right hand side shows that acoustic energy is now conserved, while it is not in the general case.

Single scattering allows for a deeper analytical analysis. Considering an acoustic beam made of a wave packet of wavenumber $\boldsymbol{k}_0$, one has

$$\frac{d}{dt}\mathcal{E}(\boldsymbol{k}_0) = \frac{4\pi}{a_\infty k_0^3}\int (\boldsymbol{k}_0\cdot\boldsymbol{p})^2 k_{0i}k_{0j}\hat{R}_{ij}(\boldsymbol{k}_0-\boldsymbol{p}) \times\left[\mathcal{E}(\boldsymbol{p})-\mathcal{E}(\boldsymbol{k}_0)\right]\delta(p^2-k_0^2)d^3\boldsymbol{p}. \tag{13.120}$$

The acoustic energy is mostly concentrated at wave vector $\boldsymbol{k}_0$ at initial time. Therefore one can assume that $\mathcal{E}(\boldsymbol{p}) \ll \mathcal{E}(\boldsymbol{k}_0)$ if $\boldsymbol{p} \neq \boldsymbol{k}_0$, leading to

$$\frac{d}{dt}\mathcal{E}(\boldsymbol{k}_0) = -a_\infty \Gamma \mathcal{E}(\boldsymbol{k}_0), \tag{13.121}$$

where the fraction of energy of the incident wave lost per unit length traversed by the wave packet, Γ, is given by

$$\Gamma = \frac{4\pi}{a_\infty k_0^3}\int (\boldsymbol{k}_0\cdot\boldsymbol{p})^2 k_{0i}k_{0j}\hat{R}_{ij}(\boldsymbol{k}_0-\boldsymbol{p})\delta(p^2-k_0^2)d^3\boldsymbol{p}. \tag{13.122}$$

This approximation is accurate if the acoustic wavelength is long compared with the integral scale of turbulence.

The scattered field is recovered considering wave vectors $\boldsymbol{k} \neq \boldsymbol{k}_0$. For small propagation distances the dominant contribution in the integrand comes from the part of $\mathcal{E}(\boldsymbol{k})$ due to incident waves, leading to

$$\left(\frac{\partial}{\partial t} + a_\infty \hat{\boldsymbol{k}}\cdot\nabla_x\right)\mathcal{E}(\boldsymbol{k}) = \frac{2\pi I_0}{a_\infty k_0^4}(\boldsymbol{k}_0\cdot\boldsymbol{k})^2 k_i k_j \hat{R}_{ij}(\boldsymbol{k}-\boldsymbol{k}_0)\delta(k-k_0) \tag{13.123}$$

where I_0 is such that the acoustic beam spectrum is given by

$$\mathcal{E}(\boldsymbol{k}) = I_0\delta(\boldsymbol{k}-\boldsymbol{k}_0). \tag{13.124}$$

The latter formula yields an unbounded growth of the scattered field, which is not physical for long propagation distances. As a consequence, this approximation is not relevant for high frequency/short wave length acoustic waves. In the limit of high frequencies, the multiple scattering theory is found to be consistent with the theory of geometrical acoustics, which is beyond the scope of the present book. More results originating in the single scattering theory can be found, e.g. Lighthill (1953), Ford and Meecham (1960), which will not be given here for the sake of brevity.

13.3 Low-Mach Thermal Régimes

The analysis of the quasi-acoustic régime presented above relies on the assumption that the density and the temperature fluctuations are governed by acoustic waves. This analysis can be extended by considering flows in which the density and temperature fluctuations are much larger than those induced by the acoustic fluctuations. In such flows, the asymptotic analysis presented in the preceding section is no longer valid and must be extended to describe the low-Mach thermal régime.

13.3.1 Asymptotic Analysis and Possible Thermal Régimes

The low-Mach thermal régime has been investigated by several authors, who proposed leading-order compressible corrections to the true incompressible Navier–Stokes equations. The discussion presented below put the emphasis on the results of Bayly and coworkers (1992) and Zank and Matthaeus (1990, 1991).

The complexity of the problem is easily understood recalling that the incompressible Navier–Stokes dynamics is recovered as the limit of the compressible Navier–Stokes equations when two small parameters are taken equal to zero: a first one, δ, related to the ratio of the fluid velocity about the speed of sound (i.e. a characteristic Mach number) and a second one, δ', related to ratio of thermal energy scales. Therefore, the problem of the relative size of these two small parameters arise when the leading-order correction to the incompressible Navier–Stokes equations is sought. Let us anticipate the discussion given below to say that several régimes can be obtained, depending on the ratio of these two control parameters.

The first step consists in non-dimensionalizing the full compressible Navier–Stokes equations and introducing the two small parameters. The resulting system is Bayly et al. (1992):

$$\frac{\partial \rho}{\partial t} + \nabla \cdot (\rho \boldsymbol{u}) = 0, \tag{13.125}$$

$$\rho \left(\frac{\partial \boldsymbol{u}}{\partial t} + \boldsymbol{u} \cdot \nabla \boldsymbol{u} \right) = -\frac{1}{\delta^2} \nabla p + \frac{1}{Re} \nabla \cdot \boldsymbol{\tau} + \rho \boldsymbol{f}, \tag{13.126}$$

$$\rho c_p \left(\frac{\partial T}{\partial t} + \boldsymbol{u} \cdot \nabla T \right) = \sigma \alpha T \left(\frac{\partial p}{\partial t} + \boldsymbol{u} \cdot \nabla p \right) + \frac{1}{2} \frac{\delta^2}{Re} \boldsymbol{\tau} : \boldsymbol{\tau} + \frac{1}{Re\, Pr} \nabla \cdot (\kappa \nabla T) + \delta' \rho q, \tag{13.127}$$

where $Re = L_r u_r \rho_r / \mu_r$ and $Pr = \mu_r c_p / \kappa_r$ are the Reynolds number and Prandtl number, respectively. α denotes the thermal expansion parameter, and $\sigma \equiv T_r \alpha_r$. The subscript r is related to reference scales. The system is supplemented by the perfect gas law (3.4). The characteristic speed u_r is associated to fluid velocity, and a

reference thermal speed $v_r = \sqrt{c_p T_r}$ is introduced. The reference pressure is defined as $p_r = \rho_r v_r^2$. Here, q is a non-dimensional thermal forcing term which accounts for the presence of heat sources/sinks in the flow (e.g. reactive flows). The two small parameters are defined as follows

$$\delta \equiv \frac{u_r}{v_r} = \sqrt{\gamma - 1} M_r, \quad \delta' \equiv \frac{q_r}{v_r^2} \tag{13.128}$$

where $M_r = u_r / a_r$ is the usual reference Mach number and q_r is a characteristic heat production scale.

The existence of these two scaling parameters yields a formal double expansion problem, whose treatment is cumbersome. The avoid such a complex development, Bayly and coworkers set $\delta' = \delta^{2/l}$ where l is a positive integer. Using this relationship, all dynamic quantities are expanded in asymptotic series of the form (here expressed for a dummy variable ϕ):

$$\phi = \phi^{(0)} + \delta^{2/l} \phi^{(1)} + \delta^{4/l} \phi^{(2)} + ... \tag{13.129}$$

Assuming that the fluid fluctuates close to the reference state, the zeroth-order terms for density and temperature must have their values for that state, yielding $\rho^{(0)} = T^{(0)} = 1$. An immediate consequence of the perfect gas law is that the zeroth-order pressure term $p^{(0)}$ also corresponds to a uniform field. Therefore, the leading order fluctuating field which accounts for the weak compressible thermal turbulence is made of $\boldsymbol{u}^{(0)}$, $\rho^{(1)}$, $T^{(1)}$ and $p^{(1)}$.

Two cases can be defined, which correspond to different thermal régimes:

(i) *Relatively small external heating* with respect to both the viscous heating and the pressure-induced temperature fluctuations: $l = 1$. In this case, the lowest-order nontrivial equations are

$$\nabla \cdot \boldsymbol{u}^{(0)} = 0, \tag{13.130}$$

$$\frac{\partial \boldsymbol{u}^{(0)}}{\partial t} + \boldsymbol{u}^{(0)} \cdot \nabla \boldsymbol{u}^{(0)} = -\nabla p^{(1)} + \frac{1}{Re} \nabla^2 \boldsymbol{u}^{(0)}, \tag{13.131}$$

$$\frac{\partial T^{(1)}}{\partial t} + \boldsymbol{u}^{(0)} \cdot \nabla T^{(1)} = \sigma \left(\frac{\partial p^{(1)}}{\partial t} + \boldsymbol{u}^{(0)} \cdot \nabla p^{(1)} \right) + \frac{1}{2Re} \boldsymbol{\tau}^{(0)} : \boldsymbol{\tau}^{(0)} + \frac{1}{RePr} \nabla^2 T^{(1)} + q, \tag{13.132}$$

supplemented by the linearized equation of state

$$p^{(1)} = \frac{\gamma - 1}{\gamma} \left(\rho^{(1)} + T^{(1)} \right). \tag{13.133}$$

These equations must be interpreted as the incompressible Navier–Stokes equations for $\boldsymbol{u}^{(0)}$ and $p^{(1)}$ supplemented by a passive scalar equation for $T^{(1)}$ with several source terms. Therefore, the fluctuating pressure is completely determined up to an additive function of time through the relation

$$\nabla^2 p^{(1)} = -\nabla \cdot \nabla \cdot (\boldsymbol{u}^{(0)}\boldsymbol{u}^{(0)}) + \nabla \cdot \boldsymbol{f} \tag{13.134}$$

The time evolution of the density perturbation is deduced from Eqs. (13.132)–(13.134).

(ii) *Strong external heating*: $l \geq 2$. In this case, the lowest-order non-trivial system is

$$\nabla \cdot \boldsymbol{u}^{(0)} = 0, \tag{13.135}$$

$$\frac{\partial \boldsymbol{u}^{(0)}}{\partial t} + \boldsymbol{u}^{(0)} \cdot \nabla \boldsymbol{u}^{(0)} = -\nabla p^{(l)} + \frac{1}{Re}\nabla^2 \boldsymbol{u}^{(0)}, \tag{13.136}$$

$$\frac{\partial T^{(1)}}{\partial t} + \boldsymbol{u}^{(0)} \cdot \nabla T^{(1)} = \frac{1}{RePr}\nabla^2 T^{(1)} + q, \tag{13.137}$$

and

$$\rho^{(1)} + T^{(1)} = 0. \tag{13.138}$$

The leading-order pressure fluctuation is given by

$$\nabla^2 p^{(l)} = -\nabla \cdot \nabla \cdot (\boldsymbol{u}^{(0)}\boldsymbol{u}^{(0)}). \tag{13.139}$$

Here again the system appears to be composed of the incompressible Navier–Stokes equations supplemented by a passive scalar equation. The latter is simpler than in the weak heating case, since pressure-induced and viscous dissipation induced temperature fluctuations are now negligible. An important difference with the previous case is that the density fluctuations are now totally enslaved to the temperature fluctuations, and are anti-correlated.

These developments are consistent with the presence of acoustic modes of order δ^2. The first dilatational correction to the velocity field is $\boldsymbol{u}^{(1)}$.

13.3.2 Statistical Equilibrium States

We now discuss the features of the statistical equilibrium states associated with the two weakly compressible thermal models discussed above. For these models, no exact analytical solutions can be found, and the analysis will be restricted to the properties of the inertial ranges of the spectra of the fluctuating quantities in a fully developed turbulent isotropic flow. In both cases, the kinetic energy spectrum and

the pressure spectrum are expected to be the same as in incompressible isotropic turbulent flows. Corresponding inertial range scalings are $E_{ss}(k) \propto k^{-5/3}$ for the former and $E_{pp}(k) \propto k^{-7/3}$ for the latter.

In the strong heating case, the temperature fluctuations obey the passive scalar equation. Assuming that the external heating acts at relatively large scales and neglecting conduction effects, one obtains the usual scaling law for the temperature spectrum $E_{TT}(k) \propto k^{-5/3}$. Since the density and temperature fluctuations are anticorrelated, they have the same spectrum, yielding $E_{\rho\rho}(k) \propto k^{-5/3}$.

In the weak heating case, it must be remembered that entropy behaves as a passive scalar and therefore exhibits the usual scaling law in the inertial range $E_s(k) \propto k^{-5/3}$. The leading-order entropy fluctuation is given by

$$s^{(1)} = T^{(1)} - p^{(1)}. \tag{13.140}$$

Comparing the spectral slopes of the entropy spectrum and the pressure spectrum, one can see that the temperature fluctuations must overwhelm the pressure fluctuations at small scales to recover a $-5/3$ slope for the entropy spectrum, leading to $E_{TT}(k) \propto k^{-5/3}$ As a consequence, in the inertial range, density fluctuations will also be governed by temperature fluctuations, leading to $E_{\rho\rho}(k) \propto k^{-5/3}$.

It is seen that both régimes lead to the same scaling laws for the inertial range spectra. But it is worth noting that these scaling laws differ from those obtained for a quasi-isentropic flow, in which $E_{\rho\rho}(k) \propto k^{-7/3}$.

13.3.3 Numerical Observations

The existence of the different régimes and the related turbulent statistical equilibrium states predicted by the theoretical analysis have been checked through numerical experiments (Bayly et al. 1992; Cai et al. 1997).

The main observations are summarized below

(i) Both weak ($l = 1$) and strong ($l = 2$) external heating régimes can be reproduced in numerical simulations, and are stable if consistent initial conditions are prescribed.

(ii) The anti-correlation between density and pressure fluctuations is observed for almost incompressible initial conditions ($\chi(0) = 0$) at relatively low initial turbulent Mach numbers ($M_t \leq 0.3$). In other cases, the growth of the acoustic mode scrambles the correlation.

(iii) In freely decaying turbulence with consistent initial conditions, the asymptotic régime, i.e. the value of l at the final stage of the simulation, depends on the Prandtl number. For low values of the Prandtl ($Pr \leq 1$) the density fluctuations are observed to decay until the $l = 1$ régime is encountered. For larger values of the Prandtl number, states with $l \geq 2$ are observed.

(iv) If initial conditions are not fully consistent with the governing equations, the pressure fluctuations are observed to grow very quickly, corresponding to a transfer of internal energy toward acoustic energy. The weakly compressible thermal régimes are then observed to bifurcate toward the pseudo-acoustic or the nonlinear subsonic régimes.

(v) Despite it was derived neglecting heat conduction effect, the weak equilibrium relation $\mathcal{F}(t) = 1$ (in which is defined according to Eq. (13.33)) is observed to hold in simulations with large initial temperature fluctuations after a short transient phase. But the oscillations of $\mathcal{F}$ about 1 are much larger than in simulations with pseudo-acoustic initial conditions.

13.3.4 Isotropic Turbulence with Frictional Heating

A case of low-Mach number isotropic turbulence with a first coupling between turbulent kinetic energy and internal energy is isotropic turbulence with frictional heating (De Marinis et al. 2013; Bos 2014; Bos et al. 2015), in which turbulent dissipation of kinetic energy is retained as a source term in the temperature equation, but without feedback on the momentum equation. In this one-way coupling problem the dynamics the velocity field is assumed to be strictly incompressible and independent from the temperature field. Therefore, its dynamics is identical to the one described in Chap. 4. The turbulent frictional heating mechanisms addressed here correspond to the generation of entropy by vorticity mode self-interactions in Kovasznay's weakly non linear theory, see Sect. 3.2.3.

The temperature (or equivalently internal energy) equation (13.127) is now

$$\frac{\partial T}{\partial t} + u_i \frac{\partial T}{\partial x_i} = \kappa \frac{\partial^2 T}{\partial x_i \partial x_i} + \frac{\nu}{c_p} \left(\frac{\partial u_i}{\partial x_j} \frac{\partial u_i}{\partial x_j} + \frac{\partial u_i}{\partial x_j} \frac{\partial u_j}{\partial x_i} \right), \tag{13.141}$$

and the associated relations for the mean temperature $\bar{T}$ and temperature fluctuation variance $\overline{T'T'}$ in the isotropic case are

$$\frac{\partial \bar{T}}{\partial t} = \frac{\nu}{c_p} \overline{\frac{\partial u_i}{\partial x_j} \frac{\partial u_i}{\partial x_j}} = \frac{\varepsilon}{c_p}, \tag{13.142}$$

$$\frac{\partial \overline{T'T'}}{\partial t} = -2\kappa \overline{\frac{\partial T'}{\partial x_i} \frac{\partial T'}{\partial x_i}} + 2\frac{\nu}{c_p} \left(\overline{T' \frac{\partial u_i}{\partial x_j} \frac{\partial u_i}{\partial x_j}} + \overline{T'\varepsilon'} \right), \tag{13.143}$$

where the local instantaneous fluctuation of dissipation ε' is defined as

$$\varepsilon' \equiv \frac{\partial u_i}{\partial x_j} \frac{\partial u_j}{\partial x_i} - \overline{\frac{\partial u_i}{\partial x_j} \frac{\partial u_j}{\partial x_i}}.$$

The temperature spectrum $E_{TT}(k,t)$ such that the temperature variance and the rate of dissipation of the temperature variance are defined as

$$\overline{T'T'}(t) = \int_0^{+\infty} E_{TT}(k,t)dk, \quad \varepsilon_T(t) = 2\kappa \int_0^{+\infty} k^2 E_{TT}(k,t)dk, \tag{13.144}$$

is solution of the following Lin-like equation, which is straightforwardly derived from the equation for T':

$$\left(\frac{\partial}{\partial t} + 2\kappa k^2\right) E_{TT}(k,t) = P_T(k,t) + T_T(k,t), \tag{13.145}$$

where $P_T(k,t)$ and $T_T(k,t)$ denote the spectra of the frictional heating term and the convection-induced transfers, respectively. Both EDQNM and classical differential closures have been proposed for these two terms. While both approaches yield satisfactory results for the later, it is observed that EDQNM and other Gaussian-approximation-based approaches are not able to accurately account for frictional heating. This is due to the fact that, as seen in Eq. (13.143), the frictional heating originates in the correlation between fluctuations of temperature and fluctuations of dissipation. The later is known to exhibit a strong intermittency and therefore a large departure from Gaussianity. Therefore, a non-Gaussian model for this term should be used to recover a physical behavior. Numerical experiments show that other terms can be modeled in a classical way, i.e. by classical EDQNM or differential models.

Such a non-Gaussian model is proposed in Bos et al. (2015), in which the production spectrum is made proportional to the spectrum of fluctuations of dissipation $E_{\varepsilon'}(k,t)$ and a time scale $\tau(k)$:

$$P_T(k,t) = \frac{1}{c_p^2}\tau(k)E_{\varepsilon'}(k,t). \tag{13.146}$$

The latter stems from the combination of the correlation time of temperature fluctuations along a Lagrangian trajectory and the correlation time of the fluctuations of the dissipation rate. Since the correlation is mostly governed by large scales, it is relevant to use

$$\tau(k) \sim \varepsilon^{-1/3}k^{-2/3}(kL)^{\alpha}, \tag{13.147}$$

with L being the integral scale. For $\alpha = 0$ and $\alpha = 2/3$, one recovers the usual Lagrangian time scale of the Kolmogorov inertial range theory and the integral time scale, respectively. The non-Gaussian model for dissipation rate proposed by Yaglom yields[12]

[12]The Kolmogorov theory would yield the inaccurate expression

$$E_{\varepsilon'}(k,t) \sim \nu^2\varepsilon^{4/3}k^{5/3}.$$

$$E_{\varepsilon'}(k,t) \sim \varepsilon^2(t) L (kL)^{-1+\mu} \tag{13.148}$$

where $0.2 < \mu < 0.5$ is an intermittency parameter. Explicit expression of the temperature spectrum in different steady-state equilibrium cases and associated statistics can be obtained using the following differential model for $T_T(k,t)$, which has been observed to yield accurate results in many incompressible thermal isotropic turbulence configurations:

$$T_T(k) = \frac{\partial}{\partial k}\left(E_{TT}(k)\sqrt{k^5 E(k)}\right). \tag{13.149}$$

Considering inertio-convective range in which viscous diffusion can be neglected, one has $T_T(k) = P_T(k,t)$, leading to

$$E_{TT}(k) \sim \varepsilon^{-1/3} k^{-5/3} \int_{1/L}^{k} P_T(p)dp = \frac{\varepsilon^{4/3} L^{2/3} k^{-5/3}}{c_p^2}\left((kL)^{\mu+\alpha-2/3} - 1\right). \tag{13.150}$$

The associated scalings for the temperature variance and the destruction rate of the temperature variance are respectively

$$\overline{T'T'} \sim \int_{1/L}^{1/\eta} E_{TT}(k)dk \sim \begin{cases} \varepsilon\nu/c_p^2 & (\alpha = 0) \\ (\varepsilon L)^{4/3}/c_p^2 & (\alpha = 2/3) \end{cases} \tag{13.151}$$

and

$$\varepsilon_T \sim \int_{1/L}^{1/\eta} P_T(k)dk \sim \begin{cases} \varepsilon^{5/3} L^{2/3}/c_p^2 & (\alpha = 0) \\ \varepsilon^{5/3} L^{2/3} Re_L^{3\mu/4}/c_p^2 & (\alpha = 2/3). \end{cases} \tag{13.152}$$

DNS results at moderate Reynolds numbers show that the combination with $\alpha = 2/3$ and $\mu = 0.37$ yields an accurate model, but Finite Reynolds effects do not allow to conclude that $\alpha = 0$ should be discarded. But they clearly show that this non-Gaussian model is much more accurate than Gaussian ones, which totally fail to predict the inertial range behavior.

13.4 Nonlinear Subsonic Régimes

The two régimes discussed in Sects. 13.2 and 13.3 are expected to occur in the limit of nearly incompressible turbulence, i.e. $M_t \ll 1$. For turbulent Mach numbers lesser than unity but not negligible, M_t can no longer be used as a small parameter. Therefore, asymptotic analyses presented above are theoretically no longer valid, since one expects that the non-linearities arising from the convective terms will play a major role. Numerical simulations performed for both freely decaying and solenoidally forced isotropic turbulence show that two subsonic régimes may occur.

In the first one, corresponding to $M_t \leq 0.3 - 0.4$, dilatational effects are very small and the flow is very similar to low-Mach régimes discussed above. For larger values of M_t compressibility plays an very significant role. As a matter of fact, numerical simulations show that very small shocks, referred to as *shocklets* or *eddy-shocklets* develop.

13.4.1 A General View at the Nonlinear Subsonic Case

The occurence of the two nonlinear subsonic régimes in forced isotropic turbulence has been studied recently via Direct Numerical Simulation by Donzis and coworkers (2013), Jagannathan and Donzis (2016). Performing a set of simulations for a wide range of Re_λ (up to $Re_\lambda = 410$) and M_t (up to $M_t = 0.6$) with high resolution simulations with up to 2048^3 grid points, these authors have provided the most detailed results presently available in the open literature. Since forced turbulence reaches a statistically steady state that is nearly independent from the initial conditions, these results provide a very useful insight into compressibility effects on turbulence. Of course, they are sensitive on the forcing term used to sustain turbulence. Solenoidal forcing terms are used by most authors, since they are expected to give rise to compressibility effects induced by the sole nonlinear turbulence dynamics. Much stronger compressibility effects, including occurence of large-scale shock waves may be obtained if a non-solenoidal forcing is used, e.g. in Wang et al. (2013) where 1/3 of the energy is injected in $\boldsymbol{u}'_d$. Such results will be discussed in the section devoted to the supersonic régime.

A first result is that the classical turbulent scaling laws between characteristic scales are the same as for incompressible turbulence, e.g.

$$\eta \equiv \left(\frac{\bar{\mu}^3}{\bar{\rho}^2\bar{\varepsilon}}\right)^{1/4} \propto \lambda Re_\lambda^{-1/2} \propto L Re_\lambda^{-3/2},\ u_\eta \equiv \left(\frac{\bar{\mu}\bar{\varepsilon}}{\bar{\rho}^2}\right)^{1/4} \propto u' Re_\lambda^{-1/2},$$

at all considered M_t.

While the perfect gas law holds for instantaneous quantities, it must be supplemented by turbulent contributions when addressing the mean flow quantities. Applying Reynolds averaging, one obtains

$$\frac{\bar{p}}{R\bar{\rho}\tilde{T}} = 1 + \frac{\overline{\rho' T'}}{\bar{\rho}\tilde{T}} = 1 + \overline{\rho^\star T^\star},\ \rho^\star = \rho'/\bar{\rho},\ T^\star = T'/\tilde{T} \tag{13.153}$$

which can be fitted as

$$\frac{\bar{p}}{R\bar{\rho}\tilde{T}} \simeq 1 + \left(\frac{M_t}{1.97}\right)^4 \quad \text{or} \quad 1 + \left(\frac{M_t}{1.72}\right)^{4.5},\ 0.1 \leq M_t \leq 0.6. \tag{13.154}$$

The exact expression for the pressure fluctuation is

$$p' = R\left(\rho'\bar{T} + \bar{\rho}T' + \rho'T' - \overline{\rho'T'}\right) \tag{13.155}$$

from which one obtains straightforwardly the following exact expression for the normalized pressure variance $\mathcal{Y}$:

$$\mathcal{Y} = \frac{\overline{p'^2}}{\left(R\bar{\rho}\bar{T}\right)^2} = \overline{\rho^{\star 2}} + \overline{T^{\star 2}} + 2\overline{\rho^\star T^\star} + 3\overline{\rho^\star T^\star}^2 + \overline{\rho^{\star 2}T^{\star 2}} + 2\overline{\rho^{\star 2}T^\star} + 2\overline{\rho^\star T^{\star 2}}. \tag{13.156}$$

Numerical results show that only the first three terms in the right hand side are non-negligible. Using the mean speed of sound $\bar{a} = \overline{\sqrt{\gamma RT}}$ and assuming $\bar{a} \simeq \sqrt{\gamma\bar{p}/\bar{\rho}}$, one obtains the following theoretical scaling law

$$\mathcal{Y} = \frac{A^2\gamma^2}{9}M_t^4, \tag{13.157}$$

where $A = 1.2$ yields a good agreement with DNS data for $M_t \geq 0.3$. This scaling is similar to the one found in strictly incompressible flows, i.e. $\overline{p'^2} = A^2\bar{\rho}^2u'^4$, as discussed in Sect. 4.9. But a better match with numerical results is found considering a steeper scaling law, i.e. $\mathcal{Y} \propto M_t^{4.4}$ showing that dilatational effects lead to a departure from the incompressible scaling law. This is also illustrated by the fitting of other second-order correlations of thermodynamic quantities:

$$\overline{\rho^{\star 2}} \propto M_t^{4.3},\ \overline{T^{\star 2}} \propto M_t^{4.4},\ \overline{\rho^\star T^\star} \propto M_t^{4.5}. \tag{13.158}$$

An interesting fact is that, despite the flow is not isentropic, the following isentropic relations[13] are observed to fit data for $M_t \geq 0.3$:

$$\frac{\overline{\rho^{\star 2}}}{\overline{p^{\star 2}}} = \frac{1}{\gamma^2},\ \frac{\overline{T^{\star 2}}}{\overline{p^{\star 2}}} = \frac{(\gamma-1)^2}{\gamma^2},\ \frac{\overline{\rho^\star T^\star}}{\overline{p^{\star 2}}} = \frac{(\gamma-1)^2}{\gamma^2}. \tag{13.159}$$

It is important to note that this agreement with isentropic relations does not indicate that the flow exhibits an isentropic dynamics. This can be seen introducing the coefficient $\mathcal{B} = (p/\bar{p})^{(\alpha-\gamma)/\alpha}$. $\alpha = \gamma$, 1 and 0 is related to isentropic, isothermal and isobaric dynamics, respectively. A first-order Taylor series expansion yields

[13] Isentropic relations are obtained starting from

$$p/\bar{p} = (\rho/\bar{\rho})^\gamma = (T/\bar{T})^{\gamma/(\gamma-1)}$$

which leads to

$$\rho'^2 = \bar{\rho}^2((p/\bar{p})^{1/\gamma} - 1)^2 = (\bar{\rho}^2/\gamma^2)p^{\star 2} - (\gamma-1)(\bar{\rho}^2/\gamma^3)p^{\star 3} + O(p^{\star 4})$$

and to take averages after truncating the Taylor series expansion at the leading order.

$$\sqrt{\overline{\mathcal{B}'^2}} \simeq \frac{\gamma-\alpha}{\alpha}\sqrt{\overline{p^{\star 2}}} \simeq \frac{\gamma-\alpha}{\alpha}\frac{A\gamma}{3}M_t^2. \tag{13.160}$$

The best fit of DNS data is obtained for $\alpha = 1.2 \neq \gamma$ and $A = 1.2$, showing that non-isentropic dilatational effects are non-negligible for $M_t \geq 0.3$.

13.4.2 Statistical Equilibrium State and Scaling of Dilatational Components

Numerical simulations (Jagannathan and Donzis 2016) show that statistical equilibrium is reached in the nonlinear subsonic case after a short transient phase. The departure from the equilibrium solutions introduced during the discussion related to the low-Mach quasi-isentropic régime is measured introducing F_w and $F_s(k)$, that are defined as

$$F_w = \frac{\gamma^2 M_t^2 \chi \bar{p}^2}{\overline{p'_d p'_d}}, \; F_s(k) = \frac{\bar{\rho}^2 \bar{a}_2 E_{dd}(k)}{E_{pp}(k)}, \tag{13.161}$$

where p'_d denotes the dilatational pressure obtained thanks to an Helmholtz decomposition of the field and $E_{pp}(k)$ the associated 3D spectrum. Weak and strong acoustic equilibrium are recovered if $F_w = 1$ and $F_s(k) = 1 \; \forall k$, respectively.

In freely decaying turbulence, the statistical equilibrium state is very similar to the one observed in the quasi-acoustic régime: weak equilibrium is observed and Sarkar's function fluctuates almost periodically about unity due to energy exchanges between internal energy and the dilatational field. The period of oscillation corresponds to the characteristic acoustic time scale, and the amplitude is an increasing function of the Mach number.

The picture obtained in the forced turbulence case (with solenoidal forcing) is slightly different. As a matter of fact, F_w exhibits a very strong dispersion for $M_t \leq 0.3$ while a constant value slightly larger than one is obtained at higher M_t ($F_w \simeq 1.1$), showing that a weak equilibrium solution is reached which does not obey exact equipartition between solenoidal and dilatational modes. The lack of equilibrium at low Mach number in the forced case may be understood since the dilatational component has a very small energy, and that, due to the solenoidal forcing, couplings with the solenoidal component are very weak. In the freely decaying case, these couplings are much more important since they drive the flow at the beginning of the decay, leading to occurence of weak equilibrium. Strong equilibrium is observed on a limited range of scales at $M_t = 0.3$ while it is observed at all scales at $M_t = 0.6$, leading to the conclusion that it takes place in forced compressible turbulence as soon as dilatational modes are important.

The equilibrium solutions can be further analyzed looking at scaling laws for the dilatational component. Donzis' DNS results are summarized in Table 13.2. Evolution of ratio of the dilatational component to the solenoidal one versus M_t is displayed in Fig. 13.12.

Table 13.2 Scaling laws obtained for the dilatational component of the flow in the non-linear subsonic régime by DNS data fitting in isotropic turbulence with solenoidal forcing in the range $0.1 \leq M_t \leq 0.6$ (Jagannathan and Donzis 2016)

	$\bar{\varepsilon}_d/\bar{\varepsilon}_s$	$\mathcal{K}_d/\mathcal{K}_s$	λ_d/λ_s	$\sqrt{\overline{p_s^2}}/\bar{p}$	$\sqrt{\overline{p_d^2}}/\bar{p}$	$\sqrt{\overline{p_d^2}}/\sqrt{\overline{p_s^2}}$
$M_t \leq 0.3$	Negligibly small	$\propto M_t^4$	$\propto M_t^{-2}$	$\propto M_t^2$	$\propto M_t^4$	<0.1
$0.3 < M_t \leq 0.6$	$\propto M_t^{4.1}$	$\propto M_t^2$	$\propto M_t^{1.2}$	$\propto M_t^2$	$\propto M_t^2$	1

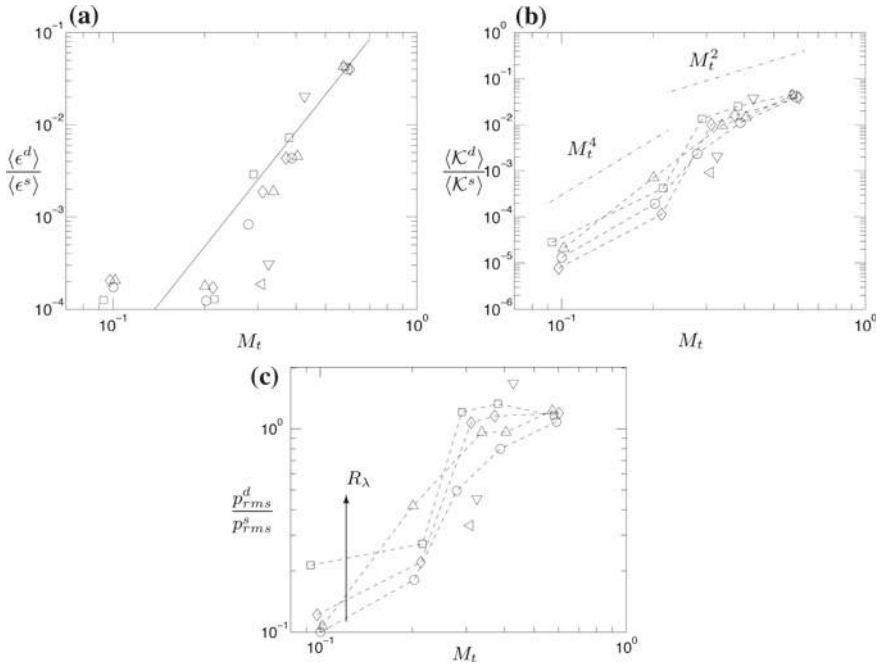

Fig. 13.12 Variation of the ratio $\bar{\varepsilon}_d/\bar{\varepsilon}_s$, $\mathcal{K}_d/\mathcal{K}_s$ and r.m.s of pressure fluctuations versus M_t in isotropic turbulence with solenoidal forcing. From Jagannathan and Donzis (2016) with courtesy of D. Donzis

It is observed that the scaling for the ratio of dilatational to solenoidal dissipation predicted by EDQNM in the quasi-isentropic régime is nearly recovered for $M_t \geq 0.3$ (with a slightly steeper exponent equal to 4.1 instead of 4, a difference which may be due to the fact the EDQNM does not account for the occurence of shocklets). This ratio cannot be accurately measured in DNS at lower M_t because it is too small. The EDQNM scaling for the kinetic energy ratio χ is recovered for $M_t \leq 0.3$. The amplification of dilatational kinetic energy for $M_t \geq 0.3$ is not predicted by EDQNM, showing that significant compressible processes are at play. The cross-correlation between the compressible and solenoidal pressure field is evaluated considering the decomposition of the full pressure variance:

$$\frac{\overline{p'^2}}{\bar{p}^2} = \frac{\overline{p_s'^2}}{\bar{p}^2} + \frac{\overline{p_d'^2}}{\bar{p}^2} + 2C_p \frac{\sqrt{\overline{p_s'^2}}}{\bar{p}} \frac{\sqrt{\overline{p_d'^2}}}{\bar{p}}. \tag{13.162}$$

A very satisfactory agreement with DNS data is found taking $C_p = -0.334\, M_t^2$ for $0.1 \leq M_t \leq 0.6$, showing that the two pressure components are anti-correlated.

13.4.3 Further Investigations of Thermodynamic Quantities

The non-linear subsonic regime can be further investigated looking at the probability density function of the pressure and its components. The general observation in freely decaying and solenoidally forced turbulence is that the pressure p.d.f. (see Fig. 13.13) is negatively skewed at low turbulent Mach number in a similar way to what is observed in the incompressible case and progressively becomes positively skewed as M_t increases. The p.d.f. exhibits a positive nearly Gaussian tail at low M_t and a negative nearly Gaussian tail at high M_t.

An intuitive explanation is that $\overline{p'^2}$ is a growing function of M_t, but that since it is a positive thermodynamical quantity, negative pressure fluctuations are bounded, $p' > -\bar{p}$, while positive fluctuations are not, leading to a progressive change in the p.d.f. shape. The far positive tail of the p.d.f. is observed to exhibit a log-normal character.

This result is further refined looking at the p.d.f.s of p_s' and p_d'. The p.d.f. of the solenoidal pressure field is observed to be almost independent of M_t and very similar to the incompressible case with a negative skewness. The p.d.f. of p_d has a negative part independent of M_t with a Gaussian shape, and becomes positively skewed for $M_t \geq 0.3$. Therefore the changes in the p.d.f. of p' originate in the combination of the change in the shape of the p.d.f. of p_d' and the increase of the relative amplitude of p_d'.

The density p.d.f. is observed to have a nearly Gaussian core with far tails obeying a log-normal distribution (see Fig. 13.13). This log-normal character is well observed for positive fluctuations $\rho' > 0$, while there is still a M_t dependence of the tail for $\rho' < 0$. An empirical explanation (Donzis and Jagannathan 2013) for the log-normal distribution of extreme events is that the Lagrangian solution to the mass conservation equation is $\rho(t) = \rho(0) \exp(-\int_0^t \nabla \cdot \boldsymbol{u} dt')$, showing long time evolution can be seen as a sum of independent random changes induced by uncorrelated shocklets and dilatation waves. Invocation of the central limit theorem then suggests the existence of a log-normal distribution. Such a rationale is valid only in a régime in which density fluctuations originate in shock and rarefaction waves only, i.e. in an asymptotic supersonic régime with $M_t \to +\infty$. In the subsonic régime other events like vortices or vortex sheets are also present and are responsible for the Gaussian distribution of weak fluctuations (Fig. 13.14).

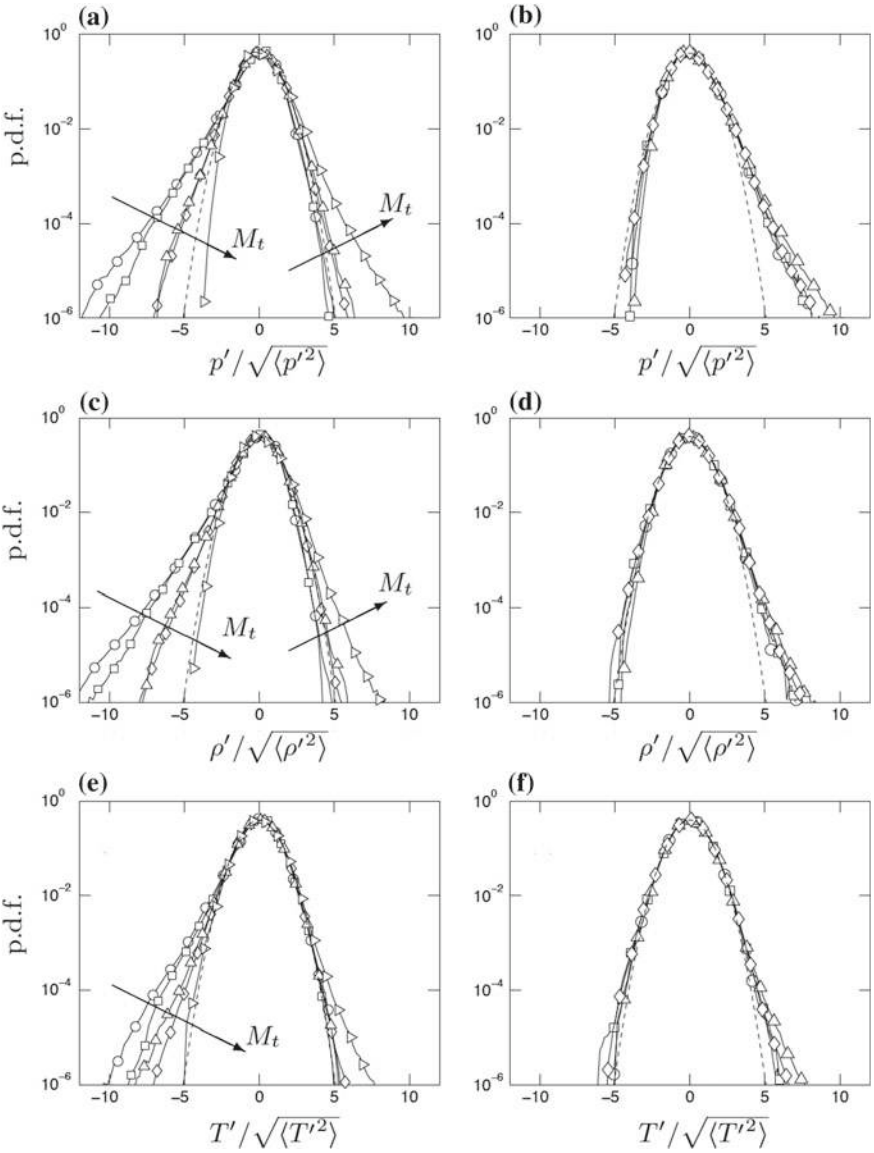

Fig. 13.13 Probability density functions of thermodynamic quantities in solenoidally forced turbulence in the range $0.1 \leq M_t \leq 0.6$ and $38 \leq Re_\lambda \leq 160$. Left column: $Re_\lambda = 100$ and $0.1 \leq M_t \leq 0.6$; Right column: $M_t = 0.6$ and $38 \leq Re_\lambda \leq 160$. From Donzis and Jagannathan (2013) with courtesy of D. Donzis

The changes in the thermodynamic quantities are also observed looking at their spectra, more precisely to their slopes in the inertial range, if the Reynolds number is large enough for such a range to exist.

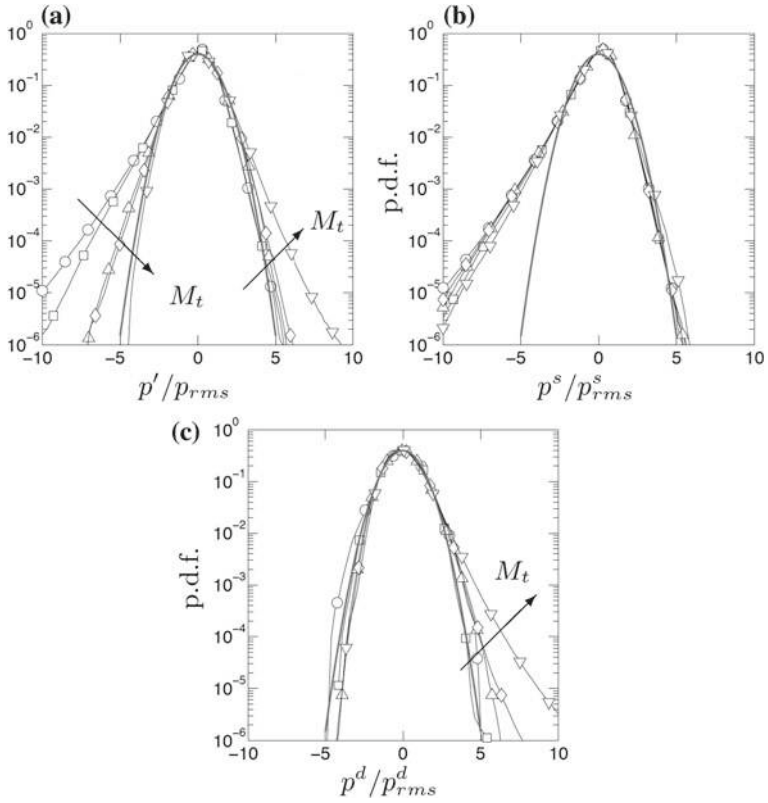

Fig. 13.14 Probability density functions of **a**) total pressure, **b**) solenoidal component of pressure and **c**) dilatational component of pressure in solenoidally forced turbulence in the range $0.1 \leq M_t \leq 0.6$ at $Re_\lambda = 160$. From Jagannathan and Donzis (2016) with courtesy of D. Donzis

At low Mach number, the temperature field can be approximated as a passive scalar, leading to

$$E_{TT}(k) = C_{oc}\varepsilon^{-1/3}\varepsilon_T k^{-5/3} \tag{13.163}$$

where C_{oc} is the Obukhov–Corrsin constant for temperature fluctuations and ε_T the dissipation rate of the variance of the temperature. This solution is reported by Donzis for $M_t \leq 0.6$.

The density spectrum $E_{\rho\rho}(k)$ is observed to be accurately deduced from the temperature spectrum in the same Mach number range using the isentropic assumption

$$\frac{\rho'}{\bar{\rho}} \sim \frac{1}{\gamma - 1}\frac{T'}{\bar{T}}$$

yielding

$$E_{\rho\rho}(k) = \frac{\bar{\rho}^2}{\bar{T}^2}\frac{1}{(\gamma-1)^2}E_{TT}(k) = C_{oc}\frac{\bar{\rho}^2}{\bar{T}^2}\frac{1}{(\gamma-1)^2}\varepsilon^{-1/3}\varepsilon_T k^{-5/3}. \tag{13.164}$$

The pressure spectrum exhibits a more complex behavior, since the inertial range is different in the two régimes. For $M_t \leq 0.3 - 0.4$ a nearly incompressible solution is found with $E_{pp}(k) \propto \varepsilon^{4/3}k^{-7/3}$, showing that the solenoidal component is dominant. At higher M_t the dilatational part becomes the most important one, and the spectrum can be deduced from the temperature spectrum thanks to the isentropic hypothesis, leading to

$$E_{pp}(k) = C_{oc}\frac{\bar{p}^2}{\bar{T}^2}\frac{\gamma^2}{(\gamma-1)^2}\varepsilon^{-1/3}\varepsilon_T k^{-5/3}. \tag{13.165}$$

13.4.4 Conditions for Occurrence of Shocklets

Shocklets are small-scale extreme events associated with a strong compression that satisfy the classical Rankine–Hugoniot jump relations for shocks with possible viscous effects. In numerical simulations they are often detected using Samtaney's criterion, i.e. as regions in which $d < -3\overline{d'^2}$ where $d = \nabla \cdot \boldsymbol{u}$.

Before discussing the properties of these shocklets and analyzing their influence on the dynamics and the statistical properties of compressible isotropic turbulence, it is worth noting that they can occur at nominally very low Mach numbers depending on the initial condition. In the case where initial acoustic pressure perturbations are very strong, the linear theory is no longer relevant to describe the dynamics. Considering such an initial condition, convective terms will play an important role, leading to the propensity for occurence of nonlinear acoustic phenomena such as wave steepening and focusing and shock formation. Therefore, a strong nonlinear transient phase will be present during which shocklets can form. Shocklets can also be obtained at low M_t if a dilatational forcing term is used.

In a similar manner, the analyses dealing with the weakly compressible thermal régime were based on the assumption that both δ and δ' as defined in Eq. (13.128) are very small. Since $\delta \propto M_r$, the asymptotic series expansion is no longer valid at higher turbulent Mach numbers. Moreover, it has been observed in numerical experiments that the thermal régimes are very sensitive to the initial conditions, and that if the initial perturbations are not consistent with the governing equations and are strong enough, acoustic waves grow and the dynamics bifurcate toward the nonlinear régime in which shocklets are present.

No exact threshold value for the turbulent Mach number M_t associated to the occurence of shocklets is known, since this phenomenon also depends on other parameters. It seems that all simulations carried out for $M_t \geq 0.4$ exhibit shocklets. But it is important to note that shocklets can appear at lower Mach numbers, depending on the initial condition.

13.4.5 Energy Budget and Shocklet Influence

Shocklets are small bow shocks which have been observed to satisfy the Rankine–Hugoniot jump conditions. Therefore, these events exhibit all properties of usual shocks. In particular, they induce sharp pressure and density gradients and, because they are associated with a compression, a negative value of the divergence of the velocity. As a consequence, one can reasonably expect that they should have a non-negligible influence on the energy balance. We summarize below observations retrieved from direct numerical simulations. Since all these simulations were carried out at small Reynolds number, viscous effects are important and they damp the effect of the shocklets. Therefore, exact values of the quantities given below must be interpreted as a qualitative description of high-Reynolds number flows rather than an accurate quantitative one.

Numerical experiments show that the probability density function of the dilatation (i.e. the divergence of the velocity field) is strongly skewed: about 2/3 of the volume is associated with an expansion ($\nabla \cdot \boldsymbol{u} > 0$), while only 1/3 corresponds to compression. On the average, the expansion regions are responsible for 80–90% of the solenoidal dissipation $\bar{\varepsilon}_s$ and 50–60% of the total dissipation ($\bar{\varepsilon}_d + \bar{\varepsilon}_s$). The global dilatational dissipation $\bar{\varepsilon}_d$ is found to be small with respect to the global solenoidal dissipation $\bar{\varepsilon}_s$: Lee and coworkers (1991) report that $\bar{\varepsilon}_d$ is less or equal than 10% of the total dissipation for M_t up to 0.6. A maximum value about 4% is reported in solenoidally forced turbulence at $M_t = 0.6$ in Jagannathan and Donzis (2016).

The shocklets fill only a few percent of the total volume: Pirrozoli and Grasso (2004) found that they represent only 1.4% of the volume at $M_t = 0.8$ while Samtaney et al. (2001) report a fraction smaller than 2% in their set of numerical experiments. Nevertheless, the shocklets strongly modify the local relative importance of the physical mechanisms: near shocklets, the dilatational dissipation is up to 10 times larger than the solenoidal dissipation. Despite they fill only a very small part of the fluid domain, shocklets are responsible for about 20% of the global dilatational dissipation.

The shocklets perturb the dilatation field. This perturbation can be roughly estimated looking at the jump condition for the dilatation for a bow shock moving into a two-dimensional inviscid steady flow provided by Kida and Orszag (1990a, 1992):

$$[[\nabla \cdot \boldsymbol{u}]] \simeq \frac{2}{R(\gamma+1)} \left(\frac{(\gamma-1)M_s^2+2}{(\gamma+1)M_s^2} - \frac{3M_s^2+1}{M_s^2-1} \tan^2\theta \right) u_n \qquad (13.166)$$

where R, u_n, M_s and θ are the radius of curvature of the shock, relative velocity normal to the shock, shocklet Mach number defined by the ratio of u_n about the upstream speed of sound, the angle between the fluid velocity and the shock normal, respectively. It is seen that the sign of the induced dilatation depends on both R and θ, and that its amplitude is a function of the square of the normal Mach number. The use of a two-dimensional simplified model was proved to be qualitatively relevant by Kida and Orszag, since the three-dimensional curved shock can be locally

Table 13.3 Transfers between turbulent kinetic energy $\mathcal{K}$ and fluctuating internal energy $\tilde{e}$ induced by strong compressions and expansions in isotropic turbulence with solenoidal forcing in the range $0.1 \leq M_t \leq 0.6$ (Jagannathan and Donzis 2016)

M_t	Event type	$\overline{p'd}$	ε	Net transfer
$M_t = 0.1$	Strong compression	$\tilde{e} \rightarrow \mathcal{K}$	$\mathcal{K} \rightarrow \tilde{e}$	Negligible
$M_t = 0.1$	Strong expansion	$\mathcal{K} \rightarrow \tilde{e}$	$\mathcal{K} \rightarrow \tilde{e}$	$\mathcal{K} \rightarrow \tilde{e}$
$M_t = 0.6$	Strong compression	$\mathcal{K} \rightarrow \tilde{e}$	$\mathcal{K} \rightarrow \tilde{e}$	$\mathcal{K} \rightarrow \tilde{e}$
$M_t = 0.6$	Strong expansion	$\tilde{e} \rightarrow \mathcal{K}$	$\mathcal{K} \rightarrow \tilde{e}$	Negligible

projected on a two-dimensional space. Lee and coworkers observed that the correlation between pressure fluctuations and dilatation fluctuations is large near shocklets, leading to a local enhancement of the transfers between the internal energy and the turbulence kinetic energy. These authors also report that the overall effect of the pressure-dilatation term $\overline{p'd}$ on the evolution of kinetic energy in freely decaying isotropic turbulence is comparable to the overall dilatational dissipation $\bar{\varepsilon}_d$. This effect is typical of the presence of the shocklets, since this term is theoretically and experimentally found to be negligible in the pseudo-acoustic régime.

The energy exchanges due to strong compressions and expansions were further investigated in forced turbulence in Jagannathan and Donzis (2016). Their main results dealing with the effects of pressure-dilatation correlation $\overline{p'd}$ and dissipation ε are summarized in Table 13.3. The results are observed to be highly sensitive to M_t. At low M_t, strong compressions have a negligible net effect on energy exchanges, while strong expansions yields a global transfer of kinetic energy $\mathcal{K}$ into internal energy $\tilde{e}$. At high M_t, the net global effect is the same, but it is governed by strong compressions while strong dilatations have a zero net effect. The main difference between the two cases is the direction of the transfers associated with $\overline{p'd}$, which changes for both compressions and expansions.

13.4.6 Enstrophy Budget and Shocklet Influence

The shocklets also have a large impact on the dynamics of vorticity and enstrophy. The general jump relation for vorticity derived from the Rankine–Hugoniot will be discussed in the chapter devoted to the shock/turbulence interaction (Chap. 15), and the interested reader can refer to it. But it is very important to emphasize that the main trends and the relative importance of the different physical mechanisms are not the same in the shocklet case as in the large-scale shock case discussed in Chap. 15. The main reason for this is a scale effect: shocklets are small shock waves which form when turbulent eddies allow for the local steepening of pressure waves, and their size is therefore comparable with those of the turbulent eddies, while large-scale shock size is much greater than the turbulent vortical structures.

We first recall some estimates related to vorticity creation by a bow shock moving in a steady, inviscid two-dimensional flow (Kida and Orszag 1990b):

$$[[\boldsymbol{\omega}]] \simeq \frac{4(M_s^2-1)\sin\theta}{R(\gamma+1)M_s^2\left((\gamma-1)M_s^2+2\right)}|\boldsymbol{u}|, \tag{13.167}$$

where the nomenclature is the same as in the previous paragraph. The sign of the created vorticity is seen to depends on the local shock curvature and the angle of incidence. The created vorticity is zero for normal shocks ($\theta = 0$) and Mach waves ($\theta = \pm\cos^{-1}(1/M_s)$). The effect of the sole baroclinic term $-(\nabla p \times \nabla\rho)/\rho^2$ is evaluated as

$$[[u_n\boldsymbol{\omega}]] \simeq \frac{4(M_s^2-1)^2}{R(\gamma+1)^2M_s^4}u_n^2\tan\theta \tag{13.168}$$

and is observed to depends on M_s^4 instead of M_s^2 for the global vorticity creation.

Numerical experiments show that the volume-averaged enstrophy budget is governed by the vortex stretching term $\boldsymbol{\omega}\cdot\mathbf{S}\cdot\boldsymbol{\omega}$ and the viscous dissipation. The former is positive and creates some vorticity, while the latter is strictly negative. The baroclinic term is negligible while the compression term $\Theta(\nabla\cdot\boldsymbol{u})$ exhibits an oscillatory behavior, with a period very similar to those of the compressive kinetic energy and the internal energy. Therefore, this phenomenon is interpreted as a coupling between acoustic waves and the vorticity.

A finer analysis can be achieved distinguishing between regions of negative dilatation and regions of positive dilatation. The compression term is observed to be dominant in shocklet areas, while the stretching term is the most important in expansion region. A careful look at direct numerical simulation data reveals that vorticity is created on shocklets through the baroclinic interaction and is enhanced in expansion regions by the vortex stretching phenomenon. The baroclinic production is relatively small because there is a clear trend for the pressure gradient and the density gradient to be aligned against each other: the global probability density function of the angle between these vectors exhibits a peak near 4°, and is almost null for angles higher than 10°, even for values of M_t as high as 0.74. It is also found that increasing the turbulent Mach number yields a stronger alignement of these vectors. Due to the weakness of the baroclinic production, Kida and Orszag observed that the barotropic relation

$$\left(\frac{p}{\bar{p}}\right) = \left(\frac{\rho}{\bar{\rho}}\right)^{\gamma} \tag{13.169}$$

is valid on the overall.

A last observation is that the vorticity has a statistical preference to align with the density gradient $\nabla\rho$ near the shocklets and to be orthogonal to it outside shocklet aeras. This influence was observed to be significant up to a distance equal to 72η downstream the shocklet (Wang et al. 2011). Since the shocklets fill a very small

fraction of the fluid domain, the overall p.d.f. of the angle between $\boldsymbol{\omega}$ and $\nabla\rho$ has a peak at 90°. As in the incompressible case, the vorticity is observed to be aligned on the overall with intermediate eigendirection of the velocity gradient tensor.

13.5 Supersonic Régime

The supersonic régime, in which the turbulent Mach number is greater than 1, is much less known than the other régimes. The main reasons why so little attention as been paid to this configuration is that it is encountered in astrophysics only, and that it escapes most theoretical tools since it does not allow small parameter expansion.

Only very few numerical experiments are available (Porter et al. 1992a, b, 1994), which all reveal the existence of two distinct quasi-equilibrium phases separated by a short transition phase:

- The *quasi-supersonic phase*, whose typical duration is of the order of a few acoustic time scale. During this initial period, nonlinear phenomena yield the formation of a myriad of small but intense shock waves. No vortical structures are observed during this period. Then, the shocks interact, leading to the existence of vortex sheets which roll-up due to Kelvin–Helmholtz-type instabilities, yielding the existence of vortex tubes. These vortex tubes then experience vortex stretching, leading to the appearance of the usual kinetic energy cascade phenomenon. During this phase, which is dominated by shock formation and shock interaction, the evolution of the vorticity is governed by the baroclinic production and the linear terms (vortex stretching and dilatation terms), which are of equal amplitude. At the end of the quasi-supersonic phase, both dilatational velocity spectrum and solenoidal velocity spectrum exhibit an inertial range with a -2 slope:

$$E_{dd}(k) \propto k^{-2}, \quad E_{ss}(k) \propto k^{-2}. \tag{13.170}$$

  It is worth noting that most of turbulent kinetic energy is contained in the solenoidal mode once the vortical structures have been created.
- The *immediate post-supersonic phase* which is governed by vortex interaction and vortical decay. The main processes involved in subsonic vortex dynamics are present, but shocks are still present and very active. As a consequence, the following inertial range scalings are observed:

$$E_{dd}(k) \propto k^{-2}, \quad E_{ss}(k) \propto k^{-1}. \tag{13.171}$$

  The vorticity dynamics is dominated by the vortex stretching and the dilation term during this phase, the baroclinic production being now much weaker due to the decrease of the turbulent Mach number.

At much longer times, an equilibrium state similar to the subsonic régime is recovered in which the shocks are much weaker and the solenoidal velocity dynamics is

decoupled (at the leading order approximation) from the acoustic field. The measured inertial range behaviors are $E_{dd}(k) \propto k^{-2}$ and $E_{ss}(k) \propto k^{-5/3}$.

A solenoidally forced supersonic turbulence with $M_t = 1.03 - 1.05$ and $Re_\lambda = 175 - 187$ was considered by Wang and coworkers (2013). Shocklets with local Mach number up to 3 were observed in this case, and both dilatational and solenoidal velocity components exhibit the same spectrum, with $E_{dd}(k) \propto k^{-5/3}$ and $E_{ss}(k) \propto k^{-5/3}$.

13.6 Structures in the Physical Space

Compressible isotropic turbulence, like incompressible isotropic turbulence, exhibits coherent events that can be classified according to some criteria. In the quasi-acoustic régime at very low Mach number, the solenoidal field is nearly decoupled from the dilatational field and they evolve almost independently. The kinetic energy being concentrated in the solenoidal velocity component, the velocity field is almost identical to the one observed in purely incompressible flows, and all the results dealing with the velocity field topology given in Sect. 4.10 hold.

The analysis must be modified to account for new configurations in the nonlinear subsonic and the supersonic régimes. This was achieved by Kevlahan et al. (1992) who proposed a topological analysis of the velocity field that accounts for compressibility effects. Main elements of this classification are displayed in Sect. 13.6.1. It has also be seen that shocklets form in this régime. Main known characteristics of these structures are discussed in Sect. 13.6.2.

13.6.1 Turbulent Structures in Compressible Turbulence

The analysis carried out by Kevlahan and coworkers (1992) relies on the local analysis of the topology of the velocity field. Introducing the anisotropic part of the instantaneous strain tensor $\mathbf{S}^* = \mathbf{S} - (S_{kk}/3)\mathbf{I}$, it is possible to define three region types:

- *Eddy-dominated regions*

$$\mathbf{W} : \mathbf{W} > 2\mathbf{S}^* : \mathbf{S}^*, \tag{13.172}$$

- *Shear zones*

$$\frac{1}{2}\mathbf{S}^* : \mathbf{S}^* \leq \mathbf{W} : \mathbf{W} \leq 2\mathbf{S}^* : \mathbf{S}^*, \tag{13.173}$$

- *Convergence zones*

$$\mathbf{W} : \mathbf{W} < \frac{1}{2}\mathbf{S}^* : \mathbf{S}^*. \tag{13.174}$$

This decomposition is supplemented by a criterion related to the local degree of compressibility. Defining the sensor $\mathcal{C}$ as

$$\mathcal{C} = \frac{(\nabla \cdot \boldsymbol{u})^2}{\mathbf{S}^* : \mathbf{S}^* + \mathbf{W} : \mathbf{W}} \tag{13.175}$$

it is proposed that

- $\mathcal{C} \leq 0.05$: structures behave as incompressible ones
- $\mathcal{C} > 0.05$: structures are compressible

The analysis can be further refined by retrieving some informations about the structure shape. Denoting λ_1^*, λ_2^* and λ_3^* the three eigenvalues of $\mathbf{S}^*$,[14] the structure shapes can be classified according to the sign of the third invariant of $\mathbf{S}^*$, $III^* = -\lambda_1^*\lambda_2^*\lambda_3^*$:

- $III^* < 0$: *cigar*-type structures
- $III^* > 0$: *pancake*-type structures

Regions can also be grouped as *focal* or compression regions and *non-focal* or expansion regions according to the sign of the determinant of $\mathbf{S}^*$, $\mathcal{D}^* = det(\mathbf{S}^*)$:

- $\mathcal{D}^* > 0$: focal/compression region
- $\mathcal{D}^* < 0$: non-focal/expansion region.

It is worth noting the $\mathcal{D}^*$ can be computed from the second and third invariants of $\mathbf{S}^*$ like

$$\mathcal{D}^* = \frac{27}{4}(III^*)^2 + (II^*)^3, \quad II^* = \lambda_1^*\lambda_2^* + \lambda_1^*\lambda_3^* + \lambda_2^*\lambda_3^*. \tag{13.178}$$

Using a wide database including flows with turbulent Mach number up to 0.8, Pirrozoli and Grasso (2004) observed that several features of isotropic turbulence are not sensitive to the Mach number and are therefore similar to those of perfectly incompressible isotropic turbulence. They are listed below:

(i) The eigenvalues of the strain tensor $\mathbf{S}^*$ are in the ratio −4:3:1
(ii) Number of pancake and cigar structures are in the ratio 3:1
(iii) Vorticity has a statistical preference to align with the intermediate eigendirection of $\mathbf{S}^*$, being either parallel or antiparallel (probabilities are equal)

[14] One can easily observe that

$$\lambda_i^* = \lambda_i - \frac{(\nabla \cdot \boldsymbol{u})}{3} \tag{13.176}$$

where λ's are the eigenvalues of $\mathbf{S}$. A direct consequence is

$$\sum_{i=1,3} \lambda_i^* = 0 \tag{13.177}$$

as in incompressible turbulence.

(iv) The joint p.d.f. of II^* and III^* does not depend on the Mach number.

Their analyses also show that focal regions are of great importance for the solenoidal field: these regions fill about 2/3 of the total volume and account for 80–90% of the enstrophy and 50–60% of the solenoidal dissipation $\bar{\varepsilon}_s$. More precisely:

(i) At low M_t, incompressible structures dominate and the fraction of the volume filled by shear zones, convergence zones and eddies are 44, 35 and 21%, respectively.
(ii) Shear regions account for 45% of the enstrophy regardless of the turbulent Mach number.
(iii) At low M_t, kinetic energy is dissipated nearly equally in focal and non-focal structures, while at high M_t focal structures are more active than the non-focal ones
(iv) At high M_t, dilatational dissipation mainly takes place in shear and convergence zones
(v) Shocklets are rare (less than 2% of the volume) but represent up to 20% of the global dilatational dissipation.

13.6.2 Probabilistic Model for Shocklets

We now present the main features of the probabilistic model for shocklet derived by Samtaney and coworkers (2001) on the grounds of direct numerical simulation data.

The initial step consists in parameterizing the probability density function of the longitudinal velocity increment, which will serve as a basis to evaluate the shocklet-based Mach number. The p.d.f. is observed to be very similar to those measured in incompressible isotropic turbulence, leading to the following exponential expression:

$$P(\Delta u) \simeq \frac{1}{\sigma_{\Delta u}} \exp\left(-b(r)\left|\frac{\Delta u}{\sigma_{\Delta u}}\right|\right), \tag{13.179}$$

where Δu is the velocity increment along the direction of $\boldsymbol{u}$ between two points separated by a distance r and $\sigma_{\Delta u} = \sqrt{\overline{(\Delta u)^2}}$. The function b can be written like $b(r) = \alpha(r/\eta)^{\beta}$, where η is the Kolmogorov length scale and $\alpha = 1.5$ and $\beta = 0.16$ are constant parameters.[15]

The second step deals with the derivation of a model p.d.f. for the shocklet strength, the shocklet being modeled as a weak shock (i.e. $M_s - 1 \ll 1$).

Let Δu be the normal velocity difference across the shocklet. Usual jump conditions yield the exact relation

[15]The value $\alpha = 1.5$ was measured in low-Reynolds number simulations. High Reynolds number wind tunnel experiments suggest $\alpha \simeq 0.5$.

$$\frac{\Delta u}{a} = -\frac{2}{\gamma+1}\left(M_s - \frac{1}{M_s}\right) \tag{13.180}$$

where a is the speed of sound in the fluid upstream the shocklet. The shocklet thickness δ_s is evaluated using the classical weak-shock theory:

$$\delta_s \simeq \frac{\nu}{a}\frac{3}{(M_s-1)} \tag{13.181}$$

where ν is related to the viscosity upstream the shock. To get a reliable model, one must evaluate all quantities using turbulence-related variables. To this end, it is assumed that the following expression for the dissipation derived in the incompressible case holds

$$\varepsilon = 15\nu\overline{\left(\frac{\partial u}{\partial x}\right)^2} \simeq 15\nu\overline{\left(\frac{\Delta u}{r}\right)^2} \tag{13.182}$$

from which the following leading-order estimates in terms of $(M_s - 1)$ are derived

$$\Delta u \simeq \frac{4a}{\gamma+1}(M_s-1), \tag{13.183}$$

$$\sigma_{\Delta u} \simeq \frac{3}{\sqrt{15}a}\sqrt{\nu\varepsilon}\frac{1}{(M_s-1)}, \tag{13.184}$$

$$\left|\frac{\Delta u}{\sigma_{\Delta u}}\right| \simeq \frac{4\sqrt{15}a^2}{3(\gamma+1)\sqrt{\nu\varepsilon}}(M_s-1)^2. \tag{13.185}$$

The last expression can be further refined introducing the mean turbulent Mach number M_t and the Taylor Reynolds number Re_λ:

$$\left|\frac{\Delta u}{\sigma_{\Delta u}}\right| \simeq \frac{4}{(\gamma+1)}\frac{Re_\lambda}{M_t^2}(M_s-1)^2, \tag{13.186}$$

leading the following expression for the p.d.f. of the shocklet strength (the constant β is taken equal to zero for the sake of simplicity):

$$P(M_s-1) \simeq \frac{8\alpha}{(\gamma+1)}\frac{Re_\lambda}{M_t^2}(M_s-1)\exp\left(-\frac{4\alpha}{(\gamma+1)}\frac{Re_\lambda}{M_t^2}(M_s-1)^2\right). \tag{13.187}$$

This expression is observed to be in good agreement with a large set of experimental data, with $Re_\lambda = 0.32 - 0.43$ and $M_t = 0.1 - 0.5$. In the same manner, a model p.d.f. can be found for the shocklet thickness:

$$P(\delta/\eta) \simeq \left(\frac{\delta}{\eta}\right)^3 \exp\left(-\frac{12\sqrt{15}\alpha}{\gamma+1}\left(\frac{\delta}{\eta}\right)^2\right) \tag{13.188}$$

One can see from Eqs. (13.187) and (13.188) that the *most probable shocklet* corresponds to

$$M_s = 1 + M_t\sqrt{\frac{\gamma+1}{8\alpha Re_\lambda}}, \quad \delta = (15)^{1/4}\eta\sqrt{\frac{8\alpha}{\gamma+1}}. \tag{13.189}$$

Using above value of α and considering air, one finds that the most probable shocklet thickness is about 5 η, which is much larger than the mean-free path of the molecules.

This model was observed to be in satisfactory agreement at moderate M_t cases, in which shocklet's strength is not too large. In supersonic isotropic turbulence with solenoidal forcing, Wang et al. (2011) observed that the super-exponential distribution (13.187) should be replaced by the following exponential distribution:

$$P(M_s - 1) \simeq 1.2\exp\left(-5.1(M_s - 1)\right), \tag{13.190}$$

which is accurate for events such that $0.5 \leq (M_s - 1) \leq 2$. They also noticed a large peak in the p.d.f. corresponding to $(M_s - 1) = 0.07$.

References

Bailly, C., Lafon, P., Candel, S.: Subsonic and supersonic jet noise predictions from statistical source models. AIAA J. **35**(11), 1688–1696 (1997)

Bataille, F.: Etude d'une turbulence faiblement compressible dans le cadre d'une modélisation Quasi-Normale avec Amortissement tourbillonnaire. Ph.D. thesis, Ecole Centrale de Lyon (in french) (1994)

Bayly, B.J., Levermore, C.D., Passot, T.: Density variations in weakly compressible flows. Phys. Fluids **4**(5), 945–954 (1992)

Bertoglio, J.P., Bataille, F., Marion, J.D.: Two-point closures for weakly compressible turbulence. Phys. Fluids **13**(1), 290–310 (2001)

Bos, W.J.T.: The temperature spectrum generated by frictional heating in isotropic turbulence. J. Fluid Mech. **746**, 85–98 (2014)

Bos, W.J.T., Chahine, R., Pushkarev, A.V.: On the scaling of temperature fluctuations induced by frictional heating. Phys. Fluids **27**, 095105 (2015)

Briard, A., Sagaut, P., Cambon, C.: Post-doctoral internal report. Available from the authors upon request (2017)

Cai, X.D., O'Brien, E.E., Ladeinde, F.: Thermodynamic behavior in decaying, compressible turbulence with initially dominant temperature fluctuations. Phys. Fluids **9**(6), 1754–1763 (1997)

Cambon, C., Scott, J.F.: Linear and nonlinear models of anisotropic turbulence. Ann. Rev. Fluid Mech. **31**, 1–53 (1999)

Cambon, C., Coleman, G.N., Mansour, N.N.: Rapid distortion analysis and direct simulation of compressible homogeneous turbulence at finite Mach number. J. Fluid Mech. **257**, 641–665 (1993)

Chu, B.T., Apfel, R.E.: Are acoustic intensity and potential energy density first- of second-order quantities? Am. J. Phys. **51**(10), 916–918 (1983)

Crow, S.C.: Visco-elastic character of fine-grained isotropic turbulence. Phys. Fluids **10**(7), 1587 (1967)
De Marinis, D., Chibbaro, S., Meldi, M., Sagaut, P.: Temperature dynamics in decaying isotropic turbulence with Joule heat production. J. Fluid Mech. **724**, 425–449 (2013)
Donzis, D.A., Jagannathan, S.: Fluctuations of thermodynamic variables in stationary compressible turbulence. J. Fluid Mech. **733**, 221–244 (2013)
Eckhoff, K.S., Storesletten, L.: A note on the stability of steady inviscid helical gas flows. J. Fluid Mech. **89**, 401 (1978)
Erlebacher, G., Sarkar, S.: Statistical analysis of the rate of strain tensor in compressible homogeneous turbulence. Phys. Fluids **5**(12), 3240–3254 (1993)
Erlebacher, G., Hussaini, M.Y., Kreiss, H.O., Sarkar, S.: The analysis and simulation of compressible turbulence. Theor. Comput. Fluid Dyn. **2**, 73–95 (1990)
Fauchet, G.: Modélisation en deux points de la turbulence isotrope compressible et validation à l'aide de simulations numériques. Thèse de Doctorat, Ecole Centrale de Lyon (in french) (1998)
Fauchet, G., Bertoglio, J.P.: A two-point closure for compressible turbulence. C.R. Acad. Sci. Paris, Série IIb **327**, 665–671 (1999a). (in french)
Fauchet, G., Bertoglio, J.P.: Pseudo-sound and acoustic régimes compressible turbulence. C.R. Acad. Sci. Paris, Série IIb **327**, 665–671 (1999b). (in french)
Favier, B., Godeferd, F.S., Cambon, C.: Modelling the far-field acoustic emission of rotating turbulence. J. Turbul. **9**(30), 1–21 (2008)
Favier, B., Godeferd, F.S., Cambon, C.: On space and time correlations of isotropic and rotating turbulence. Phys. Fluids **22**, 015101 (2010)
Ffwocs Williams, J.E.: The noise from turbulence convected at high speed. Phil. Trans. **255**, 469–503 (1963)
Ffwocs Williams, J.E., Hawkings, D.L.: Sound generation by turbulence and surfaces in arbitrary motion. Phil. Trans. A **264**, 321–342 (1969)
Ford, G.W., Meecham, W.C.: Scattering of sound by isotropic turbulence of large Reynolds number. J. Acous. Soc. America **32**, 1668–1672 (1960)
Goldstein, R.J., He, B.Y.: Energy separation and acoustic interaction in flow across a circular cylinder. J. Heat Transfer-Transactions of the ASME **123**(4), 682–687 (2001)
Howe, M.S.: Multiple scattering of sound by turbulence and other inhomogeneities. J. Sound Vib. **27**, 455–476 (1973)
Howe, M.S.: The generation of sound by aerodynamic sources in an inhomogeneous steady flow. J. Fluid Mech. **67**(3), 597–610 (1975)
Jagannathan, S., Donzis, D.A.: Reynolds and Mach number scaling in solenoidally-forced compressible turbulence using high-resolution direct numerical simulations. J. Fluid Mech. **789**, 669–707 (2016)
Kaneda, Y.: Lagrangian renormalized approximation of turbulence. Fluid Dyn. Res. **39**, 526–551 (2007). www.sciencedirect.com
Kevlahan, N., Mahesh, K., Lee, S.: Evolution of the shock front and turbulence structures in the shock/turbulence interaction. In: Proceedings of the Summer Program, CTR, Stanford University (1992)
Kida, S., Orszag, S.A.: Energy and spectral dynamics in forced compressible turbulence. J. Sci. Comput. **5**(2), 85–125 (1990a)
Kida, S., Orszag, S.A.: Enstrophy budget in decaying compressible turbulence. J. Sci. Comput. **5**(1), 1–34 (1990b)
Kida, S., Orszag, S.A.: Energy and spectral dynamics in decaying compressible turbulence. J. Sci. Comput. **7**(1), 1–34 (1992)
Kraichnan, R.H.: Comments on Space-time correlations in stationary isotropic turbulence. Phys. Fluids **2**(3), 334–334 (1959)
Lee, S., Lele, S., Moin, P.: Eddy shocklets in decaying compressible turbulence. Phys. Fluids **3**(4), 657–664 (1991)
Leslie, D.C.: Developments in the Theory of Turbulence. Clarendon Press, Oxford (1973)

Li, D., Zhang, X., He, G.: Temporal decorrelations in compressible isotropic turbulence. Phys. Rev. E **88**(4), 021001(R) (2013)
Lighthill, M.J.: On sound generated aerodynamically. I. General theory. Proc. Royal Soc. London/A **211**, 564–587 (1952)
Lighthill, M.J.: On the energy scattered from the interaction of turbulence with sound or shock waves. Proc. Cambridge Phil. Soc. **49**, 531–551 (1953)
Lighthill, M.J.: On sound generated aerodynamically. I. Turbulence as a source of sound. Proc. Royal Soc. London/A **222**, 1–32 (1954)
Lighthill, M.J.: The Bakerian Lecture, 1961. Sound generated aerodynamically. Proc. Royal Soc. London/A **267**, 147–182 (1961)
Lilley, G.M.: The radiated noise from isotropic turbulence. Theoret. Comput. Fluid Dyn. **6**(5–6), 281–301 (1994)
Lilley, G.M.: The generation of sound in turbulent motion. Aeronaut. J. **112**(1133), 381–394 (2008)
Marion, J.D., Bertoglio, J.P., Cambon, C.: Two-point closures for compressible turbulence. In: 11th International Symposium on Turbulence, Rolla (MO), Oct. 17–19. Preprints (A-89-33402 13-14) University of Missouri-Rolla, B22-1–B22-8 (1988a)
Marion, J.D., Bertoglio, J.P., Cambon, C., Mathieu, J.: Spectral study of weakly compressible turbulence. Part II: EDQNM. C. R. Acad. Sci. Paris, série II **307**, 1601–1606 (1988b)
Miura, H., Kida, S.: Acoustic energy exchange in compressible turbulence. Phys. Fluids **7**(7), 1732–1742 (1995)
Morfey, C.L.: Amplification of aerodynamic noise by convected flow inhomogeneities. J. Sound Vib. **31**(4), 391–397 (1973)
Orszag, S.A.: Lectures on the statistical theory of turbulence. In: Balian, R., Peube, J.L. (eds.) Fluid Dynamics, pp. 235–374. Gordon and Breach, London (1977)
Pirrozoli, S., Grasso, F.: Direct numerical simulations of isotropic compressible turbulence: influence of compressibility on dynamics and structure. Phys. Fluids **16**(12), 4386–4407 (2004)
Porter, D.H., Pouquet, A., Woodward, P.R.: Three-dimensional supersonic homogeneous turbulence: a numerical study. Phys. Rev. Lett. **68**(21), 3156–3159 (1992a)
Porter, D.H., Pouquet, A., Woodward, P.R.: A numerical study of supersonic turbulence. Theor. Comput. Fluid Dyn. **4**, 13–49 (1992b)
Porter, D.H., Pouquet, A., Woodward, P.R.: Kolmogorov-like spectra in decaying three-dimensional supersonic flows. Phys. Fluids **6**(6), 2133–2142 (1994)
Ribner, H.S.: On spectra and directivity of jet noise. J. Acous. Soc. America **35**, 614–616 (1963)
Samtaney, R., Pullin, D.I., Kosovic, B.: Direct numerical simulation of decaying compressible turbulence and shocklets statistics. Phys. Fluids **13**(5), 1415–1430 (2001)
Sarkar, S., Erlebacher, G., Hussaini, M.Y., Kreiss, H.O.: The analysis and modelling of dilatational terms in compressible turbulence. J. Fluid Mech. **227**, 473–493 (1991)
Simone, A., Coleman, G.N., Cambon, C.: The effect of compressibility on turbulent shear flow: a RDT and DNS study. J. Fluid Mech. **330**, 307–338 (1997)
Tatarski, V.I.: Wave Propagation in a Turbulent Medium. McGraw-Hill Book Company (1967)
Wang, J., Shi, Y., Wang, L.P., Xiao, Z., He, X., Chen, S.: Effect of shocklets on the velocity gradients in highly compressible isotropic turbulence. Phys. Fluids **23**, 125103 (2011)
Wang, J., Yang, Y., Shi, Y., Xiao, Z., He, X.T., Chen, S.: Statistics and structures of pressure and density in compressible isotropic turbulence. J. Turbul. **14**, 21–37 (2013)
Zank, G.P., Matthaeus, W.H.: Nearly incompressible hydrodynamics and heat conduction. Phys. Rev. Lett. **64**(11), 1243–1245 (1990)
Zank, G.P., Matthaeus, W.H.: The equations of nearly incompressible fluids. I. Hydrodynamics, turbulence and waves. Phys. Fluids **3**(1), 69–82 (1991)

Chapter 14
Compressible Homogeneous Anisotropic Turbulence

14.1 Effects of Compressibility in Free Shear Flows. Observations

To understand and model compressibility induced effects on turbulence is an important topic, since these effects are significant in many engineering applications, particularly in the field of propulsion and supersonic aerodynamics which is concerned by jets or wakes subjected to large velocity and density gradients. The compressible plane mixing layer is a generic problem for these applications, and explaining and modelling how compressibility reduces turbulent mixing in a shear layer has motivated the large research effort devoted to this topic during the 1980 and 1990s. Mixing usually refers to interpenetration of two streams. It is characterized by two scales: a lengthscale δ and a velocity scale ΔU which evaluate the thickness of the interface and intensity of the fluctuations, respectively. The reduction of mixing by compressibility is illustrated on Fig. 14.1 in which δ is the above mentioned thickness and $M_c = \Delta U/a$ is the *convective Mach number*, with a the average speed of sound.

There is now a consensus in the literature that the "intrinsic compressibility" (nonzero velocity divergence in Mach number dependent flows) of a turbulent velocity field tends to reduce the amplification rate of turbulent kinetic energy produced by mean velocity gradients, with respect to the solenoidal case. These effects were particularly investigated in shear flows, including both experimental and numerical studies of the plane mixing layer and DNS of homogeneous shear flows. The reader is referred to the review by Lele (1994) and the references given therein, and to Sarkar (1995), Simone et al. (1997) for more recent results.

Two preliminary questions immediately follow:

(i) To what extent homogeneous turbulence is relevant to explain such mechanisms in inhomogeneous flows?
(ii) Is compressibility always stabilizing (i.e. leading to a decrease in the turbulent kinetic growth rate) in homogeneous turbulence?

P. Sagaut and C. Cambon, *Homogeneous Turbulence Dynamics*,
https://doi.org/10.1007/978-3-319-73162-9_14

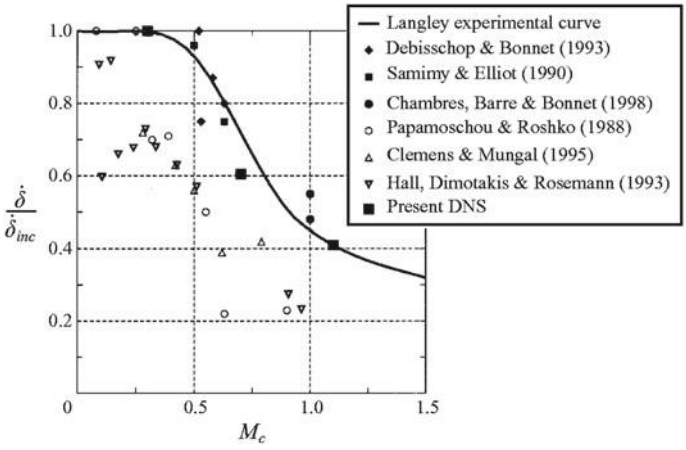

Fig. 14.1 Dependence of shear layer growth rate on convective Mach number. DNS and experimental results from Pantano and Sarkar (2002), with permission of CUP

The answer to the first question is somewhat difficult. The 'stabilizing' effect of compressibility in the mixing layer, for instance, can be attributed to the inhibition of the Kelvin–Helmholtz instability at a convective Mach number larger than 0.6. Such an instability escapes homogeneous RDT. Nevertheless, it is expected that our analysis can exploit strong analogies between the homogeneous shear and the mixing layer.

The answer to the second question is simple: no.

14.1.1 RST Equations and Single-Point Modelling

Equations for the Reynolds stress tensor are not so different from the one in the homogeneous incompressible case, at least in the absence of specific additional production by mean pressure, mean density, or mean temperature gradients. If we restrict our attention to flows in which the "production" term in the Reynolds stress tensor equations only results from mean velocity gradients, we must consider that the pressure-strain rate tensor is no longer trace-free, and that the dissipation tensor can display an explicit dilatational contribution. Using Eq. (3.102) and taking into account the homogeneity constraint, one obtains

$$\begin{aligned}\frac{\partial \bar{\rho} R_{ij}}{\partial t} = &-\bar{\rho}\left(R_{ik}\frac{\partial \tilde{u}_j}{\partial x_k} + R_{jk}\frac{\partial \tilde{u}_i}{\partial x_k}\right) + \overline{p'\left(\frac{\partial u_i''}{\partial x_j} + \frac{\partial u_j''}{\partial x_i}\right)} \\ &+\overline{u_i''}\left(\frac{\partial \bar{\tau}_{jk}}{\partial x_k} - \frac{\partial \bar{p}}{\partial x_j}\right) + \overline{u_j''}\left(\frac{\partial \bar{\tau}_{ik}}{\partial x_k} - \frac{\partial \bar{p}}{\partial x_i}\right) \\ &-\overline{\tau_{ik}'\frac{\partial u_j''}{\partial x_k}} - \overline{\tau_{jk}'\frac{\partial u_i''}{\partial x_k}}. \end{aligned} \tag{14.1}$$

The corresponding evolution equation for the turbulent kinetic energy $\mathcal{K}$ is

$$\frac{d\mathcal{K}}{dt} = P + \Pi^{(d)} - \bar{\varepsilon}_s - \bar{\varepsilon}_d, \tag{14.2}$$

in which the production term is

$$P = -\bar{\rho} R_{ik} \frac{\partial \tilde{u}_i}{\partial x_k} \tag{14.3}$$

and $\bar{\varepsilon}_s$ and $\bar{\varepsilon}_d$ are the solenoidal and dilatational dissipations introduced in Sect. 3.3.2. The pressure-dilatation correlation term, denoted $\Pi^{(d)}$ is equal to half the trace of the pressure-strain rate tensor.

Historically, two kinds of explanation were proposed to account for compressibility effects and used to derive specific turbulence models:

(i) According to the first explanation, the main effect is attributed to the explicit terms in Eq. (14.2). For instance, a reduction of the growth rate of $\mathcal{K}$ is assumed to result from a significant negative value of $\Pi^{(d)}$ and the negative term $-\bar{\varepsilon}_d$.
(ii) According to the second approach, the main mechanism responsible for the decrease of the turbulent kinetic energy growth rate is an alteration of the dynamics of pressure fluctuations. This modification results in a mollification of the pressure-strain rate tensor in Eq. (14.1) and an associated depletion of the production term P in Eq. (14.2). This effect appears as an implicit one, at least if one considers the evolution equation for $\mathcal{K}$.

An important issue is how to measure the compressibility. At least two Mach numbers are relevant in shear flows: the conventional *turbulent Mach number* $M_t = u'/a$, introduced in the previous chapter, and the *gradient Mach number*

$$M_g = \frac{SL}{a_0}. \tag{14.4}$$

The gradient Mach number compares the velocity scale SL to the speed of sound a_0, where S and L are a mean velocity gradient scale and a typical lengthscale of largest turbulent eddies, respectively. A similar parameter which accounts for the change of mean flow Mach number accross an eddy, denoted Δm, was introduced by Durbin and Zeman (1992). A more general meaning and interpretation was introduced then by Jacquin et al. (1993) and Sarkar (1995), with slightly different terminologies ("distortion" and "gradient" Mach number). Despite of the Jacquin's precedence, we adopt here the terminology gradient Mach number because it is the most popular. We think, however, that the RDT equations firstly investigated

Table 14.1 Reynolds stress anisotropy in compressible and incompressible homogeneous shear flow at large St. Values given in the two first columns come from DNS and wind tunnel experiments (if available)

Quantity	Incompressible case	Compressible case	Pressure-released RDT
b_{11}	0.203	$2/3 - 0.4e^{-0.3M_g} \pm 0.01$	$2/3$
b_{22}	-0.143	$-1/3 + 0.17e^{-0.3M_g} \pm 0.01$	$-1/3$
b_{33}	-0.06	$-1/3 + 0.23e^{-0.3M_g} \pm 0.01$	$-1/3$
b_{12}	$-0.15(0)$	$-0.17e^{-0.3M_g} \pm 0.005$	0

by Jacquin and coworkers gave the best interpretation of this parameter, since its counterpart at a fixed wavenumber, $S/(a_0 k)$, is the pivotal parameter for separating different flow regimes.

Looking at DNS results, the implicit alteration of the production is linked to a significant change in the Reynolds stress anisotropy. To illustrate this point, some values of b_{ij} are proposed for the compressible homogeneous shear flow case and compared to their counterparts in the incompressible case (see Chap. 9) in Table 14.1. Estimates for the compressible shear case presented here were proposed in Heinz (2004) on the grounds of relatively low-Reynolds DNS performed by Sarkar and coworkers.

The reduction of b_{12} in absolute value with respect to the incompressible case is directly connected to the reduction of production in this case, whereas the increase in b_{11} reflects a less efficient redistribution of the kinetic energy among the normal Reynolds stresses by the pressure-strain rate tensor, which can be interpreted as an alteration of the so-called return-to-isotropy mechanism. Even if compressibility correction factors in terms of M_g essentially come from empirical fitting, their asymptotic values are of interest, since they are observed to differ from both the incompressible and pressure-released RDT cases.

Even if the "implicit" compressibility effect mentioned above is probably more relevant than the 'explicit' one to explain the decrease in the growth rate of $\mathcal{K}$, rationales based on single-point statistics, which ignore the detailed consequences of the Helmholtz decomposition, cannot be fully satisfactory and universal. This is illustrated by the fact that some flows can be found in which the mollification of pressure-strain rate correlations at increasing gradient Mach number is not the right explanation, since it results in an *increase* of the turbulent kinetic energy growth rate. These flows include the irrotational strain case and even shear flows at moderate elapsed time, as shown by Rapid Distortion Theory and DNS results. As discussed in Chap. 9 in the pure incompressible case, the 'slow' (nonlinear) and the 'rapid' (linear) contributions to the pressure-strain rate tensor may have opposite effects on the production of $\mathcal{K}$: reducing the linear term yields increasing the production. The conventional stabilizing effect of compressibility is recovered in homogeneous shear flows at larger elapsed times, but the right explanation is different from the

one based on the sole reduction of pressure-strain terms (Sarkar 1995; Pantano and Sarkar 2002). This point will be extensively addressed in this chapter.

14.1.2 Preliminary Linear Approach: Pressure-Released Limit and Irrotational Strain

Linearizing the Euler equations for velocity and pressure fluctuations (u_i', p') around a mean flow with velocity $\bar{u}_i$ and discarding the pressure fluctuation term yields the following pressure-released solution (e.g. Cambon et al. 1985):

$$u_i^{'(pr)}(\boldsymbol{x}, t) = H_{ij}(\boldsymbol{X}, t, t_0)u_j'(\boldsymbol{X}, t_0), \tag{14.5}$$

where $\boldsymbol{x}$ is the position of a fluid particle at time t having the position $\boldsymbol{X}$ at time t_0, following a mean trajectory. The matrix H_{ij} is closely linked to the Cauchy matrix, or semi-Lagrangian displacement gradient matrix, $\mathbf{F}$, related to the mean flow (see Sect. 2.1), so that H_{ij} and F_{ij} reflect a time-accumulated effect of mean velocity gradients. They are obtained solving the following equations:

$$\dot{F}_{ij} = \frac{\partial U_i}{\partial x_m} F_{mj}, \quad F_{ij}(\boldsymbol{X}, t_0, t_0) = \delta_{ij}, \tag{14.6}$$

$$\dot{H}_{ij} = -\frac{\partial U_i}{\partial x_m} H_{mj}, \quad H_{ij}(\boldsymbol{X}, t_0, t_0) = \delta_{ij}. \tag{14.7}$$

One has $H_{ij} = F_{ji}^{-1}$ if and only if the mean velocity gradient matrix $\mathbf{A}$ is symmetric, i.e. if the mean flow is irrotational. A transposed mean velocity gradient matrix must be used in Eq. (14.6) to connect H_{ij} to the modified $\mathbf{F}$ in the general rotational case.

More generally, the linear response to an *irrotational* mean flow can be expressed using a linearized form of the Weber equation (2.31), leading to

$$u_i'(\boldsymbol{x}, t) = F_{ji}^{-1}(\boldsymbol{X}, t, t_0)u_j'(\boldsymbol{X}, t_0) + \frac{\partial \phi}{\partial x_i}, \tag{14.8}$$

in which the scalar potential ϕ accounts for the effects of fluctuating pressure. The associated equation for the vorticity fluctuation is

$$\omega_i'(\boldsymbol{x}, t) = \frac{1}{Det\mathbf{F}} F_{ij}(\boldsymbol{X}, t, t_0)\omega_j'(\boldsymbol{X}, t_0). \tag{14.9}$$

Both equations are valid not only in the solenoidal case ($u_{i,i}' = 0$), as used in Chap. 8, but also in various barotropic compressible cases. The vorticity equation is not valid in the presence of a linearized baroclinic torque, for instance. These

equations were used by several authors, including Hunt (1973), Goldstein (1978), Durbin and Zeman (1992).

As conjectured in Jacquin et al. (1993) and rediscussed in Cambon et al. (1993), Simone et al. (1997), the solenoidal linear response u_s' obtained by applying the Helmholtz decomposition to Eq. (14.8), yields the minimum kinetic energy growth rate, while its pressure-released counterpart leads to the maximum growth rate. This yields the following evolution equation

$$\boldsymbol{u}' = \boldsymbol{u}_s' + \underbrace{f(M_g)\left(\boldsymbol{u}^{'(pr)} - \boldsymbol{u}_s'\right)}_{\boldsymbol{u}_d'}, \tag{14.10}$$

where $\boldsymbol{u}^{'(pr)}$ is given by Eq. (14.5) with $\mathbf{H} =^T \mathbf{F}^{-1} = e^{-\int_{t_0}^{t} \mathbf{A}(t,t_0)dt'}$.

The following simple model can be derived (e.g. Cambon et al. 1993)

$$\mathcal{K} = \mathcal{K}_s + \underbrace{f(M_g)\left(\mathcal{K}^{(pr)} - \mathcal{K}_s\right)}_{\mathcal{K}_d} \tag{14.11}$$

for the linear history of the turbulent kinetic energy, where the weighting factor $f(M_g)$ is a monotonically increasing function of M_g. For consistency reason, one has $f(0) = 0$. This decomposition was successfully assessed for homogeneous turbulence, using both isentropic RDT and full DNS, as discussed below, and it is reasonable if the pressure-released limit is more energetic than the solenoidal limit, as it often does. Incidentally, one can mention that a simple model by Debiève et al. (1982) for the evolution of the Reynolds stress tensor in turbulence/shock wave interaction can be derived from Eq. (14.5). The reader is referred to Jacquin et al. (1993) for a detailed discussion of this approach. A short discussion is also given in Chap. 15, in the section devoted to the comparison between RDT and LIA.

This preliminary analysis has the advantage that it does not involve detailed expressions for the Helmholtz decomposition in Fourier space. But the extraction of $\boldsymbol{u}^{(s)}$ from the solution of Eq. (14.8) requires to solve the Poisson equation

$$\nabla^2\phi = -\frac{\partial u_i^{'(pr)}}{\partial x_i},$$

which comes from the dilatational balance $\boldsymbol{u}_d^{'(pr)} + \boldsymbol{\nabla}\phi = 0$.

More generally, two aspects must be kept in mind:

- The linearized Weber equation is valid for *irrotational mean flows without baroclinic effects* only. Finding the final expression of the scalar potential ϕ in terms of initial velocity remains an additional task to do anyway.
- The pressure-released linear limit (14.5) is completely general, and is valid for a rotational mean flow. But it appears as the limiting case of a linearized Weber equation for irrotational mean strains only.

14.2 A General Quasi-isentropic Approach to Homogeneous Compressible Shear Flows

Generally, if the Mach number effect is significant, the effects of compressibility are complex, since both acoustic and entropy modes are called into play, as well as the vortical mode inherited from the incompressible case (see Sect. 3.2). Irrotational mean flows have been studied by Goldstein (1978) using an inhomogeneous RDT formulation (which can be based on Eq. (14.8)), while homogeneous RDT has been extended to quasi-isentropic compressible turbulence at significant Mach number, in the presence of either irrotational compression or mean shear flows (Simone et al. 1997). For high speed compressible flows, it is no longer possible to consider the velocity field as divergence-free. Accordingly, the pressure disturbance can recover its role of thermodynamical variable. It is no longer a Lagrange multiplier enslaved to divergence-free constraint, which can be eliminated.

14.2.1 Governing Equations and Admissible Mean Flows

Compressible isentropic equations are

$$\frac{\partial \rho}{\partial t} + u_i \frac{\partial \rho}{\partial x_i} + \rho \frac{\partial u_i}{\partial x_i} = 0, \tag{14.12}$$

$$\rho \left(\frac{\partial u_i}{\partial t} + u_j \frac{\partial u_i}{\partial x_j} \right) = -\frac{\partial p}{\partial x_i} = 0, \tag{14.13}$$

$$\frac{1}{p} \left(\frac{\partial p}{\partial t} + u_i \frac{\partial p}{\partial x_i} \right) - \gamma \frac{1}{\rho} \left(\frac{\partial \rho}{\partial t} + u_i \frac{\partial \rho}{\partial x_i} \right) = 0. \tag{14.14}$$

To extend the analysis performed for strictly incompressible flows (including the special case of buoyant flows addressed in Chaps. 10 and 11), is not a easy task and can be done in several different ways.

One can at least try to obey the following rules or principles:

- To define a base flow, which could be identified with the mean flow, or $\bar{\rho}$, $\bar{\boldsymbol{u}}$, $\bar{p}$, as a special solution of the governing equations.
- To derive evolution equations for a disturbance flow, $\rho' = \rho - \bar{\rho}$, $p' = p - \bar{p}$, $\boldsymbol{u}' = \boldsymbol{u} - \bar{\boldsymbol{u}}$ by subtracting equations for the base flow from governing equations. The structure of these equations may satisfy some properties of invariance by translation, which are consistent with statistical homogeneity.
- To restrict the degree of nonlinearity to quadratic terms, neglecting higher-order nonlinear terms.

As in homogeneous incompressible turbulence, the first and second conditions can be considered independently of statistical assumptions and treatment. This is done by Craik and coworkers, who define the first condition as an *admissibility condition*. Accordingly, an admissible base flow is also compatible with a wavelike form for the disturbance flow, and the superposition of both is called 'a class of exact solutions' for Euler equations. This is nothing else than a formal rediscovery of RDT, but in which nonlinearity is rigorously excluded in the equations for the disturbance flow: only single mode perturbation are considered *and non-linearity is zero for a single Fourier mode in the incompressible case*. This is no longer true in compressible turbulence: nonlinearity does exist even for a single Fourier mode (monochromatic disturbance). We will try to define, however, a system of simplified equations in which only quadratic nonlinearities appear.

The condition that the mean velocity gradient must be uniform in space is inherited from the incompressible case, leading to

$$\frac{\partial \bar{u}_i}{\partial x_j} = A_{ij}(t).$$

An admissibility condition for the mean density follows as

$$\frac{\partial \bar{\rho}}{\partial t} + A_{jm}x_m \frac{\partial \bar{\rho}}{\partial x_j} + \bar{\rho}A_{ii} = 0.$$

This condition is compatible with the existence of a mean density gradient, or $\bar{\rho} = \rho_0(t) + C_i(t)x_i$, as in the buoyant flow case with the Boussinesq approximation addressed in Chap. 10. But this case is too complicated if the velocity field is not solenoidal, so that only

$$\bar{\rho} = \rho(t), \quad \rho_0 = \bar{\rho}(0) \tag{14.15}$$

is considered.

As a consequence, the momentum equation for the base flow is very similar to its incompressible counterpart

$$\bar{\rho}(t)\left(\frac{dA_{ij}}{dt} + A_{im}A_{mj}\right)x_j = -\frac{\partial \bar{p}}{\partial x_i},$$

One recovers the condition that $d\mathbf{A}/dt + \mathbf{A}^2$ must be a symmetric tensor, taking the Curl of the equation above, and that $\bar{\rho}(t)(dA_{ii}/dt + A_{im}A_{mi}) = -\nabla^2\bar{p}$, taking its divergence. Looking now at the linearized momentum equation for the disturbance flow:

$$\begin{aligned} &\rho'\left(\frac{dA_{ij}}{dt} + A_{im}A_{mj}\right)x_j \\ &+\bar{\rho}(t)\left(\frac{\partial u_i'}{\partial t} + A_{jm}x_m\frac{\partial u_i'}{\partial x_j} + A_{ij}(t)u_j'\right)x_j = -\frac{\partial \bar{p}}{\partial x_i}, \end{aligned} \tag{14.16}$$

it is observed that the contribution from the left-hand-side is twofold, since it combines both the mean acceleration weighted by the fluctuating density and the fluctuating acceleration weighted by the mean density. Violation of translational invariance by the first term is probable, but difficult to prove.[1] A simplified class of mean flows is finally proposed as

$$\frac{d\mathbf{A}}{dt} + \mathbf{A}^2 = 0, \quad \bar{p} = P(t). \tag{14.17}$$

Relaxing the assumption of irrotational mean strain is possible for developing at least linear RDT solutions, but the assumption of statistical homogeneity must be enforced. Even if this condition is much less stringent than it is generally admitted, the fact that the mean flow is only characterized by its spatial gradient matrix $\mathbf{A}$ has important consequences. First of all, it is not possible to define a length scale and a velocity scale for the mean flow (such as δ and ΔU in the shear layer case), but only a time-scale. This explains why linearization is not justified, as in conventional linear stability analysis, by a (small) ratio of disturbance-to-base velocity scale, but by an assumption of small elapsed time. S, which has the dimension of the inverse of a time, being a typical scalar scale for $\mathbf{A}$, the linear solution is expected to hold for small St only. But the maximum St at which it is valid depends crucially on the initial *shear rapidity* factor SL/u', where L and u' are typical scales for the disturbance flow, and other features of the flow. Practical experience shows that the validity of RDT cannot be predicted a priori, considering only St and the initial value of SL/u'. In some extreme cases, like rotating turbulence with angular velocity Ω and low Rossby number $Ro = u'/(2\Omega L)$, the nonlinearity becomes significant only after a very long time, such that $\Omega t = Ro^{-2}$ (see Chap. 7). This is partly explained by the depletion of nonlinearity due to phase mixing by dispersive inertial waves at small Rossby number. This "rapid" adjective in RDT is even less relevant here since at least two "rapid" time scales exist, namely $1/S$ and L/a. In brief, short time is a sufficient condition to ensure the validity of the linear solution, but not a necessary one.

A background mean flow is defined by space-uniform density $\bar{\rho}(t)$, pressure $P(t)$ and mean velocity gradients

$$U_i = A_{ij} x_j,$$

along with Eq. (14.17), and it is possible at least to consider that the fluctuations of density and pressure are weak with respect to their mean reference values, i.e.

$$\rho' \ll \bar{\rho}(t), \quad p' \ll P(t).$$

[1] In this case, one could check if a wavelike disturbance form for all the disturbance terms, including also ρ', can be consistently defined, without cancelling a priori the mean acceleration term.

Finally, the following simplified system of two equations is found for the fluctuating flow

$$\frac{D}{Dt}u_i' + A_{ij}u_j' + \frac{1}{\bar{\rho}}\frac{\partial p'}{\partial x_i} = -u'_j\frac{\partial u_i'}{\partial x_j} \tag{14.18}$$

$$\frac{D}{Dt}\left(\frac{p'}{\gamma P}\right) + \frac{\partial u_i'}{\partial x_i} = -u'_j\frac{\partial}{\partial x_j}\left(\frac{p'}{\gamma P}\right), \tag{14.19}$$

where

$$a_0^2 = \gamma\frac{P}{\bar{\rho}} \tag{14.20}$$

is the square of the speed of sound. The symbol $\frac{D}{Dt}$ denotes the material derivative following the mean flow streamlines. Viscous terms are omitted, in agreement with isentropic assumption, but they can be added for numerical convenience. These equations are the starting point for both the nonlinear statistically isotropic approach in the absence of mean velocity gradient (Fauchet et al. 1997) (see also Sect. 13.2), and the linear approaches in the presence of $\mathbf{A}$ (Jacquin et al. 1993; Cambon et al. 1993; Simone et al. 1997).

14.2.2 Properties of Admissible Mean Flows

A zero mean acceleration in Eq. (14.17) corresponds to

$$\ddot{F}_{ij}(t,0)X_j = 0,$$

so that the general expression for F is

$$F_{ij}(t,0) = \delta_{ij} + S_{ij}t, \tag{14.21}$$

where S_{ij} is an arbitrary constant matrix. The mean velocity gradient matrix is readily derived, using $\mathbf{A} = \frac{d\mathbf{F}}{dt}\mathbf{F}^{-1}$, as

$$\mathbf{A}(t) = \mathbf{S}(\mathbf{I}+\mathbf{S})^{-1}. \tag{14.22}$$

Using the volumetric ratio

$$J(t,0) = Det\mathbf{F}(t,t_0) = \exp\left[\int_{t_0}^{t} A_{ii}(t')dt'\right] \tag{14.23}$$

and the mean isentropic equation $P(t)\rho_0^{-\gamma}(t) = Constant$, one obtains

$$\rho_0(t) = \frac{\rho_0(0)}{J(t,0)}, \quad P(t) = \frac{P(0)}{J^\gamma(t,0)}, \tag{14.24}$$

resulting in the definition of a time-dependent speed of sound $a(t)$ if $J(t,0)$ is time-varying.

These equations were given in Cambon et al. (1993) to extend the conditions proposed by Blaisdell et al. (1991), and perhaps are not the most general solution consistent with the three admissibility conditions mentioned in the previous section. The search for more complex admissible base flows (e.g. Craik and Allen 1992) is more a mathematical skilled task than a physically relevant problem.

14.2.3 Linear Response in Fourier Space. Governing Equations

Equations (14.18) and (14.19) are linearized around a mean flow with space uniform gradient $\mathbf{A}$, discarding their right-hand-sides. As usual in RDT and in related stability analyses, the equations are simplified considering Fourier modes

$$(u_i', p')(\boldsymbol{x}, t) = \int (\hat{u}_i, \hat{p})(\boldsymbol{k}(t), t) e^{\imath \boldsymbol{k}(t)\cdot\boldsymbol{x}} d^3\boldsymbol{k},$$

with

$$\dot{k}_i = -A_{ji}k_j.$$

The only difference with incompressible RDT for the treatment of advection is the occurrence of the term A_{nn}, because the Fourier counterpart of $\dot{u'}_i$ is

$$\frac{\partial \hat{u}_i}{\partial t} - A_{nn}\hat{u}_i - A_{jm}k_j\frac{\partial \hat{u}_i}{\partial k_m}.$$

Extending the notation with the overdot to derivatives in Fourier space, the latter equation can be recast as

$$\dot{\hat{u}}_i - A_{nn}\hat{u}_i = \frac{\partial \hat{u}_i}{\partial t} + \frac{dk_m}{dt}\frac{\partial \hat{u}_i}{\partial k_m} - A_{nn}\hat{u}_i. \tag{14.25}$$

The system of Eqs. (14.18) and (14.19) yields

$$\dot{\hat{u}}_i - A_{nn}\hat{u}_i + A_{ij}\hat{u}_j = -\frac{\imath}{\rho_0}k_i\hat{p}, \tag{14.26}$$

$$\dot{\hat{p}} + (\gamma - 1)A_{nn}\hat{p} = -\gamma P \imath k_i \hat{u}_i. \tag{14.27}$$

An important step in investigating this system is to use the Helmholtz decomposition

$$\hat{\boldsymbol{u}} = \underbrace{\left(\mathbf{I} - \frac{\boldsymbol{k}\boldsymbol{k}^T}{k^2}\right)\hat{\boldsymbol{u}}}_{\hat{\boldsymbol{u}}_s} + \underbrace{\frac{\boldsymbol{k}\boldsymbol{k}^T}{k^2}\hat{\boldsymbol{u}}}_{\hat{\boldsymbol{u}}_d}. \tag{14.28}$$

In addition, the Craya–Herring frame of reference can be used for specifying the two solenoidal modes: the third vector is nothing else than $\boldsymbol{k}/k$ and is used to define the dilatational mode, with a superscript 3, consistently with

$$\boldsymbol{e}^{(3)} = \frac{\boldsymbol{k}}{k}, \quad u^{(3)} = \hat{\boldsymbol{u}} \cdot \boldsymbol{e}^{(3)},$$

from which it comes

$$\hat{\boldsymbol{u}} = \underbrace{u^{(1)}\boldsymbol{e}^{(1)} + u^{(2)}\boldsymbol{e}^{(2)}}_{\hat{\boldsymbol{u}}_s} + \underbrace{u^{(3)}\frac{\boldsymbol{k}}{k}}_{\hat{\boldsymbol{u}}_d}. \tag{14.29}$$

In agreement with the decomposition in physical space discussed in Sect. 2.1.5, the subscripts 's' and 'd' denote solenoidal and dilatational modes, respectively. Since the Craya–Herring frame of reference is a direct orthonormal frame, vortical (applying the Curl operator) and dilatational (applying the divergence) velocity contributions have simple counterpart in this frame:

$$\hat{\boldsymbol{\omega}}(\boldsymbol{k}, t) = \imath k \left(u^{(1)}\boldsymbol{e}^{(2)} - u^{(2)}\boldsymbol{e}^{(1)}\right) \tag{14.30}$$

$$\widehat{u_{i,i}}(\boldsymbol{k}, t) = \imath k u^{(3)}. \tag{14.31}$$

In order to recover an homogeneous problem, the pressure fluctuation is scaled as a velocity, and considered as the fourth component of the solution vector (Simone et al. 1997):

$$u^{(4)} = \imath \frac{\hat{p}}{\rho_0 a}. \tag{14.32}$$

This scaling is similar to the one of Eckhoff and Storesletten (1978).

Linear solutions are therefore expressed in terms of $u^{(i)}, i = 1, 4$ components, solving the following linear system of ODE:

$$\begin{pmatrix} \dot{u}^{(1)} \\ \dot{u}^{(2)} \\ \dot{u}^{(3)} \\ \dot{u}^{(4)} \end{pmatrix} + \begin{pmatrix} m_{11} - A_{nn} & m_{12} & m_{13} & 0 \\ m_{21} & m_{22} - A_{nn} & m_{23} & 0 \\ m_{31} & m_{32} & m_{33} - A_{nn} & +ak \\ 0 & 0 & -ak & \frac{3-\gamma}{2}A_{nn} \end{pmatrix} \begin{pmatrix} u^{(1)} \\ u^{(2)} \\ u^{(3)} \\ u^{(4)} \end{pmatrix} = 0 \tag{14.33}$$

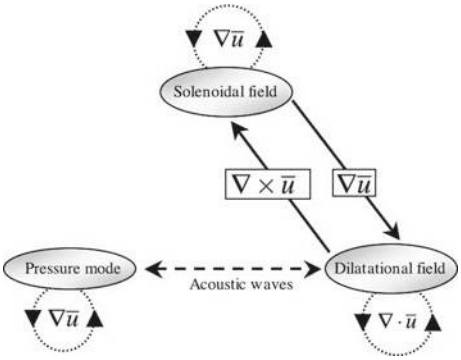

Fig. 14.2 Schematic view of interactions between modes defined in the local Craya–Herring frame according to the RDT analysis of compressible homogeneous shear flows. Dotted lines denote self-interaction

or equivalently

$$\dot{u}^{(i)} - A_{nn}u^{(i)} + m_{ij}u^{(j)} = 0, \tag{14.34}$$

where the coefficient of the RDT matrix $\mathbf{m}$ are defined as follows:

$$\begin{aligned}
m_{\alpha\beta} &= e_i^{(\alpha)}A_{ij}e_j^{(\beta)} - \dot{e}_i^{(\alpha)}e_i^{(\beta)}, \\
&= = e_i^{(\alpha)}A_{ij}e_j^{(\beta)} + \epsilon_{\alpha 3\beta}e_j^{(2)}A_{ij}e_j^{(1)}, && (14.35)\\
m_{\alpha 3} &= e_i^{(\alpha)}A_{ij}e_j^{(3)} - \dot{e}_i^{(\alpha)}e_i^{(3)} = e_i^{(\alpha)}\left(A_{ij} - A_{ji}\right)e_j^{(3)}, && (14.36)\\
m_{3\alpha} &= e_i^{(3)}A_{ij}e_j^{(\alpha)} - \dot{e}_i^{(3)}e_i^{(\alpha)} = 2e_i^{(3)}A_{ij}e_j^{(\alpha)}, && (14.37)\\
m_{33} &= e_i^{(3)}A_{ij}e_j^{(3)}, && (14.38)\\
m_{34} &= -m_{43} = -a_0k. && (14.39)
\end{aligned}$$

As previously, Greek indices take the values 1 or 2 only and refer to solenoidal modes. The calculation of the "solenoidal block" is made assuming that the polar axis $\boldsymbol{n}$ of the Craya–Herring frame of reference is one of the eigenvectors of $\mathbf{A}$.

Of course, the four-dimensional problem in physical space (u_1, u_2, u_3, p) remains a four-components problem in Fourier space. Using the Craya–Herring frame, no reduction of the number of variables is obtained as in solenoidal cases since the dilatational mode $u^{(3)}$ does not vanish, but the matrix m_{ij}, $i = 1, 4$, $j = 1, 4$ has some zero components and the role of each nonzero component is more easily understood. All the coefficients in the 'velocity block' of the matrix above, or m_{ij}, $i = 1, 3$, $j = 1, 3$ depend on $\mathbf{A}$ and therefore scale with S, which is a norm of $\mathbf{A}$. The acoustic terms m_{34} and m_{43} scale with the dispersion frequency of acoustic waves, ka_0. As a consequence, the parameter $S/(a_0k)$ is immediately found to be the *pivotal* parameter; of course it is a spectral counterpart of the gradient Mach number M_g. The different couplings between the solenoidal modes $u^{(1)}$ and $u^{(2)}$, the dilatational mode $u^{(3)}$ and the pressure mode $u^{(4)}$ are illustrated on Fig. 14.2.

The solution of Eq. (14.33) is expressed as

$$u^{(i)}(\boldsymbol{k}(t),t) = J(t,0)g_{ij}(\boldsymbol{k},t,0)u^{(j)}(\boldsymbol{K},0), \tag{14.40}$$

with J given by (14.23). As usual in RDT, the deterministic function g_{ij}, $i,j = 1,4$ can be computed analytically or numerically, solving sequentially the system (14.33) for a set of arbitrary simple initial data, such as $u^{(i)} = \delta_{i1}, \delta_{i2}, \delta_{i3}, \delta_{i4}$. Corresponding solutions for the statistical moments are obtained from the initial values of these statistical moments through g-products. Simplified forms of these initial values usually come from isotropy and 'strong' acoustic equilibrium assumptions (Simone et al. 1997).

In the general case with time-depending J, new "divergence" and "pressure" terms can be used, introducing the following new integration variables:

$$y = J^{-1}\frac{u^{(3)}}{k}, \quad z = J^{-1}\frac{u^{(4)}}{a_0}, \tag{14.41}$$

and using

$$\frac{\dot{k}}{k} = -A_{ij}\frac{k_i k_j}{k^2} \tag{14.42}$$

a useful "pressure" equation is found

$$\frac{D}{Dt}\left(\frac{\dot{z}}{k^2}\right) + a_0^2 z = a_0^2 z_s, \tag{14.43}$$

in which

$$z_s = J^{-1}\frac{\hat{p}_s}{\bar{\rho}a_0^2} = \imath\frac{J^{-1}}{ka_0^2}m_{3\alpha}u^{(\alpha)} \tag{14.44}$$

only involves the solenoidal velocity field and exactly corresponds to the solution of the Poisson equation found in the strictly incompressible case.

14.2.3.1 Recovering the Acoustic Régime

In the absence of mean flow, i.e. setting $\mathbf{A} = \mathbf{0}$ in Eq. (14.33), the solenoidal mode is strictly conserved, whereas pressure and dilatational velocity modes are governed by

$$\left(u^{(3)} \pm \imath u^{(4)}\right)(t) = e^{\pm\imath a_0 kt}\left(u^{(3)} \pm \imath u^{(4)}\right)(t=0) \tag{14.45}$$

which corresponds to the acoustic regime discussed in Chap. 13.

14.2.3.2 Recovering the Solenoidal Limit

The solenoidal limit, also known as incompressible RDT, is found solving only the block $i = 1, 2$, $j = 1, 2$, since $u^{(3)} = 0$ gives the solenoidal limit (e.g. Eq. (14.31)). The governing equation for the pressure mode is

$$u^{(4)} = u_s^{(4)} = \frac{m_{3\alpha}}{ka_0} u^{(\alpha)}. \tag{14.46}$$

This equation gives the counterpart of the solution for the Poisson equation satisfied by the fluctuating pressure in this limit, or

$$\hat{p} = \hat{p}_s = -\frac{\imath}{\rho_0} m_{3\alpha} u^{(\alpha)}, \quad m_{3\alpha} = 2\frac{k_i}{k} A_{ij} e_j^{(\alpha)}.$$

14.2.3.3 Irrotational Mean Strain Case

In addition to pure solenoidal coupling terms $m_{\alpha\beta}$, which are the same as in solenoidal RDT, and to 'acoustical' or 'pseudo-sound' terms $m_{34} = -a_0 k, m_{43} = a_0 k$, discussed above, very interesting terms are

$$m_{\alpha 3} = e_i^{(\alpha)} (A_{ij} - A_{ji}) \frac{k_j}{k}.$$

These terms represent a feedback from the dilatational mode to the solenoidal modes, and they are generated by the *rotational part* of the mean flow.

As an immediate consequence, the solenoidal flow is decoupled in the presence of an irrotational straining process. Another less obvious consequence is that the kinetic energy growth rate is larger in compressible RDT than in solenoidal RDT, since the kinetic energy of the dilatational mode, which is always positive, is just added to the kinetic energy of the solenoidal mode, which is independent of compressibility in this case. The effect of the fluctuating pressure in the solenoidal linear limit is just to kill this dilatational contribution. Accordingly, as firstly demonstrated by Jacquin et al. (1993), the kinetic energy growth rate increases monotonically with increasing gradient Mach number M_g, from solenoidal RDT to "pressure released" RDT, in full agreement with Eq. (14.11). These results were revisited and confirmed by full DNS (Cambon et al. 1993), also quoted in Lele (1994) and Simone et al. (1997) for homogeneous axial compression ($A_{ij} = S(t)\delta_{i1}\delta_{j1}$), as shown on Fig. 14.3. For the sake of convenience, the time advancement parameter is not $S(0)t$ but the inverse of the mean volumetric ratio $J(t)$, with $S(t) = -S(0)/(1 - S(0)t) = -S(0)/J(t)$. The contribution of the solenoidal mode corresponds to a quasi-linear growth of kinetic energy in terms of the mean compression ratio J^{-1}, while dilatational contribution leads to a quasi-parabolic growth. It is worth noticing that compressibility is always

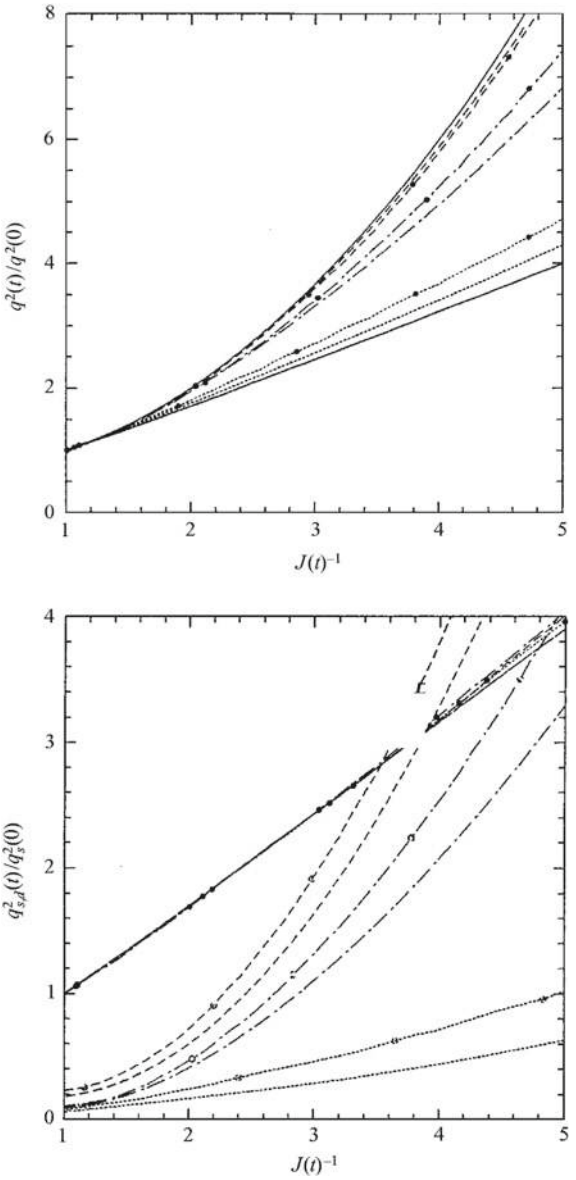

Fig. 14.3 Turbulent kinetic energy histories for different values of the gradient Mach number M_g, in the axial compression case. Top: Full DNS (dots) and linear theory (lines). Bottom: in addition, splitting into solenoidal and dilatational parts. Reproduced from Simone et al. (1997) with permission of CUP

shown to have a destabilizing effect regarding RDT for irrotational mean flow. Of course, the general relevance of this result can be questioned since it relies on both the irrotational condition and the short time condition $S(0)t < 1$ in the case of axial compression.

Analytical solutions for solenoidal RDT and pressure-released limit are

$$\frac{\mathcal{K}(t)}{\mathcal{K}(0)} = \frac{1}{2}\left(1 + J^{-2}\frac{\tan^{-1}(\sqrt{J^{-1}-1})}{\sqrt{J^{-1}-1}}\right), \tag{14.47}$$

yielding a quasi-linear growth in terms of J^{-1}, and

$$\frac{\mathcal{K}(t)}{\mathcal{K}(0)} = \frac{2+J^{-2}}{3}, \tag{14.48}$$

yielding a parabolic growth if $J^{-1} \geq 1$, respectively. Despite the presence of the varying mean volumetric ratio, the solenoidal equation is very close to the classical equation for mean incompressible axial strain given by Batchelor (see also Eqs. (8.37) and (8.38)), up to a $J^{4/3}$ factor. This result was also found by Ribner and Tucker (1953). The framework of solenoidal turbulence subjected to mean strain with variable volume is also addressed in Cambon et al. (1992), with the particular flow case addressed in the next subsection.

14.3 Incompressible Turbulence with Compressible Mean Flow Effects: Compressed Turbulence

An interesting class of solenoidal (i.e. with divergence-free velocity fluctuations) homogeneous turbulent flows can be considered in the presence of a mean flow with space-uniform gradients, which takes into account a variation in the mean volume. Provided that the Mach number is small enough, this set of assumptions is self-consistent, and it is possible to extend solenoidal RDT to *compressed turbulence*, i.e. to divergence-free fluctuating velocity field in the presence of a mean dilatational flow, neglecting acoustics and thermal effects.

The mean flow is characterized by the volumetric ratio (14.23), which differs from 1 when the constraint $A_{ii} = 0$ is relaxed. For the sake of brevity t_0 will be omitted in the following, so that abridged notations $\mathbf{F}(t)$, $J(t)$ will be now used in this section. Among different compressing mean flows, the case of isotropic compression deserves particular attention. In this case, the matrices $\mathbf{A}$ and $\mathbf{F}$, and the trajectory equations write

$$A_{ij}(t) = S(t)\delta_{ij}, \quad F_{ij}(t) = J^{1/3}(t)\delta_{ij}, \quad x_i = J^{1/3}(t)X_j, \tag{14.49}$$

in which $S = \frac{1}{3}\frac{1}{J}\frac{dJ}{dt}$. The fluctuating field is governed by

$$\frac{\partial u_i'}{\partial t} + Sx_j\frac{\partial u_i'}{\partial x_j} + Su_i' + \frac{1}{\overline{\rho}}\frac{\partial p'}{\partial x_i} = -u_j'\frac{\partial u_i'}{\partial x_j} + \nu\nabla^2 u_i', \tag{14.50}$$

in which explicit nonlinear terms and viscous terms are gathered in the right-hand-side. Setting the rigth-hand-side to zero, the RDT solution is directly found in physical space[2]:

$$\boldsymbol{u}'(\boldsymbol{x},t) = J^{-1/3}(t)\boldsymbol{u}'(\boldsymbol{X},0).$$

More interesting is the possibility to derive a rescaling for full nonlinear equation (14.50), in terms of spatial coordinates, velocity and time. It is expressed as follows

$$\boldsymbol{x}^* = J^{-1/3}\boldsymbol{x}, \quad \boldsymbol{u}^*(\boldsymbol{x}^*,t^*) = J^{1/3}\boldsymbol{u}'(\boldsymbol{x},t) \quad dt^* = J^{-2/3}(t)dt. \tag{14.51}$$

Such a dynamical rescaling can also be used in Boltzmann equations, and applied to the cosmological gas in order to account for the expansion of the universe. When substituting it in Eq. (14.50) which governs the primitive unscaled variables, the rescaled quantities are shown to satisfy the Navier–Stokes equations without the additional mean terms which depend on S in the left-hand-side. For consistency reason, the pressure is rescaled as $p^* = J^{5/3}p$, and the only difference with uncompressed freely decaying isotropic turbulence for the velocity field $\boldsymbol{u}^*(\boldsymbol{x}^*,t^*)$ is a possible influence of time-variations of the viscosity $\nu^*(t)$. The variation in Reynolds number follows directly since $u'L = u^*L^*$. If the Reynolds number is high enough, however, it is reasonable to expect that all classical results dealing with spatio-temporal dynamics and statistics of isotropic freely decaying turbulence are still valid for $(\boldsymbol{u}^*, \boldsymbol{x}^*, t^*)$, so that the corresponding laws for primitive variables $(\boldsymbol{u}', \boldsymbol{x}, t)$ can be readily derived using Eq. (14.51). The reader is referred to Cambon et al. (1992) for various applications.

This scaling deserves attention for two reasons. First, it illustrates a particular "dynamical" version of the general scale invariance (see e.g. Frisch 1995)

$$\boldsymbol{x}^* = \lambda\boldsymbol{x}, \quad \boldsymbol{u}^* = \lambda^h\boldsymbol{u}, \quad t^* = t\lambda^{1-h}, \quad \nu^* = \lambda^{1+h}\nu, \tag{14.52}$$

so that λ corresponds to the time-dependent mean density ratio $J^{-1/3}$, with $h = -1$. In the latter invariance group, the viscosity would be left unchanged if $h = -1$, but it should be borne in mind that the dynamical rescaling deals with a continuously time-varying parameter $J^{-1/3}(t)$ in contrast to λ. It is worth noting that taking $h = -1$ one recovers the scaling law I in Eq. (4.119), while transformation in Eq. (4.120) is found setting $h = 1$.

Second, it can be used to check the consistency of any model or theory, ranging from $\mathcal{K} - \varepsilon$ to elaborated EDQNM, DIA or LRA versions.

As a simple example, let us start with a classical decay law such as

$$\mathcal{K}(t) = \mathcal{K}(0)\left(1 + \frac{t}{nt_0}\right)^{-n}, \quad L(t) = L(0)\left(1 + \frac{t}{nt_0}\right)^{1-n/2},$$

[2]This is a very special case, in which the nonlocal potential term is zero in Eq. (14.8).

consistently obtained for the turbulent kinetic energy, its dissipation rate, and the single relevant integral lengthscale L, with $1/t_0 = -(1/\mathcal{K})d\mathcal{K}/dt$ at $t = 0$. Applying the rescaling, which amounts to rewrite the same equations in terms of 'starred' variables, the following equations are derived for the 'compressed' decay:

$$\mathcal{K}(t) = \mathcal{K}(0)e^{2Ct}\left(1 + \frac{e^{2Ct} - 1}{2nCt_0}\right)^{-n}, \quad L(t) = L(0)e^{-Ct}\left(1 + \frac{e^{2Ct} - 1}{2nCt_0}\right)^{1-n/2},$$

for a mean compression or dilatation at constant rate $S(t) = -C$.

These equations show immediately than the domain of relevance of RDT in terms of elapsed time is more restricted as usually conjectured, with a dominant nonlinearity having an effect opposite to the linear one. Choosing a spherical compression, i.e. $C > 0$, the RDT growth rate factor for $\mathcal{K}$, e^{2Ct}, is always balanced and rapidly dominated by a nonlinear term given by e^{-2nCt}. This reflects the fact that, when the velocity u' is affected by a linear 'RDT' factor e^{Ct}, the nonlinear term of dimension u'^2/l is affected by a factor e^{-3Ct}, the full nonlinear effect being finally accounted for by the time-rescaling $dt = dt^* e^{2Ct}$.

This flow is particular in the sense that turbulence is not really compressible, but it offers a very simple way to exactly evaluate the impact of nonlinearity; this is an unique instance for comparing linear RDT with full nonlinear theory. In contrast, a depletion of nonlinearity is rather expected in true compressible turbulence, with respect to the incompressible flow case, but in the anisotropic case, as discussed further. It is also possible to study the spherical (isotropic) compression or dilatation applied to really compressible homogeneous turbulence. Very consistent results were found by Blaisdell et al. (1996) and Simone et al. (1997), using full DNS and isentropic RDT: as a particular result, the strong acoustic equilibrium can be sustained, as illustrated by the Fig. 2 in Simone et al. (1997).

14.4 Compressible Turbulence in the Presence of Pure Plane Shear

The background velocity field of the pure plane shear addressed in this section is identical to the one considered in the incompressible case (see Chap. 9). It is defined by

$$\mathbf{A} = \begin{pmatrix} 0 & S & 0 \\ 0 & 0 & 0 \\ 0 & 0 & 0 \end{pmatrix}, \mathbf{F}(t) = \begin{pmatrix} 1 & St & 0 \\ 0 & 1 & 0 \\ 0 & 0 & 1 \end{pmatrix}. \tag{14.53}$$

The associated characteristic lines in the both Fourier and physical (trajectories) space are given by

$$k_1 = K_1, \quad k_2 = K_2 - K_1 St, \quad k_3 = K_3 \qquad x_1 = X_1 + St X_2, x_2 = X_2, x_3 = X_3. \tag{14.54}$$

In this case $J \equiv 1$, so that $\bar{\rho}$, P and a $(= a_0)$ are constant.

14.4.1 Qualitative Results

Even in the pure shear case, the pressure released limit is more energetic than the linear solenoidal limit. Accordingly, a reduction of pressure fluctuations, in the linear limit, would yield a monotonic increase of turbulent kinetic energy with increasing M_g, as for the case of irrotational mean straining ! The fact that the pressure-released growth rate is higher than the solenoidal one, in the linear limit, results from Eqs. (14.5) and (14.53), which yield a quadratic growth rate for the kinetic energy, i.e. $\mathcal{K}(t) \propto (St)^2$.[3] In the same conditions, the solenoidal RDT predicts only a linear, growth rate: $\mathcal{K}(t) \propto St$. Once recast in a relevant non-dimensional form, the kinetic energy growth rate is characterized by

$$\Lambda = \frac{1}{S\mathcal{K}} \frac{d\mathcal{K}}{dt}, \tag{14.55}$$

which is equal to

$$\Lambda = -2 \left(b_{12} + \frac{\bar{\varepsilon}_s + \bar{\varepsilon}_d - \Pi^{(d)}}{S\mathcal{K}} \right) \tag{14.56}$$

according to Eq. (14.2). In the pressure-released linear limit with isotropic initial data, the kinetic energy growth rate is equal to

$$\Lambda^{(pr)} = \frac{2St}{3 + (St)^2}. \tag{14.57}$$

This equation gives the upper solid line in Fig. 14.4-bottom. The corresponding limit of solenoidal RDT is plotted in Fig. 14.4, as the lower solid line. Is there a simple explanation for this stabilizing effect of pressure in solenoidal RDT, without looking at RDT details? As in all shear flow cases, the answer is given by the dynamics of the vertical velocity component: u_2' is passively advected in the pressure-released linear limit, while it is its Laplacian $\nabla^2 u_2'$ which is advected in the RDT solenoidal limit. According to the corresponding RDT complete solution in Fourier space, $D(k^2 \hat{u}_2)/Dt = 0$, leading to $\hat{u}_2(\boldsymbol{k}, t) = \frac{K^2}{k^2} \hat{u}_2(\boldsymbol{K}, 0)$ and a decrease of u_2' since $K/k < 1$ for $t > 0$. Using the Craya–Herring frame with the polar axis parallel to the cross-gradient direction of the mean shear, the complete RDT solution (see also Chap. 9) is much simpler than the one given by Townsend Townsend (1976) in the fixed frame. The corresponding equation dealing with $u'^{(2)}$ is

[3] The reader is referred to Chap. 9 for a detailed discussion of the incompressible shear case. Results are summarized in Table 9.2.

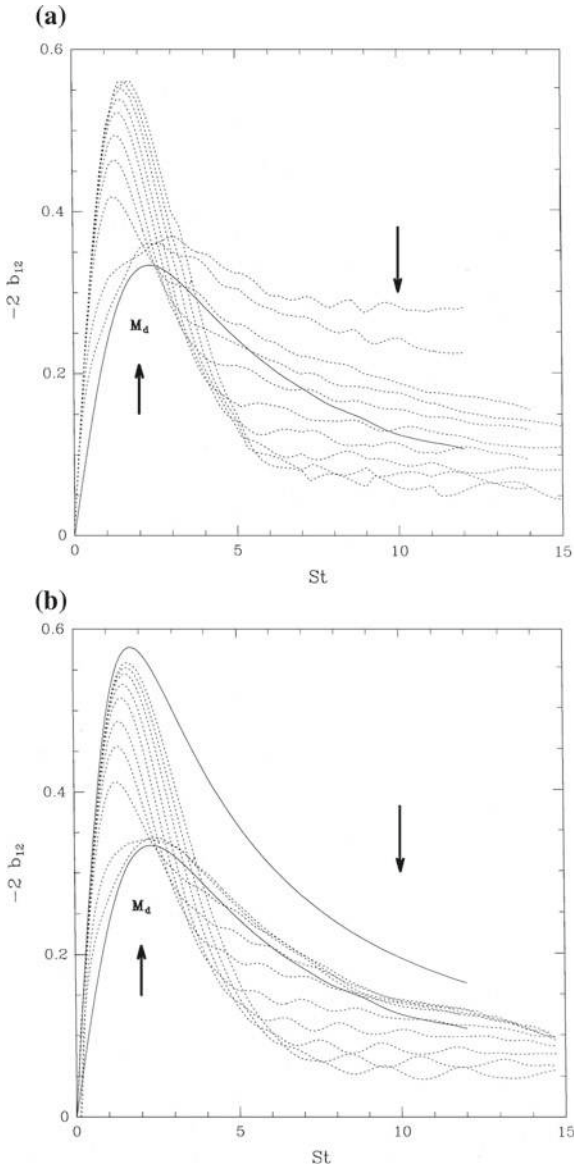

Fig. 14.4 Histories of the nondimensional production term $-2b_{12}$, Full DNS (top) and linear quasi-isentropic compressible theory (bottom), so called (improperly) RDT. Upper and lower solid lines correspond to pressure-released limit and solenoidal limit, respectively. Initial M_g (called M_d in the figure) ranges from 4 to 67 for both DNS and RDT, arrows show trend with increasing M_g. Reproduced from Simone et al. (1997) with permission of CUP

$$(k\dot{u}^{(2)}) = 0, \tag{14.58}$$

which is consistent with the pure advection of $\nabla^2 u_2$ in the physical space. Note that this analysis only confirms that the role of the so-called 'rapid' pressure-strain rate tensor in Reynolds stress equations is a stabilizing one. *This result is in qualitative agreement with crude single-point models, in which the 'rapid' pressure-strain rate*

tensor is modelled as reducing the production. Using these simple considerations, a destabilizing effect of compressibilty is observed, as shown in Fig. 14.4 for $St < 4$ in both full DNS and quasi-isentropic compressible linear theory. This result is very similar to what happened in the irrotational mean strain case, with a monotonic increase of Λ with increasing M_g, from the solenoidal to the pressure-released case.

14.4.2 Discussion of Results

As shown in Fig. 14.4, the conventional 'stabilizing' behaviour of compressibility is recovered at large times $St > 4$. It is therefore clear that this stabilizing behaviour is explained by the presence of the $m_{\alpha 3}$ coupling terms, at least in the linear limit. Figure 14.4 displays the main part of the turbulent kinetic energy growth rate Λ defined in Eq. (14.55), which reduces to $-2b_{12}$, ignoring other terms, as also justified by Sarkar (1995).

Equations for the pure plane shear case are rewritten below using Eqs. (14.35)–(14.37) and the three nontrivial components from the solenoidal Craya–Herring frame

$$e_1^{(1)} = -\frac{K_3}{K_\perp}, \quad e_2^{(2)} = -\frac{K_\perp}{k}, \quad e_1^{(2)} = \frac{K_1 k_2}{K_\perp k}.$$

It is recalled that the optimal choice for the arbitrary vector $\boldsymbol{n}$ in the definition of the local frame (see Table 2.2) is to chose the polar axis in the cross-gradient shear direction: $n_i = \delta_{i2}$. Further simplifications are obtained using integrating factors to remove some diagonal coupling terms, in agreement with Eq. (14.42). After some algebra, one obtains

$$\dot{u}^{(1)} + S\frac{K_3}{k(t)}u^{(2)} = S\frac{K_3 k_2(t)}{K_\perp}\frac{u^{(3)}}{k(t)}, \tag{14.59}$$

$$\left(k\dot{u}^{(2)}\right) = -S\frac{K_1}{K_\perp}k(t)u^{(3)}, \tag{14.60}$$

$$\left(\frac{\dot{u^{(3)}}}{k(t)}\right) = 2S\frac{K_1 K_\perp}{k^4(t)}k(t)u^{(2)} - a_0 u^{(4)}, \tag{14.61}$$

$$\dot{u}^{(4)} = a_0 k(t) u^{(3)}, \tag{14.62}$$

with

$$K_\perp = \sqrt{K_1^2 + K_3^2}, \tag{14.63}$$

as a special case of Eq. (14.33). The counterpart of Eq. (14.43) is

$$\frac{D}{Dt}\left(\frac{\dot{\hat{p}}}{k^2(t)}\right) = a_0^2\left(\underbrace{2\imath\rho_0 S\frac{K_1K_\perp}{k^4}(ku^{(2)})}_{\hat{p}_s} - \hat{p}\right). \tag{14.64}$$

Going back to the (generally expected) stabilizing effect of compressibility, it is commonly accepted, following Sarkar (1995), Pantano and Sarkar (2002), that the weakening of pressure correlation is the sole explanation. As a matter of fact, the weakening of pressure can be demonstrated from the solution of Eq. (14.64), considering the following scalar Green's function for pressure to velocity coupling:

$$\hat{p}(\mathbf{k},t) = \int_{t_0}^{t} \mathcal{G}(\mathbf{k},t,t')\hat{p}_s(\mathbf{k},t')dt'. \tag{14.65}$$

Recently, Thacker et al. (2006) proposed an analytical solution for a similar scalar Green's function in the pure shear case, generalizing the form $\mathcal{G} = \frac{\sin(a_0k(t-t'))}{a_0k}$ recovered in the shearless case (e.g. Pantano and Sarkar 2002). One can point out that this scalar Green's function is generated by the equation

$$\ddot{\hat{p}} + a_0^2k^2\hat{p} = a_0^2k^2\hat{p}^{(s)}, \tag{14.66}$$

which is simpler and less general than Eq. (14.64). Both Eqs. (14.64) and (14.66) account for the time-dependency of k via Eq. (14.54), but the removal of the divergence term was not accurately obtained in Thacker et al. (2006). In addition, the equation of type (14.65) was used to express the 'rapid' pressure-strain rate tensor in terms of the velocity spectral tensor involved in $\overline{\hat{p}^*\hat{u}_i^{(s)}}$: a solenoidal spectral model for $\overline{\hat{u}_i^{(s)*}\hat{u}_j^{(s)}}$ was used by Thacker et al. (2006) for this purpose (see also Cambon and Rubinstein 2006 for a discussion of this model).

It is advocated here that the explanation based on Eq. (14.64), i.e. weakening of pressure fluctuations, for stabilizing/destabilizing compressibility effects, is only a partial one. This equation is also a byproduct of the general study based on the full system of linear equations considered here. The conventional explanation is valid, for instance to account for the difference between the less compressible fully nonlinear case in Fig. 14.4-top which corresponds to an almost constant production rate at largest St, and the pressure released case (upper curve in solid line in Fig. 14.4-bottom). This 'explanation' is irrelevant when the plot of compressible RDT result at large M_g and large elapsed time lies below the incompressible RDT limit curve (solid line in Fig. 14.4): in this case the sole argument of mollification of pressure would lead a destabilizing effect of compressibility. In contrast, the second explanation based upon the feedback in Eq. (14.60) of the dilatational mode onto the relevant poloidal mode, which includes the whole vertical velocity component—a key component for the production by shear in any case—, is valid.

As a final remark, let us recall that the argument dealing with the weakening of pressure is always relevant in the irrotational 'mean' case, or at $St < 4$ in the shear case, but yields a *systematic destabilizing effect* because the pressure-released limit is always over the incompressible RDT limit! Of course, looking at the Reynolds stress equations, the weakening of the *nonlinear* (so-called slow) pressure-strain rate tensor yields a stabilizing effect in the pure shear flow case, but this reflects more a depletion of nonlinearity at increasing M_g than a stabilizing effect of compressibility: in addition the ratio of gradient to turbulent Mach number M_g/M_t is nothing else than the shear rapidity factor, and increasing M_g without increasing M_t in the same proportion means depleting the nonlinearity. The latter remark also holds for DNS results presented in Fig. 14.4, but not for pure linear theories.

14.4.3 Towards a Complete Linear Solution

As a direct continuation of the study by Simone et al. (1997), some work remains to be done to retrieve more information from the linear equations in the pure shear flow case. The existence of the invariant quantity

$$\xi = ku^{(2)} + \frac{S}{a_0}\frac{K_1}{K_\perp}u^{(4)}, \tag{14.67}$$

which is passively advected (i.e. conserved along the characteristic lines (14.54)), as seen combining Eqs. (14.60) and (14.62), offers new perspectives for analytical solutions. Analytical solutions by Thacker et al. (2006) for the scalar pressure Green's function can be useful for this purpose too.

A single second order equation is found at $K_1 \neq 0$ for $x = ku^{(2)}$:

$$\frac{D}{Dt}\left(\frac{\dot{x}}{k^2}\right) - K_1^2\left(2\frac{S^2}{k^4} + \frac{a_0^2}{K_\perp^2}\right)x = -\frac{K_1^2}{K_\perp^2}a_0^2\xi. \tag{14.68}$$

As in all RDT cases in the presence of pure plane shear, an analytical solution is found if $K_1 = 0$, because $\boldsymbol{k} = \boldsymbol{K}$. In this case the acoustic solution (14.45) for $u^{(3)}$ and $u^{(4)}$ is valid, whereas the solution of (14.59) and (14.60) is

$$u^{(2)}(\boldsymbol{k}, t) = u^{(2)}(\boldsymbol{k}, 0), \tag{14.69}$$

$$\begin{aligned} u^{(1)}(\boldsymbol{k}, t) = u^{(1)}(\boldsymbol{k}, 0) - St\frac{k_3}{k}u^{(2)}(0) \\ +S\frac{k_2}{k}\left(\frac{\sin(a_0kt)}{a_0k}u^{(3)}(\boldsymbol{k}, 0) - \frac{\cos(a_0kt)}{a_0k}u^{(4)}(\boldsymbol{k}, t)\right). \end{aligned} \tag{14.70}$$

The feedback from dilatational to toroidal mode is displayed in the latter equation. The probably more important (for global production) feedback from dilatational to poloidal is cancelled at $k_1 = 0$, showing the need for a general solution at any K_1.

In the line of the latter study, the very complete study by Livescu and Madnia (2004) gives many useful analytical and numerical results for the homogeneous turbulent shear flow, with emphasis on the effect of compressibility. Analytical RDT solutions show very different behavior compared to the incompressible case, with most of the contributions to second order moments coming from different regions in the wavenumber space. The analytical solutions predict the decrease of the growth rate with compressibility and the persistent anisotropy of higher order derivative moments seen in DNS.

A very important result of the RDT analysis is the derivation of the following linear third-order in time equation for the pressure fluctuation

$$\frac{\partial^3 \hat{p}}{\partial \tau^3} = -\frac{a_0^2}{S^2}\left(k^2 \frac{\partial \hat{p}}{\partial \tau} - 4k_1 k_2 \hat{p}\right), \tag{14.71}$$

with $\tau = St$. This equation is completely consistent with the system of Eqs. (14.64) and (14.62), and could be recovered in eliminating the poloidal (or vertical) mode of fluctuating velocity between them. In addition, a second order in time equation for $\hat{p}$ can be find as an integral form of Eq. (14.71), using the invariant ξ in Eq. (14.67). An equation similar to (14.68), but for the pressure, is found this way.

14.4.4 Noise Radiated by Homogeneous Compressible Pure Shear Turbulence: Lighthill Analogy

The Lighthill analogy used to evaluate the noise radiated by isentropic compressible isotropic turbulence in Sect. 13.2.10 can be extended to the case of the noise radiated by isentropic homogeneous shear turbulence in which the Lighthill tensor is restricted to

$$T_{ij} = \rho_\infty u_i u_j \tag{14.72}$$

The developments are almost the same as in the isotropic case, since the main difference arises in the expression and modeling of the Lighthill tensor for aeroacoustic sources. Therefore, the emphasis is put here on the modelling of source term, the rest of the procedure, i.e. use of the d'Alembertian Green function along with simplifications arising from further assumptions dealing with source compactness and far-field approximation being the same as in Sect. 13.2.10.

In the homogeneous shear case, the expression of the fourth-order correlation tensor must be split into a purely isotropic part and a second part related to the interactions between the mean shear and velocity fluctuations, exactly as in the incom-

pressible case discussed in Sect. 9.7,[4] leading to

$$R_{ijkl}(\boldsymbol{y},\boldsymbol{\xi},\tau) = \underbrace{\rho_\infty^2 \overline{u_i u_j u_k' u_l'}}_{\text{self-noise}} + \underbrace{4\rho_\infty^2 \delta_{1j}\delta_{1l}\overline{u_i u_k'} U_j U_l'}_{\text{shear-noise}}, \tag{14.73}$$

$$\boldsymbol{u}(\boldsymbol{y},t) = U\boldsymbol{e}_x + \boldsymbol{u}, \quad \boldsymbol{u}(\boldsymbol{y}+\boldsymbol{\xi},t+\tau) = U'\boldsymbol{e}_x + \boldsymbol{u}'. \tag{14.74}$$

The term UU' is evaluated writing a Taylor series expansion about the middle point $\boldsymbol{y}+\boldsymbol{\xi}/2$:

$$UU' \simeq U^2(\boldsymbol{y}+\boldsymbol{\xi}/2) - \frac{\xi_2^2}{4}\left(\frac{dU}{dy}(\boldsymbol{y}+\boldsymbol{\xi}/2)\right)^2, \tag{14.75}$$

which simplifies in the present case of homogeneous shear as

$$UU' \simeq U^2(\boldsymbol{y}+\boldsymbol{\xi}/2) - S^2\frac{\xi_2^2}{4}. \tag{14.76}$$

The two-point fourth-order correlation $\overline{u_i u_j u_k' u_l'}$ is modeled thanks to the Quasi-Normal hypothesis, as in the isotropic case. The two-point second-order velocity correlations are then evaluated exactly as in the isotropic case, leading to closed expressions for both shear noise and self-noise components.

The associated expression for the radiated acoustic intensity is

$$I(\boldsymbol{x}) = \underbrace{\frac{\mathcal{A}\rho_\infty^2}{x^2}\int_{\mathcal{V}} \frac{2L_u^6\mathcal{K}^2}{9\sqrt{2}C^5}\frac{d^4G^2}{d\tau^4}(0)d^3\boldsymbol{y}}_{\text{self-noise}} + \underbrace{\frac{S^2\mathcal{A}\rho_\infty^2}{x^2}\int_{\mathcal{V}} \frac{2L_u^5\mathcal{K}}{6\pi C^5}\frac{d^4G}{d\tau^4}(0)D_\theta d^3\boldsymbol{y}}_{\text{shear-noise}} \tag{14.77}$$

where $D_\theta = (\cos^4\theta + \cos^2\theta)/2$ is the shear noise directivity. One can see that contrary to the self noise which is emitted in an isotropic way, the shear noise intrinsically exhibits a non-uniform directivity, independently of convective effect.

The radiated acoustic spectrum is now given by

$$\hat{R}_{\rho\rho}(\boldsymbol{x},\omega) = \frac{\mathcal{A}}{x^2}\int_{\mathcal{V}}\left[\hat{S}_{\text{self}}(\boldsymbol{y},\omega) + \hat{S}_{\text{shear}}(\boldsymbol{y},\omega)\right]d^3\boldsymbol{y}. \tag{14.78}$$

Using Bailly's formula for the velocity two-time correlation function $G(\tau)$, one obtains for the spectra of the two noise components:

$$\hat{S}_{\text{self}}(\boldsymbol{y},\omega) = \frac{4\rho_\infty^2 L_u^3\mathcal{K}^2}{9\sqrt{2}\beta\tau_u}\omega^4\frac{C\omega\tau_u/4\beta}{\sinh(C\omega\tau_u/4\beta)} \tag{14.79}$$

[4] As a matter of fact, the solution in compressible shear case is formally the same as in the incompressible shear case, the Green function of the Laplacian operator being replaced by the one of the d'Alembertian operator.

and

$$\hat{S}_{\text{shear}}(\boldsymbol{y}, \omega) = \frac{\rho_\infty^2 L_u^5 \mathcal{K} D_\theta}{3\beta\tau_u} S^2\omega^4 \frac{1}{\cosh(C\omega\tau_u/4\beta)}. \tag{14.80}$$

As in the isotropic case, this model is observed to be very accurate in subsonic cases.

14.5 Perspectives and Open Issues

Perspectives for modelling nonhomogeneous and/or nonlinear effects can be briefly discussed. On the one hand, extending homogeneous RDT towards zonal (localized) RDT is possible, but the related assumption of short-wave disturbance can disconnect the acoustic modes in practice. A more promising case is found when disturbances are localized in the vicinity of rays (along which total energy, including the acoustic one, propagates), instead of being localized near mean trajectories. More details are given in Chap. 17.

On the other hand, in the absence of mean velocity gradients, interactions between solenoidal, dilatational and pressure modes are purely nonlinear and can be analysed and modelled in pure isotropic homogeneous turbulence. In this context, the model by Fauchet et al. (1997) gave promising spectral informations, as shown in the previous chapter. To reconcile both cases, i.e. taking into account both linear distortion by the mean flow and nonlinearity, is a formidable challenge. At least, the nonlinear model could be used for initializing in a better way the compressible RDT equations, replacing a questionable 'strong' acoustic equilibrium by a more realistic 'weak' one.

Regarding 'strong' acoustic equilibrium, even the RDT solution can significantly break it, independently of initial data, if M_g is sufficiently large, or more precisely if $S/(a_0 k)$ is large and $K_1 \neq 0$. The linear equation (14.62) is probably always valid, even in the nonlinear case, and the forcing by the solenoidal term (poloidal mode in Eq. (14.61)) can play a similar role here as the dominant part of the $T_{NL}^{(3)}$ term does in the nonlinear case.

14.5.1 Homogeneous Shear Flows

A critical survey of previous studies has shown that the alteration of pressure equation by compressibility, without significant change in its source term, is not the correct explanation for the "stabilizing" effect, at least for homogeneous shear flow. It is suggested that the alteration mentioned above results from the depletion of nonlinearity, and that this is the nonlinear part of the pressure-strain rate and not the linear (so called rapid) one which is concerned in this case. In contrast, the subtle

coupling between solenoidal and dilatational velocity modes is essential for explaining the stabilizing effect in the linear limit, and especially the feedback from the dilatational mode induced by the rotational part of the mean flow, as in Eq. (14.60). Such an analysis escapes the description permitted by Reynolds stress modelling. A general linear solution such as (14.40) contains a lot of information and it is a pity to derive from it only conventional single-point statistics: more information can be obtained about spectral distribution, since the ratio $S/(ak)$ which underlies the distortion Mach number is wavenumber-dependent, and about specific vortical and dilatational contributions.

14.5.2 Perspectives Towards Inhomogeneous Shear Flows

In an incompressible mixing layer, the velocity scale is unequally determined by the difference in the two stream velocities, $v_0 \sim \Delta U$ and variation in the lengthscale unequally depends on the velocity ratio. Compressibility changes this dimensional rule by making the speed of sound a relevant parameter with the consequence that the two above scales now possibly depends on a Mach number (the gradient Mach number $M_g \sim \Delta U/a$ or the turbulent Mach number $M_t \sim v_0/a$ with a an average of the two speeds of sound). As already mentioned, the consensus that emerged from DNS of compressible mixing layers is that compressibility stabilises a mixing layer by decreasing its pressure fluctuations, see e.g. Pantano and Sarkar (2002). This leads in particular to the reduction of the pressure-strain terms which produce the turbulent shear stress through redistribution among the Reynolds stresses of the energy provided by the work of the mean shear. Indeed, these DNSs provided us with decisive results. But, according to our above analyses, the detailed sequence of mechanisms leading to the mixing layer stabilization still escapes our understanding. It is important to note that linear analyses of compressible flows are somewhat in contradiction with the proposed interpretations because given a shear rate $\Delta U/\delta$, damped pressure fluctuations should make both the kinetic energy and the shear stress *increased* instead of decreased, through contribution of dilatational velocity fluctuations growing with the gradient Mach number. This should remain effective in the conditions which hold in a mixing layer because one does not expect a strong imbalance between linear and non linear time scales in such a free flow (actually $\delta/\Delta U$ does not depart so much from δ/v_0 and mildly rapid shear conditions must prevail). This indicates that non-linear compressibility effects should be addressed, in particular the changes in the mechanism of "isotropisation" of the fluctuations by pressure which are essential for producing kinetic energy in a shear flow. Evaluation of the respective impact of compressibility on linear and non-linear pressure terms is required for understanding and modelling correctly the compressible mixing layer. Note at last that in this inhomogeneous flow transport terms are also deeply modified by the drop of pressure fluctuations. Namely, one observes that the decrease in the production of turbulent kinetic energy is almost compensated by an equivalent decrease in its transport, letting the dissipation rate ε almost unchanged.

This last result also deserves attention. Favre averaging and normalization by ΔU and by the momentum thickness δ being used in the DNS, the result is that $\varepsilon\delta/(\Delta U)^3$ depends weakly on compressibility. If at the same time the normalized kinetic energy $v_0^2/(\Delta U)^2$ is reduced by compressibility, basic dimensional analysis leaves us with the paradox that the rate of dissipation of the turbulent kinetic energy (which is proportional to $(\Delta U)^3/\delta$) exceeds by a factor proportional to $(\Delta U/v_0)^3$ the rate of injection of the kinetic energy into the cascade (proportional to v_0^3/δ).

Indeed, this reasoning is very crude, but it indicates that the detailed mechanisms fixing energetic equilibrium in compressible mixing layers are not yet fully asserted. This was addressed for instance by the results of Jacquin et al. (1996) who observed that changing M_g thanks to variations in the total temperature of the interacting streams had almost no effect on mixing of the total pressure in their flow: weak variations in the total pressure spreading rate with compressibility were obtained and were also observed in other experiments. This may be an indication that the dissipation processes, which set the losses (i.e. the transformation of mechanical energy into heat), weakly depends on compressibility in free compressible shear flows. If this were true, this should be integrated into the models. Though it is, it remains still much to make and to understand on the subject.

Finally, explanations based on the hydrodynamic stability, as the inhibition of Kelvin–Helmholtz instabilities by compressibility, cannot be ignored, even if our main theme here is developed turbulence. The reader is referred to Friedrich (2006) for the problem of compressibility in wall bounded flows.

14.6 Topological Analysis, Coherent Events and Related Dynamics

Since it is nearly impossible to generate compressible homogeneous flows in wind tunnels, DNS is the main tool for coherent event eduction and analysis. The case of compressible homogeneous shear flows has received much less attention than the incompressible homogeneous shear flow and the compressible isotropic turbulence. Only very few papers address the issue of the dynamics of coherent events in the compressible homogeneous shear case, among which Sarkar et al. (1991), Blaisdell et al. (1993), Erlebacher and Sarkar (1993), Simone et al. (1997) and Hamba (1999).

14.6.1 Non-linear Dynamics in the Subsonic Regime

As in the case of isotropic compressible turbulence, several flow regimes can be identified, according to the level of compressibility, the relative importance of thermal versus acoustic mechanisms, etc. Only the subsonic case without strong thermal effects has been investigated, corresponding to the pseudo-acoustic regime described

in Sect. 13.2 or the non-linear subsonic regime discussed in Sect. 13.4, in which the main part of the turbulent kinetic energy is carried by the solenoidal component of the velocity field. In practice, initial turbulent Mach numbers M_t ranging from 0.1 to 0.5 have been considered in the references cited above. No results dealing with the supersonic regime and homogeneous shear with strong thermal effects are available. Only relatively weak shear effects have been investigated, since the final value non-dimensional time reached in the simulations is typically $St \simeq 10$. A noticeable exception is found in Blaisdell et al. (1993), in which simulations have been carried out up to $St = 24$. The main reason for that is that, due to the production mechanisms, the turbulent Mach number is monotonically increasing after a transient phase, leading to the occurrence of shocklets, which are poorly captured by the spectral methods used for this kind of simulation.

All simulations show that the flow converge toward a state which does not depend on the initial value of the compressibility ratio $\chi(0)$ defined in Eq. (13.34). After a transient state, the production effects associated with the mean shear seem to lead to nearly universal behavior, in which a solenoidal field and an acoustic field interacts. This evolution is illustrated in Fig. 14.5, which displays the evolution of the balance of the terms in Eq. (14.1) as a function of St, for two values of the initial Mach number. It is observed that the relative importance of each balance term does not depends on the turbulent Mach number and St (after the initial transient phase). In all cases, the dissipation is negligible. For low values of the turbulent Mach number, the solenoidal and acoustic fields are relatively decoupled in this growth regime. This is mainly due to the fact that the kinetic energy of the dilatational mode is very small compared to the one of the solenoidal field. At higher values of the turbulent Mach number, shocklets are observed, as in the isotropic case. An interesting point is that this non-linear subsonic regime is reached in all cases if the final value of St is high enough. When shocklets are present, the dilatational dissipation $\bar{\varepsilon}_d$ is enhanced. Even in the presence of shocklets, it is observed in Blaisdell et al. (1993) that, after the initial transient phase, the relative weights of dilatational and solenoidal kinetic energy dissipations reach a constant value, with $\bar{\varepsilon}_d/\bar{\varepsilon}_s = 0.1$. This ratio is reached for $M_t \geq 0.3$. In this regime, it is observed that 23% (resp. 58%) of the total dilatational dissipation is associated to the 1% (resp. 10%) volume of the flow with the most compressive dilatations.

This relative decoupling was analyzed by Erlebacher and Sarkar (1993) looking at the balance of budget terms in the equation for the dilatation variance $\overline{d^2}$ and the enstrophy variance $\overline{\omega^2}$. In the homogeneous shear case, the corresponding evolution equations are:

$$\begin{aligned}\frac{1}{2}\frac{\partial \overline{d^2}}{\partial t} = &-\frac{1}{6}\overline{d^3} - \overline{S_{ij}^I S_{ij}^I d} - \overline{S_{ij}^C S_{ij}^C} - 2\overline{S_{ij}^C S_{ij}^I d} \\ &+\frac{1}{2}\overline{\omega^2 d} - 2S\overline{d S_{12}^I} - 2S\overline{d S_{12}^C} \\ &-S\overline{\omega_3 d} - \overline{d\frac{\partial}{\partial x_j}\left(\frac{1}{\rho}\frac{\partial p}{\partial x_j}\right)} - \frac{4}{3}\nu\overline{\frac{\partial d}{\partial x_j}\frac{\partial d}{\partial x_j}},\end{aligned} \tag{14.81}$$

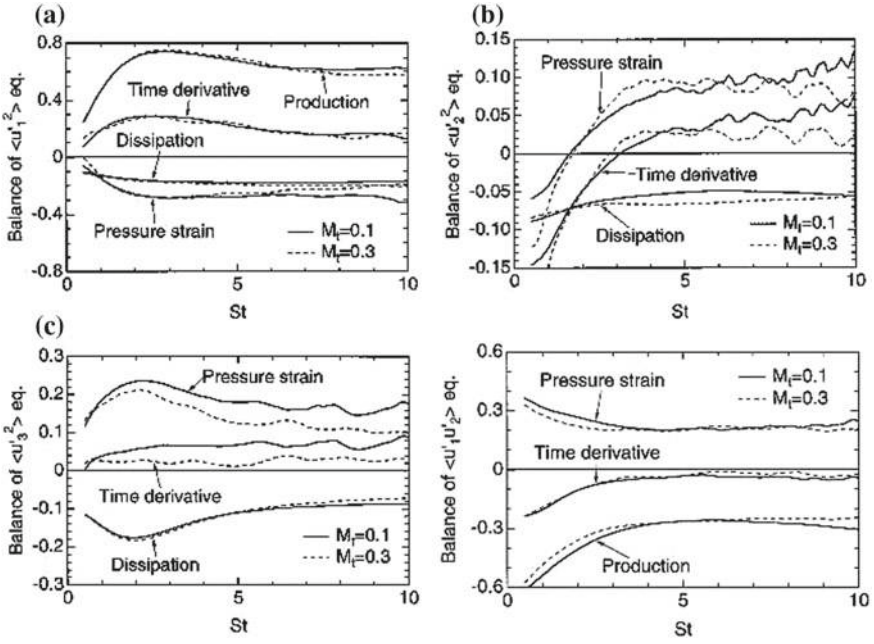

Fig. 14.5 Evolution of the budget terms of the Reynolds stresses as a function of St in compressible homogeneous shear flows. Dissipation is not plotted when it is negligible. From Hamba (1999) with permission of American Institute of Physics

and

$$\frac{1}{2}\frac{\partial\overline{\omega^2}}{\partial t} = \overline{\omega_i S^I_{ij}\omega_j} + \overline{\omega_i S^C_{ij}\omega_j} - \frac{2}{3}\overline{\omega^2 d} + S\overline{\omega_1\omega_2} + \frac{2}{3}S\overline{\omega_3 d} - S\overline{S^I_{3j}\omega_j} + S\overline{S^C_{3j}\omega_j} - \overline{\epsilon_{ijk}\omega_i\frac{\partial}{\partial x_j}\left(\frac{1}{\rho}\frac{\partial p}{\partial x_k}\right)} - \nu\overline{\frac{\partial\omega_i}{\partial x_j}\frac{\partial\omega_i}{\partial x_j}}, \tag{14.82}$$

where $\mathbf{S}^C$ and $\mathbf{S}^I$ denotes the the dilatational and solenoidal part of the turbulent velocity gradient tensor $\mathbf{S}$, respectively. Amplitudes of the balance terms which appear in the rhs of these two equations computed at $St = 9$ when $Re_\lambda = 23.4$, $M_t = 0.27$ and $S\mathcal{K}/\varepsilon = 6.05$ are displayed in Table 14.2. Looking at the dilatation variance balance, it is clear that interaction terms between solenoidal and dilatational modes are much smaller than between the dilatational components themselves. The main production term is $-2S\overline{dS^C_{12}}$, which is related to an interaction of the dilatational field with the background shear. In a similar way, it is seen that the dilatational mode has a very weak direct influence on the vorticity variance, but that the total enstrophy increase rate in the compressible case is 50% of the one found in the strictly

Table 14.2 Values of the terms in the budget equations for dilatation and vorticity variance in compressible homogeneous shear flows at $St = 9$ and $M_t = 0.27$, according to Erlebacher and Sarkar (1993). The terms are sorted from the left to the right in the rhs of the evolution equation. The third line displays the value of the budget term for the vorticity variance in the incompressible case at the same value of St and the same Reynolds number as in the compressible case

Equation	1	2	3	4	5	6	7	8	9	10
(14.81)	28	0	96	0	34	0	355	69	33	−292
(14.82)	4124	−26	−45	4555	−46	0	0	1	−6355	
(14.82), $M = 0$	6699			5301				0	−8453	

incompressible case. Here, compressibility is observed to reduce both the enstrophy variance production by the solenoidal vortex stretching term and the enstrophy variance dissipation. It is worth noting that the main production mechanism is the nonlinear vortex stretching, and that the direct production by the background shear is negligible at $St = 9$.

14.6.2 Topological Analysis of the Rate of Strain Tensor

The effect of compressibility on the statistical features of the rate of strain tensor was investigated by Erlebacher and Sarkar (1993). To this end, these authors split the rate of strain tensor $\mathbf{S}$ into a solenoidal component $\mathbf{S}^I$ and an irrotational component $\mathbf{S}^C$, which are computed applying the Helmholtz decomposition to the global fluctuating velocity field.

In the incompressible case, the rate of strain ellipsoid (based on the eigenvalues of $\mathbf{S}$) has the preferred shape (−4:1:3) in strongly dissipative regions. In the compressible case, with $St = 9$ and $M_t = 0.27$, the eigenvalues ratio of the solenoidal rate of strain tensor are almost identical to those of $\mathbf{S}$ in the incompressible case. The irrotational part exhibits a very different behavior, since pdfs of the eigenvalue ratios have two peaks. The main peak is associated with an ellipsoid of the shape (−2.2:1:1.2), while the secondary peak corresponds to (−1:−0.7:1.7). The former suggests that the structures which are associated with regions of high dilatation are sheet-like in the $x - z$ plane, the strain rates being extensional in the plane of the sheet and strongly compressive normal to it. The latter shows that regions with one large expansion strain are also associated with high dilatation. The exact shape of the two preferential dilatational rate of strain ellipsoids are certainly Reynolds and Mach number dependent, but the finding that the two rate of strain components have very different features is trustworthy.

The same simulation also shows that compressibility (at least in this regime) has no influence on the relative orientation of the vorticity vector.

14.6.3 Vortices, Shocklets and Dynamics

The vortical structures observed in available simulations are qualitatively the same as in the incompressible case discussed in Chap. 9. This is in agreement with the analysis of the balance of the budget terms of the vorticity variance presented above. Therefore, it can be concluded than in the pseudo-acoustic regime and in the non-linear subsonic regime, compressiblity does not result in a qualitative change in the vortical structures dynamics, and most of the results presented for incompressible case dealing with vortex dynamics still hold. But is should be mentioned that the existence of a self-sustaining process in compressible homogeneous shear flows has not been investigated.

The occurrence of shocklets in compressible homogeneous shear flows has been reported in several direct numerical simulations (Blaisdell et al. 1993; Sarkar et al. 1991). They appear as elongated ribbon-like structures lying at an angle about 15–20° to the x axis in the $(x - y)$ plane. The most plausible scenario is that they are created by the upwash and downwash mechanisms induced by the streamwise streaky vortical structures in the direction of the mean velocity gradient (Blaisdell et al. 1993). This entrainment effect causes high-speed and low-speed fluid pockets to come into contact, yielding a compression which causes a shocklet. DNS data show that shocklets do not contribute directly significantly to the dilatational dissipation rate $\bar{\varepsilon}_d$, but they play an important role in the dynamics of $\bar{\varepsilon}_d$.

The weak influence of shocklets on the global dynamics is also revealed by the fact that the thermodynamic fields follow a quasi isentropic behavior, despite the occurrence of the shocklets, which are entropic phenomena. Looking at the value of the polytropic coefficient n in the relation

$$\frac{\overline{p'p'}}{\overline{p}} = n\frac{\overline{\rho'\rho'}}{\overline{\rho}} = \frac{n}{n-1}\frac{\overline{T'T'}}{\overline{T}} \tag{14.83}$$

$n = 1.35$ was found in Blaisdell et al. (1993). It is recalled that $n = \gamma = 1.4$ corresponds to an isentropic flow, while $n = 0$ and $n = 1$ are related to isobaric and isothermal flows, respectively.

References

Blaisdell, G.A., Mansour, N.N. Reynolds, W.C.: Numerical simulation of compressible homogeneous turbulence. Report TF-50. Department of Mechanical Engineering, Stanford University, Stanford (1991)

Blaisdell, G.A., Mansour, N.N., Reynolds, W.C.: Compressibility effects on the growth and structure of homogeneous turbulent shear flow. J. Fluid Mech. **256**, 443–485 (1993)

Blaisdell, G.A., Coleman, G.N., Mansour, N.N.: RDT for compressible homogeneous turbulence under isotropic mean strain. Phys. Fluids **8**, 2692–2708 (1996)

Cambon, C., Teissèdre, C., Jeandel, D.: Etude d' effets couplés de déformation et de rotation sur une turbulence homogène. J. de Mécanique Théorique et Appliquée **4**(5), 629–657 (1985). (in French)

Cambon, C., Mao, Y., Jeandel, D.: On the application of time dependent scaling to the modelling of turbulence undergoing compression. Eur. J. Mech. B/Fluids **6**, 683–703 (1992)

Cambon, C., Coleman, G.N., Mansour, N.N.: Rapid distortion analysis and direct simulation of compressible homogeneous turbulence at finite mach number. J. Fluid Mech. **257**, 641–665 (1993)

Cambon, C., Rubinstein, R.: Anisotropic developments for homogeneous shear flows. Phys. Fluids **18**, 085106 (2006)

Craik, A.D.D., Allen, H.R.: J. Fluid Mech. **234**, 613–627 (1992)

Debiève, J.F., Gouin, H., Gaviglio, J.: Evolution in the reynolds stress tensor in a shock wave turbulence interaction, Indian. J. Technol. **20**, 90–97 (1982)

Durbin, P.A., Zeman, O.: RDT for homogeneous compressed turbulence with application to modelling. J. Fluid Mech. **242**, 349–370 (1992)

Eckhoff, K.S., Storesletten, L.: A note on the stability of steady inviscid helical gas flows. J. Fluid Mech. **89**, 401 (1978)

Erlebacher, G., Sarkar, S.: Statistical analysis of the rate of strain tensor in compressible homogeneous turbulence. Phys. Fluids **5**(12), 3240–3254 (1993)

Fabre, D., Jacquin, L., Sesterhenn, J.: Linear interaction of a cylindrical entropy spot with a shock wave. Phys. Fluid **13**(8), 1–20 (2001)

Fauchet, G., Shao, L., Wunenberger, R., Bertoglio, J.P.: An improved two-point closure for weakly compressible turbulence. In: 11-th Symposium Turbulence Shear Flow, Grenoble, 8–10 September 1997

Friedrich, R.: Effects of compressibility and heat release in turbulent wall-bounded and free shear flows. In: SIG4 ERCOFTAC and GST13 Workshop, Porquerolles, France, 1 June 2006

Frisch, U.: Turbulence: The Legacy of A.N. Kolmogorov. Cambridge University Press, Cambridge (1995)

Goldstein, M.E.: Unsteady vortical and entropic distortions of potential flows round arbitrary obstacles. J. Fluid Mech. **89**(3), 433–468 (1978)

Hamba, F.: Effects of pressure fluctuations on turbulence growth in compressible homogeneous shear flow. Phys. Fluids **11**(6), 1623–1635 (1999)

Heinz, S.: Statistical Mechanics of Turbulent Flows. Springer, Berlin (2004)

Hunt, J.C.R.: A theory of turbulent flow around two-dimensional bluff bodies. J. Fluid Mech. **61**, 625–706 (1973)

Jacquin, L., Cambon, C., Blin, E.: Turbulence amplification by a shock wave and rapid distortion theory. Phys. Fluids A **10**, 2539–2550 (1993)

Jacquin, L., Mistral, S., Cruaud, F.: Mixing of a heated supersonic jet with a parallel stream. Advances in Turbulence V. Springer, Berlin (1996)

Kovasznay, L.S.G.: Turbulence in supersonic flow. J. Aeronaut. Sci. **20**, 657–682 (1953)

Lele, S.K.: Compressibility effects on turbulence. Annu. Rev. fluid Mech. **26**, 211–254 (1994)

Lifschitz, A., Hameiri, E.: Local stability conditions in fluid dynamics. Phys. Fluids A **3**, 2644–2641 (1991)

Livescu, D., Madnia, C.K.: Small scale structure of homogeneous turbulent shear flow. Phys. Fluids **16**(8), 2864–2876 (2004)

Lighthill, M.J.: Waves in Fluids. Cambridge University Press, Cambridge (1978)

Pantano, C., Sarkar, S.: A study of compressibility effects in the high-speed turbulent shear layer using DNS. J. Fluid Mech. **451**, 329–371 (2002)

Ribner, H.S., Tucker, M.: Spectrum of turbulence in a contracting stream, In: NACA Report, No 113 (1953)

Sabel'nikov, V.A.: Pressure fluctuations generated by uniform distortion of homogeneous turbulence. J. Mech. Sov. Res. **4**, 46–56 (1975)

Sarkar, S., Erlebacher, G., Hussaini, M.Y.: Direct simulation of compressible turbulence in a shear flow. Theor. Comput. Fluid Dyn. **2**, 291–305 (1991)
Sarkar, S.: The stabilizing effect of compressibility in turbulent shear flow. J. Fluid Mech. **282**, 163–286 (1995)
Simone, A., Coleman, G.N., Cambon, C.: The effect of compressibility on turbulent shear flow: a RDT and DNS study. J. Fluid Mech. **330**, 307–338 (1997)
Thacker, W.D., Sarkar, S., Gatski, T.B.: Analyzing the influence of compressibility on the rapid pressure-strain rate correlation in turbulent shear flows. Theor. Comput. Fluid Dyn. **21**(3), 171–199 (2006). https://doi.org/10.1007/s00162-007-0043-4
Townsend, A.A.: The Structure of Turbulent Shear Flow, 2nd edition. Cambridge University Press, Cambridge (1976)

Chapter 15
Canonical Isotropic Turbulence/Shock Interaction and Beyond

This chapter is mainly devoted to the analysis of the interaction of an initially isotropic turbulence with a normal plane shock wave. Eventhough this case, often referred to as *canonical shock/turbulence interaction* is very simple from a geometrical viewpoint, it will be seen that it involves most physical mechanisms observed in more complex configurations. It also makes it possible to carry out an extensive theoretical analysis, leading to a deep understanding of the underlying physics. Cases with more complex physics, namely spherical shock/turbulence interaction, shock/turbulence interaction a binary mixtures and detonation/turbulence interaction are discussed at the end of the chapter.

15.1 Brief Survey of Existing Interaction Regimes

Several interaction regimes exist, which can be grouped into two families. The first one, referred to as the *destructive interaction* family, encompasses all configurations in which the structure of the shock wave is deeply modified during the interaction in the sense that a single well-defined shock wave can no longer be identified, the limiting case being the shock destruction. The second family, i.e. the *non-destructive interaction* family, is made of all cases in which the structure of the shock wave is preserved during the interaction. It is important noting that in the later case the shock wave can be strongly corrugated by the incoming turbulence.

15.1.1 Destructive Interactions

The first case of destructive interactions is the one of *unstable shocks*, in which any small disturbances will lead to the destruction of the shock wave due to instability

P. Sagaut and C. Cambon, *Homogeneous Turbulence Dynamics*,
https://doi.org/10.1007/978-3-319-73162-9_15

mechanisms. In such a case, the destruction mechanism is tied to the shock itself and not to the turbulence dynamics (see Lubchich and Pudovkin 2004 and references given therein).

According to Dyakov (1954), a shock is *absolutely unstable* if one of the two following conditions is fulfilled:

$$(\rho_2 u_2)^2 \cdot \left(\frac{\partial(1/\rho_2)}{\partial p_2}\right)_{\mathcal{H}} < -1, \tag{15.1}$$

or

$$(\rho_2 u_2)^2 \cdot \left(\frac{\partial(1/\rho_2)}{\partial p_2}\right)_{\mathcal{H}} > 1 + 2M_2, \tag{15.2}$$

where M is the Mach number and subscripts 1 and 2 refer to the shock upstream and downstream states, respectively. The index $\mathcal{H}$ indicates that the derivative is calculated along the Hugoniot curve in the pressure-specific volume plane. The absolute instability regime corresponds to cases in which the solution of the jump conditions is not unique, and small perturbations trigger the bifurcation toward stable states made of combinations of discontinuities and simple waves. It can be shown that the absolute instability cannot occur for plane shocks in perfect gases. It can be observed in perfect gases for curved shocks or plane shocks with viscous effects such that the interaction with a boundary layer.

Another shock instability, referred to as the *relative instability* was identified by Kontorovich (1957). Here, a perturbation, once having emerged at the discontinuity, stands for arbitrarily long times, emitting acoustic, vorticity and entropy waves without attenuation and amplification. The criterion for the occurrence of the relative instability is

$$\frac{1 - M_2^2(1 + (\rho_2/\rho_1))}{1 - M_2^2(1 - (\rho_2/\rho_1))} < (\rho_2 u_2)^2 \cdot \left(\frac{\partial(1/\rho_2)}{\partial p_2}\right)_{\mathcal{H}} < 1 + 2M_2. \tag{15.3}$$

It is observed that the range of the relative instability is adjacent to one of the two ranges of the absolute instability. In the relative instability regime the shock wave is not destroyed by infinitesimal initial perturbations but it cannot exists alone, since the downstream solution is made of the superposition of a uniform field and propagating perturbation waves. For initial perturbations of finite amplitude, the shock wave disintegrates to a shock wave of essentially different intensity and other elements.

Other cases of destructive interaction are associated to cases where the turbulent fluctuations are strong enough to yield a local deep modification of the shock wave. These configurations escape the linear instability theory used to define the preceding destructive regimes and can therefore be classified as nonlinear destructive interactions. The first case is associated to the case where a turbulent eddy is strong enough

to render the flow locally subsonic. When it reaches the shock wave, the latter will be locally annihilated. In the second case, the upstream flow remains supersonic but the perturbation is strong enough to make a secondary shock appearing.

15.1.2 Non-destructive Interactions

The non-destructive interactions are trivially defined as all the interactions which are not destructive, meaning that a single well-defined shock wave can be identified all thorough the interaction process. Two main cases are identified, coined as the *wrinkled shock* and the *broken shock régime* by Larsson and Lele (2009):

- the *wrinkled shock régime*, in which the shock wave is distorted by turbulent fluctuations but remains compatible with classical jump relations at all locations. Two sub-régimes are identified:
  - the *linear interaction régime* (see Sect. 15.2), in which the perturbations are assumed to be weak in the sense that the mean flow quantities obey the usual Rankine–Hugoniot jump conditions, while the turbulent fluctuations satisfy linearized jump relations. This régime is well described by the Linear Interaction Approximation at high Reynolds number, which is a linearized inviscid theory that will be discussed hereafter. A condition for the LIA to hold proposed by Ryu and Livescu (2014) is $M_{t_2} \leq 0.1 M_2$, where M_{t_2} and M_2 denote the downstream turbulent Mach number and the downstream mean flow based Mach number, respectively. This condition ensures that nonlinear effects will remain small compared to linear ones.
  - the *nonlinear interaction régime* (see Sect. 15.3), in which the turbulent intensity is so high that the mean flow is modified by the turbulent fluctuations. In this case, turbulent fluxes must be taken into account when writing jump conditions for the mean flow.
- the *broken shock régime* (see Sect. 15.4) in which turbulent fluctuations are so strong that the upstream flow may happen to be locally subsonic. At such a location the shock wave is replaced by a smooth compression wave, and jump relations are not valid. This régime occurs when $M_{t_1}/(M_1 - 1) \geq 0.6$, where M_{t_1} and M_1 denote the upstream turbulent Mach number and the upstream mean flow based Mach number, respectively Larsson and Lele (2009). Another criterion with an additional dependency on the upstream Taylor scale based Reynolds number Re_{λ_1} is proposed by Donzis (2012a): $\mathfrak{S} = M_{t_1}/Re_{\lambda_1}(M_1 - 1) \geq 0.6$. Here, the parameter $\mathfrak{S}$ is the normalized laminar shock thickness, i.e. $\mathfrak{S} \simeq \delta_l/\eta$ where the laminar shock thickness is given by the classical approximation $\delta_l \simeq \mu/\rho a(M_1 - 1)$ and η is the Kolmogorov scale. The important fact is that both criteria share the same dependency on M_t and M.

15.2 Wrinkled Shock Régime: Linear Interaction

15.2.1 Introduction to the Linear Interaction Approximation Theory

We now briefly introduce the Linear Interaction Approximation (LIA), which is a very powerful tool pioneered in the 1950s (Ribner 1953; Moore 1954) to analyze the non-destructive linear interaction regime. Details of the LIA procedure are given in Chap. 16. It relies on the following simplified dynamic scheme:

(i) The shock wave has no intrinsic scale, and therefore it is enslaved to incident perturbations. It will only acts through the jump conditions.
(ii) Both mean and fluctuating parts of the upstream field (i.e. the field in the supersonic part of the flow) are arbitrarily fixed.
(iii) The downstream field is fully determined by the upstream field and the jump conditions. More precisely, it is assumed that the interaction process between turbulent fluctuations and the shock is mostly linear, so that:

(a) The mean flow obeys the usual Rankine–Hugoniot conditions
(b) The fluctuating field obeys linearized jump conditions.

This physical scheme is illustrated in Fig. 15.1.
Two conditions must be fulfilled to ensure that the linear approximation is relevant:

(i) The fluctuations must be weak in the sense that the distorted shock wave must remain well defined.
(ii) The time required for turbulent events to cross the shock must be small compared to the turbulence time scale $\mathcal{K}/\varepsilon$ (with $\mathcal{K}$ and ε the turbulent kinetic energy and the turbulent kinetic energy dissipation rate, respectively), so that nonlinear mechanisms cannot have significant effects.

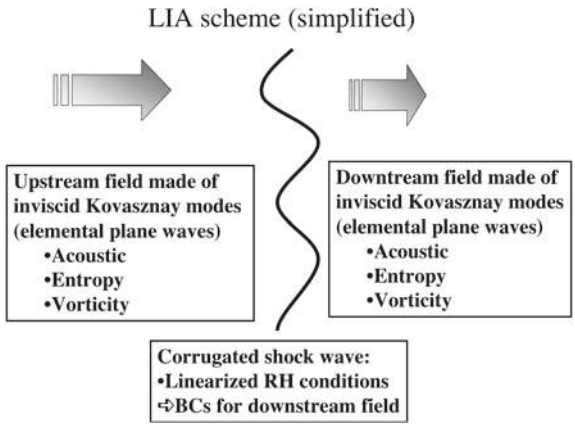

Fig. 15.1 Schematic view of the Linear Interaction Approximation for shock/turbulence interaction

The LIA analysis is made more accurate splitting the fluctuating field using the Kovasznay decomposition: both the upstream and downstream fluctuating fields are split as sums of individual modes, each mode being characterized by its nature (acoustic, vorticity or entropy mode) and wave number or frequency. Since linearized jump conditions are utilized, all cross interactions between modes are precluded, and the downstream fluctuating field is obtained via a simple superposition of the LIA results obtained for each upstream fluctuating mode. Let us emphasize here that, as it will be demonstrated below, the fact that interactions are precluded does not mean that an upstream perturbation wave is associated to an emitted downstream wave of the same nature (as a matter of fact, all physical modes are excited in the downstream region in the general case), but that the interaction process is not sensitive to shock deformations induced by other upstream fluctuations.

The resulting LIA scheme is the following: one considers two semi-infinite domains separated by the shock wave. Both the mean and fluctuating fields in the upstream domain are arbitrarily prescribed. Since the flow is hyperbolic in this domain, it is not sensitive to the presence of the shock wave. The mean downstream field is computed using the mean upstream field and the usual Rankine–Hugoniot jump relations (3.16)–(3.19). The emitted fluctuating field is then computed using the linearized jump relations as boundary conditions. Using results displayed in Chap. 16, it is important to note that the wave vectors of the emitted waves are computed using the dispersion relation associated to each physical mode, the frequency and the tangential component of the wave vector being the same as the upstream perturbation. The linearized jump conditions are used only to compute the amplitudes of the emitted waves.

15.2.2 Vortical Turbulence/Shock Interaction

We first address the case in which the incident turbulence is isotropic and composed of vorticity modes only. This case was investigated by several researchers, e.g. Lee et al. (1993, 1997), Larsson and Lele (2009), Donzis (2012a, b), Larsson et al. (2013), Ryu and Livescu (2014) using LIA and direct numerical simulation (DNS). The trends found via DNS and LIA are corroborated by wind tunnel experiments, but a strict quantitative agreement is hopeless since the exact nature of the incident turbulence in experiments cannot be controlled, due to technological limitations. Full analytical expressions of amplification ratios for the different modes, including asymptotic analysis for weak and strong shocks, have been derived in Wouchuk et al. (2009). These very useful expressions are very cumbersome and will not be reproduced here for the sake of brevity.

The main observations are the following:

(i) *Velocity fluctuations*. The streamwise distributions of the kinetic energy of the three velocity components given by both direct numerical simulation and LIA are displayed in Fig. 15.2. It is observed that all velocity components are ampli-

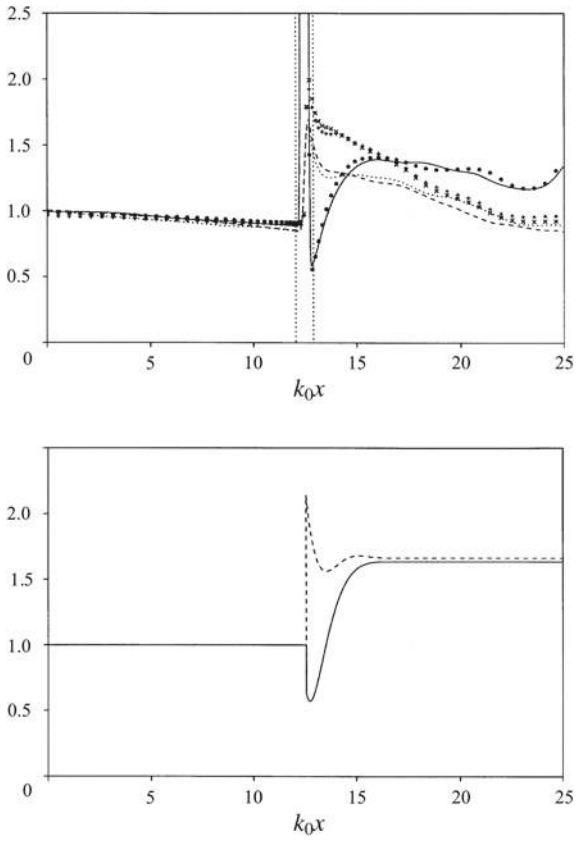

Fig. 15.2 Streamwise evolution of normalized Reynolds stresses. Top: DNS results (lines for ($M_1 = 2$, $M_t = 0.108$, $Re_\lambda = 19.0$) and symbols for ($M_1 = 3$, $M_t = 0.110$, $Re_\lambda = 19.7$)); streamwise component $R_{11} = \overline{u'u'}$: solid line and dots; spanwise component $R_{22} = \overline{v'v'}$: dashed line and 'x'; spanwise component $R_{33} = \overline{w'w'}$: dotted line and '+'. Bottom: LIA results for ($M_1 = 2$, $M_t = 0.108$); streamwise component R_{11}: solid line; spanwise components R_{22} and R_{33}: dashed line. Vertical dotted line show the limit of the shock displacement region. From Lee et al. (1997) with permission of CUP

fied, leading to a global increase in the turbulent kinetic energy. The amplification rate is well recovered by the LIA calculation, showing that the amplification is mainly due to linear mechanisms. In agreement with LIA, the velocity field behind the shock wave is axisymmetric. Both LIA and DNS predict that the amplification is Mach number dependent. The amplification level is plotted as a function of the upstream Mach number, M_1, in Fig. 15.3. It is interesting to note that the amplification of the transverse velocity components is an increasing monotonic function, while the shock normal velocity component amplification exhibits a maximum near $M_1 = 2$. The transverse components are more amplified than the streamwise component for $M_1 > 2$, and the amplification of the total turbulent kinetic energy tends to saturate beyond $M_1 = 3$. The streamwise DNS profiles reveal that the velocity field experiences a rapid evolution downstream the shock, leading to the definition of two different regions behind the shock wave. This observation is in full agreement with the LIA analysis, which predicts the existence of a near field region where the evanescent acoustic waves emitted during the interaction are not negligible. Comparing the LIA and DNS

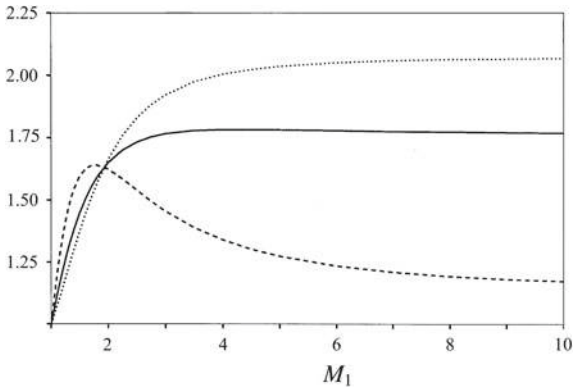

Fig. 15.3 LIA prediction of far field Reynolds stress amplification versus the upstream Mach number. Solid line: turbulent kinetic energy; dashed line: streamwise Reynolds stress $R_{11} = \overline{u'u'}$; dotted line: spanwise Reynolds stresses $R_{22} = \overline{v'v'}$ and $R_{33} = \overline{w'w'}$. From Lee et al. (1997) with permission of CUP

profiles (see Fig. 15.2) once again leads to the conclusion that the process is mainly governed by linear mechanisms. The rapid evolution in the near field region is due to the exponential decay of evanescent acoustic waves, which are responsible for the anti-correlation of the (acoustic) dilatational and (vortical) solenoidal field just downstream the shock. The nature of the relaxation process that takes place in the near-field region is better understood recalling that the solution of linearized Euler equations about a one-dimensional mean field is such that the following acoustic energy balance holds

$$\frac{\partial}{\partial x}\left(M_2\left(\frac{\mathcal{K}}{a_2^2}+\frac{1}{2}\frac{\overline{\rho'^2}}{\bar{\rho}^2}\right)+\frac{1}{\gamma}\frac{\overline{p'u''}}{\bar{p}a_2}\right)=0, \tag{15.4}$$

where

$$\mathcal{K}=\frac{1}{2}\left(\overline{u''u''}+\overline{v''v''}+\overline{w''w''}\right), \tag{15.5}$$

if viscous and entropy-dilatation correlation effects are neglected. A close examination of DNS data shows that these two contributions are small in the near field region, and that the near field evolution is associated to an energy transfer from the acoustic potential energy in the form of density or pressure fluctuations to turbulent kinetic energy. This transfer is done via the pressure transport term $\nabla\cdot(\overline{p'\boldsymbol{u}''})$. The pressure-dilation term $\overline{p'\nabla\cdot\boldsymbol{u}''}$ is observed to be strictly positive in this region, corresponding to a reversible transfer from the mean internal energy to the turbulent kinetic energy.

Outside the near-field region, the global behavior results from the competition between the viscous decay and the return to isotropy process. In low-Reynolds number DNS,[1] the viscous effect is dominant: the turbulent kinetic energy balance simplifies as an equilibrium between the convection term and the viscous

[1]The turbulent Reynolds number based on the Taylor microscale Re_λ at the inlet plane of DNS presented in Lee et al. (1993, 1997) range from 11.6 to 21.6.

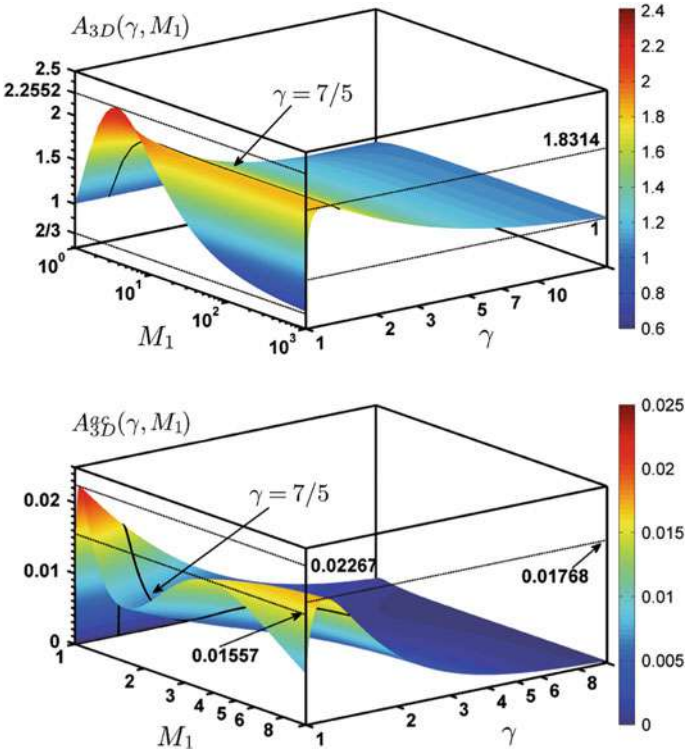

Fig. 15.4 LIA prediction of the turbulent kinetic energy amplification factor as a function of M_1 and γ. Top: amplification factor A_{3D}; Bottom: acoustic part A^{ac}_{3D}. Courtesy of C. Huete. From Wouchuk et al. (2009) with permission of APS

term, showing that the main effects are convection of turbulent velocity fluctuations by the mean field and their destruction by viscous effects.

The amplification factor of turbulent kinetic energy in the far field, $A_{3D} = \mathcal{K}_2/\mathcal{K}_1$ is plotted as a function of the upstream Mach number M_1 and the polytropic index γ in Fig. 15.4, along with A^{ac}_{3D}, defined as the ratio of the kinetic energy of the acoustic velocity field to $\mathcal{K}_1$, which measures the contribution of the acoustic field to A_{3D}. It is observed that the amplification factor response surface exhibits a complex behavior. The maximum amplification is about 2.25 and is obtained in the limit of strongly compressible gas with $\gamma = 1$ for $M_1 = 3.51$. It is also interesting to note that in the limit $M_1 \to \infty$ and $\gamma \to 1$ turbulence (very strong shock and highly compressible fluid) is not amplified but damped, with $A_{3D} \to 2/3$. In this case, the shock corrugation vanish and transverse velocity components are left unchanged when crossing the shock. In the case of very-low compressibility fluids, i.e. large values of γ, one has $A_{3D} \to 1$ for all values of M_1. Strong shock asymptotic behavior and highly compressible fluid asymptotics are displayed in Fig. 15.5. The behavior of the acoustic part

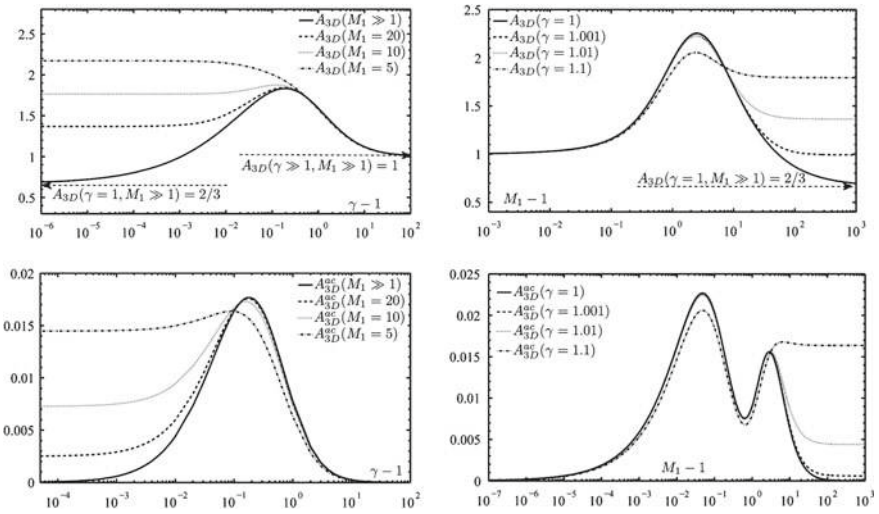

Fig. 15.5 LIA prediction of asymptotic behavior of kinetic energy amplification factor. Top-left: $A_{3D}(M_1 \gg 1, \gamma)$; Top-right: $A_{3D}(M_1, \gamma \to 1)$; Bottom-left: $A^{ac}_{3D}(M_1 \gg 1, \gamma)$; Bottom-right: $A^{ac}_{3D}(M_1, \gamma \to 1)$. Courtesy of C. Huete. From Wouchuk et al. (2009) with permission of APS

characterized by A^{ac}_{3D} is more complex since two peaks are observed in the limit of weak shocks and highly compressible fluids. The acoustic kinetic energy remains small compared to the vortical one, since the maximum value of A^{ac}_{3D} is about 0.022. Asymptotic behavior are also displayed in Fig. 15.5.

The Reynolds stress anisotropy parameter $\beta_v = (R_{11} - (R_{22} + R_{33}))/(R_{11} + (R_{22} + R_{33}))$ is plotted as a function of M_1 and γ in Fig. 15.6. The maximum value is equal to 1 and is obtained in the limit of strong shocks in highly compressible fluids, in which the longitudinal motion in the compressed fluid vanishes. The limit value $\beta_v = -1$ is never reached. It is worth noting that the two types of anisotropy, i.e. lateral anisotropy with $\beta_v < 0$ (*pancake-type flow*) and longitudinal anisotropy with $\beta_v > 0$ (*cigar-type flow*) can be obtained. The neutral curve $\beta_v = 0$, which corresponds to an isotropic Reynolds stress tensor, is illustrated in the right part of Fig. 15.6. For large values of M_1, the neutral curve is given by $\gamma = \gamma^* = 2.36$.

(ii) *Vorticity field*. The vorticity is also strongly affected by the interaction with the shock wave. The streamwise evolution of the vorticity components computed in two different simulations are presented in Figs. 15.7 and 15.8. Several typical features are observed. First, the streamwise (i.e. shock normal) vorticity component is not affected, in agreement with the conclusion drawn from the jump condition (3.23). The two other components are amplified, in a symmetric way, leading to the definition of a statistically axisymmetric vorticity field being the shock wave. This behavior was predicted by the LIA analysis. The amplification of the transverse component is Mach number dependent, and the

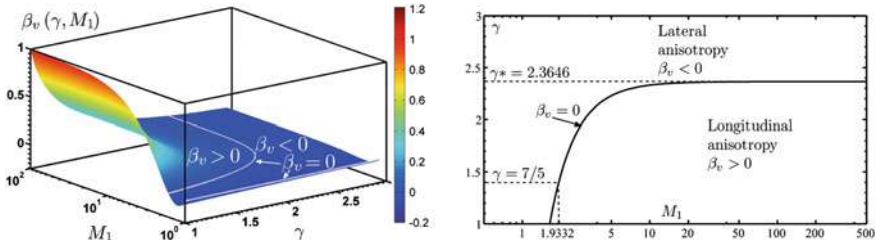

Fig. 15.6 LIA prediction of the Reynolds stress anisotropy factor as a function of M_1 and γ. Courtesy of C. Huete. From Wouchuk et al. (2009) with permission of APS

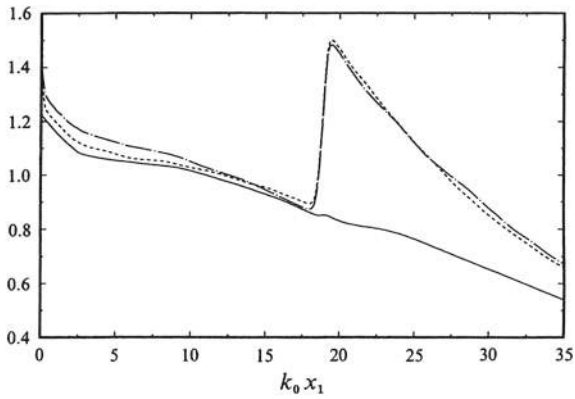

Fig. 15.7 Vorticity amplification across shock (DNS data, $M_1 = 1.2$, $Re_t = 84.8$). Solid line: streamwise component $\overline{\omega_1'\omega_1'}$; Dashed line: spanwise component $\overline{\omega_2'\omega_2'}$; Dash-dot line: spanwise component $\overline{\omega_3'\omega_3'}$. From Lee et al. (1993) with permission of CUP

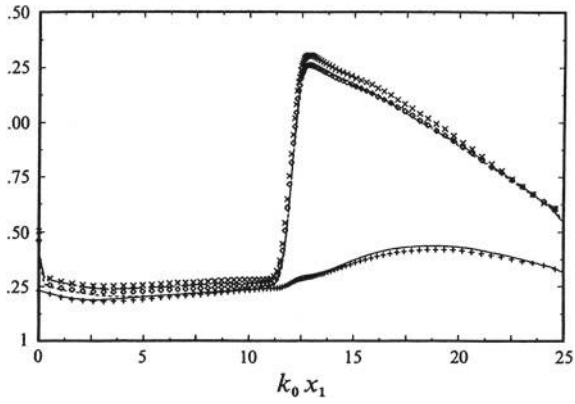

Fig. 15.8 Vorticity amplification across shock (DNS data on two computational grids, $M_1 = 1.2$, $Re_t = 238$). Solid line and '+': streamwise component $\overline{\omega_1'\omega_1'}$; Dashed line and 'x': spanwise component $\overline{\omega_2'\omega_2'}$; Dash-dot line and diamonds: spanwise component $\overline{\omega_3'\omega_3'}$. From Lee et al. (1993) with permission of CUP

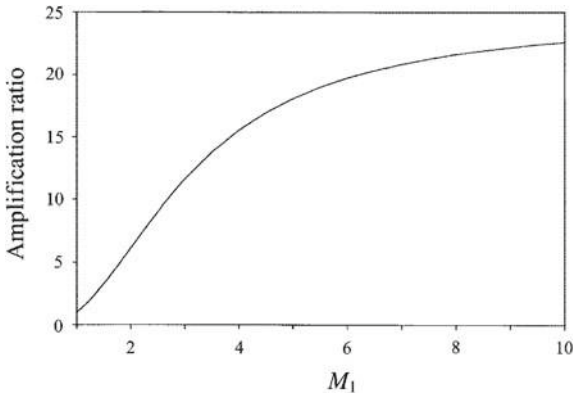

Fig. 15.9 Amplification of transverse vorticity components $\overline{\omega_2'\omega_2'}$ and $\overline{\omega_3'\omega_3'}$ across shock versus the upstream Mach number M_1: LIA results. From Lee et al. (1997) with permission of CUP

LIA analysis presented in Fig. 15.9 shows that it is a monotonically increasing function that tends to saturate at very high Mach numbers. Since the vorticity has no contribution from the acoustic modes, it does not exhibit a near field. But it is interesting to note that two different behaviors of the streamwise vorticity component are observed downstream the shock: it is monotonically decreasing at low Reynolds number, while it has a local maximum at higher Reynolds number. The explanation for this bifurcation is found looking at the evolution equation of the vorticity component variances using DNS data. Neglecting the temperature-induced fluctuations of the viscosity, the evolution equation for the fluctuating vorticity variances $\overline{\omega_\alpha'\omega_\alpha'}$ is (without summation over repeated Greek indices):

$$\underbrace{\bar{u}_j \frac{\partial}{\partial x_j}\overline{\omega_\alpha'\omega_\alpha'}}_{I} = \underbrace{2\overline{\omega_\alpha'\omega_j'}\bar{S}_{\alpha j}}_{II} + \underbrace{2\overline{\omega_\alpha'\omega_j'S_{\alpha j}'}}_{III} - \underbrace{2\overline{\omega_\alpha'\omega_\alpha'}\bar{S}_{jj}}_{IV}$$
$$- \underbrace{\overline{\omega_\alpha'\omega_\alpha'S_{jj}'}}_{V} + \underbrace{2\epsilon_{\alpha jk}\overline{\left(\frac{\omega_\alpha'\frac{\partial\rho}{\partial x_j}\frac{\partial p}{\partial x_k}}{\rho^2}\right)}}_{VI} - \underbrace{\frac{\partial}{\partial x_k}\overline{\omega_\alpha'\omega_\alpha'u_k'}}_{VII}$$
$$+ \underbrace{2\epsilon_{\alpha jk}\overline{\omega_\alpha'\frac{\partial}{\partial x_j}\left(\frac{1}{\rho}\frac{\partial\tau_{kl}}{\partial x_l}\right)}}_{VIII}. \tag{15.6}$$

Inside the shock wave, the transverse component evolution ($\alpha = 2, 3$) which leads to the existence of the jump in the LIA theory is dominated by the vorticity-compression terms (IV + V), the vorticity-mean compression term IV being the leading term. Downstream the shock region, the vortex stretching mechanism (II + III) is balanced by the viscous effects (VIII). In all DNS cases, both the

baroclinic production term (VI) and the turbulent transport (VII) are negligible. The dynamics of the streamwise component is different. Inside the shock wave, vortex stretching (II + III) and vorticity compression (IV + V) balance each other, resulting in a negligible influence of the shock, in agreement with inviscid jump relations. Downstream the shock wave, the streamwise vorticity variance $\overline{\omega_1'\omega_1'}$ is governed by the balance between two dominating mechanisms: turbulent vortex stretching (III) and viscous effects (VIII). In the low Reynolds number case, the viscous damping overwhelms the vortex stretching effects, leading to a monotonous decay. At higher Reynolds number, the turbulent stretching is large enough to yield the existence of a local downstream maximum.

The LIA amplification factor of transverse vorticity $A_{\omega_\perp^2} = \|\boldsymbol{\omega}'_{\perp_2}\|^2/\|\boldsymbol{\omega}'_{\perp_1}\|^2$ is plotted in Fig. 15.10 as a function of M_1 and γ, along with strong shock and high fluid compressibility asymptotics. It is observed that amplification increases as $\gamma \to 1$ and $M_1 \to +\infty$ and exhibits an unbounded behavior. As the gas becomes infinitely compressible, one has $\mathfrak{C}^2 = (\bar{\rho}_2/\bar{\rho}_1)^2 \sim (\gamma - 1)^{-2}$, showing that the longitudinal wavelength of emitted vorticity waves tends to zero. The unbounded character of vorticity (with bounded kinetic energy) is

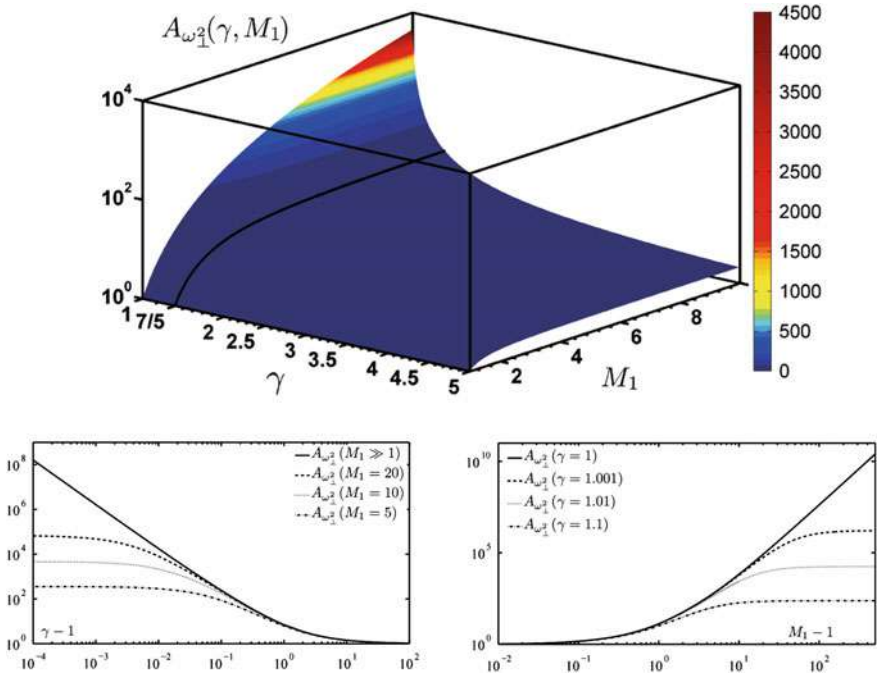

Fig. 15.10 LIA prediction of transverse vorticity amplification ration as a function of M_1 and γ (top), along with large M_1 asymptotics (bottom-left) and high compressibility asymptotics $\gamma \to 1$ (bottom-right). Courtesy of C. Huete. From Wouchuk et al. (2009) with permission of APS

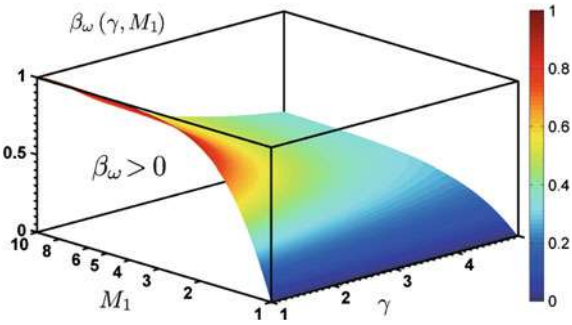

Fig. 15.11 LIA prediction of vorticity anisotropy ratio β_ω as a function of M_1 and γ. Courtesy of C. Huete. From Wouchuk et al. (2009) with permission of APS

due to the inviscid gas approximation used in present LIA developments, since viscous effects will become very important for small wavelength, introducing a regularizing effects (Miller and Ahrens 1991).

The vorticity anisotropy factor $\beta_\omega = (A_{\omega_\perp^2} - 1)/(A_{\omega_\perp^2} + 1)$ is plotted versus M_1 and γ in Fig. 15.11. In all cases one has $\beta_\omega > 0$ due to the fact that only the transverse vorticity components are amplified, the normal component being continuous on the shock front. The maximum value $\beta_\omega = 1$ is reach for $M_1 \gg 1$ and $\gamma \to 1$, corresponding to an asymptotic case in which the longitudinal vorticity component becomes negligible compared to the transverse ones.

(iii) *Turbulence lengthscales*. Characteristic scales of turbulence are observed to be modified during the interaction in a scale-dependent manner. Let us first discuss the behavior of the one dimensional spectra $E_\alpha(k_\beta)$ which are defined such that (without summation over Greek indices)

$$\overline{u'_\alpha u'_\alpha} = \int_{k_\beta=0}^{k_\beta=\infty} E_\alpha(k_\beta)\, dk_\beta \tag{15.7}$$

where u'_α and k_β are the αth component of $\boldsymbol{u}'$ and the βth component of $\boldsymbol{k}$, respectively. Both LIA and DNS results show that:

(a) In the longitudinal spectra $E_\alpha(k_1)$, small scales (i.e. large wave numbers) are more amplified than large scales (i.e. small wave numbers).
(b) The amplification pattern is more complex for transverse spectra: higher amplification at small scales is found for $E_1(k_2)$ and $E_2(k_2)$, while the large scales are the most amplified for $E_3(k_2)$.

This complex behavior makes it necessary to carry out a specific analysis for each characteristic length scale, since they are spectrum-dependent. Defining the integral scale for the dummy variable ϕ as

$$\Lambda_\phi(r, x) = \int_{r=0}^{r=+\infty} C_{\phi\phi}(r, x)\, dr \tag{15.8}$$

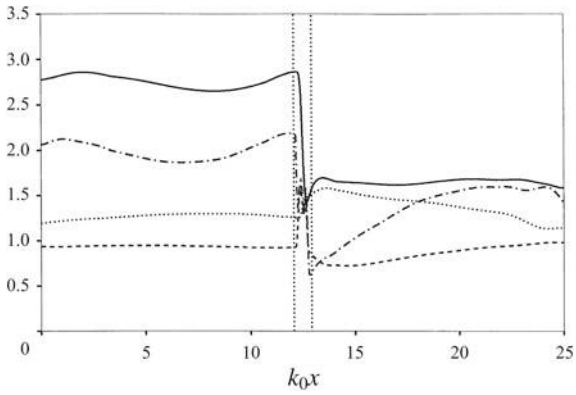

Fig. 15.12 Streamwise evolution of turbulence transverse integral scales (DNS, $M_1 = 2$, $M_t = 0.108$, $Re_\lambda = 19$). Dashed line: Λ_{u_1}; solid line: Λ_{u_2}; dotted line: Λ_{u_3}; dashed-dotted line: Λ_ρ. From Lee et al. (1997) with permission of CUP

where the transverse two-point correlation $C_{\phi\phi}(r, x)$ is given by (ϕ is assumed to be a centered random variable)

$$C_{\phi\phi}(r, x) = \frac{\overline{\phi(x, y, z, t)\phi(x, y + r, z, t)}}{\overline{\phi(x, y, z, t)\phi(x, y, z, t)}}, \tag{15.9}$$

in which the statistical averaging is carried out over time and homogeneous directions y and z, both DNS and LIA show that (see Fig. 15.12):

(a) Λ_{u_1}, Λ_{u_2} and Λ_ρ exhibit a significant Mach-number dependent decrease across the shock,
(b) Λ_{u_3} is largely increased by the interaction.

Now looking at the Taylor microscales (see Fig. 15.13), it is observed that they are all significantly reduced during the interaction, the reduction being more pronounced in the shock normal direction. It is recalled that the Taylor microscale λ_α associated to u'_α and the density microscale λ_ρ are computed here as

$$\lambda_\alpha = \sqrt{\frac{\overline{u'_\alpha u'_\alpha}}{\overline{\frac{\partial u'_\alpha}{\partial x_\alpha}\frac{\partial u'_\alpha}{\partial x_\alpha}}}}, \quad \lambda_\rho = \sqrt{\frac{\overline{\rho'\rho'}}{\overline{\frac{\partial \rho'}{\partial y}\frac{\partial \rho'}{\partial y}}}}. \tag{15.10}$$

(iv) *Thermodynamic quantities*. The thermodynamic properties of the flow downstream the shock are also modified by the interaction process. Both DNS and LIA results show that, for an isentropic incident isotropic turbulence, the downstream field remain isentropic for weak shocks such that $M_1 < 1.2$. At higher upstream wave number, the emitted entropy waves have a significant energy since their magnitude becomes comparable to that of acoustic waves. This effect is illustrated plotting the normalized correlation coefficients (see Fig. 15.14):

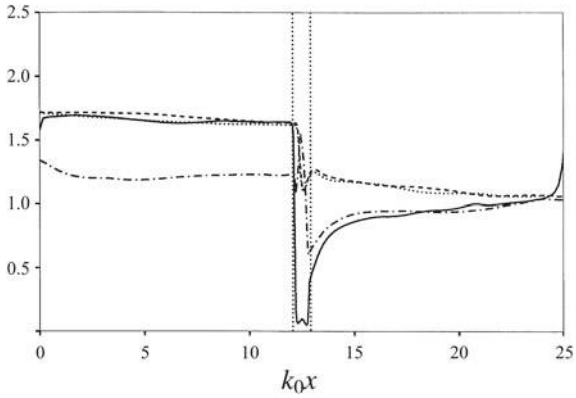

Fig. 15.13 Streamwise evolution of turbulence microscales (DNS, $M_1 = 2$, $M_t = 0.108$, $Re_\lambda = 19$). Solid line: λ_{u_1}; dashed line: λ_{u_2}; dotted line: λ_{u_3}; dashed-dotted line: λ_ρ. From Lee et al. (1997) with permission of CUP

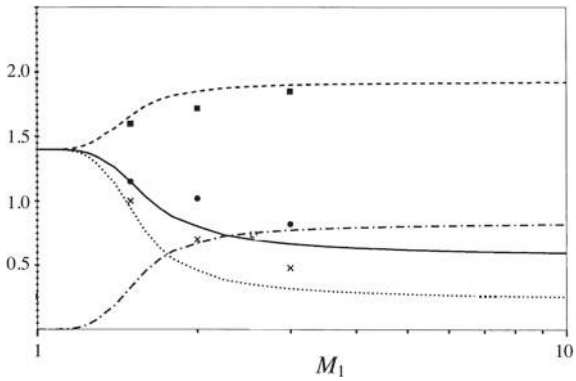

Fig. 15.14 Evolution of normalized correlation coefficients in the far field region downstream the shock versus the upstream Mach number M_1. $n_{\rho p}$: solid line (LIA) and black circles (DNS); $n_{\rho T}$: dashed line (LIA) and black circles (DNS); $C_{\rho T}$: dotted line (LIA) and 'x' (DNS); i_s: dashed-dotted line (LIA). From Lee et al. (1997) with permission from CUP

$$n_{\rho p} \equiv \frac{\sqrt{\overline{p'p'}}}{\bar{p}^2}\frac{\bar{\rho}^2}{\sqrt{\overline{\rho'\rho'}}}, \quad n_{\rho T} \equiv 1 + \frac{\sqrt{\overline{T'T'}}}{\bar{T}^2}\frac{\bar{\rho}^2}{\sqrt{\overline{\rho'\rho'}}}, \tag{15.11}$$

$$C_{\rho T} \equiv 1 + \frac{\bar{\rho}}{\tilde{T}}\frac{\sqrt{\overline{\rho'T''}}}{\sqrt{\overline{\rho'\rho'}}}, \tag{15.12}$$

along with the entropy fluctuation contribution

$$i_s \equiv \frac{\sqrt{\overline{s's'}}}{c_p^2}\frac{\bar{\rho}^2}{\sqrt{\overline{\rho'\rho'}}}. \tag{15.13}$$

It is observed that the entropy fluctuations are more significant than acoustic fluctuations for $M_1 > 1.65$. But it is worth noting that, downstream the shock, neither the isentropic hypothesis (which states that the entropy fluctuations are negligible) nor the Strong Reynolds Analogy proposed by Morkovin for shear

flows (which says that the stagnation temperature is constant, which amounts to assume that acoustic waves have a negligible effect on the density fluctuations) are valid if $M_1 > 1.2$. It is recalled that the latter can be expressed as

$$\frac{\rho'}{\bar{\rho}} = -\frac{T''}{\bar{T}} = (\gamma - 1)M_1^2 \frac{u_1''}{\tilde{u}_1}. \tag{15.14}$$

(v) *Far-field radiated noise*. The far-field radiated noise is generated by propagating acoustic waves. The acoustic energy flux vector is defined $\boldsymbol{q} = a_2 E \boldsymbol{k}_a$ in the frame of reference in which the fluid is at rest, where the energy density of the sound wave is related to the amplitude of the emitted acoustic mode by $E = \rho_2 a_2^2 A_a$. In the reference frame associated to the shock front, one has $\boldsymbol{q} = (a_2 \boldsymbol{k}_a + (U_2 - u_s)\boldsymbol{e}_x)\,(M_2 - \cos\alpha_a)E$. The existence of the critical angle α_c introduce some preferred directions in the emission of acoustic energy, resulting in a non-uniform directivity pattern. The directivity is illustrated in Fig. 15.15 in which a polar plot of the dimensionless angle-averaged streamwise component of acoustic flux vector is displayed. Normalization is made using the upstream longitudinal turbulent flux $\bar{\rho}_1 R_{11} U_1/2$. In this plot, the modified emission angle α' is used for the sake of clarity, with

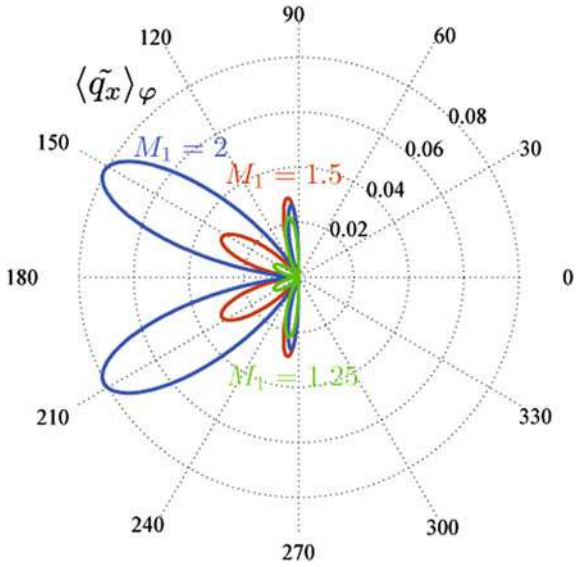

Fig. 15.15 LIA prediction of radiated far-field noise in the case of a right-facing shock wave, for $M_1 = 1.25$, 1.5 and 2. Directivity pattern for normalized streamwise acoustic flux $\boldsymbol{q} \cdot \boldsymbol{e}_x$ versus modified emission angle α'. Courtesy of C. Huete. From Wouchuk et al. (2009) with permission of APS

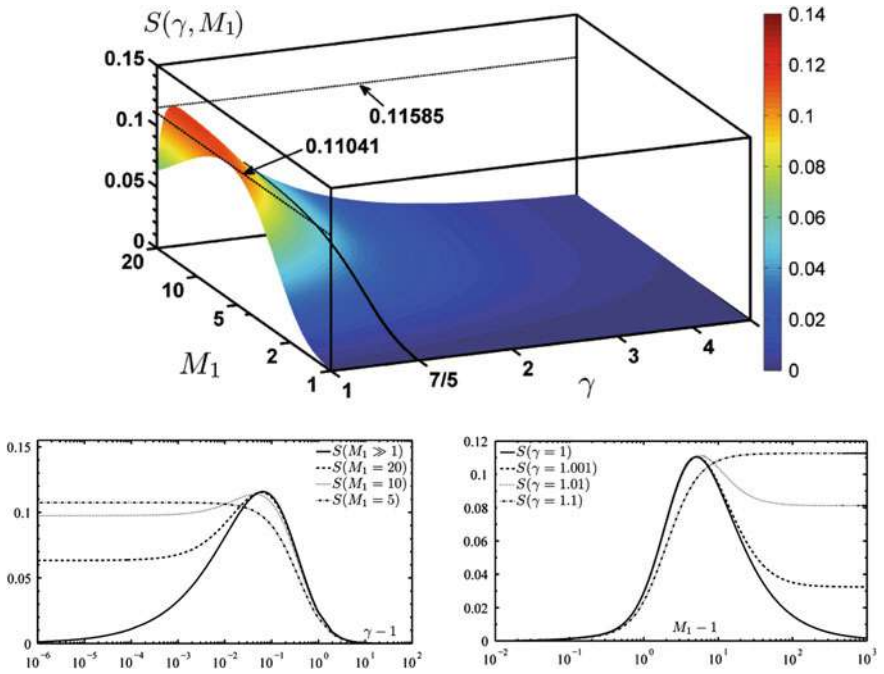

Fig. 15.16 LIA prediction of acoustic relative intensity parameter S. Top: S as a function of M_1 and γ. Bottom-left: large M_1 asymptotics; Bottom-right: high compressibility asymptotics. Courtesy of C. Huete. From Wouchuk et al. (2009) with permission of APS

$$\cos\alpha' = \frac{\cos\alpha_a - M_2}{\sqrt{1 + M_2^2 - 2M_2\cos\alpha_a}}\,.$$

With this change of coordinate, one has $\alpha' = \pi/2$ when $\alpha = \alpha_c \Leftrightarrow \cos\alpha_a = M_2$. It is observed that the directions of maximum and minimum emission are almost independent from M_1 using α', the maximum amplitude being a growing function of M_1. The global efficiency of the acoustic production mechanisms is analyzed looking at the relative intensity parameter $S = I_a/I_t$ (see Fig. 15.16), where I_a is the acoustic intensity obtained by summing $\boldsymbol{q}$ over all directions and wavenumbers and $I_t = 5\bar{\rho}_1 R_{11} U_1/6$ is the streamwise turbulent flux intensity. The maximum value is $S = 0.115$, which is obtained in the strong shock limit for $\gamma = 1.06$. In the weak shock limit, the Lighthill formula for $\gamma = 7/5$ later corrected by Ribner is recovered within 4% error. In the high compressibility limit, it is observed that $S \to 0$ as $M_1 \to +\infty$.

15.2.3 Acoustic Turbulence/Shock Interaction

The case of an incident purely acoustic isotropic field has been addressed by Mahesh and coworkers (1995) using both LIA and DNS. Full analytical expressions of amplification ratios for the physical modes, including asymptotic analysis for weak and strong shocks, are given in Huete et al. (2012b). These very useful expressions are very cumbersome and will not be reproduced here for the sake of brevity. It is observed that this case exhibits very significant differences with respect to the case of an incident purely vortical isotropic turbulence.

The main results are summarized below:

(i) *Velocity fluctuations*. As in the case of an incident vortical turbulence, the interaction yields an increase of the fluctuating kinetic energy just behind the shock wave (see Fig. 15.17). For weak shock waves (LIA analysis in Mahesh et al. 1995 is done with $M_1 = 1.2$), the kinetic energy decays monotonically downstream the shock, while for strong shocks ($M_1 = 2$ in Mahesh et al. 1995) it exhibits local extrema behind the shock. In the former case the evanescent waves are weak an have a negligible impact on the acoustic energy balance, see Eq. (15.4), while in the latter, the evanescent waves are strong and lead to the existence of a near field relaxation very similar to the one observed in the case of incident vortical turbulence. But it is worth noting that increasing the Mach number yields a decrease of the amplification immediately behind the shock front.

The behavior of far-field kinetic energy is a bit more complex. Far-field turbulence intensities are plotted versus the upstream Mach number in Fig. 15.18. A first observation is that the shock normal turbulence intensity is higher than the two transverse components. The second, more important conclusion is that the amplification factor of the far field kinetic energy does not respond monotonically to an increase in the upstream Mach number: the far field kinetic energy is

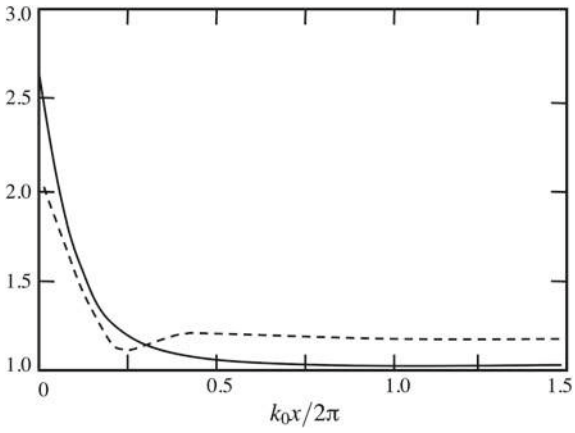

Fig. 15.17 LIA prediction of streamwise evolution of normalized turbulent kinetic energy $\mathcal{K}$ downstream the shock wave in air. Solid line: $M_1 = 1.2$; dashed line: $M_1 = 2$. From Mahesh et al. (1995) with permission of CUP

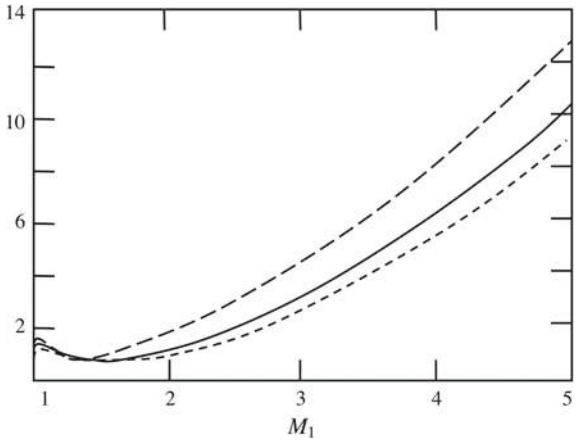

Fig. 15.18 LIA analysis of far field normalized turbulent kinetic energy and Reynolds stresses versus the upstream Mach number M_1 in air. Solid line: turbulent kinetic energy $\mathcal{K}$; long-dashed line: streamwise Reynolds stress $R_{11} = \overline{u'u'}$; short-dashed line: transverse Reynolds stresses $R_{22} = \overline{v'v'}$ and $R_{33} = \overline{w'w'}$. From Mahesh et al. (1995) with permission of CUP

lower than the incident kinetic energy for $1.25 \leq M_1 < 1.80$, while it is higher for other values. But it is worth noting that the energy of transverse components of velocity decrease over a wider range of upstream Mach number.

This phenomena can be understood decomposing the far field kinetic energy into vortical and acoustic contributions and plotting the associated kinetic energy amplification factor $K_{3D} = K_{3D}^{rot} + K_{3D}^{ac}$. These parameters are plotted as function of M_1 and γ in Fig. 15.19. It is observed that K_{3D} diverges in the limit of strong shocks and highly compressible fluids. This is a drawback of the inviscid fluid assumptions, since viscosity and thermal diffusion would regularize the singularity in this limit which is associated with asymptotically small scales. The behavior of K_{3D}^{ac} is more complex, since several extrema are detected on the response surface. This parameter remains bounded, showing that the emitted vortical field is responsible for the unbounded growth of kinetic energy. Asymptotic behaviors plotted in Fig. 15.20, in which one can see that the strong shock asymptotic behavior is very sensitive to γ for highly compressible fluids.

The case of air ($\gamma = 7/5$) is detailed in Fig. 15.21 It is observed that K_{3D}^{ac} decays monotonically in air for $M_1 > 1.2$, while K_{3D}^{rot} is a strictly increasing function of M_1. The existence of a local minimum is explained by the fact that the solenoidal kinetic energy exceeds the dilatational one for $M_1 > 2$ and the incident kinetic energy for $M_1 > 2.25$. The behavior of the far field acoustic kinetic energy is governed by the competition between two mechanisms: the amplification of the energy of incident waves, that grows with the Mach number, and the fact that the range of angles corresponding to evanescent emitted waves also increases with M_1, making less and less emitted waves contributing to the far field. The LIA analysis shows that, at high upstream Mach number, the energy of all velocity components scales as M_1^2.

The Reynolds stress anisotropy coefficient β_v is displayed in Fig. 15.22. As in the case of an incident pure vortical turbulence, the response surface exhibits a complex topology, and it is observed that all states, i.e. $\beta_v > 0$, $\beta_v < 0$ and

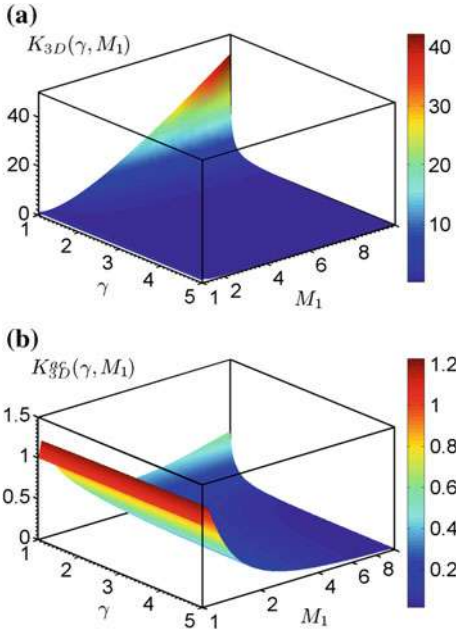

Fig. 15.19 LIA prediction of amplification of turbulent kinetic energy as a function of M_1 and γ. Top: full kinetic energy amplification factor K_{3D}; Bottom: acoustic part K^{ac}_{3D}. Courtesy of C. Huete. From Huete et al. (2012b) with permission of APS

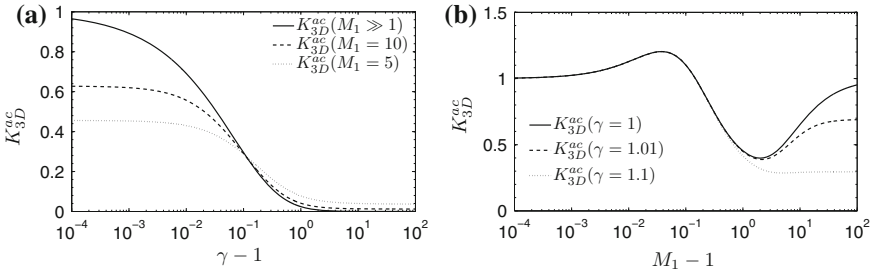

Fig. 15.20 LIA prediction of amplification factor of acoustic part of turbulent kinetic energy K^{ac}_{3D}. Left: high gas compressibility asymptotics $\gamma \to 1$; Right: strong shock asymptotics $M_1 \to +\infty$. Courtesy of C. Huete. From Huete et al. (2012b) with permission of APS

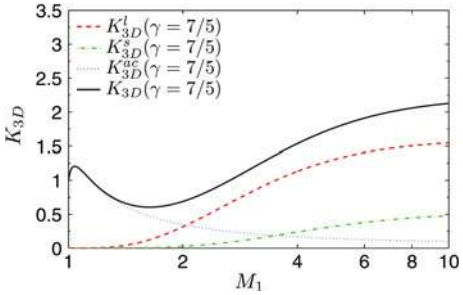

Fig. 15.21 LIA prediction of amplification factor of turbulent kinetic energy in air ($\gamma = 7/5$). K^l_{3D} and K^s_{3D} denote contributions with incidence angle such that $\alpha < \alpha_c$ and $\alpha > \alpha_c$, respectively, to the kinetic energy of the vorticity mode. Courtesy of C. Huete. From Huete et al. (2012b) with permission of APS

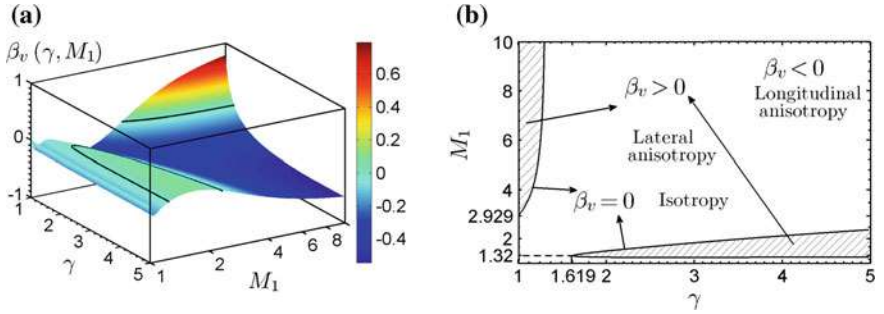

Fig. 15.22 LIA prediction of Reynolds stress anisotropy parameter β_v. Left: plot as a function of M_1 and γ; Right: level curve for $\beta_v = 0$ corresponding to isotropic Reynolds stress tensor. Courtesy of C. Huete. From Huete et al. (2012b) with permission of APS

$\beta_v = 0$ (isotropic Reynolds tensor) are possible. The limit $\beta_v = 1$ (state with negligible shock-normal kinetic energy) is obtained for $M_1 \to +\infty$ and $\gamma \to 1$, while $\beta_v = -1$ is never approached.

(ii) *Vorticity*. In this case, the production of vorticity is mainly governed by the baroclinic term (term VI in Eq. (15.6)). The jump relations for the vorticity components show that transverse components will be the most affected, the streamwise component evolution being governed by other mechanisms, as in the case of incident vortical turbulence. The shock-normal vorticity component being left unchanged by jump relations for a planar shock wave, there is no shock-normal vorticity in the downstream region in the case of a pure irrotational incident turbulent acoustic field, resulting in a very high vorticity anisotropy. The normalized (transverse) vorticity generation parameter W_{3D} such that $\|\boldsymbol{\omega}'\|^2 \propto (ka_2)^2 A_a^2 W_{3D}$, with A_a^2 the energy of the incident acoustic field, is displayed in Fig. 15.23. It is observed that the largest generation mechanisms are observed in the limit of strong shocks in highly compressible fluids, a diverg-

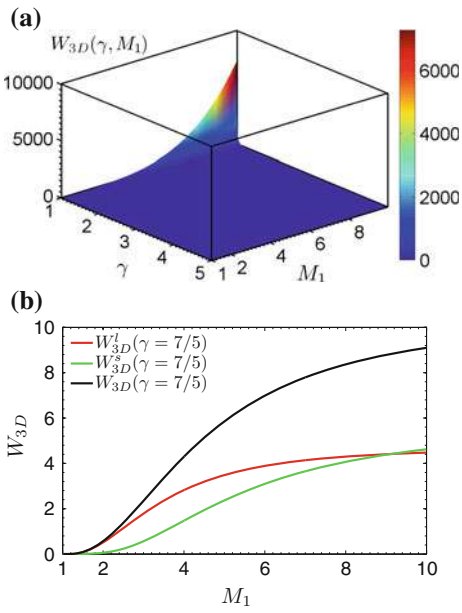

Fig. 15.23 LIA prediction of vorticity generation parameter. Top: W_{3D} as a function of M_1 and γ; Bottom: W_{3D} as a function of M_1 in air. W^l_{3D} and W^s_{3D} denote contributions with incidence angle such that $\alpha < \alpha_c$ and $\alpha > \alpha_c$, respectively. Courtesy of C. Huete. From Huete et al. (2012b) with permission of APS

ing behavior being recovered in the absence of viscous effects. In the case of air, vorticity generation is dominated by incident waves such that $\alpha < \alpha_c$ up to $M_1 \simeq 9$, while waves such that $\alpha > \alpha_c$ become more important at higher Mach number.

(iii) *Thermodynamic quantities*. The evolution of the thermodynamic quantities in the far field versus the upstream Mach number is displayed in Fig. 15.24. It is observed that the downstream fluctuations are nearly isentropic for $M_1 < 1.5$. At higher Mach numbers the emitted entropy fluctuations are significant relative to the acoustic fluctuations. The dominance of the entropy mode at high Mach number originates in two phenomena: the emission of stronger and stronger entropy waves and the decrease of acoustic energy in the far field.

15.2.4 Mixed Turbulence/Shock Interaction

We now address the cases in which the incident turbulent field is composed of different types of Kovasznay modes: hybrid vortical/acoustic turbulence (Mahesh et al. 1995) and vortical/entropic turbulence (Mahesh et al. 1996, 1997). These cases are of great interest, since physical turbulence generated in wind tunnels or observed in natural flows is never strictly vortical or acoustic. It is worth recalling here the important conclusion that a Kovasnay mode will generate modes of different natures through non-linear self interactions. Therefore, the sensitivity of the results presented

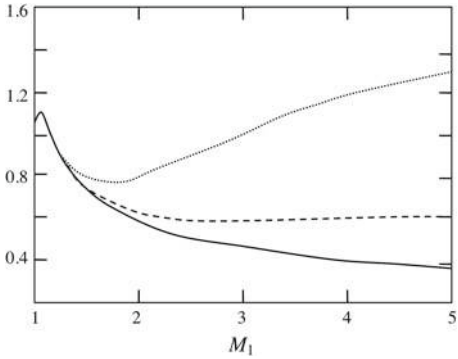

Fig. 15.24 LIA prediction of far field normalized r.m.s. fluctuations of thermodynamical quantities. Solid line: $\sqrt{\overline{p'p'}}/\bar{p}$; dashed line: $\gamma\sqrt{\overline{\rho'\rho'}}/\bar{\rho}$; dotted line: $\frac{\gamma}{\gamma-1}(\sqrt{\overline{T'T'}}/\bar{T})$. From Mahesh et al. (1995) with permission of CUP

above for pure incident fields is of major interest to gain a deeper insight into the dynamics of realistic flows. But since the experimental data exhibit a significant dispersion, it can be inferred that their sensitivity must be great (independently from the fact that such experiments are very difficult to perform for technical and technological reasons). Another point is that, in real flows, the distribution of the total energy among the three Kovasznay modes is unknown and cannot usually be controlled. Therefore, we will hereafter put the emphasis on the theoretical results dealing with the sensitivity of the results rather than giving an exhaustive presentation of some realizations.

Let us begin examining the two-dimensional linearized Euler equation for the vorticity fluctuation about a one-dimensional mean flow. We will use it as a simple phenomenological model to describe the amplification of the transverse vorticity components across the shock. The linearized evolution law is:

$$\frac{\partial \omega'}{\partial t} + U\frac{\partial \omega'}{\partial x} = -\omega'\frac{\partial U}{\partial x} - \frac{\partial \rho'}{\partial y}\frac{1}{\bar{\rho}^2}\frac{\partial \bar{p}}{\partial x} + \frac{\partial p'}{\partial y}\frac{1}{\bar{\rho}^2}\frac{\partial \bar{\rho}}{\partial x}. \tag{15.15}$$

The usual viscous model (Zel'dovich and Raizer 2002; Landau and Lifshitz 1987) for the shock front shows that $(\partial\bar{u}/\partial x) < 0$, $(\partial\bar{p}/\partial x) > 0$ and $(\partial\bar{\rho}/\partial x) > 0$ in the shock region. The first term in the right hand side of the above equation corresponds to the compression by the mean flow gradient. Since $\partial\bar{u}/\partial x$ is negative in the shock region, the net effect of vorticity amplification by the bulk compression is recovered. The two last terms are related to the baroclinic mechanisms. The second term in the right hand side of Eq. (15.15) involves the fluctuating density, and is therefore non zero for both acoustic and entropy fluctuating modes, while the third one is non zero for acoustic perturbations only. This equation also shows that the baroclinic and the bulk compression contributions can have the same or opposite signs, depending on the respective signs of the vorticity, density and pressure fluctuations. If the contributions have the same sign, the net amplification of vorticity will be increased by the cooperative interaction, while the two mechanisms will tend to cancel in the opposite case, yielding a decrease of the net vorticity fluctuation amplification. One

can see that increased amplification is recovered if $\omega' p' > 0$ or $\omega' \rho' < 0$. The very important conclusion drawn from that very simple analysis is that the results of the shock/turbulence interaction will be greatly sensitive to the correlation between the Kovasznay modes in the incident field.

15.2.4.1 Influence of the Upstream Entropy Fluctuations

Let us first consider the case of an incident field made of vorticity and entropy modes. We simplify the problem considering a single plane entropy wave with amplitude A_s and a single vorticity wave with amplitude A_v with the same wave vector $\boldsymbol{k}$. According to results presented in Sect. 3.2.2, the upstream field is given by

$$\frac{u'}{\bar{u}} = A_v \cos\alpha e^{\imath(\boldsymbol{k}\cdot\boldsymbol{x}-\omega t)}, \quad \frac{v'}{\bar{u}} = -A_v \sin\alpha e^{\imath(\boldsymbol{k}\cdot\boldsymbol{x}-\omega t)}, \quad \frac{s'}{c_p} = A_s e^{\imath(\boldsymbol{k}\cdot\boldsymbol{x}-\omega t)} \tag{15.16}$$

leading to

$$\frac{\omega'}{\bar{u}} = -A_v e^{\imath(\boldsymbol{k}\cdot\boldsymbol{x}-\omega t)}, \quad \frac{\rho'}{\bar{\rho}} = -\frac{T'}{\bar{T}} = A_s e^{\imath(\boldsymbol{k}\cdot\boldsymbol{x}-\omega t)}, \quad \frac{p'}{\gamma\bar{p}} = 0. \tag{15.17}$$

It is seen that ω' and u' on the one hand and ρ' and T' on the other hand are in phase opposition. Therefore, the condition for cooperative interaction $\omega'\rho' < 0$ is equivalent to $u'T' < 0$. Introducing the complex ratio:

$$\frac{A_s}{A_v} = c_{sv} e^{\imath\varphi}, \tag{15.18}$$

cooperative interaction is observed if $\varphi \in]-\pi/2, \pi/2[$, while partial cancelation occurs for $\varphi \in]\pi/2, -\pi/2[$. This discussion is illustrated in Fig. 15.25.

Direct numerical simulation and LIA results dealing with the amplification of velocity fluctuations in the case of an incident isotropic turbulent are presented in Fig. 15.26. They show that, in the case where the streamwise velocity component and temperature fluctuations are strongly anti-correlated ($\overline{u'T'}/u_{rms}T_{rms} \approx -1$), the amplification of all velocity components is greatly enhanced, the effect being more important on the streamwise component. The velocity field still exhibits a near field whose properties are similar to those of the near field generated by a pure vortical incident field. On the opposite, the amplification is reduced when they are correlated, i.e. $\overline{u'T'} > 0$. The evolution of the amplification of the far field velocity variances with respect to the upstream Mach number is displayed in Fig. 15.27. The LIA predicts that the amplification saturates for $M_1 > 2$, with a remarkable exception: if the upstream fluctuations satisfy the Morkovin's hypothesis given in Eq. (15.14), the amplification factor does not saturate and keeps growing with M_1. The main reason is that, if the Morkovin's hypothesis holds in the upstream region, the relative importance of the entropy modes with respect to the vorticity mode scales like M_1^2.

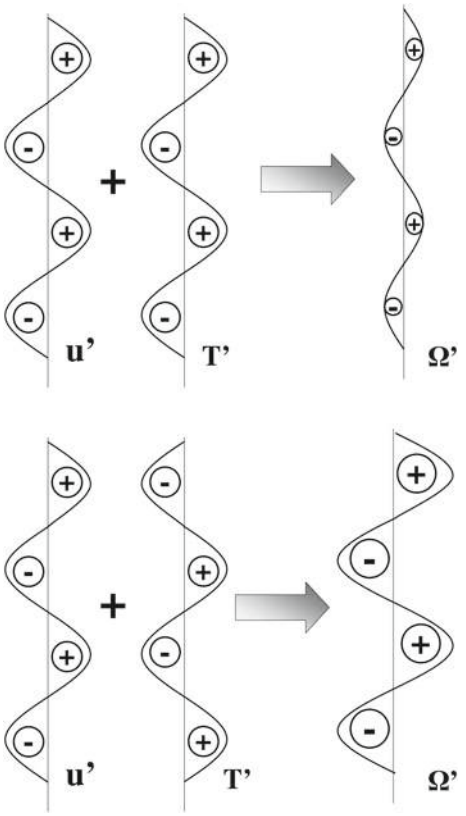

Fig. 15.25 Schematic view of the influence of the phase difference between velocity and temperature fluctuations on the emitted vorticity fluctuation. Top: velocity and temperature fluctuations are in phase, leading to a decrease of the vorticity amplification. Bottom: they are in phase opposition, yielding a large increase of the vorticity amplification

Similar conclusions hold for the vorticity field: both DNS and LIA confirm the predictions drawn from the simplified model. The amplification factor of the transverse vorticity components is plotted versus the upstream Mach number in Fig. 15.28. Once again, the amplification is enhanced if $\overline{u_1' T'} < 0$ and exhibits very strong values if the incident turbulent field satisfy Morkovin's hypothesis.

An interesting point is that the interaction with the shock results in a breakdown of the Morkovin's hypothesis downstream the shock wave, even if it holds upstream the shock. Recalling that the fundamental assumption in Morkovin's proposal is that the stagnation temperature T^0 is constant in the flow. Decomposing the stagnation temperature like

$$T^0 = \bar{T} + T' + \frac{1}{2}\frac{(U+u')^2 + v'^2 + w'^2}{c_p}, \tag{15.19}$$

the Rankine–Hugoniot jump relation for the energy (3.19) yields the continuity of T^0 across the shock wave:

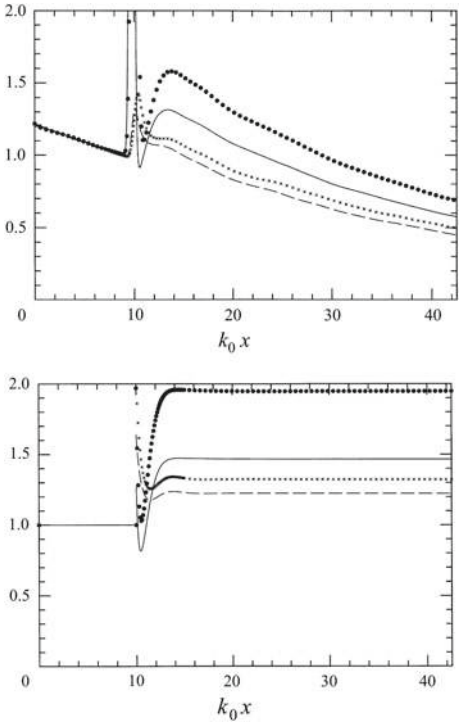

Fig. 15.26 Influence of upstream entropy fluctuations on the streamwise evolution of Reynolds stresses at $M_1 = 1.29$. Top: DNS data. Streamwise Reynolds stress $R_{11} = \overline{u'u'}$ for $u_1' T_1'/u_{rms} T_{rms} = -0.06$ (solid line) and -0.84 (black circles); transverse Reynolds stress $R_{22} = \overline{v'v'}$ for $u_1' T_1'/u_{rms} T_{rms} = -0.06$ (dashed line) and -0.84 ('x'). Bottom: LIA analysis, same cases and symbols as for DNS data. From Mahesh et al. (1997) with permission of CUP

$$\bar{T}_1 + T_1' + \frac{1}{2}\frac{(U_1 + u_1' - u_s)^2 + {v_1'}^2 + {w_1'}^2}{c_p} = \bar{T}_2 + T_2' + \frac{1}{2}\frac{(U_2 + u_2' - u_s)^2 + {v_2'}^2 + {w_2'}^2}{c_p}, \tag{15.20}$$

where u_s is the shock speed associated to the corrugation of the shock front by incident perturbations. Assuming that fluctuations are small enough, one can linearize (15.20), yielding

$$T_1' + \frac{U_1(u_1' - u_s)}{c_p} = T_2' + \frac{U_2(u_2' - u_s)}{c_p}. \tag{15.21}$$

Now assuming that the upstream flow satisfies the Morkovin hypothesis, one obtains the following expression for the linearized fluctuation of the stagnation temperature behind the shock wave:

$$T_2' + \frac{U_2 u_2'}{c_p} = \frac{u_s(U_2 - U_1)}{c_p}. \tag{15.22}$$

Using this expression, one can write:

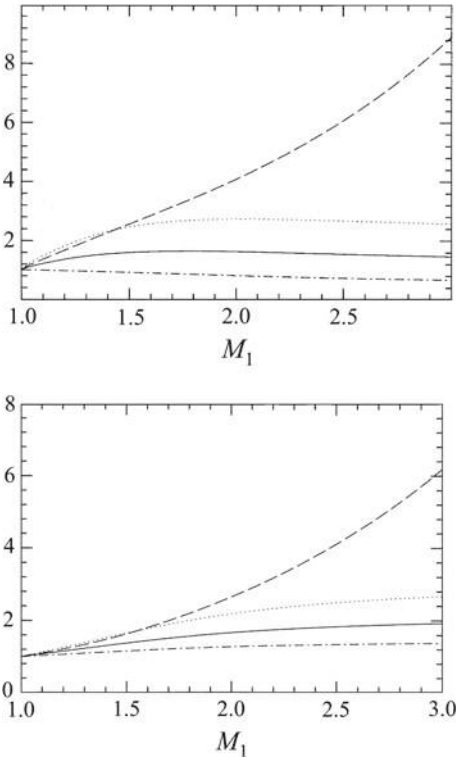

Fig. 15.27 LIA analysis of influence of upstream entropy fluctuations on the downstream evolution of Reynolds stresses versus the upstream Mach number M_1. Top: Streamwise Reynolds stress $R_{11} = \overline{u'u'}$. Solid line: pure vortical incident turbulence; dotted line: $\overline{u_1' T_1'} < 0$; dashed-dotted line: $\overline{u_1' T_1'} > 0$; dashed line: Morkovin's hypothesis satisfied upstream. Bottom: transverse Reynolds stress $R_{22} = \overline{v'v'}$, same symbols as above. From Mahesh et al. (1997) with permission of CUP

$$\frac{T_2''}{\bar{T}_2} + (\gamma - 1) M_2^2 \frac{u_2''}{U_2} = -(\gamma - 1) M_2 (\mathfrak{C} - 1) \frac{u_s}{\bar{a}_2} \tag{15.23}$$

where $\mathfrak{C}$ is the compression factor defined by U_1/U_2. Therefore, the Morkovin's hypothesis holds downstream the shock wave if and only if the right hand side of Eq. (15.23) is zero, which is observed to be false in both LIA and DNS results.

The LIA results can be accurately fitted by simple expressions as proposed in Sinha (2012). Introducing the upstream velocity-temperature correlation coefficient A_{uT} defined such that

$$\frac{\rho_1'}{\bar{\rho}_1} = -\frac{T_1''}{\bar{T}_1} = A_{uT} \frac{u_1''}{U_1} \tag{15.24}$$

the vorticity amplification factor is approximated as:

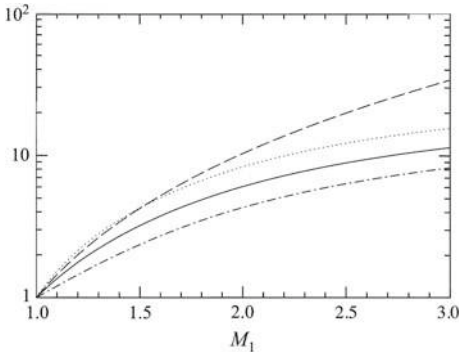

Fig. 15.28 LIA analysis of influence of upstream entropy fluctuations on the far field amplification of transverse vorticity components $\overline{\omega_2'\omega_2'} = \overline{\omega_3'\omega_3'}$ versus the upstream Mach number M_1. Solid line: pure vortical incident turbulence; dotted line: $\overline{u_1'T'} < 0$; dashed-dotted line: $\overline{u_1'T'} > 0$; dashed line: Morkovin's hypothesis satisfied upstream. From Mahesh et al. (1997) with permission of CUP

$$\frac{(\overline{\omega_i'\omega_i'})_2}{(\overline{\omega_i'\omega_i'})_1} = \left(\frac{U_1}{U_2}\right)^{c_\omega}, \quad c_\omega = 1.55\left(1 + \frac{(1+e^{1-M_1})}{8}A_{uT}\right). \tag{15.25}$$

The amplification ratio of solenoidal dissipation is modeled as

$$\frac{\bar{\varepsilon}_{s_2}}{\bar{\varepsilon}_{s_1}} = \left(\frac{\bar{T}_2}{\bar{T}_1}\right)^{0.76}\left(\frac{U_2}{U_1}\right)^{c_\omega - 1}. \tag{15.26}$$

These formula are observed to lead to a nearly perfect match of LIA results up to $M_1 = 3$ in the range $-0.58 \leq A_{uT} < 4$.

15.2.4.2 Influence of the Upstream Acoustic Fluctuations

The analysis of the influence of upstream acoustic waves is simpler than the one of entropy waves, since these waves cannot be correlated with the vortical fluctuations, their propagation speeds being different.[2] Therefore, the emitted far field is obtained via a simple superposition of the far fields corresponding to the vortical fluctuations and acoustic fluctuations considered separately.

This is illustrated considering the amplification of the total turbulent kinetic energy $\mathcal{K} = \mathcal{K}_s + \mathcal{K}_d$:

[2]It is to note here that some interactions exist if the upstream field is composed of a single wave of each type, but these interactions cancel from a statistical viewpoint in fully developed isotropic turbulent flows.

$$\frac{\mathcal{K}_2}{\mathcal{K}_1} = \frac{(\mathcal{K}_s)_2 + (\mathcal{K}_d)_2}{(\mathcal{K}_s)_1 + (\mathcal{K}_d)_1} = (1-\chi_1)\frac{(\mathcal{K}_s)_2}{(\mathcal{K}_s)_1} + \chi_1 \frac{(\mathcal{K}_d)_2}{(\mathcal{K}_d)_1} \tag{15.27}$$

where χ_1 is the ratio of dilatational acoustic energy to the total kinetic energy (see Eq. (13.34)) in the upstream state. The amplification factors of the acoustic and vortical component being different, significant differences in the amplification of the total kinetic energy can be observed varying the value of χ_1.

15.2.5 *On the Use of RDT for Linear Non-destructive Interaction Modelling*

The LIA theory has been shown to be a very accurate tool to predict and understand the linear non-destructive shock/turbulence interactions. The capability of the RDT theory to account for the same physical effects has also been investigated by many authors, among which Jacquin et al. (1993) and references given therein.

Within the RDT framework, the planar shock is essentially modelled as an unidirectional irrotational compression with a time-varying mean flow already discussed in Sect. 14.2.3.3. Therefore, all results presented in this section can be used in a straightforward way. Therefore, the amplification ratio of turbulent kinetic energy is lower-bounded by the solenoidal limit given by Eq. (14.47) and upper-bounded by the pressure-released evolution described by the relation (14.48). These two evolution laws are compared with LIA results in Fig. 15.29.

Large discrepancies are observed, the two RDT limits yielding much larger amplification ratio than both the near- and far-field LIA predictions at almost all upstream Mach numbers. The inaccuracy of RDT for this problem can be understood looking at Table 15.1 which summarizes the main differences between the RDT and LIA

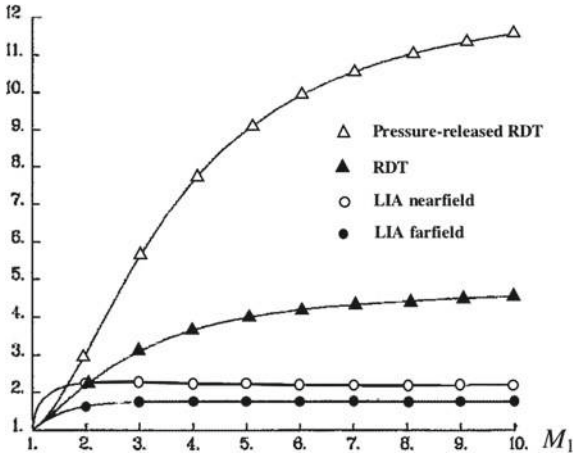

Fig. 15.29 Comparison of the turbulent kinetic energy amplification factor as a function of the upstream Mach number according to different linearized theories for a pure solenoidal upstream disturbance field. Adapted from Jacquin et al. (1993)

Table 15.1 Main features of shock/turbulence interaction modelling according to linearized theories

Theory features	LIA	RDT
Intrinsic timescale	None	$1/S$
Intrinsic lengthscale	None (infinitely small)	None (infinitely large)
Shock viscous effects	Yes (linearized Rankine–Hugoniot relations)	No
Shock corrugation effects	Yes (linearized response)	No
Vortical disturbances	Yes	Yes
Acoustic disturbances	Yes	Yes
Entropy disturbances	Yes	No

approaches. Of course, due to the isentropy assumption, RDT cannot account for entropy effects discussed in Sect. 15.2.4.1. But restricting to the case of a purely vortical incoming turbulence described in Sect. 15.2.2, one can observe that the main weaknesses of RDT are:

- The inability to account for the shock corrugation and its feedback on the emitted turbulent field.
- The inability to predict the existence of evanescent acoustic waves downstream the shock and the existence of a cutoff incidence angle for incoming disturbances (see details in Sect. 16.5.2).
- The isentropic assumption, since the entropy fluctuations are more significant than the acoustic ones for $M_1 > 1.65$ downstream the shock. The isentropic assumption for the emitted field is found to be realistic for weak shocks only, with $M_1 < 1.2$.

15.3 Wrinkled Shock Régime: Nonlinear Interaction

15.3.1 Turbulent Jump Conditions for the Mean Field

Let us denote the mean and fluctuating velocity components (U_i, V_i, W_i) and (u_i'', v_i'', w_i''), respectively, where the subscripts 1 and 2 refer to the upstream and downstream states, respectively. The mean and fluctuating enthalpy are denoted $\tilde{h}_i$ and h_i''. Using the same notations as in previous sections, assuming that a frame of reference can be found in which the mean shock wave is stationary and that viscous effects are negligible, Lele (1992) deduced from the Navier–Stokes equations written in conservative form the following jump relations for the mean flow quantities (the vector normal to the shock wave is chosen to be along the x direction):

$$\bar{\rho}_1 U_1 = \bar{\rho}_2 U_2, \tag{15.28}$$

$$\bar{\rho}_1 U_1^2 + \bar{\rho}_1 \widetilde{u_1'' u_1''} + \bar{p}_1 = \bar{\rho}_2 U_2^2 + \bar{\rho}_2 \widetilde{u_2'' u_2''} + \bar{p}_2, \tag{15.29}$$

$$\bar{\rho}_1 U_1 V_1 + \bar{\rho}_1 \widetilde{u_1'' v_1''} = \bar{\rho}_2 U_2 V_2 + \bar{\rho}_2 \widetilde{u_2'' v_2''}, \tag{15.30}$$

$$\bar{\rho}_1 U_1 W_1 + \bar{\rho}_1 \widetilde{u_1'' w_1''} = \bar{\rho}_2 U_2 W_2 + \bar{\rho}_2 \widetilde{u_2'' w_2''}, \tag{15.31}$$

$$\begin{aligned} &\bar{\rho}_1 U_1 \left(\tilde{h}_1 + \frac{1}{2} K_1 + \frac{1}{2} \mathcal{K}_1 \right) \\ &+ \bar{\rho}_1 \left(\widetilde{h_1'' u_1''} + U_1 \widetilde{u_1'' u_1''} + V_1 \widetilde{u_1'' v_1''} + W_1 \widetilde{u_1'' w_1''} + \frac{1}{2} \widetilde{\mathcal{K}_1'' \mathcal{K}_1'' u_1''} \right) = \\ &\bar{\rho}_2 U_2 \left(\tilde{h}_2 + \frac{1}{2} K_2 + \frac{1}{2} \mathcal{K}_2 \right) + \\ &\bar{\rho}_2 \left(\widetilde{h_2'' u_2''} + U_2 \widetilde{u_2'' u_2''} + V_2 \widetilde{u_2'' v_2''} + W_2 \widetilde{u_2'' w_2''} + \frac{1}{2} \widetilde{\mathcal{K}_2'' \mathcal{K}_2'' u_2''} \right), \end{aligned} \tag{15.32}$$

where the mean turbulent and mean flow kinetic energies are defined as

$$\mathcal{K}_i = \widetilde{u_i'' u_i''} + \widetilde{v_i'' v_i''} + \widetilde{w_i'' w_i''}, \quad K_i = U_i^2 + V_i^2 + W_i^2, \tag{15.33}$$

and

$$\widetilde{\mathcal{K}_i'' \mathcal{K}_i'' u_i''} \equiv \frac{1}{\bar{\rho}} \overline{\rho u_i'' (u_i'' u_i'' + v_i'' v_i'' + w_i'' w_i'')}. \tag{15.34}$$

Equations (15.28)–(15.32) show that the mean flow quantities are directly affected by the jump in the turbulent stresses across the shock, and that they cannot be computed separately. Therefore, closures for the turbulent terms are required to compute the mean flow downstream the shock front. Only very few attempts to close the jump conditions are available (Lele 1992; Zank et al. 2002). Since none of them has been fully assessed, they will not be discussed here.

It is worth noting that the mean flow solutions of the non-linear jump conditions be very different from those considered within the LIA framework. A striking example is that if the incident mean flow is normal to the mean shock front (i.e. $V_1 = W_1 = 0$), the mean flow downstream the shock can deviate from a unidirectional flow (i.e. $V_2 \neq 0$ and/or $W_2 \neq 0$). The observed effects of turbulence are the following:

(i) Turbulent fluctuations increase the mean shock speed.
(ii) Turbulent fluctuations decrease the efficiency of turbulence amplification across the shock as the amplitude of incident fluctuations is increased.

15.3.2 Jump Conditions for an Incident Isotropic Turbulence

General jump conditions given above simplify dramatically in the case of a normal upstream mean flow advecting an isotropic incident field. In this case, the mean flow stay unidirectional and one has

$$V_i = W_i = 0, \quad \widetilde{u_i'' v_i''} = \widetilde{u_i'' w_i''} = 0, \quad i = 1, 2. \tag{15.35}$$

After some algebra, one obtains the following expressions for the mean flow quantities (to be compared with Eqs. (16.17)–(16.19)):

$$\frac{\bar{p}_2}{\bar{p}_1} = 1 + \frac{2\gamma}{\gamma+1}\left(\frac{(1-\mathfrak{K})\gamma + (1+\mathfrak{K})}{2} M_1^2 - \mathfrak{K}\right) - \frac{1}{\bar{p}_1}\left[\left[\widetilde{\bar{\rho} u'' u''}\right]\right], \tag{15.36}$$

$$\mathfrak{C} = \frac{\bar{\rho}_2}{\bar{\rho}_1} = \frac{U_1}{U_2} = \frac{1}{\mathfrak{K}} \frac{(\gamma+1)M_1^2}{2 + (\gamma-1)M_1^2}, \tag{15.37}$$

$$M_2^2 = \mathfrak{L}^2 \left(1 + \frac{\gamma-1}{2} M_1^2\right) \times \left(\frac{(1+\mathfrak{L})\gamma - (1-\mathfrak{L})}{2} \frac{(1-\mathfrak{L})\gamma + (1+\mathfrak{L})}{2} M_1^2 - \frac{\gamma-1}{2}\mathfrak{L}^2\right)^{-1}, \tag{15.38}$$

with

$$\mathfrak{L} = \frac{\mathfrak{K}}{\sqrt{1 + \frac{[[H]]}{H_1}}}, \tag{15.39}$$

and

$$\mathfrak{K} = \left(1 + \frac{U_1}{U_1 - U_2}\frac{[[H]]}{H_1}\right)\left(1 - \frac{2\gamma}{(\gamma+1)(U_1 - U_2)}\left[\left[\frac{\widetilde{u'' u''}}{U}\right]\right]\right)^{-1}, \tag{15.40}$$

where $H = \tilde{h} + U^2/2$ is the mean stagnation enthalpy.

15.3.3 Direct Numerical Simulation Results

Theoretical analyses discussed above have been corroborated by numerical simulations dealing with interaction of a purely vortical isotropic turbulence with a normal shock. It must be emphasized here that a clean capture of nonlinearities requires a very

fine grid resolution since the Kolmogorov scale exhibits a strong decrease through the shock layer due to the change in the fluid viscosity (Larsson and Lele 2009). Reminding the very definition of the Kolmogorov scale η and using the relations $\varepsilon \simeq \mu\overline{\omega'^2}$ and $\mu \simeq T^{3/4}$, one has

$$\eta = \left(\frac{\nu^3}{\varepsilon/\rho}\right)^{1/4} \sim \left(\frac{\mu^2}{\rho^2\overline{\omega'^2}}\right)^{1/4} \sim \frac{\bar{T}^{3/8}}{\bar{\rho}^{1/2}\sqrt{\overline{\omega'^2}}}, \tag{15.41}$$

leading to

$$\frac{\eta_2}{\eta_1} \propto \left(\frac{\bar{T}_2}{\bar{T}_1}\right)^{3/8} \left(\frac{\bar{\rho}_1}{\bar{\rho}_2}\right). \tag{15.42}$$

This approximation is observed to match DNS results within 10% error and show that η can exhibit up to a 70% drop in the immediate post-shock region (see Fig. 15.30). This decrease in the smallest turbulent scales requires a very fine grid resolution to get converged numerical results, too coarse a grid resolution yielding a reduction in the effects on nonlinearities and an artificial agreement with LIA predictions. It is important noting that only most recent DNS are grid-converged.

A first footprint of nonlinearity is that jump relations associated to mean flow quantities are modified by turbulent fluctuations. A general result reported in all DNSs is that an increase of the upstream turbulent Mach number M_{t_1} results in a decrease of the jump on mean flow quantities with respect to the laminar Rankine–Hugoniot jump relations (Larsson and Lele 2009; Ryu and Livescu 2014; Larsson et al. 2013). As a matter of fact, the jump on mean density $\bar{\rho}$ and mean pressure $\bar{p}$ are observed to be lower than the ones predicted by laminar jump relations by a factor about $0.95(M_{t_1}/M_1)^2$ and $\gamma 0.95(M_{t_1}/M_1)^2$ in all simulations reported in Larsson et al. (2013), respectively. This behaviour is fully consistent with Eq. (15.37) in

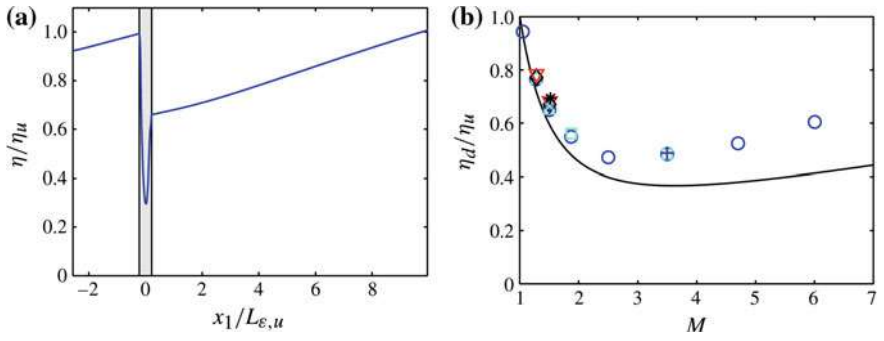

Fig. 15.30 Left: Streamwise evolution of the Kolmogorov scale η normalized by its upstream value for $(M_1, M_{t_1}) = (1.5, 0.14)$. Right: Change in η across the shock versus M_1; symbols: DNS results at different (M_1, M_{t_1}); solid line: relation (15.42). From Larsson et al. (2013) with permission of CUP

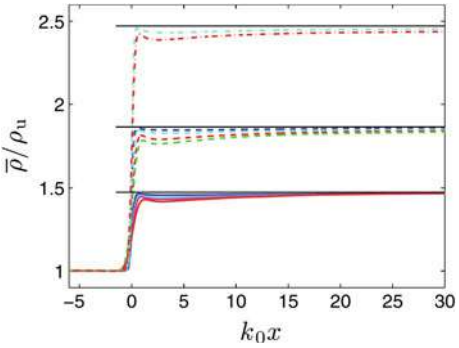

Fig. 15.31 Streamwise evolution mean density $\bar{\rho}$ normalized by its upstream value for $M_1 = 1.28, 1.5, 1.87$ and $0.16 \leq M_{t_1} \leq 0.38$. Dashed lines: DNS data; Horizontal solid line: inviscid Rankine–Hugoniot jump relation. From Larsson and Lele (2009) with permission of AIP

which the laminar jump relation is modified by the factor $1/\Re$. This is illustrated in Fig. 15.31, in which the streamwise evolution normalized by its upstream value is displayed. The sensitivity to M_{t_1} is observed, along with the fact that the mean field is not uniform downstream the shock due to the streamwise variations of the Reynolds stresses. It has been checked that DNS results converge toward LIA prediction in the limit of small M_{t_1} in Ryu and Livescu (2014), in which it is reported that deviation from LIA can be quantified by the ratio

$$\frac{\delta}{\eta} \sim 7.69 \frac{M_{t_1}}{M_1 - 1} \frac{1}{\sqrt{Re_{\lambda_1}}}. \tag{15.43}$$

The most striking effects of nonlinearity can be observed on the far field characteristics of the emitted waves. A first important results is that nonlinear effects yield an inversion in the Taylor scales behavior. While the LIA predicts that the longitudinal (shock-normal) Taylor scale λ_1 must be smaller than transverse one, i.e. $\lambda_1 < \lambda_2$, nonlinear DNS results show that $\lambda_2 < \lambda_1$. This result may seem to be paradoxical since the shock essentially acts as a compression in the shock-normal direction. A physically relevant rationale is found recalling the definition of the Taylor scale:

$$\lambda_\alpha = \sqrt{\frac{\overline{u'_\alpha u'_\alpha}}{(\partial u'_\alpha / \partial x_\alpha)^2}}, \quad \alpha = 1, 2, 3 \quad \text{(no summation)} \tag{15.44}$$

and observing that both vorticity and fluctuating stresses relax quickly toward a nearly isotropic state downstream the shock, while Reynolds stresses do not. Therefore, the increase in R_{11} induces the observed behavior of the Taylor scale.

Departure from linear results is also observable on the far-field anisotropy (see Fig. 15.32). LIA predicts a decreasing anisotropy with increasing Mach number M_1 and that the transverse Reynolds stress R_{22} should be larger than the longitudinal one, R_{11}. On the contrary, DNS and experimental results consistently show that the downstream anisotropy is such that $R_{11} > R_{22}$, due to nonlinear pressure-strain and pressure-velocity couplings just downstream the shock.

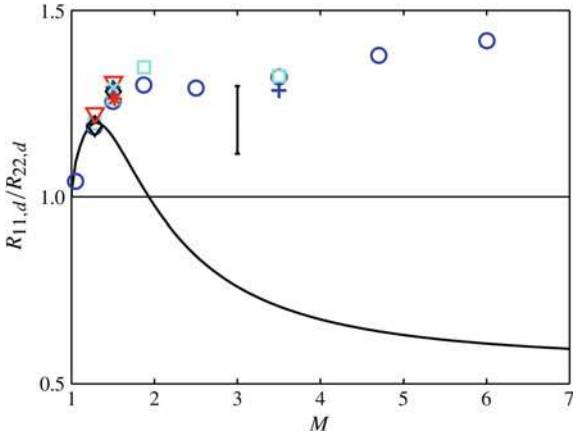

Fig. 15.32 Evolution of the far-field Reynolds tensor anisotropy versus upstream Mach number M_1. Symbols: DNS and experimental data; Solid line: LIA prediction. From Larsson et al. (2013) with permission of CUP

Detailed analysis of nonlinear effects available in the open literature is limited to the case of a purely vortical incoming turbulence. Nonlinear effects of upstream acoustic and entropic fluctuations remain to be done.

15.3.4 Shock Structure in Wrinkled Shock Régime

A detailed theoretical analysis of the shock structure in the wrinkled shock régime was proposed in Donzis (2012a), whose key elements are presented hereafter.

The classical estimate for laminar shock thickness δ_l is

$$\delta_l \simeq \frac{\mu_1}{\rho_1 a_1} \frac{1}{\Delta M}, \quad \Delta M = M_1 - 1, \tag{15.45}$$

where subscript 1 refers to upstream values. Normalizing this expression by the Kolmogorov scale, one obtains

$$\frac{\delta_l}{\eta_1} \simeq \frac{u_{\eta_1}}{U_1 - a_1} \equiv \mathfrak{S} = \frac{M_{t_1}}{\sqrt{Re_{\lambda_1}}\Delta M}, \tag{15.46}$$

in which the dimensionless parameter $\mathfrak{S}$ is defined.

Now introducing the instantaneous turbulent shock thickness δ_t, one can write:

$$\delta_t \simeq \frac{\mu_1}{\rho_1 a_1} \frac{1}{\Delta M + m'} \tag{15.47}$$

where m' denotes a random turbulence-induced fluctuation. Now prescribing a p.d.f. for m', one can recover statistics for δ_t. After some algebra, one obtains

$$\frac{\overline{\delta_t}}{\eta_1} = \mathfrak{S}\left[1 + \frac{1}{3}\left(\frac{M_{t_1}}{\Delta M}\right)^2 + a_4\left(\frac{M_{t_1}}{\Delta M}\right)^4 + a_6\left(\frac{M_{t_1}}{\Delta M}\right)^6 + \ldots\right] \tag{15.48}$$

where parameters a_i explicitly depend on the p.d.f. of m'. It is important noting that the leading order quadratic term is universal. In the same way, the variance of the turbulent shock thickness, $\sigma^2_{\delta_t}$ can be expressed as

$$\frac{\sigma^2_{\delta_t}}{\eta_1^2} = \mathfrak{S}^2\left[1 + \frac{1}{3}\left(\frac{M_{t_1}}{\Delta M}\right)^2 + O\left(\frac{M_{t_1}^4}{\Delta M^4}\right)\right], \tag{15.49}$$

independently of the p.d.f. of m'. These results are in agreement with those obtained using an incomplete similarity analysis, giving them an additional value.

Now considering the instantaneous dilatation at the shock, θ, and using the estimate $\theta \sim [[u]]/\delta_t$, one obtains at the leading order

$$\overline{\theta} = [[u]]\frac{\rho_1 a_1}{\mu_1}\Delta M, \quad \overline{\theta^2} = \left([[u]]\frac{\rho_1 a_1}{\mu_1}\right)^2\left(\Delta M + \frac{1}{3}M_{t_1}\right). \tag{15.50}$$

Therefore, the rms-to-mean ratio of dilatation, Θ, is approximated as

$$\Theta \simeq \frac{1}{\sqrt{3}}\frac{M_{t_1}}{\Delta M} + O\left(\frac{M_{t_1}^3}{\Delta M^3}\right). \tag{15.51}$$

It is important to note that this analysis is based on two key assumptions:

- turbulence does not modify the internal structure of the shock wave, so that the instantaneous local thickness is accurately approximated using the laminar thickness solution, see Eq. (15.47)
- the *quasi-equilibrium hypothesis* holds, meaning that the shock is in local equilibrium with instantaneous local flow state. This requires the relaxation time associated to internal shock dynamics to be much smaller than the one associated to the most disruptive turbulent perturbations. This ratio is found to be proportional to $\mathfrak{S}^2$. Therefore, a necessary condition is $\mathfrak{S}^2 \ll 1$.

15.4 Broken Shock Régime

The broken shock régime corresponds to cases in which the shock is locally disrupted by turbulent fluctuations, yielding the occurrence of holes in the shock front which is locally replaced by regions of smooth gradient, as illustrated in Fig. 15.33.

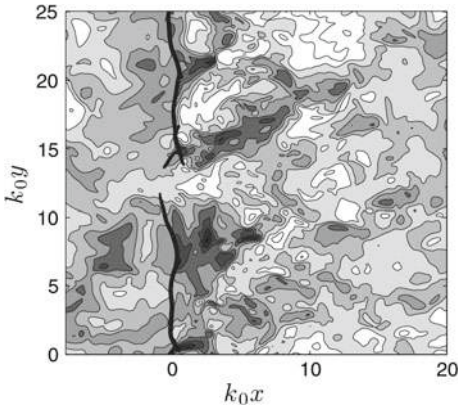

Fig. 15.33 Instantaneous 2D slice of DNS showing a shock hole. Greyscale: isovalues of streamwise momentum. Thick black line: shock front detected via local dilatation. From Larsson and Lele (2009) with permission of AIP

A first point is that, even at high turbulent Mach number M_{t_1}, such events are very rare. Considering a random local turbulent fluctuation m' of the Mach number, the flow becomes subsonic and a hole will appears if $\Delta M + m' < 0$, with $\Delta M = M_1 - 1$. Assuming that large turbulent energetic scales obey a Gaussian distribution, Donzis (2012a) evaluates the probability of such an event as

$$P(m' < -\Delta M) = \left(1 - \mathrm{erf}\left[\sqrt{\frac{3}{2}}\frac{\Delta M}{M_{t_1}}\right]\right). \tag{15.52}$$

Taking $M_{t_1}/\Delta M \sim 0.6$, which corresponds to a high turbulence level, the probability is about 0.2%. It is grows up to 6% in the supersonic case $M_{t_1}/\Delta M \sim 1.4$. This theoretical analysis is in agreement with DNS data (Larsson et al. 2013) in which it is observed that about 1% of the shock surface is occupied by holes.

The local change in the flow physics is illustrated in Fig. 15.34 in which the instantaneous streamwise evolution of density and dilatation along streamlines crossing the shock through a hole and through a well-defined front are displayed.

Since the holes occupy only a very small percentage of the total shock surface, global statistics in the broken shock régime are close to those of the wrinkled shock régime. This is illustrated by the amplification ratio of turbulent kinetic energy, which is not affected by the appearance of holes in the shock (Donzis 2012b). Main differences are observed on tails of the p.d.f.s of physical quantities near the shock wave.

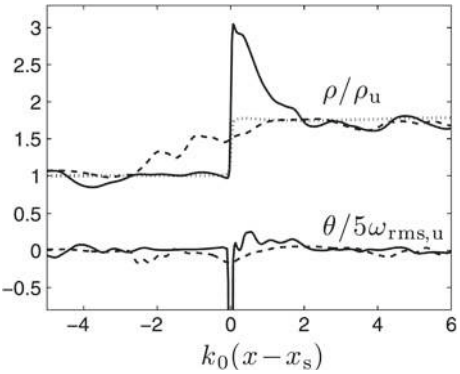

Fig. 15.34 Instantaneous streamwise evolution of density ρ normalized by its upstream value and dilatation normalized by upstream vorticity variance for $M_1 = 1.5$ and $M_{t_1} = 0.38$. Solid lines: streamline crossing the shock front; Dashed line: streamline crossing a shock hole; Dotted line: time-averaged value. From Larsson and Lele (2009) with permission of AIP

15.5 Beyond Canonical Case. I: Spherical Shock Waves

15.5.1 Case of Diverging Taylor–Sedov Blast Wave

The case of interaction between initially isotropic and a diverging spherical blast wave was addressed via DNS in Bhagatwala and Lele (2011). In the case of an inviscid laminar strong blast wave, the radius $R_s(t)$ of the shock wave is assumed to follow Taylor's self-similar solution

$$R_s(t) = A(\gamma)\rho_0^{-1/5}E^{1/5}t^{2/5}, \tag{15.53}$$

where $A(\gamma)$ is a function of γ, ρ_0 the density of the undisturbed fluid and E the energy deposited at initial time.

Interaction with a spherical diverging wave is observed to lead to results that are very different from the planar shock case, at least for small radius of curvature. At high radius of curvature, the shock is locally nearly planar and results close to those found above are recovered. An important point is that the strength of the shock is a decreasing function of time in the spherical case, while it is constant in the planar case. Therefore, the spherical blast wave case is a transient problem for which time-averaging is not meaningful.

Typical effects of the blast wave on tangentially-averaged pressure, density and radial velocity component are displayed at three different times in Fig. 15.35. In the case of strong blast wave, the shock remains almost spherical and obeys Taylor's $t^{2/5}$ law. In the case of a weak shock, strong turbulence-induced corrugation effects with possible holes similar to those discussed in the planar broken shock régime appear.

Main differences with the planar shock case are the following:

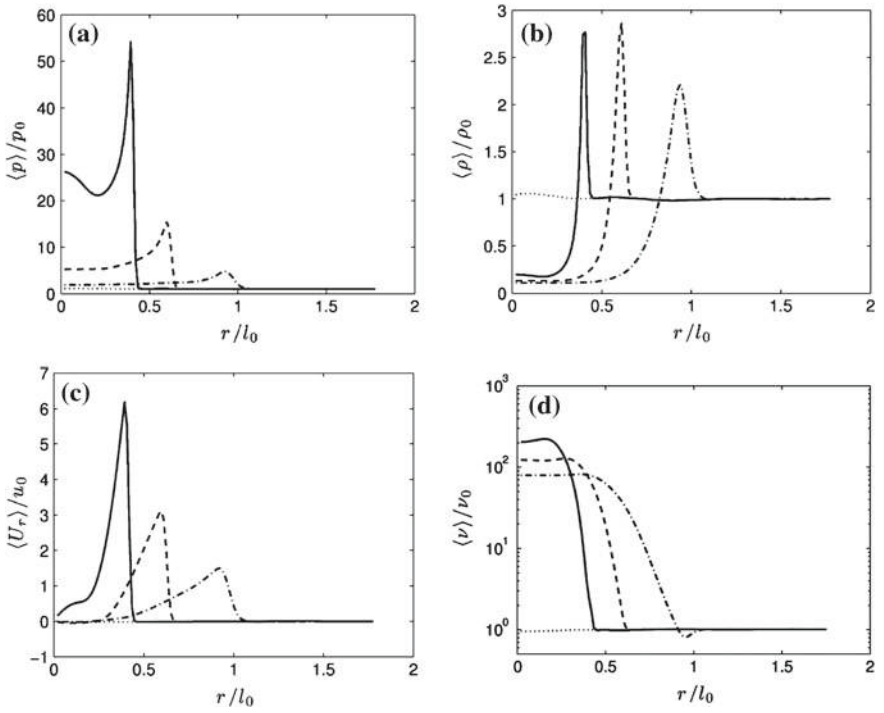

Fig. 15.35 Instantaneous tangentially-averaged quantities for strong blast wave case at three different times. From Bhagatwala and Lele (2011) with permission of AIP

- Interaction with the shock yields a dramatic decrease in the turbulent Reynolds number, by a factor up to two orders of magnitude. This is due a huge increase in fluid viscosity (up to two orders of magnitude also) due to a large increase in the temperature in the shocked region, also associated with a similar growth of the dissipation (see Fig. 15.36).
- The Kolmogorov scale is amplified by a factor up to one order of magnitude in the post-shock region (see Fig. 15.36).
- Post-shock vorticity is decreased (by a factor up to two orders of magnitude) instead of being amplified. This is mainly due to the dilatation-vorticity correlation, which acts as a very strong sink term in the post-shock region. This effect is due to positive dilatation events, which are dominant due to the shock-induced flow. The baroclinic production term is not large enough to balance this effect. A kink is observed in tangential vorticity in the shock region, which is very quickly damped.

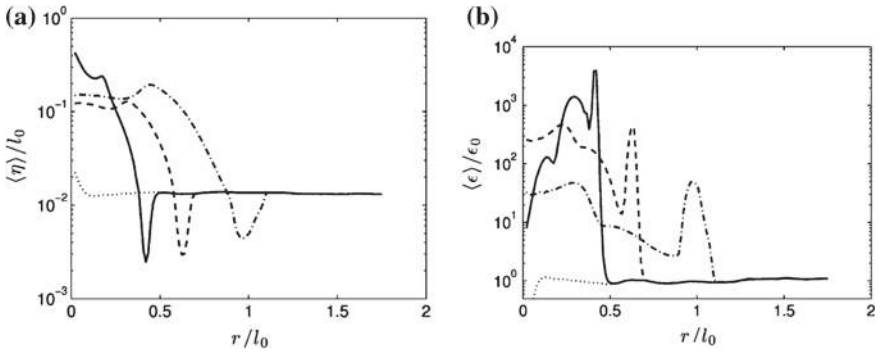

Fig. 15.36 Instantaneous tangentially-averaged turbulent dissipation and Kolmogorov scale for strong blast wave case at three different times. From Bhagatwala and Lele (2011) with permission of AIP

15.5.2 Case of Converging/Diverging Spherical Shock

The second case analyzed via DNS is related to a converging, then diverging spherical shock wave (Bhagatwala and Lele 2012). This configuration involves a re-shock phenomena (turbulence interacts with a shock and a reflected shock after that), which has been analyzed via LIA in the planar shock case in Huete et al. (2012a). This phenomena are illustrated in Fig. 15.37 in which time evolution of tangentially-averaged pressure, density, radial velocity and viscosity are displayed at different times associated to both converging incident and reflected diverging shock waves. This flow configuration is observed to yield different results from the previous case of a single diverging spherical blast wave.

The first shock wave is a converging one whose strength is growing as the radius is decreasing, which induces a compressive radial velocity field. In the post-shock region turbulent vorticity fluctuations are strongly amplified since the two main mechanisms, baroclinic terms and vorticity-dilatation correlations, act as source terms. Amplification ratio of $\overline{\omega_i'\omega_i'}$ larger than 20 are observed in DNS, along with a very large amplification of the turbulent Reynolds number by a factor larger than 40.

The second wave is a diverging initially strong blast wave. In the corresponding post-shock region vorticity-dilatation effects damp the vorticity fluctuations, as in the Sedov–Taylor blast wave case. But the damping effect is much weaker here, since turbulent vorticity does not vanish in the post-shock region but exhibits a plateau. This plateau is due to the balance between dilatation-induced damping and the advection of very strong vortical events away from the core region (in which the amplification by the converging wave was maximum) by the outward radial velocity field.

The main differences observed in the post-shock region of the reflected wave and the Sedov–Taylor blast wave are the following:

- the turbulent Reynolds number is strongly amplified (by a factor up to two orders of magnitude) instead of being reduced,

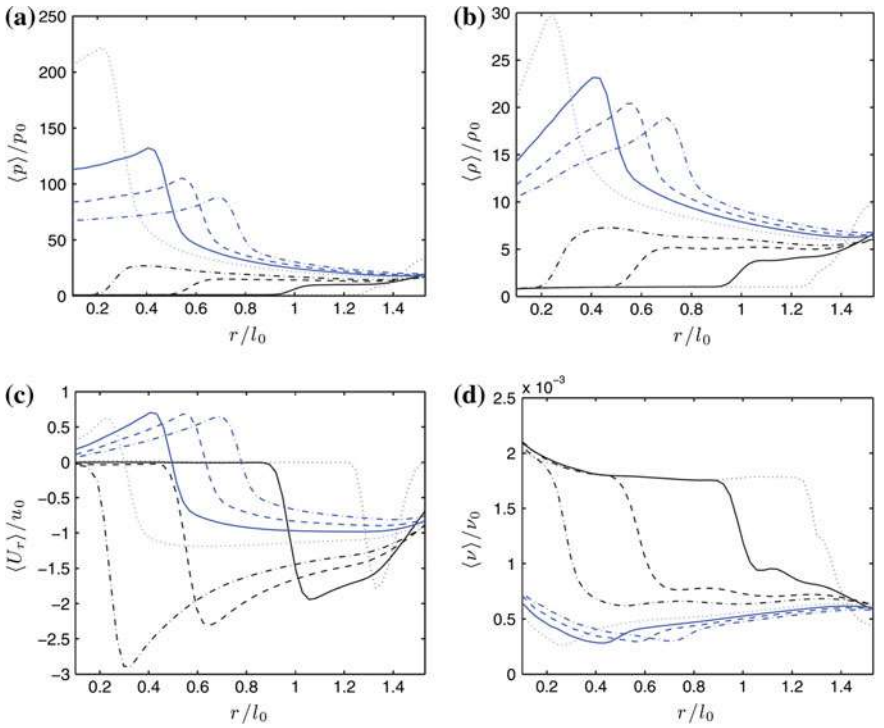

Fig. 15.37 Instantaneous tangentially-averaged quantities for converging-diverging blast wave case at different times. Black lines: incident converging wave; Blue lines: reflected diverging wave. From Bhagatwala and Lele (2012) with permission of AIP

- the Kolmogorov scale is decreased (by a factor up to six) instead of being amplified (see Fig. 15.38). This is due to a very strong reduction induced by the converging shock, which leads to an increase of the dissipation ε, an increase of viscosity μ due to an increase in the temperature, but an overall decrease of $\nu = \mu/\rho$ due to increasing ρ. The reflected shock yields a slight increase of ν and η after that, which is not large enough to balance the initial reductions.

As for the Sedov–Taylor blast wave curvature effects lead to a dramatical departure from the planar shock theory, looking at amplification ratios. Turbulence effects on the tangentially-averaged mean flow quantities are important, leading to a reduction in the observed jump with respect to the inviscid laminar theory. This decrease in maximum compression is larger for initially weak shock wave (up to 35% for density and 60% for pressure) than for strong shocks (up to 10% for density and 30% for pressure). But it is observed that the shock radius $R_s(t)$ evolves following the laminar Gurdeley model for both converging and diverging shocks:

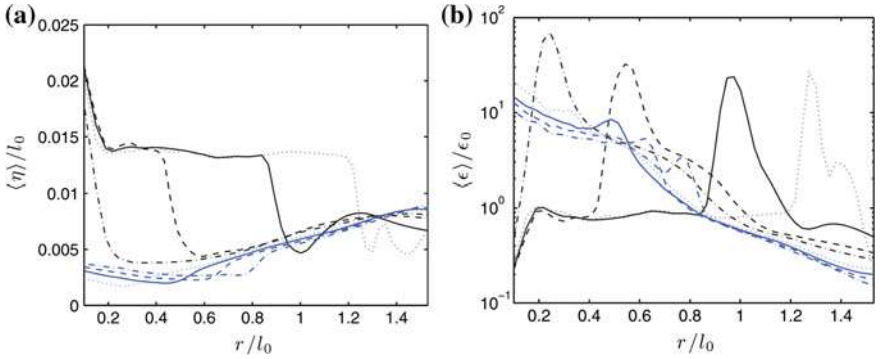

Fig. 15.38 Instantaneous tangentially-averaged turbulent dissipation and Kolmogorov scale for the converging/diverging spherical shock case at different times. From Bhagatwala and Lele (2012) with permission of AIP

$$R_s(t) = \begin{cases} R_{s0}(1 - t/t_s)^{0.717} & \text{converging wave} \\ R_{s0}(t/t_s - 1)^{0.717} & \text{diverging wave} \end{cases} \tag{15.54}$$

where R_{s0} and t_s refer to the initial shock radius and the time taken for the converging shock to reach the origin, respectively.

15.6 Beyond Canonical Case. II: Planar Shock Interacting with Turbulence in a Non-reacting Binary Mixture

The case of a planar shock interacting with isotropic turbulent fluctuations in a binary mixture of perfect gas has been addressed via extended LIA (see Sect. 16.9) in Griffond (2005), Griffond et al. (2010), Griffond and Soulard (2012). Considering a concentration spectrum of the form

$$E_{cc}(k) = \frac{32}{3k_0}\sqrt{\frac{2}{\pi}}\left(\frac{k}{k_0}\right)^4 e^{-2(k/k_0)^2}, \tag{15.55}$$

the influence of the nature of the incident concentration waves has been investigated. The extended Kovasznay decomposition coupled to the LIA procedure shows that incident waves associated with fluctuations in the concentration field c can be of two types:

- r-waves, or *molar mass waves* at constant c_v,
- c_v-waves, or *constant volume specific heat waves* at constant molar mass.

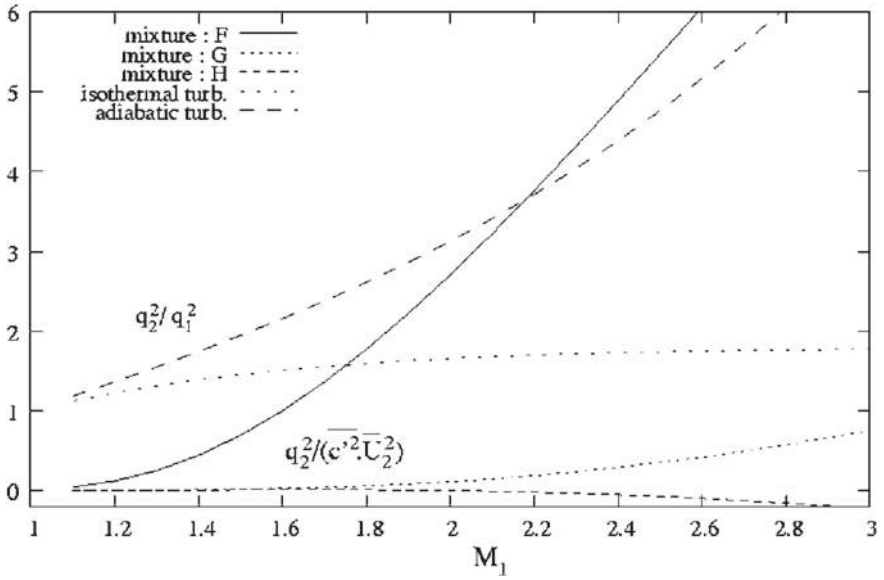

Fig. 15.39 Evolution of the downstream kinetic energy $\mathcal{K}_2$ production/amplification for shock/isotropic concentration fluctuations in a binary mixture for $\bar{\gamma} = 7/5$ versus the upstream Mach number M_1. F, G and H terms are given in Eqs. (16.243)–(16.245). Comparisons are made with canonical interaction in a pure fluid for both incident isothermal and incident adiabatic vortical isotropic turbulence. All results are LIA results. Courtesy of J. Griffond. From Griffond (2005) with permission of AIP

The effect of the interaction between a pure concentration fluctuating field with a shock wave in terms of generation of downstream turbulent kinetic energy is plotted in Fig. 15.39, and compared with results obtained in a pure fluid for an incident isotropic vortical adiabatic turbulent field and incident isotropic vortical isothermal turbulent field. It is worth noting that in the case of incident concentration waves the upstream turbulent kinetic energy is identically null, $\mathcal{K}_1 = 0$. It is seen that r-waves are responsible for most of the creation of downstream kinetic energy, and that this effect is a monotonous function of the upstream Mach number M_1. c_v-waves have a much less important effect, while interactions between these two families of waves have an negligible effect. It is also observed that the downstream kinetic energy tends to 0 in the limit of vanishing shock, $M_1 \to 1$.

The analysis can be refined looking at the longitudinal, shock-normal Reynolds stress R_{11} and the transverse one, $R_{tt} = (R_{22} + R_{33})/2$. The streamwise evolution of these two stresses is displayed in Fig. 15.40 (top). The existence of a near field region is observed as in the canonical case. The decrease is due to the exponential damping of non-propagating acoustic waves (term I_{aa} in Eq. (16.237)) and to the fact that acoustic and non-acoustic waves are decorrelated in the downstream region, leading to the decay of term I_{av} in Eq. (16.237). Therefore, the far-field solution is governed by the sole term I_{vv} in Eq. (16.237). It is observed that r-waves are more efficient

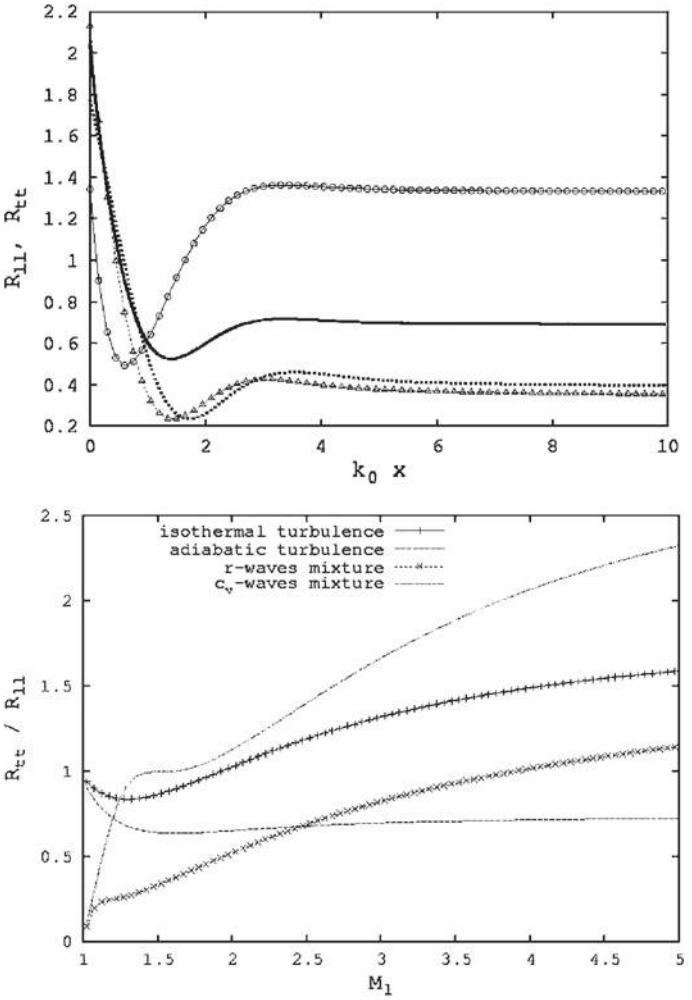

Fig. 15.40 Evolution of the longitudinal Reynolds stress R_{11} and the transverse Reynolds stress $R_{tt} = (R_{22} + R_{33})/2$ for shock/isotropic density perturbation field in a binary mixture for $\bar{\gamma} = 7/5$. Top: downstream evolution for incident pure r-wave turbulence (circles) and pure c_v-wave turbulence (triangle, with premultiplication by 10) at $M_1 = 2$; dotted lines: R_{11}, solid lines: R_{11}. Bottom: evolution of the anisotropy ratio R_{tt}/R_{11} versus the upstream Mach number M_1 for different upstream turbulence type. All results are LIA results. Courtesy of J. Griffond. From Griffond (2005) with permission of AIP

at generating downstream turbulence looking at both longitudinal and transverse Reynolds stresses. The anisotropy, measured by the ratio R_{tt}/R_{11} is displayed in Fig. 15.40 (bottom) as a function of M_1 and compared with results stemming from LIA analysis of the canonical case for incoming adiabatic and isothermal turbulence. It is observed that turbulent mixtures yield a very anisotropic state in the weak shock case, contrary to vortical turbulence. For $M_1 > 1.5$, the strongest anisotropy is obtained for c_v-wave turbulence.

15.7 Beyond Canonical Case. III: Planar Detonation Interacting with Turbulence

The case of the interaction of a planar overdriven detonation wave with an isotropic turbulent field has been addressed by a few authors only (Lasseigne et al. 1991; Huete et al. 2013, 2014). It is worth noting that detonation waves will remain stable only if the detonation Mach number is very large compared with the Chapman–Jouguet Mach number. Otherwise, the detonation front will break into cells, yielding a destructive interaction in the sense that the topology of the front is deeply modified.

The case of a detonation with zero thickness moving in a gas at rest with an isotropic perturbation field has been studied by Huete et al. (2013, 2016) via LIA and the Laplace transform approach (see Sect. 16.10 for technical details). While the results can be parameterized with respect to two parameters, namely the upstream Mach number M_1 and the gas polytropic index γ in the cold shock case, a third parameter must be introduced to account for the heat release by chemical reaction in the detonation case. Therefore, the exothermicity parameter q is defined, with $q = 0$ corresponding to an inert gas and the classical shock case.

15.7.1 Case of an Upstream Isotropic Density Field

The first investigated case is related to a detonation wave propagating in a gas at rest with an isotropic density perturbation field. This perturbation field corresponds to the ρ-waves introduced when discussing the case of the interaction between a shock and a non-reacting mixture, in the absence of vorticity and acoustic upstream modes. Downstream turbulent kinetic can be split into a vortical and an acoustic component, i.e. $\mathcal{K}_2 = \mathcal{K}^r + \mathcal{K}^a$, whose explicit formula are given in the original reference and are not given here for the sake of brevity. The evolution of values of the two components (normalized by the downstream speed of sound a_2) versus the Mach number is displayed, in Fig. 15.41 for different values of q for $\gamma = 1.2$. As in the inert shock case, the acoustic kinetic energy is larger than the vortical one

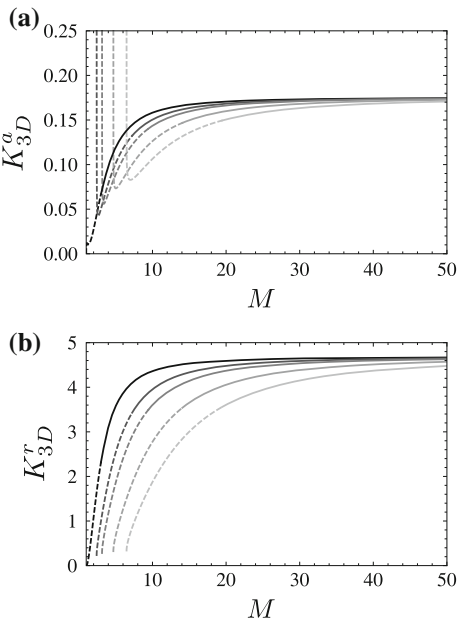

Fig. 15.41 LIA analysis of the evolution of the normalized downstream kinetic energy versus the detonation Mach number for $q = 0$ (inert gas, black line) to $q = 10$ (strongly exothermic chemical reactions, light grey). Intermediary values are $q = 1, 2, 5$. Top: Acoustic kinetic energy; Bottom: vortical kinetic energy. From Huete et al. (2013) with permission of AIP

at low Mach number, the opposite being observed at larger values of M_1. Both are observed to converge toward bounded asymptotic values as $M_1 \to \infty$. Heat release by chemical reactions is observed to damp both components.

The same analysis for downstream normalized vorticity amplitude and density fluctuation amplitude associated to the entropy mode is illustrated in Fig. 15.42. It is seen that both are growing functions of M_1 and decreasing functions of q, and that bounded asymptotic values exist at large M_1.

15.7.2 Case of an Upstream Isotropic Vorticity Field

Interaction between a strong thin detonation and an isotropic vortical turbulent field has been investigated thanks to LIA (Huete et al. 2016). In order to analyze the evolution of anisotropy, both acoustic and vortical downstream kinetic energy components, $\mathcal{K}^a$ and $\mathcal{K}^r$ respectively, can be split into a front-normal and a transverse component. Therefore, one has for the turbulent kinetic energy amplification factor

$$\frac{\mathcal{K}_2}{\mathcal{K}_1} = \frac{\mathcal{K}^a}{\mathcal{K}_1} + \frac{\mathcal{K}^r}{\mathcal{K}_1} = K_a + K_r = \frac{1}{3}(L^a + 2T^a) + \frac{1}{3}(L^r + 2T^r) \tag{15.56}$$

where L and T factors are related to longitudinal (shock-normal) and transverse component amplification factors, respectively. Evolution of L_r, T_r and K_r versus the detonation Mach number for $\gamma = 7/5$ (air) and $q = 0$ and $q = 1$ is displayed in

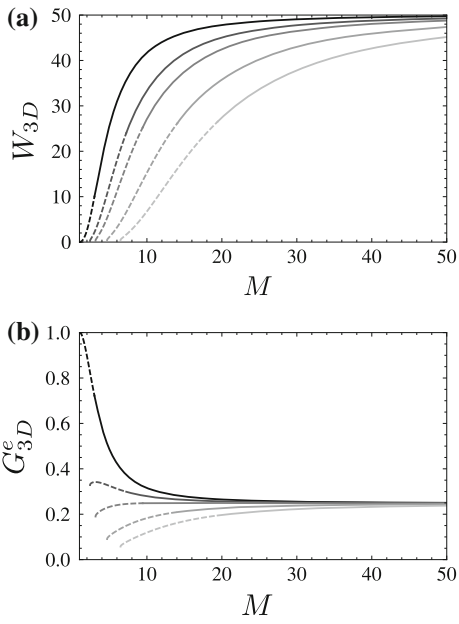

Fig. 15.42 LIA analysis of the evolution of the normalized downstream vorticity (top) and entropic density fluctuations (bottom) versus the detonation Mach number for $q = 0$ (inert gas, black line) to $q = 10$ (strongly exothermic chemical reactions, light grey). Intermediary values are $q = 1, 2, 5$. From Huete et al. (2013) with permission of AIP

Fig. 15.43. It is observed that the transverse component dominates at large enough Mach number. Heat release is observed to damp the transverse component but it enhances the longitudinal one. A similar analysis for the acoustic component is displayed in the same figure. It is observed that the longitudinal component is the most amplified for acoustic waves, and that heat release yields an enhancement of both longitudinal and transverse kinetic energy components of the acoustic field. As for inert shock case, one has $\mathcal{K}^a \ll \mathcal{K}^r$ at large enough Mach number.

Variations of L_r and T_r in the (M_1, q) plane are displayed in Fig. 15.44. It is observed that isolines are almost vertical for $q > 2$, indicating that results become almost insensitive to changes in exothermicity if the heat release is large enough. It is observed that anisotropy type (pancake-type or cigar-type) may vary, the pancake-type in which $R_{11} < R_{22} = R_{33}$ being observed at large enough Mach number. The cigar-type may exist at low-Mach and large heat release. As for the cold shock case, an isotropic emitted field can be obtained selected ad hoc values of q and M_1.

The amplification of vorticity is well understood introducing the amplification factor of the transverse vorticity component, $W_\perp$. As a matter of fact, the total vorticity amplification factor is equal to $(1 + 2W_\perp)/3$. $W_\perp$ is plotted in the (M_1, q) plane in Fig. 15.45. The effect of heat release is to increase $W_\perp$ and therefore the vorticity anisotropy. As for kinetic energy amplification, results become insensitive to heat release changes for $q > 2$.

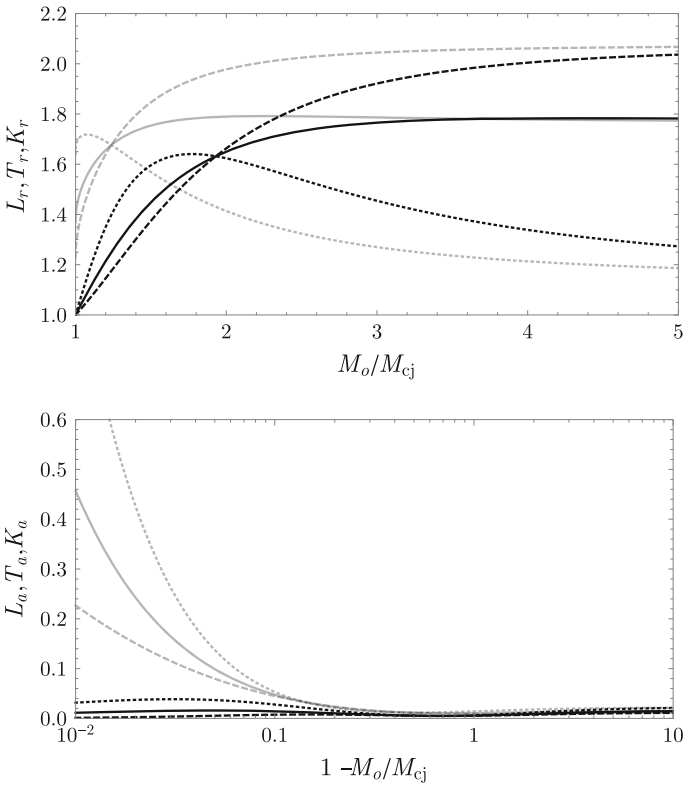

Fig. 15.43 LIA analysis of the evolution of the normalized vortical kinetic energy (top) and normalized acoustic kinetic energy (bottom) along with their longitudinal and transverse components versus the detonation Mach number for $q = 0$ (inert gas, black line) and $q = 1$ (light grey). Solid line: K_r and K_a, dotted line: L_r and L_a, dashed line: T_r and T_a. Courtesy of C. Huete

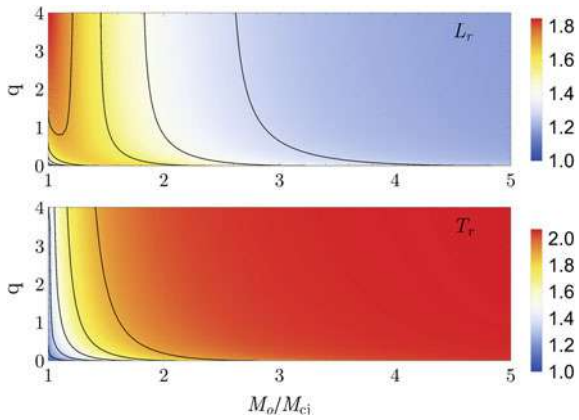

Fig. 15.44 LIA analysis of the evolution of the longitudinal vortical kinetic energy amplification factor L_r (top) and transverse vortical kinetic energy amplification factor T_r (bottom) in the $(M_1/M_{CJ}, q)$ plane. Courtesy of C. Huete

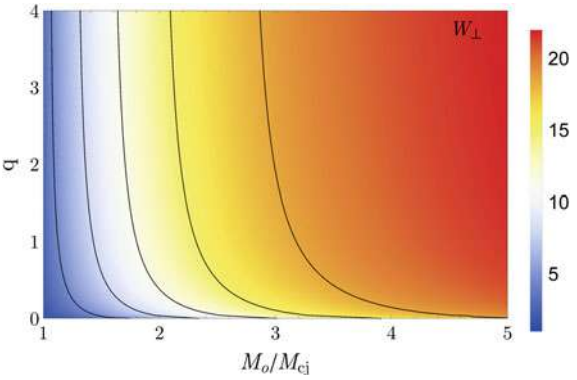

Fig. 15.45 LIA analysis of the evolution of the transverse vorticity amplification factor $W_\perp$ in the $(M_1/M_{CJ}, q)$ plane. Courtesy of C. Huete

References

Bhagatwala, A., Lele, S.K.: Interaction of a Taylor blast wave with isotropic turbulence (2012). Shock structure in shock-turbulence interaction. Phys. Fluids **23**, 035103 (2011)

Bhagatwala, A., Lele, S.K.: Interaction of a converging spherical shock wave with isotropic turbulence (2012). Shock structure in shock-turbulence interaction. Phys. Fluids **24**, 085102 (2012)

Donzis, D.A.: Shock structure in shock-turbulence interactions. Phys. Fluids **24**, 126101 (2012a)

Donzis, D.A.: Amplification factors in shock-turbulence interactions: effect of shock thickness. Phys. Fluids **24**, 011705 (2012b)

Dyakov, S.P.: On the stability of shock waves. Zh. Eksp. Teor. Fiz. **27**, 288 (1954). At. Res. Agency Establ. AERE Lib./Trans. **648** (1956)

Griffond, J.: Linear interaction analysis applied to a mixture of two perfect gases. Phys. Fluids **24**, 115108 (2005)

Griffond, J., Soulard, O., Souffland, D.: A turbulent mixing Reynolds stress model fitted to match linear interaction analysis prediction. Phys. Scr. **142**, 014059 (2010)

Griffond, J., Soulard, O.: Evolution of axisymmetric weakly turbulent mixtures interacting with shock or rarefaction waves. Phys. Fluids **17**, 086101 (2012)

Huete, C., Wouchuk, J.G., Canaud, B., Velikovich, A.L.: Analytical linear theory for the shock and re-shock of isotropic density inhomogeneities. J. Fluid Mech. **700**, 214–245 (2012a)

Huete, C., Wouchuk, J.G., Velikovich, A.L.: Analytical linear theory for the interaction of a planar shock wave with a two- or three-dimensional random isotropic acoustic wave field. Phys. Rev. E **85**, 026312 (2012b)

Huete, C., Sanchez, A.L., Velikovich, A.L.: Theory of interactions of thin strong detonations with turbulent gases. Phys. Fluids **25**, 076105 (2013)

Huete, C., Sanchez, A.L., Velikovich, A.L.: Linear theory for the interaction of small-scale turbulence with overdriven detonations. Phys. Fluids **26**, 116101 (2014)

Huete, C., Jin, T., Martinez-Ruiz, D., Williams, F.A.: Reacting shock wave effects on isotropic turbulent flows. Linear Interaction Analysis and Direct Numerical Simulations. Private Communication (2016)

Jacquin, L., Cambon, C., Blin, E.: Turbulence amplification by a shock wave and rapid distortion theory. Phys. Fluids A **5**(10), 25309–2550 (1993)

Kontorovich, V.M.: To the question on stability of shock waves. Sov. Phys. JETP **6**, 1179 (1957). At. Res. Agency Establ. AERE Lib./Trans. **648** (1956)

Landau, L.D., Lifshitz, E.M.: Fluid Mechanics. Course of Theoretica Physics, vol. 6, 2nd edn. Butterworth-Heinemann (1987)

Larsson, J., Lele, S.K.: Direct numerical simulation of canonical shock-turbulence interaction. Phys. Fluids **21**, 126101 (2009)
Larsson, J., Bermejo-Moreno, I., Lele, S.K.: Reynolds- and Mach-number effects in canonical shock-turbulence interaction. J. Fluid Mech. **717**, 293–321 (2013)
Lasseigne, D.G., Jackson, T.L., Hussaini, M.Y.: Nonlinear interaction of a detonation/vorticity wave. Phys. Fluids A **3**, 1972–1979 (1991)
Lee, S., Lele, S.K., Moin, P.: Direct numerical simulation of isotropic turbulence interacting with a weak shock wave. J. Fluid Mech. **251**, 533–562 (1993)
Lee, S., Lele, S.K., Moin, P.: Interaction of isotropic turbulence with shock waves: effect of shock strength. J. Fluid Mech. **340**, 225–247 (1997)
Lele, S.K.: Shock-jump relations in a turbulent flow. Phys. Fluids A **4**(12), 2900–2905 (1992)
Lubchich, A.A., Pudovkin, M.I.: Interaction of small perturbations with shock waves. Phys. Fluids **16**(12), 4489–4505 (2004)
Mahesh, K., Lele, S.K., Moin, P.: The interaction of an isotropic field of acoustic waves with a shock wave. J. Fluid Mech. **300**, 383–407 (1995)
Mahesh, K., Moin, P., Lele, S.K.: The interaction of a shock wave with a turbulent shear flow. Report No. TF-69, Department of Mecanical Engineering, Stanford University (1996)
Mahesh, K., Lele, S.K., Moin, P.: The influence of entropy fluctuations on the interaction of turbulence with a shock wave. J. Fluid Mech. **334**, 353–379 (1997)
Miller, G.H., Ahrens, T.J.: Shock wave viscosity measurement. Rev. Modern Phys. **63**, 919–948 (1991)
Moore, F.K.: Unsteady oblique interaction of a shock wave with a plane disturbance. Technical report 2879, NACA (1954)
Ribner, H.S.: Convection of a pattern of vorticity through a shock wave. Technical report 1164, NACA (1953)
Ryu, J., Livescu, D.: Turbulence structure behind the shock in canonical shock-vortical turbulence interaction. J. Fluid Mech. **756**(R1), 1–13 (2014)
Sinha, K.: Evolution of enstrophy in shock/homogeneous turbulence interaction. J. Fluid Mech. **707**, 74–110 (2012)
Wouchuk, J.G., Huete, C., Velikovich, A.L.: Analytical linear theory for the interaction of a planar shock wave with an isotropic turbulent vorticity field. Phys. Rev. E **79**, 066315 (2009)
Zank, P., Zhou, Y., Matthaeus, W.H., Rice, W.K.M.: The interaction of turbulence with shock waves: a basic model. Phys. Fluids **14**(11), 3766–3774 (2002)
Zel'dovich, Y.B., Raizer, Y.P.: Physics of Shock Waves and High-Temperature Hydrodynamic Phenomena. Dover Publications, Mineola (2002)

Chapter 16
Linear Interaction Approximation for Shock/Perturbation Interaction

This chapter is devoted to a detailed presentation of the Linear Interaction Approximation (LIA) (Ribner 1953; Moore 1954) theory mentioned in Chap. 15. The main assumptions which underly the LIA are discussed in Sect. 15.2.1 and will not be duplicated here. We just recall here that the LIA holds if the following constraints are fulfilled:

(i) The fluctuations must be weak in the sense that the distorted shock wave must remain well defined. As a matter of fact, LIA is an asymptotic approximation that theoretically holds in the limit case $Re_\lambda \to \infty$ and $M_t \to 0$. Numerical experiments lead Lee and coworkers Lee et al. (1993) to propose the following empirical criterion for the linear regime:

$$M_t^2 < \alpha(M_1^2 - 1) \tag{16.1}$$

where M_t and M_1 are the upstream turbulent and mean Mach numbers respectively and $\alpha \approx 0.1$. This criterion was later refined using DNS with higher resolution (Ryu and Livescu 2014), yielding

$$M_{t_2} \leq 0.1 M_2 \tag{16.2}$$

with M_{t_2} and M_2 the downstream (LIA-predicted) turbulent Mach number and the downstream mean flow based Mach number, respectively. LIA can be extended to account for viscous effects (Miller and Ahrens 1991), but this extension has not been considered by almost all authors and it is therefore not discussed here.

(ii) The time required for turbulent events to cross the shock must be small compared to the turbulence time scale $\mathcal{K}/\varepsilon$ (with $\mathcal{K}$ and ε the turbulent kinetic energy and the turbulent kinetic energy dissipation rate, respectively), so that nonlinear mechanisms cannot have significant effects.

P. Sagaut and C. Cambon, *Homogeneous Turbulence Dynamics*,
https://doi.org/10.1007/978-3-319-73162-9_16

16.1 Shock Description and Emitted Fluctuating Field

We consider here the interaction of a plane shock with a normal two-dimensional flow in the (x, y) plane. Let the undisturbed shock normal vector and the mean flow be oriented along the x axis. The disturbed shock front is defined as

$$x = x_s(y, t). \tag{16.3}$$

The position of the undisturbed shock is arbitrarily chosen to be $x = 0$. The local instantaneous normal and tangential vector, $\boldsymbol{n}$ and $\boldsymbol{t}$, are equal to

$$\boldsymbol{n} = \left(1, -\frac{\partial x_s}{\partial y}\right)^T, \quad \boldsymbol{t} = \left(\frac{\partial x_s}{\partial y}, 1\right)^T. \tag{16.4}$$

The shock speed in the reference frame associated with the mean shock location, is equal to

$$\boldsymbol{u}_s = \left(\frac{\partial x_s}{\partial t}, 0\right)^T = (u_s, 0)^T. \tag{16.5}$$

The upstream and downstream fields are split as follows:

$$\rho_i(x, y, t) = \bar{\rho}_i + \epsilon\rho_i'(x, y, t) \tag{16.6}$$
$$s_i(x, y, t) = \bar{s}_i + \epsilon s_i'(x, y, t) \tag{16.7}$$
$$T_i(x, y, t) = \bar{T}_i + \epsilon T_i'(x, y, t) \tag{16.8}$$
$$p_i(x, y, t) = \bar{p}_i + \epsilon p_i'(x, y, t) \tag{16.9}$$
$$\omega_i(x, y, t) = 0 + \epsilon\omega_i'(x, y, t) = \epsilon\text{curl}(\boldsymbol{u}_i') \tag{16.10}$$
$$u_i(x, y, t) = U_i + \epsilon u_i'(x, y, t) \tag{16.11}$$
$$v_i(x, y, t) = 0 + \epsilon v_i'(x, y, t) \tag{16.12}$$

along with

$$x_s(y, t) = 0 + \epsilon\xi(y, t) \tag{16.13}$$

where subscripts 1 and 2 are related to the upstream (incident) and downstream (emitted) fields, respectively. The parameter ϵ is assumed to be a small parameter, i.e. $\epsilon \ll 1$, so that all primed quantities and ξ are of order $O(1)$.

These small perturbations are assumed to obey the linearized Euler equations upstream and downstream the shock front, leading to the following equations for the Kovasznay modes:

$$\frac{\partial s_i'}{\partial t} + U_i\frac{\partial s_i'}{\partial x} = 0, \tag{16.14}$$

$$\frac{\partial \omega_i'}{\partial t} + U_i \frac{\partial \omega_i'}{\partial x} = 0, \tag{16.15}$$

$$\left(\frac{\partial p_i'}{\partial t} + U_i \frac{\partial p_i'}{\partial x} \right)^2 - c_i^2 \nabla^2 p_i' = 0. \tag{16.16}$$

Since the mean field obeys the classical Rankine–Hugoniot jump conditions (3.16)–(3.19) which are recovered as the zeroth-order relations inserting Eqs. (16.6)–(16.12) into jump relations (3.16)–(3.19), the following classical relations hold:

$$\mathfrak{C} \equiv \frac{\bar{\rho}_2}{\bar{\rho}_1} = \frac{U_1}{U_2} = \frac{(\gamma+1)M_1^2}{2+(\gamma-1)M_1^2}, \tag{16.17}$$

$$\frac{\bar{p}_2}{\bar{p}_1} = 1 + \frac{2\gamma}{\gamma+1}(M_1^2 - 1), \tag{16.18}$$

$$M_2 \equiv \frac{U_2}{a_2} = \sqrt{\frac{2+(\gamma-1)M_1^2}{2\gamma M_1^2 - (\gamma-1)}}, \tag{16.19}$$

where M_1 and M_2 are the upstream and downstream Mach numbers, respectively.

The incident field is composed of superimposed plane propagating waves. Thanks to the linear approximation, one can restrict the analysis to a single incident wave for each Kovasznay mode, with the orientation of the incident wave vector as a free parameter. One can remark that since the shock is assumed to have no intrinsic length scale, the LIA results will not depend on the wave vector modulus. Let $\boldsymbol{k}$ and ω be the wave vector and the frequency of the incident plane wave, respectively. Therefore, all fluctuating quantities tied to the incident wave have the following form:

$$\phi(x, y, t) = A_\phi e^{\imath(\boldsymbol{k}\cdot\boldsymbol{x} - \omega t)} \tag{16.20}$$

where ϕ and A_ϕ are a dummy variable and the corresponding amplitude parameter, respectively. Denoting α the angle between $\boldsymbol{k}$ and the x axis, one has $\boldsymbol{k}\cdot\boldsymbol{x} = k_x x + k_y y = kr$ with $k_x = k\cos\alpha$, $k_y = k\sin\alpha$ and $r = x\cos\alpha + y\sin\alpha$.

Since the shock has no intrinsic scale and is fully enslaved to incident perturbations, its displacement induced by the perturbation wave considered above is

$$\xi(y, t) = A_\xi e^{\imath(k_y y - \omega t)} = A_\xi e^{\imath(k\sin\alpha y - \omega t)} \tag{16.21}$$

where the amplitude factor A_ξ remains to be computed.

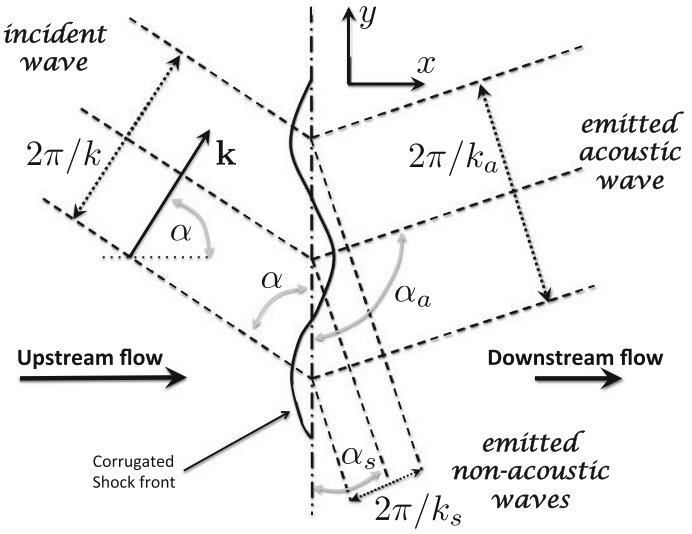

Fig. 16.1 Schematic view of the two-dimensional linear interaction approximation for shock/plane wave interaction

16.2 Calculation of Wave Vectors of Emitted Waves

16.2.1 General

We now address the problem of computing the wave vector of each emitted wave. The problem is schematized in Fig. 16.1.

A said above, any incident perturbation triggers the generation of a triad of emitted waves (one wave for each Kovasznay mode) in the downstream region. Continuity at the shock wave requires that the solution in this region has the same transverse wave number k_y and frequency as the incident perturbation wave. Therefore, all fluctuating variables behind the shock wave have the generic form

$$\phi(x, y, t) = A_\phi F(x) e^{\imath(k_y y - \omega t)} = A_\phi F(x) e^{\imath(k \sin\alpha y - \omega t)} \tag{16.22}$$

where the function $F(x)$ is still unknown and must be such that the emitted fluctuating field obeys the governing equations of the Kovasznay analysis, i.e. the linearized Euler equations. Looking for plane wave solution, one can write

$$F(x) = e^{\imath \tilde{k}_x x} \tag{16.23}$$

where the wave vector normal component $\tilde{k}_x$ is such that the dispersion relation associated with the Kovasznay mode under consideration is satisfied.

16.2.2 Incident Entropy and Vorticity Waves

We first address the problem of an incident entropy or vorticity wave, for which $\omega = k \cos \alpha U_1$.

16.2.2.1 Emitted Entropy and Vorticity Waves

For the emitted entropy and vorticity modes, the linear analysis yields the following single dispersion relation

$$\boldsymbol{k} \cdot \bar{\boldsymbol{u}} = \omega, \tag{16.24}$$

where $\bar{\boldsymbol{u}}$ is the mean velocity, leading to

$$\omega = k_x U_1 = k \cos \alpha U_1 = \tilde{k}_x U_2 \tag{16.25}$$

from which it follows that

$$\tilde{k}_x = \frac{U_1}{U_2} k \cos \alpha = \mathfrak{C} k \cos \alpha, \tag{16.26}$$

where $\mathfrak{C}$ is the compression factor defined by Eq. (16.17). Fluctuating fields associated with the entropy and vorticity modes are therefore of the form

$$\phi(x, y, t) = A_\phi e^{\imath k (\mathfrak{C} \cos \alpha x + \sin \alpha y - U_1 \cos \alpha t)}, \tag{16.27}$$

where it is important to note that k is the modulus of the wave vector of the *incident* wave. Since the entropy and vorticity modes obey the same dispersion relation, emitted waves associated with these two modes have the same wave vector, i.e. they propagate in the same direction and have the same wavelength. Let $\boldsymbol{k}_s$ and α_s be the wave vector of the emitted entropy and vorticity waves and the angle between $\boldsymbol{k}_s$ and the x axis, respectively. Relation (16.27) can be rewritten like follows

$$\phi(x, y, t) = A_\phi e^{\imath (\boldsymbol{k}_s \cdot \boldsymbol{x} - \omega t)} = A_\phi e^{\imath (k_s \cos \alpha_s x + k_s \sin \alpha_s y - \omega t)}, \tag{16.28}$$

leading to the two relations

$$\cot \alpha_s = \mathfrak{C} \cot \alpha, \tag{16.29}$$

$$\frac{k_s}{k} = \frac{\sin \alpha}{\sin \alpha_s}. \tag{16.30}$$

16.2.2.2 Emitted Acoustic Waves - Propagative and Non-propagative Regimes

The dispersion relation for the acoustic mode in the linear approximation is

$$(\omega - \boldsymbol{k} \cdot \bar{\boldsymbol{u}})^2 - a^2 k^2 = 0, \tag{16.31}$$

where a is the mean speed of sound. Using this relation in the domain located behind the shock, one obtains

$$(\omega - \tilde{k}_x U_2)^2 - a_2^2(\tilde{k}_x^2 + k^2 \sin^2 \alpha) = 0. \tag{16.32}$$

Reminding that $\omega = kU_1 \cos\alpha$, this last relation can be recast as

$$\frac{1}{\mathfrak{C}^2}\left(\frac{1}{M_2^2} - 1\right)\tilde{k}_x^2 + \frac{2k\cos\alpha}{\mathfrak{C}}\tilde{k}_x - k^2\left(\cos^2\alpha - \sin^2\alpha\frac{1}{(\mathfrak{C}M_2)^2}\right) = 0. \tag{16.33}$$

The discriminant Δ of the above quadratic relation determines if $\tilde{k}_x$ is real or imaginary. The discriminant being equal to

$$\Delta = \frac{2k\sin\alpha}{\mathfrak{C}M_2}\sqrt{\left(\frac{\cos\alpha}{\sin\alpha}\right)^2 - \frac{1}{\mathfrak{C}^2}\left(\frac{1}{M_2^2} - 1\right)}, \tag{16.34}$$

it is seen that $\tilde{k}_x$ is real if $0 \leq \alpha \leq \alpha_c$ where the critical angle α_c is such that

$$\cot\alpha_c = \frac{\sqrt{1 - M_2^2}}{\mathfrak{C}M_2} \tag{16.35}$$

and imaginary if $\alpha_c < \alpha \leq \pi/2$. Denoting $\tilde{k}_i$ and $\tilde{k}_r$ the real and imaginary parts of $\tilde{k}_x$, the emitted acoustic fluctuating field can be expressed as

$$\phi(x, y, t) = A_\phi e^{-\tilde{k}_i x} e^{\imath(\tilde{k}_r x + k\sin\alpha y - \omega t)} \tag{16.36}$$

showing that the emitted acoustic field decays exponentially behing the shock wave if $\tilde{k}_x$ is not real, i.e. if the angle of incidence of the incident wave is larger than the critical angle α_c. This threshold angle demarcates two regimes for the emitted acoustic waves: the *propagative regime* without damping, and the *non propagative regime* with damping. The latter is coined as non propagative since the emitted wave amplitude is nearly zero at a distance of the order of one wave length downstream the shock. Therefore, it is possible to identify a *near field solution* in which the non propagative perturbations have a significant contribution and a *far field solution* in which non propagative perturbations are negligible.

Elementary algebra yield the following expression for the roots of Eq. (16.33)

$$\tilde{k}_x^{\pm} = \frac{-\dfrac{2k\cos\alpha}{\mathfrak{C}} \pm \Delta}{\dfrac{2}{\mathfrak{C}^2}\left(\dfrac{1}{M_2^2} - 1\right)}, \tag{16.37}$$

where Δ is given by (16.34). It is observed that $\tilde{k}_x^+$ is the only physically admissible root, since $\tilde{k}_x^-$ leads to an exponential growth of the solution behind the shock. Therefore $\tilde{k}_x = \tilde{k}_x^+$ hereafter. The corresponding normalized form is

$$\frac{\tilde{k}_x}{k} = \mathfrak{C}\frac{M_2}{1-M_2^2}\left(-\cos\alpha M_2 + \sin\alpha\sqrt{\cot^2\alpha - \frac{1}{\mathfrak{C}^2}\left(\frac{1}{M_2^2} - 1\right)}\right). \tag{16.38}$$

In the non propagative regime, the real and imaginary parts of $\tilde{k}_x$ are equal to

$$\frac{\tilde{k}_r}{k} = -\mathfrak{C}\cos\alpha\frac{M_2^2}{1-M_2^2}, \tag{16.39}$$

and

$$\frac{\tilde{k}_i}{k} = \mathfrak{C}\sin\alpha\frac{M_2}{1-M_2^2}\sqrt{\cot^2\alpha - \frac{1}{\mathfrak{C}^2}\left(\frac{1}{M_2^2} - 1\right)}, \tag{16.40}$$

respectively. The emitted acoustic field can be re-expressed introducing the emitted wave vector $\boldsymbol{k}_a$ which is such that

$$e^{-\tilde{k}_i x}e^{\imath(\tilde{k}_r x + k\sin\alpha y - \omega t)} = e^{\imath(k_a(\cos\alpha_a x + \sin\alpha_a y + i\eta x) - \omega t)} \tag{16.41}$$

where α_a is the angle between $\boldsymbol{k}_a$ and the x axis. The geometrical characteristics of the emitted wave are given by

$$\frac{k_a}{k} = \frac{\sin\alpha}{\sin\alpha_a}, \tag{16.42}$$

and

$$\begin{cases} \mathfrak{C}\cot\alpha = \cot\alpha_a + \dfrac{1}{M_2\sin\alpha_a} & \text{(propagative regime)} \\ \dfrac{\cot\alpha_a}{\cot\alpha_a^c} = \dfrac{\cot\alpha}{\cot\alpha_c} & \text{(non propagative regime),} \end{cases} \tag{16.43}$$

while the damping factor is expressed as

$$\eta = \begin{cases} 0 & \text{(propagative regime)} \\ \dfrac{|\cot\alpha_a^c\sin\alpha_a|}{M_2}\sqrt{1 - \left(\dfrac{\cot\alpha}{\cot\alpha_c}\right)^2} & \text{(non propagative regime)} \end{cases} \tag{16.44}$$

where α_a^c is the angle of the emitted acoustic wave when $\alpha = \alpha_c$. It can be shown that $\cos \alpha_a^c = -M_2$.

16.2.3 Incident Acoustic Waves

16.2.3.1 Fast and Slow Waves

We now consider the case of an incident acoustic wave, for which we have $(\omega - k \cos \alpha U_1)^2 = a_1^2 k^2$. The method is similar to the one presented above for incident entropy and vorticity waves, but the analysis is made a bit more complex since incident waves can be classified in two types: the *fast waves* which propagate in the direction of the mean flow (i.e. $u_1 U_1 > 0$) and the *slow waves* which travel in the opposite direction (i.e. $u_1 U_1 < 0$). These two families are demarcated by the stationary Mach waves with an angle of incidence α_M such that $\cos \alpha_M = -1/M_1$. Both fast and slow waves can lead to the generation of vorticity, entropy, and propagating or evanescent acoustic waves.

16.2.3.2 Emitted Entropy and Vorticity Waves

Let us first address the case of emitted entropy and vorticity waves. Using the dispersion relations of incident and emitted waves, one obtains

$$\omega = k \cos \alpha U_1 \pm a_1 k = k U_1 \left(\cos \alpha \pm \frac{1}{M_1} \right) = \tilde{k}_x U_2, \tag{16.45}$$

where $\tilde{k}_x$ can be computed in the same way as in the case of incident vorticity and entropy waves. Signs '+' and '−' in the above equation are related to fast and slow waves, respectively. An elegant way to compute the angle of the emitted waves is proposed by Fabre and coworkers Fabre et al. (2001), who introduce the angle $\alpha' \in [0, \pi]$ such that

$$\cot \alpha' = \cot \alpha + \frac{1}{M_1 \sin \alpha}. \tag{16.46}$$

The angle α_s of the emitted entropy and vorticity waves is given by Eq. (16.29) as in the case of an incident entropy/vorticity wave, the angle of incidence α being replaced by α'. The wave vector modulus, k_s, is still given by Eq. (16.30). The plane wave operator associated to emitted fluctuating fields is similar to the one found for incident entropy/vorticity waves Eq. (16.28), the wave vector $\boldsymbol{k}_s$ being defined as said above.

16.2.3.3 Emitted Acoustic Waves

We now turn to the case of emitted acoustic waves. A difference with the case of incident entropy/vorticity waves is that fast and slow waves have different threshold angles, denoted α_c^+ and α_c^-, respectively. These two angles are solutions of

$$\cot \alpha_c^{\pm} + \frac{1}{M_1 \sin \alpha_c^{\pm}} = \pm \frac{\sqrt{1 - M_2^2}}{\mathfrak{C} M_2}. \tag{16.47}$$

For fast waves, the propagative regime is associated with $\alpha \in]0, \alpha_c^+[$ and the non propagative regime with $\alpha \in]\alpha_c^+, \alpha_M[$. For slow waves, the propagative and non propagative regimes correspond to $\alpha \in]\alpha_c^-, \pi[$ and $\alpha \in]\alpha_M, \alpha_c^-[$, respectively. In both cases, the damping factor η is given by Eq. (16.44) the angle of the incident wave α being replaced by the angle α' defined in Eq. (16.46), while the wave length k_a is still computed solving Eq. (16.42). The angle α_a of the emitted wave is defined as follows:

$$\begin{cases} \dfrac{\cot \alpha_a}{\cot \alpha_c^a} = \dfrac{\cot \alpha'}{\cot \alpha_c} - \dfrac{1}{M_2}\sqrt{\left(\dfrac{\cot \alpha'}{\cot \alpha_c}\right)^2 - 1} & \alpha_a \in]0, \pi[\quad \alpha \in]0, \alpha_c^+[\\ \dfrac{\cot \alpha_a}{\cot \alpha_c^a} = \dfrac{\cot \alpha'}{\cot \alpha_c} & \alpha_a \in]0, \pi[\quad \alpha \in]\alpha_c^+, \alpha_M[\\ \dfrac{\cot \alpha_a}{\cot \alpha_c^a} = \dfrac{\cot \alpha'}{\cot \alpha_c} & \alpha_a \in]\pi, 2\pi[\ \alpha \in]\alpha_M, \alpha_c^-[\\ \dfrac{\cot \alpha_a}{\cot \alpha_c^a} = \dfrac{\cot \alpha'}{\cot \alpha_c} + \dfrac{1}{M_2}\sqrt{\left(\dfrac{\cot \alpha'}{\cot \alpha_c}\right)^2 - 1} & \alpha_a \in]\pi, 2\pi[\ \alpha \in]\alpha_c^-, \pi[\end{cases} \tag{16.48}$$

Using these definitions for the damping rate η and the wave vector $\boldsymbol{k}_a$, the emitted acoustic field is still of the form (16.41).

16.3 Calculation of Amplitude of Emitted Waves

16.3.1 General Decompositions of the Perturbation Field

Utilizing either formulation of the exponential operator and the results given in Sect. 3.2.2 dealing with the inviscid Kovasznay decomposition, the perturbation field in the downstream domain associated to a single incident plane wave can therefore be written under the general form[1] given in Table 16.1 where F, G, H, I, K and Q are

[1] It is chosen is to normalize velocity fluctuations using U_2, and not U_1. Turning from one formulation to the other one brings in the compression factor $\mathfrak{C}$.

Table 16.1 First decomposition of the emitted field associated to a single plane incident wave with wave number k and frequency ω

		Acoustic mode		Vorticity mode		Entropy mode
$\frac{u_2(x,y,t)}{U_2}$	$=$	$Fe^{\imath\tilde{k}_x x}e^{\imath(k\sin\alpha y-\omega t)}$	$+$	$Ge^{\imath(k\mathfrak{C}\cos\alpha x+k\sin\alpha y-\omega t)}$	$+$	0
$\frac{v_2(x,y,t)}{U_2}$	$=$	$He^{\imath\tilde{k}_x x}e^{\imath(k\sin\alpha y-\omega t)}$	$+$	$Ie^{\imath(k\mathfrak{C}\cos\alpha x+k\sin\alpha y-\omega t)}$	$+$	0
$\frac{p_2'(x,y,t)}{\gamma\bar{p}_2}$	$=$	$Ke^{\imath\tilde{k}_x x}e^{\imath(k\sin\alpha y-\omega t)}$	$+$	0	$+$	0
$\frac{\rho_2'(x,y,t)}{\bar{\rho}_2}$	$=$	$Ke^{\imath\tilde{k}_x x}e^{\imath(k\sin\alpha y-\omega t)}$	$+$	0	$+$	$Qe^{\imath(k\mathfrak{C}\cos\alpha x+k\sin\alpha y-\omega t)}$
$\frac{T_2'(x,y,t)}{\bar{T}_2}$	$=$	$K(\gamma-1)e^{\imath\tilde{k}_x x}e^{\imath(k\sin\alpha y-\omega t)}$	$+$	0	$-$	$Qe^{\imath(k\mathfrak{C}\cos\alpha x+k\sin\alpha y-\omega t)}$
$\frac{s_2'(x,y,t)}{c_p}$	$=$	0	$+$	0	$-$	$Qe^{\imath(k\mathfrak{C}\cos\alpha x+k\sin\alpha y-\omega t)}$

amplitude parameters which will be computed thanks to the boundary conditions, i.e. the linearized Rankine-Hugoniot jump conditions. The full turbulent emitted field is recovered summing the emitted perturbations associated to all incident waves, i.e. carrying out the summation over k, α and the wave nature.

It is worth noting that all these parameters are not independent since the fluctuations are solutions of the linearized Euler equations. Substitution into the x momentum equation

$$\frac{\partial u_2'}{\partial t} + U_2 \frac{\partial u_2'}{\partial x} = -\frac{1}{\bar{\rho}_2} \frac{\partial p_2'}{\partial x}$$

yields

$$U_2(-\imath F k \cos\alpha U_1) + \imath U_2^2 F \tilde{k}_x = -\imath \frac{\bar{p}_2}{\bar{\rho}_2} K \tilde{k}_x, \tag{16.49}$$

from which it follows that

$$F = \frac{1}{\gamma} \frac{1}{\mathfrak{C} M_2^2} \frac{\frac{\tilde{k}_x}{k}}{\cos\alpha - \frac{\tilde{k}_x}{\mathfrak{C} k}} K. \tag{16.50}$$

The y momentum equation

$$\frac{\partial v_2'}{\partial t} + U_2 \frac{\partial v_2'}{\partial x} = -\frac{1}{\bar{\rho}_2} \frac{\partial p_2'}{\partial y}$$

leads to

$$U_2(-H\imath k \cos\alpha U_1) + U_2^2 H \imath \tilde{k}_x = -\frac{\bar{p}_2}{\bar{\rho}_2} K \imath k \sin\alpha, \tag{16.51}$$

which can be rearranged like

$$H = \frac{1}{\gamma} \frac{1}{\mathfrak{C} M_2^2} \frac{\sin\alpha}{\cos\alpha - \frac{\tilde{k}_x}{\mathfrak{C} k}} K. \tag{16.52}$$

A last constraint is that the vortical velocity field is solenoidal, i.e.

$$\frac{\partial u_2'}{\partial x} + \frac{\partial v_2'}{\partial y} = 0,$$

which is equivalent to

$$U_2 G \imath k \mathfrak{C} \cos\alpha + U_2 I \imath k \sin\alpha = 0, \tag{16.53}$$

leading to

$$I = -\mathfrak{C} \cot\alpha G. \tag{16.54}$$

It is recalled that the entropy, density, pressure and temperature fluctuations are tied by the two following linearized relations:

$$\frac{\rho_2'}{\bar{\rho}_2} = \frac{p_2'}{\gamma \bar{p}_2} - \frac{s_2'}{c_p}, \tag{16.55}$$

$$\frac{T_2'}{\bar{T}_2} = (\gamma - 1)\frac{p_2'}{\gamma \bar{p}_2} + \frac{s_2'}{c_p}. \tag{16.56}$$

The above system is supplemented by the normalized boundary conditions

$$\frac{1}{U_1}\frac{\partial \xi}{\partial t} = L e^{\imath(k \sin \alpha y - \omega t)}, \quad \frac{\partial \xi}{\partial y} = -\frac{L}{\cos \alpha} e^{\imath(k \sin \alpha y - \omega t)}, \tag{16.57}$$

where L is an amplitude factor for the shock displacement. The downstream perturbation field is therefore parameterized by four independent parameters, namely I, K, L and Q. The problem is a priori well-behaved, since there are four unknowns and four jump conditions. The problem can be recast making the transfer coefficients $Z_F, Z_G, Z_H, Z_I, Z_K, Z_L$ and Z_Q appearing, which are defined as

$$F = AZ_F, G = AZ_G, H = AZ_H, I = AZ_I, K = Z_K, L = AZ_L, Q = AZ_Q, \tag{16.58}$$

where A is the complex amplitude of the incident wave (A is therefore identical to the coefficient of the Fourier transform of the incident perturbation field associated to $\boldsymbol{k}$).

The decomposition given in Table 16.1 and Eq. (16.57) can also be rewritten making the amplitude of each Kovasznay mode explicitely appearing. This new expression is given in Table 16.2 where it is chosen here to use the second form of the exponential wave operator to illustrate it.

The shock front displacement is now expressed like

$$\xi(y, t) = Z_x e^{\imath(k \sin \alpha y - \omega t)}. \tag{16.59}$$

The coefficient ζ is defined as $\zeta = \sqrt{1 - \eta^2 + 2\imath\eta \cos \alpha_a}$. The four unknowns are now A_a, A_v, A_s and A_x, i.e. the normalized amplitudes of the acoustic, vorticity and entropy modes and shock displacement, respectively. One observes that $\zeta = 1$ in the propagative regime, while ζ is imaginary in the non propagative regime, showing that the velocity and pressure fluctuations associated to evanescent waves are not in phase.

For an incident wave with complex amplitude A the unknown amplitudes are given by

$$A_a = AZ_a, A_v = AZ_v, A_s = AZ_s, A_x = AZ_x, \tag{16.60}$$

where Z_a, Z_v, Z_s and Z_x are complex transfer functions associated with the second decomposition.

Table 16.2 Second decomposition of the emitted field associated to a single plane incident wave with wave number k and frequency ω

		Acoustic mode		Vorticity mode		Entropy mode
$\frac{u_2(x,y,t)}{U_2}$	$=$	$A_a \frac{\cos\alpha_a + \imath\eta}{M_2\zeta} e^{-k_a\eta x} e^{\imath(k_a x\cos\alpha_a + k_a y\sin\alpha_a - \omega t)}$	$+$	$A_v \sin\alpha_s e^{\imath(k_s x\cos\alpha_s + k_s y\sin\alpha_s - \omega t)}$	$+$	0
$\frac{v_2(x,y,t)}{U_2}$	$=$	$A_a \frac{\sin\alpha_a}{M_2\zeta} e^{-k_a\eta x} e^{\imath(k_a x\cos\alpha_a + k_a y\sin\alpha_a - \omega t)}$	-	$A_v \cos\alpha_s e^{\imath(k_s x\cos\alpha_s + k_s y\sin\alpha_s - \omega t)}$	$+$	0
$\frac{p_2'(x,y,t)}{\gamma\bar{p}_2}$	$=$	$A_a e^{-k_a\eta x} e^{\imath(k_a x\cos\alpha_a + k_a y\sin\alpha_a - \omega t)}$	$+$	0	$+$	0
$\frac{\rho_2'(x,y,t)}{\bar{\rho}_2}$	$=$	$A_a e^{-k_a\eta x} e^{\imath(k_a x\cos\alpha_a + k_a y\sin\alpha_a - \omega t)}$	$+$	0	-	$A_s e^{\imath(k_s x\cos\alpha_s + k_s y\sin\alpha_s - \omega t)}$
$\frac{T_2'(x,y,t)}{\bar{T}_2}$	$=$	$A_a(\gamma-1) e^{-k_a\eta x} e^{\imath(k_a x\cos\alpha_a + k_a y\sin\alpha_a - \omega t)}$	$+$	0	$+$	$A_s e^{\imath(k_s x\cos\alpha_s + k_s y\sin\alpha_s - \omega t)}$
$\frac{s_2'(x,y,t)}{c_p}$	$=$	0	$+$	0	$+$	$A_s e^{\imath(k_s x\cos\alpha_s + k_s y\sin\alpha_s - \omega t)}$

The two decompositions are tied by the following equalities:

$$k_a\eta = \tilde{k}_i, \quad k_a\cos\alpha = \tilde{k}_r, \tag{16.61}$$

$$Z_F = Z_a\frac{\cos\alpha_a + \imath\eta}{M_2\zeta},\ Z_G = Z_v\sin\alpha_s,\ Z_H = Z_a\frac{\sin\alpha_a}{M_2\zeta}, \tag{16.62}$$

$$Z_I = -Z_v\cos\alpha_s, \qquad Z_K = Z_a, \qquad Z_Q = -Z_s. \tag{16.63}$$

Both incident and emitted fields can be further decomposed to emphasize the contribution of each Kovasznay mode. The incident field can be expressed as follows

$$\frac{u_1'}{U_1} = A_i\left(\delta_{iv}\sin\alpha + \delta_{ia}\frac{\cos\alpha}{M_1}\right)e^{\imath(\boldsymbol{k}\cdot\boldsymbol{x}-\omega t)} \tag{16.64}$$

$$\frac{v_1'}{U_1} = A_i\left(-\delta_{iv}\cos\alpha + \delta_{ia}\frac{\sin\alpha}{M_1}\right)e^{\imath(\boldsymbol{k}\cdot\boldsymbol{x}-\omega t)} \tag{16.65}$$

$$\frac{\rho_1'}{\bar{\rho}_1} = A_i(-\delta_{is} + \delta_{ia})e^{\imath(\boldsymbol{k}\cdot\boldsymbol{x}-\omega t)} \tag{16.66}$$

$$\frac{p_1'}{\gamma\bar{p}_1} = A_i\delta_{ia}e^{\imath(\boldsymbol{k}\cdot\boldsymbol{x}-\omega t)} \tag{16.67}$$

$$\frac{T_1'}{\bar{T}_1} = A_i(\delta_{is} + (\gamma-1)\delta_{ia})e^{\imath(\boldsymbol{k}\cdot\boldsymbol{x}-\omega t)} \tag{16.68}$$

$$\frac{s_1'}{c_p} = A_i\delta_{is}e^{\imath(\boldsymbol{k}\cdot\boldsymbol{x}-\omega t)} \tag{16.69}$$

where A_i is the complex amplitude of the incident wave. The subscript i is the related to the Kovasnay mode associated to the incident wave, with $i = a, v, s$ for acoustic wave, vorticity wave and entropy wave, respectively. The corresponding expressions for the emitted field are

$$\frac{u_2'}{U_2} = A_i\left(Z_{iv}\sin\alpha_s e^{\imath(\boldsymbol{k}_s\cdot\boldsymbol{x}-\omega t)} + Z_{ia}e^{-k_a\eta x}\frac{\cos\alpha_a + \imath\eta}{M_2\zeta}e^{\imath(\boldsymbol{k}_a\cdot\boldsymbol{x}-\omega t)}\right) \tag{16.70}$$

$$\frac{v_2'}{U_2} = A_i\left(-Z_{iv}\cos\alpha_s e^{\imath(\boldsymbol{k}_s\cdot\boldsymbol{x}-\omega t)} + Z_{ia}e^{-k_a\eta x}\frac{\sin\alpha_a}{M_2\zeta}e^{\imath(\boldsymbol{k}_a\cdot\boldsymbol{x}-\omega t)}\right) \tag{16.71}$$

$$\frac{\rho_2'}{\bar{\rho}_2} = A_i(-Z_{is}e^{\imath(\boldsymbol{k}_s\cdot\boldsymbol{x}-\omega t)} + Z_{ia}e^{-k_a\eta x}e^{\imath(\boldsymbol{k}_a\cdot\boldsymbol{x}-\omega t)}) \tag{16.72}$$

$$\frac{p_2'}{\gamma\bar{p}_2} = A_i Z_{ia}e^{-k_a\eta x}e^{\imath(\boldsymbol{k}_a\cdot\boldsymbol{x}-\omega t)} \tag{16.73}$$

$$\frac{T_2'}{\bar{T}_2} = A_i\left(Z_{is}e^{\imath(\boldsymbol{k}_s\cdot\boldsymbol{x}-\omega t)} + (\gamma-1)Z_{ia}e^{-k_a\eta x}e^{\imath(\boldsymbol{k}_a\cdot\boldsymbol{x}-\omega t)}\right) \tag{16.74}$$

$$\frac{s_2'}{c_p} = A_i Z_{is}e^{\imath(\boldsymbol{k}_s\cdot\boldsymbol{x}-\omega t)} \tag{16.75}$$

where Z_{ij} is the transfer function associated to the emission of a wave associated to Kovasnay mode $j = v, s, a$ by and incident wave of type i. These formula are supplemented by the one related to the shock wave corrugation:

$$\xi' = A_i Z_{ix}. \tag{16.76}$$

16.3.2 Calculation of Amplitudes of Emitted Waves

Amplitudes of the emitted Kovasznay modes are related to those of the incident wave through linearized jump conditions. The first step of the procedure consists in substituting Eqs. (16.6)–(16.12) into the linearized Rankine–Hugoniot relations (see Sect. 3.1.3) written in a frame of reference that moves at the local instantaneous speed of the shock wave. Then, normalizing the fluctuating quantities using mean flow variables, one obtains the following equations which are valid at $x = 0$:

$$\frac{1}{\mathfrak{C}}\left(\frac{u_2' - \frac{\partial \xi}{\partial t}}{U_2}\right) = \left(\frac{u_2' - \frac{\partial \xi}{\partial t}}{U_1}\right) = \frac{(\gamma-1)M_1^2 - 2}{(\gamma+1)M_1^2}\left(\frac{u_1' - \frac{\partial \xi}{\partial t}}{U_1}\right) + \frac{2}{(\gamma+1)M_1^2}\left(\frac{T_1'}{\bar{T}_1}\right), \tag{16.77}$$

$$\frac{1}{\mathfrak{C}}\left(\frac{v_2'}{U_2}\right) = \left(\frac{v_2'}{U_1}\right) = \left(\frac{v_1'}{U_1}\right) + \frac{2(M_1^2-1)}{(\gamma+1)M_1^2}\frac{\partial \xi}{\partial y}, \tag{16.78}$$

$$\left(\frac{\rho_2'}{\bar{\rho}_2}\right) = \frac{4}{(\gamma-1)M_1^2+2}\left(\frac{u_1' - \frac{\partial \xi}{\partial t}}{U_1}\right) - \frac{(\gamma-1)M_1^2+4}{(\gamma-1)M_1^2+2}\left(\frac{T_1'}{\bar{T}_1}\right), \tag{16.79}$$

$$\left(\frac{p_2'}{\gamma \bar{p}_2}\right) = \frac{4M_1^2}{2\gamma M_1^2 - (\gamma-1)}\left(\frac{u_1' - \frac{\partial \xi}{\partial t}}{U_1}\right) - \frac{2M_1^2}{2\gamma M_1^2 - (\gamma-1)}\left(\frac{T_1'}{\bar{T}_1}\right). \tag{16.80}$$

Now taking into account the fact that the shock front abscissa $\xi(y, t)$ is proportional to $\exp(\imath(k_y y - \omega t))$, one has

$$\alpha' = \frac{d\xi}{dy} = \imath k_y \xi, \quad u_s' = \frac{d\xi}{dt} = -\imath\omega\xi, \tag{16.81}$$

where it is recalled that the angle α' is defined as $\alpha' = \boldsymbol{n} \cdot \boldsymbol{t}'$, one recovers after some algebra the following relations :

$$\frac{\rho_2'}{\bar{\rho}_2} + \frac{u_2'}{U_2} - \frac{\imath\omega}{U_1}(1 - \mathfrak{C})\xi = \frac{\rho_1'}{\bar{\rho}_1} + \frac{u_1'}{U_1}, \tag{16.82}$$

$$\frac{\rho_2'}{\bar{\rho}_2}+2\frac{u_2'}{U_2}+\frac{1}{M_2^2}\frac{p_2'}{\gamma\bar{p}_2}=\mathfrak{C}\left(\frac{\rho_1'}{\bar{\rho}_1}+2\frac{u_1'}{U_1}+\frac{1}{M_1^2}\frac{p_1'}{\gamma\bar{p}_1}\right), \tag{16.83}$$

$$\frac{v_2'}{U_2}+\imath k_y(1-\mathfrak{C})\xi=\mathfrak{C}\frac{v_1'}{U_1}, \tag{16.84}$$

$$\frac{u_2'}{U_2}+\left(\frac{1}{M_2^2}+\frac{1}{(\gamma-1)M_2^2}\right)\frac{p_2'}{\gamma\bar{p}_2}-\frac{1}{(\gamma-1)M_2^2}\frac{\rho_2'}{\bar{\rho}_2}+\frac{\imath\omega}{U_1}\mathfrak{C}(1-\mathfrak{C})\xi=$$
$$\mathfrak{C}^2\left(\frac{u_1'}{U_1}+\left(\frac{1}{M_1^2}+\frac{1}{(\gamma-1)M_1^2}\right)\frac{p_1'}{\gamma\bar{p}_1}-\frac{1}{(\gamma-1)M_1^2}\frac{\rho_1'}{\bar{\rho}_1}\right), \tag{16.85}$$

where all mean flow quantities and incident fluctuating perturbations (subscript 1) are known.

The second step of the LIA procedure consists in selecting an incident wave, i.e. chosing its nature and prescribing the incident wave vector $\boldsymbol{k}$ (which is equivalent to prescribing α, k and ω). A set of linear equations for the amplitudes of the emitted waves and the shock displacement is then obtained expressing both incident and emitted fluctuating fields using one of the decomposition presented above (Table 16.1 and Eq. (16.57) or Table 16.2 and Eq. (16.59)) and its compact formulation (16.64)–(16.75), in which $\boldsymbol{k}_s$, $\boldsymbol{k}_a$ and the damping factor for evanescent waves are computed thanks to the ad hoc relations.

The second decomposition is used hereafter, since it give a deep insight into flow physics via a direct access to mode-to-mode transfer function. This case was exhaustively described by Fabre and coworkers Fabre et al. (2001). The first set of expressions was historically used in the works carried out at Stanford University during the 1990s. Thanks to the fact that all exponential terms are identical at the shock location ($x=0$), they can be removed. Therefore, the complex transfer function vectors $\boldsymbol{Z}_i=(Z_{iv},Z_{is},Z_{ia},Z_{ix})^T$, where the subscript $i=s,v,a$ is related to the nature of the incident wave and where Z_{ix} is related to the shock corrugation amplitude, are solution of a linear system of the form

$$\mathcal{A}\boldsymbol{Z}_i=\boldsymbol{B}_i, \tag{16.86}$$

where $\boldsymbol{B}_i$ denotes the associated right-hand side term.

For *non-acoustic* incident waves, i.e. $i=v$ (vorticity waves) and $i=s$ (entropy waves), the matrix $\mathcal{A}$ is given by

$$\mathcal{A}=\begin{bmatrix}\sin\alpha_s & -1 & 1+\frac{\cos\alpha_a+\imath\eta}{M_2\zeta} & \imath(\mathfrak{C}-1)\cos\alpha\\ 2\sin\alpha_s & -1 & \frac{M_2^2+1}{M_2^2}+2\frac{\cos\alpha_a+\imath\eta}{M_2\zeta} & 0\\ -\cos\alpha_s & 0 & \frac{\sin\alpha_a}{M_2\zeta} & \imath(1-\mathfrak{C})\sin\alpha\\ \sin\alpha_s & \frac{1}{(\gamma-1)M_2^2} & \frac{1}{M_2^2}+\frac{\cos\alpha_a+\imath\eta}{M_2\zeta} & \imath\mathfrak{C}(1-\mathfrak{C})\cos\alpha\end{bmatrix}. \tag{16.87}$$

In the case of *incident acoustic waves*, i.e. $i = a$, the matrix $\mathcal{A}$ should be replaced by $\mathcal{A}'$, which is obtained replacing α by the angle α' defined in Eq. (16.46) in the last column:

$$\mathcal{A}' = \begin{bmatrix} \sin\alpha_s & -1 & 1 + \frac{\cos\alpha_a + \imath\eta}{M_2\zeta} & \imath(\mathfrak{C}-1)\cos\alpha' \\ 2\sin\alpha_s & -1 & \frac{M_2^2+1}{M_2^2} + 2\frac{\cos\alpha_a+\imath\eta}{M_2\zeta} & 0 \\ -\cos\alpha_s & 0 & \frac{\sin\alpha_a}{M_2\zeta} & \imath(1-\mathfrak{C})\sin\alpha' \\ \sin\alpha_s & \frac{1}{(\gamma-1)M_2^2} & \frac{1}{M_2^2} + \frac{\cos\alpha_a+\imath\eta}{M_2\zeta} & \imath\mathfrak{C}(1-\mathfrak{C})\cos\alpha' \end{bmatrix}. \tag{16.88}$$

The right-hand side terms are defined as follows

$$\boldsymbol{B}_s = \begin{pmatrix} -1 \\ -\mathfrak{C} \\ 0 \\ \frac{\mathfrak{C}^2}{(\gamma-1)M_1^2} \end{pmatrix}, \quad \boldsymbol{B}_v = \begin{pmatrix} \sin\alpha \\ 2\mathfrak{C}\sin\alpha \\ -\mathfrak{C}\cos\alpha \\ \mathfrak{C}^2\sin\alpha \end{pmatrix}, \quad \boldsymbol{B}_a = \begin{pmatrix} 1 + \frac{\cos\alpha}{M_1} \\ \mathfrak{C}\left(\frac{M_1^2+1}{M_1^2} + \frac{2\cos\alpha}{M_1}\right) \\ \mathfrak{C}\frac{\sin\alpha}{M_1} \\ \mathfrak{C}^2\left(\frac{1}{M_1^2} + \frac{\cos\alpha}{M_1}\right) \end{pmatrix}. \tag{16.89}$$

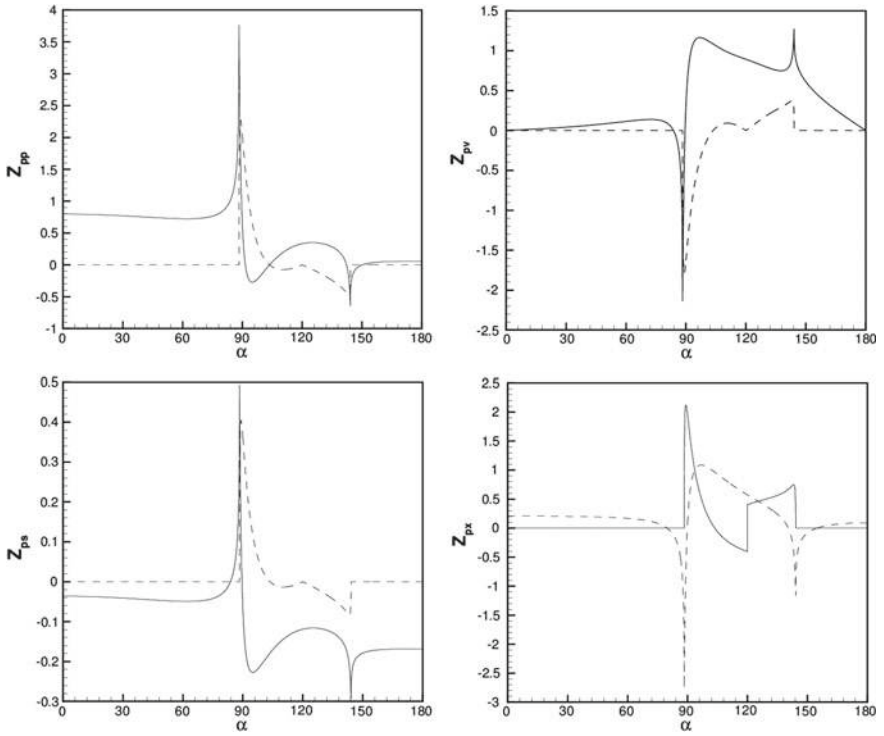

Fig. 16.2 LIA transfer functions versus the angle of the incident wave α in the case of an incident plane acoustic wave. Top: Z_a (left) and Z_v (right); Bottom: Z_s (left) and Z_x (right). Solid line: real part, dashed line: imaginary part. Courtesy of D. Fabre, IMFT, France

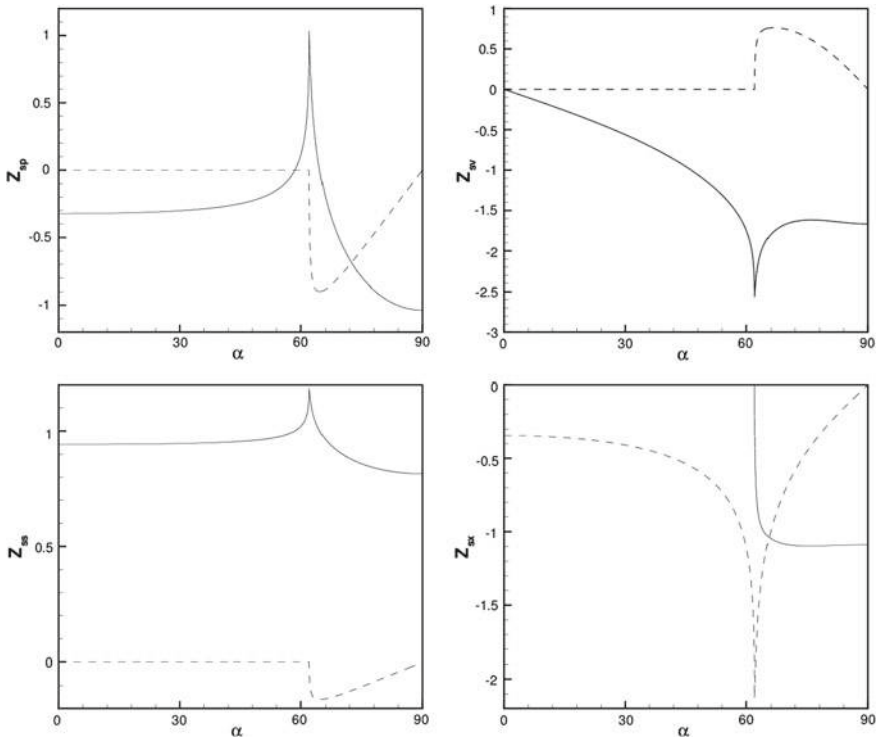

Fig. 16.3 LIA transfer functions versus the angle of the incident wave α in the case of an incident plane entropy wave. Top: Z_a (left) and Z_v (right); Bottom: Z_s (left) and Z_x (right). Solid line: real part, dashed line: imaginary part. Courtesy of D. Fabre, IMFT, France

A careful examination of these results reveals that the transfer functions depend only on γ, M_1 and α, i.e. they are not functions of the wave vector amplitude k. This is coherent with the fact that the shock wave is assumed to have no intrinsic length scale, and that viscous effects are neglected.

The computed transfer functions, angles of emission and damping factor are displayed in Figs. 16.2, 16.3, 16.4 and 16.5.

It is seen that transfer functions exhibit a kink near the critical angle α_c, which corresponds to a strong increase of the emitted energy. Therefore, the small perturbation assumption might be partially violated for waves with $\alpha \sim \alpha_c$, a fact that is used by several authors to explain some discrepancies between LIA and DNS results. It is also observed that the imaginary parts are null for $\alpha < \alpha_c$, indicating that incident and emitted waves are in phase in this case, while they are out of phase for higher values of α.

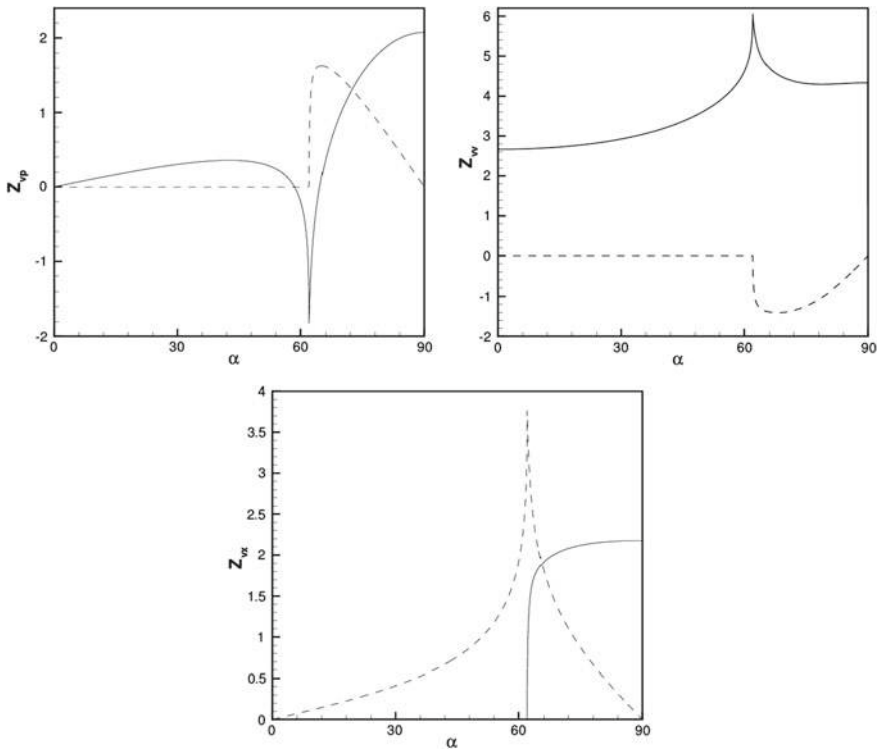

Fig. 16.4 LIA transfer functions versus the angle of the incident wave α in the case of an incident plane vorticity wave. Top: Z_a (left) and Z_v (right); Bottom: Z_x. Solid line: real part, dashed line: imaginary part. Courtesy of D. Fabre, IMFT, France

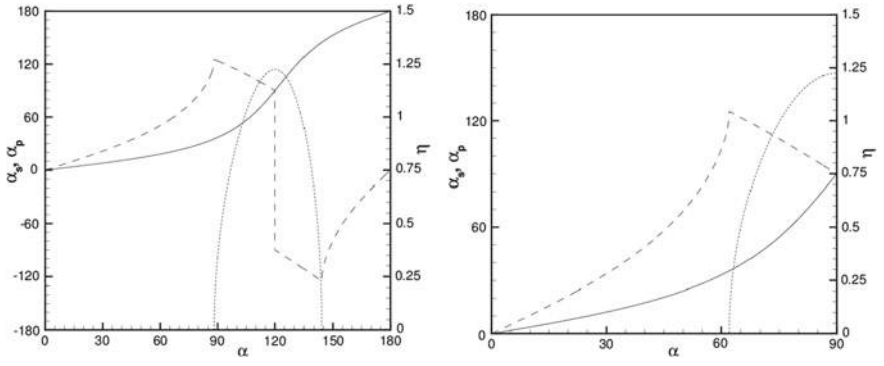

Fig. 16.5 Angle of emitted waves and damping parameter η as a function of the angle of the incident wave. Left: incident acoustic wave; Right: incident entropy/vorticity wave. Dotted line: η, solide line: α_s, dashed line: α_a. Courtesy of D. Fabre, IMFT, France

16.4 Distinguishing Between Poloidal and Toroidal Vorticity Modes

The previous results can be extended by making the distinction between poloidal and toroidal vorticity modes (Griffond and Soulard 2012), augmenting the dimension of the problem with respect to the classical Kovasznay decomposition. To this end, it is useful to rewrite the problem in cylindrical coordinates, since poloidal and toroidal modes are easily separated in this reference frame.

Denoting $(\boldsymbol{e}_x, \boldsymbol{e}_y, \boldsymbol{e}_z)$ the Cartesian reference frame, the cylindrical coordinate unit vectors are $(\boldsymbol{e}_x, \boldsymbol{e}_r = \boldsymbol{e}_\phi \times \boldsymbol{e}_x, \boldsymbol{e}_\phi = \boldsymbol{e}_x \times \boldsymbol{k}/\|\boldsymbol{e}_x \times \boldsymbol{k}\|)$ while it is recalled that the Craya-Herring reference frame is given by $(\boldsymbol{e}^{(1)} = \boldsymbol{k} \times \boldsymbol{e}_x/\|\boldsymbol{k} \times \boldsymbol{e}_x\|, \boldsymbol{e}^{(2)} = \boldsymbol{k} \times \boldsymbol{e}^{(1)}/\|\boldsymbol{k} \times \boldsymbol{e}^{(1)}\|, \boldsymbol{e}^{(3)} = \boldsymbol{k}/k)$ (with $k = \|\boldsymbol{k}\|$) leading to

$$\boldsymbol{k} = \begin{cases} k\cos\alpha\boldsymbol{e}_x + k\sin\alpha\cos\phi\boldsymbol{e}_y + k\sin\alpha\sin\phi\boldsymbol{e}_z & \text{(Cartesian frame)} \\ k\cos\alpha\boldsymbol{e}_x + k\sin\alpha\boldsymbol{e}_r + 0\boldsymbol{e}_\phi & \text{(Cylindrical frame)} \\ 0\boldsymbol{e}^{(1)} + 0\boldsymbol{e}^{(2)} + k\boldsymbol{e}^{(3)} & \text{(Craya-Herring frame)} \end{cases} \tag{16.90}$$

where α and ϕ denote the angles between $\boldsymbol{k}$ and $\boldsymbol{e}_x$ and $\boldsymbol{e}_y$ and $\boldsymbol{e}_r$, respectively. Fluctuating velocity fields associated to poloidal vorticity mode (subscript *pol*), toroidal vorticity mode (subscript *tor*) and acoustic modes are given in the Craya-Herring frame as

$$\boldsymbol{u}' = \begin{cases} \boldsymbol{u}_{tor} = -u_{(1)}\boldsymbol{e}^{(1)} \\ \boldsymbol{u}_{pol} = -u_{(2)}\boldsymbol{e}^{(2)} \\ \boldsymbol{u}_a = u_{(3)}\boldsymbol{e}^{(3)} \end{cases} \tag{16.91}$$

where the Craya-Herring amplitudes $(u_{(1)}, u_{(2)}, u_{(3)})$ are deduced from the Cartesian (u_x, u_y, u_z) and cylindrical ones (u_x, u_r, u_ϕ) according to

$$\begin{aligned} u_{(1)} &= -u_\phi = -u_y\sin\phi + u_z\cos\phi \\ u_{(2)} &= u_r\cos\alpha - u_x\sin\alpha = u_y\cos\alpha\cos\phi + u_z\cos\alpha\sin\phi - u_x\sin\alpha \\ u_{(3)} &= u_r\sin\alpha + u_x\cos\alpha = u_y\sin\alpha\cos\phi + u_z\sin\alpha\sin\phi + u_x\sin\alpha \end{aligned}$$

The Kovasznay decomposition of both incident and emitted fields can be written in cylindrical coordinates as follows, in which poloidal and toroidal vorticity modes are related to *pol* and *tor* subscripts, respectively. The upstream velocity field is expressed as (expressions for other fluctuating quantities are the same as in the previous case, see Eqs. (16.66)–(16.69)):

$$\frac{u'_{x_1}}{U_1} = A_i\left(\delta_{ipol}\sin\alpha + \delta_{ia}\frac{\cos\alpha}{M_1}\right)e^{\imath(\boldsymbol{k}\cdot\boldsymbol{x}-\omega t)}, \tag{16.92}$$

$$\frac{u'_{r_1}}{U_1} = A_i\left(-\delta_{ipol}\cos\alpha + \delta_{ia}\frac{\sin\alpha}{M_1}\right)e^{\imath(\boldsymbol{k}\cdot\boldsymbol{x}-\omega t)}, \tag{16.93}$$

$$\frac{u'_{\phi_1}}{U_1} = A_i \delta_{i\,tor} e^{\imath(\boldsymbol{k}\cdot\boldsymbol{x}-\omega t)}. \tag{16.94}$$

Introducing the transfer function vector $\boldsymbol{Z}_i = (Z_{i\,tor}, Z_{i\,pol}, Z_{is}, Z_{ia}, Z_{ix})$, one obtains for the emitted velocity field (expressions for other emitted fields are the same as in the previous case, see Eqs. (16.72)–(16.75)):

$$\frac{u'_{x_2}}{U_2} = A_i \left(Z_{i\,pol} \sin\alpha_s e^{\imath(\boldsymbol{k}_s\cdot\boldsymbol{x}-\omega t)} + Z_{ia} e^{-k_a\eta x} \frac{\cos\alpha_a + \imath\eta}{M_2\zeta} e^{\imath(\boldsymbol{k}_a\cdot\boldsymbol{x}-\omega t)} \right), \tag{16.95}$$

$$\frac{u'_{r_2}}{U_2} = A_i \left(-Z_{i\,pol} \cos\alpha_s e^{\imath(\boldsymbol{k}_s\cdot\boldsymbol{x}-\omega t)} + Z_{ia} e^{-k_a\eta x} \frac{\sin\alpha_a}{M_2\zeta} e^{\imath(\boldsymbol{k}_a\cdot\boldsymbol{x}-\omega t)} \right), \tag{16.96}$$

$$\frac{u'_{\phi_2}}{U_2} = A_i Z_{i\,tor} e^{\imath(\boldsymbol{k}_s\cdot\boldsymbol{x}-\omega t)}. \tag{16.97}$$

The computation of the complex transfer functions is carried out as in the previous case. A careful examination of this linearized system shows that the toroidal vorticity mode is decoupled from all other modes, and that only the poloidal component of the vorticity mode generates entropy and acoustic waves downstream the shock, along with shock corrugation. The expression of the transfer function for the toroidal vorticity mode simplifies as

$$Z_{i\,tor} = \mathfrak{C}\delta_{i\,tor} \tag{16.98}$$

The remaining transfer functions $Z_{i\,pol}$, Z_{is}, Z_{ia} and Z_{ix} are solutions of the same 4×4 linear system as the one given in Sect. 16.3.2 (including the treatment for incident acoustic waves), Z_{iv} being replaced by $Z_{i\,pol}$.

16.5 Reconstruction of the Second Order Moments

The general formulation of the fluctuating field behind the shock wave makes it possible to derive expressions for the second-order statistical moments and to emphasize some fundamental differences between fields generated by propagating and evanescent waves (Mahesh et al. 1995, 1996). As said above, the existence of evanescent waves with significant amplitude just behind the shock yields the existence of a thin region with peculiar behavior, referred to as the near field.

16.5.1 Case of a Single Incident Wave

Let us first consider the case of a single incident wave with wave number k and angle α. The second-order one-point cross correlation between the fluctuating quantities ψ' and φ' at downstream location x is given by

$$\overline{\psi'\varphi'}(x;k,\alpha) \equiv \Re\left(\overline{\psi'\varphi'^{*}}(x;k,\alpha)\right), \tag{16.99}$$

where $\Re$ denotes the real part and $\psi'(x)$ and $\varphi'(x)$ are the complex variables taken in the lists (16.70)–(16.75) and (16.95)–(16.97). The superscript * and the overbar denote the complex conjugate and statistical averaging, respectively.

Considering the mean fluctuating kinetic energy associated with the shock normal velocity component u'_{x_2} as an illustration, one obtains

$$\begin{aligned}\frac{\overline{u'_{x_2}{}^2}(x;k,\alpha)}{U_2^2} &= \Re\left(\overline{\left[A_i(Z_{i\,pol}\sin\alpha_s e^{\imath(\boldsymbol{k}_s\cdot\boldsymbol{x}-\omega t)} + Z_{ia}e^{-k_a\eta x}\frac{\cos\alpha_a+\imath\eta}{M_2\zeta}e^{\imath(\boldsymbol{k}_a\cdot\boldsymbol{x}-\omega t)}\right]}\right.\\ &\left.\times\,\overline{\left[A_i(-Z_{is}e^{\imath(\boldsymbol{k}_s\cdot\boldsymbol{x}-\omega t)} + Z_{ia}e^{-k_a\eta x}e^{\imath(\boldsymbol{k}_a\cdot\boldsymbol{x}-\omega t)})\right]^{*}}\right)\\ &= \overline{|A_i|^2}\left(|Z_{i\,pol}|^2\sin^2\alpha_s + |Z_{ia}|^2e^{-2k_a\eta x}\frac{\cos^2\alpha_a+\eta^2}{M_2^2\zeta^2}\right)\\ &\quad +2\overline{|A_i|^2}e^{-k_a\eta x}\sin\alpha_s\Re\left(Z_{i\,pol}Z_{ia}^{*}\frac{\cos\alpha_a-\imath\eta}{M_2\zeta}e^{\imath([\boldsymbol{k}_s-\boldsymbol{k}_a]\cdot\boldsymbol{x})}\right).\end{aligned} \tag{16.100}$$

It is observed that the longitudinal velocity autocorrelation is made of three contributions that appear in the right hand side of the final expression. The first one is the kinetic energy of the velocity component of the emitted vorticity mode, the second one is the kinetic energy of the emitted acoustic mode while the last one is the cross-correlation between emitted acoustic and vorticity modes. The acoustic mode exhibits the $e^{-k_a\eta x}$ term, which indicates that an exponentially damped near-field may exist in the non-propagative regime. A similar expression can be derived for the second poloidal velocity component, u'_{r_2}. Therefore, in the propagative regime the emitted poloidal kinetic energy has spatially uniform contributions from both the poloidal vortical and acoustic modes and an oscillating component whose argument is equal to the phase difference between them which is related to $([\boldsymbol{k}_s-\boldsymbol{k}_a]\cdot\boldsymbol{x})$. In the non propagative regime it has a spatially uniform contribution from the vorticity mode only, an exponentially decaying monotone acoustic component and exponentially damped components due to the correlation between the poloidal vorticity and the acoustic mode. Temperature and density variances exhibit a similar behavior, since they are made of a combination of the acoustic and entropy modes.

The emitted toroidal kinetic energy has a much simpler structure, since it depends on the sole toroidal vorticity mode, which is decoupled from all other modes, leading to

$$\frac{\overline{u'_{\phi_2}{}^2}(x;k,\alpha)}{U_2^2} = \overline{|A_i|^2}|Z_{i\,tor}|^2 = \mathfrak{C}^2\overline{|A_i|^2}\delta_{i\,tor} \tag{16.101}$$

It exhibits a spatially uniform distribution without possible near-field structure or far-field oscillation. The same conclusion holds for the entropy variance, since

entropy fluctuations depend on the sole entropy mode which has no evanescent regime. Quantities which depend on the sole acoustic mode such as pressure and dilatation exhibit dramatic changes when switching from one regime to the other one. Let us illustrate this point using the pressure variance:

$$\frac{\overline{p_2'^2}(x;k,\alpha)}{\gamma^2\bar{p}_2^2} = \overline{|A_i|^2}|Z_{ia}|^2 e^{-2k_a\eta x} \tag{16.102}$$

In the propagative regime, the pressure variance is spatially uniform, while in the non propagative regime it experiences an exponential decay and the pressure variance totally vanishes outside the near-field region. The width of the near field region scales like $O(1/k)$, showing that it is very thin.

Variance of shock displacement and shock speed due to shock corrugation are reconstructed as follows:

$$\overline{\xi'^2}(k,\alpha) = \overline{|A_i|^2}|Z_{ix}|^2, \quad \overline{\left(\frac{\partial \xi'}{\partial t}\right)^2}(k,\alpha) = -\overline{|A_i|^2}|Z_{ix}|^2 k^2 U_1^2 \cos^2\alpha. \tag{16.103}$$

16.5.2 Case of an Incident Turbulent Isotropic Field

It is important to note that the developments presented above are valid in the case of a single incident wave. We now address the problem of an incident isotropic turbulent field made of a single Kovasznay mode, i.e. a purely vortical, acoustic or entropic isotropic turbulence. The case of a mixed turbulence made of several Kovasznay modes will be discussed in the next section. The symmetry of the problem leads to an axisymmetric emitted field.

In the original Cartesian frame of reference, the undisturbed plane shock is assumed to lie in the $y-z$ plane, while the normal mean flow is parallel to the x axis.

Let us first consider an isotropic solenoidal velocity field generated by vorticity modes. The energy spectrum of the incident velocity field is assumed to be of the form

$$E_{ij}(\boldsymbol{k}) = \frac{E(k)}{4\pi k^2}\left(\delta_{ij} - \frac{k_i k_j}{k^2}\right), \tag{16.104}$$

where $E(k)$ is the three dimensional energy spectrum. Since the velocity field is solenoidal, the velocity vector associated to the wave vector $\boldsymbol{k}$ is orthogonal to $\boldsymbol{k}$ and may have a component orthogonal to the plane spanned by $\boldsymbol{k}$ and the x axis. Therefore, the two-dimensional analysis presented above must be extended introducing cylindrical coordinates (x, r, ϕ) (see Fig. 16.6).[2]

[2]Here, x still refers to the x axis in the original Cartesian frame of reference. Let u_x' and u_r' be the fluctuating velocity components in the x and r directions, and u_ϕ' be azimutal component. The latter

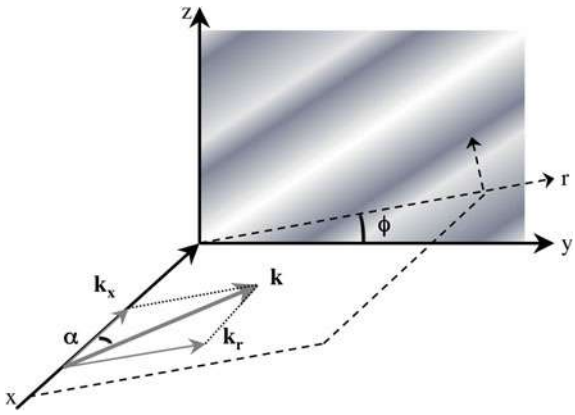

Fig. 16.6 Schematic view of the Linear Interaction Approximation for shock/turbulence interaction: reference frames for the treatment of an isotropic incident field

The change of frame of reference implies

$$u' = u'_x \tag{16.105}$$

$$u'_r = v' \cos\phi + w' \sin\phi, \quad u'_\phi = -v' \sin\phi + w' \cos\phi, \tag{16.106}$$

$$v' = u'_r \cos\phi - u'_\phi \sin\phi, \quad w' = u'_r \sin\phi + u'_\phi \cos\phi, \tag{16.107}$$

while the elemental volumes of integration are tied by the following relation

$$d\boldsymbol{k} = k^2 \sin\alpha \, d\alpha \, d\phi \, dk \tag{16.108}$$

with $k \in [0, +\infty]$, $\alpha \in [-\pi/2, \pi/2]$ and $\phi \in [0, 2\pi]$, along with

$$k_1 = k \cos\alpha, \quad k_2 = k \cos\phi \sin\alpha, \quad k_3 = k \sin\phi \sin\alpha. \tag{16.109}$$

The two-dimensional analysis presented above obviously holds for the u'_x and u'_r components, since the $x - r$ plane corresponds to the $x - y$ plane in the two-dimensional analysis. The angle α is the same in the two coordinates systems. The method consists therefore in applying the two-dimensional LIA procedure to the u'_x and u'_r components, while the u'_ϕ component is left unmodified by the interaction since it is tangential to the shock wave, according to Eq. (3.18). An important point is that the amplitude $A_v(k)$ of the incident wave with wave vector $\boldsymbol{k}$ which appears in the two-dimensional analysis (see Eqs. (16.58) and (16.60)) is now related to the magnitude of the velocity vector in the $x - r$ plane, leading to

$$|A_v(k)| = \frac{|u'_1|}{\sin\alpha}, \quad \overline{|A_v(k)|^2} = \frac{E(k)}{4\pi k^2}. \tag{16.110}$$

---

is normal to the $x - r$ plane spanned by the x axis and the wave vector $\boldsymbol{k}$. It is reminded that α and ϕ denote the angle between $\boldsymbol{k}$ and the x axis in the $x - r$ plane, while ϕ is defined as the angle between $\boldsymbol{k}$ and the y axis in the $y - z$ plane.

Now introducing the spectral components of kinetic energy behind the shock waves in both the Cartesian and cylindrical coordinates systems, Eqs. (16.105)–(16.107) yield the following relations:

$$E_{11}(k) = E_{xx}(k), \tag{16.111}$$

$$E_{22}(k) + E_{33}(k) = E_{rr}(k) + E_{\phi\phi}(k), \tag{16.112}$$

$$E_{22}(k) = \cos^2\phi E_{rr}(k) + \sin^2\phi E_{\phi\phi}(k) - \sin 2\phi E_{r\phi}(k), \tag{16.113}$$

$$E_{33}(k) = \sin^2\phi E_{rr}(k) + \cos^2\phi E_{\phi\phi}(k) + \sin 2\phi E_{r\phi}(k). \tag{16.114}$$

The spectral components are linked to the amplitude factor $A_v(k)$ via

$$\overline{|A_v(k)|^2} = \frac{E^1_{11}(k)}{\sin^2\alpha} = E^1_{11}(k) + E^1_{rr}(k) = E^1_{nn}(k) - E^1_{\phi\phi}(k), \tag{16.115}$$

where the superscript '1' refers to the incident perturbation field and $E_{nn}(k)$ is the total kinetic energy density, from which it follows that

$$E^1_{\phi\phi}(k) = E^1_{nn}(k) - \overline{|A_v(k)|^2} = \frac{E(k)}{4\pi k^2} \tag{16.116}$$

and

$$E_{22}(k) + E_{33}(k) = E_{rr}(k) + \frac{E(k)}{4\pi k^2}. \tag{16.117}$$

The streamwise kinetic energy behind the shock wave is defined as follows

$$\frac{\overline{u_2'^2}(x)}{U_2^2} = \int_{k=0}^{+\infty}\int_{\alpha=-\pi/2}^{+\pi/2}\int_{\phi=0}^{2\pi}\frac{\overline{u_{x_2}'^2}(x;k,\alpha)}{U_2^2}k^2\sin\alpha\, d\alpha\, d\phi\, dk, \tag{16.118}$$

where $\overline{u_{x_2}'^2}(x;k,\alpha)/U_2^2$ is the amplitude of the emitted wave associated to a single incident wave vector computed using the two-dimensional theory (see Eq. (16.100)). Remarking that this term is independent of ϕ and that it is symmetric about $\alpha = 0$, Eq. (16.118) simplifies as

$$\frac{\overline{u_2'^2}(x)}{U_2^2} = 4\pi\int_{k=0}^{+\infty}\int_{\alpha=0}^{+\pi/2}\frac{\overline{u_2'^2}(x;k,\alpha)}{U_2^2}k^2\sin\alpha d\alpha\, dk. \tag{16.119}$$

By identification with the definition of the spectrum of the streamwise velocity component $E_{11}(k)$, one has

$$\int_0^{+\infty} E_{11}(k)dk = \overline{u_x'u_x'} \Rightarrow E_{11}(k) = 4\pi k^2\int_{\alpha=0}^{+\pi/2}\overline{u_{x_2}'^2}(x;k,\alpha)\sin\alpha\, d\alpha \tag{16.120}$$

Equation (16.119) can be simplified emphasizing that cross-correlations between velocity fields of the emitted vorticity and acoustic waves vanish, because they have different propagation speeds and therefore cannot be correlated when considering an incident random turbulent field instead of a single deterministic monochromatic wave. Therefore, inserting remaining terms of Eq. (16.100), one has

$$\frac{\overline{u_2'^2}(x)}{U_2^2} = \int_{k=0}^{+\infty}\int_{\alpha=0}^{+\pi/2} E(k)\left(|Z_{v\,pol}|^2\sin^2\alpha_s + |Z_{va}|^2 e^{-2k_a\eta x}\frac{\cos^2\alpha_a+\eta^2}{M_2^2\zeta^2}\right)\sin\alpha d\alpha\, dk. \tag{16.121}$$

Expressions similar to Eq. (16.119) for the transverse components of kinetic energy are

$$\frac{\overline{v_2'^2}(x)}{U_1^2} = \frac{\overline{w_2'^2}(x)}{U_1^2} = \frac{1}{2}4\pi\int_{k=0}^{+\infty}\int_{\alpha=0}^{+\pi/2}\left(E_{rr}+\frac{E(k)}{4\pi k^2}\right)k^2\sin\alpha\, d\alpha\, dk. \tag{16.122}$$

We now consider scalar quantities, such as pressure and entropy. This case is much simpler since since no projection is needed. As an example, the variance of the emitted pressure wave is given by

$$\frac{\overline{p_2'^2}(x)}{\gamma^2\bar{p}_2^2} = 2\pi\int_{k=0}^{+\infty}\int_{\alpha=0}^{+\pi/2}\frac{\overline{p_2'^2}(x;k,\alpha)}{\gamma^2\bar{p}_2^2}k^2\sin\alpha\, d\alpha\, dk \tag{16.123}$$

where $\overline{p_2'^2}(x;k,\alpha)/\gamma^2\bar{p}_2^2$ is computed using Eq. (16.102) for a single incident plane wave, i.e.

$$\frac{\overline{p_2'^2}(x;k,\alpha)}{\gamma^2\bar{p}_2^2} = |A_v|^2|Z_{va}|^2e^{-2k_a\eta x} = \frac{E(k)}{4\pi k^2}|Z_{va}|^2e^{-2k_a\eta x}$$

while the downstream pressure variance three-dimensional spectrum $E_{pp}(k)$ if expressed as

$$\frac{\overline{p_2'^2}(x)}{\gamma^2\bar{p}_2^2} = \int_0^{+\infty}E_{pp}(k)dk \Rightarrow E_{pp}(k) = \frac{1}{2}E(k)\int_{\alpha=0}^{+\pi/2}|Z_{va}|^2e^{-2k_a\eta x}\sin\alpha\, d\alpha. \tag{16.124}$$

Downstream cross-correlations between velocity components, pressure, density, temperature, entropy and other quantities are obtained in the same way, keeping in mind that contributions stemming from the acoustic emitted waves are not statistically correlated with non-acoustical contributions.

The case of an incident isotropic acoustic field is much simpler, since the associated velocity field is purely dilatational and is therefore parallel to the wave vector. Consequentely, the velocity vector is entirely contained in the $x-r$ plane in the cylindrical coordinates system introduced above, i.e. the azimutal velocity component u'_ϕ

is identically zero. The same conclusion is reached considering that the upstream acoustic field is irrotational, so that both poloidal and toroidal vorticity component are null upstream the shock wave. Since the toroidal component is decoupled from other modes, it remains zero downstream the shock wave while poloidal vorticity is created, leading to the fact that u'_ϕ is null downstream the shock. Therefore, this case will not be detailed since it can be directly treated using the two-dimensional LIA theory, the two-dimensional $x-y$ plane being taken equal to the $x-r$ plane. It is just recalled that the isotropic spectral tensor is now defined as

$$E^1_{ij}(\boldsymbol{k}) = \frac{E(k)}{8\pi k^2}\frac{k_i k_j}{k^2} \tag{16.125}$$

and not by Eq. (16.104).

General expressions can be obtained for all types of incident fields in a straightforward way. This is illustrated by the following expressions for longitudinal (i.e. shock-normal) and transversal Reynolds stresses:

$$\begin{aligned}\frac{\overline{u_2'^2}(x)}{U_2^2} = 4\pi \int_{k=0}^{+\infty}\int_{\alpha=0}^{+\pi/2} \overline{|A_i(k)|^2}\Big\{ & |Z_{i\,pol}|^2 \sin^2\alpha_s \\ & + |Z_{ia}|^2 e^{-2k_a\eta x}\frac{\cos^2\alpha_a+\eta^2}{M_2^2\zeta^2} \\ & + 2e^{-k_a\eta x}\Re\left(\cos\alpha_s\frac{\sin\alpha_a}{M_2\zeta^*}Z_{iv}Z_{ia}^* e^{\imath x(k_s\cos\alpha_s - k_a\cos\alpha_a)}\right)\Big\} k^2\sin\alpha d\alpha\, dk,\end{aligned} \tag{16.126}$$

$$\begin{aligned}\frac{\overline{v_2'^2}(x)}{U_2^2} = 2\pi \int_{k=0}^{+\infty}\int_{\alpha=0}^{+\pi/2} \overline{|A_i(k)|^2}\Big\{ & |Z_{i\,tor}|^2 + |Z_{i\,pol}|^2\cos^2\alpha_s \\ & + |Z_{ia}|^2 e^{-2k_a\eta x}\frac{\sin^2\alpha_a}{M_2^2\zeta^2} \\ & - 2e^{-k_a\eta x}\Re\left(\cos\alpha_s\frac{\sin\alpha_a}{M_2\zeta^*}Z_{iv}Z_{ia}^* e^{\imath x(k_s\cos\alpha_s - k_a\cos\alpha_a)}\right)\Big\} k^2\sin\alpha d\alpha\, dk.\end{aligned} \tag{16.127}$$

16.5.3 Case of a Mixed Incident Perturbation Field

We now address the case of an incident field made of the combination of different Kovasznay modes. The above analysis is extended in a straightforward way by summing the contribution coming from the different families of incident waves. In this

case, the phase shift between waves of different nature but having the same frequency ω may have a deep impact on the emitted field.

Let us illustrate that point considering the emitted pressure field in the case of a mixed vortical-entropic incident monochromatic field. The downstream pressure field is

$$\frac{p_2'}{\gamma \bar{p}_2} = \left(A_v Z_{va} + A_s Z_{sa}\right) e^{-k_a \eta x} e^{\imath (\boldsymbol{k}_a \cdot \boldsymbol{x} - \omega t)}. \tag{16.128}$$

For the sake of clarity, the complex amplitude of the entropy mode is rewritten as

$$A_s = A_v c_{sv} e^{-\imath \phi_{sv}}, \tag{16.129}$$

where c_{sv} and ϕ_{sv} are real parameters related to the energy ratio and the phase shift between the two incoming waves, respectively. Therefore, one has

$$\frac{p_2'}{\gamma \bar{p}_2} = \left(Z_{va} + c_{sv} e^{\imath \phi_{sv}} Z_{sa}\right) e^{-k_a \eta x} A_v e^{\imath (\boldsymbol{k}_a \cdot \boldsymbol{x} - \omega t)}, \tag{16.130}$$

leading to

$$\frac{\overline{p_2'^2}(x; k, \alpha)}{\gamma^2 \bar{p}_2^2} = \overline{|A_v|^2} e^{-2 k_a \eta x} \left(|Z_{va}|^2 + c_{sv}^2 |Z_{sa}|^2 + 2 c_{sv} \Re\left(Z_{va} Z_{sa}^* e^{-\imath \phi_{sv}}\right)\right). \tag{16.131}$$

It is seen that the last term explicitly depends on ϕ_{sv}, showing that the variance of the emitted pressure fluctuations can be modulated by manipulating the phase shift. Similar results are obtained in a straightforward way for all emitted fields and for other combinations of incident waves, including the case of an incident field containing fluctuations belonging to the three Kovasznay physical groups. In the later case, two phase shift parameters must be introduced, leading to a much wider class of possible results.

These analysis is extended to the case of a mixed turbulent incident field writing the statistical correlation of the complex amplitudes as

$$\overline{A_s A_v^*} = c_{sv} \overline{|A_s|^2} e^{\imath \phi_{sv}} \tag{16.132}$$

and deriving the associated expression for second-order moments. It is worth keeping in mind that, when an incident stochastic turbulent field is considered, $\overline{A_v A_a^*} = \overline{A_s A_a^*} = 0$ because of the difference in the propagation speeds of the waves. Therefore a single phase shift parameter must be considered. This is illustrated by the expression of the pressure variance associated to Eq. (16.131) which is equal to

$$\begin{aligned}\frac{\overline{{p_2'}^2}(x)}{\gamma^2\bar{p}_2^2} &= 2\pi\int_{k=0}^{+\infty}\int_{\alpha=0}^{+\pi/2}\frac{\overline{{p_2'}^2}(x;k,\alpha)}{\gamma^2\bar{p}_2^2}k^2\sin\alpha\,d\alpha\,dk\\ &= \underbrace{2\pi\int_{k=0}^{+\infty}\int_{\alpha=0}^{+\pi/2}\overline{|A_v|^2}e^{-2k_a\eta x}|Z_{va}|^2k^2\sin\alpha\,d\alpha\,dk}_{\text{vorticity-vorticity interaction}}\\ &\quad+\underbrace{2\pi\int_{k=0}^{+\infty}\int_{\alpha=0}^{+\pi/2}\overline{|A_v|^2}e^{-2k_a\eta x}c_{sv}^2|Z_{sa}|^2k^2\sin\alpha\,d\alpha\,dk}_{\text{entropy-entropy interaction}}\\ &\quad+\underbrace{2\pi\int_{k=0}^{+\infty}\int_{\alpha=0}^{+\pi/2}\overline{|A_v|^2}e^{-2k_a\eta x}2c_{sv}\Re\left(Z_{va}Z_{sa}^*e^{-\imath\phi_{sv}}\right)k^2\sin\alpha\,d\alpha\,dk}_{\text{vorticity-entropy interaction}}.\end{aligned}\tag{16.133}$$

This expression is fully general, and both c_{sv} and ϕ_{sv} can be taken as scale-dependent parameters, i.e. to be functions of k. The cross-correlation can be also expressed in terms of $\overline{u_1'T_1'}$, since

$$\frac{\overline{u_1'T_1'}}{U_1\bar{T}_1} = 2\Re\overline{A_sA_v^*}.\tag{16.134}$$

Fully general expressions for the Reynolds stresses and other turbulent fluxes downstream the shock are obtained by summing all possible interactions. A few examples are given below:

$$\begin{aligned}\frac{\overline{\rho_2'^2}}{\bar{\rho}_2^2} &= \sum_i\sum_j\iiint\overline{A_iA_j^*}Z_{is}Z_{js}^*d^3\boldsymbol{k}\\ &\quad+\sum_i\sum_j\iiint_{\alpha\le\alpha_c}\overline{A_iA_j^*}Z_{ia}Z_{ja}^*d^3\boldsymbol{k},\end{aligned}\tag{16.135}$$

$$\begin{aligned}\frac{\overline{u_2'^2}}{U_2^2} &= \sum_i\sum_j\iiint\overline{A_iA_j^*}Z_{i\,pol}Z_{j\,pol}^*\sin^2\alpha_s d^3\boldsymbol{k}\\ &\quad+\sum_i\sum_j\iiint_{\alpha\le\alpha_c}\overline{A_iA_j^*}Z_{ia}Z_{ja}^*\cos^2\alpha_a d^3\boldsymbol{k},\end{aligned}\tag{16.136}$$

$$\begin{aligned}\frac{\overline{v_2'^2}+\overline{w_2'^2}}{2U_2^2} &= \frac{1}{2}\sum_i\sum_j\iiint\overline{A_iA_j^*}\left(Z_{i\,pol}Z_{j\,pol}^*\cos^2\alpha_s+Z_{i\,tor}Z_{j\,tor}^*\right)d^3\boldsymbol{k}\\ &\quad+\frac{1}{2}\sum_i\sum_j\iiint_{\alpha\le\alpha_c}\overline{A_iA_j^*}Z_{ia}Z_{ja}^*\sin^2\alpha_a d^3\boldsymbol{k},\end{aligned}\tag{16.137}$$

$$\frac{\overline{\rho_2' u_2'}}{\bar{\rho}_2 U_2} = \sum_i \sum_j \iiint \overline{A_i A_j^*} Z_{i\,pol} Z_{j\,s}^* \sin \alpha_s d^3\boldsymbol{k} + 0, \tag{16.138}$$

where $i, j = pol, tor, s, a$. The first term in the right-hand side of above equations is related to the contribution of emitted poloidal and toroidal vortical fluctuations and entropy fluctuations to the Reynolds stresses, while the second one represents the contributions of the radiated acoustic field. Here, only far-field contributions have been retained (i.e. $\eta = 0, \zeta = 1$) and scalar $\boldsymbol{k}$-independent coefficients have been omitted for the sake of simplicity.

16.5.4 Linearized Jump Relations for Reynolds Stresses and Turbulent Fluxes

The effect of a shock wave on turbulence is usefully analyzed looking at the transfer functions for the Reynolds stresses, which is of great importance for researches dealing with the development of RANS turbulence models for shocked flows since they provide consistency constraints for RANS models at the shock front. Considering the unknown vector $\boldsymbol{X}_m$, $(m = 1, 2)$:

$$\boldsymbol{X}_m = \left(\frac{\overline{\rho_m'^2}}{\bar{\rho}_m^2}, \frac{\overline{u_m'^2}}{U_m^2}, \frac{\overline{v_m'^2} + \overline{w_m'^2}}{2U_m^2}, \frac{\overline{\rho_m' u_m'}}{\bar{\rho}_m U_m} \right)^T \tag{16.139}$$

the emitted Reynolds stresses can be rewritten as functions of the incident ones under the form

$$\boldsymbol{X}_2 = \mathbf{S}\boldsymbol{X}_1 \tag{16.140}$$

where the 4×4 matrix $\mathbf{S}$ is the transfer matrix for Reynolds stresses, where S_{ij} denotes the transfer function between X_{1_j} and X_{2_i}. Expressions for the components of $\mathbf{S}$ are cumbersome, and the reader is referred to Griffond and Soulard (2012) for exhaustive detailed expressions of all these terms. Similar expressions can be derived for any set of second-order statistical moments of fluctuating quantities.

16.6 Further Analytical Work: Exact and Asymptotic LIA Solutions Based on Laplace Transform

Further analytical work can be performed seeking for analytical solutions of the LIA equations. Such an analysis has been carried out in a series a of papers for incident isotropic adiabatic turbulence (Wouchuk et al. 2009), pure incident acoustic turbulence (Huete et al. 2012b), pure indicent isotropic density fluctuations (including the reshock problem) (Huete et al. 2012a).

16.6.1 Problem Statement and Formulation

To obtain analytical solutions, the problem is recast as the propagation of a planar shock wave with constant speed $\boldsymbol{De}_x$ in a static (in the laboratory frame) sinusoidal perturbation field of vortical, acoustic or density nature. The upstream perturbation is of the form $A\cos(k_x x)\sin(k_y y)$, and the normalized emitted field is assumed to be like

$$\frac{\rho_2'(\boldsymbol{x},t)}{\bar{\rho}_2} = A\tilde{\rho}(x,t)\cos(k_y y), \tag{16.141}$$

$$\frac{u_2'(\boldsymbol{x},t)}{a_2} = A\tilde{u}(x,t)\cos(k_y y), \tag{16.142}$$

$$\frac{v_2'(\boldsymbol{x},t)}{a_2} = A\tilde{v}(x,t)\cos(k_y y), \tag{16.143}$$

$$\frac{p_2'(\boldsymbol{x},t)}{\bar{\rho}_2 a_2^2} = A\tilde{p}(x,t)\cos(k_y y). \tag{16.144}$$

The associated linearized Euler equation for mass, x-momentum, y-momentum and pressure are

$$\frac{\partial\tilde{\rho}}{\partial\tau} = -\frac{\partial\tilde{u}}{\partial(k_y x)} - \tilde{v}, \tag{16.145}$$

$$\frac{\partial\tilde{u}}{\partial\tau} = -\frac{\partial\tilde{p}}{\partial(k_y x)}, \tag{16.146}$$

$$\frac{\partial\tilde{u}}{\partial\tau} = \tilde{p}, \tag{16.147}$$

$$\frac{\partial\tilde{\rho}}{\partial\tau} = \frac{\partial\tilde{p}}{\partial\tau}, \tag{16.148}$$

the last equation being obtained assuming that the flow is adiabatic behind the shock wave.

These equations can be combined to recover a wave equation for pressure disturbances:

$$\frac{\partial^2\tilde{p}}{\partial\tau^2} = \frac{\partial^2\tilde{p}}{\partial(k_y x)^2} - \tilde{p}, \tag{16.149}$$

where $\tau = k_y a_2 t$ is a dimensionless time unit. This equation is a particular case of the *telegraphist equation* for lossy transmission line. The boundary conditions are obtained considering the Rankine-Hugoniot jump conditions. Initial conditions should also be provided, allowing for the analysis of transient phenomena and impulsive start.

To this end, it is convenient to introduce the following change of variables prior to applying the Laplace transform:

$$x = r\sinh\chi, \quad \tau = r\cosh\chi, \tag{16.150}$$

leading to

$$-\sinh\chi\tilde{h} + \cosh\chi\frac{\partial\tilde{p}}{\partial r} + \frac{\cosh\chi}{r}\frac{\partial\tilde{u}}{\partial\chi} - \sinh\chi\frac{\partial\tilde{u}}{\partial r} + \tilde{v} = 0,\ \tilde{h} = \frac{1}{r}\frac{\partial\tilde{p}}{\partial\chi} \tag{16.151}$$

$$-\frac{\sinh\chi}{r}\frac{\partial\tilde{u}}{\partial\chi} + \cosh\chi\frac{\tilde{u}}{r} + \cosh\chi\tilde{h} - \sinh\chi\frac{\partial\tilde{p}}{\partial r} = 0 \tag{16.152}$$

$$-\frac{\sinh\chi}{r}\frac{\partial\tilde{v}}{\partial\chi} + \cosh\chi\frac{\tilde{v}}{r} = \tilde{p} \tag{16.153}$$

$$r\frac{\partial^2\tilde{p}}{\partial r^2} + \frac{\partial\tilde{p}}{\partial r} + r\tilde{p} = \frac{\partial\tilde{h}}{\partial\chi} \tag{16.154}$$

for the mass, x-momentum, y-momentum and pressure telegraphist equation, respectively.

16.6.2 Solving the Problem via Laplace Transform

The next step to obtain exact analytical solutions is to introduce the variable change $s = \sinh q$ and to apply the Laplace transform, which is defined for a dummy function $\phi(\chi, r)$ as

$$\breve{\phi}(\chi, s) = \int_0^{+\infty} \phi(\chi, r)e^{-sr}dr$$

to Eq. (16.154), yielding the set of coupled equations:

$$\frac{\partial}{\partial q}(\cosh q\breve{p}) + \frac{\partial\breve{h}}{\partial\chi} = 0,\ \frac{\partial}{\partial\chi}(\cosh q\breve{p}) + \frac{\partial\breve{h}}{\partial q} = 0 \tag{16.155}$$

which can be integrated to find the solution

$$\breve{p}(\chi, q) = \frac{(q-\chi)F_1 + F_2}{\cosh q}, \quad \breve{h}(\chi, q) = (q-\chi)F_1 + F_2 \tag{16.156}$$

where the functions F_1 and F_2 are given by the initial conditions and the linearized jump relations. They are related to sound waves radiated downstream the shock and to the incident acoustic perturbations, respectively.

The solution in the physical space for the pressure fluctuations *on the shock front* is then obtained using the inverse Laplace transform, which takes the form of the

following integral in the complex plane (subscript s denotes quantity evaluated at the shock wave position):

$$\tilde{p}_s(r_s) = \frac{1}{2\pi\imath}\int_{c-\imath\infty}^{c+\imath\infty} \breve{p}_s(s)e^{sr_s}ds \tag{16.157}$$

where c is a real number to the right of the singularities of $\breve{p}_s(s)$. The exact expression of $\breve{p}_s(s)$ is obtained combining the jump relations and the initial conditions, and is therefore case-dependent. This integral is computed selecting a closed integration path and using the residue theorem, taking care of singularities. For a shock wave moving in an perfect gas, the only singularities are the branch points at $s = \pm\imath$, which are associated to the generation of evanescent acoustic waves downstream the shock that decay asymptotically in time as $t^{-3/2}$ and poles $s = \pm\imath\zeta_0$, which are related to constant amplitude oscillations, with

$$\zeta_0 = \frac{\mathfrak{C}M_2}{\sqrt{1-M_2^2}}\frac{k_x}{k_y} = \frac{\mathfrak{C}M_2}{\sqrt{1-M_2^2}}\frac{1}{|\tan\alpha|} \tag{16.158}$$

The final expression of the general solution is

$$\tilde{p}_s(r_s) = -\frac{2}{\pi}\int_0^1 f_p(z)\cos(zr_s)dz + \frac{2\psi}{\pi}\int_0^1 f_p(z)\left(\frac{\cos(zr_s) - cos(\zeta_0 r_s)}{\zeta_0^2 - z^2}\right)dz \tag{16.159}$$

where

$$f_p(z) = \frac{4M_1^4M_2^2z^2\sqrt{1-z^2}}{4M_1^2M_2^2z^2(1-z^2) + [(M_1^2+1)z^2 - M_1^2]^2} \tag{16.160}$$

where $r_s = \tau\sqrt{1-M_2^2}$ and in which the coefficient ψ depends on initial conditions, i.e. shock strength, polytropic index γ and incident perturbations. One can distinguish between long- ($\zeta_0 < 1$) and short-wave ($\zeta_0 > 1$) contributions, along with constant and evanescent contributions.

Long-time behavior, i.e. statistically steady regime similar to those analyzed thanks to the modal analysis discussed in previous sections is associated to constant contributions, which can be computed as asymptotic solutions for $t \to +\infty$. They are found considering the residues at the poles $s = \pm\imath\zeta_0$:

$$\lim_{t\to+\infty}\tilde{p}_s(r_s) = \begin{cases} e_{l1}\cos(\zeta_0 r) + e_{l2}\sin(\zeta_0 r) & \zeta_0 \le 1 \\ e_s\cos(\zeta_0 r) & \zeta_0 \ge 1 \end{cases} \tag{16.161}$$

with

$$e_{l1} = \frac{2M_1^2M_2^2[M_1^2 - (M_1^2+1)\zeta_0^2]\psi}{4M_1^4M_2^2\zeta_0^2(1-\zeta_0^2) + [M_1^2 - (M_1^2+1)\zeta_0^2]^2} \tag{16.162}$$

$$e_{l2} = \frac{4M_1^4 M_2^2 \zeta_0 \sqrt{1-\zeta_0^2}\psi}{4M_1^4 M_2^2 \zeta_0^2 (1-\zeta_0^2) + [M_1^2 - (M_1^2+1)\zeta_0^2]^2} \tag{16.163}$$

$$e_s = -\frac{2M_1^2 M_2 \psi}{2M_1^2 M_2 \zeta_0 \sqrt{1-\zeta_0^2} - [M_1^2 - (M_1^2+1)\zeta_0^2]}. \tag{16.164}$$

The link with physical variables is easily seen, since $\zeta_0 r_s = Dk_x t$.
A companion solution is found for the shock corrugation:

$$\tilde{\xi}(r_s) = \frac{\sin(\zeta_0 r_s)}{\zeta_0 \sqrt{1-M_2^2}} - \frac{(\gamma+1)}{2\pi M_2 \sqrt{1-M_2^2}} \int_0^1 f_p(z) \frac{\sin(z r_s)}{z} dz + \frac{(\gamma+1)\psi}{2\pi M_2 \sqrt{1-M_2^2}} \int_0^1 \frac{f_p(z)}{z\zeta_0} \left(\frac{\zeta_0 \sin(z r_s) - z \sin(\zeta_0 r)}{\zeta_0^2 - z^2} \right) dz \tag{16.165}$$

which can also be split into short- and long-wave contributions and constant and evanescent contributions. Solutions for other variables are deduced from the jump relations. Detailed solutions will not be displayed here for the sake of clarity, since they involve very cumbersome formula that are available in original references.

16.6.3 Structure of the Emitted Field

The existence of propagating and evanescent, non-propagating pressure waves downstream the shock (See Sect. 16.2) can also be recovered using the Laplace-transform-based solutions. Denoting $\chi_s = \tanh^{-1} M_2$ the value of χ at the shock front, the pressure in the downstream region is given by

$$\tilde{p}(\chi, q) = \frac{\cosh(q + \chi_s - \chi)}{\cosh q} \tilde{p}_s(q + \chi_s - \chi). \tag{16.166}$$

After some algebra, one can prove that the pressure waves will contribute with imaginary poles to the solution (i.e. will exhibit non-evanescent contributions) if and only if

$$\zeta_0 + \sqrt{\zeta_0^2 - 1} \geq \exp(\chi_s - \chi), \quad \zeta_0 > 1 \tag{16.167}$$

meaning that long-wave contributions such that $\zeta_0 < 1$ to the pressure field correspond to non-propagating damped acoustic waves, while short-wave contributions with $\zeta_0 > 1$ are related to constant-amplitude propagating acoustic mode with longitudinal wave number $\tilde{k}_x$ given by

$$\frac{\tilde{k}_x}{k_y} = \frac{M_2\zeta_0 - \sqrt{\zeta_0^2 - 1}}{\sqrt{1 - M_2^2}}. \tag{16.168}$$

Therefore, the near-field solution downstream the shock will depend on both short- and long-wave contributions, while the far-field is governed by the sole short-wave branch. Thanks to the definition (16.158), the critical value of the incident wave angle α_c associated to $\zeta_0 = 1$ is computed as

$$\sin\alpha_c = M_1^2\sqrt{\frac{\gamma+1}{2\gamma M_1^4 + (3-\gamma)M_1^2 - 2}}. \tag{16.169}$$

For $\alpha > \alpha_c$ only evanescent acoustic waves will be emitted, while a far-field acoustic field will be radiated if $\alpha < \alpha_c$.

For emitted vorticity and entropy modes, it is observed that both long- and short-wave branches contribute to the far-field solution.

16.6.4 Reconstruction of Statistical Moments of the Emitted Field

Useful quantities for physical analysis of the emitted turbulent field can be reconstructed thanks to the analytical solutions found above. An important point is that all solutions for a perfect gas can be written as explicit functions of the adiabatic exponent γ and the Mach number M_1. A complete analysis of the asymptotic behavior in the case of weak shock ($M_1 - 1 \to 0$), strong shock ($M_1 \to +\infty$) along with combination with high gas compressibility ($\gamma \to 1$) and low gas compressibility ($\gamma \to +\infty$) can also be carried out, including the separation between the contributions of vorticity, acoustic and entropy modes.

16.7 A Posteriori Assessment of LIA in the Canonical Interaction Case

A said at the beginning of this section, the LIA is observed to compare well to DNS and experimental data if $M_{t_2} \leq 0.1M_2$. Convergence of DNS results toward LIA prediction is assessed in Ryu and Livescu (2014). But a finer analysis reveals that some discrepancies arise in predicting the emitted field associated to incident waves with an angle of incidence close to the critical angle that demarcates propagating and evanescent waves. The rationale for that is that the energy of the emitted waves is high near the critical angle is high (the transfer functions exhibit a strong, narrow peak for $\alpha = \alpha_c$), leading to a breakdown of the small perturbation hypothesis.

The amplitude of the fluctuations being too high, the linear approximation should be refined to account for additional non linear effects. It is also observed that the inviscid approximation may be a problem, since it may leads to diverging amplification ratio in the limit of strong shocks $M_1 \to \infty$ in highly compressible fluids $\gamma \to 1$. In such a case, the longitudinal wavelength of emitted waves tends to zero, and viscous effects should become dominant. Therefore, regularizing effects of viscosity should be taken into account, as proposed in Miller and Ahrens (1991).

16.8 Extending LIA: I. Interaction with Rarefaction Waves

The LIA theory was originally developed to analyze the canonical interaction between a planar shock wave and a small disturbance. It can be extended to the case of the interaction between a rarefaction wave and turbulent fluctuations (Griffond and Soulard 2012). The LIA solution is developed to predict the emitted field in the downstream region outside the rarefaction wave, given the upstream incident perturbation field outside the rarefaction wave and the conservation equation that hold inside the rarefaction wave. As an output, complex transfer functions for Kovasznay modes similar to those found for the case of the shock wave will be obtained. The analysis will be restricted to non-acoustic waves, since results for this waves is much more complicated than for entropy and vorticity waves and they cannot be cast in the transfer function form. This is due to the fact that for non-acoustic waves the results do not depend on the width of the rarefaction wave but only on the compression ratio, while for acoustic waves the solution explicitly depends on the wave width.

16.8.1 Linearized Governing Equations

The problem is efficiently described considering both vorticity and entropy, which are governed by the following equations:

$$\left(\frac{\partial}{\partial t} + \boldsymbol{u}\cdot\nabla\right) s = 0, \tag{16.170}$$

$$\left(\frac{\partial}{\partial t} + \boldsymbol{u}\cdot\nabla\right)\left(\frac{\boldsymbol{\omega}}{\rho}\right) = \left(\frac{\boldsymbol{\omega}}{\rho}\cdot\nabla\right)\boldsymbol{u} + \frac{1}{\rho^3}\nabla\rho\times\nabla p. \tag{16.171}$$

Inside the rarefaction wave, one has a null base vorticity, i.e. $\nabla\times\boldsymbol{u}_0 = 0$ and a uniform base entropy $s_0 = cst$. Since the base flow is unidirectional, one has $\nabla\rho_0\times\nabla p_0 = 0$. Here, subscript 0 refers to base flow quantities inside the rarefaction wave. The linearized system associated to small disturbances is

$$\frac{d}{dt}s' = 0, \quad \frac{d}{dt} \equiv \left(\frac{\partial}{\partial t} + \boldsymbol{u}_0 \cdot \nabla\right), \tag{16.172}$$

$$\frac{d}{dt}\left(\frac{\boldsymbol{\omega}'}{\rho_0}\right) = \left(\frac{\boldsymbol{\omega}'}{\rho_0} \cdot \nabla\right)\boldsymbol{u}_0 + \frac{1}{\rho_0^3}\left(\nabla\rho' \times \nabla p_0 + \nabla\rho_0 \times \nabla p'\right). \tag{16.173}$$

Since s_0 is uniform, one has $\nabla s_0 = 0$ and therefore $\frac{\nabla p_0}{p_0} = \gamma\frac{\nabla\rho_0}{\rho_0}$, yielding

$$\frac{d}{dt}\left(\frac{\boldsymbol{\omega}'}{\rho_0}\right) = \left(\frac{\boldsymbol{\omega}'}{\rho_0} \cdot \nabla\right)\boldsymbol{u}_0 + \frac{\gamma p_0}{\rho_0^3}\nabla\rho_0 \times \left(\frac{\nabla p'}{\gamma p_0} - \frac{\nabla\rho'}{\rho_0}\right). \tag{16.174}$$

16.8.2 Case of a Single Incident Wave

The evolution of a single incident wave with wavevector $\boldsymbol{k}$ across the rarefaction wave is now addressed. To this end, the cylindrical coordinates will be used for the sake of simplicity. Every fluctuating quantity q' is expressed as

$$q'(x, r, \phi, t) = q'(x, t)e^{\imath kr\sin\alpha}, \tag{16.175}$$

where α is the angle between $\boldsymbol{k}$ and $\boldsymbol{e}_x$. Since the base flow is along the direction $\boldsymbol{e}_x$, the baroclinic term in the right hand side of Eq. (16.174) is parallel to $\boldsymbol{e}_\phi$. As a consequence, the evolution of the three component of fluctuating vorticity are

$$\frac{d}{dt}\left(\frac{\omega_x'}{\rho_0}\right) = \frac{\omega_x'}{\rho_0}\frac{\partial u_{0_x}}{\partial x} \iff \frac{d}{dt}\left(\omega_x'\right) = 0, \tag{16.176}$$

$$\frac{d}{dt}\left(\frac{\omega_r'}{\rho_0}\right) = 0, \tag{16.177}$$

$$\frac{d}{dt}\left(\frac{\omega_\phi'}{\rho_0}\right) = \frac{a_0^2}{\rho_0^2}\frac{\partial\rho_0}{\partial x}\frac{\partial\mathring{s}'}{\partial x}, \tag{16.178}$$

where $\mathring{s} = \frac{1}{\gamma}\ln\left(\frac{p}{\rho^\gamma}\right)$ is related to the perfect gas entropy by $\mathring{s} = s/c_p$.

The next step consists of introducing the similarity coordinates classically used to describe rarefaction wave, i.e. operating the change of variables $(x, t) \to (\xi = x/t, t)$. Using this mapping, the head and the tail of the base rarefaction wave are associated to constant values of ξ. The upstream and downstream regions are defined as $x/t < \xi_u$ and $x/t > \xi_d$, respectively. Rewritting the above equations using the new variables along the characteristic lines given by $\frac{d\xi}{dt} = (u_{0_x} - \xi)/t$, one obtains the following Lagrangian linearized system

$$\frac{d}{d\xi}\mathring{s}' = 0, \tag{16.179}$$

$$\frac{d}{d\xi}\omega_x' = 0, \tag{16.180}$$

$$\frac{d}{d\xi}\left(\frac{\omega_r'}{\rho_0}\right) = 0, \tag{16.181}$$

$$\frac{d}{d\xi}\left(\frac{\omega_\phi'}{\rho_0}\right) = \imath k \sin\alpha \frac{a_0^2}{\rho_0^2}\frac{d\rho_0}{d\xi}\mathring{s}'. \tag{16.182}$$

This is an autonomous ordinary differential system in ξ, whose solution is self-similar, implying the dependency of the results with respect to the rarefaction wave width which will play a role similar to the shock strength in the canonical case. The downstream fluctuating field is now computed integrating this system along the characteristic lines, leading to

$$\mathring{s}_2' = \mathring{s}_1', \tag{16.183}$$

$$\omega_{x_2}' = \omega_{x_1}', \tag{16.184}$$

$$\omega_{r_2}' = \mathfrak{C}\omega_{r_1}', \tag{16.185}$$

$$\omega_{\phi_2}' = \mathfrak{C}\omega_{\phi_1}' + \frac{2\imath a_1 k \sin\alpha}{\gamma - 3}(\mathfrak{C}^{(\gamma-1)/2} - \mathfrak{C})\mathring{s}_1', \tag{16.186}$$

where subscripts 1 and 2 refer to states on the characteristic line under consideration at $\xi = \xi_u$ (upstream field) and $\xi = \xi_d$ (downstream field), respectively. The compression ratio $\mathfrak{C} = \bar{\rho}_2/\bar{\rho}_1$ is defined as in the case of shock wave, but it is important noting that it is lower than 1 for rarefaction waves.

16.8.3 Transfer Functions Associated to Kovasznay Modes

The transfer functions for Kovasznay modes are now obtained considering the incident upstream fluctuating field as a combination of a poloidal vorticity wave with amplitude A_{pol}, a toroidal vorticity wave with amplitude A_{tor} and an entropy wave with amplitude A_s. The same nomenclature as in Sect. 16.4) will be used hereafter. The upstream and downstream fields can be written as

- Upstream field: $(x/t < \xi_u)$

$$\left(\mathring{s}', \frac{\omega_x'}{a_1}, \frac{\omega_r'}{a_1}, \frac{\omega_\phi'}{a_1}\right) = \left(A_s, A_{tor}\imath k \sin\alpha, -A_{tor}\imath k \cos\alpha, -A_{pol}\imath k\right) e^{\imath\left(kx\cos\alpha + kr\sin\alpha - k\imath U_1 \cos\alpha\right)} \tag{16.187}$$

- Downstream field: $(x/t > \xi_d)$

$$\left(\mathring{s}', \frac{\omega_x'}{a_2}, \frac{\omega_r'}{a_2}, \frac{\omega_\phi'}{a_2}\right) = (A_s, A_{tor}\imath k_s \sin\alpha_s Z_{tor\,tor}, -A_{tor}\imath k_s \cos\alpha_s Z_{tor\,tor}, -\imath k_s (A_{pol} Z_{pol\,pol} + A_{tor} Z_{tor\,tor})) \, e^{\imath(k_s x \cos\alpha_s + k_s r \sin\alpha_s - k t U_2 \cos\alpha_s)} \tag{16.188}$$

where the emitted field wave number $\boldsymbol{k}_s$ and angle α_s are given by:

$$k_{s_x} = \mathfrak{C} k_x \Longleftrightarrow k_s \cos\alpha_s = \mathfrak{C} k \cos\alpha \tag{16.189}$$

$$k_{s_r} = k_r \Longleftrightarrow k_s \sin\alpha_s = k \sin\alpha \tag{16.190}$$

yielding $\mathfrak{C} \tan\alpha_s = \tan\alpha$ as for non-acoustic waves in the case of shock/turbulence interaction. The associated expressions for the complex transfer functions are:

$$\begin{array}{ccc} Z_{tor\,tor} = \mathfrak{C}^{(1-\gamma)/2} & Z_{tor\,pol} = 0 & Z_{tor\,s} = 0, \\ Z_{pol\,tor} = 0 & Z_{pol\,pol} = \frac{\sin\alpha_s}{\sin\alpha} \mathfrak{C}^{(3-\gamma)/2} & Z_{pol\,s} = 0, \\ Z_{s\,tor} = 0 & Z_{s\,pol} = \frac{2\sin\alpha_s}{\gamma-3}(\mathfrak{C}^{(3-\gamma)/2} - 1) & Z_{s\,s} = 1. \end{array} \tag{16.191}$$

These results show that, as in the shock wave case, the toroidal vorticity mode is decoupled from the rest of the system. Conservation of entropy leads to the fact that vortical modes cannot generate entropy, along with $Z_{s\,s} = 1$, but the upstream entropy mode as an impact on the downstream poloidal vorticity mode.

16.8.4 Transfer Functions Associated with Reynolds Stresses

The effect of a rarefaction wave on turbulence can be analyzed looking at the changes on the Reynolds stresses. Keeping in mind that the analysis is restricted to incoming non-acoustic waves, formula identical to those given in Sect. 16.5.4 for shock-turbulence interactions can be used. Coefficients of 4×4 transfer matrix $\mathbf{S}$ or Reynolds stresses are plotted as function of the compression factor $\mathfrak{C}$ for $\gamma = 7/5$ in Fig. 16.7, where rarefaction waves correspond to $\mathfrak{C} < 1$ and shock wave to $\mathfrak{C} > 1$.

Several observations can be made:

- Rarefaction waves and shock waves have a comparable efficiency in creating turbulence, since the magnitude of terms S_{1i} is the same for $\mathfrak{C} < 1$ and $\mathfrak{C} > 1$.
- Rarefaction waves and shock waves yield opposite signs on S_{23}, showing that they produce turbulent mass fluxes with opposite signs. This can be understood remembering that the baroclinic vorticity production term is proportional to $\nabla\rho \times \nabla p$, and that the longitudinal pressure gradients associated with rarefaction and

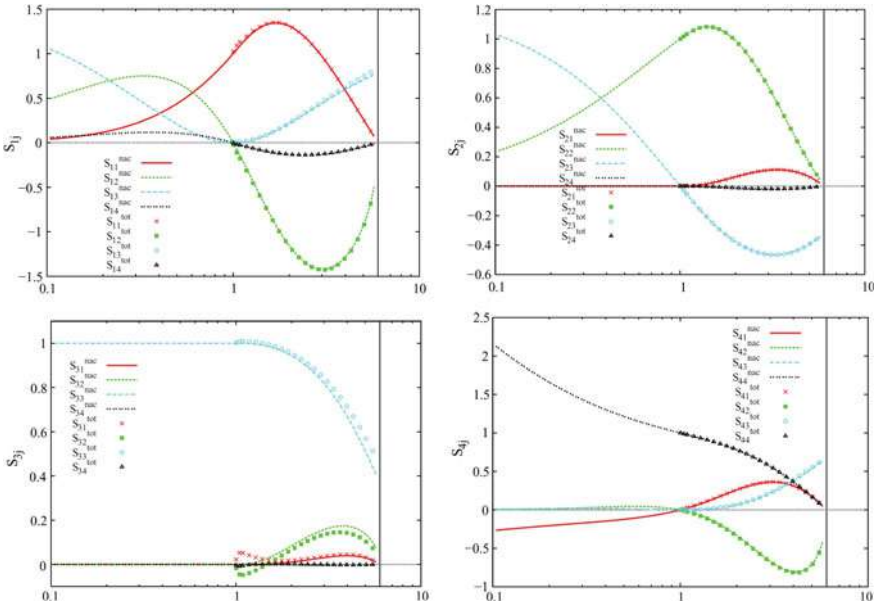

Fig. 16.7 Transfer functions S_{ij} associated to Reynolds stresses versus the compression ratio $\mathfrak{C}$ for both rarefaction waves ($\mathfrak{C} < 1$) and shock waves ($\mathfrak{C} > 1$) for $\gamma = 7/5$. Vertical lines denotes the asymptotic limit $M_1 = +\infty$. $S_{ij_{nac}}$ denotes the results obtained neglecting the contribution of the emitted acoustic field to the Reynolds stresses (but not its effects during the turbulence/wave interaction). Courtesy of J. Griffond and O. Soulard. From Griffond and Soulard (2012) with permission of AIP

shock wave have opposite sign, resulting in the generation of tangential vorticity component and induced shock normal mass flux of opposite sign.

- The emitted acoustic component has a negligible contribution on the emitted Reynolds stresses, except for specific volume variance in the weak shock case.

16.9 Extending LIA: II. Case of Non-reacting Binary Mixtures of Perfect Gas

LIA can be extended to the case of the mixture of two perfect gas, accounting for differences in molar mass and constant volume specific heat (Griffond 2005; Griffond et al. 2010). This enriched physical system involves two new perturbation waves with respect to the canonical case, namely *molar mass waves* and *constant volume specific heat waves*. The derivation of the transfer functions is basically the same as in the canonical case discussed in Sects. 16.1–16.7. Therefore, for the sake of brevity, only main modifications to the derivation of the transfer functions related to the canonical case will be given here. A full detailed description is available in Griffond (2005).

16.9.1 Governing Equations, Linearized System and Jump Relations

One considers here the non-reacting mixture of two perfect gas, a and b, which is also to be a perfect gas itself. The associated equation of state is

$$\frac{p}{\rho} = \frac{\mathcal{M}}{\mathcal{R}} T = (\gamma - 1)e, \quad e = c_v T, \tag{16.192}$$

where $\mathcal{R}$, $\mathcal{M}$, c_v and γ are the perfect gas constant, the molar mass, the constant volume specific heat and the specific heat ratio, respectively. It is important noting that the later three quantities are not constant as in a pure fluid since they explicitly depend on the local mixture composition. Let Y and $(1-Y)$ denote the mass fraction of the a gas and the b gas, respectively. Two mixture models can be used that lead to the same LIA results:

- The *partial-density partial-pressure isothermal model*:

$$\rho = \rho_a + \rho_b, \quad \rho_a = \rho Y, \rho_b = (1 - Y)\rho, \tag{16.193}$$

$$T = T_a = T_b, \tag{16.194}$$

$$p = p_a + p_b, \quad p_i = \rho_i \frac{\mathcal{M}}{\mathcal{R}_i} T = (\gamma_i - 1)\rho_i c_{v_i} T. \tag{16.195}$$

- The *isobaric-isothermal model*:

$$\frac{1}{\rho} = \frac{Y}{\rho_a} + \frac{1 - Y}{\rho_b}, \tag{16.196}$$

$$T = T_a = T_b, \tag{16.197}$$

$$p = p_a = p_b. \tag{16.198}$$

The mixture molar mass, specific heat ratio and constant volume specific heat are given by the following relations

$$\mathcal{M} = \frac{\mathcal{M}_a \mathcal{M}_b}{Y\mathcal{M}_b + (1 - Y)\mathcal{M}_a}, \tag{16.199}$$

$$\gamma = \frac{c_p}{c_v} = \frac{Y\, c_{p_a} + (1 - Y)\, c_{p_b}}{Y\, c_{v_a} + (1 - Y)\, c_{v_b}} = \frac{Y\, c_{v_a}\gamma_a + (1 - Y)\, c_{v_b}\gamma_b}{Y\, c_{v_a} + (1 - Y)\, c_{v_b}}, \tag{16.200}$$

$$c_v = Y\, c_{v_a} + (1 - Y)\, c_{v_b}, \quad c_p = Y\, c_{p_a} + (1 - Y)\, c_{p_b}. \tag{16.201}$$

The governing equations for the mixture (mass, momentum and energy conservation) are formally the same as for a pure perfect gas, see Eqs. (3.1)–(3.3) and they are supplemented by the following evolution equation for the mass fraction Y:

$$\frac{\partial \rho Y}{\partial t} + \nabla \cdot (\rho Y \boldsymbol{u}) = \nabla \cdot (\rho D \nabla Y) \tag{16.202}$$

where D is related to the molecular diffusion. It is important noting that the usual perfect gas equation of state must be replaced by the one for the mixture given above, with composition-dependent parameters.

The associated Rankine-Hugoniot jump relation systems (3.28)–(3.30) and (3.31)–(3.34) are also formally the same given that the pure fluid polytropic parameter γ is replaced by the mixture mean value $\bar{\gamma}$, coupled to the additional jump relation for the concentration Y:

$$[[\rho Y (u_n - u_s)]] = 0 \quad \Rightarrow \quad \left[\left[\bar{Y}\right]\right] = \left[\left[Y'\right]\right] = 0, \tag{16.203}$$

which shows that both mean and fluctuating concentration field are continuous at the shock front. The detailed jump relation system (16.82)–(16.85) is supplemented by

$$Y_2' = Y_1'. \tag{16.204}$$

Linearizing the mixture equation of state (16.192) and relations (16.199)–(16.201) yields

$$\frac{e'}{\bar{e}} = \frac{c_v'}{\bar{c}_v} + \frac{T'}{\bar{T}} = \frac{p'}{\bar{p}} - \frac{\rho'}{\bar{\rho}} + \frac{c_v'}{\bar{c}_v} - \frac{r'}{\bar{r}}, \tag{16.205}$$

or equivalently

$$\frac{p'}{\bar{p}} = \frac{\rho'}{\bar{\rho}} + \frac{T'}{\bar{T}} + \frac{r_a - r_b}{\bar{Y} r_a + (1 - \bar{Y}) r_b} c', \tag{16.206}$$

with $c_v' = (c_{v_a} - c_{v_b}) Y'$, $r = \mathcal{R}/\mathcal{M} = r_a Y + (1 - Y) r_b$ and $r' = (r_a - r_b) Y'$. The fluctuating internal energy e' is defined as

$$e = (Y\, c_{v_a} + (1 - Y) c_{v_b}) T \quad \Longrightarrow \quad e' = \bar{c}_v T' + Y' (c_{v_a} - c_{v_b}) \bar{T}. \tag{16.207}$$

Taking the continuity of c' into account, the linearized equation of state can be coupled to the linearized energy equation (16.85) to get

$$\begin{aligned} -\frac{1}{(\bar{\gamma} - 1) M_2^2} \frac{\rho_2'}{\bar{\rho}_2} + \frac{u_2'}{U_2} + \frac{1}{(\bar{\gamma} - 1) M_2^2} \frac{p_2'}{\bar{p}_2} + \frac{\imath \omega}{U_1} \mathfrak{C} (1 - \mathfrak{C}) \xi = \\ \mathfrak{C}^2 \left(-\frac{1}{(\bar{\gamma} - 1) M_1^2} \frac{\rho_1'}{\bar{\rho}_1} + \frac{u_1'}{U_1} + \frac{1}{(\bar{\gamma} - 1) M_1^2} \frac{p_1'}{\bar{p}_1} \right) \\ + \frac{1}{\bar{\gamma}(\bar{\gamma} - 1)} \left(\frac{\mathfrak{C}^2}{M_1^2} - \frac{1}{M_2^2} \right) \left(\frac{c_{v_a} - c_{v_b}}{\bar{c}_v} - \frac{r_a - r_b}{\bar{r}} \right) Y'. \end{aligned} \tag{16.208}$$

16.9.2 *Extended Kovasznay Decomposition for a Mixture of Perfect Gas*

The next step consists of defining Kovasnay modal waves for the mixture under consideration. Since it relies on a first-order small parameter expansion, the first question is to find criteria that will ensure that the disturbances will remain small with respect to mean flow quantities. Considering a binary mixture instead of a pure fluid involves two new conditions. Selecting r and c_v as control variables, one has

$$\epsilon_r = |r'/\bar{r}| \ll 1 \quad \text{and} \quad \epsilon_{c_v} = |c_v'/\bar{c}_v| \ll 1, \tag{16.209}$$

which can be recast in a more useful way a functions of Y

$$|\frac{(r_a - r_b)Y'}{r_a\bar{Y} + (1-\bar{Y})r_b}| \ll 1 \quad \text{and} \quad |\frac{(c_{v_a} - c_{v_b})Y'}{c_{v_a}\bar{Y} + (1-\bar{Y})c_{v_b}}| \ll 1. \tag{16.210}$$

Now introducing the two Atwood numbers

$$A_t^r = \frac{(r_a - r_b)}{\bar{r}}, \quad A_t^{c_v} = \frac{(c_{v_a} - c_{v_b})}{\bar{c}_v}, \tag{16.211}$$

the validity condition for LIA is

$$\epsilon_r = |A_t^r|A_Y \ll 1 \quad \text{and} \quad \epsilon_{c_v} = |A_t^{c_v}|A_Y \ll 1, \tag{16.212}$$

where A_Y denotes the amplitude of the concentration fluctuations. Keeping in mind the fact that the two conditions must be fulfilled to obtain relevant LIA results, one can identify two limit cases:

- Mixtures with small concentration fluctuations, i.e. $A_Y \ll 1$, and $O(1)$ Atwood numbers, i.e. significant differences in physical parameters of the two components.
- Mixtures with large concentration fluctuations, i.e. $A_Y = O(1)$ and small diferences in physical parameters, i.e. $A_t^r \ll 1$ and $A_t^{c_v} \ll 1$.

Validity criteria associated to other physical quantities are left unchanged with respect to the pure fluid case.

The second step consists of identifying the Kovasznay modes for the binary mixture, assuming that all validity criteria are fulfilled. The linearized system (3.39)–(3.41) for the pure fluid is supplemented by an equation for Y', which, in the inviscid case, is (still considering a uniform constant base flow in a reference frame associated to the base flow velocity $U\boldsymbol{e}_x$)

$$\frac{\partial Y'}{\partial t} = 0, \tag{16.213}$$

showing that concentration fluctuations are not influenced by acoustic, vortical and entropic waves. Therefore, the pure fluid waves are left unchanged and supplemented by concentration waves. The full set of Kovasznay modes for monochomatic waves with wave number $\boldsymbol{k}$ can then be rewritten as follows (in cylindrical coordinates for the sake of clarity)

$$\frac{u'_{x_1}}{U_1} = A_i\left(\delta_{i\,pol}\sin\alpha + \delta_{ia}\frac{\cos\alpha}{M_1}\right)e^{\imath(\boldsymbol{k}\cdot\boldsymbol{x}-\omega t)}, \tag{16.214}$$

$$\frac{u'_{r_1}}{U_1} = A_i\left(-\delta_{i\,pol}\cos\alpha + \delta_{ia}\frac{\sin\alpha}{M_1}\right)e^{\imath(\boldsymbol{k}\cdot\boldsymbol{x}-\omega t)}, \tag{16.215}$$

$$\frac{u'_{\phi_1}}{U_1} = A_i\delta_{i\,tor}e^{\imath(\boldsymbol{k}\cdot\boldsymbol{x}-\omega t)}, \tag{16.216}$$

$$\frac{\omega'_1}{U_1} = \imath kA_i(\delta_{iv}\sin\phi - \delta_{i\,tor}\cos\phi\cos\alpha)e^{\imath(\boldsymbol{k}_s\cdot\boldsymbol{x}-\omega t)}, \tag{16.217}$$

$$\frac{\rho'_1}{\bar{\rho}_1} = A_i(-\delta_{is} + \delta_{ia} - \delta_{iY}A_t^r)e^{\imath(\boldsymbol{k}\cdot\boldsymbol{x}-\omega t)}, \tag{16.218}$$

$$\frac{p'_1}{\gamma\bar{p}_1} = A_i\delta_{ia}e^{\imath(\boldsymbol{k}\cdot\boldsymbol{x}-\omega t)}, \tag{16.219}$$

$$\frac{T'_1}{\bar{T}_1} = A_i(\delta_{is} + (\gamma-1)\delta_{ia})e^{\imath(\boldsymbol{k}\cdot\boldsymbol{x}-\omega t)}, \tag{16.220}$$

$$\frac{s'_1}{c_p} = A_i(\delta_{is} + \delta_{iY}A_t^r)e^{\imath(\boldsymbol{k}\cdot\boldsymbol{x}-\omega t)}, \tag{16.221}$$

$$Y'_1 = A_i\delta_{iY}e^{\imath(\boldsymbol{k}\cdot\boldsymbol{x}-\omega t)}, \tag{16.222}$$

where A_i denotes the complex wave amplitude, A_Y being related to concentration waves. It is seen that concentration waves induce fluctuations in both mass entropy and density. The corresponding emitted field is expressed as

$$\frac{u'_{x_2}}{U_2} = A_i\left(Z_{i\,pol}\sin\alpha_s e^{\imath(\boldsymbol{k}_s\cdot\boldsymbol{x}-\omega t)} + Z_{ia}e^{-k_a\eta x}\frac{\cos\alpha_a + \imath\eta}{M_2\zeta}e^{\imath(\boldsymbol{k}_a\cdot\boldsymbol{x}-\omega t)}\right), \tag{16.223}$$

$$\frac{u'_{r_2}}{U_2} = A_i\left(-Z_{i\,pol}\cos\alpha_s e^{\imath(\boldsymbol{k}_s\cdot\boldsymbol{x}-\omega t)} + Z_{ia}e^{-k_a\eta x}\frac{\sin\alpha_a}{M_2\zeta}e^{\imath(\boldsymbol{k}_a\cdot\boldsymbol{x}-\omega t)}\right), \tag{16.224}$$

$$\frac{u'_{\phi_2}}{U_2} = A_iZ_{i\,tor}e^{\imath(\boldsymbol{k}_s\cdot\boldsymbol{x}-\omega t)}, \tag{16.225}$$

$$\frac{\omega'_2}{U_2} = \imath kA_i(Z_{iv}\sin\phi\sin\alpha_s\sin\alpha(1+\cot^2\alpha_s) - Z_{i\,tor}\mathfrak{C}\cos\phi\cos\alpha)e^{\imath(\boldsymbol{k}\cdot\boldsymbol{x}-\omega t)}, \tag{16.226}$$

$$\frac{\rho'_2}{\bar{\rho}_2} = A_i(-(Z_{is} + \delta_{iY}A_t^r)e^{\imath(\boldsymbol{k}_s\cdot\boldsymbol{x}-\omega t)} + Z_{ia}e^{-k_a\eta x}e^{\imath(\boldsymbol{k}_a\cdot\boldsymbol{x}-\omega t)}), \tag{16.227}$$

$$\frac{p_2'}{\gamma \bar{p}_2} = A_i Z_{ia} e^{-k_a \eta x} e^{\imath(\boldsymbol{k}_a \cdot \boldsymbol{x} - \omega t)}, \tag{16.228}$$

$$\frac{T_2'}{\bar{T}_2} = A_i \left(Z_{is} e^{\imath(\boldsymbol{k}_s \cdot \boldsymbol{x} - \omega t)} + (\gamma - 1) Z_{ia} e^{-k_a \eta x} e^{\imath(\boldsymbol{k}_a \cdot \boldsymbol{x} - \omega t)} \right), \tag{16.229}$$

$$\frac{s_2'}{c_p} = A_i Z_{is} e^{\imath(\boldsymbol{k}_s \cdot \boldsymbol{x} - \omega t)}, \tag{16.230}$$

$$Y_2' = A_i Z_{iY} e^{\imath(\boldsymbol{k}_s \cdot \boldsymbol{x} - \omega t)}, \tag{16.231}$$

where Z_{ij} with $i, j = (a, s, pol, tor, x, Y)$ denotes the complex transfer function associated to the generation of a wave of type j by an incident wave of type i. All parameters of emitted waves, i.e. wave number, angle and damping factor for non-propagating acoustic waves are the same as in the pure fluid case (see Sect. 16.2), all thermodynamical parameters being replaced by mean values in the mixture case. The continuity of the concentration field Y implies $Z_{YY} = 1$ and that concentration is not influenced by vorticity, entropy and acoustic modes, i.e. $Z_{iY} = 0, i \neq Y$.

16.9.3 Transfer Functions

Complex transfer functions are found for the binary mixture case solving the following linear problem

$$\mathcal{A} \boldsymbol{Z}_i = \boldsymbol{B}_i \tag{16.232}$$

where $\boldsymbol{Z}_i = (Z_{iY}, Z_{i\,tor}, Z_{i\,pol}, Z_{is}, Z_{ia}, Z_{ix})^T$. Since $Z_{iY} = \delta_{iY}$ and $Z_{i\,tor} = \delta_{i\,tor}\mathfrak{C}$ they can be removed from the problem and the initial 6×6 system simplifies in a 4×4 system whose matrix $\mathcal{A}$ is identical to the one of the pure fluid case. Right-hand side vectors $\boldsymbol{B}_i, i = tor, pol, s, a$ are also the same as for the pure fluid problem. The vector associated to incident concentration waves is

$$\boldsymbol{B}_Y = A_t^r \boldsymbol{B}_{c_r} + A_t^{c_v} \boldsymbol{B}_{c_{c_v}} = A_t^r \begin{pmatrix} 0 \\ (1 - \mathfrak{C}) \\ 0 \\ \frac{1}{\bar{\gamma}} \left(\frac{\mathfrak{C}^2}{M_1^2} - \frac{1}{M_2^2} \right) \end{pmatrix} + A_t^{c_v} \begin{pmatrix} 0 \\ 0 \\ 0 \\ \frac{1}{\bar{\gamma}(\bar{\gamma}-1)} \left(\frac{\mathfrak{C}^2}{M_1^2} - \frac{1}{M_2^2} \right) \end{pmatrix} \tag{16.233}$$

It is seen that two families of concentration waves, one for each part of $\boldsymbol{B}_Y$ can be defined:

(i) *molar mass waves*, or r-waves, for which $\boldsymbol{B}_Y = A_t^r \boldsymbol{B}_{c_r}$
(ii) *constant specific heat waves*, or c_v-waves, for which $\boldsymbol{B}_Y = A_t^{c_v} \boldsymbol{B}_{c_{c_v}}$

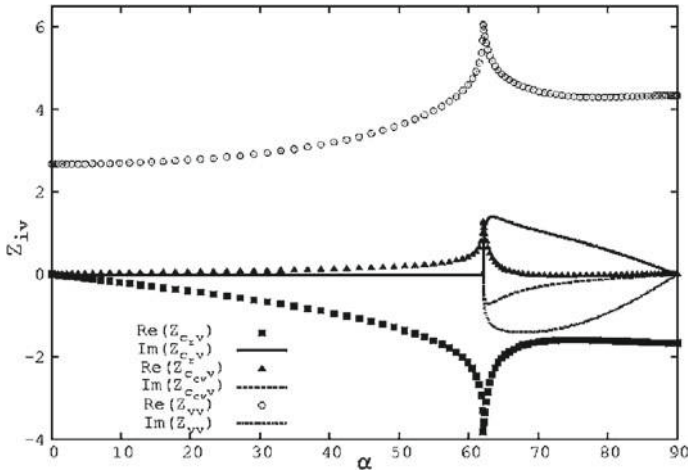

Fig. 16.8 Transfer functions associated to vorticity mode creation/amplification in a binary mixture versus the angle of incidence of the incident wave at $M_1 = 2$ and $\bar{\gamma} = 7/5$. Courtesy of J. Griffond. From Griffond (2005) with permission of AIP

These two wave families have independent amplitudes. These transfer functions are tied by the following exact relation:

$$Z_{c_r\, i} + Z_{c_{c_v}\, i} = Z_{s\, i}, \quad i = pol, tor, a, s \tag{16.234}$$

It is worth noting that the present mixture model can be used to describe two additional cases:

- *Density wave* with uniform specific heat ratio γ, which corresponds to the sum of a r-wave and a c_v-wave with equal amplitude. The associated transfer function $\mathbf{Z}_\rho$ is computed as $\mathbf{Z}_\rho = \mathbf{Z}_{c_r} + \mathbf{Z}_{c_{c_v}}$.
- *Pure specific heat ratio wave* without temperature, density and pressure fluctuation. This case is recovered taking $\mathbf{Z}_\gamma = -\frac{\bar{\gamma}}{\bar{\gamma}-1}\mathbf{Z}_{c_{c_v}}$.

Transfer functions for vorticity associated to vorticity creation/amplification for incident r-waves, c_v-waves and vorticity waves are displayed in Fig. 16.8. It is seen that for waves normal to the shock front, i.e. $\alpha = 0$, no vorticity is generated by the concentration mode. The maximum vorticity generation is observed for an incidence close to the critical angle α_c that separate propagating and non-propagating emitted acoustic waves. The same behavior was observed for incident entropy, vorticity and acoustic modes in the canonical case, see Sect. 16.3.2. It is observed that the imaginary part of transfer functions is zero for $\alpha < \alpha_c$ and non-zero for larger angles of incidence, meaning that emitted propagating waves are in-phase and non-propagating waves are out of phase.

16.9.4 Reconstruction of Second-Order Moments: Case of Isotropic Mixture

Classical turbulence statistical moments in the case of the mixture are recovered in the same way as in the pure fluid case. Since vorticity and entropy modes are decoupled from concentration waves, it is interesting to reconstruct the emitted field in the case of a shock wave travelling in a mixture with isotropic turbulent concentration field.

Considering a concentration fluctuating field Y' and the associated three-dimensional spectrum $E_{YY}(k)$, one has

$$\overline{Y'^2} = \int_0^{+\infty} E_{YY}(k)dk. \tag{16.235}$$

The normalized longitudinal emitted Reynolds stress is equal to

$$\frac{R_{11}(x)}{\overline{Y'^2}U_2^2} = \frac{\overline{u_2'^2}(x)}{\overline{Y'^2}U_2^2} = 4\pi \int_0^{\pi/2} (I_{vv} + I_{aa} + I_{va}) \sin\alpha d\alpha, \tag{16.236}$$

where

$$I_{vv} = \sin^2\alpha_s |Z_{Ypol}|^2 \int_0^{+\infty} E_{YY}(k)dk, \tag{16.237}$$

$$I_{aa} = \left| \frac{\cos\alpha_a + \imath\eta}{M_2\zeta} \right|^2 |Z_{Ya}|^2 \int_0^{+\infty} E_{YY}(k) e^{-2k_a\eta x} dk, \tag{16.238}$$

$$I_{va} = 2\Re\left[\sin\alpha_s \frac{\cos\alpha_a + \imath\eta}{M_2\zeta} Z_{Ypol} Z_{Ya}^* \int_0^{+\infty} E_{YY}(k) e^{\imath x(k_s\cos\alpha_s - k_a\cos\alpha_a)} e^{-k_a\eta x} dk \right]. \tag{16.239}$$

This expression can be simplified looking at the far-field solution, in which both I_{va} and the non-propagating part of I_{aa} can be neglected.

The far-field expression of the emitted kinetic energy is

$$\frac{\mathcal{K}_2}{\overline{Y'^2}U_2^2} = \int_0^{\pi/2} |Z_{Ypol}|^2 \sin\alpha d\alpha + \int_0^{\alpha_c} \frac{|Z_{Ya}|^2}{\bar{\gamma}M_2^2} \sin\alpha d\alpha \tag{16.240}$$

$$= (A_t^r)^2 \mathcal{F}(M_1) + (A_t^{c_v})^2 \mathcal{G}(M_1) + A_t^r A_t^{c_v} \mathcal{H}(M_1), \tag{16.241}$$

where the terms of the last expression, which displays explicitly the contributions of r-waves and c_v-waves, are defined as

$$\mathcal{F}(M_1) = \int_0^{\pi/2} |Z_{c_r\,pol}|^2 \sin\alpha d\alpha + \int_0^{\alpha_c} \frac{|Z_{c_r\,a}|^2}{\bar{\gamma}M_2^2} \sin\alpha d\alpha, \tag{16.242}$$

$$\mathcal{G}(M_1) = \int_0^{\pi/2} |Z_{c_{v_2}\,pol}|^2 \sin\alpha d\alpha + \int_0^{\alpha_c} \frac{|Z_{c_{v_2}\,a}|^2}{\bar{\gamma} M_2^2} \sin\alpha d\alpha, \tag{16.243}$$

$$\mathcal{H}(M_1) = \int_0^{\pi/2} 2\Re[Z_{c_r\,pol} Z^*_{c_{v_2}\,pol}] \sin\alpha d\alpha + \int_0^{\alpha_c} \frac{2Re[Z_{c_r\,pol} Z^*_{c_{v_2}\,pol}]}{\bar{\gamma} M_2^2} \sin\alpha d\alpha. \tag{16.244}$$

Reynolds stress anisotropy, measured as $2R_{11}/(R_{22}+R_{33})$, is expressed in the far field as

$$\frac{2R_{11}(x)}{(R_{22}(x)+R_{33}(x))} = \frac{\int_0^{\pi/2} |Z_{Ypol}|^2 \cos^2\alpha_s \sin\alpha d\alpha + \int_0^{\alpha_c} \frac{\sin^2\alpha_a |Z_{Ya}|^2}{\bar{\gamma} M_2^2} \sin\alpha d\alpha}{2\int_0^{\pi/2} |Z_{Ypol}|^2 \sin^2\alpha_s \sin\alpha d\alpha + 2\int_0^{\alpha_c} \frac{\cos^2\alpha_a |Z_{Ya}|^2}{\bar{\gamma} M_2^2} \sin\alpha d\alpha}. \tag{16.245}$$

Far-field pressure and density variance are respectively expressed as

$$\frac{\overline{p_2'^2}}{\bar{p}_2^2 \overline{Y'^2}} = \int_0^{\alpha_c} |Z_{Ya}|^2 \sin\alpha d\alpha, \tag{16.246}$$

and

$$\frac{\overline{\rho_2'^2}}{\bar{\rho}_2^2 \overline{c'^2}} = \int_0^{\pi/2} |A_r^t + Z_{Ys}|^2 \sin\alpha d\alpha + \int_0^{\alpha_c} \frac{|Z_{Ya}|^2}{\bar{\gamma}} \sin\alpha d\alpha. \tag{16.247}$$

16.10 Extending LIA: III. Thin Strong Detonation/Turbulence Interaction

16.10.1 Problem Statement and Associated Linearized Equations

LIA can also be extended to reacting waves, see Lasseigne et al. (1991), (Huete et al. 2013, 2014, 2016). Realistic models for 1D detonation waves, e.g. the Zeldovich- von Neumann - Döring (ZND) model, describe finite-thickness reacting waves. Typically, a non-reactive shock wave is followed by an induction zone in which temperature rises due to the shock initiated chemical reactions, a reaction zone in which combustion takes place, and finally a region with inert burned gas. The present analysis is restricted to strong overdriven detonation waves, since it is known that weak planar detonation wave are unstable to small perturbations (a cellular organization of the reactive front is commonly observed), resulting in a destructive interaction that precludes LIA approach.

The analysis is also restricted to the case in which the size of turbulent eddies is very large compared with the detonation thickness, so that the detonation wave can be modelled as a discontinuity moving at constant speed D in a region field by

fresh gas at rest with a prescribed superimposed fluctuating field. The combustion scheme is simplified in such a way that only exothermicity of the chemical reaction is taken into account, i.e. both fresh and burned gas are assumed to be perfect gas with the same thermodynamical parameters γ, c_p and c_v. The amount of chemical heat released in the detonation per unit mass is denoted ΔQ. In this simplified framework, the jump relation for a 1D detonation travelling at constant speed D read (written in the detonation reference frame)

$$\rho_1 u_1 = \rho_2 u_2, \tag{16.248}$$

$$\rho_1 u_1^2 + p_1 = \rho_2 u_2^2 + p_2, \tag{16.249}$$

$$\frac{1}{2}u_1^2 + h_1 = \frac{1}{2}u_2^2 + h_2, \tag{16.250}$$

$$s_2 \geq s_1, \tag{16.251}$$

along with

$$h_1 = c_p T_1, \quad h_2 = c_p T_2 - \Delta Q. \tag{16.252}$$

On both side of the reacting shock wave the flow is modelled as a non-reacting flow of perfect gas. Therefore, linearized Euler equations used to described the flow are the same as for the canonical case and will not be repeated here. The difference with the non-reacting case lies in the jump relation for energy, which explicitly depend on the heat release parameter ΔQ:

$$\frac{1}{2}\left((U_1 + u_1')^2 - (U_2 + u_2')^2\right) = -\Delta Q + \frac{\gamma r}{\gamma - 1}(T_2 - T_1). \tag{16.253}$$

Introducing the detonation Mach number $M_1 = D/a_1$, the mean flow quantities on both sides of the shock are tied by the following relations

$$\frac{\bar{\rho}_2}{\bar{\rho}_1} = \mathfrak{C} = \frac{D}{D - U_2} = \frac{(\gamma + 1)M_1^2}{(\gamma - \kappa)M_1^2 + 1}, \tag{16.254}$$

$$\frac{\bar{p}_2}{\bar{\rho}_1 D^2} = \frac{\gamma M_1^2(1 + \kappa) + 1}{\gamma(\gamma + 1)M_1^2}, \tag{16.255}$$

$$M_2 = \frac{D - U_2}{a_2} = \sqrt{\frac{(\gamma - \kappa)M_1^2 + 1}{\gamma M_1^2(1 + \kappa) + 1}}, \tag{16.256}$$

where

$$\kappa = \frac{\sqrt{(M_1^2 - 1)^2 - 4qM_1^2}}{M_1^2}, \quad q = \frac{(\gamma^2 - 1)\Delta Q}{2a_1^2}. \tag{16.257}$$

The dimensionless heat release parameter q is equal to 0 in the case of non-reacting shock wave, for which κ simplifies as $1 - M_1^2$, leading to the usual jump relation for planar shock waves.

For detonations, the minimum propagation Mach number is the Chapman-Jouguet value

$$M_{CJ} = \sqrt{1+q} + \sqrt{q}. \tag{16.258}$$

In the present case of strong overdriven detonation, one should have $M_1 \gg M_{CJ}$ corresponding to $\kappa \simeq 1$.

Derivation of linearized jump relations for detonations is performed in a way identical to the one used to treat the inert shock case. They are identical to those found for the non-reacting case, since ΔQ does not depend on upstream fluctuations in the present model and therefore vanishes during the linearization step. Therefore, both equations of the linearized problem and the associated solutions of the LIA problem are the same as in the non-reacting case (see e.g. Section 16.9 to handle the case of a detonation wave with concentration fluctuations) and will not be reproduced here for the sake of brevity. The only difference is that the downstream mean flow quantities are explicit functions of the heat release parameter q.

It is worth noting that the analysis also holds for endothermic shock waves which can be observed when the shock wave trigger a endothermic phase change or a radiative loss. The range of validity of the present model is given by physically admissible values of q, which are such that both $\mathfrak{C}$ and M_2^2 are real positive numbers:

$$q_{min} = 4(1+\gamma)(M_1^2(1-\gamma) - 2) < q < \frac{4(1-M_1^2)^2}{M_1^2} = q_{max}. \tag{16.259}$$

16.10.2 Solution via Laplace Transform

Normal-mode LIA analysis has been very briefly addressed by Jackson et al. (1993), while a full detailed study has been carried out more recently (Huete et al. 2013, 2016) using the Laplace-transform-based methodology discussed in Sect. 16.6. The procedure is exactly the same, the differences arising in the linearized jump conditions, and therefore in the expression for $\breve{p}_s(r_s)$.

The general solution for pressure perturbations on the wave front computed for an upstream fluctuating density field is

$$\begin{aligned}\tilde{p}_s(r_s) = {} & \frac{2(1+\sigma_1)\psi}{\pi}\int_0^1 f_p(z)\cos(r_s z)dz \\ & -\frac{M_2(\mathfrak{C}-\Delta)(\zeta_0^2-\sigma_2)}{\pi}\int_0^1 \frac{f_p(z)}{\zeta_0^2 - z^2}\left[\cos(r_s z) - \cos(\zeta_0 z)\right]dz\end{aligned} \tag{16.260}$$

where ζ_0 is unchanged (see Eq. (16.158)) and

$$f_p(z) = \frac{z^2\sqrt{1-z^2}}{z^2(1-z^2)+(\sigma_2-\sigma_1 z^2)^2}, \tag{16.261}$$

with

$$\sigma_1 = \frac{1+\Pi}{2M_2},\ \sigma_2 = \frac{M_2\mathfrak{C}(1-\Pi)}{2(1-M_2^2)},\ \sigma_3 = 1+\frac{1}{\sqrt{1+M_1^4-2(1+2q)M_1^2}}, \tag{16.262}$$

$$\Pi = \frac{[(1-\kappa)M_1^2+1]^2}{4M_1^2(1+q)},\quad \Delta = 1-\frac{q}{1+q}\left(\frac{1+(1-\kappa)M_1^2}{1+(\gamma-\kappa)M_1^2}\right). \tag{16.263}$$

The parameter ψ is given by the initial conditions, and is therefore case-dependent. The companion solution for the shock corrugation length $\tilde{\xi}$ is not displayed here for the sake of brevity. The method to reconstruct the full emitted field and associated statistical moments is identical to the inert shock case.

It is seen that the solution explicitly depends on M_1, γ and q. As in the cold shock case, it can be split into short- and long-wave components and constant-amplitude and evanescent contributions. The analysis is basically the same, since the definition of ζ_0 is not changed in the reacting case (but its value is changed since the values of both $\mathfrak{C}$ and M_2 depend on q). In the limit of very strong detonation $M_1 \to +\infty$ with $O(1)$ values of γ and q, its expression simplifies as

$$\zeta_0 \sim \sqrt{\frac{\gamma+1}{\gamma-1}}\left(1-\frac{(\gamma-2)(1+q)}{(\gamma-1)M_1^2}-\frac{1}{2M_1^2}\right)\frac{k_x}{k_y}.$$

16.10.3 Amplitude of Emitted Fields for Incident Monochromatic Density Waves

Variations of the amplitudes of emitted pressure mode, shock corrugation, vorticity mode and entropic mode versus the angle of incidence α are displayed in Fig. 16.9. The general shape of the plot is not modified, and the critical angle is still associated with a strong increase of the amplitude of emitted waves. The main effects of heat release are the following:

- a small decrease in the value of the critical angle α_c,
- a decrease in the amplitude of shock corrugation, emitted vorticity and entropy-induced density fluctuations,
- an increase of emitted pressure wave amplitude.

The most important effects are observed on vorticity and density.

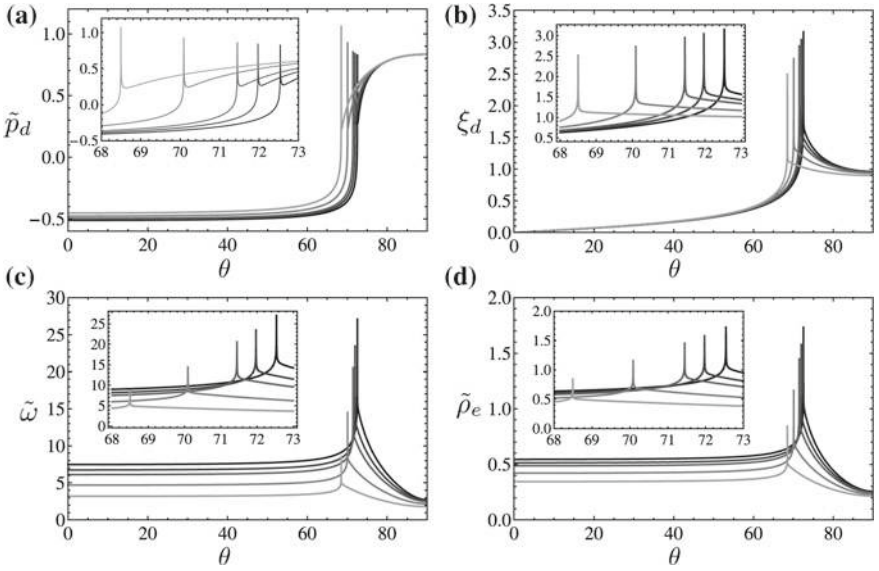

Fig. 16.9 Evolution of amplitudes of emitted non-evanescent modes in strong detonation/monochromatic density wave interaction versus the angle of incidence α at $M_1 = 10$ for different values of heat release parameter q. Color is related to exothermicity, with $q = 0$ (non-reacting shock wave) in black and $q = 10$ in light grey. Top-left: pressure fluctuation, top-right: shock corrugation, bottom-left: vorticity, bottom-right: entropy-mode-induced density fluctuation. Courtesy of C. Huete. From Huete et al. (2013) with permission of AIP

References

Fabre, D., Jacquin, L., Sesterhenn, J.: Linear interaction of a cylindrical entropy spot with a shock wave. Phys. Fluids **13**(8), 2403–2422 (2001)

Griffond, J.: Linear interaction analysis applied to a mixture of two perfect gases. Phys. Fluids **24**, 115108 (2005)

Griffond, J., Soulard, O., Souffland, D.: A turbulent mixing Reynolds stress model fitted to match linear interaction analysis prediction. Phys. Scr. **142**, 014059 (2010)

Griffond, J., Soulard, O.: Evolution of axisymmetric weakly turbulent mixtures interacting with shock or rarefaction waves. Phys. Fluids **17**, 086101 (2012)

Huete, C., Jin, T., Martinez-Ruiz, D., Williams, F.A.: Reacting Shock Wave Effects on Isotropic Turbulent Flows. Linear interaction analysis and direct numerical simulations. Private Communication (2016)

Huete, C., Sanchez, A.L., Velikovich, A.L.: Theory of interactions of thin strong detonations with turbulent gases. Phys. Fluids **25**, 076105 (2013)

Huete, C., Sanchez, A.L., Velikovich, A.L.: Linear theory for the interaction of small-scale turbulence with overdriven detonations. Phys. Fluids **26**, 116101 (2014)

Huete, C., Wouchuk, J.G., Canaud, B., Velikovich, A.L.: Analytical linear theory for the shock and re-shock of isotropic density inhomogeneities. J. Fluid Mech. **700**, 214–245 (2012a)

Huete, C., Wouchuk, J.G., Velikovich, A.L.: Analytical linear theory for the interaction of a planar shock wave with a two- or three-dimensional random isotropic acoustic wave field. Phys. Rev. E **85**, 026312 (2012b)

Jackson, T.L., Hussaini, M.Y., Ribner, H.S.: Interaction of turbulence with a detonation wave. Phys. Fluids A **5**(8), 745–749 (1993)
Lasseigne, D.G., Jackson, T.L., Hussaini, M.Y.: Nonlinear interaction of a detonation/vorticity wave. Phys. Fluids A **3**, 1972–1979 (1991)
Lee, S., Lele, S.K., Moin, P.: Direct numerical simulation of isotropic turbulence interacting with a weak shock wave. J. Fluid Mech. **251**, 533–562 (1993)
Mahesh, K., Lele, S.K., Moin, P.: The interaction of an isotropic field of acoustic waves with a shock wave. J. Fluid Mech. **300**, 383–407 (1995)
Mahesh, K., Moin, P., Lele, S.K.: The interaction of a shock wave with a turbulent shear flow. Report No. TF-69, Department of Mecanical Engineering, Stanford University (1996)
Miller, G.H., Ahrens, T.J.: Shock wave viscosity measurement. Rev. Modern Phys. **63**, 919–948 (1991)
Moore, F.K.: Unsteady oblique interaction of a shock wave with a plane disturbance. Technical report 2879, NACA (1954)
Ribner, H.S.: Convection of a pattern of vorticity through a shock wave. Technical report 1164, NACA (1953)
Ryu, J., Livescu, D.: Turbulence structure behind the shock in canonical shock-vortical turbulence interaction. J. Fluid Mech. **756**(R1), 1–13 (2014)
Wouchuk, J.G., Huete, C., Velikovich, A.L.: Analytical linear theory for the interaction of a planar shock wave with an isotropic turbulent vorticity field. Phys. Rev. E **79**, 066315 (2009)

Chapter 17
The Essentials of Linear and Nonlinear Theories and Models

17.1 Rapid Distortion Theory for Homogeneous Turbulence

Homogeneous RDT remains a questionable nomenclature, and Spectral Linear Theory (SLT) is more convenient in recent studies, especially in geophysics and astrophysics, as reported in Chap. 11. The twofold aspects of this approach can be reconcilied anyway, as a particular stability analysis or as a model for predicting evolution of initially existing turbulence, via "rapidly" evolving statistical moments.

With respect to conventional stability analysis, modes of perturbation are sought as

$$\boldsymbol{u}(\boldsymbol{x},t) = \boldsymbol{a}(t)\exp(\boldsymbol{k}(t)\cdot\boldsymbol{x}), \tag{17.1}$$

(e.g. for velocity fluctuations) instead of normal modes

$$\boldsymbol{u}(\boldsymbol{x},t) = e^{\omega t}\mathcal{U}(\boldsymbol{x}).$$

In the classical approach, the time-dependency is prescribed, under the exponential factor with complex-valued ω frequency. On the other hand, the spatial form of the fluctuation is prescribed as a Fourier mode in Eq. (17.1), but the time-dependency of the amplitude $\boldsymbol{a}$, if affected by the time-dependency of the wavevector, may permit a simplified non-modal stability analysis, useful for transient algebraic growth and bypass transition to turbulence. Of course, a general non-modal stability analysis can be carried out with a continuous spectrum of frequencies ω, using a general Laplace transform, but this is in general more cumbersome to treat.

As introduced in Chap. 8, the basic equations for inviscid "RDT" disturbances in the presence of a mean flow gradient $\mathbf{A}$ are

$$\frac{da_i}{dt} + \underbrace{\left(\delta_{im} - 2\frac{k_i k_m}{k^2}\right) A_{mj}}_{M_{ij}} a_j = 0, \tag{17.2}$$

P. Sagaut and C. Cambon, *Homogeneous Turbulence Dynamics*,
https://doi.org/10.1007/978-3-319-73162-9_17

with

$$\frac{dk_i}{dt} + A_{ji}k_j = 0. \tag{17.3}$$

According to the mathematical treatment of partial derivative equations, the latter equation also gives the characteristic lines of the operator $\frac{\partial}{\partial t} - A_{nj}k_n\frac{\partial}{\partial k_j}$ in Fourier space. Since the mean trajectories are the characteristics lines of the advection operator $\frac{\partial}{\partial t} + A_{jn}x_n\frac{\partial}{\partial x_j}$, it is clear that the eikonal equation (17.3) is the counterpart, in Fourier space, of $\dot{x}_i - A_{ij}x_j = 0$, changing A_{ij} into $-A_{ji}$ and $\boldsymbol{x}$ into $\boldsymbol{k}$. A more physical interpretation will be given in the following.

More classically, the pressure contribution is removed from consideration using the incompressibility constraint, which is equivalent to the orthogonality condition $\boldsymbol{a}\cdot\boldsymbol{k} = 0$ (see Sect. 2.5.4)

The ordinary differential equations (17.3) and (17.2) are referred to as the *Kelvin–Moffatt equations*. In the matrix $\mathbf{M}$, the factor $\frac{k_ik_n}{k^2}$ reflects the contribution from the fluctuating pressure term, with a prefactor 2 which takes into account advection in wave-space. As usual, spectral analysis allows for a straightforward treatment of the nonlocal dependence of pressure upon velocity. The time dependency of the wave vector represents the convection of the plane wave $\exp(\imath\boldsymbol{k}(t)\cdot\boldsymbol{x})$ by the base flow. Both the direction and magnitude of $\boldsymbol{k}$ change as wave crests rotate and approach or separate from each other due to mean velocity gradients.

General solutions which are valid for arbitrary initial data are expressed as follows in terms of linear transfer matrices

$$\widehat{u}_i(\boldsymbol{k}(t), t) = G_{ij}(\boldsymbol{k}, t, t_0)\widehat{u}_j(\boldsymbol{k}(t_0), t_0) \tag{17.4}$$

and

$$k_i(t) = F_{ji}^{-1}(t, t_0)k_j(t_0) \tag{17.5}$$

in which the Green's function is eventually determined by the initial conditions[1]

$$G_{ij}(\boldsymbol{k}, t_0, t_0) = \delta_{ij} - \frac{K_iK_j}{K^2}, \quad K_i = k_i(t_0). \tag{17.6}$$

Of course, $\mathbf{G}$ is governed by the same equation as $\hat{\boldsymbol{u}}$

$$\dot{G}_{ij} = -M_{in}G_{nj},$$

in which the overdot is a convenient notation to indicate that $\boldsymbol{k}$ has to be considered as a time-dependent vector in $\mathbf{G}(\boldsymbol{k}, t, t_0)$.

The general definition of the Cauchy matrix $\mathbf{F}$ for an arbitrary flow has been given previously.

[1] A different initialization $G_{ij} = \delta_{ij}$ was prescribed in Townsend (1956, 1976). The Eq. (17.6) presents some advantages, since $k_iG_{ij} = 0$ can be satisfied at any time, and the RDT Green's function can be more easily related to the Kraichnan's response function.

When comparing similar characteristics lines for the advection term in both physical and in Fourier space, i.e. $x_i = F_{ij}(t, t_0)X_j$ (trajectory) and $k_i = F^{-1}_{ji}(t, t_0)K_j$, their close analogy is obvious. One recovers the conservation of $\boldsymbol{k}\cdot\boldsymbol{x}$ $(= \boldsymbol{K}\cdot\boldsymbol{X})$ along trajectories, and also conservation of the plane wave $\exp(\imath\boldsymbol{k}(t)\cdot\boldsymbol{x}(t))$.

17.1.1 Using Solenoidal Modes for a Green's Function with a Minimal Number of Components

For instance, a reduced Green's function can be used in the Craya–Herring frame of reference, as

$$u^{(\alpha)}(\boldsymbol{k}(t), t) = g_{\alpha\beta}(\boldsymbol{k}, t, t')u^{(\beta)}(\boldsymbol{k}(t'), t'). \tag{17.7}$$

The reduced Green's function $g_{\alpha\beta}$, with only four components instead of nine for G_{ij}) can be generated by solving

$$\dot{u}^{(\alpha)} + m_{\alpha\beta}u^{(\beta)} = 0, \tag{17.8}$$

with

$$m_{\alpha\beta} = e_i^{(\alpha)}A_{ij}e_j^{(\beta)} - \dot{e}_i^{(\alpha)}e_i^{(\beta)}. \tag{17.9}$$

Here, the Einstein convention of summation over repeated indices is used for both Latin (varying from 1 to 3) and Greek (taking only the values 1 and 2) indices. The Craya–Herring frame being orthonormal, it characterizes a solid-body motion when $\boldsymbol{k}$ is time dependent, so that the entrainment term is simply

$$\dot{e}_i^{(\alpha)}e_i^{(\beta)} = \epsilon_{\alpha 3\beta}\Omega_E, \quad \Omega_E = -e_i^{(2)}A_{ij}e_j^{(1)} - n_iA_{ij}e_j^{(1)}\frac{k}{k_\perp}, \tag{17.10}$$

with $k = \mid \boldsymbol{k} \mid, k_\perp = \sqrt{k^2 - (\boldsymbol{k}\cdot\boldsymbol{n})^2}$. This term contributes to the "stropholysis" effect that affects the polarization anisotropy in Eq. (8.40).

Equation (17.10) is simplified if the axial vector $\boldsymbol{n}$ is chosen along one of the eigendirection of $\mathbf{A}$ (Cambon et al. 1985), so that

$$\Omega_E = -e_i^{(2)}A_{ij}e_j^{(1)}. \tag{17.11}$$

This condition is always fulfilled in the cases treated in this book, and an optimal choice of $\boldsymbol{n}$ has been discussed if needed.

Similar equations can be found in terms of helical modes, but they present no additional interest, except if the mean vorticity, or the mean absolute vorticity in the presence of an additional Coriolis force, is completely dominant. A first instance is given in the Chap. 7.

17.1.2 Prediction of Statistical Quantities

Throughout this book, we are using an approach which reconcile and simplify two different approaches:

- The way initiated by Moffatt (1967) in RDT, who addressed the very definition of a deterministic Green's function, prior to any statistical calculation, but without using a local frame of reference. More recent studies (since 1986) in the community of hydrodynamic stability theory (e.g. Bayly 1986; Craik and Criminale 1986), have essentially the same starting point, but are disconnected from application to statistics anyway.
- The way initiated by Craya, who put the emphasis on solving statistical equations for second-order and third-order spectral tensors, but with a reduced number of components obtained by projecting these equations and these tensors in the eponymous frame of reference. Craya never considered the fluctuating velocity field in Fourier space, what Herring (1974) did in 1974, recovering the local frame of reference, but restricting the statistical approach to axial symmetry only.

Recall that the second way yielded several studies (dealing with single-time two-point and single-point second order statistics) by J.N. Gence and coworkers (mainly his Ph. D. students), following (Courseau and Loiseau 1978) for pure strain and pure shear, namely "pure" rotation, rotating shear, buoyant flows (without mean stratification). Related publications, mainly written in French, can be obtained from the authors upon request.

About the first way, it is perhaps useful to discuss some points dealing with terminology. The time-dependent Fourier modes given in Eq. (17.1), when recovered in the hydrodynamic stability community, then in geophysics and astrophysics, were often referred to as "Kelvin modes", ignoring their use in RDT (engineering community) and considering that the first instance of such modes was given by Lord Kelvin. This may be true, but the terminology is misleading, given the huge number of Kelvin modes and Kelvin waves called into play in stability analyses. Let us illustrate this with two examples: For a specialist of aerodynamics, a Kelvin wave is a localized inertial wave confined in the core of a vortex, whereas for an oceanographer, it is a much more complex wave, also dealing with the variation of the Coriolis parameter with latitude, the stable density-stratification and the topology. We hope to have clarified the point here that 'mean-Lagrangian Fourier modes', or 'Fourier modes advected by the mean' would be less confusing than Kelvin modes. It is not necessary to recall chronologically all the authors who used a similar approach, from Lord Kelvin to Batchelor and Proudman (1954).

As an example of statistical calculation, the RDT equation for second order statistics is readily derived from Eq. (17.4) using Eq. (2.84), leading to

$$\hat{R}_{ij}[\boldsymbol{k}(t), t] = G_{in}(\boldsymbol{k}, t, t_0) G_{jm}(\boldsymbol{k}, t, t_0) \hat{R}_{nm}[\boldsymbol{k}(t_0), t_0]. \tag{17.12}$$

Given an initial solution $\hat{R}_{ij}$ at $t = t_0$, one can compute it at later times using the relation (17.12), provided that the Green's function $G_{ij}(\boldsymbol{k}, t, t')$ is known. The determination of G_{ij} is thus the main problem in applying homogeneous RDT in practice.

Applications mainly concern second-order, two-point and one-point correlations, with many results about the history of the Reynolds stress tensor when the initial data are chosen isotropic. Similarly, "rapid" pressure-strain rate tensor and dissipation tensor can be calculated.

It is not difficult to reintroduce a laminar viscous effect, or an efficient modelled damping effect, as illustrated by Townsend (1956, 1976) and some RDT applications reported in Chaps. 9 and 11. The viscous factor was calculated in the most general way by Cambon et al. (1985) as

$$V_0(\boldsymbol{k}, t) = \exp\left(-\nu \int_0^t k^2(t)dt\right),$$

so that

$$V_0(\boldsymbol{k}, t) = \exp\left(-k_l k_n \int_{t_0}^t F_{li}(t, t')F_{ni}(t, t')dt'\right). \tag{17.13}$$

This equation involves a quadratic form in terms of $\boldsymbol{k}$, using the group relations of $\mathbf{F}$ (such as $\mathbf{F}(t, t').\mathbf{F}(t', t'') = \mathbf{F}(t, t'')$) and can also be given in terms of the 'material' wavevector $\boldsymbol{K}$.

The Eq. (17.12) can also be extended to any order n, thanks to the existence of the general solution (17.4), via a product of n Green's functions: linear solutions for third-order correlations are considered per se in Chap. 7, for instance, and incorporated in triadic closures for evaluating nonlinear transfer terms.

Complete inviscid RDT equations for the Reynolds stress tensor and the integral lengthscales are given below, for isotropic initial data:

$$\overline{u_i' u_j'} = \frac{\mathcal{K}(0)}{4\pi} \iint_{|\boldsymbol{K}|=1} e_i^{(\alpha)}(\boldsymbol{k}) g_{\alpha\gamma}(\boldsymbol{k}, t) g_{\beta\gamma}(\boldsymbol{k}, t) e_j^{(\beta)}(\boldsymbol{k}) d^2\boldsymbol{K} \tag{17.14}$$

and

$$\mathcal{E}_{ij}^{(n)} = \overline{u_i' u_j'} L_{ij}^{(n)} \quad \text{no summation on i, j}$$

$$= \frac{1}{2} \int_0^\infty \frac{E(k)}{k} dk \iint_{k_l=0} e_i^{(\alpha)}(\boldsymbol{k}) g_{\alpha\gamma}(\boldsymbol{k}, t) g_{\beta\gamma}(\boldsymbol{k}, t) e_j^{(\beta)}(\boldsymbol{k}) d^2\boldsymbol{K}. \tag{17.15}$$

The latter equation makes use of the additional condition $K_l = k_l$, as for instance $k_1 = K_1$ and $k_3 = K_3$ for the pure plane shear flow case in Chap. 9).

17.1.2.1 Initial Value Problem or Forcing?

Instead of considering the initial value problem, one may add a forcing term to the linear equation, in order to mimic a nonlinear effect and/or a source of noise.

From the general solution for the fluctuating field

$$\hat{\boldsymbol{u}}(\boldsymbol{k}(t),t) = G_{ij}(\boldsymbol{k},t,t_0)\hat{\boldsymbol{u}}(\boldsymbol{k}(t_0),t_0) + \int_{t_0}^{t} G_{ij}(\boldsymbol{k},t,t')\boldsymbol{f}_j(\boldsymbol{k}(t'),t')dt', \quad (17.16)$$

it is possible to derive a related statistical solution. The contribution from the initial value can even be omitted if the Green's function is rapidly decaying. Interesting applications can be found looking at the Reynolds stress tensor, or even at its subgrid scale counterpart in Large-Eddy Simulation. Choosing an isotropic white noise for the forcing, with

$$\langle \boldsymbol{f}_i^*(\boldsymbol{p},t)\boldsymbol{f}_j(\boldsymbol{k},t')\rangle = \frac{B(k)}{4\pi k^2}\delta^3(\boldsymbol{k}-\boldsymbol{p})\delta(t-t'), \quad (17.17)$$

the Reynolds stress tensor obeys the following linear response solution

$$\overline{u_i'u_j'}(t) = \frac{\int_0^\infty B(k)dk}{4\pi}\int_{t_0}^{t} dt\left(\iint_{|\boldsymbol{K}|=1} e_i^{(\alpha)}(\boldsymbol{k})g_{\alpha\gamma}(\boldsymbol{k},t)g_{\beta\gamma}(\boldsymbol{k},t)e_j^{(\beta)}(\boldsymbol{k})d^2\boldsymbol{K}\right) \quad (17.18)$$

Even if the structure of this equation is similar to its counterpart for the initial value problem, it may be more interesting to have a steady state at large time, forgetting the intermediate history of the Reynolds stress tensor. For instance, a bounded steady state $\overline{u_i'u_j'}(\infty)$ is found in the absence of exponential or algebraic growth for $g_{\alpha\beta}$ in the inviscid case. More interesting, a steady state can be obtained even in some cases with exponential growth by reintroducing the viscous factor (17.13). For instance, the convergence of the temporal integral is analyzed in Cambon (1982) for a large class of flows subjected to strain dominated mean flow, i.e. in the presence of a hyperbolic instability. Because the mean advection is seen in wave space ($\boldsymbol{K} \to \boldsymbol{k}$), this asymptotic analysis only depends on the infrared part of the spectrum $B(k)$, since $B(k) \sim k^x$ when $k \to 0$.

Decomposing Eq. (17.18), or its viscous counterpart, in contributions related or not (in a local way) to the mean velocity gradient reveals typical coefficients, such as efficient viscosity and *Anisotropic Kinetic Alpha* (AKA) coefficients. For instance, in a quasi-parallel flow dominated by mean shear, one can formally write the Taylor series expansion of $\overline{u_i'u_2'} = R_i$ with respect to the gradient of the large-scale flow

$$R_i(\infty) = \Lambda_i U_0 - \nu_T S\delta_{i1}\ldots,$$

where two coefficients Λ_i and ν_T appear (N. Le Provost, private communication). Turbulent viscosity is well known, but RDT can also suggest negative values of ν_T, e.g. in rotating shear flows. Some recent applications of RDT to subgrid scale modelling by B. Dubrulle and coworkers appear to be related to such a calculation of an eddy viscosity.

The first term with Λ_i is known as the Λ-effect or AKA-effect (Frisch et al. 1987). Surprisingly, this term cannot be removed by Galilean invariance. It can only exist in anisotropic helical turbulence.

17.1.3 RDT for Two-Time Correlations

RDT can be used for evaluating the spectrum of the variance of a passive scalar concentration s', subject to a mean scalar gradient $\overline{s}$:

$$\dot{s'} = \frac{\partial s'}{\partial t} + u'_j \frac{\partial s'}{\partial x_j} = -\frac{\partial \overline{s}}{\partial x_j} u_j = 0,$$

in which the material derivative is replaced by a simple Eulerian time-derivative, whereas linear dynamics is only used for the bearer velocity field $\boldsymbol{u}'$. Given the strong analogy of the fluctuating trajectory equation, $\dot{x} = u'_i$, with the above-mentioned scalar's one, this approach can be used for calculating mean-square displacements, or single-particle diffusion, the particle being only a fluid element.

A different approach was initiated by Kaneda and Ishida (2000), calculating two-time velocity correlations via RDT. Homogeneous RDT cannot give access to the Lagrangian two-time correlations, because the 'Lagrangian' Fourier mode can afford oversimplified 'mean' trajectories, but not the 'fluctuating' ones. On the other hand, a simplified Corrsin hypothesis can be advocated for replacing the Lagrangian two-time velocity second-order correlations by their Eulerian counterpart. The two ways, either linearizing both scalar and velocity equations to derive second order single-time mixed correlations, or applying RDT to two-time second order velocity correlations using the simplified Corrsin hypothesis, yield the same final result for single-particle dispersion, but the second is much less demanding about physical assumptions. The simplified Corrsin hypothesis is less stringent than the crude assumption of equating $\dot{s'}$ and $\partial s'/\partial t$ from the very beginning.

The only advantage of the first way is to illustrate what information is gained using the following more sophisticated model: To incorporate the linear operators in a synthetic model of turbulence, usually referred to as Kinematic Simulation (KS), and to compute individual random trajectories from the synthetic velocity field which include linear (RDT) dynamics.

Applications to single-particle diffusion by rotating stratified turbulence are performed in Cambon et al. (2004b), with comparison of the statistical RDT model, the KS + RDT model, and DNS. Results are reported in Chap. 11.

17.2 Zonal RDT and Short-Wave Stability Analysis

The condition of extensional mean flow, having a velocity gradient matrix $\mathbf{A}$ uniform in the whole space, is very stringent, as is the statistical homogeneity (spatial invariance of any centered multi-point moment related to the fluctuating flow).

It is therefore useful to generalize the linear solutions in the presence of more complex "base" (or mean) flows, either for extending stability analyses, or for modelling non-homogeneous turbulence.

17.2.1 Irrotational Mean Flows

For irrotational mean flows, for instance potential flows, a tractable form of inviscid RDT in physical space can be based on the solution of equation that governs the fluctuating vorticity ($\omega_i = \epsilon_{ijk} u'_{j,k}$), a particular Kelvin equation for the linearized case without mean vorticity:

$$\omega_i(\boldsymbol{x}, t) = F_{ji}(\boldsymbol{X}, t, t_0)\omega_j(\boldsymbol{X}, t_0) \tag{17.19}$$

As we have seen in Chaps. 8 and 14, the related Weber equation

$$u'_i(\boldsymbol{x}, t) = F^{-1}_{ji}(\boldsymbol{X}, t, t_0)u'_j(\boldsymbol{X}, t_0) + \frac{\partial \phi(\boldsymbol{x}, t)}{\partial x_i}, \tag{17.20}$$

is particularly useful.

The mean flow may involve complex trajectories, which are defined by

$$x_i = \overline{x}_i(\boldsymbol{X}, t_0, t) \quad \text{with} \quad \dot{\overline{\boldsymbol{x}}} = \bar{u}_i(\boldsymbol{x}, t) \tag{17.21}$$

in which Lagrangian coordinates $\boldsymbol{X}$ denote the initial position at time t_0 of a particle, which reaches the position $\boldsymbol{x}$ at time t, and the overdot holds for the related 'mean' material derivative. The Cauchy matrix $\mathbf{F}$ does not need to be defined again. Of course, the more general solution such as (8.22) requires that the potential term in the right-hand-side of (17.20) be expressed in terms of initial data. This can be done using incompressibility condition with relevant boundary conditions, and even applications to compressible flows are possible (Goldstein 1978), as already discussed in Chap. 14. Of course, in the general incompressible case, integral nonlocal dependency, as in (8.22) reappears through the solution for ϕ in Eq. (17.20).

17.2.2 Zonal Stability Analysis with Disturbances Localized Around Base Flow Trajectories

As soon as the mean flow is rotational, equations such as (17.19) or (17.20) are no longer valid to tackle inhomogeneous RDT. Assuming weak inhomogeneity, considerable progress can be made without the need for irrotational mean flow, although simplifications occur in this case. As discussed earlier, turbulence which is fine-scale compared with the overall dimensions of the flow can be treated under RDT by following a notional particle advected by the mean flow. Thus, the results obtained for strictly homogeneous turbulence can be extended to the weakly inhomogeneous case, but with a mean velocity gradient matrix $A_{ij}(t)$ which reflects the $\partial \bar{u}_i/\partial x_j$ seen by the moving particle.

Even if the Green's function related to the canonical base flow (2.67) and (2.68) can give interesting information for linear stability analysis and short-time development of turbulence, this problem is somewhat unphysical in the absence of typical lengthscales for variation of the base flow gradients and disturbances. For instance, the Green's function in (17.4) only depends on the orientation, but not on the modulus, of the wavevector. Rather than to consider perturbations with an arbitrary wavelength k^{-1} in the presence of the flow (2.67), it is more physical to consider a base flow whose velocity gradients vary over a typical lengthscale ℓ, and to restrict the validity of the zonal stability analysis to perturbations with much shorter wavelengths, i.e. $k^{-1} \ll \ell$. In so doing, the disturbance field should locally experience advection and distortion effects by the base flow, similarly to the effects of an extensional flow with space-uniform gradients. Given a priori a lengthscale separation between base and disturbance flows, one can imagine to look through a mathematical magnifying glass at the vicinity of real base trajectories. This idea has been formalised in the context of flow stability (see the short-wave 'geometric optics' of Lifschitz and Hameiri 1991) using an asymptotic approach based on the WKB method, which is traditionally used to analyse the theoretical ray limit (i.e. short waves) in wave problems. The perturbation solution is written as

$$u_i'(\mathbf{x}, t) = a_i(\mathbf{x}, t) \exp(\imath \Phi(\mathbf{x}, t)/\epsilon) \tag{17.22}$$

with a similar expression for the fluctuating pressure, with amplitude $b(\boldsymbol{x}, t)$, where Φ is a real phase function and ϵ is a small parameter expressing the small scale of the "waves" represented by Eq. (17.22), while $a_i(\boldsymbol{x}, t)$ and $b(\boldsymbol{x}, t)$ are complex amplitudes which are expanded in powers of ϵ according to the WKB technique: $a_i = a_i^{(0)} + \epsilon a_i^{(1)} + \ldots$. Inserting (17.22) into the linearized equations (2.50) and (2.51) yields

$$\dot{\Phi} a_i^{(0)} + b^{(0)} \frac{\partial \Phi}{x_i} = 0,$$

and $k_i a_i^{(0)} = 0$ at the leading ϵ^{-1} order. Consequently, it is found that $b^{(0)} = 0$ and that

$$\dot{\Phi} = \frac{\partial \Phi}{\partial t} + \overline{u}_j \frac{\partial \Phi}{\partial x_j} = 0, \tag{17.23}$$

i.e. the wave crests of Eq. (17.22) are convected by the mean flow, whose trajectories are given by (17.21). It is then apparent that (17.22) is locally a plane-wave Fourier component of wavenumber

$$k_i(\boldsymbol{x}, t) = \epsilon^{-1} \frac{\partial \Phi}{\partial x_i}. \tag{17.24}$$

The spatial derivatives of $\dot{\Phi} = 0$ yield an eikonal equation:

$$\dot{k}_i = -A_{ji}(t) k_j, \tag{17.25}$$

where, as before, $A_{ij} = \partial \overline{u}_i / \partial x_j$ and the dot represents the mean-flow material derivative $\partial/\partial t + \overline{u}_i \partial/\partial x_i$. Finally, at the next ϵ^0 order, one obtains

$$\dot{a}_i^{(0)} = -M_{ij}(t) a_j^{(0)}, \tag{17.26}$$

with M_{ij} as in (17.2), after elimination of the pressure using the leading-order incompressibility condition $k_i a_i^{(0)} = 0$.

Equations (17.25) and (17.26) have exactly the same form as the basic equations of homogeneous RDT (Kelvin–Moffatt equations) and therefore, together with Eq. (17.21), describe the weakly inhomogeneous case at leading order. The only difference is that, rather than being related to simple time derivatives, the dots represent mean-flow material derivatives, implying that one should follow mean flow trajectories which differ from one to another. In homogeneous RDT, the different classes of disturbances are only labelled by the direction of the initial wavevector $\boldsymbol{K} = \boldsymbol{k}(t_0)$, and all trajectories, such as $\psi = constant$ in (2.70) are equivalent. In the zonal RDT approach, it is necessary to add the Lagrangian coordinate vector $\boldsymbol{X}$ for labelling different trajectories. In agreement with classic continuum mechanics, one has

$$d\overline{x}_i = F_{ij} dX_j + \bar{u}_i dt, \tag{17.27}$$

when differentiating the mean trajectory equation $\boldsymbol{x} = \overline{\boldsymbol{x}}(\boldsymbol{X}, t_0, t)$, so that $\dot{\Phi} = 0$ and (17.25) correspond to

$$\boldsymbol{k}\cdot\delta\boldsymbol{x} = \boldsymbol{K}\cdot\delta\boldsymbol{X}, \qquad k_i(\boldsymbol{X}, t) = F_{ji}^{-1}(\boldsymbol{X}, t, t_0) K_j, \tag{17.28}$$

which generalizes Eq. (17.5) together with $\boldsymbol{k}\cdot\boldsymbol{x} = \boldsymbol{K}\cdot\boldsymbol{X}$. It is perhaps useful to rewrite the complete system of equations, exhibiting all parameters and dependent variables (Godeferd et al. 2001)

$$\dot{x}_i = \bar{u}_i(\boldsymbol{x}) \tag{17.29}$$

$$\dot{k}_i = -\frac{\partial \bar{u}_j}{\partial x_i} k_j(\boldsymbol{X}, t) \tag{17.30}$$

$$\dot{a}_i = -\left(\delta_{in} - 2\frac{k_i k_n}{k_2}\right) \frac{\partial \bar{u}_n}{\partial x_j} a_j(\boldsymbol{X}, t), \tag{17.31}$$

with solutions (17.28) for $\boldsymbol{k}$, and

$$a_i(\boldsymbol{X}, \boldsymbol{k}, t) = G_{ij}(\boldsymbol{X}, \boldsymbol{K}, t, t_0) a_j(\boldsymbol{X}, \boldsymbol{K}, t, t_0).$$

Typical applications are presented in Chap. 11. It is even possible to consider the base flow as unsteady, and to directly use the Cauchy matrix for solving (17.31) with (17.28), without need for numerical solution of Eqs. (17.29) and (17.30), as illustrated by Guimbard and Leblanc (2006).

17.2.3 Using Characteristic Rays Related to Waves Instead of Trajectories

The WKB method by Lifschitz and Hameiri (1991) is different from those developments, which lead to 'geometric optics' and 'physical optics'. Accordingly, the first one (Lifschitz and Hameiri 1991) is referred to *short-wave* linear stability analysis, or zonal WKB RDT everywhere in this book, whereas only the second will be denoted 'geometric optics' from now on. The starting point of 'true geometric optics' is similar to Eq. (17.22), but the spatio-temporal evolution is assumed to be slow, so that $\boldsymbol{x}$ and t in (17.22) ought to be replaced by $\epsilon\boldsymbol{x}$ and ϵt, respectively. In 'true geometric optics', the leading order approximation is $\epsilon^{(0)}$, and the inhomogeneous dispersion law is exhibited, for instance in injecting Eq. (17.22) with ($\boldsymbol{x} \to \epsilon\boldsymbol{x}$, $t \to \epsilon t$) in linearized equations (2.50) and (2.51) so that:

$$\dot{\Phi} = \pm\sigma(\nabla\Phi) - \nabla\Phi \cdot \bar{\boldsymbol{u}}, \tag{17.32}$$

in which, for the sake of simplicity of notations, spatial and temporal operators concern 'slow' variables. Stressing, as before, that $\boldsymbol{k} = \nabla\Phi$, an Hamiltonian function can be defined as

$$\dot{\Phi} = H(\boldsymbol{k}, \boldsymbol{x}) = \pm\sigma(\boldsymbol{k}) - \boldsymbol{k} \cdot \bar{\boldsymbol{u}} \tag{17.33}$$

Accordingly, an Hamiltonian dynamical system is derived:

$$\dot{\boldsymbol{x}} = \frac{\partial H}{\partial \boldsymbol{k}} \tag{17.34}$$

$$\dot{\boldsymbol{k}} = -\frac{\partial H}{\partial \boldsymbol{x}}. \tag{17.35}$$

Because H includes both the dispersion frequency and the Doppler frequency due to convection by the mean flow, or $\boldsymbol{k}\cdot\bar{\boldsymbol{u}}$, the right-hand side of Eq. (17.34) is the sum of group and convection velocities, and the related characteristic line is the ray along which energy propagates. Applications of the Hamiltonian dynamical system are used by Galmiche (1999), for instance, in the case of gravity waves propagating in an inhomogeneous medium. Note that the dispersion law cannot appear at the leading order in the Lifschitz–Hameiri WKB method, so that the previous system of Hamiltonian equations reduces to the trajectory equation (17.29) and to the Eikonal equation (17.24), respectively, with $H = -\boldsymbol{k}\cdot\bar{\boldsymbol{u}}$. The dispersion law is recovered in Lifschitz and Hameiri (1991) at the next order, via the solution for the amplitude equation (17.31), similarly to RDT solutions of Chaps. 7 and 10. Using the development in terms of slow spatio-temporal variables, in 'true geometric optics', the next order (ϵ^1) leads to the 'physical optics' approximation, which yields conservation of wave action.

In the same context of gravity waves, promising perspectives, with transport of statistical spectra with nonlinear effects and diffusion, are offered by Carnevale and Frederiksen (1983). In the latter work, the Hamiltonian function which appears in Eq. (17.33) is affected by nonlinear dynamics in connection with a simplified version of DIA, and the role of resonant triad interactions is displayed.

Another interesting field of application is aeroacoustics, since zonal RDT along trajectories can be applied to a weakly compressible flow: both vortical and entropic modes can be considered, but the acoustic mode is always missed because it is not a short-wavelength one at low Mach number. On the other hand, it is possible to extend the zonal analysis along trajectories (linked to velocity $\boldsymbol{u}$) by a ray-method along acoustic rays, which are linked to $\boldsymbol{u} + a\boldsymbol{k}$ and $\boldsymbol{u} - a\boldsymbol{k}$.

17.3 Application to Statistical Modeling of Inhomogeneous Turbulence

The stability analysis framework is no longer discussed in the following for the sake of brevity, and only incompressible turbulence is considered.

Generalisation of the Craya equation can be sought in the presence of an arbitrary mean flow, in deriving a complete equation for the two-point velocity correlation tensor with centered position from Eq. (2.50):

$$R_{ij}(\boldsymbol{r}, \boldsymbol{x}, t) = \overline{u_i'(\boldsymbol{x} - \boldsymbol{r}/2)u_j'(\boldsymbol{x} + \boldsymbol{r}/2)}. \tag{17.36}$$

Fourier transform can be applied with respect to the separation distance $\boldsymbol{r}$, so that the equation for the hybrid spectral-physical tensor $\hat{R}(\boldsymbol{k}, \boldsymbol{x}, t)$ can be displayed. Equations for both $\mathbf{R}$ and $\hat{\mathbf{R}}$ are very complicated. Correlations involving the pressure cannot be expressed in terms of velocity only, as in Eq. (2.102), especially if boundary conditions have to be taken into account. Hence, it is necessary to add some assumptions, or to introduce some multi-scale approach. The remaining necessary assumption is the separation of spectral and physical space dependencies of the correlations, for example by treating the statistical inhomogeneity as weak. Even for homogeneous turbulence, going beyond the isotropic case entails a high computational cost for two-point simulations using classical nonlinear closures, a cost which is not negligible compared with that of direct numerical simulation. Thus, it is currently unattractive to solve the full set of equations resulting from closures such as DIA, TFM or EDQNM in the inhomogeneous case without simplifications.

An alternative approach can take inhomogeneity into account *via* the basis set of modes used to express the fluctuations, while, as far as possible, maintaining the structure of equations of the correlation matrix similar to that of the homogeneous case. The modes which substitute for Fourier components may, for instance, be chosen to satisfy the boundary and incompressibility conditions. Accordingly, strong inhomogeneity due to solid boundaries can be accommodated by the very definition of the fluctuation modes. This approach is illustrated by the work of Turner (1999), who considered the problem of channel flow using suitably chosen modes whose amplitude equations are analogous to those of Fourier modes in the homogeneous case and which were closed via a random phase approximation. The normal modes of the linear problem might well be good candidates in this type of approach.

17.3.1 Transport Models Along Mean Trajectories

Simplified equations for $\hat{R}(\boldsymbol{k}, \boldsymbol{x}, t)$ are suggested by the short-wave analysis of Sect. 17.2.2. In turbulent flows, the fluctuating field is not the single component (17.22), but instead consists of a random superposition of such components. As one might expect, given the behavior of the underlying local Fourier components described above, it can be shown that, at leading order, weakly inhomogeneous turbulence evolves according to

$$\dot{\hat{R}}_{ij} + M_{ik}\hat{R}_{kj} + M_{jk}\hat{R}_{ik} = 0, \tag{17.37}$$

where the dot now represents the operator

$$\frac{\partial}{\partial t} + \overline{u}_i \frac{\partial}{\partial x_i}, -\frac{\partial \overline{u}_j}{\partial x_i} k_j \frac{\partial}{\partial k_i}, \tag{17.38}$$

and expresses both convection by the mean flow and evolution of the wavenumber of individual Fourier components according to Eq. (17.25). The spectral evolution

Eq. (17.37) corresponds to the RDT limit of its homogeneous equivalent, i.e. the Craya equation, provided that the dot operator is interpreted appropriately. Thus, following the mean flow, the leading-order, local spectral tensor $\hat{R}_{ij}(\mathbf{k}, \mathbf{x}, t)$ behaves as in homogeneous RDT, being given in terms of its initial values and the RDT Green's function. The obvious way to incorporate nonlinearity and viscosity into this description is to use

$$\dot{\hat{R}}_{ij} + M_{ik}\hat{R}_{kj} + M_{jk}\hat{R}_{ik} = T_{ij} - D_{ij} - 2\nu k^2 \hat{R}_{ij} \tag{17.39}$$

rather than Eq. (17.37) to describe spectral evolution, where T_{ij} could be modelled using a homogeneous spectral closure. For the sake of completeness, the tensor D_{ij} would typically represent inhomogeneous diffusion across the mean streamline.

An interesting alternative, as proposed by Nazarenko et al. (1999), is to derive weakly inhomogeneous RDT using a Gabor transform and related WKB development. A small parameter like ϵ in Eq. (17.22) appears. It is the ratio of the wave-length of the Fourier mode to the length of its Gaussian envelope. The interest of this method is not to derive the equations for the wave vector and the amplitude of the fluctuating velocity field (the method presented above does the job in a simplest and more general way), but to calculate a space-dependent Reynolds stress tensor by integrating $\hat{R}_{ij}(\boldsymbol{x}, \boldsymbol{k}, t)$ as in Eq. (17.14). Consequently, the nonlinear term which expresses the feedback from the Reynolds stress tensor in (2.48) can be evaluated (it is zero in pure homogeneous RDT).

17.3.2 Semi-empirical Transport "Shell" Models

This approach, discussed in Godeferd et al. (2001) is mainly illustrated by semi-empirical transport models, which treat the dependency with respect to the position variable by analogy with one-point modelling. These models cannot incorporate all the information coming from the general Eq. (17.39), but they retain some element of its structure. They are very far from the 'shell models' presented by, e.g. Bohr et al. (1998), but they share with them the property that the spectral dependency is only retained through the modulus of the wave vector. Accordingly, it is assumed that primitive equations for $\hat{R}(\boldsymbol{k}, \boldsymbol{x}, t)$ are integrated over spherical shells of radius k. Because of spherical averaging, one has to forget the idea of recovering the asymptotic RDT limit, even in the homogeneous case, and needs to model the 'rapid' terms comprising distortion and pressure-strain correlations, modelling which is unnecessary in the fully anisotropic theory. Transport models for the joint physical/spectral space energy spectrum $E(k, \mathbf{x})$ have been developed, which describe inhomogeneity in a similar way to the diffusive terms in the $k - \varepsilon$ model, but allow a better treatment of dissipation, calculated from the energy spectrum. Examples include the inhomogeneous EDQNM model of Burden (1991), the SCIT (Simplified Closure for Inhomogeneous Turbulence) model developed at Lyon (Touil et al. 2000) and the

LWN (Local Wave Number) model developed at Los Alamos (Clark and Zemach 1995). These approaches are extensively discussed in Sagaut et al. (2006).

As a useful compromise between RSM and subgrid-scale modelling, with seamless transition from RANS to LES, the partially integrated Reynolds stress modelling by Chaouat and Schiestel (2005, 2007) deserves attention. The underlying spectral formalism is not based on closures but on heuristic arguments, whereas spatial Taylor expansions are used for the position coordinates in physical space.

17.4 Other Perspectives in Extended Linearized Approaches

Some analytical relations are summarized in Fig. 17.1, particularly for displaying the role of the Cauchy matrix in both homogeneous and zonal RDT (eikonal equation) in the general case, and its particular involvement for irrotational mean (base) flows.

Application of RDT to subgrid-scale modelling appears to be attractive, but it is probably premature to report related studies, and large-eddy simulation (LES) is largely outside the scope of this book. The interested reader is referred to Sagaut (2005) for an exhaustive presentation.

One can just mention a direct use of the Cauchy matrix for deriving pressure-released simplified solutions for the transport of the subgrid-scale stress tensor, very similarly to what is done for the Reynolds stress tensor. This way for improving LES,

	Euler (fully nonlinear)	Linearized (WKB RDT)	Homogeneous RDT	Pressure-released RDT
Trajectory	Any	Any Coarse grained $\delta\mathbf{x} = F\delta\mathbf{X}$	Linear $\mathbf{x} = F\mathbf{X}$	
Transported scalar (gradient)	$\nabla\mathbf{s}(\mathbf{x},t) = (F^t)^{-1}\nabla\mathbf{s}(\mathbf{X},0)$	Eikonal solution $\mathbf{k} = (F^t)^{-1}\mathbf{K}$ general case : $\mathbf{k}(\mathbf{X},t)$	Eikonal solution $\mathbf{k} = (F^t)^{-1}\mathbf{K}$	
Kelvin equation	$\omega(\mathbf{x},t) = F\omega(\mathbf{X},0)$	Valid only if $A = A^t$	idem	
Weber equation	$\mathbf{u}(\mathbf{x},t) = (F^t)^{-1}\mathbf{u}(\mathbf{X},0) + \nabla\phi$	Valid only if $A = A^t$	idem	$\mathbf{u}(\mathbf{x},t) = H\mathbf{u}(\mathbf{X},0)$ in irrotational cases : $H = (F^t)^{-1}$

Fig. 17.1 Sum of the main useful relations for RDT analysis. It is recalled that $\mathbf{F}$ is the solution of $\dot{\mathbf{F}} = \mathbf{AF}$. Transposed is denoted as $\mathbf{A}^t$, instead of $\tilde{\mathbf{A}}$ in the text

discussed by C. Meneveau (invited talk, ETC11 conference, Porto, June 2007), is in the line of the seminal study by Crow (1968), and, of course, is in agreement with many instances of pressure-released "solutions" given in this book. We think that this approach is valid for a strain-dominated coarse-grain flow, but is more questionable in the case of a vorticity-dominated flow. In applying the pressure-released approach to a rotational coarse-grain flow, it must be born in mind that $\mathbf{F}$ must be replaced by $\mathbf{H}$, whose history involves transposed $\mathbf{A}$, not to mention that the full RDT solution can be very different from its pressure-released counterpart (one uses $\dot{\tilde{\mathbf{F}}} = \mathbf{A}\tilde{\mathbf{F}}$ and $\dot{\tilde{\mathbf{F}}}^{-1} = -\tilde{\mathbf{A}}\tilde{\mathbf{F}}^{-1}$).

Other applications deal with the transport of the coarse-grain mean velocity gradient, which is governed by the following equation (as the mean flow gradient for homogeneous RDT, but with additional diffusive terms, not given explicitly):

$$\dot{A}_{ij} + A_{in}A_{nj} = \frac{\partial^2 P}{\partial x_i \partial x_j} + \text{diffusive and subgrid terms.}$$

A presentation is now (present edition) given in Chap. 4.

17.5 Isotropic Turbulence with Production: Linear and Nonlinear Dynamics Under Spherical Compression

This case, already addressed in Sect. 14.3, illustrates an optimal interplay between linear and nonlinear effects, as a watershed between the two parts of this chapter. One considers an isotropic compressing mean flow, not divergence free, such that

$$F_{ij}(t) = J(t)^{1/3}\delta_{ij},$$

with $J(t) = \det \mathbf{F}(t)$ the volumetric ratio. On the other hand, the fluctuating velocity field remains divergencefree. With respect to incompressible irrotational straining, the "rapid distortion" limit

$$u_i(\boldsymbol{x}, t) = F_{ji}^{-1}(t)u_j(\boldsymbol{X}, t) + \frac{\partial \phi}{\partial x_i}$$

simply becomes

$$u_i(\boldsymbol{x}, t) = J(t)^{-1/3}u_i(\boldsymbol{X}, 0), \tag{17.40}$$

with $\boldsymbol{x} = J^{1/3}(t)\boldsymbol{X}$. Conversely in Fourier space

$$\hat{u}_i(\boldsymbol{k}, t) = P_{mi}(\boldsymbol{\alpha})F_{jm}^{-1}(t)\hat{u}_j(\boldsymbol{K}, 0)$$

yields

$$\hat{\boldsymbol{u}}(\boldsymbol{k}, t) = J^{2/3}(t)\hat{\boldsymbol{u}}(\boldsymbol{K}, 0), \tag{17.41}$$

with $\boldsymbol{k} = J(t)^{-1/3}\boldsymbol{K}$.

The rescaling of both space coordinates and velocity is thereby given by conventional RDT. Less usual is the removal of the 'production' term by a rescaling of time, or $dt = J^{2/3}(t)dt^*$. Finally, basic Napier–Stokes equations *without production and advection by the mean flow* are recovered in term of the following 'starred' variables (Eq. (14.51))

$$\boldsymbol{u}^* = J^{1/3}(t)\boldsymbol{u}, \boldsymbol{x}^* = \boldsymbol{X} = J^{-1/3}(t)\boldsymbol{x}, t^* = \int_0^t J^{-2/3}(t')dt'.$$

But the kinematic viscosity ν ought to be considered as time-varying during the process of mean compression.

17.5.1 Discussion. Using Nonlinear Dynamical Models for HIT

A problem of turbulence undergoing spherical compression or dilatation is turned into decaying HIT with variable kinematic viscosity, that amounts to a Reynolds number varying in $1/\nu$ since $L^*u^* = Lu$. Any robust model for HIT can be used in terms of starred variables, with results easily recovered in terms of primitive variables. The example of the $\mathcal{K} - \varepsilon$ model at high Reynolds number is given in Cambon et al. (1992) (see also Sect. 14.3). Because the kinematic viscosity decreases (and the Reynolds number increases) during a compression, as illustrated by pressurised wind-tunnel experiments, conventional high-Reynolds $\mathcal{K} - \varepsilon$ are relevant if the initial Reynolds number is sufficiently high. On the other hand, a very special imbalance is created between the skewness term and the palenstrophy term: the second one (viscous destruction of enstrophy) is directly affected by the lessening of kinematic viscosity, whereas the first one (nonlinear production of enstrophy by vortex stretching) is affected with some delay. EDQNM for HIT remains an excellent candidate for exploring such a dynamical, non-conventional, spectral imbalance. Interesting features of compressed fluid are summarized as follows:

- Because of isotropic straining process, the RDT limit is drastically simplified, with no need for solving the pressure fluctuation as in the linearized Weber equation.
- A rescaling of the time can account for the nonlinear effect in this type of straining process, because a single (radial) direction and thereby a single dimension is called into play.
- Conventional separation into 'rapid' (RDT) and 'slow' (nonlinear) terms is radically questioned. For instance even basic equations show that nonlinear terms with dimension $U^2(t)/L(t)$ can be faster than linear terms in $\frac{j}{J}U(t)$ under spherical compression.

17.5.2 A Recent Application to Plasma Dynamics

The strategy of using EDQNM for decaying HIT, together with the above mentioned dynamical rescaling was applied recently $\cdots$ but to a hot plasma, in line with applications to confinement. All the formalism is the same as for a fluid until the law for the time-dependent kinematic viscosity is chosen. At this stage, a very different behavior is found. For the adiabatic compression of ideal monatomic gas, temperature evolves as $T(t) = T_0 J^{-2/3}(t)$ so that the viscosity is $\mu = \mu_0 J(t)^{-2\beta/3}$. Accordingly

$$\nu(t) = \frac{\mu}{\rho} = \nu_0 J(t)^{-2\beta/3+1}. \tag{17.42}$$

In the case of a hot plasma in kinetic regime, $\beta = 5/2$, so that $\nu(t)$ increases as $J(t)^{-2/3}$ instead of decreasing as in a gas. The difference is due to the rapid increase of the temperature of electrons, when this phase is well dissociated. Accordingly, turbulent plasmas under compression and entering the kinetic regime can experience a sudden increase of kinetic energy dissipation due to an abrupt growth of the viscosity from temperature increase. The reader is referred to Davidovits and Fisch (2016) for DNS and to Viciconte et al. (2017) for use of both DNS and EDQNM results.

17.6 Generalities on Triadic Closures

Fundamentals of anisotropic triadic closures are given in Chaps. 2, 4, 7, 8 and 12. A general discussion is offered on various aspects of these closures. Strong anisotropy is the most original aspect which is emphasized throughout this book, but it is perhaps useful to recall the role of the characteristic time (e.g. eddy damping in EDQNM) for the decorrelation of triple correlations in canonical incompressible HIT, and not only in EDQNM. The closure for compressible quasi-isentropic isotropic turbulence, which is a very interesting case of interaction of "strong" solenoidal turbulence with pseudo-acoustical "weak" wave-turbulence, also merits an additional discussion. Finally, the theory of "linear response" by Kaneda and coworkers, touched upon in Chap. 8, is rediscussed in connection with an approach to weak anisotropy.

17.6.1 Canonical HIT, Dependence on the "Eddy Damping" for the Scaling of the Energy Spectrum in the Inertial Range

All technical details about EDQNM for HIT are given in Chap. 4. In this case, and only looking at the power-law slope of the single-time energy spectrum $E(k)$ in the inertial range, all "triadic" theories, including the most sophisticated self-consistent

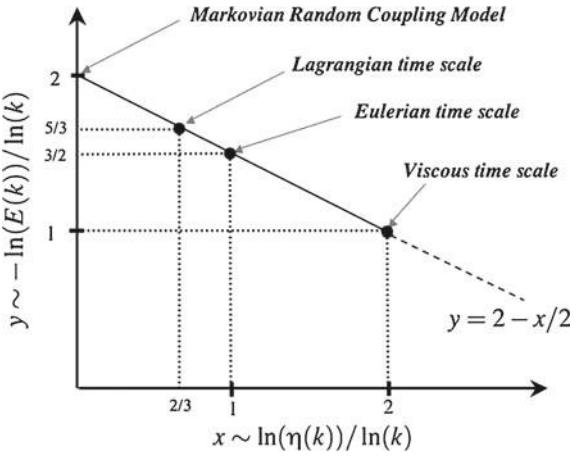

Fig. 17.2 Map on a single straight line of the $E(k)$-to-$\eta(k)$ power-law exponents. Suggested by W. Bos

ones, from DIA to TFM, LHDIA and LRA, can be analyzed from the following simple, purely dimensional and local in wavespace, argument[2]:

$$F(k) = \int_k^\infty T(k)dk \sim \eta(k)^{(-1)}k^4E^2 \to \varepsilon,$$

where $\eta(k)$ is the Eddy Damping term in EDQNM, or a constant external frequency in isotropic or isotropized wave-turbulence theory. A link of the exponent of the power-law for $E(k)$, or $E(k) \sim k^{-y}$, to the exponent of the power law for $\eta(k)$,or $\eta(k) \sim k^x$ is immediately derived as a linear law

$$y = 2 - x/2.$$

Some important cases are discussed as follows, and summarized in Fig. 17.2 with $0 \leq x \leq 2$:

- Constant $\eta(k) = f_0$: $x = 0$, $y = 2$, $E \sim k^{-2}$. This case is illustrated by some models, such as the Markovian Random Coupling Model, which amount to EDQNM with constant ED. They also illustrate oversimplified cases of wave-turbulence, in which $\eta(k)$ is not a nonlinear decorrelation time, but instead the time-frequency of the external linear wave-operator ($f_0 = 2\Omega$ in rotating turbulence, $f_0 = N$ in stratified turbulence, etc.).
- "Eulerian" time-scale: the sweeping effect, or advection of small scales by the largest ones, seen in the Eulerian framework, suggests $\eta(k) \sim Uk$, yielding $x = 1$, $y = 3/2$, and $E \sim k^{-3/2}$. The wrong exponent of original DIA is immediately derived.

[2]This analysis can be found in existing literature, e.g. in books by Frisch and Lesieur, but it was suggested by a very concise and pedagogical informal talk, given by W. Bos in the CNRS Summer School in Cargèse (France), August 13–25, 2007.

- "Lagrangian" time scale: one of the simplest proposals, by Kraichnan and Orszag, is $\eta(k) \sim \varepsilon^{1/3}k^{2/3}$, yielding $x = 2/3$, $y = 5/3$. More sophisticated proposals, as $\eta(k) \sim k^{3/2}E^{1/2}$, or $\eta(k) \sim \sqrt{\int_0^k p^2 E(p)dp}$ (see Chap. 4) are also consistent with $x = 2/3$, $y = 5/3$ in the inertial range. The correct Kolmogorov law is recovered, as found in EDQNM and in all self-consistent theories correcting DIA with Lagrangian or semi-Lagrangian approaches, not to mention the very recent self-consistent EDQNM version by Bos and Bertoglio (2006).
- Pure viscous time-scale, $\eta(k) \sim \nu k^2$: $x = 2$, $y = 1$, $E(k) \sim k^{-1}$. This correspond to a late-time of decay, or a transient zone between the inertial range and the dissipative one.

It is a bit surprising that a complex spectral flux term, which results from the difference of two large nonlocal terms (e.g. $pE(q)(k^2E(p) - p^2E(q))$ in Eq. (4.335)), which are individually high and quasi-balanced, might be so simply evaluated by $k^3E(k)^2$, using pure dimensional analysis, but this works for our simple purpose of deriving power laws.

To speak of 'Eulerian' or 'Lagrangian' time-scales is almost a caricature, without a profound survey of Lagrangian, semi-Lagrangian and Eulerian theories. We have chosen not to treat in detail these aspects in this book, but let us mention at least two points. On the one hand, the Lagrangian or Eulerian origin of the nonlinear decorrelation time-scale of triple correlations can be ignored, as it is done in the Local Energy Transfer theory by Mc Comb (1974), which is also a self-consistent theory (i.e. which involves no adjustable parameter dealing with the Kolmogorov constant) giving the correct point $x = 2/3$, $y = -5/3$ in the diagram. On the other hand, it is important to recall that the parameter $\eta(k)$ comes from the Kraichnan's response tensor, which is an essential ingredient of any triadic spectral closure, and therefore is revisited in the next section. This response tensor, either random or averaged, is a tangent Green's function to a nonlinear state, and therefore is subject to the effects of advection and deformation by the velocity field. In this sense, the RDT Green's function (in fact both $\mathbf{G}(\boldsymbol{k}, t, t')$ and $\mathbf{F}(t, t')$ in 'mean' Eulerian, $\mathbf{G}(\boldsymbol{K}, t, t')$ in Lagrangian), illustrates in an oversimplified way these advection and deformation effects by the mean flow, even if nonlinear dynamics is essential in the Kraichnan Green's function. Accordingly, we think that a physical discussion taking into account the different advection and deformation aspects cannot ignore their different translation in Lagrangian or Eulerian frameworks.

17.6.2 Anisotropic Triadic Closures at a Glance

In homogeneous isotropic turbulence, all classical closures share a common background, as discussed in the previous section. Anisotropy, even introduced in the context of homogeneous anisotropic turbulence, and illustrated by shear-driven or buoyancy-driven flows, induces new difficulties that are treated with different levels of approximation. Accordingly, multiple more or less elaborate extensions of closures

can be proposed. The Table in Fig. 17.3 is an attempt to gather the versions in which we have an experience of complete numerical solution, often with comparison to DNS. Illustration of the results can be found throughout this book.

For these reasons, we emphasize closure models and theories with QNM structure, from generalized EDQNM versions to their asymptotic limit of wave turbulence theory, when it is relevant.

Equations for Non-Markovian, two-time, triadic theories and models do exist for anisotropic and even inhomogeneous turbulence, and are addressed in this book, but there is no available tractable numerical code to solve them, without strong additional approximations. For instance, the Kraichnan's Direct Interaction Approximation (DIA), introduced for HIT (Kraichnan 1958), has been extended towards inhomogeneous shear-driven and thermally-driven flows (Kraichnan 1964). In addition to the complexity of equations in the latter cases, the diagonal form of the nonlinear Green's tensor is probably a flaw inherited from the HIT case, as discussed in the next subsection. The simplified context of HAT should have given an intermediate step between HIT and inhomogeneous shear-driven or thermally-driven turbulence: Unfortunately, it has never been addressed using DIA; even more, linear RDT and weakly nonlinear wave turbulence theory in HAT remain outside the scope of DIA. The same remark holds for other Kraichnan's theories, Test-Field Model (TFM) and Lagrangian History Direct Interaction Approximation (LHDIA), and for the Lagrangian Renormalized Approximation (LRA) (Kaneda 2007) as well.

Going back to the table in Fig. 17.3, the star indicates that a numerical code is available and has been validated for solving the model equations. Two important classes of model equations are shown. The first class with angle-dependent 3D description allows for an accurate resolution of the linear and exact part of equations for second-order two-point statistics. EDQNM1 version is sufficient for closing the contribution from third-order correlations, mediated by nonlinearity, when turbulent flows are dominated by production, in the presence of mean velocity gradients with nonzero symmetric part or in the unstably stratified case (USHT-EDQNM code). More elaborate EDQNM2-3 versions are needed for flows dominated by interacting waves, and a code is available for purely rotating turbulence (RHT-EDQNM) and purely stably stratified turbulence (SSHT-EDQNM). In the case of purely rotating turbulence only, the EDQNM3 version can match the asymptotic limit of inertial wave turbulence theory, with an Asymptotic Quasi-normal Markovian (AQNM) code (Bellet et al. 2006) that numerically captures all resonant triads.

In the second class of models, the statistical description of two-point second-order correlations is restricted to spherically-averaged descriptors. This dramatic simplification allows to treat arbitrary mean velocity gradients (including a symmetric part) moving from EDQNM1 to the model by Mons et al. (2016) with EDQNM1-S name in the table. A similar procedure, using truncation of angular harmonics at the first non-trivial order, allowed to switch from EDQNM1 (USHT-EDQNM) to the USHT-EDQNM-S code (Briard et al. 2017), with a possibility to combine effects of mean velocity gradients and mean buoyancy gradient. On the other hand, angle-averaged models cannot reproduce linear dynamics for two-point second-order statistics, so that they partially miss the RDT limit and are restricted to weak or

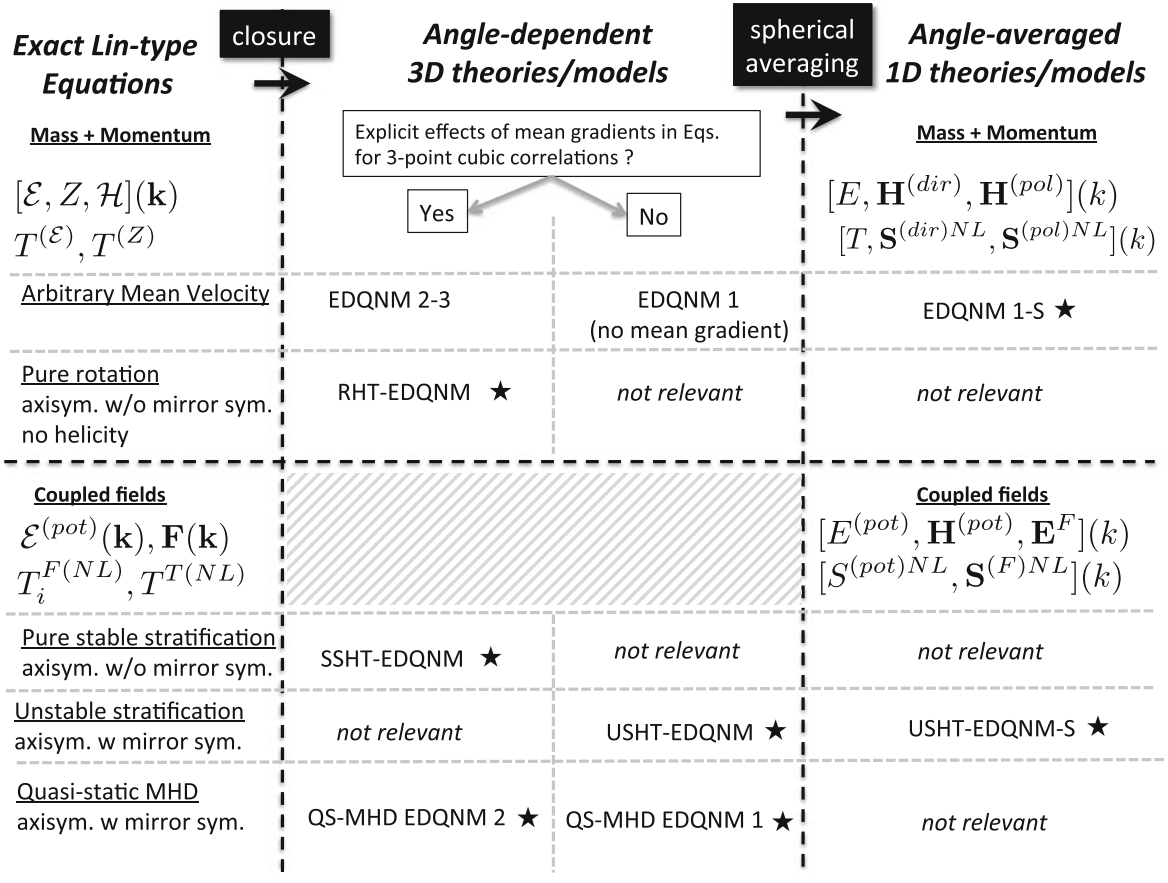

Fig. 17.3 Anisotropic QNM closures

moderate (depending on the cases) anisotropy. Finally, the angle-averaged models can afford any anisotropy, whereas the angle-dependent models (with available numerical code) are all restricted to axisymmetry.

17.7 Solving the Linear Operator to Account for Strong Anisotropy

17.7.1 Random and Averaged Nonlinear Green's Functions

The concept of *response tensor* is in the heart of all closures inherited from Kraichnan. The most general definition is obtained from writing the perturbation equation for a disturbance field $\delta\hat{\boldsymbol{u}}$ created by an external disturbance $\delta\hat{\boldsymbol{f}}$ (e.g. from a solenoidal stirring force):

$$\delta\hat{u}_i(\boldsymbol{k},t) = \iint\int_{t_0}^{t} \mathcal{G}_{ij}(\boldsymbol{k},\boldsymbol{k}',t,t')\delta\hat{f}_j(\boldsymbol{k}',t')d^3\boldsymbol{k}'dt'. \tag{17.43}$$

It is very important to stress that the perturbation is performed around any particular random realization of $\hat{\boldsymbol{u}}$, which is a solution of the fully nonlinear Navier–Stokes equations in Fourier space. The nonlinear term $\widehat{\boldsymbol{uu}}$ leads to the contribution $2\widehat{\boldsymbol{u}\delta\boldsymbol{u}}$ in the $\delta\hat{\boldsymbol{u}}$-equation. Accordingly, the response function is also a random variable, changing from realization to realization of the bearer velocity field $\hat{\boldsymbol{u}}$. Therefore, this relation is not only an integral formulation in time, but also in the wavevector space. In this sense, the response tensor before averaging is a tangent Green's function related to a *random and nonlinear* state.

Only the statistical counterpart of $\mathcal{G}$,[3] obtained from statistical ensemble averaging, becomes local in wavespace assuming spatial homogeneity, i.e.

$$\langle\mathcal{G}_{ij}\rangle = G_{ij}^{(NL)}(\boldsymbol{k},t,t')\delta^3(\boldsymbol{k}-\boldsymbol{k}'). \tag{17.44}$$

One can just recall that the eddy damping term in the previous section can be related to $\mathbf{G}^{(NL)}$ by $\eta(k)^{-1} \sim \int G^{(NL)}(\boldsymbol{k},t,t')dt'$.

Considering a homogeneous turbulent velocity field, but subjected to a mean flow which is not itself homogeneous but with uniform velocity gradients, the above equation must be modified as follows

$$\langle\mathcal{G}_{ij}\rangle = G_{ij}^{(NL)}(\boldsymbol{k},t,t')\delta^3(\boldsymbol{k}-\tilde{\mathbf{F}}^{-1}(t,t')\boldsymbol{k}'). \tag{17.45}$$

A purely diagonal form is recovered in terms of mean-Lagrangian wave-vectors, yielding a term $\delta^3(\boldsymbol{K}-\boldsymbol{K}')$.

[3] $\mathcal{G}$ must be not confused with the linear Green's function in physical space in Eq. (8.22).

From these general considerations, we consider that the confusion between $\mathcal{G}$ and $\langle \mathcal{G} \rangle \to G^{(NL)}$ is highly misleading, even without mean flow. Identification of the random response function with its averaged counterpart is made in Leslie (1973), for instance, and by many other authors. Such oversimplifications do not lead to an incorrect final form of DIA equations, for instance, but this is only because these equations are consistent with a "first loop" iterative expansion around a deterministic zeroth-order state for $\mathbf{G}^{(NL)}$. The same procedure performed in the presence of a mean flow, using (17.44) instead of (17.45) is nothing but wrong.

Introducing a perturbative expansion in terms of the basic nonlinear term in Navier–Stokes equations, the zeroth-order response function naturally appears as the viscous linear Green's function, which is really deterministic (or "statistically sharp" in Leslie's parlance). In the case of HIT without mean flow, the linear operator reduces to the viscous term, so that the basic Green's function, or zeroth order response tensor is simply

$$G_{ij}^{(0)}(\boldsymbol{k}, t, t') = P_{ij}(\boldsymbol{k}) \exp[-\nu k^2 (t - t')].$$

17.7.2 Homogeneous Anisotropic Turbulence with a Mean Flow

For HAT in the presence of a distorting mean flow, the linear operator inherited from Rapid Distortion Theory must be accounted for: it is an essential building block for constructing the nonlinear theory, and it can generate the relevant nontrivial zeroth order response function of any 'triadic' closure, including DIA, EDQNM, etc.

In the presence of an additional right-hand-side term $f_i(\boldsymbol{k}, t)$ in the basic spectral equation

$$\dot{\hat{u}}_i + M_{ij}\hat{u}_j + \nu k^2 \hat{u}_i = f_i, \tag{17.46}$$

which represents nonlinearity and possibly random forcing, the basic "RDT" solution can be generalized as

$$\begin{aligned} \hat{u}_i(\boldsymbol{k}(t), t) = {} & G_{ij}^{(0)}(\boldsymbol{k}, t, t')\hat{u}_j(\boldsymbol{k}(t'), t') \\ & + \int_{t'}^{t} G_{ij}^{(0)}(\boldsymbol{k}, t, \tau) f_j(\boldsymbol{k}(\tau), \tau) d\tau. \end{aligned} \tag{17.47}$$

It is necessary to include the viscous term, so that $\mathbf{G}^{(0)}$ is the viscous Green's function given by

$$G_{ij}^{(0)}(\boldsymbol{k}, t, t') = G_{ij}(\boldsymbol{k}, t, t') V_0(\boldsymbol{k}, t, t'), \tag{17.48}$$

where $\mathbf{G}$ (in pure inviscid RDT) and V_0 are defined in Eq. (17.13) in Sect. 17.1.2. The latter equation is generic, and similar forms can be found for the equations which govern the statistical moments of $\hat{\boldsymbol{u}}$ at any order.

For instance, the equation for the second-order spectral tensor, or Craya equation (2.102), is formally solved as

$$\hat{R}_{ij}(\boldsymbol{k}(t),t) = G^{(0)}_{im}(\boldsymbol{k},t,t_0)G^{(0)}_{jn}(\boldsymbol{k},t,t_0)\hat{R}_{mn}(\boldsymbol{k}(t_0),t_0) + \int_{t_0}^{t} G^{(0)}_{im}(\boldsymbol{k},t,t')G^{(0)}_{jn}(\boldsymbol{k},t,t')T_{mn}(\boldsymbol{k}(t'),t')dt', \quad (17.49)$$

and similarly for the third order, with a three-fold product

$$\mathbf{G}^{(0)}(\boldsymbol{k},t,t') \otimes \mathbf{G}^{(0)}(\boldsymbol{p},t,t') \otimes \mathbf{G}^{(0)}(\boldsymbol{q},t,t'), \quad \boldsymbol{k}+\boldsymbol{p}+\boldsymbol{q}=0,$$

called into play (see Eq. (2.117), revisited in the next section).

In a slightly different form, one can introduce a new variable $\boldsymbol{a}$ defined as

$$\hat{u}_i(\boldsymbol{k}(t),t) = G^{(0)}_{ij}(\boldsymbol{k},t,t_0)a_j(\underbrace{\boldsymbol{k}(t_0)}_{\boldsymbol{K}},t), \quad (17.50)$$

which replaces the initial data in the linear solution, and can be considered as *slowly* varying in time, where the initial time is fixed at $t' = t_0$. The Green's function can be used for deriving a new equation for the slow variable without any assumption from the exact, Navier–Stokes-type, $\hat{\boldsymbol{u}}$- equation:

$$\dot{a}_i = G^{(0)-1}_{ij}(\boldsymbol{k},t,t_0)P_{jmn}(\boldsymbol{k}(t)) \iint\!\!\int \underbrace{G^{(0)}_{ms}(\boldsymbol{p},t,t_0)a_s(\boldsymbol{P},t)}_{\hat{\boldsymbol{u}}(\boldsymbol{p})} \underbrace{G^{(0)}_{nr}(\boldsymbol{q},t,t_0)a_r(\boldsymbol{Q},t)}_{\hat{\boldsymbol{u}}(\boldsymbol{q})} d^3\boldsymbol{p}, \quad (17.51)$$

with $\boldsymbol{q} = \boldsymbol{k} - \boldsymbol{p}$. The latter equation suggests a systematic way to derive a suitable closure. For instance, the idea in applying generalized EDQNM is to transfer the 'machinery' of EDQNM procedures/assumptions from the $\hat{\boldsymbol{u}}$ to the slow variables $\boldsymbol{a}$. A cartoon of the optimal procedure, called EDQNM3, and successively applied to the pure rotation case in Chap. 7, can be given as follows:

- Quasi-normal (QN) procedure is the same, working with $\hat{\boldsymbol{u}}$ or with $\boldsymbol{a}$ variables. Fourth-order correlations at three points are expressed in terms of products of second-order correlations.
- Markovian (M) procedure consists in freezing the time dependency of the slow variables, and of the slow variables only, in the time integral which links third-order to second order correlations, once the QN assumption used.
- Eddy-Damping consists of replacing the "bare" viscous RDT Green's function by a possibly renormalized one as

$$G_{ij}^{(NL)}(\boldsymbol{k},t,t') = G_{ij}(\boldsymbol{k},t,t')V(\boldsymbol{k},t,t'), \tag{17.52}$$

where the term V, which is substituted to V_0 in Eq. (17.48), will be specified later on. This way is suggested by Eq. (2.117) as well.

In view of the "exact" Eq. (17.51), however, specific difficulties linked to the advection term appear, and a unique system of dependent variables has to be chosen.

Time-dependence of the wave-vectors reflects the advection by the mean flow. The general relation

$$k_i(t) = F_{ji}^{-1}(t,t')k_j(t'), \tag{17.53}$$

is always valid, but for any operator depending on $(\boldsymbol{k},t,t')$, one can ask the question whether a *fixed* wavenumber of reference, such as $\boldsymbol{K} = \boldsymbol{k}(t_0)$ is useful or not. In addition to the renormalization of $\mathbf{G}$ by a scalar term, the related question of renormalizing the Cauchy matrix in Eq. (17.53) can be raised, together with the two-time aspect in general: in spite of some proposals for modelling parallel shear flows with a saturated accumulated mean shear (F_{12} here), e.g. by Maxey and Hunt, we prefer to keep Eq. (17.53) unchanged here: in the presence of solid-body rotation or dominant mean vorticity, for instance, to saturate Ωt is meaningless.

In order to avoid any ambiguity, 'mean-Lagrangian' wavevectors will be used, such as $\boldsymbol{K} = \boldsymbol{k}(t_0)$, $\boldsymbol{P} = \boldsymbol{p}(t_0)$, $\boldsymbol{Q} = \boldsymbol{q}(t_0)$, when 'slow' variables are concerned, and the time argument, e.g. t or t' will be specified in $\boldsymbol{k}$, $\boldsymbol{p}$, $\boldsymbol{q}$.

As far as possible, eigenmode decomposition must be used to diagonalize $\mathbf{G}$. At least, a drastic reduction of the number of variables can be obtained in working with the components in the Craya–Herring frame or in similar frames of reference, as used in Cambon (1982), Cambon et al. (1985) and in all subsequent papers from the same team.

17.8 A General EDQN Closure. Different Levels of Markovianization

Using the three-fold product of Green's functions to express triple correlations in terms of fourth-order ones, the most general Eddy-Damped Quasi-normal closure for the transfer tensor T_{ij} in the Craya's equation leads to:

$$\tau_{ij}(\boldsymbol{k}(t),t) = P_{jml}(\boldsymbol{k}(t))\int_{-\infty}^{t}\iiint_{k+p+q=0} G_{in}^{(NL)}(\boldsymbol{k},t,t')G_{mr}^{(NL)}(\boldsymbol{p},t,t')G_{ls}^{(NL)}(\boldsymbol{q},t,t')$$
$$\hat{R}_{vs}(\boldsymbol{q}(t'),t')\left[\frac{1}{2}P_{nvw}(\boldsymbol{k}(t'))\hat{R}_{wr}(\boldsymbol{p}(t'),t') + P_{rvw}(\boldsymbol{p}(t'))\hat{R}_{wn}(\boldsymbol{k}(t'),t')\right]d^3\boldsymbol{p}dt', \tag{17.54}$$

with

$$T_{ij}(\boldsymbol{k},t) = \tau_{ij}(\boldsymbol{k},t) + \tau^*_{ji}(\boldsymbol{k},t). \tag{17.55}$$

If the factor V in Eq. (17.52) is generated only by adding to the 'laminar' viscous factor νk^2 a damping term $\eta(\boldsymbol{k},t)$, the result can be written as

$$V(\boldsymbol{k},t,t') = \exp\left[-\int_{t'}^{t} \nu k^2(t'') + \eta(\boldsymbol{k}(t''),t'')dt''\right]. \tag{17.56}$$

The exponential decay factor in Eq. (17.56) is related to the cumulative viscous and eddy damping between t' and t. Notice that, although eddy damping formally appears by means of the revised Green's function $G^{(NL)}_{ij}$, unlike viscosity it is really a nonlinear effect, modifying the expression of the third-order moments in terms of the second-order ones.

The time integral in Eq. (17.54) expresses memory of the third-order moments, represented by τ_{ij}, for the fourth-order moments, written as products of $\hat{\mathbf{R}}$. This memory is too long-lasting in the QN model, but eddy damping suppresses memory by progressive attenuation of the Green's function with increasing $t - t'$ by way of the η part of the exponential factor in Eq. (17.56). This will to decrease the importance of third-order memory is taken to its logical conclusion by the Markovianization process. First, the integrand in Eq. (17.56) is approximated by its value at $t'' = t$ to obtain

$$\tilde{V}(\boldsymbol{k},t,t') = \exp\left[-(\nu k^2(t) + \eta(\boldsymbol{k}(t),t)(t-t')\right]. \tag{17.57}$$

17.8.1 EDQNM2 Version

Next, the spectral tensors in Eq. (17.54) can be replaced by their values at $t' = t$, and the wavevectors too, leading to the following form (Cambon and Scott 1999)

$$\tau_{ij}(\boldsymbol{k}(t),t) = P_{jml}(\boldsymbol{k}(t)) \iiint_{k+p+q=0} \Psi_{iml;nrs}\hat{R}_{ns}(\boldsymbol{q},t)$$

$$\left[\frac{1}{2}P_{nvw}(\boldsymbol{k})\hat{R}_{wr}(\boldsymbol{p},t) + P_{rvw}(\boldsymbol{p})\hat{R}_{wn}(\boldsymbol{k},t)\right] d^3\boldsymbol{p}dt' \tag{17.58}$$

where

$$\Psi_{iml;nrs} = \int_{-\infty}^{t} G^{(NL)}_{in}(\boldsymbol{k},t,t')G^{(NL)}_{mr}(\boldsymbol{p},t,t')G^{(NL)}_{ls}(\boldsymbol{q},t,t')\tilde{V}(\boldsymbol{k},t,t')\tilde{V}(\boldsymbol{p},t,t')\tilde{V}(\boldsymbol{q},t,t')dt'. \tag{17.59}$$

Equation (17.58) yields an EDQNM model, for which the nonlinear transfer term in Eq. (2.102) is determined by $\hat{\mathbf{R}}$ at the current instant of time, rather than by the entire past history of the spectral tensor. This is the essence of Markovianization. This version was a rather logical generalization of the classical approach of Orszag (1970), allowing for mean flow effects, and was successfully applied to rotating (Cambon and Jacquin 1989)[4] and to stably stratified turbulence (Godeferd and Cambon 1994). On the other hand, it is not the optimal EDQNM version: depending on the mean flow features, a simpler or a more sophisticated version can be used.

17.8.2 A Simplified Version: EDQNM1

It is tempting to push the Markovianization one step further and set $t = t'$ in the RDT Green's functions of Eq. (17.59), in which case one obtains equations for the spectral transfer as if there were no mean flow. This amounts to replace $\mathbf{G}$ by the identity matrix, so that

$$\Psi_{iml;nrs} = \delta_{in}\delta_{mr}\delta_{ls}\theta_{kpq}(t), \tag{17.60}$$

with

$$\theta_{kpq} = \nu(k^2 + p^2 + q^2 + \eta(k,t) + \eta(p,t) + \eta(q,t).$$

The only effect of the mean flow on the spectral evolution then appears through the linear operators in the left-hand-side of Eq. (2.102). This version is also valid for anisotropic turbulence without mean flow, the isotropic case addressed in Chap. 4 being derived setting the isotropic form for $\hat{\mathbf{R}}$. Finally, a more tractable form of the transfer term is derived from the $\mathcal{E}/Z$ decomposition of the anisotropic spectral tensor, in term of $T^{(\mathcal{E})}$ and $T^{(Z)}$ (Cambon et al. 1997)

$$T^{(\mathcal{E})} = \frac{1}{2}T_{ii}(\boldsymbol{k})$$

$$= \iiint \theta_{kpq} 2kp \left[(\mathcal{E}'' + \Re X'')[(xy + z^3)(\mathcal{E}' - \mathcal{E}) - z(1-z^2)(\Re X' - \Re X)]\right] d^3\boldsymbol{p}$$

$$+ \iiint \theta_{kpq} 2kp \left[\Im X'(1-z^2)(x\Im X - y\Im X')\right] d^3\boldsymbol{p} \tag{17.61}$$

$$T^{(z)} = \frac{1}{2}T_{ij}(\boldsymbol{k})N_i(-\boldsymbol{k})N_j(-\boldsymbol{k})$$

[4]Time-dependency of the wave-vectors was not considered in the EDQNM2 version for "pure" rotation, because the formalism was developed in the rotating frame, but if the same procedure is applied to equations in the Galilean frame, in the presence of a solid-body 'mean' motion, time-shifting cannot be neglected, as discussed at the end of this section.

$$= \iiint \theta_{kpq} 2kpe^{-2\imath\lambda} \left[(\mathcal{E}'' + \Re X'')[(xy + z^3)(\Re X' - X) - z(1 - z^2)(\mathcal{E}' - \mathcal{E}) + \imath(y^2 - z^2)\Im X'] \right] d^3\boldsymbol{p}$$
$$+ \iiint \theta_{kpq} 2kpe^{2\imath\lambda} \left[\imath \Im X'(1 - z^2)(x(e + X) - \imath y \Im X') \right] d^3\boldsymbol{p}, \tag{17.62}$$

with $\mathcal{E} = \mathcal{E}(\boldsymbol{k}, t)$, $\mathcal{E}' = \mathcal{E}(\boldsymbol{k}, t)$, $\mathcal{E}'' = \mathcal{E}(\boldsymbol{q}, t)$, $X = Z(\boldsymbol{k}, t)e^{2\imath\lambda}$, $X' = Z(\boldsymbol{p}, t)e^{2\imath\lambda'}$, $X'' = Z(\boldsymbol{q}, t)e^{2\imath\lambda''}$. Angles λ, λ' and λ'' are defined in Eq. (4.283), and further in (17.87). Geometric terms that only depend on the shape of the triangle related to $\boldsymbol{k} + \boldsymbol{p} + \boldsymbol{q} = 0$, denoted x, y and z are defined as for the isotropic case, in Eq. (4.332).

With respect to arbitrary anisotropy, only the helicity spectrum and the helicity transfer are omitted, considering that these terms cannot be created and are only present if introduced in initial data. Absence of helicity spectrum is generally justified in homogeneous turbulence, despite the interest of (random) helical modes for investigating nonlinear interactions. Notice that the latter equations are most easily obtained from the sophisticated versions EDQNM2 and EDQNM3 for rotating turbulence, given in the next section, by setting $\Omega = 0$. This way to derive equations can appears as paradoxical, but, again, it follows from the fact that helical modes give the best basis for both rotating and non-rotating turbulence.

Of course the conventional EDQNM model for 3D isotropic turbulence is recovered using $\mathcal{E} = E(k)/(4\pi k^2)$, $Z = 0$, and $\iiint d^3\boldsymbol{p} = 2\pi \iint_{\Delta_k} (pq/k)dpdq$ in Eq. (17.61), whereas the averaging on λ yields $T^z = 0$ in the same conditions.

17.8.2.1 Recovering the Conventional 2D Case with Additional "Jetal" Mode

Another interesting result is the derivation of an extended isotropic 2D version, setting $k_\perp = k, k_\parallel = 0$, and using $\iiint d^3\boldsymbol{p} = \iint_{\Delta_k} (1 - x^2)^{-1/2} dpdq$, $e^{2\imath\lambda} = e^{2\imath\lambda'} = e^{2\imath\lambda''} = -1$. In this case, the expression of $T^{(\mathcal{E})} - T^{(Z)}$ in terms of $\mathcal{E} - Z$ is exactly the 2D EDQNM equation used by Leith (1971). $\mathcal{E} - Z$ at $k_\parallel = 0$ is the limit of the toroidal energy spectrum, directly linked to vertical vorticity. In addition, the expression of $T^{(\mathcal{E})} + T^{(Z)}$ in terms of both $\mathcal{E} - Z$ and $\mathcal{E} + Z$ in this limit, is exactly the EDQNM equation of a passive scalar advected by a 2D flow. $\mathcal{E} + Z$ is the limit of poloidal energy which represents a purely vertical mode, which is referred to as the jettal mode by Kassinos and Reynolds), and plays the role of the spectrum of the variance of the passive scalar (see also Cambon and Godeferd 1993). One recovers the fact that a 2D-3C (two-dimensional with three velocity components) flow, characterized by both $\mathcal{E} - Z$ (toroidal = vortical) and $\mathcal{E} + Z$ (poloidal = jetal) energy spectra, evolves towards a pure vortical flow, since the energy $\mathcal{E} - Z$ is conserved by the inverse cascade, whereas the energy $\mathcal{E} + Z$ is rapidly damped (our best application is the case of quasi-static MHD in Chap. 12.)

17.8.3 The Most Sophisticated Version: EDQNM3

In all cases in which the linear "RDT" effect is shown to be important on the dynamics of triple correlations, it is not possible to use EDQNM1, and EDQNM2 is potentially more relevant. Nevertheless, the Markovianization in EDQNM2 is not completely consistent with the decomposition in terms of slow and rapid terms from the very definition of slow variables in Eqs. (17.50) and (17.51). The most straightforward Markovianization consist of setting $t = t'$ in the slow terms and in the slow terms only. On the other hand, this version appeared as not the most relevant one in EDQNM cases with "production" and is really restricted to bridging wave turbulence theory. All details are given in Sect. 17.10, for purely rotating turbulence only.

17.9 Detailed Equations from EDQNM1 in the Model by Mons, Cambon and Sagaut

The model by Mons et al. (2016) is introduced in Chap. 8. The state-vector, extracted from the second-order spectral tensor, consists of spherically averaged descriptors with 11 (in the most general case) components: The classical "radial" energy spectrum $E(k,t)$ and two deviatoric tensors for directional anisotropy and polarization anisotropy, having 5 independent components each one (symmetric trace-free rank-3 tensors.) This state-vector is governed by the following equations:

$$\left(\frac{\partial}{\partial t} + 2\nu k^2\right) E(k,t) = \mathcal{S}^L(k,t) + T(k,t), \tag{17.63}$$

$$\left(\frac{\partial}{\partial t} + 2\nu k^2\right) E(k,t) H_{ij}^{(dir)}(k,t) = \mathcal{S}_{ij}^{L(dir)}(k,t) + \mathcal{S}_{ij}^{NL(dir)}(k,t), \tag{17.64}$$

$$\left(\frac{\partial}{\partial t} + 2\nu k^2\right) E(k,t) H_{ij}^{(pol)}(k,t) = \mathcal{S}_{ij}^{L(pol)}(k,t) + \mathcal{S}_{ij}^{NL(pol)}(k,t), \tag{17.65}$$

with

$$2\left(\frac{\delta_{ij}}{3} T(k,t) + \mathcal{S}_{ij}^{NL(dir)}(k,t) + \mathcal{S}_{ij}^{NL(pol)}(k,t)\right) = \mathcal{S}_{ij}(k,t) + \mathcal{P}_{ij}(k,t). \tag{17.66}$$

The tensors $\mathcal{S}^L(k,t)$, $\mathcal{S}_{ij}^{L(dir)}(k,t)$ and $\mathcal{S}_{ij}^{L(pol)}(k,t)$ account for the linear terms corresponding to the interactions with the mean flow, whereas $T(k,t)$, $\mathcal{S}_{ij}^{NL(dir)}(k,t)$ and $\mathcal{S}_{ij}^{NL(pol)}(k,t)$ correspond to nonlinear transfer terms. The tensor $\mathcal{P}_{ij}(k,t)$ is the spherically integrated spectral counterpart of the slow pressure-strain rate tensor, to which a return-to-isotropy is conventionally attributed. The tensor $\mathcal{S}_{ij}(k,t)$ corresponds to a 'true' transfer tensor with $\int_0^\infty \mathcal{S}_{ij}(k,t)dk = 0\ \forall t$.

17.9.1 Closure for the Linear Terms Induced by Mean-Gradient-Effects

These terms are exact and linear in the equation governing the full spectral tensor, or equivalently $\mathcal{E}(\boldsymbol{k},t)$ and $Z(\boldsymbol{k},t)$. Taken independently with zero contribution from third-order correlations, they reflect the RDT limit for the evolution of two-point second-order velocity correlations. In order to obtain the corresponding, spherically averaged terms $\mathcal{S}^L(k,t)$, $\mathcal{S}_{ij}^{L(dir)}(k,t)$ and $\mathcal{S}_{ij}^{L(pol)}(k,t)$, one has to analytically solve the spherical averaging of tensorial products of vectors $\boldsymbol{\alpha}=\boldsymbol{k}/k$. This is done following the procedure described in Cambon et al. (1981) and Mons et al. (2016). Performing the spherical integration of the linear terms in Eq. (2.102) or that of the linear terms in Eqs. (8.39) and (8.40) with the representation (8.44) and (8.45) leads to:

$$\mathcal{S}^L(k,t) = -2S_{lm}\frac{\partial}{\partial k}\left(kEH_{lm}^{(dir)}\right) - 2ES_{lm}\left(H_{lm}^{(dir)}+H_{lm}^{(pol)}\right), \tag{17.67}$$

$$\begin{aligned}\mathcal{S}_{ij}^{L(dir)}(k,t) &= \frac{2}{15}S_{ij}E - \frac{2}{7}E\left(S_{jl}H_{il}^{(pol)} + S_{il}H_{jl}^{(pol)} - \frac{2}{3}S_{lm}H_{lm}^{(pol)}\delta_{ij}\right)\\ &+ \frac{2}{7}\left(S_{il}\frac{\partial}{\partial k}\left(kEH_{lj}^{(dir)}\right) + S_{lj}\frac{\partial}{\partial k}\left(kEH_{li}^{(dir)}\right) - \frac{2}{3}S_{lm}\frac{\partial}{\partial k}\left(kEH_{lm}^{(dir)}\right)\delta_{ij}\right)\\ &- \frac{1}{7}E\left(S_{jl}H_{li}^{(dir)} + S_{il}H_{lj}^{(dir)} - \frac{2}{3}S_{lm}H_{lm}^{(dir)}\delta_{ij}\right) + E\left(A_{jn}H_{ni}^{(dir)} + A_{in}H_{jn}^{(dir)}\right)\\ &- \frac{1}{15}S_{ij}\frac{\partial}{\partial k}\left(kE\right),\end{aligned} \tag{17.68}$$

$$\begin{aligned}\mathcal{S}_{ij}^{L(pol)}(k,t) &= -\frac{2}{5}ES_{ij} - \frac{12}{7}E\left(S_{lj}H_{li}^{(dir)} + S_{il}H_{lj}^{(dir)} - \frac{2}{3}S_{lm}H_{lm}^{(dir)}\delta_{ij}\right)\\ &- \frac{2}{7}\left(S_{jl}\frac{\partial}{\partial k}\left(kEH_{il}^{(pol)}\right) + S_{il}\frac{\partial}{\partial k}\left(kEH_{lj}^{(pol)}\right) - \frac{2}{3}S_{ln}\frac{\partial}{\partial k}\left(kEH_{ln}^{(pol)}\right)\delta_{ij}\right)\\ &+ \frac{1}{7}E\left(S_{il}H_{lj}^{(pol)} + S_{jl}H_{li}^{(pol)} - \frac{2}{3}S_{lm}H_{lm}^{(pol)}\delta_{ij}\right) - \frac{1}{3}E\left(\tilde{A}_{il}H_{lj}^{(pol)} + \tilde{A}_{jl}H_{li}^{(pol)}\right),\end{aligned} \tag{17.69}$$

with $E = E(k,t), H_{ij}^{(dir)} = H_{ij}^{(dir)}(k,t), H_{ij}^{(pol)} = H_{ij}^{(pol)}(k,t), S_{ij} = (A_{ij}+A_{ji})/2$, $\tilde{A}_{ij} = (A_{ij}-A_{ji})/2$.

Incidentally, The consistency with the linear system in Cambon et al. (1981) is checked, and the following equivalence is established:

$$H_{ij}^{(dir)}(k,t) = \left(1+\frac{2}{5}a(k,t)\right)H_{ij}(k,t), \quad H_{ij}^{(pol)}(k,t) = -\frac{2}{5}a(k,t)H_{ij}(k,t), \tag{17.70}$$

so that the adjustable parameter $a(k,t)$ previously used in Cambon et al. (1981) can be interpreted as a partition parameter prescribing a direct linkage of $H_{ij}^{(dir)}$ and $H_{ij}^{(pol)}$ to the total deviatoric tensor H_{ij}.

17.9.2 Closure for the Terms Mediated by Third-Order Correlations

The transfer terms $T(k,t)$, $\mathcal{S}_{ij}^{NL(dir)}(k,t)$ and $\mathcal{S}_{ij}^{NL(pol)}(k,t)$ are obtained from the spherical integration of the expressions of the transfer terms $T^{(\mathcal{E})}(\boldsymbol{k},t)$ and $T^{(Z)}(\boldsymbol{k},t)$ closed by the EDQNM procedure (17.61) and (17.62) and using the representation (8.44) and (8.45) for $\mathcal{E}(\boldsymbol{k},t)$ and $Z(\boldsymbol{k},t)$. It is consistent to retain only linear contributions from the tensors $H_{ij}^{(dir)}(k,t)$ and $H_{ij}^{(pol)}(k,t)$ in the terms present in the right-hand-sides of the system (17.63)–(17.65). In anisotropic triadic closure, the new difficulty is to solve the integral over the orientation of the plane of the triad, which is performed analytically. Final results are:

$$T(k,t) = \iint_{\Delta_k} \theta_{kpq} 16\pi^2 p^2 k^2 q (xy + z^3)\mathcal{E}_0''(\mathcal{E}_0' - \mathcal{E}_0)\mathrm{d}p\mathrm{d}q, \tag{17.71}$$

$$\begin{aligned}\mathcal{S}_{ij}^{NL(dir)}(k,t) = &\iint_{\Delta_k} \theta_{kpq} 4\pi^2 p^2 k^2 q \mathcal{E}_0'' \Big[(y^2-1)(xy+z^3)(\mathcal{E}_0' - \mathcal{E}_0)H_{ij}^{(pol)''} \\ &+ z(1-z^2)^2 \mathcal{E}_0' H_{ij}^{(pol)'}\Big] dpdq \\ &+ \iint_{\Delta_k} \theta_{kpq} 8\pi^2 p^2 k^2 q (xy+z^3)\mathcal{E}_0'' \Big[(3y^2-1)(\mathcal{E}_0' - \mathcal{E}_0)H_{ij}^{(dir)''} \\ &+ (3z^2-1)\mathcal{E}_0' H_{ij}^{(dir)'} - 2\mathcal{E}_0 H_{ij}^{(dir)}\Big]\mathrm{d}p\mathrm{d}q,\end{aligned} \tag{17.72}$$

$$\begin{aligned}\mathcal{S}_{ij}^{NL(pol)}(k,t) = &\iint_{\Delta_k} \theta_{kpq} 4\pi^2 p^2 k^2 q \mathcal{E}_0'' \Big[(xy+z^3)\Big((1+z^2)\mathcal{E}_0' H_{ij}^{(pol)'} - 4\mathcal{E}_0 H_{ij}^{(pol)}\Big) \\ &+ z(z^2-1)(1+y^2)(\mathcal{E}_0' - \mathcal{E}_0)H_{ij}^{(pol)''} + 2z(z^2-y^2)\mathcal{E}_0' H_{ij}^{(pol)'} + 2yx(z^2-1)\mathcal{E}_0 H_{ij}^{(pol)''}\Big] dpdq \\ &+ \iint_{\Delta_k} \theta_{kpq} 24\pi^2 p^2 k^2 q z(z^2-1)\mathcal{E}_0'' \Big[(y^2-1)(\mathcal{E}_0' - \mathcal{E}_0)H_{ij}^{(dir)''} + (z^2-1)\mathcal{E}_0' H_{ij}^{(dir)'}\Big]\mathrm{d}p\mathrm{d}q,\end{aligned} \tag{17.73}$$

$$\mathcal{P}_{ij}(k,t) = \iint_{\Delta_k} \theta_{kpq} 16\pi^2 p^2 k^2 q (yz + x) \times \mathcal{E}_0'' \Big[\mathcal{E}_0' \Big(y(z^2 - y^2)\big(6H_{ij}^{(dir)''} + H_{ij}^{(pol)''}\big) - (xz + y) H_{ij}^{(pol)''} \Big) - y(z^2 - x^2)\mathcal{E}_0 \big(6H_{ij}^{(dir)''} + H_{ij}^{(pol)''}\big) \Big] \mathrm{d}p\mathrm{d}q, \tag{17.74}$$

with $\mathcal{E}_0 = \frac{E(k,t)}{4\pi k^2}$, $\mathcal{E}_0' = \frac{E(p,t)}{4\pi p^2}$, $\mathcal{E}_0'' = \frac{E(q,t)}{4\pi q^2}$, $H_{ij}^{()} = H_{ij}^{()}(k,t)$, $H_{ij}^{()'} = H_{ij}^{()}(p,t)$ and $H_{ij}^{()''} = H_{ij}^{()}(q,t)$, where $H_{ij}^{()}$ may refer to either $H_{ij}^{(dir)}$ or $H_{ij}^{(pol)}$. The integrals over p and q are performed over the domain Δ_k so that k, p and q are the lengths of the sides of the triangle formed by $\boldsymbol{k}$, $\boldsymbol{p}$ and $\boldsymbol{q}$. The expression of the "true" (zero integral, corresponds to a conserved statistical quantity in the inviscid limit) transfer $\mathcal{S}_{ij}(k,t)$ can be deduced from Eqs. (17.66) and (17.71)–(17.74).

The structure of these equations is very close to the one for EDQNM in the isotropic case. Equation (17.71) for $T(k,t)$ is exactly the same, and geometric coefficients x, y, z as well, defined in Eq. (4.332).

Application of this model are reported in both Chaps. 8 and 9.

17.10 Application of Three EDQNM(1-2-3) Versions to the Rotating Turbulence

The most general EDQNM versions were carried out towards complete achievement for pure rotation only. In this case, the zeroth order state consists of superimposed oscillating modes of motion, without amplification and interaction: They correspond to neutral dispersive inertial waves. Time integral of a three-fold product of Green's functions converges, provided an infinitesimal viscous (or eddy damping) term is added. In the limit of small interactions, two-point closures and theories of wave turbulence share an important background. Even if the latter are developed in the inviscid case, a vanishing damping term is also added, as a mathematical convenience, in order to regularize the resonant operators.

The EDQNM1 version presents little relevance since the isotropy is broken by the Green's function only at the level of triple correlations: started with isotropic initial data, EDQNM1 equations conserve isotropy and are not at all affected by rotation. Equations (17.61) and (17.62), however, remains of interest in some situations, as discussed in Sect. 17.8.2, illustrating the interest of the $(\mathcal{E}/Z)$ decomposition. In addition, one can recall the interest of an "isotropized" simplified model, in which the rotation rate Ω is simply incorporated in the eddy damping term, in Eq. (7.46).

Detailed EDQNM2 and EDQNM3 equations are written below in terms of $\mathcal{E}$ and Z (without initial helicity).

In EDQNM3 equations recalled below from Cambon et al. (2004a) ((17.79) and (17.80)), $T^{(\mathcal{E},Z,h)}$ are given by volume integrals close to the ones found in the appendix of Cambon et al. (1997)(CMG hereafter). Helicity is ignored here as in

CMG, for the sake of brevity. The integrands are completely expressed in terms of $(\mathcal{E}, Z)$ through quadratic terms involving triads. The most laborious calculation is for deriving five geometric factors, denoted $A_1(k, p, q), \ldots A_5(k, p, q)$. Fortunately, these factors were calculated once for all, and play the same role in EDQNM2 and EDQNM3.

The way to simply move from EDQNM2 to EDQNM3, in the absence of helicity, is found as follows.

The only explicit (in addition to the time dependence of the e and Z variables themselves) time-dependent term in the EDQNM2 integrand of $T^{(\mathcal{E},Z)}$ is

$$\exp[-z_{kpq}(t-t')] = \exp[(-\mu_{kpq} - \imath\Omega_{kpq})(t-t')], \quad \Omega_{kpq} = s\sigma_k + s'\sigma_p + s"\sigma_q, \tag{17.75}$$

and its integral gives

$$\int_{-\infty}^{t} e^{-z_{kpq}(t-t')}dt' = \frac{1}{z_{kpq}}. \tag{17.76}$$

The polarization anisotropy is now denoted ζ in order to avoid confusion with its slow counterpart, which is only relevant here, Z, with the relationship:

$$\zeta(s\boldsymbol{k}, t') = Z(s\boldsymbol{k}, t')e^{-2\imath s\sigma_k t'}. \tag{17.77}$$

Only Z has to be considered as "slow", so that it has to be frozen to $t' = t$ in the temporal integral over t' resulting from EDQN. Accordingly, the related phase term in ζ will give an additional (versus EDQNM2) contribution to the temporal integrand, with the following modifications:

(i) There is no modification for the terms which do not include ζ in $T^{(\mathcal{E})}$
(ii) Terms containing ζ in $T^{(\mathcal{E})}$ are altered in replacing $1/z_{kpq}$ by

$$\int_{-\infty}^{t} e^{-z_{kpq}(t-t')-\imath\Omega_z t'}dt' = \frac{e^{-\imath\Omega_z t}}{z_{kpq} - \imath\Omega_z}, \tag{17.78}$$

with $\Omega_z = 2s''\sigma_q$ for Z''-type term, $\Omega_z = 2s\sigma_k$ for Z-type term, $\Omega_z = 2s''\sigma_q + 2s\sigma_k$ for ZZ''-type terms, and $\Omega_z = 2s''\sigma_q + 2s'\sigma_p$ for $Z'Z''$-type terms.

Consequently, the EDQNM3 version without helicity of $T^{(\mathcal{E})}$ becomes

$$T^{(\mathcal{E})} = \frac{1}{2^3}\sum_{ss's''}\iiint C_{kpq}^2\left[\frac{A_1(sk, s'p, s''q)}{\mu + \imath(s\sigma_k + s'\sigma_p + s''\sigma_q)}\mathcal{E}''(\mathcal{E} - \mathcal{E}')\right]d^3\boldsymbol{p}$$

$$+\frac{1}{2^3}\sum_{ss's''}\iiint C_{kpq}^2\left[\frac{A_2(sk, s'p, s''q)}{\mu + \imath(s\sigma_k + s'\sigma_p - s''\sigma_q)}e^{2\imath s''(\lambda''-\sigma_q t)}\mathcal{E}Z(s''\boldsymbol{q})\right]d^3\boldsymbol{p}$$

$$+\frac{1}{2^3}\sum_{ss's''}\iiint C_{kpq}^2\left[\frac{A_3(sk,s'p,s''q)}{\mu+\imath(-s\sigma_k+s'\sigma_p+s''\sigma_q)}e^{2\imath s(\lambda-\sigma_k t)}\mathcal{E}''Z(s\boldsymbol{k})\right]d^3\boldsymbol{p}$$

$$-\frac{1}{2^3}\sum_{ss's''}\iiint C_{kpq}^2\left[\frac{A_5(sk,s'p,s''q)}{\mu+\imath(s\sigma_k+s'\sigma_p-s''\sigma_q)}e^{2\imath s''(\lambda''-\sigma_q t)}\mathcal{E}'Z(s''\boldsymbol{q})\right]d^3\boldsymbol{p}$$

$$+\frac{1}{2^3}\sum_{ss's''}\iiint C_{kpq}^2\left[\frac{A_4(sk,s'p,s''q)}{\mu+\imath(-s\sigma_k+s'\sigma_p-s''\sigma_q)}e^{2\imath s''(\lambda''-\sigma_q t)+2\imath s(\lambda-\sigma_k t)}Z(s''\boldsymbol{q})Z(s\boldsymbol{k})\right]d^3\boldsymbol{p}$$

$$-\frac{1}{2^3}\sum_{ss's''}\iiint C_{kpq}^2\left[\frac{A_4(sk,s'p,s''q)}{\mu+\imath(s\sigma_k-s'\sigma_p-s''\sigma_q)}e^{2\imath s''(\lambda''-\sigma_q t)+2\imath s'(\lambda'-\sigma_p t)}Z(s''\boldsymbol{q})Z(s'\boldsymbol{p})\right]d^3\boldsymbol{p},\tag{17.79}$$

where the geometric factors A_1 to A_5 are given in CMG appendix, and are recalled below. Equations are very symmetric. With respect to EDQNM2, the presence of a Z, or Z', Z'' factor results in changing the corresponding sign in the term $\pm\sigma_k \pm \sigma_p \pm \sigma_q$, and to add the specific time-oscillating phase factor $e^{-2\imath\sigma t}$. $T^{(\mathcal{E})}$ being real, it is possible to only retain $s = 1$ and to replace complex contributions by twice their real part. As in Eqs. (17.61) and (17.62), $\mathcal{E} = \mathcal{E}(\boldsymbol{k}, t)$, $\mathcal{E}' = \mathcal{E}(\boldsymbol{p}, t)$, $\mathcal{E}'' = \mathcal{E}(\boldsymbol{q}, t)$.

The EDQNM3 version of $T^{(Z)}$, given just below, is derived from its EDQNM2 counterpart in a similar way, except that the whole term is multiplied, in addition, by the oscillating term $e^{2\imath\sigma_k t}$:

$$T^{(Z)}=\frac{1}{2^3}\sum_{s's''}\iiint C_{kpq}^2 e^{2\imath(\sigma_k t-\lambda)}\left[\frac{A_3(k,-s'p,-s''q)}{\mu+\imath(\sigma_k+s'\sigma_p+s''\sigma_q)}\mathcal{E}''(\mathcal{E}'-\mathcal{E})\right]d^3\boldsymbol{p}$$

$$+\frac{1}{2^3}\sum_{s's''}\iiint C_{kpq}^2 e^{2\imath(\sigma_k t-\lambda)}\left[\frac{A_4(k,-s'p,-s''q)}{\mu+\imath(\sigma_k+s'\sigma_p-s''\sigma_q)}e^{2\imath s''(\lambda''-\sigma_q t)}\mathcal{E}Z(s''\boldsymbol{q})\right]d^3\boldsymbol{p}$$

$$+\frac{1}{2^3}\sum_{s's''}\iiint C_{kpq}^2 e^{2\imath(\sigma_k t-\lambda)}\left[\frac{A_1(k,-s'p,-s''q)}{\mu+\imath(-\sigma_k+s'\sigma_p+s''\sigma_q)}e^{2\imath(\lambda-\sigma_k t)}\mathcal{E}''Z(\boldsymbol{k})\right]d^3\boldsymbol{p}$$

$$-\frac{1}{2^3}\sum_{s's''}\iiint C_{kpq}^2 e^{2\imath(\sigma_k t-\lambda)}\left[\frac{A_5(k,-s'p,-s''q)}{\mu+\imath(\sigma_k-s'\sigma_p+s''\sigma_q)}e^{2\imath s'(\lambda'-\sigma_p t)}\mathcal{E}''Z(s'\boldsymbol{p})\right]d^3\boldsymbol{p}$$

$$+\frac{1}{2^3}\sum_{s's''}\iiint C_{kpq}^2 e^{2\imath(\sigma_k t-\lambda)}\left[\frac{A_2(k,-s'p,-s''q)}{\mu+\imath(-\sigma_k+s'\sigma_p-s''\sigma_q)}e^{2\imath s''(\lambda''-\sigma_q t)+2\imath(\lambda-\sigma_k t)}Z(s''\boldsymbol{q})Z(\boldsymbol{k})\right]d^3\boldsymbol{p}$$

$$-\frac{1}{2^3}\sum_{s's''}\iiint C_{kpq}^2 e^{2\imath(\sigma_k t-\lambda)}\left[\frac{A_2(k,-s'p,-s''q)}{\mu+\imath(\sigma_k-s'\sigma_p-s''\sigma_q)}e^{2\imath s''(\lambda''-\sigma_q t)+2\imath s'(\lambda'-\sigma_p t)}Z(s''\boldsymbol{q})Z(s'\boldsymbol{p})\right]d^3\boldsymbol{p}.\tag{17.80}$$

Accordingly, all explicit time-dependent oscillating terms cancel for the $T^{(Z)}$ term which depends on the third one, $Z(\boldsymbol{k})$.

Let us recall the definition of geometric coefficients[5]:

$$C_{kpq} = \frac{\sin(p,q)}{k} = \frac{\sin(k,q)}{p} = \frac{\sin(k,p)}{q} \tag{17.81}$$

and

$$A_1(k,p,q) = -(p-q)(k-q)(k+p+q)^2 \tag{17.82}$$

$$A_2(k,p,q) = -(p-q)(k+q)(k+p+q)(k+p-q) \tag{17.83}$$

$$A_3(k,p,q) = (p-q)(k+q)(k+p+q)(-k+p+q) \tag{17.84}$$

$$A_4(k,p,q) = (p-q)(k-q)(k+p+q)(k-p+q) \tag{17.85}$$

$$A_5(k,p,q) = -(p-q)(p+q)(k+p+q)(k+p-q) \tag{17.86}$$

The other geometric coefficients which depend not only on the triad geometry (via moduli k, p, q), but also on the orientation of its plane, are only λ, λ', λ'' terms. Following Cambon (1982), Cambon and Jacquin (1989), Waleffe (1993) they are displayed by substituting to the local frames related to the helical (or complex Craya–Herring) decomposition $(\boldsymbol{N}(s\boldsymbol{k}), \boldsymbol{N}(s'\boldsymbol{p}), \boldsymbol{N}(s''\boldsymbol{q}))$ alternative ones having their polar axis normal to the plane of the triad rather than to the plane of rotation, so that:

$$\boldsymbol{N}(s\boldsymbol{k}) = e^{s\imath\lambda}\underbrace{(\boldsymbol{\beta} + \imath s\boldsymbol{\gamma})}_{\boldsymbol{W}(s)}, \quad , \boldsymbol{N}(s'\boldsymbol{p}) = e^{s'\imath\lambda'}\underbrace{(\boldsymbol{\beta}' + \imath s'\boldsymbol{\gamma})}_{\boldsymbol{W}'(s')}, \quad \boldsymbol{N}(s''\boldsymbol{q}) = e^{s''\imath\lambda''}\underbrace{(\boldsymbol{\beta}'' + \imath s''\boldsymbol{\gamma})}_{\boldsymbol{W}''(s'')}, \tag{17.87}$$

in which $\boldsymbol{\gamma}$ is the unit vector normal to the plane of the triad, whereas $\boldsymbol{\beta}$, $\boldsymbol{\beta}'$, $\boldsymbol{\beta}''$ are unit vectors all located in the plane of the triad, and normal to $\boldsymbol{k}$, $\boldsymbol{p}$, and $\boldsymbol{q}$ respectively. Accordingly, the scalar products in terms of $\boldsymbol{k}$, $\boldsymbol{p}$, $\boldsymbol{q}$, $\boldsymbol{W}$, $\boldsymbol{W}'$, and $\boldsymbol{W}''$ depend only on the moduli k, p, q. These scalar products generate all the A_1-A_5 terms.

The last equations, derived from the previous one, which are used in general EDQNM equations (e.g. (17.79) and (17.80)), are

$$\cos\theta_p = p_\parallel/p = -z\cos\theta_k + \sqrt{1-z^2}\sin\theta_k\cos\lambda, \tag{17.88}$$

$$\cos\theta_q = q_\parallel/q = -y\cos\theta_k - \sqrt{1-y^2}\sin\theta_k\cos\lambda, \tag{17.89}$$

with $y = \cos(k,q)$, $z = \cos(k,p)$, $\sin(k,q) = C_{kpq}\,p$, $\sin(k,p) = C_{kpq}q$, with x, y, z, C_{kpq} given in Eqs. (4.286) and (4.332). Accordingly,

[5]The additional factor $2p/k$ was a mistake in CMG appendix.

$$p\cos\theta_p = -q\cos\theta_q = pqC_{kpq}\sin\lambda \tag{17.90}$$

at $k_\parallel = 0$.

The asymptotic limit of wave-turbulence in terms of $\mathcal{E}$, Z, H is (Bellet et al. 2006)

$$T^{(\mathcal{E})} = \frac{\pi}{4}\sum_{s',s''}\iint_{\mathfrak{M}_{s's''}} C_{kpq}^2\frac{A_1(k,s''q,s'p)}{s'\boldsymbol{C}_g(\boldsymbol{p})-s''\boldsymbol{C}(\boldsymbol{q})}\left[\mathcal{E}'(\mathcal{E}''-\mathcal{E})+s'\mathcal{H}'(s''\mathcal{H}''-\mathcal{H})\right]dS, \tag{17.91}$$

$$T^{(h)} = \frac{\pi}{4}\sum_{s',s''}\iint_{\mathfrak{M}_{s's''}} C_{kpq}^2\frac{A_1(k,s''q,s'p)}{s'\boldsymbol{C}_g(\boldsymbol{p})-s''\boldsymbol{C}(\boldsymbol{q})}\left[s'\mathcal{H}'(\mathcal{E}''-\mathcal{E})+\mathcal{E}'(s''\mathcal{H}''-\mathcal{H})\right]dS, \tag{17.92}$$

and

$$T^{(z)} = -Z\frac{\pi}{4}\left[\sum_{s',s''}\iint_{\mathfrak{M}_{s's''}} C_{kpq}^2\frac{A_1(k,s''q,s'p)}{s'\boldsymbol{C}_g(\boldsymbol{p})-s''\boldsymbol{C}(\boldsymbol{q})}\mathcal{E}'dS+\imath\iiint C_{kpq}^2\frac{A_1(k,s''q,s'p)}{s'\boldsymbol{C}_g(\boldsymbol{p})-s''\boldsymbol{C}(\boldsymbol{q})}\mathcal{E}'d^3\boldsymbol{p}\right], \tag{17.93}$$

in which $\mathfrak{M}_{s's''}$ is the family of resonant surfaces and $\boldsymbol{C}_g$ is the group velocity of inertial waves.

Equations (17.91) and (17.92) are fully consistent with the ones in Galtier (2003). The last equation, and Z in general, is ignored in conventional wave-turbulence theory (Waleffe 1993; Galtier 2003). The transfer term $T^{(Z)}$ is linear in Z, and it is the only term which does not reduce to a surface integral ($\iint dS$) over surfaces of resonant triads: the integral $\iiint d^3\boldsymbol{p}$ in Eq. (17.93) denotes a principal value integral in the vicinity of the resonant surface. Much more complex quadratic interactions terms which involve Z in volumetric (Eqs. (17.79) and (17.80) are discarded in AQNM when removing rapidly oscillating terms.

In the case of MHD (Magneto-Hydro-Dynamics) flows addressed in Chap. 12, the use of similar two-point closure/ wave-turbulence theories is particularly relevant (see Galtier et al. 2001 for flows dominated by Alfvén waves).

Because purely rotating flows perfectly illustrate how to bridge from anisotropic EDQNM to wave turbulence theory, some last comments on the latter theory are probably useful. In addition to reviews (Newell and Rumpf 2011 and book by Nazarenko 2011), a wealth of experimental and theoretical studies appeared in the last decade, but much more for surface waves and vibrating plates than for deep rotating or stratified flows, with internal waves. The terminology inherited from Zakharov et al. (1992) is dominant and does not contribute to clarify the linkage of AQNM (Asymptotic QNM) to wave turbulence theory: "kinetic equations" and "Random phase Approximation" refer more to the Boltzmann distribution equation, for which the use of the central limit theorem is obvious; accordingly, the recourse to a QNM approximation is often implied, and not even discussed. On the other hand, to consider "kinetic equations" as a relevant limit of Lin equations, used in developed turbulence, is clearer; accordingly, the QN ingredient is not a trivial byproduct of a central limit theorem, and it must be investigated with care. This was done by Benney and Newell (1969) and in following studies by the same team.

17.11 Other Cases of Flows with and Without Production

Throughout this book, we have distinguished between flows dominated by production and flows dominated by waves. The first class is illustrated by classical shear flows, in which a nonzero production term is displayed in the equations governing the Reynolds Stress tensor. This production is often related to growth of instabilities, when stability analysis is addressed. The second class is illustrated in Chaps. 7, 10 and 11 as being the most relevant area to apply spectral closures. Note that the dynamics can be dominated by dispersive waves, which are neutral but for a small part of the configuration space, in which exponential amplification occurs. In the latter case, e.g. for flows with weak ellipticity (i.e. $S \ll \Omega$) the production of energy is nonzero, but classic single-point closure models are of poor relevance, since only particular orientations in wave-space are subjected to parametric instability.

17.11.1 Effects of the Distorting Mean Flow

17.11.1.1 Hyperbolic and Elliptic Cases

In the hyperbolic and elliptic cases, with $0 \neq S \neq \Omega$ in Eq. (8.8), the RDT Green's function can display exponential growth, at least for particular angles of $\boldsymbol{k}$ ($k_3/k \sim 1/2$ in the case $S \ll \Omega_0$). If the bare zeroth-order response function is only modified by eddy damping, with exponential decorrelation as in Eq. (17.57), convergence is not ensured for the time integral of the three-fold product $\mathbf{GGG}$ in the generic closure relationship. Another type of nonlinear decorrelation operator, e.g. a Gaussian one, could be used.

17.11.1.2 Pure Shear

A less critical situation occurs when $S = \Omega$ (pure plane shear), since the RDT Green's function yields only algebraic growth, so that the viscous term ensures convergence of the time integral involved in the closure. Nevertheless, it is very cumbersome to develop, and especially to solve numerically with enough accuracy, a complete anisotropic EDQNM model in this case. Recall that even calculation of single-point correlations resulting from viscous RDT at high St is not easy (Beronov and Kaneda, private communication). Direct Numerical Simulations suggest that fully nonlinear effects yield exponential growth for the turbulent kinetic energy, but computations are very sensitive to cumulated errors (remeshing, low angular resolution at small k, etc.). Such a transition from algebraic growth (linear, small time) to exponential growth (nonlinear) is mimicked by simple models but not reproduced with sufficient accuracy by spectral models. Interesting scaling laws, however, for possible exponential growth, follow from self-similarity arguments, as discussed in Chap. 9.

17.11.2 Flows Without Production Combining Strong and Weak Turbulence

A particular class of flows "without production" involves both wavy and non-propagating modes, the latter being constant in the linear limit. Their dynamics can mix strong and weak turbulence. On the one hand, strong turbulence is concerned only when nonlinear interactions in terms of the non-propagating modes are considered: that includes the "toroidal turbulence" for pure stratification, the QG turbulence for the stratified rotating case, and the pure solenoidal case for the weakly compressible flow case.

Principal features of flows without production, which are addressed in this book are collected in Fig. 17.4.

Investigation of interactions with waves is a second step in the study of such flows: we are firstly faced with the problem of interacting acoustic waves in the latter case only, because the solenoidal problem is essentially solved (e.g. using conventional isotropic EDQNM consistent with a Kolmogorov energy spectrum).

17.11.2.1 Buoyant Flows in a Stably Stratified Fluid

In the purely stratified case, gravity wave turbulence is crucial only if the non-propagating mode, i.e. the toroidal part of the velocity field, is a priori discarded. This removal is generally unphysical, and oversimplified wave-turbulence studies, such as the one by Caillol and Zeitlin (2000), are only marginally relevant. The claim of explaining the horizontal layering in the latter paper is highly misleading. In contrast, emphasis on rather strong turbulence is much more relevant, at least at moderate times, looking at the "toroidal cascade", and the transition from a 3D isotropic unstructured flow to a strongly anisotropic, horizontally layered, flow can be described by the statistical theory.

17.11.2.2 Weakly Compressible Isotropic Turbulence

The case of weakly compressible turbulence is not present in Fig. 17.4. In this case, the solenoidal mode plays a role similar to the toroidal mode in stratified turbulence and to the QG mode in the rotating and stratified case — see Table 11.2 —, but the pseudo-acoustic mode is not necessarily a wave-mode: true acoustic waves are observed at very low wave numbers, while the pseudo-sound régime may hold at higher wave numbers. As for the case of buoyant turbulence in a stratified fluid, the basic equations in terms of 'slow' amplitudes are

Case	Relevant linear eigenmodes	Conservation laws (inviscid theory)		TKE cascade(s)	Nonlinear effects
		Detailed (isolated triad)	Global (sum over triads)		
Isotropic (3D)	none	➡ Kinetic energy ➡ Helicity	➡ Kinetic energy ➡ Helicity (zero net helicity)	➡ Total (poloidal + toroidal) cascade ➡ existence of both forward and reverse cascades	➡ net forward cascade at high wave numbers ➡ net backward cascade at very low wave numbers
Isotropic (2D)	none	➡ Kinetic energy ➡ Enstrophy	➡ Kinetic energy ➡ enstrophy	➡ existence of reverse cascade only	➡ net forward enstrophy cascade cascade at high wave numbers ➡ net backward energy cascade at high wave numbers
Pure rotation	Inertial waves	➡ Kinetic energy ➡ Helicity	➡ Kinetic energy, ➡ Helicity	Cascade associated to resonant triads	TKE concentration on equatorial plane
Pure stable stratification	➡ Toroidal velocity mode (constant) ➡ Gravity waves	➡ (At very low Froude number only): vertical enstrophy & toroidal kinetic energy	➡ Toroidal kinetic energy ➡ Wave (poloidal + potential) kinetic energy	➡ Toroidal cascade excluding "weak" wave-turbulence ➡ poloidal and potential modes affected by wave-turbulence	Layering due to toroidal cascade, i.e. concentration of TKE on the polar direction
Rotation + stable stratification	➡ Quasi-Geostrophic mode (constant) ➡ Inertia-gravity waves	➡(neglecting wave mode): GQ energy & Linearized potential enstrophy	➡ QG energy ➡ Wave kinetic energy (poloidal + potential)	QG cascade	Multiform, depending on f/N

Fig. 17.4 Table of different properties, including eigenmodes (if relevant), conservation law, and cascade processes

$$\frac{\partial a_s}{\partial t} = \sum_{s',s''=0,\pm 1} \int_{\boldsymbol{k}+\boldsymbol{p}+\boldsymbol{q}=0} \exp\left(-\imath\left(s\sigma_k + s'\sigma_p + s''\sigma_q\right)t\right) \times \times N_{ss's''}(\boldsymbol{k},\boldsymbol{p}) a^*_{s'}(\boldsymbol{p},t) a^*_{s''}(\boldsymbol{q},t)\, d^3\boldsymbol{p} \tag{17.94}$$

Diffusive terms can be neglected for a preliminary discussion of couplings. Of course, the coupling coefficients $N_{ss's''}$ completely differ from their counterparts in the solenoidal buoyant case subjected to stable stratification, and a_0 is two-component (solenoidal mode) in the compressible case. A similar cartoon, however, can be discussed in both flow cases, depending on the signs (s, s', s''), or triad polarities, as follows:

(i) Non-propagating slow mode, $s = 0$. It is clear that the nonlinear dynamics is dominated by interactions between slow modes only, so that the leading terms may correspond to $s' = s'' = 0$: one recovers the 'toroidal turbulence' for the stratified flow case and pure incompressible dynamics for the weakly compressible flow case. The main difference is that incompressible isotropic turbulence is well understood, at least regarding energy spectrum and energy transfer, whereas toroidal turbulence is still under investigation. Consequently, a large Reynolds number Kolmogorov energy spectrum can be specified and fixed for the solenoidal mode, as in Fig. 13.3.

(ii) Our main interest in this subsection is the mode related to $s = \pm 1$, generating "dilatational velocity" and "pressure" contributions, which are closely connected together or not via a possible acoustic equilibrium. It is very difficult to rank a priori the three kinds of interactions $(\pm 1, 0, 0)$, $(\pm 1, \pm 1, 0)$ and $(\pm 1, \pm 1, \pm 1)$ for (s, s', s''). The first one is never resonant, but cannot be completely removed from consideration if the order of magnitude of a_0 is much larger than the one of $a_{\pm 1}$. The second one will select resonant 'dyads', like $k \pm p = 0$. Only the third one will select resonant triads, as $k \pm p \pm q = 0$.

It is clear that Wave turbulence is only a part of the whole story, which is even irrelevant in some cases, like the toroidal turbulence in the stably stratified case. A simplified EDQNM3 closure strategy is applicable, but the study by Fauchet (1998) has shown the importance of a non-conventional eddy-damping term denoted V in this chapter, or, more generally of the nonlinear part of the Kraichnan's response function.

Finally, we have illustrated closure theories for weakly compressible flows in Chap. 13 by a peculiar study. This viewpoint, which may appear as idiosyncratic, is mainly motivated by the existence of detailed asymptotic laws which were derived, with practical interest. There exist an important literature on this topic, from wave turbulence for nonlinear sound (Zakharov et al. 1992), to absolute equilibrium in truncated Euler equations. For instance, a generalized $k^{-5/3}$ law can be inferred from Kraichnan (1955) for both solenoidal and acoustic modes, even in the viscous case, but radiation to infinite is excluded in this study.

17.11.3 Role of the Nonlinear Decorrelation Time-Scale

When comparing strong turbulence without production and wave-turbulence, it is important to stress significant differences:

- Conventional isotropic EDQNM works well, at least for predicting energy spectra and transfers, but we do not know really why! The role of the eddy damping is crucial, and even the QN structure only results from a heuristic closure strategy. In any case of strong turbulence less documented, as the toroidal turbulence in stably stratified flows, the conventional isotropic eddy damping probably needs refinement, especially in the spectral region where energy concentrates (quasi-VSHF 1D modes). Recourse to more sophisticated self-consistent closure theories may be useful.
- The"pure" wave turbulence theory, which appears as a limiting case of QNM closure, also works well, but we know why! QN structure can be supported by mathematical analysis (Benney and Newell 1969) or by physically relevant random phase approximation. Markovianization results from a rigorous rapid/slow time scale decomposition, and ED is unimportant in the asymptotic limit. In this limit, there is no need for a significant nonlinear renormalization of the bare dispersion frequency, too.
- The role of the eddy damping appears to be very subtle in the "mixed" case, when wave-turbulence coexists with strong turbulence. In stably-stratified turbulence, a quasi-perfect agreement was found between DNS results and EDQNM2 results (Godeferd and Staquet 2003), keeping the same eddy-damping (inherited from HIT) for all interactions, but only the relatively low Reynolds number range, which was allowed in DNS, was investigated. In the case of very high Reynolds number and very Low Froude number, with large $ReFr^2$ parameter, which is discussed at the end of Chap. 10, a refined analysis will be needed. The case of quasi-isentropic isotropic turbulence offers a very good example: Keeping the same eddy-damping for all interactions yields poor results. Very striking results are found by choosing a Gaussian kernel for V, as in the Table 13.1 instead of a exponential one. As discussed in Chap. 13, this cannot be obtained by replacing the acoustic wave-frequency by a renormalized nonlinear one. A relevant explanation, given in this book but not in the original reference Fauchet (1998), is to add a random part to the linear dispersion frequency, in agreement with the Kraichnan's random oscillator. A related problem is the possible need for a "renormalized" wave frequency in wave-turbulence. For instance, a nonlinear shift in Rossby wave frequency is demonstrated from statistical theory and DNS (Kaneda and Holloway 1994; Ishihara and Kaneda 2001), whereas such a shift seems to be useless in 3D rotating turbulence (inertial wave turbulence) and in MHD turbulence (Alfven wave turbulence). The study of Galtier et al. (2001) had the merit to show that even non-dispersive (or semi-dispersive) waves can generate 'weak' wave turbulence, against a well-established prejudice. Of course, phase-mixing results from dispersivity, and naturally damps nonlinearity. The 'prejudice', however, is possibly linked to a confusion between a pure advection term by a velocity, $\boldsymbol{V}$, yielding

$\exp(\imath \boldsymbol{k}\cdot\boldsymbol{V})$ in Fourier space, and the phase term $\pm\imath \boldsymbol{k}\cdot\boldsymbol{V}$ of non-dispersive waves, …forgetting the sign ± 1 ! Because of the sign, which allows propagation in opposite directions (generally coming from second order in time, Dalembertian-type, operator), wave operators affect the triple correlations — even in the absence of dispersive effects, whereas pure advection terms do not. Rossby waves are characterized by a first order in time operator, and therefore propagate only in one direction. We do not question here the 'wave' terminology, even if Rossby waves could be called 'westward advected oscillations' instead of 'waves'. This is a question of definition of waves, but one can point out a very different nature of inertial, Alfven and Rossby waves. The Rossby waves could be less efficient in damping nonlinearity, so that a nonlinear shift would reveal not too "weak" turbulence.

17.12 Connection with Self-consistent Theories: Single-Time or Two-Time?

The Kraichnan's DIA, in spite of some drawbacks, played a crucial role in the long history and progressive generation of "triadic closure" theory. The two-time aspect is essential in the first version, as well as in its Lagrangian or semi-Lagrangian more sophisticated subsequent variants (see Kaneda 2007 for a review). The aim of such two-time and two-point (or even three-point) statistical theory is to derive a consistent set of close equations for both the response tensor, corresponding to $\mathbf{G}^{(NL)}(\boldsymbol{k}, t, t')$ in this chapter, and to the two-time spectral tensor, which generalizes our $\hat{R}$ as $\hat{R}(\boldsymbol{k}, t, t')$.

A theory formulated in terms of two-time statistical tensors can be converted in its single-time counterpart using a so called fluctuation-dissipation theorem. For instance

$$\hat{R}_{ij}(\boldsymbol{k}, t, t') = G_{in}^{(NL)}(\boldsymbol{k}, t, t')\hat{R}_{nj}(\boldsymbol{k}, t', t'), \tag{17.95}$$

ignoring the possible time-dependency of the wavevector for the sake of simplicity. In conventional applications, the two-time dependency of the response tensor is a priori specified (for instance exponential $(t - t')$-decorrelation). EDQNM can be presented as a byproduct of DIA by this way, but we think that it is a rather complicated and indirect way to proceed. Few applications of DIA or EDQNM were made in the context of HAT. One can mention the return to isotropy from a (weak) anisotropic (axisymmetric) case by Herring (1974), and the weakly axisymmetric QG EDQNM model by the same author mentioned in Chap. 11. More sophisticated anisotropic models were developed by Sanderson et al. (1986), using a small number of spherical harmonics. None of this studies was able of incorporating as a building block the RDT Green's function as a natural zeroth order response tensor, if we exclude Wave Turbulence, of course.

A general formulation of two-time DIA yields a single Green's function in the nonlinear closure of the equation for the two-time correlation spectral tensor, and the two other factors then appear by means of the above fluctuation-dissipation relationship, leading to essentially the same form as Eq. (2.117) with a threefold product of response tensors. Of course, solving (inverting?) the modified response tensor operator for third-order single-time correlations is simpler and more direct, the three-fold product even appearing in the basic equation for velocity fluctuation, rewritten in Eq. (17.51). The final DIA-type evolution equation for the two-time spectral tensor therefore contains an integral whose structure is much the same as the EDQN expression (2.117), with terms such as $G_{lq}(\boldsymbol{q},t,t')\hat{R}_{qn}(\boldsymbol{q}',t')$ replaced by the two-time spectral tensor $\hat{R}_{ln}(\boldsymbol{q}',t,t')$, leaving one remaining Green's function from the threefold product, which is replaced by the response tensor.

A more streamlined procedure could be based on generalized EDQNM, using DIA and subsequent self-consistent theories for improving the Eddy Damping factor only without excluding other variants. This strategy can be used for deriving complete two-time statistics, as illustrated in RDT by Kaneda and Ishida (2000), in order to have access to $\hat{\mathbf{R}}(\boldsymbol{k},t,t')$. The way of solving operators linked to any product of response tensors is applicable. The only difficulty could result from a very complex equation for the response tensor $\mathbf{G}^{(NL)}(\boldsymbol{k},t,t')$, with no explicit simplified solution in terms of $\hat{\mathbf{R}}(\boldsymbol{k},t,t')$ (such as $\mathbf{G}^{(0)}(\boldsymbol{k},t,t')V(\boldsymbol{k},t,t')$).

17.13 Applications to Weak or Moderate Anisotropy

Applications to weakly anisotropic flows have been mentioned previously: Herring (1974), Sanderson et al. (1986). In addition, some recent applications of LRA to the response of turbulence to a weak linear operator in the presence of strong nonlinearity deserves attention, with a first survey in Chap. 8.

17.13.1 A Self-consistent Representation of the Spectral Tensor for Moderate Anisotropy

The most general decomposition of the spectral tensor (e.g. the $\mathcal{E}/Z/\mathcal{H}$ decomposition introduced and discussed in Chap. 2), which holds for arbitrary flow anisotropy, involves never more than four real scalars. In addition to the very existence of the polarization anisotropy Z, anisotropy is reflected by angle-dependence of these basic scalars. Looking at the trace of the spectral tensor, it is clear that $E(k)/(4\pi k^2)$ is only the zeroth-degree angular harmonic of $\mathcal{E}(\boldsymbol{k})$ and gives no information on its angular distribution in wave-space. Nevertheless, some information about this angular distribution can be obtained by spherically averaging all the components of the spectral tensor $\hat{\mathbf{R}}$, because some weighting factors, such as the projector P_{ij} (for $\mathcal{E}$) or the polarization deviator N_iN_j (for Z) generate angular harmonics until the degree 2.

As a result, the following self-consistent decomposition is found

$$\hat{R}_{ij}(\boldsymbol{k},t)=\frac{E(k)}{4\pi k^2}\left[\left(1-15H_{pq}^{(dir)}\frac{k_pk_q}{k^2}\right)P_{ij}+5\left(P_{in}P_{jm}H_{nm}^{(pol)}+\frac{1}{2}P_{ij}H_{pq}^{(z)}\frac{k_pk_q}{k^2}\right)\right], \tag{17.96}$$

in which one can identify the contribution from the directional anisotropy as

$$\hat{R}_{ij}^{(dir)}=\left(\mathcal{E}-\frac{E}{4\pi k^2}\right)P_{ij}=-15H_{pq}^{(dir)}(k)\frac{k_pk_q}{k^2}\frac{E(k)}{4\pi k^2}P_{ij}(\boldsymbol{k}), \tag{17.97}$$

and the contribution of polarization anisotropy[6] as

$$\hat{R}_{ij}^{(pol)}=5\frac{E(k)}{4\pi k^2}\left[P_{in}(\boldsymbol{k})P_{jm}(\boldsymbol{k})H_{nm}^{(pol)}(k)+\frac{1}{2}P_{ij}(\boldsymbol{k})H_{pq}^{(pol)}(k)\frac{k_pk_q}{k^2}\right], \tag{17.98}$$

in addition to the purely isotropic part

$$\hat{R}_{ij}^{(iso)}=\frac{E(k)}{4\pi k^2}P_{ij}(\boldsymbol{k}).$$

This decomposition, introduced by Cambon and Rubinstein (2006), can generalize many other similar tensorial expansions. It is self-consistent in the sense that it does not involve any adjustable parameter: Given an arbitrary anisotropic $\hat{\mathbf{R}}$, it is possible to derive from it the spherically averaged spectra $H_{ij}^{(dir)}(k)$ and $H_{ij}^{(pol)}(k)$ defined in Chap. 2, and then to reconstruct its angle-dependent form, up to a given degree of angular harmonics, using Eq. (17.96). The difference between the original, arbitrarily anisotropic, $\hat{\mathbf{R}}$, and its weakly anisotropic approximation generated by $H_{ij}^{(dir)}(k)$ and $H_{ij}^{(pol)}(k)$ is the contribution from higher degree harmonics which cannot be reconstructed from $H_{ij}^{(dir)}$ and $H_{ij}^{(pol)}$ alone. The general decomposition in Eq. (17.96) is strictly equivalent to Eqs. (8.44) and (8.45) for $\mathcal{E}$ and Z.

Going back to the approach of linear response by Ishihara et al. (2002), Yoshida et al. (2003), Eq. (17.96) is only used for translating the main results in the presence of a weak shear, as already touched upon in Chap. 8. This approach is very different from the one dedicated to strongly anisotropic turbulence, since the linear response is sought with respect to a weak perturbation (the linear "RDT" operator) to a nonlinear state in statistical equilibrium. In this sense, the tangent response function can be also weakly anisotropic and therefore far from the RDT linear limit $\mathbf{G}^{(0)}$, which is generally very anisotropic for large $t-t'$. A decomposition of $\mathbf{G}^{(NL)}$ in terms of a pure isotropic factor and a weakly anisotropic one is found consistently.

[6] This form is strictly equivalent to its counterpart in terms of Z, $\Re(ZN_iN_j)$, with $Z=(5/2)E/(4\pi k^2)H_{ij}^{(z)}N_i^*N_j^*$, without using the helical mode vector $\boldsymbol{N}$.

The linear response has some analogies with the general laws which connect fluxes and forces in statistical theory for continuum media, with similar symmetry properties as the ones prescribed by Onsager. The main equation for the response to a weak mean flow with A_{ij} velocity gradients is

$$\hat{R}_{ij}^{(aniso)} = Q_{ijnm}(\boldsymbol{k}) A_{nm},$$

and because of the symmetry of the Q_{ijnm} tensor, only the symmetric part, S_{nm}, of A_{nm} is eventually displayed. Translated in our own formalism, this yields $\hat{\mathbf{R}}^{(aniso)} = \hat{\mathbf{R}}^{(dir)} + \hat{\mathbf{R}}^{(pol)}$, and, using Eqs. (17.97) and (17.98),

$$H_{ij}^{(dir)}(k) = \frac{1}{15}(B - A)\left(\frac{k}{k_0}\right)^{-2/3} \varepsilon^{-1/3} k_0^{-2/3} S_{ij}, \tag{17.99}$$

$$H_{ij}^{(pol)}(k) = \frac{2}{5} A \left(\frac{k}{k_0}\right)^{-2/3} \varepsilon^{-1/3} k_0^{-2/3} S_{ij}. \tag{17.100}$$

For the basic state, a classical Kolmogorov inertial range is recovered, with $E(k) = C_k \epsilon^{2/3} k^{-5/3}$, so that the dimensional spectra of deviatoric tensors, $E(k) H_{ij}^{(dir)}$ and $E(k) H_{ij}^{(pol)}$, exhibit a classical scaling like $\varepsilon^{1/3} k^{-7/3}$, as suggested by Lumley (see also Chap. 9). In the above equations, k_0 is identified with the wavenumber at which the inertial range can be considered to begin, probably of the same order of magnitude as the threshold wavenumber k_S, or inverse of a Corrsin's scale, used in Chap. 9.

Accordingly, $k_0^{-2/3} \varepsilon^{2/3}$ is the typical time scale, and $k_0^{-2/3} \varepsilon^{2/3} S_{ij}$ is the relevant non-dimensional strain tensor. Finally, A and B are universal constants, obtained in a satisfactory agreement both by DNS for homogeneous pure plane shear and LRA theory (Ishihara et al. 2002; Yoshida et al. 2003).

17.13.2 Brief Discussion of Concepts, Results, and Open Issues

Given the strong constraints given by weak anisotropy, with a spectral tensor which is necessarily of the form (17.96), and dimensional analysis "à la Lumley", there are very few degrees of freedom, and the main results can be obtained by much simpler, even wrong, ways. The merit of LRA in this case, is to find the result in a rigorous and self-consistent way, avoiding useless oversimplifications. Even if the specific shear-advection term inherited from the linear operator has no significant effect on the tensor $H_{ij}^{(dir)}$, which expresses the linear response as in the short-time RDT limit (see Chap. 8), this shear-advection effect is correctly accounted for in the intermediate theoretical steps, so that the confusion between relations (17.44) and (17.45) is avoided from the beginning.

One could expect, at least in the case of pure plane shear, to reconcile an approach to strong anisotropy, more restricted to large scales, and the linear response theory, limited to very small scales.

Not even mentioning the case of combined effects of irrotational strain and vorticity, which leads to elliptical or hyperbolical instabilities with exponential growth in the linear limit, the case of solid-body rotation deserves some attention. It appears that the Coriolis force has no impact on the linear response. This is consistent with an objectivity principle satisfied in continuum mechanics. Nevertheless, it is well known that Chapman–Enskog-type developments for Boltzmann equations can question such objective laws if they are carried out at a sufficient order. The constitutive laws, or fluxes-to-forces relationship could become explicitely Coriolis-dependent in this situation. In the same way, the effect of solid-body rotation can be recovered at a further order (quadratic dependency on Ω?) using LRA.

Another point is the fact that strong anisotropy induced by the Coriolis force at sufficiently low Rossby number is found to be dominant at small scale, as shown by both wave turbulence theory and DNS results. The classical picture of strong anisotropy restricted to largest scales is radically questioned. In this situation, it seems to be difficult to match both low-Rossby and high-Rossby limits.

17.14 Open Numerical Problems

The numerical cost of solving EDQNM equations, as well as those issued from similar single-time or even two-time "triadic" theories, is very low in the isotropic case. This cost, and the complexity of the numerical procedure, can blow up, not only in an inhomogeneous configuration, as it is often said, but even in the case of strong anisotropy. The numerical solution of the equations of wave-turbulence was demanding in terms of numerical resources, with a particular care for accurately capturing the resonant surfaces with complex shapes.

Reaching very high Reynolds numbers and even asymptotic limits, e.g., vanishing Rossby numbers, is not a problem in solving these statistical model equations, in contrast with DNS. This is the number of angular variables in interaction which is responsible for the high cost, especially because the classical pseudo-spectral scheme is difficult to apply: A factorization like $A(\boldsymbol{k})\sum \hat{\boldsymbol{u}}(\boldsymbol{p})\hat{\boldsymbol{u}}(\boldsymbol{q})$, which is very simple for basic Navier–Stokes equations, yielding $A(\boldsymbol{k})\widehat{\boldsymbol{uu}}$ is very cumbersome looking at typical equations in terms of spectral tensors and response functions. A higher accuracy, however, can be obtained in statistical closures, for accounting for typical triads, such as the resonant ones but also the quasi-exact cancellation between some of them. Even very simple quantities affected by phase-mixing, e.g. in Chap. 7, whose history consists of damped oscillations with a smooth envelope, are found to exhibit chaotic wrong envelopes after a finite integration time, in any classical pseudo-spectral DNS, because of limited accuracy in terms of $\Delta k/k$, $k_\parallel/k$, etc. It is therefore pertinent to try to solve costly statistical models. Attempts to reduce this

cost, using — despite the cumbersome factorization — pseudo-spectral techniques, or Monte-Carlo methods, do exist but are outside our scope.

Since the first edition of this book, progresses were made in numerically solving elaborate anisotropic EDQNM models, even with detailed angular discretization, for both the orientation wave vector $\boldsymbol{k}$ and the orientation of the plane of triads. This permitted quantitative comparisons with high resolution DNS, then extrapolation of DNS results towards unprecedented Reynolds numbers, as reported in Sect. 10.7.7.

References

Batchelor, G.K., Proudman, I.: The effect of rapid distortion in a fluid in turbulent motion. Q. J. Mech. Appl. Math. 7–83 (1954)

Bayly, B.J.: Three-dimensional instability of elliptical flow. Phys. Rev. Lett. **57**, 2160 (1986)

Bellet, F., Godeferd, F.S., Scott, J.F., Cambon, C.: Wave-turbulence in rapidly rotating flows. J. Fluid Mech. **552**, 83–121 (2006)

Benney, D.J., Newell, A.C.: Random wave closure, Stud. Appl. Math. **48**, (1969)

Bohr, T., Jensen, M.H., Paladin, G., Vulpiani, A.: Dynamical Systems Approach to Turbulence. Cambridge University Press, Cambridge (1998)

Bos, W.J.T., Bertoglio, J.-P.: A single-time two-point closure based on fluid particle displacements. Phys. Fluids **18**, 031706 (2006)

Briard, A., Iyer, M., Gomez, T.: Anisotropic spectral modeling for unstably stratified homogeneous turbulence. Phys. Rev. Fluids **2**, 044604 (2017)

Burden, A.D.: Towards an EDQNM closure for inhomogeneous turbulence. In: Johansson, A.V., Alfredson, P.H. (eds.) Advances in Turbulence III, vol. 387. Springer, Berlin (1991)

Caillol, P., Zeitlin, W.: Kinetic equations and stationary energy spectra of weakly nonlinear internal gravity waves. Dyn. Atmos. Ocean. **32**, 81–112 (2000)

Cambon, C.: Etude spectrale d'un champ turbulent incompressible soumis à des effets couplés de déformation et rotation imposés extérieurement. Université Lyon I, France, Thèse de Doctorat d'Etat (1982)

Cambon, C., Godeferd, F.S.: Inertial transfers in freely decaying rotating, stably-stratified, and MPHD turbulence. In: Branover, H., Unger, Y. (eds.) Progress in Astronautics and Aeronautics. AIAA (1993)

Cambon, C., Jacquin, L.: Spectral approach to non-isotropic turbulence subjected to rotation. J. Fluid Mech. **202**, 295–317 (1989)

Cambon, C., Rubinstein, R.: Anisotropic developments for homogeneous shear flows. Phys. Fluids **18**, 085106 (2006)

Cambon, C., Scott, J.F.: Linear and nonlinear models of anisotropic turbulence. Annu. Rev. Fluid Mech. **31**, 1–53 (1999)

Cambon, C., Jeandel, D., Mathieu, J.: Spectral modelling of homogeneous anisotropic turbulence. J. Fluid Mech. **104**, 247–262 (1981)

Cambon, C., Teissèdre, C., Jeandel, D.: Etude d' effets couplés de rotation et de déformation sur une turbulence homogène. Journal de Mécanique Théorique et Appliquée **5**, 629 (1985)

Cambon, C., Mao, Y., Jeandel, D.: On the application of time-dependent scaling to the modelling of turbulence undergoing compression. Eur. J. Mech. B Fluids **11**, 683–703 (1992)

Cambon, C., Mansour, N.N., Godeferd, F.S.: Energy transfer in rotating turbulence. J. Fluid Mech. **337**, 303–332 (1997)

Cambon, C., Rubinstein, R., Godeferd, F.S.: Advances in wave-turbulence: rapidly rotating flows. New J. Phys. **6**, 73 (2004a)

Cambon, C., Godeferd, F.S., Nicolleau, F.C.G.A., Vassilicos, J.C.: Turbulent diffusion in rapidly rotating flows with and without stable stratification. J. Fluid Mech. **499**, 231–255 (2004b)
Carnevale, G.F., Frederiksen, J.S.: A statistical dynamical theory of strongly nonlinear internal gravity waves. Geophys. Astrophys. Fluid Dyn. **20**(8), 131–164 (1983)
Chaouat, B., Schiestel, R.: A new partially integrated transport model for subgrid-scale stresses and dissipation rate for turbulent developing flows. Phys. Fluids **17**(6), 065106 (2005)
Chaouat, B., Schiestel, R.: From single-scale turbulence models to multiple-scale and sbgrid-scale models by Fourier transform. Theor. Comput. Fluid Dyn. **21**(3), 201–229 (2007)
Clark, T.T., Zemach, C.: A spectral model applied to homogeneous turbulence. Phys. Fluids **7**(7), 1674–1694 (1995)
Courseau, P.A., Loiseau, M.: Contribution à l'analyse de la turbulence homogène anisotrope. Journal de Mécanique **17**(2), 245–297 (1978)
Craik, A.D.D., Criminale, W.O.: Evolution of wavelike disturbances in shear flows: a class of exact solutions of Navier–Stokes equations. Proc. R. Soc. Lond. Ser. A **406**, 13–26 (1986)
Crow, S.C.: Viscoelastic properties of the fine-grained incompressible turbulence. J. Fluid Mech. **33**, 1–20 (1968)
Davidovits, S., Fisch, N.J.: Sudden viscous dissipation of compressing turbulence. Phys. Rev. Lett. **16**(10), 105004 (2016)
Fauchet, G.: Modélisation en deux points de la turbulence isotrope compressible et validation à l'aide de simulations numériques. Thèse de Doctorat, Ecole Centrale de Lyon (in french) (1998)
Frisch, U., She, Z.S., Sulem, P.L.: Large-scale flow driven by the anisotropic kinetic alpha effect. Physica D **28**, 382–392 (1987)
Galmiche, M.: Thèse de Doctorat. Université de Toulouse, France (1999)
Galtier. S.: A weak inertial wave turbulence theory. Phys. Rev. E**68**, O15301-1-4 (2003)
Galtier, S., Nazarenko, S., Newell, A,C., Pouquet, A.: A weak turbulence theory for incompressible MHD. J. Plasma Phys. **63**, 447–488 (2001)
Godeferd, F.S., Cambon, C.: Detailed investigation of energy transfers in homogeneous stratified turbulence. Phys. Fluids **6**, 284–2100 (1994)
Godeferd, F.S., Staquet, C.: Statistical modelling and direct numerical simulations of decaying stably stratified turbulence. Part 2. Large-scale and small-scale anisotropy. J. Fluid Mech. **486**, 115–159 (2003)
Godeferd, F.S., Cambon, C., Leblanc, S.: Zonal approach to centrifugal, elliptic and hyperbolic instabilities in Stuart vortices with external rotation. J. Fluid Mech. **449**, 1–37 (2001)
Godeferd, F.S., Cambon, C., Scott, J.F.: Report on the workshop: two-point closures and their applications. J. Fluid Mech. **346**, 393–407 (2001)
Goldstein, M.E.: Unsteady vortical and entropic distortions of potential flows round arbitrary obstacles. J. Fluid Mech. **89**, 431 (1978)
Guimbard, D., Leblanc, S.: Local stability of the Abrashkin–Yakubovich family of vortices. J. Fluid Mech. **567**, 91–110 (2006)
Herring, J.R.: Approach of axisymmetric turbulence to isotropy. Phys. Fluids **17**, 859–872 (1974)
Ishihara, T., Kaneda, Y.: Energy spectrum in the enstrophy transfer range of two-dimensional forced turbulence. Phys. Fluids **13**(2), 544–547 (2001)
Ishihara, T., Yoshida, K., Kaneda, Y.: Anisotropic velocity correlation spectrum at small scale in a homogeneous turbulent shear flow. Phys. Rev. Lett. **88**(15), 154501 (2002)
Kaneda, Y.: Lagrangian renormalized approximation of turbulence. Fluid Dyn. Res. **39**, 526–551 (2007)
Kaneda, Y., Holloway, G.: Frequency shifts of Rossby waves in geostrophic turbulence. J. Phys. Soc. Jpn. **63**, 2974 (1994)
Kaneda, Y., Ishida, T.: Suppression of vertical diffusion in strongly stratified turbulence. J. Fluid Mech. **402**, 311–327 (2000)
Kraichnan, R.H.: Statistical mechanics of an adiabatically compressible fluid. J. Acoust. Soc. Am. **27**, 527–530 (1955)

Kraichnan, R.H.: The structure of isotropic turbulence at very high Reynolds number. J. Fluid Mech. **5**, 497–543 (1958)
Kraichnan, R.H.: Direct-interaction approximation for shear and thermally driven turbulence. Phys. Fluids **7**, 1048–1062 (1964)
Leith, C.E.: Atmospheric predictability and two-dimensional turbulence. J. Atmos. Sci. **28**, 145–161 (1971)
Leslie, D.C.: Developments in the Theory of Turbulence. Clarendon Press, Oxford (1973)
Lifschitz, A., Hameiri, E.: Local stability conditions in fluid dynamics. Phys. Fluids A **3**, 2644–2641 (1991)
Mc Comb, W.D.: A local energy transfer theory of isotropic turbulence. Phys. Fluid A **7**(5), 632 (1974)
Moffatt, H.K.: Interaction of turbulence with strong wind shear. In: Yaglom, A.M., Tatarski, V.I. (eds.) Colloquium on Atmospheric Turbulence and Radio Wave Propagation, pp. 139–156. Nauka, Moscow (1967)
Mons, V., Cambon, C., Sagaut, P.: A spectral model for homogeneous shear-driven anisotropic turbulence in terms of spherically averaged descriptors. J. Fluid Mech. **788**, 147–182 (2016)
Nazarenko, S.: Wave Turbulence. Springer, Berlin (2011)
Nazarenko, S., Kevlahan, N.N., Dubrulle, B.: A WKB theory for rapid distortion of inhomogeneous turbulence. J. Fluid Mech. **390**, 325–348 (1999)
Newell, A.C., Rumpf, B.: Wave turbulence. Annu. Rev. Fluid Mech. **43**, 59 (2011)
Orszag, S.A.: Analytical theories of turbulence. J. Fluid Mech. **41**, 363–386 (1970)
Sagaut, P.: Large-Eddy Simulation for Incompressible Flows, 3rd edn. Springer, Berlin (2005)
Sagaut, P., Deck, S., Terracol, M.: Multiscale and Multiresolution Approaches in Turbulence. Imperial College Press (2006)
Sanderson, R.C., Hill, J.C., Herring, J.R.: Transient behavior of a stably stratified homogeneous turbulent flow. In: Comte-Bellot, G., Mathieu, J. (eds.) Advances in Turbulence, pp. 184–190. Springer, Berlin (1986)
Touil, H., Bertoglio, J.P., Parpais, S.: A spectral closure applied to inhomogeneous turbulence. In: Dopazo, C. (ed.) Advances in Turbulence VIII, p. 689. CIMNE, Spain (2000)
Townsend, A.A.: The Structure of Turbulent Shear Flow. Cambridge University Press, Cambridge (1956,1976)
Turner, L.: Macroscopic structures of inhomogeneous, Navier–Stokes, turbulence. Phys. Fluids **11**, 2367–2380 (1999)
Viciconte, G., Gréa, B.-J., Godeferd, F.S.: A spectral model for sudden dissipation effect in turbulent plasma under compression. Proc. 23ème Congrès Français de Mécanique, Lille, France (2017)
Waleffe, F.: Inertial transfers in the helical decomposition. Phys. Fluids A **5**, 677–685 (1993)
Yoshida, K., Ishihara, T., Kaneda, Y.: Anisotropic spectrum of homogeneous turbulent shear flow in Lagrangian renormalized approximation. Phys. Fluids **15**(8), 2385–2397 (2003)
Zakharov, V.E., L'vov, V.S., Falkowich, G.: Kolmogorov Spectra of Turbulence. 1. Wave Turbulence. Springer Series in Nonlinear Dynamics. Springer, Berlin (1992)

Chapter 18
Conclusions and Perspectives

Description and knowledge of turbulent flows is advancing well, particularly with the increasing development of numerical ressources (Moore's law) and detailed measurements using more and more PIV, SPIV and PTV. Well documented databases are created, which can support techniques of data-compression using a dramatically reduced number of modes (POD, wavelet coefficients, master-modes, ...).

Behind this attractive show-window, however, the advance of our conceptual understanding of turbulent flows is much less satisfactorily. Advances in numerics, experiments, data-compression schemes, are firstly beneficial to applied studies, for instance those using smart combination of techniques (often referred to as *multiphysics*, with hybrid RANS-LES methods, and many others). Turbulent flows are well reproduced in the vicinity of a well documented *design-point*, but this modeling is questioned far from it ("far" in the parameter's space, or simply in elapsed time for unsteady processes). Efficiency of data-compression schemes, for instance, is ellusive since a low-dimension set of modes, identified and validated near the "design-point", can lose its relevance far from it.

We hope that this book will contribute to a honest and up-to-date survey of turbulence theory, with the special purpose of reconciling different angles of attack. In this sense, the atomization of the community into competing, and/or too (deliberately) self-isolating, chapels, is perhaps one of the main impediment for advancing theory. Difference of parlances or jargons is a related aspect, despite the universality of the mathematical formalism.

18.1 Homogenization of Turbulence. Local or Global Homogeneity? Physical Space or Fourier Space?

One may go back to the theory of homogeneous turbulence (or 'homogenization of turbulence') by George Batchelor (1920–2000), following a very interesting essay by Moffatt (2002). It is usefully recalled that Batchelor was aware from the very

P. Sagaut and C. Cambon, *Homogeneous Turbulence Dynamics*,
https://doi.org/10.1007/978-3-319-73162-9_18

begining of the importance of the Kolmogorov's approach, including the celebrated 4/5-law. He published a deep analysis of the theory as early as 1946 and 1947, having read the four-page seminal article in *Doklady* (Proceedings of USSR Academy of Sciences). It is therefore irrelevant to oppose a Batchelor's approach to turbulence to a Kolmogorov's one. One may evoke the meeting held in Marseille (1961), which is often mentioned as the 'Solvay meeting' of turbulence, quoted as a 'watershed for turbulence' by K. Moffat: *"Kolmogorov was there, together with Obukhov, Yaglom, and Millionshchikov; von Karman and G.I. Taylor were both there — the great father figures of prewar research in turbulence — and the place was humming with all the current stars of the subject — Stan Corrsin, John Lumley, Phillip Saffman, Les Kovasznay, Bob Kraichnan, Ian Proudman, and George Batchelor himself, among many others."* Finally, it is recalled how Kolmogorov himself questioned the validity of his K41 theory, opening the Pandora box with scale-dependent, intermittent distribution of $\varepsilon(r)$. This resulted in both a large interest for internal intermittency, and a frustration that afflicted Batchelor and many others from 1960 onward. After the publication of our first edition, a new meeting took place in Marseille, in 2011, as a follow-up of the one in 1961, and the introductory talk on homogeneous turbulence by Moffatt (2012) again presents a special interest.

We think that very important progresses in the theory were made following Kraichnan's approach, even before the early sixties, not to mention linear theory such as RDT, and that it is a pity to underestimate related studies, as it is often done in the "intermittency and scaling" community, especially after the publication of Frisch's book. In addition, development of practical models, mainly based on single-point closures, in RANS and (more recently) in LES, was very useful for turbulence in engineering and environment, with almost no impact of new developments of theory of internal intermittency, but often strong connection with spectral approach. Unjustified?[1] reluctancy to look at a formalism in Fourier space, and strong (justified) interest for a statistical approach in terms of velocity (or vorticity, pressure, etc.) *increments* can explain partly such an underestimation.

As a first example, it can be shown (e.g. Chap. 4) that the Kolmogorov law $\langle \delta u_{\parallel}^3 \rangle(r)/r = -(4/5)\varepsilon$ is as 'exact' as its counterpart in Fourier space $\int_k^\infty T(k)dk = \varepsilon$ is. In the same way, more general (not only valid at very high Reynolds number) laws were given by von Karman and Howarth in 1938 in physical space, and in Fourier space by Lin and von Karman in 1949.

The concept of local homogeneity raises very important questions. On the one hand, use of increments (e.g. velocity increments) for defining two-point statistics allows for a better approach to local homogeneity, eventhough "local homogeneity" is almost an oxymoron, since homogeneity means translational invariance. In addition, structure functions of order 2 and 3 can be obtained from measurements more

[1] Even the more that studies about scaling and intermittency are often supported by conventional pseudo-spectral DNS!

easily than second-order spectra and transfer spectra,[2] and spectral approach has less interest for higher order statistical moments (higher than 4). From this viewpoint, local homogeneity (and very often isotropy) is assumed at relatively small scales in exploiting physical and numerical experiments in rather complex flows; the assessment that "the flow is considered as homogeneous and isotropic in the center of a von Karman flow, in the centerline of the plane channel, near the centerline of a jet, ... etc" ... can be found in many recent papers ... whereas the same assessment would have been considered as ridiculous twenty to thirty years ago. This viewpoint, getting rid of inhomogeneous-anisotropic large scales in rather complex flows, and focusing on small scales, considered as homogeneous-isotropic-intermittent, is not wrong, partly thanks to the use of incremental statistics. This is questionable, however, from a dynamical viewpoint: Apparent local isotropy can result from quasi-balanced inhomogeneous flux terms which are present in the transport equations. More generally, we have shown from a dynamical approach that the universality of small scales, independently of the way of injecting energy at large scale, is really questioned in many cases, even at very high Reynolds number. Despite of significant advantages, the conventional viewpoint has some negative results:

- Not to encourage the building of smart experimental facilities, in which homogeneity can be really assumed in a very large spatial domain, following the ones presented in Chaps. 7– 11.
- To consider as marginally relevant the theoretical approach to flows, such as those studied in Chaps. 7, 10–12, which can be really considered as homogeneous, but strongly anisotropic, at almost any scale.

In this context, the recent analysis of the vicinity of the stagnation point in a von Kármán flow, from the viewpoint of HAT, deserves attention (see Sect. 8.8.1) and allows us to moderate the abovementioned too pessimistic considerations.

Other arguments, which illustrate the interest of considering Fourier space (modal decomposition related to the Helmholtz decomposition, treatment once for all of pressure fluctuations, giving the minimal number of dynamical modes) are presented in Chaps. 1 and 2. Regarding the description of energy cascades, it is important to stress that triadic spectral description, not even mentioning "closure", carries on much more information than third-order structure functions do. It accounts for triple correlations at three-points, and not only at two point, and allows to identify exact operators which underly detailed conservation laws, such as Eqs. (4.299) and (4.301) for detailed conservation of both energy and helicity, Eqs. (4.401)–(4.403) for detailed conservation of energy and enstrophy, Eqs. (10.18)–(10.20) for detailed conservation of toroidal energy and vertical enstrophy, and Eqs. (11.13)–(11.15) for detailed conservation of QG energy and potential vorticity. Another point which deserves to be emphasized is the power of Waleffe's instability hypothesis which, starting from the exact detailed conservation laws and the stability analysis of a low-

[2]Some measurements, however, give direct access to spectral information, and even to anisotropic one, such as scattering of ultrasound waves (C. Baudet, S. Fauve) or light (D. Grésillon) ....

dimensional system, leads to *accurate predictions* dealing with triadic tranfers and induced cascades, even in nonhomogeneous cases.

In addition, one can expect a convergence between some studies of cyclic regeneration processes discussed at the end of Chap. 9 and the analysis, performed by the astrophysical community, of transient growth and bypass transition (see the end of Chap. 11).

18.2 Linear Theory, 'Homogeneous' RDT, WKB Variants, and LIA

It is usually said that the 'problem(s) of turbulence' come(s) from the nonlinearity of basic Navier–Stokes-type equations. This is only partially true, since 'burgulence' (i.e. pseudo-turbulent behavior exhibited by the solution of the Burgers equations), not to mention its 3D generalization to the cosmological gas, is essentially solved and understood. The quadratic advection term is probably always involved in the problem, but the projection onto a solenoidal subspace, in connection with the pressure term, is another important ingredient, at least in the nearly incompressible flow case. As a slightly different illustration (from basic dynamical equations, again), the advection term is completely removed in a pure Lagrangian alternative to Navier–Stokes equations, but nonlinear complicated operators rear their ugly head through pressure and diffusive terms.

As another trivial remark, the validity of a linear approach depends on the definition of the base state about which one performs the linearization.

Linear theories addressed here retain at least a part from exact dynamical equations, and include a straightforward treatment of the pressure term, together with the Helmholtz decomposition for purely incompressible and weakly compressible fluctuatings flows.

Homogeneous RDT offers interesting possibilities to reconcile stability analysis and statistical approach, when it is consistent with exponential instability (hyperbolical instability in Chap. 8, barotropic instability for rotating shear, its baroclinic extension, and elliptical flow instability in Chap. 11). Related destabilizing effects are mimicked by much simpler single-point RSM models, such as for the shear flow rotating around the spanwise direction, but only RDT or more sophisticated linear stability analyses really explain why, in connection with dominant pressure-released modes. In other cases, when the destabilizing effect comes from a narrow band of angular modes in wave-space, with the 'rapid' fluctuating pressure allowing a resonant amplification to periodic 'production', the 'rapid' response of any RSM is poor (e.g. elliptical flow instability and periodic compression with swirl).

Even when RDT gives very few results about the evolution of statistics, it could suggest a good choice of eigenmodes for improving fully nonlinear theories, as illustrated in Chaps. 7–11. Identification of a deterministic Green's function, possibly expressed in terms of a minimal number of solenoidal modes, from the basic linearized

equation which governs the fluctuating field, is shown to be the best way for using linear theory: it is possible to predict the impact of the linear operator on any statistical moment, showing for instance a poor relevance of RDT dealing with single-time second-order moments, in contrast with interesting information given for two-time second-order statistics and third-order statistics (see Chaps. 7, 10–12).

WKB variants allows us to relax the assumption of homogeneity in the linear theory, or suggest at least a nice illustration of what could be "local homogeneity" from a dynamical viewpoint. In contrast with homogeneous RDT, it is possible to identify localized unstable zones in a base flow, which is smooth but more realistic than the admissible mean flows of homogeneous RDT, and to quantify their contribution: example of competing centrifugal, elliptical and hyperbolical instabilities is given in Chap. 11 for simple non-parallel flows with adjacent eddies.

It is important to point out some limitations. A generic instability as the Kelvin–Helmholtz one cannot be afforded, even if homogeneity is relaxed. Despite a very promising extension of RDT to stratified flows with shearing effects, and possible prediction of baroclinic mechanisms, and to compressible shear (Chap. 14), this drawback cannot be ignored. For compressible shear flows, a possible depletion of nonlinearity (with respect to the incompressible case) can explain an unexpected relevance of linear theory, at least in the homogeneous case.

Among the canonical flow cases addressed in this book, only the case of the incompressible shear flow is a bit disappointing restricting the approach to RDT: the important mechanism of redistribution of energy between RST components by nonlinear pressure terms, which is of course discarded, can be mimicked by very simple single-point closures.

WKB RDT can be applied to compressible flows, but its implicit ingredient of short-wave disturbance yields discarding the acoustic mode. Some extensions can be found in replacing the base-flow trajectories by the acoustic rays, as it is touched upon in Chap. 17. On the other hand, LIA has much in common with a purely homogeneous linear theory. Because there is no lenghtscale given by the base flow, there is no restriction of wavenumber range for the disturbance flows. One can say that the typical lengthscale of the mean flow is infinite in homogeneous RDT (or equivalently for the extensional base flow in stability analysis), whereas it is zero (the shock-wave thickness) in LIA. As in RDT, a transfer matrix can link upstream and downstream modal amplitudes of the disturbance field, but an entropic disturbance mode can be accounted for. Some wavelike response of the shock-wave and its linkage to the full linear transfer matrix for the disturbance field is another useful feature, with no equivalent in RDT. A very striking result of LIA, beyond statistical results, is the possibility to advect a temperature spot across the shock-wave and to give rise to a pair of co-rotating vortices. In addition to a mathematical transfer term from upstream entropy mode to downstream vortical mode via the baroclinic torque, a nice formation of structure is found!

18.3 Multi-point Closures for Weak and Strong Turbulence

An assessment of multi-point closures can be proposed. It was written in our former edition that their use for "production-dominated" flow was probably a too complicated task, given the "return of investment" that one can expect. This too pessimistic assessment is now questioned by some "success stories": On the one hand, the simplified spectral model in terms of spherically averaged descriptors (Mons et al. 2016) used in Chaps. 8 and 9 is now satisfactorily working with little computational cost. On the other hand, the case of Unstably Stratified Turbulence, in Sect. 10.7.7 illustrates how a rather costly anisotropic EDQNM model can be quantitatively compared with very high resolution DNS, and then used for investigation at much higher Reynolds numbers.

Application to flows "without production", which only consist of non-propagating neutral modes and wave-modes in the linear eigenmode decomposition, remains promising.

The latter case includes incompressible HIT as the simplest, the whole velocity field being a trivial neutral mode in the linear inviscid limit.

In the particular case of turbulence subjected to pure rotation, the complex structural anisotropy is created by the nonlinear cascade, with the angular dependence of energy in wave-space reflecting the loss of dimensionality. Such a behavior occurs in other flow configurations in which the presence of dispersive waves is more important than the classic 'production' mechanisms. Even without additional mean strain (such as the elliptical flow instable case), pure rotation induces complex "rapid" and "slow" effects, for which even the basic principles of single-point closures are questionable. Single-point closures look particularly poor since there is no production by the Coriolis force, whereas the dynamics is dominated by waves whose anisotropic dispersivity is induced by fluctuating pressure.

This suggests discriminating "turbulence dominated by production effects" from "turbulence dominated by wavy effects". In short, single-point closures are well adapted to simple turbulent flow patterns of the first class in rather complex geometry, whereas multi-point closures are more convenient for complex turbulent flows in simplified geometry, as illustrated by the second class.

18.3.1 The Wave Turbulence Limit

Mathematical developments in the area of wave-turbulence theory (WT), have recently renewed interest in flows that consist of superimposed dispersive waves, in which nonlinear interactions drive the long time behaviour. Individual modes are of the kind

$$u_i'(\boldsymbol{x}, t) = a_i(t) \exp[\imath (\boldsymbol{k} \cdot \boldsymbol{x} - \sigma_k t)] \tag{18.1}$$

with a known analytical dispersion law for $\sigma_k = \sigma(\boldsymbol{k})$. Similar averaged nonlinear amplitude equations can be found using either WT or Multi-Point Closures (MPC), the advantages and drawbacks of which are briefly discussed below.

In the case of wave turbulence, statistical homogeneity and quasi-normal assumption have equivalent counterparts, obtained by assuming a priori Gaussian random phases for the wave fields. In addition, *isotropic* dispersion laws such as $\sigma_k = |\boldsymbol{k}|^\alpha$ in Eq. (18.1) are almost exclusively treated in WT for deriving Kolmogorov spectra, with the key hypothesis of constant and isotropic energy fluxes across different scales associated with a wavenumber $|\boldsymbol{k}|$. By contrast, in geophysical flows, dispersion laws are anisotropic, with for instance $\sigma = \beta k_x/k^2$ in the case of Rossby waves, $\sigma = \pm 2\Omega k_\parallel/k$ for inertial waves and $\sigma = \pm N k_\perp/k$ for gravity waves (k_x, $k_\parallel$ and $k_\perp$ are the components of the associated wavevector respectively in the zonal direction, and the directions parallel or perpendicular to the rotation/gravity vectors). In the latter two 3D cases, this anisotropy is reflected by the strange conical — "St Andrew cross" — shape of iso-phase surfaces in typical experiments with a localized point forcing (see views of this type in Fig. 7.11) and by angular-dependent energy drains when looking at nonlinear interactions, as illustrated in Chaps. 7, 10 and 11.

At least if Eulerian correlations are considered, The MPC and WT theories share in general an important background. Kinetic equations for mean spectral energy densities of waves are found in WT, similar to homogeneous MPC. Their slow evolution is governed by similar energy transfer terms, which are cubic in terms of wave amplitudes (triads). There is also a possibility that these transfers involve fourth-order interactions (quartets) in WT when triple resonances are forbidden by the dispersion laws (e.g. rotating stably stratified turbulence with f/N close to 1 in Chap. 11) and/or by geometric constraints (e.g. shallow waters). Resonant quartets seem to be particularly relevant when resonances are seen in a Lagrangian description. They are naturally called into play when the nonlinearity is cubic and not quadratic, as, for instance, for quantum turbulence governed by Gross-Pitaievskii equation. When triple resonances are allowed, for instance in cases of rotating turbulence, stably stratified turbulence and MHD turbulence, Wave Turbulence (WT) kinetic equations have exactly the same structure as their counterpart in elaborate Multi-Point Closures (MPC). Hence, WT and MPC have a common limit at very small interaction parameter (e.g. Rossby number, Froude number, magnetic interaction number in MHD). Of course, interactions between neutral modes, if they are present, and wave modes, cannot be investigated by the pure theory of wave turbulence.

18.3.2 Coexistence of Weak and Strong Turbulence, with Interactions

When eigenmodes consist of both non-propagating, neutral, and wavy modes, one can expect very complex cascade processes. Wave turbulence, dominated by resonant triads, is the only modality in the absence of the non-propagating mode. Accordingly,

inertial wave turbulence in 3D rotating turbulence is really relevant if the Rossby number is sufficiently small[3] When strong nonlinearity mediated by interactions which only involve the non-propagating mode, and weak nonlinearity involving at least a wave mode are face to face, the former can be considered as dominant. Both toroidal cascade and Quasi-Geostrophic cascade are therefore of interest in stratified and rotating turbulence. Note that the emergence of toroidal (idem QG) cascade is found in neglecting wavy modes in triadic interactions; this does not mean that waves have no effect; in contrast, this is because gravity waves (idem inertia-gravity) waves severely damp nonlinear contributions other than the pure toroidal (idem QG) ones by angle-dependent phase-mixing that toroidal (idem QG) cascade emerges. For weakly compressible flows addressed in Chap. 9, the solenoidal turbulence is already well known, so that a pseudo-acoustical cascade appears as a relevant theme.

Magnetohydrodynamics in Chap. 12 offers a new domain of application for MPC far beyond previous "isotropized" EDQNM models. The Lorentz force can be linearized around a dominant mean magnetic field, and yields linear Alfvén waves, that affect weak turbulence as well. On the other hand, the Lorentz force is intrinsically nonlinear (quadratic), in contrast with Coriolis force or buoyancy force in the purely hydrodynamic case, so that cubic interactions, that affect the second-order ones for energetics and anisotropy, are mediated by both conventional spectral transfers and contributions from the Lorentz force. It is premature to propose a fully anisotropic MPC, as anisotropic EDQNM — except in the very particular case of quasi-static MHD — but all technical building blocks are given for this purpose. Especially, combined helical-Elsaesser modes are the best solenoidal modes for constructing advanced MPC, and coupled Lin equations can be derived in terms of the set of spectra and co-spectra in Eq. 12.24.

18.3.3 Revisiting Basic Assumptions in Multi-point Closures

Derivation of statistical equations of MPC is often a very formal skill, so that these theories can be considered as opaque and complicated. Let us mention (Moffatt 2002) again: *"and the new approaches, particularly Kraichnan's* (1958) *DIA, were of such mathematical complexity that it was really difficult to retain that essential link between mathematical description and physical understanding, which is so essential for real progress"*. In the same vein, A. Craya, in early sixties, evoked about DIA the Mona Lisa's (La Joconde) smile, having his strange beauty but some ambiguity. As a very interesting survey, Y. Kaneda proposed not less than 7 different ways to derive DIA equations. The essential ingredient is a formal development around a Gaussian field, but the effective second-order spectral tensor and response tensor are only eventually defined by the final set of coupled equations which govern them,

[3]The 2D manifold appears as the limit of the wavy inertial mode at vanishing dispersion frequency, it is therefore a low dimension slow mode, but not at all a 3D non-propagating mode, filling all the space, as the toroidal mode is in stably-stratified turbulence.

so that they cannot be specified a priori, and they can significantly differ from their zeroth order counterpart. Derivation of EDQNM is less subtle, but the conventional presentation is often too close to a cooking recipe, with heuristic procedures (Eddy Damping - ED, Markovianization - M) called into play in order to correct an initially too crude Quasi-Normal (QN) model. To derive EDQNM from DIA, using a specified form for the response tensor, and a so-called fluctuation-dissipation theorem to translate two-time correlations into single-time ones, may give information about ED and Markovianization; but this is really a too complicated and indirect way. Comparing EDQNM to WT theory, especially using the profound analysis of zero cumulant assumption by Benney and Newell (1969) quoted in Chap. 7, is really enlighting. It is firstly possible to understand why QN closure can be an *intrinsic (exact?) closure* in WT, getting rid of ED because the damping by phase-mixing of dispersive waves is a very efficient and physical process, whereas Markovianization is enslaved to the natural separation into rapid phases terms and slowly evolving amplitudes of waves. It is perhaps necessary to think in a more physical way to the use of cumulants, and to a more convincing link between the fourth-order cumulants and the third-order ones, yielding the basic concept of ED for strong turbulence. Nth-order Cumulants at N points represent the difference between statistical moments of order N and their factorized expression in terms of products of moments of smaller order. In this sense, a convergence to zero is ensured, which is not valid for the moments themselve, as soon as the points in the configuration space are sufficiently separated. Instead of speaking of a quasi-Gaussian distribution, which is often questioned in turbulent flow, one may address a pdf at four points, which reduces to almost a product of pdf's for sufficient separation lengths. The QN assumption, or more generally the EDQN one, could be more physically funded by an argument of maximum factorization of four-point pdf's, or maximum decorrelation between the different points, which is less constraining and does not use the word "Gaussian". Of course, this is a very preliminar proposal: we have in mind a four-point distribution without specifying more the configuration space (physical, Fourier, other ?). As a simple illustration, factorization would be achieved for any tetrad including at least a long leg: very large tetrads with more than one long leg, flat tetrads with only one long leg.

18.4 Structure Formation, Structuring Effects and Individual Coherent Structures

The two-point anisotropic description is more powerful, even if homogeneity is assumed, than is generally recognized. In rotating and stratified turbulence the anisotropic spectral description, with angular dependence of spectra and co-spectra in Fourier space, allows for quantification of columnar or pancake structuring in physical space. Among various indicators of the thickness and width of pancakes, which can be readily derived from anisotropic spectra, integral length scales $L_{ij}^{(n)}$ related to different components and orientations are the most useful. As another illustration

(see Fig. 9.5), the streak-like tendency in shear flows can be easily found by calculating with RDT both the $L_{11}^{(1)}$ component, which gives the streamwise length of the streaks, and $L_{11}^{(3)}$, which gives the spanwise separation length of the streaks (as usual, 1 and 3 refer to streamwise and spanwise coordinates, respectively). In pure homogeneous RDT at constant shear rate, both length scales can be calculated analytically and their ratio (elongation parameter) is found to increase as $(St)^2$, $S = \partial U_1/\partial x_2$ being the shear rate. Of course, more realistic quantitative aspects of the true streaky structures found in the near-wall region, are not captured, as discussed in Chap. 9.

It is often said that phase information is lost in homogeneous turbulence, but this is only true for single-time second-order statistics, and even does not exclude dynamical phase mixing, as illustrated by damped oscillations towards equipartition (equipartition in terms of poloidal and toroidal energy components for rapid rotation, with nontrivial transient evolution from initial unbalance if initial data are anisotropic, equipartition in term of poloidal and potential energy components for strong stratification, and similar evolution from initial unbalance). More informative and surprising phase mixing is found for two-time second-order statistics, even in the pure linear régime: this illustrates that dispersive waves can drive the Lagrangian diffusion (passive tracers, single-particle displacement), a role which is often attributed to purely spatial structures, such as coherent vortices, in the turbulence community. Finally, nonlinear formation of structures in rotating and stratified flows, which is emphasized in this book, means formation of vortex structures, — waves *are structures too* but are spatio-temporal (delocalized in space) coherent events —. In fact, a subtle interplay of linear and nonlinear effects is called into play.

As a final remark, statistical indicators in homogeneous anisotropic turbulence can quantify some average characteristics of structures (e.g. aspect ratios of cigar-shaped and pancake-shaped structures, vorticity skewness for quantifying asymmetry in terms of cyclonic and anticyclonic vorticity for cigar-shaped structures), whereas information on their dynamics can be given by statistical equations. In addition, some individual coherent structures, localized in space (and in time?), if not really obtained in statistical model equations, are found in snapshopts from DNS, as realizations of homogeneous turbulence.

18.5 Anisotropy Including Dimensionality, a Main Theme

This is emphasized throughout this book, except in Chaps. 4, 5, 6 and 13. It appears as a multifold and rich property of turbulent flows, even those without production, and affects both the multiscale energy distribution and the cascade process, possibly until smallest scales. Our viewpoint contrasts with what is currently admitted in the turbulence community. In the engineering community, the anisotropy is considered as only characterized by the deviatoric part of the Reynolds stress tensor (b_{ij} is "THE" anisotropy tensor), despite the more general investigation introduced by Reynolds and Kassinos in their structure-based modelling approach. In the physicist community,

inhomogeneity-anisotropy is considered only for largest scales, generally out of investigation, whereas scales which merit attention are seen as homogeneous-isotropic-intermittent. If attention is paid to anisotropy, with studies using the SO(3) symmetry group, this concern only the small anisotropy identified by a very small number of angular harmonics.

Finally, this book includes the material to revisit a general theory of axisymmetric turbulence. Axial symmetry with and without mirror symmetry is the simplest symmetry for an exhaustive statistical and dynamical approach to strong anisotropy, in both spectral and physical space, using all the theoretical tools used herein, including the most sophisticated ones. Application to MHD flows with external strong magnetic field could be the next step. This step can be useful for a collaboration between specialists of turbulence in fluid and specialists of turbulence in plasmas. The existence of the ITER world-wide project critically needs such a collaboration. Problems of turbulence, such as the "anomalous" heat and mass (for ions) transfer in the radial direction, is expected to be a severe problem in the future huge Tokamak. Geodynamo and astrophysical turbulence are other instances.

18.6 Deriving Practical Models

Finally, one may anticipate some criticisms against this book: Too many equations, too little practical results! A striking feature of several homogeneous flows discussed in this book is that they escape turbulence models used in engineering applications. The test is fair, since we have considered the best adapted mathematical formalism to deal with the subtleties of the problem, from $\mathcal{K}-\varepsilon$ models to anisotropic MPC, with a lot of intermediate links...

The way to derive more practical applications, from useful simple scaling laws to once-for-all calculation of parameters (eddy diffusivity, anisotropic ratios, etc.), must be discussed.

The terms appearing in the rate equations for Reynolds stress models in homogeneous turbulence can be exactly expressed as integrals over Fourier space of spectral contributions derived from the second order spectral tensor $\hat{R}_{ij}$, which is the Fourier transform of double correlations at two points, and from the third-order 'transfer' spectral tensor T_{ij}. All one-point quantities in the equation that governs $\overline{u_i' u_j'}$ can be expressed as integrals over wavenumber space, as for Eq. (2.83). The equation for the dissipation rate $\varepsilon = \nu\overline{\omega_i \omega_i}$ (in quasi-homogeneous and quasi-incompressible turbulence), can be derived from the exact equation that governs the fluctuating vorticity field ω_i. It should be borne in mind that the practical procedure for deriving the ε-equation hardly uses the latter exact equation and consists of basing the equation for $\dot{\epsilon}/\epsilon$ on the equation for $\dot{\mathcal{K}}/\mathcal{K}$ with adjustable constants.

About single-point closures, one may recall that the knowledge of the mean (Reynolds averaged) flow together with the Reynolds stress tensor at every point

(with a possible limited time-dependence[4]) would have been the Holy Grail in turbulence modelling twenty or thirty years ago. More information can be required now. In this sense the criticism against single-point closure techniques deals less and less with their incorrect closure assumptions, and more and more with the unsufficient information carried out by them. More information about low-probability events, dramatic unsteadiness, coherent structures, for predicting hazards, is needed in engineering and in environmental flows. Two-point two-time statistics can be useful for predicting dispersion processes and radiated noise (e.g. applying acoustic analogies to quasi-incompressible vortical flows). Looking at passive and reactive scalar fields, information on pdf is needed too.

As a last point, we hope to render more conversant the domain of engineering closures and the main domain of this book. A recent article, or essay, by Spalart (2015) on "philosophies and fallacies in turbulence modeling" addresses more the engineering domain with single-point closures, but it suggests a similar assessment for multi-scale approches, using RDT and MPC as well. RDT for calibrating constants in RSM models is now past history, since its advancing application moves to geophysics and astrophysics, with new challenges (transient growth, bypass transition, regeneration cycles). Investigation of non-local dynamics for improving RSM by Mishra and Girimaji (2017) is given here as a single recent example of incorporating RDT concepts. In addition, the whole study about unstably stratified turbulence (around Sect. 10.7.7) illustrates a more and more integrated area of research from $k - \varepsilon$ to elaborate spectral closures, with full support of very high resolution DNS. An advanced "system approach to turbulence" is in progress, that incorporates all interactions between the mean flow and the fluctuating one, with a scale-by-scale nonlinear model for fluctuating/fluctuating interactions.

References

Kraichnan, R.H.: The structure of isotropic turbulence at very high Reynolds number. J. Fluid Mech. **5**(4), 497–543 (1958)

Mishra, A.A., Girimaji, S.S.: Towards approximating non-local dynamics in single-point pressure strain correlation closures. J. Fluid Mech. **811**, 168–188 (2017)

Moffat, H.K.: G.K. Batchelor and the homogenization of turbulence. Annu. Rev. Fluid Mech. **34**, 19–35 (2002)

Moffatt, H.K.: Homogeneous turbulence: an introductory review. J. Turbul. **13**(39), 1–11 (2012)

Mons, V., Cambon, C., Sagaut, P.: A spectral model for homogeneous shear-driven anisotropic turbulence in terms of spherically averaged descriptors. J. Fluid Mech. **788**, 147–182 (2016)

Spalart, P.R.: Philosophies and fallacies in turbulence modelling. Prog. Aerosp. Sci. **71**, 1–13 (2015)

[4]Let us recall that there is no conceptual obstacle against unsteady RANS, and that seminal studies about 1975 dealt with time-development of Reynolds stresses in homogeneous turbulence subject to given mean flow.

Index

P. Sagaut and C. Cambon, *Homogeneous Turbulence Dynamics*,
https://doi.org/10.1007/978-3-319-73162-9